

Graeme Hanson
Lawrence Berliner
Editors

BIOLOGICAL MAGNETIC RESONANCE 28

High Resolution EPR

Applications to Metalloenzymes
and Metals in Medicine

 Springer

Biological Magnetic Resonance

Volume 28

For further volumes:

<http://www.springer.com/series/5693>

A Continuation Order Plan is available for this series. A continuation order will bring delivery of each new volume immediately upon publication. Volumes are billed only upon actual shipment. For further information please contact the publisher.

Graeme Hanson · Lawrence Berliner
Editors

High Resolution EPR

Applications to Metalloenzymes and Metals
in Medicine

Volume 28

 Springer

Editors

Graeme Hanson
University of Queensland
Center for Magnetic Resonance
Brisbane QLD 4072
Australia
graeme.hanson@cmr.uq.edu.au

Lawrence Berliner
University of Denver
2190 E. Iliff Avenue
F.W. Olin Hall, Room 202
Denver CO 80208-0001
USA
berliner@du.edu

ISSN 0192-6020

ISBN 978-0-387-84855-6

e-ISBN 978-0-387-84856-3

DOI 10.1007/978-0-387-84856-3

Springer Dordrecht Heidelberg London New York

Library of Congress Control Number: 2009929718

© Springer Science+Business Media, LLC 2009

All rights reserved. This work may not be translated or copied in whole or in part without the written permission of the publisher (Springer Science+Business Media, LLC, 233 Spring Street, New York, NY 10013, USA), except for brief excerpts in connection with reviews or scholarly analysis. Use in connection with any form of information storage and retrieval, electronic adaptation, computer software, or by similar or dissimilar methodology now known or hereafter developed is forbidden.

The use in this publication of trade names, trademarks, service marks, and similar terms, even if they are not identified as such, is not to be taken as an expression of opinion as to whether or not they are subject to proprietary rights.

Printed on acid-free paper

Springer is part of Springer Science+Business Media (www.springer.com)

CONTRIBUTORS

Andrei Astashkin (Chapter 14)
Department of Chemistry
University of Arizona
1306 East University Blvd.
Tucson, AZ 85721-0041 USA
+1 520-621-9968
+1 520-621-8407 (fax)
andrei@u.arizona.edu

Gerhard Bracic (Chapter 3)
Department of Biophysics
Faculty of Medicine
Saarland University
Klinikum Bau 76
66421 Homburg/Saar, Germany
+49 6841-16-26206
+49 6841-16-26227 (fax)
bpgbra@uniklinik-saarland.de

Simon Benson (Chapter 4)
Centre for Magnetic Resonance
The University of Queensland
St. Lucia, Queensland, 4072 Australia
+61 7-3365-3349
+61 7-3365-3833 (fax)
Simon.Benson@cmr.uq.edu.au

Peter Caravan (Chapter 14)
A. A. Martinos Center for Biomedical
Imaging
Department of Radiology, Massachusetts
General Hospital
Harvard Medical School
149 Thirteenth St, Suite 2301
Charlestown, MA 02129 USA
+1 617-643-0193
+1 617-726-7422 (fax)
caravan@nmr.mgh.harvard.edu

Rachel Codd (Chapter 13)
Centre for Heavy Metals Research and
Centre for Structural Biology and
Structural Chemistry
School of Chemistry, The University of
Sydney
Sydney NSW 2006, Australia
Present address:
School of Medical Sciences
The University of Sydney
Sydney NSW 2006, Australia
+61 2-9351-6738
+61 2-9351-3868 (fax)
rcodd@med.usyd.edu.au

Betty J. Gaffney (Chapter 6)
Biological Sciences Department
BIO Unit I, mail code 4370
Florida State University
Tallahassee, FL 32306-4370 USA
+1 850-644-8547
+1 850-644-0481 (fax)
gaffney@bio.fsu.edu

Graeme R. Hanson (Chapters 4, 7)
Centre for Magnetic Resonance
The University of Queensland
St. Lucia, Queensland, 4072 Australia
+61 7-3365-3242
+61 7-3365-3833 (fax)
Graeme.Hanson@cmr.uq.edu.au

Jeffrey Harmer (Chapter 2)
Physical Chemistry Laboratory
Department of Chemistry and Applied
Biosciences
Wolfgang-Pauli-Strasse 10, ETH Zurich
CH-8093 Zurich, Switzerland

Present address:

Inorganic Chemistry
University of Oxford
South Parks Road, OX1 3QR
+44 1865-2-72651
+44 1865-2-85002 (fax)
jeffrey.harmer@chem.ox.ac.uk

Jürgen Hüttermann (Chapter 3)
Department of Biophysics
Faculty of Medicine
Saarland University
Klinikum Bau 76
66421 Homburg/Saar, Germany
+49 6841-16-26200
+49 6841-16-26227 (fax)
bpjhue@uniklinik-saarland.de

Reinhard Kappl (Chapter 3)
Department of Biophysics
Faculty of Medicine
Saarland University
Klinikum Bau 76
66421 Homburg/Saar, Germany
+49 6841-16-26221
+49 6841-16-26227 (fax)
bprkap@uniklinik-saarland.de

Peter A. Lay (Chapter 13)
Centre for Heavy Metals Research and
Centre for Structural Biology and
Structural Chemistry
School of Chemistry, The University
of Sydney
Sydney NSW 2006, Australia
+61 2-9351-4269
+61 2-9351-3329 (fax)
p.lay@chem.usyd.edu.au

Lisa J. Lee (Chapter 9)
Department of Chemistry and Biochemistry
103 Chemistry/Biochemistry Building
Montana State University
Bozeman, MT 59717 USA
+1 406-994-4801
+1 406-994-5407 (fax)
llee@chemistry.montana.edu

Aviva Levina (Chapter 13)
Centre for Heavy Metals Research and
Centre for Structural Biology and
Structural Chemistry
School of Chemistry, The University of
Sydney
Sydney NSW 2006, Australia
+61 2-9351-7600
+61 2-9351-3329 (fax)
levina_a@chem.usyd.edu.au

Wolfgang Lubitz (Chapter 10)
Max Planck Institut für Bioanorganische
Chemie
Stiftstrasse 34-36
D-45470 Mülheim an der Ruhr, Germany
+49 208-306-3614
+49 208-306-3955 (fax)
lubitz@mpi-muelheim.mpg.de

Benjamin P. Luchsinger (Chapter 9)
Department of Chemistry and Biochemistry
103 Chemistry/Biochemistry Building
Montana State University
Bozeman, MT 59717 USA

Present address:

Bacterin International, Inc.
600 Cruiser Lane
Belgrade, MT 59714 USA
+1 406-388-0480
+1 406-388-0422 (fax)
bluchsinger@bacterin.com

Barry D. Liboiron (Chapter 12)
Centre for Blood Research
Department of Biochemistry and
Molecular Biology
University of British Columbia
2350 Health Sciences Mall
Vancouver, BC, V6T 1Z3, Canada

Present address:

Celator Pharmaceuticals Corp.
1779 West 75th Avenue
Vancouver, BC V6P 6P2, Canada
+1 604-675-2115
+1 604-708-5883 (fax)
bliboiron@celatorpharma.com

Nataša Mitić (Chapter 7)
School of Chemistry and Molecular
Biosciences
The University of Queensland
St. Lucia 4072, Australia
+61 7-3365-4040
+61 7-3365-4273 (fax)
n.mitic@uq.edu.au

George Mitrikas (Chapter 2)
Physical Chemistry Laboratory
Department of Chemistry and Applied
Biosciences
Wolfgang Pauli Strasse 10, ETH Zurich
CH-8093 Zurich, Switzerland

Present address:

Institute of Materials Science
NCSR “Demokritos”
15310 Aghia Paraskevi Attikis, Greece
+30 210-650-3352
+30 210-651-9430 (fax)
mitrikas@ims.demokritos.gr

Frank Neese (Chapter 5)
Lehrstuhl für Theoretische Chemie
Institut für Physikalische und Theoretische
Chemie
Universität Bonn
Wegelerstrasse 12
Bonn D-53115, Germany
+49 228-732351
+49 228-739064 (fax)
neese@thch.uni-bonn.de

Christopher J. Noble (Chapter 4)
Centre for Magnetic Resonance
The University of Queensland
St. Lucia, Queensland, 4072 Australia
+61 7-3365-3349
+61 7-3365-3833 (fax)
Chris.Noble@cmr.uq.edu.au

John R. Pilbrow (Chapter 1)
School of Physics
Building 27, Monash University
Victoria 3800, Australia
+61 3-9905-3630
+61 3-9905-3637 (fax)
John.Pilbrow@sci.monash.edu.au

Arnold Raitisimring (Chapter 14)
Department of Chemistry
University of Arizona
1306 East University Blvd.
Tucson, AZ 85721-0041 USA
+1 520-621-9968
+1 520-621-8407 (fax)
arnold@u.arizona.edu

Gerhard Schenk (Chapter 7)
School of Chemistry and Molecular
Biosciences
The University of Queensland
St. Lucia 4072, Australia
+61 7-3365-4144
+61 7-3365-4273 (fax)
schenk@uq.edu.au

Arthur Schweiger* (deceased)
Physical Chemistry Laboratory
Department of Chemistry and Applied
Biosciences
Wolfgang Pauli Strasse 10, ETH Zurich
CH-8093 Zurich, Switzerland

David J. Singel (Chapter 9)
Department of Chemistry and Biochemistry
103 Chemistry/Biochemistry Building
Montana State University
Bozeman, MT 59717 USA
+1 406-994-3960
+1 406-994-5407 (fax)
rchds@montana.edu

Edward I. Solomon (Chapter 11)
Department of Chemistry
Stanford University
333 Campus Drive
Stanford, CA 94305 USA
+1 650-723-9104
+1 650-725-0259 (fax)
edward.solomon@stanford.edu

Jonathan S. Stamler (Chapter 9)
Department of Chemistry and Biochemistry
103 Chemistry/Biochemistry Building
Montana State University
Bozeman, MT 59717 USA

Present address:

Department of Biochemistry
Duke University Medical Center
Box 2612
Durham, NC 27710 USA
+1 919-684-6933
+1 919-684-8885 (fax)
staml001@mc.duke.edu

Sabine Van Doorslaer (Chapter 8)
SIBAC Laboratory
Department of Physics
University of Antwerp
Universiteitsplein 1 (N 2.16)
B-2610 Wilrijk-Antwerp, Belgium
+32 3-820-24-61
+32 3-820-24-70 (fax)
sabine.vandoorslaer@ua.ac.be

Maurice van Gastel (Chapter 10)
Max Planck Institut für Bioorganische
Chemie
Stiftstrasse 34-36
D-45470 Mülheim an der Ruhr, Germany
+49 208-306-4
+49 208-306-3555 (fax)
vangastel@mpi-muelheim.mpg.de

Eric D. Walter (Chapter 9)
Department of Chemistry and Biochemistry
103 Chemistry/Biochemistry Building
Montana State University
Bozeman, MT 59717 USA

Present address:

Department of Chemistry and
Biochemistry
230 Physical Sciences Building
University of California
Santa Cruz, CA 95064 USA
+1 831-459-4002
+1 831-459-2935 (fax)
ewalter@chemistry.ucsc.edu

Jungjoo Yoon (Chapter 11)
Department of Chemistry
Stanford University
333 Campus Drive
Stanford, CA 94305 USA
+1 650-723-9128
+1 650-725-0259 (fax)
jjyoon2@stanford.edu



ARTHUR SCHWEIGER (1946–2006)

Arthur Schweiger died unexpectedly on January 4, 2006 at the age of 59 after a short illness. He was educated in the Laboratory of Physical Chemistry at ETH Zurich and was awarded the Werner Prize by the Swiss Chemical Society. He then worked in Professor Richard R. Ernsts' group and was promoted to full Professor in 1991. His research group focused on the development and application of new methods of pulsed electron paramagnetic resonance, and he was awarded the Zavoisky Award in 1993, the Bruker Prize in 1994, and the Gold Medal of the International EPR Society in 1998. He coauthored a comprehensive textbook on electron paramagnetic resonance spectroscopy that has since become the gospel for pulsed EPR.

PREFACE

Metalloproteins comprise approximately 30% of all known proteins, and are involved in a variety of biologically important processes, including oxygen transport, biosynthesis, electron transfer, biodegradation, drug metabolism, proteolysis, and hydrolysis of amides and esters, environmental sulfur and nitrogen cycles, and disease mechanisms. EPR spectroscopy has an important role in not only the geometric structural characterization of the redox cofactors in metalloproteins but also their electronic structure, as this is crucial for their reactivity. The advent of x-ray crystallographic snapshots of the active site redox cofactors in metalloenzymes in conjunction with high-resolution EPR spectroscopy has provided detailed structural insights into their catalytic mechanisms.

This volume was conceived in 2005 at the Rocky Mountain Conference on Analytical Chemistry (EPR Symposium) to highlight the importance of high-resolution EPR spectroscopy to the structural (geometric and electronic) characterization of redox active cofactors in metalloproteins. We have been fortunate to have enlisted internationally recognized experts in this joint venture to provide the scientific community with an overview of high-resolution EPR and its application to metals in biology. This volume, *High-Resolution EPR: Applications to Metalloenzymes and Metals in Medicine*, covers high-resolution EPR methods, iron proteins, nickel and copper enzymes, and metals in medicine. An eloquent synopsis of each chapter is provided by John Pilbrow in the Introduction which follows. Please visit <http://www.springer.com/978-0-387-84855-6> to view high-resolution full-color versions of all the color illustrations in this volume (see the list of color illustrations on p. xxiii). A second volume, *Metals in Biology: Applications of High-Resolution EPR to Metalloenzymes*, will appear later this year covering the complement of other metalloproteins.

One of the pioneers in the development of pulsed EPR and its application to metalloproteins was Arthur Schweiger, whose contribution we include in this volume. Unfortunately, he passed away suddenly during the preparation of this volume. The editors and coauthors are extremely honored to dedicate this volume to the memory of Arthur Schweiger in recognition of his technical advances and insights into pulsed EPR and its application to metalloproteins. Arthur was extremely humble and treated everyone with equal respect. He was a gifted educator with an ability to explain complex phenomena in terms of simple intuitive pictures, had a delightful personality, and continues to be sadly missed by the community.

It is an honor for the editors to facilitate the dissemination of these excellent contributions to the scientific community. Suggestions for future volumes are always appreciated.

Graeme R. Hanson
Brisbane, Queensland, Australia

Lawrence J. Berliner
Denver, Colorado, USA

CONTENTS

Preface	xi
List of Color Figures	xxiii

Chapter 1

Introduction	1
---------------------------	---

John R. Pilbrow

HIGH-RESOLUTION EPR METHODS

Chapter 2

Advanced Pulse EPR Methods for the Characterization of Metalloproteins	13
---	----

Jeffrey Harmer, George Mitrikas, and Arthur Schweiger

1. Introduction.....	13
2. Spin Hamiltonian.....	15
2.1. Static Spin Hamiltonian.....	15
2.2. Nuclear Frequency Spectra of Spin Systems with $S = \frac{1}{2}$ and Arbitrary I.....	17
2.3. Orientation Selection in Pulse EPR.....	18
3. ESEEM Basics.....	20
3.1. Origin of the Nuclear Modulation Effect.....	20
3.2. Two- and Three-Pulse ESEEM.....	22
3.3. HYSCORE.....	25
3.4. Remote Echo Detection.....	34
3.5. Matched ESEEM.....	35
3.6. DONUT-HYSCORE.....	37
3.7. Hyperfine Decoupling Techniques.....	37
4. Electron Nuclear Double Resonance (ENDOR).....	40
4.1. Mims and Davies ENDOR.....	41
4.2. Baseline Artifacts in ENDOR.....	43
4.3. Hyperfine-Correlated ENDOR Spectroscopy.....	44
4.4. Triple Resonance.....	46
4.5. Variable Mixing Time ENDOR.....	47
4.6. High-Field ENDOR.....	48

4.7. Hyperfine Enhancement of r.f. Pulses	50
4.8. Time-Domain ENDOR.....	50
5. Field-Swept EPR Experiments.....	52
5.1. Nutation Experiments	52
5.2. Electron Zeeman-Resolved EPR.....	54
6. Strategies and Outlook	54
7. Acknowledgements.....	56
8. References.....	56

Chapter 3

Probing Structural and Electronic Parameters in Randomly Oriented Metalloproteins by Orientation-Selective ENDOR Spectroscopy	63
--	-----------

Reinhard Kappl, Gerhard Bracic, and Jürgen Hüttermann

1. Introduction.....	64
2. Theory.....	65
3. Orientation Selection in EPR and ENDOR	74
4. Examples of Applications: Iron–Sulfur Proteins.....	82
4.1. Proton Hyperfine Interactions.....	82
4.2. ⁵⁷ Iron Interactions	94
4.3. Spin Densities	98
5. Summary	100
6. Acknowledgements.....	100
7. References.....	100

Chapter 4

Molecular Sophe: An Integrated Approach to the Structural Characterization of Metalloproteins: The Next Generation of Computer Simulation Software	105
---	------------

Graeme R. Hanson, Christopher J. Noble, and Simon Benson

1. Introduction.....	105
2. Molecular Sophe Computational Software Suite	114
2.1. Project Form	117
2.2. Simulation Form.....	117
2.3. Sample Form.....	118
2.4. Molecule Form	119
2.5. Adding Atoms.....	119
2.6. Atom Form	121
2.7. Electron Zeeman Interaction (β B.g.S).....	121
2.8. Hyperfine Interaction (S.A.I).....	122
2.9. Fine Structure Interaction (S.D.S)	123
2.10. Quadrupole Interaction (I.P.I)	124
2.11. Linewidth Parameters	126

2.12. Atom Isotopes.....	127
2.13. Position Form	128
2.14. Adding Bonds	129
2.15. SuperHyperfine Interactions (S.A.I).....	129
2.16. Exchange Interaction (S.J.S).....	130
2.17. Adding Experiments	132
2.18. Experiment Form.....	133
2.19. CW EPR Experiments	133
2.20. Sophe Computational Parameters	135
2.21. Spectra Input/Output.....	137
2.22. Resonator Configuration.....	138
2.23. Pulsed EPR Experiment: Hyperfine Sublevel Correlated Spectroscopy (HYSCORE).....	138
2.24. Pulsed EPR Experiment — Orientation Selective HYSCORE.....	142
2.25. Pulsed EPR–MIMS ENDOR	143
2.26. Units Conversion Calculator.....	145
2.27. Reports: Energy Level Diagrams.....	147
2.28. Main Menus.....	147
2.29. Tool Bar.....	147
2.30. Control Bar	149
3. Sophe: Computational Code.....	150
3.1. Sophe Grid.....	150
3.2. CW EPR Spectroscopy	152
3.3. Pulsed EPR Simulations	156
4. Molecular Sophe – Examples.....	159
4.1. CW-EPR Spectroscopy.....	159
4.2. Pulsed EPR Spectroscopy	167
5. Advances in Spectral Optimization	167
6. Conclusions.....	171
7. Acknowledgements.....	171
8. References.....	171

Chapter 5

Spin-Hamiltonian Parameters from First Principle Calculations: Theory and Application	175
--	------------

Frank Neese

1. Introduction.....	175
2. Electronic Structure Theory of Spin-Hamiltonian Parameters	177
2.1. Electronic Structure Methods	177
2.2. Additional Terms in the Hamiltonian	182
2.3. Sum-Over States Theory of SH Parameters.....	185
2.4. Linear Response Theory	188

2.5. Expression for Spin-Hamiltonian Parameters for Self-Consistent Field Methods.....	192
2.6. Practical Aspects.....	198
3. Case Studies	201
3.1. Structure–Spectral Relationships: Phenoxy Radicals	201
3.2. Difficult Cases: Cysteine Radicals.....	203
3.3. Solvent Effects: <i>g</i> -Tensors of Nitroxide Radicals.....	207
3.4. SH Parameters in Proteins: QM/MM Studies	212
3.5. Zero-Field Splittings: Origin of ZFS in Organic Triplets and Diradicals.....	217
3.6. Zero-Field Splittings: Origin of the ZFS in Transition Metal Complexes	220
4. Concluding Remarks.....	222
5. Acknowledgements.....	224
6. References.....	224

IRON PROTEINS

Chapter 6

EPR of Mononuclear Non-Heme Iron Proteins	233
--	------------

Betty J. Gaffney

1. EPR of Mononuclear, High-Spin Ferric Non-Heme Proteins.....	233
1.1. Assignment: The $S = 5/2$ EPR Parameter Space Is Large but Not Infinite	233
1.2. Assignment for Zero-Field Splitting: the Zeeman Term.....	236
1.3. Assignment for Zero-Field Splitting Similar to the Zeeman Term	240
1.4. High-Frequency EPR and Assignment for Zero-Field Splitting: The Zeeman Term.....	244
1.5. Contributions to Line Shapes.....	246
2. EPR of Mononuclear, Low-Spin Ferric Non-Heme Proteins.....	251
2.1. Nitrile Hydratase.....	251
3. Radical ($S = 1/2$) Probes of Ferrous ($S = 2$) Iron	251
3.1. Photosynthetic Reaction Centers	251
3.2. Nitric Oxide and Non-Heme Ferrous Centers.....	254
3.3. High-Spin NO Complexes with Non-Heme Iron Proteins.....	258
3.4. Low-Spin NO Complexes with Non-Heme Iron Proteins.....	261
4. References.....	264

Chapter 7

Binuclear Non-Heme Iron Enzymes 269*Nataša Mitić Gerhard Schenk, Graeme R. Hanson*

1. Introduction	269
2. Bacterial Multicomponent Monooxygenases	274
2.1. Methane Monooxygenase	274
2.2. Alkane ω -Hydroxylase	291
2.3. Alkene Monooxygenase	293
2.4. Phenol Hydroxylases	296
2.5. Toluene-4-Monooxygenase	299
2.6. Toluene/ <i>o</i> -Xylene Monooxygenase	300
3. Ribonucleotide Reductase	303
3.1. Biochemical and Structural Characterization.....	303
3.2. Spectroscopic Characterization of R2.....	305
3.3. Mechanistic Insights	313
4. Stearoyl-Acyl Carrier Protein Δ^9 Desaturase.....	314
4.1. Biochemical and Structural Characterization.....	314
4.2. Spectroscopic Characterization of Δ^9 Desaturase	317
4.3. Mechanistic Implications	318
5. <i>Myo</i> -Inositol Oxygenase	320
5.1. Biochemical and Structural Characterization.....	320
5.2. Spectroscopic Characterization of MIOX.....	321
5.3. Mechanistic Implications	323
6. Rubrerythrin, Nigerythrin, and Sulerythrin	326
6.1. Rubrerythrin.....	326
6.2. Nigerythrin.....	330
6.3. Sulerythrin	332
7. Ferritins and Bacterioferritins	332
7.1. Biochemical and Structural Characterization.....	332
7.2. Spectroscopic Characterization of Ferritins and Bacterioferritins	335
7.3. Mechanistic Insights	337
8. Hemerythrin	337
8.1. Biochemical and Structural Characterization.....	337
8.2. Spectroscopic Characterization of Hemerythrin	339
8.3. Mechanistic Insights	340
9. Hydrolytic Enzymes.....	341
9.1. Purple Acid Phosphatases.....	341
9.2. Metallo- β -Lactamases.....	346
10. Rubredoxin-Oxygen Oxidoreductase and Nitric Oxide Reductases.....	350
10.1. Biochemical and Structural Characterization	350
10.2. Spectroscopic Characterization of FprA and FIRd	352
10.3. Mechanistic Insights	352

11. Membrane-Bound Diiron Proteins:	
Alternative Oxidase.....	353
11.1. Biochemical and Structural Characterization	353
11.2. Spectroscopic Characterization of AOX.....	354
11.3. Mechanistic Insights	354
12. Conclusions	355
13. Acknowledgements.....	356
14. References.....	356

Chapter 8

Probing the Structure–Function Relationship of Heme Proteins Using Multifrequency

Pulse EPR Techniques.....	397
----------------------------------	------------

Sabine Van Doorslaer

1. Introduction	397
2. Ferric Forms of Heme Proteins	398
2.1. Low-Spin Ferric Forms of Heme Proteins	398
2.2. High-Spin Ferric Forms of Heme Proteins	406
3. NO-Ligated Heme Proteins	408
4. Distance Measurements in Heme Proteins	410
5. Conclusions and Outlook	411
6. Acknowledgements.....	412
7. References.....	412

Chapter 9

EPR Studies of the Chemical Dynamics of NO and Hemoglobin Interactions.....

	419
--	-----

*Benjamin P. Luchsinger, Eric D. Walter, Lisa J. Lee,
Jonathan S. Stamler, and David J. Singel*

1. Introduction	419
1.1. NO Hb Functional Interactions	420
1.2. SNO-Hemoglobin	421
1.3. SNO-Hemoglobin Function	422
2. EPR Spectroscopy of NO Hb Interactions	424
2.1. Heme-Fe(II)NO Spectral Components	424
2.2. Heme Fe(II)NO Subunit Selectivity	427
2.3. Heme Fe(II)NO Subunit Spectral Editing.....	430
3. Evolution of NO Hb Interactions	431
4. Acknowledgements.....	433
5. References.....	433

NICKEL AND COPPER ENZYMES

Chapter 10

EPR Investigation of [NiFe] Hydrogenases 441

Maurice van Gastel and Wolfgang Lubitz

1. Classification, Composition and Structure of Hydrogenases 442
2. Basic Description of the Electronic Structure 445
3. EPR Characterization of [NiFe] Hydrogenases: the **g** Tensors 448
 - 3.1. The Oxidized States Ni–A and Ni–B 448
 - 3.2. The Reduced Active State Ni–C 452
 - 3.3. The Split Ni–C Signal 452
 - 3.4. The Light-Induced State Ni–L 454
 - 3.5. The Ni–CO State 455
4. ENDOR and ESEEM Studies of [NiFe] Hydrogenase: Hyperfine Structure 456
 - 4.1. Hyperfine Couplings of Metal Nuclei 456
 - 4.2. HFCs of Ligand Nuclei 457
 - 4.3. The Bridging Ligand X 458
 - 4.4. Light Sensitivity of the Active Intermediate 460
 - 4.5. Interaction of the Active Site with the Protein Surrounding 461
5. Distance Studies of [NiFe] Hydrogenases 462
6. EPR-Silent States 462
7. Conclusions and Outlook 462
8. Acknowledgements 464
9. References 464

Chapter 11

Unique Spectroscopic Features and Electronic Structures of Copper Proteins: Relation to Reactivity 471

Jungjoo Yoon and Edward I. Solomon

1. Introduction 471
2. Mononuclear Blue “Type 1” Cu Sites 475
3. Binuclear Cu_A Sites 478
4. Coupled Binuclear “Type 3” Cu Sites 481
5. Non-Coupled Binuclear Cu Sites 483
6. Trinuclear Cu(II) Cluster Sites 486
7. Tetranuclear Cu_Z Sites 493
8. Concluding Comments 496
9. Acknowledgements 496
10. References 496

METALS IN MEDICINE

Chapter 12

Insulin-Enhancing Vanadium Pharmaceuticals: The Role of Electron Paramagnetic Resonance

Methods in the Evaluation of Antidiabetic Potential..... 507

Barry D. Liboiron

1. Introduction..... 507
 - 1.1. EPR and the Study of Insulin-Enhancing Vanadium Compounds..... 509
 - 1.2. EPR Properties of the Vanadyl Ion..... 510
 - 1.3. The Additivity Rule..... 512
2. In Vitro Studies of Vanadium Speciation and Redox Chemistry..... 512
 - 2.1. Solution Structures of Insulin-Enhancing Vanadium(IV) Complexes..... 514
 - 2.2. Interactions of Serum Proteins and Vanadyl Compounds..... 520
3. Use of EPR for In Vivo Studies of Vanadium Metabolism and Coordination Structure..... 525
 - 3.1. Absorption and In Vivo Redox Reactions of Vanadium Compounds..... 526
 - 3.2. In Vivo Pharmacokinetics of Vanadium Species by BCM-EPR..... 529
 - 3.3. In Vivo Structure Determination by CW and Pulsed EPR..... 532
4. Summary..... 540
5. Acknowledgements..... 541
6. Abbreviations..... 541
7. References..... 543

Chapter 13

Chromium in Cancer and Dietary Supplements..... 551

Aviva Levina, Rachel Codd and Peter A. Lay

1. Roles of Reactive Intermediates in Chromium(VI)-Induced Toxicity and in Anti-Diabetic Effects of Chromium(III)..... 552
2. Chromium(V) Intermediates..... 554
 - 2.1. Isolation and Characterization of Chromium(V) Complexes with Biological and Biomimetic Ligands..... 554
 - 2.2. Application of EPR Spectroscopic Parameters to the Structural Characterization of Chromium(V) Complexes..... 557
 - 2.3. Chromium(V) Complexes of Carbohydrates and Their Derivatives.... 561
3. Chromium(III) and Chromium(IV) Species..... 565
4. Free Radicals as Intermediates in Chromium Biochemistry..... 568
5. Living Cell and Animal Studies..... 569
6. Acknowledgements..... 572
7. References..... 573

*Chapter 14***High-Frequency EPR and ENDOR Characterization of MRI Contrast Agents**.....

581

*Arnold M. Raitsimring, Andrei V. Astashkin,
and Peter Caravan*

1. Introduction 581
2. Frequency Dependence of Gd(III) Electronic Relaxation in Aqueous Solution 586
3. Crystal Field Interaction (*CFI*) Parameters for Gd(III) Complexes in Glassy Solutions from High-Field EPR Experiments 590
4. High-Field Pulsed ENDOR of Water Ligands in MRI Agents and the Geometry of Water Coordination 597
 - 4.1. Effect of Weak *cfi* on Nuclear Transition Frequencies and Appearance of ENDOR Spectra 597
 - 4.2. ^{17}O ENDOR Frequencies at High Field 601
 - 4.3. Practical Aspects of Pulsed ENDOR Spectroscopy of MRI Agents 603
 - 4.4. Experimental ^1H ENDOR Spectra 605
 - 4.5. Experimental ^{17}O ENDOR Spectra 607
 - 4.6. Interpretation of ^{17}O *hfi* and *nqi* Parameters in Terms of Electronic and Geometrical Structure 609
 - 4.7. Hydration Numbers of Gd(III) Complexes Determined by High-Field Pulsed ^{17}O and ^1H ENDOR 612
5. Conclusions 616
6. Acknowledgements 616
7. References 617

Contents of Previous Volumes 623**Index** 651

LIST OF COLOR FIGURES

Please visit <http://www.springer.com/978-0-387-84855-6> to view high-resolution full-color versions of all the color illustrations in this volume.

CHAPTER 4

Figure 1 (p. 106)
Figure 2 (p. 108)
Figure 3 (p. 111)
Figure 4 (p. 113)
Figure 5 (p. 114)
Figure 6 (p. 115)
Figure 7 (p. 116)
Figure 8 (p. 116)
Figure 9 (p. 117)
Figure 10 (p. 118)
Figure 11 (p. 119)
Figure 12 (p. 120)
Figure 13 (p. 120)
Figure 14 (p. 121)
Figure 15 (p. 122)
Figure 16 (p. 123)
Figure 17 (p. 124)
Figure 18 (p. 125)
Figure 19 (p. 126)
Figure 20 (p. 127)
Figure 21 (p. 128)
Figure 22 (p. 129)
Figure 23 (p. 130)
Figure 24 (p. 131)
Figure 25 (p. 132)
Figure 26 (p. 133)
Figure 27 (p. 134)
Figure 28 (p. 135)
Figure 29 (p. 136)
Figure 30 (p. 138)
Figure 31a–d (p. 139)
Figure 31e (p. 140)
Figure 32 (p. 141)
Figure 33 (p. 141)
Figure 34 (p. 142)

Figure 35 (p. 143)
Figure 36 (p. 144)
Figure 37 (p. 146)
Figure 38 (p. 147)
Figure 39 (p. 149)
Figure 40 (p. 149)
Figure 42 (p. 153)
Figure 43 (p. 155)
Figure 44 (p. 159)
Figure 45 (p. 160)
Figure 46 (p. 163)
Figure 47 (p. 164)
Figure 48 (p. 165)
Figure 49 (p. 166)
Figure 50 (p. 167)
Figure 51 (p. 168)
Figure 52 (p. 168)
Figure 53 (p. 170)
Figure 54 (p. 171)

CHAPTER 5

Figure 1 (p. 202)
Figure 3 (p. 205)
Figure 4 (p. 205)
Figure 6 (p. 208)
Figure 7 (p. 211)
Figure 8 (p. 213)
Figure 9 (p. 214)
Figure 12 (p. 221)

CHAPTER 6

Figure 9 (p. 243)

CHAPTER 9

Figure 1 (p. 423)
Figure 2 (p. 424)
Figure 3 (p. 426)
Figure 4 (p. 428)
Figure 5 (p. 429)
Figure 7 (p. 431)
Figure 8 (p. 432)

CHAPTER 12

Figure 7 (p. 523)

CHAPTER 13

Figure 1 (p. 553)

ABOUT THE EDITORS

Prof. Graeme Hanson located in the Centre for Magnetic Resonance at the University of Queensland, has applied a unique synergistic approach involving both theoretical and experimental aspects of multifrequency continuous wave and pulsed EPR spectroscopy to structurally (geometric and electronic) characterise the metal binding sites in metalloenzymes and transition metal ion complexes. The development and commercialisation of the XSophe-Sophe-XeprView (CW EPR) and Molecular Sophe(CW EPR, Pulsed EPR and ENDOR) computer simulation software suites has been crucial in the characterisation of these biological inorganic systems.

Dr. Lawrence J. Berliner is currently at the Department of Chemistry and Biochemistry, University of Denver, where he was Professor and Chair for the past 8 years. He retired from The Ohio State University, where he spent a 32-year career in the area of biological magnetic resonance (EPR and NMR). He has been recognized by the International EPR Society with the Silver Medal for Biology/Medicine in 2000. He also received the Lifetime Achievement Award in Biological EPR Spectroscopy at EPR-2005. He is the Series Editor for *Biological Magnetic Resonance*, which he launched in 1979.

INTRODUCTION

John R. Pilbrow

*School of Physics, Monash University,
Victoria, Australia*

It is salutary to look back for a moment to some of the earliest publications that brought together biological EPR data some 40 years ago, and I have in mind particularly the conference volume, *Magnetic Resonance in Biological Systems*, edited by Ehrenberg, Malmström, and Vanngård [1]. In those days the reports were all based on continuous-wave (CW) EPR, computer simulations were in their infancy, ENDOR (Electron Nuclear Double Resonance) was dominantly still, but not exclusively, found in condensed matter physics and to some extent in chemistry. Pulsed EPR methods had not been applied at that time to biological systems. In those early days dominated by CW EPR it was tempting to think there was a universal EPR experiment — about 4 mW microwave power with a Varian rectangular cavity, 4 gauss modulation, and a relatively slow field sweep. One was aware of the role played by power saturation and sometimes passage effects, especially at lower temperatures, but on the whole these were avoided rather than exploited.

During the past two decades or so, CW-ENDOR has given way to Pulsed-ENDOR, and the growing availability of pulsed facilities has also opened up ESEEM (Electron Spin Echo Envelope Modulation) and HYSORE (Hyperfine Sublevel Correlation Spectroscopy) methods. It is quite clear that there is no universal EPR experiment.

This volume contains 13 specialist chapters covering strategies for high-resolution EPR spectroscopy and data analysis in biology and biomedicine. These diverse chapters, though all relating to advanced EPR spectroscopy of biological systems, cover a significant range of topics. To read this volume and the companion volume (*Biological Magnetic Resonance*, Volume 29) will show just how far the field has moved, not only in experimental complexity and sophistication but in elucidating structural and functional information regarding active sites in enzymes. Chapters 2–5 present strategies for achieving high resolution in EPR spectroscopy. The next three chapters (6–8) are concerned with a variety of iron enzymes. In Chapters 10 and 11 the subject shifts to nickel and copper enzymes. The final three chapters (12–14) provide an important link regarding the role of metal ions in medicine.

Chapter 2 — by Harmer, Miktrikas, and the late Arthur Schweiger — comes from a laboratory that has contributed more than most to the development of strategic pulsed EPR methodology and provides a convenient summary of much that is contained in the book by Schweiger and Jeschke [2]. It is an eminently readable “how-to” chapter that provides a bird’s-eye-view of the many pulsed EPR and ENDOR methods available for biological applications and, as such, makes a first reading of the subject easier than having to go through the greater detail of Schweiger and Jeschke’s book [2]. The authors describe the inner workings of ESEEM and pulsed ENDOR as well as the latest developments aimed at resolution and sensitivity enhancement, particularly the application of matched pulses. The basic theory of 2-pulse ESEEM, 3-pulse ESEEM, and 4-pulse HYSCORE is given in some detail. This includes discussion of various coherence pathways that have to be considered in order to understand pulsed experiments. The impact of the near cancellation condition at X-band for distant N ligands is also emphasized. Background to the Spin Hamiltonian is provided and appropriate approximations are identified particularly in cases with small distant ligand hyperfine anisotropy. The link to molecular calculations via Density Functional Theory (DFT) methods is indicated.

Since crystals of biological samples are mostly not available, single crystal-like spectra may be obtained using orientation selection. This relies on accumulation of spectral information at particular g -values corresponding to identifiable molecular orientations. Orientation selection, with a particular emphasis on ENDOR in iron-sulfur proteins is developed in rather more detail in the following chapter by Hüttermann et al. Only one example of direct biological relevance is reported, MCR_{BPS} (Ni, $S = \frac{1}{2}$ signal), an inhibitor of the enzyme coenzyme M reductase (MCR). There is some discussion of HYSCORE applications to biology.

With regard to ENDOR, the earliest of the high-resolution methods in EPR spectroscopy, the emphasis here was on a comparison between Mims and Davies ENDOR, both of which are pulsed ENDOR methods. The advantages and limitations of these techniques are demonstrated through examples found in the literature, with an emphasis on systems of biological relevance.

Chapter 3 by Hüttermann and Kappl presents detailed strategies for the analysis of CW- and pulsed-ENDOR spectroscopy from Fe–S proteins. ENDOR is by now a well-known high-resolution technique ideal for resolving small interactions between unpaired electrons and metal nuclei or with nuclei in the coordination sphere that cannot be resolved using CW-EPR. It provides important information to characterize the functional, structural, and electronic properties of paramagnetic centers found in metalloproteins. It complements ESEEM and HYSCORE methods, which are more suited to determining hyperfine interactions from distant ligand nuclei.

As proteins are not easily crystallized and samples are, therefore, mostly available only as frozen solutions, “powder”-type ENDOR spectra may be observed using the method of “orientation selection,” already referred to with reference to the previous chapter by Harmer et al. The authors provide a very detailed introduction to the calculation of orientation-selected ENDOR spectra and discuss several

approaches toward creating fast and efficient interactive simulations of high-quality ENDOR spectra. Readers should find Figures 3, 4, 7, and 8 of great value as aids in visualizing the orientations of molecules that contribute to spectra. Their method uses the EPR resonance condition for a set of g - and hyperfine-tensors from the paramagnetic center(s), first by calculating the orientational distribution of the subset of molecules that contribute to the ENDOR spectrum at a given magnetic field. As in CW-EPR, the ENDOR resonances are associated with turning points of selected orientations in defined frequency ranges. The authors emphasize that ENDOR spectra need to be recorded at several magnetic fields across an EPR spectrum. Other important information obtained includes the relative orientation of the g -tensor with respect to hyperfine tensors or, better still, with respect to the molecular frame when combined with x-ray crystal structures. Spin population distributions thus become accessible, as is information regarding delocalization on amino acid ligands.

Examples are drawn from reduced [2Fe–2S] clusters in ferredoxins with *all*-cysteine coordination, Rieske-type centers, and oxidized [4Fe–4S] clusters in HiPIP proteins. Details regarding proton and ^{57}Fe hyperfine interactions are provided. These coupled with the g -tensor orientation in the molecular frame provide detailed information regarding the site of reduction or oxidation within the cluster as well as valence delocalization of the iron ions.

In Chapter 4, Hanson, Benson, and Noble give an overview of their long-established simulation suite, XSophe, and add a new philosophical approach to EPR simulation through the new software suite, Molecular Sophe. The motivation for this particular chapter is the need to provide a generalized tool for the analysis of all forms of EPR spectra from transition metal ion complexes, metalloproteins, and a variety of new high-technological materials. As is common practice these days to obtain spectra at more than one frequency, one needs theoretical and simulation methods that can be used with a single parameter set at more than one frequency. The increased use of a plethora of pulsed experiments — for example, ESEEM, HYSCORE, Davies and Mims ENDOR — makes it imperative that simulation software also include these as well as CW simulations. There is a particular emphasis on theoretical approaches for simulating high-spin and spin-coupled pulsed EPR/ENDOR spectra. A longer-term goal, not yet achieved, is to link MoSophe to molecular calculation software such as DFT (ORCA), something explained in much more detail in the following chapter by Neese.

The authors lead the reader through the background to EPR and the spin Hamiltonian and the kinds of outputs one is able to obtain from input spin Hamiltonian parameters. The long-established XSophe software covers CW-EPR, energy level diagrams, transition surfaces and roadmaps, isolated and coupled spins, and an, in principle, unlimited number of electron and nuclear spins displayed using XepView. Natural isotopes are automatically allowed for, and there is provision for enriched isotope experiments. Spin Hamiltonian terms including the usual Zeeman, hyperfine, nuclear hyperfine, and quadrupole terms are all included. For iron

group and rare earth ions, the 4th- and 6th-order fine structure operators are fully supported. Solution, powder, and crystal spectra are all allowed for, as are all point group symmetries. Finally, multidimensional spectra as a function of temperature or microwave frequency are also allowed for.

Molecular Sophe (MoSophe) represents a whole new way of thinking about EPR spectroscopy. It begins with the molecular frame, thus putting the emphasis on structure rather than the spin Hamiltonian. This writer has trialed an early version of MoSophe and confirms that it is very insightful and intuitive. MoSophe uses a graphical user interface, the computational program Sophe as in XSophe, and various options for visualization. The program asks one to define a project and within that one or more simulations on a tree structure. One is then asked to define a molecule. In the case of a doped crystal, the “molecule” would consist of the paramagnetic ion and the surrounding nearest neighbor atoms. In a metal protein, the “molecule” would be, for example, a paramagnetic metal ion and its nearby coordinating ligands. Atoms can be added and also bonds. The concept of a bond is loosely defined and includes interactions between electrons and ligand nuclear spins or coupled electron spins. Then the user is asked to define the parameters for the various spin Hamiltonian terms and the orientations with respect to the molecular frame. Finally, one is asked to define the experiment. Under CW-EPR this includes both perpendicular and parallel field experiments. For pulsed EPR this includes Free Induction Decay (FID), 2-pulse ESEEM, 3-pulse ESEEM, HYSORE, Mims ENDOR, and Davies ENDOR. With regard to pulsed experiments, the pulse sequence is represented graphically on the user interface. The computational procedure is outlined in some detail and covers the Sophe Grid, brute force and field segmentation algorithms, the mosaic misorientation linewidth model, and some necessary theoretical background to pulsed simulations.

In Chapter 5, Neese takes the reader on a journey through modern molecular calculations that began with the original Hartree–Fock (HF) methods that originated in the 1930s. The introduction to the chapter provides important background to the general methodology, and the theory of molecular calculations is sketched in some detail, without formal proofs, and presented in a very readable and accessible manner. While the power of EPR methods to obtain the spin Hamiltonian for a particular system is well established, the goal of the methods described by Neese are focused more on seeking to simulate the behavior of spin systems in advance by means of exact quantum mechanical calculations. One limitation is that while there is a strong link between the spin Hamiltonian parameters and the microscopic physics governing molecular behavior, exact solutions using full relativistic treatments are not yet feasible. Neese describes a number of strategies to overcome this limitation. What is of great interest is to realize that Neese’s program, ORCA, can be run successfully on a standard PC running under either Linux or Windows. Neese warns that, while electronic structure theory these days is dominated by Density Functional Theory (DFT), it is inappropriate to equate DFT and quantum chemistry. He suggests that *ab initio* calculations based on HF theory will regain some importance in the future.

The chapter covers electronic structure theory of spin Hamiltonian parameters that depend on inclusion of spin-orbit coupling, spin-spin interactions, hyperfine coupling, quadrupole coupling, electron Zeeman interaction, zero field splitting, g -tensors, and field gradients. Linear response theory is described within a Self-Consistent Field ground state using either HF or DFT single determinants. One can use either trial models of the structure or known crystal or molecular structures when available. The efficiency of the calculations described here allows for much more reliable calculations of spin Hamiltonian parameters these days. In fact g -factors and A -values, and their orientations, can now be computed with considerable accuracy. These methods now yield tensor orientations that are used to supplement results that would otherwise require difficult and tedious single-crystal measurements that might not be feasible.

Case studies concerned phenoxyl and other radicals, nitroxide radicals, the copper proteins, plastocyanin and azurin, calculation of zero field splittings in organic triplets and diradicals, and a model Mn (II) complex, $\text{Mn}(\text{acac})_3$ (acac: acetylacetonate). In the case of plastocyanin, substantial agreement has been achieved between theory and experiment. For another copper protein, azurin, excellent results for nitrogen hyperfine constants were obtained. With regard to Mn (II), while the correct sign of D was obtained, its magnitude was too low, and theoretical reasons for this are indicated.

Betty Gaffney's Chapter 6 outlines a versatile approach for defining intermediate states of iron in various valence states in terms of geometry and electronic structures. Non-heme iron proteins have widely diverse functions, ranging from iron transport to redox chemistry, which is a reflection of considerable structural diversity. This chapter is a healthy reminder that x-ray structural information never stands on its own and must be supplemented by spectroscopic data from trapped intermediates. The first part of the chapter focuses on quantitative interpretation of EPR data for ferric, non-heme iron, and readers are referred to Biological Magnetic Resonance Volume 13 for more details regarding $S = 5/2$ spin systems [3]. Regimes where $h\nu < D$, important at X-band (9–10 GHz), and $h\nu > D$, which is relevant at W-band (94 GHz), are discussed. More technical issues include the "Aasa-Vanngard" factor needed in field-swept EPR, relaxation, distributions in zero field splittings, and identification of looping transitions, which can be very important at X-band.

Practical examples include the mononuclear low-spin ferric non-heme protein nitrile hydratase, several examples of $S = 1/2$ radical probes of Fe (II) including NO and non-heme Fe (II), and high-spin NO complexes with non-heme compounds, where ENDOR results elucidate ligand rearrangement in oxygenase-NO complexes. There are also cases where NO is a natural ligand for non-heme iron. Finally, results from low-spin NO complexes with non-heme iron proteins — e.g., protocatechuic 3,4 dioxygenase — are presented. The discussion of quinone-ferrous interactions in photosynthetic reaction centers and nitric oxide complexes with non-heme ferrous iron links appears in the later chapter by Luchsinger, Walter, Lee, Stander, and Singel.

In Chapter 7, Mitic, Schenk, and Hanson stated their purpose “was to provide the reader with an accessible means to navigate through an overwhelmingly rich topic in the field of bioinorganic chemistry.... The article was not intended to target the EPR specialist specifically.” This is an extensive review of binuclear non-heme iron enzymes that covers four broad classes: oxygenases, including ribonucleotide reductase; iron transport and storage proteins such as ferritin, bacterioferritin, and rubrerythrin; oxygen storage and transport proteins, hemerythrin and myohemerythrin; and hydrolytic enzymes, such as purple acid phosphatase. The role played by x-ray crystal structures in relation to a variety of spectroscopic methods is emphasized. In addition to EPR, results from the Mössbauer Effect, Extended X-Ray Absorption Fine Structure (EXAFS), Magnetic Circular Dichroism (MCD), Nuclear Magnetic Resonance (NMR), and Resonance Raman spectroscopy are included, emphasizing that one cannot rely solely on any one spectroscopic technique. The presentations for each system begin with biochemical and structural characterization followed by spectroscopic characterization and “mechanistic” insights. Given the substantial list of references and the full descriptions in each case, those with a particular interest in any one of the proteins discussed will find ready information to help in their own quest, particularly important to anyone embarking on such investigations for the first time. The summary table provides a ready reference that readers should also find valuable.

Since so many different enzymes are described here, the flavor of this particular chapter can be illustrated by ribonucleotide reductase, e.g., class I ribonucleotide reductases, found in some eubacteria, viruses, and some prokaryotes. These have two homodimeric subunits — R1 and R2 — with an $\alpha_2\beta_2$ quaternary structure. The smaller R2 subunit houses a binuclear non-heme iron active site that utilizes dioxygen to generate a stable tyrosyl radical required for catalysis. Characterization of diferric R2 involved saturation recovery EPR, Mössbauer, resonance Raman, and EXAFS. Magnetization measurements were consistent with two strongly antiferromagnetically coupled high spin Fe^{3+} ions with exchange coupling lying in the range 180–216 cm^{-1} . By way of contrast, diferrous R2 is characterized by weakly antiferromagnetically coupled Fe^{2+} ions with an exchange coupling $\sim 1 \text{ cm}^{-1}$ and $S = 2$. A mixed valence form of R2 produced by cryogenic reduction at low temperatures appears to have an $S = 9/2$ ground state due to ferromagnetic coupling between Fe^{2+} and Fe^{3+} ions. On the other hand, the chemically reduced mixed valence form of R2 is consistent with an $S = 1/2$ ground state and an antiferromagnetic exchange constant of 34 cm^{-1} and a likely $\mu\text{-OH}$ bridge. This difference is thought to have involved a structural change. Further elucidation of these systems involving amino acid radicals in ribonucleotide reductase required high-field and high-frequency EPR, ENDOR, and pulsed ELDOR, which is sensitive to coupled spins up to 80 Å apart. The catalytic steps are outlined in some detail at the end of this section.

Chapter 8 by Van Doorslaer builds on Chapter 2 by Harmer et al., applies the ideas to a range of heme proteins, and provides a brief review of these methods, highlighting the advantages, limitations, and challenges for the future. In particular, there is a focus on multifrequency EPR, which has provided important insights into

the functioning of different heme proteins. Van Doorslaer points out that while the past 40 years have witnessed considerable development in multifrequency and pulse EPR techniques, the fact is they are not universally available in all laboratories. This convinces her that the full power of the EPR “toolbox” is not being exploited. Although X-band CW-EPR remains an inescapable part of the EPR “toolbox,” it cannot by itself provide definitive information about active sites. One needs, in addition, 2- and 3-pulse ESEEM, HYSCORE, and techniques such as SMART HYSCORE, which use matched pulses to achieve improved resolution.

In discussing low-spin ferric heme proteins, Van Doorslaer emphasizes the benefits of a multifrequency approach, particularly the use of S-band frequencies as well as X-band in relation to sum peaks in 2-pulse ESEEM and 4-pulse HYSCORE. This is important in Fe–H distance determinations. Particular examples relate to low-spin ferric Hb by means of SMART HYSCORE and CW-EPR of the NO-ligated E7Gin mutant of neuroglobin. There remains the problem of relating the g -axes to the molecular frame. Many high-spin Fe (III) heme proteins have the usual $g_{\parallel} = 2$ and $g_{\perp} = 6$ for axial Fe (III) when $D \gg h\nu$. At very high frequencies, D -strain contributes to an increase in linewidth. These considerations are judged important in connection with NO-ligated heme proteins such as NO synthase and nitrite reductase.

In Chapter 9, Luchsinger, Walter, Lee, Stander, and Singel provide an in-depth introduction to the field of NO in biology through a historical review that covers the period roughly from the 1970s until the present. The underlying motivation is how EPR spectra can elucidate the chemistry of vasodilatory activity. They draw attention to an important dilemma: how can the bioactivity of NO coexist with Hb, which is known to scavenge NO! This chapter highlights ways in which EPR techniques have helped understand the dilemma, in particular through the use of higher frequencies. NO is used to produce paramagnetic species such as heme–Fe(II)NO and heme–Fe(III), providing an important role for EPR as a tool to identify the valence state of iron, but also to monitor changes during reactions. The fact that heme–NO adducts can be formed raises important questions about their biological roles. A decade ago Singel and Lancaster [4] established that a broader role existed for EPR spectroscopy in this field from being simply an analytical probe for NO into a spectroscopic method of choice for characterizing the structure and function of NO adducts.

Topics covered include the basic heme–Fe(II)NO spectra, interesting observations regarding subunit behavior in Hb, subunit selectivity, and subunit spectral editing. Pulsed methods including Echo-Detected EPR are reported. The biochemical discussion and genetic implications are very detailed and will be left to the reader. This chapter provides a good deal of detail regarding EPR experiments that assist with illuminating processes involving Hb in humans and other organisms with mature cardiovascular systems. The summary in Chapter 9 (Section 3) will be found particularly illuminating and helpful.

Chapter 10 by Gastel and Lubitz is a review of EPR studies on (NiFe) hydrogenases, enzymes that contain (NiFe) centers as active sites. The authors lead the

the reader through a labyrinth with clarity and sophistication, and Figures 1 and 2 will be found particularly helpful in setting the stage for their presentation. The active sites are well understood, and these are fully described. During the catalytic cycle the enzyme passes through several redox states, several of which are paramagnetic. Iron remains as divalent low-spin (Fe^{II} , $S = 0$) throughout. Nickel, however, changes in both valence and spin state. Several distinct paramagnetic states have been identified, all of which are formal Ni^{III} species $S = 1/2$, and have a d_{z^2} ground state, whose orbital is oriented along the molecular z axis toward the open coordination site of the Ni. “EPR silent” states are all due to Ni^{II} species. High-spin ($S = 1$) states observed with EXAFS spectroscopy have not been confirmed by EPR. ENDOR and HYSCORE data confirm the presence of a $\mu\text{-OH}^-$ bridge in one case (Ni–B), whereas in another case (Ni–C) a formal $\mu\text{-H}^-$ bridge has been identified. The identification of the electronic and geometric structure of the reaction intermediates has involved a judicious mix of spectroscopy and quantum chemical calculations, and provides the basis for establishing the nature of the reaction mechanism for (NiFe) hydrogenase.

In Chapter 11, Yoon and Solomon review the role of copper in active sites in proteins, many of which are believed to play a major role in biological processes as diverse as long-range electron transfer, binding, activation, two-/four-electron reduction of dioxygen, and two-electron reduction of nitrous oxide. Copper sites have traditionally been divided into three types based on EPR properties: type 1 “blue,” type 2 “normal,” and type 3 “coupled binuclear” sites. The situation is now known to be more complicated, and several other characteristic structures are recognized, such as mixed-valent binuclear Cu_A , trinuclear Cu clusters in multicopper oxidases, and tetranuclear Cu_Z sites. This chapter reviews EPR and other spectral features of the different copper active sites and their relation to reactivity. The unique spectroscopic features are reported in relation to novel geometric and electronic structures that are intimately related to catalytic function. For example, a high level of covalency is demonstrated to activate specific pathways for long-range electron transfer and exchange interactions between copper centers that controls the two- versus one-electron activation of O_2 for different chemistries and four-electron reduction of O_2 to H_2O .

Chapter 12 by Liboiron emphasizes the importance of EPR in the study of antidiabetic vanadium (IV) compounds, in both naturally containing vanadium species and spin-labeled or metal-substituted systems. Important contributions to in vitro and in vivo properties of these complexes have been made possible through EPR spectroscopy over the past 25 years, which has led to major advances in the optimization of chemical structures, formulation, and descriptions of vanadium metabolism in relation to vanadium antidiabetic pharmaceuticals. Vanadium compounds include potent antidiabetic agents that can normalize blood glucose levels and lipid metabolism. In particular, vanadyl ($[\text{V}^{\text{IV}}\text{O}]^{2+}$) coordination complexes offer potential new treatment options for one form of diabetes. EPR studies have assisted with improved understanding of the solution chemistry, absorption, metabolism, and bioaccumulation of antidiabetic vanadium species. However, there is yet much that remains to be understood concerning the mechanism of insulin-

enhancement by vanadium (IV) compounds. Undoubtedly, EPR, ENDOR, and ESEEM will all have a role to play in its elucidation.

Chapter 13 by Levina, Codd, and Lay, deals with possible medical applications of chromium compounds. Carcinogenicity and antidiabetic effects of chromium compounds, originally thought to be quite distinct biologically, are found to depend on varying amounts of Cr (VI) and reactive intermediates, such as Cr (V) species, formed in vivo either by reduction of Cr (VI) or by oxidation of Cr (III) complexes. The cartoon in Figure 1 should prove very helpful to those readers unfamiliar with chromium chemistry and its applications.

EPR spectroscopy is an important tool for investigations of Cr (V) and other reactive intermediates of relevance to the biological activities of Cr (VI) and Cr (III) compounds. Cr (V) complexes possess a d^1 electronic configuration that is ideal for EPR detection of Cr (V) intermediates formed in biological systems exposed to Cr (VI) and also, potentially, to Cr (III) complexes. Low-frequency (L-band) EPR spectroscopy opens up the possibility for detection of weak Cr (V) signals in whole living plants or animals. Correlations between EPR spectroscopic parameters, such as the g_{iso} values and superhyperfine splitting patterns, have been refined through extensive model studies, and these help to identify Cr (V) complexes with carbohydrate and glycoprotein ligands as the most abundant Cr (V) species formed in biological systems. EPR has proved less useful for characterizing biologically relevant Cr (III) complexes (d^3 -systems) due to low sensitivity and broad signals. The chapter covers the role of reactive intermediates in Cr (VI)-induced toxicity, antidiabetic effects of Cr (III), isolation and characterization of Cr (V) complexes with biological and biomimetic ligands, EPR spectroscopy parameters related to structural characterization of Cr (V) complexes, Cr (V) complexes of carbohydrates, Cr (III) and Cr (IV) species, free radicals as intermediates in Cr biochemistry, and reference to living cell and animal studies.

The final chapter — by Caravan, Zech, and Raitsimring — provides a broad overview of Magnetic Resonance Imaging (MRI) contrast agents and the need for EPR studies to characterize them. High-frequency EPR and ENDOR techniques have made a significant difference in the characterization of gadolinium-based MRI contrast agents and led to an improved understanding of their mechanisms of action and to improved design of potent nuclear relaxation agents. These have been focused on four areas: field-dependent electronic relaxation behavior of Gd (III) complexes in aqueous solution; an understanding of the parameters that define the fine structure among different contrast agents; the hydration number and the gadolinium–water proton distance. Each of these topics is reviewed and critiqued in some detail. The chapter is aimed at scientists interested in the design of new MRI contrast agents, the EPR of high-spin ions, and the coordination chemistry of lanthanide ions in aqueous media. A combination of multifrequency, pulsed or CW, EPR, and ENDOR methodologies are often the only means of directly probing questions such as the metal-to-hydrogen bond distance. Unlike other physical techniques, these methods are applicable to studying contrast ions in biological media at micromolar metal ion concentrations.

Particular matters covered include the frequency dependence of Gd (III) electronic relaxation in aqueous solution, elucidation of fine structure parameters for Gd (III) complexes in frozen solutions using high-field EPR, high-field pulsed ENDOR of water ligands in MRI agents, ^{17}O ENDOR measured at high fields and the benefits of Mims ENDOR, ^1H ENDOR of Gd (III) aquo ion using the central $\frac{1}{2} \leftrightarrow -\frac{1}{2}$ Gd (III) transition, and determination of the hydration numbers for Gd (III) complexes from high-field pulsed ^{17}O and ^1H ENDOR. While this investigation is about applications of EPR methods, a byproduct has been an improved understanding of the bonding of aqua ligands to lanthanide ions. The advances described here have served to make some of these applications routine, to a point where the techniques can be applied by non-spectroscopists working in the contrast agent field.

REFERENCES

1. Ehrenberg A, Malmström BG, Vanngård, T, eds. 1967. *Magnetic resonance in biological systems*. Oxford: Pergamon Press.
2. Schweiger A, Jeschke G. 2001. *Principles of pulse electron paramagnetic resonance*. Oxford: Oxford UP.
3. Gaffney BJ, Silverstone HJ. 1993. Simulation of the EMR spectra of high-spin iron in proteins. In *EMR of paramagnetic molecules*, pp. 1–57. *Biological magnetic resonance*, Vol. 13. Ed LJ Berliner, J Reuben. New York and London: Plenum.
4. Singel DJ, Lancaster Jr JR. 1996. Electron paramagnetic resonance spectroscopy and nitric oxide biology. In *Methods in nitric oxide research*, pp. 341–356. Ed M. Feelisch, JS Stamler. New York: John Wiley.

HIGH-RESOLUTION EPR METHODS

ADVANCED PULSE EPR METHODS FOR THE CHARACTERIZATION OF METALLOPROTEINS

Jeffrey Harmer, George Mitrikas, and Arthur Schweiger

Laboratory of Physical Chemistry, Department of Chemistry and Applied Biosciences, ETH-Zürich, Switzerland

Electron Spin Echo Envelope Modulation (ESEEM) and pulse Electron Nuclear Double Resonance (ENDOR) experiments are considered to be two cornerstones of pulse EPR spectroscopy. These techniques are typically used to obtain the static spin Hamiltonian parameters of powders, frozen solutions, and single crystals. The development of new methods based on these two effects is mainly driven by the need for higher resolution, and therefore, a more accurate estimation of the magnetic parameters. In this chapter, we describe the inner workings of ESEEM and pulse ENDOR experiments as well as the latest developments aimed at resolution and sensitivity enhancement. The advantages and limitations of these techniques are demonstrated through examples found in the literature, with an emphasis on systems of biological relevance.

1. INTRODUCTION

During the last decades, electron paramagnetic resonance (EPR) has become a powerful spectroscopic method for studying compounds containing paramagnetic species. Applications abound in the study of transition metal complexes, organic and inorganic radicals, and paramagnetic metalloproteins. In biological systems containing one or more unpaired electrons, EPR spectroscopy can provide unique information on the electronic and geometric structure since magnetic data such as g -values, hyperfine couplings, and nuclear quadrupole parameters are directly related to the electronic wavefunction and the local environment of the paramagnetic center. The g -values and, for species with several unpaired electrons ($S > 1/2$), the zero-field splitting often provide fingerprint information on the type of paramagnetic species. The hyperfine couplings characterize the spin density distribution in detail and can give access to distances between the nuclei and the unpaired electron up to approximately 1 nm. The nuclear quadrupole interactions provide information on the bonding of nuclei and can also be utilized to determine bond angles. For

these reasons, EPR spectroscopy is well suited for structural studies in systems lacking long-range order on length scales that are not easily accessible by other techniques.

In powders, frozen solutions and even single crystals, many of the hyperfine and nuclear quadrupole splittings are typically not resolved in the field-swept EPR spectrum due to inhomogeneous broadening effects. In transition metal complexes, for example, often only the largest hyperfine coupling from the metal ion is observed. This lack of resolution is mainly due to the transition selection rules, which show that the number of EPR lines increases multiplicatively, $N_{\text{EPR}} = \prod_k (2I_k + 1)$,

where the product is over the total number of nuclei (k) with spin quantum numbers $I_k > 0$. The resolution limitation in field-swept EPR methods can be overcome by measuring nuclear frequency spectra directly with pulse techniques. In this case the number of lines increases in an additive way, $N_{\text{NF}} = \sum_k I_k$. By directly measuring

nuclear frequency spectra, EPR spectroscopy can access both strong and very weak interactions and, consequently, characterize the system under study in more detail.

The pulse EPR methods discussed here for measuring nuclear transition frequencies can be classified into two categories. The first involves using electron nuclear double resonance (ENDOR) techniques where the signal arises from the excitation of EPR and NMR transitions by microwave (m.w.) and radiofrequency (r.f.) irradiation, respectively. In the second class of experiments, based on the electron spin echo envelope modulation (ESEEM) effect, the nuclear transition frequencies are indirectly measured by the creation and detection of electron or nuclear coherences using only m.w. pulses. No r.f. irradiation is required. ENDOR and ESEEM spectra often give complementary information. ENDOR experiments are especially suited for measuring nuclear frequencies above approximately 5 MHz, and are often most sensitive when the hyperfine interaction is not very anisotropic. Conversely, anisotropic interactions are required for an ESEEM effect, and the technique can easily measure low nuclear frequencies.

Following the rapid development of pulse EPR spectroscopy during the last few decades, pulse EPR methods based on ENDOR and ESEEM effects have been successfully applied to characterize paramagnetic systems containing transition metal ions [1–6]. Together with this ever-increasing number of applications, there is an ongoing effort to develop new methods aimed at resolution and/or sensitivity enhancement [7]. Nowadays, there is a large variety of pulse EPR experiments that can specifically address a given problem and provide optimum resolution. Furthermore, results from such advanced experiments are often more easily interpreted because fewer assumptions are required. The aim of this contribution is to give an up-to-date overview of the existing pulse EPR experiments based on ENDOR and ESEEM effects and to illustrate their advantages and limitations by reference to recent applications.

The present chapter is structured as follows. In §2 the most important terms of the spin Hamiltonian are introduced and the relevant properties of nuclear fre-

quency spectra are discussed. The concept of orientation selection, which is of particular importance in disordered systems in EPR, is also presented. Section 3 gives an overview of experiments based on the ESEEM effect, starting with a short description of the origin of the nuclear modulation effect. After introducing the basic two- and three-pulse experiments in one dimension, special attention is paid to high-resolution two-dimensional methods such as hyperfine sublevel correlation spectroscopy (HYSCORE), as well as to special detection schemes for eliminating spectral artifacts. The concept of sensitivity enhancement using matched m.w. pulses is described and specific techniques developed in order to separate interactions from each other, i.e., hyperfine decoupling, are presented. Section 4 gives an overview of pulse ENDOR experiments. A brief introduction to the standard Davies and Mims ENDOR sequences is given. We then present a description of a selection of 2D experiments, as well as methods aimed at determining the sign or relative sign of the hyperfine interaction. A brief discussion of high-field ENDOR, resolution and sensitivity, and the hyperfine enhancement effect is presented. In §5, 2D field-swept EPR techniques for unraveling different interactions that contribute to a complex EPR lineshape are discussed (nutration experiments and electron Zeeman-resolved EPR).

2. SPIN HAMILTONIAN

This section gives an explanation of the different terms of the static spin Hamiltonian. The concept of orientation selection by selective m.w. excitation, which is central to many pulse EPR experiments on disordered systems, is explained.

2.1. Static Spin Hamiltonian

The static spin Hamiltonian is used to describe the energies of states of a paramagnetic species in the ground state with an effective electron spin S and m nuclei with spins I .

$$\mathcal{H}_0 = \mathcal{H}_{EZ} + \mathcal{H}_{ZFS} + \mathcal{H}_{HF} + \mathcal{H}_{NZ} + \mathcal{H}_{NQ} \quad (1a)$$

$$= \beta_e \tilde{\mathbf{B}}_0 \mathbf{g} \mathbf{S} / \hbar + \tilde{\mathbf{S}} \mathbf{D} \mathbf{S} + \sum_{k=1}^m \tilde{\mathbf{S}} \mathbf{A}_k \mathbf{I}_k - \beta_n \sum_{k=1}^m g_{n,k} \tilde{\mathbf{B}}_0 \mathbf{I}_k / \hbar + \sum_{I_k > 1/2} \tilde{\mathbf{I}}_k \mathbf{P}_k \mathbf{I}_k. \quad (1b)$$

In this review all interactions are given in angular frequency units unless stated otherwise. \mathcal{H}_0 is called the spin Hamiltonian since it contains only phenomenological constants and spin coordinates described by the electron spin vector operator $\tilde{\mathbf{S}} = [\hat{S}_x, \hat{S}_y, \hat{S}_z]$ and the nuclear spin vector operators $\tilde{\mathbf{I}}_k = [\hat{I}_{x,k}, \hat{I}_{y,k}, \hat{I}_{z,k}]$. \mathbf{B}_0 is a vector describing the direction and strength of the permanent magnetic field. The transpose is denoted with a tilde. The terms describe: \mathcal{H}_{EZ} , electron Zeeman interaction; \mathcal{H}_{ZFS} , zero-field splitting; \mathcal{H}_{HF} , hyperfine interactions between the electron

spins and m nuclear spins; \mathcal{H}_{NZ} , nuclear Zeeman interactions; \mathcal{H}_{NQ} , nuclear quadrupole interactions for $I > 1/2$. Equation (1) ignores high-order electron spin operators, and the spin–spin interactions between pairs of nuclear spins since its magnitude is very small compared to the other terms and the usual linewidths observed in paramagnetic complexes.

The information obtained from the spin Hamiltonian, the 3×3 matrices \mathbf{g} , \mathbf{D} , \mathbf{A} , and \mathbf{P} , is very sensitive to the geometric and electronic structure of the paramagnetic center. The electron Zeeman interaction reveals information about the electronic states; the zero-field splitting describes the coupling between electrons for systems where $S > 1/2$; the hyperfine interactions contain information about the spin density distribution [8] and can be used to evaluate the distance and orientation between the unpaired electron and the nucleus; the nuclear Zeeman interaction identifies the nucleus; the nuclear quadrupole interaction is sensitive to the electric field gradient at the site of the nucleus and thus provides information on the local electron density.

The hyperfine interaction is a key source of information on the spin density distribution. It can be written as the sum of the isotropic interaction or Fermi contact interaction \mathcal{H}_{F} and the electron–nuclear dipole–dipole coupling \mathcal{H}_{DD} :

$$\mathcal{H}_{\text{HF}} = \mathcal{H}_{\text{F}} + \mathcal{H}_{\text{DD}} = a_{\text{iso}} \tilde{\mathbf{S}}\mathbf{I} + \tilde{\mathbf{S}}\mathbf{T}\mathbf{I}. \quad (2)$$

Here a_{iso} is the isotropic hyperfine coupling constant that is directly related to $|\psi_o(\mathbf{0})|^2$, the electron spin density at the nucleus:

$$a_{\text{iso}} = \frac{2\mu_0}{3\hbar} g_e \beta_e g_n \beta_n |\psi_o(\mathbf{0})|^2. \quad (3)$$

Often a_{iso} is used to estimate the s-orbital spin population on the corresponding nucleus [9] (see, e.g., [10]). In Eq. (2) matrix \mathbf{T} describes the anisotropic dipole–dipole coupling. The dominant contribution to \mathcal{H}_{DD} , for nuclei other than protons, usually comes from the interaction of an electron spin in a p-, d-, or f-type orbital with the magnetic moment of the corresponding nucleus. By reference to suitable tables the dipole–dipole coupling can also be used to estimate the spin population in these orbitals [10]. For distances $r_{\mathbf{k}}$ between the electron and nuclear spin greater than approximately 0.25 nm, the anisotropic part of the hyperfine interaction can be used to calculate the electron–nuclear distance and orientation with the electron–nuclear point–dipole formula:

$$\mathbf{T} = \frac{\mu_0}{4\pi\hbar} g_e \beta_e g_n \beta_n \sum_{\mathbf{k} \neq \mathbf{N}} \frac{\rho_{\mathbf{k}} (3\tilde{\mathbf{n}}_{\mathbf{k}} \mathbf{n}_{\mathbf{k}} - \mathbf{1})}{r_{\mathbf{k}}^3}, \quad (4)$$

where the sum is over all nuclei with spin population $\rho_{\mathbf{k}}$ at distance $r_{\mathbf{k}}$ from the nucleus with the electron–nucleus unit vector $\mathbf{n}_{\mathbf{k}}$. For an axial interaction with positive g_n , $\mathbf{T} = [-T, -T, 2T]$. Equation (4) gives very accurate information on proton positions provided the spin density distribution is known. It is also worth noting

that in many transition metal complexes there is a substantial orbital magnetic moment that adds pseudo-isotropic and pseudo-anisotropic contributions, and can be taken into account with $\mathbf{A} = a_{\text{iso}}\mathbf{1} + \mathbf{gT}/g_e$ [11,12]. For systems with large g and/or T anisotropy this contribution to \mathbf{A} cannot be neglected and needs to be included, particularly when analyzing high-resolution experiments like HYSCORE.

The spin Hamiltonian parameters of a complex or a model system can in principle be determined from a quantum chemical calculation of the electronic structure. The Density Functional Theory (DFT) [13] method is at present popular for this purpose, since it allows fairly large systems (~ 200 atoms) to be investigated. By comparing the calculated and experimental spin Hamiltonian parameters it is often possible to distinguish between different proposed models and to gain further insight into the electronic and geometric structure of the sample.

2.2. Nuclear Frequency Spectra of Spin Systems with $S = 1/2$ and Arbitrary I

Under the assumption $\mathcal{H}_{\text{EZ}} \gg \mathcal{H}_{\text{HF}} \gg \mathcal{H}_{\text{NQ}}$, the first-order nuclear frequencies ($\omega^{(1)}$) for a nuclear spin I and an arbitrary orientation of the \mathbf{B}_0 field are given by

$$\omega^{(1)}(m_s, m_l \leftrightarrow m_l + 1) = c(m_s) + \frac{3}{2}P'_{zz}(m_s)(2m_l + 1), \quad (5)$$

where

$$c(m_s) = \sqrt{\tilde{\mathbf{n}}\left(m_s \frac{\mathbf{gA}}{g} + \omega_l \mathbf{1}\right)(m_s \frac{\widetilde{\mathbf{gA}}}{g} + \omega_l \mathbf{1})\mathbf{n}}, \quad (6)$$

and

$$P'_{zz}(m_s) = \frac{1}{c(m_s)^2} \tilde{\mathbf{n}}\left(m_s \frac{\mathbf{gA}}{g} + \omega_l \mathbf{1}\right) \mathbf{P}\left(m_s \frac{\widetilde{\mathbf{gA}}}{g} + \omega_l \mathbf{1}\right) \mathbf{n}. \quad (7)$$

\mathbf{n} is a unit vector describing the orientation of \mathbf{B}_0 in the molecular frame. For the special case when \mathbf{g} , \mathbf{A} , and \mathbf{P} are coaxial and \mathbf{B}_0 is parallel to one of the principal values A_i , Eq. (5) reduces to

$$\omega^{(1)} = \left| \frac{A_i}{2} \pm \omega_l \right| \quad \text{for } I = 1/2, \quad (8a)$$

$$\omega^{(1)} = \left| \frac{A_i}{2} \pm \omega_l \pm \frac{3}{2}P_i \right| \quad \text{for } I = 1, \quad (8b)$$

$$\omega^{(1)} = \left| \frac{A_i}{2} \pm \omega_l \pm \frac{3}{2}P_i(2m_l + 1) \right| \quad \text{for } I > 1. \quad (8c)$$

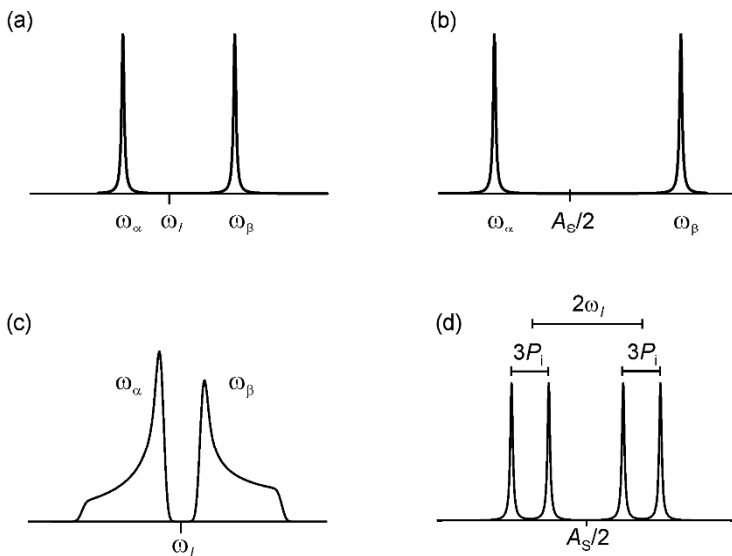


Figure 1. Typical nuclear frequency spectra for an $S = \frac{1}{2}$ spin system with one nuclear spin: (a) single-crystal, $I = \frac{1}{2}$, $2|\omega_i| > |A_S|$, $\omega_i < 0$, $A_S > 0$; (b) single crystal, $2|\omega_i| < |A_S|$; (c) powder spectrum for an axial hyperfine interaction; (d) single crystal, $I = 1$ with \mathbf{B}_0 along a principal axis. Modified with permission from [7]. Copyright © 2001, Oxford University Press.

For an $I = \frac{1}{2}$ spin system Eq. (8a) shows that there are two frequencies symmetrically centered around $|\omega_i|$ (weak coupling case; $2|\omega_i| < |A_i|$) or $A_i/2$ (strong coupling case; $2|\omega_i| > |A_i|$). If the hyperfine interaction is anisotropic and \mathbf{B}_0 is not along one of the principal values, then the peaks are shifted to higher frequencies as, shown in Figure 1a,b. This shift is exploited in 2D techniques like HYSSCORE. For nuclear spin $I > \frac{1}{2}$, there is an additional splitting of the lines due to the nuclear quadrupole interaction (Fig. 1d).

The energy level diagram for an $S = \frac{1}{2}$, $I = 1$ spin system is shown in Figure 2, and has four single-quantum (SQ) NMR transitions and two double-quantum (DQ) NMR transitions. In ENDOR spectroscopy, usually only the SQ transitions are observed; in ESEEM experiments both SQ and DQ transitions can be observed.

2.3. Orientation Selection in Pulse EPR

A resonator can be considered as a bandpass filter. The excitation bandwidth $\Delta\nu$ is determined by the resonator quality factor Q_L and is given by $Q_L = \nu/\Delta\nu$. For example, at X-band with $\nu = 9.8$ GHz and $Q_L = 100$, a total bandwidth of approximately 100 MHz or 3.5 mT is excited. In addition to the resonator, the excitation width of the m.w. pulse needs to be considered. With the maximum available microwave power and Q_L value the B_1 field strength is such that a $\pi/2$ -pulse requires typically ~ 10 ns (a rectangular pulse of width L has a sinc function in the frequency domain with a full width at half height of $\approx 3.79/(2\pi L)$ Hz).

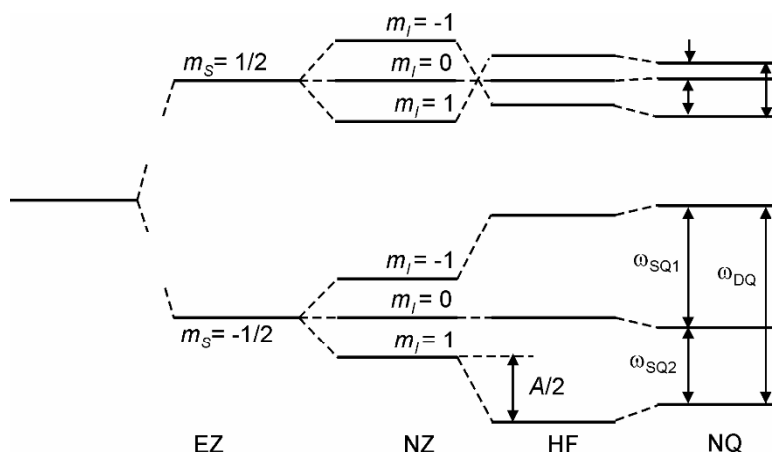


Figure 2. Energy level diagram for an $S = 1/2, I = 1$ spin system in the strong coupling case, $2|\omega_i| < |A_s|$.

The resulting excitation bandwidth may be enough to excite the complete spectrum of an organic radical at X-band, but typically only excites a narrow region of the spectrum from a transition metal complex. Consider for example the EPR spectrum of Cob(II)alamin with g -values of $g_1 = 2.272, g_2 = 2.230, g_3 = 2.004$ [14]. At X-band the EPR spectrum has a width of 90 mT (~ 2 GHz), and at W-band it is 400 mT (~ 11 GHz) wide. The effective excitation bandwidth of the pulse, in comparison to the EPR spectrum, thus provides orientation selection in disordered samples. This orientationally selective excitation allows the magnetic interactions, with respect to the g -matrix coordinate system, to be estimated.

Figure 3a shows a calculated EPR spectrum for a rhombic g -matrix (the g -values correspond to the so called “red2” signals from methyl coenzyme reductase) [15]. For a pulse experiment (e.g., ENDOR or HYSCORE) preformed at the field position corresponding to g_1 , only molecules with their g_1 axis (\mathbf{g}_1) oriented along or close to \mathbf{B}_0 contribute to the experiment. At the high-field end at the observer position corresponding to g_3 , only molecules with \mathbf{g}_3 oriented close to or along \mathbf{B}_0 contribute to the experiment. These positions, at the extreme high- and low-field ends of the EPR spectrum, are referred to as “single-crystal” like. With \mathbf{B}_0 at the observer position corresponding to the g_2 value, many orientations of the paramagnetic center are resonant with the m.w. pulse and contribute to the experiment. Figure 3b,c shows a calculation for Cob(II)alamin at X-band and Q-band, respectively. At X-band, the orientation selection for experiments performed at the field positions corresponding to g_1 and g_2 are particularly poor since the small g -anisotropy and large cobalt hyperfine interaction result in many orientations contributing to the experiment. At Q-band the situation is much improved and two “single-crystal” like positions are possible at the low- and high-field ends.

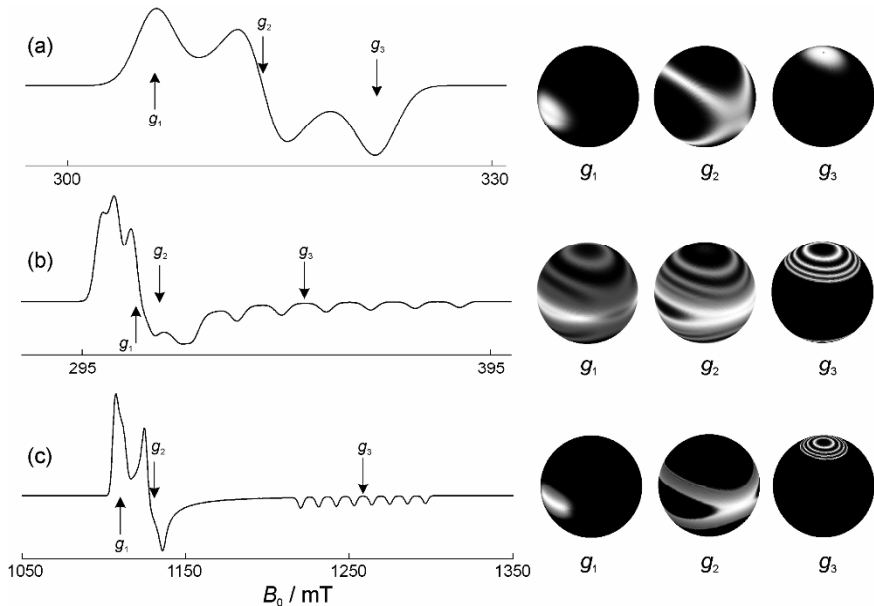


Figure 3. Calculated EPR spectra and orientation selection on the unit sphere for the observer (B_0 field) positions corresponding to g_1 , g_2 , and g_3 . White indicates orientations on-resonance with the m.w. pulse, black shading is off-resonance. The m.w. pulse for the orientation selection has a width of 25 MHz. (a) Orthorhombic spectrum of MCR_{red2} ¹⁵ at X-band (9.8 GHz) with g -values of $g_1 = 2.287$, $g_2 = 2.231$, $g_3 = 2.175$, and a linewidth of 100 MHz. (b) spectrum of Cob(II)alamin¹⁴ with $g_1 = 2.272$, $g_2 = 2.230$, $g_3 = 2.004$, cobalt ($I = 7/2$) hyperfine couplings $A_1 = 30$ MHz, $A_2 = 40$ MHz, $A_3 = 305$ MHz, and a linewidth of 50 MHz. (c) same as in (b) but at Q-band (35.3 GHz).

3. ESEEM BASICS

3.1. Origin of the Nuclear Modulation Effect

The nuclear modulation effect was first observed by Rowan, Hahn, and Mims [16], and the theory was later developed by Mims in 1972 [17]. The origin of the nuclear modulation effect can be understood with a semi-quantitative discussion using a two-spin model system consisting of one electron spin ($S = 1/2$) and one nuclear spin ($I = 1/2$). Assuming an isotropic g -matrix and an anisotropic hyperfine interaction, the spin Hamiltonian in the rotating frame can be written as

$$\mathcal{H}_0 = \Omega_S S_z + \omega_I I_z + A S_z I_z + B S_x I_x, \quad (9)$$

where $\Omega_S = \omega_S - \omega_{mw}$ is the resonance offset of the electron Zeeman frequency ($\omega_S = g\beta_e B_0 / \hbar$) from the m.w. frequency ω_{mw} , and A , B describe the secular and

pseudo-secular part of the hyperfine coupling. In the case of an axially symmetric hyperfine interaction, A and B are given by

$$A = a_{\text{iso}} + T(3 \cos^2 \theta - 1), \quad B = 3T \sin \theta \cos \theta. \quad (10)$$

T and a_{iso} are the dipolar and the isotropic hyperfine coupling and θ is the angle between the electron–nuclear vector and the external static magnetic field \mathbf{B}_0 .

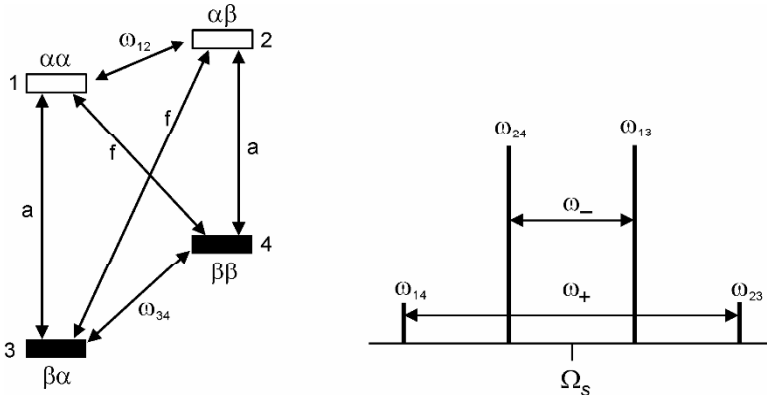


Figure 4. Energy level diagram (left) and corresponding schematic EPR spectrum (right) for an $S = 1/2$, $I = 1/2$ model system with $|A_S| < |2\omega_I|$ (weak-coupling case): **a**: allowed EPR transitions (1,3) and (2,4); **f**: forbidden EPR transitions (1,4) and (2,3); nuclear transitions (1,2) and (3,4). Modified with permission from [7]. Copyright © 2001, Oxford University Press.

In this four-level system, shown in Figure 4, there are two allowed ($\Delta m_S = \pm 1$, $\Delta m_I = 0$) and two forbidden ($\Delta m_S = \pm 1$, $\Delta m_I = \pm 1$) EPR transitions with frequencies given by

$$\begin{aligned} \omega_{13} &= \omega_S + \omega_- / 2, \\ \omega_{24} &= \omega_S - \omega_- / 2, \\ \omega_{14} &= \omega_S + \omega_+ / 2, \\ \omega_{23} &= \omega_S - \omega_+ / 2, \end{aligned} \quad (11)$$

with $\omega_+ = \omega_\alpha + \omega_\beta$, $\omega_- = \omega_\alpha - \omega_\beta$, and the nuclear frequencies ω_α and ω_β corresponding to the two NMR transitions being given by

$$\omega_\alpha = |\omega_{12}| = \left[\left(\omega_I + \frac{A}{2} \right)^2 + \left(\frac{B}{2} \right)^2 \right]^{1/2}, \quad \omega_\beta = |\omega_{34}| = \left[\left(\omega_I - \frac{A}{2} \right)^2 + \left(\frac{B}{2} \right)^2 \right]^{1/2}. \quad (12)$$

The transition probabilities of the allowed (I_a) and forbidden (I_f) EPR transitions are given by Eq. (13), where 2η is the angle between the nuclear quantization axes in the two m_S manifolds with respect to \mathbf{B}_0 [7]:

$$I_a = \cos^2 \eta = \frac{|\omega_I^2 - \frac{1}{4}\omega_-^2|}{\omega_\alpha \omega_\beta}, \quad I_f = \sin^2 \eta = \frac{|\omega_I^2 - \frac{1}{4}\omega_+^2|}{\omega_\alpha \omega_\beta}. \quad (13)$$

For the isotropic coupling case ($T = 0$) the B term vanishes and $I_a = 1$, $I_f = 0$. Then the EPR stick spectrum (Fig. 4, right) consists of only two lines corresponding to the allowed transitions split by $\omega_- = a_{\text{iso}}$. The addition of an anisotropic part to the hyperfine coupling ($T \neq 0$) mixes the energy levels so that they are no longer pure α or β with respect to the nuclear spin state. This in turn results in a nonzero probability for the forbidden EPR transitions, which provides the basis of the ESEEM effect.

3.2. Two- and Three-Pulse ESEEM

In the two-pulse ESEEM experiment (Fig. 5a), the intensity of the primary echo is recorded as a function of the time interval τ between the $\pi/2$ and π pulses. The modulation formula for an $S = 1/2$, $I = 1/2$ spin system is given by

$$V_{2p}(\tau) = 1 - \frac{k}{4} [2 - 2\cos(\omega_\alpha \tau) - 2\cos(\omega_\beta \tau) + \cos(\omega_- \tau) + \cos(\omega_+ \tau)], \quad (14)$$

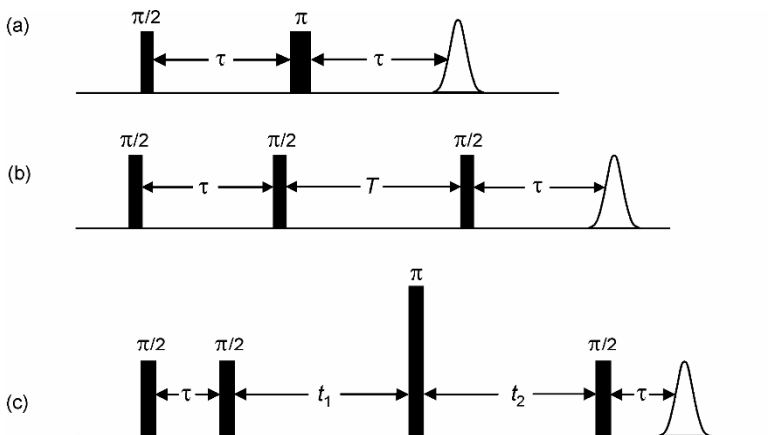


Figure 5. Pulse sequences making use of the ESEEM effect. (a) Two-pulse sequence and the primary echo. (b) Three-pulse sequence and the stimulated echo. (c) Four-pulse sequence for the HYSORE experiment.

where k is the orientation-dependent modulation depth parameter given by

$$k(\theta) = \left(\frac{B\omega_I}{\omega_\alpha\omega_\beta} \right)^2 \quad (15)$$

For the case of an isotropic hyperfine interaction $\mathbf{A}=a_{\text{iso}}\mathbf{I}$, or if \mathbf{B}_0 is oriented along one of the principal axes of the hyperfine tensor ($\theta = 0$ or $\theta = \pi/2$), the echo modulation disappears, since in either of these cases the quantity B in Eq. (15) becomes zero.

Equation 14 consists of an unmodulated part with amplitude $1 - k/2$, the basic frequencies ω_α and ω_β with amplitudes $k/2$, and the combination frequencies ω_- and ω_+ with amplitudes $k/4$, and inverted phase. To compute the frequency-domain spectrum, first the unmodulated part is subtracted, as it gives a dominant peak at zero frequency for the usual case of small k values. A cosine Fourier transform (FT) of the time trace results in a spectrum that contains the two nuclear frequencies, ω_α and ω_β , with positive intensity, and their sum and difference frequencies, ω_+ and ω_- , with negative intensity. If the initial part of the time-domain trace is missing, then the spectrum can be severely distorted by frequency-dependent phase shifts and it may be best to FT the time-domain trace and compute the magnitude spectrum.

In multinuclear spin systems the echo modulation is given by the product rule [17]:

$$V_{2p}(\tau) = \prod_i^N V_{2p}^i(\tau), \quad (16)$$

where $V_{2p}^i(\tau)$ is given by Eq. (14) and N is the number of nuclei coupled to the electron spin. In this case the spectrum contains, in addition to the four basic frequencies, combination frequencies. Combination frequencies arise from the sum or difference of nuclear frequencies from different nuclei of the same paramagnetic center. The simple form of Eq. (16) can be used to identify modulations originating from specific nuclei. This can be achieved by dividing the time traces from two samples, one before and one after isotopic substitution of the nucleus of interest. As a consequence of the product rule, all modulation components that are common to the two samples vanish when the ratios of the two ESEEM time traces are calculated [18,19].

The main shortcoming of the two-pulse experiment is that the primary echo decays within the phase memory time, T_M , which is often very short. This can prevent the observation of low-frequency modulations, and thus the estimation of the magnetic parameters can become uncertain. Another important limitation arises from the spectrometer deadtime τ_d (typically 100–150 ns at X-band frequencies), which restricts the observation of the signal to times $t > \tau_d$. The loss of the initial part of the time trace can cause severe distortions in the frequency-domain spectrum, especially in disordered systems where destructive interference from differ-

ent resonance frequencies is more pronounced. The initial part of the time trace can be recovered by employing a remote-echo detection scheme (see §3.4).

The disadvantage of the fast echo decay in two-pulse ESEEM can be circumvented with the three-pulse ESEEM experiment shown in Figure 5b. In this pulse sequence the first two $\pi/2$ pulses create nuclear coherence that develops during the evolution time T and decays with the transverse nuclear relaxation time T_{2n} , which is usually much longer than the corresponding relaxation time T_M of the electrons. The third $\pi/2$ pulse transfers the nuclear coherence back to observable electron coherence. The modulation of the stimulated echo is given by

$$V_{3p}(\tau, T) = \frac{1}{2}[V^\alpha(\tau, T) + V^\beta(\tau, T)], \quad (17a)$$

with the contribution from the α electron spin manifold

$$V^\alpha(\tau, T) = 1 - \frac{k}{2}[1 - \cos(\omega_\beta \tau)][1 - \cos(\omega_\alpha(\tau + T))], \quad (17b)$$

and an analogous expression for $V^\beta(\tau, T)$:

$$V^\beta(\tau, T) = 1 - \frac{k}{2}[1 - \cos(\omega_\alpha \tau)][1 - \cos(\omega_\beta(\tau + T))]. \quad (17c)$$

It is worth reiterating that nuclear coherence, comprising nuclear frequencies of the spin system, is created by the first two m.w. pulses. During evolution time T the nuclear coherence accumulates phase, and the transfer of this nuclear coherence back to electron coherence with the third m.w. pulse causes the stimulated echo intensity to be modulated by the nuclear frequencies, enabling their measurement.

When T is varied the echo envelope is modulated only by the two basic frequencies ω_α and ω_β , the sum and difference frequencies do not appear, in contrast to the two-pulse ESEEM experiment. This is usually advantageous, as it simplifies spectra, but it may also be a disadvantage for disordered systems where the sum-combination line is often the only narrow feature in the ESEEM spectrum. Another important difference is the dependence of the three-pulse ESEEM amplitudes on τ , as is apparent from Eq. (17) by the factors $1 - \cos(\omega_\beta \tau)$ and $1 - \cos(\omega_\alpha \tau)$. Due to this suppression effect, individual peaks in the spectrum can disappear completely. These blind spots occur for the $\alpha(\beta)$ peak when $\tau = 2\pi n/\omega_{\beta(\alpha)}$ ($n = 1, 2, \dots$). In principle they can be avoided by using $\tau < 2\pi/\omega_{\max}$, where ω_{\max} is the maximum nuclear frequency; however, this is usually precluded by the spectrometer deadtime. Consequently, the three-pulse ESEEM experiment has to be performed at several τ values to avoid misinterpretation of the spectra due to blind-spot artifacts.

For several nuclear spins the product rule gives [20]

$$V_{3p}(\tau, T) = \frac{1}{2} \left[\prod_{l=1}^N V_l^\alpha(\tau, T) + \prod_{l=1}^N V_l^\beta(\tau, T) \right]. \quad (18)$$

As a consequence of Eq. (18), combinations of the nuclear frequencies occur only within the same electron spin manifold, in contrast to the two-pulse experiment. This allows the relative sign of two hyperfine couplings to be determined if combination peaks are observed [14]. Another consequence of the product rule is an effect where nuclei with deep modulations partially or completely suppress signals from nuclei with shallow modulations [21]. For example, a ^{14}N nucleus close to the cancellation regime at X-band will have a large modulation depth, and can completely suppress weaker ^1H or ^{19}F signals. This additional suppression effect has a serious impact on spectral intensities and can lead to misinterpretation of spectral features, for instance, when spectra from a compound in nondeuterated and deuterated solvents are compared. Such experiments are often used to identify exchangeable protons by the disappearance or reduction in intensity of certain ^1H lines [22]. However, deuterons with deep modulations can suppress all ^1H peaks. Due care therefore has to be exercised when three-pulse ESEEM spectra are compared.

The suppression effects mentioned above are inherent in the spin dynamics of ESEEM experiments using the nuclear coherence generator $\pi/2 - \tau - \pi/2$. Therefore, they cannot be completely eliminated by any choice of experimental parameters. Techniques for minimizing the suppression effects are discussed in §3.4.

3.3. HYSORE

In powder samples or frozen solutions the modulation pattern usually decays very much faster than the overall amplitude of the echo, owing to the destructive interference of the different resonance frequencies. Consequently, the advantage of slow echo decay in three-pulse ESEEM cannot be fully utilized for disordered systems. This problem can be solved with the four-pulse sequence shown in Figure 5c, where an additional π pulse is introduced between the second and third $\pi/2$ pulse of the three-pulse ESEEM experiment. During the first evolution period t_1 , the nuclear coherence created by the $\pi/2 - \tau - \pi/2$ subsequence evolves in the $\alpha(\beta)$ electron spin manifold. The nonselective π pulse acts as a mixer that interchanges the nuclear coherence between the electron spin α and β manifolds. During the second evolution period t_2 , the transferred nuclear coherence evolves in the $\beta(\alpha)$ electron spin manifold and a nuclear coherence transfer echo (CTE) is created at about $t_1 = t_2$ as a result of the refocusing of the hyperfine anisotropy [23]. Finally, the nuclear coherences are transferred to electron coherence by the last $\pi/2$ pulse and are detected as an electron spin echo, which is modulated by the nuclear frequencies. The observation of the nuclear CTE allows one to measure the in-phase part of the modulation and its decay with respect to both t_1 and t_2 . This is an important advantage as compared to the three-pulse ESEEM experiment, since the spectrum consists of undistorted absorption peaks.

Three different 1D ESEEM schemes using the pulse sequence in Figure 5c and the nuclear CTE have been proposed; deadtime-free ESEEM by nuclear coherence transfer echoes (DEFENCE) [24], the combination peak (CP) experiment, and the

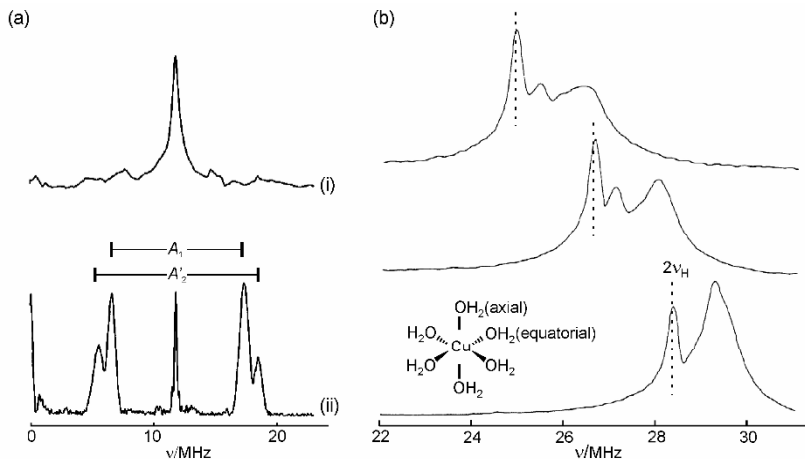


Figure 6. Examples of 1D four-pulse ESEEM experiments. (a) Comparison of three-pulse ESEEM (i) and DEFENCE (ii) experiments of bis(η^6 -benzene)vanadium(0), $\text{V}(\text{C}_6\text{H}_6)_2$, diluted into polycrystalline ferrocene; observer position, g_\perp . (b) Combination-peak spectra of $[\text{Cu}(\text{H}_2\text{O})_6]^{2+}$ centers in a frozen water/glycerol solution measured at three different observer positions. The dashed lines mark the frequency $2\nu_H$. Modified with permission from [24] and [26]. Copyright © 1995, American Institute of Physics.

hyperfine (HF) spectroscopy experiment [25]. The DEFENCE experiment, where the time interval t_1 is fixed and t_2 is swept, gives undistorted 1D ESEEM spectra that contain the nuclear frequencies ω_α and ω_β . This is demonstrated in Figure 6a, which compares the absolute-value spectra from DEFENCE and a three-pulse ESEEM experiment on bis(η^6 -benzene)vanadium(0), $\text{V}(\text{C}_6\text{H}_6)_2$, diluted into polycrystalline ferrocene. The three-pulse ESEEM spectrum is dominated by a broad and featureless matrix peak, and signals from the benzene ring protons are hardly recognizable. The resolution is drastically improved in the DEFENCE spectrum, from which one can readily read out the hyperfine couplings $A_1 = 9.2$ MHz and $A_2' = 14.4$ MHz that correspond to the extremes of the proton hyperfine couplings in the benzene ring plane.

In the CP experiment, times t_1 and t_2 are incremented under the constraints $t_1 = t_{10} + t$, $t_2 = t_{20} + t$, enabling the combination frequencies $\omega_+ = \omega_\alpha + \omega_\beta$ to be measured. This is very helpful in studies of disordered systems, where the peaks of the nuclear frequencies are often broad and difficult to observe. The combination peaks appear as narrow features in the spectrum since the orientation-dependent hyperfine interactions are partially refocused. For weak hyperfine couplings with $|B| \pm |\omega_l \pm A/2|$, the maximum of the sum-combination frequency is given by

$$(\omega_+)_{\max} = 2|\omega_l| + \frac{9}{16} \frac{T^2}{|\omega_l|}, \quad (19)$$

so that T can be inferred. CP experiments are particularly useful for assigning proton hyperfine couplings. Figure 6b shows combination-peak spectra of $[\text{Cu}(\text{H}_2\text{O})_6]^{2+}$ centers in frozen solution measured at different B_0 field positions [26]. Depending on the selected orientation, the spectra consist of two or three combination-frequency peaks. The peak at $2\nu_{\text{H}}$ arises from weakly coupled protons of the solvent molecules. The broad line with a frequency shift Δ of 1.2–1.5 MHz results from the protons of water molecules coordinated in the equatorial plane, whereas the peaks with $\Delta \approx 0.5$ MHz are assigned to axial water protons. A recent study of low-spin ferric complexes using 1D-CP experiments at different observer positions allowed the dipolar parts of the hyperfine interactions of the nearest protons of the axially coordinated imidazole ligands to be determined [27].

In the HF experiment, times t_1 and t_2 are incremented under the constraints $t_1 = t_{10} + t$, $t_2 = t_{20} - t$, with $t_1 + t_2 = t_{10} + t_{20} = T_0 = \text{const}$ (see Fig. 5c). The total accumulated phase of the nuclear coherence is given by $(\omega_{12} - \omega_{34})t + \omega_{12}t_{10} + \omega_{34}t_{20}$. Since time t is varied and t_{10} and t_{20} are kept constant, the echo is modulated with the frequency $|\omega_-| = |\omega_\alpha - \omega_\beta|$, which, for the weak coupling case, becomes $|\omega_-| = |A_S|$. Therefore, despite some peculiarities [25], this experiment allows for the measurement of undistorted hyperfine spectra.

The 1D methods described above result in undistorted ESEEM spectra and thus can drastically improve resolution. However, in multinuclear spin systems having strongly coupled nuclei with small gyromagnetic ratios and weakly coupled nuclei with large gyromagnetic ratios, peaks may overlap and the spectrum can be complicated and difficult to analyze. The resolution can be further increased by implementing the HYSORE experiment where times t_1 and t_2 are incremented independently [28]. As a consequence of the transfer of nuclear coherence by the π pulse, this 2D experiment correlates nuclear frequencies from different m_S manifolds. For an $S = 1/2$, $I = 1/2$ spin system and ideal pulses the modulation formula for the HYSORE experiment can be written as [29]

$$V_{4p}(\tau, t_1, t_2) = \frac{1}{2}[V^{\alpha\beta}(\tau, t_1, t_2) + V^{\beta\alpha}(\tau, t_1, t_2)], \quad (20)$$

with the terms

$$\begin{aligned} V^{\alpha\beta}(\tau, t_1, t_2) = & 1 - \frac{k}{2} \left\{ \frac{C_0}{2} + C_\alpha \cos \left[\omega_{12} \left(t_1 + \frac{\tau}{2} \right) \right] + C_\beta \cos \left[\omega_{34} \left(t_2 + \frac{\tau}{2} \right) \right] \right. \\ & \left. + C_c \left[\cos^2 \eta \cos \left(\omega_{12} t_1 + \omega_{34} t_2 + \omega_+ \frac{\tau}{2} \right) - \sin^2 \eta \cos \left(\omega_{12} t_1 - \omega_{34} t_2 + \omega_- \frac{\tau}{2} \right) \right] \right\} \\ V^{\beta\alpha}(\tau, t_1, t_2) = & 1 - \frac{k}{2} \left\{ \frac{C_0}{2} + C_\alpha \cos \left[\omega_{12} \left(t_2 + \frac{\tau}{2} \right) \right] + C_\beta \cos \left[\omega_{34} \left(t_1 + \frac{\tau}{2} \right) \right] \right. \\ & \left. + C_c \left[\cos^2 \eta \cos \left(\omega_{34} t_1 + \omega_{12} t_2 + \omega_+ \frac{\tau}{2} \right) - \sin^2 \eta \cos \left(\omega_{34} t_1 - \omega_{12} t_2 - \omega_- \frac{\tau}{2} \right) \right] \right\} \end{aligned} \quad (21)$$

and the coefficients

$$\begin{aligned}
 C_0 &= 3 - \cos(\omega_{12}\tau) - \cos(\omega_{34}\tau) - \sin^2 \eta \cos(\omega_+\tau) - \cos^2 \eta \cos(\omega_-\tau), \\
 C_\alpha &= \cos^2 \eta \cos((\omega_{34} - \omega_{12}/2)\tau) + \sin^2 \eta \cos((\omega_{34} + \omega_{12}/2)\tau) - \cos(\omega_{12}\tau/2), \\
 C_\beta &= \cos^2 \eta \cos((\omega_{12} - \omega_{34}/2)\tau) + \sin^2 \eta \cos((\omega_{12} + \omega_{34}/2)\tau) - \cos(\omega_{34}\tau/2), \\
 C_c &= -2 \sin(\omega_{12}\tau/2) \sin(\omega_{34}\tau/2).
 \end{aligned} \tag{22}$$

Three different kinds of peaks appear in the HYSORE spectrum after the FT of the time-domain signal along both dimensions, as depicted in Figure 7. The first terms of Eq. (21) with coefficients C_α and C_β originate from the transfer of nuclear coherence to polarization (and vice versa) and lead to the axial peaks $(0, \omega_{12})$, $(0, \omega_{34})$ and $(\omega_{12}, 0)$, $(\omega_{34}, 0)$ (open circles). These peaks are usually not of interest and are typically removed by a baseline correction.

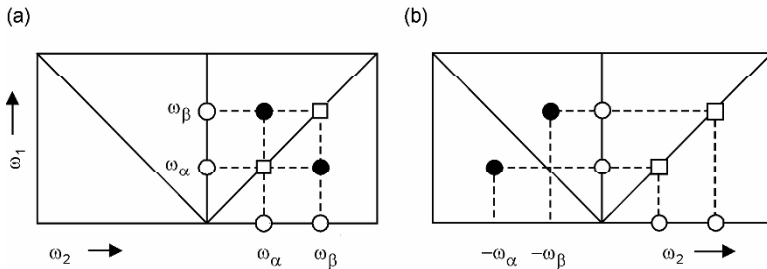


Figure 7. Peaks in HYSORE spectra. Full circles represent the wanted cross-peaks, open circles represent axial peaks due to transfer of nuclear coherence to polarization, and vice versa, by the mixing π pulse. Open squares represent diagonal peaks caused by pulse non-ideality: (a) Weak-coupling case, $|A_S| < 2|\omega_1|$; and (b) Strong coupling case $|A_S| > 2|\omega_1|$. Modified with permission from [7]. Copyright © 2001, Oxford University Press.

The terms with the coefficient C_c arise from the interchange of nuclear coherences between the two m_S manifolds and give cross-peaks at $(\omega_{12}, \omega_{34})$ and $(\omega_{34}, \omega_{12})$ with the weighting factor $\cos^2 \eta$ (full circles), and cross-peaks at $(\omega_{12}, -\omega_{34})$ and $(\omega_{34}, -\omega_{12})$ with the weighting factor $\sin^2 \eta$ (not shown). For intermediate couplings, $2|\omega_1| \sim |A_S|$, the cross-peaks have comparable intensities in the first and second quadrants. For the very weak- or strong-coupling case, the weighting factor $\sin^2 \eta$ is much smaller than $\cos^2 \eta$ and, consequently, the cross-peaks at $(\omega_{12}, \omega_{34})$ and $(\omega_{34}, \omega_{12})$ dominate the spectrum (i.e., cross-peaks are observed in either the first (third) or the second (fourth) quadrant). For the weak-coupling case, where ω_{12} and ω_{34} have the same sign, the stronger cross-peaks are observed in the first (and third) quadrants (Fig. 7a). For the strong-coupling case ω_{12} and ω_{34} have opposite signs and the stronger cross-peaks appear in the second (and fourth) quadrant (Fig. 7b). This feature introduces additional spectral

information since peaks corresponding to weak and strong couplings are separated from each other and can thus be easily identified.

Apart from axial-peaks and cross-peaks, the diagonal-peaks (ω_{12}, ω_{12}) and (ω_{34}, ω_{34}) can also be present in the HYSORE spectrum as a result of the incomplete transfer of nuclear coherence due to nonideality of the π pulse (see Fig. 7). Their intensity can be significantly reduced by using a larger excitation bandwidth for the mixing pulse (shorter pulse length) than for the $\pi/2$ pulses that generate and detect the nuclear coherence. Apart from the weighting factors $\cos^2 \eta$ and $\sin^2 \eta$, the intensities of the HYSORE cross-peaks are also determined by two important parameters: the modulation depth k and the coefficient C_c . First, the intensities of the peaks at the canonical orientations vanish since here $k = 0$ [Eq. (15)], and, second, the term C_c induces blind spots at $\nu = n/\tau$ ($n = 0, 1, 2, \dots$) in both dimensions [Eq. (22)].

The analysis of HYSORE spectra by means of peak intensities is not a straightforward process. Deviations from the analytical formulas given in Eqs. (20)–(22) can occur due to nonideality of the pulses. In addition, for multinuclear spin systems and/or systems with $I > 1$, analytical solutions become tedious and physical insight is not easily acquired. In disordered systems the task becomes very demanding because orientation selection and additional amplitude effects due to destructive interferences [30] have to be taken into account. For these reasons, numerical simulations are very important for analyzing peak positions and intensities of HYSORE spectra. Even though there is significant progress on the development of simulation programs [31,32], an accurate and general quantitative interpretation of peak intensities via numerical simulations has not yet been clearly established. Consequently, the information extracted from HYSORE spectra is often based primarily on the analysis of peak positions.

Figure 8 shows typical HYSORE powder patterns for an $S = 1/2$, $I = 1/2$ spin system. In the strong-coupling case, $|A_S| > 2|\omega_I|$, the correlation ridges orient parallel to the diagonal and are separated by $2|\omega_I|$ only at the orientations corresponding to the principal values. In the weak-coupling case, $|A_S| < 2|\omega_I|$, the two arcs are displaced from the antidiagonal at $|\omega_I|$, with a maximum frequency shift given by [33]

$$\Delta\omega_{\max} = \frac{9}{32} \frac{T^2}{|\omega_I|}. \quad (23)$$

The advantage of $\Delta\omega_{\max}$ for inferring the anisotropic part of the hyperfine interaction arises from the fact that the intensities of the endpoints of the arcs (corresponding to the principal values) vanish since here the depth parameter $k = 0$. Therefore, the hyperfine parameters cannot be determined easily from the extension of the ridges perpendicular to the diagonal. In addition to this approach, the lineshapes of ESEEM spectra for $S = 1/2$, $I = 1/2$ spin systems have been thoroughly studied [34], and useful representations of the correlation patterns in order to determine a_{iso} and T have been proposed [35].

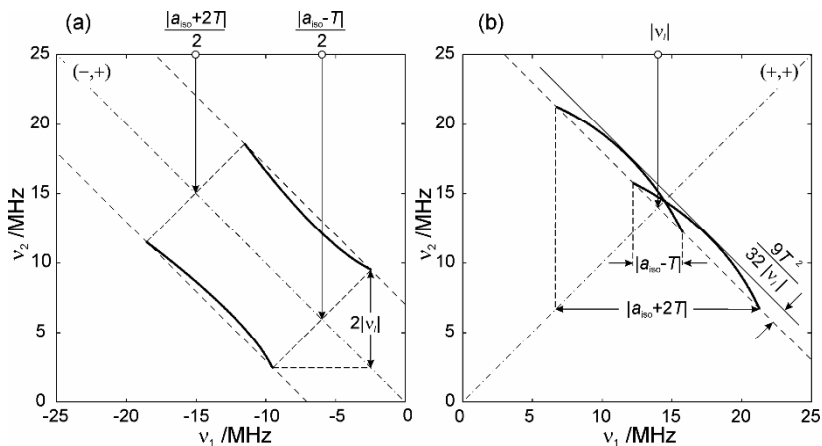


Figure 8. Theoretical HSCORE powder patterns for an $S = 1/2$, $I = 1/2$ spin system with an axial hyperfine tensor. (a) Strong-coupling case with $\nu_1 = 3.5$ MHz, $a_{\text{iso}} = 18$ MHz, and $T = 6$ MHz. (b) Weak-coupling case with $\nu_1 = 14$ MHz, $a_{\text{iso}} = 2.5$ MHz, and $T = 6$ MHz.

Figure 9 shows ^1H and ^{13}C HSCORE spectra from the complex MCR_{BPS} ($S = 1/2$, nickel-based EPR signal). MCR_{BPS} is a potent inhibitor of the enzyme methyl-coenzyme M reductase (MCR) [36] and results from reaction of $\text{Ni}^{\text{I}}\text{F}_{430}$ (active site of MCR) with 3-bromopropane sulfonate to give a bromide ion and $\text{O}_3\text{S}(\text{CH}_2)_3\text{Ni}^{\text{III}}\text{F}_{430}$ in the active site (see figure) [37,38]. An Ni alkyl bond is thus formed.

The X-band proton HSCORE spectrum (Fig. 9a) allows signals from the two H_γ protons that are bonded to the C_γ coordinated to the nickel to be resolved. Due to their close proximity to the main part of the spin density, located on the γ -carbon and nickel, the two proton hyperfine interactions have large anisotropies, $A(^1\text{H}_\gamma) \cong [-10, -1, 14]$ MHz. This displaces the signals from the antidiagonal [Eq. (23)] and allows them to be resolved from the many other protons comprising the “matrix line.” A second signal with a large isotropic hyperfine component could also be resolved and is assigned to $\text{H}_{\beta 1}$, $A(^1\text{H}_{\beta 1}) = [16.3, 8.0, 20.7]$ MHz. Figure 9b shows a Q-band ^{13}C HSCORE spectrum measured near to the echo maximum. The appearance of ^{13}C signals in both quadrants indicates that for the many sample orientations contributing at this observer position the hyperfine couplings go from the weak to the strong coupling case ($2\nu_1 = 25.5$ MHz). In the graph the principal values of the hyperfine interaction, $A(^{13}\text{C}) = [17.6, 18.3, 45.0]$ MHz, are indicated. These were determined from a set of HSCORE and ENDOR data. From a biological perspective, the detection of this alkyl-nickel species in the active site of MCR adds plausibility to proposed mechanisms proceeding via such intermediates, and this new type of alkyl-nickel species detected by EPR could play a crucial role in the C–H activation step in MCR. For example, in one proposed mechanism the Ni(I) acts as a nucleophile attacking $\text{CH}_3\text{--S--CoM}$ at the carbon of the $\text{CH}_3\text{--S}$ group, generating a $\text{CH}_3\text{--Ni(III)F}_{430}$ intermediate.

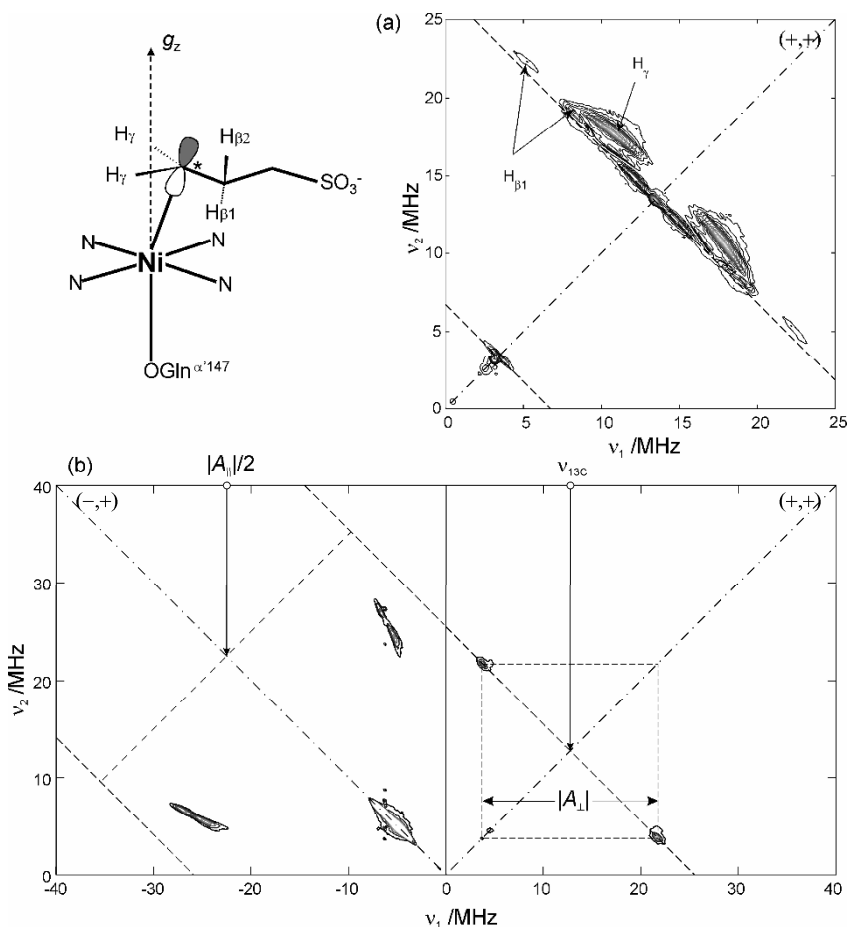


Figure 9. HYSCORE spectra of MCR_{BPS} (see schematic for structure). (a) ¹H X-band (9.7 GHz) spectrum at 20 K, with signals assigned to H_γ and H_{β1}. (b) ¹³C Q-band (35.3 GHz) spectrum at 20 K. The position of the principal values, determined from the full set of HYSCORE and ENDOR spectra, are indicated. The intense signal on the diagonal around (-5,5) MHz is due to an incomplete transfer of nuclear coherences between the two electron spin manifolds by the non-ideal π pulse. Modified with permission from [38]. Copyright © 2006, Wiley-VCH.

For a nucleus with $I = 1$ and nonnegligible quadrupole coupling, e.g., ¹⁴N, 18 correlation ridges are expected but typically not all of them are observed in the HYSCORE spectrum. This may be because of broadening due to hyperfine and quadrupole anisotropy, or low transition probabilities. The double-quantum transitions $(m_1, m_1 + 2) = (-1, 1)$ do not depend to first order on the nuclear quadrupole coupling [see Eq. (8b)], hence correlation patterns similar to those found for nuclei with $I = 1/2$ are expected. In contrast, the single-quantum transitions $(m_1, m_1 + 1) =$

(0,1) and (-1,0) depend to first order on the nuclear quadrupole coupling and, therefore, are usually broad in disordered systems. For this reason the most prominent features of ^{14}N HSCORE spectra are often the double-quantum cross-peaks. The situation is different when the nuclear quadrupole interaction is much weaker than the nuclear Zeeman and hyperfine interaction, which is the usual case for deuterium bonded to carbon. Under these conditions the transition probabilities of the double-quantum transitions are very small and the single-quantum correlation peaks dominate the spectrum [39]. Analytical formulas describing the frequencies and shapes of the cross-peaks for $I = 1$ have also been derived [40,41].

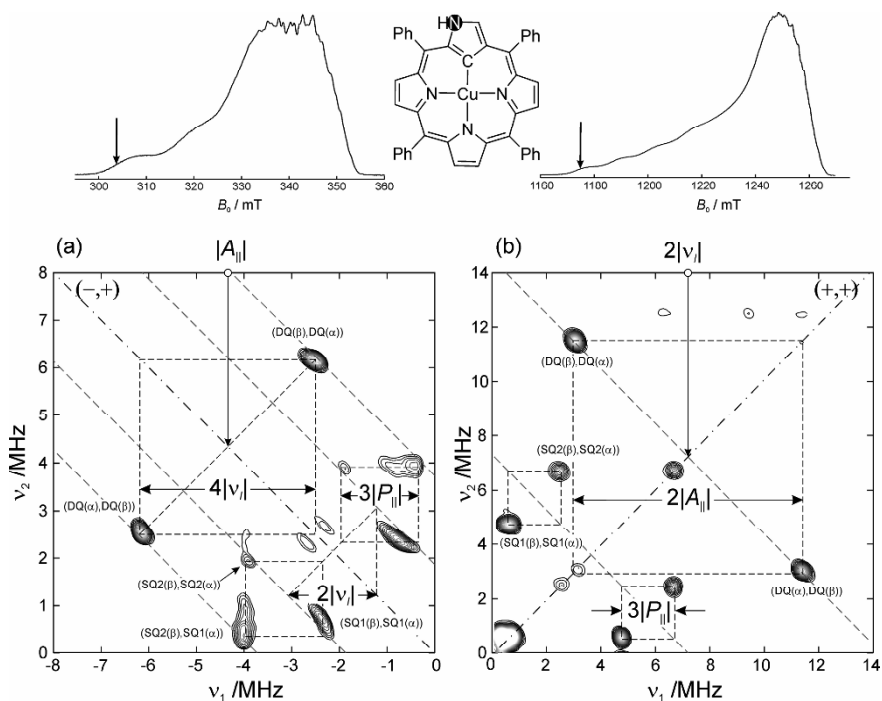


Figure 10. HSCORE spectra of the remote ^{14}N of Cu(II)NCTPP diluted in ZnTPP powder, measured at the field positions indicated by the arrows in the field-swept spectra (upper part of figure). (a) X-band spectrum; m.w. frequency, 9.7 GHz; $\nu_{14\text{N}} = 0.9$ MHz; $\tau = 100$ ns. (b) Q-band spectrum; m.w. frequency, 35.6 GHz; $\nu_{14\text{N}} = 3.6$ MHz; $\tau = 100$ ns. All interactions are given in MHz. Modified with permission from [42]. Copyright © 2005, Wiley-VCH.

Figure 10 shows ^{14}N HSCORE spectra from the Cu(II) N-confused tetraphenylporphyrin (NCTPP) complex measured at X- and Q-band frequencies [42]. The correlation peaks observed in the single-crystal like spectra, measured at g_{\parallel} , are assigned to the remote ^{14}N nucleus of the inverted pyrrole. In the Q-band spectrum (Fig. 10b, weak-coupling case) the stronger peaks appear in the first quadrant.

The cross-peaks representing double-quantum transitions lie on the antidiagonal at $2|\nu_1| = 7.2$ MHz and are separated by $2|A_s| \approx 8.5$ MHz, from which a hyperfine coupling of $|A_s| \approx 4.3$ MHz is estimated. The other four cross-peaks are assigned to single-quantum transitions; they exhibit a hyperfine splitting $|A_s| \approx 4.3$ MHz along the direction of the antidiagonal, and a quadrupole splitting $3|P| \approx 1.8$ MHz along the direction of the diagonal (P is the quadrupole coupling along this orientation, see [43]). Note that the estimation of the couplings is based on Eq. (8b), which is a first-order approximation, and valid only when \mathbf{g} , \mathbf{A} , and \mathbf{P} are coaxial and \mathbf{B}_0 is parallel to one of the principal axes. For a more accurate estimation of parameters numerical simulations of the frequency positions are necessary.

In the X-band spectrum (Fig. 10a, strong-coupling case) the peaks appear in the second quadrant, $(-,+)$. The double-quantum cross-peaks are separated by approximately $4|\nu_1| = 3.6$ MHz and centered around the hyperfine coupling $|A_s| \approx 4.3$ MHz. The cross-peaks close to the antidiagonal at $|A_s|/2 \approx 2.2$ MHz are assigned to single-quantum transitions. In addition, correlations between single- and double-quantum frequencies appear close to the diagonal. From the single-quantum frequencies a quadrupole splitting of $3|P| \approx 1.5$ MHz is evaluated that deviates slightly from the one estimated by the Q-band measurements. This discrepancy is related to the different orientation selection at the two m.w. frequencies. At X-band there are more orientations contributing to the experiment and the correlation ridges become broader.

The correlation patterns are more complex if the nuclear quadrupole, the hyperfine, and the nuclear Zeeman interactions are of the same order of magnitude. This situation is often encountered in X-band HYSCORE spectra of weakly coupled nitrogen nuclei in transition metal complexes. A special case, where the spectrum is considerably simplified, is the so-called exact cancellation condition, where $|A_s| \approx 2|\omega_1|$. Under this condition, the nuclear frequencies within one of the two m_S manifolds correspond to the nuclear quadrupole resonance (NQR) frequencies $\omega_0 = 2K\eta$, $\omega_- = K(3 - \eta)$, and $\omega_+ = K(3 + \eta)$ [43], which are orientation independent. Consequently, correlation peaks involving these frequencies appear as narrow features in the nuclear frequency spectrum.

Due to its high resolution, HYSCORE spectroscopy has become a powerful method for the characterization of paramagnetic metalloproteins [3–5]. Dikanov and coworkers [44] used orientation-selective ^{15}N -HYSCORE experiments to study the coordination environment of the Archaeal Rieske [2Fe–2S] center. From the HYSCORE spectra the authors were able to distinguish weak hyperfine couplings from both histidyl and peptide backbone nitrogens. Prisner and coworkers [45] used HYSCORE to investigate the environment of the 2Fe–2S (N1) cluster of complex I from *Yarrowia lipolytica*. This study revealed two sets of proton hyperfine couplings corresponding to two sets of β -protons of the cysteine ligands, and one weakly coupled nitrogen. Since the ^{14}N hyperfine and nuclear quadrupole coupling parameters were found to be very similar to those of ferredoxin-type FeS clusters, the authors assigned the ^{14}N coupling to a backbone nitrogen nucleus.

Lubitz and coworkers [46] employed HYSCORE to study the spin density distribution in the active site of [NiFe]-hydrogenase from *Desulfovibrio vulgaris* Miyazaki F in the reduced Ni–C state. Upon H₂O → D₂O exchange of the solvent, the HYSCORE spectrum contained ²H peaks that were assigned to an exchangeable proton residing in a bridging position between nickel and iron. An exchangeable bridging proton was also found earlier in a regulatory hydrogenase [47]. The similarity of the [NiFe] centers found in catalytically active and regulatory hydrogenase suggests that their functional differences originate from structural differences further away from the [NiFe] center.

HYSCORE spectroscopy has been successfully used to study heme-containing proteins like cytochromes [48] and hemoglobins [49]. Van Doorslaer and coworkers [50] demonstrated how a combined ¹H and ¹⁴N HYSCORE study can reveal structural information on the heme pocket of ferric mouse neuroglobin. They showed that the imidazole planes of the proximal (F8His) and distal (E7H) histidines bounded to the iron of the heme group are nonparallel. The good agreement of this result with available X-ray diffraction data shows that pulse EPR techniques can be confidently applied to study the arrangement of ligands in these metalloproteins.

For nuclei with $I > 1$ the analysis of HYSCORE spectra can be demanding due to their high degree of complexity. Although there are theoretical studies aimed at the understanding of basic features, no analytical solutions are available [51–53]. Therefore, an accurate interpretation depends on spectrum simulation. In a pulse EPR study of the ox1 form of methyl-coenzyme M reductase, HYSCORE spectroscopy was utilized to study the hyperfine ($A(^{33}\text{S}) = [10, 24, 17]$ MHz) and nuclear quadrupole ($|e^2qQ/h| = 36$ MHz, $\eta = 0.1$) interactions from the thiolate sulfur group of CoM (³³SCH₂CH₂SO₃⁻, ³³S: $I = 3/2$), which was found to bind to the nickel ion of the cofactor F₄₃₀ [54]. The ox1 complex was formally best described as an Ni(III) (d^7) thiolate in resonance with a thiyl radical/high-spin Ni(II) complex, Ni^{III} – ⁻SR ↔ Ni^{II} – ^{*}SR. The detection of an Ni–S bond in the active site of MCR provides valuable information for proposed catalytic cycles that proceed via such or related intermediates (e.g., in one proposal the Ni(I) center attacks the thioether sulfur of methyl-CoM, generating a methyl radical and the thiolate complex CoM–S–Ni(II)F₄₃₀ as intermediates).

3.4. Remote Echo Detection

The use of a remote-echo detector allows τ values shorter than the spectrometer deadtime τ_d to be employed [55]. This is important in two-pulse ESEEM experiments where the deadtime prevents the signal for times $\tau < \tau_d$ from being recorded. Also in the deadtime-free four-pulse experiments described in §3.3, a small τ value is often needed to avoid blind spots. Blind spots are a particular concern for the measurement of proton spectra at X-band, where the signals typically extend from 5 to 25 MHz, and with a $\tau = 100$ ns blind spots occur at $\nu = n/\tau = 0, 10, 20, \dots$ MHz.

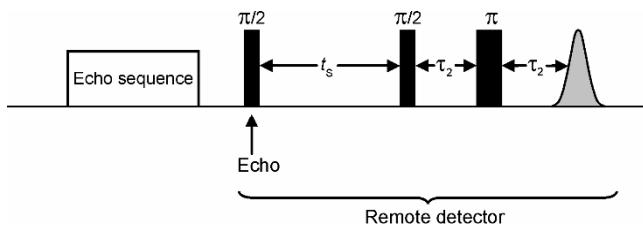


Figure 11. Pulse sequence for remote-echo detection. Modified with permission from [7]. Copyright © 2001, Oxford University Press.

The remote-echo detector is shown in Figure 11. In this method the electron spin echo at the end of the pulse sequence, which uses $\tau_1 < \tau_d$ for the nuclear coherence generator, is not recorded. Instead, at the time of echo formation an additional $\pi/2$ pulse transfers the electron coherence to longitudinal magnetization. The echo amplitude information can thus be stored for a time interval up to the order of T_1 . After a fixed time delay $t_s < T_1$, the z -magnetization is read out using a two-pulse echo sequence with a fixed time interval $\tau_2 > \tau_d$. Remote echo detection can be applied to many experiments, including three-pulse ESEEM and HYSCORE, and thus can eliminate blind spots with an appropriate choice of small τ_1 . Note, however, that it may suffer from reduced sensitivity due to the increased sequence time.

3.5. Matched ESEEM

An important issue in ESEEM experiments is sensitivity, which, apart from relaxation effects, is mainly determined by the modulation depth k . Equation (15) shows that for $I = 1/2$ nuclei the modulation depth is maximal when the hyperfine coupling is comparable to the nuclear Zeeman interaction ($|A_S| \approx |2\omega_I|$). For nuclei with very strong or very weak hyperfine interactions, and/or very small hyperfine anisotropy ($B \approx 0$), the modulation amplitude practically vanishes. An efficient sensitivity enhancement can be achieved by optimizing the strength ω_1^m and duration t_p of the m.w. pulses. These “nonideal” m.w. pulses can create nuclear coherence from electron spin polarization. The optimization of this transfer by means of the appropriate strength ω_1^m and length t_p of the nonideal m.w. pulse is called matching. Experimentally the strength ω_1 of the m.w. pulse can be satisfactorily calibrated by optimizing the primary echo intensity from a two-pulse sequence, for an $S = 1/2$ system $\omega_1 = g\beta_e B_1/\hbar = \pi/t_\pi$, where t_π is the length of the π pulse. For the case of very weak coupling $|A_S| \ll |2\omega_I|$, an optimized transfer occurs when $\omega_1^m \approx |\omega_I|$, whereas in the case of very strong coupling $|A_S| \gg |2\omega_I|$, the largest enhancement is obtained with the maximum ω_1 experimentally available [56]. For instance, for weakly coupled protons at X-band, the strength of the matched m.w. pulse has to be $\omega_1^m/2\pi \approx |\omega_I|/2\pi \approx 15.6$ MHz, corresponding to a nominal $\pi/2$ pulse of 16 ns length. For strongly coupled nuclei, ω_1^m is often restricted to the maximum experimentally achievable ω_1 , typically ranging between 30 and 50 MHz at X-band. The optimum length of the matched pulse is typically determined experimentally.

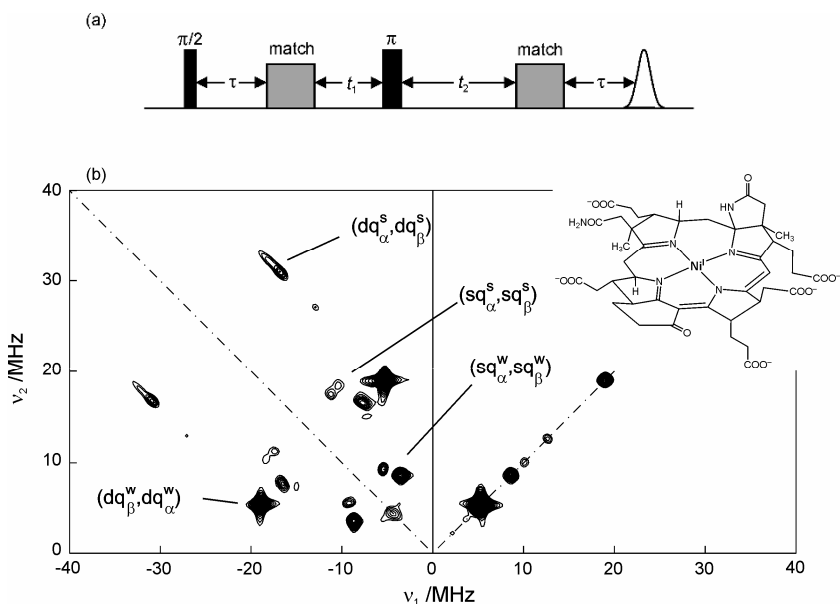


Figure 12. (a) Pulse sequence for matched HYSCORE. (b) Q-band (35.3 GHz) matched HYSCORE spectrum from the red2 species of MCR. Signals from the weakest coupled pyrrole nitrogen are labeled with superscript “w,” those from the three strongest coupled pyrrole nitrogens with superscript “s.” The later type of nitrogens were only observed using matched HYSCORE with m.w. pulses of strength $\omega_1/2\pi = 31.25$ MHz ($t_\pi = 16$ ns) and matched pulses of length 24 ns (nominal flip angle of $3\pi/2$). Inset: Cofactor F_{430} , in the red2 state the upper axially ligand is known from ^{33}S HYSCORE data to be the thiolate sulfur of CoM ($\text{H}^{33}\text{SCH}_2\text{CH}_2\text{SO}_3^-$). Modified with permission from [15]. Copyright © 2003, Springer.

Matched pulses can be implemented in all ESEEM experiments described here. Figure 12a shows a matched HYSCORE pulse sequence where the second and third $\pi/2$ pulses of the standard experiment have been replaced by matched pulses [57]. By using matched pulses the signal intensities can be enhanced by more than one order of magnitude as compared to standard HYSCORE.

A matched HYSCORE spectrum is shown in Figure 12b for the red2 species of methyl-coenzyme reductase (MCR), where the four pyrrole nitrogens of the porphyrinoid macrocycle (cofactor F_{430}) are directly coordinated to an Ni(I) ion ($S = 1/2$, d^9) [15]. HYSCORE measurements show that the complex has two sets of pyrrole nitrogens. One pyrrole nitrogen has hyperfine couplings of $A(^{14}\text{N}) = [16, 13.5, 11.8]$ MHz, which produces deep modulations at Q-band ($2\nu_1 = 7.2$ MHz). The other three pyrrole nitrogens, however, with hyperfine couplings in the range 20–27 MHz, give rise to a very shallow modulation depth and are thus not observable with the standard HYSCORE sequence. However, with matched pulses signals from these strongly coupled nitrogens are significantly enhanced and both double-

quantum and single-quantum transitions are observed. These data show that there is a significant electronic and/or geometric distortion of the cofactor F₄₃₀.

3.6. DONUT-HYSCORE

In the HYSCORE experiment only nuclear frequencies in different m_S manifolds belonging to the same paramagnetic center are correlated with each other. For multinuclear spin systems the assignment of nuclear frequencies is often not straightforward, since some of the correlation peaks may not be observed in the HYSCORE spectrum due to the small intensity of the nuclear transitions in one of the two m_S manifolds. Additional information can be gained if correlations of nuclear frequencies within the same m_S manifold can be obtained. Cross-peaks that represent such correlations can be created by replacing the nonselective transfer π pulse in the HYSCORE sequence by the double nuclear-coherence transfer (DONUT) mixer $\pi - \tau - \pi$ [58]. This DONUT-HYSCORE experiment with the pulse sequence $\pi/2 - \tau_1 - \pi/2 - t_1 - \pi - \tau_2 - \pi - t_2 - \pi/2 - \tau_1 - \text{echo}$ results in cross-peaks $(\omega_{\alpha,i}, \omega_{\alpha,j})$ and $(\omega_{\beta,i}, \omega_{\beta,j})$. The presence of these cross-peaks in the DONUT-HYSCORE spectrum is a proof that $\omega_{\alpha,i}$ and $\omega_{\alpha,j}$ belong to the same paramagnetic center, and this information can support their unambiguous assignment. An experimental example for nitrogens that are close to the exact cancellation condition has been published for the complex Co(II)TPP(py) [59], where the DONUT-HYSCORE experiment revealed one of the NQR frequencies that was missing from the HYSCORE spectrum.

3.7. Hyperfine Decoupling Techniques

The interpretation of nuclear frequency spectra can be simplified if the hyperfine interaction can be eliminated by a decoupling procedure. In principle the decoupling of the electron spin S from the nuclear spin I can be achieved using m.w. or r.f. pulses with a strength $\gamma_e B_1$ ($\gamma_n B_2$) that is larger than the hyperfine coupling. However, since the maximum technically achievable B_1 (B_2) is approximately 1 mT and the gyromagnetic ratio of the electron γ_e and nuclear γ_n spins differ by two to three orders of magnitude, it turns out that hyperfine decoupling through m.w. radiation is relatively easy, whereas decoupling through r.f. radiation is virtually impossible. For this reason hyperfine decoupling is only possible by exciting the electron spins, which are also used for detection. During hyperfine decoupling under strong resonant m.w. radiation the quantization axis of the electron spins S is rotating with the Larmor frequency in the xy -plane of the laboratory frame. The local field at nuclear spin I generated by the electron spin S thus becomes strongly time dependent and is averaged for times $t \gg 2\pi/\omega_S$. In principle it is then possible to decouple the electron spin from the nuclear spin by applying a prolonged strong m.w. pulse. However, for off-resonant spin packets there will still be a nonzero component of S along \mathbf{B}_0 , resulting in a residual hyperfine coupling. The theoretic-

cal analysis of the eigenvalues of the spin Hamiltonian under a strong m.w. pulse gives for an $S = 1/2, I = 1/2$ spin system [56]

$$\omega_{\alpha,\beta}^{\text{dec}} = \omega_I \pm \frac{A\Omega_S}{2\omega_1} - \frac{B^2(\Omega_S^2 - \omega_I^2)}{8\omega_1^2\omega_I}, \quad (24a)$$

and for an $S = 1/2, I = 1$ spin system [60]

$$\begin{aligned} \omega_{\text{SQ1}(\alpha,\beta)}^{\text{dec}} &= \omega_{\text{SQ1}} \pm \frac{A\Omega_S}{2\omega_1} \pm \frac{A^2}{4\omega_1} + \frac{B^2}{8(\omega_I \mp \omega_1)}, \\ \omega_{\text{SQ2}(\alpha,\beta)}^{\text{dec}} &= \omega_{\text{SQ2}} \pm \frac{A\Omega_S}{2\omega_1} \mp \frac{A^2}{4\omega_1} + \frac{B^2}{8(\omega_I \pm \omega_1)}, \\ \omega_{\text{DQ}(\alpha,\beta)}^{\text{dec}} &= \omega_{\text{DQ}} \pm \frac{A\Omega_S}{\omega_1} + \frac{B^2\omega_I}{4(\omega_I^2 - \omega_1^2)}, \end{aligned} \quad (24b)$$

where the subscripts SQ1 and SQ2 denote the two single-quantum nuclear spin transitions $(m_i, m_i+1) = (0,1)$ and $(-1,0)$, and DQ the double-quantum transition, $(-1,1)$. In Eqs. (24) the first term on the right-hand side gives the desired nuclear frequencies corresponding to complete decoupling ($A = 0, B = 0$), whereas the remaining terms describe the residual hyperfine splitting.

Hyperfine-decoupling methods are particularly useful when the hyperfine-decoupled spectrum is correlated to the original undecoupled spectrum in a 2D experiment [61]. The proposed hyperfine-decoupled DEFENCE [62] scheme is based on the DEFENCE sequence [24], where the third $\pi/2$ pulse is replaced by a decoupling pulse of variable length T_{dec} (Fig. 13a). This introduces a second dimension along which the hyperfine-decoupled frequencies given by Eq. (24) can be obtained. For an $S = 1/2, I = 1/2$ spin system this experiment correlates the two nuclear frequencies ω_α and ω_β of Eq. (12) with the corresponding decoupled frequency $\omega_{\text{dec}} = \omega_I$, so that the nuclear frequencies of different types of nuclei can be separated from each other. For the $S = 1/2, I = 1$ case, the six nuclear frequencies $\omega_{\text{SQ1}(\alpha,\beta)}$, $\omega_{\text{SQ2}(\alpha,\beta)}$, and $\omega_{\text{DQ}(\alpha,\beta)}$ (see Fig. 2) will be correlated with the corresponding decoupled frequencies ω_{SQ1} , ω_{SQ2} , and ω_{DQ} that contain only the nuclear Zeeman and quadrupole interactions. Consequently, a direct determination of the nuclear quadrupole interaction becomes possible.

The main drawback of this pulse sequence is the residual hyperfine splitting, which causes line broadening along the decoupling dimension. For spin packets with small off-resonance frequencies ($\Omega_S \approx 0$) narrow peaks will be obtained, but the residual hyperfine splitting arising from off-resonance spin packets scales with Ω_S/ω_1 and thus can only be reduced by applying sufficiently strong m.w. fields. However, since a typical maximum m.w. field is around $\omega_1/2\pi = 50$ MHz, complete decoupling is not possible with currently available commercial spectrometers.

The residual hyperfine splitting can be eliminated with the pulse sequence shown in Figure 13b. In contrast to the previous pulse sequence, the nuclear coherence during the decoupling pulses evolves now in both electron spin manifolds. It

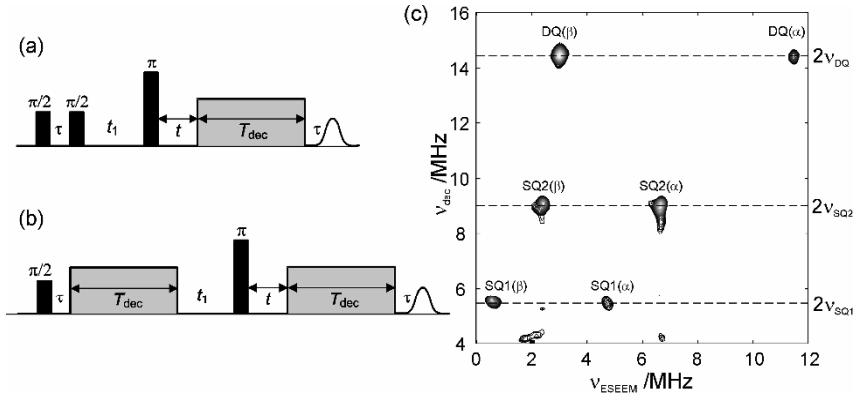


Figure 13. Pulse sequences for hyperfine-decoupled ESEEM (a,b) and 2D experimental example (c). (a) Hyperfine-decoupled DEFENCE. (b) New hyperfine-decoupled DEFENCE sequence for elimination of the residual hyperfine splitting. (c) Application of (b) on Cu(II)NCTPP diluted in Zn(TPP) powder measured at Q-band. Experimental parameters: observer position, g_{\parallel} ; m.w. field strength of decoupling pulses, $\omega_1 \approx 32$ MHz; $\tau = 140$ ns; $t_1 = 170$ ns; starting value for t , $t_0 = 96$ ns incremented in steps of $\Delta t = 16$ ns; starting value for T_{dec} , $T_0 = 16$ ns incremented in steps of $\Delta T_{dec} = 8$ ns (256×512 datapoints).

is then expected, in analogy with the combination peak experiment [24], also that the frequencies $\omega_{\pm}^{dec} = |\omega_{\alpha}^{dec} \pm \omega_{\beta}^{dec}|$ will appear in the decoupling dimension of the spectrum. For the weak hyperfine coupling case ($2|\omega_1| > |A_S|$) with $I = 1/2$, for every off-resonance spin packet the decoupled frequencies are in first order symmetrically placed around ω_1 , so that the sum-combination frequency, $\omega_+^{dec} = 2\omega_1$, is free from secular residual hyperfine contributions. Similarly, for $I = 1$, the six nuclear frequencies are correlated with the three sum-combination frequencies:

$$\begin{aligned}
 \omega_{SQ1(\alpha)}^{dec} + \omega_{SQ1(\beta)}^{dec} &= 2\omega_{SQ1} - B^2\omega_1 / 4\omega_1^2, \\
 \omega_{SQ2(\alpha)}^{dec} + \omega_{SQ2(\beta)}^{dec} &= 2\omega_{SQ2} - B^2\omega_1 / 4\omega_1^2, \\
 \omega_{DQ(\alpha)}^{dec} + \omega_{DQ(\beta)}^{dec} &= 2\omega_{DQ} - B^2\omega_1 / 2\omega_1^2.
 \end{aligned} \tag{25}$$

For sufficiently strong m.w. fields the terms containing the nonsecular hyperfine coupling B can be neglected and the sum-combination frequencies become twice the completely decoupled frequencies.

The remarkable reduction of the residual hyperfine coupling by using this new decoupling scheme has been demonstrated by numerical simulations and experimental results [60]. Its application on Cu(II)NCTPP performed at the observer position g_{\parallel} ($B_0 = 1174$ mT) is shown in Figure 13c. The correlation peaks observed in the 2D plot are assigned to the remote nitrogen ($\nu_N = 3.6$ MHz) of the inverted pyrrole. The nuclear frequencies in the ESEEM dimension correspond to those observed in the HYSORE spectrum of Figure 10b. The double-quantum frequencies $\nu_{DQ(\alpha)}$ and $\nu_{DQ(\beta)}$ are correlated with $2\nu_{DQ} = 14.4$ MHz. The single-quantum fre-

quencies $\nu_{\text{SQ1}(\alpha)}$ and $\nu_{\text{SQ1}(\beta)}$ are correlated with $2\nu_{\text{SQ1}} = 5.4$ MHz, whereas the other two $\nu_{\text{SQ2}(\alpha)}$ and $\nu_{\text{SQ2}(\beta)}$ are correlated with $2\nu_{\text{SQ2}} = 9.0$ MHz. The narrow peaks along the decoupling dimension allow for an accurate estimation of the completely decoupled frequencies $\nu_{\text{SQ1}} = 2.7$ MHz, $\nu_{\text{SQ2}} = 4.5$ MHz and $\nu_{\text{DQ}} = 7.2$ MHz. With these frequencies we find $|\nu_{\text{SQ2}} - \nu_{\text{SQ1}}| \approx 3|P| = 1.8$ MHz, which is in accordance with the value estimated from the analysis of the HYSORE peaks. Note that with this approach the quadrupole coupling parameters can be estimated with high accuracy because ν_{SQ1} , ν_{SQ2} , and ν_{DQ} are free from hyperfine coupling parameters. The latter can then also be accurately determined from the ESEEM frequencies since they now become the only unknowns. Consequently, hyperfine decoupling experiments can be very useful for the interpretation of complicated ESEEM spectra.

4. ELECTRON NUCLEAR DOUBLE RESONANCE (ENDOR)

Apart from ESEEM methods, electron nuclear double resonance (ENDOR) spectroscopy is the other well-established technique for measuring nuclear transition frequencies of paramagnetic compounds. We start with a brief discussion of the two standard pulse schemes, Davies and Mims ENDOR, before moving onto 2D sequences aimed at resolution improvement.

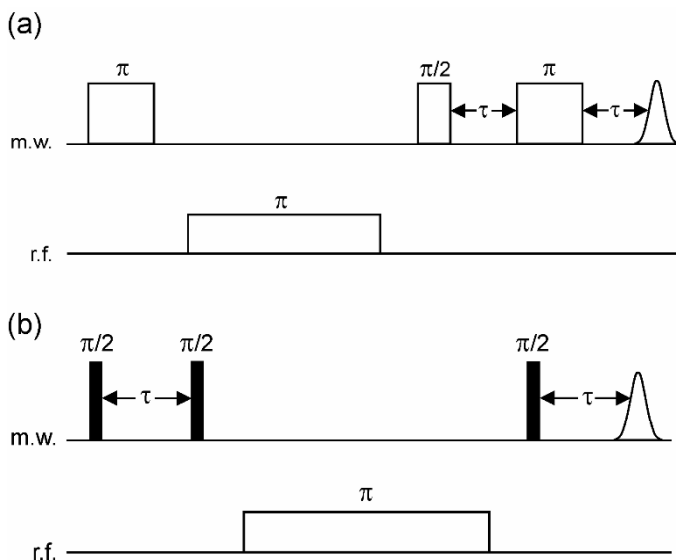


Figure 14. Pulse sequence for the Davies ENDOR (a) and Mims ENDOR (b) experiments. The inter-pulse delays are kept constant while the radio frequency is incremented over the desired frequency range. Modified with permission from [7]. Copyright © 2001, Oxford University Press.

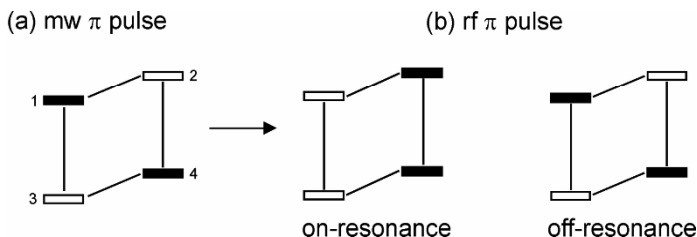


Figure 15. Populations of the energy levels of a two-spin system during the Davies ENDOR experiment: (a) selective m.w. π pulse inverts the polarization of EPR transition (1,3), (b) population after the r.f. π pulse, on-resonance with nuclear transition (1,2), or off-resonance (no effect).

4.1. Mims and Davies ENDOR

Figure 14 shows the Davies [63] and Mims [64] ENDOR pulse sequences, both of which are based on the transfer of polarization between electron and nuclear transitions.

In Davies ENDOR the first *selective* m.w. π pulse inverts the polarization of a particular EPR transition (Fig. 15a). During the mixing period a *selective* r.f. π pulse is applied. If the r.f. pulse is resonant with one of the nuclear frequencies (Fig. 15b), the polarization of this transition is inverted, which also alters the polarization of the electron spin echo observer transition (1,3) detected via a primary echo, $\pi/2 - \tau - \pi - \tau - \text{echo}$. The ENDOR spectrum is thus recorded by monitoring the primary echo intensity as the r.f. frequency is incremented stepwise over the desired frequency range.

The first m.w. pulse in Davies ENDOR is required to be selective, for example, in Figure 15a the m.w. pulse must only invert the population of level (1,3) and not (2,4). The inversion pulse can therefore be used as a filter by varying the pulse length and thus the selectivity. This concept can be used at X-band when weakly coupled proton signals overlap with strongly coupled nitrogen signals. An example is given in Figure 16, where traces 1 and 3 were measured with a relatively selective m.w. π pulse of length 200 ns, whereas traces 2 and 4 were measured with a short, and thus less selective, m.w. pulse of length 32 ns. This has the effect of attenuating signals from the weakly coupled protons ($A_S < 10$ MHz), while signals from the strongly coupled nitrogen nuclei ($A_S \sim 30$ MHz) are enhanced relative to the protons. The absolute ENDOR intensity as a function of the selectivity parameter η_s is given by [65]

$$V(\eta_s) = V_{\max} \frac{\sqrt{2}\eta_s}{\eta_s^2 + 1/2} \quad \text{with } \eta_s = a_{\text{iso}} t_{\text{mw}} / 2\pi, \quad (26)$$

where V_{\max} is the maximum ENDOR intensity obtained with $\eta_s = \sqrt{2}/2$ and t_{mw} is the length of the first m.w. π pulse.

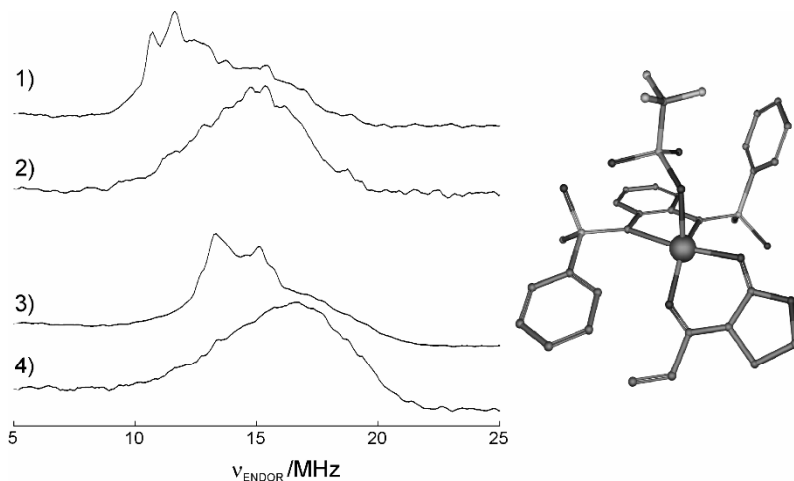


Figure 16. Hyperfine contrast selective X-band Davies ENDOR spectra of the Cu(II) bis(sulfoximine) complex (right) measured near g_{\parallel} (traces 1 and 2) and g_{\perp} (traces 3 and 4). Traces 1 and 3 were recorded using a π pulse of length 200 ns, traces 2 and 4 with a π pulse of length 32 ns to suppress the weakly coupled protons. The strongly coupled ^{14}N nuclei (trace 2 and 4) are centered at one-half of the hyperfine coupling, $A_S/2$, between 14.5 and 17 MHz. Modified with permission from [66]. Copyright © 2003, American Chemical Society.

Mims ENDOR is based on the stimulated echo sequence with three nonselective m.w. $\pi/2$ pulses (Fig. 14b). The preparation part, $\pi/2 - \tau - \pi/2$, creates a τ -dependent grating polarization pattern. During the mixing period, the polarization is changed by a selective r.f. pulse if it is on-resonance with a nuclear frequency. The electron polarization is then detected via a stimulated echo created at time τ after the last $\pi/2$ m.w. pulse. The ENDOR efficiency is given by [64]

$$F_{\text{ENDOR}} = \frac{1}{4}(1 - \cos(A_S \tau)), \quad (27)$$

and depends upon the hyperfine coupling constant A_S and the time τ . It is maximum for $\tau = (2n + 1)\pi/A_S$, and zero for $\tau = 2n\pi/A_S$, with $(n = 0, 1, 2, \dots)$. Mims ENDOR thus exhibits a blind-spot behavior similar to three-pulse ESEEM, but which now depends upon A_S (in three-pulse ESEEM the blind spots depend upon ω_{α} and ω_{β}).

The τ dependence of the signal can be used to enhance signals from weakly coupled nuclei. An example is shown in Figure 17 for the case of weakly coupled ^{19}F nuclei [66]. The complete set of spectra show the expected pattern for a pure dipole interaction, with the splitting along g_{\parallel} ($2T$) being approximately twice as large as the splitting along g_{\perp} (T). Using the point-dipole model [Eq. (4)] with a $T = 0.57$ MHz allows the average electron–fluorine distance of 0.5 nm to be estimated. With this information the coordination of the triflate anion to the copper ion can be inferred, as shown on the right of Figure 17. Significantly, these data are

uniquely obtained by EPR on a sample prepared with the relevant catalytic conditions (e.g., the bis(sulfoximine) Cu(II) catalyst in solution with the solvent CH_2Cl_2). Therefore, information is obtained on the subtle influence of counterions and solvent molecules on the efficiency and stereoselectivity of the catalytically induced C–C bond forming reaction.

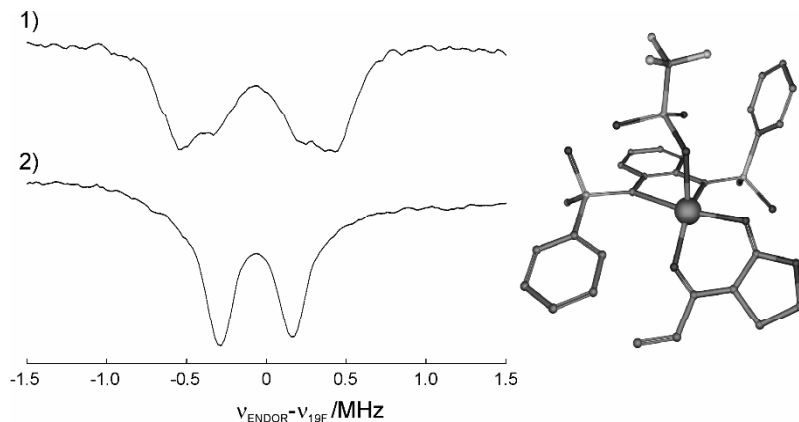


Figure 17. ^{19}F W-band Mims ENDOR spectra of the Cu(II) bis(sulfoximine) complex (right) measured at g_{\parallel} (trace 1) and g_{\perp} (trace 2). Due to the small ^{19}F hyperfine interaction and considering the phase memory time T_M , the optimum sensitivity was obtained with $\tau = 400$ ns. The ^{19}F signals originate from the triflate anion. Modified from [66]. Copyright © 2003. American Chemical Society.

For nuclei with large hyperfine couplings and large anisotropies the τ dependence of the signal can produce unwanted blind spots in the spectrum. Note that the deadtime of the spectrometer prevents very small τ values from being used: at X-band typically τ is 100 ns or more. For $\tau = 100$ ns blind spots occur when $A_S = 0, 10, 20, \dots$ MHz. For large hyperfine couplings it is thus usually preferable to employ the Davies ENDOR sequence with a well-chosen length for the m.w π pulse [Eq. (26)]. Conversely, Mims ENDOR can be particularly sensitive for measuring small hyperfine couplings if the phase memory time T_M of the sample is sufficiently long to allow an optimal τ value to be used. The blind spot behavior in Mims ENDOR can be avoided with a remote-echo detection sequence [55] or with the refocused Mims ENDOR approach [67].

4.2. Baseline Artifacts in ENDOR

A significant technical problem in ENDOR arises from r.f. heating, resulting in small changes in the resonator tuning, and leading to the appearance of baseline artifacts in the ENDOR spectrum. This problem is most severe at low temperatures, but can be overcome by varying the r.f. frequency acquisition not linearly, but randomly [68]. Convincing examples are shown in [68].

4.3. Hyperfine-Correlated ENDOR Spectroscopy

The resolution of the basic 1D Mims and Davies ENDOR sequences can be improved by disentangling the spectrum into a second appropriately chosen dimension. One approach is to correlate the ENDOR frequencies with their corresponding hyperfine frequencies, so-called hyperfine-correlated ENDOR spectroscopy. We discuss two sequences that achieve this correlation: 2D Mims ENDOR and HYEND (hyperfine correlated ENDOR).

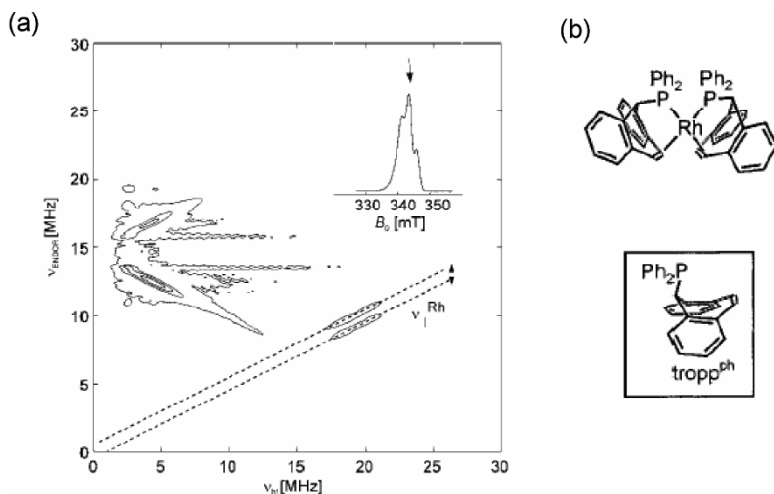


Figure 18. (a) Two-dimensional Mims ENDOR spectrum of $[\text{Rh}(\text{tropp}^{\text{ph}})_2]$. The dashed lines are separated by $2\nu_{\text{hf}}(\text{Rh})$ and cross the ν_{hf} and ν_{ENDOR} axes at $\nu_{\text{hf}}(\text{Rh})$. Proton signals are centered around $\nu_{\text{ENDOR}} = 15$ MHz and have hyperfine couplings up to ~ 10 MHz. Inset: EPR spectrum, the arrow indicates the observer position used for the ENDOR experiment. (b) Structure of $[\text{Rh}(\text{tropp}^{\text{ph}})_2]$ and the tropp^{ph} ligand. Modified with permission from [69]. Copyright © 2002, Editions Scientifiques Elsevier.

The 1D Mims ENDOR sequence can readily be extended to include a hyperfine dimension by incrementing, in addition to the r.f. frequency, the τ value. Equation (27) shows that the ENDOR efficiency oscillates with $\cos(A_{\text{ST}}\tau)$, and thus performing a FT of the time-domain traces recorded as a function of τ results in a hyperfine-correlated ENDOR spectrum. An example is shown in Figure 18 for the complex $[\text{Rh}(\text{tropp}^{\text{ph}})_2]$, which has rhodium ($I = 1/2$) hyperfine couplings in the range 16–21 MHz [69].

2D Mims ENDOR is restricted to hyperfine couplings smaller than the frequency range covered by the m.w. pulses, typically < 50 MHz, and can suffer from poor resolution along the hyperfine axis as the signal decays with the phase memory time T_{M} (which is often of the order of only a few microseconds in transition metal complexes).

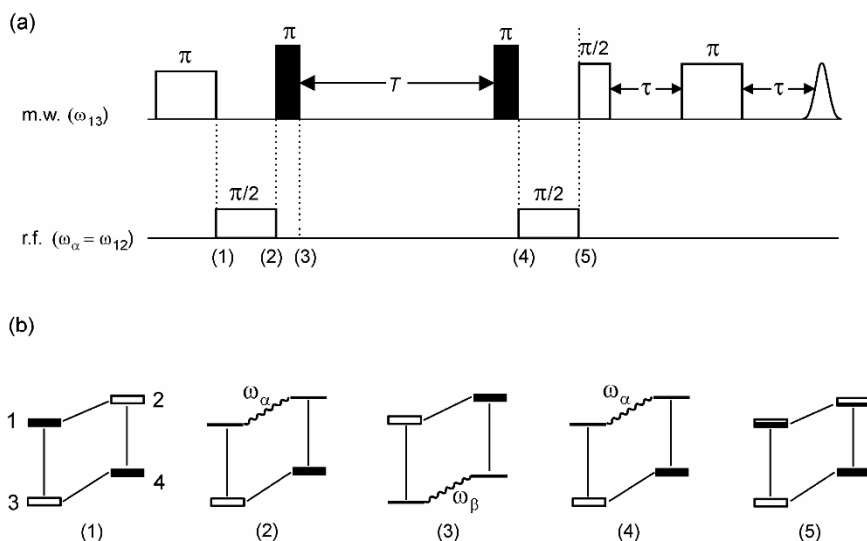


Figure 19. HYEND experiment. (a) Pulse sequence. (b) Four-level energy diagrams for an $S = 1/2, I = 1/2$ spin system illustrating the different states obtained during the experiment. Modified with permission from [7]. Copyright © 2001, Oxford University Press.

The HYEND experiment [70] also correlates ENDOR frequencies with their corresponding hyperfine couplings. The pulse sequence is shown in Figure 19a. The nuclear frequency dimension is obtained by varying the frequency of the two selective $\pi/2$ r.f. pulses, and the hyperfine dimension by the FT of the echo modulations recorded as a function of the time T . The states attained during the experiment for an $S = 1/2, I = 1/2$ spin system are shown in Figure 19b. The experiment is easily understood qualitatively. We assume that the first m.w. pulse is on resonance with the allowed EPR transition (1,3) and the r.f. pulse has the frequency ω_{α} and is thus resonant with the nuclear transition (1,2). The first m.w. pulse inverts the polarization of transition (1,3), and the selective r.f. pulse transfers the polarization of transition (1,2) to nuclear coherence (wavy line). This coherence is immediately transferred by a nonselective m.w. π pulse to the β electron spin manifold, where it evolves with the nuclear frequency ω_{β} for a time T . The second nonselective m.w. π pulse transfers the nuclear coherence back to the α manifold, where the second r.f. pulse transfers the nuclear coherence back to electron polarization, which is detected with the m.w. primary echo sequence. The two r.f. pulses must remain coherent during the sequence, and then the polarization created by the second r.f. pulse is dependent upon the phase accumulated by the nuclear coherence during the time T in the β manifold with respect to the phase of the r.f. field. This phase is given by $(\omega_{\alpha} + \omega_{\beta})T$ (weak coupling) or $(\omega_{\alpha} - \omega_{\beta})T$ (strong coupling). The HYEND signal as a function of T , for an isotropic hyperfine interaction with the r.f. pulses resonant with a nuclear transition, is given by

$$V_{\alpha/\beta}(T) = \pm \text{sign}(2\omega_I + a_{\text{iso}}) \cos(\omega_- T) \text{ with } \omega_- = \omega_\alpha - \omega_\beta = a_{\text{iso}}. \quad (28)$$

Figure 20 illustrates a HYEND spectrum from a $[\text{Rh}(\text{trop}_2\text{NCH}_2)(\text{PPh}_3)]$ complex [71], which demonstrates the resolution of ^{13}C and ^{103}Rh signals that are otherwise difficult to assign in an X-band Davies ENDOR experiment.

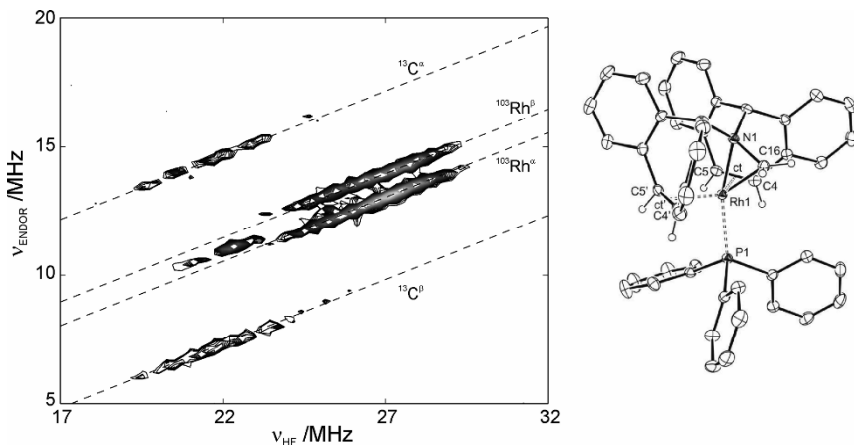


Figure 20. X-band HYEND spectrum of $[\text{Rh}(\text{trop}_2\text{NCH}_2)(\text{PPh}_3)]$ in THF measured at 15 K. The dashed lines are separated by twice the nuclear Zeeman interaction ($2\nu_I$) of ^{103}Rh and ^{13}C , and cross the ν_{ENDOR} and ν_{HF} axes at $\nu_I(^{103}\text{Rh})$ and $\nu_I(^{13}\text{C})$, respectively. Modified with permission from [71]. Copyright © 2006, Wiley-VCH.

4.4. Triple Resonance

This experiment is usually employed to determine the relative sign of two hyperfine couplings [72], or in the 2D version additionally the relative orientation between two hyperfine tensors [73,74]. In a triple resonance (or double ENDOR) experiment, the nuclear transitions are excited with two r.f. fields. Figure 21a shows the pulse sequence based on the Davies ENDOR approach. The mixing time now consists of two r.f. π pulses separated by a time ΔT . The first r.f. pulse (pump pulse) with frequency ω_{f1} must be resonant with a particular nuclear transition, while the frequency ω_{f2} of the second r.f. pulse (scan pulse) is swept through the ENDOR spectrum. Figure 21b shows the expected spectra for an $S = 1/2$, $I_1 = 1/2$, $I_2 = 1/2$ spin system in the weak coupling case ($A_{1S} > A_{2S} > 0$, $\omega_{11} = \omega_{21}$): the ENDOR spectrum (top), the triple spectrum (middle) when the pump pulse is resonant with peak 1, and the difference triple spectrum (bottom) obtained by subtraction. Since peak 2 occurs on the same side of ω_I as the pump pulse on peak 1, the two hyperfine couplings have the same sign. The difference spectrum contains only transitions that belong to the same electron spin manifold of the same paramagnetic center.

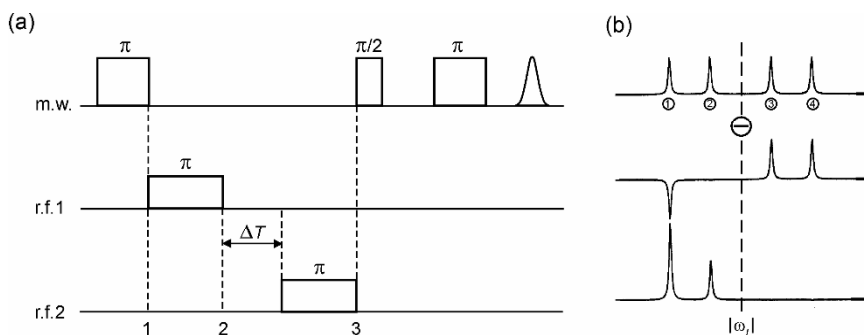


Figure 21. (a) Pulse sequence for the triple resonance experiment. (b) ENDOR spectrum (top), triple spectrum (middle), and difference triple spectrum (bottom). Modified with permission from [7]. Copyright © 2001, Oxford University Press.

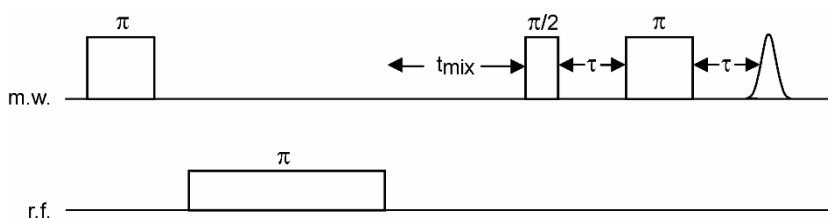


Figure 22. Pulse sequence for the variable mixing-time ENDOR experiments based on the Davies ENDOR sequence. Under suitable conditions the asymmetry of the ENDOR spectrum depends upon the variable mixing time t_{mix} , and the sign of the hyperfine coupling.

4.5. Variable Mixing Time ENDOR

Variable mixing time ENDOR experiments can be used to determine the absolute sign of a hyperfine coupling [75]. One such sequence based on Davies ENDOR is shown in Figure 22 [76], and includes an additional variable mixing time (VMT), t_{mix} . Under suitable conditions the ENDOR signals from the two electron spin manifolds become distorted (asymmetric), with the asymmetry depending upon the electron and nuclear spin-lattice relaxation and cross-relaxation times, T_{1e} , T_{1n} , and T_{1x} , respectively, the thermal polarization, and the sign of the hyperfine coupling. Under suitable experimental conditions, usually low temperature and high field, the sign of the hyperfine coupling can be determined from the relative intensity of the ENDOR signals from the two m_S manifolds. Epel and colleagues [77] provide an example of this approach using ^1H W-band ENDOR on frozen solutions of nitrous oxide reductase (N_2OR).

4.6. High-Field ENDOR

The advantages of measuring ENDOR spectra at high field are (1) separation of signals of nuclei with different γ_n , (2) increased orientation selectivity, (3) increased sensitivity for samples when only a small amount of material is available or where it is only possible to grow small single crystals, (4) improved resolution of paramagnetic centers with different g -values, and hence their ENDOR spectra, (5) spectra with low γ_n can be measured, such as ^2H nuclei, (6) simplification of spectra from high-spin systems where the electron Zeeman interaction is dominant, and (7) it is often possible to determine the absolute sign of the hyperfine interaction.

Points 1 and 2 can be easily appreciated by inspection of the spin Hamiltonian given in Eq. (1); the electron and nuclear Zeeman interactions are field dependent. For this reason overlapping spectra of different types of nuclei can be separated at higher B_0 fields. For instance, at X-band frequencies (e.g., $B_0 = 330$ mT), the ENDOR spectra of weakly coupled ^1H and ^{19}F nuclei overlap since they are approximately centered at $\nu_{\text{H}} = 14$ MHz and $\nu_{\text{F}} = 13.2$ MHz, respectively. By measuring at W-band frequencies (e.g., $B_0 = 3300$ mT) the difference between $\nu_{\text{H}} = 140$ MHz and $\nu_{\text{F}} = 132$ MHz might be sufficient to separate the two signals. Another example, often encountered in X-band ENDOR spectra of transition metal complexes, is the overlap of strongly coupled ^{14}N signals centered at $A_{\text{S}}/2 \approx 15$ MHz and weakly coupled ^1H signals centered at $\nu_{\text{H}} \approx 14$ MHz (see Fig. 16). At higher m.w. frequencies (e.g., Q-band, $\nu_{\text{H}} \approx 50$ MHz) the two signals can be fully separated.

In the case of strongly coupled nuclei with $I > 1/2$, the measurement at higher B_0 fields can improve resolution because of the increased nuclear Zeeman splitting. An example is shown in Figure 23 for the Cu(II) complex of N-confused tetraphenylporphyrin. The Davies ENDOR spectra measured close to g_{\parallel} (Fig. 23a) consist of doublets split by $2\nu_{^{14}\text{N}}$ and centered at $\nu_{\text{ENDOR}} = 30$ MHz. Consequently, these peaks are assigned to strongly coupled nitrogens of the porphyrin core. Due to the unresolved nuclear quadrupole interaction along this orientation, the resolution enhancement gained by going from X- to Q-band frequencies does not provide any further information. The situation is different for the observer position at g_{\perp} . The X-band Davies ENDOR spectrum (Fig. 23b, left) consists of five peaks corresponding to the turning points of the orientation dependent single-quantum nuclear frequencies (Fig. 23c, left). These four frequencies strongly overlap because the nuclear Zeeman and quadrupole splittings are comparable ($2\nu_{^{14}\text{N}} = 2.1$ MHz, $3P \approx 2.8$ MHz). In going to Q-band frequency (Fig. 23b, right) the nuclear Zeeman splitting increases to $2\nu_{^{14}\text{N}} = 7.6$ MHz, and this results in an almost complete separation of the nitrogen signals from the two electron spin manifolds (Fig. 23c, right). This resolution enhancement allows for a more straightforward spectrum simulation [42].

In going to higher B_0 fields, the resolution of ENDOR signals belonging to the same type of nucleus of the same paramagnetic species only improves as a result of the increased orientation selection (less contributing orientations equates to sharper

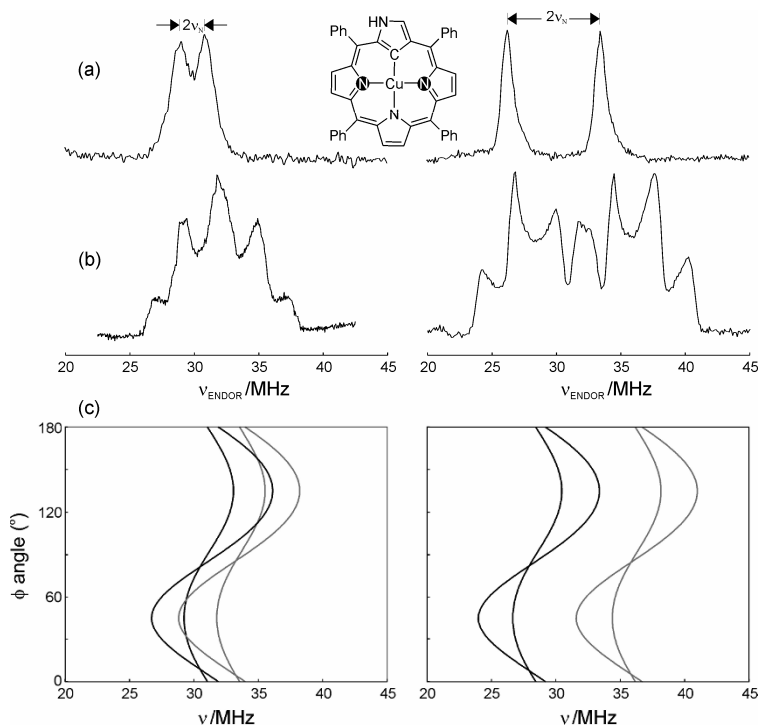


Figure 23. Comparison between X-band (left) and Q-band (right) Davies ENDOR spectra of Cu(II)NCTPP diluted in ZnTPP powder. (a) Single-crystal like spectra measured at g_{\parallel} (\mathbf{B}_0 perpendicular to the porphyrin plane). The peaks are centered at 30 MHz and split by $2\nu_N$; therefore, they are assigned to the two magnetically equivalent strongly coupled core nitrogens with a hyperfine coupling of 60 MHz and an unresolved nuclear quadrupole interaction along this orientation. (b) Spectra measured at observer positions corresponding to g_{\perp} (\mathbf{B}_0 in the porphyrin plane). (c) Theoretical in-plane ($\theta = \pi/2$) orientation dependence of the single-quantum nuclear frequencies upon the polar angle ϕ . Black curves: α electron spin manifold; gray curves: β electron spin manifold. Simulation parameters: $(A_1, A_2, A_3) = (71.5, 58.3, 59.5)$ MHz and $(P_1, P_2, P_3) = (-0.87, 1.00, -0.13)$ MHz, $\nu_N = 1.05$ MHz for X-band (left) and $\nu_N = 3.80$ MHz for Q-band (right). Modified with permission from [42]. Copyright © 2005, Wiley-VCH.

lines). However, this resolution improvement is often very modest, particularly for transition metal complexes where the g anisotropy is already resolved at X- or Q-band. A 2D experiment can help in these cases, and the best resolution may be achieved at lower m.w. frequencies. This is especially true for overlapping proton signals where HYSORE [59], or the ENDOR equivalent HYSORE-ENDOR, is ideal for separating overlapping proton signals which originate from hyperfine interactions with different anisotropies. This is because the signal shifts from the antidiagonal line are proportional to the hyperfine anisotropy and inversely proportional to the proton Larmor frequency [Eq. (23)]. A lower B_0 field also offers an

additional advantage for strongly coupled, low γ_n nuclei, since a very short r.f. π pulse can be realized as a result of the hyperfine enhancement effect (see §4.7).

4.7. Hyperfine Enhancement of r.f. Pulses

A significant technical challenge in ENDOR is to produce a strong r.f. B_2 field at the location of the sample. The effective r.f. field $B_{\text{rf}}^{\text{eff}}(t)$ that induces transitions at the nucleus is enhanced by the hyperfine interaction between the electron and the nuclear spin, an effect called hyperfine enhancement. For an isotropic hyperfine interaction and with $B_2 \ll B_0$, the component of \mathbf{B}_{hf} perpendicular to \mathbf{B}_0 can be written as $B_{\text{hf}}^\perp = a_{\text{iso}}/(\omega_1 B_2)$, and the total oscillating field amplitude B_2^{eff} with the enhancement factor E as [78]

$$B_2^{\text{eff}} = EB_2 \quad \text{with} \quad E = \left| 1 + \frac{m_s a_{\text{iso}}}{\omega_1} \right|. \quad (29)$$

More general formulae for first-order line intensities, which include hyperfine enhancement, are given in [78–81]. Pronounced hyperfine enhancements (or de-enhancements) are often found in transition metal complexes with ligand nuclei having large hyperfine couplings in comparison to their gyromagnetic ratios. This is often the case at X-band for strongly coupled nitrogens. For example, a nitrogen with a hyperfine coupling of $A_s/2\pi = 40$ MHz, $m_s = \pm 1/2$, and $\nu_1 = 1$ MHz, has a hyperfine enhancement factor of $E_\pm = 21, 19$. Practically, this means that a π r.f. pulse can be achieved in a time much shorter than would otherwise be the case, an advantage. Note that this effect will decrease at higher B_0 fields; at W-band $\nu_1 = 10$ MHz and the hyperfine enhancement factor is $E_\pm = 1, 3$ for $A_s/2\pi = 40$ MHz. This effect shows that ENDOR performed at low B_0 fields is sometimes advantageous because of the higher sensitivity afforded by a larger effective B_2 .

Equation (29) shows that for low-frequency transitions, where $A_s \approx 2|\omega_1|$, one of the E values is close to zero so that it becomes exceedingly difficult to excite these nuclear transitions. In this case ESEEM methods are required.

4.8. Time-Domain ENDOR

In this section we describe selected time-domain ENDOR experiments where the free evolution of nuclear coherence is recorded. These experiments consist of at least three building blocks: a nuclear coherence generator, a free evolution period for the nuclear coherence, and a nuclear coherence detector.

Time-Domain ENDOR methods often employ a chirp r.f. pulse; a pulse with a linearly swept frequency. This approach enables broadband excitation of the nuclear transitions that covers the entire frequency range of the ENDOR spectrum, often of the order of 30 MHz. Note that with the available r.f. power this broad excitation range is not possible without the r.f. frequency sweep (i.e., a π r.f. pulse of around 10 ns would be required, whereas a length of around 10 μ s is typically needed for protons).

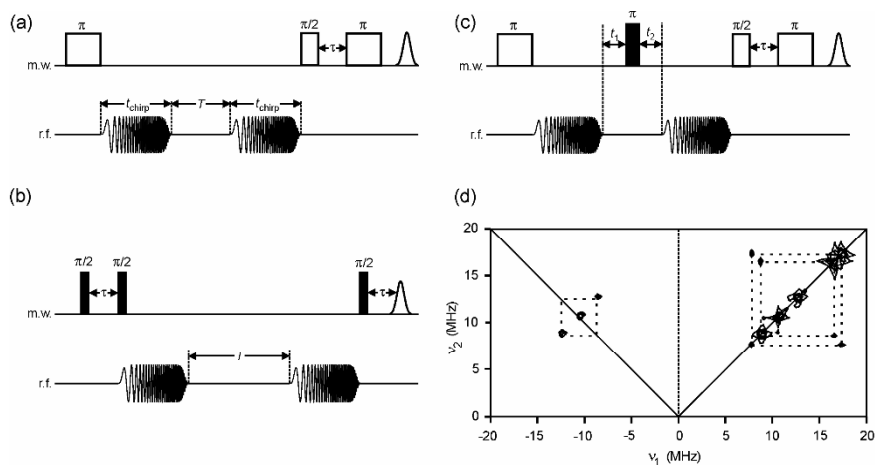


Figure 24. Sequences for chirp ENDOR experiments: (a) Davies-type chirp ENDOR; (b) Mims-type chirp ENDOR; (c) Chirp-ENDOR-HYSCORE sequence; and (d) Two-dimensional chirp ENDOR-HYSCORE spectrum of a Cu(II)-doped glycine single-crystal. Cross-peaks in the first quadrant correspond to proton ENDOR lines, cross-peaks in the second quadrant to nitrogen ENDOR lines. Modified with permission from [7]. Copyright © 2001, Oxford University Press.

The pulse sequences for a Davies-type, a Mims-type, and a Chirp-ENDOR-HYSCORE are shown in Figure 24 [82]. In the Davies-type sequence (a), the nuclear coherence generator consists of the first m.w. and r.f. chirp pulse, followed by a variable free evolution time T , and the nuclear coherence detector consisting of the second r.f. chirp pulse and the m.w. primary echo sequence. The time-domain trace is thus measured by incrementing T and recording the echo intensity. FT gives the ENDOR spectrum. The Mims-type sequence, shown in Figure 24b, functions in a similar way.

Figure 24c shows an ENDOR “equivalent” to HYSCORE, the Chirp-ENDOR-HYSCORE sequence. This sequence is based on the Davies-type chirp sequence, but with the addition of the m.w. π pulse during the free evolution time of the nuclear coherence. As with HYSCORE, the π pulse transfers nuclear coherences between the electron spin manifolds, and FT of the echo intensity as a function of the two evolution times t_1 and t_2 , gives a 2D spectrum correlating the nuclear frequencies of the different electron spin manifolds, exactly as in a HYSCORE experiment. A 2D chirp-ENDOR-HYSCORE spectrum of a copper complex is shown in Figure 24d, and shows peaks from strongly coupled nitrogens in the second quadrant and from weakly coupled protons in the first quadrant. This method thus enables a clear separation of the nitrogen and proton signals, in contrast to a conventional 1D Davies ENDOR spectrum, where they overlap. ENDOR-HYSCORE is complementary to conventional HYSCORE, since ENDOR is ideal for measuring large hyperfine couplings and isotropic hyperfine couplings, and

can measure signals when \mathbf{B}_0 is along a principal axis direction. Conversely, in ESEEM the modulation depth vanishes for isotropic hyperfine couplings (strictly true for $I = 1/2$) and when \mathbf{B}_0 is along a principal value, and the m.w. pulses must have a sufficient bandwidth to excite both allowed and forbidden transitions of the same spin packet. The excitation bandwidth usually restricts ESEEM techniques to hyperfine interactions <50 MHz.

5. FIELD-SWEPT EPR EXPERIMENTS

This class of experiments involves measuring a field-swept EPR spectrum, either with CW excitation or using m.w. pulses. A variety of 2D pulse field-swept EPR experiments exist that aim to increase the resolution by the addition of a second dimension to the B_0 sweep; T_1 and T_2 filtered EPR [83], forbidden-transition-labeled EPR (FORTE) [84], anisotropy-resolved EPR [85], and magic-angle spinning EPR [86]. Here only two types of experiments are discussed: nutation and electron Zeeman-resolved EPR.

5.1. Nutation Experiments

It is not always possible to evaluate the electron spin quantum number S of a paramagnetic species from the field-swept EPR spectrum. Often only the $(|-1/2\rangle, |+1/2\rangle)$ EPR transitions can be observed, or several species with different S values contribute to the spectrum. Under suitable conditions S can be determined from the nutation frequency ω_{nut} . If the m.w. radiation excites only a single transition then

$$\omega_{\text{nut}}(m_s, m_s + 1) = \frac{g_1 \beta_e B_1}{\hbar} [S(S+1) - m_s(m_s + 1)]^{1/2}. \quad (30)$$

B_1 can be determined separately in a calibration experiment with a standard sample such as DPPH ($S = 1/2$, $g = g_1 = 2.0036$), and g_1 is related to the laboratory frame x -axis [7].

Nutation experiments allow for the measurement of very low g -values, for example, in a Ti^{3+} -doped sapphire sample $g_{\perp} = 0.04$ was measured by nutation spectroscopy [87]. Separation of the allowed and forbidden EPR transitions can be achieved in a 2D nutation experiment (one axis has the B_0 field sweep and the other the nutation frequencies), since allowed transitions have a significantly lower nutation frequency than the forbidden transitions [88]. A 2D nutation experiment also allows spectra from different sites in a single crystal to be separated, as for example in single crystals of $\text{N,N}'$ -ethylenebis-(acetylacetonatiminato)Cu(II) [89]. There are several pulse sequences available to measure nutation frequencies (see, e.g., [90,91]). We explain briefly the PEANUT sequence given in Figure 25a [88]. The sequence begins with a $\pi/2$ pulse whose length determines the frequency range of the spins involved in the experiment. The transverse magnetization excited by this

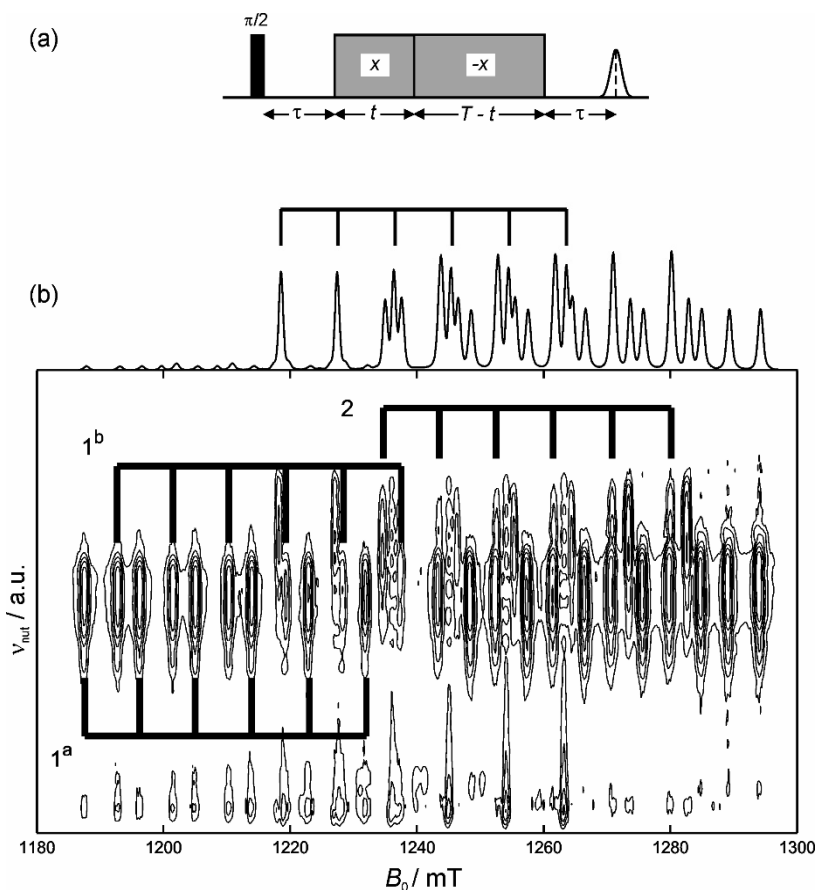


Figure 25. (a) PEANUT sequence for the measurement of nutation frequencies. (b) Peanut experiment at Q-band (35.3 GHz) on a single crystal of $\text{Zn}(\text{Im})_6$ doped with 0.4% $\text{Mn}(\text{II})$ ($S = 5/2$, $I = 5/2$). Labels $1^a, 1^b$ show the $(|-5/2, m_i\rangle, |-3/2, m_i\rangle)$ transitions for the two sites in the single crystal. Label 2 shows the $(|+3/2, m_i\rangle, |+1/2, m_i\rangle)$ transitions for site **a** in the single crystal, the six lines from site **b** are approximately 2 mT to the right of this pattern. Inset: FID-detected EPR spectrum with the $(|-1/2, m_i\rangle, |+1/2, m_i\rangle)$ transitions marked. From data provided by Dr. Inés García Rubio.

pulse evolves and defocuses during the evolution period τ . Next, a pulse of constant length T , which is subdivided into two parts of variable length t and $T-t$ with opposite m.w. phases applied. During time t the B_1 m.w. field is orientated along the x -axis and the magnetization nutates with frequency ω_{eff} around an effective field B'_{eff} , while during time $T-t$ the B_1 m.w. field is orientated along the minus x -axis and the magnetization nutates with the same frequency ω_{eff} but around an effective field B_{eff} . The phase shift at time t causes a partial refocusing to a rotary echo, which is detected via a spin-locked echo formed at time τ after the nutation

pulse. A single time-domain trace is thus obtained by measuring at a fixed field position and varying the time t during the nutation pulse of constant length T . A 2D spectrum is obtained by sweeping B_0 .

Figure 25b shows a PEANUT spectrum measured at Q-band (35.3 GHz) on a single crystal of $\text{Zn}(\text{Im})_6$ doped with 0.4% $\text{Mn}(\text{II})$ ($S = 5/2$, $I = 5/2$ spin system). The sample contains molecules in two slightly different orientations due to the twinning of the crystal. The magnetic field sweep is along the x -axis, and the y -axis plots the nutation frequencies. The transition moment between the various m_S -manifolds depends on m_S , which results in slightly different turning angles for the $(|\pm 5/2, m_I\rangle, |\pm 3/2, m_I\rangle)$, $(|\pm 3/2, m_I\rangle, |\pm 1/2, m_I\rangle)$, and $(|-1/2, m_I\rangle, |+1/2, m_I\rangle)$ transitions. In this way the different transitions can be identified in the PEANUT experiment by their position on the nutation axis. The most intense lines in the spectrum correspond to the transitions $(|\pm 5/2, m_I\rangle, |\pm 3/2, m_I\rangle)$. At a higher nutation frequency the transitions $(|\pm 3/2, m_I\rangle, |\pm 1/2, m_I\rangle)$ can be observed, and also, very weakly, the transitions $(|-1/2, m_I\rangle, |+1/2, m_I\rangle)$. The upper spectrum corresponds to the FID-detected spectrum of the single crystal sample for the same crystal orientation.

5.2. Electron Zeeman-Resolved EPR

This 2D EPR experiment makes use of the fact that the electron Zeeman interaction is the only relevant field-dependent term in the spin Hamiltonian. The pulse sequence is shown in Figure 26a, and consists of a primary echo sequence together with a sinusoidal varying magnetic field, $\Delta B_0(t)$, directed along the B_0 axis. The additional magnetic field causes an accumulation of the phase of electron coherence, so that transitions with different g -values will be separated from one another. An example of this approach to disentangle a spectrum from a powder sample with an axial g -matrix and hyperfine interaction from an $I = 3/2$ nucleus is given in Figure 26b [92].

6. STRATEGIES AND OUTLOOK

In this review we have concentrated on explaining the basic mechanisms behind ENDOR and ESEEM spectroscopy. These two methods, along with field-swept EPR experiments, provide a means to obtain a detailed description of the EPR parameters of paramagnetic centers in single crystals, powders, and frozen solutions. To obtain the most accurate EPR parameters requires not one technique, but a combination, and preferably applied at several m.w. frequencies. Measurements at multi-frequencies allow possible ambiguities that arise from data measured at only one m.w. frequency to be resolved.

For ESEEM experiments in particular, the B_0 field strength needs to be matched to the hyperfine interaction of interest; the largest echo envelope modulation occurs when the nuclear Zeeman and hyperfine interaction are equal in magnitude (strictly true only for $I = 1/2$ nuclei). For a nucleus with a particular hyperfine interaction, the modulation depth may be too weak to observe at X-band,

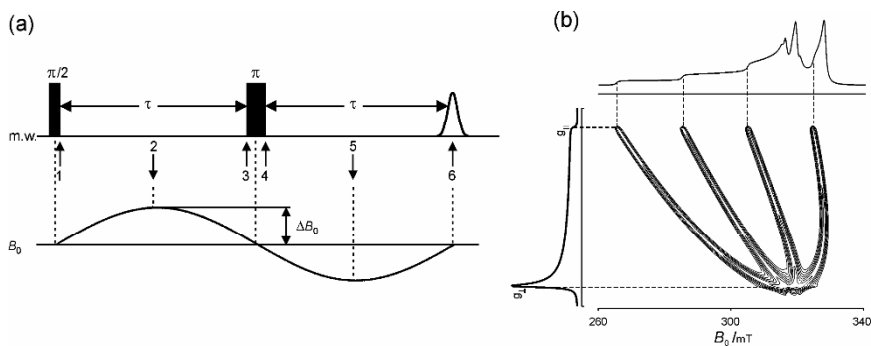


Figure 26. (a) EZ-EPR experiment consisting of a primary echo sequence and a sinusoidal B_0 variation; (b) model calculation for an $S = 1/2$, $I = 3/2$ spin system. Modified with permission from [7]. Copyright © 2001, Oxford University Press.

whereas at Q-band the sensitivity can be maximum. Even when the modulation depth is predicted to be low for a particular nucleus, sensitivity improvements can conveniently be achieved by using matched pulses with an optimal m.w. field strength and length.

Generally, ENDOR resolution is superior at higher B_0 fields. However, for nuclei with low γ_n values and large hyperfine couplings, the sensitivity may be better at lower fields (X-band) because the ENDOR enhancement effect allows very short π r.f. pulses to be used. Additionally, the EPR spectrum is less spread out and thus more orientations contribute to the measurement. At lower B_0 fields, overlapping signals from different nuclei can be disentangled by 2D ENDOR experiments. Several possibilities have been described here.

Spectrum simulation is an integral part of EPR spectroscopy of disordered systems. To obtain the most accurate EPR parameters, it is usually necessary to measure (ENDOR or ESEEM) spectra at a number of observer positions across the EPR spectrum. Ideally, spectra at enough field positions should be recorded so that the set contains signals from all orientations of the paramagnetic center with respect to B_0 . The number required depends on the width of the EPR spectrum. In disordered systems spectra taken away from the “single-crystal” positions consist of ridges whose width reflects the anisotropy of the spin Hamiltonian parameters, and the orientation selection. Sharp peaks are usually observed at “single-crystal” positions, which generally makes their interpretation straightforward. Once the data have been collected, each field position needs to be correctly interpreted and the signals simulated. For time-domain experiments, usually a computer programme based on the density matrix formalism [93] is implemented. Examples include EasySpin [94,95] and XSophe [96,97], and programmes by Madi et al. [31] and Shane et al. [98]. 1D time-domain experiments, such as two- or three-pulse ESEEM, can be simulated quickly with this approach. This allows in some situations a fitting algorithm to be implemented. However, simulation of 2D experiments such as HYSORE are very time consuming, particularly if $S > 1/2$, if more than one nu-

clear spin needs to be considered, and for nuclei with $I > \frac{1}{2}$. In these cases, we suggest that a scan of possible solutions first be undertaken by computing just the frequency positions of the cross-peaks by exact diagonalization of the spin Hamiltonian. This calculation is very rapid, and the correct orientation selection can be included. Once possible solutions are found, they should be checked with a simulation that includes both position and intensity information. For ENDOR, very often simulation programs calculate the nuclear frequencies and transitions by diagonalization of the spin Hamiltonian, an approach appropriate for resonant irradiation. In this case appropriate care should be taken when comparing this simulation to pulse ENDOR spectra (e.g., blind spots, hyperfine enhancement, pulse selectivity).

ACKNOWLEDGMENTS

This work was supported by the Swiss *National Science Foundation*. We acknowledge our collaborators: Prof. Hansjörg Grützmacher, Laboratory of Inorganic Chemistry, Department of Chemistry and Applied Biosciences, ETH-Zürich, 8093 Zürich, Switzerland (*Rh chemistry*); Prof. Dr. R. K. Thauer, Max Planck Institute for Terrestrial Microbiology, Department of Biochemistry, Karl-von-Frisch-Straße, 35043 Marburg, Germany, and Prof. Dr. B. Jaun, Laboratory of Organic Chemistry, Department of Chemistry and Applied Biosciences, ETH Zürich, 8093 Zürich, Switzerland (*MCR*). We thank all members of the EPR group at ETH for their support.

REFERENCES

1. Hoffman BM. 2003. ENDOR of metalloenzymes. *Acc Chem Res* **36**:522–529.
2. Hoffman BM. 2003. Electron-nuclear double resonance spectroscopy (and electron spin-echo envelope modulation spectroscopy) in bioinorganic chemistry. *Proc Natl Acad Sci USA* **100**:3575–3578.
3. Deligiannakis Y, Louloudi M, Hadjiliadis N. 2000. Electron spin echo envelope modulation (ESEEM) spectroscopy as a tool to investigate the coordination environment of metal centers. *Coord Chem Rev* **204**:1–112.
4. Lakshmi KV, Brudvig GW. 2001. Pulsed electron paramagnetic resonance methods for macromolecular structure determination. *Curr Opin Struct Biol* **11**:523–531.
5. Prisner T, Rohrer M, MacMillan F. 2001. Pulsed EPR spectroscopy: biological applications. *Annu Rev Phys Chem* **52**:279–313.
6. Goldfarb D, Arieli D. 2004. Spin distribution and the location of protons in paramagnetic proteins. *Annu Rev Biophys Biomol Struct* **33**:441–468.
7. Schweiger A, Jeschke G. 2001. *Principles of pulse electron paramagnetic resonance*. Oxford: Oxford UP.
8. Spin density $\rho(x,y,z)$ denotes the difference in the number of electrons per unit volume having spin up and down: $\rho(x,y,z) = \rho^\alpha(x,y,z) - \rho^\beta(x,y,z)$. Spin population ρ_x^y is interpretable as the integrated spin density $\rho(x,y,z)$ in the orbital ψ centered on nucleus x and is the difference in the populations of unpaired electrons with spin up and spin down,

- $\rho_x^{\nu} = \rho_x^{\nu\alpha} - \rho_x^{\nu\beta}$. See Gerson F, Huber W. 2003. *Electron spin resonance spectroscopy of organic radicals*. Weinheim: Wiley-VCH Verlag.
- McGarvey BR. 1967. The isotropic hyperfine interaction. *J Phys Chem* **71**:51–67.
 - Morton JR, Preston KF. 1978. Atomic parameters for paramagnetic-resonance data. *J Magn Reson* **30**:577–582.
 - Golding RM, Stubbs LC. 1978. Higher-order hyperfine terms in spin. *Proc Roy Soc London* **A362**:525–536.
 - McGarvey BR. 1987. In *Electronic magnetic resonance of the solid state*, p. 83. Ed JA Weil. Ottawa: Canadian Society of Chemistry.
 - Neese F, Solomon EI. 2002. Interpretation and calculation of Spin Hamiltonian parameters in transition metal complexes. In *Magnetism: molecules to materials*, IV. Ed JS Miller, M Drillon. Weinheim: Wiley-VCH Verlag.
 - Harmer J, Van Doorslaer S, Gromov I, Schweiger A. 2002. Corrin nitrogens and remote dimethylbenzimidazole nitrogen interactions in Cob(II)alamin studied with HYSCORE at X- and Q-band. *Chem Phys Lett* **358**:8–16.
 - Finazzo C, Harmer J, Jaun B, Duin EC, Mahlert F, Thauer RK, Van Doorslaer S, Schweiger A. 2003. Characterization of the MCRred2 form of methyl-coenzyme M reductase: a pulse EPR and ENDOR study. *J Biol Inorg Chem* **8**:586–593.
 - Rowan LG, Hahn EL, Mims WB. 1965. Electron-spin-echo envelope modulation. *Phys Rev* **A137**:61–71.
 - Mims WB. 1972. Envelope modulation in spin-echo experiments. *Phys Rev* **B5**:2409–2419.
 - Zweier J, Aisen P, Peisach J, Mims WB. 1979. Pulsed electron paramagnetic resonance studies of the copper complexes of transferrin. *J Biol Chem* **254**:3512–3515.
 - Lu J, Bender CJ, McCracken J, Peisach J, Severns JC, McMillin DR. 1992. Pulsed EPR studies of the type 2 copper binding site in the mercury derivative of laccase. *Biochemistry* **31**:6265–6272.
 - Dikanov SA, Shubin AA, Parmon VN. 1981. Modulation effects in the electron spin echo resulting from hyperfine interaction with a nucleus of an arbitrary spin. *J Magn Reson* **42**:474–487.
 - Stoll S, Calle C, Mitrikas G, Schweiger A. 2005. Peak suppression in ESEEM spectra of multinuclear spin systems. *J Magn Reson* **177**:93–101.
 - Dikanov SA, Samoilova RI, Kolling DR, Holland JT, Crofts AR. 2004. Hydrogen bonds involved in binding the Q_i-site semiquinone in the bc₁ complex, identified through deuterium exchange using pulsed EPR. *J Biol Chem* **279**:15814–15823.
 - Ponti A, Schweiger A. 1994. Echo phenomena in electron paramagnetic resonance spectroscopy. *Appl Magn Reson* **7**:363–403.
 - Ponti A, Schweiger A. 1995. Nuclear coherence-transfer echoes in pulsed EPR. *J Chem Phys* **102**:5207–5219.
 - Hubrich M, Jeschke G, Schweiger A. 1995. The generalized hyperfine sublevel coherence transfer experiment in one and two dimensions. *J Chem Phys* **104**:2172–2184.
 - Schossler PM. 1998. Electron paramagnetic resonance study of the copper (II) complexation with carbonate ligands in aqueous solution and at calcium carbonate surfaces. PhD thesis, No. 12669, ETH Zürich.
 - Vinck E, Van Doorslaer S. 2004. Analysing low-spin ferric complexes using pulse EPR techniques: a structure determination of bis (4-methylimidazole) (tetraphenylporphyrinato) iron (III). *Phys Chem Chem Phys* **6**:5324–5330.

28. Höfer P, Grupp A, Nebenführ G, Mehring M. 1986. Hyperfine sublevel correlation (HYSCORE) spectroscopy: a 2D ESR investigation of the squaric acid radical. *Chem Phys Lett* **132**:279–282.
29. Tyryshkin AM, Dikanov SA, Goldfarb D. 1993. Sum combination harmonics in four-pulse ESEEM spectra: study of the ligand geometry in aqua–vanadyl complexes in polycrystalline and glass matrices. *J Magn Reson* **A105**:271–283.
30. Dikanov SA, Tyryshkin AM, Bowman MK. 2000. Intensity of cross-peaks in Hyscore spectra of $S = 1/2$, $I = 1/2$ spin systems. *J Magn Reson* **144**:228–242.
31. Mádi Z, Van Doorslaer S, Schweiger A. 2002. Efficient simulation of ESEEM spectra. *J Magn Reson* **154**:181–191.
32. Stoll S. 2003. Spectral simulations in solid-state EPR. PhD thesis, No. 15059, ETH Zürich.
33. Pöpl A, Kevan L. 1996. A practical strategy for determination of proton hyperfine interaction parameters in paramagnetic transition metal ion complexes by two-dimensional HYSCORE electron spin resonance spectroscopy in disordered systems. *J Phys Chem* **100**:3387–3394.
34. Reijerse E, Dikanov SA. 1991. Electron spin echo envelope modulation spectroscopy on orientationally disordered systems: line shape singularities in $S = 1/2$, $I = 1/2$ spin systems. *J Chem Phys* **95**:836–845.
35. Dikanov SA, Bowman MK. 1995. Cross-peak lineshape of two-dimensional ESEEM spectra in disordered $S = 1/2$, $I = 1/2$ spin systems. *J Magn Reson* **A116**:125–128.
36. Thauer RK. 1998. Biochemistry of methanogenesis: a tribute to Marjory Stephenson. *Microbiology* **144**:2377–2406.
37. Goenrich M, Mahler F, Duin EC, Bauer C, Jaun B, Thauer RK. 2004. Probing the reactivity of Ni in the active site of methyl–coenzyme M reductase with substrate analogues. *J Biol Inorg Chem* **9**:691–705.
38. Hinderberger, D, Piskorski RP, Goenrich G, Thauer RK, Schweiger A, Harmer J, Jaun B. 2006. A nickel–alkyl bond in an inactivated state of the enzyme catalyzing methane formation. *Angew Chem, Int Ed* **45**:3602–3607.
39. Pöpl A, Böttcher R. 1997. Cross peak intensities in two-dimensional four-pulse electron spin echo modulation spectra of deuterium in single crystals. *Chem Phys* **221**:53–66.
40. Dikanov SA, Xun L, Karpel AB, Tyryshkin AM, Bowman MK. 1996. Orientationally-selected two-dimensional ESEEM spectroscopy of the Rieske-type iron–sulfur cluster in 2,4,5-trichlorophenoxyacetate monooxygenase from *Burkholderia cepacia* AC1100. *J Am Chem Soc* **118**:8408–8416.
41. Maryasov AG, Bowman MK. 2004. Hyperfine sublevel correlation (HYSCORE) spectra for paramagnetic centers with nuclear spin $I = 1$ having isotropic hyperfine interactions. *J Phys Chem* **B108**:9412–9420.
42. Mitrikas G, Calle C, Schweiger A. 2005. Asymmetric spin density distribution in the copper (II) complex of N-confused tetraphenylporphyrin: a multifrequency continuous-wave and pulse EPR study. *Angew Chem Int Ed* **44**:3301–3303.
43. The nuclear quadrupole coupling constant $K = e^2qQ/[4I(2I - 1)\hbar]$ and the asymmetry parameter $\eta = (P_x - P_y)/P_z$ are usually given in the definition of the nuclear quadrupole tensor in its principal axes system: $\mathbf{P}^d = [P_x, P_y, P_z] = [-K(1 - \eta), -K(1 + \eta), 2K]$, where Q is the nuclear electrical quadrupole moment and eq is the electric field gradient.
44. Iwasaki T, Kounosu A, Uzawa T, SamoiloVA RI, Dikanov SA. 2004. Orientation-selected ^{15}N -HYSCORE detection of weakly coupled nitrogens around the archaeal Rieske [2Fe–2S] center. *J Am Chem Soc* **126**:13902–13903.

45. Maly T, Grgic L, Zwicker K, Zickermann V, Brandt U, Prisner T. 2006. Cluster N1 of complex I from *Yarrowia lipolytica* studied by pulsed EPR spectroscopy. *J Biol Inorg Chem* **11**:343–350.
46. Foerster S, van Gastel M, Brecht M, Lubitz W. 2005. An orientation-selected ENDOR and HYSCORE study of the Ni–C active state of *Desulfovibrio vulgaris* Miyazaki F hydrogenase. *J Biol Inorg Chem* **10**:51–62.
47. Brecht M, van Gastel M, Buhrke T, Friedrich B, Lubitz W. 2003. Direct detection of a hydrogen ligand in the [NiFe] center of the regulatory H₂-sensing hydrogenase from *Ralstonia eutropha* in its reduced state by HYSCORE and ENDOR spectroscopy. *J Am Chem Soc* **125**:13075–13083.
48. Garcia-Rubio I, Martínez JL, Picorel R, Yruela I, Alonso PJ. 2003. HYSCORE Spectroscopy in the cytochrome *b*₅₅₉ of the photosystem II reaction center. *J Am Chem Soc* **125**:15846–15854.
49. Ioanitescu AI, Dewide S, Kiger L, Marden MC, Moens L, Van Doorslaer S. 2005. Characterization of nonsymbiotic tomato hemoglobin. *Biophys J* **89**:2628–2639.
50. Vinck E, Van Doorslaer S, Dewilde S, Mitrikas G, Schweiger A, Moens L. 2006. Analyzing heme proteins using EPR techniques: the heme-pocket structure of ferric mouse neuroglobin. *J Biol Inorg Chem* **11**:467–475.
51. Gutjahr, M, Böttcher, R, Pöppel A. 2002. Analysis of correlation patterns in hyperfine sublevel correlation spectroscopy of $S = 1/2$, $I = 3/2$ systems. *Appl Magn Reson* **22**:401–414.
52. Matar K, Goldfarb D. 1992. Fourier transform electron spin echo envelope modulation of a $S = 1/2$, $I = 5/2$ spin system: an exact analysis and a second order perturbation approach. *J Chem Phys* **96**:6464–6476.
53. Ponti A. 1997. Electron-spin-echo envelope modulation arising from hyperfine coupling to a nucleus of arbitrary spin. *J Magn Reson* **127**:87–104.
54. Harmer J, Finazzo C, Piskorski R, Bauer C, Jaun B, Duijn EC, Goenrich M, Thauer RK, Van Doorslaer S, Schweiger A. 2005. Spin density and coenzyme M coordination geometry of the ox1 form of methyl-coenzyme M reductase: a pulse EPR study. *J Am Chem Soc* **127**:17744–17755.
55. Cho H, Pfenninger S, Gemperle C, Schweiger A, Ernst RR. 1989. Zero deadtime pulsed ESR by remote echo detection. *Chem Phys Lett* **160**:391–395.
56. Jeschke G, Schweiger A. 1996. Generation and transfer of coherence in electron-nuclear spin systems by non-ideal microwave pulses. *Mol Phys* **88**:355–383.
57. Jeschke G, Rakhmatullin R, Schweiger A. 1998. sensitivity enhancement by matched microwave pulses in one- and two-dimensional electron spin echo envelope modulation spectroscopy. *J Magn Reson* **131**:261–271.
58. Goldfarb D, Kofman V, Libman J, Shanzer A, Rahmatouline R, Van Doorslaer S, Schweiger A. 1998. Double nuclear coherence transfer (DONUT)-HYSCORE: a new tool for the assignment of nuclear frequencies in pulsed EPR experiments. *J Am Chem Soc* **120**:7020–7029.
59. Van Doorslaer, S, Bachmann, R, Schweiger, A. 1999. A pulse EPR and ENDOR investigation of the electronic and geometric structure of cobaltous tetraphenylporphyrin (pyridine). *J Phys Chem A* **103**:5446–5455.
60. Mitrikas G, Schweiger A. 2004. Hyperfine decoupling in electron paramagnetic resonance as a powerful tool for unraveling complicated ESEEM spectra of $S = 1/2$, $I \geq 1/2$ systems. *J Magn Reson* **168**:88–96.

61. Jeschke, G, Schweiger A. 1997. Hyperfine decoupling in electron spin resonance. *J Chem Phys* **106**:9979–9991.
62. Van Doorslaer S, Schweiger A. 1999. New hyperfine-decoupling schemes in electron paramagnetic resonance spectroscopy. *Chem Phys Lett* **308**:187–194.
63. Davies ER. 1974. New pulse ENDOR technique. *Phys Lett* **A47**:1–2.
64. Mims WB. 1965. Pulsed ENDOR experiments. *Proc Roy Soc London* **283**:452.
65. Fan C, Doan PE, Davoust CE, Hoffman B. 1992. Quantitative studies of Davies pulsed ENDOR. *J Magn Reson* **98**:62–72.
66. Bolm C, Martin M, Gescheidt G, Palivan C, Neshchadin D, Bertagnolli H, Feth M, Schweiger A, Mitrikas G, Harmer J. 2003. Spectroscopic investigations of bis(sulfoximine) copper(II) complexes and their relevance in asymmetric catalysis. *J Am Chem Soc*:**125**, 6226–6227.
67. Doan PE, Hoffman B. 1997. Making hyperfine selection in Mims ENDOR independent of deadtime. *Chem Phys Lett* **269**:208–214.
68. Epel B, Arieli D, Baute D, Goldfarb D. 2003. Improving W-band pulsed ENDOR sensitivity-random acquisition and pulsed special TRIPLE. *J Magn Reson* **164**:78–83.
69. Deblon S, Liesum L, Harmer J, Schönberg H, Schweiger A, Grützmacher H. 2002. High-resolution EPR spectroscopic investigations of a homologous set of d⁹-cobalt(0), d⁹-rhodium(0), and d⁹-iridium(0) complexes. *Chem Eur J* **8**:601–611.
70. Jeschke G, Schweiger A. 1995. Hyperfine-correlated electron-nuclear double-resonance spectroscopy. *Chem Phys Lett* **246**:431–438.
71. Maire P, Sreekanth A, Büttner T, Harmer J, Gromov I, Rügger H, Breher F, Schweiger A, Grützmacher H. 2006. Synthesis of a rhoda-aza-cyclopropane and characterization of its radical cation by EPR. *Angew Chem, Int Ed* **45**:3265–3269.
72. Mehring M, Höfer P, Grupp A. 1987. Pulsed electron nuclear double and triple resonance schemes. *Ber Bunsenges Phys Chem* **91**:1132–1137.
73. Epel B, Goldfarb D. 2000. Two-dimensional pulsed TRIPLE at 95 GHz. *J Magn Reson* **146**:196–203.
74. Sammet A, Hubrich M, Spiess HW. 1995. Nature and dynamics of radicals in polyamide as studied by pulsed electron nuclear double resonance. *Adv Mater* **7**:747–750.
75. Bennebroek MT, Schmidt J. 1997. Pulsed ENDOR spectroscopy at large thermal spin populations and the absolute sign of the hyperfine interaction. *J Magn Reson* **128**:199–206.
76. Epel B, Pöpl A, Manikandan P, Vega S, Goldfarb D. 2001. The effects of spin relaxation on the ENDOR spectra recorded at high magnetic fields and low temperatures. *J Magn Reson* **148**:388–397.
77. Epel B, Manikandan P, Kroneck PMH, Goldfarb D. 2001. High-field ENDOR and the sign of hyperfine coupling. *Appl Magn Reson* **21**:287–297.
78. Abragam A, Bleaney B. 1970. *Electron paramagnetic resonance of transition ions*, §4.3, Oxford: Oxford UP.
79. Schweiger A, Günthard HsH. 1982. Transition-probabilities in electron nuclear double-resonance and multiple-resonance spectroscopy with noncoherent and coherent radio-frequency fields. *Chem Phys* **70**:1–22.
80. Schweiger A, Günthard HsH. 1981. Electron nuclear double-resonance with circularly polarized radio-frequency fields (CP-ENDOR): theory and applications. *Mol Phys* **42**:283–295.
81. Schweiger A. 1982. Electron nuclear double-resonance of transition metal complexes with organic ligands. *Struct Bonding* **51**:1–119.

82. Jeschke G, Schweiger A. 1995. Time-domain chirp electron nuclear double-resonance spectroscopy in one and 2 dimensions, *J Chem Phys* **103**:8329–8337.
83. Maly T, MacMillan F, Zwicker K, Kashani-Poor N, Brandt U, Prisner TF. 2004. Relaxation filtered hyperfine (REFINE) spectroscopy: a novel tool for studying overlapping biological electron paramagnetic resonance signals applied to mitochondrial complex I. *Biochemistry* **43**:3969–3978.
84. Willer M, Schweiger A. 1994. Forbidden-transition-labeled EPR (FORTE): an approach for the sensitive measurement of forbidden EPR transitions. *Chem Phys Lett* **230**:67–74.
85. Sierra G, Schweiger A. 1998. Anisotropy-resolved electron paramagnetic resonance spectroscopy. *Mol Phys* **95**:973–987.
86. Hessinger D, Bauer C, Hubrich M, Jeschke G, Spiess HW. 2000. Magic-angle sample spinning electron paramagnetic resonance: instrumentation, performance, and limitations. *J Magn Reson* **147**:217–255.
87. Willer M, Schweiger A. 1997. Determination of g values by a new electron spin transient nutation experiment: the g_{\perp} value of titanium-doped sapphire. *Chem Phys Lett* **264**:1–8.
88. Stoll S, Jeschke G, Willer M, Schweiger A. 1998. Nutation-frequency correlated EPR spectroscopy: the PEANUT experiment. *J Magn Reson* **130**:86–96.
89. Astashkin AV, Schweiger A. 1990. Electron-spin transient nutation: a new approach to simplify the interpretation of ESR spectra. *Chem Phys Lett* **174**:595–602.
90. Mizuochi N, Ohba Y, Yamauchi S. 1997. A two-dimensional EPR nutation study on excited multiplet states of fullerene linked to a nitroxide radical. *J Phys Chem* **A101**:5966–5968.
91. Kouskov V, Sloop DJ, Liu SB, Lin TS. 1995. Pulsed transient nutation experiments on the photoexcited triplet-state. *J Magn Reson Series* **A117**:9–15.
92. Sierra GA. 1997. Two-dimensional pulse electron spin resonance methods for spectral resolution enhancement in solids. PhD thesis, No. 12241, ETH Zürich.
93. Blum K. 1981. Density matrix theory and applications. New York: Plenum.
94. See <http://www.esr.ethz.ch>
95. Stoll S, Schweiger A. 2006. EasySpin, a comprehensive software package for spectral simulation and analysis in EPR. *J Magn Reson* **178**:42–55.
96. Wang D, Hanson GR. 1996. New methodologies for computer simulation of paramagnetic resonance spectra. *Appl Magn Res* **11**:401–415.
97. Noble CJ, Benson, S, Hanson GR. 2007. Molecular Sophie: an integrated approach to the structural characterization of paramagnetic molecules. *Biol Magn Reson* **28**. In press.
98. Shane JJ, Liesum LP, Schweiger A. 1998. Efficient simulation of ESEEM spectra using gamma. *J Magn Reson* **134**:72–75.

PROBING STRUCTURAL AND ELECTRONIC PARAMETERS IN RANDOMLY ORIENTED METALLOPROTEINS BY ORIENTATION-SELECTIVE ENDOR SPECTROSCOPY

Reinhard Kappl, Gerhard Bracic, and Jürgen Hüttermann

*Fachrichtung Biophysik, Universität des Saarlandes,
Klinikum Bau 76, 66421 Homburg, Germany*

Electron nuclear double resonance (ENDOR) spectroscopy in its continuous wave (CW) and pulsed operational modes is now widely used to characterize the functional, structural, and electronic properties particularly of paramagnetic centers found in metalloproteins. Its essential advantage is based on the intrinsic high resolution, which permits the analysis of small interactions of the metal nucleus or of nuclei in the vicinity of the metal center with the electron spin not observable by standard EPR techniques. Because most of the protein samples are available only as frozen solutions, the essential concept introduced for the analysis of such “powder”-type ENDOR spectra is a method for calculation of “orientation-selected” ENDOR spectra. In this approach the EPR resonance condition is solved for a set of g -, hyperfine-tensors of the paramagnetic center(s), yielding the orientational distribution of the subset of molecules contributing to the ENDOR spectrum recorded at a certain magnetic field value. For these orientations the ENDOR transitions can be calculated and the ENDOR powder spectrum composed. Typically, the resonance lines arise from cumulations (turning points) of the selected orientations in defined frequency ranges. By recording several ENDOR spectra across an EPR spectrum, the tensors of the interactions, not resolvable in EPR, are probed. Their evaluation provides important information regarding the relative orientation of the g -tensor with respect to relevant hyperfine tensors or, when transformed to an x-ray crystal structure, to the molecular frame. In addition the distribution of the spin population amongst several spin centers of the paramagnetic metal center becomes accessible as well as its delocalization on amino acid ligands via the isotropic hyperfine contribution. In this report we summarize the fundamental theoretical background for the calculation of orientation-selected ENDOR spectra and discuss several approaches for the realization of algorithms particularly with respect to fast and effi-

cient interactive simulation of artefact-free ENDOR spectra. As examples of this type of ENDOR analysis iron–sulfur clusters in proteins are chosen. Reduced [2Fe2S]-clusters in ferredoxins with all-cysteine coordination, the Rieske-type centers, and oxidized [4Fe4S]-clusters in HiPIP proteins are presented. The evaluation of their proton and ^{57}Fe hyperfine interactions is discussed, and it is shown that from these data not only the g -tensor position in the molecular frame but also the site of reduction or oxidation within the cluster as well as valence delocalization of the iron ions can be deduced.

1. INTRODUCTION

Electron Nuclear Double Resonance (ENDOR) spectroscopy has become an indispensable tool in the elucidation of structure–function relationships in metallo-proteins. Its role nowadays is about as important as was the role of Electron Paramagnetic Resonance (EPR) spectroscopy in that field about forty years ago. The main advantage of ENDOR derives from its spectral resolution. When an EPR line is inhomogeneously broadened by unresolved hyperfine interactions, ENDOR enables these interactions to be detected in a highly resolved manner. Typically, due to its connection with nuclear relaxation parameters, the resolution in ENDOR can be up to three orders of magnitude higher than in EPR. This advantage is, however, connected with a decreased sensitivity, of approximately the same order of magnitude. Therefore, rather stable conditions in terms of magnetic field, temperature, microwave frequency and power, as well as computer-aided data acquisition are the main prerequisites for successfully recording ENDOR spectra, combined with sufficient radio-frequency (rf) power. Since its invention by Feher as a transient phenomenon for phosphorous donors in silicon [1], technical improvements have been achieved for all the parameters of concern. Therefore, ENDOR spectroscopy, in general, has become a fairly standard technique in many laboratories, at least in its continuous wave (CW) mode and at the standard X-band frequency (~ 9.5 GHz). Apart from this band, commercial ENDOR apparatus is available at Q- (35 GHz) and W- (95 GHz) band frequencies. Many home-built spectrometers run at other frequencies. In addition, with the development of pulsed EPR machines, the past decade has seen pulsed ENDOR equipment becoming available at the three major frequencies mentioned.

With these technical prerequisites fulfilled it is perhaps surprising that the complete information about the electronic and structural parameters of the interaction of the unpaired metal ion electron with nuclei in their immediate coordination environment is still rarely exploited. One reason may be attributed to the samples themselves. The information about the g - and the hyperfine tensor(s) as primary parameters obtained by EPR/ENDOR requires, basically, single crystals as samples: more precisely, single crystals for which a high-resolution structure is available. Only then can the tensor directions that are measured experimentally with respect to the crystal morphology be related, by transformation, with the molecular structure. There are, however, only a few examples of such studies in the literature [2,3]. Often, single crystals of proteins cannot be crystallized in a size sufficient for

handling. Moreover, proteins tend to have many molecules in the unit cell, and thus, depending on the space group of the crystal, their contributions may be difficult to disentangle with precision when rotating the crystal with respect to the magnetic field. Furthermore, for each (say hyperfine) tensor there is an ambiguity in the sign of elements that often necessitates rotation not only about three orthogonal axes but also about a fourth axis, skew to the others [4].

In this situation, the use of polycrystalline or randomly oriented protein samples comes into consideration. Most, if not all, metalloproteins have at least one interaction that is strongly anisotropic and thus spreads the EPR spectrum over the magnetic field. This may be the g -tensor alone or in connection with a large metal hyperfine interaction as, e.g., in copper or cobalt systems. If so, there is a definitive relation between all of these parameters and the magnetic field position within an EPR spectrum. The resonance condition for a given magnetic field involves therefore only a subset of molecules that contribute to the EPR intensity on account of their specific orientations with respect to the magnetic field. When ENDOR is being performed at such a position, it is only that subset which responds. Assembling the ENDOR data from many field positions across the EPR spectrum allows one, in principle, to arrive at a full (non-EPR resolved) hyperfine tensor for a given nucleus in the coordination shell. This principle is denoted "orientation selection." It was mentioned first in a paper by Rist and Hyde [5]. Later it was the groups of Kreilick [6,7] and of Hoffman [8,9] who described a theoretical foundation as well as several applications of this method in which information is obtained from randomly oriented samples that otherwise is restricted to single crystals. We have summarized earlier our results obtained from mononuclear metalloproteins such as NO-ligated hemoglobin and myoglobin as well as Cu-Zn SOD [10–12]. Since then, we have extended the application of orientation-selected ENDOR to multinuclear systems like [2Fe2S] and [4Fe4S] clusters in iron-sulfur proteins [13–15].

In this report we outline the basic considerations of orientation-selective ENDOR spectroscopy and summarize the current status of the method in our group. The application of its principles will be detailed using some examples from our more recent work on iron-sulfur proteins.

2. THEORY

The theory of stationary ENDOR transition frequencies is well understood. In the framework of metalloprotein applications we consider one metal ion (or more) in the center of a coordination sphere in which ligands like protons and nitrogen nuclei are in interaction distance with the ion. Shown in Figure 1 are sketches of three different iron-sulfur clusters in proteins and their immediate environment that are of relevance for the present report. The Spin Hamiltonian applicable to this situation contains metal ion terms indexed as M and ligand terms (indexed L):

$$\hat{H} = \beta_e \vec{B}^T \cdot \mathbf{g} \cdot \hat{S} + \hat{S}^T \cdot \mathbf{A}_M \cdot \hat{I} + \hat{I}^T \cdot \mathbf{P}_M \cdot \hat{I} + \sum_L (\hat{S}^T \cdot \mathbf{A}_L \cdot \hat{I} + \hat{I}^T \cdot \mathbf{P}_L \cdot \hat{I} + \beta_N \cdot g_N \cdot \vec{B}^T \cdot \hat{I}) \quad (1)$$

in which the symbols have the usual meaning, i.e., β_c and β_N correspond to the Bohr and nuclear magnetons, respectively, \hat{S} and \hat{I} for the electron and nuclear Spin operator with superscript T indicating the transpose. \mathbf{g} , \mathbf{A} , and \mathbf{P} represent the electronic \mathbf{g} -tensor, the hyperfine and the nuclear quadrupolar interaction tensors, and \vec{B} the magnetic field vector. We have omitted a potential fine structure term in the metal-centered part assuming that the electron spin S is always 1/2. Also omitted is the metal ion nuclear Zeeman term since it does not contribute for most of the metal ions due to their small β_N values.

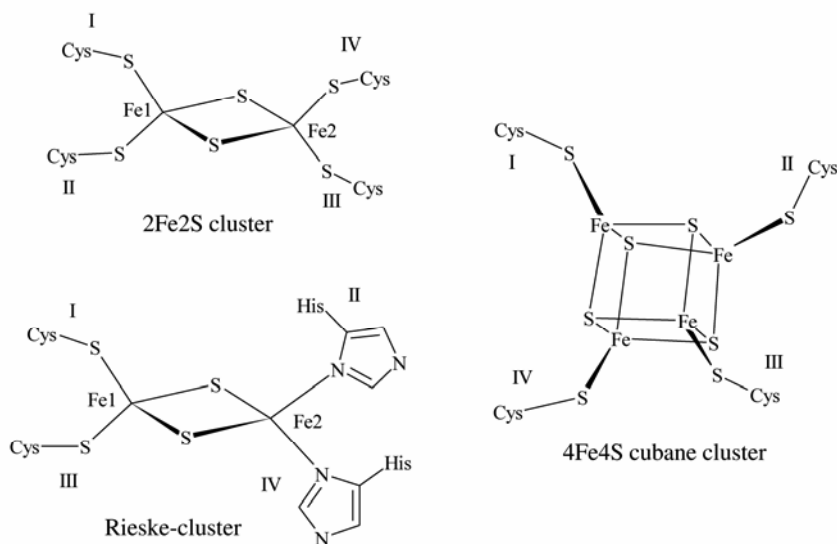


Figure 1. Schematic structures of [2Fe₂S] centers for plant- or adrenodoxin-type ferredoxins (top left) and for a Rieske-type center (bottom left). The cubane cluster of [4Fe₄S] proteins is shown in the right part. The roman numerals indicate the sequence of protein ligands to the irons.

If we now consider, as a representative model system, a four-level energy scheme arising from the (metal ion) electron spin $S = 1/2$ and a nuclear spin $I = 1/2$ of, e.g., a proton in the coordination environment, the above Hamiltonian reduces to

$$\hat{H} = \beta_e \cdot \vec{B}^T \cdot \mathbf{g} \cdot \hat{S} + \hat{S}^T \cdot \mathbf{A} \cdot \hat{I} + \beta_N \cdot g_N \cdot \vec{B}^T \cdot \hat{I}. \quad (2)$$

In the first-order perturbation approximation the energy levels E in frequency units for this system are obtained for a given field value B_0 as [16]

$$E(M_S, M_I) = g(\theta, \varphi) \cdot B_0 \cdot M_S + K(M_S) \cdot M_I, \quad (3)$$

with

$$K(M_S) = \sqrt{\vec{h}^T \cdot \mathbf{K}^T(M_S) \cdot \mathbf{K}(M_S) \cdot \vec{h}} \quad (4)$$

and

$$\mathbf{K}(M_S) = \frac{\mathbf{A} \cdot \mathbf{g}}{g} \cdot M_S - \nu_P \cdot \mathbf{1}. \quad (5)$$

The vector \vec{h} contains the direction cosines of the magnetic field orientation. The symbols ν_P and $\mathbf{1}$ describe the nuclear Zeeman frequency (for protons) and the unit matrix. In this notation, $g(\theta, \varphi)$ is the effective \mathbf{g} -factor, which describes the resonance magnetic field for a given microwave frequency ν_o , with h as Planck's constant, as

$$B_{res} = \frac{h \cdot \nu_o}{\beta_e \cdot g(\theta, \varphi)}. \quad (6)$$

The connection to the effective g is written as

$$g(\theta, \varphi) = \left[\sum_{i=1}^3 (g_i \cdot h_i)^2 \right]^{\frac{1}{2}}. \quad (7)$$

The situation is depicted schematically by the four-level diagram given in Figure 2 (left column) sketching a single crystal-type situation. There is one value of φ and θ for a given orientation that is operative for the \mathbf{g} -value as in Eq. (7) and for the hyperfine interaction as in Eq. (5). The ENDOR spectrum is obtained, under stationary (i.e., CW) conditions, by pumping (saturating) one of the EPR transitions and sweeping the r.f. frequency, thus desaturating at the respective NMR transition frequencies. The resulting spectrum is a doublet, separated by the effective hyperfine interaction A at the chosen (θ, φ) -pair and centered around the ν_P frequency applicable for the magnetic field value chosen. This applies for the case in which $\nu_P > A/2$, a situation typically encountered in cases as depicted for metalloproteins in Figure 1. The protons are then termed “weakly” interacting. When the crystal is rotated about at least three orthogonal axes, a full tensor derivation for A can be achieved from the analysis of the variation of hyperfine value A with θ and φ . This is a standard procedure detailed in textbooks typically discussing EPR, but the ENDOR case is fully analogous [17].

Consider now the randomly oriented sample. Figure 3 shows a “powder-type” EPR spectrum for a \mathbf{g} -tensor with rhombic symmetry ($g_{max} = 2.05$, $g_{int} = 1.97$, and $g_{min} = 1.93$) in its top part. This parameter is the only one resolved by EPR. When ENDOR is now performed at the field position corresponding to g_{max} (denoted I in the figure), only those molecules contribute that have their g_{max} -axes parallel to the

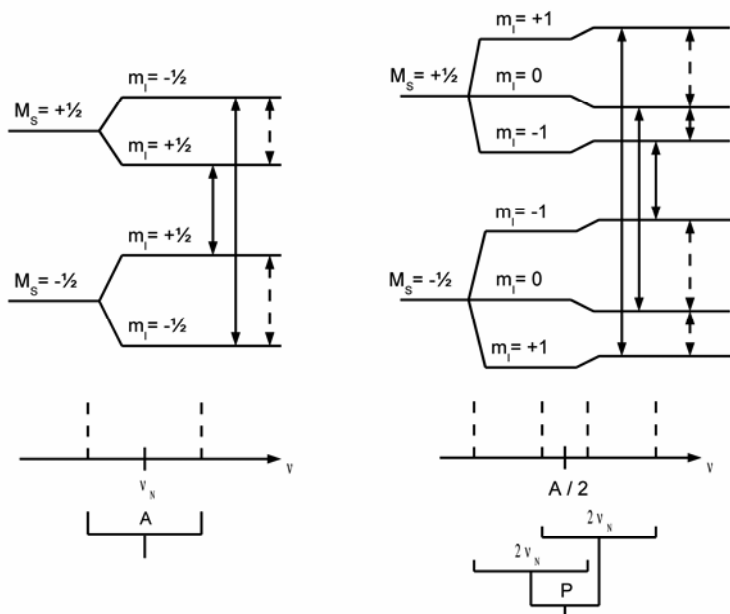


Figure 2. ENDOR transitions (dashed arrows) in the energy level diagrams for an electron interacting with a nuclear spin $I = 1/2$ (left scheme) and with a nuclear spin $I = 1$ (right scheme) for a single orientation. The resulting ENDOR resonance lines and their associated spectral parameters are shown in the bottom part.

magnetic field. The resulting spectrum due to a proton hyperfine interaction therefore consists of a single doublet, as discussed above for the single crystal case. The same basic consideration holds, given the rhombic \mathbf{g} -tensor symmetry, for the ENDOR response along g_{\min} . At both extreme \mathbf{g} -tensor values the resulting spectra are therefore described as “single-crystal type.” (This applies to any nucleus responding; the case of ^{14}N interactions will be dealt with below.) The situation at a chosen magnetic field position in between the limits set by g_{\max} and g_{\min} (e.g., at position II, indicated in the figure) is different. Here, a whole range of (θ, φ) -pairs is selected that contribute to the resonance condition of Eq. (6). This selection is indicated schematically as a g_{iso} line on a unit sphere in which the \mathbf{g} -tensor values form the orthogonal axis system (middle part of Fig. 3). The g_{iso} line connects all (θ, φ) -pairs of orientations for which the numerical value of the \mathbf{g} -factor is the same, i.e., that of position II. The consequence of this selection for a proton hyperfine tensor ellipsoid due to its relation with respect to the \mathbf{g} -tensor axes frame is also shown schematically in the middle part of Figure 3. The g_{iso} selection transforms into a selection of respective hyperfine values $A(\theta, \varphi)$. Thus, the observed ENDOR spectrum at this field position involves the range of (θ, φ) -pairs resulting in a corresponding range of superimposed doublet patterns with values of A differing for

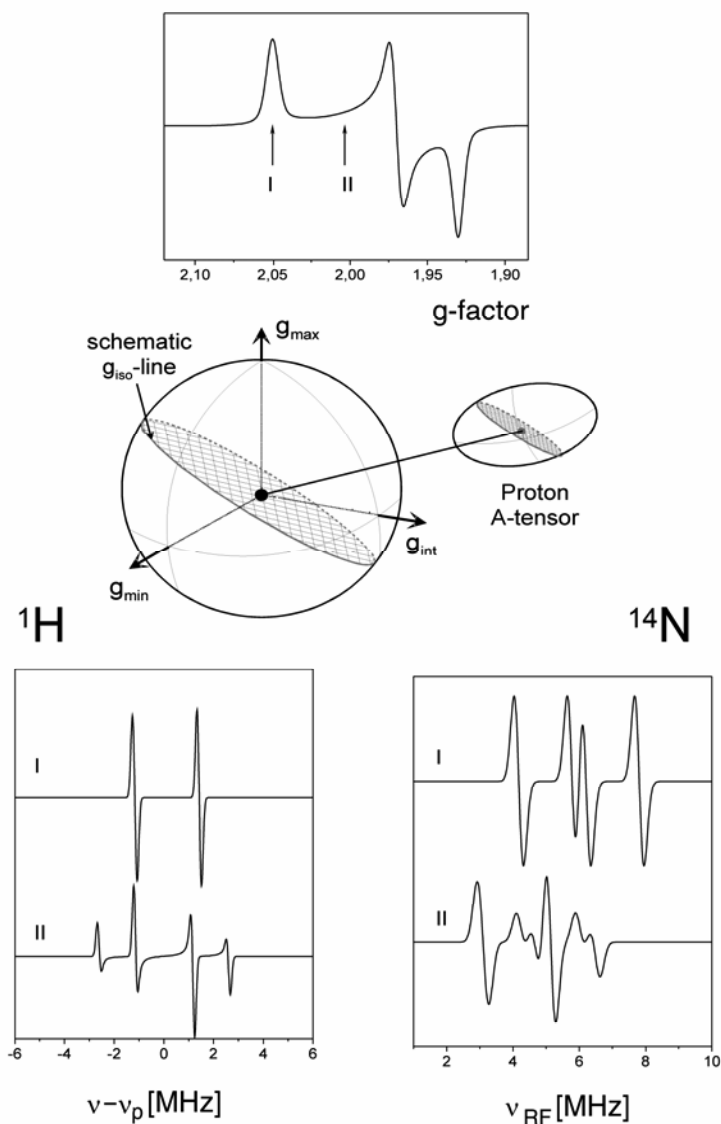


Figure 3. Typical powder EPR spectrum of a [2Fe2S] center for a \mathbf{g} -tensor of rhombic symmetry (top); the transformation of a g_{iso} selection at a field position corresponding to II in the EPR spectrum onto a (proton) hyperfine tensor is shown schematically (middle part). The simulated ENDOR spectra obtained for the g -values I and II, indicated in the EPR spectrum, for a proton ($I = \frac{1}{2}$) and a nitrogen (^{14}N ; $I = 1$) are shown in the bottom part. See text for details.

each such pair of angles. In sum, the ENDOR response changes with each field position. At any value in between the two field limits corresponding to g_{\max} and g_{\min} , many such pairs of ENDOR lines make up the total response, giving a whole range of r.f. frequencies covered according to the range of (θ, φ) -pairs selected. Typically, however, there are cumulations of contributing orientations (“turning points”) that thus give rise to discernable lines in each of the two frequency branches below and above ν_p . The example shown as the ENDOR response in the first derivative mode is a “single-crystal”-like doublet along g_{\max} (I) and a multiline pattern at field position II between g_{\max} and g_{int} (bottom left part of Fig. 3). The two spectra derive from a nearly axially symmetrical **A**-tensor (5.34 MHz, -2.58 MHz, and -2.6 MHz). If such ENDOR spectra are analyzed over the whole spread of the EPR spectrum, the full tensor information is obtained for the hyperfine interaction in terms of principal values and directions with respect to the **g**-tensor. The analysis involves spectra simulations, as detailed below.

Apart from protons, the above analysis using Eqs. (5) and (7) applies to all $I = 1/2$ nuclei. In metalloproteins, prominent examples of this case are ^{57}Fe and ^{15}N . A case in which nuclear quadrupole interaction has to be included in the analysis is for nitrogen ^{14}N ($I = 1$) interactions. The Hamiltonian of Eq. (2) then becomes

$$\hat{H} = \beta_e \cdot \vec{B}^T \cdot \mathbf{g} \cdot \hat{S} + \hat{S}^T \cdot \mathbf{A} \cdot \hat{I} + \hat{I}^T \cdot \mathbf{P} \cdot \hat{I} + \beta_N \cdot g_N \cdot \vec{B}^T \cdot \hat{I}. \quad (8)$$

This leads to the first-order perturbation theory energy levels [16]

$$E(M_S, M_I) = g(\theta, \varphi) \cdot \beta \cdot B_0 \cdot M_S + K(M_S) \cdot M_I - (\vec{k}^T \cdot \mathbf{P} \cdot \vec{k}) \cdot [(1/3) \cdot I \cdot (I+1) - M_I^2], \quad (9)$$

with

$$(\vec{k}^T \cdot \mathbf{P} \cdot \vec{k}) = \left(\vec{k}^T \cdot \mathbf{K}^T(M_S) \cdot \mathbf{P} \cdot \mathbf{K}(M_S) \cdot \vec{k} \right) / K^2(M_S). \quad (10)$$

The letter **P** stands for the quadrupole interaction tensor. The corresponding energy levels are shown schematically for a single-crystal situation in Figure 2 (right column). There are four ENDOR lines, centered typically around $A/2$ and either separated by $2\nu_N$ (assuming $A/2 > \nu_N$) or by the value P of the tensor **P**. These new positions are now the center of a doublet in each frequency branch separated by either the quadrupolar interaction or by ν_N . In our energy level example $P < \nu_N$ was chosen. The situation for a randomly oriented tensor (with values of 12, 6, and 4 MHz taken for **A**, and of 0.8, -0.4 , and -0.4 MHz for **P**), and its spectrum at the same two field positions as indicated in the powder EPR spectrum is also shown in Figure 3 (bottom right part).

Often, the proton and nitrogen interactions are of such a magnitude that they produce overlapping lines in measurements taken at a given microwave frequency (e.g., X-band). In this case, variation of that parameter is extremely helpful, e.g., going from X- to Q-band or higher frequencies. Since the nuclear frequencies of

protons and nitrogens differ strongly, this change often leads to a complete separation of the two interaction regions in frequency space. This also holds for the two other nuclei of interest in metalloproteins, ^{57}Fe and ^{15}N , which otherwise are, like the proton, $I = 1/2$ nuclei, and thus the treatment is analogous to that of the protons, if the g -tensor anisotropy is not too large.

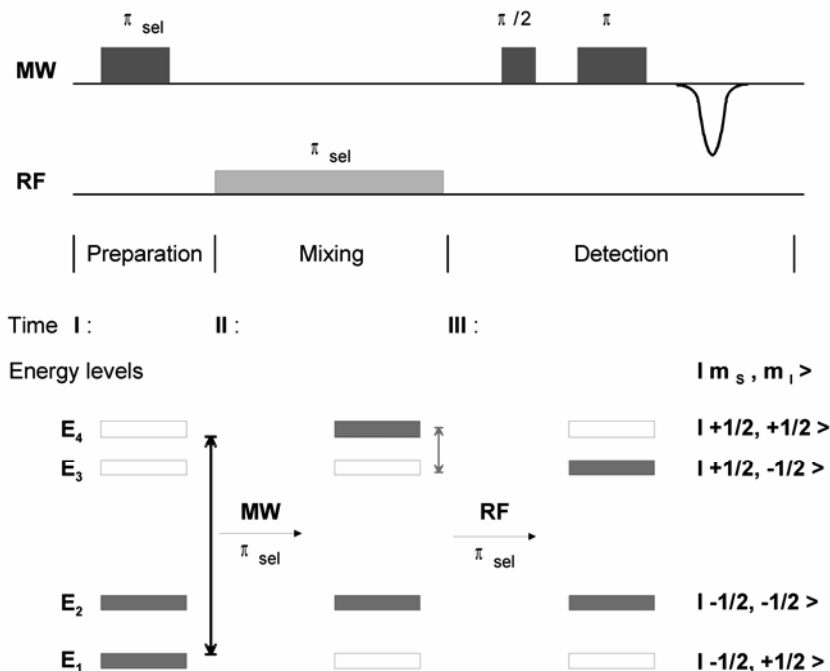


Figure 4. Schematic sequence of microwave (MW) and radiofrequency (RF) pulses of the Davies ENDOR experiment (top part) and the energy level diagram indicating the level occupation in the different time steps of the experiment.

The above description of the basic orientation selection principle applies for both CW and pulse techniques. In practice, each of these two methods has its own advantages and drawbacks. As we shall discuss below, in practical applications concerning interacting protons emphasis must be given to outer, unoverlapped lines that often are broad and of low intensity. They can be picked up well by performing Davies ENDOR. The corresponding scheme, again for an $S = 1/2$ and $I = 1/2$ system, is shown in Figure 4. Typically, a so-called π -pulse selectively inverts the population of one of the two $M_S = -1/2$ sublevels (here: level E_1) by fully polarizing its $M_S = +1/2$ counterpart level (E_4). This period is called the preparation re-

gime. It is followed by the mixing period, in which, in this case, the nuclear sub-levels of the $M_S = +1/2$ manifold (E_4, E_3) are connected with an r.f. pulse, so that the polarization resides eventually at E_3 . If, in the detection period, the same transition E_1 to E_4 , is now probed selectively in a two-pulse sequence, the change in populations (or polarizations) will become apparent and represents the ENDOR response. With the appropriate pulse lengths and pulse separations in time it is possible to emphasize the outer ENDOR lines at the expense of resolution in the inner part. It is also possible to separate different EPR active species if their relaxation behavior is sufficiently different. In that case, the ENDOR response can be selected to arise, e.g., from a more long-lived species.

In CW ENDOR, using frequency modulation of the r.f. source, the effect equivalent to emphasising outer weak lines can be achieved with large modulation amplitudes. This technique has been applied in our laboratory. It yields ENDOR spectra in the first derivative mode and thus is well suited for achieving spectra resolution, unlike the absorption mode typically gained by pulsed ENDOR. The resolution is another parameter to be addressed, since in practical work the spectra are crowded due to many proton interactions giving overlapping lines. Moreover, there is typically an intensity increase toward the center of the spectra, indicating that more protons with weaker interactions and more orientations are contributing.

Suppose that one has extracted a (e.g., proton) hyperfine tensor from orientation-selective ENDOR measurements. How can this information be utilized in terms of relation to structural and electronic properties? First, it has to be emphasized that the hyperfine tensor is established within the framework of the orthogonal axes of the \mathbf{g} -tensor. If it is possible to assign the hyperfine tensor within a protein prosthetic group to a specific proton, at the same time the \mathbf{g} -tensor with respect to the molecular frame is fixed. This is important information that is otherwise only obtained from single-crystal measurements.

The hyperfine tensor contains information about distance and directions (within the \mathbf{g} -tensor frame) via its dipolar part. It may also contain information about the spin density via the isotropic interaction. A typical hyperfine tensor (\mathbf{A}_D , i.e., in its diagonalized form) for a proton interacting with a localized spin center can be written as the sum of the isotropic and the dipolar interactions:

$$\mathbf{A}_D = a_{\text{iso}} \cdot \mathbf{1} + \mathbf{A}_{\text{dip}}, \quad (11)$$

with a_{iso} given by $a_{\text{iso}} = \text{trace}(\mathbf{A}_D)$, and the dipolar part is of the following form: $\mathbf{A}_{\text{dip}} = (2T, -T, -T)$.

The isotropic part is the trace of the diagonal elements, and the dipolar part is axially symmetric. There is, of course, an uncertainty concerning the signs. In practice, however, one often knows (e.g., from Mössbauer experiments in iron-sulfur proteins) the sign of the spin density on the metal ion and thus the sign of the isotropic interaction.

The task now arises to build a structure from these data, i.e., to place a proton into an orthogonal (x, y, z) frame from the dipolar part of the tensor and subsequently to place this fragment into a reasonable molecular structure that reflects the

metal ion coordination in the protein in question (e.g., as depicted in Fig. 1). This is facilitated if more than one (proton) tensor is available. Typical cases for this situation will be discussed below. For practical purposes, the point-dipole approximation is used for approximate distance determinations.

There is another way of approaching the same problem. It starts with a high-resolution structure of the metal ion and its surrounding and ends with hyperfine tensors. The structure gives the distance of say an interacting proton and from this, in point-dipole approximation, a dipolar tensor is established using as an adjustable parameter the spin density on the metal ion(s). An isotropic part is added based on assumptions or knowledge from related techniques (e.g., paramagnetic NMR) and with this hyperfine tensor the ENDOR spectra across the EPR spectrum are simulated. If correct, the result comprises the direction of the \mathbf{g} -tensor within the known molecular structure and the spin density as a new electronic parameter. It is obvious that in both cases the final hyperfine tensor diagonalized in the \mathbf{g} -frame must be identical. As before, the result is becoming increasingly reliable with the number of interactions being correctly reproduced. We shall detail below the limits and uncertainties of both approaches. The formalism of this kind of simulation was first described by Henderson et. al. [6,7] and is based on the following formula, which applies for proton hyperfine interactions:

$$\nu(M_S) = \left[\sum_{i=1}^3 \left[\frac{M_S}{g(\theta, \varphi)} \cdot \left(\sum_{j=1}^3 g_j \cdot h_j \cdot A_{ij} \right) - h_i \cdot \nu_p \right]^2 \right]^{\frac{1}{2}} \quad (12)$$

with

$$A_{ij} = -g_n \cdot \beta_N \cdot \beta_e \cdot h^{-1} \cdot r^{-3} \cdot g_i \cdot (3 \cdot r_i \cdot r_j - \delta_{ij}) + A_{iso} \cdot \delta_{ij} = (A_{DD})_{ij} + A_{iso} \cdot \delta_{ij} \quad (13)$$

The components A_{ij} of the hyperfine tensor \mathbf{A} in Eq. (12) comprise an anisotropic (dipolar) and an isotropic part as written in frequency units in Eq. (13). The term δ_{ij} denotes the Kronecker delta function; h in Eq. (13) is Planck's constant. The distance r and location (r_i, r_j) with respect to the center of spin density in the point-dipole approximation, as well as the isotropic coupling, determine the ENDOR response in the case of unit spin density. If a spin density ρ is distributed over various spin centres with $\rho = \sum_l \rho_l$, the components of the dipolar part of the tensor are modified to yield

$$(A_{DD})_{ij} = \sum_l \rho_l \cdot (A_{ij})_l \quad (14)$$

3. ORIENTATION SELECTION IN EPR AND ENDOR

In frozen solutions of paramagnetic proteins the molecules are static as in crystals, but they are randomly distributed and oriented, i.e., the tensors (\mathbf{g} and \mathbf{A}) of the paramagnetic center may adopt any orientation with respect to the external magnetic field direction (or laboratory frame). Such samples typically show axial or rhombic “powder-type” EPR spectra extending from a minimal (g_{\max}) to a maximal field value (g_{\min}). An example for rhombic symmetry in the \mathbf{g} -tensor has already been introduced in Figure 3 and was discussed schematically. This discussion will be extended and quantified in the present section. Consider a quite rhombic model system ($g_{\max} = 2.2$, $g_{\text{int}} = 1.9$, and $g_{\min} = 1.6$) without a resolved hyperfine interaction of, e.g., the metal nucleus. The EPR spectrum obtained in absorption and in derivative display is shown in Figure 5 (top left). The EPR experiment on such a powder sample can now be visualized by a representation in g -space. As long as the magnetic field is off-resonance at low values, the corresponding g -sphere surrounds the \mathbf{g} -tensor without having any points in common. For the first time the resonance condition is fulfilled when the g -sphere touches the \mathbf{g} -tensor at the g_{\max} value (2.20) (Fig. 5, top right). Here, only those molecules of the sample are in resonance that are oriented with their g_{\max} direction parallel to the external field. Further shrinking of the g -sphere to, say $g = 2.05$ (i.e., going to higher field), means that now a different subset of molecules is in resonance whose g_{\max} orientation is tilted at certain angles from the direction of the applied magnetic field (Fig. 5, middle left). These orientations are represented by the curve resulting from the intersection of the g -sphere and \mathbf{g} -tensor (the g_{iso} -curve). When the field is passing through the intermediate $g_{\text{int}} = 1.9$, the g_{iso} -curve adopts its greatest length, indicating that here the largest number of molecules is contributing to the EPR spectrum (i.e., the highest intensity in the absorption spectrum is found; Fig. 5, top left, absorption mode). Moving further toward g_{\min} ($g_{\text{eff}} = 1.65$, Fig. 5, bottom left) leads to a selection of molecules whose g_{\min} -orientation is again at defined angles with respect to the external field vector, until at g_{\min} again only few molecules are contributing. At this field the g -sphere is touching the \mathbf{g} -tensor ellipsoid from within at one point, i.e., along g_{\min} (Fig. 5, bottom right). At higher fields the two bodies loose contact again.

This kind of representation of the EPR experiment illustrates that each subset of molecules in resonance at a field B_{res} [Eq. (6)] is associated with a number k of vectors [\vec{h} in Eq. (7)] connecting the origin of the \mathbf{g} -tensor and k points on the g_{iso} -curve. Hence, one obtains k (θ, φ)-pairs. For each of the vectors \vec{h} the hyperfine interaction is calculated according to, e.g., Eq. (12) for a given (proton) hyperfine tensor with components A_{ij} , yielding exactly two lines (cf. Fig. 2). All the resulting doublets are finally composed to give the simulated powder spectrum. The essential task for the simulation of ENDOR powder spectra (free of artefacts as far as possible) is to determine a sufficient number (k) of these vectors, for which several possible approaches can be chosen. The vectors are created by a random number generator, or by covering the unit sphere with a grid, such as the SOPHE grid [18],

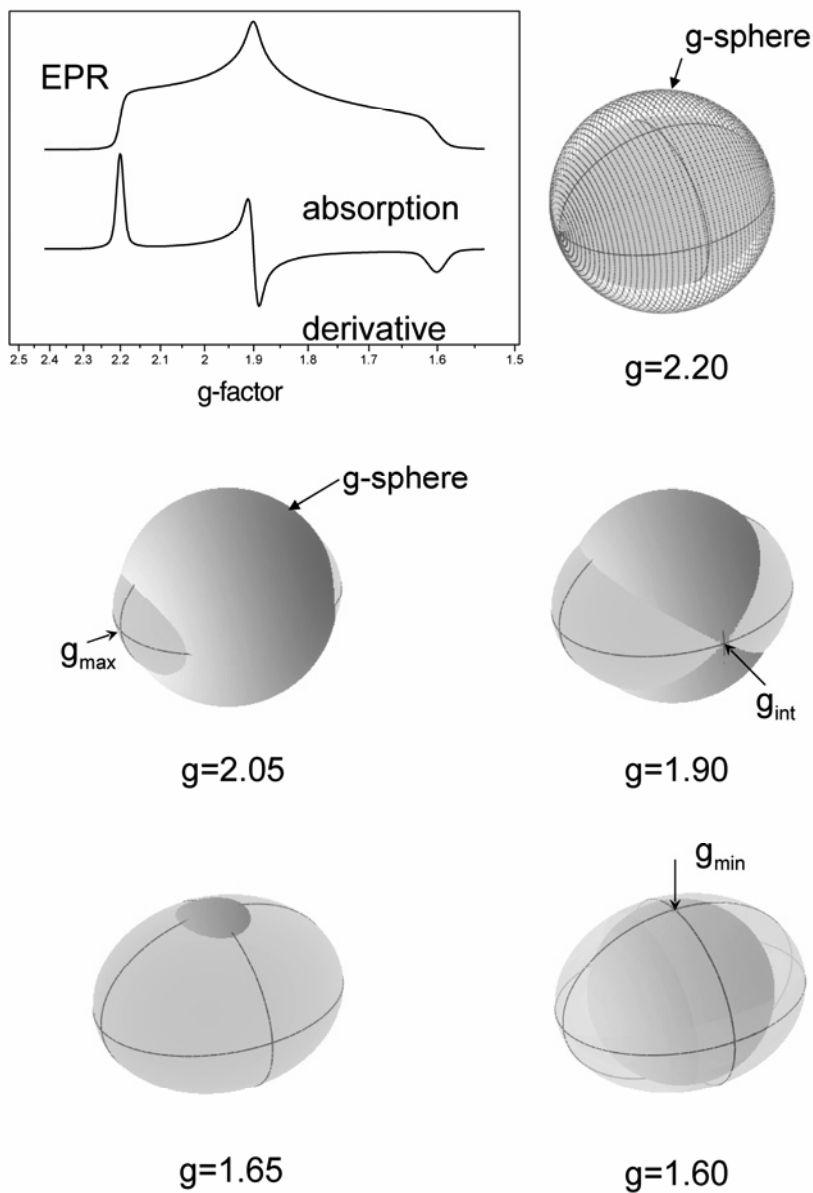


Figure 5. Visualisation of the EPR-resonance condition for a subset of molecules and the corresponding g_{iso} -curves for a rhombic model g -tensor at several effective g -factor values. The g -sphere and the principal values on the g -ellipsoid are marked with arrows. The corresponding powder EPR spectrum in absorption and first derivative mode is shown in the top left panel.

or by a direct calculation of the (θ, φ) -pairs on the g_{iso} -curve. The latter method was developed for a copper system of coaxial \mathbf{g} - and metal \mathbf{A} -tensor with axial symmetry [7]. In our laboratory this approach was extended to tensors of rhombic symmetry in a coaxial arrangement for which an explicit expression was derived and implemented in a program [11]. Subsequently, the method for direct calculation was optimized for fast processing with equal spacing of the points on the g_{iso} -curve.

Before going into further detail about the orientation selection methods, we first want to introduce the effect of a spin population distributed over several atoms of a protein metal center on the evaluation of a proton ENDOR hyperfine tensor. This situation is regularly found in polynuclear metals containing proteins, particularly in iron-sulfur proteins, where the size and also the sign of the spin density of the spin centers is changing. This is different from the case of mononuclear metalloproteins, with which we have dealt earlier [10,11]. Equation (13) describes the hyperfine tensor components of a proton at a defined location with respect to the \mathbf{g} -tensor interacting with a single spin center of unit spin density. In principle, for a distributed system, the interaction with each spin center has to be calculated and the resulting local tensors summed up weighted with the local spin densities as indicated in Eq. (14). This generally leads to rhombic hyperfine tensors for protons. In the example, related to a typical [2Fe2S]-protein (cf. Fig. 1, top left) and shown in Figure 6, the proton is interacting with two spin centers Z1 (Fe1) and Z2 (Fe2) at distances of 3.14 and 3.83 Å, and spin densities of 1.8 (Fe1) and -0.8 (Fe2), respectively. Because of its relative position to both centers, the principal tensor components are calculated with values of $A_{\text{max}} = 8.58$ MHz, $A_{\text{int}} = -5.36$ MHz and $A_{\text{min}} = -3.27$ MHz, yielding a fairly rhombic \mathbf{A} -tensor.

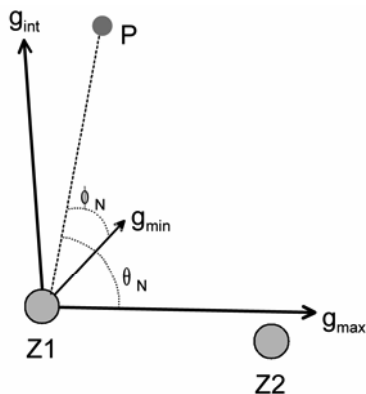


Figure 6. Spatial arrangement of two spin centers (Z1, Z2), the \mathbf{g} -tensor, and a single interacting proton for the model ENDOR simulations presented in Figure 7. The principal g -values are $g_{\text{max}} = 2.052$, $g_{\text{int}} = 1.957$, and $g_{\text{min}} = 1.887$. The proton is at a distance of 3.14 Å from Z1 and at angles $\theta_N = 76.5^\circ$ and $\varphi_N = 82.5^\circ$ with respect to the g -axis system. The arrangement of the proton with respect to the spin centers models the situation in [2Fe2S] centers of ferredoxins.

With this model situation we now consider the transformation of orientation selection by \mathbf{g} onto the hyperfine tensor \mathbf{A} and thus the ENDOR response at chosen magnetic field values. This extends the schematic discussion based on Figure 3 (middle part) given above. The EPR spectrum using the principal values of the \mathbf{g} -tensor for a typical [2Fe2S] ferredoxin sample ($g_{\max} = 2.052$, $g_{\text{int}} = 1.957$, and $g_{\min} = 1.887$) is shown in Figure 7 (bottom row, left). It is labeled with three field positions (1–3) for which the g_{iso} -curves were calculated and projected onto the \mathbf{g} -tensor ellipsoid (top row in Fig. 7). For position 1 ($g_{\text{eff}} = 2.003$) the bent g_{iso} -curve is represented by the points following the surface of the \mathbf{g} -ellipsoid at some distance from the g_{\max} principal value. It also has its mirror image in the lower part of the \mathbf{g} -ellipsoid. At the intermediate g -factor $g_{\text{int}} = 1.957$ the two g_{iso} -curves cross through this point and adopt their greatest length. At field position 3 ($g_{\text{eff}} = 1.921$) in between g_{int} and g_{\min} , the curves are surrounding the minimal g -value and its mirror image. Each of the points represents one \vec{h} vector (or a (θ, φ) -pair), and thus a possible orientation of a protein molecule in resonance. Consequently, each of the vectors is intersecting the proton \mathbf{A} -tensor, fixed with respect to the \mathbf{g} -tensor in each molecule, differently. This is visualized by the points on the surface of the \mathbf{A} -tensor ellipsoid for which the \vec{h} vectors have been transformed into the diagonal \mathbf{A} -tensor system (Fig. 7, middle row). The resulting curve is skewed with respect to the hyperfine principal values. The ENDOR resonance lines of the simulated powder spectrum (bottom row, right panel) arise from those regions of the curve where the change of the hyperfine value is smallest for changes of (θ, φ) -angles, i.e., at the inflection (turning) points of the curve indicated by arrows on the \mathbf{A} -tensor ellipsoid for field position 1. Because the \mathbf{A} -tensor is rhombic, as in our example above, the four regions cause four ranges on the frequency scale where intensity is accumulating, giving four resonance lines on each M_s -branch, as is evident from the simulated spectra. It also appears that for field position 2 the curve is approaching the A_{\max} -value producing the largest separation of lines in ENDOR spectrum 2. Hence, when the field positions are varied in sufficiently small steps across the EPR spectrum, the hyperfine tensor of an interacting proton is probed and the relevant parameters can be determined.

The quality of a simulated ENDOR powder spectrum critically depends on the number k of the \vec{h} vectors (or (θ, φ) -pairs) defining the g_{iso} -curve when selecting a certain field position in an EPR spectrum. Using a random generator requires the calculation of a very large number of orientations, so that a sufficient number of points are found on a g_{iso} -curve. In practice, several tens or hundreds of thousands of vectors, depending mainly on the anisotropy of the EPR-spectrum, are necessary to yield an artefact-free ENDOR spectrum. This requires considerable processing time (and memory) and is generally inapplicable for an interactive simulation routine that simultaneously evaluates 20 to 30 field positions for up to 15 or 20 protons interacting with several spin centers. As an alternative, a grid can be created over a unit sphere to obtain sufficient orientations. An example is shown in Figure 8A in a quadrant with 841 points on a half sphere. Here, the number of points

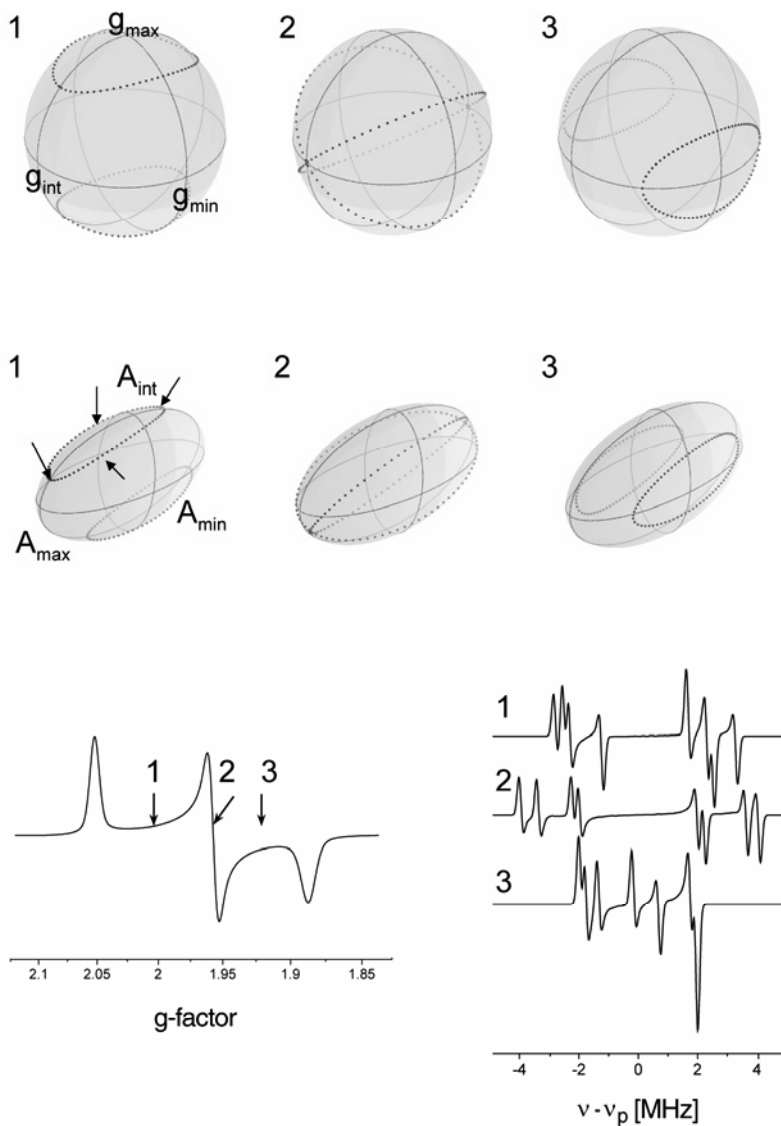


Figure 7. Simulation of the EPR spectrum and the corresponding ENDOR spectra for the model system introduced in Figure 6 at the three selected g -factors 2.003 (1), 1.957 (2), and 1.921 (3) (bottom row). The top row shows the g_{iso} -curves (dotted lines) for the three g -factors projected onto the surface of the g -tensor ellipsoid. The directions of the g_{iso} -curves are transformed onto the surface of the A -tensor (middle row). (For the simulation spin densities of 1.80 (on Z1) and -0.80 (on Z2) were used yielding a rhombic A -tensor.)

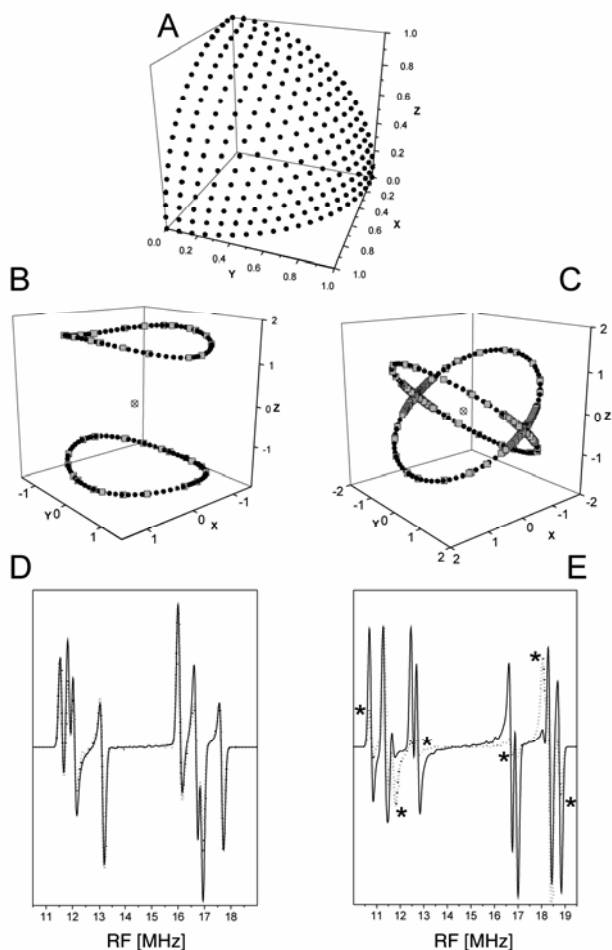


Figure 8. Panel A presents the grid distribution in a quadrant obtained with 20 steps in θ (from 0–90°) and the partitioning of φ dependent on the step size of θ . This results in 841 points on a half sphere. The g_{iso} -curves in panel B ($g = 2.003$) show the points obtained by direct calculation (filled circles) and the hits of the grid method (gray squares). The direct calculation was performed with initial step $\Delta\varphi$ of $\pi/30$ resulting in 144 equally spaced points. The grid distribution was performed with 120 steps in θ yielding only about 40 points. The g_{iso} -curves in panel C for $g = 1.957$ were calculated for the same conditions as B. The grid method yields a clustering of points near the equatorial plane. For reasons of clarity, the step size was kept low. To demonstrate the effects of the two methods, the simulated ENDOR spectra (panel D, $g = 2.003$; panel E, $g = 1.957$) are compared for the grid distribution (dotted line, 1000 steps in θ) and the direct calculation of the g_{iso} -curve (initial step $\Delta\varphi$ of $\pi/1000$). In panel E the spectral differences are marked by asterisks.

along the angle φ depends on the number of steps of the azimuthal angle θ from 0 (pole) to $\pi/2$ (equator), so that a roughly regular distribution of points is achieved. Since integer numbers for the steps are used, the occupation near the equator is somewhat higher. However, the grid can be reproducibly calculated in a much shorter time in comparison to the random approach for spectra of comparable quality because an approximately regular distribution is achieved with a significantly smaller number of orientations. Again, care has to be taken to have sufficient points located on the g_{iso} -curve for artefact-free ENDOR spectra.

The method of direct calculation of the \vec{h} vectors (or (θ, φ) -pairs) has proven to be the optimal simulation approach, because it combines fast calculation with an evenly distributed pattern of points on the g_{iso} -curve. The procedure is briefly outlined for a system without hyperfine lines from, e.g., the metal nucleus. Then the g_{iso} -curve is described by the relation

$$g_{\text{iso}}^2 = g_{\text{min}}^2 \cdot \sin^2 \theta \cdot \cos^2 \varphi + g_{\text{int}}^2 \cdot \sin^2 \theta \cdot \sin^2 \varphi + g_{\text{max}}^2 \cdot \cos^2 \theta \quad (15)$$

To obtain a constant distribution of orientations on the g_{iso} -curve, the total differential equation for the curve s in polar coordinates is given by

$$ds^2 = dr^2 + r^2 \cdot d\theta^2 + r^2 \cdot \sin^2 \theta \cdot d\varphi^2. \quad (16)$$

With $r^2 = g_{\text{iso}}^2 = \text{const}$ and $dr = dg = 0$, the equation simplifies to

$$ds^2 = g_{\text{iso}}^2 \cdot (d\theta^2 + \sin^2 \theta \cdot d\varphi^2). \quad (17)$$

Equation (15) is then solved for $\sin^2 \theta$ and θ , so that $\theta = f(\varphi)$, and correspondingly, $\frac{d\theta}{d\varphi} = f'(\varphi)$. With these substitutions, Eq. (17) can be written as

$$ds = g_{\text{iso}} \cdot \sqrt{f'(\varphi)^2 + \sin^2 \theta(\varphi)} \cdot d\varphi. \quad (18)$$

This equation can be integrated numerically to obtain the curve integral. However, for our purposes, a simplification in going to a small segment representation is preferable, yielding the segmental length Δs as

$$\Delta s = g_{\text{iso}} \cdot \sqrt{f'(\varphi)^2 + \sin^2 \theta(\varphi)} \cdot \Delta\varphi. \quad (19)$$

Starting with $\varphi = 0$, the value of θ , i.e., the first (θ, φ) -pair, is calculated. Then, for an initial increment $\Delta\varphi$ the segment Δs is determined and the second (θ, φ) -pair defined. In subsequent steps the segment Δs is kept constant, yielding consecutively new $\Delta\varphi$ values that increase φ according to $\varphi = \varphi + \Delta\varphi$. For each new φ -value the related θ is determined by calculating $\sin^2 \theta(\varphi)$. This procedure is repeated until $\varphi \approx \pi/2$. The value of θ for $\varphi = \pi/2$ is calculated separately. All the (θ, φ) -pairs are then transformed into the other quadrants by mirror symmetry

across the axes planes. In this way a regular distribution of the pairs on the g_{iso} -curve is achieved.

The differences between the grid method and the direct calculation of (θ, φ) -pairs are demonstrated for the example introduced in Figure 7. The g_{iso} -curves for 2.003 constructed by the two methods are shown in Figure 8B. The grid was set up for 120 steps in θ (from 0 to 90°), resulting in more than 29,000 points on the upper sphere, but only about 40 points (gray squares) are found on the g_{iso} -curves. They are roughly equally distributed, because the g_{iso} -curve is approximately following the pattern of the grid distribution horizontally to the xy -plane (cf. Fig. 8A). In comparison, the direct calculation method with an initial $\Delta\varphi$ increment of $\pi/30$ produced 144 equally spaced points (filled circles) on the two curves. For the demonstration the step size was kept rather low and had to be increased considerably for spectra simulation. Indeed, for the grid a bit more than 2×10^6 points were placed on the upper hemisphere, resulting in 3416 points on the g_{iso} -curve. The resulting ENDOR spectrum (dotted line) is shown in Figure 8D in comparison to the spectrum obtained for direct calculation with about 4700 points (for an initial $\Delta\varphi$ increment of $\pi/1000$) on the g_{iso} -curve. It is obvious that the inflection points and the resonance frequencies coincide, but that the relative line intensities are clearly different, and that, in addition, the spectrum simulated by the grid method is producing more “wiggles” of low intensity as a result of the uneven distribution of points on the g_{iso} -curve.

The inequivalent distribution of (θ, φ) -pairs becomes even more pronounced for $g_{\text{iso}} = 1.957$. Here, in the example with reduced step size (Fig. 8C), the grid method produces more than 260 points on the g_{iso} -curves (gray squares) compared to 160 points (filled circles) for the direct calculation. It is obvious, however, that the grid points are clustering in the equatorial plane. This effect is the reason that in the simulation spectra, apart from small differences in the resonance position, the relative line intensities are significantly different (Fig. 8E, marked with asterisks) although more points are found on the g_{iso} -curve for the grid method than for direct calculation (ca. 15000 vs. 5200).

The example presented in Figure 8 demonstrates that direct calculation of the (θ, φ) -pairs is a simple and fast method to achieve an even distribution of sufficient points on the g_{iso} -curves and circumvents the intrinsic problems of the grid method. This is seen to reproduce the statistical orientation of a large number of molecules in the sample in the most realistic way. It also provides the advantage of fast calculation, which becomes important when g -strain effects have to be included in the simulation of the ENDOR powder spectra. In such a case the (θ, φ) -pairs of several slightly different g_{iso} -curves resulting from a distribution in the principal value and/or direction have to be evaluated on the \mathbf{A} -tensor. Still, with this method an interactive simulation of ENDOR spectra of a few protons is feasible on a standard PC.

We have shown earlier [11] that the direct calculation of (θ, φ) -pairs is also applicable to systems with a rhombic \mathbf{g} - and coaxial \mathbf{A} -tensor, the latter arising from a metal or “strong” ligand hyperfine interaction already resolved in EPR. Presently,

the segmentation procedure providing an even distribution of (θ, φ) -pairs is implemented, and it is intended to extend it to a system with noncoaxial arrangement of the tensors.

4. EXAMPLES OF APPLICATIONS: IRON-SULFUR PROTEINS

4.1. Proton Hyperfine Interactions

Protons are the most abundant nuclei in the environment of metal ion(s) in metalloproteins regardless of the details of their coordination. They may be interacting with the metal ion either through space, implying that the tensor comprises only a dipolar part, or through bonds, in which case the protons are connected to the distribution of the spin-density, which typically is at least in part delocalized. As a consequence, the interaction tensor then consists not only a dipolar but also an isotropic part. Apart from that, protons can be classified chemically into exchangeable and unexchangeable ones. Those that are exchangeable produce, when treating the protein in D_2O buffer conditions, specific changes in the experimental spectra that allow secure assignments. However, often one finds that when the prosthetic group is not solvent exposable it is difficult to produce efficient H/D exchange observable in the experimental situation.

The problem with analyzing proton interactions in most practical cases arises from spectral crowding in the center part, close to the “free” proton frequency. Many protons contribute to this region since they are distant and have no significant couplings. Most interesting are the outer lines, especially when they are not overlapped by other interactions. Typically, they arise from one or two proton interactions and give “turning point” accumulations only from a small range of (θ, φ) -pairs. Therefore, their line intensity is small. It is one of the main problems in the experiment to secure the positions of the outermost weak lines since they form anchoring points in the analysis. These considerations will be emphasized in the subsequent examples.

We start with a prototypical $[2Fe_2S]$ cluster from *Arthrospira platensis* ferredoxin [15]. The structural arrangement of the prosthetic group with its two irons and four cysteine residues is shown schematically in Figure 1 (top left). Its function is electron transfer. In its oxidized form it is EPR-mute, the reduced form is paramagnetic. The spin of the system then is $S = 1/2$ due to antiferromagnetic coupling of the local valences Fe(II) ($S = 2$) and Fe(III) ($S = 5/2$). The aim of the ENDOR analysis is to determine the site of iron ion reduction, establish the position of the g -tensor in the molecular frame, and give estimates for the spin densities on both irons via determination of the hyperfine interactions of relevant protons in the cluster vicinity. Figure 9 (top part) shows the rhombic EPR spectrum ($g_{\max} = 2.052$, $g_{\text{int}} = 1.957$, and $g_{\min} = 1.887$) of the reduced cluster taken at X-band frequencies. The spectrum is spread over the magnetic field scale by the g -tensor anisotropy; there is no resolved hyperfine interaction. In contrast, hyperfine interactions are highly

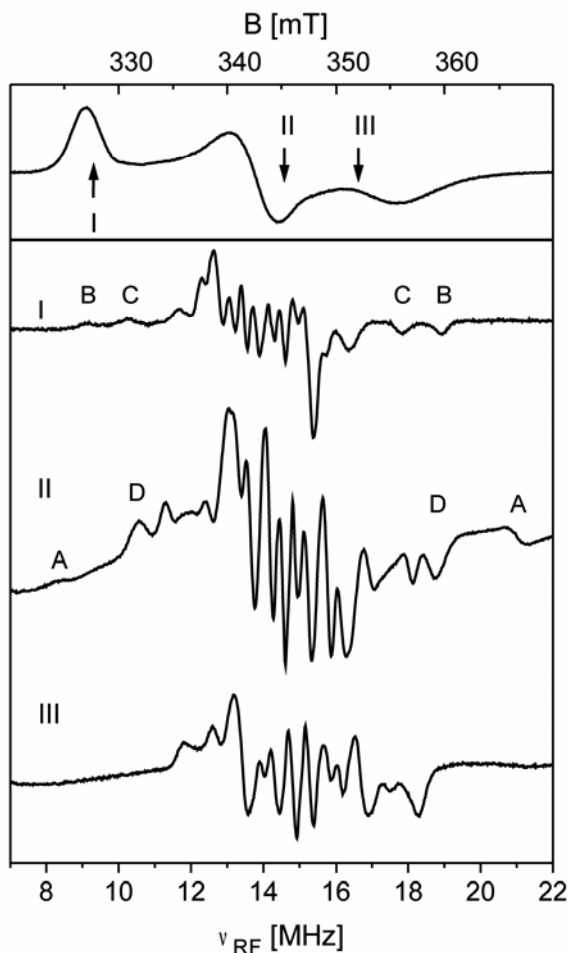


Figure 9. EPR spectrum (top) of the reduced $[2\text{Fe}_2\text{S}]$ cluster of *Arthrospira platensis* with the field positions (I–III) indicated for which experimental ENDOR spectra are presented (bottom part). The outer couplings analysed in detail in the simulations are marked A–D.

resolved by ENDOR, as shown in the lower part of the figure by three representative spectra taken at field positions marked I–III in the EPR spectrum. Resonance lines shown in first derivative mode are observed in a range from about 8 to 22 MHz, and they are nearly symmetrically arranged around the “free” proton frequency, which ranges from about 14 to 15 MHz depending on the field value, indicating that the observed resonance lines are due to weakly interacting protons. There are broad outer lines of weak intensity, and many sharp and resolved inner ones with higher intensity crowding toward the center; the latter are observable if

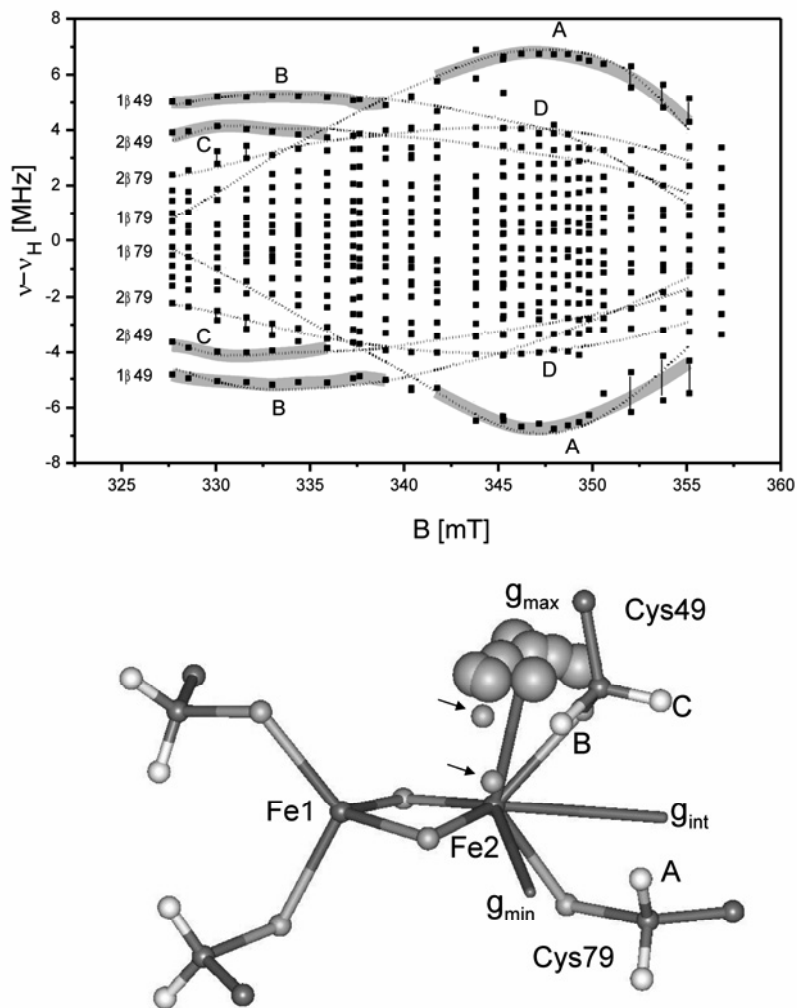


Figure 10. In the field-frequency plot (top) the field regions, in which couplings A–C are clearly discernible, are indicated by the broad gray traces. The gamut of experimental data points are given as black squares. The dotted lines represent the simulations of outer lines for all field positions across the EPR spectrum for the individual cysteine β -protons. In the bottom part the structure of the cluster (4fx.pdb, Brookhaven Protein Data Bank, www.rcsb.org) including the final g -tensor orientation and the assignment of the couplings A–C to cysteine β -protons are given. The large and small (marked with an arrow) gray spheres indicate the trace of the g_{\max} -direction obtained from simultaneous fitting of couplings A–C with the automatic calculation routine (for details see text). The variation of g_{\min} and g_{int} is omitted for clarity.

the FM modulation is not too high. Only the outer ones are initially directly amenable for analysis. A field-frequency plot given in the top part of Figure 10 shows the total set of ENDOR resonances obtained at 25 field positions (“working points”) across the EPR spectrum. The crowding in the center part becomes obvious. The outer couplings, marked A–D in the ENDOR spectra, are also indicated in the field-frequency plot. Fortunately, for resonances A–C their anisotropy coupled with their interaction strength makes it possible to follow them from one field position to the next (shaded lines in the field-frequency plot), albeit only in a limited field range before they become lost in the center part. We note, in addition, that coupling A becomes very broad toward the g_{\min} range of the EPR spectrum. In a similar way, a fourth coupling, denoted D, can be marked, which, however, barely emerges from the crowded part and is tagged with less security. These four couplings remain unchanged under D_2O buffer conditions; effects of H/D exchange become visible in at most the ± 2.5 MHz distance to the free proton frequency. Regarding primary spectral information, we note that when moving in the field-frequency plot from the outer couplings towards the center each of the couplings mentioned must be, in principle, represented by a doublet of lines at g_{\max} and g_{\min} . This then allows us to assume that the lines connected for couplings A–D represent the outermost lines of their respective coupling pattern throughout the field-frequency plot.

With this information the solution can be found that couplings B and C arise from the two β -protons bound to one of the cysteines, whereas A and D originate from two β -protons bound to another cysteine. Both cysteine residues, on the other hand, must be bound to the same iron, which has a positive spin density, i.e., the iron with the (III)-valence state. Both groups of cysteine β -protons have their maximum coupling values in different regions of the field-frequency plot. Couplings B and C are largest between g_{\max} and g_{int} , close to g_{\max} ; A and D between g_{int} and g_{\min} . This immediately implies that g_{\max} points approximately toward a cysteine residue and not toward the interconnection vector between the two irons in the cluster, as was suggested earlier based on theoretical considerations [19]. The final solution and assignment places the g -tensor into the molecular frame, as is shown in Figure 10 (bottom part), which also indicates the identified protons responsible for couplings A–C. As mentioned above, besides the g -tensor position within the cluster, further results from the analysis comprise the determination of the iron site, which is reduced together with the spin densities on both the Fe(III) and the Fe(II), and the isotropic coupling of the four cysteine β -protons [15]. For the isotropic coupling parameters and site of iron reduction, paramagnetic NMR is a complementary method with which the ENDOR data can be compared directly. For *A. platensis* the respective data were available prior to our study and compare well with the ENDOR results [20]. It turns out that, of the two iron ions, the one closer to the surface is reduced, denoted Fe1 in *A. platensis* (cf. Fig. 10). This can be explained in part by its solvent exposure and the larger number of polarizable (e.g., NH) protons in its vicinity.

It is instructive to reanalyse the proton ENDOR data for *A. platensis* with a new computer program through which the intuitive spectroscopist's approach is guided by a variation routine that selects possible solutions. For both approaches described in the theoretical section [Eqs. (4), (5), and (12), as well as Eq. (19), respectively], we have developed a program that compares the position of outer lines of a given experimental coupling with a calculated line position over the whole range of the magnetic fields of the EPR spectrum. For this, in the experimental spectra, the outer lines of a given coupling are marked with a certain range of a frequency interval. This range is chosen by the operator; it must be large enough to make sure that the calculated position for a "hit" falls into it but should be small enough to allow for a differentiation of "hit" and "miss." In the example of *A. platensis*, the spectra for coupling B between about 328 and 338 mT (cf. Fig. 10, top) would carry a mark not broader in frequency than their linewidth. For the overlapped part to higher magnetic fields, no frequency range is fixed, except for the last (or next to last) spectrum. There, a broad frequency range covers the potential coupling range, which in our example extends from -3.5 to $+3.5$ MHz. For coupling A, the unoverlapped range between 340 and 355 mT would carry a mark in the order of the linewidth, and the overlap region would be treated according to B in its corresponding part along g_{\max} . With couplings A, B, and C one would now have three proton interactions, each safely determined in a certain, limited field range. If now a structure of the [2Fe2S] core together with its coordinated cysteine residues is taken from the protein databank as a high-resolution crystal structure and applied as a source for the distances and directions (i.e., fixing the parameters r , r_i , and r_j) of relevant protons with respect to the two iron ions, then each of the experimental couplings A–C is assigned to a certain proton.

We use now, as an example, Eqs. (12) and (13) to calculate the ENDOR resonance lines at all selected field positions by varying all parameters within defined ranges, except for the proton position that is taken from the structure. The global parameters varied are the \mathbf{g} -tensor direction and the spin densities, and the individual parameters concerning each coupling separately are the isotropic parts of the hyperfine interaction. A "hit" is produced if, for the same global parameters, the outer lines produced by each of the protons simultaneously fall into the assigned marked intervals. This condition has to be fulfilled for all the preset field positions for the same set of global parameters. In our case the only restriction is that all three protons should be bound to the two cysteine residues coordinated to the same iron. Starting with an arbitrary assignment of proton and couplings A–C and varying the \mathbf{g} -tensor over the whole unit sphere, one finds the solution indicated by the larger gray balls in Figure 10 (bottom) representing the trace of possible g_{\max} -directions. It includes the solution suggested in an earlier paper [15]. The small gray spheres, marked with arrows, result from a thin trace of allowed g_{\max} -directions, which however are discarded by testing them for couplings to other H/D-exchangeable protons with the standard simulation program. It is noted that the selective criteria become very stringent if a dipolar coupled proton can be assigned in the field-frequency plot. The applied automated procedure is also very useful for exploring additional solutions for the parameters, which are not easily

found by the interactive simulation. It also can be used to refine a solution with respect to proton positions taking into account positional strain or g -strain always present in powder spectra of metal proteins.

The question arises as to whether the g -tensor is directed as shown in Figure 10 above in all [2Fe2S] ferredoxins. The EPR spectra of this class of clusters show a large variation both in symmetry as well as in values within a symmetry class. The classical distinction has been made between plant and vertebrate ferredoxins. The typical plant (spinach, parsley) ferredoxin has rhombic g -tensor symmetry and values around 2.05, 1.96, and 1.89, with an average value below 2. Representative for the vertebrate ferredoxins is adrenodoxin or putidaredoxin, in which the g -tensor has fairly axial symmetry, with g_{\max} around 2.02 and $g_{\text{ax}} \sim 1.93$, with an average g -factor also below 2. However, other groups of ferredoxin spectra can be formed when considering the two redox active [2Fe2S] clusters in molybdopterin hydroxylases, e.g., of the xanthine oxidase family. Here one has to distinguish between the so-called FeSI and the FeSII center. Both are [2Fe2S] clusters with all-cysteine coordination but show a large variation in symmetry and g -factor values. For the FeSII centers the g -factor can adopt values of g_{\max} around 2.13, but values below 2.1 also occur. FeSI centers exhibit a maximum g -factor of about 2.03 [14]. Some representative EPR spectra from five different members of this family showing the diversity of spectra appearances for [2Fe2S] clusters are given in Figure 11. In some cases one can derive directly from splittings of lines in the spectra that the two centers do interact; in others this is not obvious.

In view of this large diversity of EPR spectra, the question concerning the direction of the g -tensor becomes highly significant. Apart from *A. platensis*, which represents the typical plant ferredoxin group in symmetry and values of the g -tensor, we have recently analyzed in detail adrenodoxin, the axially symmetrical case, with smaller g_{\max} values. In that case the spin density on the irons was slightly reduced (by about 20%), but the position of the g -tensor with respect to the molecular frame was similar in comparison to *A. platensis* [21]. In addition, we have preliminary data from *Anabaena sp.* that also gives the same g -tensor position. Furthermore, the present state of our analysis from the two FeS centers in the molybdopterin cofactor protein aldehyde oxidoreductase (labelled “Mop” in Fig. 11) indicates that, apart from the FeSII center, which clearly gives the same positioning of the g -tensor as the examples before, the more obscured FeSI center also has the same basic g -tensor orientation.

One of the means of separating contributions within either center is based on relaxation. In simple EPR data acquisition, one finds that FeSI appears already around 77 K, whereas FeSII starts to grow in at much lower temperatures, typically below 30 K. This is true for all different samples of molybdopterin hydroxylases and implies differing relaxation behavior, mainly in spin lattice relaxation time T_1 . Therefore, in Davies ENDOR, one can use the time separation of the detection pulses (see Fig. 4) in order to distinguish between the two FeS centers in their ENDOR response. This is shown in Figure 12 for Mop as an example. Recording **a** is for a 400-ns time delay between the detection pulses, trace **b** is for 1200 ns. At

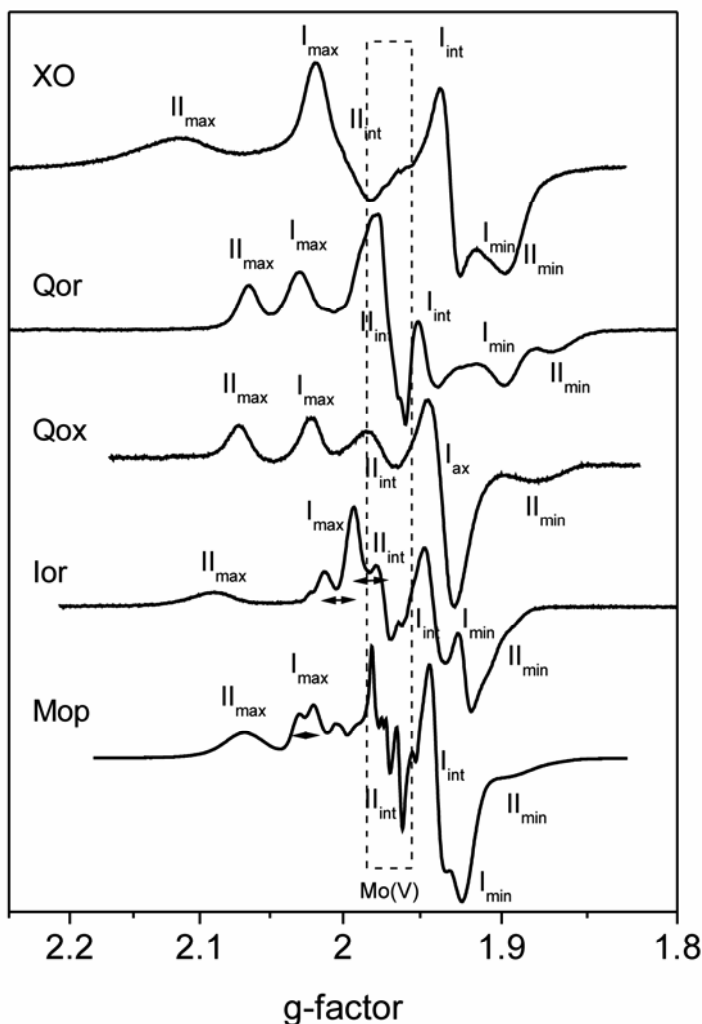


Figure 11. Comparison of the EPR powder spectra (20 K) of the two reduced $[2Fe_2S]$ clusters FeSI and FeSII of various molybdenum hydroxylases of the xanthine oxidase (XO) family showing a pronounced variation of EPR parameters of the centers. The principal g -tensor components of both clusters are indicated. The horizontal arrows mark appearance of dipolar interaction between the clusters. The dashed rectangle covers the field range of sizeable contributions from paramagnetic Mo(V) species. Qor: quinoline oxidoreductase; Qox: quinoline oxidase; Ior: isoquinoline oxidoreductase; Mop: aldehyde oxidoreductase.

the longer time, one of the outer lines clearly disappears and is thus assigned to the FeSII center. In this way an assignment for the two centers can be attempted, leading to the statement concerning the g -tensors as done above. At present it seems that g -tensor localization within the cluster structure is independent of EPR g -

tensor symmetry or absolute numerical values for the g -tensor and always looks like that shown in Figure 10 (bottom). This information is an absolute prerequisite when trying to understand the interaction parts in the EPR spectra of Figure 11, but space restrictions do not allow us to go into further detail on this complex topic.

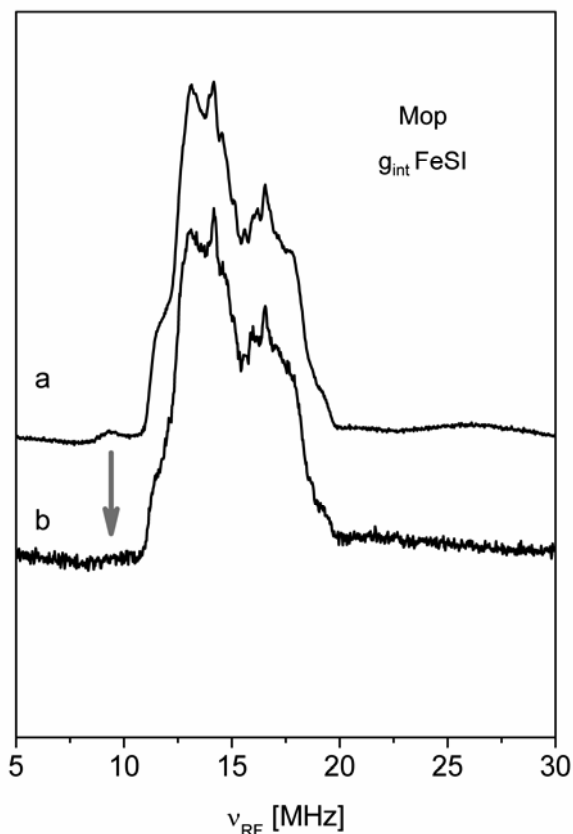


Figure 12. Pulse Davies ^1H -ENDOR of Mop at g_{int} of FeSI for pulse separations of 400 ns (a) and 1200 ns (b) of the detection pulses. The arrow indicates the clear reduction of a proton line in spectrum b that therefore can be assigned to belong to the fast relaxing FeSII cluster.

The position of the g -tensor is different, on the other hand, in the Rieske iron sulfur protein, in which, in the $[2\text{Fe}_2\text{S}]$ cluster, two of the cysteine residues coordinated to one iron are exchanged against histidines (cf. Fig. 1, left bottom structure). Here g_{max} lies along the iron–iron interconnection vector, as was proposed on theoretical grounds and supported from single-crystal EPR data [19,22]. We have recently analyzed the proton ENDOR data and found clearly the respective symmetry

of the outer proton lines in the field-frequency plot necessary for this assignment [21]. The position of the g -tensor within the Rieske cluster is shown in the stereoplot of Figure 13.

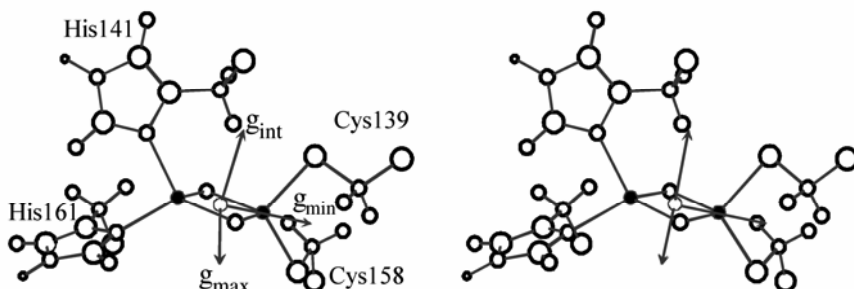


Figure 13. The stereoplot of the Rieske [2Fe2S] cluster shows the orientation of the g -tensor in the molecular frame as derived from an analysis of proton ENDOR.

Consider now [4Fe4S] clusters. There are two groups of iron–sulfur proteins utilizing the same basic cubane structure shown schematically in Figure 1 (right part). They are either reducible and thus ferredoxins, or they are oxidizable and then are called **H**igh **P**otential **I**ron sulfur **P**roteins (HiPIP) since their redox potential is positive. We shall deal here with the latter group. As an example, consider the HiPIP of *Ectothiorhodospira halophila* (*E. hal.*) II. Its basic cubane structure combined with the sequence information (also for *E. hal.* I) concerning its amino acid residue environment is given in Figure 14 (top). The typical iron spin coupling scheme for the case of *E. hal.* I is also shown (bottom part). For HiPIPs in the cluster oxidation state $[\text{Fe}_4\text{S}_4]^{3+}$ generally there is an $S = 1/2$ ground state arising from antiferromagnetic coupling of two pairs of irons: a ferric and a mixed-valence (formally ferric–ferrous) pair. The pairs are coupled in a ferromagnetic way, which involves spin maximization. In the coupling scheme shown, the total spin $S = 1/2$ would then result from the antiferromagnetic combination of $S = 9/2$ for the mixed-valence ($5/2 + 2$) and the $S = 4$ for the ferric pair ($5/2 + 3/2$), respectively. Note, however, that an $S = 1/2$ total spin state can also arise from other combinations, e.g., $S = 7/2$ and $S = 4$ or $S = 7/2$ and $S = 3$, etc. Details on this question will be given below. (In both the cubane and the coupling scheme, the final result concerning the specific assignment of the individual iron ions Fe1 to Fe4 to the two pairs is already shown: the mixed-valence pair resides on Fe2 and Fe3). The EPR spectrum is shown in Figure 15 (left part, top). It is axial with some resolved rhombic distortion ($g_{\text{max}} = 2.145$, $g_{\text{int}} = 2.034$, and $g_{\text{min}} = 2.024$). Apparently the spectrum is due to a single paramagnetic species. Therefore, considering the six cubane faces, the

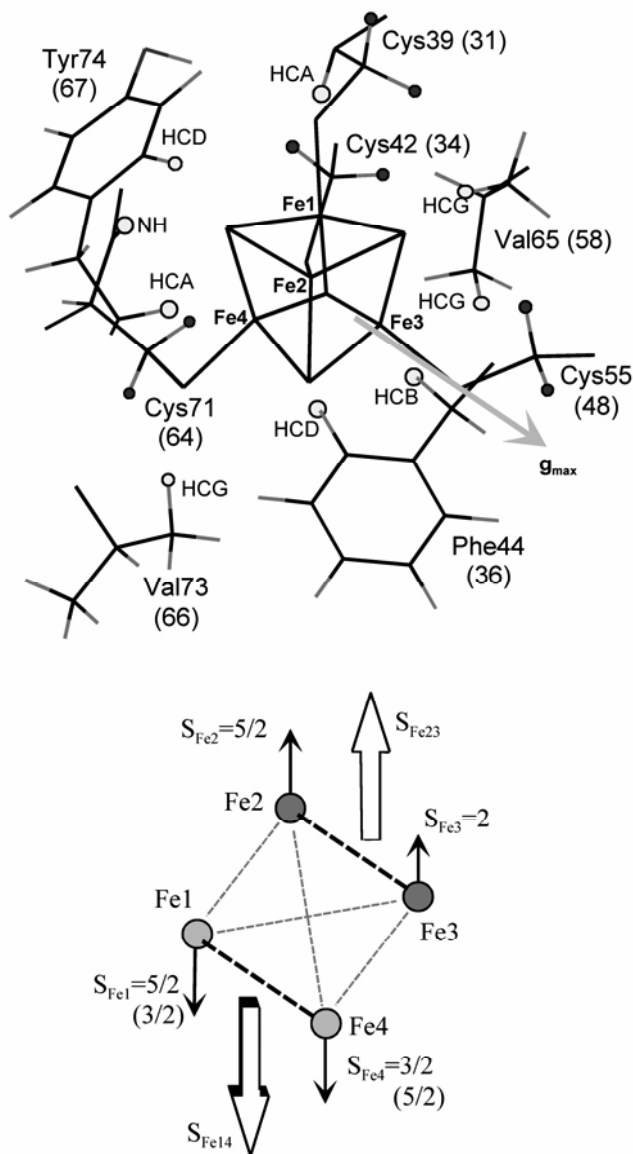


Figure 14. Environment of the HiPIP [4Fe4S] cluster (top) of *E. hal.* II (and I) showing the interacting protons observed in ENDOR (cysteine β -protons: black spheres, protons of amino acids in the immediate cluster vicinity: light gray spheres). The g_{\max} -orientation is given by the gray arrow; g_{\min} is along the vector connecting Fe2 and Fe3, g_{int} along the vector between Fe1 and Fe4 (not shown). In the bottom part the spin coupling scheme for the 4Fe4S system illustrates the combination of possible local iron spin states by ferromagnetic coupling (dashed black line) to subspins (open arrows) which antiferromagnetically coupled yield the total spin $S = 1/2$. The narrow dashed lines indicate exchange and super-exchange pathways. In the example the irons Fe2 and Fe3 constitute the mixed-valence pair; Fe1 and Fe4 the ferric pair.

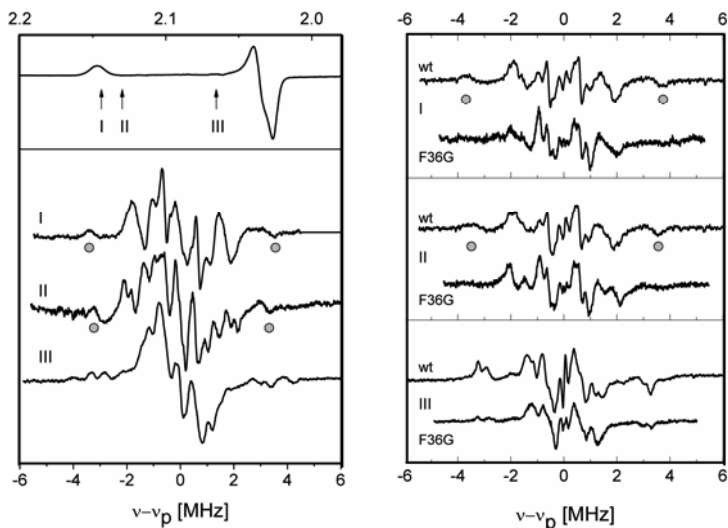


Figure 15. Comparison of ^1H -ENDOR spectra of the HiPIPs from *E. hal.* II (left panel) and *E. hal.* I and its variant F36G (right panel). Spectra were recorded at the field positions indicated in EPR spectrum (left panel, top). The gray circles mark the interaction of HCB Phe48 in *E. hal.* II and correspondingly of HCB Phe36 in *E. hal.* I. This interaction vanishes in the F36G variant.

question arises whether all possible combinations of iron pairs, mixed-valence and ferric, are occupied and thus the spectrum represents an ensemble average of these or if only one of the combinations applies and, if so, which one and for what reason. When we started our analysis [13], unlike the situation for [2Fe2S] clusters, there was much additional information available. For example, in single crystals of a model compound the oxidized state had been produced by ionizing irradiation, and the EPR showed that several spectroscopically distinct $[\text{Fe}_4\text{S}_4]^{3+}$ centers were formed potentially aligning with several possible occupations of the mixed-valence pairs [23]. Later, the same group of authors presented an ENDOR single-crystal analysis of one of these centers that was highly useful in terms of transfer to the protein data [24]. Also, sequence-specific paramagnetic NMR studies at room temperature were available for *E. halophila* II, and thus access to the position of the mixed-valence pair and isotropic hyperfine couplings had been given. In addition, a high resolution x-ray structure of the isoenzyme *E. halophila* I was available [25], from which a molecular dynamics simulation for the *E. halophila* II structure had been derived [26]. We therefore considered our study a test of the feasibility of orientation-selective ENDOR for this group of proteins since no other such studies existed. The structural details of the cubane and its amino acid residue environment (cf. Fig. 14, top part) emphasizes the potential protons with possible interactions. Apart from eight cysteine β -protons (black spheres), there are nine more protons

(light gray spheres) close enough (within 4 Å) to potentially contribute to the ENDOR spectra.

Shown together with the EPR spectrum in Figure 15 (left part) are three representative proton ENDOR spectra taken at the respective field positions marked in the EPR part. In two spectra, an outer line group is indicated (filled circle). For the detailed analysis of the field-frequency plot for all ENDOR data (not shown) one stringent parameter was applied: the direction of the g -tensor with respect to the cubane face was taken from the model complexes [23]. It had been shown that the maximum g -factor aligned with the normal to the face and the other two, “in-face” directions were parallel with the connecting vectors between the two mixed-valence (g_{\min}) and the two ferric ion pairs. With this parameter fixed it became immediately clear that the coupling of about 6.8 MHz along about g_{\max} (marked in Fig. 15) could not be ascribed to a cysteine β -proton since none of them pointed in this direction. Only the purely dipolar proton HCB of Phe44 had the right direction and distance, and the respective search in the structure showed that only for this face (which contained the irons numbered Fe2 and Fe3) was a dipolar proton available. It followed that these were the irons of the mixed-valence pair, in agreement with the paramagnetic NMR results in which the mixed-valence pair iron ions had been associated with residues Cys42 and Cys55. The direction of g_{\max} is shown in the cubane of Figure 14 (top). With these prerequisites the four β -proton resonances of these two residues were simulated and assigned to the experimental spectra. For the spin density on the two mixed-valence irons the coupling value of the dipolar proton and independent ENDOR data from ^{57}Fe substituted *E. halophila* II protein (see below) were taken as input parameters. The agreement between experiment and simulation was considered reasonable. Nevertheless, an uncertainty as to the exact value of the isotropic coupling of the cysteine β -protons remained and led to two sets of values. One of them was subsequently discarded on account of less efficient matching with the structural prerequisites from the dihedral angle analysis.

In a subsequent study the iso-protein *E. halophila* I was analyzed, which turned out to have the same basic g -tensor direction and spin density parameters as *E. halophila* II. In this protein we could, in addition, probe the assignment of the dipolar coupling to the HCB proton of Phe44 (now 36 in *E. halophila* I), which was crucial for the total assignment for both proteins. A mutant was measured in which this residue was replaced by glycine. The resulting changes in the experimental ENDOR spectra between wild-type and mutant are shown in Figure 15 (right part). It is obvious that the line assigned to this residue, which is present in the wild-type protein prominently along g_{\max} , and its vicinity (positions I and II) is missing in the mutant, whereas at other field positions the patterns show little change. This implies that the mutant has the same cluster environment as the wild type except the proton in question is missing.

It is therefore unambiguous and in line with paramagnetic NMR results that in *E. halophila* II (and I) both the ENDOR and EPR data imply that there is only one single and specific paramagnetic species formed upon oxidation of the protein that is connected with one specific site of the cubane. (With respect to *E. halophila*

I, an additional minority species of unknown origin at less than 5% contribution was detected.) It thus appears reasonable to assume that in those HiPIP proteins that exhibit more than one species detected by EPR, other faces of the cubane should be involved and carry the mixed-valence iron pair. Studies aiming at proving this experimentally are presently under way in our laboratory. A prominent example with more than one EPR-active signal is HiPIP from *Chromatium vinosum*. According to combined EPR and Mössbauer data, three different species contribute to the signal [27]. Another EPR study found four different species [28]. Paramagnetic NMR at 300 K discerned two species in a 60:40 ratio [29–31]. We are presently studying this HiPIP, and so far the data support the four-species model. Details concerning the g -tensor directions deriving from proton ENDOR will be given soon.

4.2. ^{57}Fe Iron Interactions

The iron nucleus was a very important spectroscopic probe early on in the development of an understanding of iron–sulfur clusters. Both for EPR as well as, by necessity, for Mössbauer spectroscopy, enrichment of clusters with ^{57}Fe was the first methodological approach that allowed for an insight into the basic chemical nature of the [2Fe2S] clusters in ferredoxins (see, e.g., [32] for an early review on the EPR of this field). A more recent account on the many facets involved with the whole group of iron–sulfur proteins is found in [33]. With respect to the EPR method, the article by Guigliarelli and Bertrand in that book is of specific interest since it deals, among others, with utilization of the only other observable at that time, the g -tensor principal values, and their description in terms of a ligand field model [33]. One of the main topics connected with analysis of the g -tensor and, later on, the ^{57}Fe hyperfine interaction was to understand the valence states of the iron ions and their mutual interactions. The first description of the g -tensor values in [2Fe2S] clusters that led to the so-called “spin projection coefficients” [34] has opened the field to a large number of theoretical approaches and was transferred to polynuclear clusters in addition. A more recent account dealing with the analysis of iron hyperfine couplings in clusters containing from one to four iron ions and their relation to the electronic structure in terms of spin projection coefficients is found in [35].

The first ^{57}Fe ENDOR measurements were performed on [2Fe2S] clusters of the type in Figure 1 from plant ferredoxins, and the idea of orientation selectivity of the ENDOR response was already addressed, although not fully exploited [36]. With its nuclear spin $I = 1/2$ the theoretical treatment of ^{57}Fe hyperfine coupling in terms of establishing tensors is completely analogous to that of protons. Nevertheless, the analysis of the values in terms of spin densities and spin coupling schemes in iron–sulfur clusters is a fairly complex matter. We shall deal with this below.

Let us first consider data from [2Fe2S] clusters. The experimental A_{Fe} values (isotropic couplings) obtained from plant-type and vertebrate ferredoxins yield about 48.2 MHz for the Fe(III) ion and 22.1 MHz for the Fe(II) ion (tabulated in [35]). Since for both ions the $A_{\text{Fe}}/2$ value is much larger than the nuclear Zeeman

frequency (0.4818 MHz at a magnetic field of 0.35 T), the appearance of an ^{57}Fe hyperfine interaction in the spectra involves a doublet of lines for each ion centered approximately around 24 (Fe(III)) and 11 MHz (Fe(II)), respectively, split by twice the nuclear Zeeman frequency, i.e., by nearly 1 MHz. Typically, the anisotropy of the interaction due to Fe(II) is considerably larger than that of Fe(III).

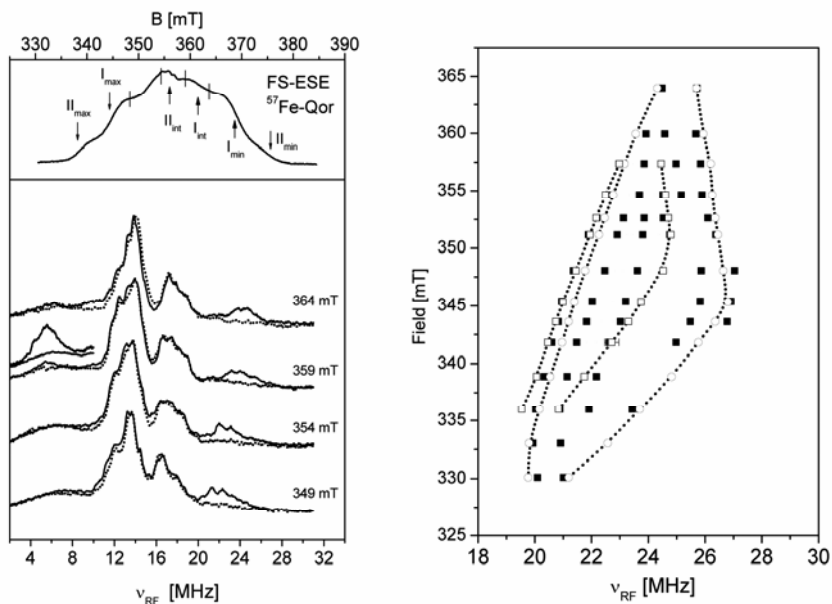


Figure 16. Observation of ^{57}Fe -ENDOR for the two $[2\text{Fe}_2\text{S}]$ clusters in quinoline oxidoreductase (Qor). The top part of the left panel shows the field-swept ESE spectrum with the arrows indicating the principal components of the \mathbf{g} -tensors of both clusters (FeII and FeSI). The sticks mark the field positions for which the ENDOR spectra of ^{57}Fe -substituted Qor (solid traces) and ^{56}Fe -Qor (dotted traces) are compared in the bottom part of the left panel. In the high-frequency part the resonances of the $^{57}\text{Fe}^{3+}$ ions of both centers are visible. The resonances of $^{57}\text{Fe}^{2+}$ appear only weakly in a narrow field range (ca. 359 mT) at low rf frequencies. The right panel shows the experimental line positions of the $^{57}\text{Fe}^{3+}$ resonances (filled squares) and the simulation of the outer lines of the ^{57}Fe interaction arising from FeII (open circles, dotted line) and FeSI (open squares, dotted line) for comparison. The data-points were taken from CW difference spectra (^{56}Fe vs. ^{57}Fe); note that the microwave frequency for this panel is different from that in the left part, yielding shifted magnetic field values for related working points. The swept radiofrequency is denoted ν_{RF} .

In the group of molybdopterin hydroxylases, there is the complication in terms of spectral overlap of two different $[2\text{Fe}_2\text{S}]$ clusters, FeSI and FeSII, which was already discussed for the proton interactions above. The main question involved with the study of ^{57}Fe interactions is whether the two sites can be distinguished, i.e.,

four ions grouped into two pairs. If so, the question is whether the ^{57}Fe hyperfine couplings derived can give a clue to understanding the strong differences observed, e.g., in \mathbf{g} -tensor values in EPR (cf. Fig. 11) in the two clusters. So far the results are not conclusive. Consider first the EPR spectrum optimized for the observation of the two FeS centers in ^{57}Fe -enriched quinoline oxidoreductase (Qor) shown in Figure 16 (left part, top) as field-sweep electron spin echo response (Hahn echo). The labels II_{max} to II_{min} and I_{max} to I_{min} indicate the three g -factors for the FeS centers I and II, respectively, as introduced in Figure 11. As noted above for the proton interactions, at field positions II_{max} and II_{min} a response from the FeSII center only is expected. Davies ENDOR spectra taken at four different, representative field positions in the overlap region of centers I and II are shown in the bottom part of Figure 16 (left part, bottom). The traces of the ^{56}Fe and the ^{57}Fe protein samples are superimposed. It is obvious that the center part, which represents the proton interaction, is flanked by a group of lines in the ^{57}Fe -enriched sample in the range between 22 and 25 MHz, which was assigned above to expected Fe(III) contributions. The counterpart, the Fe(II) contribution that should occur at about 10 to 11 MHz, is obscured mostly by the proton lines. Only at about 359.0 mT field is there a group of lines around 6 MHz that should be ascribed to Fe(II) interactions. It is not clear why there is only such a small window of fields of accessibility to this interaction, but it may be a combination of anisotropy and relaxation. In any case, this interaction cannot be analyzed properly. Concerning the Fe(III) lines, an approximate analysis based on a full set of CW-ENDOR data can be attempted utilizing the field regions free of overlap for the FeSII cluster (positions II_{max} and II_{min}). This is shown in the right part of Figure 16. The analysis gives values of 41 MHz (II_{max}) and 50.1 MHz (II_{min}), corresponding to values of $A/2_{\text{Fe}}$ of 20.5 and 25.05 MHz, respectively. The outer lines for center II as deriving from the tensor simulation with 52.5 MHz as a third value are shown as open circles and connected with dotted lines. The deviation of the principal value directions of the hyperfine tensor with respect to the \mathbf{g} -tensor is about 5° . For FeS center I we find from the simulations (open squares) slightly smaller coupling values (40, 47.6, and 48.6 MHz, in the same order as above for center II). Again, there is little deviation from coaxiality with the respective \mathbf{g} -tensor directions. For a further analysis involving also the Fe(II) contributions for both centers to the spectra, they should be taken at higher frequencies than X-band in order to separate the proton from the ^{57}Fe lines.

We now turn to the $[4\text{Fe}4\text{S}]$ clusters in HiPIP proteins. Fortunately, like for the protons as mentioned above, there were single-crystal ^{57}Fe ENDOR studies from a HiPIP model complex available [37], permitting an estimation of the potential situation in the proteins. Four different hyperfine tensors were found that could be grouped into two categories with two members in each that showed a slight inequivalence. The two categories were assigned to the ferric and the mixed-valence pair. The mean tensors (isotropic value) found for the mixed-valence pair was around 33 MHz, while for the ferric pair a value around 18.5 MHz was found. These values were in good agreement with those found earlier by Mössbauer spectroscopy from *Chromatium vinosum* HiPIP [38]. They would translate into

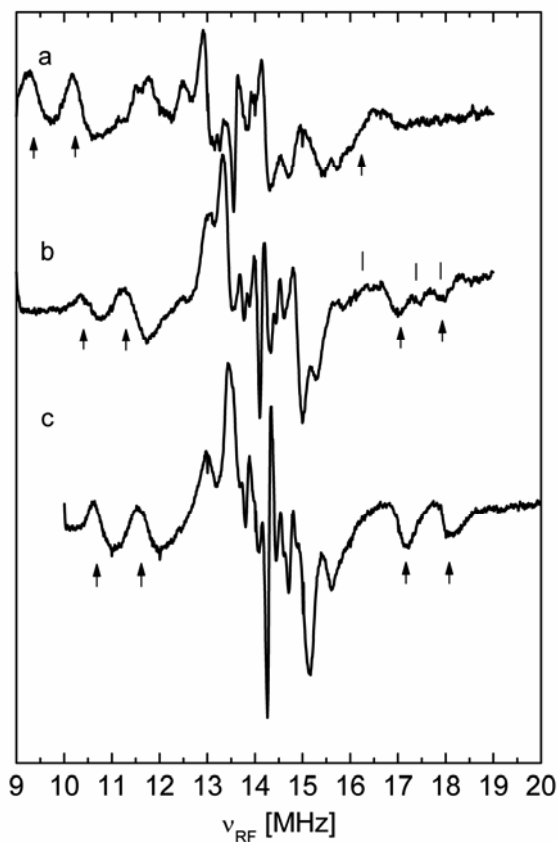


Figure 17. ENDOR spectra of ^{57}Fe -enriched HiPIP of *E. hal.* II at three g -selections: (a) $g = 2.143$, (b) $g = 2.053$, and (c) $g = 2.030$ (refer to EPR spectrum in Fig. 15). Two groups of ^{57}Fe resonances are marked with arrows and are partly overlapping with proton lines (indicated by sticks).

ENDOR patterns as (basic) doublets separated by about 1 MHz and centered at about 16.5 MHz (mixed-valence) and 9.25 MHz (ferric pair). Therefore, as for the $[\text{2Fe2S}]$ clusters, there should be considerable overlap with proton resonances when the measurements are taken at the usual X-band frequencies. Fortunately, the results for *E. halophila* II are shown in Figure 17 for three g -factors have better resolution than the ones discussed above for the $[\text{2Fe2S}]$ clusters. Although there is no distinction possible between the individual irons within one line group, the mixed-valence pair and the ferric pair are nicely distinguishable from the protons when the ^{56}Fe sample is used for comparison (data not shown). Comparison with the available data based mostly on Mössbauer spectroscopy from several HiPIP

proteins, the ^{57}Fe ENDOR data from *E. halophila* II derived from our study [13], fall well within the range of other experimental methods and other proteins [35,39].

4.3. Spin Densities

Proton and ^{57}Fe hyperfine interactions give insight into the spin density (sometimes denoted spin population) and its distribution, in the present context, over the iron ions and other nuclei of iron sulfur clusters. For protons, the dipolar part of the tensor is directly connected, apart from distance to the spin center (iron) in the structure, with the spin density at the center in the point-dipole approximation. This type of spin density is therefore not associated with any iron orbital. The isotropic part that we have considered only for the cysteine β -protons is connected with the 2π -orbital spin density on the sulfur and the dihedral angle as typical β -protons [40]. The latter spin density is usually not more than about 3–5%. The ^{57}Fe hyperfine interaction is also associated with the iron spin density, and there have been several approaches to its description.

One of the first attempts, in the context of EPR spectroscopy, to describe spectroscopic features of iron-sulfur proteins in terms of theoretical models was introduced for the [2Fe2S] cluster in spinach ferredoxin [34]. Gibson and coworkers presented a formula for the \mathbf{g} -tensor principal values that coupled a high spin ferric and a high spin ferrous ion in an antiferromagnetic fashion. Each iron carried an individual g -value (g_1 and g_2 , respectively) coupled to total g by

$$g = \frac{(g_1 + g_2)}{2} + [(g_1 - g_2) / 2S(S + 1)] \cdot [S_1(S_1 + 1) - S_2(S_2 + 1)], \quad (20)$$

With $S_1 = 5/2$, $S_2 = 2$, and $S = 1/2$ for the ferric, the ferrous and the total spin, one obtains

$$g = \frac{(7g_1 - 4g_2)}{3}. \quad (21)$$

Values were proposed for g_1 and g_2 from the energy levels of each iron ion to give the experimentally determined one. This model is basically still the one that describes the contributions of the individual ions to the total parameters. The coefficients $7/3$ and $-4/3$ for the individual g -values were later denoted spin projection coefficients, and in essence they give the spin densities on the iron ions assuming a specific coupling scheme, be it a [2Fe2S] or a [4Fe4S] cluster. For the latter, the vector coupling model shown in Figure 14 derives from it.

For the [2Fe2S] cluster the proton interactions give spin densities from the dipolar part between 1.65 (Adrenodoxin) and 1.80 (*A. platensis*) on Fe(III) and about -0.65 to -0.80 for Fe(II). These values are clearly less than $7/3$ and $-4/3$. This is connected to covalency parameters and delocalization. Nevertheless, it is obvious that the spin densities in the [4Fe4S] clusters are typically smaller. For *E. halophila* II spin densities from the proton ENDOR analysis were 1.30 for the mixed-valence

and -0.70 for the ferric pair. This corresponds to a spin coupling scheme of $S = 7/2$ for the mixed-valence pair, $S = 3$ for the ferric pair, and $S = 1/2$ for the total spin, but admixtures of other states cannot be excluded. Note that these values are different from the ones given in the scheme of Figure 14, in which the initial proposal discussed in the literature is shown. This comprised, in terms of spin maximization as observed in the $[2\text{Fe}_2\text{S}]$ clusters, the states $(9/2, 5, 1/2)$. For FeS clusters in general, the ^{57}Fe hyperfine interaction can be connected with the spin projection coefficients in a way that

$$A^{\text{exp}}(\text{Fe}_i) = K(\text{Fe}) \cdot a(\text{Fe}_i). \quad (22)$$

Here the experimentally observed isotropic interaction of iron number i is connected with the projection coefficient K for that iron and an intrinsic coupling a that would be normalized to a unit projection coefficient. The question then is the value of $a(\text{Fe}_i)$. There are several values proposed in the literature deriving mainly from Mössbauer spectroscopy of mononuclear tetrahedrally sulfur coordinated complexes FeS_4 like in rubredoxin. If we use a typical value of -22 MHz for Fe(III) and Fe(II), we obtain, for the $[2\text{Fe}_2\text{S}]$ cluster in Qor as discussed above, a spin projection coefficient close to the theoretical value of $7/3$ for Fe(III). For the Fe(II) iron we have not been able to derive the isotropic coupling. However, the proton interactions give spin densities from the dipolar part between 1.65 (Adrenodoxin) and 1.80 (*A. platensis*) on Fe(III) and about -0.65 to -0.80 for Fe(II). These values are clearly less than $7/3$ and $-4/3$. This difference has been connected to covalency parameters and delocalization [35]. It would be of interest to be able to give the hyperfine tensor values for the two centers FeSI and FeSII in the group of molybdopterin hydroxylases in order to understand the large differences in their EPR signature. Here, again, the proton interaction analysis can be helpful in the absence of ^{57}Fe data.

It is obvious that the spin densities in the $[4\text{Fe}_4\text{S}]$ clusters are typically smaller if we consider the proton interaction data. For *E. halophila* II from the proton ENDOR analysis we found 1.30 for the mixed-valence and -0.70 for the ferric pair. According to a detailed analysis of both proton and ^{57}Fe hyperfine interactions in model compounds [24,37] and in proteins [35], this corresponds to a spin coupling scheme of $7/2$ for the mixed-valence pair, 3 for the ferric pair, and $1/2$ for the total spin. Admixtures of other states cannot, however, be fully excluded. Note that this coupling and its associated spin projection coefficients correspond to the values given in parenthesis in the scheme of Figure 14 and differ from the initial proposal of the literature, which involved the states $(9/2, 5, 1/2)$. The example shows how important the spin density is for understanding the coupling scheme. This parameter, on the other hand, is indeed best obtained by ENDOR using combined proton and ^{57}Fe data.

5. SUMMARY

Orientation-selective ENDOR spectroscopy has established itself as a method to study not only structural and electronic aspects in mononuclear but also in polynuclear metalloproteins like the iron–sulfur proteins discussed here. In this context, the global parameter of the g -tensor position within the molecular structure is again of importance, in part for understanding EPR spectra that show dipolar interaction due to more than one paramagnetic species, but also for determining the cluster position with respect to a membrane normal in a membrane protein. The difference found between the g -tensor position in the Rieske [2Fe2S] cluster and that in “normal” ferredoxins is of relevance in this respect. Another very important parameter is the site specificity of the reduction in [2Fe2S] clusters for which proton ENDOR, like paramagnetic NMR, is the only spectroscopic technique yielding such information. The respective parameter in the [4Fe4S] HiPIP clusters is the site of oxidation, which is also amenable to orientation-selective proton ENDOR. Apart from this, there is information about isotropic proton couplings and the iron spin densities. The latter information can be also gained from ^{57}Fe hyperfine interaction analysis and gives access to the spin coupling scheme. It should be noted that ENDOR is a spectroscopic technique that can probe both interactions simultaneously, unlike Mössbauer and paramagnetic NMR.

The problem with the application of this principle in proteins is spectral crowding for proton interactions and, combined with this, only partial definition of hyperfine lines over the whole range of the EPR spectrum. This makes direct tensor determination somewhat ambiguous, but in connection with known molecular structures a unique solution can typically be found. A very important asset in this respect is site-directed mutagenesis, by which specific amino acid residues can be changed. For most of the examples of iron–sulfur clusters discussed, a full analysis was possible even without this tool.

ACKNOWLEDGMENTS

Work from the authors' laboratory was supported by grants from the Deutsche Forschungsgemeinschaft. We gratefully acknowledge the contribution of our co-workers C. Canne, M. Ebelshäuser, C. Cullmann, M. Frotscher, C. Cracuin, and B. Bennett. The work was made possible through collaborations with the laboratories of I. Bertini (Florence), S. Ciurli (Bologna), S. Fetzner (Münster), R. Bray (Brighton), D. Lowe (Norwich), T. A. Link (Frankfurt), L. Eltis (Toronto), and M. Romao, J.J.G. Moura (Lisbon).

REFERENCES

1. Feher G, Gere EA. 1956. Polarization of phosphorus nuclei in silicon. *Phys Rev* **103**:501–503.

- Manikandan P, Carmieli R, Shane T, Kalb AJ, Goldfarb D. 2000. W-band ENDOR investigation of the manganese-binding site of concanavalin A: determination of proton hyperfine couplings and their signs. *J Am Chem Soc* **122**:3488–3494.
- van Gastel M, Matthias S, Brecht M, Schroder O, Lenzian F, Bittl R, Ogata H, Higuchi Y, Lubitz W. 2006. A single-crystal ENDOR and density functional theory study of the oxidized states of the [NiFe] hydrogenase from *Desulfovibrio vulgaris* Miyazaki F. *J Biol Inorg Chem* **11**:41–51.
- Schonland DS. 1959. On the determination of the principal *g*-values in electron spin resonance. *Proc Phys Soc (Lond)* **73**:788–792.
- Rist GH, Hyde JS. 1970. Ligand ENDOR of metal complexes in powders. *J Chem Phys* **52**:4633–4643.
- Hurst GC, Henderson TA, Kreilick RW. 1985. Angle-selected ENDOR spectroscopy, 1: theoretical interpretation of ENDOR shifts from randomly orientated transition metal complexes. *J Am Chem Soc* **107**:7294–7299.
- Henderson TA, Hurst GC, Kreilick RW. 1985. Angle-selected ENDOR spectroscopy, 2: determination of proton coordinates from a polycrystalline sample of bis(2,4-pentanedionato)copper(II). *J Am Chem Soc* **107**:7299–7303.
- Hoffman BM, Martinsen J, Venters RA. 1984. General theory of polycrystalline ENDOR patterns: *g* and hyperfine tensors of arbitrary symmetry and relative orientation. *J Magn Reson* **59**:110–123.
- Hoffman BM, Venters RA, Martinsen J. 1985. General theory of polycrystalline ENDOR patterns: effects of finite EPR and ENDOR component linewidths. *J Magn Reson* **62**:537–542.
- Hüttermann J. 1993. ENDOR of randomly oriented mononuclear metalloproteins: toward structural determinations of the prosthetic group. *Biol Magn Reson* **13**:219–252.
- Hüttermann J, Däges GP, Reinhard H, Schmidt G. 1995. Metalloprotein-ENDOR-spectroscopy. In *Nuclear magnetic resonance of paramagnetic macromolecules*, pp. 165–192. Ed GN La Mar. New York: Kluwer Academic.
- Hüttermann J, Kappl R. 1987. ENDOR: probing the coordination environment in metalloproteins. In *Metal ions in biological systems*, Vol 22, pp1–80. Ed H Sigel. New York: Marcel Dekker.
- Kappl R, Ciurli S, Luchinat C, Hüttermann J. 1999. Probing structural and electronic properties of the oxidized [Fe₄S₄]³⁺ cluster of *Ectothiorhodospira halophila* iso-II high-potential iron–sulfur protein by ENDOR spectroscopy. *J Am Chem Soc* **121**:1925–1935.
- Canne C, Lowe DJ, Fetzner S, Adams B, Smith AT, Kappl R, Bray RC, Hüttermann J. 1999. Kinetics and interactions of molybdenum and iron-sulfur centers in bacterial enzymes of the xanthine oxidase family: Mechanistic implications. *Biochemistry* **38**:14077–14087.
- Canne C, Ebelshäuser M, Gay E, Shergill JK, Cammack R, Kappl R, Hüttermann J. 2000. Probing magnetic properties of the reduced [2Fe-2S] cluster of the ferredoxin from *Arthrospira platensis* by ¹H ENDOR spectroscopy. *J Biol Inorg Chem* **5**:514–526.
- Iwasaki M. 1974. Second-order perturbation treatment of general spin hamiltonian in an arbitrary coordinate system. *J Magn Reson* **16**:417–423.
- Weil JA, Bolton JR, Wertz JE. 1994. *Electron paramagnetic resonance*. New York: John Wiley & Sons.
- Wang DM, Hanson GR. 1995. A new method for simulating randomly oriented powder spectra in magnetic resonance: the Sydney Opera House (SOPHE) method. *J Magn Reson Series A* **117**:1–8.

19. Bertrand P, Guigliarelli B, Gayda JP, Beardwood P, Gibson JF. 1985. A ligand-field model to describe a new class of 2Fe–2S clusters in proteins and their synthetic analogs. *Biochim Biophys Acta* **831**:261–266.
20. Dugad LB, LaMar GN, Banci L, Bertini I. 1990. Identification of localized redox states in plant-type 2-iron ferredoxins using the nuclear overhauser effect. *Biochemistry* **29**:2263–2271.
21. Kappl R, Ebelshäuser M, Hannemann F, Bernhardt R, Hüttermann J. 2006. Probing electronic and structural properties of the reduced [2Fe–2S] cluster by orientation-selective ^1H ENDOR spectroscopy: adrenodoxin vs. Rieske ISP. *Appl Mag Reson* **30**:427–459.
22. Bowman MK, Berry EA, Roberts AG, Kramer DM. 2004. Orientation of the g-tensor axes of the Rieske subunit in the cytochrome bc(1) complex. *Biochemistry* **43**:430–436.
23. Gloux J, Gloux P, Lamotte B, Mouesca JM, Rius G. 1994. The different $[\text{Fe}_4\text{S}_4]^{3+}$ and $[\text{Fe}_4\text{S}_4]^+$ species created by gamma irradiation in single crystals of the $(\text{Et}_4\text{N})_2[\text{Fe}_4\text{S}_4(\text{SBenz})_4]$ model compound: their EPR description and their biological significance. *J Am Chem Soc* **116**:1953–1961.
24. Mouesca JM, Rius G, Lamotte B. 1993. Single-crystal proton ENDOR studies of the $[\text{Fe}_4\text{S}_4]^{3+}$ cluster: determination of the spin population-distribution and proposal of a model to interpret the ^1H -NMR paramagnetic shifts in high-potential ferredoxins. *J Am Chem Soc* **115**:4714–4731.
25. Breiter DR, Meyer TE, Rayment I, Holden HM. 1991. The molecular structure of the high-potential iron-sulfur protein isolated from *Ectothiorhodospira halophila* determined at 2.5 Å resolution. *J Biol Chem* **266**:18660–18667.
26. Banci L, Bertini I, Capozzi F, Carloni P, Ciarli S, Luchinat C, Piccioli M. 1993. The iron-sulfur cluster in the oxidized high-potential iron protein from *Ectothiorhodospira halophila*. *J Am Chem Soc* **115**:3431–3440.
27. Dilg AWE, Capozzi F, Mentler M, Iakovleva O, Luchinat C, Bertini I, Parak FG. 2001. Comparison and characterization of the $[\text{Fe}_4\text{S}_4]^{2+/3+}$ centre in the wild-type and C77S mutated HiPIPs from *Chromatium vinosum* monitored by Mössbauer, ^{57}Fe ENDOR and EPR spectroscopies. *J Biol Inorg Chem* **6**:232–246.
28. Priem AH, Klaassen AAK, Reijerse EJ, Meyer TE, Luchinat C, Capozzi F, Dunham WR, Hagen WR. 2005. EPR analysis of multiple forms of $[\text{4Fe-4S}]^{3+}$ clusters in HiPIPs. *J Biol Inorg Chem* **10**:417–424.
29. Bertini I, Briganti F, Luchinat C, Scozzafava A, Sola M. 1991. ^1H -NMR spectroscopy and the electronic structure of the high-potential iron sulfur protein from *Chromatium vinosum*. *J Am Chem Soc* **113**:1237–1245.
30. Bertini I, Luchinat C. 1996. Electronic isomerism in oxidized Fe_4S_4 high-potential iron-sulfur proteins. *ACS Symp Ser* **653**:57–73.
31. Bertini I, Ciarli S, Luchinat C. 1995. The electronic structure of FeS centers in proteins and models, a contribution to the understanding of their electron-transfer properties. *Struct Bonding* **83**:1–53.
32. Dunham WR, Sands RH. 2003. g-strain, ENDOR, and structure of active centers of two-iron ferredoxins. *Biochem Biophys Res Comm* **312**:255–261.
33. Guigliarelli B, Bertrand P. 1999. Application of EPR spectroscopy to the structural and functional study of iron-sulfur proteins. *Adv Inorg Chem* **47**:421–497.
34. Gibson JF, Hall DO, Thornley JH, Whatley FR. 1966. Iron complex in spinach ferredoxin. *Proc Natl Acad Sci USA* **56**:987–990.

35. Mouesca JM, Noodleman L, Case DA, Lamotte B. 1995. Spin-densities and spin coupling in iron-sulfur clusters: a new analysis of hyperfine coupling-constants. *Inorg Chem* **34**:4347–4359.
36. Fritz J, Anderson R, Fee J, Palmer G, Sands RH, Tsibris JCM, Gunsalus IC, Orme-Johnson WH, Beinert H. 1971. Iron electron-nuclear double resonance (ENDOR) of 2-iron ferredoxins from spinach, parsley, pig adrenal cortex and *Pseudomonas putida*. *Biochim Biophys Acta* **253**:110–133.
37. Rius G, Lamotte B. 1989. Single-crystal ENDOR study of a ^{57}Fe -enriched iron sulfur $[\text{Fe}_4\text{S}_4]^{3+}$ cluster. *J Am Chem Soc* **111**:2464–2469.
38. Middleton P, Dickson DPE, Johnson CE, Rush JD. 1980. Interpretation of the Mössbauer spectra of the high-potential iron protein from *Chromatium*. *Eur J Biochem* **104**:289–296.
39. Dilg AWE, Mincione G, Achterhold K, Iakovleva O, Mentler M, Luchinat C, Bertini I, Parak FG. 1999. Simultaneous interpretation of Mössbauer, EPR and ^{57}Fe ENDOR spectra of the $[\text{Fe}_4\text{S}_4]$ cluster in the high-potential iron protein I from *Ectothiorhodospira halophila*. *J Biol Inorg Chem* **4**:727–741.
40. Noodleman L, Chen JL, Case DA, Giori C, Rius G, Mouesca JM, Lamotte B. 1995. Isotropic hyperfine coupling in high-potential $[\text{Fe}_4\text{S}_4]^{3+}$ models. In *Nuclear magnetic resonance of paramagnetic macromolecules*, pp. 339–367. Ed GN La Mar. New York: Kluwer Academic.

MOLECULAR SOPHE: AN INTEGRATED APPROACH TO THE STRUCTURAL CHARACTERIZATION OF METALLOPROTEINS: THE NEXT GENERATION OF COMPUTER SIMULATION SOFTWARE*

Graeme R. Hanson, Christopher J. Noble, and Simon Benson

*Centre for Magnetic Resonance, The University of Queensland
St. Lucia, Queensland, Australia*

Herein we describe an integrated approach — *Molecular Sophe* — for determination of the molecular structure of redox active cofactors in metalloproteins from an analysis of their high-resolution EPR spectra. Molecular Sophe involves the computer simulation of continuous-wave and orientation-selective pulsed EPR and electron nuclear double resonance (ENDOR) spectra. As aids to the correct analysis of these spectra, calculation of energy level diagrams, transition roadmaps, and transition surfaces can also be performed. This approach, based on molecular structure, promises to revolutionize the three-dimensional molecular (geometric and electronic) characterization of paramagnetic materials using a combination of high-resolution EPR spectroscopy and quantum chemistry calculations.

1. INTRODUCTION

Multifrequency continuous-wave electron paramagnetic resonance (CW EPR) and pulsed EPR spectroscopy [1–8] have found application in the structural characterization of paramagnetic species (species containing one or more unpaired electrons) used in a wide range of areas from physics, materials science, chemistry, biochemistry, microbiology, and medicine. Metalloproteins comprise approximately 30% of all known proteins and are involved in a variety of biologically important processes, including oxygen transport, biosynthesis, electron transfer, biodegradation, drug metabolism, proteolysis, and hydrolysis of amides and esters,

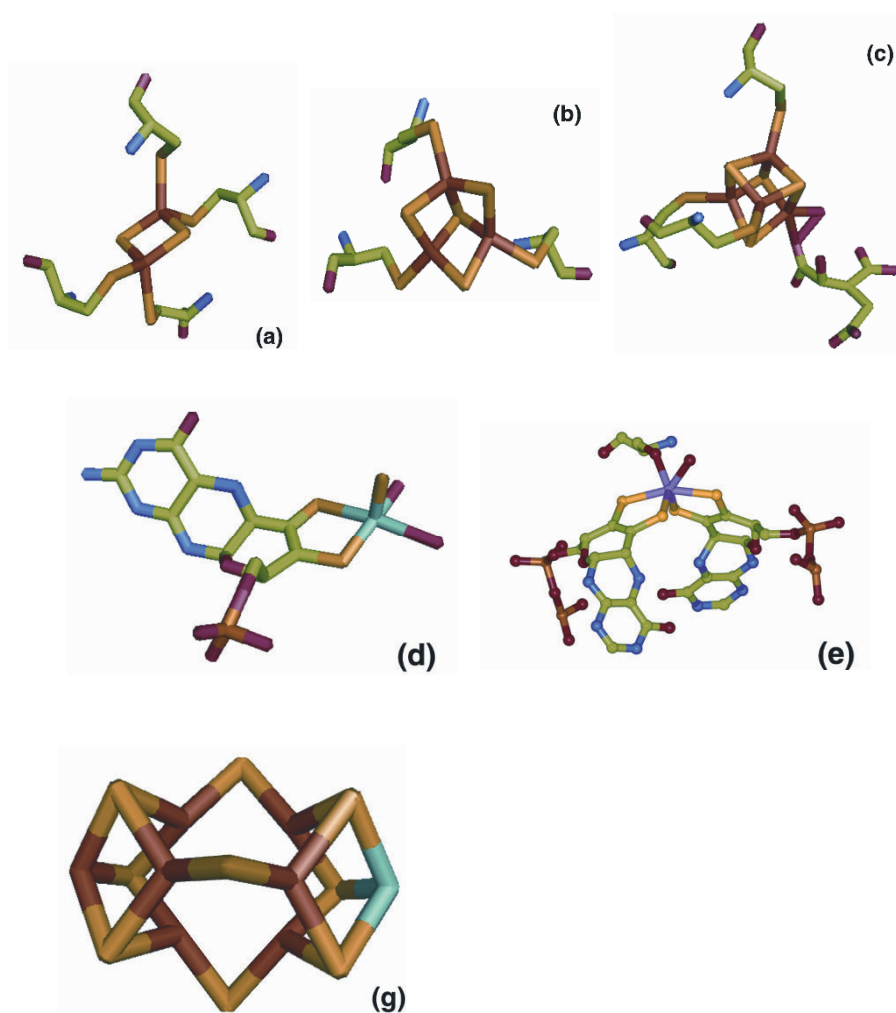


Figure 1. Examples of redox cofactors found in metalloproteins. (a) $[\text{Fe}_2\text{-S}_2]^{2+;1+}$ cluster; (b) $[\text{Fe}_3\text{-S}_4]^{1+;0}$ cluster; (c) $[\text{Fe}_4\text{-S}_4]^{3+;2+/2+;1+}$ cluster; (d) molybdenum cofactor in xanthine oxidase; (e) molybdenum cofactor in dimethylsulfoxide reductase; (f) heme prosthetic group; (g) iron molybdenum cofactor in nitrogenase.

environmental sulfur and nitrogen cycles, and disease mechanisms [9–11]. The diversity of reactions catalyzed by these metalloenzymes is reflected in the large number of different redox cofactors incorporated into and stabilized by the secondary and tertiary protein structure. Some examples of these cofactors are shown in Figure 1.

Reactive oxygen species (ROS) and other free radicals, including amino acid free radicals, play a crucial role in a broad range of biochemical reactions involving metabolism, catabolism, and respiration. The high reactivity of these free radicals is also associated with tissue damage leading to a variety of degenerative dis-

cals is also associated with tissue damage leading to a variety of degenerative diseases such as chronic inflammation and arthritis, cardiovascular diseases such as atherosclerosis, and neurodegenerative diseases such as Alzheimer's and Parkinson's, as well as acute conditions such as reperfusion injury and aging.

EPR spectroscopy has an important role in not only the geometric structural characterization of the redox cofactors in metalloproteins and free radicals but also their electronic structure, as this is crucial for their reactivity. While x-ray crystallography can provide detailed geometric structural information of redox cofactors in metalloproteins, spectroscopy (EPR, magnetic circular dichroism, electronic absorption, infrared and resonance Raman) provides detailed information concerning the electronic structure of these cofactors in metalloproteins. In addition, catalytic mechanisms can be determined through the use of high-resolution EPR spectroscopy, which enables the geometric and electronic structural characterization of resting metalloenzymes and their catalytic intermediates and product complexes.

Computer simulation of the experimental randomly oriented or single-crystal EPR spectra from isolated or coupled paramagnetic centers is often the only means available for accurately extracting the spin Hamiltonian parameters required for the determination of structural information [1,2,12–28]. EPR spectra are often complex and arise through a range of interactions involving one or more unpaired electrons, the external magnetic field, and one or more nuclei. Pictorially, these interactions are shown in Figure 2, and, in summary:

- The electron Zeeman interaction involves the interaction of the magnetic dipole moment associated with the spin and orbital angular momentum of the unpaired electron with an externally applied magnetic field. The magnitude of this interaction is described by a 3×3 g matrix (**B.g.S**).
- The fine structure interaction involves the interaction between the magnetic dipole moments of electrons on an atom containing more than one unpaired electron. The magnitude of this interaction is described by the second rank **D** tensor. Second-order terms, D and E/D correspond to the axial zero field splitting (D) and the asymmetry parameter E/D , which varies from 0 (axial symmetry) to $1/3$ (rhombic symmetry) (**S.D.S**). Fourth- and sixth-order corrections to the fine structure interaction tensor **D** may also be necessary to adequately interpret the spectrum,
- The hyperfine interaction involves the interaction between the magnetic dipole moments of the unpaired electron(s) and the nucleus of the same atom. The magnitude of this interaction is described by the hyperfine (A) 3×3 matrix (**S.A.I**).
- The superhyperfine interaction involves the interaction between the magnetic dipole moments of the unpaired electron and the nucleus of different atoms. The magnitude of this interaction is described by the hyperfine (A) 3×3 matrix (**S.A.I**).

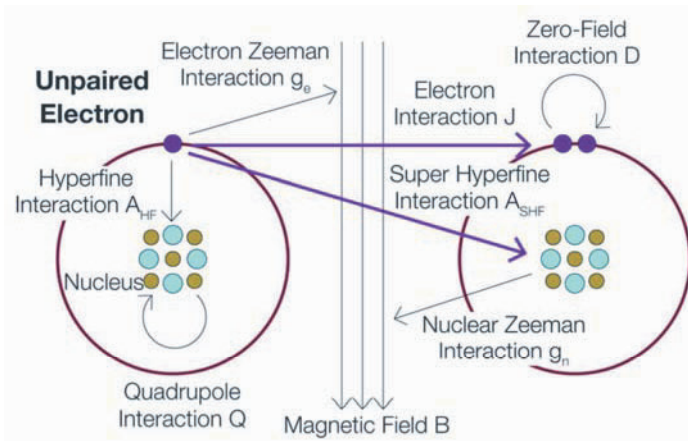


Figure 2. Spin Hamiltonian interactions.

- The quadrupole interaction requires the existence of a quadrupole moment that arises from an inhomogeneous electric field gradient at the nucleus. By necessity, the nuclear spin must be greater than $\frac{1}{2}$ and the nucleus must experience a symmetry lower than cubic. The magnitude of this interaction is described by a second-rank tensor \mathbf{Q} or \mathbf{P} , both of which are used interchangeably in the literature and throughout this chapter ($\mathbf{I.Q.I}$) or ($\mathbf{I.P.I}$).
- The nuclear Zeeman interaction involves the interaction of the magnetic dipole moment arising from the nuclear spin with an externally applied magnetic field ($\gamma\mathbf{B.I}$).
- The exchange interaction involves the interaction of magnetic dipole moments of unpaired electrons on different atoms. This interaction can occur through molecular orbitals ($\mathbf{J S.S}$, $\mathbf{G.SxS}$) or space ($\mathbf{S.J.S}$).

Mathematically these interactions can be written using the spin Hamiltonian formalism. For an isolated paramagnetic center (A) a general spin Hamiltonian (H) [1,2,12] is:

$$H_A = S \cdot \mathbf{D} \cdot S + \beta \mathbf{B} \cdot g \cdot S + \sum_{k=1}^{\text{All Nuclei}} \left[S \cdot A_k \cdot I_k + I_k \cdot Q_k \cdot I_k - \gamma_k (1 - \sigma) \mathbf{B} \cdot I_k \right], \quad (1)$$

where S and I are the electron and nuclear spin operators, respectively; \mathbf{D} is the zero field splitting tensor, g and A are the electron Zeeman and hyperfine coupling matrices, respectively; \mathbf{Q} the quadrupole tensor; γ the nuclear gyromagnetic ratio; σ the chemical shift tensor; β the Bohr magneton and \mathbf{B} the applied magnetic field. Additional hyperfine, quadrupole, and nuclear Zeeman interactions will be required when superhyperfine splitting is resolved in the experimental EPR spectrum. When

two or more paramagnetic centers (A_{ij} $i, j = 1, \dots, N$; $i \neq j$) interact, the EPR spectrum is described by a total spin Hamiltonian (H_{Total}), which is the sum of the individual spin Hamiltonians (H_{A_i} , Eq. (1)) for the isolated centers (A_i), and the interaction Hamiltonian ($H_{A_{ij}}$), which accounts for the isotropic exchange ($J_{ij} \mathbf{S}_i \cdot \mathbf{S}_j$), anti-symmetric exchange ($G_{ij} \mathbf{S}_i \times \mathbf{S}_j$) and the anisotropic spin-spin ($\mathbf{S}_i \cdot \mathbf{J}_{ij} \cdot \mathbf{S}_j$, dipole-dipole coupling) interactions between a pair of paramagnetic centers [1,13,14]:

$$H_{\text{Total}} = \sum_{i=1}^N H_{A_i} + \sum_{i,j=1, i \neq j}^N H_{A_{ij}}, \quad (2)$$

$$H_{A_{ij}} = J_{A_{ij}} \mathbf{S}_{A_i} \cdot \mathbf{S}_{A_j} + G_{A_{ij}} \mathbf{S}_{A_i} \times \mathbf{S}_{A_j} + \mathbf{S}_{A_i} \cdot \mathbf{J}_{A_{ij}} \cdot \mathbf{S}_{A_j},$$

Computer simulation of randomly oriented or single-crystal EPR spectra from isolated or coupled paramagnetic centers is required to accurately determine the spin Hamiltonian parameters (Eqs. (1) and (2)) and the electronic and geometric structure of the paramagnetic center. The simulation of randomly oriented EPR spectra is performed in frequency space through the following integration [1,26]:

$$S(B, \nu_c) = C \int_{\theta=0}^{\pi} \int_{\phi=0}^{\pi} \sum_{i=0}^N \sum_{j=i+1}^N |u_{ij}|^2 f[\nu_c - \nu_0(B), \sigma_\nu] d \cos \theta d\phi, \quad (3)$$

where $S(B, \nu_c)$ denotes the spectral intensity, $|\mu_{ij}|^2$ is the transition probability, ν_c the microwave frequency, $\nu_0(B)$ the resonant frequency, σ_ν the spectral linewidth, $f[\nu_c - \nu_0(B), \sigma_\nu]$ a spectral lineshape function that normally takes the form of either Gaussian or Lorentzian, and C a constant that incorporates various experimental parameters. The summation is performed over all the transitions (i, j) contributing to the spectrum, and the integrations, performed numerically, are performed over half the unit sphere (for ions possessing triclinic symmetry), a consequence of time reversal symmetry [1,12]. For paramagnetic centers exhibiting orthorhombic or monoclinic symmetry, the integrations in Eq. (3) need only be performed over one or two octants, respectively. Whilst paramagnetic centers with an axially symmetric spin Hamiltonian only require integration over θ between 0 and $\pi/2$, those possessing a spin Hamiltonian with cubic symmetry require only a single orientation. Whilst perturbation theory involves an analytical expression for the calculation of resonant field positions and is therefore inherently computationally very fast, it breaks down when state mixing occurs. Consequently, the better and more general approach is to employ numerical matrix diagonalization, which does not suffer from this problem, though for large spin Hamiltonian matrices this can be computationally expensive.

Experimentally the continuous-wave (CW) EPR experiment is a field-swept experiment in which the microwave frequency (ν_c) is held constant and the magnetic field varied. Computer simulations performed in field space assume a symmetric lineshape function, f in Eq. (3) ($f(B - B_{\text{res}}), \sigma_B$), which must be multiplied by $d\nu/dB$ and assume a constant transition probability across a given resonance [1,29]. Sinclair and Pilbrow [30,31] have described the limitations of this approach in relation to asymmetric lineshapes observed in high-spin Cr(III) spectra and the pres-

ence of a distribution of g -values (or g -strain broadening). The following approach has been employed by Pilbrow et al. in implementing Eq. (3) (frequency swept) into computer simulation programs based on perturbation theory [1,29]. First, at a given orientation of (θ, φ) the resonant field positions (B_{res}) are calculated with perturbation theory and then transformed into frequency space $\nu_0(B)$. Second, the lineshape [$f(\nu_c - \nu_0(B), \sigma_\nu)$] and transition probability are calculated in frequency space across a given resonance and the intensity at each frequency stored. Finally, the frequency swept spectrum is transformed back into field space. Performing computer simulations in frequency space produces asymmetric lineshapes (without having to artificially introduce an asymmetric lineshape function) and secondly, in the presence of a large distribution of g -values will correctly reproduce the down field shifts of resonant field positions [29]. Unfortunately, this approach cannot be used in conjunction with matrix diagonalization as a very large number of matrix diagonalizations would be required to calculate f and the transition probability across a particular resonance, resulting in unacceptably large computational times. In Sophe (field space version), we assume a symmetric lineshape function, multiplied by $d\nu/dB$ and a constant transition probability across a given resonance.

Previously we have developed the XSophe-Sophe-XeprView[®] computer simulation software suite [22–27] (Fig. 3) for the analysis of isotropic, randomly oriented, and single-crystal CW EPR spectra. The software suite consists of: XSophe, an X-windows graphical user interface; the Sophe authentication and Common Object Request Broker Architecture (CORBA) daemons; Sophe, a state-of-the-art computational program for simulating CW EPR spectra; and XeprView[®], Bruker Biospin's program for visualizing and comparing experimental and simulated spectra. The functionality of the XSophe software suite is shown below [23–24]:

Experiments

Continuous-Wave EPR Spectra displayed in XeprView[®].

Energy level diagrams, transition surfaces, and transition roadmaps displayed in a Web Browser (Mozilla or Firefox).

Spin Systems

Isolated and magnetically coupled spin systems.

An unlimited number of electron and nuclear spins is supported with nuclei having multiple isotopes.

Spin Hamiltonian Interactions

Second-order Fine Structure Interaction, 4th- and 6th-order corrections (S.D.S, B4, B6) [12].

Isotropic and Anisotropic Electron Zeeman interaction ($g\beta\mathbf{B}\cdot\mathbf{S}$, $\beta\mathbf{B}\cdot g\cdot\mathbf{S}$).

Isotropic and Anisotropic Hyperfine interaction ($a\mathbf{S}\cdot\mathbf{I}$, $\mathbf{S}\cdot\mathbf{A}\cdot\mathbf{I}$).

Nuclear Zeeman Interaction for nucleus N ($g_N \beta_N \mathbf{B}\cdot\mathbf{I}$).

Quadrupole interaction (I.P.I).

Isotropic Exchange interaction ($J_{\text{iso}} \mathbf{S}_i\cdot\mathbf{S}_j$).

Anisotropic Exchange interaction (dipole–dipole coupling) ($\mathbf{S}_i\cdot\mathbf{J}\cdot\mathbf{S}_j$).

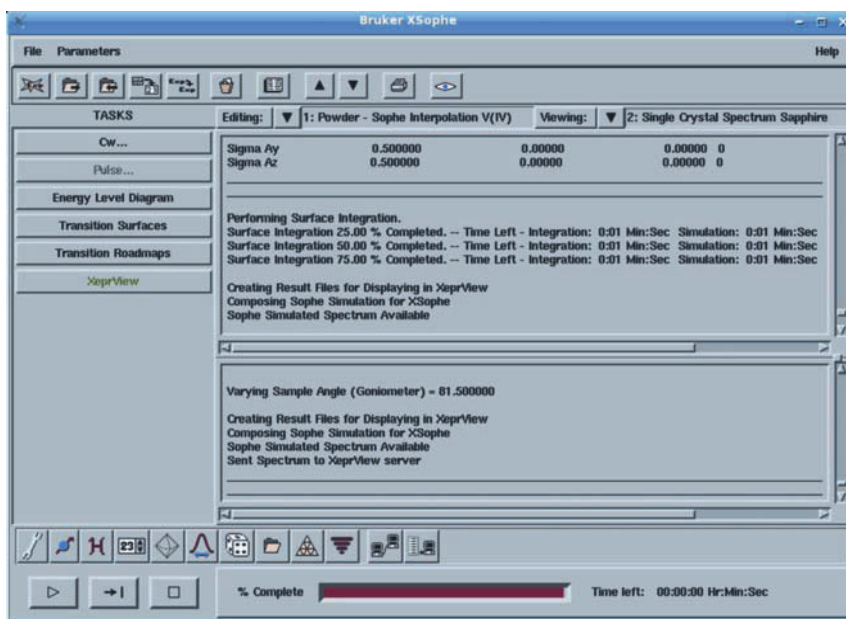


Figure 3. The XSophe (v 1.1.4) main Window. The interface allows creation and execution of multiple input files on local or remote hosts. There are macro task buttons to guide the novice through the various menus and two button bars to allow easy access to the menus. For example, the bottom bar (left to right), Experimental Parameters, Spin System, Spin Hamiltonian, Instrumental Parameters, Single Crystal Settings, Lineshape Parameters, Transition Labels/Probabilities, File Parameters, Sophe Grid Parameters, Optimisation Parameters, Execution Parameters and Batch Parameters.

Continuous Wave EPR Spectra

Spectra types:

Solution, randomly oriented and single-crystal.

Symmetries:

Isotropic, axial, orthorhombic, monoclinic and triclinic.

Multidimensional spectra:

Variable temperature, multifrequency and the simulation of single-crystal spectra in a plane perpendicular to a user defined axis.

Methods

Matrix diagonalization — mosaic misorientation linewidth model.

Sophe Interpolation.

A choice of perturbation theory or matrix diagonalization for superhyperfine interactions.

Optimization (Direct Methods)

Methods:

Hooke and Jeeves.

Quadratic variation of Hooke and Jeeves.

Simplex.

Two Simulated Annealing methods.

Spectral Comparison:

Raw data and Fourier transform.

XSophe allows transparent transfer of EPR spectra and spectral parameters between XSophe, Sophe, and XeprView[®] using platform-independent CORBA libraries. This interactivity allows the execution and interaction of the XSophe graphical user interface with Sophe on the same computer or a remote host through a simple change of the hostname. XSophe contacts the Sophe CORBA daemon, which then interacts with the Sophe authentication daemon via a Unix socket to validate the username and password, which has been encrypted with 128-bit encryption and embedded in a CORBA string. Once validated the Sophe authentication daemon forks a Sophe, which then performs the simulation.

The output of one- and two-dimensional CW EPR spectra from the Sophe program can be visualized in conjunction with the experimental spectrum in XeprView[®] or Xepr[®]. Computer simulation of single-crystal spectra measured in a plane perpendicular to a rotation axis can be performed by defining the rotation axis and the initial and final angles of the magnetic field in the plane perpendicular to this axis. Energy level diagrams, transition roadmaps, and transition surfaces aid the interpretation of complicated randomly oriented EPR spectra and can be viewed with a web browser (mozilla, firefox) and an OpenInventor scene graph viewer (ivview) (Fig. 4).

Elucidation of the three-dimensional crystallographic information (distance and orientation of nuclei with respect to the atom containing the unpaired electron) of redox active cofactors within a metalloenzyme relies on the observation of hyperfine coupling between nuclei and the electron spin, which is often unresolved in randomly orientated CW EPR spectra. Traditionally, interpretation of EPR spectra has relied on computer simulation to determine the EPR parameters that have either then been compared to parameters from well-characterized molecules to determine molecular structure or quantum chemistry calculations have been employed to reproduce the EPR parameters (Fig. 5). The advent of multidimensional pulsed EPR and electron nuclear double (triple) resonance (END(T)OR) spectroscopy in conjunction with orientation-selective experiments and computer simulation overcomes this problem and allows three-dimensional structures (electronic and geometric) of paramagnetic centers to be determined. While electron spin echo envelope modulation (ESEEM) experiments are particularly sensitive for extremely weak couplings from 4-6 Å away from the paramagnetic center, the ENDOR experiment is far more sensitive to strongly coupled nuclei 2-4 Å away from the paramagnetic center. Two-dimensional correlation experiments

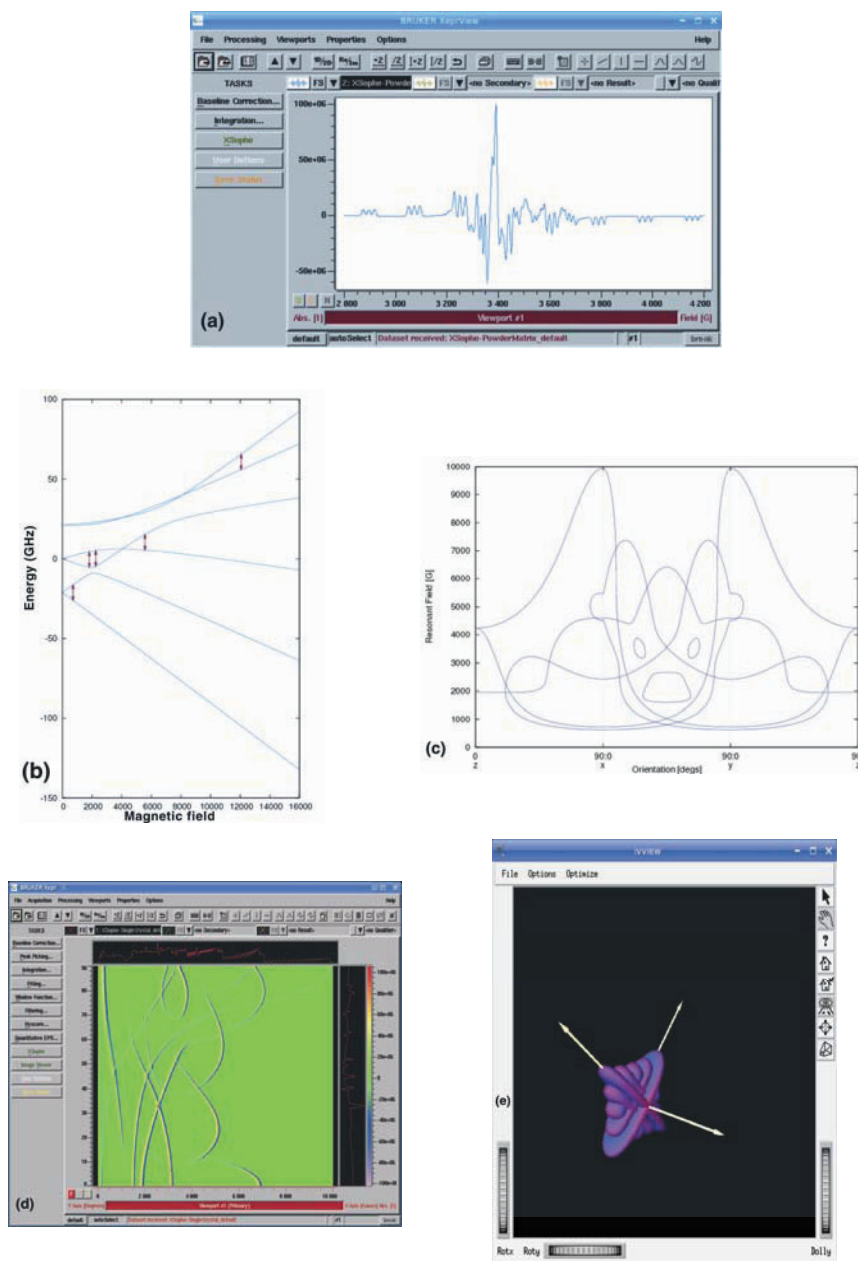


Figure 4. Output from Xsophe: (a) CW EPR Spectrum; (b) energy level diagram; (c) transition Roadmap; (d) single-crystal EPR spectrum; and (e) transition surface with a transition probability colour map

can be applied to ESEEM or ENDOR pulse sequences, yielding detailed structural information on the number and type of nuclei present and their distance and relative orientation from the paramagnetic center. For example, the complete structural characterization of the spin density distribution and consequently the structure of the photosynthetic reaction center (PS I) has been ascertained through careful two-dimensional ESEEM and END(T)OR spectroscopy by Lubitz et al. [32]. Pulse sequences based on pulsed ENTOR have been developed for directly determining crystallographic information (internuclear separations between nuclei and the paramagnetic center and their relative orientation with respect to the paramagnetic center) directly through the dipole–dipole interaction [33]. Elucidation of three-dimensional crystallographic information (distance and orientation) of multiple paramagnetic centers within a metalloenzyme relies on the observation of anisotropic exchange (dipole–dipole) coupling between the multiple electron spins. Whilst CW EPR can be used to measure the distance and orientation of redox active centers up to about 8 Å apart and power saturation studies can be used to infer slightly larger distances, pulsed ELDOR allows distances up to 80 Å to be measured directly from a Pake doublet [34].

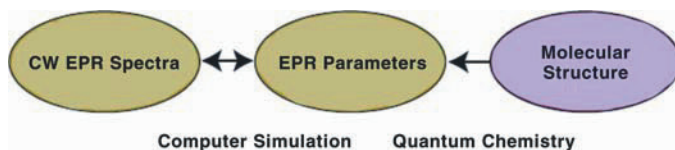


Figure 5. Traditional Approach to determining molecular structure of molecules from EPR spectra.

Herein we describe an integrated approach, *Molecular Sophe*, for the computer simulation of continuous-wave and pulsed EPR and electron nuclear double resonance (ENDOR) spectra, energy level diagrams, transition roadmaps, and transition surfaces. This approach, based on molecular structure (Fig. 6), will revolutionize the three-dimensional molecular (geometric and electronic) characterization of paramagnetic materials using high-resolution EPR spectroscopy and quantum chemistry calculations. Until now the analysis of complex CW and pulsed EPR spectra has been based on a spin system rather than molecular structure, and the analysis of pulsed EPR spectra has mainly relied upon analytical expressions involving perturbation theory.

2. MOLECULAR SOPHE COMPUTATIONAL SOFTWARE SUITE

The Molecular Sophe software suite consists of a graphical user interface, the computational program Sophe, and a variety of software tools (XeprView[®],

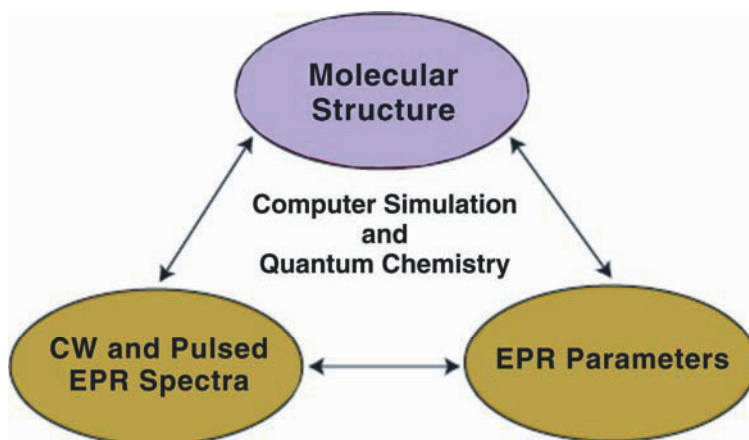


Figure 6. New approach to determining molecular structure of molecules from EPR spectra.

Gnuplot, ivview, and Ghostview) for visualizing and comparing simulations and experimental EPR spectra. This provides scientists with powerful research tools for determining the geometric and electronic structure of magnetically isolated and coupled paramagnetic centers within metalloproteins and other paramagnetic molecules. Molecular Sophe is Project oriented. Each project can contain a number of simulations, each of which contains a sample with one or more molecules consisting of atoms and bonds (interactions). The scientist can then choose a range of experiments to be applied to that sample to elucidate the geometric and electronic structure of the molecule(s). Upon starting Molecular Sophe (mosophe), a splash screen, similar to that shown in Figure 7, is displayed showing the progress of loading the software and finally allows the user to choose a project from the Project list to load into Molecular Sophe. This list of projects is stored in the user's home directory (/home/user/.mosophe/projects).

Pressing the Load button displays the graphical user interface for Molecular Sophe (Fig. 8). Molecular Sophe's graphical user interface incorporates a Menu, Tool bar, Explorer Tree, Forms, Control bar, and Message bar (Fig. 8). The main menu provides access to all functions whilst the toolbar contains some of the commonly used functions in creating a sample, adding experiments, and running external programs (XeprView[®], printing, and a units calculator). The choice of external programs and CORBA settings should be set through the Preferences window accessed from the menu (Edit, Edit Preferences) and saved to disk so that in future runs of Molecular Sophe the settings are loaded automatically upon startup. All of the Buttons, Fields, and Tree Nodes have context-sensitive help that can be accessed by moving the mouse over the desired widget.



Figure 7. Splash Screen for Molecular Sophe allowing the user to choose a project from the user's list of Projects.

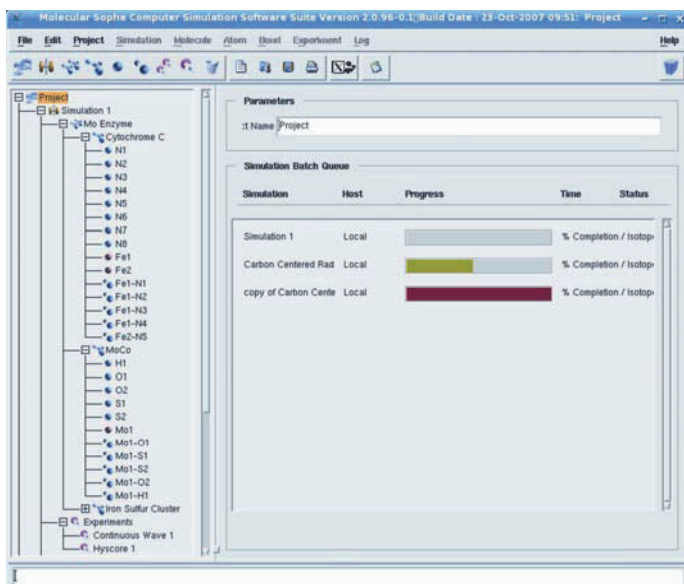


Figure 8. Molecular Sophe Graphical User Interface showing the Explorer Tree and the Project Form.

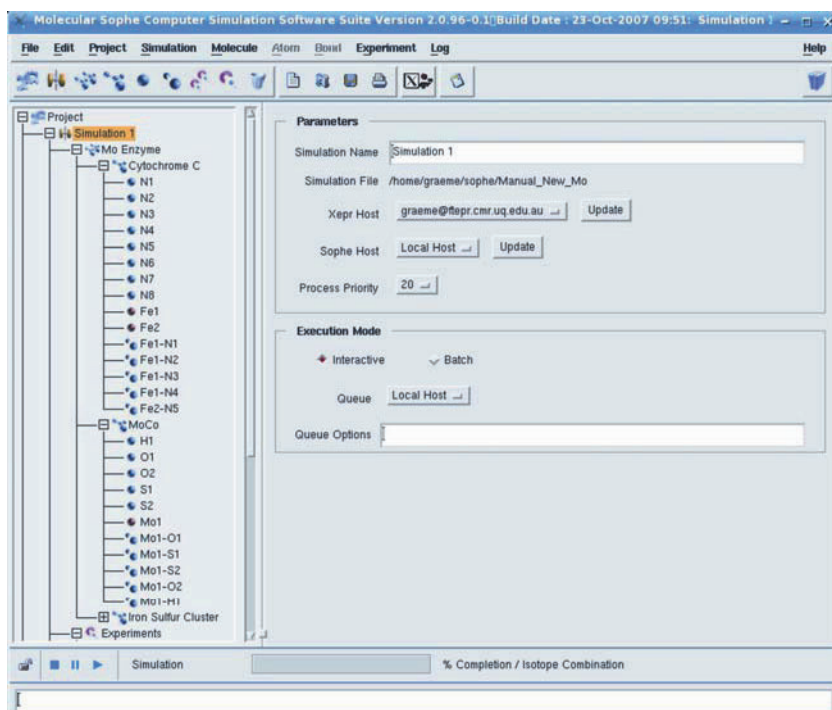


Figure 9. Molecular Sophe Graphical User Interface showing the Explorer Tree and the Simulation Form. Currently, the computational code does not contain optimisation algorithms.

2.1. Project Form

The Project Form (Fig. 8) displays the status of the multiple simulations through timing bars for each simulation. The timing bars are color coded: grey — simulation has not been started; green — simulation running; and red — simulation finished. A right mouse click on the Project Node displays a menu enabling the user to add and load a simulation, create a new project, load a project, save and delete a project.

2.2. Simulation Form

The Simulation Form (Fig. 9) displayed by a left mouse click on the Simulation Node (entitled “Mo Simulation” or “C Radical” in Fig. 9) in the Explorer Tree allows the choice of Host on which to execute the computational program Sophe (currently only localhost), the process priority, whether to run it interactively or in a batch queue (currently only interactively), and the host running the XeprView[®]

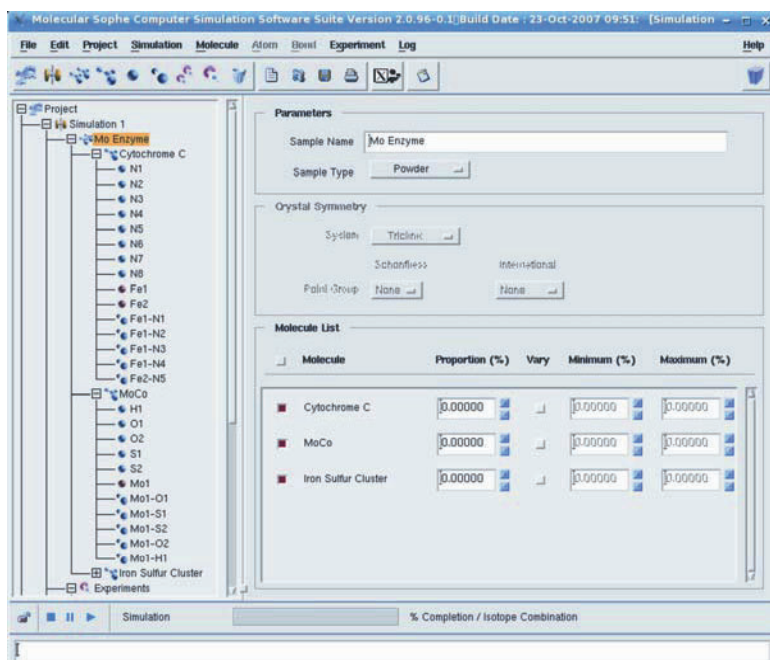


Figure 10. Molecular Sophie Graphical User Interface showing the Explorer Tree and the Sample Form.

program in which to display the resultant spectra. The name of the simulation can also be modified through the Simulation Form. A right mouse click on the Simulation Node displays a menu enabling the user to save, delete, copy, print, and run a simulation.

2.3. Sample Form

The Sample Node (entitled “Sample” or “Molybdenum Enzyme” in Fig. 8) is the next level of the Explorer Tree and a left click displays the Form shown in Figure 10. The sample can consist of multiple molecules (added through the Molecule menu (top toolbar or right mouse click) in different proportions, which itself will be able to be optimized. This is important for many paramagnetic samples. For example, metalloproteins often have more than a single prosthetic group that is paramagnetic and consequently gives rise to multicomponent EPR spectra. Inclusion or exclusion of a particular molecule/molecular fragment can be toggled with the radio button adjacent to the Molecule name in the Molecule Form.

The state of the sample (Crystal, Powder, Frozen Solution, Liquid, Gas, or Glass) may also be chosen, which will govern various aspects of the computational program, Sophie. If the Crystal state is chosen, the user can then select the Point Group for the host crystal.

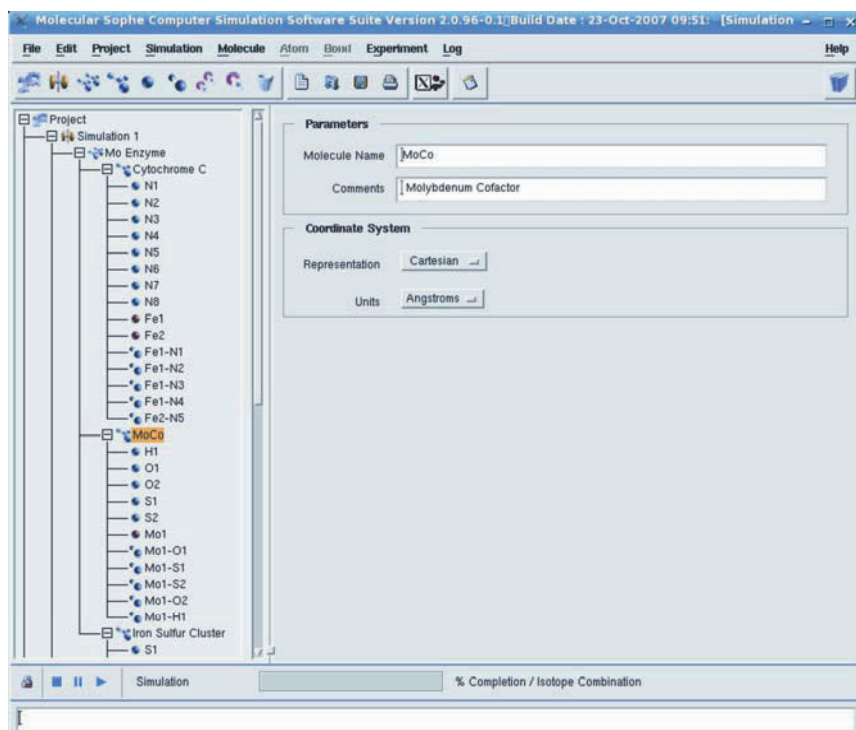


Figure 11. Molecular Sophe Graphical User Interface showing the Molecule Form.

2.4. Molecule Form

The name of the molecule (Cytochrome C, in Fig. 11) can be changed in the Molecule Form and a comment added if desired. The units for the atom's positional coordinates within the molecule and the lineshape function for all of the experiments (simulations) can be defined in the Molecule Form (Fig. 11).

2.5. Adding Atoms

Once a molecule (Fig. 11) has been added at the sample Node, the user can add atoms and subsequently bonds (see §2.14) through the Molecule menu or by a right mouse click on the Molecule Node. In this context, the term “bond” is loosely defined to include not only bonds but also interactions between electron spins and either nuclear spins (superhyperfine interaction) or other electron spins (exchange interaction). Adding an atom displays a Periodic Table (Fig. 12) from which the user can select an atom by clicking (left mouse button) on the appropriate element. The atom is then added to the Molecule in the Explorer.

Periodic Table <@ruby.cmr.uq.edu.au>

0	1																	2
n	H																	He
3	4											5	6	7	8	9	10	
Li	Be											B	C	N	O	F	Ne	
11	12											13	14	15	16	17	18	
Na	Mg											Al	Si	P	S	Cl	Ar	
19	20	21	22	23	24	25	26	27	28	29	30	31	32	33	34	35	36	
K	Ca	Sc	Ti	V	Cr	Mn	Fe	Co	Ni	Cu	Zn	Ga	Ge	As	Se	Br	Kr	
37	38	39	40	41	42	43	44	45	46	47	48	49	50	51	52	53	54	
Rb	Sr	Y	Zr	Nb	Mo	Tc	Ru	Rh	Pd	Ag	Cd	In	Sn	Sb	Te	I	Xe	
55	56	57	72	73	74	75	76	77	78	79	80	81	82	83	84	85	86	
Cs	Ba	La	Hf	Ta	W	Re	Os	Ir	Pt	Au	Hg	Tl	Pb	Bi	Po	At	Rn	
87	88	89	104	105	106	107	108	109	110	111	112	114		116				
Fr	Ra	Ac	Rf	Db	Sg	Bh	Hs	Mt	Uun	Uuu	Uub	Uuq	Uuh					
58	59	60	61	62	63	64	65	66	67	68	69	70	71					
Ce	Pr	Nd	Pm	Sm	Eu	Gd	Tb	Dy	Ho	Er	Tm	Yb	Lu					
90	91	92	93	94	95	96	97	98	99	100	101	102	103					
Th	Pa	U	Np	Pu	Am	Cm	Bk	Cf	Es	Fm	Md	No	Lr					

Figure 12. Molecular Sophie Graphical User Interface showing the Periodic Table.

Molecular Sophie Computer Simulation Software Suite Version 2.0.96-0.1; Build Date: 23-Oct-2007 09:51: [Simulation]

File Edit Project Simulation Molecule Atom Board Experiment Log Help

Project Explorer Tree:

- Simulation 1
 - Mo Enzyme
 - Cytochrome C
 - N1
 - N2
 - N3
 - N4
 - N5
 - N6
 - N7
 - N8
 - Fe1
 - Fe2
 - Fe1-N1
 - Fe1-N2
 - Fe1-N3
 - Fe1-N4
 - Fe2-N5
 - MoCo
 - H1
 - O1
 - O2
 - S1
 - S2
 - Mo1
 - Mo1-O1
 - Mo1-S1
 - Mo1-S2
 - Mo1-O2
 - Mo1-H1
 - Iron Sulfur Cluster

Mo1 Configuration:

Atomic Number: 42
Atomic Mass: 95.94
Isotopes: 24

Description:

Electron Spin: 1/2

Spin Hamiltonian View Matrix

Linewidth Isotopes Position

Electron Zeeman Fine Structure Hyperfine Quadrupole

Iron Zeeman Name:

Representation: Orthorhombic

Units: None

Parameter	Value	Vary	Minimum	Maximum
g_x	2.00000	<input type="checkbox"/>	0.00000	2.00010
g_y	2.00000	<input type="checkbox"/>	0.00000	2.00010
g_z	2.00000	<input type="checkbox"/>	0.00000	2.00010
α	0.00000	<input type="checkbox"/>	1e-04	1e-04,0

Simulation % Completion / Isotope Combination

Figure 13. Molecular Sophie Graphical User Interface showing the Explorer Tree and the Orthorhombic Electron Zeeman Interaction Form.

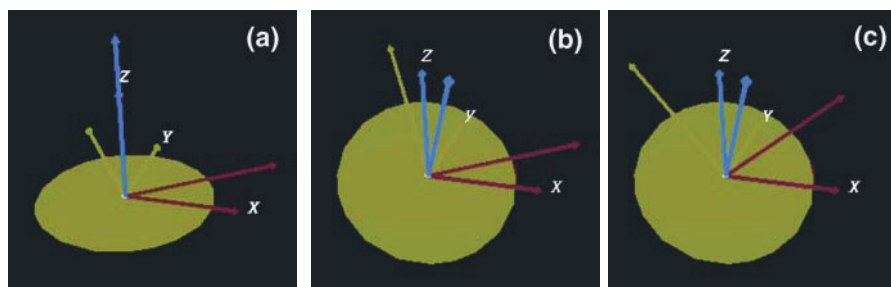


Figure 14. Euler Angle Rotations. (a) α about Z, (b) β about g_x (red, unlabeled), (c) γ about g_z (blue, unlabeled).

2.6. Atom Form

A left mouse click on the atom (Explorer Tree) displays the atom forms: Electron Zeeman (Fig. 13), Hyperfine (Fig. 15), Fine Structure (Figs. 16 and 17), Quadrupole (Fig. 18), Linewidth (Fig. 19), Isotopes (Fig. 20), and Position (Fig. 21). Each Tab also has a three-state button (color-coded tick) associated with it that may be changed by a middle mouse click. The three states are: Red Tick — *Active and Valid*; Blue Tick — *Inactive and Valid*; and No Tick — *Inactive and Invalid*. A right mouse click on the value, minimum, maximum fields enables the user to set the range of the parameter to be varied using the toggle up and down arrows to the right of the parameter field. Currently the Sophe computational code does not have any optimization algorithms present as a new method is being developed for the global optimization of all spin Hamiltonian parameters from multiple experiments.

2.7. Electron Zeeman Interaction ($\beta\mathbf{B}\cdot\mathbf{g}\cdot\mathbf{S}$) (Fig. 2)

The value of the electron spin can be selected and, if greater than zero, the atom in the Explorer Tree is colored orange (Fig. 13), and the Electron Zeeman Tab now has a Red Tick. The symmetry of the Electron Zeeman Interaction can be chosen by selecting the appropriate Representation (Orthorhombic, Axial and Isotropic). The Orthorhombic Representation is shown in Figure 13. Note the g matrix is dimensionless and therefore has no units.

For site symmetries lower than orthorhombic, one or more of the three Euler angles α , β , and γ will be greater than zero. Rotation of the principal g components (g_x , g_y and g_z) away from the internal (crystal) axes is shown in Figure 14. $\alpha(\beta = \gamma = 0)$ greater than zero rotates (about the Z axis) g_x , g_y away from the X and Y axes (Fig. 14a), corresponding to C_{2h} monoclinic sites. A rotation of $\beta(\alpha = \gamma = 0)$ rotates (about X) the g_y and g_z axes away from the Y and Z axes corresponds to C_s symmetric sites. In randomly oriented samples containing a single unpaired electron the g matrix is typically assumed to be coincident with the internal coordinate system and the hyperfine matrix is rotated from away from the g matrix.

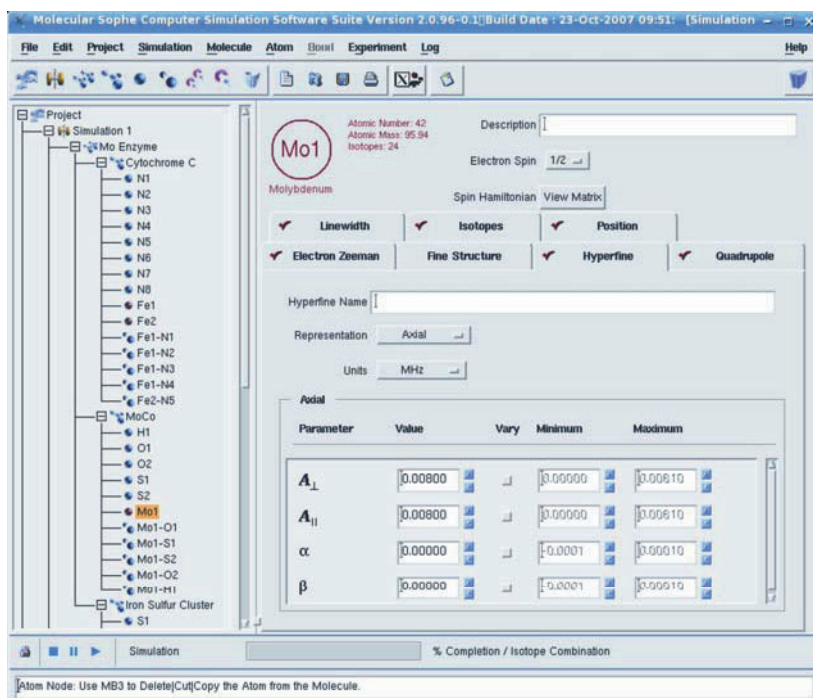


Figure 15. Molecular Sophie Graphical User Interface showing the Explorer Tree and the Axial Hyperfine Interaction Form.

The symmetry can be further lowered to triclinic symmetry (C1) by making α , β , and γ greater than zero. The angle α rotates g_x and g_y about Z (Fig. 14a), β rotates g_y and g_z about g_x (Fig. 14b), and γ rotates g_x and g_y about the new g_z (Fig. 14c). There are two Euler angles available for an axially symmetric site and none for an isotropic site.

2.8. Hyperfine Interaction (S.A.I) (Fig. 2)

The Hyperfine Tab (Fig. 15) is only valid if the atom containing one or more unpaired electrons (the electron spin is greater than zero) has isotopes with a non-zero nuclear spin. The interaction can be turned off/on with a middle mouse click on the “red/blue” tick on the hyperfine tab. Identical representations (isotropic, axial, and orthorhombic) to those for the electron Zeeman interaction are available for the hyperfine interaction. The hyperfine coupling constants correspond to the isotope of the particular atom that has the largest isotopic abundance. For randomly orientated solutions, molecules containing a single unpaired electron with monoclinic or triclinic symmetries, the Euler angles, α , β , and γ will be nonzero. α corresponds to a rotation about the z (g_z) axis, β a rotation about the new A_x axis, and γ a rotation about the new A_z axis.

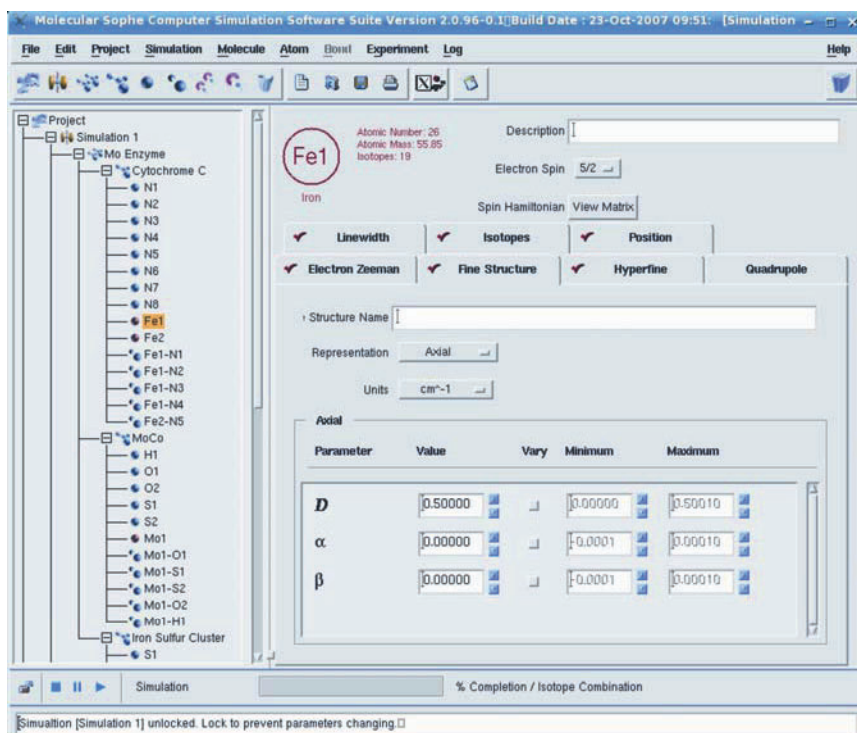


Figure 16. Molecular Sophe Graphical User Interface showing the Explorer Tree and an Axial Second-Order Fine Structure Interaction Form.

All interactions apart from the electron Zeeman interaction have their own units. For the hyperfine interaction these are: MHz and 10^{-4} cm^{-1} and can be selected from the Units drop-down list. Since the hyperfine couplings ($A/g\beta$) measured directly from the field-swept CW EPR spectrum are dependent upon the g -value, it is far easier to determine A -values if the simulation employs frequency units as the g - and A -values are then independent. Consequently, we have provided a units calculator, accessible from the main Tool bar, to convert Gauss and mT into units of frequency.

2.9. Fine Structure Interaction (S.D.S) (Fig. 2)

The fine structure interaction (Fig. 16) is only valid when the electron spin is greater than $\frac{1}{2}$ and only has Axial and Orthorhombic representations, as it is a traceless tensor. D is the axial zero field splitting and E/D , the rhombicity parameter, can vary between 0 (axial symmetry) and $1/3$ (rhombic symmetry).

In addition to axial and orthorhombic representations, the Fine Structure also has b4 (fourth-order corrections) and b6 (sixth-order corrections) [12]. If

the B4 representation is chosen (Fig. 17), then the terms b_2^0 and b_2^2 are related to D and E , respectively. The units for the Fine Structure Interaction include MHz, GHz, 10^{-4}cm^{-1} , and cm^{-1} . Note that the higher-order corrections in XSophe (B4, B6) and Molecular Sophe (b4, b6) are defined differently.

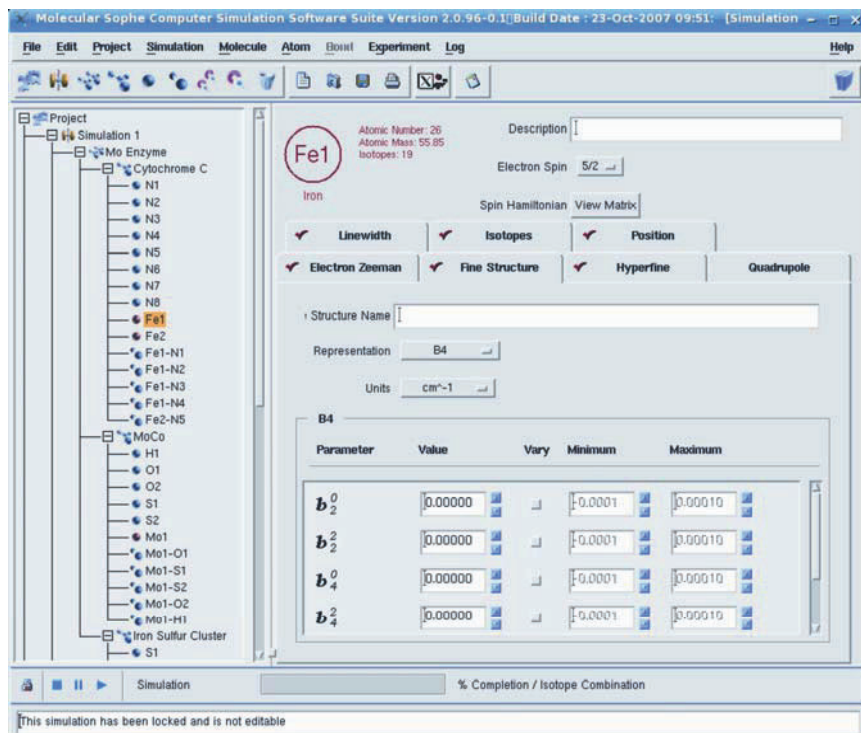


Figure 17. Molecular Sophe Graphical User Interface showing the Explorer Tree and the Fourth-Order Fine Structure Interaction Form.

2.10. Quadrupole Interaction (I.P.I) (Fig. 2)

The quadrupole interaction (Fig. 18), a traceless tensor, is only valid when an isotope of an atom contains a nuclear spin greater than $\frac{1}{2}$. This interaction only has Axial and Orthorhombic representations. The quadrupole interaction is included in the calculation if it is active and valid (red tick on the interaction tab) and may be toggled off/on through a middle mouse click on the tick. When it is valid and inactive (blue tick), the parameters are written to the simulation file, but are not used in the calculation. If there is no tick on the tab, then the interaction is invalid, as there are no isotopes that have a nuclear spin greater than $\frac{1}{2}$.

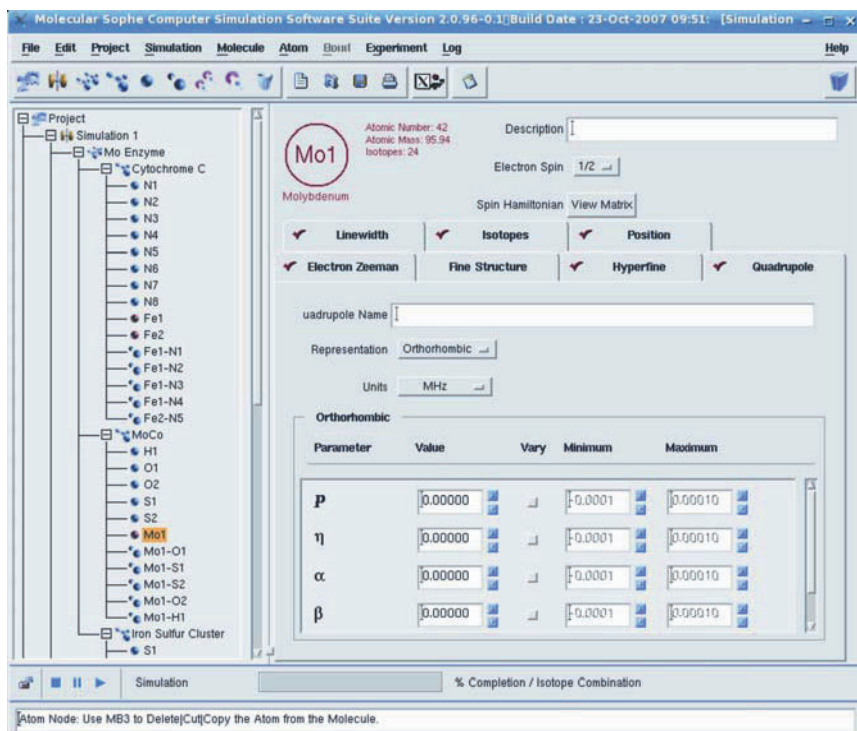


Figure 18. Molecular Sophe Graphical User Interface showing the Explorer Tree and the Orthorhombic Representation of the Quadrupole Interaction Form.

The principal components of the quadrupole tensor (P or Q) are given by

$$\begin{aligned} P_x &= -P - \eta, \\ P_y &= -P + \eta, \\ P_z &= 2P. \end{aligned} \quad (4)$$

From Schweiger and Jeschke [8]:

$$\begin{aligned} a &= e^2 q Q / (4I (2I - 1) h / 2\pi), \\ P_x &= a(-1 + \eta), \\ P_y &= a(-1 - \eta), \\ P_z &= 2a, \\ \eta &= (P_x - P_y) / P_z, \end{aligned} \quad (5)$$

hence

$$\begin{aligned}
 P(\text{MoSophe}) &= a = e^2 q Q / (4I(2I-1)h/2\pi), \\
 \eta(\text{MoSophe}) &= -a\eta = -\eta e^2 q Q / (4I(2I-1)h/2\pi),
 \end{aligned}
 \tag{6}$$

and the units for the quadrupole interaction include MHz and 10^{-4}cm^{-1} .

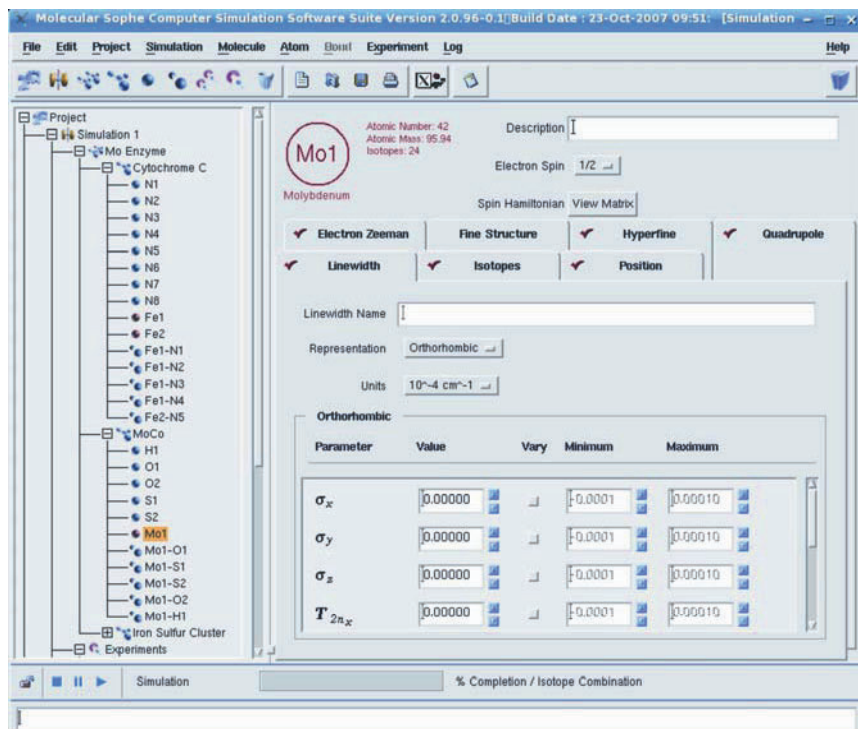


Figure 19. Molecular Sophe Graphical User Interface showing the Explorer Tree and the Orthorhombic Linewidth Parameter Form. Nuclear T_2 and Euler angles are accessible by scrolling the window.

2.11. Linewidth Parameters

Molecular Sophe currently contains only a single linewidth model for the simulation of continuous-wave EPR spectra, angular variation of g values, as described below:

$$\sigma_v^2 = (\sigma_x^2 g_x^2 l_x^2 + \sigma_y^2 g_y^2 l_y^2 + \sigma_z^2 g_z^2 l_z^2) / g^2.
 \tag{7}$$

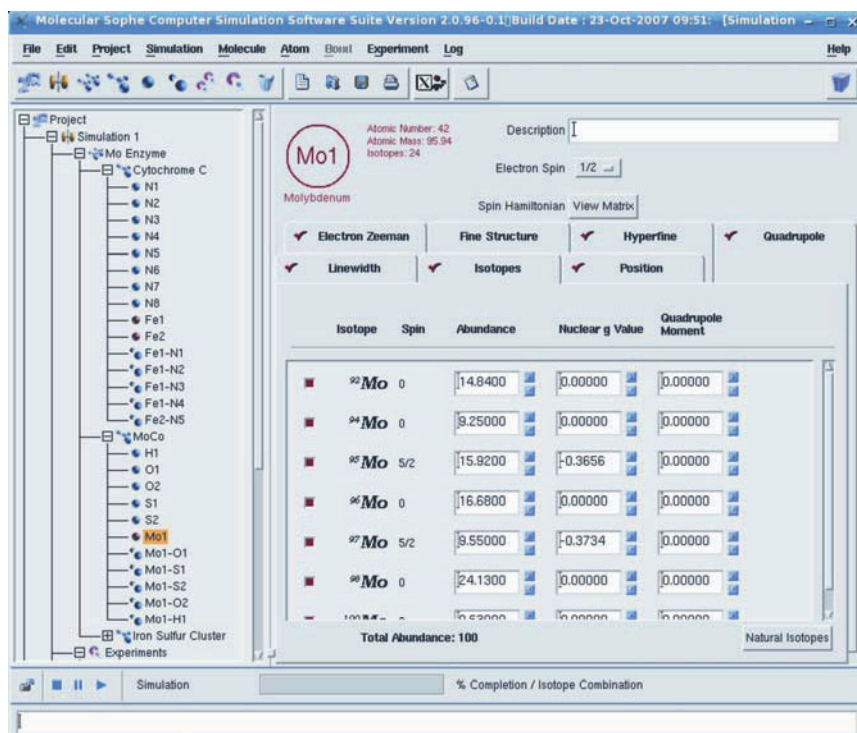


Figure 20. Molecular Sophe Graphical User Interface showing the Explorer Tree and the Isotope Form.

Representations in the Linewidth Parameter Form (Fig. 19) include orthorhombic, axial, and isotropic symmetries. Units include MHz, 10^{-4} cm^{-1} , and nanoseconds (nsec), the latter being more appropriate for pulsed EPR spectra. For pulsed EPR spectra we also include the nuclear spin–spin relaxation time T_{2N} . Addition of a more a generalized linewidth model involving a distribution of spin Hamiltonian parameters and positional coordinates (bond lengths and orientations) is forthcoming. The approach will be similar to that employed for the *D*- and *E*-strain linewidth model in the XSophe-Sophe-XeprView[®] computer simulation software suite.

2.12. Atom Isotopes

The Isotope Form (Fig. 20) contains a list of the atoms isotopes and their natural abundance, nuclear spin, if known, and the quadrupole moment if the nuclear spin is greater than $1/2$. Nuclei can be chosen by selecting the check box adjacent to the isotope. The abundance of an isotope can be modified if the user requires the simulation of spectra in which the EPR active molecule contains an enriched iso-

tope. The user should ensure that the total abundance for all isotopes corresponds to 100%. Naturally abundant isotopes can be selected by pressing the button in the right-hand bottom corner of the Form. A fictitious spin ($I = 0$) has been added to all atoms enabling a quick way of selecting an atom with ($I = 0$) and reducing overall computational times. Note that the abundance of this isotope will have to be modified in the Isotope Form.

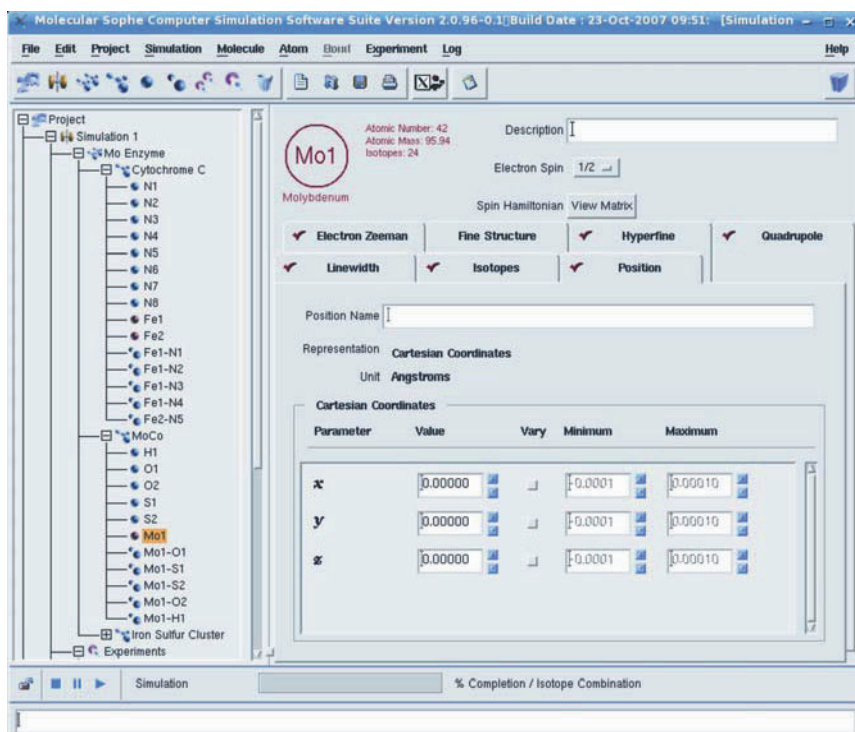


Figure 21. Molecular Sophe Graphical User Interface showing the Explorer Tree and the Position Coordinate Form.

2.13. Position Form

The atom's coordinates can be entered through the Position Form (Fig. 21). Since it makes no sense to have mixed units for the atom's coordinates, the units for the atoms coordinates are defined in the Molecule Form (Fig. 11). The atom's coordinates can be optionally used to determine the anisotropic components of either the superhyperfine or exchange interaction matrices.

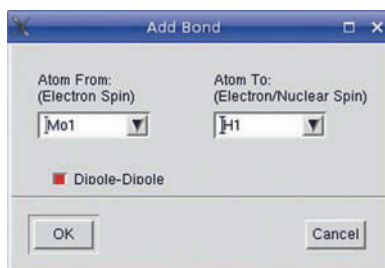


Figure 22. Molecular Sophe Graphical User Interface showing the Add Bond window. Note the atom containing unpaired electrons in the left hand combo box. In this example Fe1 is the atom containing unpaired electrons.

2.14. Adding Bonds

Superhyperfine and Exchange interactions occur between an atom containing one or more unpaired electrons and the nucleus of an atom with a nonzero nuclear spin or another atom containing unpaired electrons, respectively. In the graphical user interface these interactions are created through the Add Bond window (Fig. 22), accessed either by a right mouse click on the Molecule Node, clicking the Bond Icon (Top menu), or through the Molecule Menu. The Add Bond window allows the user to define the interaction (bond) between the atom containing the unpaired electron(s) and the atom containing the nucleus. It is important that the atom containing the unpaired electrons is identified through the left-hand combo box (Fig. 22). Inclusion of the dipole–dipole interaction can be chosen by selecting the check box. Having chosen the dipole–dipole interaction, the user should ensure that the atomic coordinates are entered for each atom defined in the bond, in this case for Mo1 and H1.

2.15. SuperHyperfine Interactions (S.A.I) (Fig. 2)

Once the bond is created in the Explorer Tree, a left mouse click on the bond opens the Superhyperfine Interaction Form (Fig. 23). The representations and units for the superhyperfine interaction are identical to those for the hyperfine interaction (§2.8).

The only difference is that the dipole–dipole interaction can be switched off or on from the Form by selecting the check box. If the check box is selected, then the internuclear distance and orientation are calculated from the positional coordinates of both atoms and the anisotropic interaction is calculated subsequently and added to the parameters. The superhyperfine interaction can be toggled off/on by clicking (middle mouse button) on the red/blue tick radio button on the superhyperfine tab.

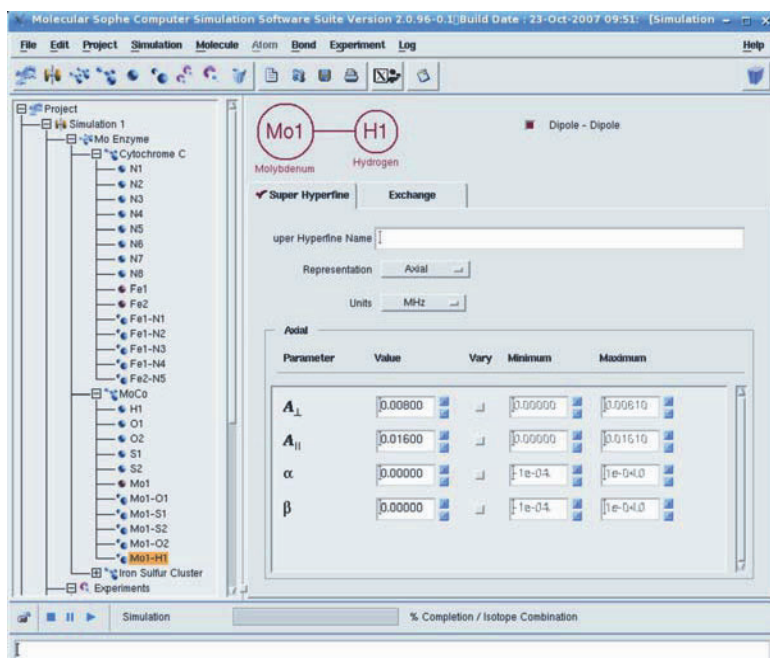


Figure 23. Molecular Sophe Graphical User Interface showing an axial Superhyperfine Interaction.

2.16. Exchange Interaction (S.J.S) (Fig. 2)

The exchange interaction involves the interaction of two or more paramagnetic centers, for example, $[\text{Fe}_2\text{S}_2]^{2+/1+}$, $[\text{Fe}_3\text{S}_4]^{1+/0}$, and $[\text{Fe}_4\text{S}_4]^{3+/2+/1+}$ (Fig. 1). The total spin Hamiltonian for an exchange-coupled system is given by the sum of the individual spin Hamiltonians and the interaction Hamiltonian (Eqs. (1) and (2), respectively). The isotropic exchange interaction involves the overlap of molecular orbitals, whilst the anisotropic exchange interaction (dipole–dipole coupling) is a through-space interaction. In the graphical user interface, the user first adds a “bond” between two atoms containing one or more unpaired electrons (i.e., $S_1, S_2 \geq \frac{1}{2}$). Of course, in metalloproteins this may be an interaction and not a real bond. Once the bond has been created, a left mouse click on the bond will open up the bond Form (superhyperfine and exchange interaction tabs). Clicking on the Exchange Interaction Tab opens the exchange Form (Fig. 24a–c). Currently there are four representations (Isotropic, Anisotropic (Axial and Orthorhombic Symmetry), and Antisymmetric). Given the spin Hamiltonian in Eq. (2), a positive value of J_{iso} corresponds to antiferromagnetic coupling between the two atoms and for inorganic chemists, who are used to working with the Hamiltonian ($H = -2J_{\text{iso}}^* S_1 \cdot S_2$, The asterisk is used here to distinguish the two values), $J_{\text{iso}}^* = -J_{\text{iso}}/2$.

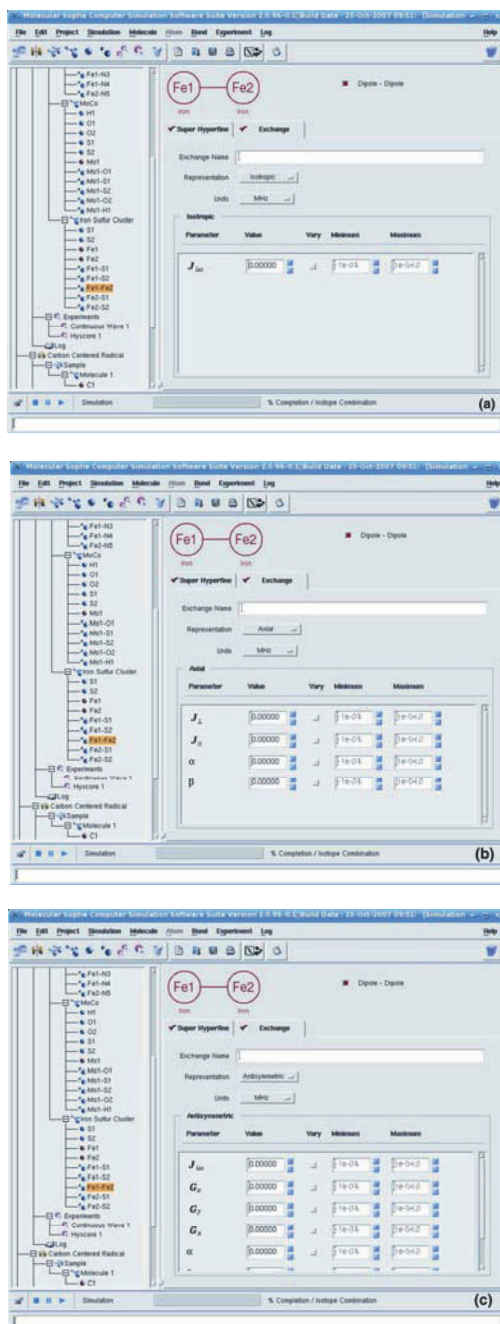


Figure 24. Molecular Sophe Graphical User Interface showing (a) the Isotropic Exchange Interaction, (b) the Axial Anisotropic Exchange Interaction, and (c) the Antisymmetric Exchange Interaction.

The anisotropic exchange parameters can either be added through the Anisotropic Representation (Axial; Fig. 24 or orthorhombic) or calculated from the positional coordinates of the two atoms through the dipole–dipole interaction, by toggling the Dipole–Dipole check box (red enabled).

The antisymmetric exchange term (Eq. (2), $G_{ab} S_a \times S_b$) can be included by selecting the Antisymmetric exchange representation (Fig. 24c), which includes J_{iso} and the principal components of the G matrix and three Euler angles. Dipole–dipole terms can be also included by selecting the Dipole–Dipole radio button (red is active). This interaction has been found to be important for trinuclear copper(II) systems, where the orbitals containing the unpaired electrons partially overlap.

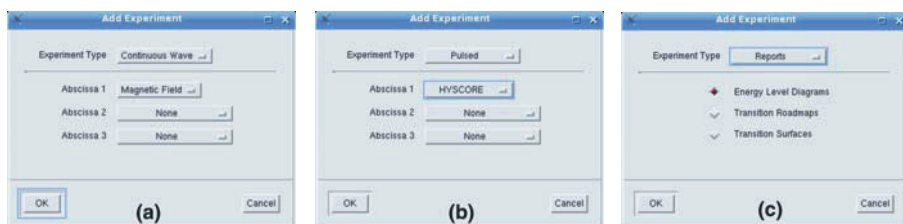


Figure 25. Molecular Sophe Graphical User Interface showing the various options in adding experiments.

2.17. Adding Experiments

Once the sample has been created, the user can now perform a range of experiments. The choice of experiment is accessed through the Experiment Menu or by a right mouse click on the Experiment Node and selecting an Experiment Type (Fig. 25). As can be seen in Figure 25, the range of experiments include: CW-EPR, Pulsed EPR (FID, 2-Pulse ESEEM, 3-Pulse ESEEM, SECSY, HYSCORE, 2-Pulse Echo, MIMS, and Davies ENDOR) and Reports (Energy Level Diagrams, Transition Roadmaps, and Transition Surfaces). Multidimensional experiments can also be performed by adding additional abscissas (Temperature, Microwave Frequency, Goniometer Angle, and Magnetic Field). Currently we have no means to visualize four-dimensional datasets, thus orientation-selective HYSCORE measurements cannot be visualized as a single dataset. This can be overcome in the short term by duplicating the HYSCORE Experiment (right mouse click on the HYSCORE Experiment and select Copy Experiment) and adjusting the static magnetic field in the copied Experiment. The output spectrum name should also be changed. This process can be repeated as often as necessary.

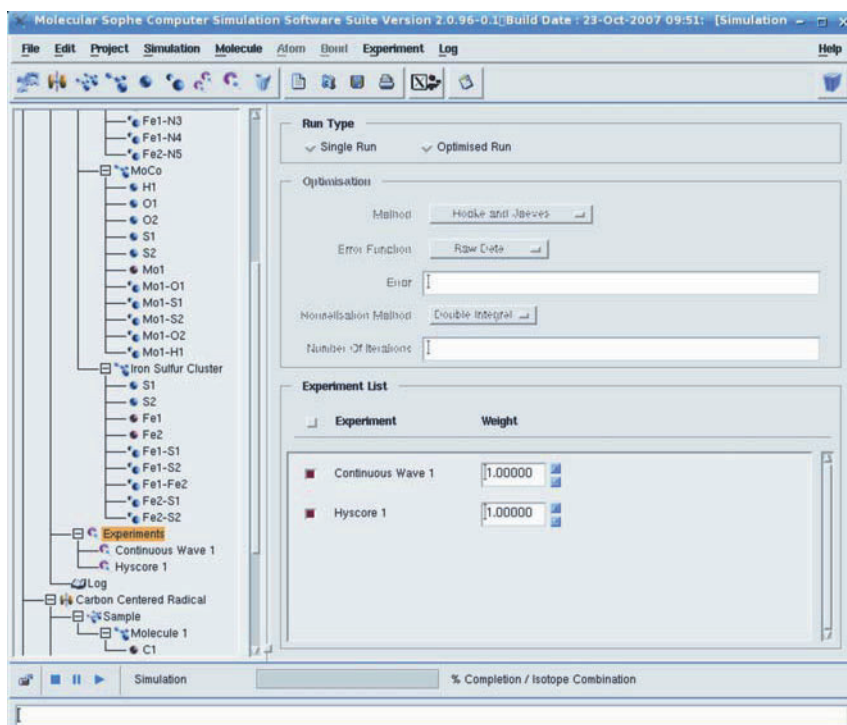


Figure 26. Molecular Sophe Graphical User Interface showing the Experiment Form.

2.18. Experiment Form

The Experiment Form (Fig. 26) contains the list of experiments available for selection. Individual experiments can be included/excluded by selecting/deselecting the check box adjacent to the experiment option. Each experiment also has a weighting that will be used when optimizing spin Hamiltonian parameters from multiple experiments.

The following sections describe four experiments: CW EPR, HYSORE, MIMS ENDOR, and Energy Level Calculations.

2.19. CW EPR Experiments

Once a CW EPR Experiment has been added to the Explorer Tree, the CW EPR Experiment forms can be viewed by a left mouse click on the CW EPR Experiment Node in the Explorer Tree. The Continuous Wave EPR Experiment Form has Continuous Wave, Sophe, Spectra, and Configuration Tabs. The Sophe, Spectra, and Configuration Tabs are common to all experiments and will be dealt with separately.

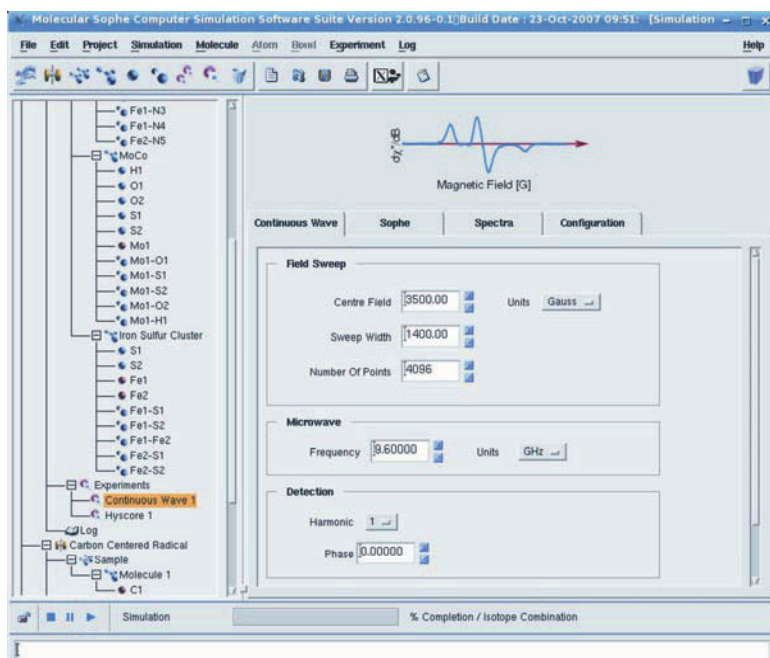


Figure 27. Molecular Sophie Graphical User Interface showing the Continuous Wave Experiment Form and specifically the Continuous Wave tab.

The Continuous Wave EPR Form (Fig. 27) allows the user to enter values concerning the field-sweep (center field, sweep width, and the number of data-points), microwave frequency, detection mode, and temperature. The units for the field-sweep parameters include Gauss, mTesla, and Tesla, and those for the microwave frequency are MHz, GHz, and THz. The harmonic corresponds to the n th derivative spectrum, where $n = 0, 1,$ and $2,$ the first derivative being the normal mode acquired on an EPR spectrometer using phase-sensitive detection. Whilst experimentally the phase of the EPR spectrum can vary anywhere between 0 and 180° , only the limits are really useful at present. Setting the phase to 180° inverts the spectrum. Boltzmann populations for each energy level are automatically included and consequently the temperature will affect the intensity of the EPR transition between two different energy levels. For exchange-coupled systems the magnitude and sign of J_{iso} may be obtained from a variable-temperature spectrum/simulation. Similarly, if the zero field splitting is larger than the microwave quantum, then a variable temperature spectrum/simulation can provide the sign and magnitude of the axial zero field splitting (D). If D is less than the microwave quantum, then this information can be easily determined from a simulation of the experimental spectrum.

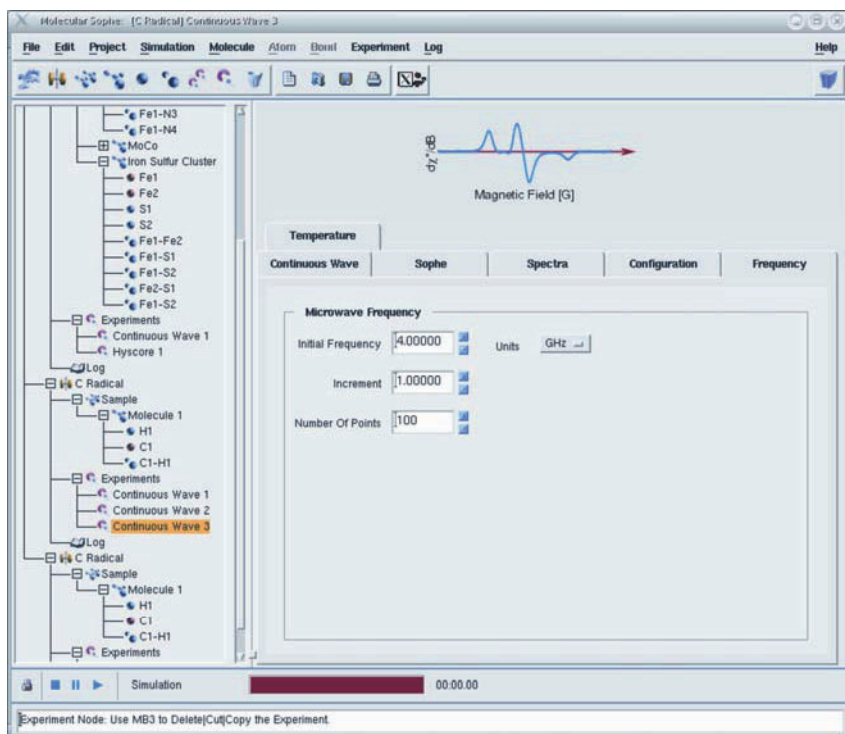


Figure 28. Molecular Sophe Graphical User Interface showing the Frequency Form of a Multidimensional Experiment.

If the user selected a multidimensional CW EPR spectrum, for example, a multifrequency variable-temperature experiment (Fig. 28), then additional tabs are added to the CW EPR Experiment Form, namely, Temperature and Frequency. These tabs allow the user to define the start and increment values for the particular parameter and the number of datapoints in the additional dimension. The parameters in this Tab, for example the temperature tab, override the temperature setting in the Continuous Wave tab. This also applies to the microwave frequency and Goniometer Angle.

2.20. Sophe Computational Parameters

The Sophe tab (Fig. 29) allows the user to input various parameters required for the computational calculation, definition of the SOPHE Grid (§3.1), and determination of the transition probability (selection rules to be used). In the Calculation Panel, matrix diagonalization is currently the only method available for performing continuous wave and pulsed EPR simulations. The field segmentation algorithm

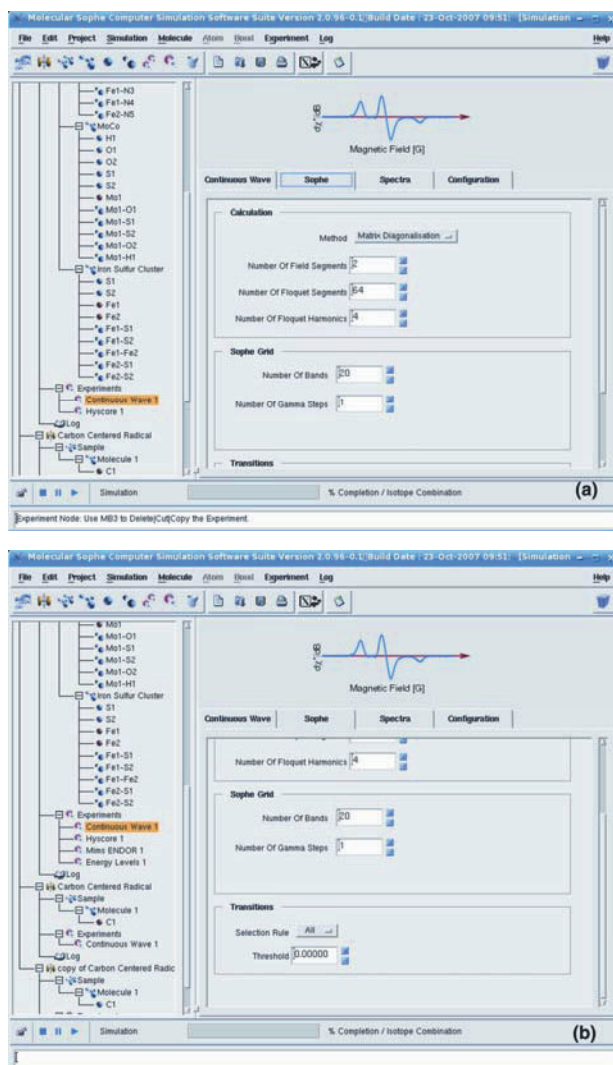


Figure 29. Molecular Sophe Graphical User Interface showing the (a) upper and (b) lower parts of the Sophe Tab within the CW EPR Experiment Form.

employed in the computational program (Sophe) requires the user to define the number of field segments where matrix diagonalization will be employed. Whilst the number of field segments can usually be set to one or two, sometimes sharp features (vertical lines) may be apparent in the spectrum, and these arise from the presence of multiple transitions within a segment. If this occurs then the number of segments should be increased.

Floquet Theory is often used to describe the evolution of a periodic time-dependent semiclassical spin Hamiltonian in magnetic resonance. The numbers of Floquet Segments and Floquet Harmonics are only used in the simulation of Pulsed EPR experiments. The number of Floquet Segments refers to the number of segments microwave pulses are divided into, so that within each segment the time-dependent spin Hamiltonian is “assumed” to be time independent. These segments are used to calculate the average Hamiltonian for the pulse. When the number of Floquet Segments is set to zero, the representation is reduced to the rotating frame, which is only appropriate for species in which there is no significant electron spin state mixing, for example, species containing only a single unpaired electron. For high-spin and exchange-coupled molecules, the number of Floquet Segments should be greater than zero.

The SOPHE grid (§3.1) is defined by the number of orientations between the “z” and “x” global coordinate system. The number of gamma steps, used in the simulation of pulsed EPR experiments, is used to calculate the transition probabilities of the echo intensities.

The Selection Rules are used to define the transition threshold for inclusion of transitions in the simulation. Setting the selection rules to “ALL” sets the transition threshold to zero, “None” sets it to one and “Some” is somewhere in between, which the user can define to only observe forbidden or allowed transitions. In principle, the Selection Rules should always be set to “ALL.”

2.21. Spectra Input/Output

Molecular Sophe employs a data directory to store all of the information associated with a particular simulation, including the input file for the computational program, Sophe, and all of the input and output spectra. This simplifies the organization of simulations. The Spectra Form (Fig. 30) allows the import of an experimental spectrum into the Molecular Sophe data directory and the export of simulated spectra from this directory. A title for the experiment can also be added that is added to the resultant simulation spectrum. The user can also choose the file type (Be3st and ESP Bruker formats) of the spectrum to import into the data directory and the output file format (Be3st and ESP Bruker formats, Gnuplot, Image Plot, Postscript, and OpenInventor).

Apart from the OpenInventor file format specifically used for the visualization of transition surfaces, ALL of the other file formats are generated when you run a simulation. You can change the output file type and select View spectrum to see the results in a different format. Both the Bruker Be3st and ESP format files are displayed within Bruker's XeprView[®], and the gnuplot file is displayed in a gnuplot X11 terminal window. The Image (portable network graphics “xxx.png” format) and postscript files are displayed in an appropriate viewer defined in the Preferences window. Typically the default viewers are the web browser mozilla/firefox and ghostview, respectively, and representative examples showing all displays can be seen in Figure 31.

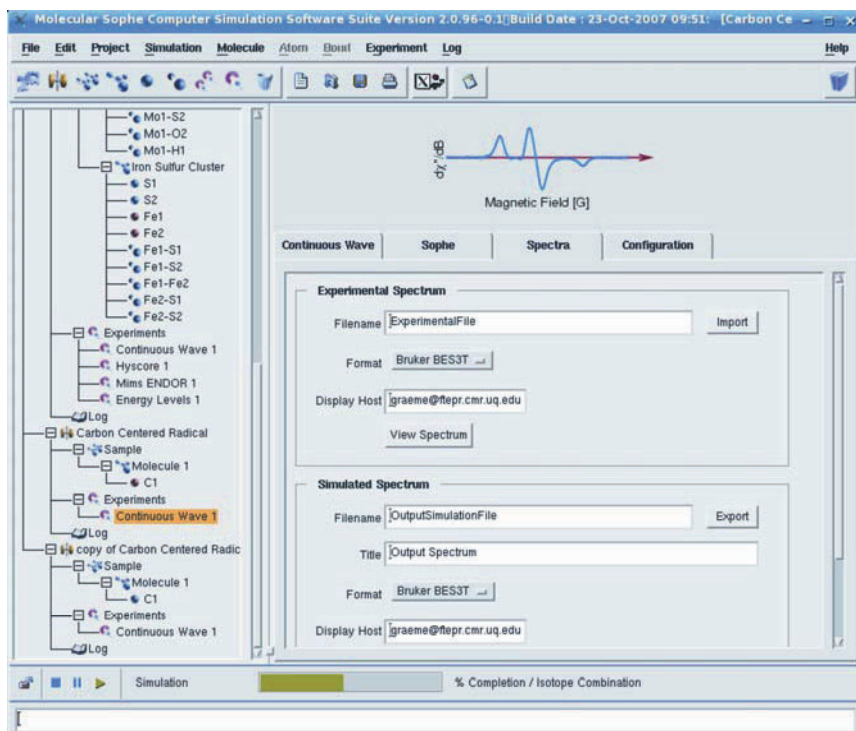


Figure 30. Molecular Sophe Graphical User Interface showing the Spectra Tab within the CW EPR Experiment Form.

2.22. Resonator Configuration

The resonator Configuration Form (Fig. 32) allows the user to choose: the Bruker spectrometer resonator type; the orientation of the microwave magnetic field with respect to the external applied magnetic field (B_0); the microwave magnetic field strength (B_1) at 0 dB; the radio frequency (RF) magnetic field strength (B_2) at 0 dB. Apart from the dual mode resonator (ER4116DM) that may have B_1 either parallel or perpendicular to B_0 , all of the other resonators have B_1 perpendicular to B_0 .

2.23. Pulsed EPR Experiment: Hyperfine Sublevel Correlated Spectroscopy (HYSCORE)

The HYSCORE Experiment Form (Fig. 33) is accessible after having loaded a HYSCORE Experiment (§2.17) and selected the HYSCORE Experiment Node

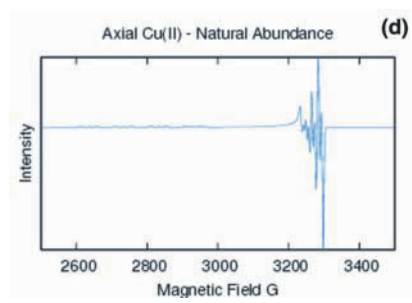
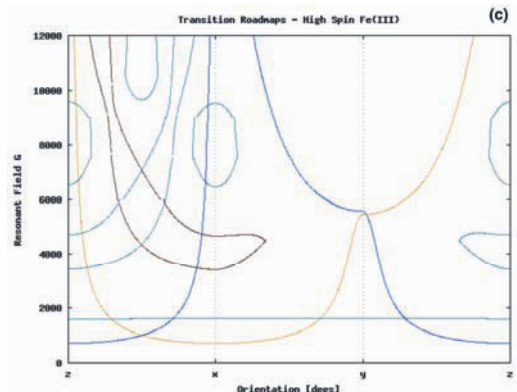
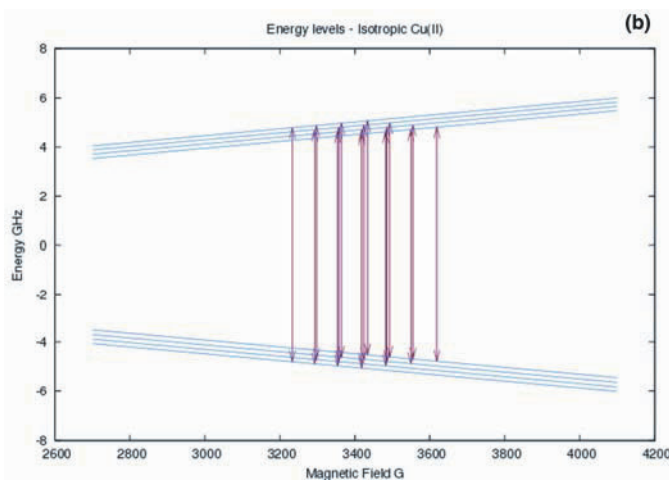
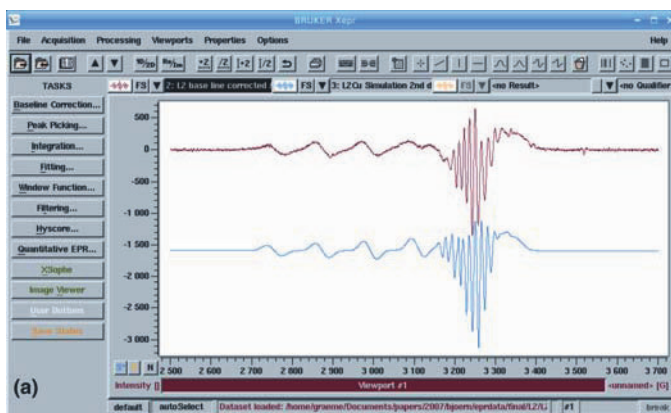
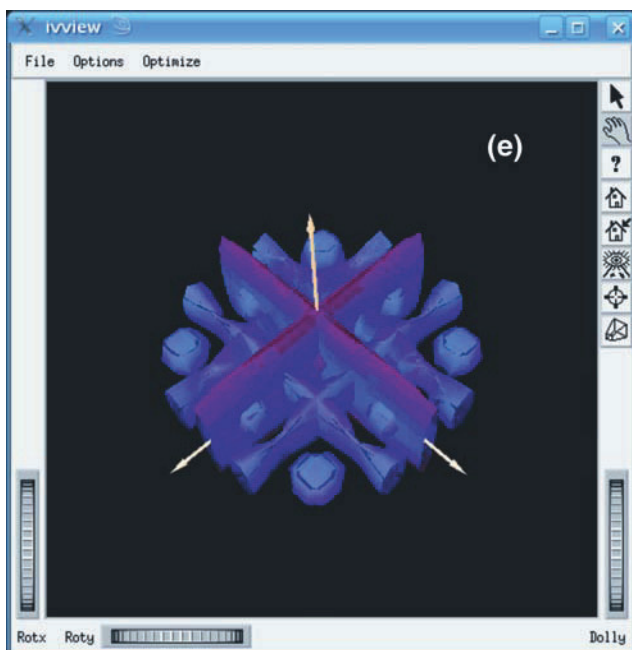


Figure 31. Spectral Outputs from Molecular Sophe: (a) Bruker's XeprView[®] (or Xepr if available), (b) Gnuplot, (c) Image plot (portable network graphics 'xxx.png'), (d) GhostView (postscript viewer), and (e) Open Inventor Viewer (ivview) (see next page).



from the Explorer Tree. The pulse sequence is displayed in the HYSORE Experiment Form (Fig. 33). The HYSORE Experiment (Fig. 33) contains the following tabs: HYSORE, Sophe (§2.20), Spectra (§2.21), and Resonator Configuration (§2.22).

Within the HYSORE tab the user can define the Pulse Length of the $\pi/2$ and π pulses, (p_0 and p_2 , respectively), Delay times (d_0 , d_1 , and d_2), Abscissa Times, Phase cycle, static Magnetic Field, the Microwave Frequency, Attenuation, and the Temperature of the experiment. Creation of the $\pi/2$ and π pulses is dependent upon the pulse length (p_0 and p_2), the microwave attenuation, and the microwave magnetic field strength (B_1) at 0 dB. The latter is defined in the Resonator Configuration Tab. The attenuation required to obtain a $\pi/2$ flip angle with the $\pi/2$ pulse length (p_0) and B_1 can be obtained by selecting the Experiment Setup Toggle Button and running the experiment. The number of bands can be set to one for this setup experiment. This will produce a plot of attenuation versus echo intensity (Fig. 34). The Position Qualifier within XeprView[®] or gnuplot can be used to determine the power associated with the maximum echo intensity.

Currently the HYSORE is monitored at a single point (detection gate delay d_0), rather than integrating over a detection gate. “dx” and “dy” define the time increments in the two dimensions and “sx” and “sy” correspond to the number of data (time) points calculated. Whilst the pulse sequence assumes “dx” and “dy” are identical, as is often the case experimentally, this condition is not strictly required

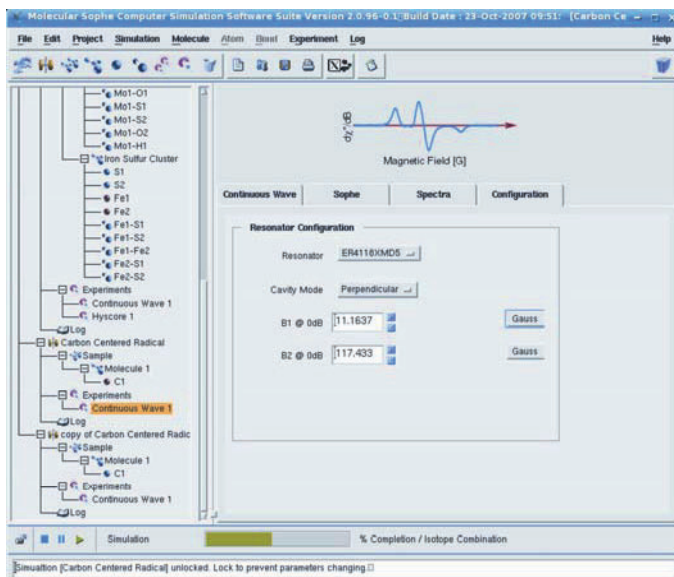


Figure 32. Molecular Sophe Graphical User Interface showing the Resonator Configuration Tab within the CW EPR Experiment Form.

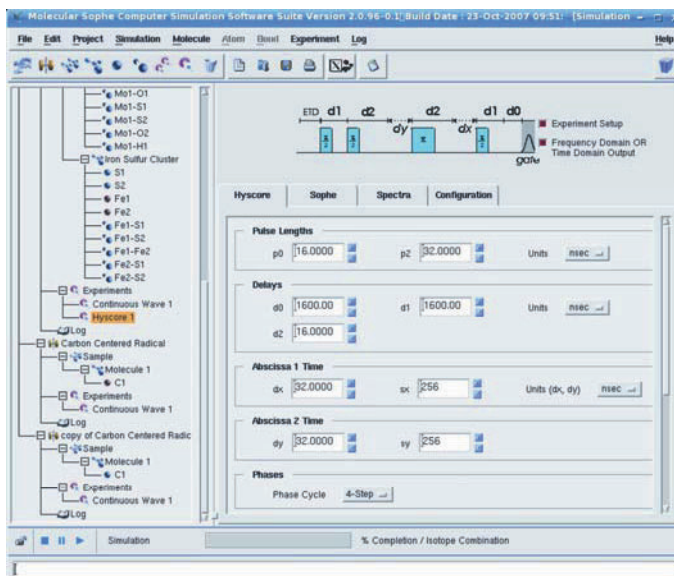


Figure 33. Molecular Sophe Graphical User Interface showing the HYSCORE Tab within the HYSCORE Experiment Form.

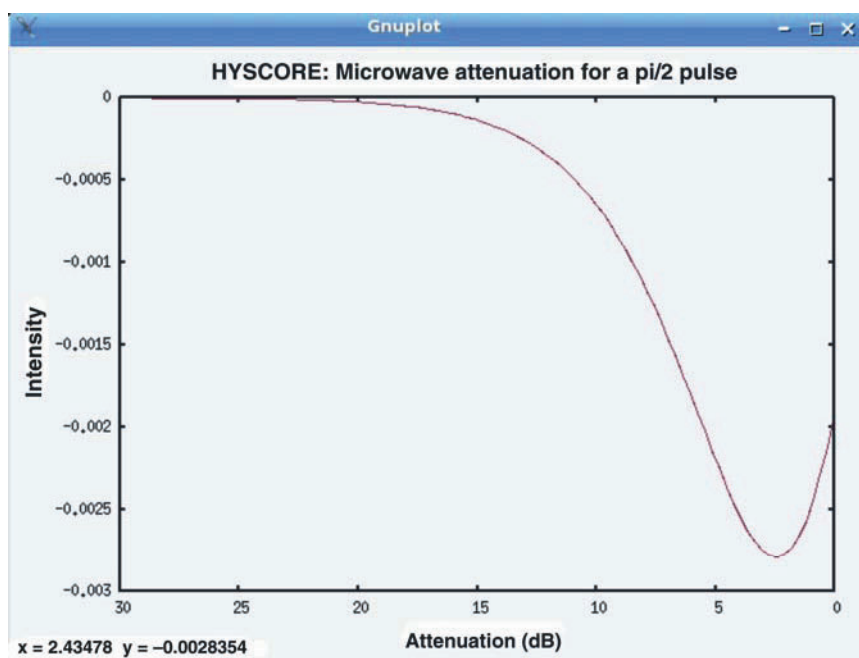


Figure 34. Gnuplot output showing the result from a Setup Experiment. Attenuation for $\pi/2$ pulse = 2.43 dB.

in the Sophe software. The units for both “dx” and “dy” are selected from the Units Menu for “dx.” The HYSCORE tab is a scrollable window, and as such all of the parameters may not be visible upon selecting the tab. This is also the case for the MIMS ENDOR experiment (Fig. 36), where the static magnetic field and temperature are hidden but can be entered by scrolling the window. The remaining parameters (magnetic field and temperature) and the parameters in the other tabs have been defined previously in the CW EPR Experiment Form (§§2.20–2.22). The HYSCORE simulation can be output in either frequency or time domain by selecting (red) or deselecting (blue) the check box labeled “Frequency Domain OR Time Domain.”

2.24. Pulsed EPR Experiment – Orientation Selective HYSCORE

Orientation-selective experiments involve performing a pulsed EPR experiment, such as HYSCORE, as a function of orientation (magnetic field). The orientation-selective HYSCORE Experiment will provide a four-dimensional dataset from which the complete hyperfine matrix for the remote nucleus can be determined. Subsequently the internuclear distance and orientation of the nucleus from the electron spin can be determined from the anisotropic components of the hyperfine matrix. Computer simulation of an orientation-selective HYSCORE Experi-

ment, or indeed any other pulsed experiment, involves adding a pulsed experiment and choosing Magnetic Field as the second abscissa. Unfortunately, XepView[®] cannot currently visualize one or more four-dimensional datasets. The Orientation Selective HYSCORE Experiment Form is shown in Figure 35, and the only difference from that of the HYSCORE Experiment Form is the addition of a Magnetic Field Tab, which allows the initial field, increment field, and the number of data-points to be added (Fig. 35). An alternative approach is to duplicate (copy) the HYSCORE experiment and change the static field position.

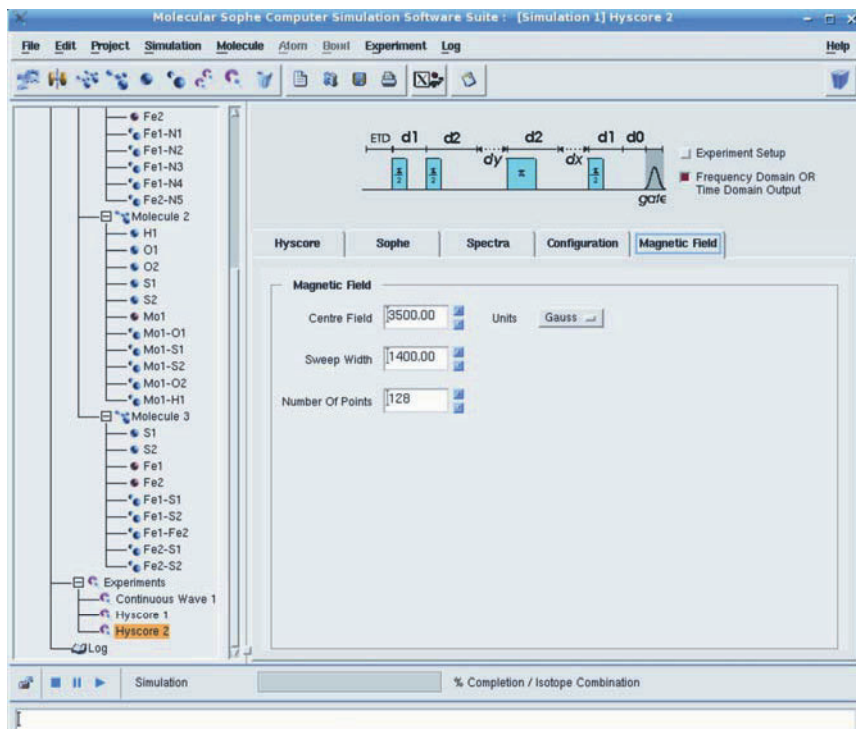


Figure 35. Molecular Sophe Graphical User Interface showing the Orientation Selective HYSCORE Experiment.

2.25. Pulsed EPR – MIMS ENDOR

The MIMS Electron Nuclear Double Resonance (ENDOR) Experiment Form (Fig. 36) is accessible after having loaded a MIMS ENDOR Experiment (§2.17) and selected the MIMS ENDOR Experiment Node from the Explorer Tree. The MIMS ENDOR Experiment is acquired by recording the amplitude versus the frequency of the radiofrequency (RF), pulse as shown in the pulse sequence within

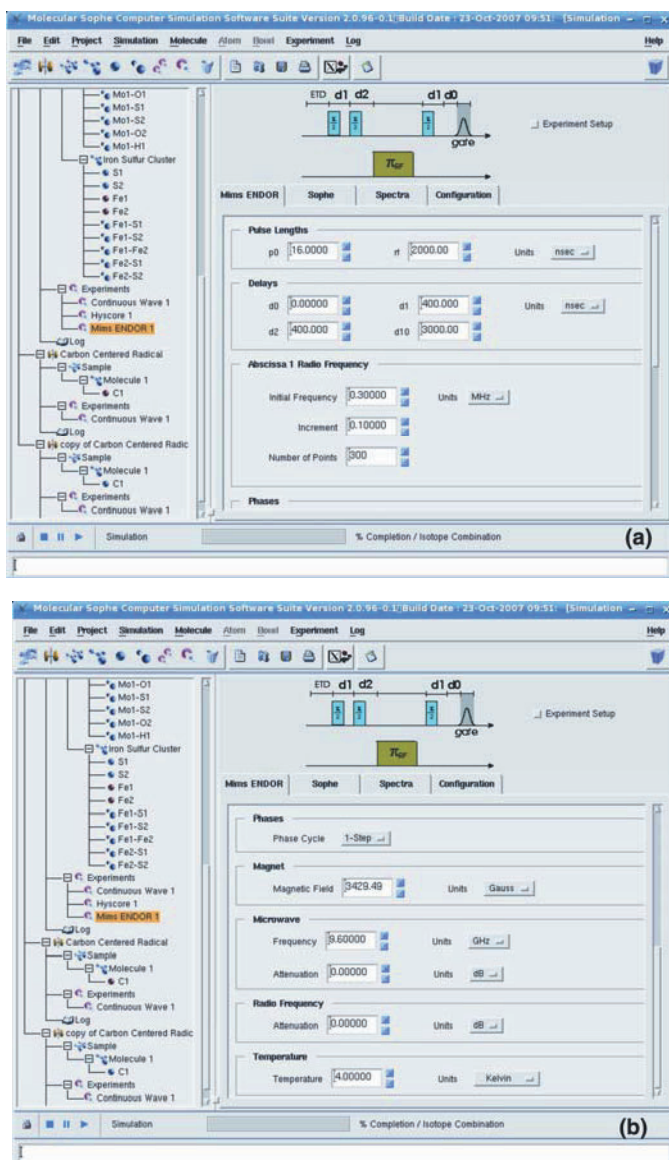


Figure 36. Molecular Sophe Graphical User Interface showing (a) the MIMS ENDOR Tab within the MIMS ENDOR Experiment Form, (b) the lower section of the MIMS ENDOR Tab.

the MIMS ENDOR Experiment Form (Fig. 36). The MIMS ENDOR Experiment (Fig. 36) contains the following tabs: MIMS ENDOR, Sophe (§2.20), Spectra (§2.21), and Resonator Configuration (§2.22). Within the MIMS ENDOR tab the user can define the microwave Pulse Length of the $\pi/2$ pulse (p_0), the length of the

radio frequency π pulse (rf), Delays, the range of radio frequencies (Abscissa 1 Radio Frequency), Phase Cycle, the static Magnetic Field, the Microwave Frequency, Attenuation, Radio Frequency Attenuation, and the Temperature of the experiment. Creation of the microwave $\pi/2$ pulse is dependent upon the pulse length (p_0), the microwave attenuation and the microwave magnetic field strength (B_1) at 0 dB. Creation of the radio frequency π pulse is dependent upon the pulse length (rf), the radio frequency attenuation, and the radio frequency magnetic field strength (B_2) at 0 dB. B_1 and B_2 are defined in the Resonator Configuration Tab.

The microwave attenuation required to obtain a $\pi/2$ flip angle with a $\pi/2$ pulse length (p_0) and B_1 can be obtained by selecting the Experiment Setup Toggle Button and running the experiment. This will produce a plot of microwave attenuation versus echo intensity (Fig. 34). The Position qualifier within XepView[®] or gnuplot can be used to determine the power associated with the maximum echo intensity. Currently the MIMS ENDOR is monitored at a single point (detection gate delay d_0) rather than integrating over a detection gate.

The MIMS ENDOR tab is a scrollable window, and as such all of the parameters may not be visible upon selecting the tab. This is the case in Figure 36, where the magnetic field strength, microwave frequency and attenuation, radio frequency attenuation, and temperature are hidden but can be entered by scrolling the window (Fig. 36). The remaining parameters (magnetic field and temperature) and the parameters in the other tabs have been defined previously in the CW EPR Experiment Form (§§2.20–2.22).

2.26. Units Conversion Calculator

The Units calculator based on kcalc has several additional buttons enabling the calculation of (i) g -values from a given frequency and magnetic field, (ii) a magnetic field from a given g value and microwave frequency, (iii) the microwave pulse angle given the g value, microwave pulse attenuation and pulse length, (iv) RF pulse angle given the nuclear g value, RF pulse attenuation and RF pulse length, (v) the microwave $\pi/2$ pulse length given the g value and attenuation, and (vi) the RF π pulse length given the nuclear g value and the RF attenuation. The default kcalc configuration file (/usr/mosophe/kcalcrc/admin) is shown below:

```
#
# Values enclosed in square brackets are stored as constants
# Other values need to be entered
#
# Constant 0
# Calculate :  $g = [h/\beta] * \text{microwave frequency (GHz)} / \text{Magnetic field (Gauss)}$ 
# Calculate :  $B \text{ (Gauss)} = [h/\beta] * \text{microwave frequency (GHz)} / g$ 
#
# Constant 1
# Conversion of Gauss to  $10^{-4} \text{ cm}^{-1}$ :  $A \text{ (} 10^{-4}\text{cm}^{-1}\text{)} = [\beta/h] * g * \text{delta B}$ 
#
```

```

# Constant 2
# Calculate Microwave Pulse Angle
# Calculate : Angle (Radians) = [beta/[2 * hbar]] * g * Attenuation (B1,
    Gauss) * pulse length (ns)
#
# Constant 3
# Calculate RF Pulse Angle
# Calculate : Angle (Radians) = [beta_n/[2 * hbar]] * g_n * Attenuation (B2,
    Gauss) * pulse length (ns)
#
# Constant 4
# Calculate Microwave Pulse Length
# Calculate : MW Pulse length (ns) = [1.5707963 * 2 * hbar / beta] / g *
    Attenuation (Gauss)
#
# Constant 5
# Calculate RF Pulse Length
# Calculate : RF Pulse length (ns) = [ 3.1415927 * 2 * hbar / beta_n] / g_n *
    Attenuation (B2, Gauss)

```

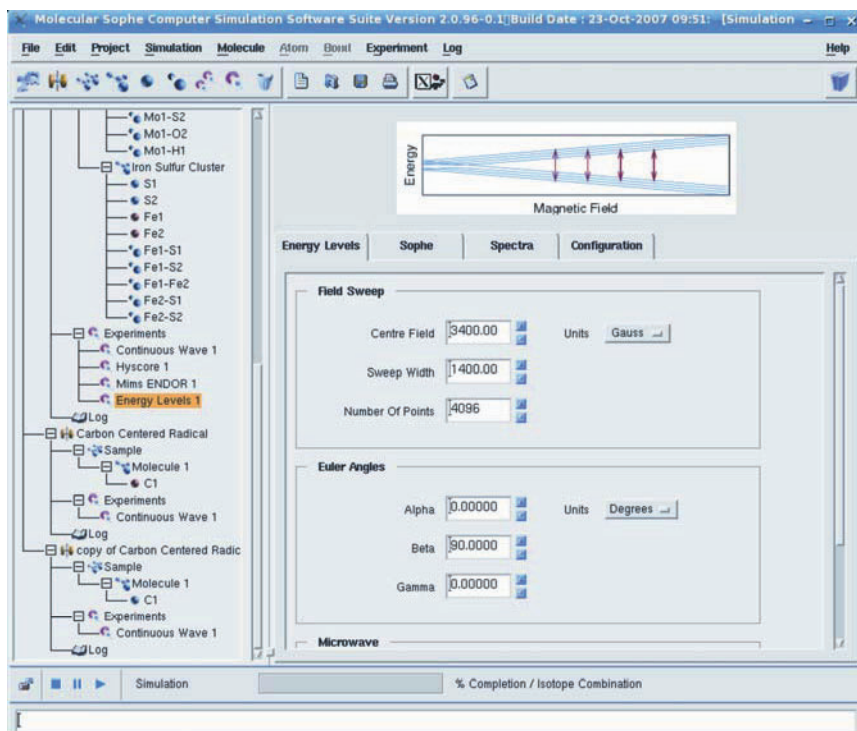


Figure 37. Molecular Sophe Graphical User Interface showing the Energy Level Experiment Form and specifically the Energy Level Tab.

2.27. Reports: Energy Level Diagrams

Once an Energy Level Experiment has been added to the Explorer Tree, the Energy Level Experiment forms can be viewed by a left mouse click on the Energy Level Experiment Node in the Explorer Tree. The Energy Level Experiment Form has Energy Level, Sophe (§2.20), Spectra (§2.21), and Resonator Configuration (§2.22). Within the Energy Level Tab (Fig. 37), the user can enter values concerning the field sweep (center field, sweep width, and number of datapoints), Euler Angles (orientation of the magnetic field), microwave frequency, and temperature. The units for the field-sweep parameters include Gauss, mTesla, and Tesla, and those for the microwave frequency are MHz, GHz, and THz. The number of field segments should be increased (from 2) to provide sufficient resolution along the magnetic field axis. Boltzmann populations for each energy level are automatically included and consequently the temperature will affect the intensity (and presence or absence) of the EPR transition between two different energy levels. The resultant energy level diagram showing energy levels (blue) as a function of magnetic field and the allowed transitions (transitions with a probability greater than the threshold) shown in red can only be viewed using Gnuplot, Image Plot, or Post-script viewers. The choice of format can be chosen in the Spectra tab. (§2.21).

2.28. Main Menus

The Main Menu is shown in Figure 38 and the following Table 1 shows all the Menu and Sub Menu items and explains their functions.

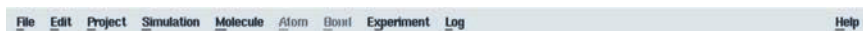


Figure 38. The main menu in the Molecular Sophe Graphical User Interface.

The Main Menu items can be accessed by placing the mouse over the particular option and performing a left click or, alternatively, pressing the <Alt> key in conjunction with the underlined letter in the Menu Item. For example, the File menu can be accessed by pressing <Alt>f.

2.29. Tool Bar

The Tool Bar (Fig. 39) provides quick access to some common tasks in building the project.

The buttons left to right perform the following functions:

- Load a project from disk,
- Add a simulation to the project,
- Remove the molecules, atoms and bonds from the sample,
- Add a molecule,
- Add an atom,

Table 1. Functionality of the Main Menu in Molecular Sophe

Main menu item	Submenu item	Explanation
File	XeprView®	Start Bruker's XeprView® Software
	Nameclean	Clean up the Orbacus Corba Nameserver
	Exit	Exit Molecular Sophe
Edit	Edit Preferences	Modify choice of external programs and CORBA settings
	Save Preferences	Save user preferences
	Hide Tool Bar	Hide (and show) the Tool Bar
	Hide Control Bar	Hide (and show) the Control Bar
	Hide Message Bar	Hide (and show) the Message Bar
	Load User Preferences	Load user preferences
Project	Load System Preferences	Load system wide preferences
	New	Create a new project
	Save	Save the current project
	Load ...	Load a project from disk
	Delete	Delete the current project
Simulation	Add Simulation	Add a simulation to the project
	Delete Simulation	Delete a simulation from the project
	Add	Add a simulation
	Load	Load a simulation
	Save	Save the current simulation
	Delete	Delete the current simulation
	Copy	Duplicate the selected simulation
	Print	Print the current simulation input file
	Run	Run the current simulation
	Stop	Stop the current simulation
Molecule	Lock	Lock the current simulation
	Add	Add a new molecule
	Paste	Greyed out, NOT currently supported
	Clear All	Delete all molecules including all atoms and bonds
	Delete	Delete current molecule including all atoms & bonds
	Cut	Greyed out, NOT currently supported
	Copy	Duplicate Molecule
	Add Atom	Add atom to the molecule
	Paste Atom	Greyed out, NOT currently supported
	Clear Atoms	Remove all atoms within the molecule
Atom	Add Bond	Add a bond (interaction) between two atoms
	Clear Bonds	Remove all bonds between atoms
	Delete	Only Active when the atom Node is selected
	Cut	Delete atom
	Copy	Greyed out, NOT currently supported
Bond	Copy	Duplicate atom
	Delete	Only Active when the bond Node is selected
Experiment	Delete bond	Delete bond
	Add	Add an experiment
	Paste	Greyed out, NOT currently supported
	Clear All	Remove all experiments
	Delete	Delete experiment
Log	Cut	Greyed out, NOT currently supported
	Copy	Duplicate experiment
	Clear	Clear both Sophe and MoSophe log windows
	Print	Print both Sophe and MoSophe log windows
Help	Save	Save both Sophe and MoSophe log windows to disk
	Click for Help	NOT Currently Supported
	Overview	Displays Product Information
	Index	NOT Currently Supported
	Keys	NOT Currently Supported
	Keys and Shortcuts	NOT Currently Supported
Product Information	Displays name of the binary executable	
Manual	Manual for Molecular Sophe	



Figure 39. The Tool Bar within the Molecular Sophe Graphical User Interface.

- Add a bond,
- Remove all experiments,
- Add an experiment,
- A Generic delete function being able to delete the currently active Node in the Explorer Tree,
- New simulation,
- Load simulation from disk,
- Save simulation to disk,
- Print the simulation using the printer defined in the preferences dialog,
- Start the XeprView[®] software,
- Units conversion calculator and
- The manual.

2.30. Control Bar

The Control Bar (Fig. 40) is used to start, pause, and stop simulations. Once the simulation has started, the simulation is locked, so that the parameters within the simulation cannot be altered.



Figure 40. The Control Bar within the Molecular Sophe Graphical User Interface.

The components of the control bar from left to right include a toggle button that can lock and unlock the simulation, stop, pause, and start buttons, and a timing bar. Upon starting the simulation, the color of the start button changes to green. The Timing Bar (Fig. 40) shows the state (grey, red, and green) of the simulation. A grey timing bar indicates the simulation has not been started and a red timing bar that the simulation has completed. A green timing bar indicates the percentage completion of a particular isotope combination; i.e., if the simulation has atoms with multiple isotopes, the green timing bar will start multiple times.

There is a problem with threading in the X-server that can sometimes block the update of the timing bar, which can be readily seen by the timing bar stopping. If this occurs, simply re-press the start button and the timing bar will be updated, reflecting the current status of the simulation.

3. SOPHE: COMPUTATIONAL CODE

Sophe is a sophisticated computer simulation software program written entirely in C++ employing a number of innovative technologies, including the SOPHE partition scheme, a field segmentation algorithm, the mosaic misorientation linewidth model, and spectral optimization (under development). In conjunction with the SOPHE partition scheme, the field segmentation algorithm [22–25,35] and the mosaic misorientation linewidth model [24,26] greatly increase the speed of simulations for most samples. Sophe has been completely rewritten in order to incorporate both continuous-wave and pulsed EPR simulations. There are versions for both 32 bit (ix86; $x = 3, 4, 5, 6$) and 64 bit (x86_64) platforms, the latter running significantly faster.

The simulation of a randomly oriented EPR spectrum involves integration over a unit sphere (Eq. (3)) that is performed numerically by partitioning a unit sphere and calculating the resonant field positions and transition probabilities at all of the vertex points.

3.1. Sophe Grid

Whilst a number of different partition schemes have been reported in the literature for performing the numerical integrations in Eq. (3), including the igloo [36–38], triangular [39], spiral [40], and a triangular arrangement with octahedral symmetry [41], Molecular Sophe uses a partition scheme involving spherical triangles [35]. The SOPHE partition scheme [35] allows any portion of the unit sphere ($\theta \in [0, \pi/2]$, $\phi \in [\phi_1, \phi_2]$ or $\theta \in [\pi/\pi]$, $\phi \in [\phi_1, \phi_2]$) to be partitioned into triangular convexes. For a single octant ($\theta \in [0, \pi/2]$, $\phi \in [0, \pi/2]$) the triangular convexes can be defined by three sets of curves:

$$\begin{aligned}\theta &= \frac{\pi}{2} \frac{i}{N}, \\ \theta\phi &= \frac{\pi}{2} \frac{i-1}{N} (\phi_2 - \phi_1), \\ \theta\phi &= \theta(\phi_2 - \phi_1) - \frac{\pi}{2} \frac{i-1}{N} (\phi_2 - \phi_1), \quad (i = 1, 2, \dots, N),\end{aligned}\tag{8}$$

where N is defined as the partition number and gives rise to $N + 1$ values of θ . Similar expressions can be easily obtained for $\theta \in [\pi/2, \pi]$, $\phi \in [\phi_1, \phi_2]$. A three-dimensional visualization of the SOPHE partition scheme is given in Figure 41b. And the triangular grid resembles the roof of the famous **Sydney Opera House** (SOPHE).

In the SOPHE grid there are N curves in each set, with the number of grid points varying from 2 to $N + 1$ in steps of 1. In order to produce simulated spectra of high quality, the unit sphere is often required to be finely partitioned, in other words, a large number of vertex points are required to reduce computational noise

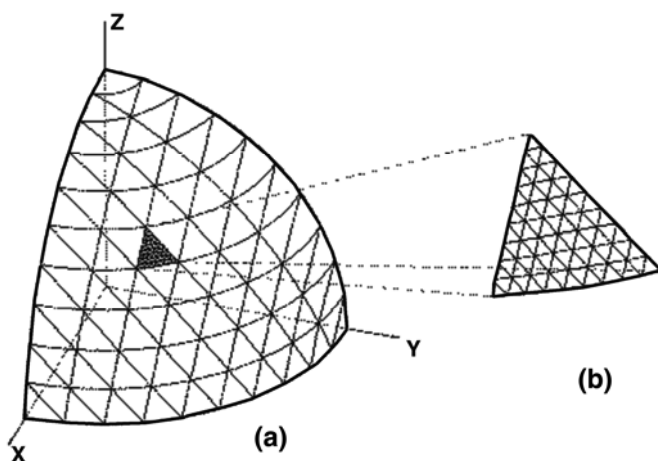


Figure 41. A schematic representation of the SOPHE partition scheme: (a) SOPHE partition grid in which the three sets of curves are described by Eq. (8); SOPHE partition number N equals 10; (b) subpartitioning into smaller triangles can be performed by using either Eq. (8) or alternatively the points along the edge of the triangle are interpolated by the cubic spline interpolation method and each point inside the triangle is linearly interpolated three times and an average is taken.

often observed when the spin Hamiltonian parameters are highly anisotropic and the linewidths small. Each triangle in Figure 41 can be easily subpartitioned into smaller triangles, referred to as “tiny triangles.” In Figure 41b a selected triangle is further partitioned into 81 tiny triangles with a subpartition number $N = 10$. The grid formed in such a subpartition can still be described by Eq. (8). In this particular case, θ is stepped in a smaller step of $\pi/(2(N-1)(M-1))$ from $\theta = 45^\circ$ to $\theta = 54^\circ$, the two corresponding curves that bound the triangle (Fig. 41b). A similar process is applied to curves in sets 2 and 3. Alternatively, various interpolation schemes may be used to generate finer grids for simulating randomly oriented EPR spectra [39, 40, 42]. In 1995 we described the highly efficient SOPHE interpolation scheme [35].

The advantage of the SOPHE partition scheme over other schemes (igloo [36–38], triangular [39], spiral [40], and a triangular arrangement with octahedral symmetry [41]) is that it allows the implementation of interpolation schemes, such as the SOPHE interpolation scheme and the mosaic misorientation linewidth model that reduce the number of matrix diagonalizations required to eliminate computer noise. Since matrix diagonalization is an N^3 process, where N is the rank of the matrix, reducing the number of matrix diagonalizations leads to significant reductions in the computational time (see §3.5). In addition, the SOPHE grid can be described by three analytical expressions (Eq. (8)) that are only dependent upon a single parameter, the partition number.

3.2. CW EPR Spectroscopy

3.2.1. Calculation of Resonant Field Positions

The very nature of EPR spectroscopy as a field-swept technique imposes a computational challenge to computer simulation of randomly oriented spectra. In essence, during an EPR experiment, the spin system under investigation is constantly modified through the Zeeman interactions as the magnetic field is swept. In a general situation where two or more interactions have comparable energies, the search for resonance field positions is not a trivial task as the dependence of the energies of the spin states on field strength (B_0) can be very complex. The complication involved is best manifested by the presence of multiple transitions between a given pair of energy levels.

3.2.2. Brute Force: Matrix Diagonalization and Field Segmentation Algorithms

A number of search schemes have been used in the full matrix diagonalization approach for locating resonant field positions [19,43–46]. Generally, they can be grouped into two categories. In category I, the resonant field position is searched independently for every transition. Among the schemes belonging to this category, the so-called iterative bisection method is the safest but probably the most inefficient [16]. Other more efficient methods such as the Newton-Raphson method have also been used [19]. In general, these search schemes are time consuming, as a large number of diagonalizations are normally required. The search schemes belonging to category II may be called segmentation methods. In these schemes, the field-sweep range is divided equally into k segments, and for each segment the whole energy matrix is diagonalized once for the center field value of that segment. Thus, only k diagonalizations are performed for each orientation. A perturbation theory is then employed for determining the presence of a transition in each segment. This search scheme is still limited to situations where in each segment there is no more than one possible transition. However, if k is not too large, the chance of having two resonances in a single segment is rare. Reijerse et al. [43] use a first-order perturbation approach for exploring transitions in each segment. However, from our experience, first-order perturbation theory cannot be guaranteed to produce resonance field positions with satisfactory precision. In Sophe we have adopted the second-order perturbation theory [47], where for each orientation on the SOPHE grid the field range is divided into a number of intervals. Matrix diagonalization [48] is performed once in each interval, and second-order perturbation theory is then employed to locate the resonant field positions within the interval. We have found that this approach has proven to be efficient and reliable for locating the resonance field positions in field-swept EPR spectra and can also deal with complicated situations where multiple transitions or looping transitions are present. A saving factor in the segmentation method lies in the fact that full matrix diagonalization is only performed k times irrespective of the number of transitions involved. By contrast, in the other schemes, a few diagonalizations are required for

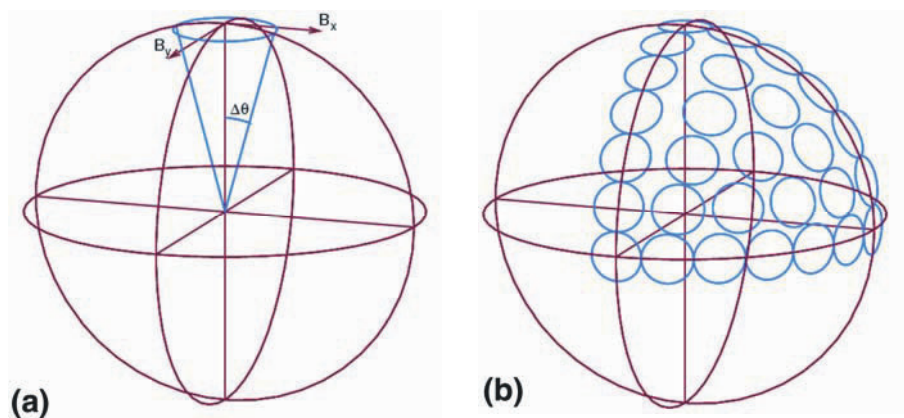


Figure 42. Mosaic misorientation linewidth model.

each transition, and for large spin systems this number can become very large. The precision of the resonance field positions normally depends on the segment number k as well as on the spin system. For $S = 1/2$ spin systems a value of 2 for the segment number is usually suitable, but for high-spin systems where the linewidth is narrow and the magnetic field sweep is large larger values are required. Simulations can be performed with different segmentation numbers, providing an easy test of precision and also to test whether apparent resonances are noise or real.

3.2.3. Mosaic Misorientation Linewidth Model

When the linewidth is small compared to the anisotropy of the system, it is necessary to integrate over a large number of orientations to avoid simulation noise in the simulated spectrum. This increases the computational time considerably. The SOPHE grid and Interpolation schemes were developed as a way to overcome this problem. A new approach based on the mosaic misorientation linewidth model [24,49] has recently been developed (Fig. 42). In the mosaic misorientation linewidth model a Gaussian distribution of molecular geometry axes about an average crystal c -axis is assumed. In the current implementation the partial derivatives of the eigenvalues with respect to a rotation about the x and y axes are calculated using first-order perturbation theory.

The contribution of a Gaussian distribution, of halfwidth $\Delta\theta$, to the linewidth can then be calculated with the following equation:

$$\sigma_m^2 = \left(\Delta\theta \frac{\partial E_{ij}}{\partial \theta_x} \right)^2 + \left(\Delta\theta \frac{\partial E_{ij}}{\partial \theta_y} \right)^2, \quad E_{ij} = E_i - E_j. \quad (9)$$

In the simulation of powder spectra each point in the SOPHE grid is considered to be a microcrystallite with a Gaussian distribution of orientations (Fig. 42a), such that there is an overlap between adjacent grid points (Fig. 42b):

$$\Delta\theta = \frac{\pi}{4(N-1)}. \quad (10)$$

At turning points in the spectrum the partial derivatives of the eigenvalues and hence σ_m are zero and the linewidths are determined by other contributions. At other orientations where the resonant field varies strongly with orientation, the linewidths will be broadened (smoothed). This model simulates an EPR spectrum where the important features, the turning points, are resolved in a significantly reduced time. Increasing N , the number of bands in the SOPHE grid, will lead to a convergence to the “true” spectrum. For a large number of spin systems, N can initially be set to 20. The mosaic misorientation linewidth model can be contrasted with interpolation schemes by considering it as an extrapolation method.

3.2.4. *A Comparison of Brute Force Matrix Diagonalization and Mosaic Misorientation*

An example demonstrating the efficiency of the SOPHE partition scheme in conjunction with the SOPHE interpolation scheme and the mosaic misorientation linewidth model is shown in Figure 43a–d, where we have calculated a randomly oriented spectrum for a high-spin rhombically distorted naturally abundant Cr(III) ion for which an appropriate spin Hamiltonian is

$$H = g_e B \cdot S + D \left[S_z^2 - \frac{1}{3} S(S+1) \right] + E(S_x^2 - S_y^2) + \text{S.A.I.} - g_n \beta B \cdot I. \quad (11)$$

The spin Hamiltonian parameters employed were $g_e = 2.00$, $D = 0.10 \text{ cm}^{-1}$, $E/D = 0.25$, $A_x = 120.0$, $A_y = 120.0$, and $A_z = 240.0 \times 10^{-4} \text{ cm}^{-1}$. A narrow linewidth was chosen (30 MHz) in order to demonstrate the high efficiency of these schemes. The unit sphere has to be partitioned very finely in order to produce simulated spectra with high signal-to-noise ratios when there is large anisotropy and the spectral linewidths are narrow.

The simulated spectra employing brute force matrix diagonalization with $N = 18$ and $N = 400$ are shown in Figure 43a and 43b, respectively. Including the SOPHE interpolation scheme with a partition number $N = 18$ (Fig. 43c) dramatically improves the signal-to-noise ratio with a considerable reduction in computational time. Application of the mosaic misorientation linewidth model (Fig. 43d) also dramatically improves the signal-to-noise ratio and is computationally faster than the SOPHE interpolation method as interpolation has many overheads. The spectra in Figure 43a–d were calculated using the XSophe-Sophe-XeprView[®] computer simulation software suite. Clearly the mosaic misorientation linewidth

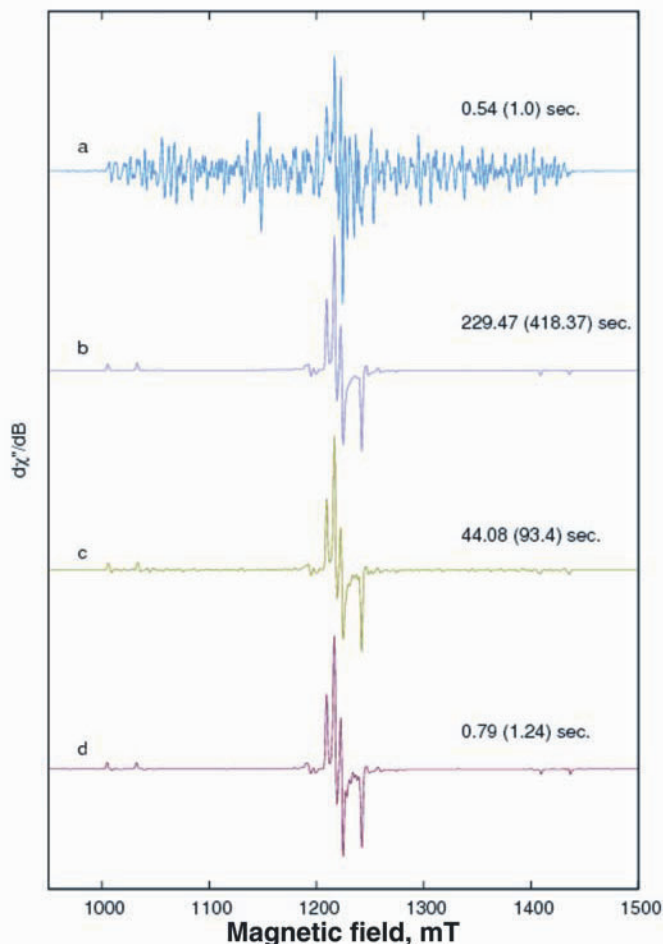


Figure 43. Computer simulations of the powder EPR spectrum from a naturally abundant Cr(III) spin system ($S = 3/2$; $I = 3/2$) that demonstrates the efficiency of the SOPHE interpolation scheme: (a) without the SOPHE interpolation scheme, $N = 18$; (b) without the SOPHE interpolation scheme, $N = 400$; (c) with the SOPHE interpolation scheme, $N = 18$; and (d) with the mosaic misorientation linewidth model, $N = 18$. Computational times were obtained on both a Linux PC (AMD Athlon XP2400+ CPU with the Mandrake 9.1 operating system) and an SGI supercomputer (MIPS R14K CPU with the IRIX 6.5.20 operating system); the latter times are given in brackets, $\nu = 34$ GHz; field axis resolution 4096 points; an isotropic Gaussian lineshape with a halfwidth at half-maximum of 30 MHz was used in the simulation.

model is the fastest approach and now replaces the brute force matrix diagonalization approach within the computational program Sophe and is also preferred over SOPHE interpolation. An identical spectrum to Figure 43d is found using Molecular Sophe, except the computational time was slightly longer: 1.49 vs. 0.79 sec.

Running the same simulation on a 64-bit notebook (Athlon XP3400) using Mandriva Linux 2006 as the operating system produced a computational time of 0.94 sec, a factor 1.5 to 2 times faster than a 32-bit computer.

3.2.5. Linewidth Models

At present only a single linewidth model, namely, the angular variation of g -values, has been incorporated into Sophe:

$$\sigma_v^2 = \left(\sigma_x^2 g_x^2 l_x^2 + \sigma_y^2 g_y^2 l_y^2 + \sigma_z^2 g_z^2 l_z^2 \right) / g^2, \quad (12)$$

where $g^2 = g_x^2 l_x^2 + g_y^2 l_y^2 + g_z^2 l_z^2$, σ_i ($i = x, y, z$) are the input linewidth parameters and l_i ($i = x, y, z$) are the direction cosines of the magnetic field with respect to the principal axes of the g matrix.

A similar approach to that used for the distribution of zero-field splittings in XSophe [23,24] will be implemented for all spin Hamiltonian and structural parameters.

3.2.6. Visual Aids for Analyzing Complex CW EPR Spectra

Molecular Sophe provides three tools (Energy level Diagrams, Transition Roadmaps, and Transition Surfaces) for aiding the analysis of complex CW EPR spectra. The Energy Level Diagrams and Transition Roadmaps can be displayed using Gnuplot, Ghostview (postscript files), or through an image viewer (portable network graphics files) such as a web browser (Firefox or Mozilla). The transition surface scene graphs are plotted with an OpenInventor scene graph viewer (ivview) using cartesian coordinates, which is extremely useful for highly anisotropic spin systems such as high-spin systems (e.g., Fig 4e). This requires the minimum field to be set to zero, which is defined as the origin. In contrast, for nearly isotropic systems it is important to examine a single transition at a time. The choice of transitions can be made through the Transition Labels/Probabilities window and either setting the transition threshold or defining the transitions.

3.3. Pulsed EPR Simulations

The simulation of pulsed EPR spectra involves calculating the evolution of an observable (\bar{O} ; Eq. (13)) during the microwave pulses, radiofrequency pulses, and free evolution periods that comprise the pulse sequence. The signal in an arbitrary pulsed EPR experiment can be simply described in superoperator notation [8,50]:

$$\langle \bar{O} \rangle = \left\langle \rho_0 \left| \hat{R}_1 \hat{R}_2 \dots \hat{R}_n \right| O \right\rangle. \quad (13)$$

In most experiments the initial density matrix (ρ_0) is the equilibrium density matrix (ρ) with diagonal elements given by the Boltzmann population of the energy levels in the eigenbasis of the static Hamiltonian:

$$\rho_{ii} = \frac{e^{\frac{-E_i}{kT}}}{\sum_{j=1}^n e^{\frac{-E_j}{kT}}}. \quad (14)$$

The density matrix for a two level spin system ($S = 1/2$) is

$$\rho = \begin{bmatrix} \rho_{11} & \rho_{12} \\ \rho_{21} & \rho_{22} \end{bmatrix}, \quad (15)$$

and the corresponding superbra is

$$\langle \rho | = [\rho_{11} \quad \rho_{12} \quad \rho_{21} \quad \rho_{22}]. \quad (16)$$

The detection operator (observable) in Eq. (13) is given by

$$O = \begin{bmatrix} O_{11} & O_{12} \\ O_{21} & O_{22} \end{bmatrix}, \quad (17)$$

and the corresponding superket is

$$|O\rangle = \begin{bmatrix} O_{11} \\ O_{21} \\ O_{12} \\ O_{22} \end{bmatrix}, \quad (18)$$

The transverse magnetization (M_x , M_y) are proportional to S_x , S_y , respectively, and are determined by the g value in the x - y plane, the microwave power, and other experimental factors.

In general, a pulse sequence is comprised of one or more microwave pulses, free evolution periods, and possibly radio frequency pulses. For example, the pulse sequences for the HYSORE and MIMS ENDOR experiments are shown in Figures 33 and 36, respectively. Each of these components can be mathematically described by a superpropagator (\hat{R}) (Eq. (13)), which in turn is derived from a direct product of the propagators:

$$\hat{R} = R \otimes R^{-1},$$

$$\hat{R} = \begin{bmatrix} R_{11} & R_{12} \\ R_{21} & R_{22} \end{bmatrix} \otimes \begin{bmatrix} R_{11}^* & R_{21}^* \\ R_{12}^* & R_{22}^* \end{bmatrix} = \begin{bmatrix} R_{11}R_{11}^* & R_{11}R_{21}^* & R_{12}R_{11}^* & R_{12}R_{21}^* \\ R_{11}R_{12}^* & R_{11}R_{22}^* & R_{12}R_{12}^* & R_{12}R_{22}^* \\ R_{21}R_{11}^* & R_{21}R_{21}^* & R_{22}R_{11}^* & R_{22}R_{21}^* \\ R_{12}R_{12}^* & R_{12}R_{22}^* & R_{22}R_{12}^* & R_{22}R_{22}^* \end{bmatrix} \quad (19)$$

Coherence transfer pathways provide a way of visualizing the transfer of magnetization during a pulse sequence and in general an element of the density matrix undergoes the following transformation:

$$\rho_{ij} \xrightarrow{R} \sum_{l=0}^n \sum_{k=0}^n R_{ik} R_{lj}^* \rho_{kl}. \quad (20)$$

In the eigenbasis of the static Hamiltonian the superpropagator for each free evolution period is diagonal. The time dependence of each element in the density matrix (ρ) is simply given by

$$\rho_{ij} \xrightarrow{Et} e^{-2i\pi E_{ij}t} \rho_{ij}. \quad (21)$$

During the microwave pulses the Hamiltonian is no longer time independent and contains a term oscillating at the microwave frequency. Using Floquet theory [51] the superpropagators for the microwave pulses can be expressed as a Fourier series. For many spin systems the series converges rapidly and can be truncated at a low number of harmonics:

$$\hat{R}(t) = \sum_{m=-n}^n \hat{R}_m e^{-im\omega_{mw}t}. \quad (23)$$

Pulsed EPR experiments typically involve phase cycling where the experiment is repeated with different combinations of the phases of the microwave pulses. It can be seen that for a single pulse the phase cycle $[0, \pi]$ filters out all odd Floquet harmonics while the phase cycle $[0, -\pi]$ filters out all even Floquet harmonics:

$$\hat{R}_n e^{-in(\omega_{mw}t + \pi)} = (-1)^n \hat{R}_n e^{-in\omega_{mw}t}. \quad (23)$$

The use of phase cycling reduces the number of coherence pathways that must be followed. This can be further reduced if we include the condition that the initial Fourier index is 0 at equilibrium and at the time of detection must be given by $p = \pm 1$. This is shown in Figure 44 for a two-pulse sequence. The first pulse has $\Delta p = +1$, the second pulse $\Delta p = -2$. One pathway through the density matrix (in superbra notation) is shown in Figure 44. Each coherence pathway yields a peak that is then added to the spectrum. The spectrum may have one or more frequency dimensions depending on how the time periods are incremented in the experiment. The final spectrum is obtained by averaging over all pathways. For powder spectra the integration over the orientation disorder using the SOPHE grid is also performed [35].

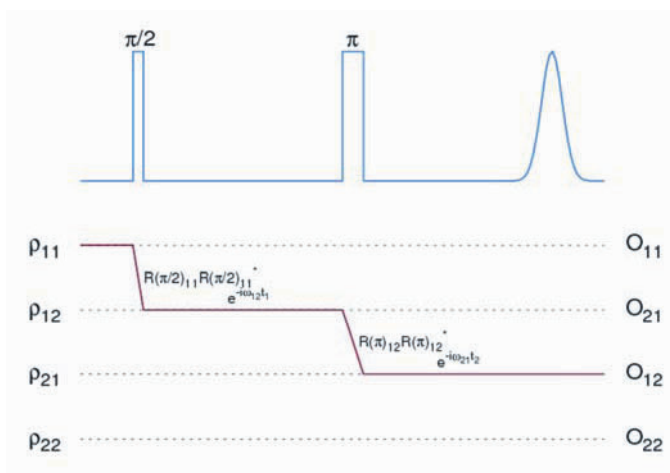


Figure 44. A schematic diagram of a pulsed EPR sequence and the evolution of the density matrix that is traced through each of the microwave pulses and free evolution periods. One coherence pathway from the equilibrium density matrix through to the detection operator is indicated.

The above approach to the simulation of pulsed EPR spectra allows the simulation of pulsed EPR spectra from not only isolated paramagnetic samples containing a single unpaired electron but also from samples containing multiple unpaired electrons, for example, high-spin Fe(III) centers found in cytochromes and non-heme iron proteins, and coupled centers, such as the type III copper-containing enzymes and the binuclear metallohydrolyases.

4. MOLECULAR SOPHE – EXAMPLES

4.1. CW-EPR Spectroscopy

4.1.1. *Mo(V) (S=1/2) Bioinorganic Chemistry*

Reaction of $\text{Tp}^*\text{Mo}^{\text{V}}\text{SCl}_2$ with a variety of phenols and thiols in the presence of triethylamine produces mononuclear, thiomolybdenyl complexes $\text{Tp}^*\text{Mo}^{\text{V}}\text{SX}_2$ [Tp^* = hydrotris(3,5-dimethylpyrazol-1-yl)borate; X = 2-(ethylthio) phenolate (etp), 2-(n-propyl)phenolate (pp), phenolate; X_2 = benzene-1,2-dithiolate (bdt), 4-methylbenzene-1,2-dithiolate (tdt), benzene-1,2-diolate (cat)] (Fig. 45) [51].

Multifrequency (S-, X-, Q-band) EPR spectra (Fig. 45) [51] of the complexes and selected molybdenyl analogues were acquired at 130 and 295 K, and yielded a spin Hamiltonian of C_s symmetry or lower, with $g_{zz} < g_{yy} < g_{xx} < g_e$ and $A_{zz'} > A_{xx'} \approx A_{yy'}$, and a non-coincidence angle in the range of $\beta = 24\text{--}39^\circ$ (Table 2). Multifrequency EPR, especially at S- and Q-band, was found to be particularly valuable in

the unambiguous assignment of spin Hamiltonian parameters for these low-symmetry sites. While Q-band measurements provided greater g -value resolution, larger state mixing, and reduced g - and A -strain at low frequencies (S-band) allowed an accurate determination of the hyperfine matrix, including its orientation with respect to the g matrix. This single set of g and A parameters (Table 2) were then used to simulate the S-, X-, and Q-band spectra. The weaker π -donor terminal sulfido ligand yields a smaller HOMO–LUMO gap and reduced g -values for the thiomolybdenyl complexes compared with molybdenyl analogues.

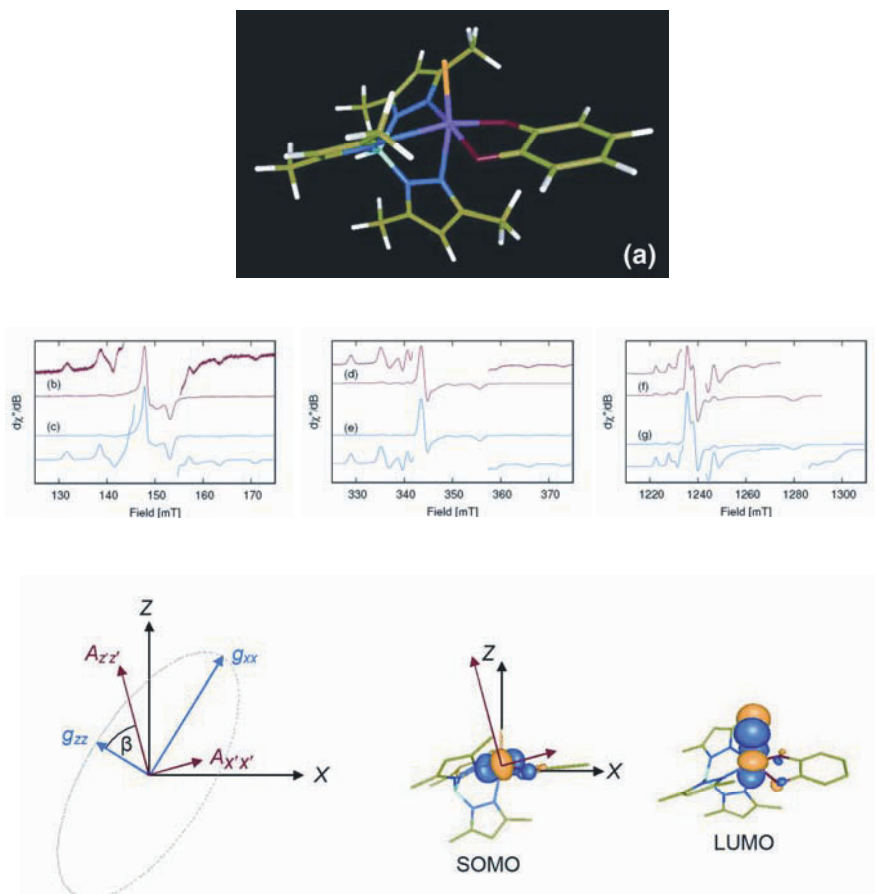


Figure 45. Multifrequency EPR and DFT Calculations (ORCA) for $\text{Tp}^*\text{Mo}^{\text{V}}\text{S}(\text{cat})$; cat = catecholate. (a) x-ray crystal structure of $\text{Tp}^*\text{Mo}^{\text{V}}\text{S}(\text{cat})$. Experimental spectra: (b) S-band, (d) X-band, (f) Q-band recorded at 130 K. (c, e, g) Computer-simulated spectra. $g_{xx} = 1.9646$, $g_{yy} = 1.9595$, $g_{zz} = 1.8970$, $A_{xx} = 30.0$, $A_{yy} = 29.0$, $A_{zz} = 67.5 \times 10^{-4} \text{ cm}^{-1}$, $\alpha = 0^\circ$, $\beta = 34.5^\circ$, $\gamma = 0^\circ$. (h) ORCA calculations of the HOMO and LUMO for $\text{Tp}^*\text{Mo}^{\text{V}}\text{S}(\text{cat})$ and the orientation of the principal components of the g - and A -matrices [52].

Table 2. Anisotropic Spin Hamiltonian Parameters for Mo(V) Model Complexes Determined from DFT Calculations Using BP86 and B3LYP Functionals and Comparison with Experimental Data (results for $A = A_F + A^{\text{dip}}$ and $A = A_F + A^{\text{dip}} + A^{\text{SO}}$ have been tabulated separately)

Complex	g_{xx}	g_{yy}	g_{zz}	$\langle g \rangle^\dagger$	A_{xx}	A_{yy}	A_{zz}	$\langle A \rangle^\dagger$	α^\ddagger	β^\ddagger	γ^\ddagger
Tp*MoO(cat)											
BP86	1.9867	1.9796	1.9402	1.9688	9.2	9.5	40.5	19.8	10	43	44
BP86+ A^{SO}	"	"	"	"	11.7	11.1	46.8	23.3	1	39	-10
B3LYP	1.9790	1.9725	1.9276	1.9597	16.1	16.4	50.2	27.6	10	42	34
B3LYP+ A^{SO}	"	"	"	"	19.7	18.6	57.4	31.9	0	37	-2
Experiment ^a	1.9680	1.9660	1.9194	1.9511	27.0	26.0	64.2	39.1	0	36	0
Experiment ^b	1.969	1.969	1.920	1.953	34.0	20.0	66.2	40.1	0	0	0
Tp*MoS(cat)											
BP86	1.9796	1.9757	1.9042	1.9524	13.3	12.7	42.6	22.9	0	36	10
BP86+ A^{SO}	"	"	"	"	14.8	16.6	49.6	27.0	2	34	6
B3LYP	1.9698	1.9651	1.8874	1.9408	20.5	19.6	51.8	30.7	1	36	9
B3LYP+ A^{SO}	"	"	"	"	25.0	22.6	59.9	35.9	2	34	6
Experiment ^d	1.9646	1.9595	1.8970	1.9404	30.0	29.0	67.5	42.2	0	34.5	0
Tp*MoO(bdt)											
BP86	2.0161	1.9863	1.9508	1.9844	10.77	10.71	38.2	19.9	3	46	16
BP86+ A^{SO}	"	"	"	"	12.24	12.18	42.6	22.3	2	44	-14
B3LYP	2.0115	1.9784	1.9413	1.9771	16.4	15.9	47.2	26.5	0	48	-1
B3LYP+ A^{SO}	"	"	"	"	18.9	18.1	52.6	29.9	0	46	0
Experiment ^e	2.0025	1.9730	1.9360	1.9705	24.0	26.0	60.0	36.7	0	45	0
Experiment ^c	2.004	1.972	1.934	1.970	50.0	11.4	49.7	37.0	0	0	0
Tp*MoS(bdt)											
BP86	2.0079	1.9858	1.9300	1.9745	12.6	13.9	39.6	22.1	2	38	-2
BP86+ A^{SO}	"	"	"	"	15.8	14.3	44.6	24.9	2	36	-2
B3LYP	2.0009	1.9756	1.9163	1.9643	19.1	19.7	48.7	29.2	-2	40	-1
B3LYP+ A^{SO}	"	"	"	"	22.0	22.5	54.9	33.1	2	38	-4
Experiment ^a	1.9975	1.9680	1.9159	1.9607	26.0	26.5	59.2	37.2	0	39	0
Tp*MoO(etp) ₂											
BP86	1.9843	1.9568	1.9324	1.9578	16.9	18.3	46.4	27.2	18	34	15
BP86+ A^{SO}	"	"	"	"	19.1	21.0	53.2	31.1	18	31	4
B3LYP	1.9772	1.9483	1.9175	1.9477	22.5	24.1	55.3	33.9	17	33	11
B3LYP+ A^{SO}	"	"	"	"	25.5	27.7	63.3	38.9	17	30	2
Experiment ^a	1.9647	1.9417	1.9073	1.9379	33.0	34.0	74.5	47.2	0	26.5	0

Continued on following page.

Crystal field description of spin Hamiltonian parameters: Large non-coincidence angles can be explained by a model in which extensive mixing among Mo 4d orbitals takes place. Although ligand-to-metal charge transfer and metal-to-ligand charge transfer states of appropriate symmetry may also contribute, for transition metals the dominant contribution to g_{ij} is usually Δg_{ij}^{d-d} , which arises from transitions within the Mo 4d manifold. In C_s symmetry with a $\sigma^{(xz)}$ mirror plane, in

Table 2, cont'd

Tp*MoS(otp) ₂											
BP86	1.9852	1.9386	1.8963	1.9400	16.6	19.0	45.9	27.2	3	34	26
BP86+A ^{SO}	“	“	“	“	19.5	22.5	53.8	32.0	3	29	16
B3LYP	1.9759	1.9256	1.8751	1.9255	23.3	24.7	54.2	33.8	6	34	20
B3LYP+A ^{SO}	“	“	“	“	26.3	29.5	63.4	39.8	6	30	11
Experiment ^d	1.9558	1.9114	1.8623	1.9098	32.0	34.0	72.0	46.0	0	26	0
Tp*MoS(pp) ₂											
BP86	1.9836	1.9356	1.8912	1.9368	16.1	19.3	46.0	27.2	-5	34	-21
BP86+A ^{SO}	“	“	“	“	19.0	23.1	54.1	32.1	-4	30	-14
B3LYP	1.9743	1.9229	1.8696	1.9223	21.6	25.0	54.1	33.6	-7	34	-16
B3LYP+A ^{SO}	“	“	“	“	25.6	30.1	63.5	39.8	-6	31	-11
Experiment ^d	1.9575	1.9111	1.8575	1.9087	33.0	34.0	72.0	45.5	0	25	0

[†] $\langle g \rangle = 1/3(g_{xx} + g_{yy} + g_{zz})$, $\langle A \rangle = 1/3(A_{x'x'} + A_{y'y'} + A_{z'z'})$; Units for coupling constants = 10^{-4} cm^{-1} .

[‡] Euler rotations (in degrees) are defined as $R(\alpha\beta,\gamma) = R_z(\gamma)R_y(\beta)R_x(\alpha)$.

^a ref. [51].

^b ref. [54].

^c ref. [55].

which the X axis lies between the metal–ligand bonds, the $d_{x^2-y^2}$, d_{xz} , and d_{z^2} orbitals transform as A' and the d_{xy} and d_{yz} orbitals transform as A'' . The metal-based antibonding wavefunctions are therefore

$$\begin{aligned}
 \Psi_{x^2-y^2}^{a'*} &= \alpha \left[a_1 d_{x^2-y^2} + b_1 d_{xz} + c_1 d_{z^2} \right], \\
 \Psi_{xz}^{a'*} &= \beta \left[a_2 d_{xz} + b_2 d_{x^2-y^2} + c_2 d_{z^2} \right], \\
 \Psi_{z^2}^{a'*} &= \gamma \left[a_3 d_{z^2} + b_3 d_{x^2-y^2} + c_3 d_{xz} \right], \\
 \Psi_{xy}^{a'*} &= \delta \left[a_4 d_{xy} + b_4 d_{yz} \right], \\
 \Psi_{yz}^{a'*} &= \varepsilon \left[a_5 d_{yz} + b_5 d_{xy} \right],
 \end{aligned} \tag{25}$$

where, by definition, $a_q > b_q, c_q$ ($q = 1, 2, \dots$). Here covalency appears only implicitly through the metal-centered orbital coefficients $\alpha, \dots, \varepsilon$. Since the molecular X and Y axes are placed between the metal–ligand bonds, the groundstate wavefunction is $\Psi_{x^2-y^2}$.

Density Functional Theory Calculations (ORCA) [52]: The electronic g matrix and ^{95,97}Mo hyperfine matrix were calculated as second-order response properties from the coupled-perturbed Kohn-Sham equations. The scalar relativistic zero-order regular approximation (ZORA) was used with an all-electron basis and an accurate mean-field spin-orbit operator that included all one- and two-electron terms. A comparison of the principal values and relative orientations of the g and A interaction matrices (Table 2) obtained from unrestricted Kohn-Sham calculations at the BP86 and B3LYP levels with the values obtained from experimental spectra shows excellent agreement at the B3LYP level. A quasi-restricted approach has

been used to analyze the contributions of the various molecular orbitals to g and A . In all complexes the ground state magnetic orbital is $d_{x^2-y^2}$ -based and the orientation of the A matrix is directly related to the orientation of this orbital (Fig. 45). The largest single contribution to the orientation of the g matrix arises from the spin-orbit coupling of the d_{yz} -based lowest-unoccupied molecular orbital into the ground state (Fig. 45). A number of smaller, cumulative charge transfer contributions augment the $d-d$ contributions.

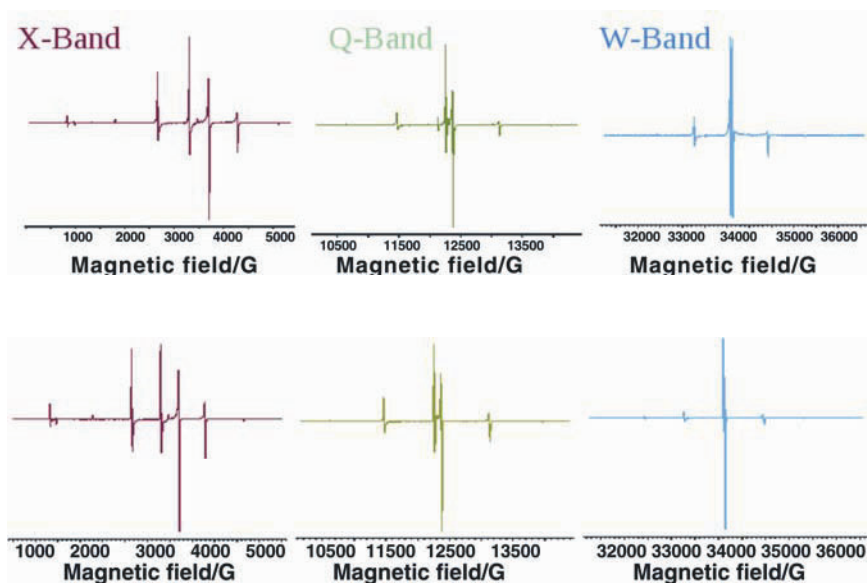


Figure 46. Multifrequency EPR spectra of 1% $^{53}\text{Cr(III)}$ doped into $\text{CsAl}(\text{SO}_4)$. Experimental spectra (top) and computer-simulated spectra (bottom). The spin Hamiltonian is given in Eq. (11) and the spin Hamiltonian parameters are $g_{\text{iso}} = 1.975$, $D = -0.078 \text{ cm}^{-1}$, and $E/D = 0$. Reproduced with permission of Bruker Biospin.

4.1.2. Multifrequency EPR Study of High Spin Cr(III) and the Analysis of Allowed and Forbidden Transitions using Perpendicular and Parallel Mode EPR Spectroscopy.

$^{53}\text{Cr(III)}$ was doped into $\text{CsAl}(\text{SO}_4)$ to a level of 1% and multifrequency EPR spectra recorded at X-, Q-, and W-band frequencies (Fig. 46). Computer simulation of all three spectra was achieved with a single set of spin Hamiltonian parameters, $g_{\text{iso}} = 1.975$, $D = -0.078 \text{ cm}^{-1}$, and $E/D = 0$, and the spin Hamiltonian given in Eq. (11). Measurement of the perpendicular ($B_1 \perp B_0$) and parallel ($B_1 \parallel B_0$) mode EPR spectra (Fig. 47) allows the observation and identification of the allowed and forbidden transitions. Computer simulation of each of these spectra with the above spin Hamiltonian parameters reproduces the spectral features accurately (Fig. 47).

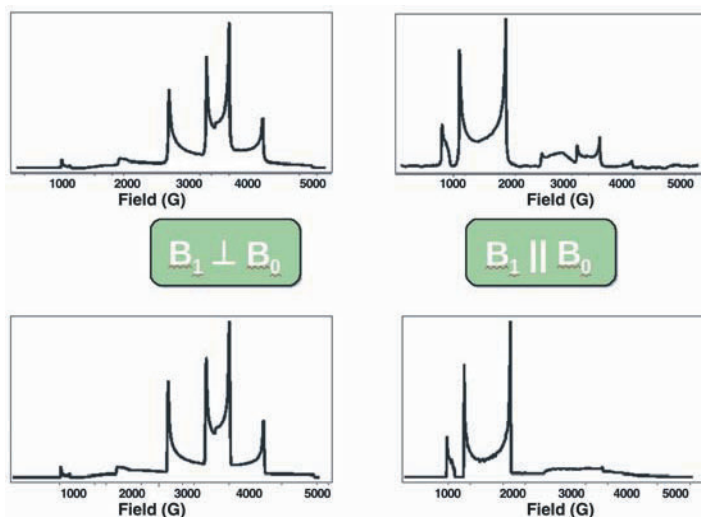


Figure 47. Computer simulation of EPR spectra of 1% $^{53}\text{Cr}(\text{III})$ doped into $\text{CsAl}(\text{SO}_4)_3$ measured in the perpendicular and parallel modes of the ER4116 DM dual mode resonator: (a) perpendicular mode showing the allowed transitions; (b) parallel mode showing the forbidden resonances; (c,d) computer simulation of (a) and (b), respectively. Computer simulation details are given in Figure 46. Reproduced with permission of Bruker Biospin.

4.1.3. Copper(II) Cyclic Peptide Complexes

Copper(II) forms both mononuclear and binuclear complexes with cyclic peptides (Patellamides, Ascidiacyclamide, Westiellamide (Fig. 48), and synthetic analogs) isolated from *Lissoclinum patella* and *L. bistratum* [55–60]. Examination of the perpendicular region of the first derivative EPR spectrum of the mononuclear copper(II) Westiellamide complex reveals nitrogen hyperfine coupling. Differentiation of the spectra and Fourier filtering produce well-resolved EPR spectra with nitrogen hyperfine coupling on the perpendicular resonances, and also on the parallel $M_1 = 3/2$ resonance (Fig. 48). Computer simulation of both the first- and second-derivative EPR spectra, based on the spin Hamiltonian,

$$\begin{aligned}
 H = & \sum_{i=x,y,z} (B_i \cdot g_i \cdot S_i + S_i \cdot A_i(\text{Cu}) \cdot I_i(\text{Cu}) - g_n \beta_n B_i \cdot I_i) \\
 & + \sum_{j=1}^{3,4} (S_i \cdot A_i(\text{N}) \cdot I_i(\text{N}) - g_n \beta_n B_i \cdot I_i),
 \end{aligned} \tag{26}$$

and with the following parameters (g_x 2.083, g_y 2.051, g_z 2.267; (^{63}Cu) A_x 14.0, A_y 16.2, A_z 175.0; (^{14}N two magnetically equivalent nuclei) A_x 12.40, A_y 6.2, A_z 10.4; (^{14}N , two magnetically equivalent nuclei) A_x 16.50, A_y 12.7, A_z 13.4) yield the spectra shown in red.

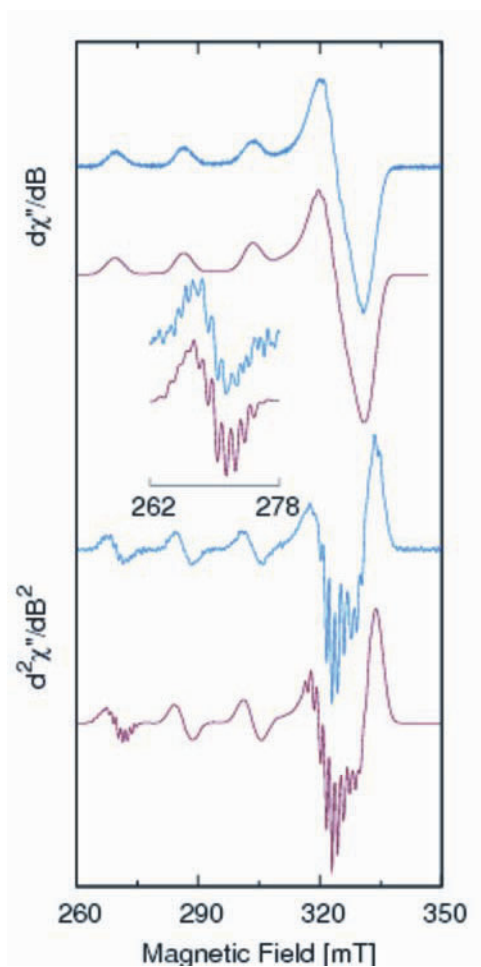


Figure 48. Experimental (blue) and simulated (red) first- and second-derivative X-band EPR spectra of the mononuclear Westiellamide copper(II) complex ($[\text{Cu}^{\text{II}}(\text{H}_2\text{L}^{\text{wa}})]^+$) in methanol at 50 K, $\nu = 9.3588$ GHz.

4.1.4. Dinuclear Exchange Coupled Copper(II) EPR Spectra

Binuclear metalloenzymes are prevalent in nature, performing a range of functions on various substrates. Dicopper sites have an important role in the activation of biological oxygen, and the study of structural and functional aspects of copper metalloenzymes via model systems is a subject of intense research. One member of the family of dicopper proteins is catechol oxidase, which features a type 3 copper

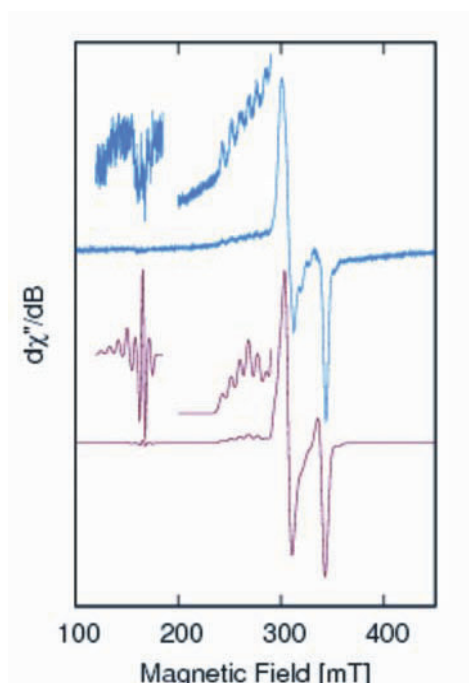


Figure 49. Experimental (blue) and computer simulation (red) of $[\text{Cu}_2\text{BPMP}(\text{OAc})_2][\text{ClO}_4]$.

center with two proximate copper ions coordinated primarily by histidine donors. This enzyme catalyses the two-electron oxidation of *o*-diphenols to the corresponding quinones. The recent x-ray crystallographic characterization of the catechol oxidase from sweet potatoes reveals a nitrogen-rich coordination environment, with 3 histidine donors to each copper. Both copper centers are in a trigonal bipyramidal geometry. Design and study of model complexes for catechol oxidase has been an area of much study and various nitrogen-containing binucleating ligands have been used to generate dicopper complexes [61]. The EPR spectrum (red) of a dinuclear copper(II) complex of BPMP with terminal, rather than bridging, acetate ligands (Fig. 49) has been simulated (blue) using the spin Hamiltonian given in Eqs. (1) and (2) with the following parameters: sites 1,2: g_{\parallel} 2.235, g_{\perp} 2.065, A_{\parallel} 179.0, A_{\perp} $15.0 \cdot 10^{-4} \text{ cm}^{-1}$, r 4.58 Å, J_{iso} -0.59 cm^{-1} . The g and A matrices for the first Cu center are rotated $+\beta^{\circ}$ (10) and those for the second are rotated $-\beta^{\circ}$ (10). The spin Hamiltonian parameters reveal that the two copper(II) ions have a tetragonal geometry and that the interaction between them occurs through dipole–dipole coupling and a very small component of exchange coupling. A small amount of exchange coupling was required to obtain a satisfactory simulation of the allowed and forbidden resonances. The magnitude of J was confirmed by fitting the magnetic susceptibility data.

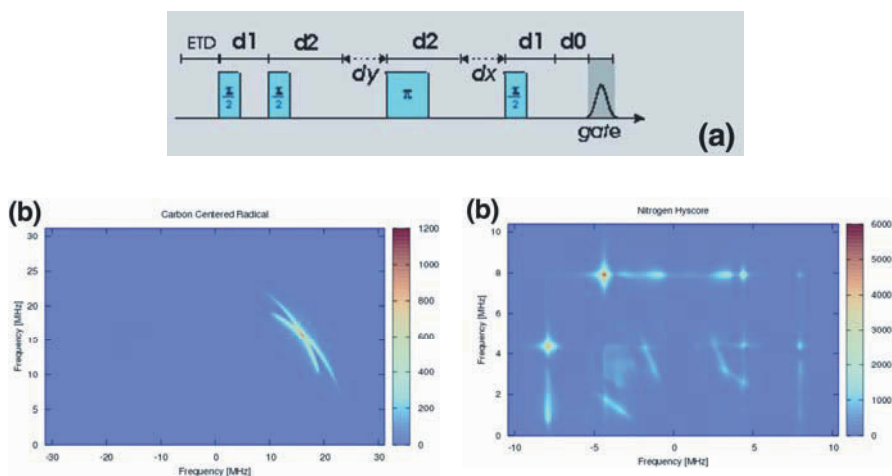


Figure 50. Examples of proton and nitrogen HYSORE simulations: (a) HYSORE pulse sequence; (b) Proton HYSORE simulation. $g_{\text{iso}} = 2.0$, $A_{\parallel} = -18$ MHz, $A_{\perp} = 9$ MHz, $T_{2\text{Niso}} = 0.1$ MHz. Microwave ($\pi/2$) pulse length equals 16.0 nsec, and the delays d_0 , d_1 , and d_2 are 0.0, 40.0, and 200.0 nsec, respectively. dx , $dy = 16.0$ nsec, sx , $sy = 512$. Number of orientations equals 100. $B = 342.949$ mT and $= 9.6$ GHz. (c) Nitrogen HYSORE simulation. $g_{\text{iso}} = 2.0$, $A_{\text{Niso}} = 5$ MHz, $P = -1$ MHz, $T_{2\text{Niso}} = 0.1$ MHz. Microwave ($\pi/2$) pulse length equals 16.0 nsec and the delays d_0 , d_1 , and d_2 are 0.0, 160.0, and 0.0 nsec, respectively. dx , $dy = 48.0$ nsec, sx , $sy = 512$. Number of orientations equals 200. $B = 342.949$ mT and 9.6 GHz.

4.2. Pulsed EPR Spectroscopy

Within Molecular Sophe there are a number of standard (default) experiments that have been optimized and are stored in `/usr/mosophe/examples`. Over time the number of examples will increase. Shown in the figures above and below are some of the results. Proton and nitrogen HYSORE simulated spectra are shown in Figure 50. A pulsed MIMS ENDOR spectrum is shown in Figure 51, and a SECSY experiment in Figure 52.

5. ADVANCES IN SPECTRAL OPTIMIZATION

Automatic fitting of EPR spectra is possible, although most techniques have problems with false minima and some degree of manual steering is necessary. One of the frequently encountered problems is that the least-squares difference is rarely an adequate measure of goodness of fit. In practice it is usually necessary to obtain a reasonable fit manually before automatic fitting is capable of further optimizing the spin Hamiltonian parameters.

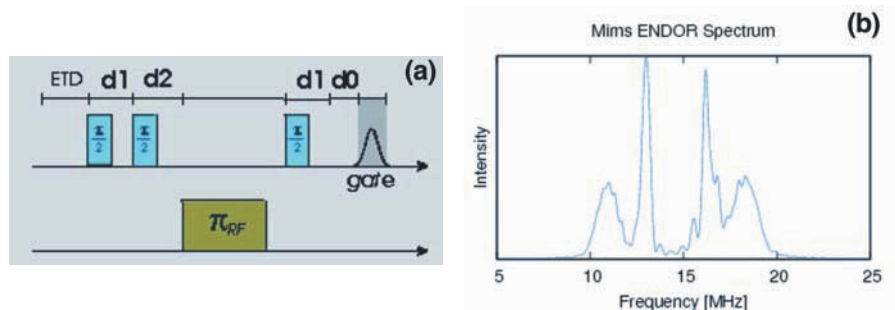


Figure 51. Proton Powder MIMS ENDOR spectrum: (a) MIMS ENDOR pulse sequence; (b) $g_{\text{iso}} = 2.0$, $A_{\parallel} = 4$ MHz, $A_{\perp} = 10$ MHz, $T_{2\text{Niso}} = 0.0$ MHz. Microwave ($\pi/2$) and RF (π) pulse lengths, 16.0 and 2000.0 nsec, respectively. Delays d_0 , d_1 , d_2 , and d_{10} are 0.0, 200.0, 400.0, 3000.0, respectively. Number of orientations equals 100. $B = 342.949$ mT and 9.6 GHz.

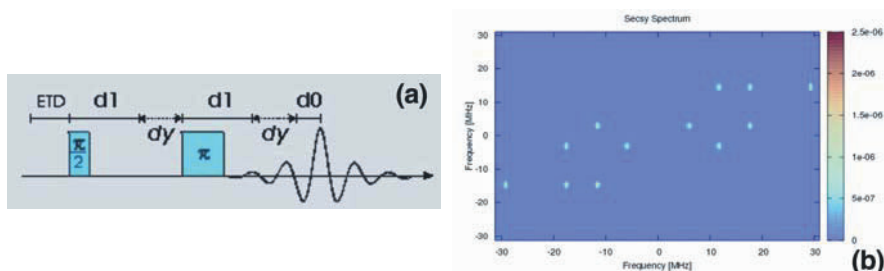


Figure 52. An example of a SECSY experiment: (a) SECSY pulse sequence and (b) the resultant simulation for $g_{\text{iso}} = 2.0$, $A_{\parallel} = 4$ MHz, $A_{\perp} = 8$ MHz, $T_{2\text{Niso}} = 0.02$ MHz. Microwave ($\pi/2$) pulse length equals 16.0 nsec and the delays d_0 and d_1 are 0.0 and 1000.0 nsec, respectively. dx , $dy = 16.0$ nsec, s_x , $s_y = 256$. Number of orientations equals 1 (45°). $B = 342.949$ mT and 9.6 GHz.

A novel method for the interactive fitting of CW EPR spectra is presented below. This method allows a user to directly manipulate the simulated spectrum in an intuitive manner in order to achieve a fit to the experimental data. Peaks in the simulated spectrum are simply dragged and dropped to align them with the corresponding peaks in the experimental spectrum. As the features in the spectrum itself are manipulated rather than the spin Hamiltonian parameters, a detailed understanding of the relationship between the two is not required by the user.

The basic CW EPR simulation involves the search for the resonant field position, B_i , for each transition, i . The intensity, I_i , and linewidth, σ_i are calculated and with the resonant field define the peak $[B_i, I_i, \sigma_i]$. The simulated spectrum is then generated by adding each peak to the spectrum using an appropriate lineshape function.

With only a small amount of extra computation it is also possible to approximate the change in resonant field corresponding to a small change in each of the spin Hamiltonian parameters by computing partial derivatives of the energies using the Hellman-Feynman theorem:

$$\frac{\partial E_i}{\partial P_j} = \left\langle \Psi_i \left| \frac{\delta H}{\delta P_j} \right| \Psi_i \right\rangle, \quad (27)$$

$$\Delta B = \sum_{j=0}^n \frac{\partial B}{\partial P_j} \Delta P_j. \quad (28)$$

The linewidth can also be treated in an analogous manner by calculating the change in linewidth with respect to each of the linewidth parameters:

$$\Delta \sigma = \sum_{j=0}^n \frac{\partial \sigma}{\partial \sigma_j} \Delta \sigma_j. \quad (29)$$

Each peak — with resonant field, intensity, linewidth, and derivatives — is then stored in a temporary data structure. The spectrum can then be recalculated efficiently with small changes in the spin Hamiltonian parameters without the computationally expensive matrix diagonalizations used in the resonant field search algorithm.

The shortest possible vector in the parameter space that gives the desired changes in resonant field position and linewidth can then be calculated from the normal to the line/plane/etc defined in Eq. (28).

Figure 53 shows an experimental spectrum (green) calculated with this spin Hamiltonian and an initial “guess” (blue). Each arrow is generated by clicking on a feature in the simulation, moving the cursor, and dropping the feature at the new position. The x -component of the arrow is used to calculate the desired change in resonant field position, ΔB , and the y -component is used to calculate the change in linewidth, $\Delta \sigma$. ΔB and $\Delta \sigma$ are then used to calculate the changes to the spin Hamiltonian parameters ΔP_j and $\Delta \sigma_j$. The spectrum is then recalculated for the new spin Hamiltonian parameters. The process is repeated until a fit is achieved.

While it is not necessary for the user to have an understanding of the spin Hamiltonian and the relationship of the spin Hamiltonian parameters to the spectrum, the program provides useful information and feedback. The sensitivity of the field position of a peak to each of the spin Hamiltonian parameters can be determined from the derivatives.

Figure 54 shows the spin Hamiltonian parameters at each iteration in the fitting process depicted in Figure 53. Only five iterations are necessary to obtain good approximations of the spin Hamiltonian parameters for the experimental spectrum.

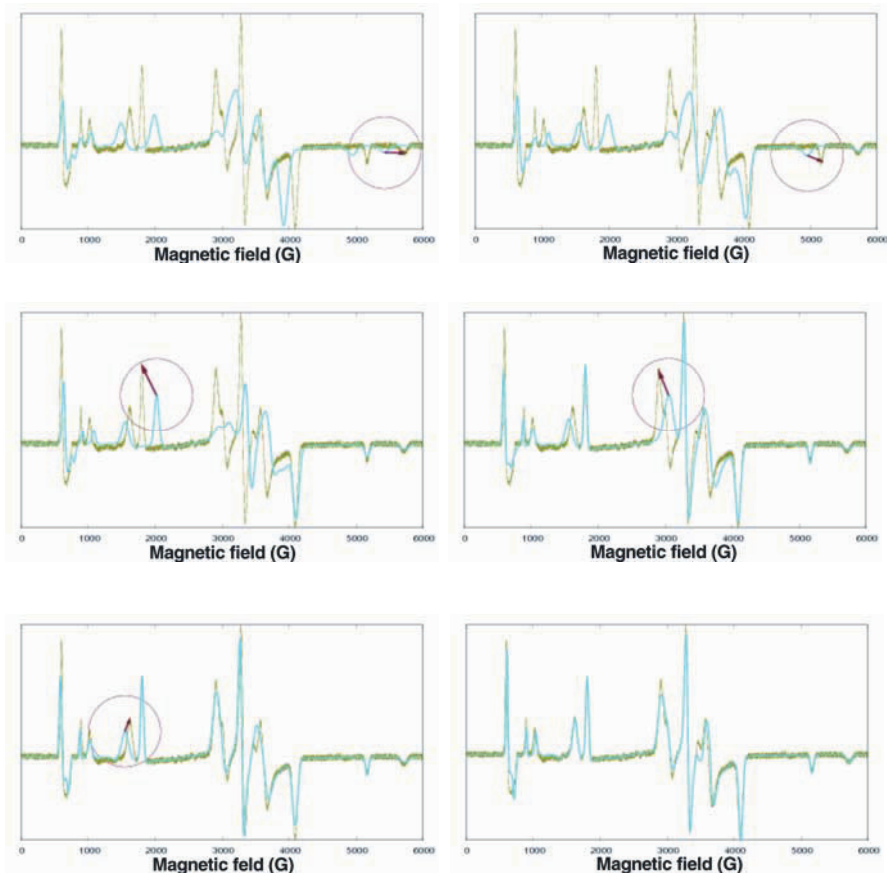


Figure 53. Progressive optimization of spectral simulation. Each step represents one correction of a peak position and linewidth. The arrow represents the desired shift in field position (x component) and the desired change in linewidth (y component).

In principle, the technique can also be extended to the fitting of pulsed EPR spectra using the frequency domain approach [62]. Each peak in the ESEEM spectrum is given by one or more frequencies, a complex intensity, and a linewidth. Derivatives of the ESEEM frequencies with respect to each of the spin Hamiltonian parameters can be calculated and utilized in an identical fashion to that used for CW spectra simulations.

Fully automated fitting of experimental spectra using this methodology is also possible. This requires an algorithm to identify features in both experimental and simulated spectra.

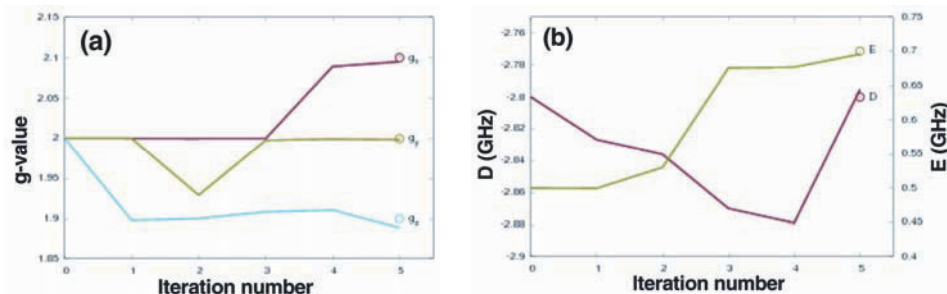


Figure 54. Spin Hamiltonian parameters as a function of the iteration number. Circles are the initial parameters used to generate the experimental spectrum: (a) g -values; (b) D and E values.

6. CONCLUSIONS

The Molecular Sophe software described herein provides scientists with an integrated tool for the determination of the molecular (geometric and electronic structure) of redox cofactors in metalloproteins and also other paramagnetic species found in other areas such as solid-state physics, materials science, nanotechnology, chemistry, biochemistry, microbiology, and medicine.

ACKNOWLEDGMENTS

We would like to thank the Australian Research Council and the EPR Division of Bruker Biospin for financial support.

REFERENCES

1. Pilbrow JR. 1990. *Transition ion electron paramagnetic resonance*. Oxford: Clarendon.
2. Mabbs FE, Collison DC. 1992. *Electron paramagnetic resonance of transition metal compounds*. Amsterdam: Elsevier.
3. Basosi R, Antholine WE, Hyde JS. 1993. Multifrequency ESR of copper: biophysical applications. In *Biological magnetic resonance*, Vol. 13, pp. 103–150. Ed LJ Berliner, J Reuben. New York: Plenum.
4. Hanson GR, Brunette AA, McDonnell AC, Murray KS, Wedd AG. 1981. *J Am Chem Soc* **103**:1953–1959.
5. Lebedev YS. 1994. *Appl Magn Reson* **7**:339–362.
6. Brunel LC. 1996. *Appl Magn Reson* **11**:417–423.
7. Reijerse EJ, vanDam PJ, Klaassen AAK, Hagen WR, van Bentum PJM, Smith GM. 1998. *Appl Magn Reson* **14**:153–167.

8. Schweiger A, Jeschke G. 2001. *Principles of pulse electron paramagnetic resonance*. Oxford: Oxford UP.
9. Frausto da Silva JJR, RJP Williams, eds. 2001. *The biological chemistry of the elements: the inorganic chemistry of life*. Oxford: Oxford UP.
10. Sigel H, ed. 1973. *Metal ions in biological systems*, New York: Marcel Dekker.
11. Bertini I, ed. 2006. *Biological inorganic chemistry: structure and reactivity*. Sausalito, CA: University Science Books.
12. Abragam A, Bleaney B. 1970. *Electron paramagnetic resonance of transition ions*. Oxford: Clarendon.
13. Bencini A, Gatteschi D. 1990. *EPR of exchange coupled systems*. Berlin: Springer-Verlag.
14. Smith TD, Pilbrow JR. 1974. *Coord Chem Rev* **13**:173–278.
15. Taylor PC, Baugher JF, Kriz HM. 1975. *Chem Rev* **75**:203–240.
16. Swalen JD, Gladney HM. 1964. *IBM J Res Dev* **8**:515–526.
17. Swalen JD, Lusebrink TRL, Ziessow D. 1973. *Magn Reson Rev* **2**:165–184.
18. Vancamp HL, Heiss AH. 1981. *Magn Reson Rev* **7**:1–40.
19. Gaffney BJ, Silverstone HJ. 1993. Simulation of the EMR spectra of high-spin iron in proteins. In *EMR of paramagnetic molecules*, pp. 1–57. Ed LJ Berliner, J Reuben. *Biological magnetic resonance*, Vol. 13. New York & London: Plenum.
20. Brumby S. 1980. *J Magn Reson* **39**:1–9.
21. Brumby S. 1980. *J Magn Reson* **40**:157–165.
22. Wang D, Hanson GR. 1996. *Appl Magn Reson* **11**:401–415.
23. Hanson GR, Gates KE, Noble CJ, Mitchell A, Benson S, Griffin M, Burrage K. 2003. XSophe–Sophe–XeprView: a computer simulation software suite for the analysis of continuous wave EPR spectra. In *EPR of free radicals in solids: trends in methods and applications*, pp. 197–237. Ed M Shiotani, A Lund. New York: Kluwer.
24. Hanson GR, Gates KE, Noble CJ, Griffin M, Mitchell A, Benson S. 2004. *J Inorg Biochem* **98**:903–916.
25. Griffin M, Muys A, Noble C, Wang D, Eldershaw C, Gates KE, Burrage K, Hanson GR. 1999. *Mol Phys Rep* **26**:60–84.
26. Heichel M, Höfer P, Kamlowski A, Griffin M, Muys A, Noble C, Wang D, Hanson GR, Eldershaw C, Gates KE, Burrage K. 2000. *Bruker Rep* **148**:6–9.
27. Hanson GR. 2003. XSophe release notes, 1.1.3. *Bruker Biospin*, pp 1–68.
28. Stoll S, Schweiger A. 2006. *J Magn Res* **178**:42.
29. Pilbrow JR. 1984. *J Magn Reson* **58**:186–203.
30. Sinclair GR. 1988. PhD thesis, Monash University.
31. Pilbrow JR, Sinclair GR, Hutton DR, Troup GJ. 1983. *J Mag Reson* **52**:386–399.
32. (a) Kaess H, Rautter J, Zweggart W, Struck A, Scheer H, Lubitz W. 1994. *J Phys Chem* **98**:354–363. (b) Kaess H, Rautter J, Boenigk B, Hofer P, Lubitz W. 1995. *J Phys Chem* **99**:436–448. (c) Lenzian F, Huber M, Isaacson RA, Endeward B, Plato M, Bonigk B, Mobius K, Lubitz W, Feher G. 1993. *Biochim Biophys Acta* **1183**:139–160. (d) Käss H, Bittersmann-Weidlich E, Andréasson L-E, Bönigk B, Lubitz W. 1995. *Chem Phys* **194**:419–432.
33. Thomann H, Goldfarb D, Bernardo M, Kroneck PMH, Ullrich V. 1995. *J Inorg Biochem* **59**:G01.
34. (a) Berliner LJ, Eaton SS, Eaton GR, eds. 2001. *Biological magnetic resonance: distance measurements in biological systems by EPR*, Vol. 19. New York: Kluwer Academic. (b) Jeschenke G, Pannier M, Spiess HW. 2001. Double electron–electron resonance. In *Biological magnetic resonance: distance measurements in biological systems*

- by EPR, Vol. 19, pp. 493–518. Ed LJ Berliner, SS Eaton, GR Eaton. New York: Kluwer Academic.
35. Wang D, Hanson GR. 1995. *J Magn Reson* **A117**:1–8.
 36. Belford RL, Nilges MJ. 1979. In *EPR Symposium 21st Rocky Mountain Conference*. Denver, Colorado.
 37. Maurice AM. 1980. PhD thesis, University of Illinois, Urbana.
 38. Nilges MJ. 1979. PhD thesis, University of Illinois, Urbana.
 39. Alderman DW, Solum MS, Grant DM. 1986. *J Chem Phys* **84**:3717–3725.
 40. Mombourquette MJ, Weil JA. 1992. *J Magn Reson* **99**:37–44.
 41. Stoll S. 2003. Easy-Spin: a software package for the computation of CW EPR and ENDOR spectra. *EPR News* **13**:24–26.
 42. van Veen G. 1978. *J Magn Reson* **38**:91–109.
 43. Gribnau MCM, van Tits JLC, Reijerse EJ. 1990. *J Magn Reson* **90**:474–485.
 44. Nettar D, Villafranca NI. 1985. *J Magn Reson* **64**:61–65.
 45. Scullane MI, White LK, Chasteen ND. 1982. *J Magn Reson* **47**:383–397.
 46. McGavin DG, Mombourquette MJ, Weil JA. 1993. *EPR ENDOR user's manual*. University of Saskatchewan, Saskatchewan, Canada.
 47. Belford GG, Belford RL, Burkhalter JF. 1973. *J Magn Reson* **11**:251–265.
 48. Anderson E, Bai Z, Bischof C, Demmel J, Dongarra J, Du Croz J, Greenbaum A, Hammarling S, McKenney A, Ostrouchov S, Sorensen D. 1992. *LAPACK users' guide*. Philadelphia: SIAM.
 49. Shalteil D, Low W. 1961. *Phys Rev* **124**:1062–1067.
 50. Jeener J. 1982. *Adv Magn Res* **10**:1–51.
 51. Drew SC, Hill JP, Lane I, Hanson GR, Gable RW, Young CG. 2007. *Inorg Chem* **46**:2373–2387.
 52. Drew SC, Young CG, Hanson GR. 2007. *Inorg Chem* **46**:2388–2397.
 53. Basu P, Bruck MA, Li Z, Dhawan IK, Enemark JH. 1995. *Inorg Chem* **34**:405–412.
 54. Dhawan IK, Enemark JH. 1996. *Inorg Chem* **35**:4873–4884.
 55. van den Brenk AL, Byriel KA, Fairlie DP, Gahan LR, Hanson GR, Hawkins CJ, Jones A, Kennard CHL, Moubaraki B, Murray KS. 1994. *Inorg Chem* **33**:3549–3547.
 56. van den Brenk AL, Fairlie DP, Hanson GR, Gahan LR, Hawkins CJ, Jones A. 1994. *Inorg Chem* **33**:2280–2289.
 57. Comba P, Cusack R, Fairlie DP, Gahan LR, Hanson GR, Kazmaier U, Ramlow A. 1998. *Inorg Chem* **37**:6721–6727.
 58. Bernhardt PV, Comba P, Fairlie DP, Gahan LR, Hanson GR, Lötzbeyer L. 2002. *Chem Eur J* **8**:1527–1536.
 59. van den Brenk AL, Tyndall JDA, Cusack RM, Jones A, Fairlie DP, Gahan LR, Hanson GR. 2004. *J Inorg Biochem* **98**:1857–1866.
 60. Comba P, Gahan LR, Haberhauer G, Hanson GR, Noble CJ, Seibold B, van den Brenk AL. 2008. *Chem Eur J* **14**:4393–4403.
 61. Smith SJ, Noble CJ, Palmer RC, Hanson GR, Schenk G, Gahan LR, Riley MJ. 2008. *J Biol Inorg Chem* **13**:499–510.
 62. Goldfarb D. 1998. *Mol Phys* **95**:1295–1308.

SPIN-HAMILTONIAN PARAMETERS FROM FIRST PRINCIPLE CALCULATIONS: THEORY AND APPLICATION

Frank Neese

*Lehrstuhl für Theoretische Chemie,
Institut für Physikalische und Theoretische Chemie,
Universität Bonn, Germany*

1. INTRODUCTION

EPR spectroscopists have refined the art of interpreting experimental results by means of an effective spin-Hamiltonian (SH) to a high degree of sophistication [1]. The SH parameters are the principal outcome of an EPR experiment and represent a concise summary of the information content of the experiments. However, the power of the SH approach extends far beyond summarizing experimental results. The SH describes the physics of spin systems so well that it can be used to creatively design new experiments. The behavior of the spin system can be simulated in advance through exact solutions of the quantum mechanical equations of motions in the SH formalism. In this respect it is of major utility that the SH is so simple—it usually works in a low-dimensional Hilbert space that is only spanned by the (effective) spin degrees of freedom of the system under investigation [2]. Due to this simplicity, exact solutions are relatively easy to generate with ordinary computational hardware, or, in many cases, just with paper and pencil. The price to pay for this invaluable convenience is that the SH contains adjustable parameters, the values of which are determined from fitting them to experimental measurements. Clearly, if the SH formalism is well designed, as in fact it is, there must be a direct connection between the SH parameters and the microscopic physics that governs the behavior of molecules under all conceivable circumstances [3]. Unfortunately, exact solutions to these microscopic (relativistic) wave equations are, with very few exceptions, out of the question. Thus, many different pathways exist that allow the matching of the SH parameters to the outcome of quantum chemical calculations at various levels of sophistication.

In order to more precisely state the nature of the problem, the leading spin-Hamiltonian parameters are briefly introduced. The SH is an effective Hamiltonian

and contains only spin-variables of a “fictitious” electron spin S and the nuclear spins I_A, I_B, \dots . All reference to the spatial part of the many-electron wavefunction and therefore to detailed molecular electronic and geometric structure is implicitly contained in the well-known SH parameters \mathbf{D} (zero-field splitting), \mathbf{g} (g -tensor) \mathbf{A} (hyperfine coupling), \mathbf{Q} (quadrupole coupling), $\boldsymbol{\sigma}$ (chemical shift), and \mathbf{J} (spin–spin coupling), which are considered as adjustable parameters in the analysis of experiments and which will be explained in detail below. Thus, the SH is “a convenient place to rest” in the analysis of experimental data by theoretical means [4]. The SH that includes the interactions covered above is [1,2,5,6]

$$\hat{H}_{SPIN} = \hat{\mathbf{S}}\mathbf{D}\hat{\mathbf{S}} + \beta\mathbf{B}\mathbf{g}\hat{\mathbf{S}} + \sum_A \left[\hat{\mathbf{S}}\mathbf{A}^{(A)}\hat{\mathbf{I}}^{(A)} + \beta_N \mathbf{B}\mathbf{g}_N^{(A)}\hat{\mathbf{I}}^{(A)} + \hat{\mathbf{I}}^{(A)}\mathbf{Q}^{(A)}\hat{\mathbf{I}}^{(A)} \right] + \sum_{A < B} \left[\hat{\mathbf{I}}^{(A)}\mathbf{J}^{(AB)}\hat{\mathbf{I}}^{(B)} \right], \quad (1)$$

where the sum over “ A ” refers to the magnetic nuclei, \mathbf{B} is the magnetic flux density and β and β_N are the electronic and nuclear Bohr magneton, respectively. The SH acts on a basis of product functions $|SM_S\rangle \otimes |I^{(A)}M_I^{(A)}\rangle \otimes \dots \otimes |I^{(N)}M_I^{(N)}\rangle$. For not too many spins this basis is often small enough to allow for exact diagonalization of the SH and therefore exact quantum mechanical treatments of the spin-physics in the SH framework. For high-dimensional SH problems, both brute-force [7] and a variety of perturbation theoretical methods can be employed in order to arrive at exact or good approximate solutions.

The role of theory is then to derive the connection of first-principle electronic structure approaches to the SH parameters and to devise practical algorithms for the prediction of the values of these parameters. In this way, calculations can help to develop the full information content of spectra and thus allow conclusions about the geometric and electronic structure of the system under investigation to be drawn.

In the past ten years, our group has contributed to this line of research through development of theoretical methods and their use in a number of collaborative studies. As a result of the development work, the methods described below have been implemented in the general purpose quantum chemical program package ORCA [8], which is available free of charge to the academic community. We hope that this chapter contributes to a more widespread use of quantum chemical methods in EPR spectroscopy by showing that for many EPR properties quite acceptable results can be obtained for many molecules of current interest. In fact, as of today, the programs have matured to an extent that they can be productively and creatively used by non-experts. The second purpose of this chapter is to provide a brief introduction into the presently most commonly used techniques. It is hoped that this will help the reader to appreciate the fundamental physical content of the calculations. Third, the chapter is meant to illustrate the scope and opportunities of the currently available approaches with some examples taken from recent studies performed in our group. However, this chapter is not meant to be a comprehensive review of the literature on theory and application of SH parameters. Such treat-

ments can be found elsewhere [3,9–15] Also, in order to keep the size of the chapter within reasonable bounds, the theory of NMR parameters (chemical shift tensor and spin–spin coupling in Eq. (1)) will not be covered. It is mentioned, however, that precisely analogous techniques as the ones explained below are used in this large field of investigation (see, e.g., the chapters in [14] dealing with NMR spectroscopy).

Present-day electronic structure theory is—at least in the applied domain—somewhat dominated by the methods of density functional theory (DFT) [16]. Consequently, the majority of the chapter will deal with this very successful approach since most of the readers are likely to use DFT methods in their own applications. However, it would be a misconception to use the terms “quantum chemistry” and “DFT” interchangeably, as appears to be widely practiced. In fact, there are good reasons to believe that *ab initio* methods based on Hartree–Fock (HF) theory [17] will regain more importance in the future, and we at least want to hint at their existence as alternatives to DFT at this point.

2. ELECTRONIC STRUCTURE THEORY OF SPIN-HAMILTONIAN PARAMETERS

In this section the basic theory of EPR SH parameters is presented in the way it is implemented in contemporary electronic structure program packages such as the ORCA [8], Gaussian03 [18], Dalton [19], ADF [20], or MagRespect [21] programs, all of which have significant but differing capabilities in the prediction of EPR properties. Since it is not assumed that the readers are experts in quantum chemistry, it is necessary to briefly introduce the underlying theory of N -electron systems. Some practical advice for performing the calculations will be provided in §2.6. This section should be reasonably self-contained and does not require the detailed study of the more formal material that is contained in §§2.1–2.5.

2.1. Electronic Structure Methods

In order to introduce the subject of electronic structure methods, we start from the Born–Oppenheimer (BO) Hamilton operator, which only considers the leading electrostatic interactions (in atomic units) [17,22]:

$$\begin{aligned}\hat{H}_{BO} &= -\frac{1}{2} \sum_i \nabla_i^2 - \sum_{i,A} \frac{Z_A}{|\mathbf{r}_i - \mathbf{R}_A|} + \frac{1}{2} \sum_{i \neq j} \frac{1}{|\mathbf{r}_i - \mathbf{r}_j|} + \frac{1}{2} \sum_{A \neq B} \frac{Z_A Z_B}{|\mathbf{R}_A - \mathbf{R}_B|} \\ &= \hat{T} + \hat{V}_{eN} + \hat{V}_{ee} + \hat{V}_{NN} \\ &= \hat{h} + \hat{V}_{ee} + \hat{V}_{NN}.\end{aligned}\tag{2}$$

The terms describe the kinetic energy of the electrons, the electron–nuclear attraction, the electron–electron repulsion, and the nuclear–nuclear repulsion, respectively. In Eq. (2), i, j sum over electrons at positions \mathbf{r}_i , A, B over nuclei with

charge Z_A at positions \mathbf{R}_A . The nuclear positions are assumed to be fixed and the electrons supposed to readjust immediately to the positions of these (classical) nuclei. The BO-operator contains just the leading electrostatic interactions between the negatively charged electrons and the positively charged nuclei. It accounts for the vast amount of the molecular total energy, and most problems of chemical structure and energetics can be satisfactorily discussed in terms of these comparatively simple interactions. Yet, the BO-operator contains the coupled motion of N -electrons and to find the exact eigenfunctions and eigenvalues of the (time-independent) BO-Schrödinger equation,

$$\hat{H}_{BO} \Psi(\mathbf{x}_1, \dots, \mathbf{x}_N | \mathbf{R}) = E(\mathbf{R}) \Psi(\mathbf{x}_1, \dots, \mathbf{x}_N | \mathbf{R}), \quad (3)$$

is a hopelessly complicated task for any but the simplest systems. In Eq. (3) the many-electron wavefunction $\Psi(\mathbf{x}_1, \dots, \mathbf{x}_N | \mathbf{R})$ has been introduced, which depends on the space (r) and spin (σ) variables of the N -electrons ($\mathbf{x}_i \equiv (\mathbf{r}_i, \sigma_i)$). \mathbf{R} collectively denotes the positions of the nuclei on which the many-electron wavefunction and the eigenvalues $E(\mathbf{R})$ depend parametrically. According to basic quantum theory, everything that can be known about the molecular system in the time-independent case is contained in $\Psi(\mathbf{x}_1, \dots, \mathbf{x}_N | \mathbf{R})$. It is also important to note that *all* measurements always probe the N -electron system. Molecular orbitals (MOs) to be introduced below are *never* observable, and, in fact, the entire theory of molecules can be exactly formulated without any recourse to orbitals. Yet, MOs are very convenient building blocks in the majority of approximate methods that have been developed to date.

MOs first appear in the framework of the Hartree–Fock (HF) method, which is a mean-field treatment [17,22]. The basic idea is to start from an N -particle wavefunction that is appropriate for a system of non-interacting electrons. Having fixed the *Ansatz* for the N -particle wavefunction in this way, the variational principle is used in order to obtain the best possible approximation for the fully interacting system. Such “independent particle” wavefunctions are Slater-determinants, which consist of antisymmetrized products of single-particle wavefunctions $\{\psi(\mathbf{x})\}$ (the antisymmetry brought about by the determinantal form is essential in order to satisfy the Pauli principle). Thus, the Slater-determinant is written as

$$\Psi(\mathbf{x}_1, \dots, \mathbf{x}_N) = \det|\psi_1 \dots \psi_N|, \quad (4)$$

and is abbreviated as $|\psi_1 \dots \psi_N|$. The HF approach consists of varying the shapes of these orbitals in order to minimize the Rayleigh-functional $\langle \Psi | \hat{H}_{BO} | \Psi \rangle / \langle \Psi | \Psi \rangle$. The result is an upper bound to the total molecular energy. The minimization leads to the following pseudo-single-particle equations (HF-equations) that must be fulfilled by the orbitals $\psi_i(\mathbf{x})$:

$$\hat{F} \psi_i = \left[\hat{h} + \sum_j \hat{J}_j - \hat{K}_j \right] \psi_i = \varepsilon_i \psi_i. \quad (5)$$

Here ε_i is the orbital energy for the i th MO. The Coulomb and exchange operators \hat{J}_j and \hat{K}_j are defined by their actions on an orbital $\psi_i(\mathbf{x})$:

$$\hat{J}_j \psi_i(\mathbf{x}) = \psi_i(\mathbf{x}) \int \frac{|\psi_j(\mathbf{x}')|^2}{|\mathbf{r} - \mathbf{r}'|} d\mathbf{x}', \quad (6)$$

$$\hat{K}_j \psi_i(\mathbf{x}) = \psi_j(\mathbf{x}) \int \frac{\psi_j^*(\mathbf{x}') \psi_i(\mathbf{x}')}{|\mathbf{r} - \mathbf{r}'|} d\mathbf{x}'. \quad (7)$$

The HF equations describe the motion of electrons in the field of the nuclei and the average field of the other electrons (hence the name “mean-field” treatment). The HF equations are a major simplification of the N -electron problem. However, this simplification comes at the price of introducing a coupled set of nonlinear equations—the Coulomb- and exchange-operators depend on the eigenfunctions of the Fock operator, which are unknown before the HF-equations are solved. Thus, an iterative approach is necessary. In practice it is not even possible to solve the HF equations exactly since the orbitals assume fairly complicated shapes. Therefore, one commonly introduces a set of auxiliary one-electron functions $\{\varphi(\mathbf{x})\}$ (basis functions) that are used to expand the orbitals:

$$\psi_i(\mathbf{x}) = \sum_{\mu} c_{\mu i} \varphi_{\mu}(\mathbf{x}). \quad (8)$$

Now, minimization is performed with respect to the coefficients $c_{\mu i}$ while the basis functions are held fixed. The expansion is only exact in the limit of a mathematically complete basis set $\{\varphi(\mathbf{x})\}$, which is impossible to obtain in practice. Thus, the results depend on the size and nature of the employed basis functions, but there is a well-defined *basis set limit*. Since the BO-operator is spin free, it is customary to let the orbitals be eigenfunctions of the single-electron spin-operator by choosing them to be either spin-up or spin-down orbitals. This leads to the spin-unrestricted (UHF) method ($\sigma = \alpha, \beta$):

$$\hat{F}^{\sigma} \psi_i^{\sigma} = \left[\hat{h} + \sum_{j\sigma'} \hat{J}_j^{\sigma'} - \delta_{\sigma\sigma'} \hat{K}_j^{\sigma} \right] \psi_i^{\sigma} = \varepsilon_i^{\sigma} \psi_i^{\sigma}. \quad (9)$$

For a closed-shell system, the spin-up and spin-down Fock operators are equal and the spin-orbitals are obtained in pairs of equal shape and energy. Instead of dividing the set of orbitals into spin-up and spin-down orbitals, it is also possible to pursue a division into closed-shell and open-shell orbitals. This leads to the restricted open-shell HF (ROHF) method [23–25]. The formalism for this method is slightly more involved than the UHF formalism, but the general ideas are identical. The ROHF wavefunction is an eigenfunction of the total spin squared (\hat{S}^2) operator, while the UHF wavefunction does not have this feature. The energy of the UHF wavefunction, on the other hand, is lower than that of the ROHF wavefunc-

tion due to the increased variational freedom in the UHF case. The matrix elements of the Fock-operator become in the UHF case

$$F_{\mu\nu}^{\sigma} = h_{\mu\nu} + \sum_{\kappa\tau} P_{\kappa\tau} (\mu\nu | \kappa\tau) - P_{\kappa\tau}^{\sigma} (\mu\kappa | \nu\tau). \quad (10)$$

With the one- and two-electron integrals over basis functions being defined as

$$h_{\mu\nu} = \int \varphi_{\mu}(\mathbf{r}) \hat{h} \varphi_{\nu}(\mathbf{r}) d\mathbf{r}, \quad (11)$$

$$(\mu\nu | \kappa\tau) = \iint \varphi_{\mu}(\mathbf{r}_1) \varphi_{\nu}(\mathbf{r}_1) \frac{1}{|\mathbf{r}_1 - \mathbf{r}_2|} \varphi_{\kappa}(\mathbf{r}_2) \varphi_{\tau}(\mathbf{r}_2) d\mathbf{r}_1 d\mathbf{r}_2. \quad (12)$$

Here, the “density matrix” was introduced:

$$P_{\mu\nu}^{\sigma} = \sum_i c_{\mu i}^{\sigma} c_{\nu i}^{\sigma}. \quad (13)$$

The sum over i is restricted to the occupied MOs with spin σ and consists of N_{α} and N_{β} terms for spin-up and spin-down, respectively. The total density matrix is $\mathbf{P} = \mathbf{P}^{\alpha} + \mathbf{P}^{\beta}$ in terms of which the electron density at point \mathbf{r} can be written

$$\rho(\mathbf{r}) = \sum_{\mu\nu} P_{\mu\nu} \varphi_{\mu}(\mathbf{r}) \varphi_{\nu}(\mathbf{r}). \quad (14)$$

In the context of EPR spectroscopy it is also important to define the spin-density matrix $\mathbf{P}^{\alpha-\beta} = \mathbf{P}^{\alpha} - \mathbf{P}^{\beta}$ in terms of which $\rho^{\alpha-\beta}(\mathbf{r}) = \sum_{\mu\nu} P_{\mu\nu}^{\alpha-\beta} \varphi_{\mu}(\mathbf{r}) \varphi_{\nu}(\mathbf{r})$. In the finite basis set, the UHF equations assume the form of a pseudo-eigenvalue problem:

$$\mathbf{F}^{\sigma}(\mathbf{c})\mathbf{c}^{\sigma} = \epsilon\mathbf{S}\mathbf{c}. \quad (15)$$

\mathbf{S} is the overlap matrix $S_{\mu\nu} = (\mu | \nu)$ and ϵ is a diagonal matrix of orbital energies. \mathbf{F} has been written as $\mathbf{F}^{\sigma}(\mathbf{c})$ to emphasize the fact that \mathbf{F} depends on its own eigenvectors, which emphasizes the iterative nature of the problem. The total energy of the UHF-approximation is

$$\begin{aligned} E_{UHF} &= \frac{1}{2} \sum_{\mu\nu} P_{\mu\nu}^{\alpha} (h_{\mu\nu} + F_{\mu\nu}^{\alpha}) + P_{\mu\nu}^{\beta} (h_{\mu\nu} + F_{\mu\nu}^{\beta}) \\ &= \sum_{\mu\nu} P_{\mu\nu} h_{\mu\nu} + \frac{1}{2} \sum_{\kappa\tau} \left[P_{\mu\nu} P_{\kappa\tau} (\mu\nu | \kappa\tau) - (\mu\kappa | \nu\tau) (P_{\mu\nu}^{\alpha} P_{\kappa\tau}^{\alpha} + P_{\mu\nu}^{\beta} P_{\kappa\tau}^{\beta}) \right] + V_{NN}. \end{aligned} \quad (16)$$

This equation shows clearly that the nonlocal exchange “interaction” is only present for electrons of the same spin.

HF calculations can nowadays be performed with reasonable basis sets for quite large molecules. On standard personal computers, molecules with up to ~500 atoms are within reach, and using state-of-the-art linear scaling technology [26,27] even systems with more than a thousand atoms can be studied. In the basis set limit

the HF methods recover typically around 99% of the total molecular energy. Unfortunately, even the remaining error is still very large on the chemical scale and amounts to hundreds of kcal/mol. Thus many properties cannot be accurately enough predicted by HF theory. Since the HF method describes a mean-field approach to the N -electron problem, the residual error is called *correlation error*, and a very large amount of work has gone into calculating the so-called correlation energy, which is the difference between the exact eigenvalue of the BO-Hamiltonian and the HF-energy. If one follows the ab initio philosophy, one starts from the HF solution and tries to calculate the correlation energy using a variety of approaches such as configuration interaction (CI), many-body perturbation theory (MBPT; also known as Møller–Plesset perturbation theory; the simplest approximation is the second-order estimate, widely known as MP2), or the powerful coupled-cluster (CC) theory (for an introduction see [28,29]). Such “correlated ab initio approaches,” if taken far enough, can systematically and reliably approach the exact BO-results. However, they are known to be notoriously expensive in terms of computational resource requirements. There is good hope, however, that very good approximations to the rigorous ab initio methods will be made available in the foreseeable future even for large molecules owing to the development of so-called *linear scaling* approaches [30–36].

A radically different approach to the N -electron problem is provided by density functional theory [16,37]. Owing to the celebrated Hohenberg–Kohn theorems it is known that, *in principle*, the knowledge of $\rho(\mathbf{r})$ is already sufficient in order to deduce the exact ground state energy. This comes at the price of introducing an unknown exchange–correlation functional $E_{xc}[\rho]$. Since a systematic procedure to approach the exact $E_{xc}[\rho]$ appears to be unknown, physically motivated guesses have to be introduced. Over the years, many such approximations have been suggested and new functionals appear in the literature almost on a weekly basis. Unfortunately, each functional has its own strengths and weaknesses, which need to be assessed through extensive series of test calculations.

Without going into much detail, it is noted that the so-called Kohn–Sham procedure allows one to solve a set of pseudo-single-particle equations that would provide the exact ground state energy if the exact $E_{xc}[\rho]$ would be known. This procedure introduces the so-called “non-interacting reference system” which is described by a single Slater determinant and that shares with the physical system the electron density calculated through Eq. (14). The spin-unrestricted Kohn–Sham equations look similar to the UHF equations. In a finite basis set they read (upon dividing the electron density into its spin components $\rho^\alpha(\mathbf{r})$ and $\rho^\beta(\mathbf{r})$):

$$F_{\mu\nu}^\sigma = h_{\mu\nu} + \sum_{\kappa\tau} P_{\kappa\tau}(\mu\nu|\kappa\tau) + \int \varphi_\mu(\mathbf{r})\varphi_\nu(\mathbf{r})V_{xc}^\sigma[\rho^\alpha, \rho^\beta](\mathbf{r})d\mathbf{r}. \quad (17)$$

Thus, in place of the HF exchange term, there now appears a *local* exchange–correlation potential, which is defined as the functional derivative of $E_{xc}[\rho^\alpha, \rho^\beta]$ with respect to $\rho(\mathbf{r})$:

$$V_{XC}^{\sigma}[\rho^{\alpha}, \rho^{\beta}](\mathbf{r}) = \frac{\delta E_{XC}[\rho]}{\delta \rho^{\sigma}(\mathbf{r})} \quad (\sigma = \alpha, \beta). \quad (18)$$

The total Kohn–Sham energy is

$$E_{UKS} = \sum_{\mu\nu} P_{\mu\nu} h_{\mu\nu} + \frac{1}{2} \sum_{\kappa\tau} P_{\mu\nu} P_{\kappa\tau} (\mu\nu | \kappa\tau) + E_{XC}[\rho^{\alpha}, \rho^{\beta}] + V_{NN}. \quad (19)$$

The second term consists of the Coulombic self-interaction of the electron cloud and can be written in a perhaps somewhat more illuminating way as

$$E_J = \frac{1}{2} \iint \rho(\mathbf{r}_1) \frac{1}{|\mathbf{r}_1 - \mathbf{r}_2|} \rho(\mathbf{r}_2) d\mathbf{r}_1 d\mathbf{r}_2. \quad (20)$$

Likewise, the Coulomb contribution to the Kohn–Sham matrix is

$$\begin{aligned} J_{\mu\nu} &= \iint \varphi_{\mu}(\mathbf{r}_1) \varphi_{\nu}(\mathbf{r}_1) \frac{1}{|\mathbf{r}_1 - \mathbf{r}_2|} \rho(\mathbf{r}_2) d\mathbf{r}_1 d\mathbf{r}_2 \\ &= \iint \varphi_{\mu}(\mathbf{r}) \varphi_{\nu}(\mathbf{r}) V_C(\mathbf{r}) d\mathbf{r}, \end{aligned} \quad (21)$$

which emphasizes the local nature of the Coulomb potential $V_C(\mathbf{r})$. Since this potential is of long range, its calculation usually dominates the computational effort of an HF or KS calculation. The precise functional forms of the various approximations to $E_{XC}[\rho^{\alpha}, \rho^{\beta}]$ are complicated and involve “odd powers” of $\rho(\mathbf{r})$ such as $\rho(\mathbf{r})^{4/3}$. If the functional also depends on the gradient of ρ ($\vec{\nabla}\rho(\mathbf{r})$), one obtains functionals from the “generalized gradient approximation” (GGA) family. Modern functionals may also depend on the Laplacian of the density ($\vec{\nabla}^2\rho(\mathbf{r})$) and the kinetic energy density ($\tau(\mathbf{r})$), which leads to the family of “meta-GGA” functionals. In recent years, so called “hybrid functionals” have become very popular, which involve a fraction of the nonlocal Hartree–Fock exchange, and this was found to improve the results for total energies as well as many molecular properties [16].

There are many important conceptual and practical subtleties in DFT that cannot be discussed in the framework of this chapter, and the interested reader is referred to the specialist literature [16,37].

2.2. Additional Terms in the Hamiltonian

Given an approximation to the ground state energy of the BO-Hamiltonian by some method, one needs to introduce the smaller field- and spin-dependent terms in the Hamiltonian that give rise to the interactions one actually probes by EPR spectroscopy. These terms can be derived through relativistic quantum chemistry, which is outside the scope of this chapter. Among the many terms that arise, we will mainly need the following interactions:

a. The spin-orbit coupling. Unlike as found in many textbooks, this term in the Hamiltonian is of a *two*-electron nature and reads within the Breit–Pauli approximation (for a detailed discussion see [38–41]):

$$\hat{H}_{SOC} = \hat{H}_{SOC}^{(1)} + \hat{H}_{SOC}^{(2)}, \quad (22)$$

$$\hat{H}_{SOC}^{(1)} = \sum_i \hat{h}_i^{1el-SOC} = \sum_i \hat{\mathbf{h}}_i^{1el-SOC} \hat{\mathbf{s}}_i = \frac{\alpha^2}{2} \sum_i \sum_A Z_A r_{iA}^{-3} \hat{\mathbf{l}}_{iA} \hat{\mathbf{s}}_i, \quad (23)$$

$$\hat{H}_{SOC}^{(2)} = \hat{H}_{SSO}^{(2)} + \hat{H}_{SOO}^{(2)} = \sum_i \sum_{j \neq i} \hat{\mathbf{g}}_{i,j}^{2el-SOC} = -\frac{\alpha^2}{2} \sum_i \sum_{j \neq i} r_{ij}^{-3} \hat{\mathbf{l}}_{ij} (\hat{\mathbf{s}}_i + 2\hat{\mathbf{s}}_j). \quad (24)$$

Here, $\alpha = c^{-1}$ in atomic units is the fine structure constant ($\sim 1/137$), $\hat{\mathbf{r}}_i, \hat{\mathbf{p}}_i, \hat{\mathbf{s}}_i$ are the position, momentum, and spin operators of the i th electron, and $\hat{\mathbf{l}}_{iA} = (\hat{\mathbf{r}}_i - \mathbf{R}_A) \times \hat{\mathbf{p}}_i$ is the angular momentum of the i th electron relative to nucleus A . The vector $\hat{\mathbf{r}}_{iA} = \hat{\mathbf{r}}_i - \mathbf{R}_A$ of magnitude r_{iA} is the position of the i th electron relative to atom A . Likewise, the vector $\hat{\mathbf{r}}_{ij} = \hat{\mathbf{r}}_i - \hat{\mathbf{r}}_j$ of magnitude r_{ij} is the position of the i th electron relative to electron j and $\hat{\mathbf{l}}_{ij} = (\hat{\mathbf{r}}_i - \hat{\mathbf{r}}_j) \times \hat{\mathbf{p}}_i$ is its angular momentum relative to this electron. The one-electron term is familiar from many phenomenological treatments, for example, in atomic spectroscopy and ligand field theory [4,42]. The two-electron term has contributions from the spin-same-orbit (SSO) and spin-other-orbit (SOO) terms, which are both important for a quantitatively correct treatment of SOC. They essentially provide a screening of the one-electron term in much the same way as the nuclear–electron attraction and electron–electron repulsion contributions counteract each other in the Born–Oppenheimer Hamiltonian. Since the full SOC operator is difficult to handle in large-scale molecular applications, it is desirable to approximate it as accurately as possible. This is possible through the spin-orbit mean-field approximation (SOMF) developed by Hess et al. [38–40,43]. Without going into the details of the derivation we merely state the form of this operator discussed recently [41,44]:

$$\hat{h}^{SOMF} = \sum_i \hat{\mathbf{z}}^{SOMF}(i) \hat{\mathbf{s}}(i), \quad (25)$$

with the matrix elements of the k th component of the SOMF operator given by

$$\begin{aligned} \langle \varphi_\mu | \hat{z}_k^{SOMF} | \varphi_\nu \rangle &= \langle \varphi_\mu | \hat{h}_k^{1el-SO} | \varphi_\nu \rangle \\ &+ \left[\sum_{\kappa\tau} P_{\kappa\tau} \left(\varphi_\mu \varphi_\nu | \hat{\mathbf{g}}_k^{SO} | \varphi_\kappa \varphi_\tau \right) \right. \\ &\left. - \frac{3}{2} \left(\varphi_\mu \varphi_\kappa | \hat{\mathbf{g}}_k^{SO} | \varphi_\tau \varphi_\nu \right) - \frac{3}{2} \left(\varphi_\tau \varphi_\nu | \hat{\mathbf{g}}_k^{SO} | \varphi_\mu \varphi_\kappa \right) \right] \end{aligned} \quad (26)$$

and

$$\hat{h}_k^{\text{rel-SO}}(\mathbf{r}_i) = \frac{\alpha^2}{2} \sum_i \sum_A Z_A r_{iA}^{-3} \hat{\mathbf{l}}_{iA;k}, \quad (27)$$

$$\hat{g}_k^{\text{SO}}(\mathbf{r}_i, \mathbf{r}_j) = -\frac{\alpha^2}{2} \hat{\mathbf{l}}_{ij;k} r_{ij}^{-3}. \quad (28)$$

Here, \mathbf{P} is the total charge density matrix calculated by some theoretical method. Essentially like the HF approximation, which gives 99% of the total molecular energy, the SOMF operator covers around 99% of the two-electron SOC operator. It will be exclusively used below in order to approximate the SOC terms that will arise in the equations for the SH parameters.

b. The direct magnetic dipolar spin-spin interaction. This interaction is described by a genuine two-electron operator of the form:[45]

$$\hat{H}_{SS} = \frac{g_e^2 \alpha^2}{8} \sum_{i \neq j} \left[\frac{\hat{s}_i \hat{s}_j}{r_{ij}^3} - 3 \frac{(\hat{s}_i \mathbf{r}_{ij})(\hat{s}_j \mathbf{r}_{ij})}{r_{ij}^5} \right], \quad (29)$$

where the free-electron g -value $g_e = 2.002319\dots$ appears.

c. The hyperfine coupling. This term describes the well-known dipolar-interaction between the electron spin and the nuclear spins [45]:

$$\hat{H}_{SI} = \frac{\alpha}{2} g_e \beta_N \sum_A g_N^{(A)} \sum_i \left[\frac{\mathbf{s}_i \hat{\mathbf{I}}^{(A)}}{r_{iA}^3} - 3 \frac{(\mathbf{s}_i \mathbf{r}_{iA})(\hat{\mathbf{I}}^{(A)} \mathbf{r}_{iA})}{r_{iA}^5} \right]. \quad (30)$$

Here, β_N is the nuclear magneton, $g_N^{(A)}$ is the g -value of the A th nucleus, and $\hat{\mathbf{I}}^{(A)}$ is the spin-operator for the nuclear spin of the A th nucleus. While the isotropic Fermi contact term is frequently introduced as a separate operator, it arises naturally as a boundary term in the partial integration of the singular operator in Eq. (30).

d. The nuclear-orbit interaction. The interaction of the nuclear spin with the orbital angular momentum of the electrons leads to the following term in the Hamiltonian [45,46]:

$$\hat{H}_{LI} = \frac{\alpha}{2} \beta_N \sum_A g_N^{(A)} \sum_i \frac{\mathbf{l}_i^A \hat{\mathbf{I}}^{(A)}}{r_{iA}^3}. \quad (31)$$

e. The quadrupole coupling. The quadrupole coupling describes the interaction of the electric field gradient (EFG) at a given nucleus with the quadrupole moment of that nucleus (only present for nuclei with spin $I > 1/2$). The electronic quantity of interest is the field gradient operator. The quadrupole interaction may be written as an operator of the following form [47]:

$$\hat{H}_Q = e^2 \sum_{A,i} Q^{(A)} \hat{\mathbf{I}}^{(A)} \hat{\mathbf{F}}^{(A)}(i) \hat{\mathbf{I}}^{(A)}, \quad (32)$$

where $Q^{(A)}$ is the quadrupole moment of the A th nucleus, e is the elementary charge, and the field gradient operator is given by

$$\hat{F}_{\mu\nu}^{(A)}(i) = \frac{r_{iA}^2 \delta_{\mu\nu} - 3r_{iA,\mu} r_{iA,\nu}}{r_{iA}^5}. \quad (33)$$

f. The electronic Zeeman-interaction. The interaction of the electrons with a static external magnetic field is described by [48]

$$\hat{H}_{LB} = \frac{\alpha}{2} \sum_i \mathbf{B}(\mathbf{I}_i + g_e \hat{\mathbf{s}}_i). \quad (34)$$

From the fully relativistic treatment there arises a “kinetic energy correction” (relativistic mass correction) to the spin-Zeeman energy that is given by [45]

$$\hat{H}_{SB}^{RMC} = \frac{\alpha^3 g_e}{2} \sum_i \nabla_i^2 \mathbf{B} \mathbf{s}_i. \quad (35)$$

2.3. Sum-Over States Theory of SH Parameters

In general, a ground state with total spin S gives rise to $2S + 1$ “magnetic sub-levels” with $M_S = S, S - 1, \dots, -S$. At the level of the BO-Hamiltonian these $2S + 1$ sublevels are all degenerate. Upon introduction of the additional terms from §2.2 (collectively denoted as \hat{H}_1) this degeneracy is lifted and the task at hand is to describe the splittings of the magnetic sublevels through an effective Hamiltonian of the same form as the SH. An illuminating approach has been outlined by McWeeny [22,48,49], and as in previous works [50–54] it is followed here in order to give formally exact expressions of the various terms that arise in the SH. Suppose that the entire spectrum of exact eigenfunctions of the BO-Hamiltonian is available and the effect of the much smaller additional terms is to be introduced through perturbation theory. The ground state many-electron wavefunction is denoted as $|0SM\rangle$ and the excited states are written as $|bS'M'\rangle$, where b is a compound index that summarizes everything that is necessary in order to unambiguously identify the given excited state of total spin S' and magnetic quantum number M' . In order for the perturbation theory to be valid, it is assumed that the energy separation $\Delta_b = E_b - E_0$ with

$$E_b = \langle bS'M' | \hat{H}_{BO} | bS'M'' \rangle = \delta_{M'M''} \langle bS'S' | \hat{H}_{BO} | bS'S' \rangle \quad (36)$$

much larger than the matrix elements of the additional terms in the Hamiltonian. Since for a reasonably well-isolated ground state Δ_b is on the order of thousands of

wavenumbers, and the additional terms are on the order of at most a few hundred wavenumbers, this is in most cases a reasonable assumption. Using the partitioning theory outlined in detail elsewhere [50,52], the effective Hamiltonian in the space of the magnetic sublevels becomes second order:

$$\begin{aligned} & \langle 0SM | \hat{H}_{eff} | 0SM' \rangle \\ &= E_0 \delta_{MM'} + \langle 0SM | \hat{H}_1 | 0SM' \rangle \\ & - \sum_{bS'M''} \Delta_b^{-1} \langle 0SM | \hat{H}_1 | bS'M'' \rangle \langle bS'M'' | \hat{H}_1 | 0SM' \rangle. \end{aligned} \quad (37)$$

The first term on the right-hand side is the total energy of the reference state and might be dropped since it does not lead to splittings between the magnetic sublevels. The second term is of first order in perturbation theory, and the third term is of second order and involves an infinite sum over excited states. The task to deduce the correct expressions of the SH parameters from this equations involves a considerable amount of algebra that is not carried out here [50,52]. Basically, one looks at operators or pairs of operators that carry the same spin- or field terms as the corresponding terms in the SH. Next, one studies whether these terms have the same M , M' , and M'' dependence as the corresponding SH terms. This is best done through the application of the Wigner–Eckart theorem (for detailed derivations see [9,22,46,48–53]). The results are the following formally exact second-order expressions for the various SH parameters (note that in all the expressions below only the “standard components” of each multiplet with $M=S$ appear):

a. Zero-Field Splitting. The ZFS consists of a first-order term arising from the direct spin–spin interaction [45]:

$$D_{\mu\nu}^{(SS)} = \frac{1}{2} \frac{\alpha^2}{S(2S-1)} \left\langle 0SS \left| \sum_i \sum_{j \neq i} \frac{r_{ij}^2 \delta_{\mu\nu} - 3(\mathbf{r}_{ij})_\mu (\mathbf{r}_{ij})_\nu}{r_{ij}^5} \{ 2\hat{s}_{zi}\hat{s}_{zj} - \hat{s}_{xi}\hat{s}_{xj} - \hat{s}_{yi}\hat{s}_{yj} \} \right| 0SS \right\rangle, \quad (38)$$

and a second-order term that arises from SOC. Using the effective one-electron SOC operator described above, the components of the \mathbf{D} -tensor can be shown to be [50]:

$$\begin{aligned} D_{kl}^{SOC(-0)} &= -\frac{1}{S^2} \sum_{b(S_b=S)} \Delta_b^{-1} \left\langle 0SS \left| \sum_i z_{k;i}^{SOMF} \hat{s}_{i,z} \right| bSS \right\rangle \left\langle bSS \left| \sum_i z_{l;i}^{SOMF} \hat{s}_{i,z} \right| 0SS \right\rangle, \quad (39) \\ D_{kl}^{SOC(-1)} &= -\frac{1}{S(2S-1)} \sum_{b(S_b=S-1)} \Delta_b^{-1} \left\langle 0SS \left| \sum_i z_{k;i}^{SOMF} \hat{s}_{i,+1} \right| bS-1S-1 \right\rangle \\ & \times \left\langle bS-1S-1 \left| \sum_i z_{l;i}^{SOMF} \hat{s}_{i,-1} \right| 0SS \right\rangle, \quad (40) \end{aligned}$$

$$D_{kl}^{SOC-(+)} = -\frac{1}{(S+1)(2S+1)} \sum_{b(S_b=S+1)} \Delta_b^{-1} \left\langle 0SS \left| \sum_i z_{k;i}^{SOMF} \hat{s}_{i,-1} \right| bS+1S+1 \right\rangle \quad (41)$$

$$\times \left\langle bS+1S+1 \left| \sum_i z_{l;i}^{SOMF} \hat{s}_{i,+1} \right| 0SS \right\rangle.$$

Thus, the SOC contribution has three terms that arise from excited states with the same total spin as the ground state and from terms that differ by unit of total spin-angular momentum.

b. *g*-Tensor. The *g*-tensor can be written as a sum of four parts [45,48,49,55–60]. The first part is the free-electron *g*-value and is usually dominant. However, since it is a natural constant it adds nothing to the information content of the *g*-tensor in analyzing molecular geometric and electronic structure. The second and third terms are of first order and are usually fairly small. The dominant contribution to $\Delta \mathbf{g} = \mathbf{g} - \mathbf{1}g_e$ arises from the cross term between the SOC and the orbital Zeeman-interactions (fourth term):

$$g_{zz}^{(SB)} = g_e, \quad (42)$$

$$g_{kl}^{(RMC)} = \delta_{kl} \frac{\alpha^2}{2} \frac{1}{S} \frac{g_e}{2} \left\langle 0SS \left| \sum_i \nabla_i^2 \hat{s}_{z;i} \right| 0SS \right\rangle, \quad (43)$$

$$g_{kl}^{(GC)} = \frac{1}{S} \left\langle 0SS \left| \sum_{i,A} \xi(r_{iA}) \{ \mathbf{r}_{iA} \mathbf{r}_i - r_{iA,k} r_{i,l} \} s_{z;i} \right| 0SS \right\rangle, \quad (44)$$

$$g_{kl}^{(OZ/SOC)} = -\frac{1}{S} \sum_{b(S_b=S)} \Delta_b^{-1} \quad (45)$$

$$\times \left\{ \left\langle 0SS \left| \sum_i l_{i,k} \right| bSS \right\rangle \left\langle bSS \left| \sum_i z_{i;l}^{SOMF} s_{z;i} \right| 0SS \right\rangle + \left\langle 0SS \left| \sum_i z_{k;i}^{SOMF} s_{z;i} \right| bSS \right\rangle \left\langle bSS \left| \sum_i l_{i,l} \right| 0SS \right\rangle \right\}.$$

The first term is simply the spin-Zeeman term, the second term is the reduced mass correction, and the third term is a gauge correction to the SOC, which has been written in somewhat simplified form here (explained in detail elsewhere [60]).

c. Hyperfine Coupling. The hyperfine coupling consists of three contributions where we have separated the Fermi contact term from the traceless dipolar contribution [9,45,56]:

$$A_{kl}^{(A;c)} = \delta_{kl} \frac{8\pi}{3} \frac{\alpha}{2} \frac{1}{S} g_e \beta_N g_N^{(A)} \left\langle 0SS \left| \sum_i s_{z;i} \delta(r_{iA}) \right| 0SS \right\rangle, \quad (46)$$

$$A_{kl}^{(A;d)} = \frac{\alpha}{2} \frac{1}{S} g_e \beta_N g_N^{(A)} \left\langle 0SS \left| \sum_i s_{z;i} r_{iA}^{-5} \{ \delta_{kl} r_{iA}^2 - 3r_{iA,k} r_{iA,l} \} \right| 0SS \right\rangle, \quad (47)$$

$$A_{kl}^{(A;SO)} = -\frac{\alpha}{2S} g_e \beta_N g_N^{(A)} \sum_{b(S_b=S)} \Delta_b^{-1} \left\{ \left\langle 0SS \left| \sum_i I_{i;k}^A r_{iA}^{-3} \right| bSS \right\rangle \left\langle bSS \left| \sum_i z_{l;i}^{SOMF} s_{z,i} \right| 0SS \right\rangle \right. \\ \left. + \left\langle 0SS \left| \sum_i z_{k;i}^{SOMF} s_{z,i} \right| bSS \right\rangle \left\langle bSS \left| \sum_i I_{i;l}^A r_{iA}^{-3} \right| 0SS \right\rangle \right\}. \quad (48)$$

The first two terms are widely known, while the third term is a contribution from the SOC and has only more recently received significant attention [9,46,61–63].

d. Field gradients. Finally, the computation of field gradients is given by

$$V_{kl}^{(A)} = \left\langle 0SS \left| \sum_i r_{iA}^{-5} \left\{ \delta_{kl} r_{iA}^2 - 3r_{iA;k} r_{iA;l} \right\} \right| 0SS \right\rangle. \quad (49)$$

Note that this term is a simple spin-independent first-order property of the system.

2.4. Linear Response Theory

The equations given in §2.3 are important from a conceptual point of view as they show the basic physics involved in SH parameters most clearly. However, as a basis of actual calculations, they are unfortunately much less useful owing to the presence of the second-order terms. The evaluation of these terms would require an infinite sum over excited many-electron states. In practice, at most a few dozen many-electron states can be calculated. Although quite useful results have been obtained with this approach [52–57,64–67], the convergence of the perturbation sum is uncertain and can, in the general case, hardly be guaranteed. In the case of DFT, the excited states cannot be obtained explicitly since the Hohenberg–Kohn theorems only apply to the electronic ground state. Hence, it is important to look for an alternative definition of the various SH parameters. An approach of substantial generality and elegance is provided by so-called linear response theory (LRT). In our view, LRT is just one realization of a family of methods that are all formulated in a similar spirit. If time does not explicitly occur in the equations (which is not necessary for the formulation of EPR and NMR parameters), these methods can also be called “analytic derivative approaches” [68]. In the framework of HF and DFT methods, they are known as “coupled-perturbed self-consistent field” (CP-SCF [69–72]) methods or “double-perturbation theory” (DPT [73]), respectively. All of these acronyms stand for computational methods that provide identical results, and it is a matter of taste as to which framework one prefers. These methods have been developed to high degree of sophistication in quantum chemistry and have been proven to be extremely useful in many contexts, including geometry optimization and frequency calculations (geometric derivatives), as well as in the precise prediction of many molecular properties. In fact, the LRT approaches can be shown to implicitly involve an untruncated sum over excited states of the system that are (implicitly) described at the same level of sophistication as the ground state [74–76]. The key quantities of interest in LRT are the derivatives of the (approximate) total ground state energy with respect to external perturbation param-

ters λ, κ, \dots where λ and κ may denote components of an external field or a nuclear magnetic moment of an electronic magnetic moment. Formally, we could take the derivative of the perturbation sum in Eq. (36) and then make the connection to the response formalism by it with the appropriate derivative of the approximate total energy calculated with the theoretical method of choice. Since all SH parameters are bilinear in external perturbations, the desired quantity is the second partial derivative of the total energy.

In order to appreciate the general concepts that are involved, the linear response equations for a Self-Consistent Field (SCF) ground state will be sketched below. This description is appropriate if the state of interest is well described by a HF (Hartree–Fock) or DFT single determinant (§2.1). The ground state energy is written here as

$$E = V_{NN} + \sum_i h_{ii} + \frac{1}{2} \sum_{i,j} (ii|jj) - c_{HF} (ij|ij) + c_{DF} E_{XC}[\rho]. \quad (50)$$

The parameters c_{HF} and c_{DF} are scaling parameters for the HF exchange energy and the XC-energy respectively. Thus, HF theory corresponds to $c_{HF} = 1$; $c_{DF} = 0$, “pure” DFT corresponds to $c_{HF} = 0$; $c_{DF} = 1$, while hybrid DFT methods choose $0 < c_{HF} < 1$. The energy has been written here in terms of the occupied orbitals $\psi_i(\mathbf{x})$. They are determined self-consistently from the SCF (HF or KS) equations:

$$\left\{ \hat{h} + \int \frac{\rho(\mathbf{x}')}{|\mathbf{x} - \mathbf{x}'|} d\mathbf{x}' - c_{HF} \sum_i \hat{K}^{ii} + c_{DF} \frac{\delta E_{XC}[\rho]}{\delta \rho(\mathbf{x})} \right\} \psi_i(\mathbf{x}) = \varepsilon_i \psi_i(\mathbf{x}). \quad (51)$$

For illustrating the concepts, it is sufficient to consider the case where the basis functions are chosen to be independent of the external perturbations. To include such a dependence (as is necessary, for example, for geometric or magnetic field perturbations) is straightforward but would lead to more lengthy equations that are not of interest for the purpose of this chapter. Since the MO coefficients c are determined in a variational procedure, one has

$$\frac{\partial E}{\partial c_{\mu i}} \frac{\partial c_{\mu i}}{\partial \lambda} = 0, \quad (52)$$

and therefore the first derivative of the energy with respect to a perturbation λ is

$$\left. \frac{\partial E}{\partial \lambda} \right|_{\lambda=0} = \sum_{\mu\nu} P_{\mu\nu} \left\langle \varphi_\mu \left| \hat{h} \right| \varphi_\nu \right\rangle_\lambda, \quad (53)$$

where

$$\left\langle \varphi_\mu \left| \hat{h} \right| \varphi_\nu \right\rangle_\lambda = \left\langle \varphi_\mu \left| \frac{\partial \hat{h}}{\partial \lambda} \right| \varphi_\nu \right\rangle, \quad (54)$$

if λ is a one-electron perturbation and if the basis functions are independent of λ . Through an additional differentiation, the second partial derivative becomes

$$\left. \frac{\partial^2 E}{\partial \lambda \partial \kappa} \right|_{\lambda=0, \kappa=0} = \sum_{\mu\nu} P_{\mu\nu} \langle \varphi_\mu | \hat{h} | \varphi_\nu \rangle_{\lambda\kappa} + \sum_{\mu\nu} \frac{\partial P_{\mu\nu}}{\partial \kappa} \langle \varphi_\mu | \hat{h} | \varphi_\nu \rangle_{\lambda}. \quad (55)$$

This important equation contains two contributions: the first term is referred to as a first-order contribution since it only depends on the ground state density. The second term is a second-order contribution since it requires the knowledge of the first derivative of the density matrix with respect to an external perturbation. These two terms substitute the two first- and second-order terms in the perturbation sum of Eq. (36). It remains to be shown how the perturbed density matrix can be calculated.

A simple approach will be followed for the calculation of the perturbed density matrix. To this end the perturbed orbitals $\psi_i^{(\lambda)} \equiv |i^{(\lambda)}\rangle$ are calculated in terms of the zeroth order orbitals $\psi_i^{(0)} \equiv |i^{(0)}\rangle$. Differentiation of the SCF equations yields

$$\{\hat{F}^{(0)} - \varepsilon_i^{(0)}\} |i^{(\lambda)}\rangle + \{\hat{F}^{(\lambda)} - \varepsilon_i^{(\lambda)}\} |i^{(0)}\rangle = 0. \quad (56)$$

The perturbed orbitals $|i^{(\lambda)}\rangle$ are expanded as

$$|i^{(\lambda)}\rangle = \sum_a U_{ai}^{(\lambda)} |a^{(0)}\rangle \quad (57)$$

(here and below, labels i, j, k, l refer to occupied orbitals, and a, b, c, d to unoccupied ones). The unitary matrix \mathbf{U} has only occupied/virtual blocks in the case that the basis functions do not depend on the perturbation. In order to determine the unique elements of \mathbf{U} one uses the perturbed SCF equations:

$$\sum_b U_{bi}^{(\lambda)} \langle a^{(0)} | \hat{F}^{(0)} - \varepsilon_i^{(0)} | b^{(0)} \rangle + \langle a^{(0)} | \hat{F}^{(\lambda)} - \varepsilon_i^{(\lambda)} | i^{(0)} \rangle = 0, \quad (58)$$

$$= U_{ai}^{(\lambda)} (\varepsilon_a^{(0)} - \varepsilon_i^{(0)}) + \langle a^{(0)} | \hat{F}^{(\lambda)} | i^{(0)} \rangle = 0. \quad (59)$$

However, $\hat{F}^{(\lambda)}$ depends on the perturbed orbitals. Therefore, one needs to take the derivative of the SCF operator carefully:

$$\begin{aligned} \hat{F}^{(\lambda)} &= \hat{h}^{(\lambda)} + \int \frac{\rho^{(\lambda)}(\mathbf{x}')}{|\mathbf{x} - \mathbf{x}'|} - c_{HF} \sum_{jb} U_{bj}^{(\lambda)*} \hat{K}^{bj} + U_{bj}^{(\lambda)} \hat{K}^{jb} + c_{DF} \iint \frac{\delta^2 E_{XC}[\rho]}{\delta \rho(\mathbf{x}) \delta \rho(\mathbf{x}')} \rho^{(\lambda)}(\mathbf{x}') d\mathbf{x} d\mathbf{x}' \\ &= \hat{h}^{(\lambda)} + \sum_{jb} U_{bj}^{(\lambda)*} \hat{J}^{bj} + U_{bj}^{(\lambda)} \hat{J}^{jb} - c_{HF} U_{bj}^{(\lambda)*} \hat{K}^{bj} - c_{HF} U_{bj}^{(\lambda)} \hat{K}^{jb} + c_{DF} \int f_{xc}[\rho] \rho^{(\lambda)}(\mathbf{x}) d\mathbf{x} \\ &= \hat{h}^{(\lambda)} + \sum_{jb} U_{bj}^{(\lambda)*} [\hat{J}^{bj} - c_{HF} \hat{K}^{bj} + c_{DF} \int f_{xc}[\rho] \psi_b^{(0)*}(\mathbf{x}) \psi_j^{(0)}(\mathbf{x}) d\mathbf{x}] \\ &\quad + U_{bj}^{(\lambda)} [\hat{J}^{jb} - c_{HF} \hat{K}^{jb} + c_{DF} \int f_{xc}[\rho] \psi_j^{(0)*}(\mathbf{x}) \psi_b^{(0)}(\mathbf{x}) d\mathbf{x}]. \end{aligned} \quad (60)$$

Here, the “XC-kernel” $f_{xc}[\rho]$ has been defined as the second functional derivative with respect to ρ , and it has been tacitly assumed that for all functionals in use this yields a factor $\delta(\mathbf{x} - \mathbf{x}')$, which reduces the double integral to a single integral. Taken together, this results in the first-order equations

$$\begin{aligned} U_{ai}^{(\lambda)} \left(\varepsilon_a^{(0)} - \varepsilon_i^{(0)} \right) + \left\langle a^{(0)} \left| \hat{h}^{(\lambda)} \right| i^{(0)} \right\rangle \\ + \sum_{jb} U_{bj}^{(\lambda)*} \left[(bj|ai) - c_{HF} (ba|ji) + (ai|f_{xc}|jb) \right] \\ + U_{bj}^{(\lambda)} \left[(jb|ai) - c_{HF} (ja|bi) + (ai|f_{xc}|jb) \right] = 0. \end{aligned} \quad (61)$$

At this point it is useful to distinguish two different types of perturbation: first, “electric field-like perturbations” yield purely real $\left\langle a^{(0)} \left| \hat{h}^{(\lambda)} \right| i^{(0)} \right\rangle$ and consequently, also purely real and symmetric \mathbf{U} matrices. In this case one has

$$\mathbf{A}^{(E)} \mathbf{U}^{(\lambda)} = -\mathbf{V}^{(\lambda)}, \quad (62)$$

with

$$A_{ia,jb}^{(E)} = \delta_{ij} \delta_{ab} \left(\varepsilon_a^{(0)} - \varepsilon_i^{(0)} \right) + 2(jb|ia) + 2c_{DF} (ai|f_{xc}|jb) - c_{HF} \left\{ (ba|ji) + (ja|bi) \right\}, \quad (63)$$

$$V_{ai}^{(\lambda)} = \left\langle a^{(0)} \left| \hat{h}^{(\lambda)} \right| i^{(0)} \right\rangle. \quad (64)$$

Note that the \mathbf{A} -matrix (the “electric Hessian”) is independent of the nature of the perturbation and that the \mathbf{U} and \mathbf{V} matrices have been written as vectors with a compound index (ai) .

Secondly, “magnetic field-like perturbations” yield purely hermitian imaginary $\left\langle a^{(0)} \left| \hat{h}^{(\lambda)} \right| i^{(0)} \right\rangle$ and consequently also purely imaginary and hermitian \mathbf{U} matrices. This leads to

$$\mathbf{A}^{(M)} \mathbf{U} = -\mathbf{V}^{(\lambda)}, \quad (65)$$

with

$$A_{ia,jb}^{(M)} = \delta_{ij} \delta_{ab} \left(\varepsilon_a^{(0)} - \varepsilon_i^{(0)} \right) + c_{HF} \left\{ (ib|ja) - (ba|ij) \right\}. \quad (66)$$

Thus, magnetic field-like perturbations yield much easier response (or “coupled perturbed”) equations in which the contributions from any local potential vanish. In fact, in the absence of HF exchange the \mathbf{A} -matrix becomes diagonal and the linear equation system is trivially solved. This then leads to a “sum-over-orbital”-like equation for the second derivative that resembles in some way a “sum-over-states” equation. One should, however, carefully distinguish the sum-over-states picture from linear response or analytic derivative techniques since they have a very different origin. For electric field-like perturbations or magnetic field-like perturba-

tions in the presence of HF exchange one thus has to solve a linear equation system of the size N (occupied) \times N (virtual), which may amount to dimensions of several hundred thousand coefficients in large-scale applications. However, there are efficient iterative techniques to solve such large equation systems without ever explicitly constructing the full \mathbf{A} -matrix [69]. Once the perturbed orbitals have been determined, the perturbed density is found as

$$P_{\mu\nu}^{(\lambda)} = \sum_i U_{ai}^{(\lambda)*} c_{\mu a}^{(0)} c_{vi}^{(0)} + U_{ai}^{(\lambda)} c_{\mu i}^{(0)} c_{va}^{(0)}. \quad (67)$$

2.5. Expression for Spin-Hamiltonian Parameters for Self-Consistent Field Methods

Using the results of the preceding sections, it is now possible to provide explicit expressions for all SH parameters.

a. Zero-Field Splitting. The ZFS is the least well-developed SH parameter in EPR spectroscopy. It is also the most complicated one since the SS contribution is a genuine two-electron property. For this contribution McWeeny and Mizuno have shown [77,78]

$$D_{kl}^{(SS)} = \frac{g_e^2}{16} \frac{\alpha^2}{S(2S-1)} \sum_{\mu\nu} \sum_{\kappa\tau} \{ P_{\mu\nu}^{\alpha-\beta} P_{\kappa\tau}^{\alpha-\beta} - P_{\mu\kappa}^{\alpha-\beta} P_{\nu\tau}^{\alpha-\beta} \} \langle \mu\nu | r_{12}^{-5} \{ 3r_{12,k} r_{12,l} - \delta_{kl} r_{12}^2 \} | \kappa\tau \rangle. \quad (68)$$

The integrals appearing in Eq. (68) look complicated at first glance but are readily calculated and owing to the factorization of the two-particle spin-density matrix, Eq. (68) can be implemented for large-scale application without creating storage of computation time bottlenecks. However, generally applicable programs have only appeared recently [76,78–85]. It is very interesting to look at the physical content of Eq. (68) in a little more detail. From the form of the operator and the appearance of the spin-density matrix, it is obvious that it describes the (traceless) direct electron–electron magnetic dipole–dipole interaction between unpaired electrons. Such a term is widely used in modeling the EPR spectra of interacting electron spins within the “point dipole” approximation [1,86–91]. Equation (68) consists of two parts. In analogy to HF theory, the first part should be recognized as a “Coulomb” contribution, while the second one is an “exchange” contribution. Thus, even the direct dipolar spin–spin interaction contains an exchange contribution that is of fundamentally different origin than the “genuine” exchange interaction used in the modeling of interacting spins [92]. This point does not appear to be widely recognized. Nevertheless, assuming an exponential decay of the basis functions, it becomes evident that the exchange term is expected to fall off much more quickly with interspin distance than the Coulomb contribution. The “distributed point dipole”-like equations can be recovered from Eq. (68) by: (a) neglecting the exchange contribution, (b) assuming that the spin density matrix is diagonal in the chosen basis, and (c) “compressing” the basis functions to δ -functions centered at the atomic positions. One then obtains

$$D_{kl} \approx \frac{g_e^2}{16} \frac{\alpha^2}{S(2S-1)} \sum_{AB} P_A^{\alpha-\beta} P_B^{\alpha-\beta} R_{AB}^{-5} [3\mathbf{R}_{AB;k} \mathbf{R}_{AB;l} - \delta_{kl} R_{AB}^2], \quad (69)$$

where A and B sum over nuclei and $P_A^{\alpha-\beta} = \sum_{\mu \in A} P_{\mu\mu}^{\alpha-\beta}$ is the “gross” spin-population on atom A .

Equation (69) describes the interaction of point dipoles centered at atomic positions where each atom pair is weighted by the product of the spin-populations that reside on this atom. Note this gross atomic spin-population differs from the usual numbers that are predicted by Mulliken or Löwdin analysis and that are part of the output of many-electronic structure programs since the latter contain terms that depend on the basis function overlap while $P_A^{\alpha-\beta}$ does not. However, since the approximation leading to the point-dipole formula, Eq. (69), have been rather crude, large additional errors may not be expected if Mulliken or Löwdin spin-populations are inserted into Eq. (69). If the distance between two spin-carrying fragments is large enough, it may even be possible to reduce Eq. (69) to a single term where R_{AB} must then refer to an “effective” distance. We propose to calculate it as follows. First the center of gravity of the spin-density of fragments “F1” and “F2” are defined as

$$\mathbf{R}^{(F1)} = \sum_{A \in F1} \bar{P}_A^{\alpha-\beta} \mathbf{R}_A, \quad (70)$$

$$\mathbf{R}^{(F2)} = \sum_{B \in F2} \bar{P}_B^{\alpha-\beta} \mathbf{R}_B, \quad (71)$$

and then we replace the vector \mathbf{R}_{AB} in Eq. (69) by $\mathbf{R}_{12} = \mathbf{R}^{(F1)} - \mathbf{R}^{(F2)}$. The barred quantity $\bar{P}_A^{\alpha-\beta}$ refers to a normalized spin-population such that the sum $\sum_{A \in F1} \bar{P}_A^{\alpha-\beta} = 1$. This appears to be a slightly more rigorous approach than the commonly used approach in which the intercenter distance is fixed by subjective plausible choices which may, however, differ between different workers. Note also that the full \mathbf{g} -tensor does not enter either Eq. (68) or Eq. (69). We have already criticized the use of the \mathbf{g} -tensor in the point dipole approximations for the hyperfine couplings [46] and a similar situation also applies to the case of the dipolar ZFS tensor.

The SOC contribution to the ZFS involves the response of the orbitals to the SOC. The formalism to achieve an analytic derivative formulation of this part of the SH has been worked out recently by the present author and is somewhat more involved than the analogous methodology for the \mathbf{g} -tensor. Without going into too much detail, the three contributions to the \mathbf{D} -tensor in Eqs. (39)–(41) may be re-written as follows [175]:

$$D_{kl}^{(0)} = -\frac{1}{4S^2} \sum_{\mu\nu} \langle \mu | h_k^{SOC} | \nu \rangle \frac{\partial P_{\mu\nu}^{(0)}}{\partial S_l^{(0)}}, \quad (72)$$

$$D_{kl}^{(+)} = \frac{1}{2(S+1)(2S+1)} \sum_{\mu\nu} \langle \mu | h_k^{SOC} | \nu \rangle \frac{\partial P_{\mu\nu}^{(-)}}{\partial S_l^{(+)}}, \quad (73)$$

$$D_{kl}^{(-)} = \frac{1}{2S(2S-1)} \sum_{\mu\nu} \langle \mu | h_k^{SOC} | \nu \rangle \frac{\partial P_{\mu\nu}^{(+)}}{\partial S_l^{(-)}}. \quad (74)$$

The components $S_l^{(m)}$ ($m = 0, \pm 1$) are the vector operator components of the total spin. The spin-densities $\mathbf{P}^{(m)}$ are the response densities with respect to a SOC perturbation. They are calculated from a non-standard set of coupled-perturbed equations analogous to the ones described above for the \mathbf{g} -tensor as

$$\frac{\partial P_{\mu\nu}^{(0)}}{\partial S_l^{(0)}} = \sum_{i_\alpha a_\alpha} U_{a_\alpha i_\alpha}^{(0);l} c_{\mu i}^\alpha c_{\nu a}^\alpha + \sum_{i_\beta a_\beta} U_{a_\beta i_\beta}^{(0);l} c_{\mu i}^\beta c_{\nu a}^\beta, \quad (75)$$

$$\frac{\partial P_{\mu\nu}^{(+1)}}{\partial S_l^{(-1)}} = \sum_{i_\alpha a_\beta} U_{a_\beta i_\alpha}^{(-1);l} c_{\mu i}^\alpha c_{\nu a}^\beta - \sum_{i_\beta a_\alpha} U_{a_\alpha i_\beta}^{(-1);l} c_{\mu a}^\alpha c_{\nu i}^\beta, \quad (76)$$

$$\frac{\partial P_{\mu\nu}^{(-1)}}{\partial S_l^{(+1)}} = -\sum_{i_\alpha a_\beta} U_{a_\beta i_\alpha}^{(+1);l} c_{\mu a}^\beta c_{\nu i}^\alpha + \sum_{i_\beta a_\alpha} U_{a_\alpha i_\beta}^{(+1);l} c_{\mu i}^\beta c_{\nu a}^\alpha, \quad (77)$$

With the U -coefficients calculated from

$m = 0$:

$$\left(\varepsilon_{a_\alpha}^{(0)} - \varepsilon_{i_\alpha}^{(0)} \right) U_{a_\alpha i_\alpha}^{k(0)} + c_{HF} \sum_{j_\alpha b_\alpha} U_{b_\alpha j_\alpha}^{k(0)} \left\{ (b_\alpha i_\alpha | a_\alpha j_\alpha) - (j_\alpha i_\alpha | a_\alpha b_\alpha) \right\} = - (a_\alpha | h_k^{SOC} | i_\alpha), \quad (78)$$

$$\left(\varepsilon_{a_\beta}^{(0)} - \varepsilon_{i_\beta}^{(0)} \right) U_{a_\beta i_\beta}^{k(0)} + c_{HF} \sum_{j_\beta b_\beta} U_{b_\beta j_\beta}^{k(0)} \left\{ (b_\beta i_\beta | a_\beta j_\beta) - (j_\beta i_\beta | a_\beta b_\beta) \right\} = - (a_\beta | h_k^{SOC} | i_\beta), \quad (79)$$

$m = +1$:

$$\begin{aligned} & \left(\varepsilon_{a_\alpha}^{(0)} - \varepsilon_{i_\beta}^{(0)} \right) U_{a_\alpha i_\beta}^{k(+1)} + c_{HF} \sum_{j_\alpha b_\alpha} U_{b_\alpha j_\alpha}^{k(+1)} (b_\beta i_\beta | a_\alpha j_\alpha) - c_{HF} \sum_{b_\alpha j_\beta} U_{b_\alpha j_\beta}^{k(+1)} (j_\beta i_\beta | a_\alpha b_\alpha) \\ & = - (a_\alpha | h_k^{SOC} | i_\beta), \end{aligned} \quad (80)$$

$$\left(\varepsilon_{a_\beta}^{(0)} - \varepsilon_{i_\alpha}^{(0)} \right) U_{a_\beta i_\alpha}^{k(+1)} + c_{HF} \sum_{j_\beta b_\beta} U_{b_\beta j_\beta}^{k(+1)} (b_\alpha i_\alpha | a_\beta j_\beta) - c_{HF} \sum_{b_\beta j_\alpha} U_{b_\beta j_\alpha}^{k(+1)} (j_\alpha i_\alpha | a_\beta b_\beta) = 0, \quad (81)$$

$m = -1$:

$$\begin{aligned} & \left(\varepsilon_{a_\beta}^{(0)} - \varepsilon_{i_\alpha}^{(0)} \right) U_{a_\beta i_\alpha}^{k(-1)} + c_{HF} \sum_{j_\beta b_\alpha} U_{b_\alpha j_\beta}^{k(-1)} \left(b_\alpha i_\alpha \mid a_\beta j_\beta \right) - c_{HF} \sum_{b_\beta j_\alpha} U_{b_\beta j_\alpha}^{k(-1)} \left(j_\alpha i_\alpha \mid a_\beta b_\beta \right) \\ & = - \left(a_\beta \mid h_k^{SOC} \mid i_\alpha \right), \end{aligned} \quad (82)$$

$$\left(\varepsilon_{a_\alpha}^{(0)} - \varepsilon_{i_\beta}^{(0)} \right) U_{a_\alpha i_\beta}^{k(-1)} + c_{HF} \sum_{j_\alpha b_\alpha} U_{b_\beta j_\alpha}^{k(-1)} \left(b_\beta i_\beta \mid a_\alpha j_\alpha \right) - c_{HF} \sum_{b_\beta j_\alpha} U_{b_\beta j_\alpha}^{k(-1)} \left(j_\beta i_\beta \mid a_\alpha b_\alpha \right) = 0. \quad (83)$$

This formalism is the exact analogue of the ones used to compute the \mathbf{g} -tensor and the SOC contribution to the HFC tensor and directly follows from general Eqs. (39)–(41). It is available in the ORCA package and has been shown to correct some deficiencies of earlier formulation of the ZFS tensor in the DFT framework [175]. Since the latter procedures are more commonly met in the literature, they are briefly described. Pederson and Khanna have suggested the equation [93]:

$$\begin{aligned} D_{kl}^{(SOC)} &= -\frac{1}{4S^2} \sum_{i_\beta, a_\beta} \frac{\langle \psi_i^\beta \mid h_k^{SOC} \mid \psi_a^\beta \rangle \langle \psi_a^\beta \mid h_l^{SOC} \mid \psi_i^\beta \rangle}{\varepsilon_a^\beta - \varepsilon_i^\beta} \\ &\quad - \frac{1}{4S^2} \sum_{i_\alpha, a_\alpha} \frac{\langle \psi_i^\alpha \mid h_k^{SOC} \mid \psi_a^\alpha \rangle \langle \psi_a^\alpha \mid h_l^{SOC} \mid \psi_i^\alpha \rangle}{\varepsilon_a^\alpha - \varepsilon_i^\alpha} \\ &\quad + \frac{1}{4S^2} \sum_{i_\alpha, a_\beta} \frac{\langle \psi_i^\alpha \mid h_k^{SOC} \mid \psi_a^\beta \rangle \langle \psi_a^\beta \mid h_l^{SOC} \mid \psi_i^\alpha \rangle}{\varepsilon_a^\beta - \varepsilon_i^\alpha} \\ &\quad + \frac{1}{4S^2} \sum_{i_\beta, a_\alpha} \frac{\langle \psi_i^\alpha \mid h_k^{SOC} \mid \psi_a^\alpha \rangle \langle \psi_a^\alpha \mid h_l^{SOC} \mid \psi_i^\beta \rangle}{\varepsilon_a^\alpha - \varepsilon_i^\beta}, \end{aligned} \quad (84)$$

which is valid in the case of DFT functionals that do not contain the HF exchange ($c_{HF} = 0$). It can be shown to be a special case of the more general treatment outlined above if the prefactors in front of the individual terms in Eq. (84) are all set to $1/4S^2$ rather than the more rigorous values in Eqs. (39)–(41). We had previously implemented this equation and compared it to the following equation, which had also been motivated from general Eqs. (39)–(41) [84]:

$$\begin{aligned} D_{kl}^{(SOC)} &= -\frac{1}{4S^2} \sum_{i,p} \frac{\langle \psi_i \mid h_k^{SOC} \mid \psi_p \rangle \langle \psi_p \mid h_l^{SOC} \mid \psi_i \rangle}{\varepsilon_p^\beta - \varepsilon_i^\beta} \\ &\quad - \frac{1}{4S^2} \sum_{p,a} \frac{\langle \psi_p \mid h_k^{SOC} \mid \psi_a \rangle \langle \psi_a \mid h_l^{SOC} \mid \psi_p \rangle}{\varepsilon_a^\alpha - \varepsilon_p^\alpha} \\ &\quad + \frac{1}{4} \frac{1}{S(2S-1)} \sum_{p \neq q} \frac{\langle \psi_p \mid h_k^{SOC} \mid \psi_q \rangle \langle \psi_q \mid h_l^{SOC} \mid \psi_p \rangle}{\varepsilon_q^\beta - \varepsilon_p^\alpha} \\ &\quad + \frac{1}{2} \frac{1}{(S+1)(2S+1)} \sum_{i,a} \frac{\langle \psi_i \mid h_k^{SOC} \mid \psi_a \rangle \langle \psi_a \mid h_l^{SOC} \mid \psi_i \rangle}{\varepsilon_a^\alpha - \varepsilon_i^\beta}. \end{aligned} \quad (85)$$

In this equation, there enters a set of “quasi-restricted” orbitals (QROs) that are explained in detail in [84]. It may be appreciated that both formulations involve the terms that are already apparent in the general treatment (Eqs. (39)–(41)). Namely, the first two terms correspond to the contributions from the spin-conserving excitations, while the third and fourth terms correspond to the contributions from the excited states of lower and higher multiplicity than the ground state, respectively. However, this QRO formalism is now superseded by the more general development in Eqs. (72)–(74). More information on the relative importance of the individual terms can be found below (§§3.5, 3.6).

b. *g*-Tensor. The *g*-tensor is well studied by now, with many implementations and applications available (for reviews see [13,15,94]). One obtains the following expressions for the four contributions [60]:

$$\mathbf{g}_{kl} = g_e \delta_{kl} + \Delta \mathbf{g}_{kl}^{RMC} + \Delta \mathbf{g}_{kl}^{GC} + \Delta \mathbf{g}_{kl}^{OZ/SOC}, \quad (86)$$

$$\Delta \mathbf{g}_{kl}^{RMC} = -\frac{\alpha^2}{S} \sum_{\mu,\nu} P_{\mu\nu}^{\alpha-\beta} \langle \varphi_\mu | \hat{T} | \varphi_\nu \rangle, \quad (87)$$

$$\Delta \mathbf{g}_{kl}^{GC} = \frac{1}{2S} \sum_{\mu,\nu} P_{\mu\nu}^{\alpha-\beta} \left\langle \varphi_\mu \left| \sum_A \xi(r_A) [\vec{r}_A \vec{r} - \vec{r}_{A,k} \vec{r}_l] \right| \varphi_\nu \right\rangle, \quad (88)$$

$$\Delta \mathbf{g}_{kl}^{(OZ/SOC)} = \frac{1}{2S} \sum_{\mu,\nu} \frac{\partial P_{\mu\nu}^{(\alpha-\beta)}}{\partial B_k} \langle \varphi_\mu | \hat{z}_l^{SOMF} | \varphi_\nu \rangle, \quad (89)$$

Here \hat{T} is the kinetic energy operator. It is noted that the *g*-tensor expressions make, through the operators \mathbf{r} in Eq. (88) and \mathbf{l} (implicit in Eq. (89), see §2.4), reference to the global origin of the coordinate system. This would seem to imply the unphysical and unfortunate situation that the results of the computations depend on the choice of origin. This is indeed so in *g*-tensor calculations and would only disappear in the basis set limit, which is, in practice, never reached. The way around this artifact is to employ magnetic field-dependent basis functions (“gauge including atomic orbitals,” GIAOs) [95–97]. The GIAOs are an elegant way to solve the gauge problem but require some additional computational effort. They have been very successful in the prediction of NMR chemical shifts where it is essential to remove the gauge dependence entirely. The alternative “independent gauge for localized orbitals” (IGLO) [98], which is also popular in chemical shift calculations, is not successful in EPR spectroscopy since the separate localization of spin-up and spin-down orbitals introduces artifacts into the results (this statement was first made in [99] and has been independently confirmed by the author). Fortunately, the gauge problem in EPR spectroscopy is not large, and one obtains meaningful results even if a slight origin dependence persists. In order to make results comparable, a reasonable choice of origin is still required and is, according to Luzanov and coworkers [100], conveniently provided by the center of electronic charge. The error made by this approximation is much smaller than other remain-

ing errors due to the functional, the basis set, the molecular model. or the treatment of environmental effects.

c. Hyperfine Coupling. One finds for the three parts of the HFC the following expressions [46,101,102]:

$$A_{kl}^{(A;c)} = \delta_{kl} \frac{8\pi}{3} \frac{P_A}{2S} \rho^{\alpha-\beta}(\mathbf{R}_A), \quad (90)$$

$$A_{kl}^{(A;d)} = \frac{P_A}{2S} \sum_{\mu\nu} P_{\mu\nu}^{\alpha-\beta} \left\langle \varphi_\kappa \left| r_A^{-5} \left(r_A^2 \delta_{\mu\nu} - 3r_{A;\mu} r_{A;\nu} \right) \right| \varphi_\tau \right\rangle, \quad (91)$$

$$A_{kl}^{(A;SO)} = -\frac{P_A}{S} \sum_{\mu\nu} \frac{\partial P_{\mu\nu}^{\alpha-\beta}}{\partial \hat{I}_k^{(A)}} \left\langle \varphi_\mu \left| z_l^{SOMF} \right| \varphi_\nu \right\rangle, \quad (92)$$

with $P_A = g_e g_N \beta_e \beta_N$. Thus, the first two terms are straightforward expectation values, while the SOC contribution is a response property [46]. In this case, one has to solve a set of coupled-perturbed equations with the nucleus—orbit interaction taken as the perturbing operator. Since the solution of the coupled-perturbed equations becomes time consuming for larger molecules, this should only be done for a few selected heavier nuclei. For light nuclei, the SOC correction is usually negligible [176].

d. Electric Field Gradient. The EFG tensor is straightforwardly calculated from

$$V_{\mu\nu}^{(A)} = \sum_{\kappa,\tau} P_{\kappa\tau} \left\langle \varphi_\kappa \left| r_A^{-5} \left(r_A^2 \delta_{\mu\nu} - 3r_{A;\mu} r_{A;\nu} \right) \right| \varphi_\tau \right\rangle. \quad (93)$$

Once available, the EFG tensor can be diagonalized. The numerically largest element V_{\max} (in atomic units) defines the value of q , which is in turn used to calculate the quadrupole splitting parameter as $e^2 q Q = 235.28 V_{\max} Q$, where Q is the quadrupole moment of the nucleus in barn. Transformed to its eigensystem, the quadrupole splitting enters the SH in the following form [1]:

$$\hat{H}_Q = \hat{\mathbf{Q}} \hat{\mathbf{I}} = \frac{e^2 q Q}{4I(2I-1)} \hat{\mathbf{I}} \begin{pmatrix} -(1-\eta) & 0 & 0 \\ 0 & -(1+\eta) & 0 \\ 0 & 0 & 2 \end{pmatrix} \hat{\mathbf{I}}. \quad (94)$$

The asymmetry parameter η is defined as

$$\eta = \frac{|V_{\text{mid}} - V_{\text{min}}|}{V_{\text{max}}}. \quad (95)$$

It is to be noted that this is the only term that involves the total electron density rather than the spin density. The field gradient tensor is consequently of a quite

different nature than the hyperfine coupling, which depends on the same dipolar interaction integrals but in the case of the HFC they are contracted with the spin density instead of the electron density.

It is important to realize that the equations of this section are not only valid in the case of a SCF ground state description but are of much wider applicability. In the case of correlated *ab initio* methods, the equations to be solved in order to determine the effective density and its response merely becomes much more complicated than the relatively simple CP-SCF equations sketched above. The general line of thought is, however, identical and merely the “mechanics” of the calculation become more involved.

2.6. Practical Aspects

The following practical advice is based on several years of experience with the calculation of EPR properties. However, it is also of a subjective nature, and other investigators may prefer different approaches.

a. Choice of molecular model. The most important step in a theoretical study of SH parameters is the choice of molecular model. Whenever possible, the largest and most realistic model that is compatible with the available computational resources should be chosen if the aim of the study is to predict the spectroscopic parameters as accurately as possible. However, large models tend to be of low symmetry and their potentially complicated structure makes it sometimes difficult to understand the physical and chemical origin of the computational results. Thus, in this case, the computed numbers are as incomprehensible to the investigator as the SH parameter values obtained from fitting the experimental spectra. If the only aim of the investigation is to obtain the theoretical numbers, perhaps as substitute for experimental measurements that cannot be performed, this may not be considered a drawback. Yet, if the goal of the study is to obtain insight into the origin of the SH parameters, one is well advised to choose an as-small-as-possible model and to theoretically study the structure/spectral relationships in this model system. Such investigations can give invaluable insight that may even lead to better calculations on the large target system.

b. Choice of geometry. The second critical step in a theoretical study is to choose a geometry for the calculation. Unless one has a very good reason to the contrary, it is highly desirable to employ quantum chemically optimized geometries—that is, to minimize the total energy with respect to all nuclear coordinates \mathbf{R} . Automatic procedures for performing such calculations are part of virtually all quantum chemical programs. Theoretical geometries are well defined once a suitable “model chemistry” and a starting structure are selected. This is important in order to satisfy the criterion of reproducibility. Second, the theoretical structures do not depend on the resolution of a crystallographic experiment. In particular, the optimized positions of hydrogens are usually more reliable than the ones obtained from crystal structures. Note that even good protein crystal structures have uncertainties in the bond distances (~ 0.1 Å) that are not tolerable for quantum chemical

studies. Third, the theoretical structures are in many if not most cases of good to excellent quality. However, there are some situations where a fully optimized structure is more harmful than helpful. One such case arises if the theoretical model chemistry fails to predict a certain geometrical feature that is known to be present in the system. A second case is met when the model consists only of a part of the actual system and the remaining part imposes geometric constraints that will be violated in an unconstrained optimization. This situation arises typically if active sites of proteins are studied. In this case, one may freeze a small amount of geometrical parameters in order to satisfy the constraints provided by the protein pocket. A much more rigorous approach is to model the entire protein using a combined quantum mechanically/molecular mechanical (QM/MM) approach [103–105]. Here, one treats a small part (the active site) with a quantum mechanical model while the rest of the structure is treated with molecular mechanics. Such calculations are expected to accurately reflect the geometric constraints of the protein and furthermore include the leading long-range electrostatic effects of the protein environment together with its first solvation shell. In some situations it will not be sufficient to look at individual optimized structures, and the dynamics of the system must be taken into account. These situations are best handled by molecular dynamics calculations. One then selects a sufficiently large number of “snapshots” from the MD trajectory [106]. Calculations performed at these snapshot geometries provide the average values of the desired spectroscopic parameters and also give, through proper statistics, an estimate of the inhomogeneous linewidth of the spectra [107]. However, the treatment of QM/MM and dynamic effects has not yet reached a “black box” level, and presently experts are still required in order to carry out such calculations.

c. Choice of theoretical method. In the framework of the present chapter, the choice of a theoretical method is identical to the choice of an appropriate density functional. Owing to the large number of different functionals that have been developed over the years, it is important to select a functional with a well-documented performance in the area of interest. If no calibration studies have been performed for the given functional, an important requisite for a successful study is to perform such a calibration on a series of related molecules with known structure and spectroscopic properties. Perhaps the two best-tested functionals in chemistry and EPR spectroscopy are the hybrid B3LYP (see [16] for a discussion of different functionals) functional and the “pure” GGA functional BP86. The performance of both functionals in EPR spectroscopy has been extensively studied, and the error bars to be expected from the calculations are known for many types of systems [15,41,60,62,63,108–110]. Overall, the B3LYP functional seems to be the best choice for EPR spectral predictions. This is fortunate since B3LYP is also the de facto standard for many chemical applications concerning structure and energetics. Thus, one appears to be on safe ground if this functional is used. This is not to say that other functionals may not perform with very similar quality, and among the hybrid functionals the PBE0 model [111,112] may be specifically mentioned [60,113]. The advantage of non-hybrid functionals is that, owing to the ab-

sence of HF exchange, the KS equations can be solved much more efficiently and performance gains by a factor of ~ 10 are possible using modern computational techniques. This is particularly important in geometry optimizations that require typically many individual KS calculations. In our experience, geometries of organic systems predicted by BP86 are not much worse than those predicted by B3LYP, and the geometries of transition metal complexes are in many cases even better than the B3LYP structures. Thus, one can invest the savings offered by the GGA functionals in a better basis set or a more realistic chemical model in studying the system of interest.

Some investigators advocate varying the amount of Hartree–Fock exchange in hybrid functionals in an attempt to obtain better agreement with experimental values. In the opinion of this author, there is little reason to invest computer time in such a study. The “optimal” amount of HF exchange varies from system to system and from property to property. Thus, it would be difficult to claim that an overall more realistic electronic structure has been obtained by the fitting procedure compared to the results obtained with standard functionals for which extensive calibration calculations are often available. One may also ask what additional physical insight is obtained from the variation of the fractional HF exchange compared to the more traditional approach of correcting for systematic deficiencies of the theoretical procedures by scaling procedures based on linear regression.

d. Choice of basis set. In general one has to balance the cost of the calculation versus the accuracy of the results. Ideally, the results obtained only reflect the chemical model and the theoretical method chosen, and basis set effects do not show up at all. This is, unfortunately, only possible if very large basis sets are used, and in practice one always has a dependence of the results on the employed basis set. Experience has shown that the smallest reasonable basis sets for the prediction of structures and energies are of so-called double- ζ plus polarization quality. Such basis sets consist of a “split” representation of each valence orbital, a single basis function for each core orbital and one set of higher angular momentum “polarization” functions. Typical members of such basis sets are the 6-31G* (or 6-31G**) basis set [114], the SV(P) (or SVP) basis set [115] or the DGAUSS-DZVP basis set [116]. Among these, the SVP basis set has the smallest number of primitives and therefore leads to the fastest calculations. Fairly good results in comparison to the basis set limit are typically already obtained if polarized triple- ζ basis sets are used. Typical members are 6-311G** [117], cc-pVTZ [118], or TZVP [119], where the latter, again, is the most efficient in terms of computational requirements. If a second and third set of polarization functions is employed (as in cc-pVTZ or in 6-311G(2df,2pd) or in TZVPP), the results become very accurate but the computations may take as much as an order of magnitude longer than those with simple split-valence bases. Thus, a reasonable strategy is to first perform the geometry optimization with a small basis set and to reoptimize with a larger basis set once convergence has been obtained. For the EPR property predictions at the optimized geometries somewhat different basis sets should be chosen. However, the only parameter that seems to be critical in this respect is the isotropic hyperfine coupling. All other properties appear to be adequately predicted by the standard bases men-

tioned above. The isotropic hyperfine coupling requires basis sets with additional flexibility in the core region. This flexibility is provided, for example, by the EPR-II and EPR-III basis sets [120], which are otherwise equivalent to split-valence and polarized triple- ζ basis sets, respectively. They are available for the first row elements. Alternatively, the IGLO-II and IGLO-III basis sets [98] have been developed for NMR calculations and are available for most first- and second-row elements. First row transition metals are usually well treated by the TZVP basis set. However, for hyperfine calculations a “brute force” set termed CP(PPP) has been defined [121] based on the developments of the Ahlrich group [122]. For transition metals beyond the first transition row, the effects of relativity become important and should be treated on an all-electron level if hyperfine or quadrupole couplings are to be predicted. For other properties the use of effective core potentials may be adequate, but small cores should be employed.

e. Summary and recommendations. Calculations of EPR parameters can now be performed on a routine basis using highly efficient and user-friendly program packages together with cheap mass market personal computers running under the Windows or Linux operating systems. For example, our group has developed the ORCA program [8], which is particularly well suited for EPR property predictions and is available free of charge. Alternative programs have been mentioned before [18–21]. For most applications it is recommended to first optimize the geometry of the system using the BP86 functional (together with the efficient so-called RI approximation [123,124]) and the SVP basis set followed by reoptimization with the TZVP basis set. The B3LYP functional may also be used for the structure optimization but will require longer computation times (factor 10–20). For the EPR property predictions the B3LYP functional is recommended together with the EPR-II basis set for first row atoms, IGLO-II or TZVP for the second row, and CP(PPP) for the first row transition metals. For higher accuracy, the EPR-III and IGLO-III basis sets should be employed. The size of the systems that can be treated with this methodology in reasonable computation times is around 100–300 atoms. If parallel computational facilities (such as Linux clusters) are available, even larger systems may already be targeted.

3. CASE STUDIES

In this section some recent case studies are quoted in order to illustrate the performance of the methods used. Since space does not permit to go into the details of the sometimes elaborate analysis, only the leading conclusions of these works are presented without detailed proof.

3.1. Structure–Spectral Relationships: Phenoxy Radicals

In order to demonstrate the accuracy that can be obtained nowadays in g -tensor calculations with DFT, we quote a recent study on modified phenoxy radicals fused with an imidazole ring in an attempt to model Tyrosine D in photosys-

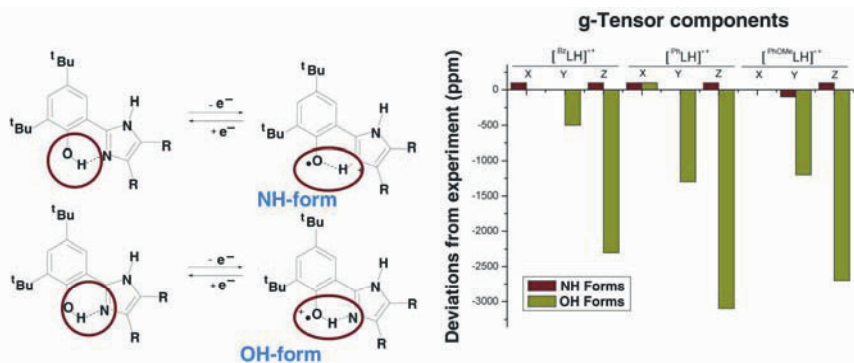


Figure 1. Identification of an oxidation product by a combination of high-field EPR spectroscopy and DFT property calculations. Left: one-electron oxidation of the parent compounds leads either to proton migration (NH-forms) or the corresponding OH-forms. On the right side, the deviation between calculated and experimental g -values is shown under assumption of the NH-forms (in red) or the OH-forms (in green). Reproduced with permission from [125]. Copyright © 2005, Wiley–VCH.

tem II [125]. In fact, in many cases agreement between theory and experiment within ~ 100 ppm is observed for g -tensors. These compounds were synthesized (Fig. 1) in their neutral forms and were then electrochemically oxidized to the radical form. However, it was not clear whether the radicals persist with the proton still attached to the phenolic oxygen or whether it has been transferred to the imidazole nitrogen upon oxidation. B3LYP calculations predicted that the result of one-electron oxidation of the parent compounds depends on the substituents on the imidazole rings. For C_6H_5 substituents the NH form was predicted more stable, while for $MeOC_4H_4$ the OH form was predicted 7.7 kJ/mol more stable. However, comparison of the calculated and measured g -tensors revealed that in all oxidation products only the NH forms occur. In this case, the calculated g -values were in better than 100 ppm agreement with experiment, while the errors predicted for the OH forms amounted to several thousand ppm (Fig. 1). Thus, the OH forms could be safely ruled out as oxidation products. Although this is an isolated example, it illustrates that spectroscopic parameters can be much more sensitive reporters of the actual situation than total energies, which are, in a sense, bulk properties that are insensitive to certain structural features and depend on all aspects of the modeling. The important point is to seek the feedback from the available experimental data in order to come to correct interpretations.

Theoretical studies of the g -tensors of aromatic free radicals [126,127] indicate that variations in the g_x -value of a phenoxyl radical may be understood as arising from a combination of two effects, changes in: (a) the unpaired spin-population at the oxygen, the constituent atom with the largest spin-orbit coupling constant, and (b) the relative energies of two oxygen-based orbitals, the out-of-plane p_z orbital

(which that has a significant contribution to the SOMO of a phenoxy radical) and the in-plane p_y lone pair orbital, the contribution of which to the g -shift arises due to spin-orbit coupling with the electron in the SOMO. This latter effect produces a magnetic moment along the C–O axis that increases the value of g_x . Formation of an in-plane hydrogen bond stabilizes the p_y lone pair, increasing the energy difference between this orbital and the SOMO, resulting in less effective spin-orbit coupling and a reduction of the g_x -value. In that respect, the OH-radical forms represent the extreme cases where the p_y lone pair is directly involved in the OH-bond and is thus not involved in efficient spin-orbit coupling with the SOMO, which explains the very low g_x -values obtained from the calculation for these species. For the NH-radical cations, the DFT calculations indicate that the strength of the hydrogen-bond increases across this series, i.e., the $-\text{O}^\bullet \dots \text{HN}$ distance decreases along the series of substituents (R = Bz, Ph, or PhOMe) from 1.867 to 1.832 and finally to 1.781 Å. Correspondingly, this leads to a reduced g_x -value. However, a full appreciation of the results also requires a detailed analysis of the spin-density distribution, as reported in [125].

3.2. Difficult Cases: Cysteine Radicals

A particularly difficult case has been met for cysteine radicals. Such radicals are important models for thiyl radicals in proteins. Such radicals are known to display very large g -shifts that furthermore are strongly dependent on the nature of the environment. Recently a detailed experimental and theoretical study was undertaken in order to clarify the observed effects [128]. In the first step, the conformations of the cysteine radical were studied with respect to variations in the dihedral angle S–C $_{\beta}$ –C $_{\alpha}$ –C.



Scheme 1. Newman projections along the C $_{\alpha}$ –C $_{\beta}$ axis for the three structures that correspond to energy minima.

Constrained geometry optimizations led to the potential energy surface shown in Figure 2. The three minima observed correspond to the structures shown in Figure 3. It is evident that the three minima are almost isoenergetic, and consequently the system can assume any of the three forms.

The calculation of the spectroscopic parameters at the three minima showed that the g -tensor is surprisingly sensitive to the conformation of the cysteine radical and that, indeed, very large g -shifts are calculated. However, the calculated g -shifts

are much smaller than the experimentally observed numbers in Table 1, which requires a detailed analysis of the origin of these effects.

Table 1. Summary of the C–C α –C β –S γ Dihedral Angles (degrees), Excitation Energies $E_{0 \rightarrow 1}$ (cm $^{-1}$) from the Ground State to the First Excited State and g -Values for the Three Geometries that Correspond to Minima on the Potential Energy Surface

	1 st minimum			2 nd minimum			3 rd minimum		
C–C α –C β –S γ	286.6			171.3			61.4		
$E_{0 \rightarrow 1}$	1732			1083			2917		
	g_x	g_y	g_z	g_x	g_y	g_z	g_x	g_y	g_z
2 nd order	2.2649	2.0215	2.0024	2.3692	2.0214	2.0023	2.1680	2.0161	2.0023
3 rd order	2.2649	2.0043	1.9852	2.3692	1.9877	1.9686	2.1680	2.0092	1.9954
	x	y	z	x	y	z	x	y	z
C β –S γ	1.3	88.7	89.9	1.6	89.5	88.5	2.6	89.7	87.4
C α –C β –S γ	347.7	170.3	80.3	53.8	174.7	95.3	121.2	37.6	127.6

The g -values up to second order stem from the calculations. Those up to third order are calculated by Eq. (1). Also included are the angles (degrees) between the principal axes and the C β –S γ direction, and the dihedral angle with the C α –C β –S γ plane. A graphic representation of the principal axes is given in Figure 3. Reproduced with permission from [128]. Copyright © 2004, American Chemical Society.

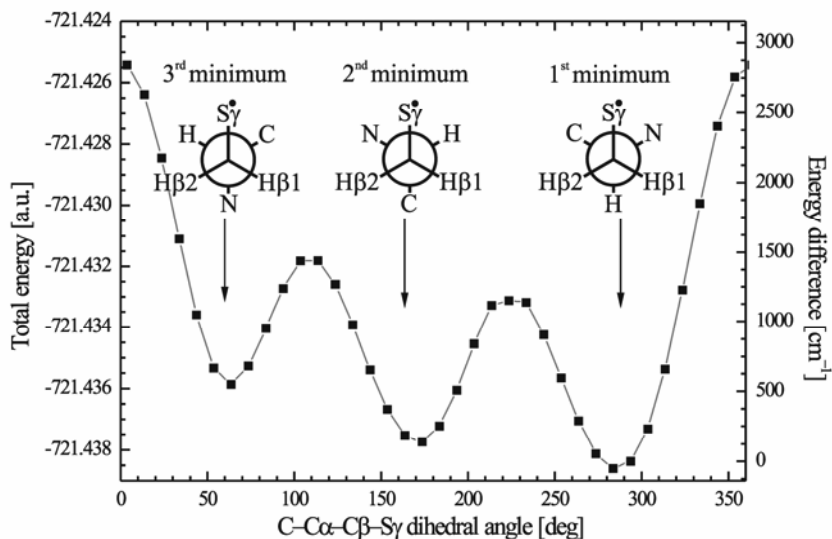


Figure 2. Potential energy surface for the cysteine thyl radical resulting from a constrained geometry optimization with respect to the C–C α –C β –S γ dihedral angle. Reproduced with permission from [128]. Copyright © 2004, American Chemical Society.

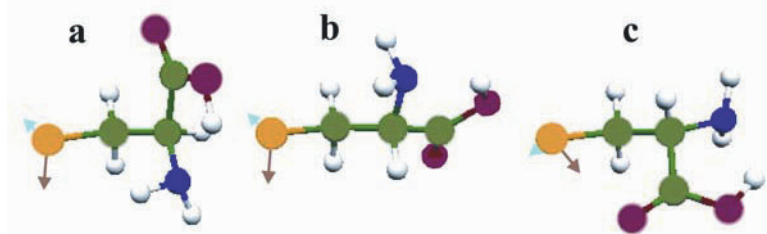


Figure 3. Overview of the three geometry-optimized structures of the cysteine thiyl radical, (a) 1st minimum, (b) 2nd minimum, and (c) 3rd minimum. The directions of the principal axes of the g -tensor: z (brown, parallel to the symmetry axis of the $3p$ orbital in the SOMO) and the y (light-blue) principal axis of the g -tensor are indicated. The x axis is parallel to the $C\beta-S\gamma$ direction. Reproduced with permission from [128]. Copyright © 2004, American Chemical Society.

The reason for the large errors in the calculations and the large g -shifts observed in crystals or frozen solutions containing the cysteine radical are readily understood upon examination of the electronic structure of this radical. The diagram in Figure 4 shows that the sulfur atom has two available lone pairs that are oriented perpendicular to the $C-S$ bond direction.

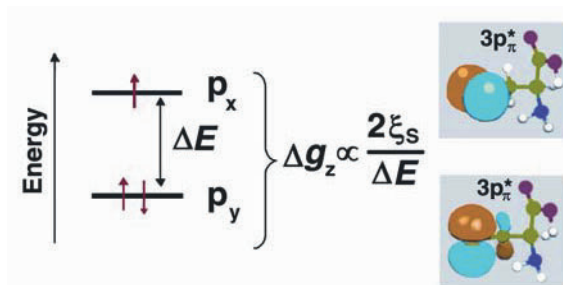


Figure 4. The sulfur lone pair orbitals of the cysteine radical (in the first minimum) and the relation of their energy separation to the g -shift (to second order).

For methyl-thiolate these two lone pairs are degenerate and, consequently, this radical exists in an orbitally degenerate ground state that is Jahn–Teller active. Under these conditions perturbation theory—which assumes an orbitally nondegenerate ground state—must fail and higher-order effects become important. In the case of the cysteine radical, the degeneracy is of course lifted by the low symmetry of the environment. Yet, the lowest lone pair \rightarrow SOMO excitation is still extremely low in energy. According to the high-level *ab initio* calculations reported in [128], this excited state occurs between ~ 1000 and 3000 cm^{-1} depending on the conformation of the cysteine radical. Since the SOC between the ground state and this first excited state induces a magnetic moment along the $C-S$ bond vector, the posi-

tion of this excited state will largely determine the g_{\max} shift along this direction. As the excitation energy is in the same range as the SOC matrix elements (the SOC constant is $\sim 382 \text{ cm}^{-1}$ for sulfur), higher-order effects of the SOC have been approximately taken into account and are listed as third-order results in Table 1.

Table 2. Experimental g -Values and Isotropic Hyperfine Parameters (MHz) for both β Protons and ^{33}S for Thiyl Radicals in Different Crystals or Disordered Systems

	g_x	g_y	g_z	$a_{\text{iso}}(H_1)$	$a_{\text{iso}}(H_2)$	$a_{\text{iso}}(^{33}\text{S})$
Crystals:						
HCl, e^- , 77 K	2.29	1.99	1.99	109	44	
HCl, UV, 77 K	2.251	2.004	1.985	101	34	
Penicillamine HCl, X, 4 K	2.297	2.037	1.921			
	2.217	2.000	1.983			
HCl, X, 4 K	2.244	2.001	1.984	100.8		
Cysteamine, γ , 77 K	2.242	1.999	1.980	92.4	42.0	
1,4-Dithiane, γ , 77 K	2.224	2.028	1.999	95.2	33.6	
N-acetylcysteine, e^- , 77 K	2.214	2.006	1.990	81.2	61.6	
N-acetylcysteine, X, 77 K	2.214	2.006	1.990	81.2	61.6	43 ⁺⁺
N-acetylcysteine, X, 4 K, H	2.493	1.923	1.897	113		7 ⁺⁺⁺
4 K, Y	2.164	2.012	2.003	110	55	+++
4 K, Dd ⁺	2.239	2.005	1.986	86	64	53 ⁺⁺
4 K, K ⁺	2.231	1.976	1.962	81	78	52 ⁺⁺
Frozen solutions/powder:						
		g_{\parallel}		g_{\perp}		
BSA 4mM, pH 7, 20 mM asc. [*]		2.17		2.008		
BSA lyophilized		2.16		2.006		
BSA dry film		2.17		2.006		
Cysteine HCl 300 mM, pH 3,						
1 M LiCl, 10 min 140 K ⁺		2.11		2.011		
Cysteine HCl 300 mM, pH 3,						
12 M LiCl, 10 min 150 K ⁺		2.10		2.015		
Cysteine crystalline powder		2.15		2.011		
Cysteine 300 mM, pH 3 [*]		2.30		2.008		

^{*}200 mM phosphate buffer.

⁺After annealing for 12 hours at room temperature.

⁺⁺Recalculated after taking the appropriate signs of the principal values into account (see [128], Table 3, for calculated values), i.e., the signs of principal values from the references have been changed to (199, -38, -32) MHz (X, 77 K), (200, -41, 0) MHz (Dd) and (178, -23, 0) MHz (K).

⁺⁺⁺Only observable at some orientations. Recalculated from principal values of (151, -78, -53) MHz.

⁺⁺⁺⁺No ^{33}S structure could be observed.

Reproduced with permission from [128]. Copyright © 2004, American Chemical Society.

The range of g -values found experimentally in various crystals and randomly oriented samples span a range from $g_x = 2.10$ to 2.49, and most of them are close to either 2.25 or 2.15. This range of g_x values is reproduced well by our calculations. However, the calculations are not able to reproduce the experimentally found g_z value, which seems to be consistently smaller than the free electron g value (for

some complexes, cf. Table 2; also, the g_y value is smaller than 2.0023). General expressions for the third-order correction to the \mathbf{g} -tensor are given by Atkins and Jamieson [129]. In our analysis, we considered a simple two-state model that included the SOMO (i.e., p_y) and the SOMO-1 (i.e., p_z) [128]. The resulting g -values are included in Table 1. Up to third order, the shift of g_z away from the free electron g -value (and for the 2nd minimum also that of g_y) has indeed become negative and now falls within the range of the experimental g_x values. We therefore concluded that the negative shifts of the g_z values observed for cysteine thiyl radicals are the result of higher than second-order contributions to the \mathbf{g} -tensor. For fully quantitative accuracy with respect to the experiment, one would have to go beyond third order, as can be done, for example, using two-component DFT methods that introduce the SOC into the SCF calculation [130–132].

While this result already gave sufficient insight in order to qualitatively understand the EPR spectroscopy of thiyl radicals, an unambiguous assignment of the individual species listed in Table 2 to one of the three minima was not unambiguously possible. Therefore, the hyperfine couplings of the C_β -protons were studied theoretically and compared to the available experimental data. As expected from McConnell type relations, the HFCs were strongly dependent on the conformation of the radical. In addition, both, the \mathbf{g} -tensor as well as the hyperfine couplings were strongly dependent on hydrogen bonds formed with the surrounding. This effect was modeled with either one or two additional water molecules. The comparison between theory and experiment in conjunction with the results obtained for the g -values made it possible to assign the conformation of the observed cysteine radical species with a good degree of confidence [128].

3.3. Solvent Effects: g -Tensors of Nitroxide Radicals

The above two examples made it clear that the immediate environment of the radicals has a distinct effect on the g -values and hyperfine couplings of the spin-carrying fragments. There are two principal types of effects to be distinguished: (a) “bulk” or unspecific effects that are mainly related to the polarity of the solvent, and (b) specific effects that depend on selective interactions between solvent and solute. In most cases these effects are related to the formation of hydrogen bonds.

In a systematic study of these effects, the EPR parameters of two nitroxide radicals (Fig. 5) were studied as a function of the polarity of the solvent [133,134].

The dominant mechanism for the g_{\max} -shift is straightforward (Fig. 6) and closely analogous to the case of the phenolic radicals or the cysteine radical discussed above. The oxygen molecule possesses an in-plane and an out-of-plane lone pair that is slightly higher in energy. Upon oxidation, the out-of-plane lone pair becomes the SOMO. The excitation from the in-plane to the out-of-plane lone pair is associated with a significant SOC matrix element along the N–O bond direction and leads to a dominant positive g_{\max} -shift along this direction.

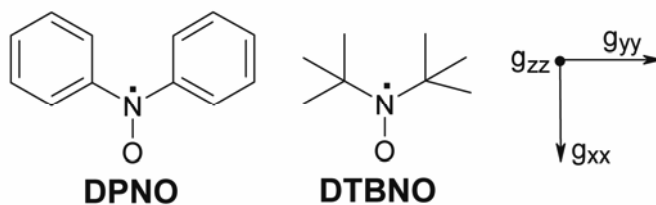


Figure 5. Molecular structures of the diphenyl nitric oxide (DPNO) and di-*tert*-butyl nitric oxide (DTBNO) radicals, and the g -tensor orientation. The largest component g_{xx} points along the N-O bond. Reproduced with permission from [133]. Copyright © 2006, American Chemical Society.

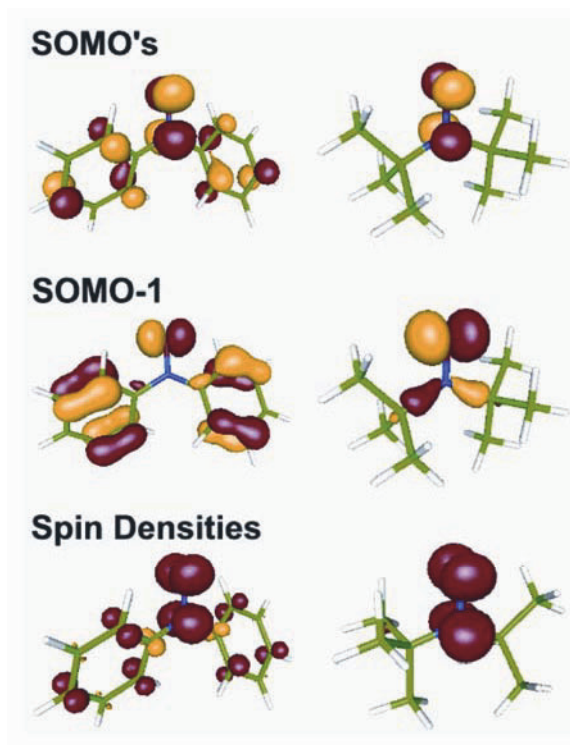


Figure 6. The semioccupied molecular orbitals (SOMOs), the doubly occupied SOMO-1 orbitals, and the spin densities of the DPNO (left) and DTBNO radicals (right). The SOMOs give an impression of the delocalization of the unpaired electron in these systems. The dominating Δg_{xx} shift is mainly the result of an electronic excitation from the SOMO-1 level to the SOMO orbitals. Reproduced with permission from [133]. Copyright © 2006, American Chemical Society.

The solvent effect on the g -tensor can be conveniently studied using popular polarizable continuum models [135]. In these approaches the solute is embedded in a molecular cavity. From the electrostatic potential exerted by the solute on the surface of the cavity one can calculate the screening charge on each surface segment, which is meant to model the polarization of the solvent by the solute [136]. The surface charges now interact with the electronic charge distribution via the potential they create inside the cavity. The solution of this coupled set of equations must therefore proceed iteratively in order to find a self-consistent set of screening charges together with the electronic charge distribution of the solute. The popular PCM model was already evaluated by Ciofini et al. [135,137–139] as well as by Rinkevicius et al. [134], and quite good results were found for aprotic solvents. In our study, we have evaluated the conductor-like screening (COSMO) model of Klamt and Schüürman [136]. With the B3LYP functional, the SOMF operator and reasonably large basis set (EPR-II and enhanced IGLO-III), our results differed by less than 100 ppm from the experimental values in the case of aprotic solvents and the solvent shifts on the isotropic g -values were very well reproduced. These results are clearly the most accurate available in the literature. However, it is also evident from Table 4 that the g -shifts are not as well modeled in the case of protic solvents that can readily be attributed to the formation of hydrogen bonds to the oxygen of the spin carrying N–O unit.

Table 3. Calculated g -shifts for the Di-*tert*-Butyl Nitric Oxide Radical DTBNO (see Scheme 1).

Solvent	BP86				B3LYP				Exptl.
	Δg_{xx}	Δg_{yy}	Δg_{zz}	Δg_{iso}	Δg_{xx}	Δg_{yy}	Δg_{zz}	Δg_{iso}	Δg_{iso}
Vacuum	6635	3734	-174	3399	7402	4114	-198	3773	–
TCL	6528	3702	-170	3353	7236	4074	-194	3705	3751 ± 20
Toluene	6525	3700	-170	3351	7228	4071	-195	3701	3741 ± 10
Acetone	6411	3659	-179	3297	7032	4014	-204	3614	3721 ± 50
Acetonitrile	6357	3658	-170	3282	6971	4013	-196	3596	3651 ± 10
Methanol	6359	3651	-176	3278	6972	4005	-201	3592	3471 ± 20
Water	6354	3651	-174	3277	6964	4005	-199	3590	3241 ± 10

All values in ppm. Solvent optimized geometries were used. Reproduced with permission from [133]. Copyright © 2006, American Chemical Society.

Thus, the models were straightforwardly enhanced by explicit water and methanol molecules that were attached to the oxygen of the nitroxide group (Fig. 7). Upon recalculating these “supermolecules” inside a COSMO cavity, accurate results were found in comparison to the experimental values. Thus, it was concluded that the COSMO model enables one to accurately study the solvent effect on the g -tensors of organic radicals if possible hydrogen bonds with the solvent are explicitly treated.

Table 4. Calculated *g*-Shifts for the Diphenyl Nitric Oxide Radical DPNO in Water or Methanol (MeOH), Including Explicit Solvent Molecules

Solvent	BP86				B3LYP			
	Δg_{xx}	Δg_{yy}	Δg_{zz}	Δg_{iso}	Δg_{xx}	Δg_{yy}	Δg_{zz}	Δg_{iso}
Gas phase calculations with explicit solvent molecules								
DPNO / 1 H ₂ O	6447	2632	-79	3000	7092	3076	-122	3349
DPNO / 2 H ₂ O	5915	2443	-51	2769	6396	2843	-108	3044
DPNO / 3 H ₂ O	5812	2375	-58	2709	6248	2763	-112	2966
DPNO / 1 MeOH	6463	2632	-40	3018	7098	3056	-105	3350
DPNO / 2 MeOH	5940	2457	-40	2786	6408	2830	-108	3043
DPNO / 3 MeOH	5860	2367	-62	2722	6311	2735	-116	2976
COSMO calculations with explicit solvent molecules^a								
DPNO / 1 H ₂ O	5986	2535	-57	2821	6448	2945	-99	3098
DPNO / 2 H ₂ O	5599	2359	-50	2636	5959	2734	-98	2865
DPNO / 3 H ₂ O	5462	2414	-171	2568	5891	2774	-200	2822
DPNO / 1 MeOH	6001	2543	-36	2836	6464	2932	-92	3101
DPNO / 2 MeOH	5545	2374	-26	2631	5897	2718	-94	2840
DPNO / 3 MeOH	5340	2260	+12	2537	5661	2602	-59	2735

All values in ppm. In the experiments, Δg_{iso} shifts of $+2761 \pm 10$ and $+3181 \pm 10$ ppm were found for the DPNO radical in water and methanol, respectively (see [133] for references to the original literature).

^a Solvent-optimized structures were employed for the *g*-tensor calculations.

Reproduced with permission from [133]. Copyright © 2006, American Chemical Society.

However, this approach also shows the limitations of this type of modeling: the positions and orientations of the additional solvent molecules are not well defined. The potential energy surfaces are extremely flat, and there certainly exist many minima in which the system could reside. Furthermore, it is likely that the system may interconvert rapidly between the different minima. Thus, even though such a supermolecule approach is attractive and straightforward, it is associated with considerable uncertainties. This situation could be resolved by explicit molecular dynamics calculations (see [140]), but this approach is still too expensive for general use.

In the original paper [133], the extension of the standard COSMO model to the self-consistent COSMO-RS model was reported. COSMO-RS is a further development of COSMO to “real solvents” [141], and it is supposed to model explicit effects like hydrogen bonding in a more accurate way without having to introduce explicit solvent molecules into the modeling. All that is needed is a screening charge profile of the solvent from a standard COSMO calculation. In [133] it was possible for the first time to include the COSMO-RS model explicitly into the SCF process in such a way that the screening charges now reflect the COSMO-RS model rather than the simpler standard COSMO. The resulting screening charges are visualized in Figure 8 and compared to the standard COSMO model for the DPNO radical. Positive screening charges (red color) were found at the nitroxide oxygen atom with its negative net charge. The difference plot of the screening

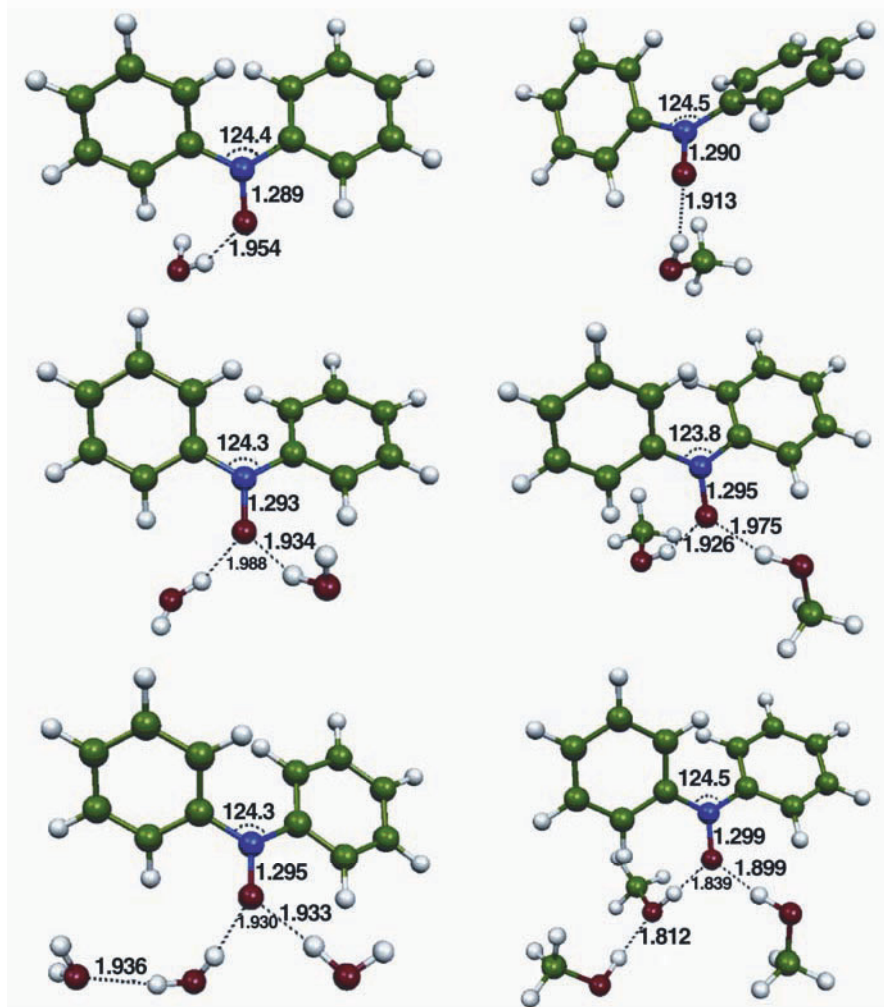


Figure 7. The DPNO radical in coordination with explicit solvent molecules (one, two, and three water or methanol molecules). Two solvent molecules form H-bonds to the nitroxide oxygen atoms, while the third solvent molecule is hydrogen bonded to another solvent molecule. The COSMO model was used in the geometry optimization ($\epsilon = 80.4$ for water and $\epsilon = 32.63$ for methanol). Reproduced with permission from [133]. Copyright © 2006, American Chemical Society.

charges from COSMO and D-COSMO-RS (Fig. 8d) shows that the D-COSMO-RS approach additionally increases the positive screening charges at the nitroxide oxygen atom. This stabilizes the lone pair orbitals on the oxygen and leads to a larger in-plane/out-of-plane energy gap, which then accounts for the observed variations

in the **g**-shift. These effects are quantitatively analyzed in Table 5. From this data one is able to conclude that—at least to some extent—the COSMO-RS model is able to simulate the effect of the explicit water molecules despite the fact that these water molecules have not been included in the model. However, they enter into the electronic structure determination via the modified COSMO-RS screening charges.

Table 5: Comparison of Spin Densities, Orbital Energies (eV), and **g**-Tensor Contributions (Relativistic Mass Correction [RMC], Diamagnetic Spin–Orbit [DSO], and Paramagnetic Spin–Orbit [PSO] Contributions) of the DPNO Radical in Water, Obtained from COSMO, D-COSMO-RS, and from COSMO Employing Additionally the Supermolecule Approach (B3LYP/IGLO-II)

Supermolecule approach ^a	COSMO	D-COSMO-RS	COSMO
Orbital energies (E_h)			
SOMO-1	-7.22	-7.46	-7.31
SOMO	-5.43	-5.77	-5.69
ΔE^b	1.79	1.69	1.62
g -tensor contributions (ppm)			
$\Delta g_{ii, RMC}$	-274	-269	-269
$\Delta g_{xx, DSO}$	+153	+153	+154
$\Delta g_{xx, PSO}$	+7046	+6261	+6074
$\Delta g_{yy, DSO}$	+213	+205	+176
$\Delta g_{yy, PSO}$	+3203	+3085	+2827
$\Delta g_{zz, DSO}$	+162	+157	+132
$\Delta g_{zz, PSO}$	+20	+32	+39
Mulliken spin-populations			
N	+0.36	+0.40	+0.42
O	+0.44	+0.39	+0.35
Atomic contributions to g_{psO} (ppm)			
$\Delta g_{xx} (N)$	+445	+547	+649
$\Delta g_{yy} (N)$	+809	+787	+904
$\Delta g_{zz} (N)$	0	0	-2
$\Delta g_{iso} (N)$	+418	+445	+517
$\Delta g_{xx} (O)$	+6453	+5565	+5309
$\Delta g_{yy} (O)$	+2115	+1967	+1716
$\Delta g_{zz} (O)$	-53	-54	-52
$\Delta g_{iso} (O)$	+2838	+2493	+2325

^a Model system with two explicit solvent molecules.

^b In vacuum, an energy difference of 1.91 eV was obtained for the SOMO and SOMO-1 levels. Reproduced with permission from [133]. Copyright © 2006, American Chemical Society.

3.4. SH Parameters in Proteins: QM/MM Studies

While the study presented in §3.3 is already quite encouraging in terms of including the leading environment effects via polarizable continuum models, the next level of sophistication is needed for detailed protein studies. As explained in §2.6,

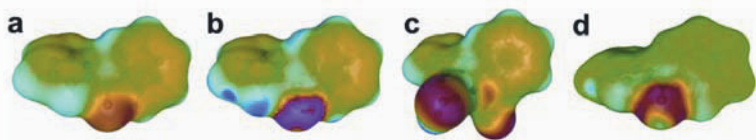


Figure 8. Visualization of the screening charges on the COSMO surface obtained for the DPNO radical in water. The plots were generated employing (a) the COSMO correction, (b) the D-COSMO-RS approach, (c) the supermolecule approach in combination with the COSMO method, and (d) a difference plot of the screening charges from COSMO and D-COSMO-RS. Positive screening charges are given in red. Reproduced with permission from [133]. Copyright © 2006, American Chemical Society.

this can be accomplished via QM/MM approaches that model the entire protein, active site, and at least the first solvation shell explicitly [105]. While such calculations are still quite time consuming, they show the enormous potential for the study of macromolecules with a combination of quantum mechanics and molecular mechanics. In [105] we have applied the QM/MM methodology to a well-known metalloprotein: the blue copper protein plastocyanin (Pc). Pc is one of the “trademark” systems of bioinorganic chemistry, and the electronic structure and spectroscopy of the active site in the Cu(II) state is very well understood [142–152]. In Figure 9 the system that was studied is explained. In Figure 9A the entire system is shown, where the solvent water molecules are shown in red and the protein backbone in green. This system was equilibrated and subjected to MD runs. In Figure 9B an 8 Å sphere around the active site is shown that was active in the following geometry relaxation. Finally, two models were selected for explicit quantum treatment: the model PCU-S is a small model and only has the copper ion, two histidines, one cysteine, and one methionine residue (all in a truncated form) in the quantum region. Model PCU-L includes the amino acids in their non-truncated forms and also adds an important residue (Asn38) to the quantum region that is supposed to strongly influence the properties of the cupric active site through hydrogen bonding to the cysteine sulfur. The Cu(II)–S_{Cys} bond is a famous bond in bioinorganic chemistry and gives rise to the blue color of the protein that arises from π -bonding to the π -antibonding transition between the two orbitals shown in Figure 9. The extremely high covalency of this bond is held responsible for most of the unique properties of the Cu(II) site in Pc compared to low-molecular-weight Cu(II) complexes [142–152].

Therefore, we have first studied the influence of the protein on the spin-populations in the Cu–S bond. In this study, the effects of scalar relativity were also probed on the basis of the popular ZORA approach [153], which is implemented into the ORCA package as described by van Wüllen [154]. Rather pronounced effects of the protein environment were found in these calculations. Although the spin-population is not a physical observable, our reference value was taken to be 41% spin-population on copper, which was advocated after the extensive studies of Solomon and coworkers [144,146–152]. If this value is accepted,

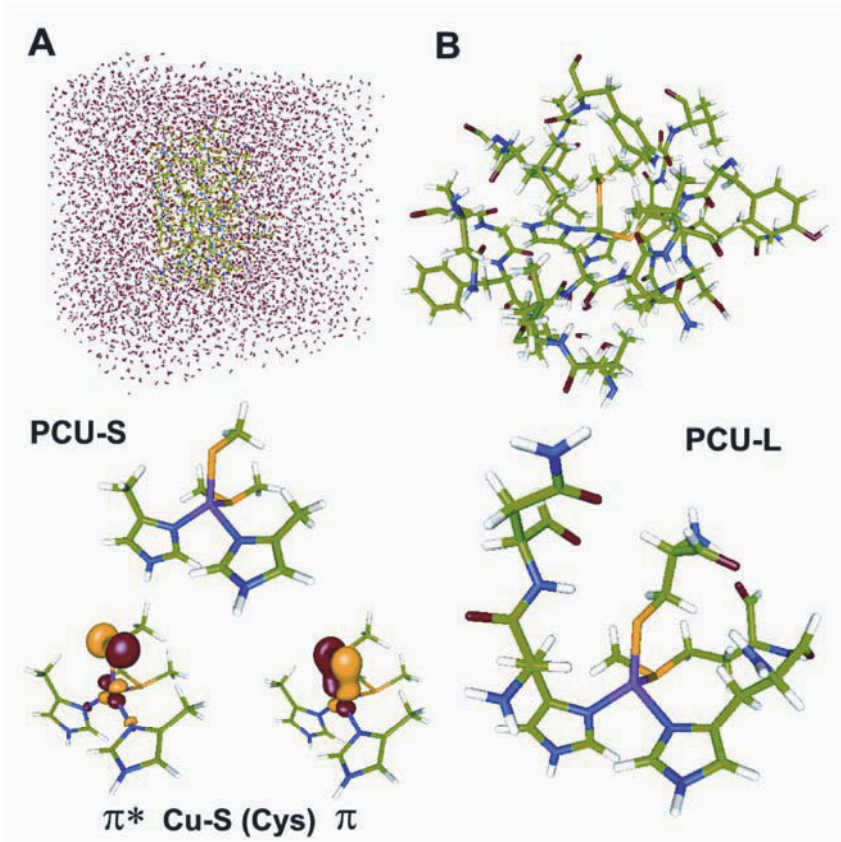


Figure 9. Models of the active site of Pc used in the QM/MM study (see text for explanation). Reproduced with permission from [105]. Copyright © 2006, Wiley.

Table 6 shows that the PCU-S in the gas phase rather dramatically underestimates the spin-population on copper. This has previously been taken as an indication for a failure of DFT and has led to revised functionals with increased amounts of HF exchange, which is known to correct the metal–ligand covalencies into the ionic direction [155]. Upon immersing the site in a dielectric continuum with $\epsilon = 4$, which is the standard value taken for a protein environment [156,157], the spin slightly shifts in direction of the copper while the entire protein effect brings the calculated value close to the best experimental estimate of 41% spin-population on Cu. The effects of scalar relativity are visible in the results but are not dominant. Similar effects were found for the large model without any dramatic differences, which shows that the additional hydrogen bond to Asn38 is not of dominant importance for the spin distribution within the active site of Pc

but that rather long-range electrostatic protein effects have a large effect on the spin distribution.

Table 6. Calculated Mulliken Spin Populations of the Copper Ion and the Cysteine Sulfur Atom

Model	Atom	NonRel			ZORA		
		Gas	Continuum	Protein	Gas	Continuum	Protein
PCU-S	Cu	0.32	0.36	0.41	0.35	0.39	0.44
	S	0.57	0.53	0.46	0.54	0.50	0.43
PCU-L	Cu	0.33	0.37	0.39	0.36	0.40	0.43
	S	0.53	0.49	0.46	0.50	0.46	0.43

Results from single-point calculations on the QM layer of the QM/MM geometry optimization without surrounding ("gas"), employing the COSMO dielectric continuum approach with a dielectric constant of 4 ("continuum"), and including the MM point charges in the calculations ("protein"). 41% Cu $d_{x^2-y^2}$ character of the SOMO were obtained in the experiments.

Reproduced with permission from [105]. Copyright © 2006, Wiley.

The calculated **g**-tensor thoroughly reflects the results obtained for the spin-populations. While g_{\min} ($= g_1$) and g_{mid} ($= g_2$) are predicted with good accuracy, the value of g_{\max} ($= g_3$) is underestimated in all calculations. This is a DFT error commonly observed for Cu(II) and has been analyzed in some detail previously [60]. It is mainly due to errors in the $d-d$ transition energies, and in the original paper a semi-empirical estimate of this error was made on the basis of ligand field theory, which brought the results into acceptable agreement with experiment.

Table 7. Calculated **g**-Tensor of Plastocyanin

		NonRel			ZORA			Exptl.
		Gas	Continuum	Protein	Gas	Continuum	Protein	
g_1	PCU-S	2.039	2.044	2.050	2.043	2.048	2.055	2.047
	PCU-L	2.039	2.044	2.047	2.043	2.048	2.051	
g_2	PCU-S	2.064	2.065	2.066	2.067	2.068	2.070	2.059
	PCU-L	2.062	2.064	2.064	2.067	2.068	2.068	
g_3	PCU-S	2.119	2.132	2.151	2.132	2.147	2.166	2.226
	PCU-L	2.117	2.133	2.142	2.133	2.148	2.157	
g_{iso}	PCU-S	2.074	2.080	2.089	2.081	2.088	2.097	2.111
	PCU-L	2.073	2.080	2.084	2.081	2.088	2.092	

Reproduced with permission from [105]. Copyright ©2006, Wiley.

Even more challenging than the determination of the **g**-tensor is the calculation of the copper hyperfine tensor since it has large contributions from three terms of

very different origin that are all of the same order of magnitude but are of opposing signs. The relatively low quality of the “raw” DFT values becomes apparent from inspecting the results in Tables 3 and 4 in [105], where none of the calculations show good agreement with experiment. This is a result of two reinforcing errors. The error in the SOC part is closely related to the error in the \mathbf{g} -tensor, while the error in the Fermi contact term is a genuine DFT error. Based on the analysis of these errors, we [105] proposed a scaling of the isotropic HFC of Cu(II) by 1.09, which brought the values of the Cu–HFC into good agreement with the experimental values. Thus, this study together with others [46,108] show that, at this point, DFT is not able to provide accurate values for metal HFCs. However, the DFT errors are very systematic and can be greatly reduced by scaling procedures [46,54,104,158–166].

While the dominant EPR parameters (\mathbf{g} -tensor, metal hyperfine, and also ZFS [§3.6]) are difficult to calculate with high accuracy by DFT methods, the situation is more fortunate for the magnetic parameters (HFCs, NQCs) of the remote ligand nuclei that can be probed by high-resolution magnetic resonance experiments. This is also confirmed by our results on the nitrogen HFCs of Pc that are collected in Table 8. The results are of quite good quality, and the effects of the protein and of relativity were found to be limited. Calculated proton HFCs are also presented in [105] and show good agreement with the experimental data.

Table 8. Calculated ^{14}N Hyperfine Coupling Constants A (MHz), Nuclear Quadrupole Coupling Constants e^2qQ/h (MHz), and Asymmetry Parameters η of the Large Model System PCU-L

	NonRel			ZORA.			Exptl.
	Gas	Continuum	Protein	Gas	Continuum	Protein	
His 37, $N_{\delta 1}$							
A_{FC}	+13.7	+16.0	+17.4	+13.7	+15.7	+16.9	+18.1
$A_{1, SD}$	+2.8	+3.4	+3.7	+3.0	+3.5	+3.9	+1.0
$A_{2, SD}$	-1.2	-1.5	-1.6	-1.3	-1.5	-1.7	-0.1
$A_{3, SD}$	-1.6	-1.9	-2.1	-1.7	-2.0	-2.2	-0.9
e^2qQ/h	-2.4	-2.2	-2.1	-2.2	-2.1	-2.0	+2.9
η	0.7	0.8	0.9	0.6	0.7	0.8	0.5
His 87, $N_{\delta 1}$							
A_{FC}	+23.4	+25.8	+28.3	+23.0	+25.1	+27.3	+25.1
$A_{1, SD}$	+3.9	+4.6	+5.1	+4.2	+4.8	+5.3	+2.7
$A_{2, SD}$	-1.7	-2.0	-2.3	-1.8	-2.1	-2.4	-1.1
$A_{3, SD}$	-2.2	-2.6	-2.9	-2.3	-2.7	-2.9	-1.5
e^2qQ/h	-2.4	-2.3	-2.1	-2.4	-2.3	-2.1	2.5
η	0.6	0.7	0.8	0.5	0.6	0.7	0.6
His 37, $N_{\epsilon 2}$							
A_{FC}	+0.63	+0.74	+0.80	+0.63	+0.72	+0.76	+0.87
$A_{1, SD}$	+0.18	+0.21	+0.23	+0.19	+0.22	+0.24	+0.23
$A_{2, SD}$	-0.03	-0.04	-0.05	-0.03	-0.04	-0.05	-0.07
$A_{3, SD}$	-0.15	-0.17	-0.18	-0.17	-0.18	-0.19	-0.18
e^2qQ/h	-2.7	-2.5	-2.2	-2.6	-2.4	-2.1	-1.37
η	0.1	0.1	0.3	0.2	0.2	0.2	0.86

Table 8, cont'd

His 87, N _{e2}							
A_{FC}	+1.04	+1.10	+1.19	+1.01	+1.04	+1.13	+1.30
$A_{1, SD}$	+0.18	+0.21	+0.24	+0.19	+0.22	+0.25	+0.35
$A_{2, SD}$	-0.06	-0.07	-0.09	-0.06	-0.07	-0.09	-0.04
$A_{3, SD}$	-0.11	-0.14	-0.15	-0.13	-0.15	-0.16	-0.32
e^2qQ/h	-2.7	-2.5	-2.2	-2.6	-2.5	-2.2	-1.43
η	0.1	0.1	0.3	0.2	0.2	0.2	0.95

Experimental results from azurin, assigned to the ^{14}N nuclei of His 117 and His 46 (for references to the original data, see [105]). Reproduced with permission from [105]. Copyright © 2006, Wiley.

Based on the results obtained for the spin distribution between copper and sulfur, it is not surprising that the C_{β} -proton couplings of Pc react much more sensitively to the protein environment since it affects the spin-population on the nearby sulfur to a large extent and this spin-population is largely responsible for the observed ^1H -HFCs. If we take the ZORA calculations on the large model inside the protein environment as the best theoretical estimate, it becomes apparent that the calculations overestimate the proton HFCs by ~20%. Part of this can be traced back to slight errors in the calculated dihedral angle $\text{H}-\text{C}_{\beta}-\text{S}-\text{Cu}$ to which the proton HFCs react very sensitively [167,168]. The remaining error may be blamed on a slight overestimation of the spin-population on the sulfur, but we also note that different groups experimentally obtained rather different values for the HFCs (Table 9).

Table 9. Cysteine 84 Isotropic HFCs of the $\text{H}_{\beta 2}$ and $\text{H}_{\beta 1}$ Nuclei (MHz)

		NonRel			ZORA			Exptl.
		Gas	Continuum	Protein	Gas	Continuum	Protein	
PCU-S	Cys 84 $\text{H}_{\beta 1}$	35.4	33.5	28.1	34.3	32.3	27.1	17.4
	Cys 84 $\text{H}_{\beta 2}$	45.6	41.7	36.2	44.3	40.3	35.0	23.2
PCU-L	Cys 84 $\text{H}_{\beta 1}$	33.4	30.9	27.3	32.3	32.8	26.2	17.4
	Cys 84 $\text{H}_{\beta 2}$	35.8	33.2	31.0	40.3	34.3	29.0	23.2

Werst et al. obtained experimental values of 27 and 16 MHz [167]. Bertini et al. measured values of 17.4 and 23.2 MHz [169]. Reproduced with permission from [105]. Copyright © 2006, Wiley.

In summary, the results of [105] show the possibilities of entire protein QM/MM modeling of metalloproteins but also demonstrate the limitations that the theoretical approaches still have.

3.5. Zero-Field Splittings: Origin of ZFS in Organic Triplets and Diradicals

The final SH parameter for which until very recently no large-scale DFT implementation has been available is the SS contribution to the ZFS. Since the SS contribution does dominate the ZFS of organic triplets and diradicals, we have

tested our implementation within the ORCA program on a series of organic molecules in triplet states (Fig. 10).

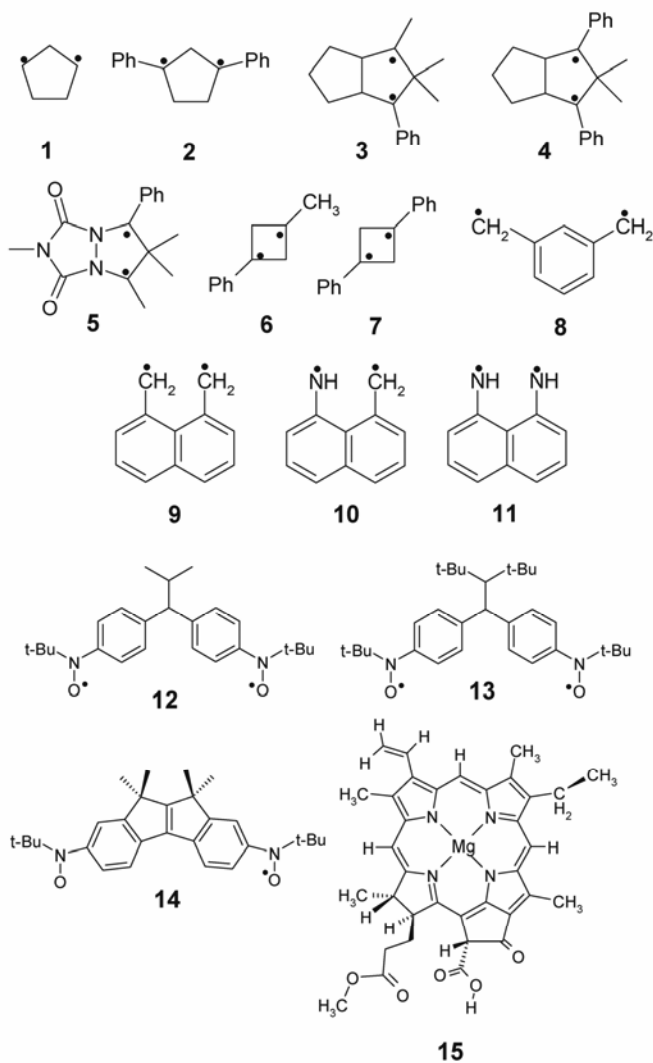


Figure 10. Molecules chosen for evaluating the accuracy of DFT in the prediction of ZFSs of organic molecules in triplet states. Reproduced with permission from [85]. Copyright © 2006, American Chemical Society.

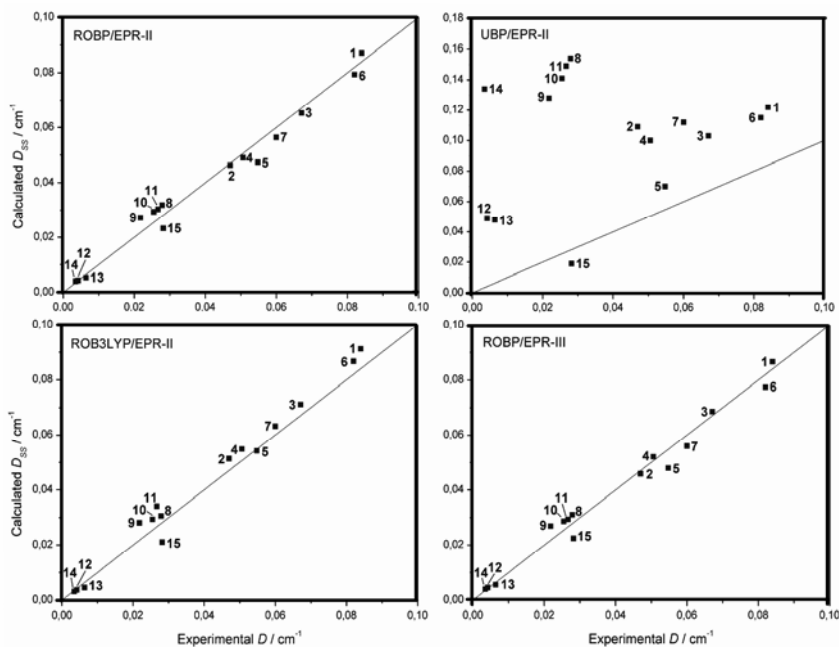


Figure 11. Correlation of calculated D_{SS} with measured D values for organic radicals 1–15 from Figure 10. Comparison of restricted open shell ROBP86/EPR-II (top left), unrestricted UBPP86/EPR-II (top right), ROB3LYP/EPR-II (bottom left), and ROBPP86/EPR-III (bottom right) calculations. In all cases, single-point calculations on triplet state geometries were performed. RMSD values of 0.0035 cm^{-1} (BP86/EPR-II), 0.0772 cm^{-1} (UBPP86/EPR-II), 0.0035 cm^{-1} (BP86/EPR-III), and 0.0045 cm^{-1} (B3LYP/EPR-II) were obtained. Reproduced with permission from [85]. Copyright © 2006, American Chemical Society.

The SS contribution was calculated according to Eq. (68) without any further approximation. The structures of the molecules were optimized using RI-BP86/SV(P), while the properties were calculated with either BP86 or B3LYP together with the EPR-II and EPR-III basis sets. Both bases were found to be adequate for the purpose of predicting ZFSs [85]. In particular, for $^3\text{O}_2$ they were found to give results close enough to those obtained with the very large QZVP basis set [170], which is believed to provide results close to the basis set limit.

The results are documented in Figure 11 and were found to be puzzling and encouraging at the same time. The curious effect was observed that spin-unrestricted calculations that are quite successful in predicting other EPR parameters failed badly in the prediction of ZFSs. However, open-shell spin restricted calculations provided results that were in excellent agreement with the experimental values. The RMSD values were as low as 0.0035 cm^{-1} (ROBP86/EPR-III) and 0.0045 cm^{-1} (ROB3LYP/EPR-II). It is to be noted that the results with the larger EPR-III basis set present no improvement over those obtained with EPR-II and

gave the same RMS values when used with the BP86 functional. At present we have no convincing explanation of why RODFT does as good as it does while UDFT does as poorly as observed. The effects of spin-contamination are of minor importance in these molecules and the differences between the spin distributions calculated with the two approaches are also not pronounced. Consequently, the effect must be quite subtle and warrants a much closer theoretical investigation.

Nevertheless, the results obtained with ROB86 are quite encouraging, and the fact that the calculations can be readily carried out even for molecules as large as **15** on a single processor of a standard personal computer shows that the method is indeed applicable to “real-life” problems.

However, as a word of caution, we present the data in Table 10. It is observed that the DFT calculations follow the general trend to decreasing ZFSs with larger size of the aromatic system. However, they clearly underestimate the ZFS beyond benzene. However, the results are quite sensitive to the geometries employed (ground state singlet or optimized triplet)—another subtle effect that is difficult to trace. We tentatively speculate that the failures of DFT may be due to the neglect of medium-range correlation by DFT methods. This has been spectacularly demonstrated by Grimme most recently in a study dealing with isomerization energies of simple alkanes and for which DFT methods failed badly [171]. Nevertheless, the study of Loboda et al. [79] as well as our study [85] demonstrated that better predictions of the SS part of the ZFS can actually be obtained on the basis of CASSCF wavefunctions.

Table 10. Comparison of Experimental and Calculated *D* Parameters for Benzene and Polyacenes

	BP86/EPR-II	BP86/EPR-III	B3LYP/EPR-III	Exptl.
Benzene	0.163	0.159	0.162	0.1593
Naphthalene	0.053	0.052	0.051	0.1004
Anthracene	0.042	0.042	0.041	0.0702
Tetracene	0.032	0.031	0.032	0.0573

Reproduced with permission from [85]. Copyright © 2006, American Chemical Society.

3.6. Zero-Field Splittings: Origin of the ZFS in transition metal complexes

As for all other SH parameters, transition metal complexes are particularly challenging; and even more so when it comes to the ZFS, which is arguably the most complicated of the SH parameters. We have recently reported a high-level MRCI implementation of the SOC contribution to the ZFS and have obtained very accurate results for the SOC splittings of the atomic multiplet terms for main group atoms, transition metal atoms, and small diatomic molecules [172]. In addition, we

have evaluated the SS part by a mean-field approximation in the multideterminantal ab initio framework, and it has been shown that this simple approximation works well for $^3\text{O}_2$ [85,172]. Unfortunately, these accurate calculations cannot be extended to the case of large transition metal complexes due to the excessive computational effort involved. Nevertheless, of the available ab initio approaches it is still possible to apply the CASSCF method or the simplified SORCI method to molecules of the size of $\text{Mn}(\text{acac})_3$, which we have chosen as our initial test molecule for studying ZFS in transition metal complexes ([84]; see Fig. 12).

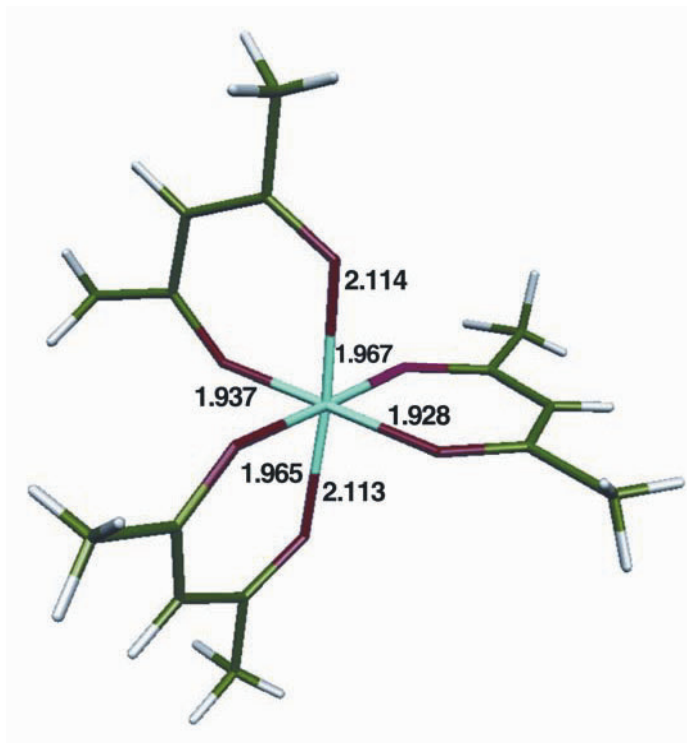


Figure 12. Structure of the complex $\text{Mn}(\text{acac})_3$ used for evaluation of ZFS effects in transition metal complexes. Rproduced with permission from [84]. Copyright © 2006, American Chemical Society.

$\text{Mn}(\text{acac})_3$ is a high-spin d^4 system with tetragonal distortion. Its ZFS has been measured to high precision by Barra et al. [173] and by Krzystek et al. [174], who arrived at values of $D = -4.52 \text{ cm}^{-1}$ and $E/D = 0.05 \text{ cm}^{-1}$. Krzystek et al. also provided a concise ligand field explanation of the origin of the ZFS: due to the Jahn–Teller active d^4 ion, the complex distorts in the direction of tetragonal elongation, which leaves the d_{z^2} -based MO empty, and according to the standard ligand-field

analysis, this leads to a negative D -value [174] (for further ligand field arguments, see [9]).

The DFT calculations documented in Table 11 predict the correct sign and an overall reasonable rhombicity. However, the absolute value of D is considerably underestimated. As expected, the SOC part contains two significant contributions: the first contribution comes from the $\alpha \rightarrow \alpha$ excitations. These correspond primarily to the spin-allowed (quintet \rightarrow quintet) ligand field excitations and have usually been solely held responsible for the ZFS. However, compared to the final value they contribute only $\sim -0.4 \text{ cm}^{-1}$ ($\sim 16\%$), which renders arguments based on spin-allowed ligand field excitations alone in high-spin d^4 systems unreliable. As anticipated, a second and even larger SOC contribution arises from the $\alpha \rightarrow \beta$ (quintet \rightarrow triplet) excitations. These excitations contribute $\sim 40\text{--}50\%$ of the final D -value. Perhaps the most surprising number in Table 11 is the large contribution of the direct spin-spin coupling term. It contributes as much as -1 cm^{-1} to the final D -value and therefore significantly improves the agreement with the experimental values. The final predicted D is then still underestimated, but since all terms have been treated with a minimum number of approximations (SOC and spin-spin integrals), it is believed that this number properly reflects the intrinsic accuracy of the DFT-based procedures for the prediction of ZFSs in transition metal complexes. Again, it has been found in [84] that ab initio procedures provide somewhat better agreement with experiment, and this has been attributed to the fact that the spin-flip excitations can be rigorously and correctly represented in a multiterminal framework, while this does not seem to be possible within a DFT philosophy [84]. Nevertheless, this study has come to the important conclusions that: (a) the spin-spin contributions to the ZFS are much larger than has been assumed for decades in transition metal EPR spectroscopy and must be taken into account in any quantitative analysis and (b) the spin-flip contributions that are often neglected in the analysis of transition metal ZFSs are of major importance. The latter statement even holds in the case of the high-spin d^4 configuration and is of course particularly true also for the high-spin d^5 configuration, where no allowed sextet-sextet ligand field transitions could contribute to the observed SOC contribution of the ZFS.

4. CONCLUDING REMARKS

In the present chapter the theory of SH parameters as it is implemented today in sophisticated quantum chemical program packages has been presented and illustrated through a series of representative applications. Although this review already contains a significant number of equations, it has not been possible to describe all important recent developments in detail (for a review, see [13]). It is nevertheless hoped that the general lines of reasoning became transparent to the interested reader in this way. Hopefully, it also became evident that the theoretical approaches based on DFT are already highly useful in complementing experimental investigations. The methods have been developed to a stage where the programs

Table 11. Comparison of Contributions to the Calculated Zero-Field Splitting between the Quasi-Restricted DFT Method and the Pederson–Khanna–Kortus Approach as well as Comparison of the Results Obtained with the SOMF and V^{eff} SOC operators (BP86/TZVP, all numbers in cm^{-1})

Method		D	E
BP86-QR ^a	$\alpha \rightarrow \alpha$	-0.42	-0.03
	$\beta \rightarrow \beta$	-0.03	-0.00
	$\alpha \rightarrow \beta$	-1.07	-0.10
	$\beta \rightarrow \alpha$	+0.00	+0.00
	Spin-Spin	-0.99	-0.17
	Total	-2.51	-0.316
BP86-PKK ^b	$\alpha \rightarrow \alpha$	-0.32	-0.04
	$\beta \rightarrow \beta$	+0.02	-0.01
	$\alpha \rightarrow \beta$	-1.29	-0.14
	$\beta \rightarrow \alpha$	-0.01	+0.01
	Spin-Spin	-0.99	-0.18
	Total	-2.59	-0.36
Exp.		-4.52	-0.25

^a with quasi-restricted method; Eq. (85). ^b with Pederson/Khanna/Kortus method; Eq. (84).
 Reproduced with permission from [84]. Copyright © 2006, American Chemical Society.

can be readily used by non-experts and provide results that frequently compare well with the experimental measurements. This is to a large extent true for organic radicals and triplets, while the area of transition metal EPR spectroscopy is still an enormous challenge to theory. Nevertheless, if viewed with sufficient care, the calculations can be of tremendous help in analyzing complicated spectra. For example, the calculations tend to give tensor orientations that are quite good, and this information is often difficult to determine from the experimental spectra without any additional source of information such as laborious single-crystal measurements. Thus, a reasonable strategy will often be to start extended simulation procedures from a set of theoretically calculated parameters and refine them through nonlinear least-squares fitting. In many cases it will be found that the theoretical values will need adjustment. Even if the calculations give errors on the order of 10–30%, they usually provide correct trends and can therefore be of invaluable aid in the deconvoluting highly complex spectral patterns. We hope that this chapter contributes to this line of thought in the following ways: (a) to explain the general strategies that lead to the currently used methods, (b) to document precisely what is being done in the available program packages, (c) to hint about how the calculations can be done in practice, and (d) to show what can be achieved on the basis of the available methods. There is no doubt that the development of theoretical methods for the prediction of EPR parameters has to continue in order for theory to become an even stronger partner of experiment. However, the rapid progress that has been

made in this field over the last ten years provides an optimistic view for the future of this exciting partnership.

ACKNOWLEDGMENTS

I wish to express my deep gratitude to the numerous colleagues and coworkers listed in the original literature, who have contributed their incredible expertise, insight, and enthusiasm to the respective studies. All of these studies cited were performed in the spirit of open collaboration, and it has been a real pleasure to be involved in them. I am also very grateful for having had the opportunity to work with many highly motivated students and postdocs without whom the work presented here would have been impossible. Furthermore, financial support from the Deutsche Forschungsgemeinschaft (priority program 1137, “molecular magnetism”), the SFB 663 (“Molecular response to electronic excitation,” University of Düsseldorf), and the German–Israeli Foundation (grant I*746-137.9/2002) are gratefully acknowledged.

REFERENCES

1. Schweiger A, Jeschke G. 2001. *Principles of pulse electron paramagnetic resonance*. Oxford: Oxford UP.
2. Pake GE, Estle TL. 1973. *The physical principles of electron paramagnetic resonance*. London: W.A. Benjamin.
3. Neese F. 2003. *Curr Opin Chem Biol* 7:125
4. Griffith JS. 1964. *The theory of transition metal ions*. Cambridge: Cambridge UP.
5. Abragam A, Bleaney B. 1970. *Electron paramagnetic resonance of transition ions*. Oxford: Clarendon Press.
6. Atherton NM. 1993. *Principles of electron spin resonance*, 2nd ed. New York: Ellis Horwood, Prentice-Hall.
7. Piligkos S, Bill E, Collison D, McInnes EJJ, Timco GA, Weihe H, Winpenny REP, Neese F. 2007. *J Am Chem Soc* 129:760
8. Neese F. 2006. ORCA: an ab initio density functional and semiempirical program package, Version 2.6.0. University of Bonn, Germany. Free download at <http://www.thch.uni-bonn.de/tc/orca/>.
9. Neese F, Solomon EI. 2002. In *Magnetoscience: from molecules to materials*, Vol. 4, p. 345. Ed JS Miller, M Drillon. Weinheim: Wiley-VCH.
10. Neese F. 2004. In *The quantum chemical calculation of NMR and EPR properties*, p. 581. Ed M Kaupp, M Bühl, V Malkin. Heidelberg: Wiley-VCH.
11. Neese F. 2004. In *The quantum chemical calculation of NMR and EPR properties*, p. 541. Ed M Kaupp, M Bühl, V Malkin. Heidelberg: Wiley-VCH.
12. Neese F, Munzarova ML. 2004. In *The quantum chemical calculation of NMR and EPR properties*, p. 21. Ed M Kaupp, M Bühl, V Malkin. Heidelberg: Wiley-VCH.
13. Neese F. 2006. In *Specialist periodical reports on EPR spectroscopy*, pp. 73ff. Ed B Gilbert. London: Royal Society of Chemistry.
14. Kaupp M, Malkin V, Bühl M. 2004. *The quantum chemical calculation of NMR and EPR properties*. Heidelberg: Wiley-VCH.

15. Patchkovskii S, Schreckenbach G. 2004. In *Calculation of NMR and EPR parameters*, p. 505. Ed M Kaupp, V Malkin, M Bühl. Weinheim: Wiley-VCH.
16. Koch W, Holthausen MC. 2000. *A chemist's guide to density functional theory*. Weinheim: Wiley-VCH.
17. Szabo A, Ostlund NS. 1982. *Modern theoretical chemistry*. New York: Macmillan.
18. Frisch MJ, Trucks GW, Schlegel HB, Scuseria GE, Robb MA, Cheeseman JR, Montgomery JJA, Vreven T, Kudin KN, Burant JC, Millam JM, Iyengar SS, Tomasi J, Barone V, Mennucci B, Cossi M, Scalmani G, Rega N, Petersson GA, Nakatsuji H, Hada M, Ehara M, Toyota K, Fukuda R, Hasegawa J, Ishida M, Nakajima T, Honda Y, Kitao O, Nakai H, Klene M, Li X, Knox JE, Hratchian HP, Cross JB, Bakken V, Adamo C, Jaramillo J, Gomperts R, Stratmann RE, Yazyev O, Austin AJ, Cammi R, Pomelli C, Ochterski JW, Ayala PY, Morokuma K, Voth GA, Salvador P, Dannenberg JJ, Zakrzewski VG, Dapprich S, Daniels AD, Strain MC, Farkas O, Malick DK, Rabuck AD, Raghavachari K, Foresman JB, Ortiz JV, Cui Q, Baboul AG, Clifford S, Cioslowski J, Stefanov BB, Liu G, Liashenko A, Piskorz P, Komaromi I, Martin RL, Fox DJ, Keith T, Al-Laham MA, Peng CY, Nanayakkara A, Challacombe M, Gill PMW, Johnson B, Chen W, Wong MW, Gonzalez C, Pople JA. 2004. Gaussian 03 (<http://www.gaussian.com/>), revision C.02. Wallingford CT.
19. Ågren H, Helgaker T, Jørgensen P, Klopper W, Olsen J, Ruud K, Vahtras O, and co-workers. 2005. DALTON, a molecular electronic structure program, Release 2.0.
20. Baerends EJ, Ziegler T, and coworkers. 2005. ADF2004.01 (<http://www.scm.com>). Amsterdam, The Netherlands.
21. Malkin VG, Malkina OL, Reviakine R, Arbuznikov AV, Kaupp M, Schimmelpfennig B, Malkin I, Helgaker T, Ruud K. 2003. MAG-ReSpect, version 1.1. Würzburg and Bratislava.
22. McWeeny R. 1992. *Methods of molecular quantum mechanics*. London: Academic press.
23. Stavrev KK, Zerner MC. 1997. *Int J Quantum Chem* **65**:877.
24. Zerner MC. 1989. *Int J Quantum Chem* **35**:567.
25. Edwards WD, Zerner MC. 1987. *Theor Chem Acta* **72**:347.
26. Scuseria GE. 1999. *J Phys Chem A* **103**:4782.
27. Ochsenfeld C, Kussmann J, Koziol F. 2004. *Angew Chem, Int Ed* **43**:4485.
28. Jensen F. 1999. *Introduction to computational chemistry*. New York: Wiley.
29. Gauss J. 2000. In *Modern methods and algorithms in quantum chemistry*, p. 1. Ed J Grotendorst. Jülich: John von Neumann Institute for Computing.
30. Saebø S, Pulay P. 1987. *J Chem Phys* **86**:914.
31. Saebø S, Pulay P. 1988. *J Chem Phys* **88**:1884.
32. Pulay P, Saebø S. 1986. *Theor Chim Acta* **69**:357.
33. Schütz M, Werner H-J. 2001. *J Chem Phys* **114**:661.
34. Schütz M, Werner H-J, Manby FR. 2004. *J Chem Phys* **121**:737.
35. Werner H-J, Manby FR. 2006. *J Chem Phys* **124**:054114.
36. Werner H-J, Manby FR, Knowles PJ. 2003. *J Chem Phys* **118**:8149.
37. Parr RG, Yang W. 1989. *Density functional theory of atoms and molecules*. Oxford: Oxford UP.
38. Marian CM. 2001. In *Reviews in computational chemistry*, Vol 17. Ed KB Lipkowitz, DB Boyd. New York: Wiley-VCH.
39. Hess BA, Marian CM, Peyerimhoff SD. 1995. In *Modern electronic structure theory*, pp. 152–278. Ed D Yarkony. Singapore: World Scientific Publishing.

40. Hess BA, Marian CM. 2000. In *Computational molecular spectroscopy*, pp. 169ff. Ed P Jensen, PR Bunker. New York: John Wiley & Sons.
41. Neese F. 2005. *J Chem Phys* **122**:034107/1.
42. Cohen Tanudji C, Diu B, Laloe F. 1977. *Quantum mechanics*, Vol. 2. Paris: Wiley.
43. Hess BA, Marian CM, Wahlgren U, Gropen O. 1996. *Chem Phys Lett* **251**:365.
44. Berning A, Schweizer M, Werner HJ, Knowles PJ, Palmieri P. 2000. *Mol Phys* **98**:1823.
45. Harriman JE. 1978. *Theoretical foundations of electron spin resonance*. New York: Academic Press.
46. Neese, F. 2003. *J Chem Phys* **118**:3939.
47. Luken EAC. 1969. *Nuclear quadrupole coupling constants*. London: Academic Press.
48. McWeeny R. 1970. *Spins in chemistry*. New York: Academic Press.
49. McWeeny R. 1965. *J Chem Phys* **42**:1717.
50. Neese F, Solomon EI. 1998. *Inorg Chem* **37**:6568.
51. Neese F, Solomon EI. 1999. *Inorg Chem* **38**:1847.
52. Neese F. 2001. *Int J Quantum Chem* **83**:104.
53. Neese F. 2003. *Chem Phys Lett* **380**:721.
54. Neese F. 2004. *Magn Reson Chem* **42**:S187.
55. Bündgen P, Lushington GH, Grein F. 1995. *Int J Quantum Chem* **29**:283.
56. Bruna PJ, Lushington GH, Grein F. 1996. *Chem Phys Lett* **258**:427.
57. Lushington GH, Grein F. 1997. *J Chem Phys* **106**:3292.
58. Vahtras O, Minaev B, Agren H. 1997. *Chem Phys Lett* **281**:186.
59. Engström M, Minaev B, Vahtras O, Agren H. 1998. *Chem Phys Lett* **237**:149.
60. Neese F. 2001. *J Chem Phys* **115**:11080.
61. van Lenthe E, van der Avoird A, Wormer ES. 1998. *J Chem Phys* **108**:4783.
62. Arbuznikov A, Vaara J, Kaupp M. 2004. *J Chem Phys* **120**:2127.
63. Remenyi C, Arbuznikov A, Reviakine R, Vaara J, Kaupp M. 2004. *J Phys Chem A* **108**:5026.
64. Brownridge S, Grein F, Tatchen J, Kleinschmidt M, Marian CM. 2003. *J Chem Phys* **118**:9552.
65. Lushington GH, Bündgen P, Grein F. 1995. *Int J Quantum Chem* **55**:377.
66. Lushington GH, Grein F. 1996. *Theor Chim Acta* **93**:259.
67. Lushington GH, Grein F. 1996. *Int J Quantum Chem: Quantum Chem Symp* **30**:467.
68. Yamaguchi Y, Goddard JD, Osamura Y, Schaefer H. 1994. *Analytic derivative approaches: a new dimension to quantum chemistry*. Oxford: Oxford UP.
69. Pople JA, Krishnan R, Schlegel HB, Binkley JS. 1979. *Int J Quantum Chem: Quantum Chem Symp* **13**:225.
70. Colwell SM, Handy NC. 1994. *Chem Phys Lett* **217**:271.
71. Lee AM, Colwell SM, Handy NC. 1994. *Chem Phys Lett* **229**:225.
72. Gerratt J, Mills IM. 1968. *J Chem Phys* **49**:1719.
73. Autschbach J, Ziegler T. 2003. *Coord Chem Rev* **238/239**:83.
74. Vahtras O, Minaev B, Ågren H. 1997. *Chem Phys Lett* **281**:186.
75. Luo Y, Jonsson D, Norman P, Ruud K, Vahtras O, Minaev B, Ågren H, Rizzo A, Mikelsen KV. 1998. *Int J Quantum Chem* **70**:219.
76. Vahtras O, Loboda O, Minaev B, Agren H, Ruud K. 2002. *Chem Phys* **279**:133.
77. McWeeny R, Mizuno Y. 1961. *Proc Roy Soc (London)* **A259**:554.
78. Petrenko TT, Petrenko TL, Bratus VY. 2002. *J Phys: Condens Matter* **14**:12433.
79. Loboda O, Minaev B, Vahtras O, Schimmelpfennig B, Agren H, Ruud K, Jonsson D. 2003. *Chem Phys* **286**:127.
80. Minaev BF, Khomenko EM, Bilan EA, Yashchuk LB. 2005. *Opt Spectrosc* **98**:209.

81. Loboda O, Tunell I, Minaev B, Agren H. 2005. *Chem Phys* **312**:299.
82. Minaev B, Yaschuk L, Kukueva V. 2005. *Spectrochim Acta A* **61**:1105.
83. Shoji M, Koizumi K, Hamamoto T, Taniguchi T, Takeda R, Kitagawa Y, Kawakami T, Okumura M, Yamanaka S, Yamaguchi K. 2005. *Polyhedron* **24**:2708.
84. Neese F. 2006. *J Am Chem Soc* **128**:10213.
85. Sinnecker S, Neese F. 2006. *J Phys Chem A* **110**:12267.
86. Berliner LJ, Eaton SS, Eaton GR. 2000. *Distance measurements in biological systems by EPR*. New York: Kluwer Academic.
87. Eaton GR, Eaton SS. 1988. *Acc Chem Res* **21**:107.
88. Eaton SS, Eaton GR. 1988. *Coord Chem Rev* **83**:29.
89. Schiemann O, Piton N, Mu YG, Stock G, Engels JW, Prisner TF. 2004. *J Am Chem Soc* **126**:5722.
90. Zanker PP, Jeschke G, Goldfarb D. 2005. *J Chem Phys* **122**:024515.
91. Bertrand P, More C, Guigliarelli B, Fournel A, Bennett B, Howes B. 1994. *J Am Chem Soc* **116**:3078.
92. Kahn O. 1993. *Molecular magnetism*. New York: VCH Publishers.
93. Pederson MR, Khanna SN. 1999. *Phys Rev B* **60**:9566.
94. Schreckenbach G, Ziegler T. 1998. *Theor Chem Acc* **99**:71.
95. Ditchfield R. 1974. *Mol Phys* **27**:789.
96. Schreckenbach G, Ziegler T. 1997. *J Phys Chem A* **101**:3388.
97. Van Lenthe E, Wormer PES, van der Avoird A. 1997. *J Chem Phys* **107**:2488.
98. Kutzelnigg W, Fleischer U, Schindler M. 1991. In *NMR basic principles and progress*, pp. 165–262. Ed P Diehl, E Fluck, H Günther, R Kosfield, J Seeling. Heidelberg: Springer.
99. Kaupp M, Gress T, Reviakine R, Malkina OL, Malkin VG. 2003. *J Phys Chem B* **107**:331.
100. Luzanov AV, Babich EN, Ivanov VV. 1994. *J Mol Struct (Theochem)* **311**:211.
101. Improta R, Barone V. 2004. *Chem Rev* **104**:1231.
102. Engels B, Eriksson LA, Lunell S. 1996. *Adv Quantum Chem* **27**:297.
103. Gao J. 1996. *Rev Comp Chem* **7**:119.
104. Schöneboom J, Neese F, and Thiel W. 2005. *J Am Chem Soc* **127**:5840.
105. Sinnecker S, Neese F. 2006. *J Comp Chem* **27**:1463.
106. Asher JR, Doltsinis NL, Kaupp M. 2005. *Magn Reson Chem* **43**:S237.
107. Barone V, Polimeno P. 2006. *Phys Chem Chem Phys* **8**:4609.
108. Munzarova ML, Kaupp M. 1999. *J Phys Chem A* **103**:9966.
109. Malkina OL, Vaara J, Schimmelpfenning B, Munzarova M, Malkin V, Kaupp M. 2000. *J Am Chem Soc* **122**:9206.
110. Rinkevicius Z, Telyatnyk L, Salek P, Vahtras O, Agren H. 2003. *J Chem Phys* **119**:10489.
111. Perdew JP, Burke K, Ernzerhof M. 1996. *Phys Rev Lett* **77**:3865.
112. Adamo C, Barone V. 1999. *J Chem Phys* **110**:6158.
113. Mattar SM. 2005. *Chem Phys Lett* **405**:382.
114. Hehre WJ, Ditchfield R, Pople JA. 1972. *J Chem Phys* **56**:2257.
115. Schäfer A, Horn H, Ahlrichs R. 1992. *J Chem Phys* **97**:2571.
116. Godbout N, Salahub DR, Andzelm J, Wimmer E. 1992. *Can J Chem* **70**:560.
117. Krishnan R, Binkley JS, Seeger R, Pople JA. 1980. *J Chem Phys* **72**:650.
118. Dunning JTH. 1980. *J Chem Phys* **90**:1007.
119. Schäfer A, Huber C, Ahlrichs R. 1994. *J Chem Phys* **100**:5829.

120. Barone V. 1995. In *Recent advances in density functional methods*, Part I, pp. 287–334. Ed DP Chong. Singapore: World Scientific.
121. Neese F. 2002. *Inorg Chim Acta* **337C**:181.
122. Ahlrichs R, and coworkers. 2006. ftp.chemie.uni-karlsruhe.de/pub/basen Karlsruhe.
123. Eichkorn K, Treutler O, Öhm H, Häser M, Ahlrichs R. 1995. *Chem Phys Lett* **240**:283.
124. Eichkorn K, Weigend F, Treutler O, Ahlrichs R. 1997. *Theor Chem Acc* **97**:119.
125. Benisvy L, Bittl R, Bothe E, Garner CD, McMaster J, Ross S, Teutloff C, Neese F. 2005. *Angew Chem, Int Ed* **44**:5314.
126. Stone AJ. 1963. *J Mol Phys* **6**:509.
127. Stone AJ. 1964. *J Mol Phys* **7**:311.
128. Van Gastel M, Lassman G, Lubitz W, Neese F. 2004. *J Am Chem Soc* **126**:2237.
129. Atkins PW, Jamieson AM. 1967. *Mol Phys* **14**:425.
130. Mayer M, Krüger S, Rösch N. 2001. *J Chem Phys* **115**:4411.
131. Di Valentin C, Neyman KM, Risse T, Sterer M, Fischbach E, Freund H-J, Nasluzov VA, Pacchioni G, Rösch N. 2006. *J Chem Phys* **124**:044708.
132. Malkin I, Malkina O, Malkin V, Kaupp M. 2005. *J Chem Phys* **123**:244103.
133. Sinnecker S, Rajendran A, Klamt A, Diedenhofen M, Neese F. 2006. *J Phys Chem A* **110**:2235.
134. Rinkevicius Z, Telyatnyk L, Vahtras O, Ruud K. 2004. *J Chem Phys* **121**:5051.
135. Ciofini I. 2004. In *Calculation of NMR and EPR parameters*, p. 505. Ed M Kaupp, V Malkin, M Bühl. Weinheim: Wiley-VCH.
136. Klamt A, Schüürmann G. 1993. *Perkin Trans* **799**.
137. Ciofini I, Reviakine R, Arbuzyanov A, Kaupp M. 2004. *Theor Chem Acc* **111**:132.
138. Ciofini I. 2004. *Magn Reson Chem* **42**:S48.
139. Ciofini I, Adamo C, Barone V. 2004. *J Chem Phys* **121**:6710.
140. Asher JR, Doltsinis NL, Kaupp M. 2004. *J Am Chem Soc* **126**:9854.
141. Klamt A. 1995. *J Phys Chem* **99**:2224.
142. Penfield KW, Gay RR, Himmelwright RS, Eickman NC, Norris VA, Freeman HC, Solomon EI. 1981. *J Am Chem Soc* **103**:4382.
143. Solomon EI. 1984. *Comments Inorg Chem* **3**:227.
144. Penfield KW, Gewirth AA, Solomon EI. 1985. *J Am Chem Soc* **107**:4519.
145. Gewirth AA, Cohen SL, Schugar HJ, Solomon EI. 1987. *Inorg Chem* **26**:1133.
146. Gewirth AA, Solomon EI. 1988. *J Am Chem Soc.* **110**:3811.
147. Solomon EI, Gewirth AA, Westmoreland TD. 1989. In *Advanced EPR: applications in biology and biochemistry*, p. 865. Ed AJ Hoff. Amsterdam: Elsevier.
148. Solomon EI, Baldwin MJ, Lowery MD. 1992. *Chem Rev* **92**:521.
149. Solomon EI, Lowery MD. 1993. *Science* **259**:1575.
150. Solomon EI, Lowery MD. 1993. In *The chemistry of copper and zinc triads*, p. 12. Ed AJ Welch, SK Chapman. Cambridge: Royal Society of Chemistry.
151. Solomon EI, Lowery MD, LaCroix LB, Root DE. 1993. *Meth Enzymol* **226**:1.
152. Solomon EI, Lowery MD, Root DE, Hemming BL. 1995. In *Mechanistic bioinorganic biochemistry*, p. 121. Ed HH Thorp, VL Pecoraro. Washington, DC: American Chemical Society.
153. van Lenthe E, Snijders JG, Baerends EJ. 1996. *J Chem Phys* **105**:6505.
154. van Wüllen C. 1998. *J Chem Phys* **109**:392.
155. Szyłagi R, Metz M, Solomon EI. 2002. *J Phys Chem A* **106**:2994.
156. Siegbahn PEM. 2001. *J Comp Chem* **22**:1634.
157. Siegbahn PEM, Blomberg MRA. 2000. *Chem Rev* **100**:421.
158. Neese F. 2006. *J Inorg Biochem* **100**:716.

159. Kababya SJN, Calle C, Neese F, Goldfarb D. 2006. *J Am Chem Soc* **128**:2017.
160. Berry JF, Bill E, Neese F, Garcia-Serres R, Weyhermüller T, Wieghardt K. 2006. *Inorg Chem* **45**:2027.
161. Sinnecker S, Neese F, Lubitz W. 2005. *J Biol Inorg Chem* **10**:231.
162. Praneeth VKK, Neese F, Lehnert N. 2005. *Inorg Chem* **44**:2570.
163. Mader-Cosper M, Neese F, Astashkin AV, Carducci MA, Raitsimring AM, Enemark JH. 2005. *Inorg Chem* **44**:1290.
164. Astashkin AV, Neese F, Raitsimring AM, Cooney JJA, Bultman E, Enemark JH. 2005. *J Am Chem Soc* **127**:16713.
165. Sinnecker S, Noodleman L, Neese F, Lubitz W. 2004. *J Am Chem Soc* **126**:2613.
166. Baute D, Arieli D, Zimmermann H, Neese F, Weckhuysen B, Goldfarb D. 2004. *J Am Chem Soc* **126**:11733.
167. Werst MM, Davoust CE, Hoffman BM. 1991. *J Am Chem Soc* **113**:1533.
168. Neese F, Kappl R, Zumft WG, Hüttermann J, Kroneck PMH. 1998. *J Biol Inorg Chem* **1**:53.
169. Bertini I, Ciurli S, Dikiy A, Gasanov R, Luchinat C, Martini G, Safarov N. 1999. *J Am Chem Soc* **121**:2037.
170. Weigend F, Furche F, Ahlrichs R. 2003. *J Chem Phys* **119**:12753.
171. Grimme S. 2006. *Angew Chem* **118**:4571.
172. Ganyushin D, Neese F. 2006. *J Chem Phys* **125**:024103.
173. Barra AL, Caneschi A, Cornia A, de Biani FF, Gatteschi D, Sangregorio C, Sessoli R, Sorace L. 1999. *J Am Chem Soc* **121**:5302.
174. Krzystek J, Yeagle GJ, Park J-H, Britt RD, Meisel MW, Brunel L-C, Telser J. 2003. *Inorg Chem* **42**:4610.
175. Neese F. 2007. *J Chem Phys* **127**:164112.
176. Neese F. 2001. *J Phys Chem A* **105**:4290.

IRON PROTEINS

EPR OF MONONUCLEAR NON-HEME IRON PROTEINS

Betty J. Gaffney

Department of Biological Science, Florida State University

Flexible geometry of three- to six-protein side-chain ligands to non-heme iron in proteins is the basis for widely diverse reactivities ranging from iron transport to redox chemistry. The gap between fixed states determined by x-ray analysis can be filled by spectroscopic study of trapped intermediates. EPR is a versatile and relatively quick approach to defining intermediate states in terms of the geometry and electronic structures of iron. A number of examples in which the iron chemistry of non-heme proteins is understood through x-ray structures at subbond length resolution, refined calculations, and spectroscopy exist now. Some examples in which EPR has provided unique insight are summarized in Table 1. Assignment and quantitative evaluation of the EPR resonances in ferric, non-heme iron sites is the focus of the first section of this review. An earlier chapter in this series provides more background on the theory specific to EPR of $S = 5/2$ metal ions [1]. Besides EPR spectra of ferric mononuclear sites, EPR of ferrous iron coupled to a spin $1/2$ radical, as it pertains to the categories mononuclear and non-heme, will also be covered, in the second half of this chapter. Examples include the quinone–ferrous interactions in photosynthetic reaction centers and nitric oxide complexes with non-heme ferrous iron. Other recent reviews of the biochemistry and spectroscopy of non-heme iron proteins provide additional background [2–6].

1. EPR OF MONONUCLEAR, HIGH-SPIN FERRIC NON-HEME PROTEINS

1.1. Assignment: The $S = 5/2$ EPR Parameter Space Is Large but Not Infinite

Two accidentally similar EPR spectra provide a focus for discussion of assigning transitions in high-spin, non-heme ferric proteins. Several superoxide reductase (SOR) enzymes have been characterized recently [7]. The SOR from *Pyrococcus furiosus* has an EPR spectrum, shown in Figure 1 [8], superficially resembling that

Table 1. References for Representative High-Spin Ferric Proteins Characterized by EPR, X-Ray Structure, and Calculation

Protein	EPR analysis	x-ray structure	Calculation
Phenylalanine hydroxylase	13, 6	67	69
Lipoxygenase	14	68	70
Transferrin	13	11	none

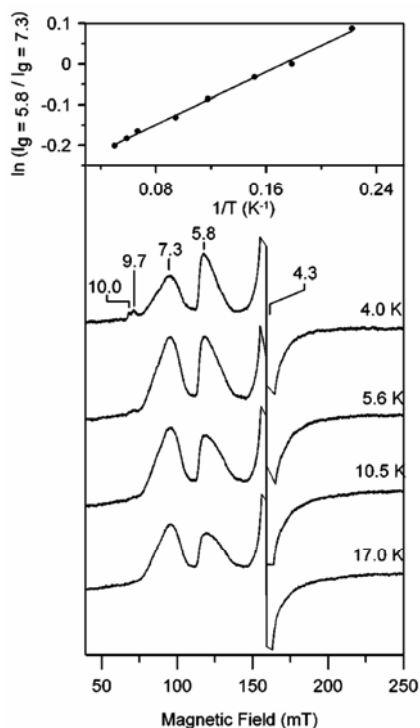


Figure 1. EPR spectra of ferric iron in superoxide reductase (SOR) of *Pyrococcus furiosus*. X-band EPR spectra, at low temperature (as indicated on the figure), of recombinant SOR (0.5 mM) in 50 mM HEPES, pH 7.5, are shown. The ratio of intensities at $g = 5.8$ (middle Kramers doublet) and $g = 7.3$ (lower Kramers doublet) is shown in the upper panel. The figure is from Fig. 2 of Clay et al. [8], with permission of the publisher.

of the oxalate complex of ferric transferrin, shown in Figure 2 [9]. Iron ligands in SOR are four histidines, the thiolate of a cysteine, and either a carboxylate or water [10]. In contrast, the sidechains ligating iron in transferrin are two Tyr, one His, and one Asp. The remaining transferrin iron ligands are provided by bidentate coordination of an anion [9,11]. Diferric transferrin, with high-spin iron bound in both lobes, has a variety of EPR spectra depending on the associated anion and

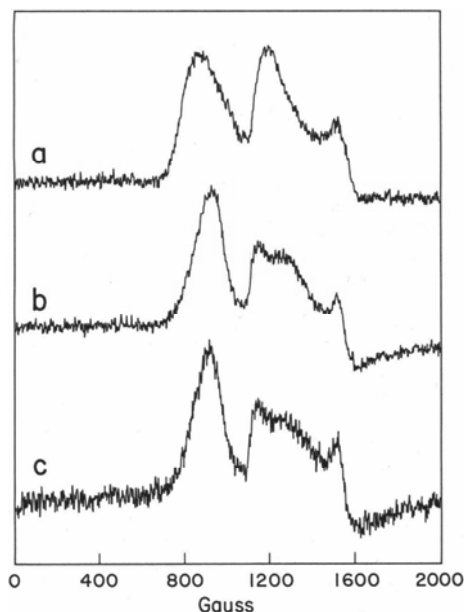


Figure 2. EPR spectra of transferrin samples in 0.09 M HEPES, pH 7.5, diluted with 2 M NaCl to final NaCl concentrations of 0 M (a), 0.5 M (b), and 1.0 M (c), and final protein concentrations of 1.0, 0.75, and 0.5 mM transferrin in a, b, and c, respectively. The figure is reproduced from Fig. 5 of Dubach et al. [9], with permission of the publisher.

ionic conditions of the buffer. It is the oxalate complex that has an EPR spectrum most similar to the SOR spectrum. The resonances shown in the examples of Figures 1 and 2 cover g -values greater than 4, although the full spectra extend to g -values of 2.0 or less. The low-field regions of X-band EPR spectra provide the basis for assigning values of the zero-field splitting (zfs) terms E and D in spectra of numerous non-heme, high-spin ferric proteins. Low-field regions of the EPR spectra are much more diverse for ferric non-heme proteins than for the heme counterparts, but as will be illustrated, there is more to assigning the spectra than the g -values of the resonances. Assignment of features in EPR spectra of high-spin iron proteins is the first step in quantitative assessment of the number and nature of the species present.

Non-heme iron proteins frequently require reconstitution with iron after they are isolated. Reconstitution of *P. furiosus* SOR yields samples with iron in two kinds of site, each with a unique EPR spectrum. Determining which EPR spectrum corresponds to the catalytically active iron site required correlation of an increase in one with increases in enzyme activity. In addition, assignment of one of the EPR resonances to the redox active iron component was made by quantitative comparison of ferric signals obtained at points through a dye-mediated redox titration [8]. In a similar problem regarding reconstituted phenylalanine hydroxylase (PAH),

one ferric site, among several sites contributing to the EPR spectrum, had to be assigned to active site iron [12]. A model including a distribution in the zero-field splitting parameter E/D was adopted to make the quantitative comparison of the two EPR spectra arising from reconstituted PAH ([13] and references therein). Ferric lipoxygenase also has two overlapping EPR spectra, the ratio of which is sensitive to buffer conditions. Both components of lipoxygenase EPR spectra are from active enzyme. Again, spectra were fit according to a distribution in the central E/D value for each site, and the amount of each component was then determined [14]. In the diferric transferrins, assignment of resonances and computer fitting of EPR spectra were used to compare spectra of the carbonate complex to those of complexes with other anions, such as oxalate [9,13].

The following discussion covers approaches to accurate and quantitative assignment of EPR spectra and the role of the experimental variables, temperature, and multiple EPR frequencies in making the assignments. As will be seen, the two ferric subjects of Figures 1 and 2 differ in the sign and magnitude of the zero-field splitting parameter D .

1.2. Assignment for Zero-Field Splitting: the Zeeman Term

The spin Hamiltonian Eq. (1) has well-known solutions when the microwave frequency is less than the zero-field splitting D (at X-band, $\nu \sim 9.4$ GHz or $\nu/c \sim 0.3$ cm^{-1}). The six energy levels for $S = 5/2$ arrange in three Kramers doublets at zero field and, for D large compared with $h\nu$, diverge linearly with magnetic field until the fields are larger than usually used for X-band spectroscopy:

$$\begin{aligned} H_S &= g\beta_e H_0 \cdot \mathbf{S} + \mathbf{S} \cdot \mathbf{D} \cdot \mathbf{S} \\ &= g\beta_e H_0 \cdot \mathbf{S} + D(S_z^2 - S(S+1)/3) + E(S_x^2 - S_y^2) \\ &\quad + \text{terms fourth order in } \mathbf{S} \text{ (minor for most proteins samples)}. \end{aligned} \quad (1)$$

Figure 3 summarizes how the g -values of the transitions vary with orientation of principal magnetic axes in the magnetic field and with the zero-field terms D (positive) and E . The numbers shown at selected points on the figure are transition probabilities. The bold numbers (e.g., 5 to 6) signify the order of the six energy levels; 6 is highest in energy. Some notable features in Figure 3 are that cases with E/D of zero or $\sim 1/3$ yield simple spectra because only one transition has significant probability. A transition at $g = 6.0$ dominates the spectrum when E/D is 0 (axial), and alternatively a transition at $g = 4.3$ dominates when E/D is $1/3$ (rhombic). Note also that the absorption at lowest field (highest g -value) corresponds to different principal directions of the D tensor for different transitions. The transition probabilities for the highest-energy-level pair (levels 5 to 6) are small, and absorptions arising from transitions between these levels are usually significant only when symmetry is near rhombic. The specification of principal axis directions to x , y , or z (see Fig. 3) results from choice of a coordinate system for the traceless \mathbf{D} matrix such that $|D_z| \geq |D_y| \geq |D_x|$ and $1/3 \geq E/D \geq 0$ [1].

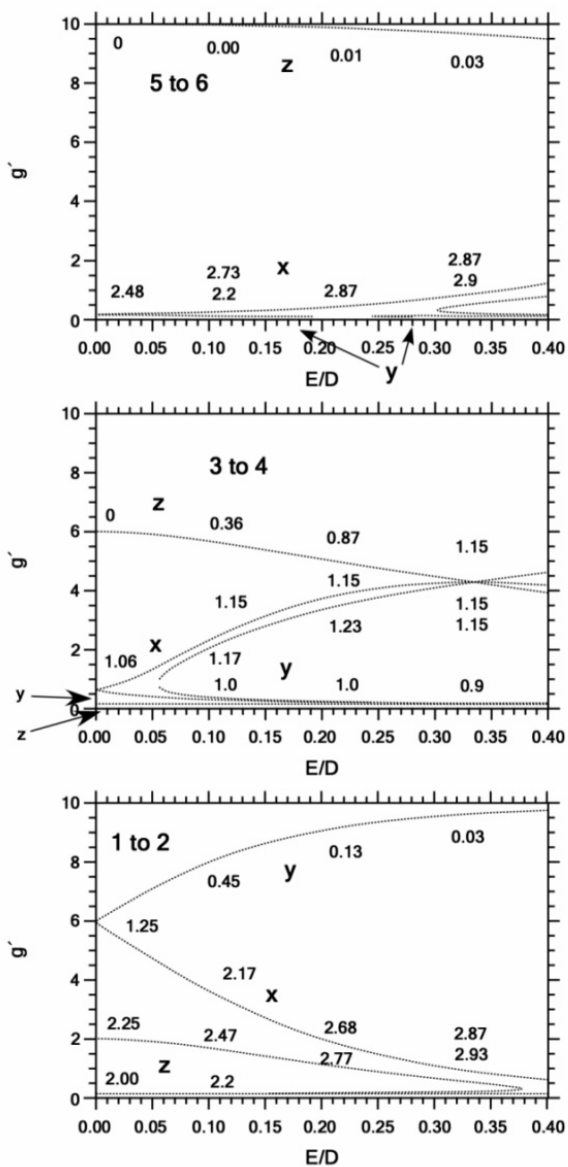


Figure 3. Calculated g' -values for the full range of E/D . Calculations were performed with a value of $D = 2.0 \text{ cm}^{-1}$ and X-band frequency. Transitions between pairs of energy levels are numbered in bold on each panel (1 to 2, etc.). The g' -values along molecular x, y, and z principal axes are shown by dotted lines, and representative squared transition moments are given along those lines. The figure is reproduced from Fig. 9 of Gaffney and Silverstone [1], with permission of the publisher.

For D negative, the shape of the plot shown in the top panel of Figure 3 will replace the shape of the one at the bottom and vice versa: the shape of the bottom plot replaces that of the top. This switch has practical consequences in that temperature variation can be used to determine the order of the energy levels, and hence the sign of D , for symmetries yielding significant absorption from two doublets.

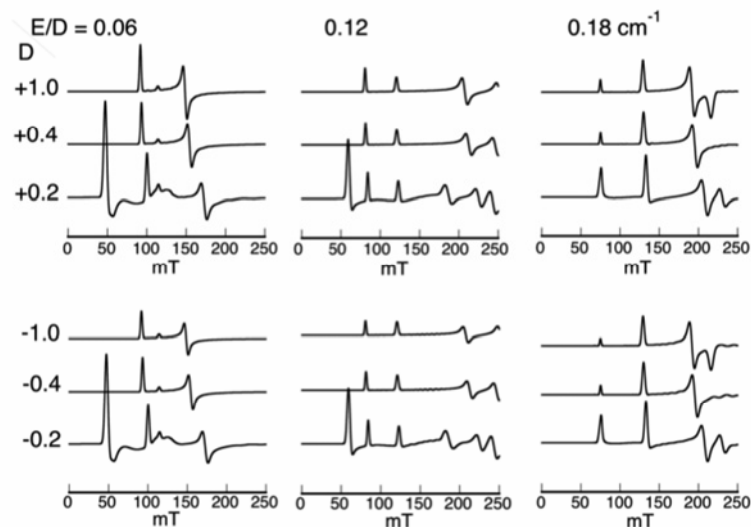


Figure 4. The low-field portions of calculated X-band EPR spectra of $S = 5/2$ for various values of D and E/D . Small changes in intensity differentiate spectra for positive (upper) and negative (lower) values of D . Spectra were calculated (with XSophe [37]) with frequency = 9.4 GHz, temperature = 15 K, linewidth = 140 MHz (Gaussian), magnetic field segments = 5 mT, and 32 angular grid partitions. The amplitudes of the spectra are adjusted to represent equivalent numbers of spins. The spectra have additional resonances at fields higher than those shown, but these are rarely observed experimentally because of broadening by distributions in E and D .

Metal centers of intermediate symmetry, with E/D in the range ~ 0.05 – 0.30 , give rise to significant EPR transitions within more than one doublet. The pairing of g -values (see Fig. 3) permits assignment of the spectrum to one iron electronic state with multiple transitions rather than to single transitions from multiple states of iron in the same sample. For example, with $E/D = 0.06$, transition between levels 1 and 2 (for D positive and $>h\nu$) gives principal low-field g_y - and g_x -values of 7.3 and 4.5, and the low-field g_z -value for the 3 to 4 transition is ~ 5.9 . Figure 4 shows calculated X-band EPR spectra for the range of E/D values from 0.06 to 0.18 to illustrate changes in the low-field features. The values of D are positive in the upper panel and negative in the lower one. The values of D used in the calculations are also varied from $\pm 1.0 \text{ cm}^{-1}$ (top row) and $\pm 0.4 \text{ cm}^{-1}$ (middle row) to ± 0.2

cm^{-1} (lower row), illustrating the shifts in g -values that occur as D becomes significantly smaller than the X-band frequency, 0.3 cm^{-1} . Note also that a new resonance is evident at low field in the lower row of each panel, left and middle spectra. This new resonance, an interdoublet transition, arises from a transition in levels 2 and 3 when the difference in energy of two Kramers doublets (between $2D$ and $3D$ at zero field) is smaller than the microwave energy applied. Interdoublet transitions will be discussed in more detail in §1.3.

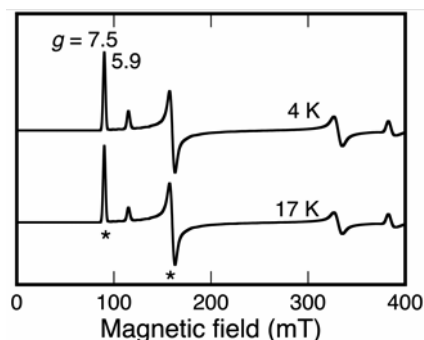


Figure 5. Variation with temperature of the relative intensities in a high-spin ferric EPR signal (D negative). The resonances from transitions in the lowest doublet are marked with stars. The resonance at $g = 5.9$ arises from the $3 \rightarrow 4$ transition. Increasing temperature increases the ratio of resonance at $g = 7.5$ to that at $g = 5.9$. The overall intensities of the spectra at the two temperatures are adjusted so that the first resonance is of the same amplitude in the two spectra. Additional resonances occur at higher fields than the region shown. The spectra were calculated (with XSophe [37]) with microwave frequency = 9.4 GHz , $D = -0.5 \text{ cm}^{-1}$, $E/D = 0.07$, linewidth = 140 MHz , 60 magnetic field segments (0.6 T scan), and 32 angular partitions.

The temperature dependence of the ratio of overlapping EPR resonances provides information about the value of D . The spectra in Figure 5 are calculated for $D = -0.5$, $E/D = 0.07$, at two temperatures. The lowest doublet is marked by stars, and the middle doublet contributes the resonance at $g = 5.9$. The ratio of absorption at $g = 5.9$ divided by that at 7.5 increases with increasing temperature when D is positive. D negative gives a ratio of these resonances that decreases as temperature increases. The dependence on temperature of the relative intensities of two transitions depends on the Boltzmann population factors Eq. (2) for the n energy levels involved:

$$\left[e^{-E_n(B)/kT} \right] / \sum_{i=1}^6 e^{-E_i(B)/kT} . \quad (2)$$

When the energies are small relative to kT , series expansions of the exponentials give the approximation Eq. (3) for the temperature dependence of relative intensi-

ties, I_k/I_l , of resonances arising from the separate pairs of levels, k and l , contributing to the spectrum

$$\ln(I_k / I_l) \propto 1/T. \quad (3)$$

The intensities in Eq. (3) are those of transitions within different doublets, so the slope of a plot of $\ln(I_k/I_l)$ against $(1/T)$ gives the sign and value of D . This approach was taken, for example, in assignment of a negative sign, and a magnitude near $|0.5| \text{ cm}^{-1}$, to the D -value of the iron center in oxidized SOR [8]. The two resonances at lowest field (g -values 7.5 and 5.9) are most convenient to use in application of Eq. (3) because they are less subject to broadening by distribution in E/D than the higher field resonances (refer to Fig. 4).

1.3. Assignment for Zero-Field Splitting Similar to the Zeeman Term

Many non-heme iron proteins have zero-field splitting energy similar to that of the Zeeman term when X-band EPR is measured. The angular variation of resonant fields and transition probabilities become interestingly nonlinear for these cases in which two terms are dominant, Zeeman (field dependent) and zero-field splitting (field independent), in the spin Hamiltonian. The EPR spectrum is being measured under conditions where all six levels of the $S = 5/2$ spin are close in energy, so significant contributions to the spectrum are possible from many of the 15 possible transitions between the six energy levels. The experimental sample transferrin oxalate has a D -value of $\sim +0.27 \text{ cm}^{-1}$ and provides a good illustration (see Fig. 2). Choosing the magnetic field at one pair of angles, θ and ϕ , with respect to the molecular axes, produces the calculated energies and separations of energies shown in Figure 6. In the lower plot of separation of energies, the resonant fields for this molecular orientation are found from a horizontal line drawn at the applied microwave frequency. At X-band frequency, more than five different transitions from this single molecular orientation arise, as indicated by the line drawn on the figure. The usual Kramers doublet transitions are between levels 1 and 2, 3 and 4, and 5 and 6. The interdoublet transitions $2 \rightarrow 3$ and $4 \rightarrow 5$ also contribute significantly to resonances in the magnetic field range 0–400 mT. A characteristic of interdoublet transitions is that the separations of energy levels are curved for a wide range of θ and ϕ . The full angular variation of resonant fields for the $2 \rightarrow 3$ transition ($D = +0.27 \text{ cm}^{-1}$ and $E/D = 0.06$) is illustrated by a three-dimensional plot in Figure 7. In this figure the direction of the applied magnetic field relative to the molecular x , y , and z axes is signified by expression of the resonant magnetic field for each orientation in the B_x , B_y , and B_z space. A single octant is shown in the figure, but the pattern is symmetric and would appear as a dumbbell surface in four octants. One can immediately see from this figure why this interdoublet transition is called a “looping transition.”

An instructive view of how transitions from all molecular orientations contribute to the observed EPR spectrum appears in a plot (Fig. 8) showing magnetic field

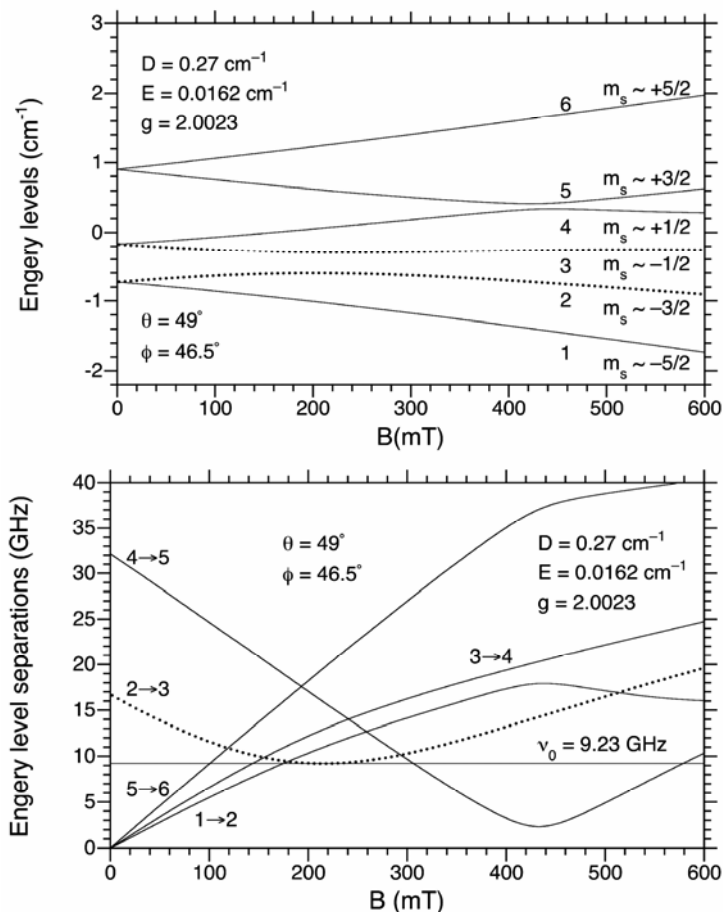


Figure 6. Energy levels and energy separations at selected molecular orientations. The energies calculated are part of simulations of transferrin oxalate EPR spectra. The molecular axes are oriented with respect to the magnetic field at $(\theta, \phi) = (49^\circ, 46.5^\circ)$. Transition between levels 2 and 3 is highlighted by dotted lines. Levels are numbered as in Figure 3, and parameters of the calculation are given on the figure. The horizontal line in the lower panel is drawn at an X-band frequency of 9.23 GHz. The figure is reproduced from Fig. 5 of Gaffney and Silverstone [21], with permission of the publisher.

variation in the intensity factor Eq. (4) for all θ and ϕ , for a transition between initial and final levels, i and f :

$$\text{Intensity factor} = | \langle i | S_{\perp} | f \rangle |^2 \sin \theta. \quad (4)$$

Examination of this type of plot reveals that regions with a high density of transitions and a high intensity factor would dominate the associated EPR spectrum.

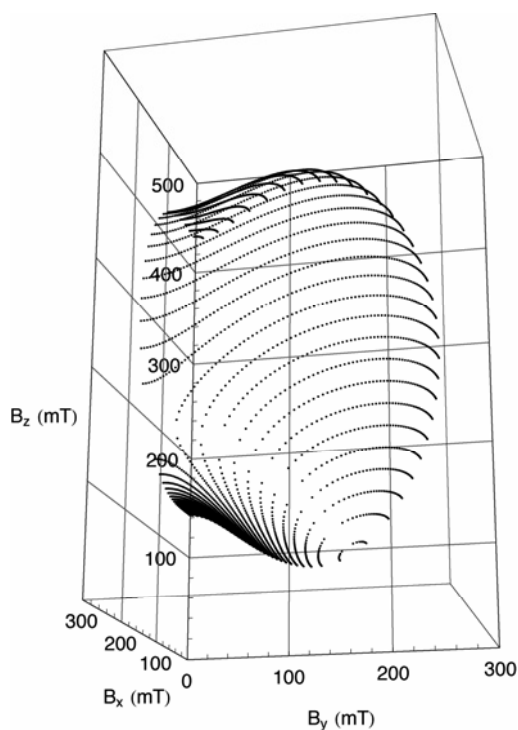


Figure 7. Three-dimensional representation of one octant of a looping transition. The resonant magnetic field for each angular orientation is plotted in magnetic field-space, where each vector from the origin to a point is graphed according to the x , y , and z components. Calculation parameters are the same as in Figure 6. The figure is reproduced from Fig. 7 of Gaffney and Silverstone [21], with permission of the publisher.

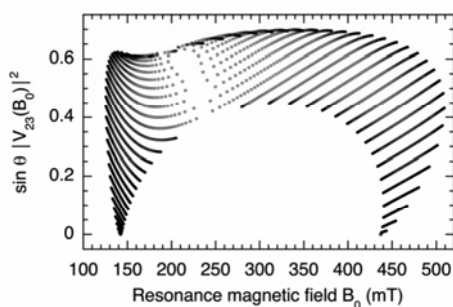


Figure 8. Intensity of resonances in a looping transition as a function of magnetic field. The intensity factor (y -axis) is shown for transitions between levels 2 and 3, using Eq. (4). Calculation parameters were $D = 0.27 \text{ cm}^{-1}$, $E = 0.0162 \text{ cm}^{-1}$, and microwave frequency = 9.23 GHz. The figure is reproduced from Fig. 11 of Gaffney and Silverstone [21], with permission of the publisher.

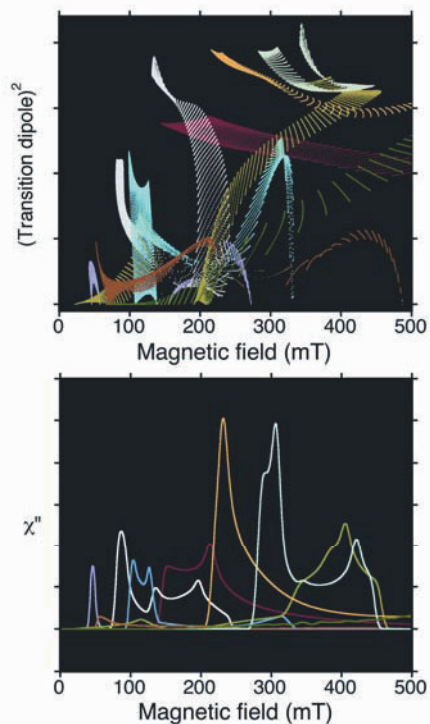


Figure 9. Intensity of all significant resonances for small D -value and X-band EPR. The upper figure shows the square of the transition dipole for each of the pairs of energy levels that contribute significantly to the low-field region of an X-band spectrum with small value of D . The lower figure shows the corresponding absorption spectra. The color code for transitions between pairs of energy levels is 1→2 (red), 1→3 (orange), 1→4 (pink), 2→3 (yellow), 2→4 (bright blue), 3→4 (turquoise), 3→5 (white), 4→5 (light green), and 5→6 (dark green). The input parameters for the IronHS program [1] were $D = 0.1 \text{ cm}^{-1}$, $E/D = 0.06$, frequency = 9.4 GHz, linewidth = 140 MHz, field segments = 1 mT, steps in θ of 1° , and steps in ϕ of 2° . Regions of looping transitions were calculated using a cubic polynomial [21].

Some biomineral samples contain high-spin iron with values of $D < 0.2$, and the $S = 5/2$ spectra of some manganese centers in proteins have similarly small zero-field splittings. At X-band, for $D < \sim 0.2$, most of the 15 possible transitions between pairs of energy levels become possible, and the spectra are a complex set of overlapping transitions. As an aid in assigning the EPR spectra of manganese lipoxxygenase at X- and W-band frequencies, a plot of X-band intensity factors against magnetic field was examined for all of the significant transitions (9 of 15 possible in this case) with $S = 5/2$, $D = 0.1 \text{ cm}^{-1}$, without the manganese hyperfine [15]. This set of parameters is equivalent to a high-spin ferric center with very small D . Figure 9, in which the intensity factors (upper figure) are colored differently for each transition, illustrates the calculation. The corresponding absorption

spectra are given in the lower figure. The red points are for the well-behaved 1→2 transition, and the spectrum of this transition would have low-field maxima at points where the density of points is high, at about 140 and 210 mT. The other transitions shown also give intensity within the same magnetic-field region and, in the case of transitions 2→3 (yellow), 2→4 (bright blue), 3→4 (turquoise), and 3→5 (white), have high density of points and high enough intensity factors that they would add to the 1→2 transition in contributing to the spectrum. This figure readily explains why assignment of X-band EPR spectra of some ferric or manganese proteins with small D -value is daunting.

1.4. High-Frequency EPR and Assignment for Zero-Field Splitting: The Zeeman Term

In the previous sections, quantitative evaluation of the amount of ferric iron contributing to an EPR spectrum was referenced to the partial spectrum in the low-field region. This process is somewhat analogous to estimating the extent of an iceberg from the portion visible above water. The complexity of multiple overlapping transitions illustrated in Figures 6–9 can be avoided by choice of a different microwave frequency such that either $h\nu > D$ or $h\nu < D$. For $h\nu > D$, high-frequency EPR at numerous frequencies is now available [16,17]. When the Zeeman term is dominant in Eq. (1) ($h\nu > D$), the energy levels of $S = 5/2$ are close to a nested set of doublets, diverging linearly with field except for the very-low-field region. Five transitions between the six levels occur (1→2, 2→3, 3→4, 4→5, and 5→6), and these are centered near $g = 2$. EPR spectra at 94 GHz (W-band) of diferric transferrin carbonate show this simplification (Fig. 10, experimental (a) and calculated (b)) [18]. The simulation illustrates the broadening of selected transitions (dotted lines above and below the calculated spectrum) that would result from a distribution in E and D . Comparing the experimental and calculated spectra reveals extra, low-intensity features on each side of the central region in the experimental spectrum that arise from a second component. Two components in the transferrin X-band EPR spectra are resolved in the low-field region [13]. The parameters from earlier assignments of transferrin X-band spectra [13] were chosen for the simulation of the W-band spectrum shown in Figure 10.

An experimental spectrum of manganese lipoxxygenase, measured at 94 GHz [15], is shown in Figure 11 to illustrate the simplification achieved at higher frequency for an $S = 5/2$ sample with a D value ~ 0.07 cm⁻¹. Because this spectrum was recorded under saturating conditions, it has the appearance of an absorption spectrum, and the manganese hyperfine is overmodulated, so the spectrum is almost identical to that expected for high-spin ferric with the same value of D . A simulated spectrum is shown in the Figure 11 lower panel. A strong central resonance from transition in levels 3 and 4 dominates the spectrum. The outer wings of the spectrum arise from transitions in levels 1 and 2 and 5 and 6. Closer to the center of the spectrum, transitions in levels 2 and 3 and 4 and 5 contribute. The slightly more pronounced features on the low-field side of the spectrum than on the higher-field side are consistent with a positive D -value.

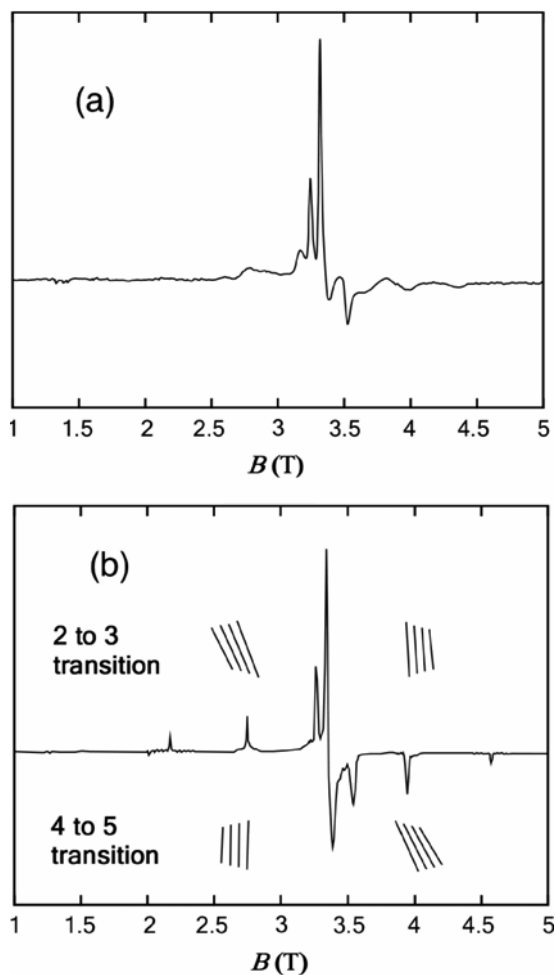


Figure 10. Experimental and calculated spectra of diferric transferrin carbonate at 94 GHz. Transferrin was ~ 1.5 mM in pH 7.4 buffer/salt solution with 50% glycerol. The experimental spectrum recorded at 40 K is shown in (a), and the conditions under which it was recorded were frequency = 94.090 GHz, modulation = 1.0 mT amplitude at 100 kHz, microwave power = 1 μ W, and sampling rate = 8192 points/2T and 0.328 s/point. The spectrum shown in (b) was calculated (40 K) with the IronHS program [1] and the following parameters: frequency = 94.1 GHz, $D = 0.28$ cm^{-1} , $E/D = 0.333$, width of Gaussian distribution in $E/D = 0.087$, linewidth = 150 MHz. Points are also shown above and below the calculated spectrum to illustrate how the magnetic-field positions of features for the interdoublet transitions between levels 2 and 3 and levels 4 and 5 would vary throughout a distribution in D (horizontal shifts) or E (vertical shifts). Similar width contributions would also apply to the outer transitions between levels 1 and 2 and 5 and 6. The figures are reproduced from Figs. 3 and 5 of Gaffney et al. [18], with permission of the publisher.

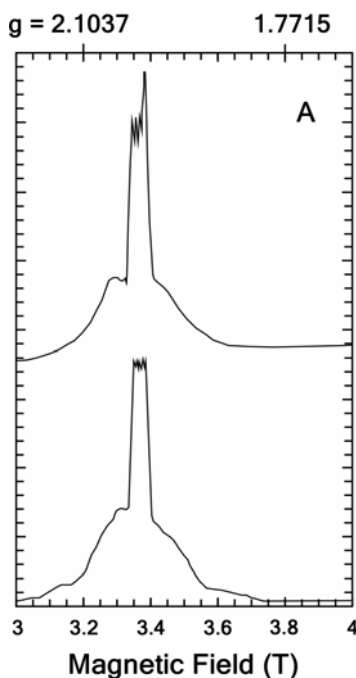


Figure 11. Manganese lipoxygenase 94 GHz experimental EPR spectrum and calculation. Manganese lipoxygenase was 0.5 mM in a pH 7.3 buffer with 28% glycerol. The experimental spectrum (upper) was recorded at 20 K and 94.094 GHz, with field modulation = 100 kHz, 1.0 mT amplitude; microwave power = 15.8 μ W; time constant = 0.082 s; scan rate = 2 T/0.373 h, 8192 points. The spectrum is the average of one scan each of increasing and decreasing field. The calculated (XSophe [37]) absorption spectrum (lower) used D and E = 0.08 and 0.015 cm^{-1} , respectively, manganese hyperfine = 0.0086 cm^{-1} , linewidth = 84 MHz, and microwave frequency = 94.22 GHz. The figure is reproduced from Fig. 7a of Gaffney et al. [15], with permission of the publisher.

1.5. Contributions to Line Shapes

1.5.1. The "Aasa-Vännngård Factor"

In 1975, Aasa and Vännngård [19] pointed out that correct integrals of EPR spectra would be obtained from *frequency-swept* spectra, but because in EPR the magnetic field is usually swept, the spin-packet linewidth in field-swept EPR requires additional consideration. The linewidth has proper units of frequency (MHz), and the integral of the lineshape function with respect to frequency is normalized to one. The frequency to field change of variables is given by Eq. (5), where ν_0 is the microwave frequency and $\nu(B_0)$ is the frequency separation of the two levels involved in the transition at magnetic field B_0 [20,21]:

$$f(\sigma_\nu, (\nu(B) - \nu_0)) = f(\sigma_\nu, (B - B_0)) \frac{d\nu(B_0)}{dB_0} + \frac{1}{2}(B - B_0)^2 \frac{d^2\nu(B_0)}{dB_0^2} + \dots \quad (5)$$

Under conditions (low magnetic field, $D > h\nu$) giving energy levels diverging linearly with field, the practical result of Eq. (5) is that the field-swept linewidth is proportional to the frequency-swept linewidth divided by the effective g -factor:

$$\sigma_{\text{field}} \propto \frac{h\sigma_{\text{frequency}}}{g_{\text{eff}}\beta} \quad (6)$$

Although g_{eff} is used in Eq. (6) to distinguish it from the electron g -factor, the remaining discussion will be phrased in terms simply of g , as is common in EPR. The increasing apparent linewidth with decreasing g -value in a field-swept EPR spectrum is apparent, for example, in the calculated spectra of Figure 5. Simulation of lineshapes provides the best approach to quantitative spin counts in field-swept EPR of ferric iron. Another approach to determining spin concentration in samples with wide EPR spectra is comparison to the double integral of a standard covering a similar magnetic-field range [12].

1.5.2. Relaxation

From a historical perspective, the insight provided by Aasa and Vännegård probably was not noticed in earlier EPR experiments with high-spin iron because heme proteins provided the subjects of many early biological EPR experiments. A characteristic of ferric heme EPR spectra is that the apparent field-swept linewidths at $g \sim 6$ and $g \sim 2$ do not vary as implied by Eq. (6). Instead, the apparent linewidths have significant relaxation-determined contributions [22,23] that vary across the spectrum. Relaxation times of high-spin iron in proteins, heme or non-heme, are of obvious importance for contemporary experiments designed to determine distances by EPR of iron-containing proteins [24–26]. For example, in a biological example involving a non-heme iron to spin-label distance measurement, an estimate of 23–30 Å between a hinge region in the ligand-gated channel, FepA, and the bound iron chelate, enterobactin, was obtained [27].

The relaxation times of enterobactin [27] can be compared with relaxation times of other biological non-heme, $S = 5/2$, iron examples, transferrin carbonate, and oxalate [28]. The observed EPR linewidths (>100 MHz) [13] of these non-heme iron proteins exhibit little temperature dependence (4–100 K), in contrast to observed widths of heme proteins. The measured phase memory times ($T_m \leq T_2$) of the transferrins correspond to relaxation-determined linewidth contributions of <2 MHz in the range 4–30 K. The T_m values of enterobactin bound to FepA indicate similarly small relaxation-determined widths. The apparent widths of these non-heme-iron EPR spectra therefore have an origin other than relaxation.

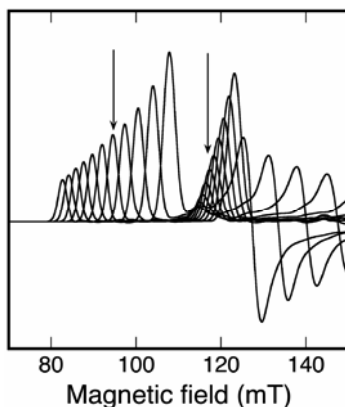


Figure 12. An ensemble of calculated EPR spectra related to distributions in E/D for $S = 5/2$. The low-field region of resonances for a constant value of D (-0.5 cm^{-1}) and variable E , at 4 K, is shown. The range of E/D is from 0.03 to 0.11. The arrows point to the g -values corresponding to E/D of 0.07, similar to those in the EPR spectrum of superoxide reductase [8]. In the figure, each spectrum is scaled to represent equivalent spins. In the case of a distribution in values of E/D , the amplitudes of the subspectra would be multiplied by an appropriate distribution function. Other calculation parameters (XSophe [37]) are microwave frequency = 9.6 GHz, magnetic field partitions = 0.5 mT, 64 angular grid partitions, and linewidth = 140 mT. The resonances in the magnetic field range 84–117 mT are the g_y features of transitions in the lowest doublet; only two of the g_x features from the same transition appear in the magnetic field region shown: they are the two resonances at the extreme right side of the figure. There are other resonances at higher magnetic fields than those shown.

1.5.3. Distributions in Zero-Field Splitting

Distributions in zero-field splittings are generally accepted as the dominant form broadening the apparent linewidths in EPR spectra of non-heme, high-spin iron proteins [13,14,22,29]. Because transition probabilities vary with E/D (Fig. 3), shapes arising from distributions are different from ones calculated with a single frequency-swept lineshape of width similar to experimentally observed ones. This point is illustrated in Figure 12. Each full subspectrum, only part of which is shown, has a double integral corresponding to the same number of spins (more transitions occur at fields higher than those shown).

The parameters chosen for Figure 12 give spectra that might be included, for example, in fitting the low-field lineshape of ferric superoxide reductase (Fig. 1), or (with some change in the value and sign of D) transferrin oxalate (Fig. 2), or the high-salt form of ferric lipoyxygenase [14]. As the value of E/D decreases, the two sets of resonances shown in the figure move closer together, converging on $g = 6$ when E/D is zero. Fitting would involve applying a distribution model (Gaussian or multicomponent, for example) to adjust the amplitudes of the subspectra within the distribution. The lowest-field set of maxima (~ 84 – 117 mT) in Figure 12 covers a

wider field range than the next set (~ 118 – 122 mT). As a result, a distribution of E/D would have the effect of diminishing the intensity of the lowest-field maximum in the spectrum relative to that of the second-to-lowest-field maximum. This consideration probably applies to the experimental SOR spectrum in Figure 1. On the other hand, the smaller D -value, as well as distribution of E/D , contributes to relative intensities in the transferrin oxalate spectra in Figure 2. Distributions in D might also contribute to breadth in EPR spectra of the types considered here.

1.5.4. Looping Transitions

Interesting cases for simulation arise when looping transitions occur, mentioned earlier in §1.3 and Figures 6–8 [20,21,30]. A looping transition occurs when a pair of energy levels is in resonance at two separate magnetic fields. For a "powder" EPR sample, a range of angular orientations may contribute looping transitions to the spectrum, whereas outside of that range no transitions occur between the same pair of levels (Fig. 7). When the two transitions of a looping transition are separated in a magnetic field by a few linewidths, special simulation methods are required to represent the spectrum accurately while minimizing the number of calculated field points and matrix diagonalizations. With reference to Eq. (5), as conditions (angular orientation) approach the point at which the two resonances overlap, and $d\nu(B_0)/dB_0$ goes to zero, a different approach to the lineshape function is required. One approach is to approximate $(\nu(B) - \nu_0)$ by a cubic polynomial in B , Eq. (7), where the constants c_0 and c_1 are defined in terms of the two resonant fields (B_{01} and B_{02}) and the derivatives $d\nu(B)/dB$ at points 1 and 2 [21]:

$$\nu(B) - \nu_0 \sim (B - B_{01})(B - B_{02})(c_0 + c_1 B). \quad (7)$$

In essence, $h(\nu(B) - \nu_0)$ is the difference between the curved energy separation (for example, the 2 \rightarrow 3 transition in Fig. 6) and the microwave energy, $h\nu_0$. The transition probability variation requires similar adjustment. Figure 13 illustrates the considerations for the selected angular orientation used in earlier figures (Figs. 6–8). In Figure 13a, the dots are the calculated separations of energy levels through the region of the loop; the straight lines are the slopes, $d\nu(B_0)/dB_0$, at the two resonant fields; the cubic fit is shown by the solid line; and the shaded area corresponds to a linewidth $\pm\sigma_\nu$ (150 MHz). Clearly, $d\nu(B_0)/dB_0$ is not constant over a linewidth. The standard approximation (two diagonalizations) would apply a shape function to the two points where the loop crosses $(\nu(B) - \nu_0) = 0$ and approximate $(\nu(B) - \nu_0)$ by $(B - B_0)$ in the normalized lineshape function. An exact calculation uses a frequency-swept function calculated at closely spaced intervals (many diagonalizations) through the looping region. These approaches can be compared to the "cubic approximation" in which $(\nu(B) - \nu_0)$ is approximated by Eq. (7), using just two points (Fig. 13b,c). The approximate calculation is the dashed line, and the dots are the overlap of exact calculation or cubic approximation.

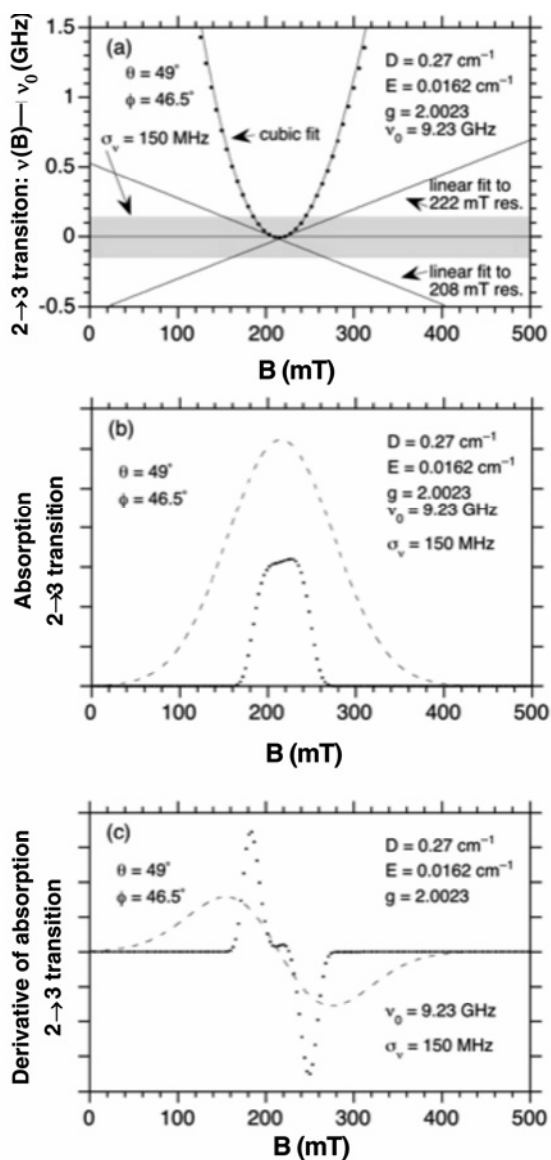
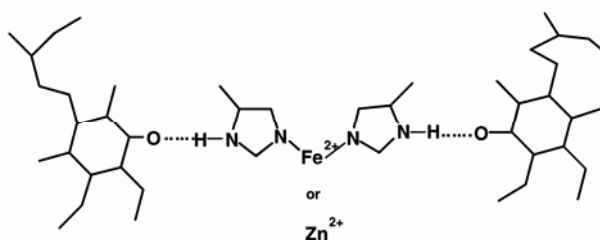


Figure 13. Simulation of a “looping” transition using linear and cubic fits. (a) Cubic fits (solid line) and calculated difference between the transition frequency and the microwave frequency (dots), compared with linear fits (straight lines) in the region of a looping transition. (b) Corresponding absorption spectra with (dashed line) and without (dotted line) the cubic approximation. (c) Derivative spectra. Calculation parameters are the same as in Figure 6. The figure is reproduced from Fig. 6 of Gaffney and Silverstone [21], with permission of the publisher.

2. EPR OF MONONUCLEAR, LOW-SPIN FERRIC NON-HEME PROTEINS

2.1. Nitrile Hydratase

Low-spin ferric iron is common in heme and in some iron–sulfur proteins, but nitrile hydratase is presently the lone example among mononuclear, non-heme, non-iron–sulfur iron proteins [31]. The ferric form of the enzyme is obtained by photolysis of the as-isolated nitric oxide d^6 form. The g -values of the photodissociated ferric protein are 2.27, 2.13, and 1.97, and photointermediates of differing g -values are observed. The relatively narrow linewidths allowed the ^{57}Fe hyperfine to be measured at g_z (40 MHz), establishing that the g - and iron \mathbf{A} -tensors are 45° out of alignment.



Scheme 1.

3. RADICAL ($S = 1/2$) PROBES OF FERROUS ($S = 2$) IRON

3.1. Photosynthetic Reaction Centers

Photosynthetic reaction centers are the classic example of ferrous iron: EPR invisible at 9 GHz because of large zero-field splitting, rendered visible by interaction with close radical spins. The nature of the path ($\sim 7\text{--}9 \text{ \AA}$, Scheme 1) between iron and quinones A and B (Q_A and Q_B) is favorable for a spin–spin coupling to be the dominant form of interaction. Essentially, each level of the $S = 2$ system is split by the $S = 1/2$ spin, giving energy separations accessible at 9 GHz. The A or B quinone radical interactions with the metal ion can be probed separately by means of preparation light pulses and temperature cycles [32] or by selective extraction procedures [33]. Recent summaries are available of the history of assigning the complex Q–Fe spectra and selecting individual quinone interactions with iron [32,34]. Feher has written a personal and historical account of his experimental studies, extending from development of EPR spectrometers and the ENDOR technique to pathways of electron transfer in photosynthesis [35].

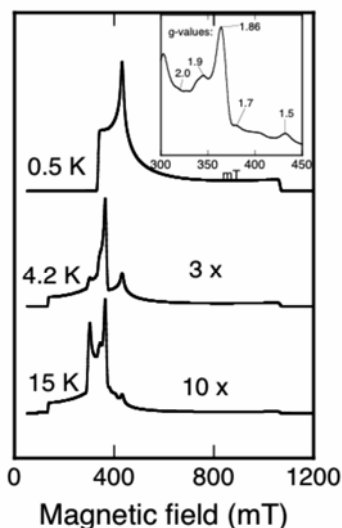


Figure 14. Calculated absorption EPR spectra of ferrous iron ($S = 2$) interacting by J -coupling with a radical at 8.7 Å. The temperatures in the calculations are 0.5, 4.2, and 15 K. The amplitudes of calculated spectra corresponding to equivalent spins were multiplied by the values given on the figure for display. The inset marks selected g -values in the 15 K spectrum. The 0.5 K spectrum is complete as shown, but the 15 K spectrum extends to near 1 T (not shown). The calculation parameters (XSophe [37]) are simplified (isotropic value of J) from those reported in [36] and [41]: iron g -values = 2.16, 2.27, and 2.04; $J = 0.4 \text{ cm}^{-1}$; $D = 5.2 \text{ cm}^{-1}$; and $E/D = 0.25$. Other calculation parameters include microwave frequency = 9.0 GHz and linewidth = 30 G (narrower than experimental). Spectra were calculated with 80 field partitions and 64 grid segments.

For purposes of discussing the EPR of iron–semiquinone interactions in reaction centers, simplified simulations of the spectra are given in Figure 14. The parameters chosen for the simulation are similar to those of Calvo et al. [36]. The spin Hamiltonian relevant to a one-electron reduced $Q_A\text{--Fe--}Q_B$ system has terms involving the iron zero-field splitting and the semiquinone–iron electron spin–spin interactions:

$$H = (\text{iron Zeeman}) + (\text{quinone radical Zeeman}) + \mathbf{S} \cdot \mathbf{D} \cdot \mathbf{S} + \mathbf{S}_{\text{FeII}} \cdot \mathbf{J} \cdot \mathbf{S}_Q. \quad (8)$$

Zero-field splitting ($\mathbf{S} \cdot \mathbf{D} \cdot \mathbf{S}$) dominates the overall appearance of the spectrum for the $Q\text{--Fe}$ case. In the absence of a radical, ferrous iron with $D = 5.2 \text{ cm}^{-1}$ would have no spectrum unless frequencies considerably higher than 9 GHz were used. The radical splits the iron energy levels through a spin–spin interaction. The relevant term, $\mathbf{S}_{\text{FeII}} \cdot \mathbf{J} \cdot \mathbf{S}_Q$, includes isotropic exchange and an anisotropic part that consists of both dipolar and exchange interaction components. The isotropic exchange component can be expressed as $J_0 \mathbf{S}_{\text{FeII}} \mathbf{S}_Q$. When the point dipole approximation is appropriate for one spin (semiquinone), the anisotropic in-

teraction can be described by a vector connecting the spins and by two angles defining the orientation of the interspin vector in the magnetic axis frame of the other spin (ferrous iron, $S = 2$). Different conventions are used for the sign of J . The convention used in Eq. (8) is that of the XSophe simulation program [37], for which the input parameters for spin–spin interaction are J_0 , r , χ , and ρ . Positive J_0 signifies antiferromagnetic spin–spin interaction in XSophe. The notation used by Feher and colleagues [36] is that negative J_0 signifies the antiferromagnetic spin–spin interaction.

Experimental conditions for observing semiquinone–iron interactions by EPR, at low temperature, favor absorption-like rapid-passage spectra. Calculated *absorption* spectra are shown in Figure 14 to illustrate major characteristics of EPR spectra of the $S = 2$, $S = 1/2$ interactions in Q–Fe centers. In the figure, the portion of the spectrum arising from the ground $S = 2$ doublet is illustrated in the calculation with temperature taken as 0.5 K. As the temperature is raised (4.2 and 15 K), more complex spectra that include transitions between higher pairs of levels are seen. The linewidth chosen for the illustration in Figure 14 is considerably less than the experimental linewidth, to show the details of the transitions. In experimental spectra, the overall signal is broad and has a maximum at $g' = \sim 1.8$ when the temperature is 1.4 K or higher [38,39]. Experimental samples also differ from the calculation in Figure 14 in having an intense $g = 2$ signal from several radicals.

The Figure 14 inset identifies g -values in the region where semiquinone–iron signals are often monitored. The positions of the g -values are sensitive to D , to E/D , and somewhat to J and are relatively insensitive to the iron–radical distance, r , in the relevant 7- to 9-Å range (the coordinates of Q_B vary in this range with sample conditions [40]). The two reaction-center quinones have very similar magnetic properties and distances to iron, so the approximate calculation shown in Figure 14 could apply to either Q–Fe interaction. In photosystem II (PSII) of the cyanobacterium *Thermosynechococcus elongatus*, a peak at a g -value of 1.97 is attributed to the Q_B semiquinone–iron interaction, and peaks at g -values in the 1.93–1.95 range to either radical–iron interaction [32]. In addition, the biradical state in which both Q_A and Q_B are semiquinones has a well-defined peak at a g -value of 1.66 in the *T. elongatus* photosystem sample. The biradical state is of course not spectroscopically equivalent to the monoradical state discussed so far.

Characterizing the semiquinone as a point dipole in simulations of Q–Fe EPR works well because the radical is a small perturbation on the highly anisotropic ferrous iron energy levels, but for a high-resolution understanding of why the electron interaction between reaction-center quinones is so efficient, a better picture of the electronic properties of each semiquinone is desired. The paramagnetism of iron is not necessary for electronic interaction between the quinones, and iron either can be driven to low-spin ($S = 0$) by cyanide addition or can be replaced by the diamagnetic metal Zn^{2+} in photosynthetic systems. Under these conditions, and with high-frequency EPR, the relative intensities of $Q_A^{-\bullet}$ and $Q_B^{-\bullet}$, as a function of the state of the sample, can be examined [33]. In addition, the exchange interaction

of quinones in the biradical state ($Q_A^{\cdot-}Q_B^{\cdot-}$) of zinc-substituted reaction centers has been examined by relaxation and by high-frequency EPR [36,41].

3.2. Nitric Oxide and Non-Heme Ferrous Centers

Nitric oxide (NO) is used commonly by EPR spectroscopists as a tool to render ferrous iron measurable [42,43]. In oxidases, nitric oxide interacting with iron serves as a mimic of oxygen activation. Through advances in higher-frequency ENDOR, the intimate details of the structure of non-heme iron oxidase intermediates are being revealed by studies of Fe–NO complexes [44]. Interest is also increasing in the proteins involved in natural NO-dependent biological responses. Bacterial stress regulons are activated by agents including NO, reactive oxygen, and drugs in a variety of categories [45]. The NO-response regulons are involved in bacterial defense against macrophage attack, a process including NO generation by these animal cells. Crosstalk also occurs between genes regulated by iron levels and the NO regulons [46]. Progress in characterizing the non-heme iron–NO complexes of several transcription regulators will be mentioned below. These include Fur, a regulator of iron acquisition, and NorR, an NO-responsive transcription factor. Superoxide reductase (SOR), mentioned earlier in the ferric EPR sections, is an enzyme component of the stress response to superoxide. The SOR mononuclear Fe–NO complex has been a useful analog of the Fe-superoxide interaction in this enzyme. The reader is referred to the chapter on iron–sulfur proteins for further discussion of another category of NO additions to iron. The many examples of heme–iron proteins interacting with NO are also covered in Chapters 8 and 9.

Experimentally, nitric oxide complexes of iron proteins have excellent properties for sensitive spectroscopy. The EPR signals are strong enough that they can sometimes be measured within intact *Escherichia coli* expressing the target protein [47], and EPR signals can be observed at higher temperatures, sometimes including room temperature, than are normally required for study of other spin states of non-heme iron [48]. Among the factors contributing to the strong signals are large zero-field splitting (only the ground state is populated at lower temperatures), relatively small deviations from axial symmetry, small distributions in E/D (the short Fe–NO bond is a well-defined axial ligand), and of near-coincidence of the g - and hyperfine tensors. Some of these favorable properties contribute to the spectra in Figure 15, which shows the EPR spectra of the iron–nitric oxide complex of lipoxygenase at two frequencies, 9.26 and 92.6 GHz, scaled to the same g -value scale. The essentially identical g -values in the two spectra indicate that the D -value of this Fe–NO complex is >93 GHz (~ 3 cm $^{-1}$). These spectra show the presence of two species, the relative amounts of which vary with pH and other factors [49]. Variability of two components exhibited in spectroscopy of lipoxygenase is also a property of both the ferric and ferrous forms of the protein [14,50]. The apparent linewidth in the 92.6 GHz spectrum is narrower on the g -value scale shown than that in the 9.26 GHz spectrum, indicating that relaxation is probably a significant component of the linewidth, especially of the outer features in the spectrum. This spectrum is part of an ongoing investigation (Gaffney, *unpublished*).

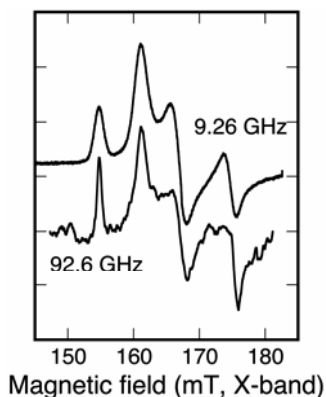


Figure 15. EPR spectra of the high-spin Fe–NO complex of soybean LOX-1 at two frequencies. The soybean lipoxygenase (LOX-1)–nitric oxide complex (3.2 mM in 0.1 M potassium phosphate, pH 7.0) was sealed under argon in a quartz EPR tube of 0.7 mm ID. Spectra were recorded 9.26 GHz and 94 GHz, and the temperature was 6 K. The original 94 GHz spectrum was scaled to the same g -value scale as the 9.26 GHz spectrum, and the magnetic field units are shown for the X-band spectrum. Because of the scaling, the high-frequency spectrum is labeled in the figure as if it was recorded at 92.6 GHz, and the corresponding magnetic field scale would be ten times that shown.

3.2.1. Model Compounds

The similarities and differences between iron–NO and iron–oxygen bonding have been the subjects of debate, and model compounds provide important correlations between structure, spectroscopy, and redox chemistry of iron nitrosyls. The nitrosyl groups in these complexes can be described as NO^+ ($S = 0$), NO^{\cdot} ($S = 1/2$), NO^- ($S = 0$), NO^- ($S = 1$), and NO^{2-} ($S = 1/2$). The associated iron ions have charges and spins such that the overall numbers of iron d electrons plus $\text{NO } \pi^*$ electrons are 6–8 in most experimentally accessible model compounds. The notation for these complexes follows the Enemark and Feltham conventions [51]. The EPR visible complexes are d^7 , or $(\text{Fe–NO})^7$, and d^9 , or $(\text{Fe–(NO)}_2)^9$. Both $S = 3/2$ and $S = 1/2$ d^7 complexes are found. Table 2 summarizes possible electronic states that might be considered for d^{6-8} iron–nitrosyl complexes. Representative references to those electronic states that are experimentally observed, or calculated, are given in the table footnotes.

Although $S = 1/2$ nitrosyl complexes with heme iron are well known and described, low-spin ($S = 1/2$) non-heme iron–NO examples are uncommon. Debate on the electronic descriptions of the low-spin d^{6-8} series has focused on whether the redox chemistry is ligand centered, as suggested by variation in infrared NO stretching frequencies, or metal centered, as implied by Mössbauer isomer shifts. What Serres et al. [52] describe as “a unified picture of the electronic structure of low-spin non-heme iron nitrosyls in perhaps unprecedented detail” has recently

been achieved by combined spectroscopy and density functional theory (DFT) calculations. Iron in this d^{6-8} series was in complex with the pentadentate [Fe(II)NO(cyclam-Ac)] (cyclam = 1,4,8,11-tetraazacyclotetradecane; Ac = a pendant acetyl). Oxidation and reduction were achieved by both electrochemical and chemical redox reactions. The d^7 oxidation state is EPR active, as expected, and is low spin. Experimental and simulated spectra from this work are shown in Figure 16. Two components, a- (70%) and b- (30%), were required to fit the EPR data. Also, linewidths with frequency and g -variation were assigned to yield fits over a decade of frequencies. Solvation effects on EPR of the experimental sample present some difficulties, but overall, density functional calculations gave EPR parameters in reasonable agreement with experiment (Table 3). At 34 GHz, resolved nitrogen hyperfine of ~ 74 MHz is clearly seen associated with the middle g -value in the spectrum of the minor component. This experimental hyperfine value agrees well with a B3LYP calculation that gives a deviation of 21° between axes of middle g -value and maximum hyperfine (86 MHz), giving a calculated value of $\cos(21^\circ) \times 86$ MHz ~ 80 MHz. From combined spectroscopy and calculation, the low-spin d^7 complex is best described as (Fe(II) ($S = 0$) (NO \bullet) ($S = 1/2$))⁷. The (Fe–NO)⁸ component, described as “elusive,” was partially characterized by experiment and fully by calculation in this same paper. In summary, calculations and spectroscopy lead to a picture of oxidation/reduction in the low-spin d^{6-8} series as ligand centered, with iron remaining Fe(II) through the series.

Table 2. Possible Electronic States and Total Spin (S_{tot}) of (Fe–NO)^{6–8} Complexes^a

(Fe–NO) ⁶ $S_{\text{tot}} = 0$	(Fe–NO) ⁷ $S_{\text{tot}} = 1/2$	(Fe–NO) ⁷ $S_{\text{tot}} = 3/2$	(Fe–NO) ⁸ $S_{\text{tot}} = 0$	(Fe–(NO) ₂) ⁹ $S_{\text{tot}} = 1/2$
[Fe(II)NO ⁺] $S = 0, S = 0^{\text{b,d}}$	[Fe(II)NO [•]] $S = 0, S = 1/2^{\text{b,c}}$	[Fe(II)NO \bullet] $S = 2, S = 1/2$	[Fe(II)NO [–]] $S = 0, S = 0^{\text{b}}$	Nonequivalent NOs
[Fe(III)NO \bullet] $S = 1/2, S = 1/2^{\text{f}}$	[Fe(III)NO [–]] $S = 1/2, S = 0$	[Fe(III)NO [–]] $S = 5/2, S = 1^{\text{c}}$	[Fe(III)NO ^{2–}] $S = 1/2, S = 1/2$	
[Fe(IV)NO [–]] $S = 1, S = 1^{\text{g}}$	[Fe(III)NO [–]] $S = 1/2, S = 1$			

^a Table modeled, in part, after Chart 1 in Serres et al. [52]. Representative references to states assigned in model compounds are designated in footnotes b–g. ^b [52]. ^c [53,54]. ^d [66]. ^e Typical of heme Fe(II)NO. See D. Singel, Chapter 9, this volume. ^f [61]. ^g [31].

Several model iron–nitrosyl compounds with $S = 3/2$ group spins were examined by optical, infrared, resonance Raman, x-ray absorption, and calculations [53]. The data indicate a description of the complexes as antiferromagnetically coupled (Fe(III) ($S = 5/2$) (NO[–]) ($S = 1$))⁷. A number of other studies of model compounds agree with this assignment of $S_{\text{tot}} = 3/2$ Fe–NO model compounds. In a separate study, the *cis*- and *trans*- isomers of the iron complex of 1,4,8,11-tetraazacyclo-

tetradecane (cyclam), [(cyclam)Fe(II)(NO)(I)], were examined by Mössbauer [54]. The *trans*-cyclam derivative exhibits $S = 1/2$, whereas the *cis*-compound is $S = 3/2$. The *cis*-complex rapidly converts to *trans*- on slight warming of a freeze-trapped sample of the *cis*-cyclam.

Table 3. EPR Parameters from Experiment and DFT Calculation for $S = 1/2$ d^7 Model^a

EPR parameter	Experimental ^b	Calculated ^c
g_x, g_y, g_z	2.042, 2.022, 1.977	2.017, 1.997, 1.940
A_x, A_y, A_z (MHz)	30, 75, 3	52.9, 86.2, 11.4

^aFrom Serres et al. (52), Tables 3 and 10.

^bOf the two components, the major, a (70%), with more poorly resolved ¹⁴N (of NO) hyperfine, is cited.

^cB3LYP DFT calculation.

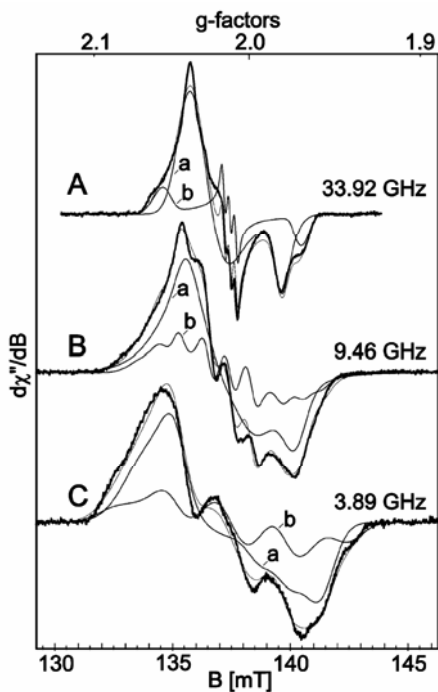


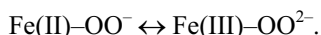
Figure 16. EPR spectra at three frequencies of low-spin model Fe—NO compounds. The EPR spectra of a frozen solution (in butyronitrile) of 1,4,8,11-tetraazacyclotetradecane-1-acetic acid nitrosyl(iron) (PF₆) was measured at low temperature (40 K, 33.9202 GHz; 10 K, 9.4565 GHz; 13K, 3.8835 GHz). The *g*-values are given in the labels for the upper abscissa. The lower abscissa is labeled with the corresponding magnetic field for the 3.8835 GHz EPR spectrum. Two forms, in a ratio of 70:30, were used in a simulation (thin lines). The figure is reproduced from Fig. 9 of Serres et al. [52], with permission of the publisher.

3.2.2. *Fe-NO as a Model of Iron-Reactive Oxygen Intermediates in Proteins*

Nitric oxide reacts with non-heme, mononuclear iron in proteins that have diverse interactions with reactive oxygen. The way in which Fe-NO serves as a model of the interaction therefore varies. The ferrous form of facial triad oxygenases [4] reacts with oxygen, forming initially a ferric superoxide intermediate followed by O-O bond cleavage to give the reactive species Fe(IV)-OH. When NO is substituted for oxygen, the analog of the superoxide intermediate is formed as a stable species:



In contrast, superoxide reacts with ferrous iron in SOR, and in this case, the ferrous-NO \leftrightarrow ferric-NO⁻ interaction must model formation of a ferric-peroxy complex, but with one less electron [55]:



In the third example, no evidence has been obtained, despite serious effort [56], for direct interaction of oxygen with the ferrous iron in lipoyxygenase, but NO forms a complex with a pH-dependent K_d in the range 10–95 μM [49]. Instead, the lipoyxygenase iron-NO complex (Figure 15) could be viewed as a model of an intermediate in the catalytic cycle:



Regardless of the details of the model, the various stable complexes of ferrous iron with NO prepare non-heme mononuclear iron proteins for high-resolution local structure EPR studies, especially by ENDOR.

3.3. High-Spin NO Complexes with Non-Heme Iron Proteins

3.3.1. *ENDOR Studies of Ligand Rearrangement in Facial Triad Oxygenase-NO Complexes*

A function of the iron center in the “facial triad” oxygenases is to bring three exogenous ligands into alignment for reaction while also remaining tightly attached to three protein sidechains. Nitric oxide serves as a noncleaved oxygen surrogate in structural studies of substrate/inhibitor binding to these oxygenases. Questions regarding rearrangements of exogenous ligand sites have arisen in comparisons of x-ray structures of various facial triad oxygenases in different intermediate states [57]. Magnetic resonance of the solution state provides a versatile companion to the structural studies.

High-resolution ENDOR of iron-NO complexes has proven ideal for resolving questions about the relative orientations of exogenous iron ligands in facial triad oxygenases. Because this volume has a chapter devoted to recent ENDOR studies (see Chapter 3), only a brief account of one example, in which an Fe-NO complex

is examined by ENDOR, will be given here. The enzyme 1-aminocyclopropane-1-carboxylic acid oxidase (ACCO) is a facial triad oxygenase involved in ethylene formation. The high resolution achieved in ENDOR studies of ACCO included higher-frequency (35 GHz) pulsed techniques and genetic manipulations designed to facilitate selective isotope labeling [44,58]. The protein-derived metal ligands of ACCO are provided by two His and a carboxylate, bound in bidentate fashion. Nitric oxide reacts with ferrous ACCO to form a high-spin d^7 ($S = 3/2$) complex exhibiting an EPR spectrum indicative of near axial symmetry ($g_{1,2,3} = 4.11, 3.94, 1.99$; $E/D = 0.008$). With substrate or inhibitor present, the EPR spectrum is less axial ($g_{1,2,3} = 4.23, 3.82, 1.99$; $E/D = 0.035$) [44]. Besides the change in rhombicity, another indication of considerable differences in the electronic structure of the Fe–NO centers between ACCO–NO and the ACCO–NO–substrate complex (ACCO–ACC–NO) is that the latter saturates at ~ 10 -fold lower power than the former.

The problem posed by earlier crystallography studies of other facial triad oxygenases [57] is that the carboxylate of the bidentate substrate and a water ligand are bound to iron in different arrangements in crystal structures of different members of the facial triad oxygenase family. A variety of approaches have now resolved the structural questions by showing that the arrangement of ligands can change when both NO (or, by analogy, oxygen) and substrate bind. The ENDOR studies [44] of ACCO–NO–substrate illustrate this point nicely. All of the protein and ligand nuclei coordinated to iron, except the substrate –COOH oxygen, were labeled with ^{14}N , ^{15}N , or ^{17}O in this study. Overall, combined pulsed and CW ENDOR techniques yielded spectra from both ν_+ and ν_- branches and a full range of g -values. In CW mode, only the ν_+ branch is seen, simplifying the spectra. CW ENDOR was also best in providing information near $g = 2$ (g_3) and at angles intermediate between the extreme g -values in angle-selected experiments. Davies-pulsed 35-GHz ENDOR spectra were better resolved than CW ENDOR spectra around g_1 and g_2 . The presence of an iron–water bond in ACCO–NO (no substrate) was detected in two ways. CW ENDOR at g_3 of the enzyme prepared in H_2O^{17} gave a very large ^{17}O resonance at 13 MHz. Also, a 35-GHz refocused-Mims-pulsed ENDOR experiment detected a 2-MHz splitting for the deuterons of D_2O . Whether one or two waters contributed to the data could not be determined. In nitrogen ENDOR of substrate-free ACCO–NO, the two nitrogen nuclei of histidines coordinated to Fe are magnetically identical along g_3 (the Fe– N_{NO} bond direction) and must, therefore, lie in the plane perpendicular to the Fe– N_{NO} direction. In the ACCO–NO–ACC complex, however, they are distinct, one being aligned with g_3 and the other with g_2 . Figure 17 shows the angle-selected, 35-GHz CW ENDOR results for the (^{15}N -His)–ACCO–NO–ACC complex. Note that, in the lowest spectrum, taken along g_3 , the two ^{15}N -His signals are distinctly different. This finding signifies that one of the Fe– N_{His} bonds has become *trans* to the Fe– N_{NO} direction. If NO is viewed as a paramagnetic oxygen surrogate, then the ENDOR results show that the orientation of oxygen is directed to a unique ligand position on iron, the correct position for subsequent reaction, by the substrate displacing waters and binding in a bidentate fashion [44].

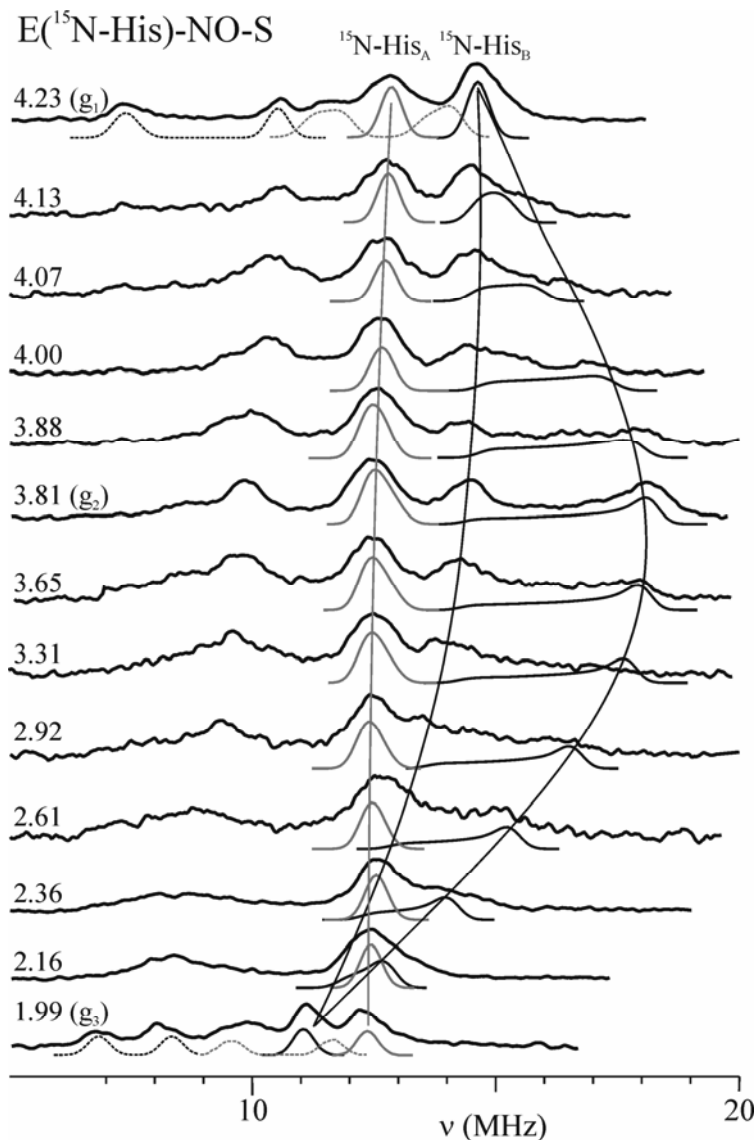


Figure 17. Orientation-selected CW ENDOR spectra ($^{15}\text{N-His}$ at 35 GHz) of the enzyme, 1-aminocyclopropane-1-carboxylic acid oxidase (ACCO). At each g -value, the upper spectrum is experimental, and below each a simulation is shown. Simulations of individual $^{15}\text{N-His}$ spectra are shown as gray and black for His_A and His_B , respectively. The simulation at g_1 ($g = 4.23$) also includes ^{14}NO (long dashes). Note that the two nitrogens of histidine ligands are not equivalent along g_3 (the Fe-N_{NO} bond direction), so one of the histidines is *trans* to the NO ligand. The apparent absence of angle dependence of the $^{15}\text{N-His}_A$ spectra arises from compensating shifts in $\nu_{\text{N}}(^{15}\text{N})$ and nitrogen hyperfine coupling. The figure is reproduced from Fig. 6 of Tierney et al. [44], with permission of the publisher.

3.3.2. Proteins in which NO Is a Natural Ligand to Mononuclear Non-Heme Iron

3.3.2.1. *NO responsive transcription factor NorR.* *E. coli* genes for proteins involved in reduction of nitric oxide are transcribed in response to NorR. Transcriptional activation controlled by NorR involves three domains in the protein. An N-terminal GAF domain is the sensor, a middle domain is in the AAA+ family of adenosine triphosphatases (ATPases), and the C-terminal domain is a helix–loop–helix deoxyribonucleic acid (DNA) binding domain. The AAA+ domain is only active when NO has bound to the GAF domain [59]. The GAF domain contains iron and undergoes a conformational change when NO binds iron. In the NO-bound state, NorR then activates transcription. Mutation of one of the iron ligands, D99A, gives a GAF domain that does not bind Fe. The EPR spectrum of NorR–Fe–NO is typical of a $d^7 S = 3/2$ species ($E/D = 0.03$) [47].

3.3.2.2. *Nitrile hydratase.* Nitric oxide is a naturally occurring ligand in inactive Fe nitrile hydratase, as isolated. This state is EPR silent. In addition to the natural NO ligand, the iron ligand environment is unique in other ways. Three ligands derive from cysteine, but in the highest-resolution x-ray structure two of the sulfur ligands are oxidized sulfurs, sulfinic and sulfonic acids, and the third sulfur is cysteinate [60]. Photolysis of the NO ligand from nitrile hydratase replaces NO by water and yields an enzymatically active state with a low-spin ferric EPR signal [31]. On the basis of several forms of spectroscopy, the Fe(III)–NO form of nitrile hydratase is assigned as low-spin Fe(III)NO, d^6 . This interesting iron center is the subject of ongoing modeling and theory, showing that the charge density on iron in the NO-bound d^6 form is similar to that in the photolysed FeIII form [61]. The center is therefore closer to $[\text{Fe(III)NO}]^+$, [$S = 1/2$, $S = 1/2$], than to other charge and spin designations (Table 2).

3.4. Low-Spin NO Complexes with Non-Heme Iron Proteins

3.4.1. d^7 Example: Protocatechuate 3,4-Dioxygenase

Under most conditions, ferrous protocatechuate 3,4-dioxygenase (3,4-PCD) gives EPR spectra of a high-spin, $S = 3/2$, nitrosyl adduct, but when NO is added to a preformed 3,4-PCD–cyanide complex, a well-resolved EPR spectrum of a low-spin adduct (d^7 , $S = 1/2$) is seen [62]. A calculation using the published parameters of this low-spin ^{15}NO adduct is illustrated in Figure 18. In variously isotope-labeled samples, the signals have resolved splittings from $^{15,14}\text{NO}$, a histidine ^{14}N , and ^{13}C –cyanide ligands with resolution as high as many previously reported for NO associated with iron in heme proteins. Binding of both cyanide and NO depends on the order of addition. When CN^- binds first, a tyrosine ligand is probably displaced, maintaining charge neutrality, and subsequently NO and one more CN^- bind. The Fe–NO bond is photolabile. Assignment of the EPR spectra helped establish how the conformation of the iron center adapts to exogenous ligands. The highly resolved hyperfine splittings indicate close alignment of the principal axes of the **g**- and **A**-tensors.

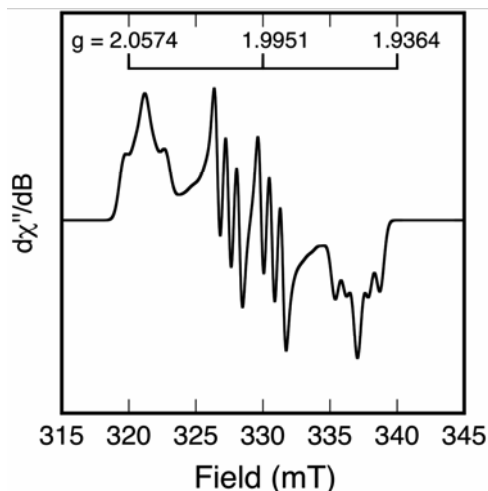


Figure 18. A simulation, after that of Orville and Lipscomb [62], of the EPR spectrum of 3,4-protocatechuate dioxygenase with cyanide and ^{15}N -nitric oxide. The original appears in Fig. 3B of Orville and Lipscomb [62]. The simulation here was performed with XSophe [37] with $g_1 = 2.050$, $g_2 = 2.001$, $g_3 = 1.9535$; ^{15}N -NO $A_1 = 41.9$, $A_2 = 91$, $A_3 = 45$ MHz; ^{14}N -protein A = 2.3 MHz (isotropic); linewidths at $g_{1,2,3} = 0.425$, 0.225, and 0.35 mT; microwave frequency = 9.2158 GHz; 40 field partitions; and 32 grid segments. It is interesting to compare this spectrum to those of a model d^9 , $S = 1/2$ compound shown in Figure 16.

3.4.2. d^9 Example: When Spin Counts Matter: *Fur*-(NO) $_2$

Fur, the iron uptake regulator of Gram-negative bacteria, binds to “iron boxes” and is a corepressor for genes involved in iron homeostasis and oxygen stress [46]. Fe*Fur* includes six iron donor ligands (oxygen plus nitrogen), and the mechanism of *Fur* regulation involves association–dissociation of the iron–protein complex. The *E. coli* Fe*Fur* repressor activity is inhibited by NO, concomitant with formation of a complex having an EPR spectrum with $g_{\text{iso}} = 2.03$ [48]. This nitric–oxide interaction links bacterial NO stress responses to iron homeostasis. The protein has a second metal ion center, a zinc site in an $(\text{S}_2(\text{O}/\text{N})_2)$ environment, and it also has two free sulfhydryls that are not involved in either metal center (shown by mutagenesis). When NO binds to Fe*Fur*, the resulting EPR spectrum is identical to the well-known d^9 iron-dinitrosyl species formed when NO reacts with iron sulfur centers. This result is illustrated in Figure 19, where the d^9 iron dinitrosyl species resulting from an iron–sulfur protein [63] is compared to a simulation using the EPR parameters that fit the Fe*Fur* spectrum [48].

A remaining question is whether the new d^9 iron-nitrosyl center might involve a rearrangement to include the sulfurs of the zinc center. The extremely tight binding of zinc to the second metal site in *Fur* suggests not, but accounting quantita-

tively for the number of nitric oxides involved in forming NO–FeFur has been important. Fur has higher affinity for NO than deoxymyoglobin has, and the equivalents of NO needed to saturate FeFur could therefore be determined optically in the presence of deoxymyoglobin (see supporting information in [48]). The answer obtained was that 2.7 equivalents of NO were needed to saturate the FeFur site. The extra NO equivalent served as a reductant to give the paramagnetic d^9 complex. The conclusion then is that FeFur forms predominantly (85%) a protein– $(\text{Fe}(\text{NO})_2)^9$ ($S = 1/2$) complex and a minor amount of an EPR-silent $(\text{Fe}(\text{NO})_2)^8$ ($S = 0$) complex (assigned by Mössbauer). In contrast to d^7 Fe–NO EPR spectra, the d^9 species in FeFur has a small nitrogen hyperfine (around 10 MHz or less) and a large ^{57}Fe hyperfine, showing that the spin density is high on iron and low on NO.

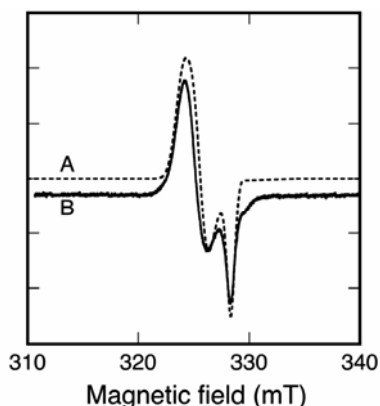


Figure 19. The calculated EPR spectrum of the d^9 , $S = 1/2$, $\text{FeFur}(\text{NO})_2$ complex compared with the experimental iron dinitrosyl complex from an iron–sulfur protein, RumA. The upper spectrum (dashed line) is a simulation (XSophe [37]) based on the parameters given by D'Autréaux et al. [48] (their Fig. 3 legend] for the EPR of an FeFur complex with two ^{14}N –NO molecules. Simulation parameters used here were spin state, $S = 1/2$; $g_{1,2,3}$ -values, 2.042, 2.032, 2.015; linewidths at each g -value, 7.9, 7.0, 4.0. The ^{14}N –NO hyperfine was not used in the simulation shown, but incorporating hyperfine splitting from ^{14}N of up to 10, 10, and 5 MHz (x, y, z) produced no significant change in the calculated lineshape. The lower curve is an experimental spectrum that results from NO addition to the $[\text{Fe}_4\text{S}_4]^{2+}$ cluster in the *E. coli* RNA methylase, RumA. The frequency used in simulation was 9.26 GHz, to match the RumA EPR spectrum. The experimental spectrum was published earlier as Fig. 5b of Agarwalla et al. [63].

The x-ray structure of Fur from *Pseudomonas aeruginosa*, solved recently [64], is the first structure of a Fur protein. In this organism the protein has only one sulfhydryl, and it lacks the domain with the high-affinity zinc site of the *E. coli* homolog. Still, it was found to have two metal sites, one (O_4/N_2) octahedral site for iron and one tetrahedral (O_2/N_2) site occupied by zinc. All the metal-binding amino acids are conserved in the *P. aeruginosa* and *E. coli* homologs, so an unidentified

metal (M) in a tetrahedral site in Fur proteins, such as the one from *E. coli*, might yield a dinitrosyl complex with geometry similar to those formed in Fe–S proteins. However, more recent examination of metal affinities of *E. coli* Fur cast doubt on the existence of the putative tetrahedral site in this version of the protein [65]. Evidently the story of Fur EPR is not over.

REFERENCES

1. Gaffney BJ, Silverstone HJ. 1993. Simulation of the EMR spectra of high-spin iron in proteins. In *EMR of paramagnetic molecules*, pp. 1–57. Ed LJ Berliner, J Reuben. *Biological magnetic resonance*, Vol. 13. New York & London: Plenum Press.
2. Abu-Omar MM, Loaiza A, Hontzeas N. 2005. Reaction mechanisms of mononuclear non-heme iron oxygenases. *Chem Rev* **105**(6):2227–2252.
3. Costas M, Mehn MP, Jensen MP, Que L. 2004. Dioxygen activation at mononuclear nonheme iron active sites: enzymes, models, and intermediates. *Chem Rev* **104**(2):939–986.
4. Hausinger RP. 2004. FeII/alpha-ketoglutarate-dependent hydroxylases and related enzymes. *Crit Rev Biochem Mol Biol* **39**(1):21–68.
5. Solomon EI, Brunold TC, Davis MI, Kemsley JN, Lee SK, Lehnert N, Neese F, Skulan AJ, Yang YS, Zhou J. 2000. Geometric and electronic structure/function correlations in non-heme iron enzymes. *Chem Rev* **100**(1):235–349.
6. Kappock TJ, Caradonna JP. 1996. Pterin-dependent amino acid hydroxylases. *Chem Rev* **96**(7):2659–2756.
7. Kurtz DM. 2004. Microbial detoxification of superoxide: the non-heme iron reductive paradigm for combating oxidative stress. *Acc Chem Res* **37**(11):902–908.
8. Clay MD, Jenney FE, Hagedoorn PL, Goerge GN, Adams MWW, Johnson MK. 2002. Spectroscopic studies of *Pyrococcus furiosus* superoxide reductase: implications for active-site structures and the catalytic mechanism. *J Am Chem Soc* **124**(5):788–805.
9. Dubach J, Gaffney BJ, More K, Eaton GR, Eaton SS. 1991. Effect of the synergistic anion on electron paramagnetic resonance spectra of iron–transferrin anion complexes is consistent with bidentate binding of the anion. *Biophys J* **59**(5):1091–1100.
10. Yeh AP, Hu YL, Jenney FE, Adams MWW, Rees DC. 2000. Structures of the superoxide reductase from *Pyrococcus furiosus* in the oxidized and reduced states. *Biochemistry* **39**(10):2499–2508.
11. Baker HM, Anderson BF, Brodie AM, Shongwe MS, Smith CA, Baker EN. 1996. Anion binding by transferrins: importance of second-shell effects revealed by the crystal structure of oxalate-substituted diferric lactoferrin. *Biochemistry* **35**(28):9007–9013.
12. Bloom LM, Benkovic SJ, Gaffney BJ. 1986. Characterization of phenylalanine hydroxylase. *Biochemistry* **25**(15):4204–4210.
13. Yang AS, Gaffney BJ. 1987. Determination of relative spin concentration in some high-spin ferric proteins using E/D-distribution in electron paramagnetic resonance simulations. *Biophys J* **51**(1):55–67.
14. Gaffney BJ, Mavrophilipos DV, Doctor KS. 1993. Access of ligands to the ferric center in lipoxigenase-1. *Biophys J* **64**(3):773–783.
15. Gaffney BJ, Su C, Oliw EH. 2001. Assignment of EPR transitions in a manganese-containing lipoxigenase and prediction of local structure. *Appl Magn Reson* **21**(3–4):411–422.

16. Bennati M, Prisner TF. 2005. New developments in high field electron paramagnetic resonance with applications in structural biology. *Rep Prog Phys* **68**(2):411–448.
17. Andersson KK, Schmidt PP, Katterle B, Strand KR, Palmer AE, Lee SK, Solomon EI, Graslund A., Barra AL. 2003. Examples of high-frequency EPR studies in bioinorganic chemistry. *J Biol Inorg Chem* **8**(3):235–247.
18. Gaffney BJ, Maguire BC, Weber RT, Maresch GG. 1999. Disorder at metal sites in proteins: a high-frequency-EMR study. *Appl Magn Reson* **16**(2):207–221.
19. Aasa R, Vänngård T. 1975. EPR signal intensity and powder shapes: a reexamination. *J Magn Reson* **19**(3):308–315.
20. Pilbrow JR, Sinclair GR, Hutton DR, Troup GJ. 1983. Asymmetric lines in field-swept EPR: Cr^{3+} looping transitions in ruby. *J Magn Reson* **52**(3):386–399.
21. Gaffney BJ, Silverstone HJ. 1998. Simulation methods for looping transitions. *J Magn Reson* **134**(1):57–66.
22. Fiamingo FG, Brill AS, Hampton DA, Thorkildsen R. 1989. Energy distributions at the high-spin ferric sites in myoglobin crystals. *Biophys J* **55**(1):67–77.
23. Rakowsky MH, Zecevic A, Eaton GR, Eaton SS. 1998. Determination of high-spin iron(III)-nitroxyl distances in spin-labeled porphyrins by time-domain EPR. *J Magn Reson* **131**(1):97–110.
24. Berliner LJ, Eaton GR, Eaton SS, eds. 2000. *Distance measurements in biological systems by EPR. Biological magnetic resonance*, Vol. 19. New York: Kluwer Academic/Plenum.
25. MacArthur R, Sazinsky MH, Kuhne H, Whittington DA, Lippard SJ, Brudvig GW. 2002. Component B binding to the soluble methane monooxygenase hydroxylase by saturation-recovery EPR spectroscopy of spin-labeled MMOB. *J Am Chem Soc* **124**(45):13392–13393.
26. Bennati M, Robblee JH, Mugnaini V, Stubbe J, Freed JH, Borbat P. 2005. EPR distance measurements support a model for long-range radical initiation in *E. coli* ribonucleotide reductase. *J Am Chem Soc* **127**(43):15014–15015.
27. Klug CS, Eaton SS, Eaton GR, Feix JB. 1998. Ligand-induced conformational change in the ferric enterobactin receptor FepA as studied by site-directed spin labeling and time-domain ESR. *Biochemistry* **37**(25):9016–9023.
28. Gaffney BJ, Eaton GR, Eaton SS. 1998. Electron spin relaxation rates for high-spin Fe(III) in iron transferrin carbonate and iron transferrin oxalate. *J Phys Chem B* **102**(28):5536–5541.
29. Hendrich MP, Debrunner PG. 1989. Integer-spin electron paramagnetic resonance of iron proteins. *Biophys J* **56**(3):489–506.
30. Wang DM, Pilbrow JR. 1988. Symmetry relationships for the 4 energy levels and the angular property of the EPR spectra for a spin-3/2 system. *J Magn Reson* **77**(3):411–423.
31. Popescu VC, Munck E, Fox BG, Sanakis Y, Cummings JG, Turner IM, Nelson MJ. 2001. Mössbauer and EPR studies of the photoactivation of nitrile hydratase. *Biochemistry* **40**(27):7984–7991.
32. Fufezan C, Zhang CX, Krieger-Liszkay A, Rutherford AW. 2005. Secondary quinone in photosystem II of *Thermosynechococcus elongatus*: semiquinone-iron EPR signals and temperature dependence of electron transfer. *Biochemistry* **44**(38):12780–12789.
33. Utschig LM, Thurnauner MC, Tiede DM, Poluektov OG. 2005. Low-temperature interquinone electron transfer in photosynthetic reaction centers from *Rhodobacter sphaeroides* and *Blastochloris viridis*: characterization of Q(B)(-) states by high-

- frequency electron paramagnetic resonance (EPR) and electron-nuclear double resonance (ENDOR). *Biochemistry* **44**(43):1413–14142.
34. Lakshmi KV, Brudvig GW. 2000. Electron paramagnetic resonance distance measurements in photosynthetic reaction centers. In *Distance measurements in biological systems by EPR*, pp. 513–567. Ed LJ Berliner, GR Eaton, SS Eaton. New York: Kluwer Academic/Plenum.
 35. Feher G. 2002. My road to biophysics: picking flowers on the way to photosynthesis. *Annu Rev Biophys Biomol Struct* **31**:1–44.
 36. Calvo R, Abresch EC, Bittl R, Feher G, Hofbauer W, Isaacson RA, Lubitz W, Okamura MY, Paddock ML. 2000. EPR study of the molecular and electronic structure of the semiquinone biradical $Q_A^-Q_B^-$ in photosynthetic reaction centers from *Rhodobacter sphaeroides*. *J Am Chem Soc* **122**(30):7327–7341.
 37. Hanson GR, Gates KE, Noble CJ, Griffin M, Mitchell A, Benson S. 2004. XSophe-Sophe-XeprView: a computer simulation software suite (v. 1.1.3) for the analysis of continuous wave EPR spectra. *J Inorg Biochem* **98**(5):903–916.
 38. Butler WF, Johnston DC, Shore HB, Fredkin DR, Okamura MY, Feher G. 1980. The electronic structure of Fe^{2+} in reaction centers from *Rhodospseudomonas sphaeroides*, I: static magnetization measurements. *Biophys J* **32**(3):967–992.
 39. Butler WF, Calvo R, Fredkin DR, Isaacson RA, Okamura MY, Feher G. 1984. The electronic structure of Fe^{2+} in reaction centers from *Rhodospseudomonas sphaeroides*, III: EPR measurements of the reduced acceptor complex. *Biophys J* **45**(5):947–973.
 40. Xu Q, Baciou L, Sebban P, Gunner MR. 2002. Exploring the energy landscape for Q_A^- to Q_B^- electron transfer in bacterial photosynthetic reaction centers: effect of substrate position and tail length on the conformational gating step. *Biochemistry* **41**(31):10021–10025.
 41. Calvo, R, Isaacson, RA, Abresch, EC, Okamura, MY and Feher, G. 2002. Spin-lattice relaxation of coupled metal-radical spin dimers in proteins: application to Fe^{2+} -cofactor (Q_A^- , Q_B^- , ϕ^+) dimers in reaction centers from photosynthetic bacteria. *Biophys J* **83**(5):2440–2456.
 42. Hori H, Ikeda-Saito M, Yonetani M. 1981. Single crystal EPR of myoglobin nitroxide: freezing-induced reversible changes in the molecular orientation of the ligand. *J Biol Chem* **256**(15):7849–7855.
 43. Galpin JR, Veldink GA, Vliegthart JFG, Boldingh J. 1978. The interaction of nitric oxide with soybean lipoxygenase-1. *Biochim Biophys Acta* **536**(2):356–362.
 44. Tierney DL, Rocklin AM, Lipscomb JD, Que L, Hoffman BM. 2005. ENDOR studies of the ligation and structure of the non-heme iron site in ACC oxidase. *J Am Chem Soc* **127**(19):7005–7013.
 45. Cao M, Moore CM, Helmann JD. 2005. *Bacillus subtilis* paraquat resistance is directed by σ_M , an extracytoplasmic function sigma factor, and is conferred by YqjL and BcrC. *J Bacteriol* **187**(9):2948–2956.
 46. Mukhopadhyay P, Zheng M, Bedzyk LA, LaRossa RA, Storz G. 2004. Prominent roles of the NorR and Fur regulators in the *Escherichia coli* transcriptional response to reactive nitrogen species. *Proc Natl Acad Sci USA* **101**(3):745–750.
 47. D'Autreaux B, Tucker NP, Dixon R, Spiro S. 2005. A non-haem iron centre in the transcription factor NorR senses nitric oxide. *Nature* **437**(7059):769–772.
 48. D'Autreaux B, Horner O, Oddou JL, Jeandey C, Gambarelli S, Berthomieu C, Latour JM, Michaud-Soret I. 2004. Spectroscopic description of the two nitrosyl-iron complexes responsible for fur inhibition by nitric oxide. *J Am Chem Soc* **126**(19):6005–6016.

49. Nelson MJ. 1987. The nitric oxide complex of ferrous soybean lipoxygenase-1: substrate, pH, and ethanol effects on the active-site iron. *J Biol Chem* **262**(25):12137–12142.
50. Schenk G, Neidig ML, Zhou J, Holman TR, Solomon EI. 2003. Spectroscopic characterization of soybean lipoxygenase-1 mutants: the role of second coordination sphere residues in the regulation of enzyme activity. *Biochemistry* **42**(24):7294–7302.
51. Enemark JH, Feltham RD. 1974. Principles of structure, bonding, and reactivity for metal nitrosyl complexes. *Coord Chem Rev* **13**(9):339–406.
52. Serres RG, Grapperhaus CA, Bothe E, Bill E, Weyhermuller T, Neese F, Wieghardt K. 2004. Structural, spectroscopic, and computational study of an octahedral, non-heme [Fe–NO]^(6–8) Series: [Fe(NO)(cyclam-ac)]^{2+/+0}. *J Am Chem Soc* **126**(16):5138–5153.
53. Brown CA, Pavlosky MA, Westre TE, Zhang Y, Hedman B, Hodgson KO, Solomon EI. 1995. Spectroscopic and theoretical description of the electronic structure of *S* = 3/2 iron-nitrosyl complexes and their relation to O₂ activation by non-heme iron enzyme active sites. *J Am Chem Soc* **117**(2):715–732.
54. Hauser C, Glaser T, Bill E, Weyhermuller T, Wieghardt K. 2000. The electronic structures of an isostructural series of octahedral nitrosyliron complexes {Fe–NO}_{6,7,8} elucidated by Mössbauer spectroscopy. *J Am Chem Soc* **122**(18):4352–4365.
55. Clay MD, Coper CA, Jenney FE, Adams NWW, Johnson MK. 2003. Nitric oxide binding at the mononuclear active site of reduced *Pyrococcus furiosus* superoxide reductase. *Proc Natl Acad Sci USA* **100**(7):3796–3801.
56. Knapp MJ, Klinman JP. 2003. Kinetic studies of oxygen reactivity in soybean lipoxygenase-1. *Biochemistry* **42**(39):11466–11475.
57. Zhang ZH, Ren JS, Harlos K, McKinnon CH, Clifton IJ, Schofield CJ. 2002. Crystal structure of a clavamate synthase–Fe(II)–2-oxoglutarate–substrate–NO complex: evidence for metal centered rearrangements. *FEBS Lett* **517**(1–3):7–12.
58. Rocklin AM, Tierney DL, Kofman V, Brunhuber NMW, Hoffman BM, Christoffersen RE, Reich NO, Lipscomb JD, Que L. 1999. Role of the nonheme Fe(II) center in the biosynthesis of the plant hormone ethylene. *Proc Natl Acad Sci USA* **96**(14):7905–7909.
59. Tucker NP, D'Autreaux B, Studholme DJ, Spiro S, Dixon R. 2004. DNA binding activity of the *Escherichia coli* nitric oxide sensor NorR suggests a conserved target sequence in diverse proteobacteria. *J Bacteriol* **186**(19):6656–6660.
60. Nagashima S, Nakasako M, Dohmae N, Tsujimura M, Takio K, Odaka M, Yohda M, Damiya N, Endo I. 1998. Novel non-heme iron center of nitrile hydratase with a claw setting of oxygen atoms. *Nat Struct Biol* **5**(5):347–351.
61. Dey A, Chow M, Taniguchi K, Lugo-Mas P, Davin S, Maeda M, Kovacs JA, Odaka M, Hodgson KO, Hedman B, Solomon EI. 2006. Sulfur K-edge XAS and DFT calculations on nitrile hydratase: geometric and electronic structure of the non-heme iron active site. *J Am Chem Soc* **128**(2):533–541.
62. Orville AM, Lipscomb JD. 1997. Cyanide and nitric oxide binding to reduced protocatechuate 3,4-dioxygenase: insight into the basis for order-dependent ligand binding by intradiol catecholic dioxygenases. *Biochemistry* **36**(46):14044–14055.
63. Agarwalla S, Stroud RM, Gaffney BJ. 2004. Redox reactions of the iron-sulfur cluster in a ribosomal RNA methyltransferase, RumA: optical and EPR studies. *J Biol Chem* **279**(33):34123–34129.
64. Pohl E, Haller JC, Mijovilovich A, Meyer-Kaucke W, Garman E, Vasil ML. 2003. Architecture of a protein central to iron homeostasis: crystal structure and spectroscopic analysis of the ferric uptake regulator. *Mol Microbiol* **47**(4):903–915.

65. Mills SA, Marletta MA. 2005. Metal binding characteristics and role of iron oxidation in the ferric uptake regulator from *Escherichia coli*. *Biochemistry* **44**(41):13553–13559.
66. Lee CM, Hsieh CH, Dutta A, Lee GH, Liaw WF. 2003. Oxygen binding to sulfur in nitrosylated iron–thiolate complexes: relevance to the Fe-containing nitrile hydratases. *J Am Chem Soc* **125**(38):11492–11493.
67. Erlandsen H, Fusetti F, Martinez A, Hough E, Flatmark T, Stevens, RC. 1997. Crystal structure of the catalytic domain of human phenylalanine hydroxylase reveals the structural basis for phenylketonuria. *Nat Struct Biol* **4**(12):995–1000.
68. Minor W, Steczko J, Stec B, Otwinowski Z, Bolin JT, Walter R, Axelrod B. 1996. Crystal structure of soybean lipoxygenase L-1 at 1.4 Å resolution. *Biochemistry* **35**(33):10687–10701.
69. Shiota Y, Yoshizawa K. 2004. QM/MM study of the mononuclear non-heme iron active site of phenylalanine hydroxylase. *J Phys Chem B* **108**(44):17226–17237.
70. Lehnert N, Solomon EI. 2003. Density-functional investigation on the mechanism of H-atom abstraction by lipoxygenase. *J Biol Inorg Chem* **8**(3):294–305.

BINUCLEAR NON-HEME IRON ENZYMES

Nataša Mitić,¹ Gerhard Schenk,¹ Graeme R. Hanson²

¹*School of Chemistry and Molecular Biosciences, and* ²*Centre for Magnetic Resonance, The University of Queensland, Brisbane, Australia*

Binuclear non-heme iron enzymes are a large group of enzymes that catalyze a variety of chemical reactions and are involved in numerous metabolic functions. In this review, the structural and biochemical properties of representatives of every class of this group of enzymes are described. The contributions of electron paramagnetic resonance-related techniques to our understanding of structure and reactivity of binuclear non-heme iron enzymes are discussed, and, where appropriate, supported by data obtained from complementary spectroscopic methods. This chapter is intended as a guide to illustrate the usefulness of electron paramagnetic resonance-related techniques in the study of these enzymes. Consequently, technical details were kept to a minimum.

1. INTRODUCTION

Binuclear non-heme iron enzymes are versatile with respect to the reactions they catalyze and their proposed biological functions. Reactions catalyzed include oxidations, hydroxylations, epoxidations, desaturations, reversible oxygen binding, N-oxide formation, ferroxidation, dehalogenation, NO reduction, NADH peroxidation, reduction of oxyribonucleotides to deoxyribonucleotides, oxygenations, and hydrolyses. The spectrum of physiological functions binuclear non-heme iron enzymes are involved in range from iron storage, transport and metabolism, DNA biosynthesis and repair, to bone metabolism and bioremediation. Many binuclear non-heme iron enzymes are characterized by their extraordinary catalytic efficiencies. For example, methane monooxygenase (see below) catalyzes the oxidation of methane to methanol, a reaction that is energetically very costly [1–3]. In Table 1 representatives of the group of binuclear non-heme iron enzymes are listed, together with their metal ion composition, the reaction they catalyze, and their proposed biological functions.

Address all correspondence to Nataša Mitić, phone: +61 7 3365 4040; fax: +61 7 3365 4273; email: n.mitic@uq.edu.au.

Table 1. Representative Binuclear Non-Heme Iron Enzymes (the chemical reactions catalyzed by these enzymes and their metabolic functions are also listed)

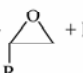
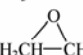
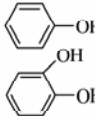
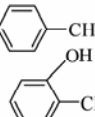
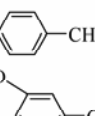
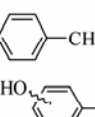
Enzyme	Reaction type	Catalytic reaction	Metabolic role(s)
Methane Monooxygenase (MMO)	Hydroxylation	$\text{Fe}^{2+} - \text{Fe}^{2+} + \text{CH}_4 + \text{O}_2 \longrightarrow \text{Fe}^{3+} - \text{Fe}^{3+} + \text{CH}_3\text{OH}/\text{H}_2\text{O}$	Carbon fixation, methane metabolism
Alkane ω -hydroxylase (AlkB)	Hydroxylation	$\text{Fe}^{2+} - \text{Fe}^{2+} + \text{C}_{18}\text{H}_{18} + \text{O}_2 \longrightarrow \text{Fe}^{3+} - \text{Fe}^{3+} + \text{C}_8\text{H}_{18}\text{O}/\text{H}_2\text{O}$	Alkane hydroxylation
Alkene monooxygenase (AMO)	Epoxidation	$\text{Fe}^{2+} - \text{Fe}^{2+} + \text{RCH}=\text{CH}_2 + \text{O}_2 \longrightarrow \text{Fe}^{3+} - \text{Fe}^{3+} + \text{epoxide} + \text{H}_2\text{O}$ 	Alkene metabolism
Xanobacter alkene monooxygenase (XAMO)	Epoxidation	$\text{Fe}^{2+} - \text{Fe}^{2+} + \text{CH}_3\text{CH}=\text{CH}_2 + \text{O}_2 \longrightarrow \text{Fe}^{3+} - \text{Fe}^{3+} + \text{epoxide} + \text{H}_2\text{O}$ 	Propene metabolism
Phenol hydroxylase (PH)	Oxidation	$\text{Fe}^{2+} - \text{Fe}^{2+} + \text{C}_6\text{H}_5\text{OH} + \text{O}_2 \longrightarrow \text{Fe}^{3+} - \text{Fe}^{3+} + \text{C}_6\text{H}_4(\text{OH})_2 + \text{H}_2\text{O}$ 	Phenol degradation
Toluene-2-monooxygenase (T2MO)	Oxidation	$\text{Fe}^{2+} - \text{Fe}^{2+} + \text{C}_6\text{H}_4(\text{CH}_3) + \text{O}_2 \longrightarrow \text{Fe}^{3+} - \text{Fe}^{3+} + \text{C}_6\text{H}_3(\text{CH}_3)(\text{OH}) + \text{H}_2\text{O}$ 	Toluene oxidation
Toluene-4-monooxygenase (T4MO)	Oxidation	$\text{Fe}^{2+} - \text{Fe}^{2+} + \text{C}_6\text{H}_4(\text{CH}_3) + \text{O}_2 \longrightarrow \text{Fe}^{3+} - \text{Fe}^{3+} + \text{C}_6\text{H}_3(\text{CH}_3)(\text{OH}) + \text{H}_2\text{O}$ 	Toluene oxidation
Toluene/ <i>o</i> -Xylene monooxygenase (ToMO)	Hydroxylation	$\text{Fe}^{2+} - \text{Fe}^{2+} + \text{C}_6\text{H}_4(\text{CH}_3) + \text{O}_2 \longrightarrow \text{Fe}^{3+} - \text{Fe}^{3+} + \text{C}_6\text{H}_3(\text{CH}_3)(\text{OH}) + \text{H}_2\text{O}$ 	Toluene, <i>o</i> -xylene hydroxylation

Table 1, cont'd

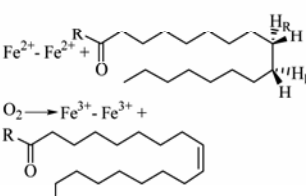
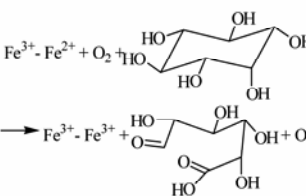
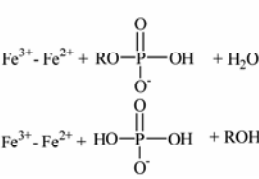
Enzyme	Reaction type	Catalytic reaction	Metabolic role(s)
Ribonucleotide reductase R2 subunit (RNR)	One-electron oxidation	$Fe^{2+} - Fe^{2+} + Tyr + O_2 \longrightarrow Fe^{3+} - Fe^{3+} + Tyr^{\bullet}$	Biosynthesis of DNA precursors
Stearoyl-ACP Δ^9 desaturase (Δ^9D)	Desaturation	$Fe^{2+} - Fe^{2+} + O_2 \longrightarrow Fe^{3+} - Fe^{3+} +$ 	Fatty acid + desaturation
<i>Myo</i> -inositol oxygenase (MIOX)	Four-electron oxidation	$Fe^{3+} - Fe^{2+} + O_2 +$  $\longrightarrow Fe^{3+} - Fe^{3+} + O_2$	<i>Myo</i> -inositol catabolism (regulation of inositol levels)
Rubrerythrin	NADH peroxidation	$Fe^{2+} - Fe^{2+} + H_2O_2 + 2H^+ \longrightarrow Fe^{3+} - Fe^{3+} / 2H_2O$	Peroxidase activity, protection against oxidative stress
Nigerythrin	NADH peroxidation	$Fe^{2+} - Fe^{2+} + H_2O_2 + 2H^+ \longrightarrow Fe^{3+} - Fe^{3+} / 2H_2O$	Peroxidase activity
Sulerythrin	NADH peroxidation	$Fe^{2+} - Fe^{2+} + H_2O_2 + 2H^+ \longrightarrow Fe^{3+} - Fe^{3+} / 2H_2O$	Peroxidase activity
Ferritins and bacterioferritins	Ferroxidation	$Fe^{2+} - Fe^{2+} + O_2 + 2H^+ \longrightarrow Fe^{3+} - Fe^{3+} + H_2O_2$	Iron storage, iron homeostasis and metabolism
Hemerythrin (Hr)	Reversible dioxygen binding	$Fe^{2+} - Fe^{2+} + O_2 \longrightarrow Fe^{3+} - Fe^{3+} - OOH$	Oxygen transport
Purple acid phosphatases	Hydrolysis	$Fe^{3+} - Fe^{2+} + RO - P(=O)(OH)_2 + H_2O \longrightarrow Fe^{3+} - Fe^{2+} + HO - P(=O)(OH)_2 + ROH$ 	Bone metabolism, iron transport

Table 1, cont'd

Enzyme	Reaction type	Catalytic reaction	Metabolic role(s)
Metallo- β -lactamases	Hydrolysis	$\text{Fe}^{2+} - \text{Fe}^{2+} + \text{R}_1\text{OCHN} \begin{array}{c} \diagup \\ \diagdown \\ \text{O} \\ \text{N} \end{array} \longrightarrow$ $\text{Fe}^{2+} - \text{Fe}^{2+} + \text{R}_1\text{OCHN} \begin{array}{c} \diagup \\ \diagdown \\ \text{O} \\ \text{HN} \end{array}$	Antibiotic resistance
Rubredoxin: O ₂ oxidoreductase (ROO)	Oxidase	$\text{Fe}^{2+} - \text{Fe}^{2+} + \text{O}_2 + 4\text{H}^+ \xrightarrow{+ 2 e^-} \text{Fe}^{3+} - \text{Fe}^{3+} + 2\text{H}_2\text{O}$	Protection against oxidative and nitrosative stress
Nitric oxide reductase (NOR)	NO reduction	$\text{Fe}^{2+} - \text{Fe}^{2+} + 2\text{NO} \longrightarrow \text{Fe}^{3+} - \text{Fe}^{3+} + \text{N}_2\text{O}/\text{H}_2\text{O}$	Protection against nitrosative stress
Alternative Oxidase (AOX)	Oxidase	$\text{Fe}^{2+} - \text{Fe}^{2+} + \text{O}_2 + 4\text{H}^+ \xrightarrow{+ 2 e^-} \text{Fe}^{3+} - \text{Fe}^{3+} + 2\text{H}_2\text{O}$	Quinol oxidation, chloro-respiration
Plastid terminal oxidase (PTOX)	Oxidase	$\text{Fe}^{2+} - \text{Fe}^{2+} + \text{O}_2 + 4\text{H}^+ \xrightarrow{+ 2 e^-} \text{Fe}^{3+} - \text{Fe}^{3+} + 2\text{H}_2\text{O}$	Quinol oxidation, carotenoid and chlorophyll biosynthesis
DMQ hydroxylase	Hydroxylation	$\text{Fe}^{2+} - \text{Fe}^{2+} + 5\text{-demethoxyquinol} + \text{O}_2 \longrightarrow \text{Fe}^{3+} - \text{Fe}^{3+} + 5\text{-hydroxy-UQ}/\text{H}_2\text{O}$	Chloro-respiration, ubiquinone biosynthesis
Mg-protoporphyrin IX MME hydroxylase	Hydroxylation	$\text{Fe}^{2+} - \text{Fe}^{2+} + \text{MME} + \text{O}_2 \longrightarrow \text{Fe}^{3+} - \text{Fe}^{3+} + \text{divinyl protochlorophyllide}$	Carotenoid and chlorophyll biosynthesis
Arylamine oxygenases	N-oxygenation	$\text{Fe}^{2+} - \text{Fe}^{2+} + \text{H}_2\text{N} \begin{array}{c} \text{COOH} \\ \\ \text{C}_6\text{H}_4 \end{array} + \text{O}_2 \longrightarrow \text{Fe}^{3+} - \text{Fe}^{3+} + \text{O}_2\text{N} \begin{array}{c} \text{COOH} \\ \\ \text{C}_6\text{H}_4 \end{array}$	Biosynthesis of nitro compounds, aurcothin biosynthesis

Previously, binuclear non-heme iron enzymes have been grouped into four distinct classes [4]. Class I contains oxygenases, including ribonucleotide reductase R2, p53 ribonucleotide reductase, methane monooxygenase, stearyl-acyl carrier protein Δ^9 desaturase, toluene 4-monooxygenase, phenol hydroxylase, alkene hydroxylase, xylene monooxygenase, and alkane ω -hydroxylase. The iron transport and storage proteins ferritin, bacterioferritin, and rubrerythrin are grouped in class II, while class III contains the oxygen storage and transport proteins hemerythrin and myohemerythrin. Class IV comprises hydrolytic enzymes such as purple acid phosphatases and some β -lactamases. In more recent years, additional members of the family of binuclear non-heme iron enzymes have emerged, including membrane-bound diiron proteins such as the alternative oxidase [5], plastid terminal oxidase [6], 5-demethoxyquinone hydroxylase [7], and aerobic Mg-protoporphyrin IX monomethylester hydroxylase [8], and reductases such as O_2 oxidoreductase and NO reductase. Most members of these different classes are commonly referred to as non-heme diiron carboxylate-bridged proteins that contain similar coupled diiron clusters with predominantly O/N ligation in the immediate coordination environment [9]. These six amino acid residues are highly conserved, and they represent the iron binding motif in these proteins. Apart from these active site residues, the overall sequence homology amongst the members of the binuclear non-heme iron enzymes is low.

High-resolution x-ray crystal structures, often in various oxidation states, are available for several binuclear non-heme iron enzymes, and are mentioned where appropriate in the sections below. Despite the variety of reactions catalyzed (Table 1), many of these enzymes display structural similarities, and it is thus often not possible to investigate factors that contribute to differences in reactivities from crystallographic data alone. The catalytic mechanism of a small number of binuclear non-heme iron enzymes has been studied in great detail using a large variety of methods, including site-directed mutagenesis, enzyme kinetics, crystallography, and a variety of spectroscopic techniques, such as magnetic circular dichroism, Mössbauer, nuclear magnetic resonance, electron paramagnetic resonance (EPR), x-ray absorption, and resonance Raman spectroscopies. In order to obtain a detailed description of the molecular mechanism employed by binuclear non-heme iron enzymes, it is essential to characterize the geometric and electronic structures of their iron active sites. Since these enzymes may exist in various oxidation states, with different paramagnetic properties, EPR-related techniques have been particularly useful in obtaining insight into factors that govern their reactivities. Importantly, such methods have been successful in the characterization of labile reaction intermediates, providing information about structural and electronic changes that take place during a reaction cycle. Here, we summarize advances in the study of multinuclear non-heme iron-catalyzed reactions, focusing predominantly on the contributions from EPR-related techniques. Although it is our aim to cover binuclear non-heme iron enzymes comprehensively, the breadth of the topic has required a selective approach. "Classical" systems such as methane monooxygenases and ribonucleotide reductases have been discussed at length, while other systems

have been treated more cursorily. We thus would like to apologize to researchers whose contributions may not have been included here. The following sections are subdivided into three segments describing (i) biochemical and structural, (ii) some relevant spectroscopic, and (iii) mechanistic aspects of the various enzyme systems. Notably, the descriptions of proposed reaction mechanisms are kept brief, focusing mainly on those aspects where EPR-related techniques provided important insights.

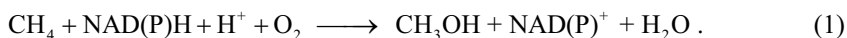
2. BACTERIAL MULTICOMPONENT MONOOXYGENASES

Bacterial multicomponent oxygenases containing binuclear non-heme iron active centers are soluble proteins that carry out a large array of oxidation reactions and activate dioxygen using a variety of hydrocarbons as substrates (alkanes, alkenes, and aromatic compounds) [10,11]. They generally reside in the aerobic/anaerobic interface and utilize their respective hydrocarbon substrates as the only source of carbon and energy [12]. They have also become major targets for various bioremediation/biodegradation and industrial catalytic and environmental applications [13]. Multicomponent oxygenases exhibit a high degree of structural homology and are divided into four major subgroups based on their structural and biochemical properties: (i) soluble methane monooxygenases, (ii) alkene/arene monooxygenases, (iii) phenol hydroxylases, and (iv) $\alpha\beta$ alkene monooxygenases. Furthermore, they all contain either three or four components (subunits) that are required for activity [12]. The carboxylate-bridged binuclear iron active site is located within the hydroxylase component [14–18] and is highly homologous to that in ribonucleotide reductases and Δ^9 desaturases (§§3 and 4) [19,20].

2.1. Methane Monooxygenase

2.1.1. Biochemical and Structural Characterization

Methane monooxygenase (MMO) is the most extensively studied bacterial binuclear oxygenase. It catalyzes the selective oxidation of methane to methanol, which is the first step in the metabolic pathway of methanotrophic bacteria [21,22], and which is energetically one of the most demanding reactions in nature (bond dissociation energy for methane is ~ 104 kcal/mole). Since methane monooxygenase is the only enzyme capable of activating inert C–H bonds under ambient temperatures and pressures [2], it has become a paradigm for the design of synthetic catalysts. The conversion of methane to methanol occurs according to the following equation:



In this monooxygenation reaction, two reducing equivalents from NAD(P)H are used to cleave the O–O bond of O₂, where one oxygen atom is reduced to H₂O and the other is used to oxidize methane to methanol. Apart from methane, MMO utilizes a broad range of substrates, including linear, branched, cyclic, satu-

rated, unsaturated, aromatic, heterocyclic, and halogenated reagents [22–24], and depending on the identity of the substrate the enzyme catalyzes hydroxylations, epoxidations, dehalogenations and the formation of N-oxides [25–27]. Recently, it has also been demonstrated that methane monooxygenase is able to catalyze desaturation reactions [28].

There are two distinct forms of methane monooxygenase, a membrane-bound particulate and a soluble type. Methanotrophic bacteria express one or both of these forms, and while both are capable of hydroxylating methane to methanol, only the soluble type contains a binuclear non-heme iron center [15]. Particulate methane monooxygenase contains copper and zinc ions in its active site [29,30] and will not be discussed further here. The soluble form has been isolated, purified, and characterized from two sources, *Methylococcus capsulatus* (Bath) [2,31] and *Methylosinus trichosporium* OB3b [3]. The enzyme consists of three components: a 245-kDa hydroxylase component (MMOH) that contains the binuclear iron center, a 39-kDa reductase component (MMOR), and a 16-kDa component B (MMOB), which is known to have a regulatory function [2]. MMOH is a dimer of trimers, and has an $\alpha_2\beta_2\gamma_2$ quaternary structure (α , 60.6 kDa; β , 45 kDa; γ , 19.8 kDa) [14,32,33]. The binuclear iron active site is located within the α subunit, where both O_2 activation and methane oxidation take place. The diiron cluster of MMOH can exist in three oxidation states: fully oxidized diferric ($Fe^{3+}-Fe^{3+}$), mixed-valent ($Fe^{3+}-Fe^{2+}$), and fully reduced diferrous ($Fe^{2+}-Fe^{2+}$). MMOR contains two cofactors: flavin adenine dinucleotide and a $[2Fe-2S]^{2+}$ iron-sulfur cluster, and it is responsible for shuttling electrons from NAD(P)H to MMOH [14,32,34–39]. The third component, MMOB, is a small effector protein proposed to regulate MMO catalysis, and has no associated cofactors [40,41], and which is known to (i) increase MMO reactivity with O_2 by 1000-fold [42], (ii) alter the redox potential of MMOH [43–46], and (iii) affect the regioselectivity of substrate oxidation [47]. MMOB also couples electron and O_2 consumption with methane oxidation, and it may influence the accessibility of the substrates into the active site [48–50]. While the precise structure of the MMO complex is not known, maximum turnover of substrate requires an MMOB:MMOH ratio of 2:1 [51].

Several crystal structures of MMOH from both *M. capsulatus* (Bath) (PDB codes 1MTY, 1MMO, 1FZ0-1FZ9, 1FYZ, 1FZI, 1FZH, 1XMF, 1XMG, 1XMH) and *M. trichosporium* (OB3b) (PDB codes 1MHY, 1MHZ) have been reported [15,52–59]. In addition, NMR structures of the FAD (PDB code 1TVC) and the $[2Fe-2S]$ ferredoxin (PDB code 1JQ4) domains of MMOR have also been reported [35,37]. The overall structure of MMOH is a heart-shaped dimer of trimers, and is predominantly α -helical (Fig. 1). The binuclear iron center is located within a four- α -helix bundle of the α subunit, a structural motif common to many binuclear iron proteins [19,60,61]. In the oxidized, diferric form both irons in the active site have distorted octahedral geometry, with Fe1 and Fe2 being coordinated by His147, monodentate Glu114, and a terminal water ligand, and by His246, Glu209, and Glu243, respectively (unless stated otherwise, numbering of residues is according



Figure 1. Overall structure of MMOH from *Methylococcus capsulatus* (Bath) (PDB code 1FZ2).

to the sequence of MMOH extracted from *M. trichosporium* OB3b; Fig. 2A). The two metal ions are linked by a μ -1,3 carboxylate group from Glu144, a hydroxide, and a third ligand, which may be a second hydroxide ion, an acetate group, or formate, depending on the crystallization conditions [15,56–58]. In the structure of *M. capsulatus* (Bath) MMOH in the reduced, biferrous state, each metal ion has five ligands, with Fe1 and Fe2 coordinated by Glu114, His147, and a terminal water molecule, and by Glu243, Glu209, and His246, respectively [57]. In addition to the μ -1,3 carboxylate bridge from Glu144, the two metal ions are also linked via a μ -1,1 carboxylate from Glu243 (Fig. 2C); no other bridging ligands are observed. Although both iron centers are coordinatively unsaturated, reduced MMOH is not reactive with O₂. The crystal structure of the mixed-valent form of MMOH from *M. capsulatus* (Bath) has also been reported [56]. The ferric ion is six-coordinate, while the ferrous one is four-coordinate, and the two metal ions are bridged via a single hydroxide group (Fig. 2B). MMOH has also been crystallized in the presence of various product/substrate analogs such as phenol, bromoethanol, 6-bromo-hexanol, 3-bromo-3-butenol, or chloropropanol [52], iodoethane, and dibromomethane [54] in order to mimic possible interactions between enzyme and

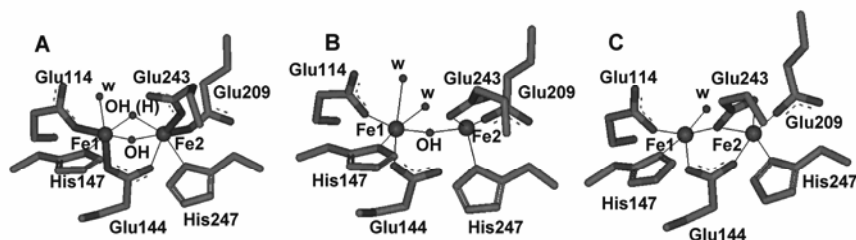


Figure 2. Active site structures of MMOH (A) oxidized from *Methylosinus trichosporium* OB3b (PDB code 1MHY), (B) mixed-valent from *Methylococcus capsulatus* (Bath) (PDB code 1FZ2), and (C) reduced from *Methylococcus capsulatus* (Bath). A. Rosenzweig, personal correspondence.

substrate, and residue Leu110 in a hydrophobic region of the enzyme has been ascribed a role as a “gate,” i.e., it controls access of substrate and solvent molecules into the active site [2]. The crystal structures were also obtained for the apo enzyme, Mn(II)- and Co(II)-reconstituted MMOH [53], and with bound xenon [54]. However, isolated reduced MMOH reacts remarkably slowly with dioxygen; full enzymatic activity is only achieved in the presence of MMOB. While the crystal structure of the MMOH–MMOB complex is not yet available, NMR solution structures of MMOB from both *M. capsulatus* (Bath) (PDB code 1CKV) and *M. trichosporium* (OB3b) (PDB code 2MOB) have indicated likely sites of interaction between the two MMO components [62,63]. Interestingly, while MMOH–MMOB interactions in the complex from *M. trichosporium* (OB3b) are predominantly electrostatic in nature [63], hydrophobic interactions are crucial in the complex from *M. capsulatus* (Bath) [62].

2.1.2. Spectroscopic Characterization of MMOH

Origin of EPR spectra from dinuclear iron centers. EPR spectra of dinuclear iron species can be described by a total spin Hamiltonian involving the sum of the individual spin Hamiltonians and the interaction Hamiltonian [64–66]:

$$H_{\text{tot}} = \sum_{i=1}^2 H_{A_i} + \sum_{i,j=1,i \neq j}^2 H_{A_j}, \quad (2)$$

$$H_{A_i} = S_i \cdot D_i \cdot S_i + \beta \mathbf{B} \cdot \mathbf{g}_i \cdot S_i + S_i \cdot \mathbf{A}_i \cdot I_i + I_i \cdot \mathbf{Q}_i \cdot I_i - \gamma(1 - \sigma_i) \mathbf{B} \cdot I_i$$

$$H_{A_j} = -2J_{A_j} \cdot S_{A_i} \cdot S_{A_j} + G_{A_j} S_{A_i} \times S_{A_j} + S_{A_i} \cdot D_{A_j} \cdot S_{A_j},$$

where S and I are the electron and nuclear spin operators, respectively, D the zero-field splitting tensor, \mathbf{g} and \mathbf{A} are the electron Zeeman and hyperfine coupling matrices, respectively, \mathbf{Q} the quadrupole tensor, γ the nuclear gyromagnetic ratio, σ the chemical shift tensor, β the Bohr magneton, and \mathbf{B} the applied magnetic field. Additional hyperfine, quadrupole, and nuclear Zeeman interactions will be required

when superhyperfine splitting is resolved in the experimental EPR spectrum. Due to the fast relaxation times (T_1 and T_2) the large linewidth of the EPR resonances in the continuous-wave EPR spectra generally prohibits the observation of these interactions. Consequently, high-resolution techniques such as electron spin echo envelope modulation (ESEEM), hyperfine sublevel correlation (HYSCORE), and pulsed electron nuclear double resonance (ENDOR) spectroscopy are exploited as a function of orientation to determine the distance and orientation of nuclei coordinated to the dinuclear center [67].

The interaction Hamiltonian (H_A ; Eq. (2)) accounts for the isotropic exchange ($\mathcal{H}_{\text{ex}} = -2JS_1 \cdot S_2$), antisymmetric exchange ($\mathcal{H} = S_1 \cdot G \cdot S_2$), and the anisotropic spin-spin (dipole-dipole coupling, $\mathcal{H} = S_1 \cdot J \cdot S_2$) interactions between the two paramagnetic centers [64–66]. There are two types of isotropic exchange, namely, anti-ferromagnetic ($J < 0$) and ferromagnetic ($J > 0$) coupling. The former involves the overlap of molecular orbitals on each iron ion through a bridging ligand, giving rise to a spin paired ground spin state (*vide infra*), whilst in a ferromagnetically coupled center the molecular orbital on each iron atom is diametrically opposed preventing overlap. The anisotropic exchange interaction (dipole-dipole coupling) is a through-space interaction, and the anisotropic exchange matrix J can be used to determine the internuclear distance and orientation of the two paramagnetic ions, but is often much weaker than the isotropic term. The antisymmetric term is generally important for trinuclear centers but may be relevant in mixed metal ion dinuclear centers such as purple acid phosphatases (§9.1).

For high-spin iron centers (Fe^{3+} , $S = 5/2$; Fe^{2+} , $S = 2$) there are three different exchange regimes (strong, intermediate, and weak) that are dependent on the relative magnitude of the exchange coupling (J_{iso}) and the zero-field splitting (D_i , $i = 1, 2$), i.e., $|J_{\text{iso}}| \gg |D_i|$, $|J_{\text{iso}}| \sim |D_i|$, $|J_{\text{iso}}| \ll |D_i|$, respectively (Fig. 3). Whilst the EPR spectra from dinuclear centers that belong to the strong and weak exchange regimes can be relatively easily interpreted, this is not the case for the intermediate exchange regime where full matrix diagonalization is required to assess the spectral data (Fig. 3B). Fortunately, for the majority of dinuclear iron containing metallo-proteins, $|J| \gg |D|$, and the spectra are relatively straightforward to understand. A brief description of the theory behind the EPR spectra of dinuclear iron centers that lie in the strong and weak exchange regimes is presented below.

Strong exchange regime: In the strong exchange limit the spin system is best characterized by a total spin operator $S_{\text{tot}} = S_1 + S_2$, and for two antiferromagnetically coupled high-spin ($S = 5/2$) ferric ions there are a total of six spin multiplets, characterized by $S_{\text{tot}} = 0, 1, 2, 3, 4$, and 5, where $S_{\text{tot}} = 0$ is the ground spin state and each of the spin multiplets is $(2S_{\text{tot}} + 1)$ -fold degenerate. The energies of these levels (Fig. 3A) are given by

$$E(S_{\text{tot}}) = -J \left[S_{\text{tot}} (S_{\text{tot}} + 1) - S_1 (S_1 + 1) - S_2 (S_2 + 1) \right], \quad (3)$$

and the energy level difference between adjacent levels is

$$E(S_{\text{tot}}) - E(S_{\text{tot}} - 1) = -2S_{\text{tot}}J. \quad (4)$$

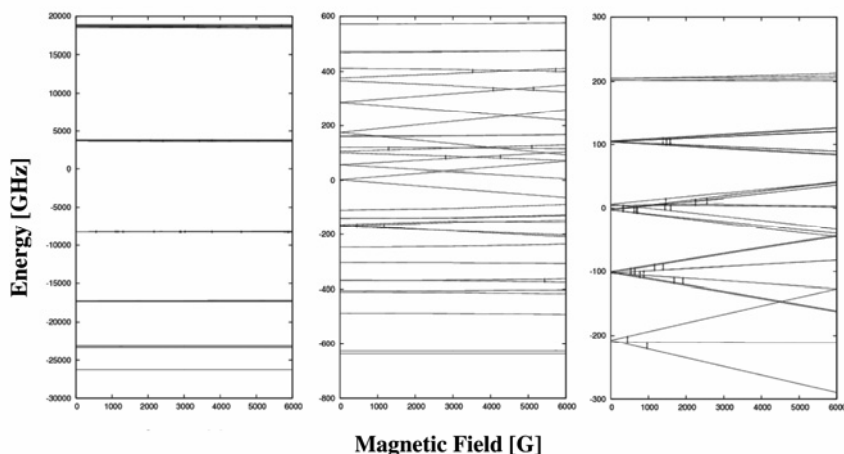


Figure 3. Energy level diagrams (calculated using Molecular Sophe, Chap. 4) for the three exchange regimes for an antiferromagnetically coupled dinuclear Fe^{3+} center $g_i = 2$, $D_i = -1 \text{ cm}^{-1}$, $E/D_i = 0.3$ ($i = 1, 2$). (A) Strong exchange regime, $-2J = 100 \text{ cm}^{-1}$, (B) intermediate exchange regime, $-2J = 2 \text{ cm}^{-1}$, and (C) weak exchange regime, $-2J = 0.01 \text{ cm}^{-1}$.

Consequently, for an antiferromagnetically coupled dinuclear Fe^{3+} center with a large negative value of J , the ground spin state ($S_{\text{tot}} = 0$) is populated and the system is EPR silent. This is the case when there is a μ -oxo bridging ligand between the Fe^{3+} centers, and even at room temperature there may only be a partial population of higher spin states. However, protonation of the μ -oxo bridging ligand reduces the J value to around $10\text{--}20 \text{ cm}^{-1}$, which permits thermal population of the higher spin states producing complex EPR spectra. It is often desirable to perform a variable-temperature study at multiple frequencies to allow the assignment of resonances to a particular spin multiplet (S_{tot}) as its relative population ($I(S_{\text{tot}})$) is given by [65, 68]

$$I(S_{\text{tot}}) = \frac{C e^{\frac{JS_{\text{tot}}(S_{\text{tot}}+1)}{kT}}}{\sum_{S_{\text{tot}}=0}^5 (2S_{\text{tot}}+1) e^{\frac{JS_{\text{tot}}(S_{\text{tot}}+1)}{kT}}} \quad (5)$$

Thus, a variable temperature continuous-wave EPR (cwEPR) study can be employed to not only determine the magnitude of the exchange coupling constant and its sign, but also the spin state of each iron atom as the plots of $I(S_{\text{tot}})$ versus temperature are sensitive to the spin states, for example, Figure 4.

For mixed-valent, partially reduced antiferromagnetically coupled dinuclear ($\text{Fe}^{3+}\text{--}\text{Fe}^{2+}$) centers, the spin states in order of increasing energy are $S_{\text{tot}} = 1/2, 3/2,$

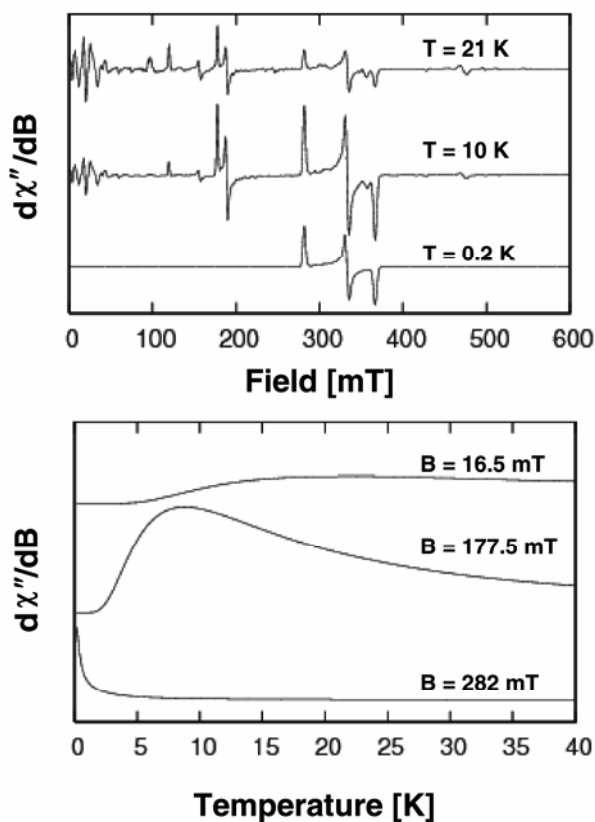


Figure 4. Variable temperature EPR spectra (calculated using Molecular Sophe, Chap. 4) of a hydroxy-bridged mixed-valent dinuclear $\text{Fe}^{3+}\text{-Fe}^{2+}$ center. Spin-Hamiltonian parameters, Fe^{3+} : $g = 2$, $D = -1\text{ cm}^{-1}$, $E/D = 0.3$; Fe^{2+} : $g_x = 1.96$, $g_y = 1.85$, $g_z = 1.75$, $D = 1\text{ cm}^{-1}$, $E/D = 0.3$; $-2J = -6\text{ cm}^{-1}$. (A) Continuous wave spectra and (B) temperature dependence of particular resonant field positions.

$5/2$, $7/2$, and $9/2$, and if $|J|$ is large the EPR spectrum is typical of an $S_{\text{tot}} = 1/2$ ground state (Fig. 4, $T = 0.2\text{ K}$); however, if J is small or the temperature is increased allowing thermal population of the $S_{\text{tot}} = 3/2$ spin multiplet, then the EPR spectrum may be more complex (Fig. 4, $T = 10$ and 21 K), but allows an unambiguous determination of J and the zero-field splitting parameters.

Often fully reduced samples of dinuclear iron containing proteins contain a ferromagnetically coupled dinuclear Fe^{2+} center that has as its ground state $S_{\text{tot}} = 4$ (*vide infra*). In many cases formally forbidden $\Delta M_s = \pm 4$ transitions between the $M_s = \pm 2$ spin states produce resonances in the EPR spectrum with $g_{\text{eff}} \sim 16$ (Fig. 5).

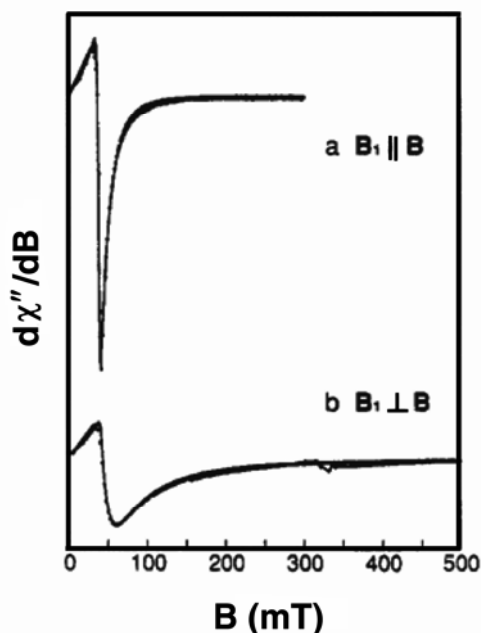


Figure 5. Low-temperature (4 K) EPR spectra of the fully reduced MMOH from *Methylosinus trichosporium* OB3b using (a) microwave field parallel and (b) microwave field perpendicular to the static magnetic field **B**. Reprinted with permission from [76]. Copyright © 1990, American Chemical Society.

The observation of these resonances relies on the rhombic zero-field splitting term (E) being less than the microwave quantum ($h\nu$). However, strain broadening can produce a distribution of energy levels resulting in a finite, albeit small population of energy levels where $E < h\nu$. The intensity of these resonances can be enhanced by performing parallel mode EPR spectroscopy where the microwave magnetic field is parallel rather than perpendicular to the externally applied magnetic field.

Weak exchange regime: When the magnitude of the axial zero-field splitting parameter is greater than the exchange coupling for a dinuclear high-spin Fe^{3+} center, the spectra can be interpreted in terms of the coupling of the Kramers doublets of each isolated Fe^{3+} ion (Fig. 3C). The weak exchange regime is often observed in ferromagnetically coupled binuclear ferrous centers, for example, the azide complex of deoxyhemerythrin [69]. Ideally, measuring the EPR spectra at high microwave frequencies will simplify the interpretation of the spectra as the zero-field splitting can be treated with perturbation theory for the electron Zeeman interaction.

Diferriic MMOH. Fully oxidized, diferriic MMOH is diamagnetic ($S_{\text{tot}} = 0$) at low temperatures, indicating the presence of two antiferromagnetically coupled high-spin Fe^{3+} ions ($S_{\text{Fe}1} = S_{\text{Fe}2} = 5/2$) [70]. Using parallel mode X-band continuous-

wave EPR (cwEPR) an integer-spin EPR signal is observed at $g_{\text{eff}} = 8.0$ [70]. This resonance is seen only at temperatures higher than 10 K, reaching an intensity peak at ~ 30 K, and is likely to arise from $\Delta M_S = \pm 4$ transitions within the excited $S_{\text{tot}} = 2$ state [70]. This excited state manifold is ~ 45 cm^{-1} above the diamagnetic ground state. The temperature dependence of this $g_{\text{eff}} = 8.0$ resonance allows the exchange coupling constant $J = -7.5$ cm^{-1} ($\mathcal{H}_{\text{ex}} = -2J S_1 \cdot S_2$) [70], suggesting (in agreement with extended x-ray absorption fine structure [71–74] and Mössbauer experiments [70,75]), the presence of a μ -hydroxo group as the bridging ligand in oxidized MMOH (Fig. 2A).

Diferrous MMOH. The catalytically competent diferrous form of MMOH exhibits a low-field EPR signal at $g_{\text{eff}} = 16$, which is indicative of an integer spin electronic system with two ferromagnetically coupled high-spin Fe^{2+} ($S = 2$) ions [76,77] (Fig. 5). The temperature dependence of this $g_{\text{eff}} = 16$ resonance has been analyzed using a full-spin Hamiltonian for the cases of both strong and weak ferromagnetic exchange coupling [76]. The non-Kramers ground state doublet of fully reduced MMOH is characterized by the quantum numbers $|S, M_S\rangle = |4, \pm 4\rangle$, while the first excited state sublevel is either the $|4, \pm 3\rangle$ state with $g_{\text{eff}} = 12$ (EPR active), or one of the diamagnetic $|4, 0\rangle$, $|3, 0\rangle$ states. The observed weak ferromagnetic coupling (~ 0.4 cm^{-1}) [78] between the two ferrous metal centers is likely to be mediated via the μ -1,1 bridging carboxylate in the active site (Fig. 2C) [79]. As will be discussed below, the integer-spin EPR signal at $g_{\text{eff}} = 16$ has been very useful in monitoring interactions between dioxygen and reduced MMOH [42]. ESEEM and ENDOR measurements of fully reduced MMOH from both *M. trichosporium* OB3b and *M. capsulatus* (Bath) have identified coupling to ^{14}N from either one or two His residues directly coordinated to the diferrous center of both enzymes (Fig 6) [77].

Mixed-valent MMOH. In the cwEPR spectrum of the chemically reduced mixed-valence $\text{Fe}^{3+}\text{--Fe}^{2+}$ form of MMOH resonances with g values of $g_z = 1.94$, $g_y = 1.86$, and $g_x = 1.75$ ($g_{\text{av}} = 1.85$) are observed [70,71,75,80], suggesting anti-ferromagnetic coupling between the Fe^{3+} ($S = 5/2$) and Fe^{2+} ($S = 2$) centers (ground state $S_{\text{tot}} = 1/2$) (Fig. 4). The small deviation of the g -values from $g = 2.0$ has been attributed to the octahedral ferrous site (which allows mixing of the low-lying orbital states with the ground state), as well as to the comparable magnitudes of the exchange-coupling parameter J and axial zero-field splitting parameter D [75]. From both EPR and Mössbauer studies the magnitude of J was estimated to be -30 cm^{-1} ($\mathcal{H}_{\text{ex}} = -2J S_1 \cdot S_2$) [70,71]. Both the cwEPR spectrum and the magnitude of the exchange coupling constant of mixed-valent MMOH closely resemble those of the mixed-valent forms of the oxygen transport protein hemerythrin (§8) and the hydrolytic enzyme purple acid phosphatase (§9) [81,82], indicating that the metal ions are bridged via a (hydr)oxo group, thus agreeing with the crystal structure of mixed-valent MMOH (*vide supra*). The nature of the bridging ligand was further investigated by Q-band ENDOR (Fig. 7) and pulsed EPR (ESEEM and Davies ENDOR) spectroscopy [83,84]. Three classes of resonances were observed, two of which are associated with exchangeable protons while the third (with hyperfine

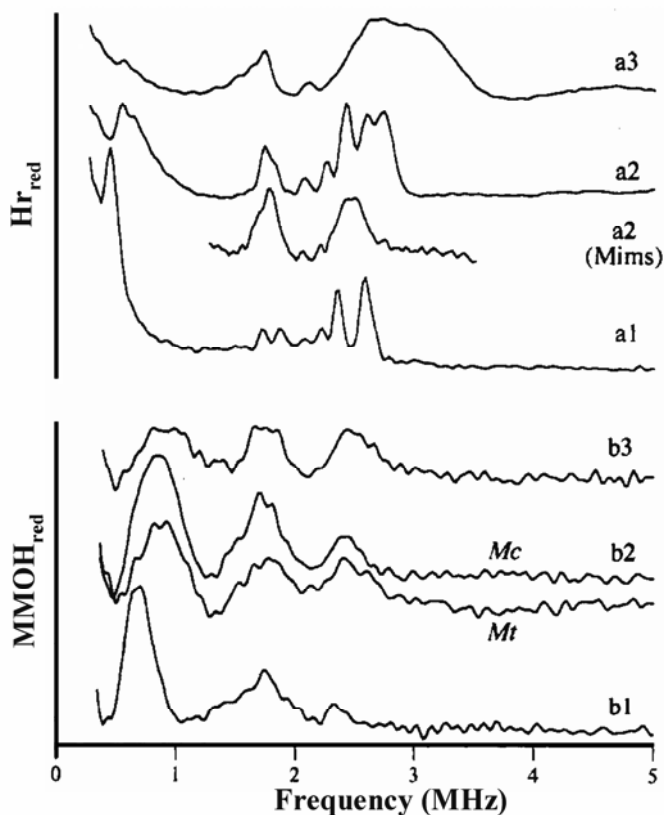


Figure 6. Low-temperature (2 K) three-pulse ESEEM frequency domain spectra of the fully reduced MMOH from *Methylosinus trichosporium* OB3b and *Methylococcus capsulatus* (Bath). Comparison with the corresponding ESEEM spectra of reduced hemerythrin-azide complex. Reprinted with permission from [77]. Copyright © 1994. American Chemical Society.

coupling constants $A \leq 4$ MHz) is ascribed to non-exchangeable protons. The latter are likely to belong to amino acid ligands [83]. The resonances associated with one of the exchangeable protons have a hyperfine coupling constant of ~ 8 MHz and are nearly isotropic, indicating that they may be due to a terminally Fe^{3+} -coordinated water/hydroxide ligand [83]. The second set of resonances associated with an exchangeable proton appears as a doublet at ~ 14 MHz at $g_1 = 1.94$. These resonances are characterized by large anisotropy with a maximum coupling constant of ~ 30 MHz at g_2 [83]. A comparison of the hyperfine tensor of these resonances with the corresponding parameters determined for semimet azido hemerythrin [84] identifies a metal center-bridging hydroxo group as the likely source for the exchangeable proton.

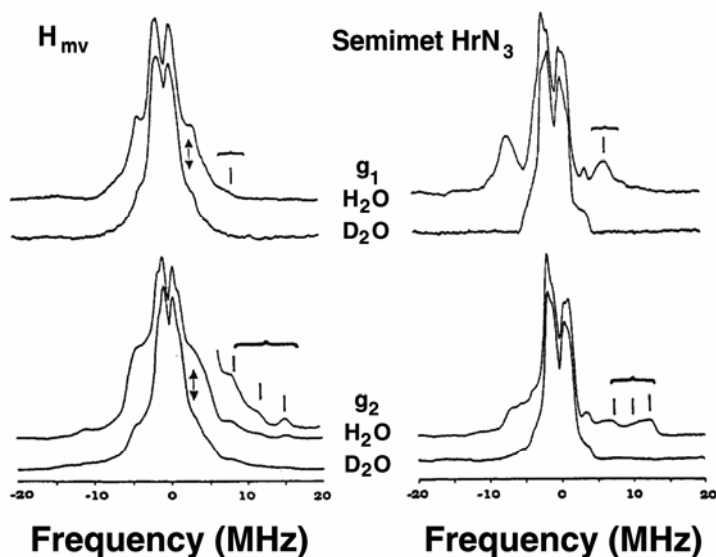


Figure 7. Low-temperature proton ENDOR spectra of mixed-valent MMOH from *Methylococcus capsulatus* (Bath) in H₂O and D₂O showing different proton resonances (see text for details). Reprinted with permission from [83]. Copyright © 1993, American Chemical Society.

¹H and ²H ENDOR spectroscopy was used to probe solvent accessibility of the active site in mixed-valent MMOH [83–85]. There are a total of nine magnetically unique coupled protons, and at least three of these are exchangeable in deuterated solvent. These protons exchange only slowly in ²H₂O (over 15–25 hours), which is consistent with the hypothesis that the iron active site of MMOH is buried and not readily accessible to the solvent [84,85]. This is in contrast to the binuclear iron clusters in hemerythrin (§8) or ribonucleotide reductase (§3), where solvent has direct access to the active sites of these proteins [86].

The ¹⁴N ENDOR spectroscopy of mixed-valent MMOH has identified two sets of nitrogen resonances (superhyperfine coupling constants of 13.6 and 2–5 MHz) that were assigned to the two N-containing ligands (histidines) directly coordinated to the Fe³⁺ and Fe²⁺ ions, respectively, in agreement with the crystal structure shown in Figure 2B [85].

An alternative method to generate the heterovalent Fe³⁺–Fe²⁺ form of MMOH involves the use of γ -irradiation at low temperatures (77 K; radiolytic reduction) [87,88]. Since the one-electron reduction is carried out at low temperature, structural changes to the MMOH active site are anticipated to be minimal, essentially leaving the conformation of the diferric MMOH cluster virtually intact [87]. Thus, radiolytic reduction provides an avenue to study by EPR (i) the geometric structure

of the diferric center in MMOH, and (ii) structural changes that may occur during catalysis by comparing spectroscopic parameters of the chemically and radiolytically reduced mixed-valent forms of MMOH. In the cwEPR spectrum of radiolytically reduced MMOH from *M. capsulatus* (Bath), two chemically distinct species (labeled H1 and H2) were detected [88]. Their g -matrices are distinctly different from that obtained from the chemically reduced form with different relaxation properties (effective g values: 1.94, 1.86, and 1.79 ($g_{\text{av}} = 1.85$) for H1, 1.82, 1.77, and 1.68 ($g_{\text{av}} = 1.74$) for H2, as compared to 1.94, 1.87, and 1.72 ($g_{\text{av}} = 1.82$) for MMOH_{mv} generated chemically). An analysis of the temperature dependence (between 6 and 15 K) of the EPR resonances associated with species H1 and H2 indicated a predominant contribution of the distribution of the former (~80%) [88]. A similar result was obtained upon cryogenic reduction of diferric MMOH from *M. trichosporium* OB3b, with the approximate contribution ratios of the two species from EPR spectra estimated to be 65% (species I with g values at 1.94, 1.86, and 1.79) and 35% (species II with g values at 1.85, 1.75, and 1.70) [87]. The presence of these two structural variants of the diferric form, i.e., (MMOH_{ox})_{mv}, is also supported both by extended x-ray absorption fine structure and x-ray crystallographic studies [15,57,58,74]. The two forms are believed to have two bridging (hydr)oxides (species H1) or one bridging (hydr)oxide and one bridging water ligand (species H2), respectively [88], in addition to the μ -1,3 carboxylate group from Glu144 (Fig. 2). Upon incubation of the radiolytically reduced sample at 230 K for 3 minutes or 293 K for 3–7 minutes (“annealing”), the resonances associated with species I and II, and H1 and H2, disappear and the resulting spectrum is characteristic for the chemically reduced heterovalent form of MMOH. This observation demonstrates that structural changes do occur during the catalytic turnover, more specifically upon reduction of the diferric cluster of MMOH to the Fe³⁺–Fe²⁺ mixed-valent form.

Substrate/product interactions with MMOH. In order to probe interactions between the substrates methane and O₂ and the product methanol with the active site of MMOH, advanced EPR techniques have been employed. In particular, the inhibitor DMSO has been used to mimic enzyme–substrate interactions in the active site of mixed-valent MMOH from *M. capsulatus* (Bath) [89]. ^{1,2}H ENDOR spectra of mixed-valent MMOH in the presence of DMSO still display the resonances characteristic of both the Fe²⁺-bound terminal water or hydroxide ligand and the μ -hydroxide (*vide supra*), indicating that the addition of the substrate analog does not displace these two ligands [89]. ⁵⁷Fe ENDOR studies in the absence and presence of DMSO have identified two sets of resonances, one ascribed to the Fe³⁺ ion (predominantly isotropic with $A \sim 62$ MHz) and the other belonging to the Fe²⁺ (highly anisotropic with $A \sim 36$ –38 MHz) [89]. Since the addition of DMSO does mainly affect the resonances associated with the ferric metal ion, it appears that the substrate analog interacts predominantly at this site in MMOH_{mv} from *M. capsulatus* (Bath). Furthermore, the ^{14,15}N ENDOR study by DeRose et al. has shown that DMSO binding to MMOH_{mv} from *M. capsulatus* (Bath) perturbs both His ligands

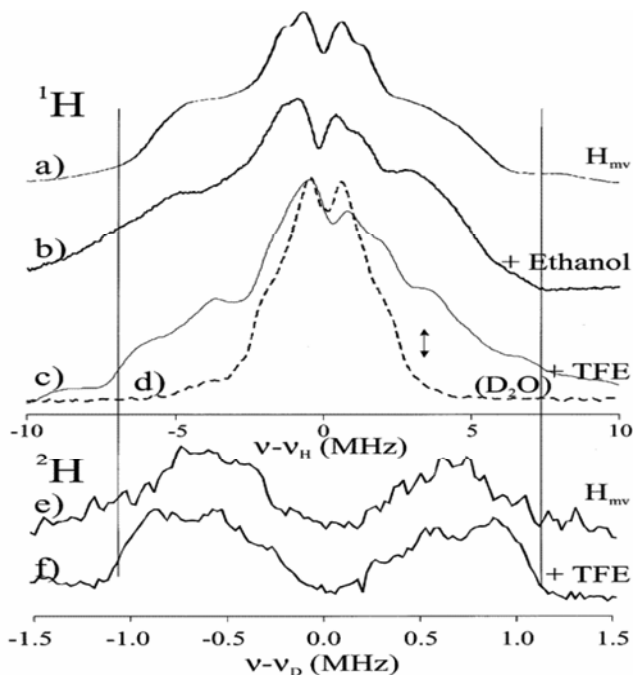


Figure 8. ^1H and ^2H ENDOR spectra of mixed-valent MMOH from *Methylococcus capsulatus* (Bath). (a) MMOH_{mv} alone, $g = 1.87$ and negative scan direction, (b) MMOH_{mv} in the presence of ethanol, $g = 1.862$, (c) MMOH_{mv} in the presence of TFE, $g = 1.840$ and negative scan direction, (d) same as (a) but positive scan direction and $g = 1.841$, (e) four pulse sequence, $g = 1.86$, and (f) same as (e) but with TFE. Reprinted with permission from [91]. Copyright © 2002, American Chemical Society.

that are coordinated to the two iron centers without displacing them: a μ -hydroxo bridge, or the terminally coordinated solvent ligand on the Fe^{2+} center [89]. Each of the metal ions is coordinated by a single, different histidine residue (Fig. 2), but significant changes in the coordination environment upon the addition of DMSO are only recorded in the Fe^{3+} site. Fe^{3+} -localized binding interactions of ^{13}C - or ^2H -labeled DMSO have also been demonstrated with Q-band Mims pulsed ENDOR and X-band three-pulse ESEEM measurements [89]. Furthermore, ENDOR measurements of mixed-valent MMOH from *M. capsulatus* (Bath) in the presence of ^2H -DMSO and ^{13}C -labeled methanol have shown that the substrate analog and reaction product do not compete for the same binding site in the active center, but both molecules can bind simultaneously [90]. The exchange coupling between the metal ions is not affected by the addition of DMSO and methanol, indicating that the bridging hydroxide is retained [90]. Interestingly, in contrast to MMOH from *M. capsulatus* (Bath), cwEPR and ^1H , ^{14}N ENDOR measurements on MMOH_{mv} from *M. trichosporium* OB3b have indicated that the Fe^{2+} ion is predominantly perturbed upon addition of DMSO [70,85].

The cwEPR spectrum of mixed-valent MMOH in the presence of methanol differs from that of the free enzyme, indicating direct ligation of methanol to the metal cluster. Since DMSO has been shown to bind to Fe^{3+} , and since methanol does not compete with DMSO, it follows that the product is likely to interact with the Fe^{2+} site without displacing the terminally coordinated water ligand on this iron center. This conclusion has been supported by both ^1H and ^{17}O ENDOR studies [90]. Similarly, a combination of methods including Q-band cwEPR and both $^{1,2}\text{H}$ and ^{19}F pulsed ENDOR spectroscopy have been employed to demonstrate that the product analogs ethanol and 1,1,1-trifluoroethanol (TFE) also bind terminally to the ferrous center of the mixed-valent form of MMOH, thus not competing with DMSO (Fig. 8) [91]. In addition, a $^{1,2}\text{H}$ ENDOR study monitoring the interactions between ethanol or TFE with the one-electron cryogenically reduced MMOH, i.e., $(\text{MMOH}_{\text{ox}})_{\text{mv}}$, has implied a different mode of alcohol binding to oxidized MMOH (binding in semi-bridging or bridging mode) as opposed to the mixed-valent MMOH (binding to the Fe^{2+} center), a result consistent with the MMOH_{ox} -alcohol crystal structure [55]. Furthermore, the diferric center of $(\text{MMOH}_{\text{ox}})_{\text{mv}}$ from *M. capsulatus* (Bath) is able to bind methanol and phenols, as demonstrated by X-band EPR [88]. However, DMSO or methane binding to the $(\text{MMOH}_{\text{ox}})_{\text{mv}}$ does not perturb the EPR spectra, indicating that most likely they do not bind directly to the diferric cluster.

Nitric oxide as a mimic for dioxygen. Nitric oxide (NO) has been extensively used as a probe for dioxygen binding to non-heme iron enzymes [92–95]. NO interacts with ferrous iron, forming an antiferromagnetically coupled $\{\text{Fe}(\text{NO})\}^7$ complex with an X-band cwEPR spectrum characteristic of a system with $S = 3/2$ (Fe^{3+} ($S = 5/2$) and NO^- ($S = 1$) [95,96]. The reaction of NO with fully reduced, diferrous MMOH from *M. capsulatus* (Bath) in the absence/presence of MMOB yields predominantly an EPR-silent dinitrosyl species, $[\{\text{Fe}(\text{NO})\}^7]_2$ [97]. A smaller proportion of active sites (20–30%) appeared to contain mononuclear iron centers, characterized by distinct cwEPR resonances with g_{eff} values of 4.08, 4.02, and 2.00. The time course of the reaction between reduced MMOH and NO was investigated using a combination of stopped-flow kinetics measurements and rapid freeze-quench (RFQ) cwEPR. Various intermediates were detected [97]. Two labile species are formed within the first 200 ms of the reaction. The first forms in the first 100 ms (with a first-order rate constant of $10\text{--}20\text{ s}^{-1}$) decays slowly and is identified as a mononuclear $\{\text{Fe}(\text{NO})\}^7$ complex. The second species forms more slowly, is more abundant, and is identified, from RFQ-Mössbauer data, as the diamagnetic dinitrosyl species [97]. The dinitrosyl species has been proposed as a likely mimic of the peroxodiferric reaction intermediate (labeled intermediate **P**) in the catalytic cycle of MMO (rate constants for the formation of the dinitrosyl species and intermediate **P** in the presence of MMOB at 4°C are essentially the same, 26 and 25 s^{-1} , respectively) [97–99]. An EPR study of the reduced MMO–NO adduct has given insight into the possible effects of MMOB component on the diiron center of MMOH required for its interaction with dioxygen.

Interactions between MMOH and MMOB. Interactions between MMOH and MMOB are essential for MMO to reach its full catalytic potential [14]. Although the mechanism with which MMOB binding increases the turnover rate of MMOH is still not fully understood, spectroscopic techniques, in the absence of crystallographic data of the MMOH-MMOB complex, have been instrumental in providing insight into the nature of the interactions between these two protein components. Binding of MMOB to the chemically reduced mixed-valent form of MMOH from *M. trichosporium* OB3b affects the cwEPR spectrum by (i) shifting the observed g -values, (ii) altering the power saturation properties, and (iii) decreasing the magnitude of the exchange coupling between the two iron centers ($J \sim -5 \text{ cm}^{-1}$, $\mathcal{H}_{\text{ex}} = -2JS_1 \cdot S_2$), which has been interpreted in terms of an MMOB-induced conformational change of the MMOH active site [70]. X-band cwEPR was employed to investigate the effect of MMOB binding on the mixed-valent center (generated by chemical and radiolytic reduction) of MMOH, indicating that the interactions between MMOH and MMOB are different for different oxidation states of the active site [70,87,88]. The EPR spectra of radiolytically reduced MMOH ((MMOH_{ox})_{mv}) and MMOH-MMOB ((MMOH_{ox}-MMOB)_{mv}) from *M. capsulatus* (Bath) are very similar, with the major change affecting the relative contributions of the species H2 (*vide supra*) to the spectrum. In contrast, MMOB binding to chemically reduced mixed-valence MMOH alters the EPR spectrum significantly (g values at 1.94, 1.87, and 1.72 for MMOH_{mv} and 1.88, 1.77, and 1.63 for MMOH_{mv}-MMOB), indicating structural changes that may be of importance for the activation of the MMOH active site [88]. Furthermore, MMOB binding to the cryogenically reduced MMOH promotes binding of exogenous ligands such as DMSO and glycerol.

Saturation-recovery EPR has also been employed to study fully oxidized (diferric) MMOH from *M. capsulatus* (Bath) and its complex with MMOB [100]. The spin-label methane thiosulfonate (MTSL) was incorporated specifically into residue Cys89 of MMOB. Monitoring the spin-lattice relaxation time (T_1) of MTSL provided evidence that MMOB binding occurs $\sim 15 \text{ \AA}$ away from the metal ions of MMOH, and that the magnitude of the exchange coupling ($J = -18.5 \text{ cm}^{-1}$, assuming $\mathcal{H}_{\text{ex}} = -2JS_1 \cdot S_2$) between the two irons increases, suggesting a shortening of the Fe-Fe distance [100]. This is in contrast to MMOH from *M. trichosporium* OB3b, where MMOB binding to mixed-valent MMOH decreases J from -15 to -2.5 cm^{-1} [51,70] (*vide supra*). Possible explanations for the increase in the exchange coupling constant J between the iron centers in the presence of MMOB include (Fig. 2): (i) the flexible residue Glu243 can provide the necessary exchange pathway, (ii) residue Glu144 can shorten its oxygen bond to the iron center, or (iii) the deprotonation of the bridging hydroxide. In combination with NMR studies [62,63], these saturation-recovery EPR measurements have limited possible points of interactions between MMOB and MMOH to two helices in the latter that contain metal ion ligands Glu209 and Glu243 (Fig. 2).

The mode of interactions between MMOH and MMOB from *M. trichosporium* OB3b has recently been investigated using a combination of site-directed spin labeling (SDSL) [101] and small metal chelate paramagnetic relaxation [102], allow-

ing an estimate of the binding affinity of MMOB to reduced MMOH of 4.5 μM at pH 7.0 [50].

From kinetic and NMR data, several hydrophilic amino acid residues (Asn107, Ser109, Ser110, Thr111) close to the C-terminal end of MMOB have been identified to form the binding interface with MMOH [48,49]. The functional importance of this C-terminal region and its potential role in the interactions with MMOH were investigated using a combination of mutagenesis, kinetics, and EPR spectroscopy [40]. Three deletion mutants in the C-terminal region of MMOB were generated: $\Delta 126$ (with 13 last residues deleted), $\Delta 131$ (with last 8 residues deleted), and $\Delta 134$ (with last 5 residues deleted). The X-band cwEPR spectrum of chemically reduced mixed-valent MMOH (*vide supra*) is characterized by g values of 1.94, 1.86, and 1.75, whereas the mixed-valent MMOH–wtMMOB complex exhibits characteristic resonances at $g = 1.87, 1.77, \text{ and } 1.60$ [40]. The EPR spectra of the complexes with the mutant MMOB forms were shown to be dependent on the size of the deletion: the larger the deletion, the more similar the spectrum to that of free MMOH [40], suggesting that the entire C-terminal domain of MMOB is required for proper interactions with MMOH.

2.1.3. Mechanistic Insights

A combination of spectroscopic, crystallographic, and mechanistic studies produced remarkable progress over the last decade in elucidating the catalytic cycle of MMO. The proposed reaction mechanism for the catalytic cycle of MMO is shown in Figure 9. The resting diferric form of MMOH is reduced by two electrons from MMOR, resulting in diferrous MMOH. The O_2 binds to the diferrous enzyme, forming the initial intermediate labeled **O**, where the O_2 is not yet directly bound to any of the diferrous ions. Subsequently, intermediate **O** decays to compound **P***, where the loss of the $g_{\text{eff}} = 16$ signal, characteristic of diferrous MMOH (Fig. 5), indicates a direct interaction between O_2 and the metal center [76,103]. Intermediate **P*** then further decays to form intermediate **P**, a diferric peroxo species. This short-lived intermediate has been characterized by absorption and Mössbauer spectroscopies [43,99,104,105]. It was found to be diamagnetic at 4 K as a result of the two antiferromagnetically coupled Fe^{3+} centers (Fig. 3), and is proposed to be a μ -1,2-peroxo diiron(III) complex. In the following step, compound **P** is converted to compound **Q**, which has been trapped and characterized in great detail by absorption, Mössbauer, and extended x-ray absorption fine structure spectroscopies [105,106]. Compound **Q** has been described as a high-valent iron–oxygen intermediate having an $\text{Fe}_2^{\text{IV}}\text{O}_2$ bis- μ -oxo “diamond core” structure, and is believed to be the hydroxylating intermediate in the catalytic cycle. The ground state of intermediate **Q** is diamagnetic ($S_T = 0$) as a result of two antiferromagnetically coupled Fe^{4+} ions ($S_1 = S_2 = 2$). Compound **Q** reacts with the hydrocarbon substrate, forming compound **T**. In the final step of catalysis, the product is released from **T**, and resting diferric MMOH is regenerated.

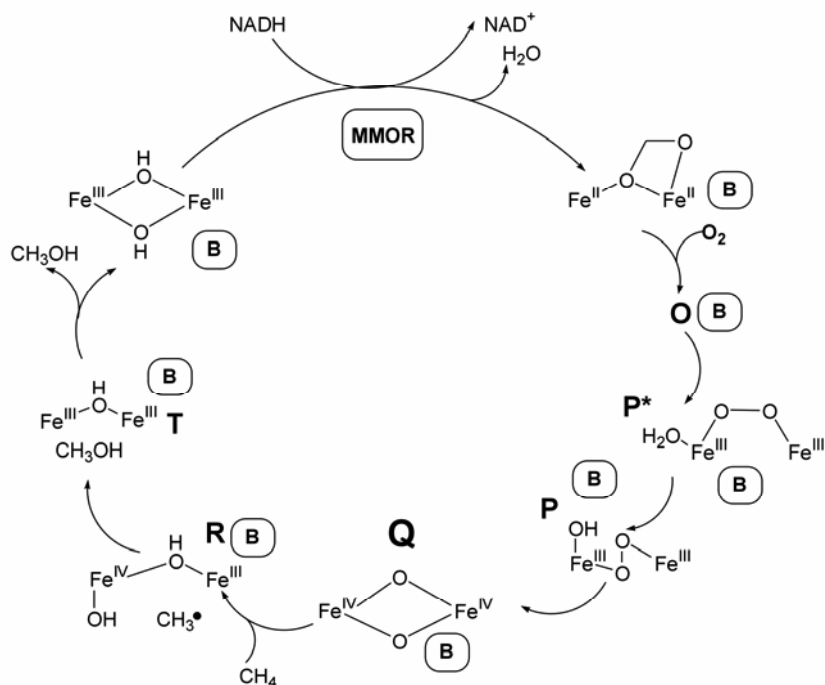


Figure 9. Proposed catalytic cycle for MMO. MMOR and B refer to reductase and component B, respectively. Adapted with permission from [40]. Copyright © 2006, American Chemical Society.

Due to its diamagnetic ground state, intermediate **Q** is not readily accessible to study by EPR-related techniques. However, radiolytic reduction of **Q** has been shown to produce a structurally preserved but paramagnetic Fe³⁺-Fe⁴⁺ species, designated **Q_x** [107] (in analogy to intermediate **X** in ribonucleotide reductase; *vide infra*). Annealing of this intermediate above 200 K produced a structure essentially identical to that of the chemically reduced intermediate at room temperature.

The reaction mechanism of methane oxidation and the actual O–O bond cleavage (heterolytic vs. homolytic) have been under intense investigation and still remain the subject of debate. Numerous studies have been carried out to address specific aspects of the MMO reaction mechanism using substrate analogs such as fluoromethanes, ethers, various alkanes, furan, nitrobenzene, and methylcubane [49,108–110]. While some studies seem to favor the radical rebound mechanism initially proposed in cytochrome P450 chemistry [27,111–115], those involving radical clock probes suggest a concerted mechanism [116–119]. Computational studies have also argued for alternative mechanisms that involve variations of the reaction mechanisms mentioned above, as well as an Fe-substrate carbon bond

intermediate [120–122]. Aiming to probe substrate radical formations, some mechanistic studies have focused on the detection of radical/cation intermediates [28,111,113,117,123]. Suitable spin-trap probes (nitron or nitroso compounds) can be utilized, which can trap transient radical species to form nitroxide adducts detectable by EPR spectroscopy [124,125]. Recently, an EPR spin-trapping study has demonstrated the use of nitrosobenzene (NOB) as a substrate as well as a radical trap [126]. This study has shown that a long-lived radical species ($t_{1/2} = 1$ hour) is generated in the MMO active site using NOB as a probe, thus strongly favoring a stepwise mechanism similar to that of cytochrome P450.

2.2. Alkane ω -Hydroxylase

2.2.1. Biochemical and Structural Characterization

The bacterial alkane ω -hydroxylase from *Pseudomonas putida* GPo1 (also known as *P. oleovorans*) is an integral membrane oxygenase that catalyzes the oxidation of unactivated terminal methyl groups of alkanes and fatty acids (Table 1) [127]. In addition to hydroxylating *n*-alkanes (C5–C12 chain length), this enzyme can also carry out epoxidations of terminal olefins and allyl alcohol derivatives, aliphatic sulfoxidations, and O-demethylations of branched alkyl and vinyl methyl ethers [128–130]. Various homologs of alkane ω -hydroxylase have also been extracted from polluted marine environments and soil as a result of oil and fuel spillages and industrial waste accumulation [131–133]. More recently, alkane hydroxylases from *P. aeruginosa* PAO1, *P. fluorescens* CHA0, *Alcanivorax borkumensis* AP1, and *Mycobacterium tuberculosis* H37Rv have been cloned [134,135]. Alkane hydroxylases have been attracting increasing scientific interest due to their biocatalytic versatility with respect to chemical reactions performed and substrates used.

The best-characterized alkane hydroxylase from *P. putida* GPo1 is comprised of three protein components: the membrane-bound oxygenase component (AlkB), where substrate hydroxylation takes place; the soluble rubredoxin component AlkG, which is responsible for shuttling the required electrons to AlkB [127,136]; and the NADH-dependent flavoprotein rubredoxin reductase component (AlkT) [137,138]. A sequence comparison of AlkB with other non-heme iron integral membrane enzymes has revealed a characteristic conserved eight-histidine motif [139]. A similar motif is also found in coenzyme A-dependent rat Δ^9 desaturase and other desaturases from the cyanobacterium *Synechocystis* and *Arabidopsis thaliana*, and it has thus been speculated that residues within this motif may play a crucial role in the catalytic mechanism of these enzymes [139–142]. This hypothesis is further supported by the observation that these residues occupy similar locations relative to their transmembrane domains [143]. The eight-histidine motif was also found in other enzymes such as acetylenases, conjugases, epoxidases, ketolases, and decarboxylase [141,144,145]. Site-directed mutagenesis studies with AlkB from *P. putida* Gp01 have recently demonstrated the catalytic importance of the eight-

histidine residues; the substitution of any of the eight-histidine residues with alanine produced inactive mutants, while mutations of other, non-conserved histidine residues within the motif still yielded partially active derivatives [143]. No crystal structure of an alkane ω -hydroxylase is yet available, but it is speculated that the eight essential histidine residues may coordinate to the two irons in the active site, providing a coordination environment different from the carboxylate-rich active sites of MMOH and other related enzymes [140].

2.2.2. Spectroscopic Characterization of AlkB

In the absence of crystallographic data, EPR and Mössbauer spectroscopies have been crucial for the characterization of the diiron cluster of AlkB [139]. In its resting (oxidized) form, AlkB contains two high-spin ferric ions, antiferromagnetically coupled with quadrupole splitting ($\Delta E_Q(1) = 1.70$ mm/s, $\Delta E_Q(2) = 1.13$ mm/s), and isomer shift parameters ($\delta(1) = 0.55$ mm/s, $\delta(2) = 0.51$ mm/s) similar to those reported previously for the distantly related toluene-4-monooxygenase [146] (discussed below). The exchange coupling constant $|J|$ was estimated to be ≥ 40 cm⁻¹ from Mössbauer data assuming slow or intermediate relaxation rates for the diiron cluster [139]. The magnitude of J in oxidized AlkB is consistent with the presence of a μ -oxo bridge. Chemical reduction of AlkB leads to an oxygen-stable diferrous form of the enzyme [139]. Examination of the fully reduced diferrous AlkB by Mössbauer spectroscopy confirmed the presence of two high-spin Fe²⁺ ions with an isomer shift of about 1.05–1.15 mm/s. The smaller isomer shift observed for the diferrous center of AlkB is similar to that of deoxyhemerythrin [147] (*vide infra*) and strongly supports nitrogen ligation in the coordination environment of the diiron cluster [139]. The addition of both dioxygen and the substrate octane leads to oxidation of the diiron center with concomitant catalytic turnover [139]. No EPR resonances due to a mixed-valent form of AlkB were detected in this study.

2.2.3. Mechanistic Insights

On the basis of mechanistic studies with wild-type AlkB from *P. putida* GPO1 and *E. coli* using norcarane as the diagnostic substrate probe, an “oxygen rebound mechanism” has been proposed (Fig. 10) [148,149]. Evidence for the formation of a short-lived carbon-centered radical intermediate (lifetime of ~ 1 ns) has been obtained. It is speculated that AlkB might thus involve a reaction intermediate similar to compound **Q** in MMO-catalyzed reactions (Fig. 9). In addition, $\sim 15\%$ of the reaction product for the AlkB-catalyzed reaction was found to be 3-(hydroxymethyl)-cyclohexene, implicating a radical rearrangement pathway. Active site structural changes that may dictate the formation and lifetime of the radical intermediate were investigated using whole cells and specific compounds as substrates for AlkB [150]. The lifetime of the radical appears to depend on substrate concentration; at low concentrations an unusually long lifetime of ~ 19 ns was observed, the longest lifetime for a radical intermediate to be reported for a monooxygenase [150]. It has been hypothesized that substrate binding to AlkB may perturb the

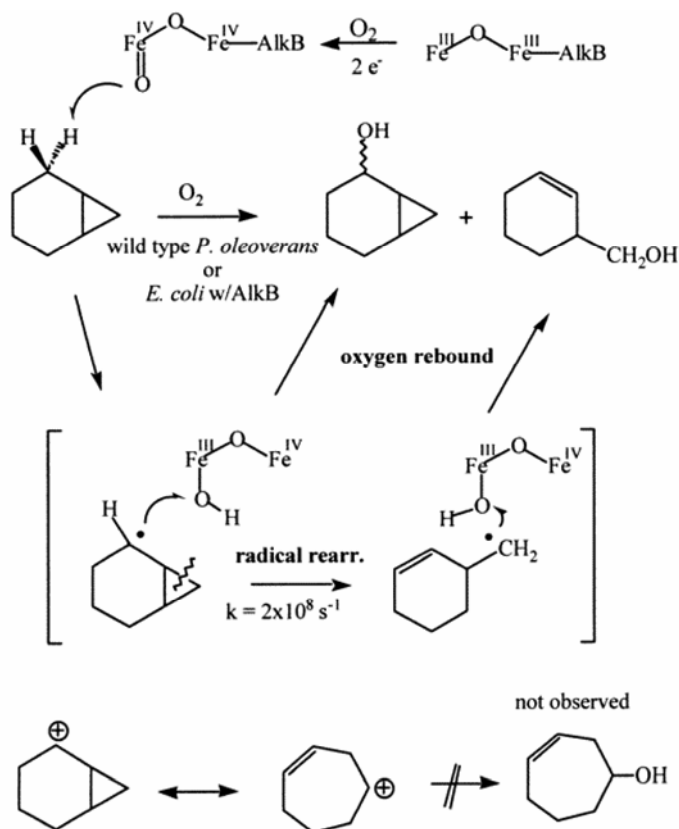


Figure 10. Mechanism of norcaradiene hydroxylation by alkane ω -hydroxylase (AlkB). Reprinted with permission from [148]. Copyright © 2000, American Chemical Society.

active site of the enzyme, causing a change in its reactivity. Specifically, a substrate channel close to the active site and within the transmembrane part of the protein has been invoked that may affect the active site in a manner dependent on the presence of solvent or substrate molecules. However, the molecular details of substrate-induced active site structural changes have yet to be investigated.

2.3. Alkene Monooxygenase

2.3.1. Biochemical and Structural Characterization

Alkene monooxygenase (AMO) from *Rhodococcus rhodochromus* B-276 (also known as *Nocardia corallina*) is a multicomponent oxygenase that catalyzes the stereoselective insertion of an oxygen atom from O_2 into aliphatic alkenes, yielding the corresponding chiral epoxides (Table 1) [151]. This reaction is the first step in the pathway of the alkene metabolism. AMO utilizes substrates ranging from C3–

C4 chain length 1- and 2-alkenes and styrenes, to chloroalkenes, and the reaction products are predominantly R enantiomers [16,151,152]. Since optically active epoxides are of interest in the development of pharmaceutical compounds, AMO has been attracting increasing attention in recent years. Although AMO possesses biochemical properties similar to those of MMO [151], it does not hydroxylate the unactivated C–H bonds of alkanes [153,154]. Similar to MMO, AMO consists of three protein components that are necessary for catalysis; an epoxygenase component (containing subunits α and β , of 53 and 35 kDa, respectively), a 40-kDa reductase component (AmoD, containing one [2Fe–2S] cluster and one flavin group), and a small 14-kDa coupling protein (AmoB) [151,155]. A sequence comparison between the epoxygenase component of AMO, MMOH, and ribonucleotide reductase has revealed the presence of a conserved iron-binding motif, suggesting a similar active site structure for all of these enzymes [156]. In the absence of a crystal structure of AMO, homology modeling studies in combination with chemical modifications were used to probe the significance of specific amino acid residues for the interactions of substrates and products with the active site of AMO from *N. corallina* B-276 [157]. Two residues, Ala91 and Ala185, were proposed to govern the stereoselectivity of AMO due to their ability to anchor the substrate or reaction product. In contrast, in MMOH the corresponding residues are glycines that do not facilitate a proper anchoring of the reaction intermediate (due to the lack of steric hindrance). Consequently, the reaction products of MMOH-catalyzed reactions are not chiral [157].

2.3.2. Spectroscopic Characterization of AMO

EPR spectroscopy has been the primary technique utilized to probe the active site structure of AMO. The fully oxidized epoxygenase component of AMO exhibits a weak, rhombic EPR signal at $g_{\text{eff}} = 4.3$, and a free radical EPR signal at $g = 2.01$ [16]. It has been speculated that the EPR resonance at $g_{\text{eff}} = 4.3$ with significantly broad features arises from two weakly coupled high-spin Fe^{3+} centers ($S = 5/2$). Partial reduction of the epoxygenase with dithionite yields a mixed-valence form ($S_{\text{tot}} = 1/2$) with a characteristic EPR signal at $g_{\text{av}} = 1.9$ ($g_x = 1.93$, $g_y = 1.87$, and $g_z = 1.84$). Therefore, the mixed-valent form of the epoxygenase component is similar to that of the mixed-valent forms of MMOH (*vide supra*) and ribonucleotide reductase (*vide infra*) [71,75,80,158]. The fully reduced epoxygenase component exhibits an EPR signal at $g_{\text{eff}} = 15$ indicative of a binuclear center with two weakly ferromagnetically coupled Fe^{2+} ions, as observed in reduced MMOH [14,16,71,76] (Fig. 5). Thus, as anticipated from the above-mentioned sequence comparison the epoxygenase component of AMO, and the hydroxylase component of MMO are likely to contain similar diiron active sites.

2.3.3. Mechanistic Insights

EPR techniques have proven pivotal in establishing the identity of the prosthetic groups and the determination of the midpoint potential of the reductase component of AMO [159]. From these studies the following mechanism for the elec-

iron transfer between the reductase and epoxygenase components of AMO emerged. The FAD prosthetic group gets reduced by two electrons originating from NADH, which are then transferred to the [2Fe–2S] cluster in two one-electron steps, ultimately reducing the diiron cluster of the epoxygenase component. The role of reductase component in AMO is very similar to that of the reductase component associated with MMO, and the role of the small coupling protein AmoB may be similar to that of MMOB in the MMO complex (see §2.1) [159].

However, in contrast to MMO, AMO is not inhibited by ethyne, and its reactivity is only mildly affected by the presence of propyne [16]. Since both enzymes also display different stereochemistries despite having homologous active sites, it has been speculated that MMO and AMO employ alternative catalytic mechanisms [16]. While the observation of AMO activation by hydrogen peroxide [160] suggests the formation of a possible diiron–peroxo intermediate in the reaction cycle, the enzyme's inability to oxidize methane indicates that no Q-like diferryl-oxo species may be formed [98]. Hence, small differences in the coordination environment of the diiron centers in AMO and MMO lead to significant variations in substrate specificity and reactivity.

2.3.4. Other Alkene Monooxygenases

Several other alkene monooxygenases have also been isolated and partially characterized. For example, the alkene monooxygenase from the Gram-negative bacterium *Xanthobacter* Py2 (XAMO) has been purified and characterized biochemically [161]. XAMO is also homologous to MMOH with the iron-binding ligands conserved, and catalyzes the epoxidation of alkenes (C2–C6 chain length) to the corresponding epoxides, and the oxidation of benzene, toluene, and phenol [162,163]. In addition, XAMO is capable of catalyzing the degradation of various chlorinated alkenes, such as trichloroethene, vinyl chloride, 1,3-dichloropropene [164], thus making it an interesting target for the design of novel pathways for the degradation of environmentally hazardous chemicals [161]. XAMO is a four-component protein complex comprised of a 212-kDa oxygenase component (with a multimeric $\alpha_2\beta_2\gamma_2$ structure containing two binuclear iron active sites per holoenzyme), a 35.5-kDa reductase component (containing one FAD and an [2Fe–2S] cluster as prosthetic groups), whose role is the shuttling of reducing equivalents from NADH to the oxygenase component, a 13.3-kDa Rieske-type iron–sulfur cluster ferredoxin, and a small 11-kDa coupling protein with no associated metal ions or prosthetic groups. Whilst EPR has been used to determine the midpoint reduction potential of the Rieske-type iron–sulfur cluster of the ferredoxin component (-49 ± 10 mV) [161], no resonances have been observed for the reduced or oxidized oxygenase component [161]. Thus, the characterization of the diiron catalytic center of XAMO awaits further investigation.

2.4. Phenol Hydroxylases

2.4.1. Biochemical and Structural Characterization

Phenol hydroxylases belong to the class of multicomponent (three-component) aromatic oxygenases and are responsible for the oxidation of phenol and some methyl-substituted phenol derivatives to the corresponding catechols (Table 1) [165–168]. These enzymes are utilized by a large number of microorganisms to degrade toxic compounds to carbon dioxide and water as part of their catabolic pathways. Two phenol hydroxylases—the DMP phenol hydroxylase from *Pseudomonas* sp. strain CF600 [165,167–171] and the toluene *o*-monooxygenase from *Burkholderia cepacia* G4 (TOM), also known as toluene-2-monooxygenase [172]—have so far been isolated and characterized. These enzymes exhibit features and properties that are similar to MMO (§2.1), both with respect to their reactivity and structure [2]. Specifically, each of these systems contains three functional components that are required for catalysis: a hydroxylase component containing a carboxylate-bridged binuclear iron center, a reductase component, and a small effector protein. They also require O₂ and the electron donor NADH for hydroxylations to occur.

The phenol hydroxylase from *Pseudomonas* sp. Strain CF600 catalyzes the first step of the phenol degradation pathway, converting it to catechol, which subsequently undergoes further degradation. Its three components are a heteromultimeric ($\alpha\beta\gamma$) hydroxylase component (DmpLNO) accommodating the binuclear non-heme iron center, a reductase component (DmpP) containing FAD and a [2Fe–2S] cluster as cofactors, and a small coupling (activator) protein (DmpM) with no associated metal ions or cofactors [167,170,171]. Biochemical studies and sequence comparisons of these components indicate a significant homology to the corresponding components of MMO [168], with an especially high degree of similarity with respect to the ligands in the iron-binding domain of the hydroxylase components [173]. Furthermore, an amino acid sequence alignment of the coupling proteins MMOB (16 kDa) and DmpM (10.4 kDa), and the comparison of their NMR solution structures indicate similar secondary structures [174]. It is therefore likely that the roles of DmpM and MMOB in their respective protein complexes are equivalent, i.e., altering redox potential of the oxygenase component, increasing the reactivity with O₂, and affecting the product yield. DmpM is necessary for maximum turnover of DMP phenol hydroxylase, which reaches a maximum at an approximately 1.5:1 DmpM/DmpLNO ratio [165,168,175].

Interestingly, an additional component is associated with DMP phenol hydroxylase, the so-called auxiliary protein DmpK, which seems to be responsible for the iron-dependent assembly of DmpLNO [171]. More specifically, DmpK has been proposed to play a significant role during the post-translational incorporation of iron into apoDmpLNO. DmpK appears to be unique amongst binuclear non-heme iron oxygenases.

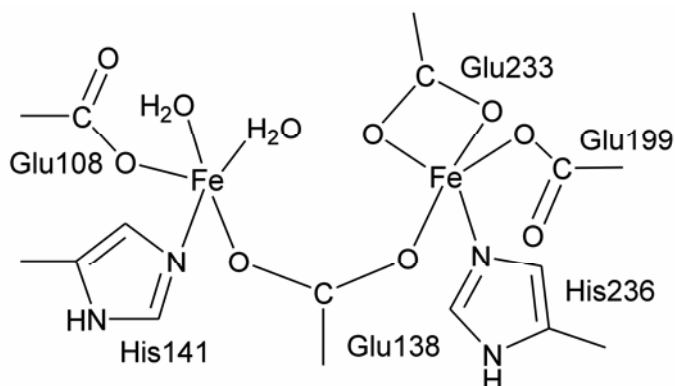


Figure 11. Active site structure of phenol hydroxylase from *Pseudomonas* sp. OX1.

A crystal structure of the phenol hydroxylase-regulatory protein complex from *Pseudomonas* sp. OX1 has been recently reported [176]. The diiron center of PH is essentially the same in the absence and presence of its regulatory protein (Fig. 11) and resembles that of the diiron center of MMOH in its mixed-valent form (Fig. 2B). This may be due to the photoreduction of the samples by synchrotron radiation. While these structures provide some insight into the potential role of the regulatory protein (preventing reduction of high-valence iron–oxygen intermediates during catalysis), detailed spectroscopic investigation is required to assess the geometric and electronic structure changes of the diiron active site in the absence/presence of the regulatory protein.

2.4.2. Spectroscopic Characterization of PH

Mössbauer studies have been instrumental in characterizing the diiron cluster of DmpLNO. Two types of diferric binuclear iron clusters are observed, each containing two equivalent iron sites. Clusters I and II comprise approximately 85% and 15% of the total amount of DmpLNO, respectively, and the catalytic activity of DmpLNO correlates with the amount of cluster I present in the sample [175]. The magnitude of the exchange coupling constant J ($\mathcal{H}_{\text{ex}} = -2JS_1 \cdot S_2$) in cluster I is estimated to be $>60 \text{ cm}^{-1}$, indicative of an oxo bridge between the two high-spin ferric centers and possibly additional bridging carboxylate ligands [177]. In contrast, the magnitude of J in cluster II is much smaller, thereby implicating a μ -hydroxo or μ -aqua bridge between the two iron centers, as observed in MMOH (§2.1) [2]. Low-temperature parallel mode X-band EPR of dithionite-reduced DmpLNO exhibits an integer spin signal at $g_{\text{eff}} = 16.6$ (Fig. 5), indicative of two weakly ferromagnetically coupled Fe^{2+} ions having an $|S, M_s\rangle = |4, \pm 4\rangle$ doublet as the ground state. Since an analysis of the spin concentration has shown that the observed EPR signal corresponds to only 19% of the total concentration of binuclear centers, it has been proposed that only cluster II is EPR active [175]. The existence of two different

forms of diferric clusters in DmpLNO is reminiscent of Δ^9 desaturase [178,179] (§4) and toluene-4-monooxygenase [146] (§2.5), suggesting a similar reaction mechanism (*vide infra*).

2.4.3. Other Phenol Hydroxylases

Phenol hydroxylase from *Acinetobacter radioresistens* S13 is another multi-component monooxygenase that catalyzes the hydroxylation of phenol, chloro- and methyl-substituted phenols, and naphthol [180–182]. It also requires three protein components for full catalytic activity, an oxygenase (PHO) that contains the binuclear non-heme iron center required for catalysis, a reductase (PHR), and a small regulatory protein (PHI). A distinct protein complex is formed between the three components; maximum catalytic turnover is achieved when the PHR:PHI:PHO ratio is 2:1:1. Similar to the DMP phenol hydroxylase and MMO, the small regulatory component PHI appears to be responsible for promoting interactions between the substrate and the iron active site of the PHO component, but in this case the effector protein interacts with the reductase component, thus facilitating electron transfer between the reductase and oxygenase components.

Other phenol hydroxylases that are homologous to the DMP phenol hydroxylase, MMO, and the alkene monooxygenase from *N. coralline* have been isolated from *Comamonas testosteroni* R5 [183] and *Ralstonia eutropha* E2 [184], but they remain to be characterized structurally spectroscopically and mechanistically. Toluene-2-monooxygenase from *Burkholderia cepacia* G4 (also known as T2MO or TOM) is another three-component monooxygenase that catalyzes reactions of the toluene catabolic pathway, which include the oxidations of toluene to *o*-cresol and *o*-cresol to 3-methylcatechol (Table 1) [172,185]. In addition, T2MO also catalyzes the degradation of halogenated compounds such as trichloroethylene, thus making this enzyme an interesting target for use in bioremediation [186,187]. The three components comprising T2MO include a 211-kDa hydroxylase component with an $(\alpha\beta\gamma)_2$ quaternary structure, a 40-kDa reductase component containing one FAD and one [2Fe–2S] cluster, and a 10.5-kDa regulatory protein with no metal ions or organic cofactors [172]. The regulatory component increases the rate of toluene oxidation by approximately 10-fold, and is speculated to play a role during catalysis similar to that proposed for MMOB in MMO (§2.1). Amino acid sequence comparisons between corresponding components from T2MO and other related multicomponent monooxygenases suggest that these enzymes have similar structural and functional properties [173].

The fully reduced, mixed-valent and fully oxidized forms of the hydroxylase component of T2MO have been studied by EPR [172]. The fully reduced form exhibits a low-field EPR signal at $g_{\text{eff}} = 16$, indicative of a ferromagnetically coupled binuclear $\text{Fe}^{2+}\text{--Fe}^{2+}$ center, similar to that observed for reduced MMOH [71,75] (Fig. 5). Exposure to air leads to the disappearance of this signal, with the fully oxidized form being EPR silent, indicating antiferromagnetic coupling between two Fe^{3+} ions [172] ($S_{\text{tot}} = 0$; Fig. 3). In further analogy to MMO (§2.1), the mixed-valent form of T2MO hydroxylase yields an EPR spectrum with $g_{\text{av}} =$

1.84 ($g_x = 1.74$, $g_y = 1.85$, and $g_z = 1.93$), indicating that the two metal ions, Fe^{3+} ($S = 5/2$) and Fe^{2+} ($S = 2$), are antiferromagnetically coupled to give an $S_{\text{tot}} = 1/2$ ground state.

2.5. Toluene-4-Monooxygenase

2.5.1. Biochemical and Structural Characterization

Toluene-4-monooxygenase (T4MO) from *P. mendocina* KR1 belongs to the group of soluble four-component bacterial alkene/aromatic monooxygenases [188], and is responsible for NADH- and O_2 -dependent hydroxylation of toluene to *p*-cresol with 96% regioselectivity (Table 1) [189,190]. T4MO is able to oxidize a variety of other substrates, including some heterocyclic aromatic, halogenated compounds such as indole, trichloroethylene, chloroform, benzene, chlorobenzene, 1,2-dichloroethane, and C3–C8 alkanes [191–197]. Furthermore, T4MO also catalyzes the epoxidation of alkenes such as butene, butadiene, pentene, and hexane, and current studies involving direct evolution of T4MO are aimed at evolving this enzyme for specific hydroxylation reactions [198,199]. T4MO is comprised of a 212-kDa hydroxylase component (T4MOH), a 12-kDa Rieske-type ferredoxin (T4MOC), a 11.6-kDa effector protein (T4MOD) with no associated cofactors, and a 36-kDa NADH oxidoreductase (T4MOF) that contains one FAD and one [2Fe–2S] cluster [146]. All four components are required for full catalytic activity. T4MOH has a $(\alpha\beta\gamma)_2$ quaternary structure similar to T2MO (§2.4.3), with the di-iron center located in the α subunit. The sequence motif E...EX₂H occurs in two copies within T4MOH, contains all metal-coordinating ligands, and is also found in MMOH, Δ^9 desaturase (§4), and ribonucleotide reductase (§3). Apart from this motif, the sequence homology between these enzymes is limited, accounting for the observed variations in substrate specificity and regioselectivities [173]. While T4MOH alone can carry out the hydroxylation of toluene under single turnover conditions, the presence of T4MOC increases the rate of hydroxylation by ~100-fold, thus supporting the proposal that T4MOC is responsible for the mediation of electron transfer between the T4MOH and T4MOF components [146]. The rate of the hydroxylation reaction is further enhanced by the addition of the effector protein T4MOD [146]. T4MOD is homologous to MMOB both in sequence and structure, strongly supporting a mechanistic proposal whereby T4MOD fulfills a catalytic role similar to that proposed for MMOB [146,188,194,200,201] (§2.1). The structure of T4MOD has been characterized both crystallographically and by protein NMR spectroscopy [188,201] and it appears likely that, similar to the MMOH–MMOB complex, the T4MOH–T4MOD interactions are predominantly of electrostatic nature [62,63]. However, in contrast to MMOB, T4MOD does not seem to interact via its N-terminal domain [188,201]. The NMR solution structure of the T4MOC component containing a Rieske-type [2Fe–2S] cluster has also recently been reported [202].

2.5.2. Spectroscopic Characterization of T4MO

The diiron site in T4MOH has not been studied in great detail. A combination of EPR and Mössbauer spectroscopic data indicates that the active site in T4MOH is very similar to that of MMOH. Its diferric form is EPR silent due to the antiferromagnetic coupling of the two $S = 5/2$ Fe^{3+} centers [146] (Fig. 3). Mössbauer spectroscopy indicates that at 23 K the $S = 1$ level is already partially populated, indicating an exchange coupling constant $-J = 7.5\text{--}15\text{ cm}^{-1}$ ($\mathcal{H}_{\text{ex}} = -2JS_1 \cdot S_2$) [146], consistent with the presence of a μ -hydroxo or a μ -alkoxo bridge. The mixed-valent center of T4MOH has not yet been studied, but the fully reduced form exhibits a low-field integer spin EPR signal at $g_{\text{eff}} \approx 16$, reminiscent of the EPR signal observed for reduced MMOH [76] (Fig. 5), and indicating ferromagnetic coupling between the two Fe^{2+} centers.

2.5.3. Mechanistic Insights

Most of the studies examining the T4MO reaction mechanism have involved the use of radical and cationic diagnostic probes (so-called “radical clock” probes), which are capable of forming transient radical/cationic intermediates [150,203] or kinetic isotope studies exploiting various substrate analogs [204]. Intramolecular isotope effect studies with various substrates have shown that T4MO employs different mechanistic strategies depending on the type of substrates used (aromatic vs. aliphatic hydrocarbons) [204]. This observation is analogous to those reported for other hydroxylases, which seem to employ different mechanisms depending on the nature and strength of the C–H bond in a particular substrate [98,205]. The effector protein T4MOD is likely to play an important role in the proper entry and orientation of the substrate in the iron active site [204]. Recently, studies have been extended to probe the nature of various component interactions within the T4MO complex using fluorophore-labeled T4MOD and fluorescence anisotropy [206]. These studies have enabled the determination of binding constants between various protein components and have demonstrated the formation of a T4MO catalytic complex similar to the MMO complex [34,47]. For T4MO, it is likely that the T4MOD and T4MOC components first form a complex, which facilitates proper and efficient interaction with the T4MOH component, thus forming a catalytic ternary complex. The T4MOF component seems to affect the interaction between the T4MOD and T4MOC components [206], but the precise details of the involvement of each component in the catalytic cycle await further investigation.

2.6. Toluene/*o*-Xylene Monooxygenase

2.6.1. Biochemical and Structural Characterization

Toluene/*o*-xylene (ToMO) from *P. stutzeri* OX1, which has recently been expressed and purified, belongs to a class of bacterial multicomponent monooxygenases, and is also closely related to MMO [11,12,207]. It catalyzes the oxidation



Figure 12. Active site structure of toluene/*o*-xylene monooxygenase (ToMOH) from *Pseudomonas stutzeri* OX1: (A) fully oxidized native ToMOH (PDB code 2INC), (B) $\text{Mn}^{2+}/\text{Mn}^{2+}$ ToMOH (PDB code 2IND), and (C) reduced ToMOH–azide complex (PDB code 1TOR).

of a broad variety of substrates, including aromatic hydrocarbons like xylene, toluene, benzene, naphthalene, styrene, and alkenes, and chlorinated alkenes such as chloroform, trichloroethylene, and tetrachloroethylene (Table 1) [208–210]. ToMO is a multicomponent protein consisting of a hydroxylase component (ToMOH), where the catalytic reaction takes place, an oxidoreductase component (ToMOF), responsible for electron transfer from NADH to ToMOC, a Rieske-type ferredoxin protein necessary for electron shuttling to the hydroxylase component, and a coupling protein (ToMOD) with a possible regulatory role. Preliminary x-ray crystallographic and absorption studies have recently been carried out [211,212]. A comparison, by x-ray absorption spectroscopy, between reduced ToMOH in the absence and presence of ToMOD and the corresponding data from MMOH in the absence and presence of MMOB, has indicated that ToMOD (i) directly affects the first-shell ligation of reduced ToMOH and (ii) decreases the distance between the two ferrous ions. In contrast, MMOB binding to reduced MMOH seems to primarily affect the outer-shell ligands (§2.1). It is likely that these differences between ToMOH and MMOH reflect the reactivity differences between the two enzymes. Crystal structures have been reported for oxidized ToMOH, an $\text{Mn}^{2+}/\text{Mn}^{2+}$ derivative of ToMOH, azido ToMOH, and the ToMOH–4-bromophenol complex [211,213]. The diiron active site of ToMOH is very similar to that of MMOH, with both Fe^{3+} ions displaying octahedral environments (Fig. 12A). The crystal structure of the oxidized ToMOH–azide complex is speculated to mimic the potential peroxo intermediate, and it suggests that initial dioxygen binding may occur at the Fe2 site (Fig. 12C). Although the diiron active sites of ToMOH and MMOH look very similar, there are distinct differences between the two enzymes with respect to their substrate binding pockets. In ToMOH there is a wide channel (6–10 Å) that is rather long (35–40 Å) and extends from the diiron center to the surface of the protein and can accommodate various aromatic substrates. In contrast, MMOH has five hydrophobic cavities, and only three of them have direct access to the protein surface, thus making the diiron site in MMOH less accessible for the bulk solvent than that in ToMOH [2, 10]. The crystallographic evidence from a dimanganese(II) derivative of ToMOH (Fig. 12B) indicates that reduced, diferrous ToMOH is likely

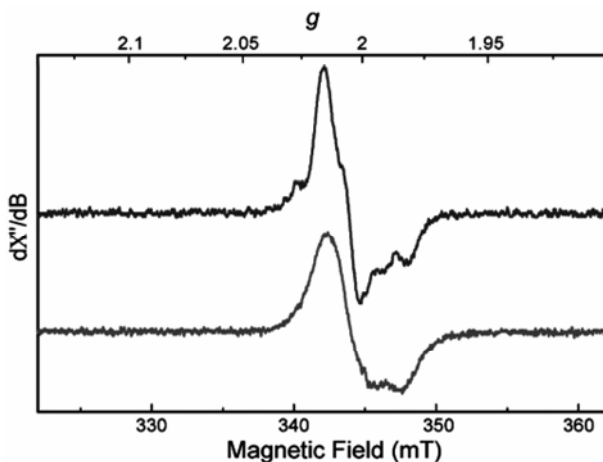


Figure 13. EPR spectra of the $\text{Fe}^{3+}\text{-Fe}^{4+}\text{-W}^*$ intermediate generated in the reaction of reduced I110W mutant of toluene/*o*-xylene monooxygenase with dioxygen. Reprinted with permission from [214]. Copyright © 2006, American Chemical Society.

to resemble the differous center of MMOH [213]. Finally, a conserved asparagine residue in the Mn^{2+} derivative of ToMOH exhibits a rotameric shift (80°) relative to the oxidized diiron structure and is proposed to be crucial for the interaction between ToMOH and its regulatory protein ToMOD [213].

2.6.2. Spectroscopic Characterization of ToMOH

While the diiron active sites of ToMOH and MMOH are very similar, EPR and Mössbauer spectroscopic evidence suggests somewhat different intermediates in their catalytic cycles [214]. With the I1000W mutant of ToMOH, it has been possible to trap and characterize transient reaction intermediates by stopped-flow kinetics, rapid freeze-quench-EPR, and rapid freeze-quench-Mössbauer spectroscopies. An intermediate species with an absorption maximum at 500 nm and a $g = 2.00$ EPR signal, and which reached maximum concentration ~ 3.5 s after initiating the reaction, has been observed. The intermediate shows hyperfine broadening in its EPR spectrum that is consistent with that of a spin-coupled $\text{Fe}^{4+}\text{-Fe}^{3+}\text{-W}^*$ species (Fig. 13), and its Mössbauer parameters are similar to those observed in the ribonucleotide reductase mutant R2-W48F [214,215] (§3). An analysis, also by Mössbauer spectroscopy, of the precursor of the $\text{Fe}^{4+}\text{-Fe}^{3+}\text{-W}^*$ intermediate, quenched after 70 ms, has led to its tentative assignment as a peroxodiiron $^{3+}$ intermediate despite the lack of optical absorption in the 650 nm region, as usually observed in peroxodiiron $^{3+}$ intermediates formed in other diiron-containing non-heme iron enzymes. Specifically, the diiron $^{3+}$ species observed in the ToMOH-I100W mutant exhibits Mössbauer parameters different from those characteristic of a $\mu\text{-1,2-peroxo}$ intermediate found in MMOH [2]. Based on current spectroscopic and kinetic data, it seems likely that the peroxodiiron intermediate in ToMOH is struc-

turally different from that in MMOH, consistent with the observed differences in substrate specificity and reactivity [10].

3. RIBONUCLEOTIDE REDUCTASE

3.1. Biochemical and Structural Characterization

Ribonucleotide reductases are metalloenzymes that catalyze the rate-limiting step in DNA biosynthesis: the reduction of ribonucleotides to deoxyribonucleotides (Table 1) [216–223]. Over the last decade, due to their crucial role in DNA synthesis and repair, and cell growth, ribonucleotide reductases have become important targets for the design of anticancer drugs and therapies [224]. The recent discovery of the human p53 ribonucleotide reductase (R2 subunit), regulated by the p53 tumor suppressor protein, has provided a new avenue for the design of more effective therapies against various human cancers [225–228]. Since several reviews about ribonucleotide reductases have been published recently, including some that focus specifically on the use of EPR-related techniques in the study of these enzymes [221,223,229–244], here only selected spectroscopic developments are discussed.

Ribonucleotide reductases are classified into four major groups according to their composition, oxygen, and cofactor requirements [219,221,229]. Class I ribonucleotide reductases are found in all eukaryotes, some eubacteria, viruses, as well as some prokaryotes, and are comprised of the two homodimeric subunits, R1 and R2, arranged in an $\alpha_2\beta_2$ quaternary structure (Fig. 14) [19,245–248]. The best-characterized class I ribonucleotide reductases to date are the *E. coli*, mouse, and calf-thymus enzymes [240,249–251]. The larger R1 subunit contains one substrate (nucleotide) binding site and two allosteric effector sites, while the smaller R2 subunit houses a binuclear non-heme iron active site that utilizes dioxygen to generate a stable tyrosyl radical necessary for catalysis to occur (Tyr122' in *E. coli*) [19,246,252]. Reductive activation of O₂ at the diiron active site of the R2 subunit generates the Tyr122' radical, which acts as the “pilot light” and triggers catalysis via a long-range radical transfer (proton-coupled electron transfer; PCET) mechanism between the R1 and R2 subunits, thus generating a thiyl radical on Cys439 of the R1 subunit (Fig. 14), which is ultimately responsible for initiation of the nucleotide reduction process [223]. Both the diiron cluster and the Tyr122' radical are 35 Å away from the R1 active site (Fig. 14), and the mechanism of radical propagation over such a long distance has been the subject of intense research. Residues involved in this long-range radical transfer are Tyr356, Trp48, and Asp237 in the R2 subunit and Cys439, Ty730, and Tyr731 in the R1 subunit (unless mentioned otherwise, the residue numbering refers to the sequence of the *E. coli* enzyme). The stable tyrosyl radical is highly conserved amongst almost all sequenced R2 subunits, and according to site-directed mutagenesis studies it is essential for catalysis [253]. Unlike MMOH, which catalyzes two-electron oxidations, the reaction of diferrous R2 with O₂ leads to a one-electron oxidation of the nearby Tyr122 residue, forming the stable radical mentioned above.

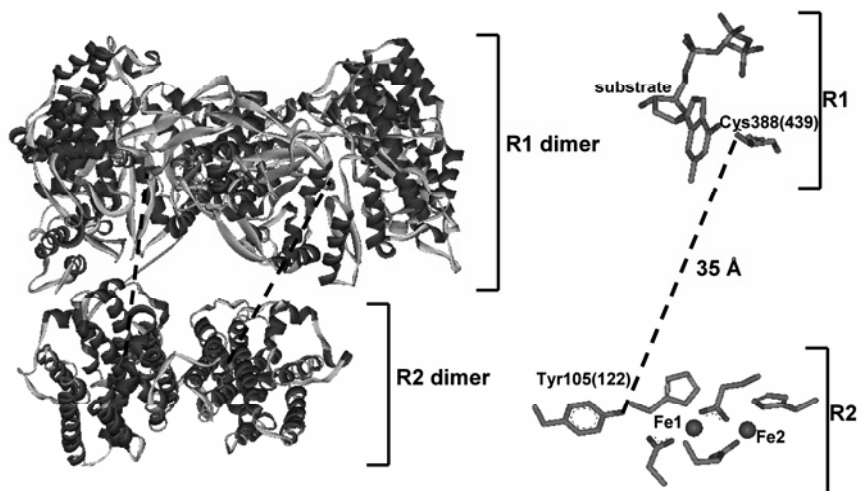


Figure 14. Overall structure of R1 and R2 subunits of RNR from *Salmonella typhimurium* (PDB code 2BQ1).

Various crystal structures of *E. coli* R1 and R2 subunits have been reported, including some of the complexes of R1 with substrates or effectors [19,246,254–257]. In addition, the structures of mouse, yeast, and mammalian R2 have also been determined [258–263]. The crystal structures of R2 proteins from other species are also available, including those from *Salmonella typhimurium*, *Corynebacterium ammoniagenes*, *Mycobacterium tuberculosis*, and *Chlamydia trachomatis* [257,264–268]. Furthermore, the first crystallographic determination of the R1/R2 holocomplex from *S. typhimurium* has recently been reported [269]. The overall structural fold of the R2 subunit is a heart-shaped dimer (predominantly helical in structure) containing two equivalent diiron clusters separated by 25 Å (Fig. 14). While there is low homology between the *E. coli* and mouse R2 proteins, they contain the highly conserved sequence motif EXXH, also present in MMO (§2.1) and Δ^9 desaturase (§4) [57,60]. In the fully oxidized form of R2 the two Fe^{3+} ions are both six-coordinate, with Fe1 being coordinated by His118, bidentate Asp84 and a water molecule, and Fe2 by His241, Glu204, Glu238, and one solvent molecule (Fig. 15A). The octahedral geometry of each ferric iron is completed by a μ -1,3 carboxylate bridge (from Glu115) and an additional μ -oxo bridge. The Tyr122' radical is located approximately 5.3 Å from the diiron active site and \sim 10 Å from the surface of the protein [247]. In the reduced form of *E. coli* R2 (including azide-bound as well as Mn-substituted forms), a substantial degree of variation with respect to the immediate coordination environment of the diiron center is observed, probably as a consequence of different crystallization conditions and reduction methods [256,270–272]. Both metal ions in diferrous R2, reduced chemically or

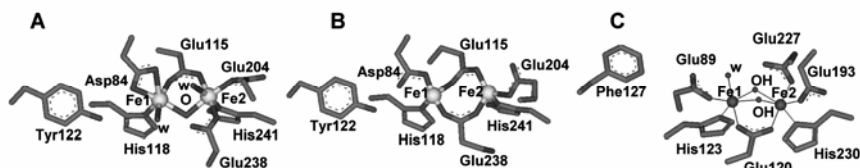


Figure 15. Active site structures of R2 subunit: (A) oxidized R2 from *E. coli* (PDB code 1RIB), (B) reduced R2 from *E. coli* (PDB code 1XIK), and (C) oxidized R2 from *Salmonella typhimurium* (PDB code 1SYU).

photolytically, are four-coordinate, whereby Fe1 is coordinated by His118 and Asp84, and Fe2 by His241 and Glu204; additionally, the two irons are linked via μ -1,3 carboxylates from Glu238 and Glu115 (Fig. 15B). In contrast, in “ferrous soaked” R2 (soaked apo R2 crystals in the solution of ferrous ammonium sulfate) the Fe1 is still four-coordinate, while Fe2 is five-coordinate, consistent with spectroscopic studies using (magnetic) circular dichroism [256,273–275]. The major difference between the oxidized and reduced structures of R2 is the conformation of Glu238 (Figs. 15A,B). In the oxidized form this residue coordinates monodentately to Fe2, while in the reduced form it interacts with the Fe2 bidentately in an asymmetric fashion and adopts a bridging μ -1,1(η^1, η^2) coordination mode [256]. Similar to the *E. coli* enzyme, reduced mouse R2 is believed to have considerable coordination flexibility, with either one four-coordinate and one five-coordinate site, or two four-coordinate sites [261]. Interestingly, oxidized *C. trachomatis* R2 contains a somewhat different diiron active site when compared to the *E. coli* enzyme (Fig. 15C) [267]. Here, the two iron ions are coordinated by two histidines and four glutamates (two μ -OH bridges and a terminal water molecule complete the coordination environment), instead of the three glutamates and one aspartate observed in *E. coli* R2. Thus, the active site of *C. trachomatis* R2 resembles that of diferric MMOH enzyme [2] (Figs. 15C and 2A). In addition, *C. trachomatis* R2 lacks the Tyr residue corresponding to Tyr122 in the *E. coli* enzyme, having a phenylalanine (Phe127) in the corresponding position instead. It is thus likely that the *C. trachomatis* enzyme has evolved an alternative mechanism to catalyze ribonucleotide reductase-type reactions [267].

3.2. Spectroscopic Characterization of R2

Diferric R2. The combined application of a range of techniques including saturation-recovery EPR, Mössbauer, resonance Raman, and extended x-ray fine structure absorption spectroscopies, and magnetization measurements supports the presence of two strongly antiferromagnetically coupled high-spin Fe^{3+} ions, bridged via a μ -oxo group in oxidized *E. coli* R2 (J is in the range between -90 and -108 cm^{-1} , where $\mathcal{H}_{\text{ex}} = -2JS_1 \cdot S_2$) [276–281]. Saturation-recovery EPR experiments with oxi-

dized R2 proteins from mouse and the type 1 herpes simplex virus have resulted in similar exchange coupling constants ($J = -77$ and -66 cm^{-1} , respectively) [277].

Diferrous R2. Mössbauer spectroscopy, magnetic susceptibility measurements, as well as nuclear magnetic resonance, (magnetic) circular dichroism, and variable-temperature/variable-field magnetic circular dichroism studies indicate that the two Fe^{2+} ions in reduced *E. coli* R2 are weakly antiferromagnetically coupled ($J \approx -0.5 \text{ cm}^{-1}$, with $\mathcal{H}_{\text{ex}} = -2JS_1 \cdot S_2$, $S_{\text{tot}} = 2$ and $M_S = \pm 2$) [273,276,282,283]. Azide was added to diferrous R2 in an attempt to mimic O_2 binding to the catalytically competent enzyme. The EPR spectrum of azide-bound reduced R2 shows an integer spin signal with $g_{\text{eff}} = 17.0$ (Fig. 5), indicative of a ferromagnetically coupled diferrous cluster with an $M_S = \pm 4$ ground state [273,284]. This result has demonstrated the availability of the open coordination sites on the two ferrous ions for O_2 binding, supporting a metal ion-bridging coordination based on the observed altered exchange coupling interaction.

Mixed-valent R2. Mixed-valent *E. coli* Fe^{3+} - Fe^{2+} R2, generated by cryogenic reduction at low temperature, exhibits an EPR spectrum with g_{eff} values at 14.0, 6.6, and 5.4, suggesting an $S_{\text{tot}} = 9/2$ ground state (Fig. 16) as a result of ferromagnetic coupling between the Fe^{3+} and Fe^{2+} ions [285–288]. In contrast, the chemically reduced mixed-valent form of R2 produces an EPR spectrum with g values at 1.93, 1.85, 1.83, and 1.64, consistent with an $S_{\text{tot}} = 1/2$ ground state resulting from antiferromagnetic coupling [158,289]. The magnitude of the exchange coupling constant ($J \approx -17 \text{ cm}^{-1}$; $\mathcal{H}_{\text{ex}} = -2JS_1 \cdot S_2$) supports the presence of a μ -OH bridge [286]. The presence of two distinct mixed-valent species with $S = 9/2$ and $S = 1/2$ has been interpreted in terms of a conformational change of residue Glu238 from monodentate coordination to Fe2 to a bidentate and bridging mode of coordination, as well as the protonation of the μ -oxo bridge [288] (Fig. 15).

Oxygen intermediates in R2. The mechanism of self-assembly of the radical diiron $^{3+}$ cofactor of *E. coli* R2 has been studied by various spectroscopic methods, including EPR, ENDOR, Mössbauer, stopped-flow absorption, and resonance Raman spectroscopies [290–293]. The reaction of reduced R2 with O_2 under limiting Fe^{2+} and non-reducing conditions leads to the formation of a first transient reaction intermediate known as U, identified by a characteristic absorption band at 560 nm and an EPR signal at $g = 2.00$ [293]. Intermediate U has been described as an Fe^{4+} - Fe^{3+} species coupled to a tryptophan radical cation (Trp48^+) [215,294]. The overall process of electron-shuttling in R2 is mediated by this Trp48 residue.

A second reaction intermediate, labeled X, has been observed both in wild-type and some variants of *E. coli* R2 [292,295]. Intermediate X exhibits a broad absorption band at $\sim 360 \text{ nm}$ and a sharp, isotropic EPR signal at $g = 2.00$ (Fig. 17) [290,296]. Detailed spectroscopic characterization employing EPR, ^{57}Fe , ^{17}O , and $^{1,2}\text{H}$ ENDOR, Mössbauer, and extended x-ray absorption spectroscopies and (magnetic) circular dichroism have shown that intermediate X is best described as an antiferromagnetically coupled Fe^{4+} - Fe^{3+} species (high-spin Fe^{4+} with $S_1 = 2$ and high-spin Fe^{3+} with $S_2 = 5/2$), giving rise to an $S_{\text{tot}} = 1/2$ ground state [290,297–302]. Mössbauer and ^{57}Fe ENDOR studies with X are consistent with (i) substantial spin

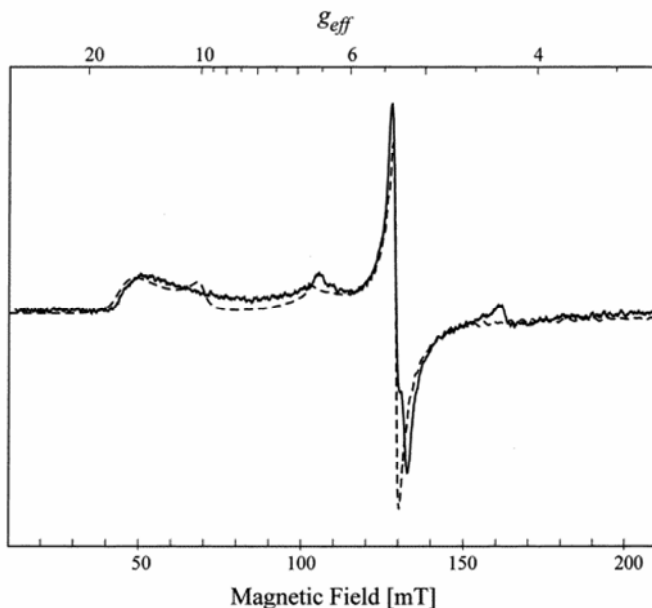


Figure 16. Low-temperature (5 K) EPR spectrum of mixed-valence R2 from *E. coli*. Dashed line shows a simulation of the experimental EPR spectrum with parameters $S = 9/2$, $D = 1.5 \text{ cm}^{-1}$, $E/D = 0.05$, and $\sigma_{E/D} = 0.023$. Reprinted with permission from [288]. Copyright © 2000. American Chemical Society.

delocalization onto the oxygen ligands, (ii) the Fe^{4+} ion having a small isomer shift of $\delta = 0.26 \text{ mm/s}$ and a moderate anisotropy, and (iii) the Fe^{3+} ion being closer to Tyr122 than the Fe^{4+} [297,303]. The active site structure of **X** has further been elucidated by S-band EPR, cw and pulsed Q-band EPR, as well as ^1H and ^{17}O pulsed ENDOR (Fig. 18) and rapid freeze-quench magnetic circular dichroism studies [298–300,302,304]. These studies have demonstrated that **X** is likely to contain a single μ -oxo bridge and a terminal water ligand on the Fe^{3+} , an interpretation that is also supported by the short metal–metal distance measured with extended x-ray absorption spectroscopy [301]. Detailed MCD study of intermediate **X** in wt-R2 and two of its variants has been extended, supporting a μ -oxo/ μ -hydroxo [$\text{Fe}^{3+}(\mu\text{-O})(\mu\text{-OH})\text{Fe}^{4+}$] core structure for intermediate **X** (Fig. 19) [305].

A combination of kinetic studies and EPR spectroscopy has allowed characterization of intermediate **X** in R2 from *C. trachomatis* [306]. Since R2 from *C. trachomatis* has a phenylalanine in the position corresponding to Tyr122 in *E. coli* R2, an exceptionally stable intermediate **X** is formed in the R1/R2/substrate holo-complex. Observed hyperfine couplings in a ^{57}Fe -substituted sample are consistent with the presence of an $\text{Fe}^{4+}\text{-Fe}^{3+}$ cluster that stores an extra electron equivalent required for catalysis [307]. While the tyrosyl radical is believed to be the initiator

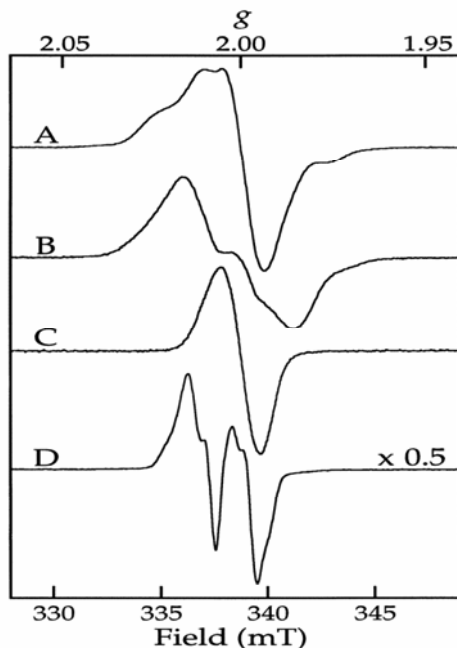


Figure 17. X-band RFQ-EPR spectra of (A) intermediate X-W48⁺ prepared with ⁵⁶Fe, (B) intermediate X-W48⁺ prepared with ⁵⁷Fe, (C) intermediate X in R2-Y122F mutant, and (D) Y122^{*}. Reprinted with permission from [294]. Copyright © 2000, American Chemical Society.

of catalysis in *E. coli* R2 in *C. trachomatis* R2, the Fe⁴⁺–Fe³⁺ diiron cluster is proposed to function in this role [307]. Furthermore, this study has demonstrated direct correlation between the presence of intermediate X and the catalytic activity of ribonucleotide reductase.

An additional reaction intermediate, labeled intermediate P, has been observed and kinetically as well as spectroscopically characterized in two variants of *E. coli* R2: D84E R2 and W48F/D84E R2. Intermediate P is best described as a symmetrically bridged μ -1,2-diferric peroxo complex similar to peroxo intermediates trapped in MMO (§2.1) and Δ^9 desaturase (§4) [99,105,308–313].

Various studies have also focused on probing the mechanism of the ribonucleotide reduction process [314–316]. Notably, a compound proposed to be an intermediate in the reduction process, 3'-keto-2'-deoxynucleotide, has recently been trapped and characterized by high-field EPR spectroscopy [317].

Application of EPR in the study of amino acid radicals in ribonucleotide reductase. Advanced EPR methods (high-field and high-frequency EPR, ENDOR, and ELDOR) have been employed extensively in the study of intermediate amino

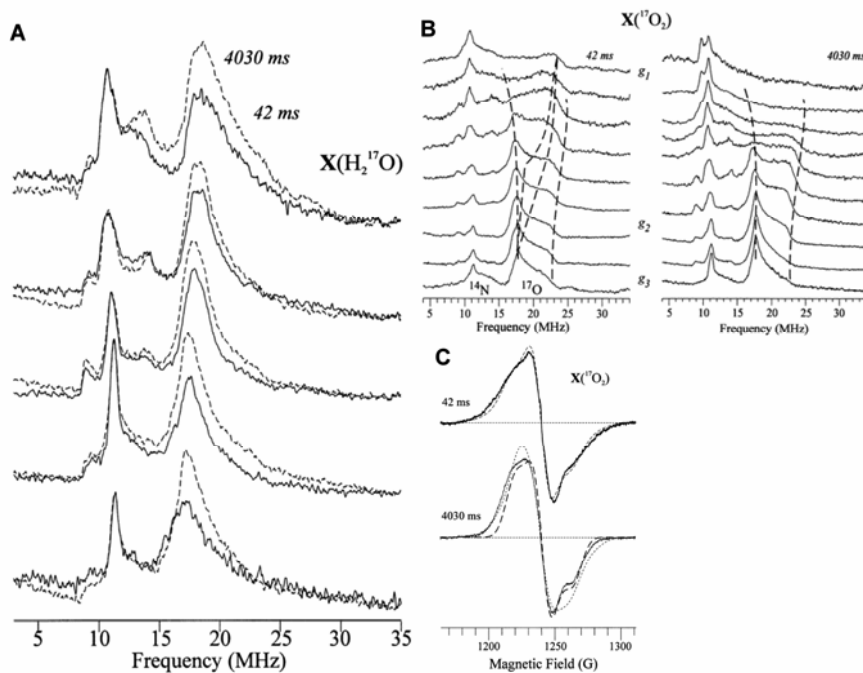


Figure 18. EPR and ENDOR characterization of intermediate **X** in *E. coli* R2. (A) CW ENDOR spectra of H_2^{17}O -labeled intermediate **X** in *E. coli* R2-Y122F mutant (samples quenched at 42 and 4030 ms, respectively). (B) CW ENDOR spectra of $^{17}\text{O}_2$ -labeled intermediate **X** in *E. coli* R2-Y122F mutant (samples quenched at 42 and 4030 ms, respectively). (C) S-band EPR spectra of $^{17}\text{O}_2$ -labeled intermediate **X** in *E. coli* R2-Y122F mutant (samples quenched at 42 and 4030 ms, respectively). Reprinted with permission from [299]. Copyright © 1998, American Chemical Society.

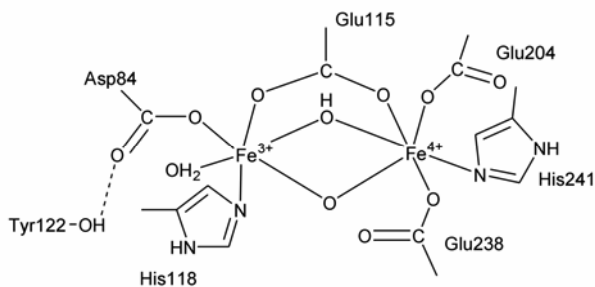


Figure 19. Proposed structure of intermediate **X** in *E. coli* R2 subunit of ribonucleotide reductase.

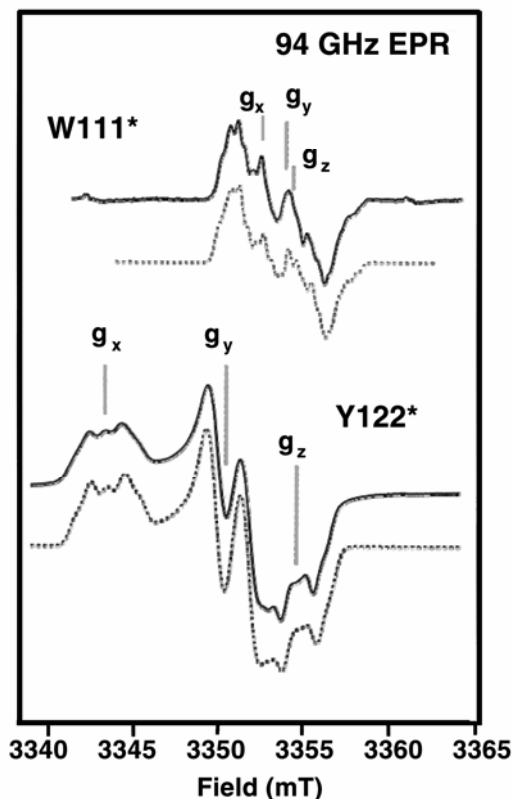


Figure 20. High-field EPR (94 GHz) spectroscopic signatures for Trp radical (W111*) in *E. coli* R2-Y122F mutant and Tyr radical (Y122*) in wt *E. coli* R2 at 20 and 40 K, respectively. Reprinted with permission from [323]. Copyright © 2001, American Chemical Society.

acid radicals of ribonucleotide reductases in order to elucidate the electronic structure, function, and mechanism of the R1–R2 holocomplex [230,232,316,318–322]. Amino acid radicals are found in all three steps of ribonucleotide reductase catalysis: (i) generation of Tyr122' in the R2 subunit, (ii) the radical transfer pathway between Tyr122' in R2 and Cys429 in R1, and (iii) the reduction of ribonucleotides [217–219,223,229,235]. The different amino acid radicals (tyrosyl (e.g., Tyr122), thiyl (e.g., Cys439), tryptophanyl (e.g., Trp48)) can be identified and characterized by the principal values of their \mathbf{g} matrices and anisotropies (Fig. 20) [253,323,324]. In general, high-field and high-frequency methods allow the determination of the relative orientations of the principal components of the \mathbf{g} and hyperfine matrices. Since both the \mathbf{g} and hyperfine matrices are sensitive to their environment, accurate detection of any changes in their principal values provides information about (i) geometric and electronic structural changes, (ii) relevant H-bonding interactions,

(iii) conformational changes and dynamic processes required for reactivity and catalysis, as well as (iv) distances between catalytically significant radical species, and their electrostatic and chemical environments [231,318,323,325].

The above-mentioned tyrosyl radical (Tyr122' in *E. coli* R2)—in particular from *E. coli*, mouse, and yeast R2—has been the subject of detailed high-field EPR and ENDOR studies [231,232,326–328]. H-bonding interactions play an important role in the radical transfer pathway between the R2 and R1 subunits of ribonucleotide reductase, and the g_x component of Tyr radicals can be used as a fingerprint indicating H-bonded and non-H-bonded Tyr radicals in R2 proteins [230,325,329]. It may thus be a reflection of mechanistic versatility that, in contrast to the Tyr122' of *E. coli* R2, the corresponding Tyr' radicals in mouse, yeast, and the herpes simplex virus R2 proteins are H-bonded through the oxygen atom of the tyrosine ring to a water molecule, while *M. tuberculosis* R2 has both weakly H-bonded and non-H-bonded populations of the coresponding Tyr' radicals [323,327–329].

A combination of x-ray crystallography and high-field EPR has also been applied to study Tyr122' upon its formation in the R2 active site [330]. The results were consistent with a significant tyrosyl sidechain rotation (10°), away from the diiron center relative to reduced Tyr122. A similar study was carried out with the binuclear metal center-containing subunit of *Salmonella typhimurium* ribonucleotide reductase [331] (R2F subunit). Although radical formation of the corresponding tyrosine residue (Tyr105) induces a rotation in the opposite direction relative to that observed in the *E. coli* R2 subunit, the overall effect in both enzymes is the same since similar distances between the tyrosyl radicals and the binuclear center were observed.

In two mutants of *E. coli* R2—Phe208Tyr and Phe208Tyr/Tyr122Phe—a new paramagnetic species, denoted **Z**, has been observed and described as an $\text{Fe}^{4+}\text{-Fe}^{3+}$ center in equilibrium with the $\text{Fe}^{3+}\text{-Fe}^{3+}\text{-Tyr208}'$ radical [332]. In these mutants, there are two competitive pathways in the course of diiron cluster reconstitution reaction with apo enzyme, Fe^{2+} , and O_2 depending on ascorbate concentration. One pathway leads to Tyr208 oxidation, while the other leads to the accumulation of species **Z**. The second pathway leads to stabilization of the tyrosyl radical in the wt-R2, and in these two mutants it leads to the different delocalization of the unpaired spin. Therefore, small structural changes are able to tune and govern delocalization and distribution of the unpaired electron spin density [332]. Furthermore, the recent characterization by cwEPR and ^1H , ^{15}N - and ^{57}Fe - ENDOR of the Tyr122His single mutant has demonstrated the formation of a stable iron-coordinated paramagnetic species, labeled **H**, where the $\text{Fe}^{3+}\text{-Fe}^{3+}$ center is strongly coupled to the phenoxyl radical from Phe208, which appears to be directly coordinated to one of the iron ions [333]. While Tyr122His has no measurable catalytic activity, it leads to hydroxylation of Phe208 residue, demonstrating that small structural changes in the R2 active site are able to alter the reactivity of the diiron center, making it capable of carrying out an MMO-type of reaction, i.e., oxygenation of a hydrocarbon in this instance.

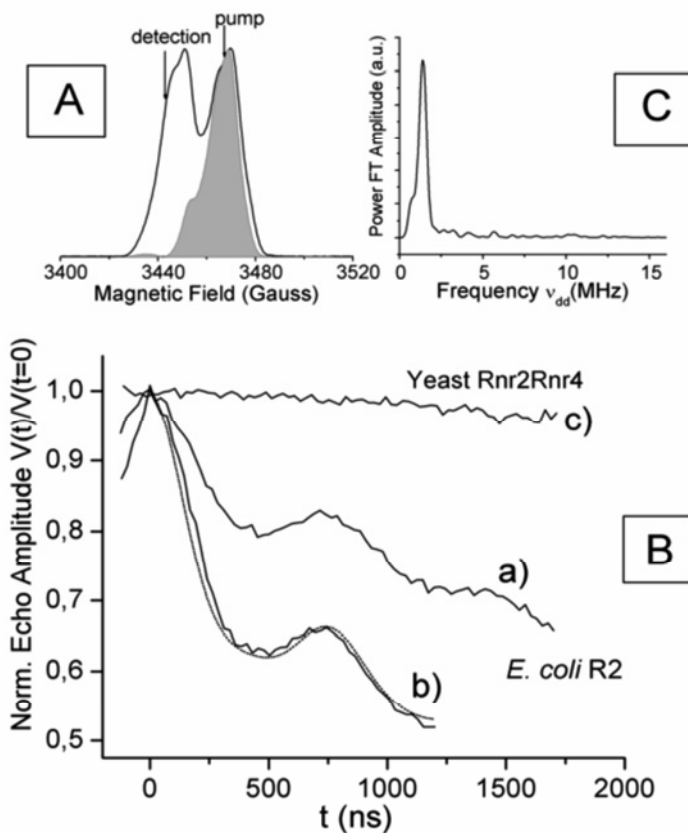


Figure 21. Pulsed ELDOR data of *E. coli* R2 and Rnr2Rnr4 from yeast: (A) low-temperature (5 K) spin-echo detected spectrum of Tyr* in *E. coli* R2, (B) time traces normalized with the echo signal intensity at zero time, and (C) frequency spectrum. Reprinted with permission from [334]. Copyright © 2003, American Chemical Society.

The distance between the Tyr122' radicals in the two monomers of the *E. coli* R2 homodimer and the corresponding Tyr radicals in mouse R2 has been estimated using pulsed electron double resonance (PELDOR) spectroscopy (Fig. 21) [319,334]. PELDOR allows detection of weak dipolar interactions between the electron spins of radical species separated by distances up to 80 Å, thus facilitating the accurate measurement of long-range distances [231,335,336]. In *E. coli* and mouse R2, the distance between the two Tyr radicals is 33.1 and 32.5 Å, respectively, in good agreement with crystallographic data [19,330]. Furthermore, PELDOR has allowed determination of the dipolar coupling between the two catalytically essential tyrosyl radicals, thereby providing direct information about the relative orientation of the two radicals in solution [337]. PELDOR has also been

instrumental for determining selected distances between the R1 and R2 subunits of *E. coli* ribonucleotide reductase in the presence and/or absence of various substrates, allosteric effectors, and inhibitors. For example, in combination with double quantum coherence (DQC) PELDOR has allowed the measurement of the distance between the Tyr122[•] radical in R2 and the N[•] radical covalently attached to Cys225 in R1 to 47–50 Å [338]. This result is consistent with a proposed docking model of the two ribonucleotide reductase subunits and a long-range radical transfer pathway [223]. A recent study using fluorinated tyrosine analogs has shown that another residue in the *E. coli* R1 subunit, Tyr356, is also part of the radical propagation pathway of ribonucleotide reductase [339,340].

Another *E. coli* R1-based radical proposed in the radical propagation and thus catalytic mechanism of ribonucleotide reductase is Cys439[•], believed to initiate ribonucleotide reduction by H-atom abstraction from the 3' position of the substrate nucleotide [217,223]. Thiyl radicals have been generated artificially in the R1 subunit using several different methods, and their spectral properties have been investigated by EPR spectroscopy [341,342]. Oxidation of Cys residues in the wild-type enzyme with Ce^{IV}/nitrolotriacetate or flash photolysis of the nitrosylated R1 subunit in order to generate thiyl radicals have not provided samples accessible for further spectroscopic characterization, probably due to the short lifetimes of thiyl radicals at room temperature [341]. However, the Glu441Gln mutation in R1 reduces the reaction rate sufficiently to enable characterization of radical intermediates in the R1–R2 complex with bound substrate, cytosine diphosphate [316,343,344]. Two transient radical intermediate species have been observed by high-frequency EPR (140 GHz) spectroscopy: a cysteinyl (disulfide anion radical) and a substrate-centered 4'-ketyl radical [316].

3.3. Mechanistic Insights

The general reaction mechanism of oxygen activation proposed for wild-type *E. coli* R2 based on current kinetic, spectroscopic, and crystallographic data is shown in Figure 22 and described in more detail in a recent review [345]. The first step of the reaction involves Fe²⁺ binding to the apo R2 subunit to form the catalytically competent diferrous cluster. In the second step, O₂ binds to the Fe²⁺–Fe²⁺ cluster, leading to the formation of several sequential short-lived intermediates. Intermediate **P**, a μ-1,2-peroxodiferric complex characterized in the Asp84Glu mutant of *E. coli* R2 (*vide supra*), is proposed to form first upon the reaction of R2 with O₂ [308–311]. The application of chemical “rescue” experiments has also allowed the detection of a state denoted as **L**, consisting of at least two distinct peroxo diferric complexes that interconvert rapidly [345,346], and which decays to a state characterized by the presence of the **X** intermediate and a tryptophan (Trp48) cation radical (intermediate **U**).

Subsequently, Tyr122 is oxidized in a manner that depends on the absence or presence of external reductants, and intermediate **X** is reduced to the stable diferric

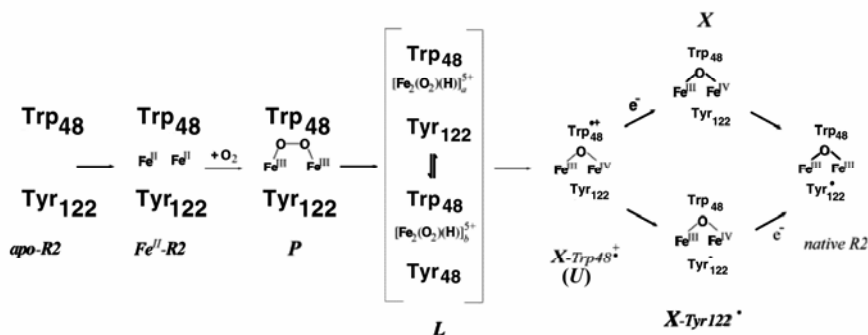


Figure 22. Proposed reaction mechanism for O_2 activation by *E. coli* R2 subunit of ribonucleotide reductase. Reprinted and adapted with permission from [345]. Copyright © 2006, Elsevier.

state [294]. The radical $Tyr122^{\cdot}$ is the starting point for a long-range electron transfer chain that ultimately leads to the formation of a thiyl free radical on a cysteine residue (Cys439), which is located close to the substrate in the R1 subunit, and which initiates reduction of the substrate. An interesting variation of the above mechanism is observed in the R2 subunit of *C. trachomatis* ribonucleotide reductase [307]. In the absence of a tyrosine residue equivalent to Tyr122 in *E. coli* R2, the $Fe^{4+}-Fe^{3+}$ cluster itself acts as the initiator of catalysis. The proposed reaction scheme is shown in Figure 23 and involves, in brief, the formation of intermediate X via a high-valent $Fe^{4+}-Fe^{4+}$ state. Substrate binding to the R1 subunit induces electron transfer between the binuclear metal center in R2 and residue Cys672 in R1 via an electron transfer chain.

4. STEAROYL-ACYL CARRIER PROTEIN Δ^9 DESATURASE

4.1. Biochemical and Structural Characterization

Fatty acid desaturases are responsible for catalysis of the O_2 - and NADH-dependent desaturation reactions, the insertion of a *cis* double bond in saturated fatty acids (Table 1) [144]. Such reactions are important in fatty acid metabolism and processes that facilitate the delivery of lipid precursors to prostaglandins and cell membranes [347]. Both soluble and membrane-bound desaturases exist, which exhibit different substrate specificities and reactivities [144,348]. The soluble stearoyl-acyl carrier protein Δ^9 desaturase from *Ricinus communis* (castor seeds) is the best characterized desaturase and catalyzes the insertion of a *cis* double bond between the C-9 and C-10 carbon atoms of stearoyl ACP to yield an important in

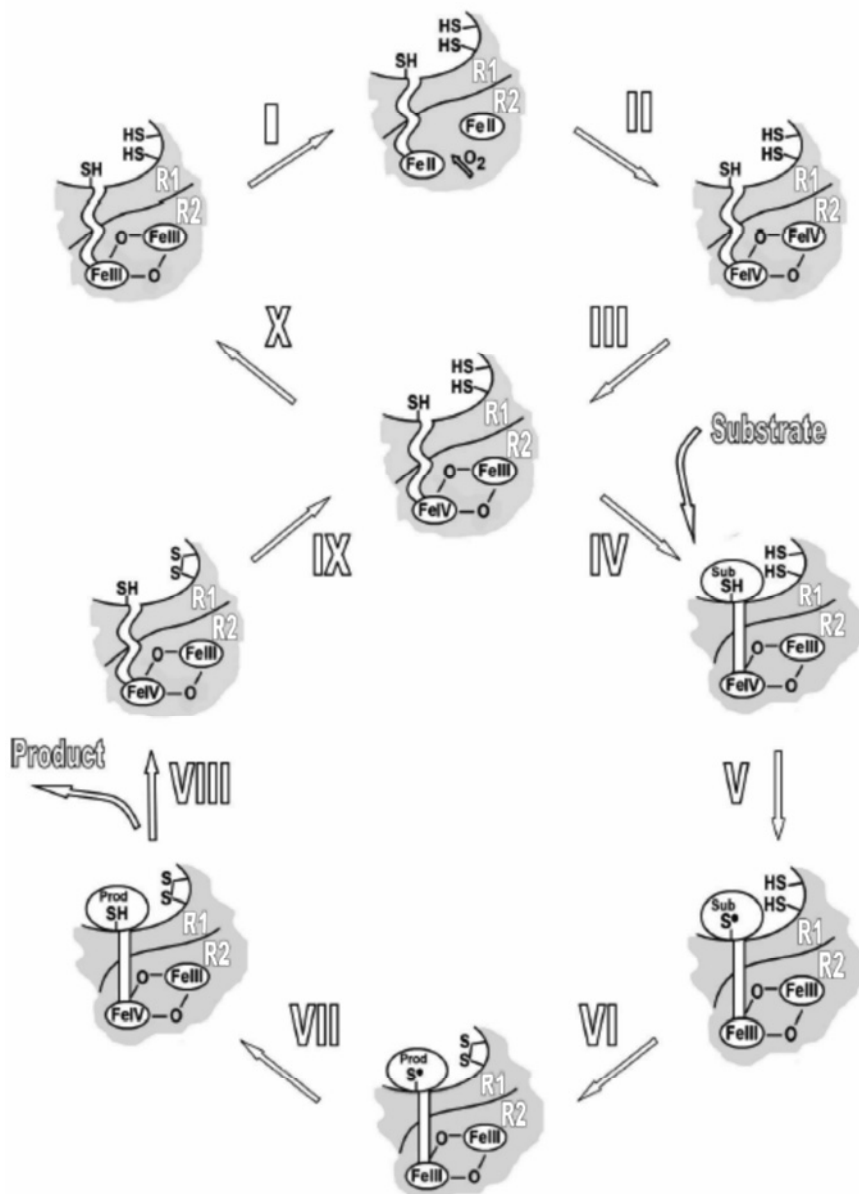


Figure 23. Proposed catalytic cycle for ribonucleotide reductase from *Chlamydia trachomatis*. High-valent iron oxygen intermediate X is shown in step III. Reprinted with permission from [306]. Copyright © 2006, National Academy of Sciences, USA.

intermediate in unsaturated cellular lipid biosynthesis, oleoyl-ACP [60,179,313,349–358]. Δ^9 desaturase is closely related to other carboxylate-bridged binuclear non-heme iron enzymes, including MMO and other bacterial monooxygenases (§2), and ribonucleotide reductase (§3), which all contain the highly conserved diiron binding motif [20]. Δ^9 desaturase is a homodimer with a molecular weight of 84 kDa, and each of the two subunits contains a binuclear non-heme iron center important for catalysis [359]. The biological electron donor for Δ^9 desaturase is a [2Fe–2S] ferredoxin, which transfers the required electrons for the reduction of the diiron center [360]. Two genes in *Mycobacterium tuberculosis* encoding proteins highly homologous to soluble stearoyl acyl-carrier desaturases in plants have also been identified [361,362]. Most recently a multicomponent membrane-bound acyl CoA desaturase from *M. tuberculosis* related to alkane hydroxylase and xylene monooxygenase (with the highly conserved eight-His diiron binding motif) has been characterized [363].



Figure 24. Active site structure of Δ^9 desaturase from *Ricinus communis*: (A) reduced Δ^9 desaturase (PDB code 1AFR), (B) reduced Δ^9 desaturase complexed with acetate (PDB code 1OQ9), and (C) reduced Δ^9 desaturase complexed with azide (PDB code 1OQ4).

The crystal structures of both reduced Δ^9 desaturase and its complexes with azide and acetate have been reported [60,355]. The binuclear iron center is buried in the four-helix bundle, as observed for other binuclear iron enzymes (see text discussion of Fig. 1), and the immediate coordination environment of the diiron center in reduced Δ^9 desaturase is symmetric and highly similar to the iron active site of the R2 subunit in ribonucleotide reductase (Fig. 15). One Fe^{2+} is coordinated by Glu196 and His232 (Fe1 site), while the other is coordinated by Glu105 and His146 (Fe2 site), with both Glu196 and Glu105 binding in bidentate fashion (Fig. 24A). The two metal-binding sites exhibit different affinities for iron, with Fe1 having a higher affinity [355]. The two iron centers are also bridged by two μ -1,3 carboxylates from Glu229 and Glu143. The long metal–metal distance (4.2 Å) is consistent with the lack of bridging hydroxo or oxo groups. A deep hydrophobic cavity extending from the surface to the interior of the enzyme (~20 Å) has been identified, and it is speculated to be the cavity through which substrate can access the iron active site. Molecular modeling of stearic acid into the substrate binding pocket places the substrate with its C-9 and C-10 atoms in close proximity to the binuclear iron site (~5.5 Å) [355]. In the crystal structures of the Δ^9 desaturase-

azide (Fig. 24B) and Δ^9 desaturase-acetate (Fig. 24C) complexes, both azide and acetate are bound to the irons in a μ -1,3 bridging mode, with Fe–N and Fe–O distances of 2.5–2.6 Å. However, apart from Glu196 in the acetate complex, which switches its coordination from bidentate to monodentate, the remaining coordination environment of the diiron centers remain unchanged compared to the structure of reduced Δ^9 desaturase alone. Both the azide and the acetate complex of Δ^9 desaturase have been proposed to mimic the active site structure of a possible peroxodiferric intermediate.

4.2. Spectroscopic Characterization of Δ^9 Desaturase

The fully oxidized and reduced forms of Δ^9 desaturase have been studied in great detail by various spectroscopic methods, including optical, resonance Raman, Mössbauer, (magnetic) circular dichroism, and extended x-ray absorption fine structure [20,179,352,364]. Specifically, an analysis of the oxidized system by Mössbauer spectroscopy has shown the presence of high-spin Fe^{3+} ions, antiferromagnetically coupled with an exchange coupling constant of $-J > 30 \text{ cm}^{-1}$ ($\mathcal{H}_{\text{ex}} = -2JS_1 \cdot S_2$) [20,179]. Furthermore, extended x-ray absorption fine structure data are consistent with the presence of two distinctly different diferric clusters, one containing a μ -oxo bridge (Fe–Fe distance: 3.12 Å) and another with a μ -OH bridge (Fe–Fe distance: 3.41 Å) [179]. The presence of a μ -oxo bridge exchangeable with solvent was also confirmed by resonance Raman spectroscopy [20]. The reduced, diferrous form of Δ^9 desaturase has been investigated using (magnetic) circular dichroism [352]. The two ferrous ions have equivalent five-coordinate sites. Upon the addition of the ACP substrate, one of the two ferrous ions adopts a four-coordinate geometry, a structural rearrangement implicated in the observed increase in reactivity of the Δ^9 desaturase-ACP complex with O_2 [313]. Resonance Raman studies have also indicated a perturbation in the μ -oxo bridged diferric center in the presence of substrate relative to the that of diferric Δ^9 desaturase–substrate free form (change in the Fe–O–Fe angle) [364].

The radiolytically reduced mixed-valent form of Δ^9 desaturase has recently been studied by EPR and ENDOR, providing structural information about the diamagnetic fully oxidized (diferric) form [356]. Based on Q-band cw EPR spectroscopy, and similar to ribonucleotide reductase (§3), the predominant species is a strongly antiferromagnetically coupled, μ -oxo bridged system characterized by g values of 1.945, 1.926, and 1.898 [286]. A minor species containing a μ -OH bridge has also been observed in this EPR spectrum (weak resonances in the high-field region). The mixed-valent form of Δ^9 desaturase has also been examined in the presence of substrate (1-ACP) and a substrate analog (9-thiastearoyl-ACP or 2-ACP). Cryoreduction of the Δ^9 desaturase-1-ACP complex results in an EPR spectrum that is distinctly different from that of the free mixed-valent enzyme with two contributing species (an axial one with $g_{\perp} = 1.938$ and $g_{\parallel} = 1.727$ and a rhombic one with g values of 1.945, 1.84, and 1.765). This observation has led to the conclusion that substrate induces a conformational change within the diferric center of

Δ^9 desaturase; the fact that two different species are observed implies the presence of two conformers at equilibrium in the fully oxidized Δ^9 desaturase–substrate complex, both containing a μ -oxo bridge [286]. The EPR spectrum of the cryoreduced Δ^9 desaturase–2-ACP complex reveals EPR signals due to four species, a major axial component with $g_{\perp} = 1.937$ and $g_{\parallel} = 1.754$, and three weaker rhombic components. Thus, although 1-ACP and 2-ACP are structurally very similar (the only difference is at position C-9, with a carbon or sulfur atom in 1-ACP or 2-ACP, respectively), their interactions with the enzyme are different.

Annealing of cryoreduced free Δ^9 desaturase at 170 K yields an EPR spectrum characteristic for a μ -hydroxide bridged Fe^{3+} – Fe^{2+} binuclear iron center [88,287]. In contrast, a similar protonation of the μ -oxo bridge was not observed in the Δ^9 desaturase–1-ACP complex upon annealing up to 230 K. This observation suggests that the substrate may block the access of the required proton to the active site.

The binuclear iron center in Δ^9 desaturase has also been characterized by ENDOR spectroscopy [356]. ^1H ENDOR measurements imply that each iron in the diferric enzyme has a terminal water ligand. In general, ENDOR data indicate that diferric, i.e., cryoreduced mixed-valent Δ^9 desaturase, contains a binuclear iron active site similar to that of the corresponding center in the R2 subunit of ribonucleotide reductase [270,356]. Furthermore, both non-exchangeable and exchangeable protons in D_2O were observed for the major species in a cryoreduced sample of Δ^9 desaturase–1-ACP. Similar to MMO (§2.1), the signal with the smaller hyperfine coupling constant ($A \leq 5$ MHz) has been assigned to the terminal water ligand of the Fe^{2+} ion [89], while the signal with the larger hyperfine coupling constant ($A \leq 16$ – 17 MHz) and low g anisotropy is consistent with a terminal water ligand on the Fe^{3+} . ^{14}N ENDOR studies (Fig. 25) of cryoreduced Δ^9 desaturase with and without substrate analogs have allowed the identification of two nitrogen-based ligands (His146 and His232), one coordinated to Fe^{3+} ($A_{\text{max}} = 9.1$ MHz) and the other to Fe^{2+} ($A_{\text{max}} = 3.34$ MHz) [356]. In summary, EPR spectroscopic data are consistent with the hypothesis that substrate binding to Δ^9 desaturase prevents solvent access to the iron active site.

4.3. Mechanistic Implications

Spectroscopic, crystallographic, and kinetic isotope effect studies have contributed to the elucidation of the molecular mechanism of Δ^9 desaturase. Substrate binding is required to increase the reactivity of this enzyme with dioxygen [20,244,313]. In contrast to the reduced R2 subunit of ribonucleotide reductase [218], resting diferrous Δ^9 desaturase does not react with O_2 , but its O_2 reactivity is increased by $\sim 10^4$ -fold in the presence of substrate [313]. Based on a magnetic circular dichroism study, substrate binding to the diferrous center of Δ^9 desaturase generates an additional vacant coordination site on one of the two iron centers (one Fe adopting a four-coordinate distorted tetrahedral geometry, while the other remains five-coordinate) [352]. The reaction of substrate-bound diferrous Δ^9 desaturase with dioxygen results in a blue complex, identified as a symmetric

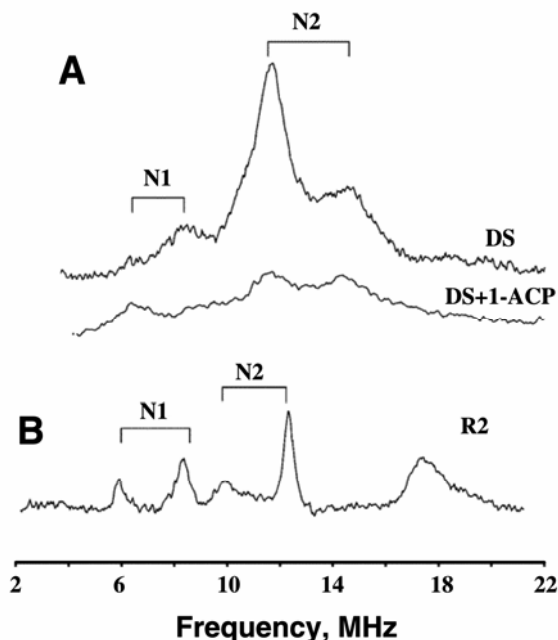


Figure 25. CW ^{15}N ENDOR (35 GHz) spectra of (A) cryoreduced Δ^9 desaturase and Δ^9 desaturase in complex with substrate 1-ACP at $g = 1.894$, and (B) cryoreduced *E. coli* R2 at $g = 1.82$. Reprinted with permission from [356]. Copyright © 2005, American Chemical Society.

μ -1,2-peroxy diferric intermediate by Mössbauer and Raman studies [313]. This intermediate is very similar to the peroxo intermediates formed in the ribonucleotide reductase R2 mutants Trp48Phe/Asp84Glu and Asp84Glu, is exceptionally stable at room temperature ($t_{1/2}$ of ≈ 26 min), and has been proposed to be formed immediately prior to O–O bond cleavage [309]. The fate of the peroxodiferric intermediate is not fully established and may entail a direct H-atom abstraction from the substrate, or, alternatively, a homo- or heterolytic cleavage of the O–O bond to yield a high-valent iron intermediate that initiates desaturation [244]. Studies using substrate analogs (acyloxy-ACPs) have implied that desaturation may possibly be initiated by H-abstraction on the C-10 position of the substrate [365,366]. While the precise molecular details of the catalytic mechanism of Δ^9 desaturase still await elucidation, resonance Raman studies have indicated that, in contrast to the oxidized R2 subunit of ribonucleotide reductase, ^{18}O -labeled oxygen atoms are not incorporated into the μ -oxo bridge linking the two Fe^{3+} ions in Δ^9 desaturase [364]. This suggests that the reaction mechanism of O–O bond cleavage in these two enzymes may differ.

It is interesting to note that chemically reduced Δ^9 desaturase acts as an oxidase while the enzymatically reduced enzyme (using ferredoxin reductase and [2Fe–2S] ferredoxin) is able to carry out desaturation reactions [313]. Thus, the active site of Δ^9 desaturase is able to partition two distinct pathways involving oxidase and desaturation chemistry, possibly as a result of specific conformational and redox state changes in the diiron cluster. Fluorescence anisotropy techniques have been used to probe the binding interactions between Δ^9 desaturase and its substrate, and kinetic studies have shown that the length of the acyl chain of the substrate directly correlates with the stability of the enzyme–substrate complex [354]. Chemical crosslinking and kinetic studies have also been used to investigate the protein–protein interactions between Δ^9 desaturase and [2Fe–2S] ferredoxin in the catalytic complex [357]. Only one binding site for ferredoxin was identified on the surface of Δ^9 desaturase, which suggests that the two required electrons for catalysis are provided by two ferredoxin molecules, which in turn must bind successively, resulting in two single electron transfer steps.

5. MYO-INOSITOL OXYGENASE

5.1. Biochemical and Structural Characterization

Myo-inositol oxygenase (MIOX) catalyzes the first step in the metabolic pathway of *myo*-inositol to form D-glucuronate (Table 1) [367–370]. MIOX was first identified as an iron-containing enzyme several decades ago, and kinetic characterization focused on the proteins isolated from porcine and hog kidneys [368,371,372]. Meanwhile MIOX from several different mammalian sources including pig, mouse, rat, and human kidney has been cloned and expressed in *E. coli* [373,374]. Sequence analysis reveals that MIOX from these organisms is highly conserved, with a molecular weight of 33 kDa [375].

MIOX has been classified both as an oxygenase and an oxidase, and the enzyme is often referred to as an internal monooxygenase, intramolecular mixed-function oxidase or renal-specific oxidoreductase [376,377]. At least in humans the four-electron oxidation reaction catalyzed by MIOX takes place primarily in kidneys and is the only known pathway for *myo*-inositol catabolism [375,378]. D-glucuronate subsequently undergoes several different steps before it reaches the pentose phosphate cycle [379]. MIOX regulates inositol levels *in vivo*, and the catabolism of *myo*-inositol is an important process since this molecule constitutes the sugar backbone of the phosphoinositide signaling molecules [373]. It has been speculated that impairment of MIOX activity contributes to the development of a number of disorders in patients suffering from diabetes mellitus, including diabetic neuropathy, retinopathy, nephropathy, infantile respiratory distress, and peripheral arterial disease [380–384]. Since MIOX expression levels and its activity are increased in tissues with diabetic complications, the enzyme has become an important target for drug design and development [385].

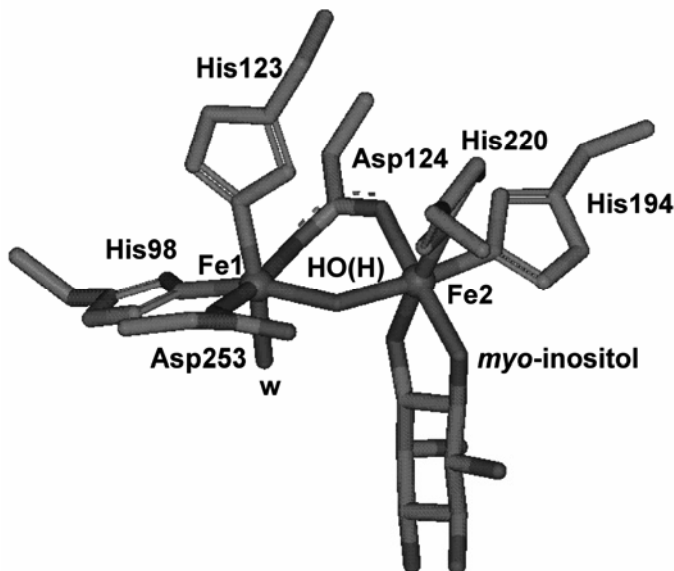


Figure 26. Active site structure of *myo*-inositol oxygenase (MIOX) from *Mus musculus* (PDB code 2HUO).

Mouse MIOX has recently been crystallized in the fully oxidized form, and its structure has been solved to 2.0 Å resolution in the presence of its substrate *myo*-inositol [386]. The two ferric ions are doubly bridged by a carboxylate from Asp124 and a water/hydroxide molecule. Both ferric ions display a distorted octahedral geometry, with the Fe1 also coordinated by His98, His123, Asp253, and a solvent molecule, and the Fe2 coordination environment completed by His194, His220, and two oxygen atoms of the *myo*-inositol substrate (Fig. 26). An interesting feature of this crystal structure is the bidentate binding mode of substrate to only one ferric ion, which is of mechanistic relevance for the catalytic cycle of MIOX (*vide infra*).

5.2. Spectroscopic Characterization of MIOX

Recombinant MIOX from *Mus musculus* kidney was recently subjected to a detailed spectroscopic and kinetic characterization. The nature of the iron active site in the presence and absence of substrate *myo*-inositol was examined using both EPR and Mössbauer methodologies [387]. The outcome of this study has not only confirmed that MIOX contains a binuclear non-heme iron center, but also that its diiron cluster is stable in its mixed-valent form and the fully oxidized state. Specifically, the low-temperature X-band EPR spectrum of fully reduced, diferrous MIOX reveals a $g_{\text{eff}} = 16$ resonance that disappears upon sample exposure to O_2 , consistent with a conversion of the diferrous center to its mixed-valent form. The

$g_{\text{eff}} = 16$ EPR signal is similar to that of reduced MMOH (§2.1, Fig. 5), indicating that the two Fe^{2+} ions are weakly ferromagnetically coupled, producing an $S_{\text{tot}} = 4$ ground state. The mixed-valent form of MIOX can readily be generated in vitro in the presence of limiting amounts of O_2 and the reductant, and its low-temperature X-band EPR spectrum is characterized by a broad axial feature with $g_{\parallel} = 1.95$ and $g_{\perp} = 1.66$ [387], indicative of antiferromagnetically coupled high-spin Fe^{3+} ($S = 5/2$) and a high-spin Fe^{2+} ($S = 2$), generating an $S_{\text{tot}} = 1/2$ ground state (Fig. 4). From the temperature dependence of the EPR resonances and the significant g strain, the presence of a μ -OH-bridge can be deduced (the presence of different diiron clusters with different spin-Hamiltonian parameters did not allow for exact determination of the exchange coupling constant in MIOX samples). Furthermore, Mössbauer parameters obtained for mixed-valent MIOX are similar to those reported for other binuclear non-heme iron enzymes such as MMO and ribonucleotide reductase [70,286].

A significant change in the EPR spectrum of mixed-valent MIOX is observed upon addition of the substrate *myo*-inositol, yielding a different axially symmetric signal ($g_{\parallel} = 1.95$ and $g_{\perp} = 1.81$) with smaller g anisotropy and more narrow linewidth [387]. Interestingly, the substrate-induced changes observed in MIOX are opposite to those observed for the Fe^{3+} - Fe^{2+} purple acid phosphatase (PAP) from pig uterine fluid, where binding of the substrate analog phosphate increases g anisotropy and broadens the linewidth. Furthermore, the magnitude of the exchange coupling constant between the iron centers in PAP is reduced from -10 to -3 cm^{-1} ($\mathcal{H}_{\text{ex}} = -2JS_1 \cdot S_2$) upon addition of phosphate [388,389]. In MIOX, it thus seems likely that substrate binding may lead to increased exchange coupling between the two metal ions. Two possible models have been proposed involving either a conformational change in the vicinity of the diiron center or a direct substrate coordination to the metal ions [387]. The latter scheme was proposed in analogy to PAPs, where the substrate analog phosphate coordinates in μ -1,3 fashion to both metal ions [390]. The different effect of substrate binding on the exchange coupling was rationalized by speculating that in MIOX the metal ions are linked via an additional μ -alkoxide bridge, which may provide a more efficient superexchange pathway. However, in the recently reported structure of mouse MIOX with bound *myo*-inositol, no μ -alkoxide bridge was apparent; instead, the substrate binds bidentately to only one of the metal ions [386].

Substrate binding also affects the electronic structure of the fully oxidized diferric form of MIOX. Mössbauer spectroscopic data reveal the presence of two antiferromagnetically coupled high-spin Fe^{3+} ions with a diamagnetic $S_{\text{tot}} = 0$ ground state [387]. The addition of *myo*-inositol to the diferric enzyme perturbs the iron active site, but the binding mode is unknown.

EPR spectroscopy in combination with stopped-flow absorption and rapid freeze-quench techniques has been employed (i) to probe the catalytically relevant oxidation state(s) of MIOX and (ii) to investigate the reaction between MIOX, substrate, and O_2 . While most other oxygen-activating binuclear non-heme iron enzymes are catalytically active in their fully reduced form, MIOX exhibits a rather different behavior. In single-turnover reactions of the diferrous recombinant *Mus*

musculus kidney, MIOX–*myo*-inositol complex with limiting amounts of O₂ stable mixed-valent complexes with an axial EPR spectrum ($g_{\parallel} = 1.95$ and $g_{\perp} = 1.81$) were formed [391]. Spin quantitation of this EPR signal demonstrated a stoichiometric conversion of diferrous MIOX to its mixed-valent form. Since it was not possible to regenerate the reduced enzyme, it was concluded that the diferrous form of MIOX is not a catalytically relevant species.

Similarly, the catalytic competence of the diferric form of recombinant *M. musculus* kidney MIOX was probed both by EPR and Mössbauer spectroscopy and kinetic studies [391]. Diferric MIOX exhibits very low activity (<2% of the maximum activity), but is fully active upon treatment with reductants such as L-Cys or ascorbate, which results in the mixed-valent form. In addition, since substrate binding to diferric MIOX was found to be slow and weak, it was concluded that the fully oxidized enzyme was also not a catalytically relevant species.

The reaction of the mixed-valent MIOX–*myo*-inositol complex with limiting amounts of O₂ was monitored by rapid freeze-quench EPR [391]. An analysis of samples obtained after various time intervals (Fig. 27) has shown that the mixed-valent MIOX–substrate complex reacts rapidly with dioxygen and the mixed-valent state is regenerated at the end of the reaction. Two transient intermediates were detected, trapped, and characterized: (i) an initial precursor intermediate, labeled **G**, which decays to a second intermediate, denoted **H** with a rhombic EPR spectrum ($g < 2$) [391,392]. Deuterated substrates are necessary to observe and trap intermediate **G** since it is formed rapidly (within 25 ms); it is characterized by a rhombic EPR signal with g values of 2.05, 1.98, and 1.90, consistent with an $S_{\text{tot}} = 1/2$ spin system (Fig. 4). An analysis by EPR of the ⁵⁷Fe-enriched intermediate **G** shows hyperfine coupling to an $I = 1/2$ nuclei, thus suggesting the nature of this intermediate species to be some kind of an iron complex, possibly a (superoxo)diiron(III/III) complex [392].

Recent ²H ENDOR data were interpreted in terms of substrate binding to the Fe³⁺–Fe²⁺ center of recombinant *Mus musculus* kidney MIOX via a bridging alkoxide [393]. However, the crystal structure of mouse MIOX indicates quite a different binding mode for the substrate *myo*-inositol, as discussed above [386].

5.3. Mechanistic Implications

Recent kinetic and spectroscopic characterization of MIOX has greatly contributed toward an understanding of the reaction mechanism of the glycol-cleavage reaction. While MIOX belongs to the class of binuclear non-heme iron oxygenases/oxidases, the observation that the resting mixed-valent Fe³⁺–Fe²⁺ oxidation state is catalytically relevant implies that the reaction mechanism employed by MIOX is different from that proposed for other diiron oxygenases (i.e., where the full reduced Fe²⁺–Fe²⁺ state is catalytically relevant binding and activating O₂ [244]). However, currently it is believed that mixed-valent MIOX cannot promote O–O bond cleavage, thus making this enzyme a unique member among the

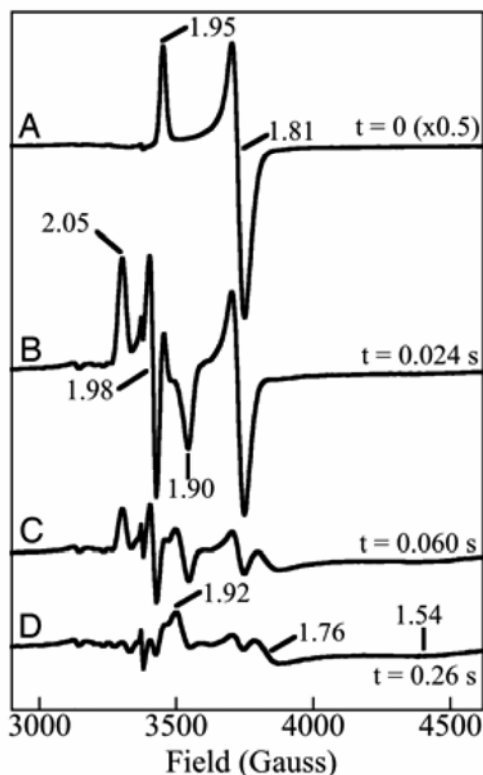


Figure 27. Low-temperature (10 K) X-band EPR spectra of samples generated by reaction of Fe^{2+} - Fe^{3+} -MIOX-substrate complex with dioxygen. Samples were quenched at shown time intervals. EPR resonances belonging to intermediates **G** and **H** are shown in B and D, respectively. Adapted with permission from [392]. Copyright © 2006, National Academy of Sciences, USA.

non-heme diiron-containing enzymes. It seems that the mechanism employed by MIOX lies between a standard reaction mechanism involving superoxo- Fe^{3+} species and a mechanism used by binuclear hydrolytic enzymes (§9). The role of the Fe^{3+} center in MIOX is likely to be similar to that of the trivalent metal ion in PAPs, i.e., to use its Lewis acidity to facilitate ionization of the hydroxyl group on C1 atom of substrate MI. The formation of a bridging alkoxide would thus be able to activate and catalyze the C1-H bond cleavage.

MIOX catalyzes a four-electron oxidation reaction, and a recently proposed mechanism for O_2 activation based on kinetic and spectroscopic data is shown in Figure 28 [386,391]. While substrate MI is believed to coordinate directly to the Fe^{3+} - Fe^{2+} cluster in the bridging mode based on the EPR and Mössbauer studies

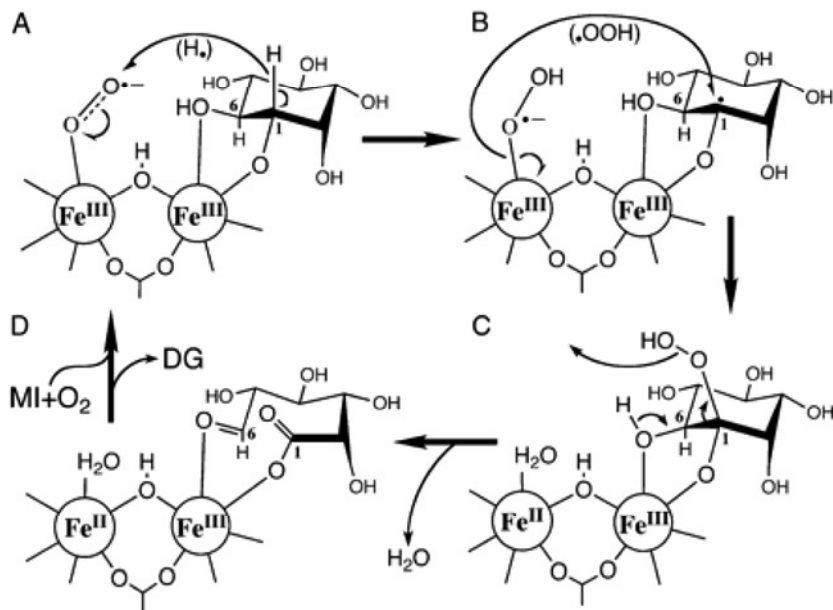


Figure 28. Proposed reaction mechanism for *myo*-inositol oxygenase-catalyzed reaction. Reprinted with permission from [386]. Copyright © 2006, National Academy of Sciences, USA.

[387,393], this μ -alkoxide bridge is anticipated to facilitate the ionization of the C1 hydroxy group and result in O_2 binding to the Fe^{2+} center of the mixed-valence MIOX–MI complex. However, an alternative mode of substrate binding (bidentate coordination to only one ferric ion), as suggested by the crystal structure of the MIOX–substrate complex [386], has significant implications for the catalytic mechanism of MIOX, activating the substrate for attack and tuning the reactivity of the diiron cluster for dioxygen binding and activation. While the Fe^{2+} site binds the substrate, binding of O_2 is proposed to occur on the Fe^{3+} site via displacement of the solvent ligand on this iron, thus leading to the formation of the proposed (superoxo)diferric complex. This superoxo complex is likely to activate C1–H bond cleavage in the substrate, and the H-atom abstraction from C1 would form a radical species that then generates a hydroperoxo- Fe^{3+} – Fe^{3+} complex. Subsequently, the hydroperoxo species interacts with the substrate C1 radical (hydroperoxyl-radical rebound step), leading to formation of the 1-hydroperoxy-substrate intermediate that has been invoked in earlier studies using kinetic deuterium and tritium isotope effect measurements [394]. Finally, complete mechanistic understanding of MIOX necessitates further spectroscopic investigations of the diiron center during various steps of the catalytic cycle.

6. RUBRERYTHRIN, NIGERYTHRIN AND SULERYTHRIN

6.1. Rubrerythrin

6.1.1. Biochemical and Structural Characterization

Rubrerythrin has been identified in various anaerobic and microaerophilic bacteria and archaea, and was initially isolated from *Desulfovibrio vulgaris*, an anaerobic sulfate-reducing bacterium [395–398]. The *D. vulgaris* enzyme is a 44-kDa homodimer and catalyzes the peroxidation of NADH [396,399–402] (Table 1). Although the precise physiological roles of rubrerythrin are still uncertain, several functions have been proposed, including a protective role against oxidative stress, a role in iron metabolism, per- and ferr-oxidase activity, as well as pyrophosphatase activity [395,400,402–407]. Reduced rubrerythrin reacts very rapidly with H_2O_2 (millisecond timescale) [395], but in contrast to MMO or ribonucleotide reductase, its reactivity with dioxygen is rather slow (minute timescale) [399].

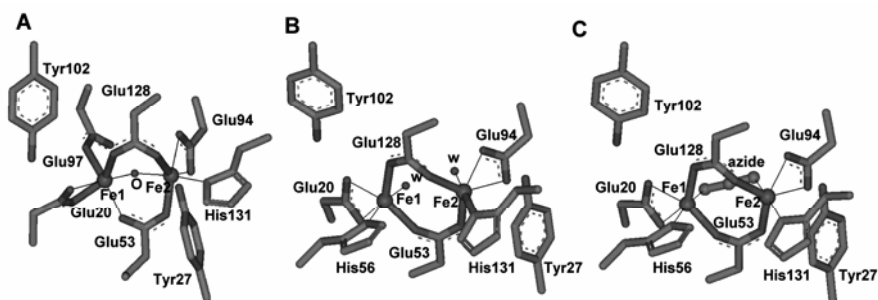


Figure 29. Active site structure of rubrerythrin from *Desulfovibrio vulgaris*: (A) oxidized rubrerythrin (PDB code 1LKM), (B) reduced rubrerythrin (PDB code 1LKO), and (C) reduced rubrerythrin complexed with azide (PDB code 1LKP).

Apart from a binuclear non-heme iron center, rubrerythrin also contains a rubredoxin-like $[\text{Fe}(\text{SCys})_4]$ site. The presence of the conserved iron-binding sequence motif also observed in other oxygenases indicates that rubrerythrin is likely to possess a diiron active site similar to those of MMO and ribonucleotide reductase [408,409] (Figs. 2 and 15). Fully oxidized rubrerythrin contains a four-helix bundle (similar to that observed in ferritin and bacterioferritin; §7), and the diiron active site is located within this bundle [409]. The two Fe^{3+} ions are six-coordinate in a distorted octahedral environment (Fig. 29A). They are bridged by two carboxylates, from Glu53 and Glu128, and a μ -oxo ligand. The coordination of Fe1 is completed by the bidentate Glu20 and a terminal carboxylate from Glu97, whereas a bidentate carboxylate from Glu94 and His131 are coordinated to Fe2. Thus, there are no vacant coordination sites on either Fe^{3+} site of oxidized rubrerythrin for O_2 binding. Furthermore, in contrast to other O_2 -activating enzymes such as MMO

and ribonucleotide reductase, oxidized rubrerythrin has only one histidine residue directly coordinated to one of the iron centers, and its diiron active site is rather solvent accessible.

The crystal structures of reduced rubrerythrin and its complex with azide have also been solved (Figs. 29B,C) [410]. The Fe^{2+} sites of the resting diferrous center exhibit a pseudo-octahedral geometry and are also bridged by the carboxylate groups from Glu53 and Glu128 (Fig. 29B). But, in contrast to the oxidized form, both iron centers are coordinated by a bidentate Glu, one His residue, and a water molecule. In essence, the reduction of the binuclear center leads to a 1.8 Å shift of Fe1 toward His56, which is not a ligand in oxidized rubrerythrin. Hence, His56 replaces Glu97 as a ligand of the Fe1 ion in reduced rubrerythrin, making the binuclear center symmetric (Fig. 29B). The azide replaces two water molecules in reduced rubrerythrin and coordinates to the two ferrous ions in a bridging μ -1,3 mode (Fig. 29C).

Finally, due to partial reduction of the diiron site during x-ray data collection, two distinct mixed-valent cores have been characterized in the crystal structures of oxidized rubrerythrin, where the iron in the rubredoxin-like $[\text{Fe}(\text{SCys})_4]$ site has been replaced by zinc [411]. In both structures, the Fe^{2+} center displays a four-coordinate geometry, and the bridging ligation differs, with two bridging carboxylates and a μ -OH bridge in one form, and only two bridging carboxylates in the other (in the latter the hydroxide is terminally bound to the Fe^{3+} ion). It has been suggested that the two mixed-valent forms represent relevant structures during the peroxidation reaction catalyzed by rubrerythrin.

6.1.2. Spectroscopic Characterization of Rubrerythrin

An initial EPR study of rubrerythrin reported a predominantly EPR-silent species, indicating the presence of two antiferromagnetically coupled Fe^{3+} centers resulting in a diamagnetic ($S = 0$) ground state [396]. Resonances with g_{eff} values of 9.4 and 4.3 ($E/D = 0.26$) were assigned to the mononuclear high-spin ferric iron ($S = 5/2$) in the rhombic environment of the rubredoxin-like FeS_4 site (resonances at $g_{\text{eff}} = 9.4$ and 4.3 are due to transitions within the ground state and first excited state Kramers doublets, respectively). Furthermore, a weak EPR signal at $g < 2$ was also observed (g values at 1.98, 1.76, and 1.57), indicating a small proportion of mixed-valent $\text{Fe}^{3+}\text{-Fe}^{2+}$ binuclear centers, similar to those observed in MMO (§2.1) [396].

A more detailed spectroscopic characterization of the diiron active site of rubrerythrin was carried out using the recombinant enzyme expressed in *E. coli*, as well as a truncated form of the enzyme, lacking the rubredoxin-like site ("chopped" rubrerythrin) [412]. The midpoint potential for the rubredoxin-like center of recombinant rubrerythrin was determined to be +260 mV, measured from EPR-monitored redox titrations [412]. In addition, the midpoint potentials for $\text{Fe}^{3+}\text{-Fe}^{3+}/\text{Fe}^{3+}\text{-Fe}^{2+}$ and $\text{Fe}^{3+}\text{-Fe}^{2+}/\text{Fe}^{2+}\text{-Fe}^{2+}$ redox couples were estimated to be +286 and +222 mV, respectively.

Parallel mode EPR spectra of reduced recombinant and “chopped” rubrerythrin exhibit a very weak signal at $g_{\text{eff}} \approx 16$. The subsequent addition of azide leads to more intense EPR spectra with $g_{\text{eff}} \approx 19.8$ and $g_{\text{eff}} \approx 17.5$ for the recombinant and “chopped” enzymes, respectively [412]. These integer-spin EPR signals are consistent with the two Fe^{2+} centers ($S = 2$) of rubrerythrin being ferromagnetically coupled producing an $S_{\text{tot}} = 4$ ground state spin system.

The mixed-valent form of recombinant rubrerythrin generated by chemical reduction with dithiothreitol has also been investigated by cwEPR and pulsed ENDOR spectroscopy. As pointed out above, up to 25% of isolated rubrerythrin contains mixed-valent binuclear centers with EPR resonances at $g < 2$ resulting from the $S = 1/2$ ground state. The exchange interaction between the Fe^{3+} and Fe^{2+} ions was evaluated by a power saturation analysis of the X-band EPR spectrum, indicating weak antiferromagnetic coupling with $J \sim 8 \text{ cm}^{-1}$ ($\mathcal{H}_{\text{ex}} = -2JS_1 \cdot S_2$) [413]. The magnitude of the exchange coupling constant has been interpreted in terms of the presence of a μ -hydroxide bridge, similar to mixed-valent MMO [51,413] (§2.1). A ^{14}N ENDOR study of mixed-valent rubrerythrin identifies a single nitrogen atom with a hyperfine coupling constant of $\sim 6 \text{ MHz}$ as ligand of the Fe^{2+} center. This nitrogen atom has been ascribed to His131. Thus, in contrast to x-ray crystallography, ENDOR facilitates an unambiguous assignment of the Fe^{3+} and Fe^{2+} ions to their respective sites in the binuclear center.

^1H ENDOR spectroscopy of mixed-valent rubrerythrin was also carried out, revealing a strongly coupled proton ($A_{\text{max}} = 25 \text{ MHz}$) that was exchangeable in D_2O and can be assigned to either a terminal water/hydroxide ligand of the Fe^{3+} or a bridging ligand between the two irons [300]. In an attempt to distinguish between these two possibilities, two-dimensional field-frequency features of the ^1H ENDOR spectra were examined, supporting an assignment of the exchangeable proton to the bridging μ -OH ligand (Fig. 30) [413].

The structure of the diferric center of rubrerythrin was probed by cryoreducing the fully oxidized enzyme to the mixed-valent form at 77 K. The resulting EPR spectrum of the cryoreduced sample was essentially indistinguishable from that obtained from the chemically reduced sample, indicating that one-electron reduction of the oxidized enzyme does not lead to significant structural changes [413]. The main difference between the two oxidation states is the presence of a μ -oxo or a μ -hydroxo bridge in the fully oxidized or mixed-valent forms, respectively [409].

6.1.3. Mechanistic Insights

Combined spectroscopic, structural, and kinetic data have led to the proposal of the following reaction mechanism for rubrerythrin-catalyzed peroxidation [410]. In the initial phase H_2O_2 enters the active site and displaces the solvent molecules coordinated to the ferrous ions, leading to formation of a *cis* μ - η^2 diferrous-hydroperoxo adduct. In the second step O–O bond cleavage occurs with concomitant transfer of two electrons from the two Fe^{2+} ions to the hydroperoxo species. Subsequently, proton transfer and release of a water molecule result in the

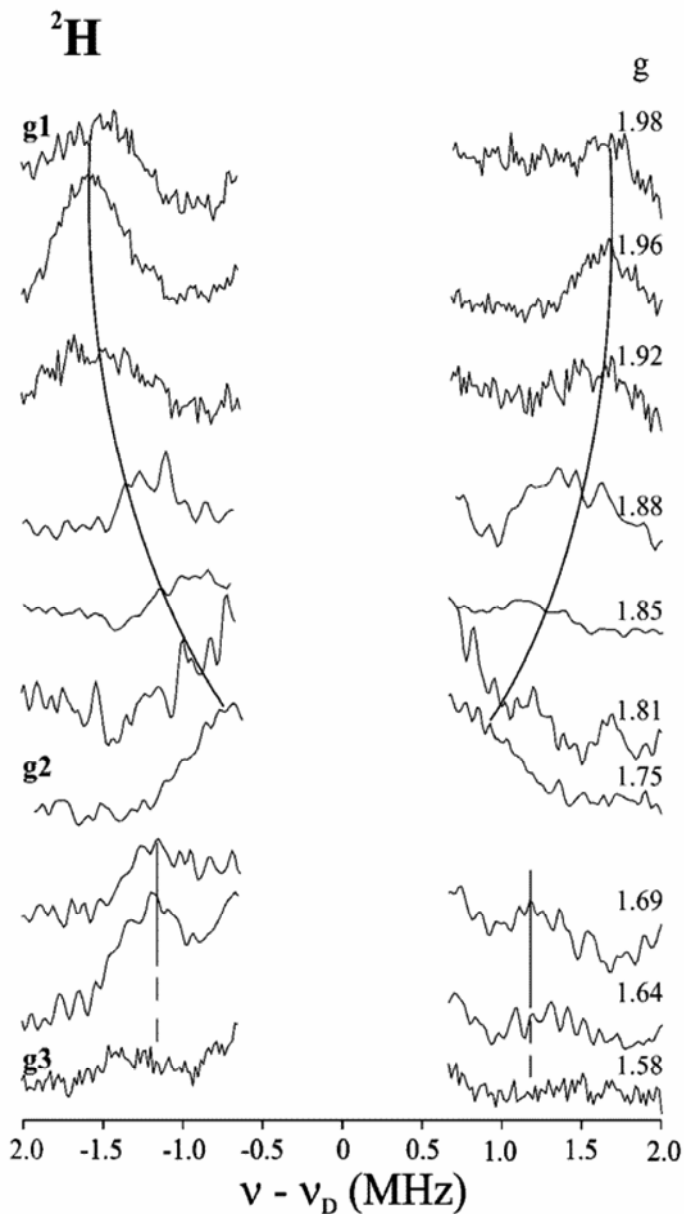


Figure 30. ^2H pulsed ENDOR spectra of mixed-valence rubrerythrin from *Desulfovibrio vulgaris* in D_2O . Reprinted with permission from [413]. Copyright © 2003, American Chemical Society.

formation of the μ -oxo bridged diferric active site. Stopped-flow kinetic evidence suggests that the intramolecular electron transfer from the rubredoxin-like site to the diiron active site occurs prior to formation of the μ -oxo bridged diferric structure [410]. It is speculated that the formation of the μ - η^2 diferrous-hydroperoxo adduct mediates the concerted process of two-electron transfer (one from each Fe^{2+}) to the hydroperoxo species, and is also considered to provide a protective role from oxidative damage caused by Fenton chemistry. The two tyrosine residues in the vicinity of the diiron active site (*vide supra*) have also been proposed to play an important role in the protection of rubrerythrin against damaging hydroxyl radicals that may be generated from one-electron reduction of H_2O_2 [410].

6.2. Nigerythrin

6.2.1. Biochemical and Structural Characterization

Nigerythrin from *D. vulgaris* is closely related to rubrerythrin. A comparison of the amino acid sequences of the two enzymes indicates 33% sequence identity, suggesting that the two enzymes have similar structures (all the iron-coordinating residues to both the non-heme diiron center and FeS_4 are conserved in both enzymes) and functions [414–416]. Nigerythrin is a soluble protein and is found in the cytoplasm, and it does not exhibit any of the activities (i.e., oxygenations, hydroxylations, desaturations, as well as phosphatase or catalase activities) usually found in the diiron-containing oxygen-activating proteins [412,414,415]. The physiological role of nigererythrin is yet to be determined, but roles similar to those proposed for rubrerythrin have been proposed, including the regulation of iron homeostasis and iron metabolism, including a role in the protection against oxidative stress via removing or supplying iron to $[\text{4Fe-4S}]$ proteins [415].

The iron-binding motif observed in rubrerythrin, MMO, and the R2 subunit of ribonucleotide reductase is fully conserved and, like rubrerythrin, nigererythrin exists as a homodimer. The structural similarity between the two enzymes from *D. vulgaris* has recently been confirmed crystallographically [416]. With only a few minor exceptions, their overall structures are identical, containing a four-helix bundle that houses the diiron center and the rubredoxin-like C-terminal domain with a mononuclear $[\text{Fe}(\text{SCys})_4]$ site. However, while the rubredoxin-like domain and the four-helix bundle are perpendicular to each other in rubrerythrin, they are approximately parallel in nigerythrin (the distance between the diiron center and the $[\text{Fe}(\text{SCys})_4]$ site is approximately 12–14 Å). During the collection of synchrotron x-ray diffraction data it was found that the binuclear iron center was partially reduced to the mixed-valent form and the diffraction data were modeled accordingly. In the mixed-valent form of nigerythrin the two iron centers are six-coordinate and are bridged by either a hydroxo or a water ligand, and two carboxylates from glutamate residues (Glu73 and Glu149) (Fig. 31A). The coordination of the Fe1 center is completed by the terminal bidentate Glu40 and a carboxylate oxygen from Glu118, while His152 and the bidentate Glu115 complete the coordination

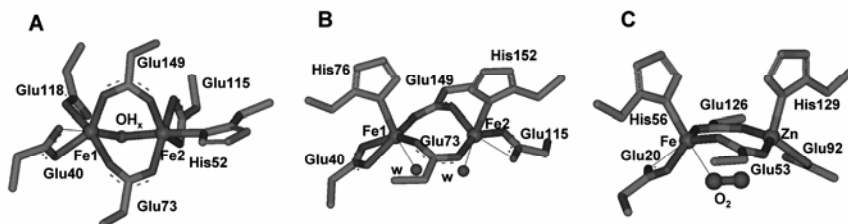


Figure 31. Active site structures of (A) mixed-valence nigerythrin from *Desulfovibrio vulgaris* (PDB code 1YUX), (B) reduced nigerythrin from *Desulfovibrio vulgaris* (PDB code 1YV1), and (C) Fe³⁺/Zn²⁺ sulerythrin from *Sulfolobus tokadaii* strain 7 (PDB code 1J30).

environment of the Fe2 center [416]. In the diferrous form, the two iron centers retain their six-coordinate environments (Fig. 31B), but instead of the bridging solvent ligand, each iron center now contains a terminally bound water ligand. Furthermore, in comparison to mixed-valent nigerythrin, the carboxylate oxygen Fe1 ligand from Glu118 is replaced by a nitrogen atom from His76 in the fully reduced form [416]. A similar switching between Glu and His coordination in one of the iron centers has also been observed in rubrerythrin upon conversion from the diferric to the fully reduced form [410] (Figs. 29A,B). This so-called “redox-induced toggling” of one iron site is a characteristic structural feature of this family of proteins, and may be an important factor in governing their reactivity. An additional structural feature common to both enzymes is the presence of two conserved tyrosine residues in the second coordination sphere of the diiron center. It has been speculated that a role of these Tyr residues may be the scavenging of free radicals as a way of preventing Fenton-type chemistry in the presence of hydrogen peroxide [410,416].

6.2.2. Spectroscopic Characterization of Nigerythrin

The diiron center of nigerythrin has been studied by absorption and EPR spectroscopy [414]. The low-temperature EPR spectrum showed three resonances at $g < 2$ ($g_{av} = 1.74$), consistent with two antiferromagnetically coupled irons (Fe³⁺ with $S = 5/2$ and Fe²⁺ with $S = 2$), yielding an $S_{tot} = 1/2$ spin ground state. The spectrum is reminiscent of those observed for mixed-valent MMO (§2) and hemerythrin (§8) [80,81]. EPR spectroscopy was also used to determine the redox potentials of the non-heme diiron center and the mononuclear iron of the FeS₄ site in nigerythrin, which were found to be $> +200$ mV.

6.2.3. Mechanistic Insights

The mechanistic details of the nigerythrin-catalyzed reaction, and in particular the molecular basis for its preference for hydrogen peroxide as substrate, are not yet established. A mechanism has recently been proposed for the peroxidation re-

action catalyzed by nigerythrin [416]. The proposed mechanistic scheme is similar to the one proposed for rubrerythrin (*vide supra*) [410]. Specifically, the reaction of H_2O_2 with diferrous nigerythrin leads to the formation of the diferric μ -1,2-hydrogen peroxide intermediate, and it is speculated, based on computational studies, that electrons are transferred from the ferrous FeS_4 rubredoxin-like site to the ferric Fe_2 of the diiron cluster via a network involving the “through-bond” electron transfer pathway [417].

6.3. Sulerythrin

Sulerythrin is a novel member of the family of non-heme iron proteins, and has recently been isolated from a strictly aerobic and thermoacidophilic archaeon, *Sulfolobus tokodaii* strain 7 [418,419]. Sulerythrin belongs to the family of rubrerythrin-like proteins, but unlike rubrerythrin or nigerythrin, it lacks the C-terminal, rubredoxin-like FeS_4 domain. However, sulerythrin also exists as a homodimer (16 kDa), but is the only rubrerythrin-like protein so far isolated from an aerobic organism [419]. The biological role(s) of sulerythrin is not yet established. Since all the iron-coordinating residues present in rubrerythrin and nigerythrin are also highly conserved in sulerythrin, it is implied that the latter has a binuclear non-heme iron center similar to those observed in the former. However, while the identity of the *in-vivo* metal ions is still a matter of contention, metal ion analysis indicates the presence of a binuclear $Fe-Zn$ center [419].

Sulerythrin has not yet been the subject of spectroscopic investigations, but its crystal structure in the oxidized form shows a similar four-helix bundle domain, as the one found in rubrerythrin and nigerythrin, with the “head-to-head” configuration of the two dimers relative to each other [409,420]. The unique feature of sulerythrin is the “domain-swapped” structure (two helices of one chain form a hybrid four-helix bundle with two other helices from a different chain) of the subunits of the homodimer, which may lead to limited flexibility of the metal centers, thus regulating the enzyme’s specific function. The crystal structure also supports the presence of an asymmetric binuclear $Fe^{3+}-Zn^{2+}$ center where the iron and zinc ions are μ -1,3-bridged by two carboxylates from Glu53 and Glu126 (Fig. 31C). The Fe^{3+} has a distorted octahedral geometry, and its coordination is completed by a nitrogen atom from His56, the bidentate Glu20, and an oxygen atom from O_2 , while Zn^{2+} has a tetrahedral geometry and is also coordinated by His129 and Glu92. Interestingly, a comparison between the active sites of sulerythrin and the $Fe-Zn$ derivative of rubrerythrin shows that the metal sites are switched in the two proteins, i.e., the Fe binding site in sulerythrin corresponds to the Zn site in rubrerythrin and vice versa [420,421].

7. FERRITINS AND BACTERIOFERRITINS

7.1. Biochemical and Structural Characterization

Ferritins and bacterioferritins constitute a large family of ubiquitous iron storage proteins that are responsible for the oxidation of Fe^{2+} to Fe^{3+} , and the reversible

sequestering of iron in a mineral form for later use by the cells (Table 1). They occur in most organisms, including vertebrates and invertebrates, plants, aerobic and anaerobic bacteria, archaea, and mammalian organisms [422–426]. Apart from their essential role in iron storage, homeostasis, and metabolism, (bacterio)ferritins are important for detoxification processes [427,428]. The biological importance of ferritins is demonstrated by the observation that the deletion of ferritin-encoding genes is lethal for mammals, while in bacteria the lack of ferritin affects their response to oxidants [429–431]. It has recently been suggested that the design of iron chelators that specifically target ferritins may be a novel avenue to battle iron-related diseases such as Cooley's anemia and thalassemia [432–435]. A thermostable ferritin from the hyperthermophilic archaeal anaerobe *Pyrococcus furiosus* has recently been isolated and characterized, and may be exploited for biotechnological applications [436].

Ferritins and bacterioferritins share distinct structural similarities (a four α -helix bundle containing a non-heme diiron center) with other binuclear non-heme iron enzymes and, in particular, are closely related to rubrerythrin [437]. Although ferritins from different sources share little sequence similarity (~15%), their overall structures are highly conserved [438,439]. Bacterial and plant ferritins generally consist of 24 identical subunits, whereas mammalian ferritins exist as assemblies of 24 subunits, 12 of H and 12 of L type, with molecular weights of ~21 and ~19.5 kDa, respectively, and ~55% amino acid sequence identity between them [423,440]. These 24 subunits form a large hollow protein sphere or cavity with an outer and inner diameter of ~125 and ~80 Å, respectively, and which can bind and encapsulate up to 4500 iron atoms in the form of a hydrated ferric oxide mineral core [423,425]. Some prokaryotes possess a smaller type of ferritin; for example, the protein isolated from *Listeria innocua* consists of only 12 identical 18-kDa subunits and can accommodate approximately 500 iron atoms [441–445]. Ferritins with 12 subunits are also described as “mini-ferritins,” in contrast to the 24-subunit “maxi-ferritins” [446]. Lastly, bacterioferritins, which are only found in fungi and bacteria, are distinguished from ferritins due to the presence of an additional heme group [436]. Bacterioferritins contain 3–12 iron heme groups per 24 subunits, but their function is not yet fully established [423,426,447]. There are suggestions that they may be important in mediation of the electron transfer during reduction and iron release [445].

Crystal structures for a number of ferritins and bacterioferritins from different sources have become available, and have recently been reviewed [448]. These structures include those for ferritins from horse spleen, bullfrog, the H subunit and the mitochondrial form from human, the L subunits from horse and mouse, as well as for bacterioferritin from *E. coli*, *Rhodobacter capsulatus*, and *D. desulfuricans* ATCC 27774 [433,447,449–462]. In addition, the crystal structures of ferritins from the halophile *Halobacterium salinarium*, from *S. solfataricus*, from the hyperthermophilic archaeon *Archaeoglobus fulgidus*, and from *Azotobacter vinelandii* have recently been solved [463–467]. Each ferritin subunit independent of source and type is folded into a characteristic four α -helix bundle (each helix ~27 Å long),

with a fifth shorter α -helix positioned at $\sim 60^\circ$ relative to the other helices [448,465]. The four-helix bundles form the hollow spherical protein cavity that can accommodate the iron atoms. The binuclear non-heme iron center also known as the “ferroxidase center,” which is necessary for catalytic iron oxidation in ferritins [468], is also located within the ferritin subunits. Its coordination environment resembles that of other diiron-containing enzymes that activate O_2 [244,446], consisting primarily of carboxylate and histidine ligands with one/two μ -1,3 carboxylate bridges.

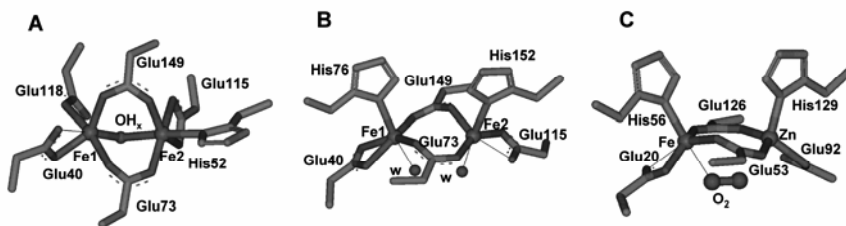


Figure 32. Active site structure of bacterioferritin (Bfr) from *Azotobacter vinelandii*: (A) oxidized Bfr (PDB code 2FL0), and (B) reduced Bfr (PDB code 2FKZ).

Three separate kinetic phases have been proposed in the overall mechanism of iron oxidation. The initial binding of Fe^{2+} to the binuclear active site is followed by a rapid oxidation of Fe^{2+} to Fe^{3+} in the presence of O_2 , and the subsequent transfer of Fe^{3+} into the ferritin core [469,470]. In mammalian ferritins, the ferroxidase active site is located within the H subunits, while the L subunits are proposed to contain a nucleation site that may be responsible for the mineralization process [471]. Despite all the efforts, there are not many high-resolution crystal structures of diferric/diferrous ferritins, and most of the structural information is based on mixed-metal derivatives of ferritins [472]. In the H subunit from human ferritin, Fe1 is coordinated by Glu27, His65, and solvent molecules, and Fe2 by Glu61 and Glu107 (this coordination environment is based upon the crystal structure with Tb^{3+} ferritin derivative) [451]. The two metal ions are bridged by a single carboxylate group from Glu62. The diiron active site of *A. vinelandii* bacterioferritin is somewhat different (Fig. 32) with the two Fe^{3+} ions being bridged by two carboxylate groups (from Glu51 and Glu127) and presumably a water molecule, although the distances between the metal ions and the bridging oxygen argue against it [466]. Both irons are five-coordinate in the fully oxidized form, with Fe1 also coordinated by Glu18 and His54, and Fe2 by Glu94 and His130 (Fig. 32A). Upon reduction, His130 ligand moves away from the Fe2 center and becomes no longer coordinated to it (Fig. 32B) [467]. Many ferritins and bacterioferritins have been crystallized in the presence of other metal ions [447,455,458,472]. Interestingly, in ferritins from *E. coli* and the archaeon *A. fulgidus*, a third binding site for iron

appears to be positioned very close to the diiron ferroxidase center [465,472]. The availability of a third binding site for iron is speculated to play an important role in the stabilization of the ferroxidase diiron center.

7.2. Spectroscopic Characterization of Ferritins and Bacterioferritins

Various aspects of ferritin and bacterioferritin reactivity, including iron incorporation by the apoenzymes, oxidation of Fe^{2+} in the presence of molecular oxygen, and the mechanism of core formation, have been investigated by an extensive number of kinetic and spectroscopic studies [468,473–487]. Early EPR studies of iron binding to horse spleen apoferritin have provided evidence for the formation of EPR silent antiferromagnetically coupled diferric species [484,488]. Formation of the μ -oxo-bridged diferric cluster was also confirmed in the recombinant H subunit of human ferritin and some of its variants [485,489]. Since NO has been implicated in the mediation of iron release from ferritins, EPR spectroscopy has also been employed to probe the effects of NO binding to several mammalian ferritins and bacterioferritins [490–493]. These studies have shown that addition of NO to diferrous ferritin generates iron-nitrosyl complexes with EPR features characteristic of both $S = 1/2$ and $S = 3/2$ spin systems. Three different EPR resonances were attributed to the presence of (i) a rhombic $S = 1/2$ species ($g_x = 2.055$, $g_y = 2.033$, and $g_z = 2.015$), (ii) an axial $S = 1/2$ species with $g_{\perp} = 2.033$ and $g_{\parallel} = 2.014$, and (iii) an $S = 3/2$ species with $g_{\text{eff}\perp} = 4$ and $g_{\text{eff}\parallel} = 2$. Although these studies could not unambiguously establish the functional role of NO in the mechanism of ferritin, they were able to identify amino acids that are important for the binding of iron in mammalian ferritins as well as formation of Fe–NO complexes (His128 and Cys130 in human ferritin).

In combination with the rapid freeze-quench methodology, EPR spectroscopy has been instrumental in the detection of reaction intermediates during the reconstitution of horse spleen ferritin from apoferritin, Fe^{2+} , and O_2 [486]. Within the first second after mixing of the reactants, a monomeric Fe^{3+} –protein complex with a characteristic resonance at $g_{\text{eff}} = 4.3$, a mixed-valent Fe^{3+} – Fe^{2+} species with a peak at $g_{\text{eff}} = 1.87$ (which accumulates quantitatively from the monomeric Fe^{3+} species), and a radical species ($g_{\parallel} = 2.042$, $g_{\perp} = 2.0033$) that may be associated with either Fe^{2+} or Fe^{3+} (whose function may potentially involve storage of the oxidizing equivalents for subsequent Fe^{2+} oxidation) have been observed.

Similarly, the oxidation of Fe^{2+} during iron core formation in recombinant human H subunit ferritin and its variants has been investigated by stopped-flow kinetics and Mössbauer spectroscopy [494]. An intermediate species, attributed to the purple Fe^{3+} –Tyr34 complex in the Fe2 site, was shown to form rapidly ($k_{\text{ox}} = 1000 \text{ s}^{-1}$) and to decay within the first 5–10 s. This Fe^{3+} –tyrosinate complex was shown to form following the rapid uptake and oxidation of Fe^{2+} , and was proposed as one of the initial steps in the fast mineralization process [474]. The oxidation of Fe^{2+} has been shown to lead to the formation of various species, including Fe^{3+} monomers, dimers, and some larger clusters. Specifically, the observed fast oxida-

tion of Fe^{2+} is also associated with the formation of diferric μ -oxo-bridged complexes in the ferroxidase center [494].

The mechanism of iron uptake by H-type recombinant frog ferritin, and the formation of reaction intermediates during the initial mineralization process, have also been investigated by rapid freeze-quench Mössbauer and EPR spectroscopies [495]. Four different types of Fe^{3+} -oxy species were identified, three of them binuclear iron centers and the fourth a trinuclear iron cluster, which ultimately decays to a superparamagnetic species (larger polynuclear ferric clusters), the so-called "young" mineral core. The two EPR signals observed ($g_{\text{eff}} = 4.3$ and $g_{\text{eff}} = 2.0$) were attributed to the formation of the trinuclear species and a protein-based radical. Furthermore, the rate of Fe^{2+} oxidation (1026 s^{-1}) was consistent with the formation rate constant for the purple Fe^{3+} -tyrosinate complex (920 s^{-1}). The combined kinetic and EPR data imply that, similar to human ferritin, all observed Fe^{3+} -oxy species may involve a protein tyrosine residue, and that the formation of this purple Fe^{3+} -tyrosine complex is the initial step of Fe^{2+} oxidation [474,495]. The subsequent mineralization process and the slow translocation of the resulting products to the ferritin cavity conclude the reaction cycle. It appears likely that specific changes in protein folding as well as packing interactions are of vital importance for these processes [495].

Apart from the occurrence of the Fe^{3+} -tyrosinate intermediate, the detection, trapping, and characterization of a peroxodiferric intermediate has contributed significantly to our understanding of the ferroxidase-catalyzed reaction [468,475,477, 478,496]. The ferroxidase reaction catalyzed by frog ferritin has been probed by rapid freeze-quench Mössbauer spectroscopy, which has led to the characterization of a blue, transient catalytic intermediate with $\lambda_{\text{max}} = 650 \text{ nm}$, a diamagnetic ground state and Mössbauer parameters $\Delta E_{\text{Q}} = 1.08 \pm 0.03 \text{ mm/s}$ and $\delta = 0.62 \pm 0.02 \text{ mm/s}$ [468]. During the catalytic cycle this transient accumulates considerably to $\sim 70\%$ of the total ferroxidase concentration. These results were interpreted in terms of the formation of a peroxodiferric intermediate in which the two high-spin Fe^{3+} ions are antiferromagnetically coupled. A similar peroxodiferric species has also been observed in the recombinant H subunit of human ferritin, as well as in *E. coli* ferritin [475,496]. The peroxodiferric intermediate has also been characterized by resonance Raman spectroscopy. The band at 851 cm^{-1} is attributed to a $\nu(\text{O}-\text{O})$ stretch vibration of the Fe-coordinated peroxide and the bands at 485 and 499 cm^{-1} to ν_{s} and ν_{as} of the Fe-O₂-Fe moiety [477]. The observed Raman bands are consistent with the presence of a μ -1,2 diferric peroxide species similar to the diferric peroxo intermediates observed in MMO (§2.1), ribonucleotide reductase (§3), and Δ^9 desaturases (§4) [59,105,295,313]. However, in contrast to these dioxygen-activating enzymes, the ferric iron in ferritin is not retained in the active site but is released for mineral core formation. The electronic structure of the peroxo intermediate formed in frog ferritin has also been investigated using x-ray absorption spectroscopy [478]. The unusually short observed Fe-Fe distance of 2.53 \AA has led to the proposal that in addition to the peroxo bridge (μ -1,2), two additional single-atom bridges are present in this intermediate (μ -oxo).

EPR spin labeling (with a cysteine specific spin label) has been useful to probe and establish the role of cysteine residues during the iron-loading and oxidation process in the study of recombinant human ferritin [497]. The Cys90 residue was found to be directly involved in ferritin aggregation during iron loading [497]. A recent EPR spin-trapping study of the H subunit of human ferritin investigated the role of this protein in the protection of cells from oxidative stress. The production of hydroxyl radicals was monitored during the ferroxidase-catalyzed oxidation of Fe^{2+} by H_2O_2 , and these measurements indicated that the H-subunit of ferritin is able to regulate the formation of the radicals, implicating a role in detoxification [498]. This proposal was further supported by EPR spin-trapping experiments that monitored the H_2O_2 -mediated oxidation of Fe^{2+} by the smaller *L. in-nocua* ferritin [443].

7.3. Mechanistic Insights

The catalytic mechanism employed by ferritins is yet to be fully elucidated. The Fe1 site in the binuclear ferroxidase center has a coordination environment reminiscent of the corresponding sites in diiron-containing oxygenases such as MMO and ribonucleotide reductase (*vide supra*). However, in comparison to these oxygen-activating enzymes, the Fe2 site in ferritins contains a weaker ligand environment [59]. It has been suggested that this difference in Fe2 coordination is responsible for the altered function of ferritins [446,479,499], i.e., it may be a major factor determining the fate of the metal ions. While the diiron active sites in MMO and other oxygenases are retained as cofactors, in ferritins iron is the substrate and is released at the end of the reaction [500].

As mentioned above, the initial reaction of diferrous ferritin with O_2 leads to the formation of a peroxodiferric intermediate, which decays to form different ferric oxy species [468,495,501]. A recent study involving a chimeric protein, where the catalytic ferroxidase site from frog ferritin was introduced into a catalytically inactive ferritin protein (animal specific L ferritin), has led to identification of several residues (Glu23, Glu103, Gln137, and Asp140) involved in the formation of the peroxo diferric reaction intermediate [499] (*vide supra*). It is speculated that the formation of an oxo-bridged diferric center initiates the iron release [453]. Although the precise details for this process await further investigations, it has emerged that ferritins and bacterioferritins employ a similar mechanistic strategy with some differences [482,502,503].

8. HEMERYTHRIN

8.1. Biochemical and Structural Characterization

Hemerythrin is a dioxygen carrier protein responsible for reversible O_2 binding and oxygen transport, and it was the first enzyme from the class of binuclear non-

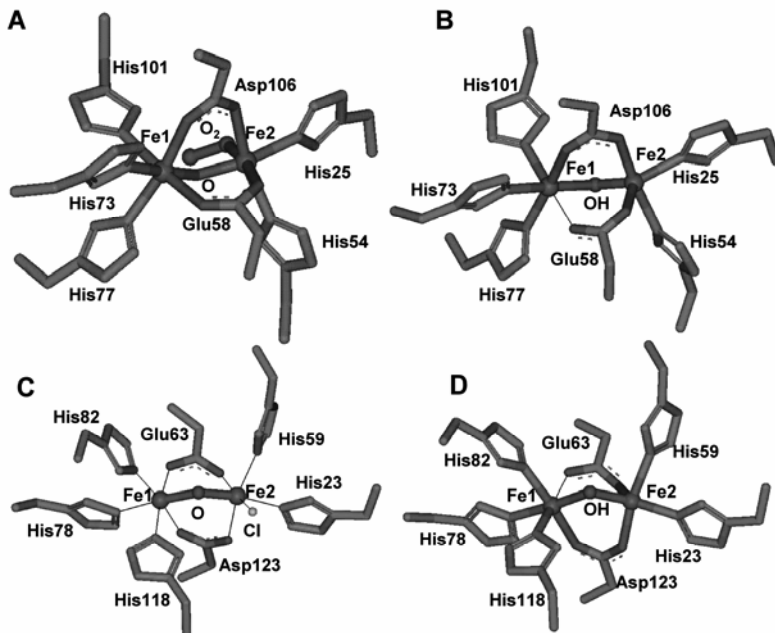


Figure 33. Active site structures of (A) oxy hemerythrin (PDB code 1HMO), (B) deoxy hemerythrin (PDB code 1HMD), (C) oxy DcrH-hemerythrin (PDB code 2AWY), and (D) deoxy DcrH-hemerythrin (PDB code 2AWC).

heme iron enzymes that was extensively characterized by biochemical, kinetic, and spectroscopic methods (Table 1) [244,504–506]. It is found especially in some marine invertebrates and usually exists as an octamer (molecular weight of approximately 13.5 kDa for each subunit) [507]. Most of the initial biochemical and spectroscopic studies were carried out with the enzyme extracted from *Phascolopsis gouldii* and *Themiste dyscrita*. Sequence comparisons have shown that the iron-coordinating residues employed by hemerythrins from various sources are highly conserved. The two physiologically relevant forms of the enzyme are the diferrous or deoxyhemerythrin and the diferric or oxyhemerythrin forms [505].

The crystal structures of several different forms of hemerythrin from different sources are available [508–515]. In the deoxy form, the two Fe^{2+} sites are inequivalent, with Fe1 and Fe2 being six- and five-coordinate, respectively (Fig. 33B). The six-coordinate iron site is coordinated by three histidine residues, two bridging carboxylates (from Asp106 and Glu58), and an additional bridging hydroxide [513]. The Fe2 site is coordinatively unsaturated, involving two histidines in addition to the two bridging carboxylates and a bridging hydroxide. In contrast, in diferric oxyhemerythrin O_2 binds to the vacant position on Fe2 (Fig. 33A). Upon interaction with dioxygen, two electrons (one from each Fe^{2+}) and the proton from the

bridging hydroxide are donated to Fe²⁺-bound O₂, yielding a μ -oxo bridged diferric center [513]. In comparison to other members of the binuclear non-heme iron enzymes, where O₂ binds in a metal ion-bridging mode, hemerythrin is rather unique in the sense that it has only one vacant coordination site on one of the metal ions, accessible for O₂ binding in monodentate end-on fashion [244]. Furthermore, hemerythrin contains a primarily histidine-rich coordination environment (Fig. 33) (five histidine residues and only two carboxylates) that seems to facilitate and favor reversible O₂ binding. More recently, a hemerythrin-like domain of a bacterial chemotaxis protein DcrH with the likely dioxygen-sensing function from *Desulfovibrio vulgaris* has been identified and crystallized [515,516]. The diiron center of this enzyme resembles that of invertebrate hemerythrins (Figs. 33C,D) and oxygen-sensing is proposed to be initiated by O₂ binding to the diferrous center and its autoxidation to the diferric form.

8.2. Spectroscopic Characterization of Hemerythrin

The different forms of hemerythrin have been characterized with a great number of spectroscopic techniques, including Mössbauer, (magnetic) circular dichroism, resonance Raman, extended x-ray absorption fine structure, and EPR-related techniques, and several reviews have emerged recently [244,517–519]. Here, we will focus only on some of the more recent developments involving EPR and related techniques. Diferrous deoxyhemerythrin is EPR silent with a singlet ground state. The two high-spin Fe²⁺ ions are antiferromagnetically coupled with $J = -14 \text{ cm}^{-1}$ ($\mathcal{H}_{\text{ex}} = -2JS_1 \cdot S_2$), determined by magnetic susceptibility measurements [520]. The azide adduct of deoxyhemerythrin contains two ferromagnetically coupled Fe²⁺ ions ($J = 1.7 \text{ cm}^{-1}$) with $g_{\text{eff}} \sim 16$ EPR [69,521]. In contrast, the two Fe³⁺ ions in oxyhemerythrin are strongly antiferromagnetically coupled due to the presence of a μ -oxo bridge ($J = -77 \text{ cm}^{-1}$; $\mathcal{H}_{\text{ex}} = -2JS_1 \cdot S_2$) [522].

Radiolytic reduction of deoxyhemerythrin and the diferrous azido form of the enzyme result in the generation of mixed-valent systems (methemerythrin and its azido derivative), both with one high-spin Fe³⁺ ($S = 5/2$) and one high-spin Fe²⁺ ($S = 2$), which are antiferromagnetically coupled resulting in $S_{\text{tot}} = 1/2$ [286,523]. ENDOR and ESEEM spectroscopy have been particularly useful in the characterization of these two mixed-valent systems, in particular in probing their nitrogen coordination environments [77,524,525]. Even in the presence of a large number of magnetically nonequivalent nitrogen atoms (10–13 in the case of hemerythrin), it is possible to estimate the values of individual hyperfine coupling constants, thus probing the iron active site structure to a high degree. Specifically, ESEEM measurements (Fig. 34) have illustrated structural changes that occur as a consequence of azide binding to the active site of the enzyme. Since azide is believed to be a suitable mimic for O₂, similar structural rearrangements are anticipated during the catalytic cycle. Specifically, hyperfine coupling constants for the iron-coordinating histidine nitrogens are affected upon azide binding, suggesting significant geometric changes in the first coordination sphere.

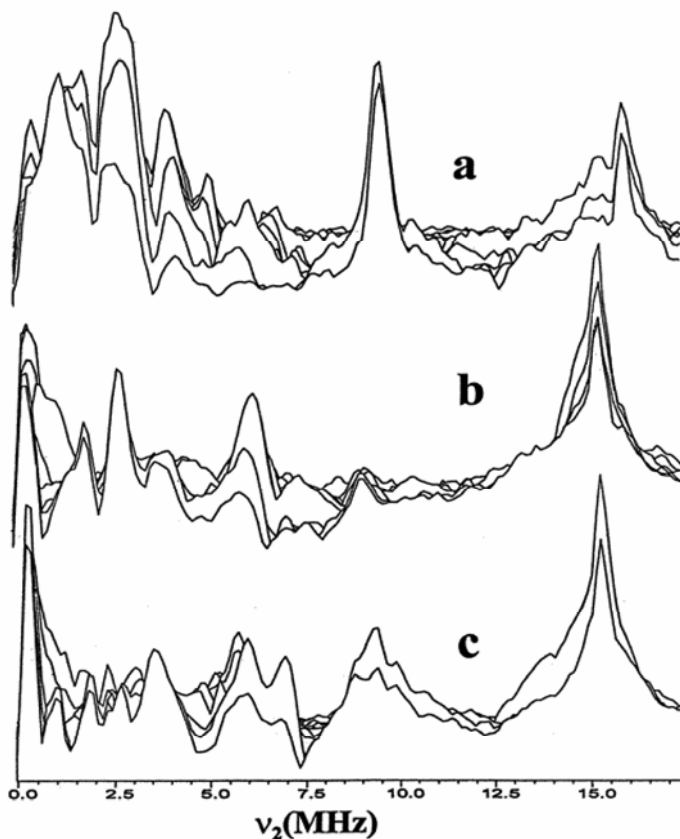


Figure 34. Three-pulse ESEEM spectra of semimethemerythrin as a function of time τ (a) at $g = 1.86$, and (b) at $g = 1.945$, and (c) azidosemimethemerythrin at $g = 1.94$. Reprinted with permission from [525]. Copyright © 1998, American Chemical Society.

Earlier EPR studies were also extended to the nitrosyl adducts of deoxyhemerythrin since the NO adduct is believed to be a reasonable mimic of the superoxide intermediate expected to be formed upon reaction of hemerythrin with O_2 [92,93,95,526]. The spin-Hamiltonian parameters for the $Fe^{2+}-\{FeNO\}^7$ unit of NO-deoxyhemerythrin are consistent with antiferromagnetic coupling between the two iron centers, and the coordination of NO to the five-coordinate Fe_2 , as expected for dioxygen binding.

8.3. Mechanistic Insights

EPR spectroscopy has played an important part in the characterization of the iron active site of hemerythrin, and in combination with various other spectro-

scopic, kinetic, biochemical, and theoretical techniques has led to the following currently accepted reaction mechanism. O_2 first diffuses into the diiron active site of the enzyme, interacting with the five-coordinate Fe_2 , thus forming a terminally bound hydroperoxide intermediate, which is H-bonded to the μ -oxo bridge [244]. The formation of the hydroperoxide can be described as a proton-coupled two-electron transfer process [522]. Furthermore, theoretical calculations strongly support that the presence of the μ -oxo bridge provides an extremely efficient superexchange pathway for the electron transfer from the remote iron center to dioxygen [244]. The histidine-rich environment and the presence of the μ -OH bridge in diferrous deoxyhemerythrin are the main factors that facilitate the formation of a terminally Fe_2 -bound hydroperoxide intermediate instead of a bridging μ -1,2 species observed in the carboxylate-rich coordination environments of MMO or ribonucleotide reductase [79]. Thus, the iron active site structure of hemerythrin directly governs its reactivity, favoring reversible O_2 binding rather than O_2 activation.

9. HYDROLYTIC ENZYMES

Metallohydrolases form a large group of predominantly binuclear enzymes that are involved in a wide array of biological functions. We have previously reviewed recent advances in their structure and function relationships [527]. Here, we focus on two members that have established iron centers, and which have been studied with EPR-related techniques.

9.1. Purple Acid Phosphatases

9.1.1. Biochemical and Structural Characterization

Catalytically active purple acid phosphatases (PAPs) contain heterovalent $Fe^{3+}M^{2+}$ centers in their active sites, where M is Fe in enzymes extracted from animal sources, and Zn or Mn in plant enzymes [527]. The characteristic purple color of PAPs is due to a ligand-to- Fe^{3+} charge transfer transition. Since PAPs hydrolyze a wide range of phosphate esters and anhydrides (Table 1), no physiologically significant substrates have yet been clearly identified. Consequently, the precise biological role(s) of PAPs remains obscure. Evidence has accumulated that supports a role for the animal enzymes in iron transport [528]: the generation of reactive oxygen species (ROS) by macrophages as part of the immune system's response to pathogens [529], and bone metabolism [530], which has made PAP a major target for the development of anti-osteoporotic chemotherapeutics [531,532]. Plant PAPs may also be involved in the production of ROS during an immune response [533], but the study of the physiological functions of PAPs in plants is greatly complicated by the presence of a multitude of isoforms [534–536]. No bacterial PAPs have yet been reported. However, based on sequence homology it is likely that this enzyme occurs in a limited number of bacterial organisms, including mycobacteria

and photosynthetically active cyanobacteria [534,536]. It has been speculated that especially in mycobacteria PAP may play an essential role in the pathogen's survival in an invaded host [534].

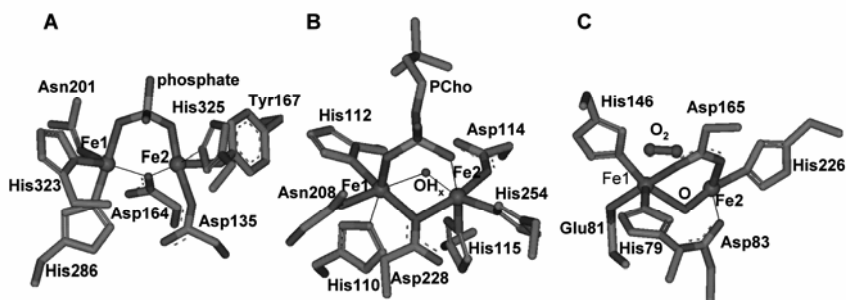


Figure 35. Active site structures of (A) $\text{Fe}^{3+}/\text{Zn}^{2+}$ red kidney bean purple acid phosphatase in complex with phosphate (PDB code 4KBP), (B) phosphorylcholine esterase domain of the virulence factor choline-binding protein E from *Streptococcus pneumoniae* (PDB code 1WRA), and (C) rubredoxin:oxygen oxidoreductase (ROO) from *Desulfovibrio gigas* (PDB code 1E5D).

Several crystal structures of PAPs have been described over the last decade. Despite a low degree of overall amino acid sequence homology between enzymes from different kingdoms [535,536], their catalytic sites display a remarkable similarity. The two metal centers are coordinated by seven invariant ligands (Fig. 35A), with an aspartate residue bridging the two ions [390,537–542]. The identity of the remaining ligands is subject to debate. In the only known structure of a PAP (from red kidney bean) in the resting state, the resolution is too low to allow identification of water ligands [537]. Nonetheless, the coordination spheres of the two metal ions in this enzyme have been completed by modeling two terminally bound and one bridging water molecule into the active site [537] (Fig. 35A). The presence of the bridging water ligand has since been observed in crystal structures of pig, human, and rat PAPs, which were crystallized in the presence of either phosphate (pig and human enzymes) or sulfate (rat PAP) [390,539,542]. In both pig and human PAP the remaining vacant positions in the coordination spheres of the two metal ions are occupied by oxygen atoms of a μ -1,3 bridging phosphate group [390,542]. In the structure of the rat enzyme, sulfate binds monodentately to the divalent metal ion, while a hydroxide is coordinating the ferric ion [539]. Most recently, red kidney bean PAP has been crystallized in the presence of sulfate. The bridging oxygen atom is in a position equivalent to that in the animal PAPs. However, in contrast to the rat enzyme, the sulfate group does not directly coordinate to the divalent metal ion. Instead, it forms several strong hydrogen bonds with amino acids in the second coordination sphere and the bridging water molecule [543]. We

speculate that this structure represents a precatalytic complex. An interesting variation is observed in the active site structure of sweet potato PAP. To date this is the only PAP with a confirmed $\text{Fe}^{3+}\text{-Mn}^{2+}$ center, and in comparison to other PAPs it has a significantly enhanced rate of hydrolysis for a broad range of substrates [544]. In contrast to other PAPs, the sweet potato enzyme appears to be very selective with respect to its divalent metal ion; only Mn^{2+} has been shown to reconstitute a fully active enzyme [545]. In the crystal structure of sweet potato PAP, phosphate coordinates the two metal ions in an unusual tripodal mode. The μ -1,1 bridging oxygen atom of the phosphate group is in a position equivalent to the bridging oxygen atoms in pig, human, rat and red kidney bean PAP [527]. This observation has been interpreted in terms of the bridging oxygen acting as the reaction-initiating nucleophile [541].

9.1.2. Spectroscopic Characterization of PAP

EPR-related methodologies have been instrumental in establishing the heterovalent oxidation state as the catalytically relevant one [546,547], and in probing the active site structures, both in the resting and in the inhibitor-bound states. The catalytically inactive diferric form of animal PAPs is characterized by a diamagnetic ground state due to antiferromagnetic exchange coupling between the two $S = 5/2$ Fe^{3+} ions (Fig. 3; $J \sim -100 \text{ cm}^{-1}$; $\mathcal{H}_{\text{ex}} = -2JS_1 \cdot S_2$) [82,546–549]. The diferrous state of animal PAPs has not been investigated spectroscopically, partially because the metal ion affinity in this fully reduced form is low. This fact is generally exploited for the preparation of metal ion derivatives of PAPs, where the incubation of the enzyme with reductants (e.g., dithionite) and chelators leads to the metal-free apoform [550–552].

The catalytically relevant mixed-valent form of the diiron PAPs from pig, cow, human, and rat is typically characterized by $g_{\text{av}} < 2$, indicating antiferromagnetic exchange coupling resulting in $S_{\text{tot}} = 1/2$ (Fig. 4) [546,547,553,554]. From the temperature dependence of the EPR spectrum and from multifold/multitemperature magnetization measurements, the exchange coupling constant was estimated to be $\sim -10 \text{ cm}^{-1}$ ($\mathcal{H}_{\text{ex}} = -2JS_1 \cdot S_2$) [388,546,547].

Inhibitor binding to PAP affects the electronic structure of the active site of the enzyme, and EPR is a convenient and diagnostic tool to study structural changes and aspects of the catalytic mechanism. For instance, the addition of the moderate competitive inhibitor phosphate to mixed-valent pig PAP reduces the exchange coupling interaction to less than half the magnitude observed in the resting enzyme, increases the g anisotropy, and the reduction potential is also lowered considerably [388,555–557]. In combination with magnetic circular dichroism [389], extended x-ray absorption fine structure [558,559], and crystallographic studies [390,538,542], EPR data support the formation of a μ -1,3 phosphate complex in pig PAP. A similar binding mode has been inferred for the substrate from recent ENDOR studies [560].

For PAPs and related binuclear metallohydrolases, a point of contention has been the number of water/hydroxide molecules coordinating to the resting active

site [527]. The only available crystal structure of a resting PAP is of insufficient resolution to identify exogenous ligands [542]. EPR and magnetization measurements indicate the presence of a bridging μ -(hydr)oxide at catalytically optimal pH [388,545,547]. This finding is supported by a recent ^2H Q-band ENDOR study with pig PAP [560] (Fig. 36). In addition to the bridging hydroxide, only signals due to a terminal, Fe^{2+} -bound water/hydroxide molecule were identified. The Fe^{3+} ion has no terminal exogenous ligand and is five-coordinate in the resting state. ^{95}Mo and ^{75}As ENDOR measurements are in agreement with the hypothesis that these substrate analogs displace the terminal water ligand. Although ^{31}P ENDOR measurements were unable to detect ^{31}P signals upon addition of phosphate to pig PAP, EPR line broadening observed in the phosphate complex of the $\text{Fe}^{3+}\text{Zn}^{2+}$ derivative of pig PAP indicates that the tetraoxo anion interacts with Fe^{3+} [555]. Thus, a substrate (analog) binding mode is envisioned whereby the phosphate group coordinates to the mixed-valent cluster in the active site in a μ -1,3 fashion [560]. This mode of substrate binding is supported by the crystal structures of pig, human, red kidney bean, and sweet potato PAP [390,538,541,542].

A range of observations evolving from isotope effects and labeling studies as well as site-directed mutagenesis, and the apparent lack of transphosphorylation, indicate that the phosphate group of the substrate is directly transferred to a metal-coordinated, nucleophilic solvent (water/(hydr)oxide) molecule [561–564]. Based on the results described in the paragraph above, only one nucleophilic candidate remains: the μ -(hydr)oxide. Fluoride is known to be able to replace nucleophilic (hydr)oxides, and has been used to probe the catalytic mechanism and mode of substrate binding in the $\text{Fe}^{3+}\text{Zn}^{2+}$ derivative of pig PAP [565]. The disappearance of the EPR signals ($g_{\text{eff}} = 9.6$ and 4.3) characteristic for a rhombic ($E/D = 0.33$) $S = 5/2$ state, and the emergence of the less rhombic ($E/D = 0.18$) $S = 5/2$ signals at $g_{\text{eff}} = 8.6$ and 5.1 upon titration of the pig PAP–phosphate complex with fluoride was interpreted in terms of fluoride binding to Fe^{3+} . Accompanying extended x-ray absorption fine structure and resonance Raman measurements support the model where the fluoride ion displaces the bridging hydroxide, thus rendering the enzyme inactive. A similar binding mode for fluoride has recently also been inferred for the $\text{Fe}^{3+}\text{Zn}^{2+}$ active site of red kidney bean PAP from inhibition [566] and crystallographic [543] studies. Interestingly, the EPR spectra recorded for the ternary PAP–substrate–fluoride complexes are independent of the identity of the substrate [565]. Thus, substrates and analogs such as phenyl phosphate, AMP, and arsenate bind in a mode to the active site of pig PAP identical to that of phosphate, i.e., in a μ -1,3 fashion (*vide supra*). Furthermore, the EPR spectra determined for enzyme–phosphate and enzyme–phosphate–fluoride complexes of bovine PAP are very similar to those reported for the pig enzyme [567], indicating that the active site structure and interactions with the substrate analog phosphate are well conserved within this family of enzymes. The formation of a ternary enzyme–phosphate–fluoride complex has recently also been deduced from EPR spectra of human PAP [568].

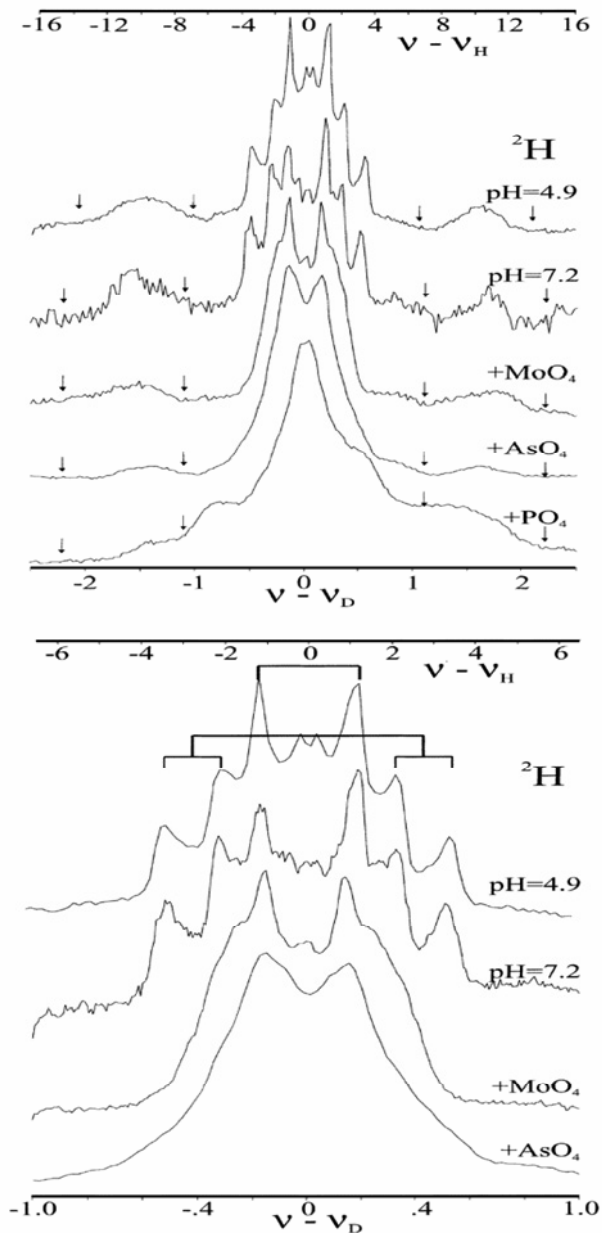


Figure 36. ^2H ENDOR spectra of uteroferrin in D_2O buffer and in complex with molybdate, arsenate, and phosphate (top panel showing broad sweep and bottom panel showing narrow sweep). Reprinted with permission from [560]. Copyright © 2002, American Chemical Society.

9.1.3. Mechanistic Insights

The catalytic mechanisms employed by binuclear metallohydrolases have recently been reviewed by us, and will only be discussed briefly here [527]. Its general features are illustrated in Figure 37. Stopped-flow measurements support an initial binding of the substrate to the second coordination sphere, forming a precatalytic complex [569]. The μ -hydroxide is likely to stabilize the substrate in this initial phase via hydrogen bonding, and may be relevant for the proper orientation of the phosphate group within the active site. Subsequently, rearrangement of the substrate leads to the formation of the catalytically competent μ -1,3 phosphate complex. The μ -1,3 coordination mode of the substrate is supported both spectroscopically and crystallographically (*vide supra*), and places the metal-bridging hydroxide group of the binuclear cluster in an ideal position for a nucleophilic attack on the phosphorus atom of the substrate. Substrate binding is likely to increase the nucleophilic character of the μ -hydroxide, possibly by inducing conformational changes upon coordinating to the binuclear center. A (magnetic) circular dichroism study has demonstrated that binding of the substrate analog phosphate leads to a shift of the μ -hydroxide toward the divalent metal ion and away from Fe^{3+} , thus increasing its nucleophilicity [389]. This observation is also in agreement with extended x-ray absorption measurements of the pig PAP-phosphate-fluoride complex, which did not only demonstrate that fluoride displaces the μ -hydroxide in the metal-bridging position, but also shows that fluoride is closer to the di- than the trivalent metal ion [565].

Nucleophilic attack by the μ -hydroxide is followed by the release of the alcohol product, with phosphate remaining bound in a tripodal mode to the binuclear center [541]. The subsequent steps in the mechanism are not well understood, but the regeneration of the resting active site requires the exchange of bound phosphate by at least two water molecules. It is speculated that the initial ligand exchange at the divalent metal site leads to a cluster characterized by monodentate $\text{M}^{2+}\text{-H}_2\text{O}$ and Fe^{3+} -phosphate complexes, in agreement with an earlier EPR study, which indicated that such a cluster may be formed upon the addition of phosphate to pig PAP [555]. Deprotonation of the M^{2+} -bound water, possibly mediated via H-bond interaction with the bound phosphate group, enables the regeneration of the μ -hydroxide and the concomitant release of the phosphate. An additional water molecule binds to the divalent metal ion, thus completing the catalytic cycle.

9.2. Metallo- β -Lactamases

9.2.1. Biochemical and Structural Characterization

An increasingly critical problem for mankind is the alarming ability of pathogenic bacteria to acquire resistance to antibiotics, which has been triggered as a result of the excessive application of these compounds by health care systems. Amongst the strategies employed by the bacteria to render these antibiotics inefficient is the expression of enzymes that hydrolyze, and thus inactivate, the

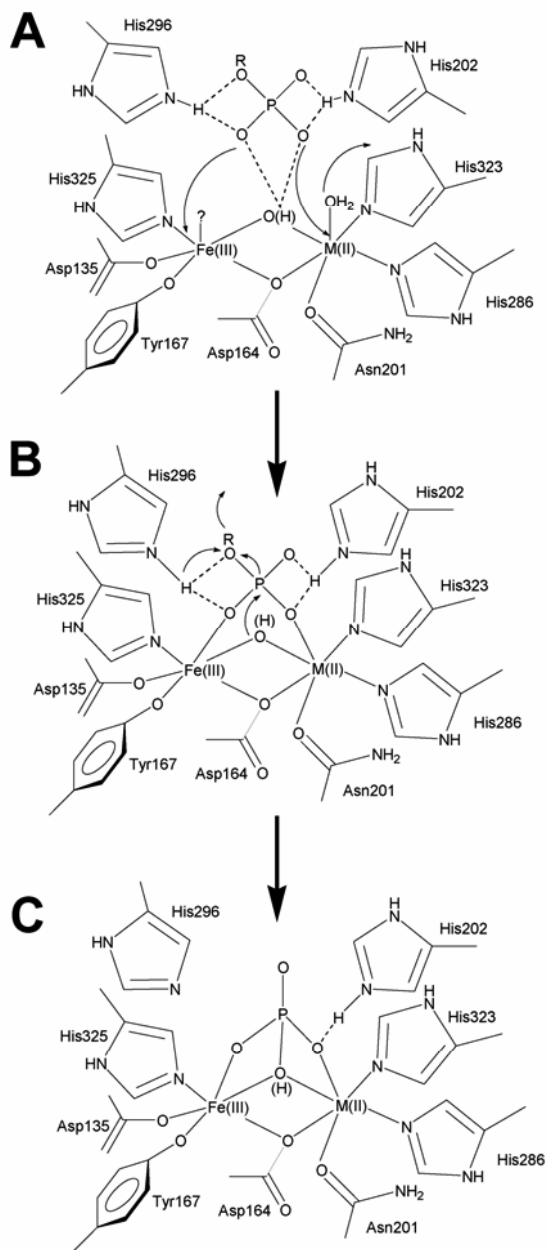


Figure 37. Proposed mechanism of hydrolysis by purple acid phosphatases. Reprinted with permission from [527]. Copyright © 2006, American Chemical Society.

chemotherapeutic reagent [570,571]. One of the most common groups of enzymes with anti-chemotherapeutic activity is the family of β -lactamases, which hydrolyze β -lactam antibiotics (Table 1) such as penicillins and cephalosporins, and which were originally categorized into four distinct groups, based on their molecular properties [572,573]. Of these, group 3 enzymes, which belong to the superfamily of metallo- β -lactamases, are the most troublesome since they inactivate virtually all known β -lactams and because there are no efficient inhibitors known to date [574,575]. At present, several types of metallo- β -lactamases have been identified [576,577] that catalyze a wide range of reactions, ranging from the hydrolysis of β -lactams (e.g., L1 from *Stenotrophomonas maltophilic*) [575] to the reduction of oxygen to water (e.g., rubredoxin:oxygen oxidoreductase (ROO) from *D. gigas*) [578]. The majority of metallo- β -lactamases appear to require two Zn(II) ions for full activity [579–581], although the specific metal ion requirements of metallo- β -lactamases are still subject to debate and may depend on the nature of the catalyzed reactions. For instance, ROO from *D. gigas* requires iron to catalyze its redox reactions (§10) [578]. In contrast, gloxylase II (GOX II), a metallo- β -lactamase that acts together with GOX I to convert a range of α -ketoaldehydes into hydroxy acids in the presence of glutathione [582], appears to be more flexible with iron, manganese, and zinc present in the active site [583–585].

Crystal structures of members of five of the 17 metallo- β -lactamase groups have been solved to date [576,578,585–589]. The majority of metal ion ligands are conserved in all these enzymes. In the crystal structures of GOX II from human [586], RNase Z from *Bacillus subtilis* [589], and the phosphorylcholine esterase (Pce) domain of the virulence factor choline-binding protein E from *Streptococcus pneumoniae* [576], the two metal ions are bridged by an aspartate residue in a μ -1,1 mode, as observed in PAPs (Fig. 35B). In contrast, in ROO from *D. gigas* the aspartate residue coordinates in a μ -1,3 mode to the two metal ions (Fig. 35C) [578], while in the zinc-dependent metallo- β -lactamase FEZ-1 from *Fluoribacter gormanii* [588] and in GOX II from *Arabidopsis thaliana* [585] no bridging amino acid is present. Similar to PAPs, all structurally characterized metallo- β -lactamases appear to have a metal-ion bridging water (hydroxide) ligand (Fig. 35B), which has been proposed as the reaction-initiating nucleophile in hydrolytically active metallo- β -lactamases (i.e., GOX II [586], RNase Z [589], FEZ-1 [588], and Pce) [576]. A feature common to all known metallo- β -lactamases is the presence of a hydrogen bond between the bridging water molecule and a terminal aspartate ligand. This hydrogen bond may increase the acidity of the bridging ligand, and thus may be an important contributor to reactivity [575,576,587–589]. Two metallo- β -lactamases, Pce and RNase Z, were crystallized in the presence of phosphate [576,589], which coordinates bidentately in a μ -1,3 mode, similar to PAPs.

9.2.2. Spectroscopic Characterization of Metallo- β -Lactamases

Since the vast majority of enzymes that belong to the metallo- β -lactamase family are usually purified as di-zinc proteins [583], only a limited number of studies have been reported at present that describe EPR-spectroscopic parameters of

metallo- β -lactamases. For instance, rapid-freeze-quench EPR of the Co(II)-substituted form of the di-zinc metallo- β -lactamase L1 from *S. maltophilia* has provided evidence that (i) the intermediate of this enzyme's reaction is likely to be metal-ion bound, and (ii) the reaction product may bind reversibly to the metal centers in the active site [590]. Naturally occurring iron centers in metallo- β -lactamases are rare (to date), and the only systems that have been investigated in some detail by EPR-related techniques are two isoforms of GOX II from *A. thaliana* [583–585]. EPR (together with extended x-ray absorption spectroscopy) has been instrumental in determining the metal ion composition in the active site of recombinant GOX II. In the EPR spectrum of the cytosolic *A. thaliana* isoform, a number of different metal ion combinations have been identified including $\text{Fe}^{3+}\text{Fe}^{2+}$, $\text{Fe}^{3+}\text{Zn}^{2+}$, $\text{Mn}^{2+}\text{Mn}^{2+}$, and possibly $\text{Mn}^{2+}\text{Zn}^{2+}$ centers [583]. The addition of 250- μM ammonium ferrous sulfate to the standard culture medium [591] does not significantly affect the EPR spectra of recombinant cytosolic *A. thaliana* GOX II extracted from the *E. coli* cultures, indicating that the bioavailability of iron is tightly controlled in *E. coli* cells [584]. Resonances at $g < 2$ are similar to those observed for some PAPs, MMOs, and ribonucleotide reductases (*vide supra*) and are likely to be due to antiferromagnetically coupled $\text{Fe}^{3+}\text{Fe}^{2+}$ centers [583]. Features at $g_{\text{eff}} = 4.6$ and 9.7 are assigned to isolated, high-spin Fe^{3+} centers (e.g., in the form of $\text{Fe}^{3+}\text{Zn}^{2+}$ centers), while the $g_{\text{eff}} = 4.3$ resonance is interpreted in terms of adventitious Fe^{3+} . Interestingly, a broad EPR signal at $g_{\text{eff}} = 16$ is recorded that is consistent with the presence of a proportion of weakly ferromagnetically coupled $\text{Fe}^{2+}\text{Fe}^{2+}$ centers (Fig. 5), as observed in MMOs (§2.1) and ribonucleotide reductases (§3). Finally, the multiline feature at $g_{\text{eff}} = 2.1$ is ascribed to the presence of a ferromagnetically coupled $\text{Mn}^{2+}\text{Mn}^{2+}$ center, and possibly some mononuclear Mn^{2+} centers [583]. The addition of 250- μM manganese chloride to the *E. coli* culture medium does lead to a significant increase in the proportion of Mn^{2+} -containing centers in recombinant *A. thaliana* GOX II, and the resulting EPR spectrum closely resembles that measured for the $\text{Mn}^{2+}\text{Mn}^{2+}$ catalase [583,592]. Apart from the various EPR-active metal centers, the presence of EPR-silent $\text{Fe}^{3+}\text{Mn}^{2+}$, $\text{Fe}^{3+}\text{Fe}^{3+}$, or $\text{Zn}^{2+}\text{Zn}^{2+}$ centers cannot be excluded. Hence, *A. thaliana* GOX II appears to be distinct from most other metallo- β -lactamases by its versatile use of different metal ion combinations for its catalytic function without significant loss of reactivity [583]. In this respect GOX II is reminiscent of some PAPs that have been shown to be active with a range of different metal ion combinations, including $\text{Fe}^{3+}\text{Fe}^{2+}$, $\text{Fe}^{3+}\text{Zn}^{2+}$, $\text{Fe}^{3+}\text{Mn}^{2+}$, $\text{Fe}^{3+}\text{Cu}^{2+}$, $\text{Ga}^{3+}\text{Fe}^{2+}$, $\text{Ga}^{3+}\text{Zn}^{2+}$, and $\text{Al}^{3+}\text{Zn}^{2+}$ [550,552,593–595]. However, in contrast to PAPs, the catalytically relevant oxidation states of the metal ions in the active site of GOX II is not yet firmly established. Also, there appears to be no site specificity for metal ion binding in GOX II [583], but metal ion binding appears to be positively cooperative [584]. Metal ion analysis of recombinant *A. thaliana* GOX II (extracted from *E. coli* cells grown in minimal medium) [584,596] has shown that only one equivalent of metal ions binds per active site. However, spin integrations of EPR spectral data support the interpretation that the bound metal ions are predominantly present as binuclear centers [584].

In contrast to the cytosolic isoform, the metal ion content of mitochondrial GOX II contains almost exclusively iron and zinc [585]. Nonetheless, the EPR spectrum of the mitochondrial isoform resembles that of cytosolic GOX II. Consequently, like its cytosolic counterpart, mitochondrial GOX II consists of a mixture of metal centers, including antiferromagnetically coupled $\text{Fe}^{3+}\text{Fe}^{2+}$ ($S = 1/2$), $\text{Fe}^{3+}\text{Zn}^{2+}$ ($S = 5/2$), EPR-silent $\text{Fe}^{3+}\text{Fe}^{3+}$, and diamagnetic $\text{Zn}^{2+}\text{Zn}^{2+}$ centers [585].

10. RUBREDOXIN-OXYGEN OXIDOREDUCTASE AND NITRIC OXIDE REDUCTASES

10.1. Biochemical and Structural Characterization

Various anaerobic archaea, bacteria, as well as protozoa that are able to survive in oxygen-rich environments utilize metalloflavoproteins that contain diiron centers [597–601]. An example is the previously mentioned ROO (rubredoxin-oxygen oxidoreductase; Table 1; §9.2) from the sulfate-reducing bacterium *D. gigas* [602]. Together with NADH-rubredoxin oxidoreductase and rubredoxin, ROO forms an electron transfer chain that is responsible for oxidation of pyridine nucleotides [603]. Specifically, NADH-rubredoxin oxidoreductase reduces rubredoxin, which subsequently shuttles the electrons to ROO, which catalyzes the four-electron reduction of dioxygen to water while preventing the formation of reactive oxygen species [602,604,605]. In addition to its oxidoreductase function, ROO may also reduce NO, and consequently it has been speculated that the primary physiological role of ROO is to provide a protective mechanism against oxidative and nitrosative stress [606]. ROO exists as a homodimer of 43-kDa subunits, each of which contains one flavin mononucleotide (FMN) cofactor and a binuclear non-heme iron center [602]. The crystal structure of oxidized ROO indicates the presence of two distinct domains—a metallo- β -lactamase-like domain housing the diiron active site (*vide supra*) and a flavodoxin-like domain where the FMN cofactor is located [578]. Interestingly, although ROO contains a metallo- β -lactamase-like structural domain, it has no hydrolytic activity. The immediate coordination environment of the diiron center in ROO from *D. gigas* resembles that of MMO (Fig. 2), ribonucleotide reductase (Fig. 15), and hemerythrin (Fig. 33) (§8). The two metal ions are separated by a distance of 3.4 Å and are bridged via a carboxylate group from an aspartate residue (Asp165) and a μ -oxo or μ -hydroxide (Fig. 35C) [578]. In addition, Fe1 is coordinated by two histidines (His146 and His79) and one glutamate (Glu81), while Fe2 is coordinated by one histidine (His226), one aspartate (Asp83), and a water molecule. An additional highly conserved histidine (His84) is in the immediate vicinity of Fe2 but does not coordinate.

Another member of the family of diiron flavoproteins is the recently characterized A-type flavoprotein FprA from the anaerobic, Gram-positive acetogenic bacterium *Moorella thermoacetica* [607]. Similar to ROO, recombinant FprA also exists as a homodimer of 45-kDa subunits and may function both as an oxido and

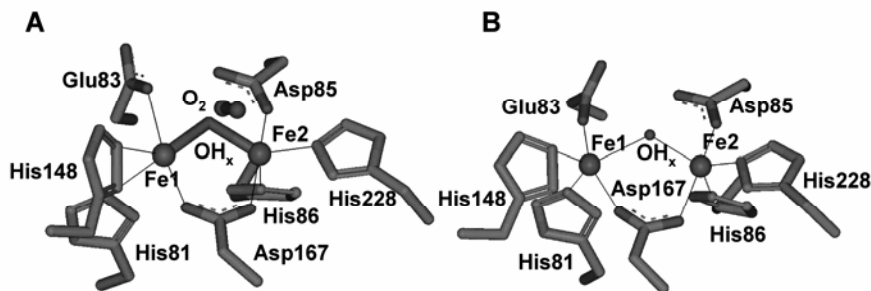


Figure 38. Active site structure of nitric oxide reductase, metalloflavoprotein FprA from *Moorella thermoacetica*: (A) oxidized FprA (PDB code 1YCF), and (B) reduced FprA (PDB code 1YCG).

NO reductase *in vivo* [607]. Similar nitric oxide reductase activity has been reported for enzymes from *E. coli*, *Salmonella enterica*, and *Desulfovibrio vulgaris* [608–611]. The catalytic efficiency of FprA using NO as substrate is approximately six times higher than that using O₂. Furthermore, the reduction of O₂ leads to a complete and irreversible inactivation of FprA, while the enzyme activity is retained during NO turnover. These observations have led to the proposal that FprA may play an important role in the organism's protection against nitrosative stress. Consequently, FprA has been classified as a scavenging NO reductase (S-NOR) [607,612]. The crystal structure of FprA from *M. thermoacetica* has been solved in three different forms—oxidized, reduced, and reduced but reacted with NO [612]. The overall structure is reminiscent of that found in metallo- β -lactamases, and the residues constituting the diiron active site of FprA are homologous to those of ROO from *D. gigas*. In the oxidized form of FprA, the two Fe³⁺ ions are five-coordinate and bridged via a carboxylate from an aspartate residue (Asp167) and a solvent molecule (μ -oxo, μ -OH or μ -aqua) (Fig. 38A). The remaining, terminal ligands are one glutamate (Glu83) and two histidines (His148 and His81) for Fe1, and one aspartate (Asp85) and two histidines (His228 and His86) for Fe2. His86 corresponds to His84 in ROO (*vide supra*) but remains an iron-coordinating ligand independent of the oxidation state of the binuclear center. In contrast, His84 in ROO may only coordinate to Fe2 in the reduced enzyme. In general, the structure of the iron active site of FprA appears to be largely unaffected by changes in the oxidation state (Figs. 38A,B) [612], with a more exposed metal center in the reduced form being the only exception. Modeling studies with the diferrous FprA–NO structure have indicated that two NO molecules can be accommodated within the diiron active site, with one NO molecule coordinating in end-on fashion to each iron [612].

Another novel member of the family of highly conserved A-type flavoproteins is flavorubredoxin (FIRd) from *E. coli* [613]. It could be shown that FIRd is able to carry out reduction of O₂ to water [614]. However, similar to ROO and FprA, FIRd

also functions as an NO reductase, and its major role in anaerobic *E. coli* is NO detoxification [609,615]. The structural core of FIRd is comprised of two domains: the flavodoxin-like domain containing one FMN cofactor and the metallo- β -lactamase-like domain, where the binuclear non-heme iron center is located [615].

10.2. Spectroscopic Characterization of FprA and FIRd

EPR spectroscopy has been instrumental in confirming the presence of binuclear non-heme iron centers in diiron flavoproteins. For FIRd, the mixed-valent form exhibits a rhombic signal with g values at ~ 2 (1.93, 1.88, and 1.82), indicative of a spin system with an $S_{\text{tot}} = \frac{1}{2}$ ground state [616]. Fully reduced FIRd has an EPR resonance in the parallel mode at $g_{\text{eff}} \sim 11.3$, consistent with the presence of two exchange-coupled Fe^{2+} ions, resulting in an $S_{\text{tot}} = 4$ ground state (Fig. 3). Addition of NO to reduced FIRd altered the EPR spectrum, resulting in g values at 2.04 and 2.0016, indicative of an $S = \frac{1}{2}$ ground state (Fig. 3) [614]. The electronic structure of this complex has not yet been investigated. The diferric form of FIRd is EPR silent as a result of two high-spin Fe^{3+} ions ($S = 5/2$) being antiferromagnetically coupled, producing an $S_{\text{tot}} = 0$ ground state. The redox properties of the binuclear non-heme iron active site in FIRd were analyzed by redox titrations and monitored by EPR spectroscopy. The redox potentials for both the $\text{Fe}^{3+}\text{Fe}^{3+}/\text{Fe}^{3+}\text{Fe}^{2+}$ and $\text{Fe}^{3+}\text{Fe}^{2+}/\text{Fe}^{2+}\text{Fe}^{2+}$ couples were estimated to be -20 ± 20 mV and -90 ± 20 mV, respectively [616]. In the presence of NADH-flavorubredoxin oxidoreductase, the physiological redox partner of FIRd, the reduction potentials for both couples are shifted by +40 mV [616].

Due to the likely antiferromagnetic exchange coupling between the two ferric ions of FprA from *M. thermoacetica* (fully oxidized FprA is EPR silent with a weak $g_{\text{eff}} = 4.3$ resonance attributed to adventitious ferric iron and a $g = 2.005$ resonance due to the presence of a small amount of an FMN semiquinone radical), Mössbauer spectroscopy has been employed to investigate the nature of the exchange coupling between the two Fe^{3+} centers. As anticipated, high-field ^{57}Fe Mössbauer measurements of oxidized FprA from *M. thermoacetica* has indicated the presence of two high-spin Fe^{3+} ions that are antiferromagnetically coupled, producing a diamagnetic ground state [607]. Furthermore, the presence of two quadrupole doublets is consistent with two Fe^{3+} ions with different coordination environments and, in agreement with the crystal structure (*vide supra*), the presence of a single bridging water ligand [612].

10.3. Mechanistic Insights

The reaction mechanism of ROO has not yet been studied in detail, but based on analogy with related binuclear non-heme iron enzymes, a mechanistic scheme has been proposed whereby binding of O_2 to the reduced enzyme leads to the formation of a bridging peroxo intermediate, followed by the transfer of electrons from the FMN cofactor [578].

A combination of structural, molecular modeling, spectroscopic, and kinetic data for FprA from *M. thermoacetica* has shed light on some aspects of a possible reaction mechanism for NO reduction [612]. A diferrous dinitrosyl species ($[\{\text{FeNO}\}^7]_2$) is proposed as an initial reaction intermediate in the catalytic cycle. Subsequently, this intermediate is reduced by FMNH₂, yielding $[\{\text{FeNO(H)}\}^8]_2$. The remaining catalytic steps are subject to future investigations. With respect to interactions with O₂, diferrous FprA is expected to generate a diferric peroxy or a diferryl species, as proposed for various binuclear non-heme iron enzymes involved in O₂ activation (*vide supra*). The interaction of reduced FprA with O₂ does ultimately lead to irreversible inactivation of the enzyme, but the molecular details for this process are not yet understood.

11. MEMBRANE-BOUND DIIRON PROTEINS: ALTERNATIVE OXIDASE

11.1. Biochemical and Structural Characterization.

A new class of membrane-bound diiron carboxylate proteins has emerged recently that are responsible for metabolic roles different from those of bacterial monooxygenases, ribonucleotide reductases or desaturases, including functions associated with chlororespiration, carotenoid and chlorophyll biosynthesis, and photosynthesis [617]. Members include alternative oxidase, plastid terminal oxidase, the diiron 5-demethoxyquinone hydroxylase, and the aerobic Mg-protoporphyrin IX monomethylester hydroxylase (Table 1) [6,618]. These enzymes contain the highly conserved six amino acid residues (four glutamate and two histidine residues) that form the iron-binding motif found also in most other soluble non-heme diiron-containing proteins mentioned above. Homology modeling studies using crystal structures of other, soluble non-heme diiron proteins as a reference have provided predicted structures of these integral membrane diiron proteins [7,619].

Alternative oxidase is a diiron-containing ubiquinol oxidase that catalyzes ubiquinol oxidation and the concomitant reduction of oxygen to water. The enzyme has been identified in plants, green algae, and some protozoa and fungi, and is part of the mitochondrial respiratory chain [620,621]. Alternative oxidases from plants are homodimers (molecular weight of 40 kDa per subunit), while those from fungi and protozoas are predominantly monomeric [622]. The precise physiological roles of alternative oxidase are not yet established, but may be organism dependent. Plant and yeast alternative oxidases are possibly involved in the protection against oxidative stress, preventing the formation of reactive oxygen species by controlling the amount of reducing equivalents present in the quinol pool [620,623–625]. Alternative oxidase has also become an important target enzyme for design of new therapeutic agents against African sleeping disease causing parasites as a result of its potential role in trypanosome respiration [626]. Two possible

models for the active site structure of alternative oxidase have been obtained from modeling studies [619,627]. In both models the diiron center is located in a four-helix bundle [5]. Of interest is residue Tyr280 in the vicinity of the binuclear center since it occupies a position similar to that of the corresponding tyrosine residue in bacterioferritin (§7), rubrerythrin (§6), and the R2 subunit of ribonucleotide reductase [409,447,628].

11.2. Spectroscopic Characterization of AOX

The recent recombinant expression of *Arabidopsis thaliana* alternative oxidase in *E. coli* membranes has facilitated spectroscopic studies of the diiron active site [629]. The fully reduced enzyme exhibits an EPR signal (parallel mode) at $g_{\text{eff}} = 15$ (Fig. 3), consistent with the presence of two weakly ferromagnetically coupled high-spin Fe^{2+} ions ($S_1 = S_2 = 2$; $S_{\text{tot}} = 4$) [629]. Fully oxidized alternative oxidase is EPR silent as a result of two high-spin Fe^{3+} ions being antiferromagnetically coupled ($S_1 = S_2 = 5/2$; $S_{\text{tot}} = 0$). The mixed-valent form (generated by air oxidation of dithionite-reduced membranes over different periods of time) shows a highly anisotropic EPR signal with $g_{\text{av}} = 1.65$ (g values at 1.86, 1.67, and 1.53), indicative of an antiferromagnetically coupled $\text{Fe}^{3+}\text{-Fe}^{2+}$ spin system with $S_{\text{tot}} = 1/2$ (Fig. 4), and similar to EPR spectra reported for mixed-valent MMO, mouse ribonucleotide reductase, rubrerythrin, uteroferrin, and hemerythrin [71,75,80,82,630–633]. The exchange coupling constant for the mixed-valent has been estimated to be $J = -5.5 \text{ cm}^{-1}$ ($\mathcal{H}_{\text{ex}} = -2JS_1 \cdot S_2$) based on the half saturation power dependence on absolute temperature for the mixed-valent alternative oxidase [629]. This relatively weak antiferromagnetic exchange coupling indicates the likely presence of a metal ion-bridging μ -hydroxide or a μ -aqua ligand. The same study has also indicated that the interaction of dioxygen with reduced alternative oxidase is rapid, and the mixed-valent form of the enzyme has been proposed as a possible reaction intermediate. Alternative proposals for the role of the mixed-valent form of alternative oxidase have been reported. Approximately 5% of the enzyme is in the mixed-valent oxidation state, but the expression levels of alternative oxidase are not directly correlated to the concentration of mixed-valent centers [629]. Thus, it has been speculated that the formation of mixed-valent centers may be of physiological (regulatory) relevance, assuming that only the fully reduced or oxidized forms of alternative oxidase are catalytically active, and that the enzyme can easily and reversibly be inactivated by oxidation/reduction to its mixed-valent form. Interestingly, in two mutants of alternative oxidase—Glu222Ala and Glu273Ala—no EPR resonances due attributable to a mixed metal center are found. The mechanistic relevance of this observation is not yet understood.

11.3. Mechanistic Insights

The molecular basis for the catalytic process in alternative oxidase has not yet been studied in great detail, but in the proposed reaction mechanism the diferric oxidation state is considered as the resting state of the enzyme [5]. In the initial

phase of the catalytic cycle, the diferric center is reduced by quinol. It has been proposed that a second quinol molecule interacts subsequently with the first one prior to oxygen binding to the diferrous metal center. The binding of two substrate molecules is considered as a possible protection mechanism, preventing side reactions of the highly reactive oxygen species. Upon O₂ binding to the diferrous metal center, a diferric peroxo intermediate species is likely to be formed, which may lead to the generation of a high-valent, oxidizing intermediate with an electronic structure similar to that of intermediates **X** or **Q** from the R2 subunit of ribonucleotide reductase (§3) or MMO (§2.1), respectively. The existence of such intermediate species in the alternative oxidase-catalyzed reaction awaits, however, further studies. Alternatively, it is possible that the putative diferric peroxo intermediate oxidizes the substrate quinol directly, instead of relying on the formation of a high-valent iron–oxygen intermediate.

12. CONCLUSIONS

Binuclear non-heme iron enzymes form a large and diverse superfamily of enzymes that carry out a multitude of biological functions. The spectrum of catalyzed reactions is immense and presents an impressive display of nature's ingenuity. Although our knowledge about their biology and chemistry has increased dramatically over the last decades, new members that employ altogether different mechanistic strategies and/or cover alternative physiological aspects are likely to emerge. As an example, the class of enzymes known as arylamine oxygenases is worth a mention, as they are responsible for catalyzing the oxidation of arylamines to arylnitro compounds, which represent an important component of many metabolic functions [634–636]. Specifically, the range of biological properties of arylnitro compounds include antifungal, antitumoral, antibiotic, and insecticidal functions [637–639]. The two presently known enzymes from this group are aminopyrrolnitrin oxygenase and *p*-aminobenzoate oxygenase (Table 1) [640,641]. *p*-Aminobenzoate oxygenase is an N-oxygenase that catalyzes the biosynthesis of aureothin, an important cytostatic metabolite in *Streptomyces thioluteus* [641]. It contains the EX_{28–37}DEXXH sequence motif, highly conserved among other non-heme diiron-containing oxygenases [139,634] (*vide supra*). Furthermore, a preliminary characterization by EPR of fully reduced, fully oxidized, and mixed-valent *p*-aminobenzoate oxygenase indicates the presence of a binuclear non-heme iron active site with properties similar to those of MMO and other members of this superfamily [634].

The projected aim of this review was to provide the reader with an accessible means to navigate through an overwhelmingly rich topic in the field of bioinorganic chemistry. Specifically, the novice may find the article useful to enter a “new territory,” while the expert may find its benefit as a point of reference providing comparative information for a comprehensive if not complete number of related enzymes. The article was not intended to target the EPR specialists specifically. On the contrary, it was our goal to prevent technical jargon and illustrate the generic

use of EPR-related techniques in the study of the electronic properties of binuclear non-heme enzymes instead. In any event, it is hoped that the readership has enjoyed reading the article as much as we did writing it.

ACKNOWLEDGMENTS

This project was funded by a grant from the Australian Research Council (DP0558652). N.M. is recipient of a University of Queensland Strategic Research Fellowship. The authors kindly appreciate the assistance of Miss Elaine Schenk in the preparation of this manuscript.

REFERENCES

1. Dalton H. 2005. The Leeuwenhoek lecture 2000: the natural and unnatural history of methane-oxidizing bacteria. *Phil Trans R Soc B* **360**:1207–1222.
2. Merx M, Kopp DA, Sazinsky MH, Blazyk JL, Müller J, Lippard SJ. 2001. Dioxygen activation and methane hydroxylation by soluble methane monooxygenase: a tale of two irons and three proteins. *Angew Chem Int Ed* **40**:2782–2807.
3. Wallar BJ, Lipscomb JD. 1996. Dioxygen activation by enzymes containing binuclear non-heme iron clusters. *Chemical Rev* **96**:2625–2657.
4. Nordlund P, Eklund H. 1995. Di-iron-carboxylate proteins. *Curr Opin Struct Biol* **5**:758–766.
5. Berthold DA, Andersson ME, Nordlund P. 2000. New insight into the structure and function of the alternative oxidase. *Biochim Biophys Acta* **1460**:241–254.
6. Kuntz M. 2004. Plastid terminal oxidase and its biological significance. *Planta* **218**:896–899.
7. Stenmark P, Grünler J, Mattsson J, Sindelar PJ, Nordlund P, Berthold DA. 2001. A new member of the family of di-iron carboxylate proteins: Coq7 (clk-1), a membrane-bound hydroxylase involved in ubiquinone biosynthesis. *J Biol Chem* **276**:33297–33300.
8. Moseley J, Quinn J, Eriksson M, Merchant S. 2000. The Crd1 gene encodes a putative di-iron enzyme required for photosystem I accumulation in copper deficiency and hypoxia in *Chlamydomonas reinhardtii*. *EMBO J* **19**:2139–2151.
9. Nordlund P. 2001. Structure-function of non-heme iron proteins with oxygen- and nitrogen-dominated coordination. In *Handbook of metalloproteins*, pp. 461–570. Ed I Bertini, A Sigel, H Sigel. New York: Marcel Dekker.
10. Sazinsky MH, Lippard SJ. 2006. Correlating structure with function in bacterial multi-component monooxygenases and related diiron proteins. *Acc Chem Res* **39**:558–566.
11. Lippard SJ. 2005. Hydroxylation of C–H bonds at carboxylate-bridged diiron centres. *Phil Trans R Soc A* **363**:861–877.
12. Leahy JG, Batchelor PJ, Morcomb SM. 2003. Evolution of the soluble diiron monooxygenases. *FEMS Microbiol Rev* **27**:449–479.
13. Rodríguez-Martínez EM, Pérez EX, Schadt CW, Zhou J, Massol-Deyá AA. 2006. Microbial diversity and bioremediation of a hydrocarbon-contaminated aquifer (Vega Baja, Puerto Rico). *Int J Environ Res Public Health* **3**:292–300.

14. Fox BG, Froland WA, Dege JE, Lipscomb JD. 1989. Methane monooxygenase from *Methylosinus richosporium* OB3b: purification and properties of a three-component system with high specific activity from a type-II methanotroph. *J Biol Chem* **264**:10023–10033.
15. Rosenzweig AC, Frederick CA, Lippard SJ, Nordlund P. 1993. Crystal structure of a bacterial non-heme iron hydroxylase that catalyzes the biological oxidation of methane. *Nature* **366**:537–543.
16. Gallagher SC, Cammack R, Dalton H. 1997. Alkene monooxygenase from *Nocardia corallina* B-276 is a member of the class of dinuclear iron proteins capable of stereospecific epoxidation reactions. *Eur J Biochem* **247**:635–641.
17. Zhou NY, Jenkins A, Chion C, Leak DJ. 1998. The alkene monooxygenase from *Xanthobacter* Py2 is a binuclear non-haem iron protein closely related to toluene 4-monooxygenase. *FEBS Lett* **430**:181–185.
18. Byrne AM, Kukor JJ, Olsen RH. 1995. Sequence analysis of the gene cluster encoding toluene-3-monooxygenase from *Pseudomonas pickettii* PKO1. *Gene* **154**:65–70.
19. Nordlund P, Sjöberg BM, Eklund H. 1990. Three-dimensional structure of the free radical protein of ribonucleotide reductase. *Nature* **345**:593–598.
20. Fox BG, Shanklin J, Ai JY, Loehr TM, Sandersloehr J. 1994. Resonance Raman evidence for an Fe–O–Fe center in stearoyl-Acp desaturase: primary sequence identity with other diiron-oxo proteins. *Biochemistry* **33**:12776–12786.
21. Hanson RS, Hanson TE. 1996. Methanotrophic bacteria. *Microbiol Rev* **60**:439–471.
22. Dalton H. 1980. Oxidation of hydrocarbons by methane monooxygenases from variety of microbes. *Adv Appl Microbiol* **26**:71–87.
23. Andersson KK, Froland WA, Lee SK, Lipscomb JD. 1991. Dioxxygen independent oxygenation of hydrocarbons by methane monooxygenase hydroxylase component. *New J Chem* **15**:411–415.
24. Rataj MJ, Kauth JE, Donnelly MI. 1991. Oxidation of deuterated compounds by high specific activity methane monooxygenase from *Methylosinus trichosporium*: mechanistic implications. *J Biol Chem* **266**:18684–18690.
25. Colby J, Stirling DI, Dalton H. 1977. The soluble methane mono-oxygenase of *Methylococcus capsulatus* (Bath): its ability to oxygenate n-alkanes, n-alkenes, ethers, and alicyclic, aromatic and heterocyclic compounds. *Biochem J* **165**:395–402.
26. Green J, Dalton H. 1989. Substrate specificity of soluble methane monooxygenase: mechanistic implications. *J Biol Chem* **264**:17698–17703.
27. Fox BG, Borneman JG, Wackett LP, Lipscomb JD. 1990. Haloalkene oxidation by the soluble methane monooxygenase from *Methylosinus trichosporium* OB3b: mechanistic and environmental implications. *Biochemistry* **29**:6419–6427.
28. Jin Y, Lipscomb JD. 2001. Desaturation reactions catalyzed by soluble methane monooxygenase. *J Biol Inorg Chem* **6**:717–725.
29. Lieberman RL, Rosenzweig AC. 2005. Crystal structure of a membrane-bound metalloenzyme that catalyses the biological oxidation of methane. *Nature* **434**:177–182.
30. Lieberman RL, Kondapalli KC, Shrestha DB, Hakemian AS, Smith SM, Telser J, Kuzelka J, Gupta R, Borovik AS, Lippard SJ, Hoffman BM, Rosenzweig AC, Stemmler TL. 2006. Characterization of the particulate methane monooxygenase metal centers in multiple redox states by x-ray absorption spectroscopy. *Inorg Chem* **45**:8372–8381.
31. Kopp DA, Lippard SJ. 2002. Soluble methane monooxygenase: activation of dioxxygen and methane. *Curr Opin Chem Biol* **6**:568–576.

32. Colby J, Dalton H. 1978. Resolution of the methane mono-oxygenase of *Methylococcus capsulatus* (Bath) into three components: purification and properties of component C, a flavoprotein. *Biochem J* **171**:461–468.
33. Green J, Dalton H. 1985. Protein-B of soluble methane monooxygenase from *Methylococcus capsulatus* (Bath): a novel regulatory protein of enzyme activity. *J Biol Chem* **260**:5795–5801.
34. Gassner GT, Lippard SJ. 1999. Component interactions in the soluble methane monooxygenase system from *Methylococcus capsulatus* (Bath). *Biochemistry* **38**:12768–12785.
35. Chatwood LL, Müller J, Gross JD, Wagner G, Lippard SJ. 2004. NMR structure of the flavin domain from soluble methane monooxygenase reductase from *Methylococcus capsulatus* (Bath). *Biochemistry* **43**:11983–11991.
36. Blazyk JL, Lippard SJ. 2002. Expression and characterization of ferredoxin and flavin adenine dinucleotide binding domains of the reductase component of soluble methane monooxygenase from *Methylococcus capsulatus* (Bath). *Biochemistry* **41**:15780–15794.
37. Müller J, Lugovskoy AA, Wagner G, Lippard SJ. 2002. NMR structure of the 2Fe–2S ferredoxin domain from soluble methane monooxygenase reductase and interaction with its hydroxylase. *Biochemistry* **41**:42–51.
38. Kopp DA, Gassner GT, Blazyk JL, Lippard SJ. 2001. Electron-transfer reactions of the reductase component of soluble methane monooxygenase from *Methylococcus capsulatus* (Bath). *Biochemistry* **40**:14932–14941.
39. Liu Y, Nesheim JC, Paulsen KE, Stankovich MT, Lipscomb JD. 1997. Roles of the methane monooxygenase reductase component in the regulation of catalysis. *Biochemistry* **36**:5223–5233.
40. Zhang JY, Lipscomb JD. 2006. Role of the C-terminal region of the B component of *Methylosinus trichosporium* OB3b methane monooxygenase in the regulation of oxygen activation. *Biochemistry* **45**:1459–1469.
41. Chang SL, Wallar BJ, Lipscomb JD, Mayo KH. 2001. Residues in *Methylosinus trichosporium* OB3b methane monooxygenase component B involved in molecular interactions with reduced- and oxidized-hydroxylase component: a role for the N-terminus. *Biochemistry* **40**:9539–9551.
42. Liu Y, Nesheim JC, Lee S-K, Lipscomb JD. 1995. Gating effects of component b on oxygen activation by the methane monooxygenase hydroxylase component. *J Biol Chem* **270**:24662–24665.
43. Liu KE, Valentine AM, Wang DL, Huynh BH, Edmondson DE, Salifoglou A, Lippard SJ. 1995. Kinetic and spectroscopic characterization of intermediates and component interactions in reactions of methane monooxygenase from *Methylococcus capsulatus* (Bath). *J Am Chem Soc* **117**:10174–10185.
44. Kazlauskaite J, Hill HAO, Wilkins PC, Dalton H. 1996. Direct electrochemistry of the hydroxylase of soluble methane monooxygenase from *Methylococcus capsulatus* (Bath). *Eur J Biochem* **241**:552–556.
45. Paulsen KE, Liu Y, Fox BG, Lipscomb JD, Münck E, Stankovich MT. 1994. Oxidation-reduction potentials of the methane monooxygenase hydroxylase component from *Methylosinus trichosporium* OB3b. *Biochemistry* **33**:713–722.
46. Liu KE, Lippard SJ. 1991. Redox properties of the hydroxylase component of methane monooxygenase from *Methylococcus capsulatus* (Bath): effects of protein b, reductase, and substrate. *J Biol Chem* **266**:12836–12839.

47. Froland WA, Andersson KK, Lee SK, Liu Y, Lipscomb JD. 1992. Methane monooxygenase component B and reductase alter the regioselectivity of the hydroxylase component-catalyzed reactions: a novel role for protein-protein interactions in an oxygenase mechanism. *J Biol Chem* **267**:17588–17597.
48. Brazeau BJ, Lipscomb JD. 2003. Key amino acid residues in the regulation of soluble methane monooxygenase catalysis by component B. *Biochemistry* **42**:5618–5631.
49. Wallar BJ, Lipscomb JD. 2001. Methane monooxygenase component B mutants alter the kinetics of steps throughout the catalytic cycle. *Biochemistry* **40**:2220–2233.
50. Zhang JY, Wallar BJ, Popescu CV, Renner DB, Thomas DD, Lipscomb JD. 2006. Methane monooxygenase hydroxylase and B component interactions. *Biochemistry* **45**:2913–2926.
51. Fox BG, Liu Y, Dege JE, Lipscomb JD. 1991. Complex formation between the protein components of methane monooxygenase from *Methylosinus trichosporium* OB3b: identification of sites of component interaction. *J Biol Chem* **266**:540–550.
52. Sazinsky MH, Lippard SJ. 2005. Product bound structures of the soluble methane monooxygenase hydroxylase from *Methylococcus capsulatus* (Bath): protein motion in the alpha-subunit. *J Am Chem Soc* **127**:5814–5825.
53. Sazinsky MH, Merckx M, Cadieux E, Tang S, Lippard SJ. 2004. Preparation and x-ray structures of metal-free, dicobalt and dimanganese forms of soluble methane monooxygenase hydroxylase from *Methylococcus capsulatus* (Bath). *Biochemistry* **43**:16263–16276.
54. Whittington DA, Rosenzweig AC, Frederick CA, Lippard SJ. 2001. Xenon and halogenated alkanes track putative substrate binding cavities in the soluble methane monooxygenase hydroxylase. *Biochemistry* **40**:3476–3482.
55. Whittington DA, Sazinsky MH, Lippard SJ. 2001. X-ray crystal structure of alcohol products bound at the active site of soluble methane monooxygenase hydroxylase. *J Am Chem Soc* **123**:1794–1795.
56. Whittington DA, Lippard SJ. 2001. Crystal structures of the soluble methane monooxygenase hydroxylase from *Methylococcus capsulatus* (Bath) demonstrating geometrical variability at the dinuclear iron active site. *J Am Chem Soc* **123**:827–838.
57. Rosenzweig AC, Nordlund P, Takahara PM, Frederick CA, Lippard SJ. 1995. Geometry of the soluble methane monooxygenase catalytic diiron center in two oxidation states. *Chem Biol* **2**:409–418.
58. Elango N, Radhakrishnan R, Froland WA, Wallar BJ, Earhart CA, Lipscomb JD, Ohlendorf DH. 1997. Crystal structure of the hydroxylase component of methane monooxygenase from *Methylosinus trichosporium* OB3b. *Protein Sci* **6**:556–568.
59. Rosenzweig AC, Brandstetter H, Whittington DA, Nordlund P, Lippard SJ, Frederick CA. 1997. Crystal structures of the methane monooxygenase hydroxylase from *Methylococcus capsulatus* (Bath): implications for substrate gating and component interactions. *Proteins: Struct, Funct, Genet* **29**:141–152.
60. Lindqvist Y, Huang WJ, Schneider G, Shanklin J. 1996. Crystal structure of Delta(9) stearoyl-acyl carrier protein desaturase from castor seed and its relationship to other di-iron proteins. *EMBO J* **15**:4081–4092.
61. Lombardi A, Summa CM, Geremia S, Randaccio L, Pavone V, DeGrado WF. 2000. Retrostructural analysis of metalloproteins: application to the design of a minimal model for diiron proteins. *Proc Natl Acad Sci USA* **97**:6298–6305.
62. Walters KJ, Gassner GT, Lippard SJ, Wagner G. 1999. Structure of the soluble methane monooxygenase regulatory protein B. *Proc Natl Acad Sci USA* **96**:7877–7882.

63. Chang SL, Wallar BJ, Lipscomb JD, Mayo KH. 1999. Solution structure of component B from methane monooxygenase derived through heteronuclear NMR and molecular modeling. *Biochemistry* **38**:5799–5812.
64. Pilbrow JR. 1990. *Transition ion electron paramagnetic resonance*. Oxford: Clarendon Press.
65. Bencini A, Gatteschi D. 1990. *EPR of exchange coupled systems*. Berlin: Springer-Verlag.
66. Smith TD, Pilbrow JR. 1974. Determination of structural properties of dimeric transition metal ion complexes from EPR spectra. *Coord Chem Rev* **13**:173–278.
67. Schweiger A, Jeschke G. 2001. *Principles of pulse electron paramagnetic resonance*. Oxford: Oxford UP.
68. Owen J. 1961. Paramagnetic resonance measurements of exchange interactions. *J Appl Phys* **32**:S213–S217.
69. Hendrich MP, Pearce LL, Que Jr L, Chasteen ND, Day EP. 1991. Multifield saturation magnetization and multifrequency EPR measurements of deoxyhemerythrin azide: a unified picture. *J Am Chem Soc* **113**:3039–3044.
70. Fox BG, Hendrich MP, Surerus KK, Andersson KK, Froland WA, Lipscomb JD, Münck E. 1993. Mössbauer, EPR, and ENDOR studies of the hydroxylase and reductase components of methane monooxygenase from *Methylosinus trichosporium* OB3b. *J Am Chem Soc* **115**:3688–3701.
71. Dewitt JG, Bentsen JG, Rosenzweig AC, Hedman B, Green J, Pilkington S, Papaefthymiou GC, Dalton H, Hodgson KO, Lippard SJ. 1991. X-ray absorption, mössbauer, and epr studies of the dinuclear iron center in the hydroxylase component of methane monooxygenase. *J Am Chem Soc* **113**:9219–9235.
72. Ericson A, Hedman B, Hodgson KO, Green J, Dalton H, Bentsen JG, Beer RH, Lippard SJ. 1988. Structural characterization by EXAFS spectroscopy of the binuclear iron center in protein a of methane monooxygenase from *Methylococcus capsulatus* (Bath). *J Am Chem Soc* **110**:2330–2332.
73. Dewitt JG, Rosenzweig AC, Salifoglou A, Hedman B, Lippard SJ, Hodgson KO. 1995. X-ray absorption spectroscopic studies of the diiron center in methane monooxygenase in the presence of substrate and the coupling protein of the enzyme system. *Inorg Chem* **34**:2505–2515.
74. Shu LJ, Liu Y, Lipscomb JD, Que Jr L. 1996. X-ray absorption spectroscopic studies of the methane monooxygenase hydroxylase component from *Methylosinus trichosporium* OB3b. *J Biol Inorg Chem* **1**:297–304.
75. Fox BG, Surerus KK, Münck E, Lipscomb JD. 1988. Evidence for a μ -oxo-bridged binuclear iron cluster in the hydroxylase component of methane monooxygenase: Mössbauer and electron paramagnetic resonance studies. *J Biol Chem* **263**:10553–10556.
76. Hendrich MP, Münck E, Fox BG, Lipscomb JD. 1990. Integer-spin EPR studies of the fully reduced methane monooxygenase hydroxylase component. *J Am Chem Soc* **112**:5861–5865.
77. Hoffman BM, Sturgeon BE, Doan PE, DeRose VJ, Liu KE, Lippard SJ. 1994. ESEEM and ENDOR magnetic-resonance studies of the non-Kramer doublet in the integer-spin diiron(ii) forms of two methane monooxygenase hydroxylases and hemerythrin azide. *J Am Chem Soc* **116**:6023–6024.
78. Pulver S, Froland WA, Fox BG, Lipscomb JD, Solomon EI. 1993. Spectroscopic studies of the coupled binuclear non-heme iron active site in the fully reduced hydroxylase

- component of methane monooxygenase: comparison to deoxy and deoxy-azide hemerythrin. *J Am Chem Soc* **115**:12409–12422.
79. Wei PP, Skulan AJ, Wade H, DeGrado WF, Solomon EI. 2005. Spectroscopic and computational studies of the de novo designed protein DF2t: correlation to the biferrous active site of ribonucleotide reductase and factors that affect O₂ reactivity. *J Am Chem Soc* **127**:16098–16106.
 80. Woodland MP, Patil DS, Cammack R, Dalton H. 1986. Electron spin resonance studies of protein-A of the soluble methane monooxygenase from *Methylococcus capsulatus* (Bath). *Biochim Biophys Acta* **873**:237–242.
 81. Muhoberac BB, Wharton DC, Babcock LM, Harrington PC, Wilkins RG. 1980. EPR spectroscopy of semi-methemerythrin. *Biochim Biophys Acta* **626**:337–345.
 82. Davis JC, Averill BA. 1982. Evidence for a spin-coupled binuclear iron unit at the active site of the purple acid phosphatase from beef spleen. *Proc Natl Acad Sci USA* **79**:4623–4627.
 83. DeRose VJ, Liu KE, Kurtz Jr DM, Hoffman BM, Lippard SJ. 1993. Proton ENDOR identification of bridging hydroxide ligands in mixed-valent diiron centers of proteins: methane monooxygenase and semimet azidohemerythrin. *J Am Chem Soc* **115**:6440–6441.
 84. Thomann H, Bernardo M, McCormick JM, Pulver S, Andersson KK, Lipscomb JD, Solomon EI. 1993. Pulsed EPR studies of mixed-valent [Fe(II)Fe(III)] forms of hemerythrin and methane monooxygenase: evidence for a hydroxide bridge. *J Am Chem Soc* **115**:8881–8882.
 85. Hendrich MP, Fox BG, Andersson KK, Debrunner PG, Lipscomb JD. 1992. Ligation of the diiron site of the hydroxylase component of methane monooxygenase: an electron nuclear double resonance study. *J Biol Chem* **267**:261–269.
 86. Shiemke AK, Loehr TM, Sanders-Loehr J. 1984. Resonance Raman study of the μ -oxo-bridged binuclear iron center in oxyhemerythrin. *J Am Chem Soc* **106**:4951–4956.
 87. Davydov A, Davydov R, Gräslund A, Lipscomb JD, Andersson KK. 1997. Radiolytic reduction of methane monooxygenase dinuclear iron cluster at 77 K: EPR evidence for conformational change upon reduction or binding of component B to the diferric state. *J Biol Chem* **272**:7022–7026.
 88. Davydov R, Valentine AM, Komar-Panicucci S, Hoffman BM, Lippard SJ. 1999. An EPR study of the dinuclear iron site in the soluble methane monooxygenase from *Methylococcus capsulatus* (Bath) reduced by one electron at 77 K: the effects of component interactions and the binding of small molecules to the diiron(III) center. *Biochemistry* **38**:4188–4197.
 89. DeRose VJ, Liu KE, Lippard SJ, Hoffman BM. 1996. Investigation of the dinuclear Fe center of methane monooxygenase by advanced paramagnetic resonance techniques: on the geometry of DMSO binding. *J Am Chem Soc* **118**:121–134.
 90. Willems J-P, Valentine AM, Gurbier R, Lippard SJ, Hoffman BM. 1998. Small molecule binding to the mixed-valent diiron center of methane monooxygenase hydroxylase from *Methylococcus capsulatus* (Bath) as revealed by ENDOR spectroscopy. *J Am Chem Soc* **120**:9410–9416.
 91. Smoukov SK, Kopp DA, Valentine AM, Davydov R, Lippard SJ, Hoffman BM. 2002. Product binding to the diiron(III) and mixed-valence diiron centers of methane monooxygenase hydroxylase studied by ^{1,2}H and ¹⁹F ENDOR spectroscopy. *J Am Chem Soc* **124**:2657–2663.

92. Nocek JM, Kurtz Jr DM, Sage JT, Debrunner PG, Maroney MJ, Que Jr L. 1985. Nitric-oxide adduct of the binuclear iron center in deoxyhemerythrin from *Phascolopsis gouldii*: analog of a putative intermediate in the oxygenation reaction. *J Am Chem Soc* **107**:3382–3384.
93. Nocek JM, Kurtz Jr DM, Sage JT, Xia YM, Debrunner P, Shiemke AK, Sanders-Loehr J, Loehr TM. 1988. Nitric-oxide adducts of the binuclear iron site of hemerythrin: spectroscopy and reactivity. *Biochemistry* **27**:1014–1024.
94. Haskin CJ, Ravi N, Lynch JB, Münck E, Que Jr L. 1995. Reaction of NO with the reduced R2 protein of ribonucleotide reductase from *Escherichia coli*. *Biochemistry* **34**:11090–11098.
95. Schenk G, Pau MYM, Solomon EI. 2004. Comparison between the geometric and electronic structures and reactivities of $\{\text{FeNO}\}^7$ and $\{\text{FeO}_2\}^8$ complexes: a density functional theory study. *J Am Chem Soc* **126**:505–515.
96. Brown CA, Pavlosky MA, Westre TE, Zhang Y, Hedman B, Hodgson KO, Solomon EI. 1995. Spectroscopic and theoretical description of the electronic structure of $S = 3/2$ iron-nitrosyl complexes and their relation to O_2 activation by non-heme iron enzyme active sites. *J Am Chem Soc* **117**:715–732.
97. Coufal DE, Tavares P, Pereira AS, Hyunh BH, Lippard SJ. 1999. Reactions of nitric oxide with the reduced non-heme diiron center of the soluble methane monooxygenase hydroxylase. *Biochemistry* **38**:4504–4513.
98. Valentine AM, Stahl SS, Lippard SJ. 1999. Mechanistic studies of the reaction of reduced methane monooxygenase hydroxylase with dioxygen and substrates. *J Am Chem Soc* **121**:3876–3887.
99. Liu KE, Valentine AM, Qiu D, Edmondson DE, Appelman EH, Spiro TG, Lippard SJ. 1995. Characterization of a diiron(III) peroxo intermediate in the reaction cycle of methane monooxygenase hydroxylase from *Methylococcus capsulatus* (Bath). *J Am Chem Soc* **117**:4997–4998.
100. MacArthur R, Sazinsky MH, Kuhne H, Whittington DA, Lippard SJ, Brudvig GW. 2002. Component B binding to the soluble methane monooxygenase hydroxylase by saturation-recovery EPR spectroscopy of spin-labeled MMOB. *J Am Chem Soc* **124**:13392–13393.
101. Hubbell WL, Cafiso DS, Altenbach C. 2000. Identifying conformational changes with site-directed spin labeling. *Nat Struct Biol* **7**:735–739.
102. Altenbach C, Froncisz W, Hemker R, Mchaourab H, Hubbell WL. 2005. Accessibility of nitroxide side chains: Absolute Heisenberg exchange rates from power saturation EPR. *Biophys J* **89**:2103–2112.
103. Lee S-K, Nesheim JC, Lipscomb JD. 1993. Transient intermediates of the methane monooxygenase catalytic cycle. *J Biol Chem* **268**:21569–21577.
104. Lee S-K, Lipscomb JD. 1999. Oxygen activation catalyzed by methane monooxygenase hydroxylase component: proton delivery during the O–O bond cleavage steps. *Biochemistry* **38**:4423–4432.
105. Shu LJ, Nesheim JC, Kauffmann K, Münck E, Lipscomb JD, Que Jr L. 1997. An $\text{Fe}_2^{\text{IV}}\text{O}_2$ diamond core structure for the key intermediate Q of methane monooxygenase. *Science* **275**:515–518.
106. Lee S-K, Fox BG, Froland WA, Lipscomb JD, Münck E. 1993. A transient intermediate of the methane monooxygenase catalytic cycle containing an $\text{Fe}^{\text{IV}}\text{Fe}^{\text{IV}}$ cluster. *J Am Chem Soc* **115**:6450–6451.
107. Valentine AM, Tavares P, Pereira AS, Davydov R, Krebs C, Hoffman BM, Edmondson DE, Huynh BH, Lippard SJ. 1998. Generation of a mixed-valent

- Fe(III)Fe(IV) form of intermediate Q in the reaction cycle of soluble methane monooxygenase, an analog of intermediate X in ribonucleotide reductase R2 assembly. *J Am Chem Soc* **120**:2190–2191.
108. Beauvais LG, Lippard SJ. 2005. Reactions of the diiron(IV) intermediate Q in soluble methane monooxygenase with fluoromethanes. *Biochem Biophys Res Commun* **338**:262–266.
 109. Beauvais LG, Lippard SJ. 2005. Reactions of the peroxo intermediate of soluble methane monooxygenase hydroxylase with ethers. *J Am Chem Soc* **127**:7370–7378.
 110. Choi S-Y, Eaton PE, Hollenberg PF, Liu KE, Lippard SJ, Newcomb M, Putt DA, Upadhyaya SP, Xiong YS. 1996. Regiochemical variations in reactions of methylcubane with tert-butoxyl radical, cytochrome P-450 enzymes, and a methane monooxygenase system. *J Am Chem Soc* **118**:6547–6555.
 111. Priestley ND, Floss HG, Froland WA, Lipscomb JD, Williams PG, Morimoto H. 1992. Cryptic stereospecificity of methane monooxygenase. *J Am Chem Soc* **114**:7561–7562.
 112. Nesheim JC, Lipscomb JD. 1996. Large kinetic isotope effects in methane oxidation catalyzed by methane monooxygenase: evidence for C–H bond cleavage in a reaction cycle intermediate. *Biochemistry* **35**:10240–10247.
 113. Ruzicka F, Huang DS, Donnelly MI, Frey PA. 1990. Methane monooxygenase catalyzed oxygenation of 1,1-dimethylcyclopropane: evidence for radical and carbocationic intermediates. *Biochemistry* **29**:1696–1700.
 114. Jin Y, Lipscomb JD. 1999. Probing the mechanism of C–H activation: oxidation of methylcubane by soluble methane monooxygenase from *Methylosinus trichosporium* OB3b. *Biochemistry* **38**:6178–6186.
 115. Ortiz de Montellano PR. 2005. *Cytochrome P450: structure, mechanism, and biochemistry*, 3rd ed. New York: Kluwer Academic/Plenum.
 116. Liu KE, Johnson CC, Newcomb M, Lippard SJ. 1993. Radical clock substrate probes and kinetic isotope effect studies of the hydroxylation of hydrocarbons by methane monooxygenase. *J Am Chem Soc* **115**:939–947.
 117. Choi S-Y, Eaton PE, Kopp DA, Lippard SJ, Newcomb M, Shen R. 1999. Cationic species can be produced in soluble methane monooxygenase-catalyzed hydroxylation reactions; radical intermediates are not formed. *J Am Chem Soc* **121**:12198–12199.
 118. Valentine AM, LeTadic-Biadatti MH, Toy PH, Newcomb M, Lippard SJ. 1999. Oxidation of ultrafast radical clock substrate probes by the soluble methane monooxygenase from *Methylococcus capsulatus* (Bath). *J Biol Chem* **274**:10771–10776.
 119. Feig AL, Lippard SJ. 1994. Reactions of nonheme iron(II) centers with dioxygen in biology and chemistry. *Chem Rev* **94**:759–805.
 120. Gherman BF, Baik MH, Lippard SJ, Friesner RA. 2004. Dioxygen activation in methane monooxygenase: a theoretical study. *J Am Chem Soc* **126**:2978–2990.
 121. Gherman BF, Lippard SJ, Friesner RA. 2005. Substrate hydroxylation in methane monooxygenase: quantitative modeling via mixed quantum mechanics/molecular mechanics techniques. *J Am Chem Soc* **127**:1025–1037.
 122. Yoshizawa K. 2000. Two-step concerted mechanism for methane hydroxylation on the diiron active site of soluble methane monooxygenase. *J Inorg Biochem* **78**:23–34.
 123. Brazeau BJ, Austin RN, Tarr C, Groves JT, Lipscomb JD. 2001. Intermediate Q from soluble methane monooxygenase hydroxylates the mechanistic substrate probe norcarane: evidence for a stepwise reaction. *J Am Chem Soc* **123**:11831–11837.

124. Dalton H, Wilkins PC, Deighton N, Podmore ID, Symons MCR. 1992. Electron paramagnetic resonance studies of the mechanism of substrate oxidation by methane monooxygenase. *Faraday Discuss* **93**:163–171.
125. Wilkins PC, Dalton H, Podmore ID, Deighton N, Symons MCR. 1992. Biological methane activation involves the intermediacy of carbon-centered radicals. *Eur J Biochem* **210**:67–72.
126. Liu AM, Jin Y, Zhang JY, Brazeau BJ, Lipscomb JD. 2005. Substrate radical intermediates in soluble methane monooxygenase. *Biochem Biophys Res Commun* **338**:254–261.
127. Peterson JA, Basu D, Coon MJ. 1966. Enzymatic omega-oxidation, I: electron carriers in fatty acid and hydrocarbon hydroxylation. *J Biol Chem* **241**:5162–5164.
128. Katopodis AG, Smith HA, May SW. 1988. New oxyfunctionalization capabilities for omega-hydroxylases. Asymmetric aliphatic sulfoxidation and branched ether demethylation. *J Am Chem Soc* **110**:897–899.
129. Colbert JE, Katopodis AG, May SW. 1990. Epoxidation of *cis*-1,2-dideuterio-1-octene by *Pseudomonas oleovorans* monooxygenase proceeds without deuterium exchange. *J Am Chem Soc* **112**:3993–3996.
130. Fu H, Newcomb M, Wong CH. 1991. *Pseudomonas oleovorans* monooxygenase catalyzed asymmetric epoxidation of allyl alcohol derivatives and hydroxylation of a hypersensitive radical probe with the radical ring-opening rate exceeding the oxygen rebound rate. *J Am Chem Soc* **113**:5878–5880.
131. Smits THM, Röthlisberger M, Witholt B, van Beilen JB. 1999. Molecular screening for alkane hydroxylase genes in Gram-negative and Gram-positive strains. *Environ Microbiol* **1**:307–317.
132. Whyte LG, Smits THM, Labbe D, Witholt B, Greer CW, van Beilen JB. 2002. Gene cloning and characterization of multiple alkane hydroxylase systems in *Rhodococcus* strains Q15 and NRRL B-16531. *Appl Environ Microbiol* **68**:5933–5942.
133. Margesin R, Labbe D, Schinner F, Greer CW, Whyte LG. 2003. Characterization of hydrocarbon-degrading microbial populations in contaminated and pristine alpine soils. *Appl Environ Microbiol* **69**:3085–3092.
134. Smits THM, Balada SB, Witholt B, van Beilen JB. 2002. Functional analysis of alkane hydroxylases from Gram-negative and Gram-positive bacteria. *J Bacteriol* **184**:1733–1742.
135. van Beilen JB, Marín MM, Smits THM, Röthlisberger M, Franchini AG, Witholt B, Rojo F. 2004. Characterization of two alkane hydroxylase genes from the marine hydrocarbonoclastic bacterium *Alcanivorax borkumensis*. *Environ Microbiol* **6**:264–273.
136. Ueda T, Lode ET, Coon MJ. 1972. Enzymatic omega-oxidation, 6: isolation of homogeneous reduced diphosphopyridine nucleotide-rubredoxin reductase. *J Biol Chem* **247**:2109–2116.
137. McKenna EJ, Coon MJ. 1970. Enzymatic omega-oxidation, 4: purification and properties of omega-hydroxylase of *Pseudomonas oleovorans*. *J Biol Chem* **245**:3882–3889.
138. Kok M, Oldenhuis R, van der Linden MPG, Raatjes P, Kingma J, van Lelyveld PH, Witholt B. 1989. The *Pseudomonas oleovorans* alkane hydroxylase gene: sequence and expression. *J Biol Chem* **264**:5435–5441.
139. Shanklin J, Achim C, Schmidt H, Fox BG, Münck E. 1997. Mössbauer studies of alkane omega-hydroxylase: evidence for a diiron cluster in an integral-membrane enzyme. *Proc Natl Acad Sci USA* **94**:2981–2986.

140. Shanklin J, Whittle E, Fox BG. 1994. 8 histidine-residues are catalytically essential in a membrane-associated iron enzyme, stearoyl-CoA desaturase, and are conserved in alkane hydroxylase and xylene monooxygenase. *Biochemistry* **33**:12787–12794.
141. Taton M, Husselstein T, Benveniste P, Rahier A. 2000. Role of highly conserved residues in the reaction catalyzed by recombinant $\Delta(7)$ -sterol-C5(6)-desaturase studied by site-directed mutagenesis. *Biochemistry* **39**:701–711.
142. Avelange-Macherel M-H, Macherel D, Wada H, Murata N. 1995. Site-directed mutagenesis of histidine residues in the Delta-12 acyl-lipid desaturase of *Synechocystis*. *FEBS Lett* **361**:111–114.
143. Shanklin J, Whittle E. 2003. Evidence linking the *Pseudomonas oleovorans* alkane omega-hydroxylase, an integral membrane diiron enzyme, and the fatty acid desaturase family. *FEBS Lett* **545**:188–192.
144. Shanklin J, Cahoon EB. 1998. Desaturation and related modifications of fatty acids. *Annu Rev Plant Physiol Plant Mol Biol* **49**:611–641.
145. Cahoon EB, Carlson TJ, Ripp KG, Schweiger BJ, Cook GA, Hall SE, Kinney AJ. 1999. Biosynthetic origin of conjugated double bonds: production of fatty acid components of high-value drying oils in transgenic soybean embryos. *Proc Natl Acad Sci USA* **96**:12935–12940.
146. Pikus JD, Studts JM, Achim C, Kauffmann KE, Münck E, Steffan RJ, McClay K, Fox BG. 1996. Recombinant toluene-4-monooxygenase: catalytic and Mössbauer studies of the purified diiron and Rieske components of a four-protein complex. *Biochemistry* **35**:9106–9119.
147. Clark PE, Webb J. 1981. Mössbauer spectroscopic studies of hemerythrin from *Phascolosoma lurco* (syn. *Phascolosoma arcuatum*). *Biochemistry* **20**:4628–4632.
148. Austin RN, Chang HK, Zylstra GJ, Groves JT. 2000. The non-heme diiron alkane monooxygenase of *Pseudomonas oleovorans* (AlkB) hydroxylates via a substrate radical intermediate. *J Am Chem Soc* **122**:11747–11748.
149. Groves JT. 2003. The bioinorganic chemistry of iron in oxygenases and supramolecular assemblies. *Proc Natl Acad Sci USA* **100**:3569–3574.
150. Bertrand E, Sakai R, Rozhkova-Novosad E, Moe L, Fox BG, Groves JT, Austin RN. 2005. Reaction mechanisms of non-heme diiron hydroxylases characterized in whole cells. *J Inorg Biochem* **99**:1998–2006.
151. Miura A, Dalton H. 1995. Purification and characterization of the alkene monooxygenase from *Nocardia corallina* B-276. *Biosci Biotechnol Biochem* **59**:853–859.
152. Saeki H, Akira M, Furuhashi K, Averhoff B, Gottschalk G. 1999. Degradation of trichloroethene by a linear-plasmid-encoded alkene monooxygenase in *Rhodococcus corallinus* (*Nocardia corallina*) B-276. *Microbiology-UK* **145**:1721–1730.
153. Vanginkel CG, Welten HGJ, Debont JAM. 1987. Oxidation of gaseous and volatile hydrocarbons by selected alkene-utilizing bacteria. *Appl Environ Microbiol* **53**:2903–2907.
154. Vanginkel CG, Debont JAM. 1986. Isolation and characterization of alkene-utilizing *Xanthobacter* spp. *Arch Microbiol* **145**:403–407.
155. Smith TJ, Lloyd JS, Gallagher SC, Fosdike WLJ, Murrell JC, Dalton H. 1999. Heterologous expression of alkene monooxygenase from *Rhodococcus rhodochrous* B-276. *Eur J Biochem* **260**:446–452.
156. Saeki H, Furuhashi K. 1994. Cloning and characterisation of a *Nocardia corallina* B-276 gene cluster encoding alkene monooxygenase. *J Ferment Bioeng* **78**:399–406.

157. Gallagher SC, George A, Dalton H. 1998. Sequence-alignment modelling and molecular docking studies of the epoxigenase component of alkene monooxygenase from *Nocardia corallina* B-276. *Eur J Biochem* **254**:480–489.
158. Gerez C, Gaillard J, Latour J-M, Fontecave M. 1991. Reduction of the small subunit of ribonucleotide reductase by diimide: evidence for the formation of the mixed-valence feii-feiii center. *Angew Chem, Int Ed* **30**:1135–1136.
159. Gallagher SC, Cammack R, Dalton H. 1999. Electron transfer reactions in the alkene mono-oxygenase complex from *Nocardia corallina* B-276. *Biochem J* **339**:79–85.
160. Fosdike WLJ, Smith TJ, Dalton H. 2005. Adventitious reactions of alkene monooxygenase reveal common reaction pathways and component interactions among bacterial hydrocarbon oxygenases. *FEBS J* **272**:2661–2669.
161. Small FJ, Ensign SA. 1997. Alkene monooxygenase from *Xanthobacter* strain Py2: purification and characterization of a four-component system central to the bacterial metabolism of aliphatic alkenes. *J Biol Chem* **272**:24913–24920.
162. Allen JR, Ensign SA. 1997. Purification to homogeneity and reconstitution of the individual components of the epoxide carboxylase multiprotein enzyme complex from *Xanthobacter* strain Py2. *J Biol Chem* **272**:32121–32128.
163. Zhou N-Y, Jenkins A, Chion CKNCK, Leak DJ. 1999. The alkene monooxygenase from *Xanthobacter* strain Py2 is closely related to aromatic monooxygenases and catalyzes aromatic monohydroxylation of benzene, toluene, and phenol. *Appl Environ Microbiol* **65**:1589–1595.
164. Ensign SA, Hyman MR, Arp DJ. 1992. Cometabolic degradation of chlorinated alkenes by alkene monooxygenase in a propylene-grown *Xanthobacter* strain. *Appl Environ Microbiol* **58**:3038–3046.
165. Nordlund I, Powlowski J, Shingler V. 1990. Complete nucleotide sequence and polypeptide analysis of multicomponent phenol hydroxylase from *Pseudomonas* sp. Strain CF 600. *J Bacteriol* **172**:6826–6833.
166. Nordlund I, Powlowski J, Hagstrom A, Shingler V. 1993. Conservation of regulatory and structural genes for a multicomponent phenol hydroxylase within phenol-catabolizing bacteria that utilize a meta-cleavage pathway. *J Gen Microbiol* **139**:2695–2703.
167. Powlowski J, Shingler V. 1990. In-vitro analysis of polypeptide requirements of multicomponent phenol hydroxylase from *Pseudomonas* Sp. strain CF 600. *J Bacteriol* **172**:6834–6840.
168. Powlowski J, Shingler V. 1994. Genetics and biochemistry of phenol degradation by *Pseudomonas* sp. CF 600. *Biodegradation* **5**:219–236.
169. Shingler V, Franklin FCH, Tsuda M, Holroyd D, Bagdasarjian M. 1989. Molecular analysis of a plasmid-encoded phenol Hydroxylase from *Pseudomonas* CF 600. *J Gen Microbiol* **135**:1083–1092.
170. Cadieux E, Powlowski J. 1999. Characterization of active and inactive forms of the phenol hydroxylase stimulatory protein DmpM. *Biochemistry* **38**:10714–10722.
171. Powlowski J, Sealy J, Shingler V, Cadieux E. 1997. On the role of DmpK, an auxiliary protein associated with multicomponent phenol hydroxylase from *Pseudomonas* sp. strain C F600. *J Biol Chem* **272**:945–951.
172. Newman LM, Wackett LP. 1995. Purification and characterization of toluene 2-monooxygenase from *Burkholderia cepacia* G4. *Biochemistry* **34**:14066–14076.
173. Coufal DE, Blazzyk JL, Whittington DA, Wu WW, Rosenzweig AC, Lippard SJ. 2000. Sequencing and analysis of the *Methylococcus capsulatus* (Bath) soluble methane monooxygenase genes. *Eur J Biochem* **267**:2174–2185.

174. Qian H, Edlund U, Powlowski J, Shingler V, Sethson I. 1997. Solution structure of phenol hydroxylase protein component P2 determined by NMR spectroscopy. *Biochemistry* **36**:495–504.
175. Cadieux E, Vrajmasu V, Achim C, Powlowski J, Münck E. 2002. Biochemical, Mössbauer, and EPR studies of the diiron cluster of phenol hydroxylase from *Pseudomonas* sp. strain CF 600. *Biochemistry* **41**:10680–10691.
176. Sazinsky MH, Dunten PW, McCormick MS, Di Donato A, Lippard SJ. 2006. X-ray structure of a hydroxylase-regulatory protein complex from a hydrocarbon-oxidizing multicomponent monooxygenase: *Pseudomonas* sp. OX1 phenol hydroxylase. *Biochemistry* **45**:15392–15404.
177. Kurtz Jr DM. 1990. Oxo-bridged and hydroxo-bridged diiron complexes: a chemical perspective on a biological unit. *Chem Rev* **90**:585–606.
178. Fox BG, Shanklin J, Somerville C, Münck E. 1993. Stearoyl-acyl carrier protein Delta-9 desaturase from *Ricinus communis* is a diiron-oxo protein. *Proc Natl Acad Sci USA* **90**:2486–2490.
179. Shu LJ, Broadwater JA, Achim C, Fox BG, Münck E, Que Jr L. 1998. EXAFS and Mössbauer characterization of the diiron(III) site in stearoyl-acyl carrier protein Delta(9) desaturase. *J Biol Inorg Chem* **3**:392–400.
180. Harayama S, Kok M, Neidle EL. 1992. Functional and evolutionary relationships among diverse oxygenases. *Annu Rev Microbiol* **46**:565–601.
181. Divari S, Valetti F, Caposio P, Pessione E, Cavaletto M, Griva E, Gribaudo G, Gilardi G, Giunta C. 2003. The oxygenase component of phenol hydroxylase from *Acinetobacter radioresistens* S13. *Eur J Biochem* **270**:2244–2253.
182. Griva E, Pessione E, Divari S, Valetti F, Cavaletto M, Rossi GL, Giunta C. 2003. Phenol hydroxylase from *Acinetobacter radioresistens* S13: isolation and characterization of the regulatory component. *Eur J Biochem* **270**:1434–1440.
183. Teramoto M, Futamata H, Harayama S, Watanabe K. 1999. Characterization of a high-affinity phenol hydroxylase from *Comamonas testosteroni* R5 by gene cloning, and expression in *Pseudomonas aeruginosa* PAO1c. *Mol Gen Genet* **262**:552–558.
184. Hino S, Watanabe K, Takahashi N. 1998. Phenol hydroxylase cloned from *Ralstonia eutropha* strain E2 exhibits novel kinetic properties. *Microbiology-UK* **144**:1765–1772.
185. Shields MS, Montgomery SO, Chapman PJ, Cuskey SM, Pritchard PH. 1989. Novel pathway of toluene catabolism in the trichloroethylene-degrading bacterium G4. *Appl Environ Microbiol* **55**:1624–1629.
186. Krumme ML, Timmis KN, Dwyer DF. 1993. Degradation of trichloroethylene by *Pseudomonas cepacia* G4 and the constitutive mutant strain G4-5223 Pr1 in aquifer microcosms. *Appl Environ Microbiol* **59**:2746–2749.
187. Winkler J, Timmis KN, Snyder RA. 1995. Tracking the response of *Burkholderia* G4 5223-PR1 in aquifer microcosms. *Appl Environ Microbiol* **61**:448–455.
188. Hemmi H, Studts JM, Chae YK, Song JK, Markley JL, Fox BG. 2001. Solution structure of the toluene 4-monooxygenase effector protein (T4moD). *Biochemistry* **40**:3512–3524.
189. Whited GM, Gibson DT. 1991. Toluene-4-monooxygenase, a 3-component enzyme system that catalyzes the oxidation of toluene to *p*-cresol in *Pseudomonas mendocina* KR1. *J Bacteriol* **173**:3010–3016.
190. Fox BG. 1998. Catalysis by non-heme iron. In *Comprehensive biological catalysis*, pp. 261–348. Ed M Sinnott. London: Academic Press.

191. McClay K, Fox BG, Steffan RJ. 1996. Chloroform mineralization by toluene-oxidizing bacteria. *Appl Environ Microbiol* **62**:2716–2722.
192. McClay K, Boss C, Keresztes I, Steffan RJ. 2005. Mutations of toluene-4-monooxygenase that alter regiospecificity of indole oxidation and lead to production of novel indigoid pigments. *Appl Environ Microbiol* **71**:5476–5483.
193. Yen KM, Karl MR, Blatt LM, Simon MJ, Winter RB, Fausset PR, Lu HS, Harcourt AA, Chen KK. 1991. Cloning and characterization of a *Pseudomonas mendocina* KR1 gene-cluster encoding toluene-4-monooxygenase. *J Bacteriol* **173**:5315–5327.
194. Mitchell KH, Studts JM, Fox BG. 2002. Combined participation of hydroxylase active site residues and effector protein binding in a para to ortho modulation of toluene 4-monooxygenase regiospecificity. *Biochemistry* **41**:3176–3188.
195. Pikus JD, Studts JM, McClay K, Steffan RJ, Fox BG. 1997. Changes in the regiospecificity of aromatic hydroxylation produced by active site engineering in the diiron enzyme toluene 4-monooxygenase. *Biochemistry* **36**:9283–9289.
196. Tao Y, Fishman A, Bentley WE, Wood TK. 2004. Oxidation of benzene to phenol, catechol, and 1,2,3-trihydroxybenzene by toluene 4-monooxygenase of *Pseudomonas mendocina* KR1 and toluene 3-monooxygenase of *Ralstonia pickettii* PKO1. *Appl Environ Microbiol* **70**:3814–3820.
197. Oppenheim SF, Studts JM, Fox BG, Dordick JS. 2001. Aromatic hydroxylation catalyzed by toluene 4-monooxygenase in organic solvent/aqueous buffer mixtures. *Appl Biochem Biotechnol* **90**:187–197.
198. McClay K, Fox BG, Steffan RJ. 2000. Toluene monooxygenase-catalyzed epoxidation of alkenes. *Appl Environ Microbiol* **66**:1877–1882.
199. Fishman A, Tao Y, Bentley WE, Wood TK. 2004. Protein engineering of toluene 4-monooxygenase of *Pseudomonas mendocina* KR1 for synthesizing 4-nitrocatechol from nitrobenzene. *Biotechnol Bioeng* **87**:779–790.
200. Johnson GR, Olsen RH. 1995. Nucleotide-sequence analysis of genes encoding a toluene benzene-2-monooxygenase from *Pseudomonas* Sp strain Js150. *Appl Environ Microbiol* **61**:3336–3346.
201. Lountos GT, Mitchell KH, Studts JM, Fox BG, Orville AM. 2005. Crystal structures and functional studies of T4moD, the toluene 4-monooxygenase catalytic effector protein. *Biochemistry* **44**:7131–7142.
202. Skjeldal L, Peterson FC, Doreleijers JF, Moe LA, Pikus JD, Westler WM, Markley JL, Volkman BF, Fox BG. 2004. Solution structure of T4moC, the Rieske ferredoxin component of the toluene 4-monooxygenase complex. *J Biol Inorg Chem* **9**:945–953.
203. Moe LA, Hu Z, Deng D, Austin RN, Groves JT, Fox BG. 2004. Remarkable aliphatic hydroxylation by the diiron enzyme toluene 4-monooxygenase in reactions with radical or cation diagnostic probes norcarane, 1,1-dimethylcyclopropane, and 1,1-diethylcyclopropane. *Biochemistry* **43**:15688–15701.
204. Mitchell KH, Rogge CE, Gierahn T, Fox BG. 2003. Insight into the mechanism of aromatic hydroxylation by toluene 4-monooxygenase by use of specifically deuterated toluene and *p*-xylene. *Proc Natl Acad Sci USA* **100**:3784–3789.
205. Vaz ADN, McGinnity DF, Coon MJ. 1998. Epoxidation of olefins by cytochrome P450: Evidence from site-specific mutagenesis for hydroperoxo-iron as an electrophilic oxidant. *Proc Natl Acad Sci USA* **95**:3555–3560.
206. Moe LA, McMartin LA, Fox BG. 2006. Component interactions and implications for complex formation in the multicomponent toluene 4-monooxygenase. *Biochemistry* **45**:5478–5485.

207. Cafaro V, Scognamiglio R, Viggiani A, Izzo V, Passaro I, Notomista E, Dal Piaz F, Amoresano A, Casbarra A, Pucci P, Di Donato A. 2002. Expression and purification of the recombinant subunits of toluene/*o*-xylene monooxygenase and reconstitution of the active complex. *Eur J Biochem* **269**:5689–5699.
208. Bertoni G, Bolognese F, Galli E, Barbieri P. 1996. Cloning of the genes for and characterization of the early stages of toluene and *o*-xylene catabolism in *Pseudomonas stutzeri* OX1. *Appl Environ Microbiol* **62**:3704–3711.
209. Chauhan S, Barbieri P, Wood TK. 1998. Oxidation of trichloroethylene, 1,1-dichloroethylene, and chloroform by toluene/*o*-xylene monooxygenase from *Pseudomonas stutzeri* OX1. *Appl Environ Microbiol* **64**:3023–3024.
210. Ryoo D, Shim H, Canada K, Barbieri P, Wood TK. 2000. Aerobic degradation of tetrachloroethylene by toluene/*o*-xylene monooxygenase of *Pseudomonas stutzeri* OX1. *Nat Biotechnol* **18**:775–778.
211. Sazinsky MH, Bard J, Di Donato A, Lippard SJ. 2004. Crystal structure of the toluene/*o*-xylene monooxygenase hydroxylase from *Pseudomonas stutzeri* OX1: insight into the substrate specificity, substrate channeling, and active site tuning of multicomponent monooxygenases. *J Biol Chem* **279**:30600–30610.
212. Rudd DJ, Sazinsky MH, Lippard SJ, Hedman B, Hodgson KO. 2005. X-ray, absorption spectroscopic study of the reduced hydroxylases of methane monooxygenase and toluene/*o*-xylene monooxygenase: differences in active site structure and effects of the coupling proteins MMOB and ToMOD. *Inorg Chem* **44**:4546–4554.
213. McCormick MS, Sazinsky MH, Condon KL, Lippard SJ. 2006. X-ray crystal structures of manganese(II)-reconstituted and native toluene/*o*-xylene monooxygenase hydroxylase reveal rotamer shifts in conserved residues and an enhanced view of the protein interior. *J Am Chem Soc* **128**:15108–15110.
214. Murray LJ, García-Serres R, Naik S, Huynh BH, Lippard SJ. 2006. Dioxygen activation at non-heme diiron centers: characterization of intermediates in a mutant form of toluene/*o*-xylene monooxygenase hydroxylase. *J Am Chem Soc* **128**:7458–7459.
215. Krebs C, Chen S, Baldwin J, Ley BA, Patel U, Edmondson DE, Huynh BH, Bollinger Jr MJ. 2000. Mechanism of rapid electron transfer during oxygen activation in the r2 subunit of *Escherichia coli* ribonucleotide reductase, 2: evidence for and consequences of blocked electron transfer in the W48F variant. *J Am Chem Soc* **122**:12207–12219.
216. Reichard P. 1993. From RNA to DNA, why so many ribonucleotide reductases?. *Science* **260**:1773–1777.
217. Sjöberg B-M. 1997. Ribonucleotide reductases: A group of enzymes with different metallosites and a similar reaction mechanism. *Metal Sites Proteins Models* **88**:139–173.
218. Stubbe J, Riggs-Gelasco P. 1998. Harnessing free radicals: formation and function of the tyrosyl radical in ribonucleotide reductase. *Trends Biochem Sci* **23**:438–443.
219. Stubbe J, van der Donk WA. 1998. Protein radicals in enzyme catalysis. *Chem Rev* **98**:705–762.
220. Zhou BBS, Elledge SJ. 2000. The DNA damage response: putting checkpoints in perspective. *Nature* **408**:433–439.
221. Eklund H, Uhlin U, Färnegårdh M, Logan DT, Nordlund P. 2001. Structure and function of the radical enzyme ribonucleotide reductase. *Prog Biophys Mol Biol* **77**:177–268.
222. Sahlin M, Sjöberg B-M. 2000. A virtual playground for electron transfer reactions. *Subcell Biochem* **35**:405–443.

223. Stubbe J, Nocera DG, Yee CS, Chang MCY. 2003. Radical initiation in the class I ribonucleotide reductase: Long-range proton-coupled electron transfer. *Chem Rev* **103**:2167–2201.
224. Shao J, Zhou B, Chu B, Yen Y. 2006. Ribonucleotide reductase inhibitors and future drug design. *Curr Cancer Drug Targets* **6**:409–431.
225. Tanaka H, Arakawa H, Yamaguchi T, Shiraishi K, Fukuda S, Matsui K, Takei Y, Nakamura Y. 2000. A ribonucleotide reductase gene involved in a p53-dependent cell-cycle checkpoint for DNA damage. *Nature* **404**:42–49.
226. Guittet O, Hakansson P, Voevodskaya N, Fridd S, Gräslund A, Arakawa H, Nakamura Y, Thelander L. 2001. Mammalian p53R2 protein forms an active ribonucleotide reductase in vitro with the R1 protein, which is expressed both in resting cells in response to DNA damage and in proliferating cells. *J Biol Chem* **276**:40647–40651.
227. Shao JM, Zhou BS, Zhu LJ, Qiu WH, Yuan YC, Xi BX, Yen Y. 2004. In vitro characterization of enzymatic properties and inhibition of the p53R2 subunit of human ribonucleotide reductase. *Cancer Res* **64**:1–6.
228. Zhou B, Shao J, Su L, Yuan Y-C, Qi C, Shih J, Xi BX, Chu B, Yen Y. 2005. A diiron-tyrosyl-diiron radical cofactor center is essential for human ribonucleotide reductases. *Mol Cancer Ther* **4**:1830–1836.
229. Kolberg M, Strand KR, Graff P, Andersson KK. 2004. Structure, function, and mechanism of ribonucleotide reductases. *Biochim Biophys Acta* **1699**:1–34.
230. Bennati M, Lenzian F, Schmittel M, Zipse H. 2005. Spectroscopic and theoretical approaches for studying radical reactions in class I ribonucleotide reductase. *Biol Chem* **386**:1007–1022.
231. Jeschke G. 2005. EPR techniques for studying radical enzymes. *Biochim Biophys Acta* **1707**:91–102.
232. Lenzian F. 2005. Structure and interactions of amino acid radicals in class I ribonucleotide reductase studied by ENDOR and high-field EPR spectroscopy. *Biochim Biophys Acta* **1707**:67–90.
233. Nordlund P, Reichard P. 2006. Ribonucleotide Reductases. *Annu Rev Biochem* **75**:681–706.
234. Han WG, Liu TQ, Lovell T, Noodleman L. 2006. Seven clues to the origin and structure of class I ribonucleotide reductase intermediate X. *J Inorg Biochem* **100**:771–779.
235. Stubbe J. 2003. Di-iron-tyrosyl radical ribonucleotide reductases. *Curr Opin Chem Biol* **7**:183–188.
236. Poole AM, Logan DT, Sjöberg B-M. 2002. The evolution of the ribonucleotide reductases: much ado about oxygen. *J Mol Evol* **55**:180–196.
237. Fontecave M, Gerez C. 2002. Tyrosyl radicals and ribonucleotide reductase. In *Protein sensors and reactive oxygen species, Pt B, thiol enzymes and proteins*, pp. 21–30. Heidelberg: Elsevier Science.
238. Sjöberg B-M, Sahlin M. 2002. Thiols in redox mechanism of ribonucleotide reductase. In *Protein sensors and reactive oxygen species, Pt B, thiol enzymes and proteins*, pp. 1–21. Heidelberg: Elsevier Science.
239. Reichard P. 2002. Ribonucleotide reductases: the evolution of allosteric regulation. *Arch Biochem Biophys* **397**:149–155.
240. Gräslund A. 2002. Ribonucleotide reductase: Kinetic methods for demonstrating radical transfer pathway in protein R2 of mouse enzyme in generation of tyrosyl free radical. In *Enzyme kinetics and mechanism, Pt F: detection and characterization of enzyme reaction intermediates*, pp. 399–414. New York: Academic Press.

241. Stubbe J, Ge J, Yee CS. 2001. The evolution of ribonucleotide reduction revisited. *Trends Biochem Sci* **26**:93–99.
242. Eklund H. 2001. Ribonucleotide reductase. In *Handbook of metalloproteins*, pp. 699–711. Ed A Messerschmidt, EI Solomon. Chichester: John Wiley & Sons.
243. Stubbe J. 2000. Ribonucleotide reductases: the link between an RNA and a DNA world. *Curr Opin Struct Biol* **10**:731–736.
244. Solomon EI, Brunold TC, Davis MI, Kemsley JN, Lee SK, Lehnert N, Neese F, Skulan AJ, Yang YS, Zhou J. 2000. Geometric and electronic structure/function correlations in non-heme iron enzymes. *Chem Rev* **100**:235–349.
245. Stubbe J. 1998. Ribonucleotide reductases in the twenty-first century. *Proc Natl Acad Sci USA* **95**:2723–2724.
246. Uhlin U, Eklund H. 1994. Structure of ribonucleotide reductase protein R1. *Nature* **370**:533–539.
247. Nordlund P, Eklund H. 1993. Structure and function of the *Escherichia coli* ribonucleotide reductase protein R2. *J Mol Biol* **232**:123–164.
248. Barlow T, Eliasson R, Platz A, Reichard P, Sjöberg B-M. 1983. Enzymic modification of a tyrosine residue to a stable free radical in ribonucleotide reductase. *Proc Natl Acad Sci USA* **80**:1492–1495.
249. Fontecave M, Eliasson R, Reichard P. 1987. NAD(P)H-flavin oxidoreductase of *Escherichia coli*: a ferric iron reductase participating in the generation of the free-radical of ribonucleotide reductase. *J Biol Chem* **262**:12325–12331.
250. Thelander M, Gräslund A, Thelander L. 1985. Subunit M2 of mammalian ribonucleotide reductase: characterization of a homogeneous protein isolated from M2-overproducing mouse cells. *J Biol Chem* **260**:2737–2741.
251. Filatov D, Ingemarson R, Johansson E, Rova U, Thelander L. 1995. Mouse ribonucleotide reductase: from genes to proteins. *Biochem Soc Trans* **23**:903–905.
252. Stubbe J. 1990. Ribonucleotide reductases: amazing and confusing. *J Biol Chem* **265**:5329–5332.
253. Pötsch S, Lenzian F, Ingemarson R, Hornberg A, Thelander L, Lubitz W, Lassmann G, Gräslund A. 1999. The iron–oxygen reconstitution reaction in protein R2-Tyr-177 mutants of mouse ribonucleotide reductase: EPR and electron nuclear double resonance studies on a new transient tryptophan radical. *J Biol Chem* **274**:17696–17704.
254. Uhlin U, Eklund H. 1996. The ten-stranded beta/alpha barrel in ribonucleotide reductase protein R1. *J Mol Biol* **262**:358–369.
255. Eriksson M, Uhlin U, Ramaswamy S, Ekberg M, Regnström K, Sjöberg B-M, Eklund H. 1997. Binding of allosteric effectors to ribonucleotide reductase protein R1: reduction of active-site cysteines promotes substrate binding. *Structure* **5**:1077–1092.
256. Voegtli WC, Sommerhalter M, Saleh L, Baldwin J, Bollinger Jr MJ, Rosenzweig AC. 2003. Variable coordination geometries at the diiron(II) active site of ribonucleotide reductase R2. *J Am Chem Soc* **125**:15822–15830.
257. Andersson ME, Högbom M, Rinaldo-Matthis A, Blodig W, Liang YH, Persson B-O, Sjöberg BM, Su X-D, Nordlund P. 2004. Structural and mutational studies of the carboxylate cluster in iron-free ribonucleotide reductase R2. *Biochemistry* **43**:7966–7972.
258. Nielsen BB, Kauppi B, Thelander M, Thelander L, Larsen IK, Eklund H. 1995. Crystallization and crystallographic investigations of the small subunit of mouse ribonucleotide reductase. *FEBS Lett* **373**:310–312.

259. Voegtli WC, Ge J, Perlstein DL, Stubbe J, Rosenzweig AC. 2001. Structure of the yeast ribonucleotide reductase Y2Y4 heterodimer. *Proc Natl Acad Sci USA* **98**:10073–10078.
260. Kauppi B, Nielsen BA, Ramaswamy S, Larsen IK, Thelander M, Thelander L, Eklund H. 1996. The three-dimensional structure of mammalian ribonucleotide reductase protein R2 reveals a more-accessible iron-radical site than *Escherichia coli* R2. *J Mol Biol* **262**:706–720.
261. Strand KR, Karlsen S, Kolberg M, Røhr ÅK, Görbitz CH, Andersson KK. 2004. Crystal structural studies of changes in the native dinuclear iron center of ribonucleotide reductase protein R2 from mouse. *J Biol Chem* **279**:46794–46801.
262. Strand KR, Karlsen S, Andersson KK. 2002. Cobalt substitution of mouse R2 ribonucleotide reductase as a model for the reactive diferrous state: spectroscopic and structural evidence for a ferromagnetically coupled dinuclear cobalt cluster. *J Biol Chem* **277**:34229–34238.
263. Sommerhalter M, Voegtli WC, Perlstein DL, Ge J, Stubbe J, Rosenzweig AC. 2004. Structures of the yeast ribonucleotide reductase Rnr2 and Rnr4 homodimers. *Biochemistry* **43**:7736–7742.
264. Eriksson M, Jordan A, Eklund H. 1998. Structure of *Salmonella typhimurium* nrdF ribonucleotide reductase in its oxidized and reduced forms. *Biochemistry* **37**:13359–13369.
265. Högbom M, Huque Y, Sjöberg B-M, Nordlund P. 2002. Crystal structure of the di-iron/radical protein of ribonucleotide reductase from *Corynebacterium ammoniagenes*. *Biochemistry* **41**:1381–1389.
266. Uppsten M, Davis J, Rubin H, Uhlin U. 2004. Crystal structure of the biologically active form of class 1b ribonucleotide reductase small subunit from *Mycobacterium tuberculosis*. *FEBS Lett* **569**:117–122.
267. Högbom M, Stenmark P, Voevodskaya N, McClarty G, Gräslund A, Nordlund P. 2004. The radical site in chlamydial ribonucleotide reductase defines a new R2 subclass. *Science* **305**:245–248.
268. Xu H, Faber C, Uchiki T, Racca J, Dealwis C. 2006. Structures of eukaryotic ribonucleotide reductase I define gemcitabine diphosphate binding and subunit assembly. *Proc Natl Acad Sci USA* **103**:4028–4033.
269. Uppsten M, Farnegardh M, Domkin V, Uhlin U. 2006. The first holocomplex structure of ribonucleotide reductase gives new insight into its mechanism of action. *J Mol Biol* **359**:365–377.
270. Logan DT, Su X-D, Åberg A, Regnström K, Hajdu J, Eklund H, Nordlund P. 1996. Crystal structure of reduced protein R2 of ribonucleotide reductase: the structural basis for oxygen activation at a dinuclear iron site. *Structure* **4**:1053–1064.
271. Andersson ME, Högbom M, Rinaldo-Matthis A, Andersson KK, Sjöberg B-M, Nordlund P. 1999. The crystal structure of an azide complex of the diferrous R2 subunit of ribonucleotide reductase displays a novel carboxylate shift with important mechanistic implications for diiron-catalyzed oxygen activation. *J Am Chem Soc* **121**:2346–2352.
272. Atta M, Nordlund P, Åberg A, Eklund H, Fontecave M. 1992. Substitution of Manganese for Iron in Ribonucleotide Reductase from *Escherichia coli*: spectroscopic and Crystallographic Characterization. *J Biol Chem* **267**:20682–20688.
273. Pulver SC, Tong WH, Bollinger Jr MJ, Stubbe J, Solomon EI. 1995. Circular dichroism and magnetic circular dichroism studies of the fully reduced binuclear non-heme iron active site in the *Escherichia coli* R2 subunit of ribonucleoside diphosphate reductase. *J Am Chem Soc* **117**:12664–12678.

274. Yang YS, Baldwin J, Ley BA, Bollinger Jr JM, Solomon EI. 2000. Spectroscopic and electronic structure description of the reduced binuclear non-heme iron active site in ribonucleotide reductase from *E. coli*: comparison to reduced Delta(9) desaturase and electronic structure contributions to differences in O₂ reactivity. *J Am Chem Soc* **122**:8495–8510.
275. Wei PP, Skulan AJ, Mitić N, Yang YS, Saleh L, Bollinger Jr JM, Solomon EI. 2004. Electronic and spectroscopic studies of the non-heme reduced binuclear iron sites of two ribonucleotide reductase variants: comparison to reduced methane monooxygenase and contributions to O₂ reactivity. *J Am Chem Soc* **126**:3777–3788.
276. Lynch JB, Juarezgarcia C, Münck E, Que Jr L. 1989. Mössbauer and EPR studies of the binuclear iron center in ribonucleotide reductase from *Escherichia coli*: a new iron-to-protein stoichiometry. *J Biol Chem* **264**:8091–8096.
277. Galli C, Atta M, Andersson KK, Gräslund A, Brudvig GW. 1995. Variations of the diferric exchange coupling in the R2 subunit of ribonucleotide reductase from four species as determined by saturation-recovery EPR spectroscopy. *J Am Chem Soc* **117**:740–746.
278. Petersson L, Gräslund A, Ehrenberg A, Sjöberg B-M, Reichard P. 1980. The iron center in ribonucleotide reductase from *Escherichia coli*. *J Biol Chem* **255**:6706–6712.
279. Scarrow RC, Maroney MJ, Palmer SM, Que Jr L, Roe AL, Salowe SP, Stubbe J. 1987. EXAFS studies of binuclear iron proteins: hemerythrin and ribonucleotide reductase. *J Am Chem Soc* **109**:7857–7864.
280. Sjöberg B-M, Loehr TM, Sandersloehr J. 1982. Raman spectral evidence for a μ -oxo bridge in the binuclear iron center of ribonucleotide reductase. *Biochemistry* **21**:96–102.
281. Sjöberg B-M, Sanders-Loehr J, Loehr TM. 1987. Identification of a hydroxide ligand at the iron center of ribonucleotide reductase by resonance raman spectroscopy. *Biochemistry* **26**:4242–4247.
282. Atta M, Scheer C, Fries PH, Fontecave M, Latour J. M. 1992. Multifield saturation magnetization measurements of oxidized and reduced ribonucleotide reductase from *Escherichia coli*. *Angew Chem, Int Ed* **31**:1513–1515.
283. Sahlin M, Gräslund A, Petersson L, Ehrenberg A, Sjöberg BM. 1989. Reduced forms of the iron-containing small subunit of ribonucleotide reductase from *Escherichia coli*. *Biochemistry* **28**:2618–2625.
284. Elgren TE, Hendrich MP, Que Jr L. 1993. Azide binding to the diferrous clusters of the R2 protein of ribonucleotide reductase from *Escherichia coli*. *J Am Chem Soc* **115**:9291–9292.
285. Hendrich MP, Elgren TE, Que Jr L. 1991. A mixed-valence form of the iron cluster in the B2 protein of ribonucleotide reductase from *Escherichia coli*. *Biochem Biophys Res Commun* **176**:705–710.
286. Davydov R, Kuprin S, Gräslund A, Ehrenberg A. 1994. Electron paramagnetic resonance study of the mixed-valent diiron center in *Escherichia coli* ribonucleotide reductase produced by reduction of radical-free protein R2 at 77 K. *J Am Chem Soc* **116**:11120–11128.
287. Davydov RM, Smieja J, Dikanov SA, Zang Y, Que Jr L, Bowman MK. 1999. EPR properties of mixed-valent μ -oxo and μ -hydroxo dinuclear iron complexes produced by radiolytic reduction at 77 K. *J Biol Inorg Chem* **4**:292–301.
288. Krebs C, Davydov R, Baldwin J, Hoffman BM, Bollinger Jr JM, Huynh BH. 2000. Mössbauer and EPR characterization of the S = 9/2 mixed-valence Fe(II)Fe(III) cluster

- in the cryoreduced R2 subunit of *Escherichia coli* ribonucleotide reductase. *J Am Chem Soc* **122**:5327–5336.
289. Gerez C, Fontecave M. 1992. Reduction of the small subunit of *Escherichia coli* ribonucleotide reductase by hydrazines and hydroxylamines. *Biochemistry* **31**:780–786.
290. Bollinger Jr JM, Edmondson DE, Huynh BH, Filley J, Norton JR, Stubbe J. 1991. Mechanism of assembly of the tyrosyl radical dinuclear iron cluster cofactor of ribonucleotide reductase. *Science* **253**:292–298.
291. Ravi N, Bollinger Jr JM, Huynh BH, Edmondson DE, Stubbe J. 1994. Mechanism of assembly of the tyrosyl radical-diiron(III) cofactor of *Escherichia coli* ribonucleotide reductase, 1: Mössbauer characterization of the diferric radical precursor. *J Am Chem Soc* **116**:8007–8014.
292. Bollinger Jr JM, Tong WH, Ravi N, Huynh BH, Edmondson DE, Stubbe J. 1994. Mechanism of assembly of the tyrosyl radical-diiron(III) cofactor of *E. coli* ribonucleotide reductase, 2: kinetics of the excess Fe^{2+} reaction by optical, EPR, and Mössbauer spectroscopies. *J Am Chem Soc* **116**:8015–8023.
293. Bollinger Jr JM, Tong WH, Ravi N, Huynh BH, Edmondson DE, Stubbe J. 1994. Mechanism of assembly of the tyrosyl radical-diiron(III) cofactor of *E. coli* ribonucleotide reductase, 3: kinetics of the limiting Fe^{2+} reaction by optical, EPR, and Mössbauer spectroscopies. *J Am Chem Soc* **116**:8024–8032.
294. Baldwin J, Krebs C, Ley BA, Edmondson DE, Huynh BH, Bollinger Jr JM. 2000. Mechanism of rapid electron transfer during oxygen activation in the R2 subunit of *Escherichia coli* ribonucleotide reductase, 1: evidence for a transient tryptophan radical. *J Am Chem Soc* **122**:12195–12206.
295. Tong W, Burdi D, Riggs-Gelasco P, Chen S, Edmondson D, Huynh BH, Stubbe J, Han S, Arvai A, Tainer J. 1998. Characterization of Y122F R2 of *Escherichia coli* ribonucleotide reductase by time-resolved physical biochemical methods and X-ray crystallography. *Biochemistry* **37**:5840–5848.
296. Bollinger Jr JM, Stubbe J, Huynh BH, Edmondson DE. 1991. Novel diferric radical intermediate responsible for tyrosyl radical formation in assembly of the cofactor of ribonucleotide reductase. *J Am Chem Soc* **113**:6289–6291.
297. Sturgeon BE, Burdi D, Chen SX, Huynh BH, Edmondson DE, Stubbe J, Hoffman BM. 1996. Reconsideration of X, the diiron intermediate formed during cofactor assembly in *E. coli* ribonucleotide reductase. *J Am Chem Soc* **118**:7551–7557.
298. Burdi D, Sturgeon BE, Tong WH, Stubbe JA, Hoffman BM. 1996. Rapid freeze-quench ENDOR of the radical X intermediate of *Escherichia coli* ribonucleotide reductase using $^{17}\text{O}_2$, H_2^{17}O , and $^2\text{H}_2\text{O}$. *J Am Chem Soc* **118**:281–282.
299. Burdi D, Willems J-P, Riggs-Gelasco P, Antholine WE, Stubbe J, Hoffman BM. 1998. The core structure of X generated in the assembly of the diiron cluster of ribonucleotide reductase: $^{17}\text{O}_2$ and H_2^{17}O ENDOR. *J Am Chem Soc* **120**:12910–12919.
300. Willems J-P, Lee HI, Burdi D, Doan PE, Stubbe J, Hoffman BM. 1997. Identification of the protonated oxygenic ligands of ribonucleotide reductase intermediate X by Q-band ^1H CW and pulsed ENDOR. *J Am Chem Soc* **119**:9816–9824.
301. Riggs-Gelasco PJ, Shu LJ, Chen SX, Burdi D, Huynh BH, Que Jr L, Stubbe J. 1998. EXAFS characterization of the intermediate X generated during the assembly of the *Escherichia coli* ribonucleotide reductase R2 diferric tyrosyl radical cofactor. *J Am Chem Soc* **120**:849–860.
302. Mitić N, Saleh L, Schenk G, Bollinger JM, Solomon EI. 2003. Rapid-freeze-quench magnetic circular dichroism of intermediate X in ribonucleotide reductase: new structural insight. *J Am Chem Soc* **125**:11200–11201.

303. Bollinger Jr JM, Chen SX, Parkin SE, Mangravite LM, Ley BA, Edmondson DE, Huynh BH. 1997. Differential iron(II) affinity of the sites of the diiron cluster in protein R2 of *Escherichia coli* ribonucleotide reductase: tracking the individual sites through the O₂ activation sequence. *J Am Chem Soc* **119**:5976–5977.
304. Veselov A, Scholes CP. 1996. X-band ENDOR of the liganding environment from the radical X intermediate of *Escherichia coli* ribonucleotide reductase. *Inorg Chem* **35**:3702–3705.
305. Mitić N, Clay MD, Saleh L, Bollinger Jr JM, Solomon EI. 2007. Spectroscopic and electronic structure studies of intermediate X in ribonucleotide reductase R2 and two variants: a description of the Fe^{IV}-oxo bond in the Fe^{III}-O-Fe^{IV} dimer. *J Am Chem Soc* **129**:9049–9065.
306. Voevodskaya N, Lenzian F, Gräslund A. 2005. A stable Fe^{III}-Fe^{IV} replacement of tyrosyl radical in a class I ribonucleotide reductase. *Biochem Biophys Res Commun* **330**:1213–1216.
307. Voevodskaya N, Narvaez AJ, Domkin V, Torrents E, Thelander L, Gräslund A. 2006. Chlamydial ribonucleotide reductase: tyrosyl radical function in catalysis replaced by the Fe^{III}-Fe^{IV} cluster. *Proc Natl Acad Sci USA* **103**:9850–9854.
308. Bollinger Jr JM, Krebs C, Vicol A, Chen SX, Ley BA, Edmondson DE, Huynh BH. 1998. Engineering the diiron site of *Escherichia coli* ribonucleotide reductase protein R2 to accumulate an intermediate similar to H_{peroxo}, the putative peroxodiiron(III) complex from the methane monooxygenase catalytic cycle. *J Am Chem Soc* **120**:1094–1095.
309. Moënné-Loccoz P, Baldwin J, Ley BA, Loehr TM, Bollinger Jr JM. 1998. O₂ activation by non-heme diiron proteins: identification of a symmetric μ -1,2-peroxide in a mutant of ribonucleotide reductase. *Biochemistry* **37**:14659–14663.
310. Baldwin J, Voegtli WC, Khidekel N, Moënné-Loccoz P, Krebs C, Pereira AS, Ley BA, Huynh BH, Loehr TM, Riggs-Gelasco PJ, Rosenzweig AC, Bollinger Jr JM. 2001. Rational reprogramming of the R2 subunit of *Escherichia coli* ribonucleotide reductase into a self-hydroxylating monooxygenase. *J Am Chem Soc* **123**:7017–7030.
311. Skulan AJ, Brunold TC, Baldwin J, Saleh L, Bollinger Jr JM, Solomon EI. 2004. Nature of the peroxo intermediate of the W48F/D84E ribonucleotide reductase variant: implications for O₂ activation by binuclear non-heme iron enzymes. *J Am Chem Soc* **126**:8842–8855.
312. Lu S, Libby E, Saleh L, Xing G, Bollinger Jr JM, Moënné-Loccoz P. 2004. Characterization of NO adducts of the diiron center in protein R2 of *Escherichia coli* ribonucleotide reductase and site-directed variants; implications for the O₂ activation mechanism. *J Biol Inorg Chem* **9**:818–827.
313. Broadwater JA, Ai JY, Loehr TM, Sanders-Loehr J, Fox BG. 1998. Peroxidiferrous intermediate of stearyl-acyl carrier protein Delta(9) desaturase: oxidase reactivity during single turnover and implications for the mechanism of desaturation. *Biochemistry* **37**:14664–14671.
314. Gerfen GJ, van der Donk WA, Yu GX, McCarthy JR, Jarvi ET, Matthews DP, Farrar C, Griffin RG, Stubbe J. 1998. Characterization of a substrate-derived radical detected during the inactivation of ribonucleotide reductase from *Escherichia coli* by 2'-fluoromethylene-2'-deoxycytidine-5'-diphosphate. *J Am Chem Soc* **120**:3823–3835.
315. van der Donk WA, Gerfen GJ, Stubbe J. 1998. Direct EPR spectroscopic evidence for an allylic radical generated from (E)-2'-fluoromethylene-2'-deoxycytidine-5'-diphosphate by *E. coli* ribonucleotide reductase. *J Am Chem Soc* **120**:4252–4253.

316. Lawrence CC, Bennati M, Obias HV, Bar G, Griffin RG, Stubbe J. 1999. High-field EPR detection of a disulfide radical anion in the reduction of cytidine 5'-diphosphate by the E441Q R1 mutant of *Escherichia coli* ribonucleotide reductase. *Proc Natl Acad Sci USA* **96**:8979–8984.
317. Fritscher J, Artin E, Wnuk S, Bar G, Robblee JH, Kacprzak S, Kaupp M, Griffin RG, Bennati M, Stubbe J. 2005. Structure of the nitrogen-centered radical formed during inactivation of *E. coli* ribonucleotide reductase by 2'-azido-2'-deoxyuridine-5'-diphosphate: Trapping of the 3'-ketonucleotide. *J Am Chem Soc* **127**:7729–7738.
318. Andersson KK, Barra AL. 2002. The use of high field/frequency EPR in studies of radical and metal sites in proteins and small inorganic models. *Spectrochim Acta Part A Mol Biomol Spectrosc* **58**:1101–1112.
319. Biglino D, Schmidt PP, Reijerse EJ, Lubitz W. 2006. PELDOR study on the tyrosyl radicals in the R2 protein of mouse ribonucleotide reductase. *Phys Chem Chem Phys* **8**:58–62.
320. Andersson KK, Schmidt PP, Katterle B, Strand KR, Palmer AE, Lee SK, Solomon EI, Gräslund A, Barra AL. 2003. Examples of high-frequency EPR studies in bioinorganic chemistry. *J Biol Inorg Chem* **8**:235–247.
321. Mobius K. 2001. High-field and high-frequency electron paramagnetic resonance. *Appl Magn Reson* **21**:255.
322. Bennati M, Stubbe J, Griffin RG. 2001. High-frequency EPR and ENDOR: time-domain spectroscopy of ribonucleotide reductase. *Appl Magn Reson* **21**:389–410.
323. Bleifuss G, Kolberg M, Pötsch S, Hofbauer W, Bittl R, Lubitz W, Gräslund A, Lassmann G, Lenzian F. 2001. Tryptophan and tyrosine radicals in ribonucleotide reductase: A comparative high-field EPR study at 94 GHz. *Biochemistry* **40**:15362–15368.
324. Lenzian F, Sahlén M, MacMillan F, Bittl R, Fiege R, Pötsch S, Sjöberg B-M, Gräslund A, Lubitz W, Lassmann G. 1996. Electronic structure of neutral tryptophan radicals in ribonucleotide reductase studied by EPR and ENDOR spectroscopy. *J Am Chem Soc* **118**:8111–8120.
325. Un S, Gerez C, Elleingand E, Fontecave M. 2001. Sensitivity of tyrosyl radical g-values to changes in protein structure: a high-field EPR study of mutants of ribonucleotide reductase. *J Am Chem Soc* **123**:3048–3054.
326. Bennati M, Farrar CT, Bryant JA, Inati SJ, Weis V, Gerfen GJ, Riggs-Gelasco P, Stubbe J, Griffin RG. 1999. Pulsed electron-nuclear double resonance (ENDOR) at 140 GHz. *J Magn Reson* **138**:232–243.
327. van Dam PJ, Willems J-P, Schmidt PP, Pötsch S, Barra A-L, Hagen WR, Hoffman BM, Andersson KK, Gräslund A. 1998. High-frequency EPR and pulsed Q-Band ENDOR studies on the origin of the hydrogen bond in tyrosyl radicals of ribonucleotide reductase R2 proteins from mouse and herpes simplex virus type 1. *J Am Chem Soc* **120**:5080–5085.
328. Bar G, Bennati M, Nguyen H-HT, Ge J, Stubbe J, Griffin RG. 2001. High-frequency (140-GHz) time domain EPR and ENDOR spectroscopy: the tyrosyl radical-diiron cofactor in ribonucleotide reductase from yeast. *J Am Chem Soc* **123**:3569–3576.
329. Liu AM, Barra AL, Rubin H, Lu GZ, Gräslund A. 2000. Heterogeneity of the local electrostatic environment of the tyrosyl radical in *Mycobacterium tuberculosis* ribonucleotide reductase observed by high-field electron paramagnetic resonance. *J Am Chem Soc* **122**:1974–1978.
330. Högbom M, Galander M, Andersson M, Kolberg M, Hofbauer W, Lassmann G, Nordlund P, Lenzian F. 2003. Displacement of the tyrosyl radical cofactor in ribonu-

- cleotide reductase obtained by single-crystal high-field EPR and 1.4-Å X-ray data. *Proc Natl Acad Sci USA* **100**:3209–3214.
331. Galander M, Uppsten M, Uhlin U, Lendzian F. 2006. Orientation of the tyrosyl radical in *Salmonella typhimurium* class Ib ribonucleotide reductase determined by high-field EPR of R2F single crystals. *J Biol Chem* **281**:31743–31752.
332. Liu A, Sahlin M, Pötsch S, Sjöberg BM, Gräslund A. 1998. New paramagnetic species formed at the expense of the transient tyrosyl radical in mutant protein R2 F208Y of *Escherichia coli* ribonucleotide reductase. *Biochem Biophys Res Commun* **246**:740–745.
333. Kolberg M, Logan DT, Bleifuss G, Pötsch S, Sjöberg BM, Gräslund A, Lubitz W, Lassmann GN, Lendzian F. 2005. A new tyrosyl radical on Phe(208) as ligand to the diiron center in *Escherichia coli* ribonucleotide reductase, mutant R2-Y122H: combined X-ray diffraction and EPR/ENDOR studies. *J Biol Chem* **280**:11233–11246.
334. Bennati M, Weber A, Antonic J, Perlstein DL, Robblee J, Stubbe JA. 2003. Pulsed ELDOR spectroscopy measures the distance between the two tyrosyl radicals in the R2 subunit of the *E. coli* ribonucleotide reductase. *J Am Chem Soc* **125**:14988–14989.
335. Milov AD, Maryasov AG, Tsvetkov YD. 1998. Pulsed electron double resonance (PELDOR) and its applications in free-radicals research. *Appl Magn Reson* **15**:107–143.
336. Jeschke G. 2002. Determination of the nanostructure of polymer materials by electron paramagnetic resonance spectroscopy. *Macromol Rapid Commun* **23**:227–246.
337. Denysenkov VP, Prisner TF, Stubbe J, Bennati M. 2006. High-field pulsed electron-electron double resonance spectroscopy to determine the orientation of the tyrosyl radicals in ribonucleotide reductase. *Proc Natl Acad Sci USA* **103**:13386–13390.
338. Bennati M, Robblee JH, Mugnaini V, Stubbe J, Freed JH, Borbat P. 2005. EPR distance measurements support a model for long-range radical initiation in *E. coli* ribonucleotide reductase. *J Am Chem Soc* **127**:15014–15015.
339. Seyedsayamdost MR, Yee CS, Reece SY, Nocera DG, Stubbe J. 2006. pH rate profiles of FnY356-R2s ($n = 2, 3, 4$) in *Escherichia coli* ribonucleotide reductase: evidence that Y-356 is a redox-active amino acid along the radical propagation pathway. *J Am Chem Soc* **128**:1562–1568.
340. Seyedsayamdost MR, Reece SY, Nocera DG, Stubbe J. 2006. Mono-, di-, tri-, and tetra-substituted fluorotyrosines: New probes for enzymes that use tyrosyl radicals in catalysis. *J Am Chem Soc* **128**:1569–1579.
341. Kolberg M, Bleifuss G, Sjöberg B-M, Gräslund A, Lubitz W, Lendzian F, Lassmann G. 2002. Generation and electron paramagnetic resonance spin trapping detection of thiyl radicals in model proteins and in the R1 subunit of *Escherichia coli* ribonucleotide reductase. *Arch Biochem Biophys* **397**:57–68.
342. Kolberg M, Bleifuss G, Gräslund A, Sjöberg B-M, Lubitz W, Lendzian F, Lassmann G. 2002. Protein thiyl radicals directly observed by EPR spectroscopy. *Arch Biochem Biophys* **403**:141–144.
343. Persson AL, Eriksson M, Katterle B, Pötsch S, Sahlin M, Sjöberg B-M 1997. A new mechanism-based radical intermediate in a mutant R1 protein affecting the catalytically essential Glu(441) in *Escherichia coli* ribonucleotide reductase. *J Biol Chem* **272**:31533–31541.
344. Persson AL, Sahlin M, Sjöberg B-M. 1998. Cysteinyll and substrate radical formation in active site mutant E441Q of *Escherichia coli* class I ribonucleotide reductase. *J Biol Chem* **273**:31016–31020.

345. Bollinger Jr JM, Krebs C. 2006. Stalking intermediates in oxygen activation by iron enzymes: motivation and method. *J Inorg Biochem* **100**:586–605.
346. Saleh L, Krebs C, Ley BA, Naik S, Huynh BH, Bollinger Jr JM. 2004. Use of a chemical trigger for electron transfer to characterize a precursor to cluster X in assembly of the iron-radical cofactor of *Escherichia coli* ribonucleotide reductase. *Biochemistry* **43**:5953–5964.
347. Funk CD. 2001. Prostaglandins and leukotrienes: advances in eicosanoid biology. *Science* **294**:1871–1875.
348. Numa S. 1984. *Fatty acid metabolism and its regulation*. New York: Elsevier.
349. Lindqvist Y. 2001. D⁹ stearoyl-acyl carrier protein desaturase. In *Handbook of metalloproteins*, pp. 725–737. Ed A Messerschmidt. Chichester: John Wiley & Sons.
350. Fox BG, Lyle KS, Rogge CE. 2004. Reactions of the diiron enzyme stearoyl-acyl carrier protein desaturase. *Acc Chem Res* **37**:421–429.
351. Nagai J, Bloch K. 1966. Enzymatic desaturation of stearyl acyl carrier protein. *J Biol Chem* **241**:1925–1927.
352. Yang YS, Broadwater JA, Pulver SC, Fox BG, Solomon EI. 1999. Circular dichroism and magnetic circular dichroism studies of the reduced binuclear non-heme iron site of stearoyl-ACP Delta(9)-desaturase: substrate binding and comparison to ribonucleotide reductase. *J Am Chem Soc* **121**:2770–2783.
353. Broadwater JA, Achim C, Münck E, Fox BG. 1999. Mössbauer studies of the formation and reactivity of a quasi-stable peroxo intermediate of stearoyl-acyl carrier protein Delta(9)-desaturase. *Biochemistry* **38**:12197–12204.
354. Haas JA, Fox BG. 2002. Fluorescence anisotropy studies of enzyme-substrate complex formation in stearoyl-ACP desaturase. *Biochemistry* **41**:14472–14481.
355. Moche M, Shanklin J, Ghoshal A, Lindqvist Y. 2003. Azide and acetate complexes plus two iron-depleted crystal structures of the di-iron enzyme Delta 9 stearoyl-acyl carrier protein desaturase: implications for oxygen activation and catalytic intermediates. *J Biol Chem* **278**:25072–25080.
356. Davydov R, Behrouzian B, Smoukov S, Stubbe J, Hoffman BM, Shanklin J. 2005. Effect of substrate on the diiron(III) site in stearoyl acyl carrier protein Delta(9)-desaturase as disclosed by cryoreduction electron paramagnetic resonance/electron nuclear double resonance spectroscopy. *Biochemistry* **44**:1309–1315.
357. Sobrado P, Lyle KS, Kaul SP, Turco MM, Arabshahi I, Marwah A, Fox BG. 2006. Identification of the binding region of the [2Fe–2S] ferredoxin in stearoyl-acyl carrier protein desaturase: insight into the catalytic complex and mechanism of action. *Biochemistry* **45**:4848–4858.
358. Schmidt H, Heinz E. 1990. Involvement of ferredoxin in desaturation of lipid-bound oleate in chloroplasts. *Plant Physiol* **94**:214–220.
359. Shanklin J, Somerville C. 1991. Stearoyl-acyl-carrier-protein desaturase from higher-plants is structurally unrelated to the animal and fungal homologs. *Proc Natl Acad Sci USA* **88**:2510–2514.
360. Jacobson BS, Jaworski JG, Stumpf PK. 1974. Fat metabolism in higher-plants, 62: stearyl-acyl carrier protein desaturase from spinach-chloroplasts. *Plant Physiol* **54**:484–486.
361. Cole ST, Brosch R, Parkhill J, Garnier T, Churcher C, Harris D, Gordon SV, Eiglmeier K, Gas S, Barry III CE, Tekaiia F, Badcock K, Basham D, Brown D, Chillingworth T, Connor R, Davies R, Devlin K, Feltwell T, Gentles S, Hamlin N, Holroyd S, Hornby T, Jagels K, Krogh A, McLean J, Moule S, Murphy L, Oliver K, Osborne J, Quail M-A, Rajandream MA, Rogers J, Rutter S, Seeger K, Skelton J,

- Squares R, Squares S, Sulston JE, Taylor K, Whitehead S, Barrell BG. 1998. Deciphering the biology of *Mycobacterium tuberculosis* from the complete genome sequence. *Nature* **393**:537–544.
362. Dyer DH, Lyle KS, Rayment I, Fox BG. 2005. X-ray structure of putative acyl-ACP desaturase DesA2 from *Mycobacterium tuberculosis* H37Rv. *Protein Sci* **14**:1508–1517.
363. Chang Y, Fox BG. 2006. Identification of Rv3230c as the NADPH oxidoreductase of a two-protein DesA3 acyl-CoA desaturase in *Mycobacterium tuberculosis* H37Rv. *Biochemistry* **45**:13476–13486.
364. Lyle KS, Moënne-Loccoz P, Ai JY, Sanders-Loehr J, Loehr TM, Fox BG. 2000. Resonance Raman studies of the stoichiometric catalytic turnover of a substrate-stearoyl-acyl carrier protein Delta(9) desaturase complex. *Biochemistry* **39**:10507–10513.
365. Rogge CE, Fox BG. 2002. Desaturation, chain scission, and register-shift of oxygen-substituted fatty acids during reaction with stearoyl-ACP desaturase. *Biochemistry* **41**:10141–10148.
366. Behrouzian B, Buist PH, Shanklin J. 2001. Application of KIE and thia approaches in the mechanistic study of a plant stearoyl-ACP Delta(9) desaturase. *Chem Commun* 401–402.
367. Charalampous FC, Lyras C. 1957. Biochemical studies on inositol, 4: conversion of inositol to glucuronic acid by rat kidney extracts. *J Biol Chem* **228**:1–13.
368. Charalampous FC. 1959. Biochemical studies on inositol, 5: purification and properties of the enzyme that cleaves inositol to D-glucuronic acid. *J Biol Chem* **234**:220–227.
369. Howard CF, Anderson L. 1967. Metabolism of *myo*-inositol in animals, 2: complete catabolism of *myo*-inositol-14c by rat kidney slices. *Arch Biochem Biophys* **118**:332–339.
370. Moskala R, Reddy CC, Minard RD, Hamilton GA. 1981. An oxygen-18 tracer investigation of the mechanism of *myo*-inositol oxygenase. *Biochem Biophys Res Commun* **99**:107–113.
371. Reddy CC, Swan JS, Hamilton GA. 1981. *Myo*-inositol oxygenase from hog kidney, 1: purification and characterization of the oxygenase and of an enzyme complex containing the oxygenase and D-glucuronate reductase. *J Biol Chem* **256**:8510–8518.
372. Reddy CC, Pierzchala PA, Hamilton GA. 1981. *Myo*-inositol oxygenase from hog kidney, 2: catalytic properties of the homogeneous enzyme. *J Biol Chem* **256**:8519–8524.
373. Arner RJ, Prabhu KS, Thompson JT, Hildenbrandt GR, Liken AD, Reddy CC. 2001. *Myo*-inositol oxygenase: molecular cloning and expression of a unique enzyme that oxidizes *myo*-inositol and D-*chiro*-inositol. *Proc Natl Acad Sci USA* **360**:313–320.
374. Arner RJ, Prabhu KS, Reddy CC. 2004. Molecular cloning, expression, and characterization of *myo*-inositol oxygenase from mouse, rat, and human kidney. *Biochem Biophys Res Commun* **324**:1386–1392.
375. Arner RJ, Prabhu KS, Krishnan V, Johnson MC, Reddy CC. 2006. Expression of *myo*-inositol oxygenase in tissues susceptible to diabetic complications. *Biochem Biophys Res Commun* **339**:816–820.
376. Hamilton GA, Reddy CC, Swan JS, Moskala R, Mulliez E, Naber NI. 1982. Aspects of oxygenases in general and *myo*-inositol oxygenase in particular. In *Oxygen and*

- oxygen metabolism*, pp. 111–123. Ed M Nozaki, S Yamamoto, Y Ishimura. New York: Academic Press.
377. Yang QW, Dixit B, Wada J, Tian YF, Wallner EI, Srivastva SK, Kanwar YS. 2000. Identification of a renal-specific oxido-reductase in newborn diabetic mice. *Proc Natl Acad Sci USA* **97**:9896–9901.
378. Hanks LV, Politzer WM, Touster O, Anderson L. 1969. *Myo*-inositol catbaolism in human pentosurics: predominant role of glucuronate-xylulose-pentose phosphate pathway. *Ann NY Acad Sci* **165**:564–576.
379. Touster O, Shaw DRD. 1962. Biochemistry of acyclic polyols. *Physiol Rev* **42**:181–225.
380. Whiting PH, Palmano KP, Hawthorne JN. 1979. Enzymes of *myo*-inositol and inositol lipid-metabolism in rats with streptozotocin-induced diabetes. *Biochem J* **179**:549–553.
381. Hallman M, Epstein BL. 1980. Role of *myo*-inositol in the synthesis of phosphatidyl-glycerol and phosphatidylinositol in the lung. *Biochem Biophys Res Commun* **92**:1151–1159.
382. Sundkvist G, Dahlin LB, Nilsson H, Eriksson KF, Lindgarde F, Rosen I, Lattimer SA, Sima AAF, Sullivan K, Greene DA. 2000. Sorbitol and *myo*-inositol levels and morphology of sural nerve in relation to peripheral nerve function and clinical neuropathy in men with diabetic, impaired, and normal glucose tolerance. *Diabet Med* **17**:259–268.
383. Prabhu KS, Arner RJ, Vunta H, Reddy CC. 2005. Up-regulation of human *myo*-inositol oxygenase by hyperosmotic stress in renal proximal tubular epithelial cells. *J Biol Chem* **280**:19895–19901.
384. Khan ZA, Farhangkhome H, Mahon JL, Bere L, Gonder JR, Chan BM, Uniyal S, Chakrabarti S. 2006. Endothelins: regulators of extracellular matrix protein production in diabetes. *Exp Biol Med* **231**:1022–1029.
385. Nayak B, Xie P, Akagi S, Yang QW, Sun L, Wada J, Thakur A, Danesh FR, Chugh SS, Kanwar YS. 2005. Modulation of renal-specific oxidoreductase/*myo*-inositol oxygenase by high-glucose ambience. *Proc Natl Acad Sci USA* **102**:17952–17957.
386. Brown PM, Caradoc-Davies TT, Dickson JMJ, Cooper GJS, Loomes KM, Baker EN. 2006. Crystal structure of a substrate complex of *myo*-inositol oxygenase, a di-iron oxygenase with a key role in inositol metabolism. *Proc Natl Acad Sci USA* **103**:15032–15037.
387. Xing G, Hoffart LM, Diao YH, Prabhu KS, Arner RJ, Reddy CC, Krebs C, Bollinger Jr JM. 2006. A coupled dinuclear iron cluster that is perturbed by substrate binding in *myo*-inositol oxygenase. *Biochemistry* **45**:5393–5401.
388. Day EP, David SS, Peterson J, Dunham WR, Bonvoisin JJ, Sands RH, Que Jr L. 1988. Magnetization and electron paramagnetic resonance studies of reduced uteroferrin and its "EPR-silent" phosphate complex. *J Biol Chem* **263**:15561–15567.
389. Yang YS, McCormick JM, Solomon EI. 1997. Circular dichroism and magnetic circular dichroism studies of the mixed-valence binuclear non-heme iron active site in uteroferrin and its anion complexes. *J Am Chem Soc* **119**:11832–11842.
390. Guddat LW, McAlpine AS, Hume D, Hamilton S, de Jersey J, Martin JL. 1999. Crystal structure of mammalian purple acid phosphatase. *Struct Fold Des* **7**:757–767.
391. Xing G, Barr EW, Diao YH, Hoffart LM, Prabhu KS, Arner RJ, Reddy CC, Krebs C, Bollinger Jr JM. 2006. Oxygen activation by a mixed-valent, diiron(II/III) cluster in the glycol cleavage reaction catalyzed by *myo*-inositol oxygenase. *Biochemistry* **45**:5402–5412.
392. Xing G, Diao YH, Hoffart LM, Barr EW, Prabhu KS, Arner RJ, Reddy CC, Krebs C, Bollinger Jr JM. 2006. Evidence for C–H cleavage by an iron-superoxide complex in

- the glycol cleavage reaction catalyzed by *myo*-inositol oxygenase. *Proc Natl Acad Sci USA* **103**:6130–6135.
393. Kim SH, Xing G, Bollinger Jr JM, Krebs C, Hoffman BM. 2006. Demonstration by ²H ENDOR spectroscopy that *myo*-inositol binds via an alkoxide bridge to the mixed-valent diiron center of *myo*-inositol oxygenase. *J Am Chem Soc* **128**:10374–10375.
394. Naber NI, Swan JS, Hamilton GA. 1986. L-*myo*-inosose-1 as a probable intermediate in the reaction catalyzed by *myo*-inositol oxygenase. *Biochemistry* **25**:7201–7207.
395. Coulter ED, Shenvi NV, Beharry ZM, Smith JJ, Prickril BC, Kurtz Jr DM. 2000. Rubrerythrin-catalyzed substrate oxidation by dioxygen and hydrogen peroxide. *Inorg Chim Acta* **297**:231–241.
396. LeGall J, Prickril BC, Moura I, Xavier AV, Moura JGG, Huynh BH. 1988. Isolation and characterization of rubrerythrin, a non-heme iron protein from *Desulfovibrio vulgaris* that contains rubredoxin centers and a hemerythrin-like binuclear iron cluster. *Biochemistry* **27**:1636–1642.
397. Moura I, Tavares P, Ravi N. 1994. Characterization of three proteins containing multiple iron sites: rubrerythrin, desulfoferrodoxin, and a protein containing a 6-iron cluster. In *Inorganic microbial sulfur metabolism*, pp. 216–240. *Methods in enzymology*, Vol. 243. New York: Academic Press.
398. Lehmann Y, Meile L, Teuber M. 1996. Rubrerythrin from *Clostridium perfringens*: cloning of the gene, purification of the protein, and characterization of its superoxide dismutase function. *J Bacteriol* **178**:7152–7158.
399. Coulter ED, Shenvi NV, Kurtz Jr DM. 1999. NADH peroxidase activity of rubrerythrin. *Biochem Biophys Res Commun* **255**:317–323.
400. Coulter ED, Kurtz Jr DM. 2001. A role for rubredoxin in oxidative stress protection in *Desulfovibrio vulgaris*: catalytic electron transfer to rubrerythrin and two-iron superoxide reductase. *Arch Biochem Biophys* **394**:76–86.
401. Alban PS, Popham DL, Rippere KE, Krieg NR. 1998. Identification of a gene for a rubrerythrin/nigerythrin-like protein in *Spirillum volutans* by using amino acid sequence data from mass spectrometry and NH₂-terminal sequencing. *J Appl Microbiol* **85**:875–882.
402. Lumpio HL, Shenvi NV, Summers AO, Voordouw G, Kurtz Jr DM. 2001. Rubrerythrin and rubredoxin oxidoreductase in *Desulfovibrio vulgaris*: a novel oxidative stress protection system. *J Bacteriol* **183**:101–108.
403. Jenney Jr FE, Verhagen MFJM, Cui XY, Adams MWW. 1999. Anaerobic microbes: oxygen detoxification without superoxide dismutase. *Science* **286**:306–309.
404. Alban PS, Krieg NR. 1998. A hydrogen peroxide resistant mutant of *Spirillum volutans* has NADH peroxidase activity but no increased oxygen tolerance. *Can J Microbiol* **44**:87–91.
405. Sztukowska M, Bugno M, Potempa J, Travis J, Kurtz Jr DM. 2002. Role of rubrerythrin in the oxidative stress response of *Porphyromonas gingivalis*. *Mol Microbiol* **44**:479–488.
406. Bonomi F, Kurtz Jr DM, Cui XY. 1996. Ferroxidase activity of recombinant *Desulfovibrio vulgaris* rubrerythrin. *J Biol Inorg Chem* **1**:67–72.
407. Liu M-Y, Le Gall J. 1990. Purification and characterization of two proteins with inorganic pyrophosphatase activity from *Desulfovibrio vulgaris*: rubrerythrin and a new, highly-active, enzyme. *Biochem Biophys Res Commun* **171**:313–318.

408. Kurtz Jr DM, Prickril BC. 1991. Intrapeptide sequence homology in rubrerythrin from *Desulfovibrio vulgaris*: identification of potential ligands to the diiron site. *Biochem Biophys Res Commun* **181**:337–341.
409. deMaré F, Kurtz Jr DM, Nordlund P. 1996. The structure of *Desulfovibrio vulgaris* rubrerythrin reveals a unique combination of rubredoxin-like FeS₄ and ferritin-like diiron domains. *Nat Struct Biol* **3**:539–546.
410. Jin S, Kurtz Jr DM, Liu ZJ, Rose J, Wang BC. 2002. X-ray crystal structures of reduced rubrerythrin and its azide adduct: a structure-based mechanism for a non-heme diiron peroxidase. *J Am Chem Soc* **124**:9845–9855.
411. Jin S, Kurtz Jr DM, Liu ZJ, Rose J, Wang BC. 2004. X-ray crystal structure of *Desulfovibrio vulgaris* rubrerythrin with zinc substituted into the [Fe(SCys)₄] site and alternative diiron site structures. *Biochemistry* **43**:3204–3213.
412. Gupta N, Bonomi F, Kurtz Jr DM, Ravi N, Wang DL, Huynh BH. 1995. Recombinant *Desulfovibrio vulgaris* rubrerythrin: isolation and characterization of the diiron domain. *Biochemistry* **34**:3310–3318.
413. Smoukov SK, Davydov RM, Doan PE, Sturgeon B, Kung IY, Hoffman BM, Kurtz Jr DM. 2003. EPR and ENDOR evidence for a 1-His, hydroxo-bridged mixed-valent diiron site in *Desulfovibrio vulgaris* rubrerythrin. *Biochemistry* **42**:6201–6208.
414. Pierik AJ, Wolbert RBG, Portier GL, Verhagen MFJM, Hagen WR. 1993. Nigerythrin and rubrerythrin from *Desulfovibrio vulgaris* each contain two mononuclear iron centers and two dinuclear iron clusters. *Eur J Biochem* **212**:237–245.
415. Lumpio HL, Shenvi NV, Garg RP, Summers AO, Kurtz Jr DM. 1997. A rubrerythrin operon and nigerythrin gene in *Desulfovibrio vulgaris* (Hildenborough). *J Bacteriol* **179**:4607–4615.
416. Iyer RB, Silaghi-Dumitrescu R, Kurtz Jr DM, Lanzilotta WN. 2005. High-resolution crystal structures of *Desulfovibrio vulgaris* (Hildenborough) nigerythrin: facile, redox-dependent iron movement, domain interface variability, and peroxidase activity in the rubrerythrin. *J Biol Inorg Chem* **10**:407–416.
417. Kennepohl P, Solomon EI. 2003. Electronic structure contributions to electron-transfer reactivity in iron-sulfur active sites: 3. Kinetics of electron transfer. *Inorg Chem* **42**:696–708.
418. Zhang Q, Iwasaki T, Wakagi T, Oshima T. 1996. 2-oxoacid:ferredoxin oxidoreductase from the thermoacidophilic archaeon: *Sulfolobus* sp strain 7. *J Biochem* **120**:587–599.
419. Wakagi T. 2003. Sulerythrin, the smallest member of the rubrerythrin family, from a strictly aerobic and thermoacidophilic archaeon. *Sulfolobus tokodaii* strain 7. *FEMS Microbiol Lett* **222**:33–37.
420. Fushinobu S, Shoun H, Wakagi T. 2003. Crystal structure of sulerythrin, a rubrerythrin-like protein from a strictly aerobic archaeon: *Sulfolobus tokodaii* strain 7, shows unexpected domain swapping. *Biochemistry* **42**:11707–11715.
421. Li M, Liu MY, Le Gall J, Gui LL, Liao J, Jiang T, Zhang JP, Liang DC, Chang WR. 2003. Crystal structure studies on rubrerythrin: enzymatic activity in relation to the zinc movement. *J Biol Inorg Chem* **8**:149–155.
422. Theil EC. 2001. Ferritin. In *Handbook of metalloproteins*, pp. 711–781. Ed A Messerschmidt, R Huber, T Poulos, K Wieghardt. Chichester: John Wiley & Sons.
423. Harrison PM, Arosio P. 1996. Ferritins: molecular properties, iron storage function and cellular regulation. *Biochim Biophys Acta* **1275**:161–203.
424. Theil EC. 1987. Ferritin: structure, gene-regulation, and cellular function in animals, plants, and microorganisms. *Annu Rev Biochem* **56**:289–315.

425. Chasteen ND, Harrison PM. 1999. Mineralization in ferritin: an efficient means of iron storage. *J Struct Biol* **126**:182–194.
426. Andrews SC. 1998. Iron storage in bacteria. *Adv Microb Physiol* **40**:281–351.
427. Liu XF, Hintze K, Lonnerdal B, Theil EC. 2006. Iron at the center of ferritin, metal/oxygen homeostasis and novel dietary strategies. *Biol Res* **39**:167–171.
428. Hintze K, Theil EC. 2006. Cellular regulation and molecular interactions of the ferritins. *Cell Mol Life Sci* **63**:591–600.
429. Ferreira C, Bucchini D, Martin M-E, Levi S, Arosio P, Grandchamp B, Beaumont C. 2000. Early embryonic lethality of H ferritin gene deletion in mice. *J Biol Chem* **275**:3021–3024.
430. Rocha ER, Owens G, Smith CJ. 2000. The redox-sensitive transcriptional activator OxyR regulates the peroxide response regulon in the obligate anaerobe *Bacteroides fragilis*. *J Bacteriol* **182**:5059–5069.
431. Kauko A, Haataja S, Pulliainen AT, Finne J, Papageorgiou AC. 2004. Crystal structure of *Streptococcus suis* dps-like peroxide resistance protein Dpr: implications for iron incorporation. *J Mol Biol* **338**:547–558.
432. Liu XF, Theil EC. 2005. Ferritin as an iron concentrator and chelator target. *Ann NY Acad Sci* **1054**:136–140.
433. Takagi H, Shi DS, Ha Y, Allewell NM, Theil EC. 1998. Localized unfolding at the junction of three ferritin subunits: A mechanism for iron release. *J Biol Chem* **273**:18685–18688.
434. Jin WL, Takagi H, Pancorbo B, Theil EC. 2001. "Opening" the ferritin pore for iron release by mutation of conserved amino acids at interhelix and loop sites. *Biochemistry* **40**:7525–7532.
435. Liu XF, Jin WL, Theil EC. 2003. Opening protein pores with chaotropes enhances Fe reduction and chelation of Fe from the ferritin biomineral. *Proc Natl Acad Sci USA* **100**:3653–3658.
436. Tatur J, Hagedoorn PL, Overijssel ML, Hagen WR. 2006. A highly thermostable ferritin from the hyperthermophilic archaeal anaerobe *Pyrococcus furiosus*. *Extremophiles* **10**:139–148.
437. Sieker LC, Holmes M, Le Trong I, Turley S, Santarsiero BD, Liu MY, LeGall J, Stenkamp RE. 1999. Alternative metal-binding sites in rubrerythrin. *Nat Struct Biol* **6**:308–309.
438. Proulx-Curry PM, Chasteen ND. 1995. Molecular aspects of iron uptake and storage in ferritin. *Coord Chem Rev* **144**:347–368.
439. Bou-Abdallah F, Lewin AC, Le Brun NE, Moore GR, Chasteen ND. 2002. Iron detoxification properties of *Escherichia coli* bacterioferritin: attenuation of oxyradical chemistry. *J Biol Chem* **277**:37064–37069.
440. Crichton RR. 2001. *Inorganic biochemistry of iron metabolism: from molecular mechanisms to clinical consequences*, 2nd ed. Chichester: Wiley.
441. Yang XK, Chiancone E, Stefanini S, Ilari A, Chasteen ND. 2000. Iron oxidation and hydrolysis reactions of a novel ferritin from *Listeria innocua*. *Biochem J* **349**:783–786.
442. Stefanini S, Cavallo S, Montagnini B, Chiancone E. 1999. Incorporation of iron by the unusual dodecameric ferritin from *Listeria innocua*. *Biochem J* **338**:71–75.
443. Su MH, Cavallo S, Stefanini S, Chiancone E, Chasteen ND. 2005. The so-called *Listeria innocua* ferritin is a Dps protein: iron incorporation, detoxification, and DNA protection properties. *Biochemistry* **44**:5572–5578.

444. Zhao GH, Ceci P, Ilari A, Giangiacomo L, Laue TM, Chiancone E, Chasteen ND. 2002. Iron and hydrogen peroxide detoxification properties of DNA-binding protein from starved cells: a ferritin-like DNA-binding protein of *Escherichia coli*. *J Biol Chem* **277**:27689–27696.
445. Andrews SC, Robinson AK, Rodriguez-Quinones F. 2003. Bacterial iron homeostasis. *FEMS Microbiol Rev* **27**:215–237.
446. Theil EC, Matzapetakis M, Liu XF. 2006. Ferritins: iron/oxygen biominerals in protein nanocages. *J Biol Inorg Chem* **11**:803–810.
447. Frolow F, Kalb AJ, Yariv J. 1994. Structure of a unique twofold symmetrical heme-binding site. *Nat Struct Biol* **1**:453–460.
448. Carrondo MA. 2003. Ferritins, iron uptake and storage from the bacterioferritin viewpoint. *EMBO J* **22**:1959–1968.
449. Banyard SH, Stammers DK, Harrison PM. 1978. Electron-density map of apoferritin at 2.8 Å resolution. *Nature* **271**:282–284.
450. Rice DW, Ford GC, White JL, Smith JMA, Harrison PM. 1983. The spatial structure of horse spleen apoferritin. *Adv Inorg Biochem* **5**:39–50.
451. Lawson DM, Artymiuk PJ, Yewdall SJ, Smith JMA, Livingstone JC, Treffry A, Luz-zago A, Levi S, Arosio P, Cesareni G, Thomas CD, Shaw WV, Harrison PM. 1991. Solving the structure of human H-ferritin by genetically engineering intermolecular crystal contacts. *Nature* **349**:541–544.
452. Hempstead PD, Yewdall SJ, Fernie AR, Lawson DM, Artymiuk PJ, Rice DW, Ford GC, Harrison PM. 1997. Comparison of the three-dimensional structures of recombinant human H and horse L ferritins at high resolution. *J Mol Biol* **268**:424–448.
453. Ha Y, Shi DS, Small GW, Theil EC, Allewell NM. 1999. Crystal structure of bullfrog M ferritin at 2.8 Å resolution: analysis of subunit interactions and the binuclear metal center. *J Biol Inorg Chem* **4**:243–256.
454. Gallois B, d'Estaintot BL, Michaux M-A, Dautant A, Granier T, Précigoux G, Soruco J-A, Roland F, Chavas-Alba O, Herbas A, Crichton RR. 1997. X-ray structure of recombinant horse L-chain apoferritin at 2.0 Å resolution: implications for stability and function. *J Biol Inorg Chem* **2**:360–367.
455. Stillman TJ, Hempstead PD, Artymiuk PJ, Andrews SC, Hudson AJ, Treffry A, Guest JR, Harrison PM. 2001. The high-resolution X-ray crystallographic structure of the ferritin (EcFtnA) of *Escherichia coli*: comparison with human H ferritin (HuHF) and the structures of the Fe³⁺ and Zn²⁺ derivatives. *J Mol Biol* **307**:587–603.
456. Granier T, Gallois B, d'Estaintot AD, Dautant A, Chevelier J-M, Mellado J-M, Beaumont C, Santambrogio P, Arosio P, Précigoux G. 2001. Structure of mouse L-chain ferritin at 1.6 Å resolution. *Acta Crystallogr Sect D Biol Crystallogr* **57**:1491–1497.
457. Granier T, d'Estaintot BL, Gallois B, Chevalier JM, Précigoux G, Santambrogio P, Arosio P. 2003. Structural description of the active sites of mouse L-chain ferritin at 1.2 angstrom resolution. *J Biol Inorg Chem* **8**:105–111.
458. d'Estaintot BL, Santambrogio P, Granier T, Gallois B, Chevalier JM, Précigoux G, Levi S, Arosio P. 2004. Crystal structure and biochemical properties of the human mitochondrial ferritin and its mutant Ser144Ala. *J Mol Biol* **340**:277–293.
459. Dautant A, Meyer JB, Yariv J, Précigoux G, Sweet RM, Kalb AJ, Frolow F. 1998. Structure of a monoclinic crystal form of cytochrome b1 (bacterioferritin) from *E. coli*. *Acta Crystallogr Sect D Biol Crystallogr* **54**:16–24.
460. van Eerde A, Wolternik-van Loo S, van der Oost J, Dijkstra BW. 2006. Fortuitous structure determination of "as-isolated" *Escherichia coli* bacterioferritin in a novel crystal form. *Acta Crystallogr Sect F Struct Biol Crystall Commun* **62**:1061–1066.

461. Cobessi D, Huang LS, Ban M, Pon NG, Daldal F, Berry EA. 2002. The 2.6 Å resolution structure of *Rhodobacter capsulatus* bacterioferritin with metal-free dinuclear site and heme iron in a crystallographic "special position." *Acta Crystallogr Sect D Biol Crystallogr* **58**:29–38.
462. Macedo S, Romão CV, Mitchell E, Matias PM, Liu MY, Xavier AV, LeGall J, Teixeira M, Lindley P, Carrondo MA. 2003. The nature of the di-iron site in the bacterioferritin from *Desulfovibrio desulfuricans*. *Nat Struct Biol* **10**:285–290.
463. Zeth K, Offermann S, Essen L-O, Oesterhelt D. 2004. Iron-oxo clusters biomineralizing on protein surfaces: structural analysis of *Halobacterium salinarum* DpsA in its low- and high-iron states. *Proc Natl Acad Sci USA* **101**:13780–13785.
464. Gauss GH, Benas P, Wiedenheft B, Young M, Douglas T, Lawrence CM. 2006. Structure of the DPS-like protein from *Sulfolobus solfataricus* reveals a bacterioferritin-like dimetal binding site within a DPS-like dodecameric assembly. *Biochemistry* **45**:10815–10827.
465. Johnson E, Cascio D, Sawaya MR, Gingery M, Schröder I. 2005. Crystal structures of a tetrahedral open pore ferritin from the hyperthermophilic Archaeon *Archaeoglobus fulgidus*. *Structure* **13**:637–648.
466. Swartz L, Kuchinkas M, Li HY, Poulos TL, Lanzilotta WN. 2006. Redox-dependent structural changes in the *Azotobacter vinelandii* bacterioferritin: new insights into the ferroxidase and iron transport mechanism. *Biochemistry* **45**:4421–4428.
467. Liu HL, Zhou HN, Xing WM, Zhao HF, Li SX, Huang JF, Bi RC. 2004. 2.6 Å resolution crystal structure of the bacterioferritin from *Azotobacter vinelandii*. *FEBS Lett* **573**:93–98.
468. Pereira AS, Small W, Krebs C, Tavares P, Edmondson DE, Theil EC, Huynh BH. 1998. Direct spectroscopic and kinetic evidence for the involvement of a peroxodiferic intermediate during the ferroxidase reaction in fast ferritin mineralization. *Biochemistry* **37**:9871–9876.
469. Lebrun NE, Wilson MT, Andrews SC, Guest JR, Harrison PM, Thomson AJ, Moore GR. 1993. Kinetic and structural characterization of an intermediate in the biomineralization of bacterioferritin. *FEBS Lett* **333**:197–202.
470. Lebrun NE, Andrews SC, Guest JR, Harrison PM, Moore GR, Thomson AJ. 1995. Identification of the ferroxidase center of *Escherichia coli* bacterioferritin. *Biochem J* **312**:385–392.
471. Crichton RR, Herbas A, Chavez-Alba O, Roland F. 1996. Identification of catalytic residues involved in iron uptake by L-chain ferritins. *J Biol Inorg Chem* **1**:567–574.
472. Stillman TJ, Connolly PP, Latimer CL, Morland AF, Quail MA, Andrews SC, Treffry A, Guest JR, Artymiuk PJ, Harrison PM. 2003. Insights into the effects on metal binding of the systematic substitution of five key glutamate ligands in the ferritin of *Escherichia coli*. *J Biol Chem* **278**:26275–26286.
473. Xu B, Chasteen ND. 1991. Iron oxidation chemistry in ferritin: increasing Fe/O₂ stoichiometry during core formation. *J Biol Chem* **266**:19965–19970.
474. Waldo GS, Theil EC. 1993. Formation of iron(III)-tyrosinate is the fastest reaction observed in ferritin. *Biochemistry* **32**:13262–13269.
475. Treffry A, Zhao Z, Quail MA, Guest JR, Harrison PM. 1995. Iron(II) oxidation by H-chain ferritin: evidence from site-directed mutagenesis that a transient blue species is formed at the dinuclear iron center. *Biochemistry* **34**:15204–15213.

476. Yang XK, Chen-Barrett Y, Arosio P, Chasteen ND. 1998. Reaction paths of iron oxidation and hydrolysis in horse spleen and recombinant human ferritins. *Biochemistry* **37**:9743–9750.
477. Moëgne-Loccoz P, Krebs C, Herlihy K, Edmondson DE, Theil EC, Huynh BH, Loehr TM. 1999. The ferroxidase reaction of ferritin reveals a diferric μ -1,2 bridging peroxide intermediate in common with other O_2 -activating non-heme diiron proteins. *Biochemistry* **38**:5290–5295.
478. Hwang J, Krebs C, Huynh BH, Edmondson DE, Theil EC, Penner-Hahn JE. 2000. A short Fe–Fe distance in peroxodiferric ferritin: control of Fe substrate versus cofactor Decay? *Science* **287**:122–125.
479. Jameson GNL, Weili J, Krebs C, Pereira AS, Tavares P, Liu XF, Theil EC, Huynh BH. 2002. Stoichiometric production of hydrogen peroxide and parallel formation of ferric multimers through decay of the diferric-peroxo complex, the first detectable intermediate in ferritin mineralization. *Biochemistry* **41**:13435–13443.
480. Bou-Abdallah F, Papaefthymiou GC, Scheswohl DM, Stanga SD, Arosio P, Chasteen ND. 2002. μ -1,2-peroxobridged di-iron(III) dimer formation in human H-chain ferritin. *Biochem J* **364**:57–63.
481. Zhao GH, Bou-Abdallah F, Arosio P, Levi S, Janus-Chandler C, Chasteen ND. 2003. Multiple pathways for mineral core formation in mammalian apoferritin: the role of hydrogen peroxide. *Biochemistry* **42**:3142–3150.
482. Bou-Abdallah F, Zhao GH, Mayne HR, Arosio P, Chasteen ND. 2005. Origin of the unusual kinetics of iron deposition in human H-chain ferritin. *J Am Chem Soc* **127**:3885–3893.
483. Bunker J, Lowry T, Davis G, Zhang B, Brosnahan D, Lindsay S, Costen R, Choi S, Arosio P, Watt GD. 2005. Kinetic studies of iron deposition catalyzed by recombinant human liver heavy, and light ferritins and *Azotobacter vinelandii* bacterioferritin using O_2 and H_2O_2 as oxidants. *Biophys Chem* **114**:235–244.
484. Bauminger ER, Harrison PM, Nowik I, Treffry A. 1989. Mössbauer spectroscopic study of the initial stages of iron core formation in horse spleen apoferritin: evidence for both isolated Fe(III) atoms and oxo-bridged Fe(III) dimers as early intermediates. *Biochemistry* **28**:5486–5493.
485. Bauminger ER, Harrison PM, Hechel D, Nowik I, Treffry A. 1991. Mössbauer spectroscopic investigation of structure-function relations in ferritins. *Biochim Biophys Acta* **1118**:48–58.
486. Sun S, Chasteen ND. 1994. Rapid kinetics of the EPR-active species during initial iron uptake in horse spleen apoferritin. *Biochemistry* **33**:15095–15102.
487. Waldo GS, Ling JS, Sanders-Loehr J, Theil EC. 1993. Formation of an Fe(III)–tyrosinate complex during biomineralization of H-subunit ferritin. *Science* **259**:796–798.
488. Chasteen ND, Antanaitis BC, Aisen P. 1985. Iron deposition in apoferritin: evidence for the formation of a mixed-valence binuclear iron complex. *J Biol Chem* **260**:2926–2929.
489. Treffry A, Hirzmann J, Yewdall SJ, Harrison PM. 1992. Mechanism of catalysis of Fe(II) oxidation by ferritin-H chains. *FEBS Lett* **302**:108–112.
490. Reif DW, Simmons RD. 1990. Nitric-oxide mediates iron release from ferritin. *Arch Biochem Biophys* **283**, 537–541.
491. Drapier JC, Pellat C, Henry Y. 1991. Generation of EPR detectable nitrosyl–iron complexes in tumor target cells cocultured with activated macrophages. *J Biol Chem* **266**:10162–10167.

492. Lebrun NE, Cheesman MR, Thompson AJ, Moore GR, Andrews SC, Guest JR, Harrison PM. 1993. An EPR investigation of non-haem iron sites in *Escherichia coli* bacterioferritin and their interaction with phosphate: a study using nitric oxide as a spin probe. *FEBS Lett* **323**:261–266.
493. Lee MH, Arosio P, Cozzi A, Chasteen ND. 1994. Identification of the EPR-active iron nitrosyl complexes in mammalian ferritins. *Biochemistry* **33**:3679–3687.
494. Bauminger ER, Harrison PM, Hechel D, Hodson NW, Nowik I, Treffry A, Yewdall SJ. 1993. Iron (II) oxidation and early intermediates of iron-core formation in recombinant human H-chain ferritin. *Biochem J* **296**:709–719.
495. Pereira AS, Tavares P, Lloyd SG, Danger D, Edmondson DE, Theil EC, Huynh BH. 1997. Rapid and parallel formation of Fe³⁺ multimers, including a trimer, during H-type subunit ferritin mineralization. *Biochemistry* **36**:7917–7927.
496. Zhao ZW, Treffry A, Quail MA, Guest JR, Harrison PM. 1997. Catalytic iron(II) oxidation in the non-haem ferritin of *Escherichia coli*: the early intermediate is not an iron tyrosinate. *J Chem Soc Dalton Trans* 3977–3978.
497. Welch KD, Reilly CA, Aust SD. 2002. The role of cysteine residues in the oxidation of ferritin. *Free Radic Biol Med* **33**:399–408.
498. Zhao GH, Arosio P, Chasteen ND. 2006. Iron(II) and hydrogen peroxide detoxification by human H-chain ferritin: an EPR spin-trapping study. *Biochemistry* **45**:3429–3436.
499. Liu XF, Theil EC. 2004. Ferritin reactions: direct identification of the site for the diferrous peroxide reaction intermediate. *Proc Natl Acad Sci USA* **101**:8557–8562.
500. Theil EC, Takagi H, Small GW, He L, Tipton AR, Danger D. 2000. The ferritin iron entry and exit problem. *Inorg Chim Acta* **297**:242–251.
501. Liu XF, Kijeong K, Leighton T, Theil EC. 2006. Paired *Bacillus anthracis* Dps (miniferritin) have different reactivities with peroxide. *J Biol Chem* **281**:27827–27835.
502. Baaghil S, Lewin A, Moore GR, Le Brun NE. 2003. Core formation in *Escherichia coli* bacterioferritin requires a functional. *Biochemistry* **42**:14047–14056.
503. Lewin A, Moore GR, Le Brun NE. 2005. Formation of protein-coated iron minerals. *Dalton Trans* 3597–3610.
504. Lankester ER. 1873. A contribution to the knowledge of hemoglobin. *Proc R Soc London* **21**:70–81.
505. Stenkamp RE. 1994. Dioxygen and hemerythrin. *Chem Rev* **94**:715–726.
506. Kurtz Jr DM. 1997. Structural similarity and functional diversity in diiron-oxo proteins. *J Biol Inorg Chem* **2**:159–167.
507. Klotz IM, Keresztesy S. 1963. Hemerythrin: molecular weight and dissociation into subunits. *Biochemistry* **2**:445–452.
508. Hendrickson WA, Klippenstein GL, Ward KB. 1975. Tertiary structure of myohemerythrin at low resolution. *Proc Natl Acad Sci USA* **72**:2160–2164.
509. Ward KB, Hendrickson WA, Klippenstein GL. 1975. Quaternary and tertiary structure of hemerythrin. *Nature* **257**:818–821.
510. Stenkamp RE, Sieker LC, Jensen LH, Loehr JS. 1976. Structure of methemerythrin at 5 Å resolution. *J Mol Biol* **100**:23–34.
511. Smith JL, Hendrickson WA, Addison AW. 1983. Structure of trimeric haemerythrin. *Nature* **303**:86–88.
512. Stenkamp RE, Sieker LC, Jensen LH. 1976. Structure of iron complex in methemerythrin. *Proc Natl Acad Sci USA* **73**:349–351.

513. Holmes MA, Letrong I, Turley S, Sieker LC, Stenkamp RE. 1991. Structures of deoxy and oxy hemerythrin at 2.0 Å resolution. *J Mol Biol* **218**:583–593.
514. Farmer CS, Kurtz DM, Liu ZJ, Wang BC, Rose J, Ai JY, Sanders-Loehr J. 2001. The crystal structures of *Phascolopsis gouldii* wild type and L98Y methemerythrins: structural and functional alterations of the O₂ binding pocket. *J Biol Inorg Chem* **6**:418–429.
515. Isaza CE, Silaghi-Dumitrescu R, Iyer RB, Kurtz Jr DM, Chan MK. 2006. Structural basis for O₂ sensing by the hemerythrin-like domain of a bacterial chemotaxis protein: substrate tunnel and fluxional N terminus. *Biochemistry* **45**:9023–9031.
516. Xiong JJ, Kurtz Jr DM, Ai JY, Sanders-Loehr J. 2000. A hemerythrin-like domain in a bacterial chemotaxis protein. *Biochemistry* **39**:5117–5125.
517. Kurtz Jr DM. 2004. Dioxygen binding proteins. In *Comprehensive coordination chemistry II*, pp. 229–260. Ed JA McCleverty, TJ Meyer. Oxford: Elsevier.
518. Kryatov SV, Rybak-Akimova EV, Schindler S. 2005. Kinetics and mechanisms of formation and reactivity of non-heme iron oxygen intermediates. *Chem Rev* **105**:2175–2226.
519. Stenkamp RE. 2001. Hemerythrin. In *Handbook of metalloproteins*, pp. 687–698. Ed A Messerschmidt. Chichester: John Wiley & Sons.
520. Brunold TC, Solomon EI. 1999. Reversible dioxygen binding to hemerythrin, 1: electronic structures of deoxy- and oxyhemerythrin. *J Am Chem Soc* **121**:8277–8287.
521. Reem RC, Solomon EI. 1987. Spectroscopic studies of the binuclear ferrous active site of deoxyhemerythrin: coordination number and probable bridging ligands for the native and ligand bound forms. *J Am Chem Soc* **109**:1216–1226.
522. Brunold TC, Solomon EI. 1999. Reversible dioxygen binding to hemerythrin, 2: mechanism of the proton-coupled two-electron transfer to O₂ at a single iron center. *J Am Chem Soc* **121**:8288–8295.
523. Davydov RM, Ménage S, Fontecave M, Gräslund A, Ehrenberg A. 1997. Mixed-valent μ -oxo-bridged diiron complexes produced by radiolytic reduction at 77 K studied by EPR. *J Biol Inorg Chem* **2**:242–255.
524. Sturgeon BE, Doan PE, Liu KE, Burdi D, Tong WH, Nocek JM, Gupta N, Stubbe J, Kurtz Jr DM, Lippard SJ, Hoffman BM. 1997. Non-Kramers ESEEM of integer-spin diferrous carboxylate-bridged clusters in proteins. *J Am Chem Soc* **119**:375–386.
525. Dikanov SA, Davydov RM, Gräslund A, Bowman MK. 1998. Two-dimensional ESEEM spectroscopy of nitrogen hyperfine couplings in methemerythrin and azidomethemerythrin. *J Am Chem Soc* **120**:6797–6805.
526. Rodriguez JH, Xia YM, Debrunner PG. 1999. Mössbauer spectroscopy of the spin coupled Fe²⁺-{FeNO}⁷ centers of nitrosyl derivatives of deoxy hemerythrin and density functional theory of the {FeNO}⁷ (*S* = 3/2) motif. *J Am Chem Soc* **121**:7846–7863.
527. Mitić N, Smith SJ, Neves A, Guddat LW, Gahan LR, Schenk G. 2006. The catalytic mechanisms of binuclear metallohydrolases. *Chem Rev* **106**:3338–3363.
528. Nuttleman PR, Roberts RM. 1990. Transfer of iron from uteroferrin (purple acid phosphatase) to transferrin related to acid phosphatase activity. *J Biol Chem* **265**:12192–12199.
529. Räisänen SR, Alatalo SL, Ylipahkala H, Halleen JM, Cassady AI, Hume DA, Väänänen HK. 2005. Macrophages overexpressing tartrate-resistant acid phosphatase show altered profile of free radical production and enhanced capacity of bacterial killing. *Biochem Biophys Res Commun* **331**:120–126.
530. Oddie GW, Schenk G, Angel NZ, Walsh N, Guddat LW, De Jersey J, Cassady AI, Hamilton SE, Hume DA. 2000. Structure, function, and regulation of tartrate-resistant acid phosphatase. *Bone* **27**:575–584.

531. Valizadeh M, Schenk G, Nash K, Oddie GW, Guddat LW, Hume DA, de Jersey J, Burke TR, Hamilton S. 2004. Phosphotyrosyl peptides and analogues as substrates and inhibitors of purple acid phosphatases. *Arch Biochem Biophys* **424**:154–162.
532. Mitić N, Valizadeh M, Leung EWW, de Jersey J, Hamilton S, Hume DA, Cassady AI, Schenk G. 2005. Human tartrate-resistant acid phosphatase becomes an effective ATPase upon proteolytic activation. *Arch Biochem Biophys* **439**:154–164.
533. Bozzo GG, Raghothama KG, Plaxton WC. 2002. Purification and characterization of two secreted purple acid phosphatase isozymes from phosphate-starved tomato (*Lycopersicon esculentum*) cell cultures. *Eur J Biochem* **269**:6278–6286.
534. Schenk G, Korsinczky MLJ, Hume DA, Hamilton S, DeJersey J. 2000. Purple acid phosphatases from bacteria: similarities to mammalian and plant enzymes. *Gene* **255**:419–424.
535. Schenk G, Guddat LT, Ge Y, Carrington LE, Hume DA, Hamilton S, de Jersey J. 2000. Identification of mammalian-like purple acid phosphatases in a wide range of plants. *Gene* **250**:117–125.
536. Flanagan JU, Cassady AI, Schenk G, Guddat LW, Hume DA. 2006. Identification and molecular modeling of a novel, plant-like, human purple acid phosphatase. *Gene* **377**:12–20.
537. Sträter N, Klabunde T, Tucker P, Witzel H, Krebs B. 1995. Crystal structure of a purple acid phosphatase containing a dinuclear Fe(III)–Zn(II) active site. *Science* **268**:1489–1492.
538. Klabunde T, Sträter N, Fröhlich R, Witzel H, Krebs B. 1996. Mechanism of Fe(III)–Zn(II) purple acid phosphatase based on crystal structures. *J Mol Biol* **259**:737–748.
539. Lindqvist Y, Johansson E, Kaija H, Vihko P, Schneider G. 1999. Three-dimensional structure of a mammalian purple acid phosphatase at 2.2 Å resolution with a μ -(hydr)oxo bridged di-iron center. *J Mol Biol* **291**:135–147.
540. Uppenberg J, Lindqvist F, Svensson C, Ek-Rylander B, Andersson G. 1999. Crystal structure of a mammalian purple acid phosphatase. *J Mol Biol* **290**:201–211.
541. Schenk G, Gahan LR, Carrington LE, Mitić N, Valizadeh M, Hamilton SE, de Jersey J, Guddat LW. 2005. Phosphate forms an unusual tripodal complex with the Fe–Mn center of sweet potato purple acid phosphatase. *Proc Natl Acad Sci USA* **102**:273–278.
542. Sträter N, Jasper B, Scholte M, Krebs B, Duff AP, Langley DB, Han RL, Averill BA, Freeman HC, Guss JM. 2005. Crystal structures of recombinant human purple acid phosphatase with and without an inhibitory conformation of the repression loop. *J Mol Biol* **351**:233–246.
543. Schenk G, Elliott TW, Leung E, Carrington LE, Mitić N, Gahan LR, Guddat LW. 2008. Crystal structures of a purple acid phosphatase, representing different steps of this enzyme's catalytic cycle. *BMC Struct Biol* **8**:6.
544. Schenk G, Ge YB, Carrington LE, Wynne CJ, Searle IR, Carroll BJ, Hamilton S, de Jersey J. 1999. Binuclear metal centers in plant purple acid phosphatases: Fe–Mn in sweet potato and Fe–Zn in soybean. *Arch Biochem Biophys* **370**:183–189.
545. Schenk G, Boutchard CL, Carrington LE, Noble CJ, Moubaraki B, Murray KS, de Jersey J, Hanson GR, Hamilton S. 2001. A purple acid phosphatase from sweet potato contains an antiferromagnetically coupled binuclear Fe–Mn center. *J Biol Chem* **276**:19084–19088.
546. Antanaitis BC, Aisen P, Lilienthal HR. 1983. Physical characterization of two iron uteroferrin: evidence for a spin-coupled binuclear iron cluster. *J Biol Chem* **258**:3166–3172.

547. Averill BA, Davis JC, Burman S, Zirino T, Sandersloehr J, Loehr TM, Sage JT, Debrunner PG. 1987. Spectroscopic and magnetic studies of the purple acid phosphatase from bovine spleen. *J Am Chem Soc* **109**:3760–3767.
548. Mockler GM, De Jersey J, Zerner B, O'Connor CJ, Sinn E. 1983. Active site of allantoic purple acid phosphatase and a model complex for strongly coupled diiron sites. *J Am Chem Soc* **105**:1891–1893.
549. Lauffer RB, Antanaitis BC, Aisen P, Que Jr L. 1983. ^1H NMR studies of porcine uteroferrin: magnetic interactions and active site structure. *J Biol Chem* **258**:14212–14218.
550. Beck JL, Keough DT, de Jersey J, Zerner B. 1984. Enzymatically active zinc, copper and mercury derivatives of the one-iron form of pig allantoic fluid acid phosphatase. *Biochim Biophys Acta* **791**:357–363.
551. Beck JL, McConachie LA, Summors AC, Arnold WN, de Jersey J, Zerner B. 1986. Properties of a purple phosphatase from red kidney bean: a zinc-iron metalloenzyme. *Biochim Biophys Acta* **869**:61–68.
552. Merckx M, Averill BA. 1999. Probing the role of the trivalent metal in phosphate ester hydrolysis: preparation and characterization of purple acid phosphatases containing $\text{Al}^{\text{III}}\text{Zn}^{\text{II}}$ and $\text{In}^{\text{III}}\text{Zn}^{\text{II}}$ active sites, including the first example of an active aluminum enzyme. *J Am Chem Soc* **121**:6683–6689.
553. Funhoff EG, Ljusberg J, Wang YL, Andersson G, Averill BA. 2001. Mutational analysis of the interaction between active site residues and the loop region in mammalian purple acid phosphatases. *Biochemistry* **40**:11614–11622.
554. Funhoff EG, Klaassen CHW, Samyn B, Van Beeumen J, Averill BA. 2001. The highly exposed loop region in mammalian purple acid phosphatase controls the catalytic activity. *ChemBioChem* **2**:355–363.
555. David SS, Que Jr L. 1990. Anion binding to uteroferrin: evidence for phosphate coordination to the iron(III) ion of the dinuclear active site and its interaction with the hydroxo bridge. *J Am Chem Soc* **112**:6455–6463.
556. Wang DL, Holz RC, David SS, Que Jr L, Stankovich MT. 1991. Electrochemical properties of the diiron core of uteroferrin and its anion complexes. *Biochemistry* **30**:8187–8194.
557. Bernhardt PV, Schenk G, Wilson GJ. 2004. Direct electrochemistry of porcine purple acid phosphatase (uteroferrin). *Biochemistry* **43**:10387–10392.
558. Wang XD, Randall CR, True AE, Que Jr L. 1996. X-ray absorption spectroscopic studies of the FeZn derivative of uteroferrin. *Biochemistry* **35**:13946–13954.
559. Wang XD, Que Jr L. 1998. Extended x-ray absorption fine structure studies of the anion complexes of FeZn uteroferrin. *Biochemistry* **37**:7813–7821.
560. Smoukov SK, Quaroni L, Wang XD, Doan PE, Hoffman BM, Que Jr L. 2002. Electron-nuclear double resonance spectroscopic evidence for a hydroxo-bridge nucleophile involved in catalysis by a dinuclear hydrolase. *J Am Chem Soc* **124**:2595–2603.
561. Mueller EG, Crowder MW, Averill BA, Knowles JR. 1993. Purple acid phosphatase: a diiron enzyme that catalyzes a direct phospho group transfer to water. *J Am Chem Soc* **115**:2974–2975.
562. Wynne CJ, Hamilton SE, Dionysius DA, Beck JL, De Jersey J. 1995. Studies on the catalytic mechanism of pig purple acid-phosphatase. *Arch Biochem Biophys* **319**:133–141.
563. Martin BL, Graves DJ. 1994. Isotope effects on the mechanism of calcineurin catalysis: kinetic solvent isotope and isotope exchange studies. *Biochim Biophys Acta* **1206**:136–142.

564. Mertz P, Yu L, Sikkink R, Rusnak F. 1997. Kinetic and spectroscopic analyses of mutants of a conserved histidine in the metallophosphatases calcineurin and lambda protein phosphatase. *J Biol Chem* **272**:21296–21302.
565. Wang XD, Ho RYN, Whiting AK, Que Jr L. 1999. Spectroscopic characterization of a ternary phosphatase-substrate-fluoride complex: mechanistic implications for dinuclear hydrolases. *J Am Chem Soc* **121**:9235–9236.
566. Elliott TW, Mitić N, Gahan LR, Guddat LW, Schenk G. 2006. Inhibition studies of purple acid phosphatases: implications for the catalytic mechanism. *J Braz Chem Soc* **17**:1558–1565.
567. Pinkse MWH, Merckx M, Averill BA. 1999. Fluoride inhibition of bovine spleen purple acid phosphatase: characterization of a ternary enzyme-phosphate-fluoride complex as a model for the active enzyme-substrate-hydroxide complex. *Biochemistry* **38**:9926–9936.
568. Funhoff EG, de Jongh TE, Averill BA. 2005. Direct observation of multiple protonation states in recombinant human purple acid phosphatase. *J Biol Inorg Chem* **10**:550–563.
569. Aquino MAS, Lim JS, Sykes AG. 1994. Mechanism of the reaction of different phosphates with the iron(II)/iron(III) form of purple acid phosphatase from porcine uteri (uteroferrin). *J Chem Soc Dalton Trans* 429–436.
570. Neu HC. 1992. The crisis in antibiotic resistance. *Science* **257**:1064–1073.
571. Levy SB. 1998. The challenge of antibiotic resistance. *Sci Am* **278**:46–53.
572. Bush K, Miller GH. 1998. Bacterial enzymatic resistance: beta-lactamases and aminoglycoside-modifying enzymes. *Curr Opin Microbiol* **1**:509–515.
573. Bush K. 1998. Metallo-beta-lactamases: a class apart. *Clin Infect Dis* **27**:S48–S53.
574. Siemann S, Brewer D, Clarke AJ, Dmitrienko GI, Lajoie G, Viswanatha T. 2002. IMP-1 metallo-beta-lactamase: effect of chelators and assessment of metal requirement by electro-spray mass spectrometry. *Biochim Biophys Acta* **1571**:190–200.
575. Garrity JD, Pauff JM, Crowder MW. 2004. Probing the dynamics of a mobile loop above the active site of L1, a metallo-beta-lactamase from *Stenotrophomonas maltophilia*, via site-directed mutagenesis and stopped-flow fluorescence spectroscopy. *J Biol Chem* **279**:39663–39670.
576. Garau G, Lemaire D, Vernet T, Dideberg O, Di Guilmi AM. 2005. Crystal structure of phosphorylcholine esterase domain of the virulence factor choline-binding protein E from *Streptococcus pneumoniae*: new structural features among the metallo-beta-lactamase superfamily. *J Biol Chem* **280**:28591–28600.
577. Garau G, Di Guilmi AM, Hall BG. 2005. Structure-based phylogeny of the metallo-beta-lactamases. *Antimicrob Agents Chemother* **49**:2778–2784.
578. Frãzao C, Silva G, Gomes CM, Matias P, Coelho R, Sieker L, Macedo S, Liu MY, Oliveira S, Teixeira M, Xavier AV, Rodrigues-Pousada C, Carrondo MA, Le Gall J. 2000. Structure of a dioxygen reduction enzyme from *Desulfovibrio gigas*. *Nat Struct Biol* **7**:1041–1045.
579. Wang ZG, Fast W, Valentine AM, Benkovic SJ. 1999. Metallo-beta-lactamase: structure and mechanism. *Curr Opin Chem Biol* **3**:614–622.
580. Cricco JA, Vila AJ. 1999. Class B beta-lactamases: The importance of being metallic. *Curr Pharm Des* **5**:915–927.
581. Cricco JA, Orellano EG, Rasia RM, Ceccarelli EA, Vila AJ. 1999. Metallo-beta-lactamases: does it take two to tango?. *Coord Chem Rev* **190-192**:519–535.

582. Thornalley PJ. 1998. Glutathione-dependent detoxification of alpha-oxoaldehydes by the glyoxalase system: involvement in disease mechanisms and antiproliferative activity of glyoxalase I inhibitors. *Chem-Biol Interact* **112**:137–151.
583. Schilling O, Wenzel N, Naylor M, Vogel A, Crowder M, Makaroff C, Meyer-Klaucke W. 2003. Flexible metal binding of the metallo-beta-lactamase domain: glyoxalase II incorporates iron, manganese, and zinc in vivo. *Biochemistry* **42**:11777–11786.
584. Wenzel NF, Carenbauer AL, Pfiester MP, Schilling O, Meyer-Klaucke W, Makaroff CA, Crowder MW. 2004. The binding of iron and zinc to glyoxalase II occurs exclusively as di-metal centers and is unique within the metallo-beta-lactamase family. *J Biol Inorg Chem* **9**:429–438.
585. Marasinghe GPK, Sander IM, Bennett B, Periyannan G, Yang KW, Makaroff CA, Crowder MW. 2005. Structural studies on a mitochondrial glyoxalase II. *J Biol Chem* **280**:40668–40675.
586. Cameron AD, Ridderström M, Olin B, Mannervik B. 1999. Crystal structure of human glyoxalase II and its complex with a glutathione thiolester substrate analogue. *Structure* **7**:1067–1078.
587. García-Sáez I, Hopkins J, Papamicael C, Franceschini N, Amicosante G, Rossolini GM, Galleni M, Frère J-M, Dideberg O. 2003. The 1.5-Å structure of *Chryseobacterium meningosepticum* zinc beta-lactamase in complex with the inhibitor, D-captopril. *J Biol Chem* **278**:23868–23873.
588. García-Sáez I, Mercuri PS, Papamicael C, Kahn R, Frere JM, Galleni M, Rossolini GM, Dideberg O. 2003. Three-dimensional structure of FEZ-1, a monomeric subclass B3 metallo-beta-lactamase from *Fluoribacter gormanii*, in native form and in complex with D-captopril. *J Mol Biol* **325**:651–660.
589. de la Sierra-Gallay IL, Pellegrini O, Condon C. 2005. Structural basis for substrate binding, cleavage and allostery in the tRNA maturase RNase Z. *Nature* **433**:657–661.
590. Garrity JD, Bennett B, Crowder MW. 2005. Direct evidence that the reaction intermediate of metallo-beta-lactamase L1 is metal bound. *Biochemistry* **44**:1078–1087.
591. Zang TM, Hollman DA, Crawford PA, Crowder MW, Makaroff CA. 2001. *Arabidopsis* glyoxalase II contains a zinc/iron binuclear metal center that is essential for substrate binding and catalysis. *J Biol Chem* **276**:4788–4795.
592. Pessiki PJ, Khangulov SV, Ho DM, Dismukes GC. 1994. structural and functional models of the dimanganese catalase enzymes, 2: structure, electrochemical, redox, and EPR properties. *J Am Chem Soc* **116**:891–897.
593. Beck JL, McArthur MJ, de Jersey J, Zerner B. 1988. Derivatives of the purple acid phosphatase from red kidney bean: replacement of zinc with other divalent metal ions. *Inorg Chim Acta* **153**:39–44.
594. Beck JL, Durack MCA, Hamilton SE, de Jersey J. 1999. Irreversible inactivation of purple acid phosphatase by hydrogen peroxide and ascorbate. *J Inorg Biochem* **73**:245–252.
595. Twitchett MB, Schenk G, Aquino MAS, Yiu DTY, Lau TC, Sykes AG. 2002. Reactivity of M^{II} metal-substituted derivatives of pig purple acid phosphatase (Uteroferrin) with phosphate. *Inorg Chem* **41**:5787–5794.
596. Rajagopalan PTR, Grimme S, Pei DH. 2000. Characterization of cobalt(II)-substituted peptide deformylase: function of the metal ion and the catalytic residue Glu-133. *Biochemistry* **39**:779–790.
597. Krekeler D, Teske A, Cypionka H. 1998. Strategies of sulfate-reducing bacteria to escape oxygen stress in a cyanobacterial mat. *FEMS Microbiol Ecol* **25**:89–96.

598. Andersson JO, Sjögren ÅM, Davis LAM, Embley TM, Roger AJ. 2003. Phylogenetic analyses of diplomonad genes reveal frequent lateral gene transfers affecting eukaryotes. *Curr Biol* **13**:94–104.
599. Saraiva LM, Vicente JB, Teixeira M. 2004. The role of the flavodiiron proteins in microbial nitric oxide detoxification. *Adv Microb Physiol* **49**:77–129.
600. Gomes CM, Frazão C, Xavier AV, LeGall J, Teixeira M. 2002. Functional control of the binuclear metal site in the metallo-beta-lactamase-like fold by subtle amino acid replacements. *Protein Sci* **11**:707–712.
601. Jouanneau Y, Meyer C, Asso M, Guigliarelli B, Willison JC. 2000. Characterization of a nif-regulated flavoprotein (FprA) from *Rhodobacter capsulatus*: redox properties and molecular interaction with a 2Fe–2S ferredoxin. *Eur J Biochem* **267**:780–787.
602. Chen L, Liu MY, Legall J, Fareleira P, Santos H, Xavier AV. 1993. Rubredoxin oxidase, a new flavo-hemo-protein, is the site of oxygen reduction to water by the strict anaerobe *Desulfovibrio gigas*. *Biochem Biophys Res Commun* **193**:100–105.
603. Fareleira P, Legall J, Xavier AV, Santos H. 1997. Pathways for utilization of carbon reserves in *Desulfovibrio gigas* under fermentative and respiratory conditions. *J Bacteriol* **179**:3972–3980.
604. Chen L, Liu MY, Legall J, Fareleira P, Santos H, Xavier AV. 1993. Purification and characterization of an nadh-rubredoxin oxidoreductase involved in the utilization of oxygen by *Desulfovibrio gigas*. *Eur J Biochem* **216**:443–448.
605. Gomes CM, Silva G, Oliveira S, LeGall J, Liu M-Y, Xavier AV, RodriguesPousada C, Teixeira M. 1997. Studies on the redox centers of the terminal oxidase from *Desulfovibrio gigas* and evidence for its interaction with rubredoxin. *J Biol Chem* **272**:22502–22508.
606. Rodrigues R, Vicente JB, Félix R, Oliveira S, Teixeira M, Rodrigues-Pousada C. 2006. *Desulfovibrio gigas* flavodiiron protein affords protection against nitrosative stress in vivo. *J Bacteriol* **188**:2745–2751.
607. Silaghi-Dumitrescu R, Coulter ED, Das A, Ljungdahl LG, Jameson GNL, Huynh BH, Kurtz Jr DM. 2003. A flavodiiron protein and high molecular weight rubredoxin from *Moorella thermoacetica* with nitric oxide reductase activity. *Biochemistry* **42**:2806–2815.
608. Silaghi-Dumitrescu R, Ng KY, Viswanathan R, Kurtz Jr DM. 2005. A flavo-diiron protein from *Desulfovibrio vulgaris* with oxidase and nitric oxide reductase activities: evidence for an in vivo nitric oxide scavenging function. *Biochemistry* **44**:3572–3579.
609. Gardner AM, Helmick RA, Gardner PR. 2002. Flavorubredoxin, an inducible catalyst for nitric oxide reduction and detoxification *Escherichia coli*. *J Biol Chem* **277**:8172–8177.
610. Mukhopadhyay P, Zheng M, Bedzyk LA, LaRossa RA, Storz G. 2004. Prominent roles of the NorR and Fur regulators in the *Escherichia coli* transcriptional response to reactive nitrogen species. *Proc Natl Acad Sci USA* **101**:745–750.
611. Büsch A, Pohlmann A, Friedrich B, Cramm R. 2004. A DNA region recognized by the nitric oxide-responsive transcriptional activator NorR is conserved in beta- and gamma-proteobacteria. *J Bacteriol* **186**:7980–7987.
612. Silaghi-Dumitrescu R, Kurtz Jr DM., Ljungdahl LG, Lanzilotta WN. 2005. X-ray crystal structures of *Moorella thermoacetica* FprA: novel diiron site structure and mechanistic insights into a scavenging nitric oxide reductase. *Biochemistry* **44**:6492–6501.
613. Wasserfallen A, Ragetti S, Jouanneau Y, Leisinger T. 1998. A family of flavoproteins in the domains Archaea and Bacteria. *Eur J Biochem* **254**:325–332.

614. Gomes CM, Vicente JB, Wasserfallen A, Teixeira M. 2000. Spectroscopic studies and characterization of a novel electron-transfer chain from *Escherichia coli* involving a flavorubredoxin and its flavoprotein reductase partner. *Biochemistry* **39**:16230–16237.
615. Gomes CM, Giuffrè A, Forte E, Vicente JB, Saraiva LM, Brunori M, Teixeira M. 2002. A novel type of nitric-oxide reductase: *Escherichia coli* flavorubredoxin. *J Biol Chem* **277**:25273–25276.
616. Vicente JB, Teixeira M. 2005. Redox and spectroscopic properties of the *Escherichia coli* nitric oxide-detoxifying system involving flavorubredoxin and its NADH-oxidizing redox partner. *J Biol Chem* **280**:34599–34608.
617. Berthold DA, Stenmark P. 2003. Membrane-bound diiron carboxylate proteins. *Annu Rev Plant Biol* **54**:497–517.
618. Josse E-M, Alcaraz J-P, Labouré A-M, Kuntz M. 2003. In vitro characterization of a plastid terminal oxidase (PTOX). *Eur J Biochem* **270**:3787–3794.
619. Andersson ME, Nordlund P. 1999. A revised model of the active site of alternative oxidase. *FEBS Lett* **449**:17–22.
620. Veiga A, Arrabaça JD, Loureiro-Dias MC. 2000. Cyanide-resistant respiration is frequent, but confined to yeasts incapable of aerobic fermentation. *FEMS Microbiol Lett* **190**:93–97.
621. Dinant M, Baurain D, Coosemans N, Joris B, Matagne RF. 2001. Characterization of two genes encoding the mitochondrial alternative oxidase in *Chlamydomonas reinhardtii*. *Curr Genet* **39**:101–108.
622. Siedow JN, Umbach AL. 2000. The mitochondrial cyanide-resistant oxidase: structural conservation amid regulatory diversity. *Biochim Biophys Acta* **1459**:432–439.
623. Moller IM. 2001. Plant mitochondria and oxidative stress: electron transport, NADPH turnover, and metabolism of reactive oxygen species. *Annu Rev Plant Physiol Plant Mol Biol* **52**:561–591.
624. Maxwell DP, Wang Y, McIntosh L. 1999. The alternative oxidase lowers mitochondrial reactive oxygen production in plant cells. *Proc Natl Acad Sci USA* **96**:8271–8276.
625. Yip JYH, Vanlerberghe GC. 2001. Mitochondrial alternative oxidase acts to dampen the generation of active oxygen species during a period of rapid respiration induced to support a high rate of nutrient uptake. *Physiol Plant* **112**:327–333.
626. Chaudhuri M, Ajayi W, Temple S, Hill GC. 1995. Identification and partial purification of a stage-specific 33 kDa mitochondrial protein as the alternative oxidase of the *Trypanosoma brucei*-Brucei blood-stream trypomastigotes. *J Eukaryot Microbiol* **42**:467–472.
627. Siedow JN, Umbach AL, Moore AL. 1995. The active site of the cyanide-resistant oxidase from plant mitochondria contains a binuclear iron center. *FEBS Lett* **362**:10–14.
628. Åberg A, Nordlund P, Eklund H. 1993. Unusual clustering of carboxyl side-chains in the core of iron-free ribonucleotide reductase. *Nature* **361**:276–278.
629. Berthold DA, Voevodskaya N, Stenmark P, Gräslund A, Nordlund P. 2002. EPR studies of the mitochondrial alternative oxidase: evidence for a diiron carboxylate center. *J Biol Chem* **277**:43608–43614.
630. McCormick JM, Reem RC, Solomon EI. 1991. Chemical and spectroscopic studies of the mixed-valent derivatives of the nonheme iron protein hemerythrin. *J Am Chem Soc* **113**:9066–9079.
631. Ravi N, Prickril BC, Kurtz Jr DM, Huynh BH. 1993. Spectroscopic characterization of ⁵⁷Fe-reconstituted rubrerythrin, a nonheme iron protein with structural analogies to ribonucleotide reductase. *Biochemistry* **32**:8487–8491.

632. Debrunner PG, Hendrich MP, de Jersey J, Keough DT, Sage JT, Zerner B. 1983. Mössbauer and electron paramagnetic resonance study of the binuclear iron center in purple acid phosphatase. *Biochim Biophys Acta* **745**:103–106.
633. Atta M, Andersson KK, Ingemarson R, Thelander L, Gräslund A. 1994. EPR Studies of mixed-valent $[\text{Fe}^{\text{II}}\text{Fe}^{\text{III}}]$ clusters formed in the R2 subunit of ribonucleotide reductase from mouse or herpes simplex virus: mild chemical reduction of the diferric centers. *J Am Chem Soc* **116**:6429–6430.
634. Simurdiak M, Lee J, Zhao HM. 2006. A new class of arylamine oxygenases: evidence that *p*-aminobenzoate N-oxygenase (AurF) is a di-iron enzyme and further mechanistic studies. *ChemBioChem* **7**:1169–1172.
635. Winkler R, Hertweck C. 2005. Sequential enzymatic oxidation of aminoarenes to nitroarenes via hydroxylamines. *Angew Chem, Int Ed* **44**:4083–4087.
636. King RR, Lawrence CH, Calhoun LA. 1998. Unusual production of 5-nitroanthranilic acid by *Streptomyces scabies*. *Phytochemistry* **49**:1265–1267.
637. He J, Magarvey N, Pirae M, Vining LC. 2001. The gene cluster for chloramphenicol biosynthesis in *Streptomyces venezuelae* ISP5230 includes novel shikimate pathway homologues and a monomodular non-ribosomal peptide synthetase gene. *Microbiology-SGM* **147**:2817–2829.
638. Arima K, Fukuta A, Imanaka H, Kousaka M, Tamura G. 1964. Pyrrolnitrin new antibiotic substance produced by *Pseudomonas*. *Agric Biol Chem* **28**:575–577.
639. Schwartz JL, Tishler M, Arison BH, Shafer HM, Omura S. 1967. Identification of mycolutein and pulvomycin as aureothin and labilomycin respectively. *J Antibiot* **29**:236–241.
640. Lee JK, Simurdiak M, Zhao HM. 2005. Reconstitution and characterization of aminopyrrolnitrin oxygenase, a Rieske N-oxygenase that catalyzes unusual arylamine oxidation. *J Biol Chem* **280**:36719–36728.
641. He J, Hertweck C. 2003. Iteration as programmed event during polyketide assembly: molecular analysis of the aureothin biosynthesis gene cluster. *Chem Biol* **10**:1225–1232.

PROBING THE STRUCTURE–FUNCTION RELATIONSHIP OF HEME PROTEINS USING MULTIFREQUENCY PULSE EPR TECHNIQUES

Sabine Van Doorslaer

*University of Antwerp, SIBAC Laboratory,
Department of Physics, Antwerp, Belgium*

Although EPR has been used regularly in the study of heme proteins for more than 40 years now, the use of multifrequency and/or pulse-EPR techniques is still quite scarce. Here, a review of the use of these methods is presented, highlighting the advantages, limitations, and challenges for the future.

1. INTRODUCTION

Heme-based proteins are found in all kingdoms of nature and cover functions as diverse as ligand uptake, transport, and storage, electron transfer, and catalysis of a large variety of biochemical reactions. It is safe to say that heme proteins, and in general metalloporphyrin-based proteins, lie at the basis of life. Unsurprisingly, heme proteins are discussed extensively in all standard books on (inorganic) biochemistry ([1–3], and many others). Although a lot is already known about the inner workings of some of these proteins, many questions remain unsolved and surprising functions of heme proteins are revealed at a regular pace. The interest in the biophysical analysis of heme proteins is therefore still as large as it was at the start of heme-protein research.

Because some of the forms of heme proteins are intrinsically paramagnetic, electron paramagnetic resonance (EPR) has been used extensively to study the structure and structure–function relations of these proteins. By far the majority of these investigations are done using continuous-wave (cw) EPR at the conventional X-band microwave frequency (~9.5 GHz), and these cw-EPR studies have formed the basis of many excellent reviews [4–6]. In the last two decennia, the field of EPR spectroscopy has, however, been revolutionized by many technical developments. Indeed, the construction of pulse-EPR spectrometers, the accompanying developments of the pulse-EPR methodology, and the (ongoing) development of

EPR spectrometers operating at high microwave frequencies ($\gg 9.5$ GHz) [7,8] have tremendously increased the amount of information that can be obtained using EPR spectroscopy.

This chapter will focus on how a multifrequency EPR approach can be used to gain insight into the workings of different heme proteins. Although X-band cw-EPR studies constitute an inherent part of this approach, they will not form the center of this discussion. The focus will lie on the strength and limitations of modern state-of-the-art EPR spectroscopy in addressing heme-protein problems, and the results of the X-band cw-EPR studies will only be discussed to a level necessary to present a coherent story to the reader. For detailed reviews on these cw-EPR analyses of heme proteins, I refer to the earlier mentioned literature [4–6]. Figure 1 gives an overview of the pulse-EPR and ENDOR (electron nuclear double resonance) techniques that are referred to in the text.

2. FERRIC FORMS OF HEME PROTEINS

The iron ion of the heme group is known to occur in the ferrous, ferric, or ferryl form. The ferric forms of cytochromes, heme-containing peroxidases, and catalases play an essential biological role (electron-transfer reactions), but the ferric (or met) form of globins was long considered to be only a globin degradation product. However, the recent discovery that myoglobin is also involved in the removal of toxic NO in cardiac and striated muscle with formation of the met form, which may in turn be reduced by an enzymatic system [9], has renewed the interest in the ferric form of globins.

The spin state of the ferric forms is found to vary from a low-spin ($S = 1/2$) to high-spin ($S = 3/2$ or $5/2$) state. The difference between the states follows from ligand-field theory [5,6] and is governed by the strength of the axial ligands (Fig. 2). As an example, the ferric form of mammalian myoglobin, whereby the F8 histidine and a water molecule are axially coordinating to the heme iron, is in a high-spin state ($S = 5/2$), because water is a weak ligand. In neuroglobin, a recently discovered mammalian nerve globin, the exogenous water ligand is replaced by the endogenous E7-histidine residue, and the bis-histidine coordinated ferric form of this protein is characterized by a low-spin iron(III) state [10]. As will be shown in the following section, EPR analysis of low-spin and high-spin ferric heme systems requires different methodological approaches.

2.1. Low-Spin Ferric Forms of Heme Proteins

The principal g values of low-spin ferric heme proteins are found to vary strongly based upon the type and orientation of the axially coordinating ligands. F.A. Walker identified three types of low-spin ferric heme centers [6]. *Type I* centers have a $(d_{xy})^2(d_{xz}, d_{yz})^3$ electronic ground state with the axial ligands aligned in quasi-perpendicular planes. The centers are sometimes referred to as HALS (highly

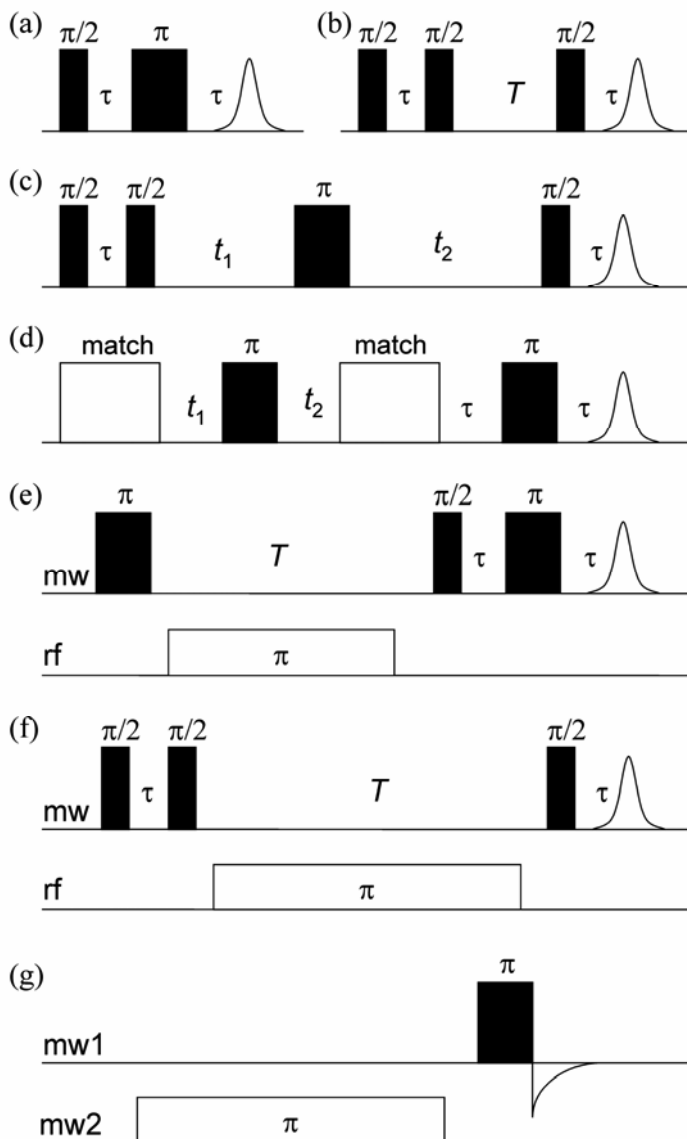


Figure 1. Scheme of the pulse EPR sequences mentioned in this chapter. (a) Two-pulse ESEEM. (b) Three-pulse ESEEM. (c) Four-pulse ESEEM. When times t_1 and t_2 are stepped under the constraint of $t_1 = t_2 = T$, a combination-peak experiment is performed. Two-dimensional HYSCORE spectroscopy is done using the same sequence, whereby t_1 and t_2 are stepped independently. The second and third $\pi/2$ pulse are replaced by high-turning-angle (HTA) pulses in a matched HYSCORE experiment. (d) SMART-HYSCORE. The first and third pulses are HTA pulses. (e) Davies ENDOR. (f) Mims ENDOR. (g) ELDOR-detected NMR.

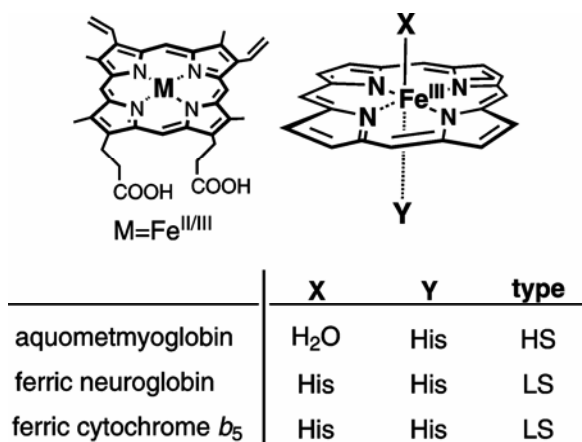


Figure 2. Iron protoporphyrin IX structure (heme). The nature of the axial ligands X and Y will determine the spin state of the ferric center. Some typical high- and low-spin ferric heme proteins are given.

anisotropic low-spin) species [11,12]. The corresponding X-band cw-EPR spectrum is usually characterized by a single feature, known as the “large g_{\max} ” signal, and is only observed at low temperatures (4–20 K). The maximum principal g value (g_{\max}) is usually higher than 3.3. Typical examples of these type I centers are cyanide-ligated myoglobin [4] and ferric mitochondrial cytochrome b_{562} [13]. *Type II* ferric heme centers are also characterized by a $(d_{xy})^2(d_{xz}, d_{yz})^3$ electronic ground state, but with the axial ligands now aligned in approximately parallel planes. They show well-resolved rhombic EPR signals at X-band that can be observed up to *ca.* 70 K. Ferric cytochrome b_5 [14], ferric cytochrome c_2 [15], and ferric tomato hemoglobin [16] are typical examples. Finally, *type III* ferric heme centers have been identified, which have a $(d_{xz}, d_{yz})^4(d_{xy})^1$ electronic ground state with axial ligands in any directions. They are characterized by axial \mathbf{g} matrices. Several type III ferric porphyrins have been synthesized [6,17]. Table 1 shows the g values of a selection of typical type I, II, and III ferric heme centers.

Two of the pioneers of EPR analyses of low-spin ferric heme proteins are undoubtedly J. Peisach and W.E. Blumberg. Their so-called “truth tables” allow for a prediction of the axial ligands of the iron heme center from the principal g values [18]. Although the truth tables are based on crude assumptions and do not include type I or type III centers, they can nevertheless give in many cases a valuable first clue as to the type of axial ligands. As an example, based on X-band cw-EPR lysine was predicted to be the sixth ligand of native cytochrome *f* [19,20]. However, in order to obtain more detailed and conclusive information on the heme pocket, the X-band cw-EPR studies need to be supplemented with more advanced EPR experiments.

Table 1. Principal g Values for Typical Examples of Type I, Type II and Type III Low-Spin Ferric Heme Systems

System	g_x	g_y	g_z	Ref.
Type I				
CN-ligated myoglobin	0.93	1.89	3.45	4
Mitochondrial cytochrome b_{562}	n.d.	n.d.	3.44	13
Type II				
Cytochrome b_5	1.35	2.22	3.07	14
Cytochrome c_2	1.23	2.11	3.13	15
Tomato hemoglobin	1.44	2.23	2.98	16
Type III				
[TPPFe(2,6-xylylNC) $_2$] $^+$	-2.2	2.2	-1.94	17

n.d. = not detected. 2,6-xylylNC = 2,6-xylylisocynide, TPP = tetraphenylporphyrin.

In 1986, C.P. Scholes and coworkers showed in a very detailed manner how cw-ENDOR can be used to elucidate the heme and imidazole nitrogen hyperfine couplings and the ligand proton hyperfine interactions for different synthetic bis-imidazole ligated low-spin ferric heme systems and for imidazole myoglobin [21]. In this work, combinations of porphyrins and imidazoles containing either naturally occurring ^{14}N or isotopically enriched ^{15}N were used to distinguish the spectral contributions of the heme and imidazole nitrogens. Furthermore, the use of deuterated tetraphenylporphyrin allowed for elucidation of the proton-ENDOR spectra. The information obtained in this way for the model complexes was then used to interpret the data of imidazole-ligated metmyoglobin. Despite the fact that the study was pioneering, there were several limitations to the work. Although the nitrogen and proton hyperfine values could be determined in the principal g directions, Scholes and coworkers could not derive the full hyperfine matrices and their principal directions, let alone derive detailed structural information from the data. In fact, they used the existing x-ray data to predict the dipolar contribution to the proton hyperfine matrix, which they then matched to the observed couplings. The reasons for these encountered problems are inherent to the methodology. Indeed, in the X-band cw-ENDOR spectra the signals stemming from the different nitrogen nuclei overlap, which hugely complicates the analysis. This also explains the need for specific isotope labeling of the model complexes, a procedure that is very difficult, if not impossible, in heme proteins. Furthermore, the use of frozen solutions (thus disordered systems) complicates the interpretation. With the exception of the spectra taken at the single-crystal-like positions, the powder ENDOR spectra contain contributions of a large number of orientations. Clearly, the spectral interpretation would have been considerably easier if single crystals had been available. However, for many (heme) proteins, it is impossible to grow single crystals, and even if they can be grown they rarely have the size needed for X-band EPR/ENDOR spectroscopy. Additionally, the ENDOR spectra were not interpreted through computational simulation of the spectra, but through a rough manual as-

signment of the line positions. And finally, although the authors did a commendable attempt to interpret their hyperfine data in terms of the electronic structure, their interpretations were (and could at the time only be) qualitative. In fact, the limitations that Scholes and colleagues encountered here and in some of their other studies on low-spin iron systems [22,23] summarize nicely the basis of what has been the driving force in the development of EPR in the last two decennia, namely the quest for increased spectral resolution through instrumental and methodological improvements, the search for the development of EPR spectrometers that can handle small samples, the urge to develop adequate spectral simulation programs, and the need to match the EPR data with quantum-chemical computations in order to extract the maximum amount of information from the experimental data.

As will be shown, spectral-resolution optimization can in principle only be obtained through the use of different pulse-EPR and ENDOR techniques in a multi-frequency approach. Fahnenschmidth et al. used X-band Davies-ENDOR spectroscopy to investigate de-novo synthesized heme proteins [24]. However, this approach basically led to the same possibilities and limitations as observed in the earlier mentioned X-band cw-ENDOR analyses of Scholes and coworkers [21]. Already at the end of the 1970s, J. Peisach, W.B. Mims, and J.L. Davis recognized the potential of using 3-pulse ESEEM (electron spin echo envelope modulation) spectroscopy to obtain information about the hyperfine and nuclear-quadrupole couplings of the heme and imidazole nitrogens of low-spin ferric heme proteins [25]. Peisach and coworkers subsequently applied the 3-pulse ESEEM technique in several of their studies on these types of systems [26–28]. Although again pioneering in their kind, the 3-pulse ESEEM studies suffer from similar problems as the cw-ENDOR analyses. The 3-pulse ESEEM spectra are one dimensional, and the signals stemming from the different nitrogens are therefore again overlapping, rendering spectral interpretation and consequent extraction of structural information difficult, especially when investigating disordered systems. Furthermore, 3-pulse ESEEM spectra suffer from τ -dependent blind spots that can corrupt the interpretation [7]. However, as shown by H. Thomann, D. Goldfarb, and coworkers, 2-pulse and 3-pulse ESEEM can sometimes be used advantageously in combination with isotope labeling [29]. They investigated water binding to the low-spin ferric form of P450 by measuring the 2-pulse and 3-pulse ESEEM spectra of substrate-free cytochrome P450cam with ^{17}O -enriched and non-enriched water. The ^{17}O ESEEM frequencies were obtained from Fourier transformation of the ratio of the ESEEM waveforms. Numerical simulation of these frequencies gave structural information on the water ligation in P450cam. The information was in a later work corroborated by ^1H Davies-ENDOR and 4-pulse ESEEM (i.e., one-dimensional combination peak) experiments [30].

All foregoing studies were performed at X-band microwave frequencies. B. Hoffman and coworkers showed, however, in a number of studies on chloroperoxidase and P450cam that a combination of cw-, Davies- and Mims-ENDOR experiments at Q-band (35 GHz) can largely facilitate the analysis of low-spin ferric heme proteins [31,32]. Indeed, due to the magnetic-field dependence of the nuclear Zeeman interaction, the spectral contributions stemming from ^{14}N , ^{15}N , ^1H , ^2H , and

^{13}C nuclei can be better separated at higher frequencies. Furthermore, through the clever use of different ENDOR techniques to separate the contributions of the different nuclei, the researchers could deduce that the allylbenzene-bound heme of inactivated chloroperoxidase is an N-alkylhemin metallocycle with the C-1 of allylbenzene bonded to the pyrrole nitrogen [32].

Astashkin et al. showed, in contrast, that there may also be advantages of using lower microwave frequencies (e.g., S-band (2–4 GHz)) when studying low-spin ferric heme systems [33,34]. This is particularly the case for type II systems with a large \mathbf{g} anisotropy or for type I centers, whereby the g_{\min} feature is only rarely observable in the X-band cw-EPR spectra due to large \mathbf{g} -strain effects. The same holds, of course, for the electron spin echo intensity at the high-field side. Increase of the microwave frequency will only worsen this case, whereby decrease of the microwave frequency makes ESEEM and ENDOR measurements at the high-field edge of the EPR spectrum feasible. In a series of papers, it was shown how the proton sum-frequency peaks obtained from 2-pulse or 4-pulse ESEEM experiments at X- and S-band microwave frequencies can be used to determine the orientation of the axial ligands versus the \mathbf{g} tensor [33,35,36]. The shift of the sum frequency of the nearby protons of the axial ligands versus twice the proton Zeeman frequency directly relates to the Fe–H distance and the Fe–H vector orientation [33–36], which can be translated into the ligand orientation.

Although two-dimensional pulse-EPR techniques, such as HYSCORE (hyperfine sublevel correlation) spectroscopy, have been applied extensively in the study of metalloproteins [7], it was surprisingly only in 2003 that the HYSCORE technique was for the first time applied to low-spin ferric heme systems [37]. In their work, García-Rubio et al. selectively isotopically labeled a bis-imidazole heme model compound in order to assign the different cross-peaks in the nitrogen HYSCORE spectra to the corresponding nuclei. They could then extrapolate this assignment to the analysis of cytochrome b_{559} . The authors derived some information on the nitrogen hyperfine and nuclear–quadrupole coupling, but were limited by the fact that they did not have adequate HYSCORE simulation programs available. In our recent work [38], we showed for a bis-imidazole ferric porphyrin model system that a combination of the earlier-mentioned Astashkin–Raitisimring–Walker approach [33–36] with the HYSCORE technique and appropriate spectral simulation can lead to valuable information that exceeds any of the other introduced approaches separately. Figure 3 shows schematically the basis of this combined approach. In a first stage, the X-band nitrogen HYSCORE spectra are recorded. If needed, matching pulses [39] or SMART HYSCORE [40] can be applied to enhance spectral quality. The assignment of the major cross-peaks is done based on the work of García-Rubio et al. [37]. Subsequently, the HYSCORE contributions of the porphyrin nitrogens are simulated. From the orientation of the nuclear–quadrupole tensor in the \mathbf{g} -tensor frame, the orientation of the \mathbf{g} principal axes in the molecular frame can be derived. This orientation procedure is based on the fact that the direction of the largest principal g value corresponds approximately with

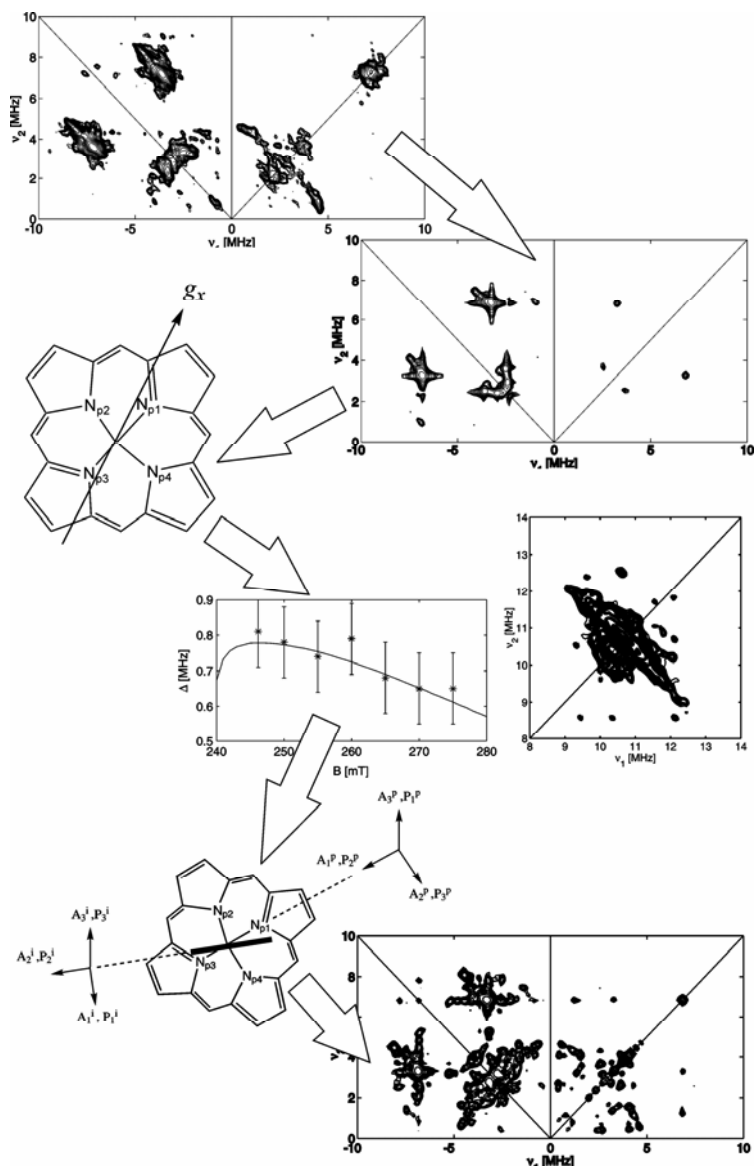


Figure 3. Cartoon of an EPR approach to determine the orientation of the axial ligands in the heme pocket of low-spin ferric heme proteins. The methodology consists of measurement of the X-band HYSCORE spectra and simulation of the contribution stemming from the porphyrin nitrogens, which leads to determination of the orientation of the g tensor axes in the molecular frame. Subsequent analysis of the proton HYSCORE spectra and proton combination frequencies leads to a determination of the axial ligand orientation in the g axes frame, and therefore in the molecular frame. The last step of the procedure consists of a full simulation of the nitrogen HYSCORE spectra. The full methodology is explained in the text.

the heme normal (which can be verified from the proton HYSCORE spectra) and on the knowledge that in metalloporphyrin systems the largest nuclear-quadrupole principal value lies in the porphyrin plane, perpendicular to the metal- N_{porph} bond [38,41]. In a next step, we focus on the analysis of the hyperfine couplings of the nearby protons of the axial imidazole ligands, as outlined in the work by Astashkin, Raitsimring, and Walker [33–36]. However, the analysis of the sum-peak frequencies obtained by X-band two- and four-pulse ESEEM are now combined with the simulation of the X-band proton HYSCORE spectra, which increases the accuracy of the spectral interpretation. From the proton hyperfine interactions, information on the Fe–H distance and orientation of the Fe–H vector in the \mathbf{g} -tensor frame can be derived that directly relates to the orientation of the imidazole planes in the \mathbf{g} -tensor frame. Since we derived in the first step the orientation of the latter frame versus the molecular frame, we now know the orientation of the axial imidazole ligand planes in the heme pocket. The angular information can in a last step be used to simulate the contributions of the imidazole nitrogens to the nitrogen HYSCORE spectra. In theory, direct simulation of the latter should also allow us to determine the orientation of the imidazole ligands. However, simulations revealed that the HYSCORE contributions of the imidazole nitrogens vary only marginally under rotation of the hyperfine and nuclear-quadrupole tensors over a large angle about the heme normal [38].

Although the above methodology is in principle a sound one, there are some problems that arise when it is applied to low-spin ferric heme proteins [16,38]. First of all, there is of course an experimental uncertainty in the determination of the \mathbf{g} -tensor orientation versus the molecular frame in step 1 and the determination of the ligand-plane orientation versus the \mathbf{g} -tensor frame in step 2. The added experimental errors may generate a large uncertainty about the orientation of the ligand planes. The degrees of freedom can be limited by the use of the counter-rotation principle introduced by Shokhirev and Walker, which is valid for most type I and II systems [42]. This principle states that the magnetic axes (thus \mathbf{g} -tensor axes) will counter-rotate when the planar axial ligands are rotated about the heme normal away from the porphyrin nitrogens toward the meso positions and beyond. Use of this principle will pin down the position of the axial ligands very nicely for bis-imidazole coordinated hemes with quasi-parallel axial ligands, but the situation may not be so clear when the coplanarity of the ligands is broken [16]. Furthermore, for systems with large \mathbf{g} anisotropy the X-band ESE (electron-spin-echo) intensity becomes very low at the high-field position of the spectrum due to the large \mathbf{g} strain effects. HYSCORE spectroscopy is then no longer feasible at these positions, so that the above experiments need to be extended with X-band Mims ENDOR experiments [43] or with S-band HYSCORE spectra (I. Ioanitescu, unpublished results on ferric cytoglobin).

It is important to note that, despite the above remarks, the recording of the ESE-detected EPR spectra is still favored over cw-EPR spectroscopy to determine the lowest principal g value in low-spin ferric systems with high \mathbf{g} anisotropy (supplementary material of [44]). Furthermore, for type I systems, 2D nutation spec-

troscopy may help in the observation of the high-field features at X-band, as was shown for ferric myoglobin cyanide [45].

Finally, the recent major evolutions in quantum chemistry (especially the development of DFT [density functional theory]) have made it feasible to compute the EPR parameters of low-spin heme systems, as was demonstrated for simple ferric porphyrin systems [46,47]. However, state-of-the-art quantum chemistry is still a long way from an identical match between experimental and computed EPR parameters, and the further development of these quantum-chemical methods form undoubtedly one of the biggest challenges for the next years.

2.2. High-Spin Ferric Forms of Heme Proteins

A large part of the ferric forms of known heme proteins are in a high-spin state. One of the classic examples is given by the aquomet form of mammalian myoglobin ($S = 5/2$). The observed X-band cw-EPR spectra of high-spin ferric heme proteins resemble those of an $S_{\text{eff}} = 1/2$ system with $g_{\perp,\text{eff}} \approx 6$ and $g_{\parallel,\text{eff}} \approx 2$. Indeed, since the microwave quantum energy, $h\nu$, is much smaller at X-band (~ 9.5 GHz) than the zero-field splitting (on the order of $5\text{--}10$ cm $^{-1}$), the observed (effective) EPR spectrum arises from transitions of the lowest Kramers doublet [5,48]. In the case of a pure tetragonal symmetry, the observed X-band cw-EPR spectra can be simulated by assuming an $S_{\text{eff}} = 1/2$ with $g_{\perp,\text{eff}} = 6$ and $g_{\parallel,\text{eff}} = 2$. Incorporation of the hemin into a protein often constrains the heme in such a manner that there is departure from tetragonal towards rhombic symmetry, which translates itself in the broadening or splitting of the $g = 6$ signal [49]. In some cases admixed spin states ($S = 3/2, 5/2$) have been identified for high-spin ferric heme proteins [50].

One obvious way to determine the zero-field splitting parameter, D , with cw-EPR spectroscopy, is to go to higher microwave frequencies, where the $h\nu/D$ ratio becomes larger than 1. E. Reijerse, W. Hagen, and coworkers measured the cw-EPR spectra of aquometmyoglobin from 1 to 285 GHz [51]. As the microwave frequency approaches the zero-field splitting, the value of $g_{\perp,\text{eff}}$ reduces notably, giving direct information on the D value. From 130 GHz onwards, an anomalous increase of the linewidth is observed that relates directly to D strain effects.

Again, detailed information on the heme-pocket structure can only be obtained by performing additional ENDOR or pulsed EPR experiments. In a detailed X-band cw-ENDOR study of single crystals of aquometmyoglobin, C.P. Scholes et al. unraveled the hyperfine and nuclear-quadrupole tensors of the heme and histidine nitrogens [52]. From this, the authors could derive a lot of information on the electronic and geometric structure of the heme pocket, and the study has become an important work of reference.

The amount of information that one can derive using X-band cw-ENDOR decreases enormously when no single crystals of the protein are available for similar reasons as discussed in the previous section on low-spin ferric heme centers. Again the solution to overcome this problem lies in a multifrequency pulse-EPR/ENDOR approach. In their cw and pulse ^{19}F and $^{1,2}\text{H}$ ENDOR study of fluorometmyoglobin, B.M. Hoffman and coworkers demonstrated the advantage of combining X- and Q-

band microwave frequencies [53]. From their study, Hoffman et al. could determine that the F^- is hydrogen-bonded to the $N(\epsilon)H$ of the distal histidine at all pH values between 5.5 and 11. Furthermore, they could derive the D parameter from the ^{19}F ENDOR spectra taken at $g_{\perp,eff} = 6$. When the high-spin ferric system is described as an $S_{eff} = 1/2$ system, there is an unusually large “pseudonuclear” contribution to the fluorine Zeeman tensor in the effective spin Hamiltonian given by [52,53]

$$g_{n,\perp}^F = g_n^F + \frac{(g_x + g_y)\beta_e A_{\perp}^F}{3\beta_n D}, \quad (1)$$

$$g_{n,\parallel}^F = g_n^F, \quad (2)$$

where g_n^F is the tabulated nuclear g value of ^{19}F , β_n and β_e are the nuclear and Bohr magneton, respectively, and g_x , g_y and A_{\perp}^F are the real in-plane principal g values and principal fluorine hyperfine values of the high-spin ferric system. From the apparent deviation of the effective g_n value from the tabulated g_n value, the D value and the absolute sign of the hyperfine values can be determined using Eq. (1). Hoffman and coworkers failed to detect changes in the spin densities and p-orbital populations of the proximal and heme nitrogens upon variation of the pH using their cw-ENDOR approach. Hong-In Lee showed that this was due to intrinsic inhomogeneous EPR line-broadening effects of MbF in frozen solutions, and he demonstrated how the hyperfine sensitivity of Mims ENDOR can be used advantageously to circumvent this problem [54].

A search of the literature reveals that the number of ESEEM studies performed on high-spin ferric heme proteins are very scarce, and the ESEEM spectra are only performed for observation positions corresponding to the $g_{\parallel,eff} = 2$ position [55,56]. Two obvious reasons for this observation can be identified:

1. The above-mentioned pseudo-nuclear contribution to the g_n value, combined with the low nuclear Zeeman frequency of the protons at the $g = 6$, position makes interpretation of the proton ESEEM spectra very difficult
2. Although the principal hyperfine values of the heme and imidazole nitrogens lie on the order of 9 to 15 MHz, the effective hyperfine values in the heme plane are a factor 3 higher. [This is analogous to the difference between the g principal values in the $S = 5/2$ description ($g_{\parallel} = 2$, $g_{\perp} = 1.98$) and those in the $S_{eff} = 1/2$ description ($g_{\parallel,eff} = 2$, $g_{\perp,eff} = 6$) [52]]. Using standard ESEEM experiments, effective nitrogen hyperfine interactions of 30–45 MHz cannot be observed.

Although the standard ESEEM experiments may fail in this case, we recently showed that the nitrogen couplings can still be observed using X-band matched

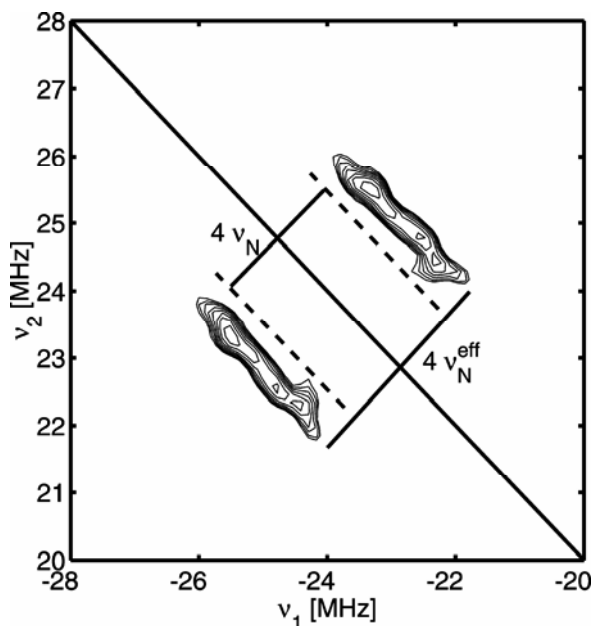


Figure 4. X-band SMART HYSORE spectrum of aquometmyoglobin taken at observer position $g = 6$. The double-quantum cross-peaks are separated over four times the effective nuclear Zeeman frequency, $4\nu_N^{\text{eff}}$, which clearly differs from the tabulated value (dashed lines, separation $4\nu_N$). From this shift, the positive sign of the hyperfine value can be determined [93,94].

HYSORE and SMART HYSORE (see Fig. 4; manuscript in preparation). The pseudonuclear effect to the g_n value can nicely be observed in the double-quantum cross-peaks and used beneficially to determine the sign of the hyperfine values (Fig. 4). Furthermore, the use of ELDOR (electron double resonance) detected NMR techniques [57] at W-band largely facilitates the analysis of high-spin iron(III) heme proteins [94].

3. NO-LIGATED HEME PROTEINS

The reaction of nitric oxide (NO) with heme enzymes such as NO synthase and nitrite reductase has important biological significance [58]. Furthermore, the recent discovery that myoglobin is involved in the removal of toxic NO in cardiac and striated muscle has revived the interest in the studies on the NO-ligated ferrous form of globins [9]. These forms of the globins are paramagnetic and have been studied extensively with X-band cw-EPR (see [59–64], and references therein). Heme proteins in a histidine–Fe(II)–NO conformation, such as NO-ligated ferrous neuroglobin, are characterized by a temperature-dependent EPR spectrum (Fig. 5)

[59,60,62–64]. At high temperatures (>150 K) the cw-EPR spectra are dominated by an axial species (denoted state A). Upon decrease of the temperature, a partial transformation of this species into a rhombic species (species R) occurs. Although the analysis of the temperature dependence of the EPR spectra is largely facilitated by a multifrequency approach (combining X-, K-, Q-, and W-band frequencies) [65,66], additional techniques are needed to gain information about the structural differences between states A and R. Where the nitrogen ENDOR spectra reveal detailed information on the nitrogen of the NO ligand, on the directly coordinating histidine nitrogen, and on the proton hyperfine couplings [67–71], ESEEM techniques, such as HYSCORE, allow characterization of the interactions with the pyrrole nitrogens and the remote histidine nitrogens [72–74].

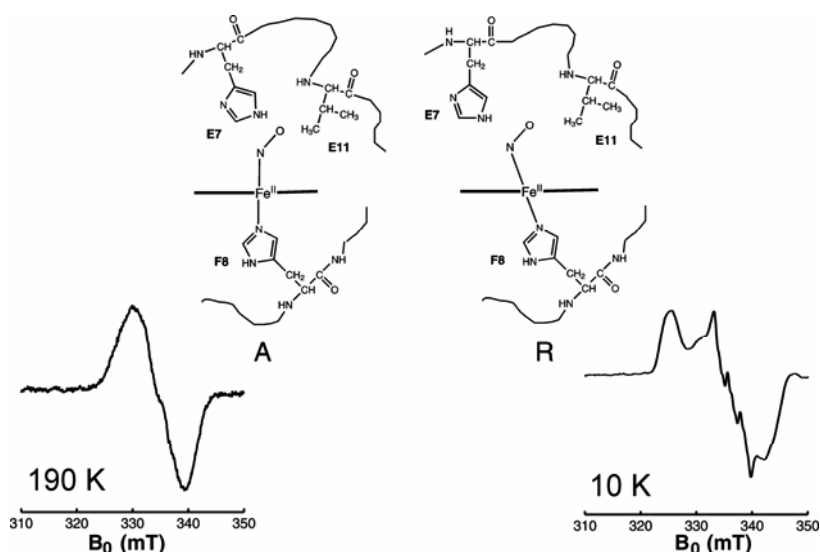


Figure 5. Cartoon of the axial (A) and rhombic (R) state of NO-ligated ferrous heme proteins and an example of the corresponding X-band cw-EPR spectra for the NO-ligated ferrous form of an E7Gln mutant of neuroglobin at 10 and 190 K.

Based on X-band cw-ENDOR, three-pulse ESEEM, and HYSCORE experiments, the rhombic component has been ascribed to a hexacoordinated nitrosyl Fe(II) heme where the proximal F8 histidine acts as a second axial ligand and the Fe–N_{NO} bond does not coincide with the heme normal [67–72] (Fig. 5). DFT computations confirm a small tilt of this axis and indicate that the NO is oriented toward a meso-C atom of the porphyrin ring (i.e., the Fe–NO plane is quasi-bisecting the N_{porph}–Fe–N_{porph}) [75]. The nature of state A is still somewhat controversial. Several authors ascribe state A at low temperature to a species where the Fe–N_{NO} bond is approximately along the heme normal [65,69–72], although also a bent

end-on orientation of the NO with the NO eclipsing one of the equatorial Fe–N_{porph} bonds or a partially dissociated hexacoordinated structure with freely rotating NO has been suggested [75]. The latter interpretation seems very unlikely to be able to describe the axial state observed at 10 K.

The proton-ENDOR study of nitrosyl horse heart myoglobin suggests that the E7-His and E11-Val residues are present in the heme pocket of both forms A and R and stabilize the bound NO [71]. The ESEEM and HYSCORE study of NO-ligated myo- and hemoglobin reveals an interaction of the unpaired electron with the N_ε nitrogen of the distal E7-His in state A, which was not found for the rhombic species [72]. Several globins appear to adopt a large variety of new Fe–NO configurations between 240 and 100 K [65]. These forms most probably lack hydrogen bonding. The fact that for mammalian myoglobin, hemoglobin, and neuroglobin the plot of the relative fraction of axial to rhombic species as a function of $1/T$ deviates from linear behavior confirms the existence of more than two conformational states [64,66].

In a very detailed X-band cw-ENDOR study, LoBrutto et al. revealed an essential difference between the NO-ligated heme *a*₃ in cytochrome *c* oxidase and those of NO-ligated myoglobin and model NO–heme–imidazole complexes [70]. They discovered in the former protein a unique proton stemming from a nearby protein sidechain that perturbs the axial ligand.

At this point it is also interesting to note that, not only ferrous globins can bind NO, but also their related Fe(III) form binds NO, giving rise to an EPR-silent complex. Upon illumination (photolysis) of ferric NO-ligated globins, the EPR-active product, the ferric high-spin heme, and the NO molecule become detectable [76]. Upon photolysis at low temperature, the photoinduced intermediates trapped in the distal heme cavity exhibit new EPR spectra that reflect the interaction between the photo-dissociated NO ($S = 1/2$) and the ferric heme species ($S = 5/2$). For ferric NO-ligated myoglobin, this experiment revealed that the photo-dissociated NO cannot leave the protein matrix at temperatures below 100 K [76]. Combining these experiments with selective mutagenesis in the heme pocket allowed for selective probing of the influence of the different amino acids in the heme cavity. The mobility of the NO molecule was found to be strongly governed by the amino acid at position E11, confirming again the important role of this amino acid in the heme pocket, as was also derived from the ENDOR study of ferrous NO-ligated myoglobin [71].

4. DISTANCE MEASUREMENTS IN HEME PROTEINS

In the previous sections, we focused on the heme pocket of the heme proteins, whereby the intrinsic paramagnetic centers were used as the probes for structural information. However, the introduction of site-directed spin labeling has revolutionized the world of EPR in the sense that now also intrinsic diamagnetic proteins can be studied by EPR [77,78]. Indeed, in site-directed labeling, a paramagnetic spin label is attached to the protein through reaction of its functional group with the

thiol group of the protein's cysteine(s). These cysteines can either be native or introduced through site-directed mutagenesis. Information on the protein dynamics and/or inter-spin distances (and thus the protein structure) can then be derived [77–79]. Transposing this idea to the field of heme proteins, several possible experiments spring to mind. Indeed, one could mono-label a heme protein in its paramagnetic form and investigate whether information on the distance between the nitroxyl label and the paramagnetic heme center can be extracted. Furthermore, one can think of mono- and bi-labeling the diamagnetic forms of the heme proteins and study the dynamics and inter-spin distances in the same way as shown for other intrinsic diamagnetic proteins [77–79].

G. and S. Eaton and their coworkers showed in an extensive series of experiments the possibilities of determining spin label to iron distances in spin-labeled ferric heme proteins using a series of cw-EPR, ESE, and saturation recovery (SR) experiments [80–86]. They clearly elucidate how the experimental results and their interpretation are affected by the spin state of the heme iron. These studies are nicely reviewed in [85].

In the previous sections we only highlighted the low- and high-spin ferric and NO-ligated ferrous forms of heme proteins. However, in many biologically relevant heme proteins, the heme iron is in a high-spin Fe(II) ($S = 2$) state. This state is paramagnetic, but EPR silent at the conventional microwave frequencies. However, when a high-spin Fe(II) heme protein is spin labeled or when it contains an intrinsic radical such as a tyrosyl radical, the spin-lattice relaxation will be enhanced by the interaction with the high-spin Fe(II) [87]. This information could be used to determine distances between the tyrosyl radical and the Fe(II) center in photosystem II [88].

5. CONCLUSIONS AND OUTLOOK

In this chapter, I have tried to summarize the current applications of different EPR techniques in the study of low- and high-spin ferric heme proteins, NO-ligated heme systems, and spin-labeled heme proteins, with emphasis on the use of ENDOR and pulse-EPR techniques in a multifrequency approach. Note that there are many other heme-related centers that were not dealt with in this chapter, such as the very nice work of the Hoffman group on the cryoreduced heme centers in cytochrome P450cam [89,90]. This chapter should therefore not be seen as a full review of all EPR work on heme proteins, not even for those themes that were specifically selected. I have merely tried to give examples of the different EPR tools that are currently used in heme research.

I would now like to point out the biggest challenges for the future in heme EPR research. Although a number of pulse-EPR and ENDOR techniques are already used in the analysis of heme proteins (Fig. 1), there is still an immense discrepancy between the actually used techniques and the state-of-the-art pulse-EPR toolbox as collected in standard works on EPR methodology [7]. It is my profound belief that we are not yet using the full potential of these tools in the analysis of

heme proteins and also in general in the study of metalloproteins. From the point of view of EPR methodology, I think that important goals for the future of heme research can be identified, amongst which are intensified use of two-dimensional pulse-EPR and ENDOR methods at different microwave frequencies, development of computer programs that can simulate the pulse-EPR experiments of complex spin systems (including high-spin iron systems), optimization of the DFT computations to interpret the observed EPR parameters of heme systems, and an extension of the use of pulse-EPR and ELDOR techniques at different microwave frequencies to determine metal–metal [91,92] or metal–spin label distances [85].

ACKNOWLEDGMENTS

This work was supported by the Fund for Scientific Research–Flanders (research grant G.0468.03).

REFERENCES

1. Kaim W, Schwederski B. 1994. *Bioinorganic chemistry: Inorganic elements in the chemistry of life: an introduction and guide*. Chichester: John Wiley & Sons.
2. Mathews CK, van Holde KE, Ahern KG. 2000. *Biochemistry*. San Francisco: Addison Wesley Longman.
3. Cowman JA. 1997. *Inorganic biochemistry: an introduction*. New York: Wiley-VCH.
4. Dickinson LC, Symons MCR. 1983. Electron Spin Resonance of Haemoglobin and Myoglobin. *Chem Soc Rev* **12**(4):387–414.
5. Smith DT, Pilbrow JR. 1980. ESR of iron proteins. In *Biological Magnetic Resonance*, Vol. 2, p. 85. Ed LJ Berliner, J Reuben. New York: Plenum.
6. Walker FA. 1999. Magnetic spectroscopy (EPR, ESEEM, Mössbauer, MCD and NMR) studies of low-spin ferriheme centers and their corresponding heme proteins. *Coord Chem Rev* **186**:471–534.
7. Schweiger A, Jeschke G. 2001. *Principles of pulse electron paramagnetic resonance*. Oxford: Oxford University Press.
8. Prisner T, Rohrer M, MacMillan F. 2001. Pulsed EPR spectroscopy: biological applications. *Annu Rev Phys Chem* **52**:279–313.
9. Brunori M. 2001. Nitric oxide moves myoglobin centre stage. *Trends Biochem Sci* **26**(4):209–210.
10. Nistor SV, Goovaerts E, Van Doorslaer S, Dewilde S, Moens L. 2002. EPR-spectroscopic evidence of a dominant His-FeIII-His coordination in ferric neuroglobin. *Chem Phys Lett* **361**(5–6):355–361.
11. Walker FA, Huynh BH, Scheidt WR, Osvath SR. 1986. Models of the cytochromes b: effect of axial ligand plane orientation on the electron paramagnetic resonance and mossbauer spectra of low-spin ferrihemes. *J Am Chem Soc* **108**(17):5288–5297.
12. Migita CT, Iwaizumi M. 1981. Low-temperature electron-paramagnetic resonance study of highly anisotropic low-spin (protoporphyrinato)iron(III) complexes. *J Am Chem Soc* **103**(15):4378–4381.

13. Salerno JC. 1984. Cytochrome electron spin resonance line shapes, ligand fields and components stoichiometry in ubiquinol-cytochrome-c oxidoreductase. *J Biol Chem* **259**(4):2331–2336.
14. Guzov VM, Houston HL, Murataliev MB, Walker FA, Feyereisen R. 1996. Molecular cloning, overexpression in *Escherichia coli*, structural and functional characterization of house fly cytochrome *b₅*. *J Biol Chem* **271**(43):26637–26645.
15. Rhynard D, Lang G., Spartalian K, Yonetani T. 1979. Mössbauer studies of low-symmetry crystal fields in low-spin ferric heme complexes. *J Chem Phys* **71**(9):3715–3721.
16. Ioanitescu I, Dewilde S, Kiger L, Marden MC, Moens L, Van Doorslaer S. 2005. Characterization of nonsymbiotic tomato hemoglobin. *Biophys J* **89**(4):2628–2639.
17. Simonneaux G, Schünemann V, Morice C, Carel L, Toupet L, Winkler H, Trautwein AX, Walker FA. 2000. Structural, magnetic, and dynamic characterization of the $(d_{xz}, d_{yz})^4(d_{xy})^1$ ground-state low-spin iron(III) tetraphenylporphyrinate complex [(p-TTP)Fe(2,6-XylylNC)₂]CF₃SO₃. *J Am Chem Soc* **122**(18):4366–4377.
18. Blumberg WE, Peisach J. 1971. A unified theory for low spin forms of all ferric heme proteins as studied by EPR. In *Probes of structure and function of macromolecules and membranes*, Vol. 2, pp. 215ff. Ed B Chance, T Yonetani, AS Mildvan. New York: Academic Press.
19. Siedow JN, Vickery LE, Palmer G. 1980. The nature of the axial ligands of spinach cytochrome *f*. *Arch Biochem Biophys* **203**(1):101–107.
20. Rigby SEJ, Moore GR, Gray JC, Gadsby PMA, George SJ, Thomson AJ. 1988. Nmr, epr and magnetic-cd studies of cytochrome *f*: identity of the haem axial ligands. *Biochem J* **256**(2):571–577.
21. Scholes CP, Falkowski KM, Chen S, Bank J. 1986. Electron nuclear double resonance (ENDOR) of bis(imidazole)-ligated low-spin ferric heme systems. *J Am Chem Soc* **108**(7):1660–1671.
22. Scholes CP, Van Camp HL. 1976. ENDOR from nitrogens and protons in low spin ferric heme and hemoprotein. *Biochim Biophys Acta* **434**(1):290–296.
23. Mulks CF, Scholes CP, Dickinson LC, Lapidot A. 1979. Electron nuclear double resonance from high- and low-spin ferric hemoglobins and myoglobins. *J Am Chem Soc* **101**(7):1645–1654.
24. Fahnenschmidt M, Bittl R, Rau HK, Haehnel W, Lubitz W. 2000. Electron paramagnetic resonance and electron nuclear double resonance spectroscopy of a heme protein maquette. *Chem Phys Lett* **323**(3–4):329–339.
25. Peisach J, Mims WB, Davis JL. 1979. Studies of the electron-nuclear coupling between Fe(III) and ¹⁴N in cytochrome P450 and in a series of low spin heme compounds. *J Biol Chem* **254**(24):12379–12389.
26. Magliozzo RS, Peisach J. 1992. Electron spin echo envelope modulation spectroscopic study of iron–nitrogen interactions in myoglobin hydroxide and Fe(III) tetraphenylporphyrin models. *Biochemistry* **31**(1):189–199.
27. Magliozzo RS, Peisach J. 1993. Evaluation of nitrogen nuclear hyperfine and quadrupole coupling parameters for the proximal imidazole in myoglobin-azide, -cyanide and -mercaptoethanol complexes by electron spin echo envelope modulation. *Spectroscopy* **32**(33):8446–8456.
28. Theodorakis JL, Garber EAE, McCracken J, Peisach J, Schejter A, Margoliash E. 1995. A chemical modification of cytochrome-c lysines leading to changes in heme iron ligation. *Biochim Biophys Acta* **1252**(1):103–113.

29. Thomann H, Bernardo M, Goldfarb D, Kroneck PMH, Ullrich V. 1995. Evidence for water binding to the Fe center in cytochrome P450cam obtained by ^{17}O electron spin echo envelope modulation spectroscopy. *J Am Chem Soc* **117**(31):8243–8251.
30. Goldfarb D, Bernardo M, Thomann H, Kroneck PMH, Ullrich V. 1996. Study of water binding to low-spin Fe(III) in cytochrome P450 by pulsed ENDOR and four-pulse ESEEM spectroscopies. *J Am Chem Soc* **118**(11):2686–2693.
31. Fann YC, Gerber NC, Osmulski PA, Hager LP, Sligar SG, Hoffman BM. 1994. ENDOR determination of heme ligation in chloroperoxidase and comparison with cytochrome P450cam. *J Am Chem Soc* **116**(13):5989–5990.
32. Lee HI, Dexter AF, Fann YC, Lakner FJ, Hager LP, Hoffman BM. 1997. Structure of the modified heme in allylbenzene-inactivated chloroperoxidase determined by Q-band CW and pulsed ENDOR. *J Am Chem Soc* **119**(17):4059–4069.
33. Astashkin AV, Raitsimring AM, Walker FA. 1999. Two- and four-pulse ESEEM studies of the heme binding center of a low-spin ferriheme protein: the importance of a multi-frequency approach. *Chem Phys Lett* **306**(1–2):9–17.
34. Astashkin AV, Raitsimring AM, Walker FA. 2001. ^1H pulsed ENDOR and ESEEM evidence that the bis-imidazole complexes of iron(III) tetraphenylchlorin and tetraphenylporphyrin have the same order of g values, and the same electronic ground state. *J Am Chem Soc* **123**(9):1905–1913.
35. Raitsimring AM, Borbat P, Shokhireva TK, Walker FA. 1996. Magnetic field (g-value) dependence of proton hyperfine couplings obtained from ESEEM measurements: Determination of the orientation of the magnetic axes of model heme complexes in glassy media. *J Am Chem Soc* **100**(13):5235–5244.
36. Raitsimring AM, Walker FA. 1998. Porphyrin and ligand protons as internal labels for determination of ligand orientation in ESEEMs of low-spin d^5 complexes in glassy media: ESEEM studies of the orientation of the g tensor with respect to the planes of axial ligands and porphyrin nitrogens of low-spin ferriheme systems. *J Am Chem Soc* **120**(5):991–1002.
37. García-Rubio I, Martínez JI, Picorel R, Yruela I, Alonso PJ. 2003. HYSORE spectroscopy in the cytochrome b_{559} of the photosystem II reaction center. *J Am Chem Soc* **125**(51):15846–15854.
38. Vinck E, Van Doorslaer S. 2004. Analysing low-spin ferric complexes using pulse EPR techniques: a structure determination of bis (4-methylimidazole) (tetraphenylporphyrinato)iron(III). *Phys Chem Chem Phys* **6**(23):5324–5330.
39. Jeschke G, Rakhmatullin R, Schweiger A. 1998. Sensitivity enhancement by matched microwave pulses in one- and two-dimensional electron spin echo envelope modulation spectroscopy. *J Magn Reson* **131**(2):261–271.
40. Liesum L, Schweiger A. 2001. A multiple quantum coherence in HYSORE spectra. *J Chem Phys* **114**(21):9478–9488.
41. Brown TG, Hoffmann BM. 1980. ^{14}N , ^1H and metal ENDOR of single crystal Ag(II)(TPP) and Cu(II)(TPP). *Mol Phys* **39**(5):1073–1109.
42. Shokhirev NV, Walker FA. 1998. Co- and counterrotation of magnetic axes and axial ligands in low-spin ferriheme systems. *J Am Chem Soc* **120**(5):981–990.
43. Vinck E, Van Doorslaer S, Dewilde S, Mitrikas G, Schweiger A, Moens L. 2006. Analyzing heme proteins using EPR techniques: the heme-pocket structure of ferric mouse neuroglobin. *J Biol Inorg Chem* **11**(4):467–475.
44. Vinck E, Van Doorslaer S, Dewilde S, Moens L. 2004. Structural change of the heme pocket due to disulfide bridge formation is significantly larger for neuroglobin than for cytoglobin. *J Am Chem Soc* **126**(14):4516–4517.

45. Ohba Y. 2003. Application of two-dimensional pulsed EPR nutation spectroscopy to a disordered system with large g anisotropy. *Appl Magn Reson* **23**(3–4):539–556.
46. van Lenthe E, van der Avoird A, Hagen WR, Reijerse EJ. 2000. Density functional calculations of g tensors of low-spin iron(I) and iron(III) porphyrins. *J Phys Chem A* **104**(10):2070–2077.
47. Johansson MP, Sundholm D, Gerfen G, Wilkström M. 2002. The spin distribution in low-spin iron porphyrins. *J Am Chem Soc* **124**(39):11771–11780.
48. Abragam A, Bleaney B. 1970. *Electron paramagnetic resonance of transition ions*. Oxford: Oxford UP.
49. Peisach J, Blumberg WE, Ogawa S, Rachmilewitz EE, Oltzik R. 1971. The effects of protein conformation on the heme symmetry in high spin ferric heme proteins as studied by electron paramagnetic resonance. *J Biol Chem* **246**(10):3342–3355.
50. Munro OQ, de Wet M, Pollak H, van Wyk J, Marques HM. 1998. Haempeptide models for haemoproteins, part 3L: N-Acetylmicroperoxidase-8: EPR, Mössbauer and magnetic susceptibility studies on an iron(III) porphyrin in thermal equilibrium between $S = 3/2$, $5/2$ and $S = 1/2$ states. *J Chem Soc, Faraday Trans* **94**(12):1743–1752.
51. van Kan PJM, van der Horst E, Reijerse EJ, van Bentum PJM, Hagen WR. 1998. Multi-frequency EPR spectroscopy of myoglobin: spectral effects for high-spin iron(III) ion at high magnetic fields. *J Chem Soc, Faraday Trans* **94**(19):2975–2978.
52. Scholes CP, Lapidot A, Mascarenhas R, Inubushi T, Isaacson RA, Feher G. 1982. Electron nuclear double resonance (ENDOR) from heme and histidine nitrogens in single crystals of aquometmyoglobin. *J Am Chem Soc* **104**(10):2724–2735.
53. Fann Y, Ong J, Nocek JM, Hoffman BM. 1995. ^{19}F and ^{12}H ENDOR study of distal-pocket N(ϵ)-H...F hydrogen bonding in fluorometmyoglobin. *J Am Chem Soc* **117**(22):6109–6116.
54. Lee HI. 2002. ^{14}N Mims pulsed ENDOR of proximal histidine and heme of aquometmyoglobin and fluorometmyoglobin. *Bull Korean Chem Soc* **23**(12):1769–1772.
55. Bachmann R, Schweiger A, Aissaoui H, Woggon WD. 1998. On the origin of the low spin character of the resting state of cytochrome P450cam: investigation of enzyme models by 2D-HYSCORE spectroscopy. In *Magnetic resonance and related phenomena*, Vol. 2, pp. 822ff. Ed D Ziessow, W Lubitz, F Lendzian. Berlin: Technische Universität Berlin.
56. Aissaoui H, Bachmann R, Schweiger A, Woggon WD 1998. On the origin of the low-spin character of cytochrome P450(cam) in the resting state: investigations of enzyme models with pulse EPR and ENDOR spectroscopy. *Angew Chem, Int Ed* **37**(21):2998–3002.
57. Jeschke G, Spiess W. 1998. NMR-correlated high-field electron paramagnetic resonance spectroscopy. *Chem Phys Lett* **293**(1–2):9–18.
58. Cooper CE. 1999. Nitric oxide and iron proteins. *Biochim Biophys Acta* **1411**(2–3):290–309.
59. Hori H, Ikeda-Saito M, Yonetani T. 1981. Single crystal EPR of myoglobin nitroxide: freezing induced reversible changes in the molecular orientation of the ligand. *J Biol Chem* **256**(15):7849–7855.
60. Morse RH, Chan SI. 1980. Electron paramagnetic resonance studies of nitrosyl ferrous heme complexes: determination of an equilibrium between two conformations. *J Biol Chem* **255**(16):7876–7882.
61. Bemski G. 1997. Contribution of electron paramagnetic resonance to the studies of hemoglobin: the nitrosylhemoglobin system. *Mol Biol Rep* **24**(4):263–269.

62. Wajnberg E, Linhares MP, El-Jaick LJ, Bemski G. 1992. Nitrosyl hemoglobin: EPR components at low temperatures. *Eur Biophys J* **21**(1):57–61.
63. Wajnberg E, Bemski G, El-Jaick J, Alves OC. 1996. Nitrosyl hemoglobins: EPR above 80 K. *Int J Biol Macromol* **18**(3):231–235.
64. Trandafir F, Van Doorslaer S, Dewilde S, Moens L. 2004. Temperature dependence of NO binding modes in human neuroglobin. *Biochim Biophys Acta* **1702**(2):153–161.
65. Schmidt PP, Kappl R, Hüttermann. 2001. On the mode of hexacoordinated NO-binding to myo- and hemoglobin: Variable-temperature EPR studies at multiple microwave frequencies. *Appl Magn Reson* **21**(3–4):423–440.
66. Flores M, Wajnberg E, Bemski G. 1997. Temperature dependence of Q-band electron paramagnetic resonance spectra of nitrosyl heme proteins. *Biophys J* **73**(6):3225–3229.
67. Höhn M, Hüttermann J, Chien JCW, Dickinson LC. 1983. ^{14}N and ^1H ENDOR of nitrosylhemoglobin. *J Am Chem Soc* **105**(1):109–115.
68. Kappl R, Hüttermann. 1989. An ENDOR study of nitrosyl myoglobin single crystals. *Isr J Chem* **29**(1):73–84.
69. Hüttermann J, Burgard C, Kappl R. 1994. Proton ENDOR from randomly oriented NO-ligated hemoglobin: approaching the structural basis for the R-T transition. *J Chem Soc, Faraday Trans* **90**(20):3077–3087.
70. LoBrutto R, Wei YH, Mascarenhas R, Scholes CP, King TE. 1983. Electron nuclear double resonance and electron paramagnetic resonance study on the structure of the NO-ligated heme a_3 in cytochrome *c* oxidase. *J Biol Chem* **258**(12):7437–7448.
71. Flores M, Wajnberg E, Bemski G. 2000. Proton electron nuclear double resonance from nitrosyl horse heart myoglobin: the role of His-E7 and Val-E11. *Biophys J* **78**(4):2107–2115.
72. Tyryshkin AM, Dikanov SA, Reijerse EJ, Burgard C, Hüttermann. 1999. Characterization of bimodal coordination structure in nitrosyl heme complexes through hyperfine couplings with pyrrole and protein nitrogens. *J Am Chem Soc* **121**(14):3396–3406.
73. Gilbert DC, Dikanov SA, Doetschman DC, Smeija JA. 1999. A study of pyridyl nitrosyl iron(II) tetraphenyl $^{15}\text{N}_4$ -porphyrin: NO geometry and spin coupling to the pyrrole nitrogens. *Chem Phys Lett* **315**(1–2):43–48.
74. Gilbert DC, Doetschman DC. 2001. Five-coordinate nitrosyl iron(II) tetraphenylporphyrin exhibits porphyrin ring ^{14}N symmetry about the Fe-NO plane: a hyperfine sublevel correlation spectroscopy study. *Chem Phys Lett* **269**(1–3):125–135.
75. Patchkovskii S, Ziegler T. 2000. Structural origin of two paramagnetic species in six-coordinated nitrosoiron(II) porphyrins revealed by density functional theory analysis of the g tensors. *Inorg Chem* **39**(23):5354–5364.
76. Hori H, Masuya F, Dou Y, Ikeda-Saito M. 2000. EPR studies on the photoinduced intermediates of NO complexes in recombinant ferric Mb trapped at low temperature. *J Inorg Biochem* **82**(1–4):181–187.
77. Hubbell WL, Cafiso DS, Altenbach C. 2000. Identifying conformational changes with site-directed spin labeling. *Nature Struct Biol* **7**(9):735–739.
78. Hubbell WL, Gross A, Langen R, Lietzow MA. 1998. Recent advances in site-directed spin labeling of proteins. *Curr Opin Struct Biol* **8**(5):649–656.
79. Eaton SS, Eaton GG. 2000. Distance measurements by CW and Pulsed EPR. In *Biological magnetic resonance*, Vol. 19: *Distance measurements in biological systems by EPR*, pp. 1ff. Ed LJ Berliner, SS Eaton, GR Eaton. New York: Kluwer Academic/Plenum Publishers.
80. Budker V, Du JL, Seiter M, Eaton GR, Eaton SS. 1995. Electron–electron spin–spin interaction in spin-labeled methemoglobin. *Biophys J* **68**(6):2531–2542.

81. Rakowsky MH, More K, Kulikov AV, Eaton GR, Eaton SS. 1995. Time-domain electron paramagnetic resonance as a probe of electron–electron spin–spin interaction in spin-labeled low spin iron porphyrins. *J Am Chem Soc* **117**(7):2049–2057.
82. Rakowsky MH, Zecevic A, Eaton GR, Eaton SS. 1998. Determination of high-spin iron(III)-nitroxyl distances in spin-labeled porphyrins by time-domain EPR. *J Magn Reson* **131**(1):97–110.
83. Seiter M, Budker V, Du JL, Eaton GR, Eaton SS. 1998. Interspin distances determined by time domain EPR of spin-labeled high-spin methemoglobin. *Inorg Chim Acta* **273**(1–2):354–356.
84. Klug CS, Eaton SS, Eaton GR, Feix JB. 1998. Ligand-induced conformational change in the ferric enterobactin receptor FepA as studied by site-directed spin labeling and time-domain ESR. *Biochemistry* **37**(25):9016–9023.
85. Eaton SS, Eaton GR. 2000. Determination of distances based on T_1 and T_m effects. In *Biological magnetic resonance*, Vol. 19: *Distance measurements in biological systems by EPR*, pp. 347ff. Ed LJ Berliner, SS Eaton, GR Eaton. New York: Kluwer Academic/Plenum Publishers.
86. Zhou Y, Bowler BE, Lynch K, Eaton GR, Eaton SS. 2000. Interspin distances in spin-labeled metmyoglobin variants determined by saturation recovery EPR. *Biophys J* **79**(2):1039–1052.
87. Hirsh DJ, Beck WF, Innes JB, Brudvig GW. 1992. Using saturation recovery EPR to measure distance in proteins. *Biochemistry* **31**(2):523–541.
88. Hirsh DJ, Brudvig GW. 1993. Long-range electron spin–spin interactions in the bacterial photosynthetic reaction center. *J Phys Chem* **97**(50):13216–13222.
89. Davydov R, Perera R, Jin SX, Yang TC, Bryson TA, Sono M, Dawson JH, Hoffman BM. 2005. Substrate modulation of the properties and reactivity of the oxy-ferrous and hydroperoxo-ferric intermediates of cytochrome P450cam as shown by cryoreduction EPR/ENDOR spectroscopy. *J Am Chem Soc* **127**(5):1403–1413.
90. Kim SH, Yang TC, Perera R, Jin SX, Bryson TA, Sono M, Davydov R, Dawson JH, Hoffman BM. 2005. Cryoreduction EPR and ^{13}C , ^{19}F ENDOR study of substrate-bound substates and solvent kinetic isotope effects in the catalytic cycle of cytochrome P450cam and its T252A mutant. *Dalton Trans* **21**:3464–3469.
91. van Amsterdam IMC, Ubbink M, Canters GW, Huber W. 2003. Measurement of a Cu–Cu distance of 26 Å by a pulsed EPR method. *Angew Chem, Int Ed* **43**(1):62–64.
92. Siddiqui MK, Lyubenovab S, de vries MJMP, Prisner TF, Ludwig B. 2004. Distance and orientation studies of the Cu_A fragment of cytochrome *c* oxidase with different cytochrome *c* by pulsed EPR spectroscopy. *Biochim Biophys Acta Bioenerg* **1658**:154–154.
93. Trandafir F, ter Heerdt P, Fittipaldi M, Vinck E, Dewilde S, Moens L, van Doorslaer S. 2007. Studying high-spin ferric heme proteins using pulsed EPR spectroscopy: analysis of the ferric form of the E7Q mutant of human neuroglobin. *Appl Magn Reson* **31**:553–572.
94. Fittipaldi M, García-Rubio I, Trandafir F, Gromov I, Schweiger A, Bouwen A, Van Doorslaer S. 2008. A multi-frequency pulse EPR and ENDOR approach to study strongly coupled nuclei in frozen solutions of high-spin ferric heme proteins. *J Phys Chem B* **112**:3859–3870.

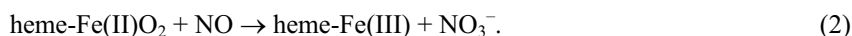
EPR STUDIES OF THE CHEMICAL DYNAMICS OF NO AND HEMOGLOBIN INTERACTIONS

Benjamin P. Luchsinger,¹ Eric D. Walter,¹ Lisa J. Lee,¹
Jonathan S. Stamler,² and David J. Singel¹

¹*Department of Chemistry and Biochemistry, Montana State University,
Bozeman, Montana;* ²*Department of Biochemistry Department of Medicine,
Duke University Medical Center, Durham, NC*

1. INTRODUCTION

The field of NO biology began two decades ago with the identification of nitric oxide, NO, as the endothelium-derived vascular relaxing factor (EDRF) discovered by Furchgott [1]. Since then, the scope of the field has dramatically expanded to view the NO moiety as a ubiquitous signaling agent [2] that can modulate effector function through a variety of chemistries, most prevalently reactions with oxygen, thiols, and metal centers [3]. The seminal work of identifying EDRF with nitric oxide (NO) was based in significant part on such chemistry, specifically the reaction with oxygen or metal centers in hemoglobin (Hb); these reactions had the same inactivating effect on both NO and EDRF [4]. Hb was known to react quickly and completely with NO to form nitrate from oxy-Hb or a heme-iron nitrosyl adduct with deoxy-Hb, as summarized in Eqs. (1) and (2) [5,6]:



This chemistry of NO, which produces paramagnetic species heme-Fe(II)NO or heme-Fe(III), immediately suggests EPR (electron paramagnetic resonance) spectroscopy as a choice *analytical* tool for detection of NO in biological systems. Indeed, this connection was immediately recognized: in the first decade of the field, EPR played a recurring role in detecting NO and monitoring its biochemical trans-

Address all Correspondence to: David J. Singel, Department of Chemistry and Biochemistry, Montana State University, Bozeman, Montana 59717, email: dsingel@chemistry.montana.edu.

formations. The realm of these analytical applications of EPR spectroscopy in NO biology continues to enlarge, but the fundamental EPR methods—in particular, the variety of EPR-detectable species employed to reveal the presence of NO—are largely the same as reviewed previously [7,8]. In those earlier reviews, we suggested that some of these species, namely NO adducts that form with *endogenous* metal ions and ligands, raise intriguing questions about the possible biological roles of these species, and “thus portend a broader role for EPR spectroscopy in this field: growing from a simple analytical probe for NO into a choice *spectroscopic* tool for characterizing the structure and function of the biological targets NO” [7].

In the ensuing years, this suggestion has been best realized in terms of NO interactions with Hb. While the heme-Fe(II)NO and heme-Fe(III) species are ideal for analytes for EPR spectroscopy, neither of them exert NO vasodilatory bioactivity. On a fundamental level, then, these efficient reactions raise an intriguing question about the manner in which NO exerts its function in the blood: how can the bioactivity of NO coexist with Hb, which is known to scavenge NO by Eqs. (1) and (2) [3,9]? Over the past decade this question has been addressed from a variety of different perspectives [11]. The studies spurred by this question ultimately led to discoveries that helped to illuminate general ideas about redox-coupled NO signaling in biology. They led to a renewed appreciation of the subtlety of nonlinear effects in the chemistry that occurs with interactions of NO and Hb, in which this tetrameric protein provides a simple, prototypical example of a complex biological system [11,12]. The understanding of this chemistry removed conceptual barriers that blocked understanding of a basic physiological role played by NO interactions with Hb—a surprising, newly discovered role, for this most-studied of proteins. In this chapter, we highlight EPR spectroscopy that has advanced this work, and that continues to provide new methodologies that propel it. We begin with a broad overview of the chemical biology, then turn to unique applications of EPR spectroscopy.

1.1. NO Hb Functional Interactions

A number of investigators examined the biophysical problem of the effects of flow and cellular packaging on the interaction of NO and Hb in blood [9,13–22]. Their collective work suggests that in flowing blood, NO and Hb encounters are reduced by several orders of magnitude as compared to in-vitro behavior. Another route to protect NO bioactivity involves the oxidative formation of S-nitrosothiols (thionitrites) [2,3,23].



In Eq. (3), A is an electron acceptor whose reduction is coupled to the oxidative activation of the NO for nitrosylation of the thiol. In principle, A (or A^-) can serve as an EPR marker of the NO redox reaction; in practice, Hb heme-Fe(III) has been shown to be competent to play this role [24,25]. The active product, S-nitrosylated

low-molecular-weight thiols or protein thiols, exhibit equal or higher molar vasodilatory potencies in bioassays than NO [26–30]. Moreover, they appear to be the most abundant compounds exhibiting NO-related bioactivity in the blood and blood vessel walls, existing at basal levels orders of magnitude greater than NO itself [29]. While the biophysical studies suggested ways in which NO in blood can evade Hb or other scavengers in the red blood cell (RBC), chemical processing to make SNO [Eq. (3)] provides a means to circumvent and limit reactions 1 and 2, even in the RBC.

This chemical processing in the RBC is crucial to the regulation of the RBC's primary function, namely, the delivery of O₂ to tissues. Blood flow in the microcirculation is principally regulated by position-to-position variations in O₂ levels that are quickly reflected in changes in HbO₂ saturation and coupled to regulated vasoconstriction or vasodilation through local modulation of vascular tension [31–35]. O₂ delivery is thus matched to metabolic demand: decreases in the O₂ content of blood are coupled to decreases in vessel tension, increases in blood flow, and recruitment of more oxygen-rich RBCs. In this light, the scavenging chemistry [Eqs. (1) and (2)] presents a paradox, as it would lead to vasoconstriction, which would impede blood flow and O₂ delivery [10]. The resolution of this paradox required the development of a broader understanding of the chemistry of NO–Hb interactions, and has led to a molecular model of the manner in which O₂ gradients are sensed and transduced to evoke the physiological vasodilatory response.

1.2. SNO-Hemoglobin

The ideal O₂ sensor in this regulatory process would appear to be Hb itself, particularly since it is the O₂ saturation of blood-Hb rather than the pO₂ that determines blood flow [32]. Hb's scavenging chemistry [Eqs. (1) and (2)] with NO, however, presented a conceptual roadblock: how could O₂ signals detected by Hb transduced to elicit NO-mediated vasodilation? The discovery by Stamler and co-workers that Hb itself is among the blood proteins that sustain S-nitrosylation broke this roadblock and initiated resolution of the paradox. Specific cysteine residues of Hb form S-nitrosothiols both *in vivo* and *in vitro* [10]. In tetrameric ($\alpha_2\beta_2$) Hb, S-nitrosylation occurs on the β -subunits on the cysteine adjacent to the proximal histidine (cys- β 93 in human numbering); this cysteine is conserved in all mammalian and avian species. S-nitrosylated-Hb (SNO-Hb) has been characterized by mass-spectrometry [36] and x-ray crystallography [37,38]. In bioassay studies, SNO-Hb exhibits a potency equivalent to authentic NO [11]. The reactivity of these cysteines toward NO reagents has been shown to depend on the quaternary structure of the tetramer [10,39]: SNO-Hb forms preferentially in the oxygenated (or R) structure; conditions favoring the deoxygenated (T) structure, such as low pO₂, favor release of NO groups [11]. SNO-Hb containing RBCs have been shown to actuate a unique, rapid, and graded vasodilator and vasoconstrictor response across a physiological range of pO₂ [40]. The biological activity of SNO-Hb and

RBCs thus exhibit the requisite dependence on Hb oxygen-saturation, apparently coupled to the allosteric behavior of Hb [41].

1.3. SNO-Hemoglobin Function

The core elements of the paradigm of SNO-Hb's mediation of RBC-induced vasodilation entail: (1) the sensing of oxygen levels by Hb; and (2) release of NO bioactivity in response to reduced oxygen tension. In the paradigm, SNO-Hb is identified as the active species through which oxygen-responsive NO-group transfer occurs. This model requires that SNO-Hb can be formed and delivered in the small amounts sufficient for regulated dilation of constricted vessels, notwithstanding the potential scavenging represented by reactions 1 and 2. Moreover, the ambient oxygen-signal must be transduced by Hb to dispense NO-bioactivity from SNO-Hb. Clearly, the chemical interactions of NO with Hb must be tightly regulated for modulating blood flow and oxygen delivery. This adaptive chemical response presumably includes limited dispensing of NO-bioactivity in hypoxic vasodilation, capture of NO in the complementary process of hyperoxic vasoconstriction, and, potentially, trapping and/or reactive elimination of NO under conditions of NO overproduction [42,43]. Moreover, in the limit of the very high NO levels used in the early in-vitro studies, it must faithfully reflect the predominant production of nitrate and heme-Fe(II)-NO in reactions 1 and 2. Hb's NO chemistry is complex [12]; the condition dependent adaptation of the products formed when NO encounters Hb is, and has always been, a fundamental feature of the paradigm [44].

NO has unique reactivity with Hb. In addition to its binding to the heme-iron in place of oxygen and coupling to thiol, it further reacts to form higher oxides and, reciprocally, is produced by Hb from higher oxides (reductive nitrosylation). NO coordinates to both oxidized and reduced heme irons and couples with Hb in redox reactions. In contrast to most heme ligands, NO expresses substantial subunit inequivalence in its reactions with Hb. Overall, complexity emerges in Hb interactions with NO from: the variety of the chemical species formed in reactions of NO and hemoglobin; the branched network of coupled kinetic equations underlying this chemistry; the tetrameric nature and allosteric behavior of Hb that enables modulation of reactivities. Accordingly, in encounters of NO and Hb, the fate of the NO group—its “disposition” on the protein (or elsewhere) and its reactive posture—is thus a function of many variables, including pH, $p\text{CO}_2$, $p\text{O}_2$, amount of NO, and the ratio of their concentrations, and the ligand occupancies and oxidation states of each heme in the tetramer [42,45–51]. Hb can be viewed as a programmable reactor that senses ambient levels of oxygen tension (and pH, anion levels, etc.), processes this information through structural alterations of the protein, and thereby modulates chemical formulation (disposition of the NO group) and reactivity. Overall, it adaptively modulates NO chemistry (input/output) to yield products that provide the optimal NO response to the ambient conditions. Emerging ideas about the salient aspects of the chemical program of this reactor are illustrated in Figure 1.

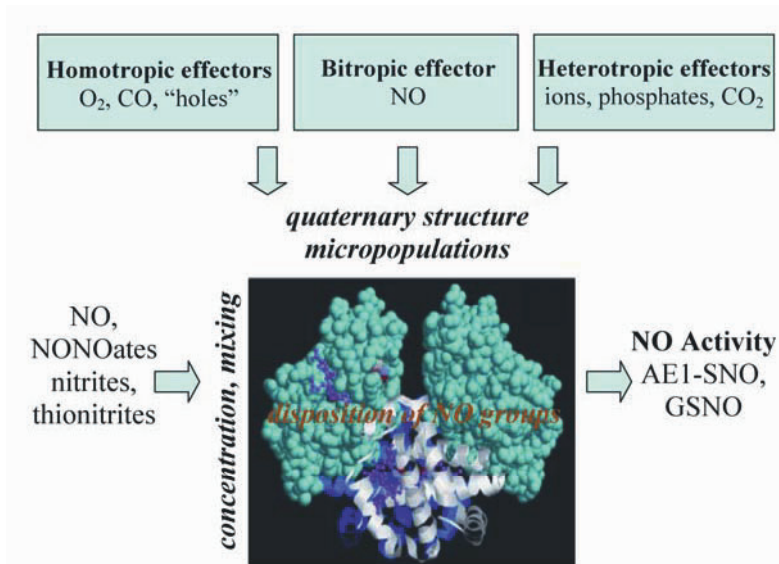


Figure 1. Chemical Dynamics of NO Interactions with Hemoglobin. This perspective envisions Hb as a programmable chemical reactor in which NO chemistry is modulated, as illustrated, by ambient conditions of NO, oxygen, and redox potentials. Allosteric effectors would likewise modulate the chemistry through effects on oxygen-saturation, oxidation-states, and spin-states. NO signal input, entailing NO, NO donors, nitrites, thionitrites are processed—as directed by effector levels, absolute and relative concentrations of reagents, and reagent mixing—to provide a disposition of NO products on the protein appropriate for signal output. For hypoxic vasodilation, output appears to involve dispensing of vasodilatory activity through formation of S-nitrosylated RBC membrane proteins and perhaps low-molecular-weight thiols. In the case of high levels of NO, for example in sepsis, the adaptive chemistry works to brake NO release. The species indicated should be taken as exemplary, but underscore the role of minority species and micropopulations in this chemistry.

The complexity of the chemical interactions of NO and Hb points to the importance of specific micropopulations of Hb in the chemistry of SNO-formation. Certain reactive micropopulations now clearly appear to be responsible for S-nitrosylation, but their identity remains to be fully elucidated [52]. A general model that rationalizes the dependence of SNO-formation and release on the basis of the different micropopulations that exist under different physiological conditions remains to be advanced. Reaching this goal will require the characterization of micropopulations of active species in the presence of a background (majority) of inactive species. This situation is very familiar in EPR spectroscopy, where the paramagnetic species probed are typically a minority species in the sample. The selectivity of EPR for trace nitrosylated or oxidized hemes, especially without interference from deoxy- or oxy-Hbs, continues to be the salient advantage of EPR spectroscopy in this work.

2. EPR SPECTROSCOPY OF NO Hb INTERACTIONS

2.1. Heme-Fe(II)NO Spectral Components

In the early studies of Hb NO interactions, where the NO ligand was used as a surrogate for O₂, two striking properties of the heme-Fe(II)NO EPR spectra were discovered. First, tetrameric ($\alpha_2\beta_2$) Hbs exhibit pronounced subunit-inequivalences in their heme-Fe(II)NO EPR spectra; these subunit inequivalences make it possible to determine proportions of NO on the α - vs. β -subunits by decomposition of the spectra according to their subunit contributions [48]. This analysis has become routine in studies of NO Hb interactions *in vitro*, but has more recently been used in the analysis of blood samples drawn from live subjects under high doses of NO or NO donors [42,47,53–56]. Second, heme-Fe(II)NO EPR spectra show a prominent hyperfine structure from the NO nitrogen, when the bond between the iron and proximal imidazole in the α -subunits is ruptured, as occurs in the quaternary T-state (deoxy-Hb state) of Hb. Thus EPR can report on the quaternary state and subunit distributions of nitrosyl populations. These spectral archetypes are exhibited together with an authentic spectrum of Hb(NO)₄ in Figure 2.

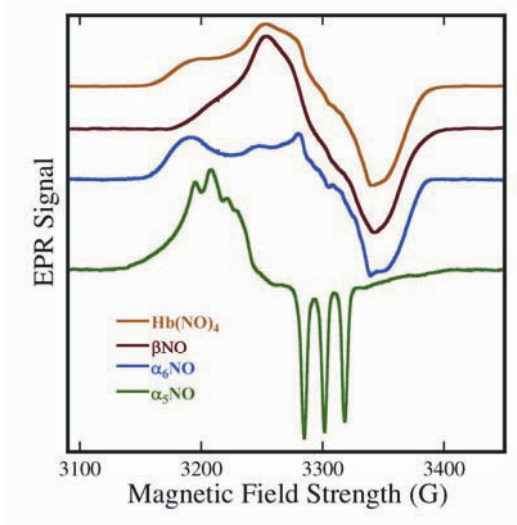


Figure 2. X-band EPR spectra, at liquid nitrogen temperatures, of standard heme-Fe(II)NO components in human Hb: (green) α -subunit five-coordinate species; (blue) α -subunit six-coordinate species; (red) β -subunit species; (orange) Hb(NO)₄.

Kon [57] and Wayland and Olson [58] were the first to associate the emergence of the prominent triplet hyperfine structure (Fig. 2, green) with a “rupture or distortion” of the proximal imidazole N–Fe bond. The prominence of this spectral feature was soon found to be influenced by pH [59], organophosphate effectors

[60,61], and heme pocket mutations [61]. Szabo and Perutz linked the presence (or absence) of the prominent hyperfine structure with the hemoglobin quaternary T (or R) state [62]. This view is supported by the studies of Sahlany, Ogawa, and Shulman, who found correlated spectral markers of the R/T transition in EPR, NMR, and CD spectra [63]. Shiga et al. [64] and Henry and Banerjee [65] obtained spectra from “isolated” subunits of human hemoglobin (β -subunit tetramers and likely α -subunit dimers) fully saturated with NO. The subunit spectra (Fig. 1) clearly show distinctions: the α -subunit spectrum (Fig. 2, blue) exhibits rhombic character (three distinct g -values); the β -subunit spectrum (Fig. 2, red) is axial (two distinct g -values). The composite spectrum formed simply by addition of the subunit spectra (Fig. 2, orange) is essentially identical to that of the tetrameric $\alpha_2\beta_2$ Hb(Fe(II))(NO)₄ (Fig. 2, Hb(NO)₄). The Hb “hybrids” α_2 (NO)/ β_2 (deoxy) and α_2 (deoxy)/ β_2 (NO) were prepared from the chemically isolated subunits and shown to exhibit spectra equivalent to those of the isolated α - or β -subunits, respectively [65]. Treatment of such hybrids with organic phosphates [66] definitively established that the hyperfine structure discussed above derives exclusively from the α -subunits. Taken together, these results establish the current approach for analyzing HbNO EPR spectra: simple decomposition of the EPR spectra into three components. The type of analysis described here has been used in numerous EPR-based studies of the kinetic and equilibrium properties of NO binding by Hb [24,40,45,47,54,67–72].

It should be noted that each of the subunit EPR spectra appear to be composites, involving species whose subtle differences have not been entirely characterized. Shortly after Kon's initial studies, Yonetani et al. [73] noted extra features in the EPR spectra of the nitrosyl derivatives of a number of heme proteins (for example, sperm whale myoglobin), suggestive of the presence of multiple species. Intriguingly, the EPR spectrum of (monomeric) myoglobin is extremely similar to that of tetrameric human hemoglobin. Hori and coworkers [66] examined nitrosyl Hb EPR spectra at liquid helium and liquid nitrogen temperatures. They observed changes in the Hb(NO)₄ lineshape that suggested an increased rhombicity of the β -subunit spectrum at the lower temperature [66]. Morse and Chan [74] cleverly identified two components in the myoglobin spectrum by factor analysis of a series of spectra obtained over the temperature range of 30 to 180 K. Their results demonstrate the presence of an equilibrium between two heme-Fe(II)NO species—one, favored at lower temperatures, has a rhombic spectrum, the other an axial one. Bemski and coworkers used CW power saturation methods to identify three spectral components in nitrosyl Hb, and Q-band EPR to further characterize the temperature dependence of the spectral components [75–77]. The most comprehensive study of the spectral components was carried out by Hüttermann and coworkers [78], who obtained X- and Q-band EPR spectra for Hb(Fe(II))(NO)₄ and isolated subunits over the temperature range of ~4–300 K. Their results were rationalized by the presence of a rhombic and an axial (two distinct g -values) component in the spectra of *both* the α - and the β -subunits; with increasing temperature, the rhombic species are converted to axial ones. At temperatures beyond ~150 K there is a fur-

ther narrowing of the lineshape that may result from motion of the NO group. The Q-band EPR work [77,78] seemed to reveal additional spectral components not seen in the X-band spectra. This emergence of new spectral components motivated us to extend the spectroscopy of nitrosyl-Hb to W-band.

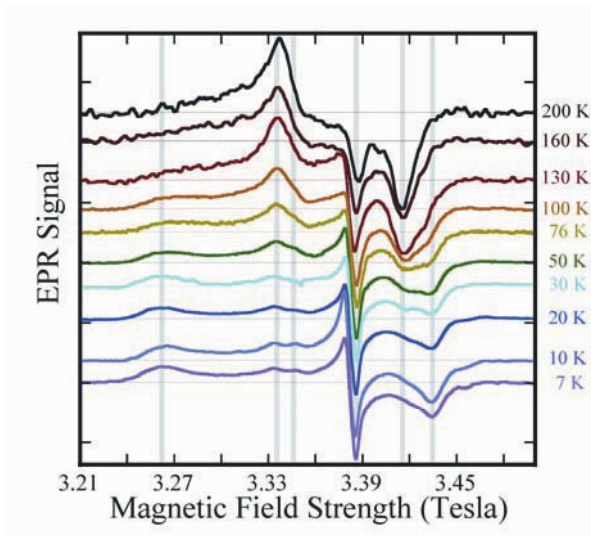


Figure 3. W-Band (94.9 GHz) EPR spectra of human $\text{Hb}(\text{NO})_4$ at sample temperatures ranging from 7 to 200 K. The spectra were obtained in CW mode with field modulation of 10 G amplitude at a frequency of 100 kHz. $\text{Hb}(\text{NO})_4$ was prepared by reaction of a phosphate-buffered (pH 7.4) saline solution of Hb A₀ (deoxygenated with ultrahigh-purity argon) with a deoxygenated aqueous solution of sodium nitrite (preceded by addition of sodium dithionite); excess reagents were removed by G-25 chromatography. For certain spectral features, highlighted with the shaded lines, the W-band spectra show a notable increase in resolution of temperature-dependent lineshape changes as compared to X- and Q-band spectra. EPR spectra exhibit both axial and rhombic spectral components in equilibrium that favors the axial components with increasing temperature.

A series of 94.9 GHz EPR spectra of $\text{Hb}(\text{NO})_4$ recorded at temperatures from ~7 to 200 K is shown in Figure 3. These spectra are remarkable for their resolution of features. The resolution is, at first glance, somewhat surprising, as one might have expected g -anisotropy and g -strain to predominate spectral lineshape and line-broadening. Of course, in the interior of the line, where the orbital contributions to the Zeeman interaction ultimately vanish, the field-dependent scaling is also suppressed, thus rationalizing, at least impart, the enhanced resolution. Regions of the EPR spectra that show a clear temperature-conversion of one spectral component into another are highlighted with shaded vertical lines on the stacked plot. It should be noted that at the lowest temperatures new components, not well-evidenced in the prior Q-band work, are seen (e.g., the doublet structure at 3.33–3.35). With increasing temperature to 100 K, there is a shift from species with greater anisot-

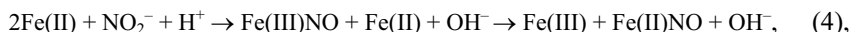
ropy to those with less anisotropy. Only above 130 K is there a change in structure (at the low-field edge) that is suggestive of motional averaging. These spectra can be reasonably simulated following the basic premises of the Hüttermann model.

A coherent picture that emerges from all of these experiments is that six-coordinate heme-Fe(II)NO species undergo an equilibrium shift from a species with a more rhombic EPR spectrum to one with a more axial spectrum with increasing temperature. The critical temperature at which the predominating species changes from the rhombic to axial species, however, is different for the two different subunits in Hb. The critical temperature is lower for the Hb β -subunits than for the α -subunits. Thus, at boiling nitrogen temperatures the β -subunit spectrum is largely converted to the axial component while the α -subunit spectrum remains rhombic. The pronounced differences of the subunit EPR spectra, illustrated in Figure 2, derive from this subtle effect; it is fortuitous that the spectral distinction is most pronounced at a temperature of convenience for the spectroscopist.

2.2. Heme Fe(II)NO Subunit Selectivity

Highly surprising subunit inequivalences have been uncovered through our studies of NO Hb micropopulations. Typically in the uptake of heme-ligands, subunit inequivalences are at best modest. In elegant cryo-gel electrophoresis experiments, Perrella and DiCera have recently documented a three-fold preference for the β -subunit at low saturation of Hb with CO [79]. NO is exceptional. While considered to exhibit little cooperativity or subunit-selectivity in NO uptake, it is also widely understood to deviate strongly from random binding by exhibiting a profound α -subunit preference for NO [45,46,70]. In pioneering studies, Hille, Olson, and Palmer [70] established the picture that NO, at doses leading to $\sim 25\%$ saturation, is initially coordinated at roughly equivalent rates by the heme-iron in both α - and β -subunits; then, on a timescale of minutes, NO migrates to α -subunits and forms the well-known five-coordinate heme-Fe(II)NO species [80]. The tendency to form this particular iron-nitrosyl species is strong enough that it has been prepared at 50% NO saturation (where α -hemes are fully and exclusively NO occupied) by Yonetani and coworkers [46].

The remarkable aspect of the chemistry that we have reported is the preferential population of β -subunit hemes, primarily in largely oxidized [24] or oxygenated [12,40] Hbs. We have reported that gradual decomposition of the SNO moiety in neat solutions of SNO-oxy-Hb, as well as more rapid reactions accelerated by added reductants, results in autocapture of NO on the β -subunits [12,40,48]. Selectivity is essentially complete. This effect appears to be governed by the proximity of the β -cys 93 and heme-iron; reduction of co-solute low-molecular-weight nitrosothiols in oxy-Hb solutions results in very limited heme-Fe(II)NO yield and no subunit-selectivity [48]. Similarly, the reaction of deoxy-Hb with low-levels of nitrite [24],



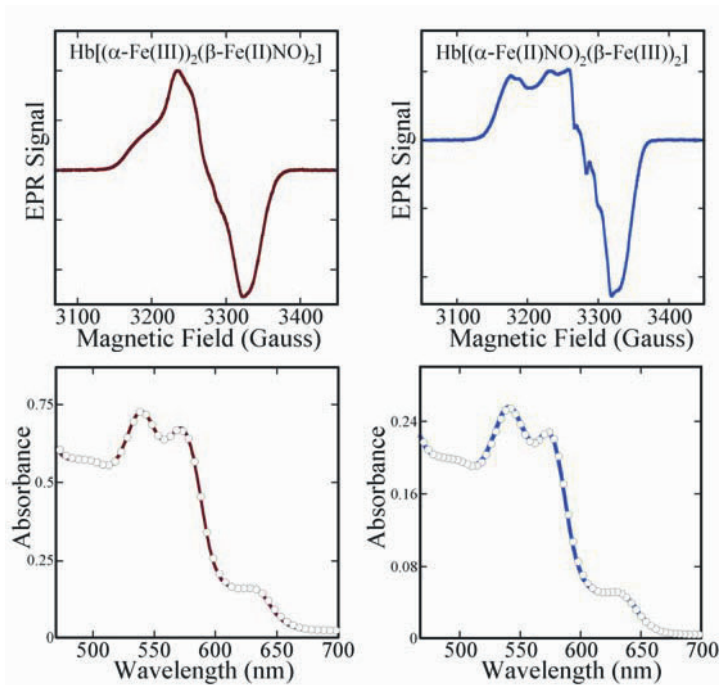


Figure 4. EPR (top) and UV/Vis (bottom) spectra of synthetic Hb hybrids. Reductive nitrosylation [24] of met-Hb (prepared from Hb A₀ by potassium ferricyanide oxidation followed by G-25 chromatography) with one equivalent of NO give Hb[(α -Fe(III))₂(β -Fe(II)NO)₂] (left), while limited air oxidation of Hb(NO)₄ furnishes Hb[(α -Fe(II)NO)₂(β -Fe(III))₂] (right). Solid lines are the experimental spectra, the dotted line on the UV/Vis spectra represents a simulation constructed from equal mixtures of heme-Fe(III) and heme-Fe(II)NO standard Hb spectra. EPR spectra were obtained at X-band (9.3 GHz), with samples at 76 K, and detected with a field modulation amplitude of 5 G and frequency of 100 kHz.

produces heme-Fe(II)NO with a strong β -subunit preference. Such a subunit preference in heme-Fe(II)NO-Hb has been seen by others, but has escaped comment [81]. In the reductive nitrosylation of met-Hb,



the iron nitrosyl product is furnished with a strong β -subunit preference. Indeed, with one equivalent of NO, the reaction leads to the formation of Hb[(α -Fe(III))₂(β -Fe(II)NO)₂] hybrids. This product is identified by decomposition of spectral components in both UV/Vis and EPR spectra, as illustrated in Figure 4 (left panel). The UV/Vis spectrum indicates an equal mixture of Fe(III) and Fe(II)NO hemes; the EPR shows that the Fe(II)NO are largely, if not exclusively, on the β -subunits.

The β -subunit preference in the distribution of the Fe–NO and met-heme products of the reaction of deoxy-Hb with NO and its biological precursors is highly significant to any mechanism of SNO-Hb formation that involves the coupling of NO and heme redox chemistry [11,24], as it could generate specific micropopulations of Fe(III) and Fe(II)NO hemes that are selectively competent for SNO-Hb formation [52]. This significance also applies to β -subunit selective oxidations of Hb(NO)₄ that provide a route to the complementary hybrid Hb[(α -Fe(II)NO)₂(β -Fe(III))₂] (Fig. 4, right panel). This selective oxidation is most easily carried out by exposure to air, quenching the reaction when half of the hemes are oxidized. This hybrid species has been seen in blood samples treated with nitrite and in blood of subjects treated with nitrite [82]. These two hybrid-forming reactions may be coupled and viewed as steps in a cycle (Fig. 5) that formally effect the relocation of the NO ligands (and holes):

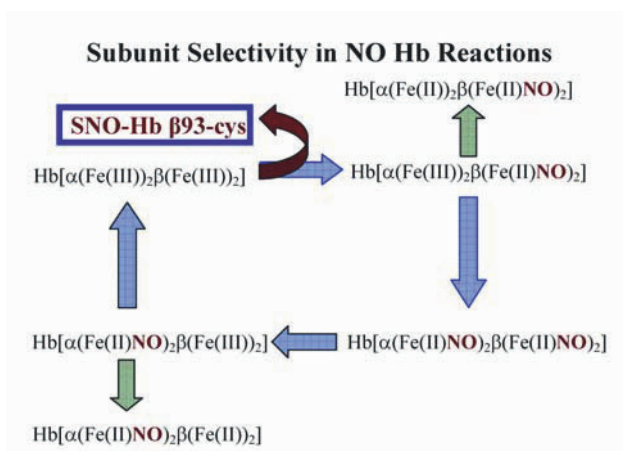


Figure 5. Reaction cycle depicting the flexibility of the disposition of the NO group in tetrameric Hb. The blue arrows outline a path beginning (upper left) with met-Hb, Hb[heme-Fe(III)₄], which is converted through partial reductive nitrosylation to the hybrid Hb[α (Fe(III))₂ β (Fe(II)NO)₂], then, upon complete reaction, to Hb(NO)₄, Hb[(heme-Fe(II)NO)₄] (lower right). Partial oxidation of Hb(NO)₄ yields the complementary hybrid Hb[α (Fe(II)NO)₂ β (Fe(III))₂], which, upon further oxidation, completes the cycle to yield met-Hb. Reduction of the hybrids (green arrows) generate the corresponding Fe(II)/Fe(II)NO hybrids. SNO-Hb formation (red arrow) can accompany reductive nitrosylation.

This reaction cycle underscores the previously unanticipated flexibility that exists in positioning the NO-group on the Hb tetramer, and subtlety of NO interactions with Hb. The Hb [(α -Fe(II)NO)₂(β -Fe(III))₂] hybrid can be reduced to furnish Hb[(α -Fe(II)NO)₂(β -Fe(II))₂], which is predominately comprised of five coordinate nitrosyl-hemes, as is evident from the characteristic EPR signature apparent in

Figure 6 [70,80]. This spectrum—which by decomposition analysis contains ~70% α_5 -nitrosyl hemes—is typical of α -subunit nitrosyl-Hb spectra obtained at ~neutral pH, and without additional T-state inducing heterotropic allosteric effectors [46].

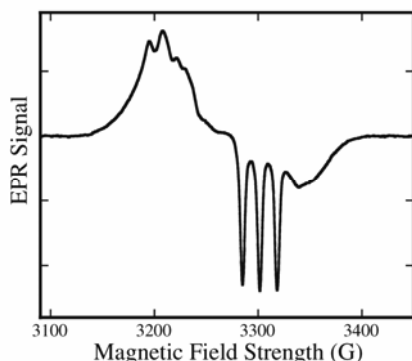


Figure 6. EPR spectrum of Hb[(α_5 -Fe(II)NO) $_2$ (β -Fe(II)) $_2$] hybrid obtained by sodium dithionite reduction of Hb[(α_6 -Fe(II)NO) $_2$ (β -Fe(III)) $_2$] (Fig. 4). Spectral decomposition with the basis spectra of Figure 2 indicate that over 90% of the Fe(II)NO is from the α -subunits with ~70% five-coordinate α -heme Fe(II)NO.

2.3. Heme Fe(II)NO Subunit Spectral Editing

The investigation of the distinct spectral components that comprise the EPR spectrum of Hb(NO) $_4$ began, as noted above, with the chemical separation of the α - and β -subunits, from which heme-Fe(II)NO spectra of the isolated subunits could be obtained. This procedure also enables the preparation of Fe(III)/Fe(II)NO hybrids by oxidation of separated subunits prior to reconstitution of the tetramer. As compared to this approach, the chemical cycle delineated in Figure 5 outlines a far simpler means to generate these hybrids that obviates the need for chemical separation of the subunits. We imagined, however, that it might be possible to take this simplification to the next level by using spectroscopic methods to selectively obtain α - and β -subunit spectra from Hb(NO) $_4$ samples. The early work of Bemski and coworkers [75], in which spectral components were distinguished by different saturation behaviors—together with recent pulsed EPR studies of nitrosyl Hb—suggested that the Hb(NO) $_4$ spectra might be parsed by relaxation-time-based editing methods.

We tested this idea in a W-band pulsed EPR spectrometer [83]. A series of echo-detected spectra were obtained by preceding two echo-generating pulses with a picket-fence saturating pulse-train followed by variable delay. A selected set of experimental results is shown in Figure 7. The left panel shows the experimental response; the spectra in the right panel are peak normalized to highlight the distinc-

tive manner in which the spectral components recover from saturation. The narrow component relaxes on a microsecond timescale, while the broader component relaxes more than an order of magnitude more slowly. This difference enabled us to process the different time slices via a simple subtraction and differentiation scheme to separate the two distinct spectral components shown in Figure 8. These broad and narrow components are immediately identified, on the basis of the studies of isolated subunits at X- and Q-band, with the α - and β -subunit spectra, respectively. These experiments represent a novel use of pulsed EPR methods for isolating spectral components.

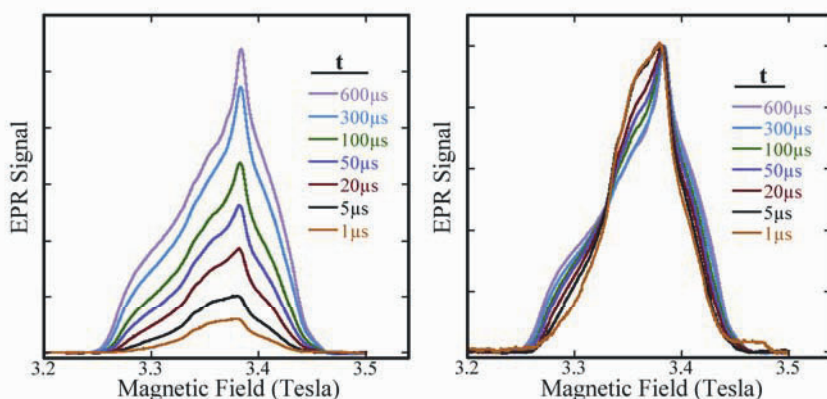


Figure 7. Spectral editing of spectral components of human Hb(NO)₄ at 13 K. (Left) Echo-detected W-band (94.9 GHz) EPR spectra. The two-pulse echo sequence was preceded by a 50- μ s picket fence of 25-ns pulses 200 ns apart, and a variable recovery time (t), ranging as indicated in the panel from 1 to 600 μ s. (Right) Peak normalized depiction of the same spectra, highlighting the faster recovery of the narrow spectral components.

The spectral editing of EPR contributions from the different subunits marks a spectroscopic milestone. It is, however, an intriguing surprise that heme-nitrosyl species within the different subunits exhibit saturation-recovery times that are sufficiently different to enable their spectroscopic separation. In continuing work, we are extending this editing methodology to probe for species, such as met/nitrosyl hybrids, that have been postulated as precursors for redox-coupled SNO-Hb formation [12,24,84,85] and for release of NO from SNO-Hb [86,87].

3. EVOLUTION OF NO Hb INTERACTIONS

This chapter details EPR experiments—some vintage and some new—that continue to assist in the development of a new perspective on the function of hemoglobin in humans, or more broadly, in organisms with mature cardiovascular

systems. In this perspective, the crucial function of O₂ delivery is affected by the channeling of blood to oxygen depleted tissues. On the molecular level this process involves sensing of ambient oxygen levels by SNO-Hb, which promptly transduces this signal to dispense NO to dilate resistance vessels; O₂ plays a role of allosteric modulator in the NO release function. As noted earlier, the cysteine residue active for S-nitrosylation in human Hb is rigorously conserved in birds and mammals; prior to the discovery of SNO-Hb function, this absolute requirement had no rationale.

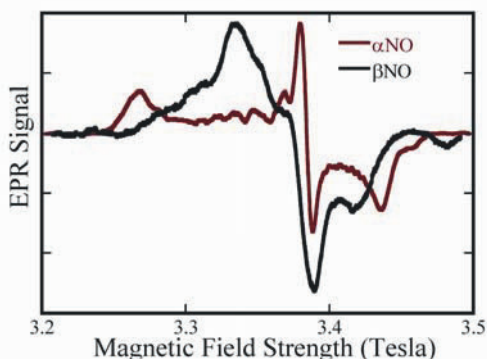


Figure 8. Saturation-recovery edited W-band (94.9 GHz) echo-detected EPR spectra of human Hb(NO)₄ at 13 K. Spectral components characteristic of heme-Fe(II)NO in the α - and β -subunits are shown separately in the red and black traces, respectively.

In closing, it is interesting to note that this ostensibly new perspective on Hb chemistry is, in fact, an “ancient” idea. Owing to the genomic revolution, the ubiquity of Hbs and closely related globins—even in archaea—is recognized [88]. It is now suggested “that the predominant functions of globins are enzymatic and that oxygen transport is a specialized development that accompanied the evolution of metazoans” [89]. Hbs in more primitive organisms feature NO chemistry with heme-iron, thiols, and oxygen for NO or O₂ detoxification. In bacteria [90] and yeast [91], flavohemoglobins counter NO stress either anaerobically (\rightarrow HNO, N₂O) or aerobically (\rightarrow NO₃⁻). In higher organisms the loss of the flavoreductase domain appears to be compensated by the incorporation of critical thiols that facilitate analogous processes through nitrosothiol chemistry. In the nematode *Ascaris lumbricoides* [92], ambient oxygen tensions are kept low through NO-primed, heme/thiol-assisted deoxygenase activity; NO detoxification operates in plants such as *Arabidopsis thaliana* [93]. Far from being a novelty, the panoply of chemical interactions of NO and Hb is a fundamental feature of Hbs that has been conserved throughout evolutionary time, from the simplest to the most advanced organisms.

ACKNOWLEDGMENTS

This work was supported by National Science Foundation Grant MCB 0981228 (to D.J.S) and National Heart, Lung, and Blood Institute Grant R01 HL421444 to J.S.S).

REFERENCES

1. Furchgott R, Zawadzki JV. 1980. The obligatory role of endothelial cells in the relaxation of arterial smooth muscle by acetylcholine. *Nature* **288**(5789):373–376.
2. Hess DT, Matsumoto A, Kim SO, Marshall HE, Stamler JS. 2005. Protein S-nitrosylation: purview and parameters. *Nat Rev Mol Cell Biol* **6**(2):150–166.
3. Stamler JS, Singel DJ, Loscalzo J. 1992. Biochemistry of nitric oxide and its redox-activated forms. *Science* **258**(5090):1898–1902.
4. Ignarro LJ, Buga GM, Wood KS, Byrns RE, Chaudhuri G. 1987. Endothelium-derived relaxing factor produced and released from artery and vein is nitric oxide. *Proc Natl Acad Sci USA* **84**:9265–9269.
5. Gibson QH, Roughton FJW. 1957. The Kinetics and equilibria of the reactions of nitric oxide with sheep haemoglobin. *J Physiol* **136**:507–526.
6. Doyle MP, Hoekstra JW. 1981. Oxidation of nitrogen oxides by bound dioxygen in hemoproteins. *J Inorg Biochem* **14**(4):351–358.
7. Singel DJ, Lancaster JR. 1996 Electron Paramagnetic resonance spectroscopy and nitric oxide biology. In *Methods in nitric oxide research*, pp. 341–356. Ed M Feelisch, JS Stamler. West Sussex: John Wiley & Sons.
8. Henry YA, Singel DJ. 1996 Metal–nitrosyl interactions in nitric oxide biology probed by electron paramagnetic resonance spectroscopy. In *Methods in nitric oxide research*, pp. 357–372. Ed M Feelisch, JS Stamler. West Sussex: John Wiley & Sons.
9. Lancaster Jr JR 1994. Simulation of the diffusion and reaction of endogenously produced nitric oxide. *Proc Natl Acad Sci USA* **91**(17):8137–8141.
10. Jia L, Bonaventura C, Bonaventura J, Stamler JS. 1996. S-nitrosohaemoglobin: a dynamic activity of blood involved in vascular control [see comments]. *Nature* **380**(6571):221–226.
11. Singel DJ, Stamler JS. 2005. Chemical physiology of blood flow regulation by red blood cells: the role of nitric oxide and S-nitrosohemoglobin. *Annu Rev Physiol* **67**:99–145.
12. Singel DJ, Stamler JS. 2004. Blood traffic control. *Nature* **430**(6997):297.
13. Liu X, Miller MJ, Joshi MS, Sadowska-Krowicka H, Clark DA, Lancaster Jr JR. 1998. Diffusion-limited reaction of free nitric oxide with erythrocytes. *J Biol Chem* **273**(30):18709–18713.
14. Liao JC, Hein TW, Vaughn MW, Huang KT, Kuo L. 1999. Intravascular flow decreases erythrocyte consumption of nitric oxide. *Proc Natl Acad Sci USA* **96**(15):8757–8761.
15. Vaughn MW, Huang KT, Kuo L, Liao JC. 2000. Erythrocytes possess an intrinsic barrier to nitric oxide consumption. *J Biol Chem* **275**(4):2342–2348.
16. Liu X, Samouilov A, Lancaster Jr JR, Zweier JL. 2002. Nitric oxide uptake by erythrocytes is primarily limited by extracellular diffusion not membrane resistance. *J Biol Chem* **277**(29):26194–2619.

17. Tsoukias NM, Popel AS. 2002. Erythrocyte consumption of nitric oxide in presence and absence of plasma-based hemoglobin. *Am J Physiol Heart Circ Physiol* **282**(6):H2265–H2277.
18. Tsoukias NM, Popel AS. 2003. A model of nitric oxide capillary exchange. *Microcirculation* **10**(6):479–495.
19. El-Farra NH, Christofides PD, Liao JC. 2003. Analysis of nitric oxide consumption by erythrocytes in blood vessels using a distributed multicellular model. *Ann Biomed Eng* **31**(3):294–309.
20. Tsoukias NM, Kavdia M, Popel AS. 2004. A theoretical model of nitric oxide transport in arterioles: frequency- vs. amplitude-dependent control of cGMP formation. *Am J Physiol Heart Circ Physiol* **286**(3):H1043–H1056.
21. Zhang Y, Hogg N. 2005. S-nitrosothiols: cellular formation and transport. *Free Radic Biol Med* **38**(7):831–838.
22. Hyduke DR, Liao JC. 2005. Analysis of nitric oxide donor effectiveness in resistance vessels. *Am J Physiol Heart Circ Physiol* **288**(5):H2390–H2399.
23. Stamler JS, Simon DI, Osborne JA, Mullins ME, Jaraki O, Michel T, Singel DJ, Loscalzo J. 1992. S-nitrosylation of proteins with nitric oxide: synthesis and characterization of biologically active compounds. *Proc Natl Acad Sci USA* **89**(1):444–448.
24. Luchsinger BP, Rich EN, Gow AJ, Williams EM, Stamler JS, Singel DJ. 2003. Routes to S-nitroso-hemoglobin formation with heme redox and preferential reactivity in the beta subunits. *Proc Natl Acad Sci USA* **100**(2):461–466.
25. Luchsinger BP, Rich EN, Yan Y, Williams EM, Stamler JS, Singel DJ. 2005. Assessments of the chemistry and vasodilatory activity of nitrite with hemoglobin under physiologically relevant conditions. *J Inorg Biochem* **99**(4):912–921.
26. Bates JN, Harrison DG, Myers PR, Minor RL. 1991. EDRF: nitrosylated compound or authentic nitric oxide. *Basic Res Cardiol* **86**(Suppl 2):17–26.
27. Myers PR, Minor Jr RL, Guerra Jr R, Bates JN, Harrison DG. 1990. Vasorelaxant properties of the endothelium-derived relaxing factor more closely resemble S-nitrosocysteine than nitric oxide. *Nature* **345**(6271):161–163.
28. Gaston B, Drazen JM, Jansen A, Sugarbaker DA, Loscalzo J, Richards W, Stamler JS. 1994. Relaxation of human bronchial smooth muscle by S-nitrosothiols in vitro. *J Pharmacol Exp Ther* **268**(2):978–984.
29. Foster MW, McMahon TJ, Stamler JS. 2003. S-nitrosylation in health and disease. *Trends Mol Med* **9**(4):160–168.
30. Stamler JS. 1995. S-nitrosothiols and the bioregulatory actions of nitrogen oxides through reactions with thiol groups. *Curr Top Microbiol Immunol* **196**:19–36.
31. Jackson WF. 1987. Arteriolar oxygen reactivity: where is the sensor? *Am J Physiol* **253**(5 Pt 2):H1120–H1126.
32. Gonzalez-Alonso J, Richardson RS, Saltin B. 2001. Exercising skeletal muscle blood flow in humans responds to reduction in arterial oxyhaemoglobin, but not to altered free oxygen. *J Physiol* **530**(Pt 2):331–341.
33. Gorczynski RJ, Duling BR. 1978. Role of oxygen in arteriolar functional vasodilation in hamster striated muscle. *Am J Physiol* **235**(5):H505–H515.
34. Duling BR, Berne RM. 1970. Longitudinal gradients in periarteriolar oxygen tension: a possible mechanism for the participation of oxygen in local regulation of blood flow. *Circ Res* **27**(5):669–678.
35. Guyton AC, Ross JM, Carrier Jr O, Walker JR. 1964. Evidence for tissue oxygen demand as the major factor causing autoregulation. *Circ Res* **15**(Suppl):60–69.

36. Ferranti P, Malorni A, Mamone G, Sannolo N, Marino G. 1997. Characterisation of S-nitrosohaemoglobin by mass spectrometry. *FEBS Lett* **400**(1):19–24.
37. Chan NL, Rogers PH, Arnone A. 1998. Crystal structure of the S-nitroso form of liganded human hemoglobin. *Biochemistry* **37**(47):16459–16464.
38. Chan NL, Kavanaugh JS, Rogers PH, Arnone A. 2004. Crystallographic analysis of the interaction of nitric oxide with quaternary-T human hemoglobin. *Biochemistry* **43**(1):118–132.
39. Stamler JS, Jia L, Eu JP, McMahon TJ, Demchenko IT, Bonaventura J, Gernert K, Piantadosi CA. 1997. Blood flow regulation by S-nitrosohemoglobin in the physiological oxygen gradient. *Science* **276**(5321):2034–2037.
40. McMahon TJ, Moon RE, Luchsinger BP, Carraway MS, Stone AE, Stolp BW, Gow AJ, Pawloski JR, Watke P, Singel DJ, Piantadosi CA, Stamler JS. 2002. Nitric oxide in the human respiratory cycle. *Nat Med* **8**(7):711–717.
41. Imai K. 1982. *Allosteric effects in haemoglobin*. Cambridge: Cambridge UP.
42. Kosaka H, Sawai Y, Sakaguchi H, Kumura E, Harada N, Watanabe M, Shiga T. 1994. ESR spectral transition by arteriovenous cycle in nitric oxide hemoglobin of cytokine-treated rats. *Am J Physiol* **266**(5 Pt 1):C1400–C1405.
43. McMahon TJ, Stamler JS. 1999. Concerted nitric oxide/oxygen delivery by hemoglobin. *Methods Enzymol* 301:99–114.
44. Gow AJ, Singel D. 2006. NO, SNO, and hemoglobin: Lessons in complexity. *Blood* **108**(9):3224–3225; author reply 3226–3227.
45. Taketa F, Antholine WE, Chen JY. 1978. Chain nonequivalence in binding of nitric oxide to hemoglobin. *J Biol Chem* **253**(15):5448–5451.
46. Yonetani T, Tsuneshige A, Zhou Y, Chen X. 1998. Electron paramagnetic resonance and oxygen binding studies of alpha-nitrosyl hemoglobin: a novel oxygen carrier having NO-assisted allosteric functions. *J Biol Chem* **273**(32):20323–20333.
47. Jaszewski AR, Fann YC, Chen YR, Sato K, Corbett J, Mason RP. 2003. EPR spectroscopy studies on the structural transition of nitrosyl hemoglobin in the arterial-venous cycle of DEANO-treated rats as it relates to the proposed nitrosyl hemoglobin/nitrosothiol hemoglobin exchange. *Free Radic Biol Med* **35**(4):444–451.
48. Luchsinger BP. 2004. *Chemical interaction of nitric oxide and human hemoglobin*. PhD dissertation, Montana State University, Bozeman.
49. Gow AJ, Luchsinger BP, Pawloski JR, Singel DJ, Stamler JS. 1999. The oxyhemoglobin reaction of nitric oxide [see comments]. *Proc Natl Acad Sci USA* **96**(16):9027–9032.
50. Gow AJ, Stamler JS. 1998. Reactions between nitric oxide and haemoglobin under physiological conditions. *Nature* **391**(6663):169–173.
51. Herold S, Rock G. 2003. Reactions of deoxy-, oxy-, and methemoglobin with nitrogen monoxide: mechanistic studies of the S-nitrosothiol formation under different mixing conditions. *J Biol Chem* **278**(9):6623–6634.
52. Angelo RM, Singel DJ, Stamler JS. 2006. An S-nitrosothiol (SNO) synthase function of hemoglobin that employs nitrite as a substrate. *Proc Natl Acad Sci USA* **103**(22):8366–8371.
53. Weinberg JB, Gilkeson GS, Mason RP, Chamulitrat W. 1998. Nitrosylation of blood hemoglobin and renal nonheme proteins in autoimmune MRL-lpr/lpr mice. *Free Radic Biol Med* **24**(1):191–196.
54. Piknova B, Gladwin MT, Schechter AN, Hogg N. 2005. Electron paramagnetic resonance analysis of nitrosylhemoglobin in humans during NO inhalation. *J Biol Chem* **280**(49):40583–40588.

55. Kirima K, Tsuchiya K, Sei H, Hasegawa T, Shikishima M, Motobayashi Y, Morita K, Yoshizumi M, Tamaki T. 2003. Evaluation of systemic blood NO dynamics by EPR spectroscopy: HbNO as an endogenous index of NO. *Am J Physiol Heart Circ Physiol* **285**(2):H589–H596.
56. Tsuchiya K, Kanematsu Y, Yoshizumi M, Ohnishi H, Kirima K, Izawa Y, Shikishima M, Ishida T, Kondo S, Kagami S, Takiguchi Y, Tamaki T. 2005. Nitrite is an alternative source of NO in vivo. *Am J Physiol Heart Circ Physiol* **288**(5):H2163–H2170.
57. Kon H. 1968. Paramagnetic resonance study of Nitric Oxide hemoglobin. *J Biol Chem* **243**(16):4350–4357.
58. Wayland BB, Olson LW. 1974. Spectroscopic studies and bonding model for nitric oxide complexes of iron porphyrins. *J Am Chem Soc* **96**(19):6037–6041.
59. Trittelvitz E, Sick H, Gersonde K. 1972. Conformational isomers of nitrosyl-haemoglobin: an electron-spin-resonance study. *Eur J Biochem* **31**(3):578–584.
60. Rein H, Ristau O, Scheler W. 1972. On the influence of allosteric effectors on the electron paramagnetic spectrum of nitric oxide hemoglobin. *FEBS Lett* **24**(1):24–26.
61. Trittelvitz E, Gersonde K, Winterhalter KH. 1975. Electron-spin resonance of nitrosyl haemoglobins: normal alpha and beta chains and mutants Hb M Iwate and Hb Zurich. *Eur J Biochem* **51**(1):33–42.
62. Szabo A, Perutz MF. 1976. Equilibrium between six- and five-coordinated hemes in nitrosylhemoglobin: interpretation of electron spin resonance spectra. *Biochemistry* **15**(20):4427–4428.
63. Shulman RG, Ogawa S, Hopfield JJ. 1972. An allosteric model of hemoglobin, II: the assumption of independent binding. *Arch Biochem Biophys* **151**(1):68–74.
64. Shiga T, Hwang KJ, Tyuma I. 1968. An electron paramagnetic resonance study of nitric oxide hemoglobin derivatives. *Arch Biochem Biophys* **123**(1):203–205.
65. Henry Y, Banerjee R. 1973. Electron paramagnetic studies of nitric oxide haemoglobin derivatives: isolated subunits and nitric oxide hybrids. *J Mol Biol* **73**(4):469–482.
66. Nagai K, Hori H, Yoshida S, Sakamoto H, Morimoto H. 1978. The effect of quaternary structure on the state of the alpha and beta subunits within nitrosyl haemoglobin: low temperature photodissociation and the ESR spectra. *Biochim Biophys Acta* **532**(1):17–28.
67. Henry Y, Cassoly R. 1973. Chain non-equivalence in nitric oxide binding to hemoglobin. *Biochem Biophys Res Commun* **51**(3):659–665.
68. Reisberg P, Olson JS, Palmer G. 1976. Kinetic resolution of ligand binding to the alpha and beta chains within human hemoglobin. *J Biol Chem* **251**(14):4379–4383.
69. Hille R, Palmer G, Olson JS. 1977. Chain equivalence in reaction of nitric oxide with hemoglobin. *J Biol Chem* **252**:403–405.
70. Hille R, Olson JS, Palmer G. 1979. Spectral transitions of nitrosyl hemes during ligand binding to hemoglobin. *J Biol Chem* **254**(23):12110–12120.
71. Louro SR, Ribeiro PC, Bemski G. 1981. EPR spectral changes of nitrosyl hemes and their relation to the hemoglobin T-R transition. *Biochim Biophys Acta* **670**(1):56–63.
72. Gow AJ, Luchsinger BP, Pawloski JR, Singel DJ, Stamler JS. 1999. The oxyhemoglobin reaction of nitric oxide. *Proc Natl Acad Sci USA* **96**(16):9027–9032.
73. Yonetani T, Yamamoto H, Erman JE, Leigh Jr JS, Reed GH. 1972. Electromagnetic properties of hemoproteins, V: optical and electron paramagnetic resonance characteristics of nitric oxide derivatives of metalloporphyrin–apohemoprotein complexes. *J Biol Chem* **247**(8):2447–2455.

74. Morse RH, Chan SI. 1980. Electron paramagnetic resonance studies of nitrosyl ferrous heme complexes: determination of an equilibrium between two conformations. *J Biol Chem* **255**(16):7876–7882.
75. Wajenberg E, Linhares MP, el-Jaick LJ, Bemski G. 1992. Nitrosyl hemoglobin: EPR components at low temperatures. *Eur Biophys J* **21**(1):57–61.
76. Wajenberg E, Bemski G, el-Jaick LJ, Alves OC. 1996. Nitrosyl hemoglobins: EPR above 80 K. *Int J Biol Macromol* **18**(3):231–235.
77. Flores M, Wajenberg E, Bemski G. 1997. Temperature dependence of Q-band electron paramagnetic resonance spectra of nitrosyl heme proteins. *Biophys J* **73**(6):3225–3229.
78. Hüttermann J, Burgard C, Kappl R. 1994. Proton ENDOR from randomly oriented NO-ligated haemoglobin: approaching the structural basis for the R-T transition. *J Chem Soc Faraday Trans* **90**:3077–3087.
79. Perrella M, Di Cera E. 1999. CO ligation intermediates and the mechanism of hemoglobin cooperativity. *J Biol Chem* **274**(5):2605–2608.
80. Kon H. 1975. An interpretation of the three line EPR spectrum of nitric oxide hemoproteins and related model systems: the effect of the heme environment. *Biochim Biophys Acta* **379**(1):103–113.
81. Huang Z, Louderback JG, Goyal M, Azizi F, King SB, Kim-Shapiro DB. 2001. Nitric oxide binding to oxygenated hemoglobin under physiological conditions. *Biochim Biophys Acta* **1568**(3):252–260.
82. Kruszyna R, Kruszyna H, Smith RP, Thron CD, Wilcox DE. 1987. Nitrite conversion to nitric oxide in red cells and its stabilization as a nitrosylated valency hybrid of hemoglobin. *J Pharmacol Exp Ther* **241**(1):307–313.
83. Schwartz DA, Walter ED, McIlwain SJ, Krymov VN, Singel DJ. 1999. High-frequency (94.9 GHz) EPR spectroscopy of paramagnetic centers in a neutron-irradiated sapphire single-crystal fiber. *Appl Magn Reson* **16**(2):223–236.
84. Romeo AA, Filosa A, Capobianco JA, English AM. 2001. Metal chelators inhibit S-nitrosation of Cys beta 93 in oxyhemoglobin. *J Am Chem Soc* **123**(8):1782–1783.
85. Romeo AA, Capobianco JA, English AM. 2003. Superoxide dismutase targets NO from GSNO to Cysbeta93 of oxyhemoglobin in concentrated but not dilute solutions of the protein. *J Am Chem Soc* **125**(47):14370–14378.
86. Pezacki JP, Ship NJ, Kluger R. 2001. Release of nitric oxide from S-nitrosohemoglobin: electron transfer as a response to deoxygenation. *J Am Chem Soc* **123**(19):4615–4616.
87. Ship N, Pezacki JP, Kluger R. 2003. Rates of release of nitric oxide from HbSNO and internal electron transfer. *Bioorg Chem* **31**(1):3–10.
88. Freitas TA, Hou S, Dioum EM, Saito JA, Newhouse J, Gonzalez G, Gilles-Gonzalez MA, Alam M. 2004. Ancestral hemoglobins in Archaea. *Proc Natl Acad Sci USA* **101**(17):6675–6680.
89. Vinogradov SN, Hoogewijs D, Bailly X, Arredondo-Peter R, Guertin M, Gough J, Dewilde S, Moens L, Vanfleteren JR. 2005. Three globin lineages belonging to two structural classes in genomes from the three kingdoms of life. *Proc Natl Acad Sci USA* **102**(32):11385–11389.
90. Hausladen A, Gow A, Stamler JS. 2001. Flavohemoglobin denitrosylase catalyzes the reaction of a nitroxyl equivalent with molecular oxygen. *Proc Natl Acad Sci USA* **98**(18):10108–10112.
91. Liu L, Zeng M, Hausladen A, Heitman J, Stamler JS. 2000. Protection from nitrosative stress by yeast flavohemoglobin. *Proc Natl Acad Sci USA* **97**(9):4672–4676.

92. Minning DM, Gow AJ, Bonaventura J, Braun R, Dewhirst M, Goldberg DE, Stamler JS. 1999. *Ascaris* haemoglobin is a nitric oxide-activated "deoxygenase." *Nature* **401**(6752):497–502.
93. Perazzolli M, Dominici P, Romero-Puertas MC, Zago E, Zeier J, Sonoda M, Lamb C, Delledonne M. 2004. *Arabidopsis* nonsymbiotic hemoglobin AHb1 modulates nitric oxide bioactivity. *Plant Cell* **16**(10):2785–2794.

NICKEL AND COPPER ENZYMES

EPR INVESTIGATION OF [NiFe] HYDROGENASES

Maurice van Gastel and Wolfgang Lubitz

*Max-Planck-Institut für Bioanorganische Chemie,
Mülheim an der Ruhr, Germany*

EPR studies of the [NiFe] hydrogenases are reviewed. These enzymes contain a heterobimetallic [NiFe] center as the active site. The nickel is ligated to four cysteine residues, two of which form a bridge to the iron. The iron carries additionally 3 small inorganic diatomic ligands (2CN^- , CO). A third small ligand X is situated in the bridge between Ni and Fe. In the catalytic cycle the enzyme passes through a number of redox states, several of which are paramagnetic. The iron remains in the divalent low-spin (Fe^{II} , $S = 0$) state, whereas the nickel changes its valence and spin state during this cycle. Nickel is believed to bind the hydrogen and to be directly involved in the catalytic process. The available EPR data are interpreted in terms of a simple model, based on ligand field theory. The model indicates that the paramagnetic Ni–A, Ni–B, and Ni–C states are best described as formal Ni^{III} low-spin species with a spin of $S = 1/2$ and a d_{z^2} ground state. The d_{z^2} orbital is oriented along the molecular z axis (g_z axis, $g_z \approx g_e$) and points to the open coordination site of the Ni. The “EPR-silent” states are all Ni^{II} species. XAS spectroscopy provides evidence that these states are high-spin ($S = 1$) states; however, supporting EPR spectra have not yet been reported. The light-induced Ni–L states are characterized by a nickel d_{z^2} ground state with an admixture of the $d_{x^2-y^2}$ orbital. The identity of the third bridging ligand X between nickel and iron changes upon going from Ni–A to Ni–B to Ni–C and to Ni–L. ENDOR and HYSCORE data indicate that a $\mu\text{-OH}^-$ bridge is present in Ni–B, for Ni–C a formal $\mu\text{-H}^-$ has been identified, while for Ni–L the bridge is empty. The bridging ligand of the Ni–A state is still under debate. The identification of the electronic and geometric structure of the reaction intermediates employing spectroscopy and quantum chemical calculations form the basis for setting up a reaction mechanism for the [NiFe] hydrogenase.

1. CLASSIFICATION, COMPOSITION AND STRUCTURE OF HYDROGENASES

Hydrogenases catalyze the reversible heterolytic splitting of molecular hydrogen:



These enzymes are found in many archae, bacteria, and even a few eukaryotes [1]. One of the most common groups are the sulfate-reducing bacteria of the *Desulfovibrio* (*D.*) species. Because of their ability not only to utilize hydrogen as an energy source but also to produce molecular hydrogen from protons, they have been the subject of many investigations with the aim to better understand the catalytic activity. Hydrogenases are commonly divided into classes according to the metal content of the active site, where the catalytic activity takes place. Presently, three classes of hydrogenases have been identified: the [Fe], the [FeFe], and the [NiFe] hydrogenases [1]. For the [NiFe] hydrogenases, x-ray structures exist for the enzymes of the organisms of *D. gigas* [2–5], *D. vulgaris* Miyazaki F [6–9], *D. fructosovorans* [5,10], *D. baculatum* [4], and *D. desulfuricans* [11]. Other [NiFe] hydrogenases that have been extensively studied are from *Allochromatium* (*A.*) *vinosum* [12–20] and *Ralstonia* (*R.*) *eutropha* [21–28]. In *R. eutropha* a membrane-bound standard hydrogenase, a soluble (NADP-reducing) hydrogenase and a regulatory hydrogenase (RH) have been found. The latter (RH) acts as a hydrogen sensor and has an active site similar to the catalytic hydrogenase [29].

The [NiFe] hydrogenases consist of two subunits with molecular weights of about 30 and 60 kDa (Fig. 1). For the membrane-bound enzymes a small membrane anchor is present as well, which is cleaved during the purification process. The large subunit contains the active site. The geometry of the active site is highly conserved throughout all [NiFe] hydrogenases (Fig. 1). The nickel and iron atoms are separated by a distance of about 2.5 to 2.9 Å and are bridged by the sulfur atoms of two cysteines. The nickel is coordinated by two more cysteines bound in a terminal position. For some hydrogenases one of the latter cysteines is replaced by a selenocysteine, and these enzymes form the subclass of [NiFeSe] hydrogenases. The iron atom carries three inorganic diatomic ligands that have been identified by infrared spectroscopy as two CN⁻ and one CO [30]. In the oxidized state (in general a mixture of the so-called “unready” Ni–A and the “ready” Ni–B states), additional density is visible between nickel and iron that stems from a third bridging ligand “X” [3,6]. In the reduced Ni–C state this density is absent [4,7]. However, from the x-ray data it cannot be concluded if position X is empty or occupied by an atom or molecule with low electron density. Recent spectroscopic results will be discussed that point to the presence of a bridging hydride H⁻ in this state.

The small subunit contains three [FeS] clusters that are involved in the electron transport to/from the active [NiFe] center (Fig. 1). In the catalytically active hydrogenases, a [4Fe4S] “proximal” cluster is located near the [NiFe] center,

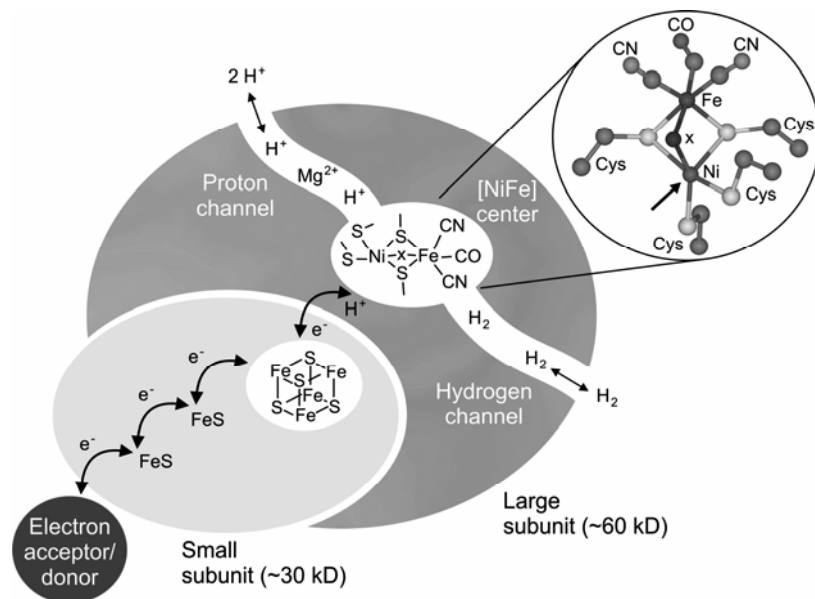


Figure 1. Schematic view of an [NiFe] hydrogenase and the active site. Shown are the 2 subunits with the active site (NiFe center), the proton channel, and the hydrogen access channel in the large subunit and the electron transport chain (3 FeS centers) in the small subunit. The structure of the catalytic site is shown on the right, which is based on the x-ray crystallographic analysis of *D. vulgaris* Miyazaki F [6]. Note that Fe is six-coordinate, while Ni is only five-coordinate; the free coordination site at Ni is marked by an arrow. For further details see text.

flanked by a [3Fe4S] cluster. Near the protein surface another [4Fe4S] “distal” cluster is present. Also indicated in Figure 1 is a magnesium ion found in the crystal structure, which is probably located in the proton transfer channel. A possible pathway for molecular hydrogen to travel between the protein surface and the active site has been found in crystallographic studies using high-pressure Xe gas [31,32].

The [NiFe] center is rich in redox states. The oxidized states (Ni–A, Ni–B) are catalytically inactive and can be activated by reduction with molecular hydrogen. They differ in their activation kinetics: Ni–A takes hours to be activated under hydrogen, while Ni–B takes only minutes [33]. For this reason the Ni–A state is also called the “unready” state and the Ni–B state the “ready” state. Both states are paramagnetic and are characterized by different *g*-values (Table 1). Upon one-electron reduction of Ni–A and Ni–B, the EPR-silent states Ni–SU and Ni–SIR are formed. For *A. vinosum* hydrogenase it has been shown that the Ni–A → Ni–SU reduction is reversible, but the Ni–B → Ni–SIR reduction strongly depends on pH and temperature. At pH 6.0 and 2°C the reduction was completely irreversible, at pH 8 and 30°C both reductions were reversible [16]. For *A. vinosum* hydrogenase

Table 1. Summary of *g* Values of the EPR Active States in Standard [NiFe] Hydrogenases

	$g_x (g_1)$	$g_y (g_2)$	$g_z (g_3)$
Ni-A	2.32	2.24	2.01
Ni-B	2.33	2.16	2.01
Ni-C	2.20	2.15	2.01
Ni-L1	2.30	2.12	2.05
Ni-L2	2.26	2.11	2.05
Ni-L3	2.41	2.16	n.d.
Ni-CO	2.12	2.07	2.02

All values taken from *D. vulgaris* Miyazaki F [51] except for Ni-CO (*A. vinosum*) [36] and Ni-L3 (*D. gigas*) [35]. For the orientation of axes see Figure 7. n.d. = not determined.

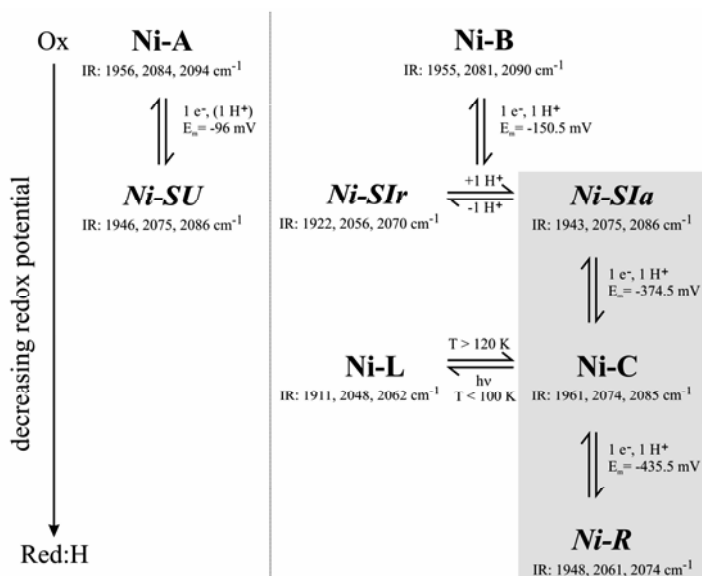


Figure 2. Overview of the redox states of [NiFe] hydrogenases, from the most oxidized (top) to the most reduced (bottom) form. Indicated are the IR frequencies (IR) of the CO ligand and the two CN^- ligands to Fe for *D. vulgaris* Miyazaki F hydrogenase and the midpoint potentials (E_m) for the redox transitions at pH = 6 (Ni-A/*NiSU*) and at pH = 7.4 (all others). The paramagnetic states are given in bold face, the EPR-silent states in italics. The two states *Ni-SIr* and *Ni-SIa* are in an acid–base equilibrium. The states involved directly in the catalytic cycle are highlighted by a shaded box. The paramagnetic Ni-CO state (not shown) is probably derived from the Ni-L state.

under reducing conditions and at temperatures greater than or equal to 30°C, the Ni-SIr is converted into another EPR-silent state, Ni-SIa, which can be quickly reduced to give another EPR active state Ni-C [15]. The Ni-C state exhibits a characteristic rhombic *g* tensor, and this state is found in all enzymes studied so far

(Table 1). The Ni–C state is light sensitive. Upon illumination with white light, the characteristic EPR signal disappears and a new signal appears [34], which is called Ni–L. At least two subforms have been identified with different g values, Ni–L1 and Ni–L2, depending on the temperature and the duration of light exposure [35]. Upon further reduction in the presence of H_2 , the most reduced state, Ni–R, is formed. Ni–R is EPR silent. Three subforms of Ni–R have been identified for *A. vinosum* hydrogenase [14]; however, the presence of all these substates has not yet been experimentally confirmed in hydrogenases from other sources. The [NiFe] hydrogenase can be inhibited by the addition of CO. It has been shown by x-ray crystallography of single crystals treated with CO [8] that the CO binds at the sixth free coordination site of the nickel (see Fig. 1). A paramagnetic Ni–CO state has been described and characterized [19,34,36,37]. This Ni–CO is also photosensitive, and upon illumination at low temperatures, CO photodissociates, resulting in the same Ni–L state as Ni–C. The different EPR active and EPR-silent redox states of the [NiFe] hydrogenase are depicted in the scheme shown in Figure 2.

In this contribution, an overview is given of the EPR studies performed so far on the EPR active states Ni–A, Ni–B, Ni–C, Ni–L, and Ni–CO. The emphasis here lies on the identification of the structure of the active site in all these intermediate states, including the assignment of the bridging ligand “X.” Knowledge of the exact structures of all intermediates is an essential prerequisite for quantum chemical studies, from which a reaction mechanism can be proposed. Especially, advanced EPR methods like ENDOR, ESEEM, and HYSCORE have played a crucial role in determining the hyperfine coupling constants (HFCs) of the metal nuclei and identifying protons or nitrogens from nearby amino acids or non-protein ligands, and in this way have helped to characterize both the electronic and the geometric structure of the site. The EPR-silent states have been investigated by other spectroscopic methods like XAS [38–41] and FTIR spectroscopy [14,42,43].

2. BASIC DESCRIPTION OF THE ELECTRONIC STRUCTURE

Many of the spectroscopic observables, especially those related to EPR spectroscopy, can be rationalized, when considering the crystal field of the metal ions. The x-ray structure shows [5,9] that the iron is hexacoordinate in all states. ENDOR data (*vide infra*) indicate that this atom remains in the non-paramagnetic ($S = 0$) low-spin Fe^{II} state in all EPR active redox states. This is probably caused by the tightly bound CO and CN^- ligands. The nickel ion is coordinated by five ligands in the Ni–A and Ni–B states [2], four of which (three sulfurs of cysteines and the bridging ligand “X”) form the base plane of a square pyramid. The fifth ligand (the sulfur of the fourth cysteine) occupies an axial position, and the other axial ligation position is unoccupied (see Fig. 1). The square pyramidal crystal field gives rise to a characteristic energy splitting of the five 3d orbitals at nickel.

The effect of the ligand field on a five-coordinate metal has been described by Solomon et al. [44]. The results presented in [44] were obtained for an Fe^{II} with four equatorial oxygen ligands and a unique axial ligand. The symmetry of this crystal field also applies to a five-coordinate nickel. A schematic overview of a

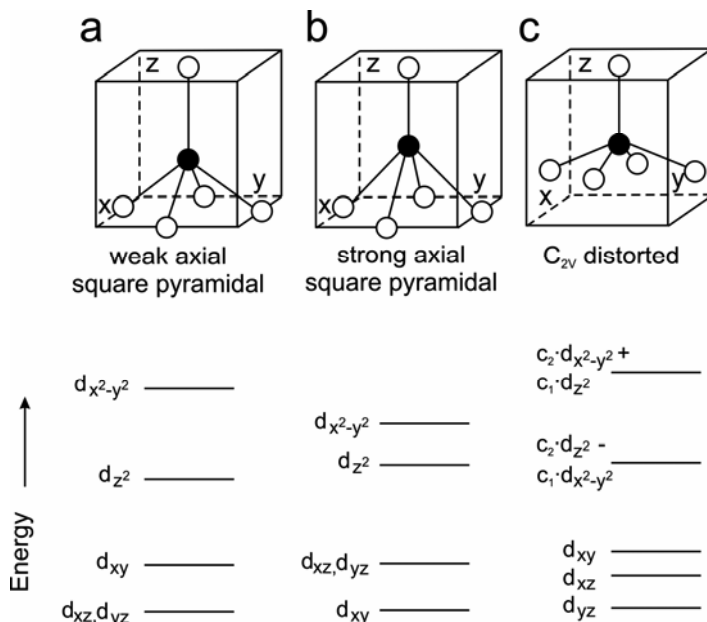


Figure 3. Schematic representation of the ligand field splitting of the 3d orbitals of a five-coordinate transition metal. The diagrams are reproduced and modified from [44]. Shown are a square pyramidal ligand field with a weak axial ligand (a); a strong axial ligand (b); C_{2v} distortion (c). In (c) a mixture of d_{z^2} and $d_{x^2-y^2}$ occurs ($c_1^2 + c_2^2 = 1$).

square pyramidal crystal field environment with a weak axial ligand, in which the metal is only slightly lifted out of the equatorial plane, gives rise to a splitting of the d orbitals, as indicated in Figure 3a. The d orbitals of lowest energy are the degenerate d_{xz} and d_{yz} orbitals. For a formal Ni^{III} ion, seven electrons are present in the 3d shell. For this d^7 case the d_{xz} , d_{yz} and d_{xy} orbitals are doubly occupied, and the unpaired electron resides in the d_{z^2} orbital, with the z axis defined as being parallel to the axis that connects the nickel and the atom of the axially coordinated ligand.

In this ligand field, the \mathbf{g} -tensor is characterized by one small principal g -value ($g_z \sim g_e$) and two larger g -values g_i ($i = x, y$). The \mathbf{g} tensor components of the d_{z^2} state can be expressed in terms of the spin-orbit-coupling parameter λ at Ni (note that $\lambda_{\text{Ni}} < 0$ [45]), and the energies of the d orbitals:

$$g_x = g_e - \frac{6\lambda}{E_{z^2} - E_{yz}}, \quad g_y = g_e - \frac{6\lambda}{E_{z^2} - E_{xz}}, \quad g_z = g_e. \quad (2)$$

The g_x and g_y values are degenerate (axial symmetry) in a ligand field with C_{4v} symmetry but are expected to become unequal in the [NiFe] hydrogenase, due to the asymmetric protein environment. A rhombic \mathbf{g} tensor is observed for all hydrogenases.

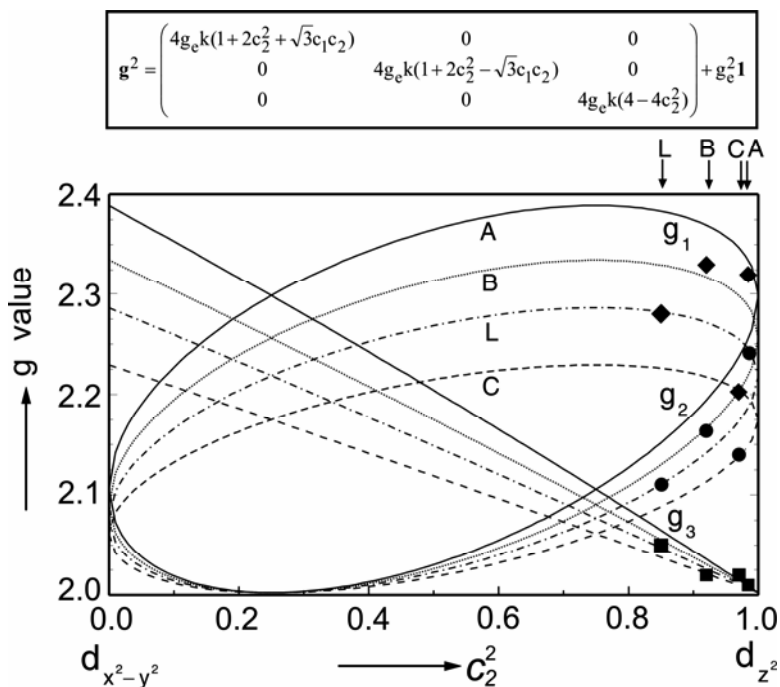


Figure 4. The \mathbf{g} -tensor components of Ni-A, Ni-B, Ni-C, and Ni-L as a function of d orbital mixing (d_{z^2} and $d_{x^2-y^2}$) for four cases with different perturbation parameters $k = \lambda_{\text{Ni}}/\Delta E_{dd}$, which were chosen to be: $k(\text{Ni-A}) = 0.053$ (solid line), $k(\text{Ni-B}) = 0.045$ (dotted line), $k(\text{Ni-C}) = 0.030$ (dashed line), and $k(\text{Ni-L}) = 0.038$ (dashed/dotted line). The experimental values of the four states are indicated by \blacklozenge (g_1), \bullet (g_2), and \blacksquare (g_3). In the model the Ni character of the singly occupied molecular orbital is described by $\Psi_{\text{Ni}} = c_1 d_{x^2-y^2} + c_2 d_{z^2}$, the energy of the other molecular orbitals with Ni(3d) character being lower by ΔE_{dd} . The expression derived for the \mathbf{g} tensor is given at the top of the figure. For further details, see [46].

We now briefly summarize the effect of distortions to the ligand field [44] that are relevant for [NiFe] hydrogenases. When the axial ligand is strongly coordinated, the d_{xy} orbital becomes lowest in energy and the energy of the d_{z^2} orbital approaches that of the $d_{x^2-y^2}$ orbital (the z direction is along the four-fold symmetry axis of the system) (see Fig. 3b). A distortion along one of the two equatorial axes causes a slight mixing of the $d_{x^2-y^2}$ and d_{z^2} orbitals (indicated in Fig. 3c). The effect of such a distortion on the g values has been discussed previously [46], where it was shown that a small admixture of $d_{x^2-y^2}$ orbital causes an increase of the g_z value and an increase in rhombicity without significantly changing the orientation of the g_z axis of the \mathbf{g} tensor (see Fig. 4).

The above-described ligand field also holds for the Ni^{II} (d^8) and Ni^{I} (d^9) valence states. Ni^{I} is paramagnetic ($S = 1/2$), and has a $d_{x^2-y^2}$ ground state, for which the \mathbf{g} tensor components are

$$g_x = g_e - \frac{2\lambda}{E_{xy} - E_{xz}}, \quad g_y = g_e - \frac{2\lambda}{E_{xy} - E_{yz}}, \quad g_z = g_e - \frac{8\lambda}{E_{xy} - E_{x^2-y^2}}. \quad (3)$$

In this case the z principal axis is associated with the largest g value, whereas for a d_{z^2} ground state the principal z axis is associated with the smallest g value. For Ni^{II} the low-spin form is diamagnetic, and the high-spin state has $S = 1$. In case of the Ni-L state, in which one equatorial ligand is removed (*vide infra*), the $d_{x^2-y^2}$ and d_{z^2} orbitals come very close in energy and orbital mixing and the order of the two orbitals may change.

Although a description in terms of pure d orbitals gives insight into the electronic structure, the binding of polarizable (“soft”) ligands (cysteine sulfurs) may lead to a significant spin delocalization, leaving only a fraction of the spin at the metal. This delocalization also has consequences for the hyperfine coupling constants (HFCs) of magnetic nuclei near the [NiFe] center. Particularly large HFCs (^{33}S , ^1H) are expected for the cysteine residue bound in the axial position along the symmetry axis of the spin carrying d_{z^2} orbital (see Fig. 1).

3. EPR CHARACTERIZATION OF [NiFe] HYDROGENASES: THE G TENSORS

In this section the EPR spectra of the EPR active redox states are discussed. An overview of the spectra for *D. vulgaris* Miyazaki F is given in Figure 5, and a summary of g values can be found in Table 1.

3.1. The Oxidized States Ni-A and Ni-B

The first EPR spectrum of the Ni-A state was reported in 1982 [47] for the enzyme *D. gigas*. In this work, the Ni-B state was also observed and appeared as a minority species. In other species like *D. vulgaris* Miyazaki F [48], the two states exist as mixtures with a more equal ratio in the aerobic “as-isolated” form of the enzyme. Different methods of preparation have been used to separate the Ni-A and Ni-B redox states, such that they appear as pure redox states in the EPR spectrum and can be therefore studied individually [13]. The Ni-A and Ni-B states have the same oxidation level, yet they differ in their g values, as observed by EPR (see Fig. 5 and Table 1). The activation times are different [33] and the FTIR spectra show differences with respect to the stretching frequencies of the CN^- and CO ligands attached to iron [14]. The midpoint potential for the Ni-A/Ni-SU couple in *D. gigas* hydrogenase has been investigated by EPR and redox titrations [49], and was found to depend on pH. By using electrochemistry combined with FTIR spectroscopy, the midpoint potentials of other redox states, including Ni-B, have also been investigated [42]. Both states are inactive and do not take part in the catalytic cycle. However, in order to understand the activation (deactivation) of the enzyme

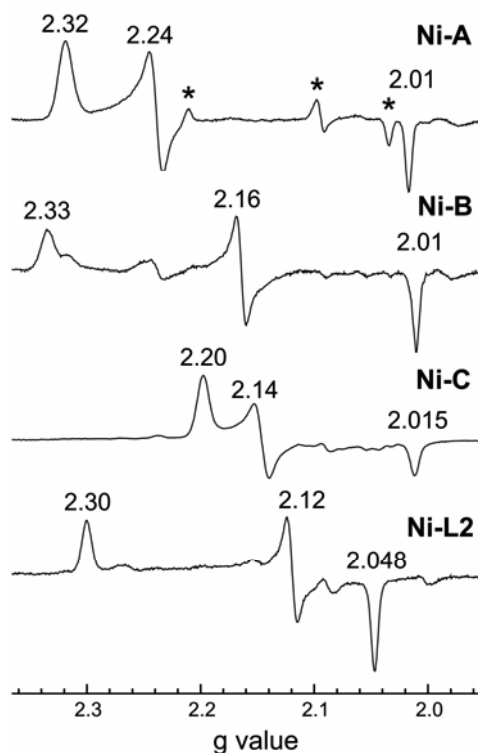


Figure 5. Overview of the EPR spectra of a standard [NiFe] hydrogenase. The spectra were obtained from *D. vulgaris* Miyazaki F in the Ni-A, Ni-B, Ni-C, and Ni-L2 redox states (see text for details). In the spectrum of Ni-A, lines from an additional redox state are observed that are marked with an asterisk. Experimental conditions: $\nu_{mw} = 9.43$ GHz, mod. freq. = 100 kHz, mod. depth = 5 G, recording time for each spectrum = approx. 15 min. For details, see [58].

and the aerobic inhibition, the spectroscopic and chemical differences of the Ni-A and Ni-B states have been the topic of many recent investigations that aim to elucidate the origin of these differences.

Until the mid-1990s, all EPR investigations of hydrogenases have been performed on frozen solutions and the g values have mainly been used as “fingerprints” for the identification of redox states (Table 1). With the advent of [NiFe] hydrogenase crystals of sufficient size, the first single-crystal EPR studies became possible and were performed on the enzyme from *D. vulgaris* Miyazaki F [48,50,51]. This opened the possibility to determine, in addition to the g tensor principal values, also the tensor axes and their orientations in the molecular frame. With this information the g values could be assigned to the geometrical structure

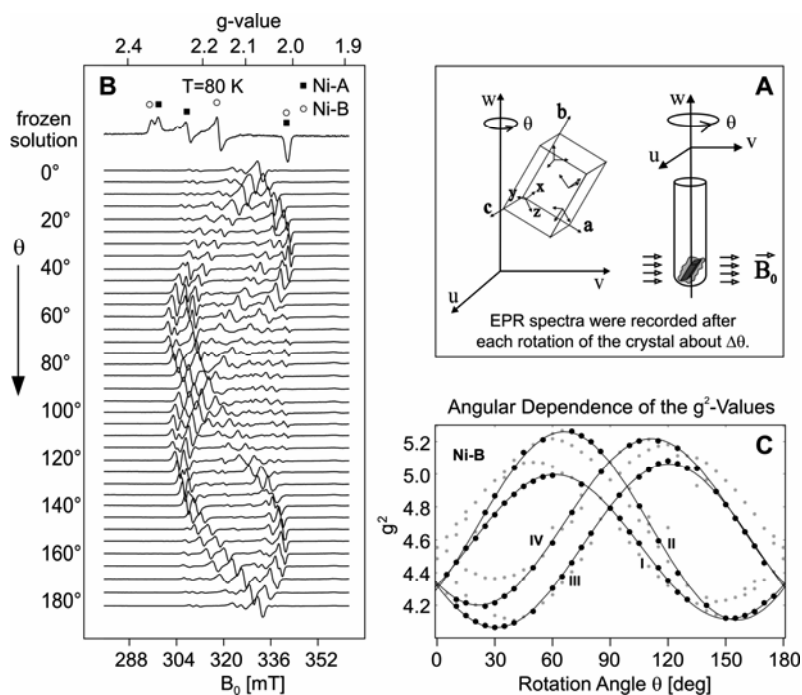


Figure 6. Schematic overview of single-crystal EPR experiments. EPR spectra are taken for different orientations of the crystal with respect to the magnetic field. The orientational dependence of the resonances can be analyzed to elucidate the directions of the principal axes of the g tensor with respect to the crystallographic axes. When the crystal structure is known, the information can be combined to obtain the directions of the principal axes with respect to bond directions and the geometry of the active site. The data shown are taken for the Ni-A and Ni-B redox states of *D. vulgaris* Miyazaki F hydrogenase. For details, see [48,50]. (A) Single crystal mounted in an EPR sample tube; shown are the laboratory reference frame (u , v , w), the crystal axes (a , b , c) of the orthorhombic single crystal with four sites in the unit cell (space group $P2_12_12_1$), and the molecular/ g tensor axes (x , y , z). (B) Top: Frozen solution EPR spectrum (X-band) of an “as-isolated” [NiFe] hydrogenase sample containing Ni-A: Ni-B \sim 2:3. Bottom: Angular variation of the EPR spectra of a single crystal ($T = 10$ K) in an arbitrary orientation showing lines from both Ni-A and Ni-B (and some smaller disoriented crystallites). Note that a maximum of 4 lines (4 sites) is expected for each species. (C) Angular dependence of the g^2 tensors of Ni-A (grey) and Ni-B (black). The analysis yields the g tensor principal values and the g tensor axes in the crystallographic axes system that can be converted to the molecular axes via the known crystallographic structure.

and be related to the d orbitals of the metal. Furthermore, single-crystal EPR experiments can be performed over a wide range of temperatures (from ambient to liquid helium), which allows to follow the structural changes of the enzyme [50]. A schematic overview of the single-crystal experiments performed on Ni-A and Ni-B for *D. vulgaris* Miyazaki F [50] is given in Figure 6. An additional stereoview of the principal axes of the g tensor in the Ni-A and Ni-B states is depicted in Figure 7. It was found that the principal g_z axis, corresponding to the smallest g value

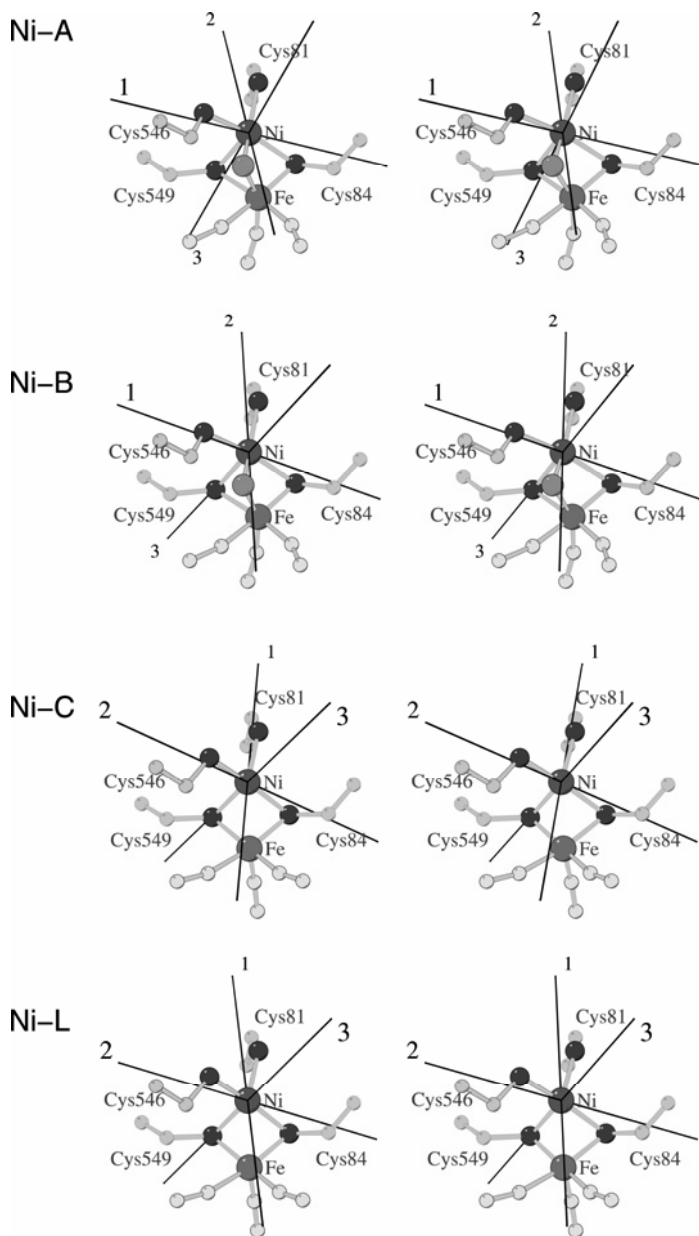


Figure 7. Stereoviews of the directions of the principal axes of the g tensors with respect to the geometry of the active site in the Ni-A, Ni-B, Ni-C, and Ni-L2 redox states of [NiFe] hydrogenase from *D. vulgaris* Miyazaki F. Reproduced with permission from [51]. Copyright © 2003, American Chemical Society.

(2.01), is approximately parallel to the bond direction of nickel toward the sulfur of the axial cysteine. This defines the direction of the C_{∞} symmetry axis of the $3d_{z^2}$ orbital, which contains the bulk spin density. The g_z axis also points from nickel toward the free coordination position of the square pyramid. This is compatible with a nickel that is either in a square pyramidal or in an octahedral ligand field with a weak axial ligation in both Ni–A and Ni–B forms. The temperature dependence of the EPR spectra between 295 and 10 K exhibited no structural changes of the active site. This is of general importance for the investigation of this enzyme, since it shows that the same g values are obtained both under physiological conditions at ambient temperature as well as at cryogenic temperatures. It should also be noted that the principal \mathbf{g} tensor values are the same within experimental error in frozen solution and in single crystals. Thus, crystallization does not change the electronic structure of the active site.

3.2. The Reduced Active State Ni–C

The Ni–C intermediate state is the only EPR active state that takes part in the catalytic cycle. It is two electrons more reduced than the Ni–A and Ni–B states (Fig. 2), and the density of the bridging ligand “X”, present in the A and B states, has disappeared in the electron density map of the x-ray data of reduced crystals [4,7]. The Ni–C state is characterized by g values of 2.01, 2.15, and 2.20 (see, e.g., for *D. vulgaris* Miyazaki F hydrogenase [51]). Similar to the Ni–A and Ni–B states, such a set of g values, with one being close to the free electron g value, g_e , and two shifted from g_e , indicate that the unpaired electron occupies the $3d_{z^2}$ orbital of nickel and that the nickel is most probably five-coordinated. The single crystal EPR studies [51] indeed showed that the direction of the principal z axis of the \mathbf{g} tensor is oriented similar to Ni–A and Ni–B, i.e., parallel to the bond direction from nickel to the sulfur of the axial cysteine, and pointing from nickel to the vacant axial coordination position (see Fig. 7). This also indicates that the bridging position “X,” one of the equatorial ligation positions of nickel, is still occupied (see Fig. 1). Since no significant electron density was observed in x-ray crystallography, this ligand must therefore be a light atom (or atoms).

In relation to the formal oxidation state, the Ni–C state was first expected to be an Ni^I (d^9) species. This is, however, not in line with XAS studies that show no significant change of the valence state [38], upon comparing Ni–A/Ni–B to Ni–C. The EPR parameters indicate the presence of a d_{z^2} ground state as found for Ni–A/Ni–B. A careful analysis of the single-crystal EPR data together with DFT calculations on various models of Ni–C incorporating different bridging ligands, indeed showed that this state is best described by a formal Ni^{III} d_{z^2} ground state, accommodating a hydride (H^-) in the bridge between Ni and Fe [51].

3.3. The Split Ni–C Signal

In general it is difficult to study the Ni–C state by EPR at low temperatures (<40 K). The reason for this is that the proximal [4Fe4S] cluster is usually also

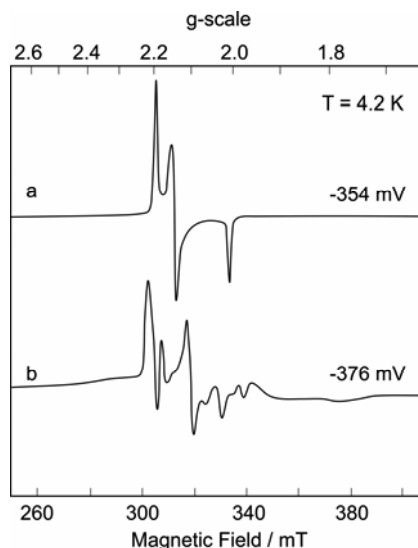


Figure 8. EPR spectra of (a) “unsplit” and (b) “split” Ni–C signal for *D. gigas* [NiFe] hydrogenase. The redox potential for (a) was set to -354 mV, for (b) to -376 mV. Experimental conditions: temperature, 4.2 K; microwave frequency, 9.378 GHz; microwave power, 0.01 mW (a) and 1 mW (b); modulation frequency, 100 kHz; modulation amplitude, 1 mT. Reproduced with permission from [53]. Copyright © 1995, American Chemical Society.

reduced and paramagnetic ($S = 1/2$). The spin–spin interaction between the [NiFe] center and the proximal $[4\text{Fe}4\text{S}]^+$ cluster splits and broadens the EPR spectrum [35,52,53]. Above this temperature, the electronic relaxation time of the $[4\text{Fe}4\text{S}]^+$ cluster is so fast that the spin–spin interaction is averaged out. An exception is the regulatory hydrogenase of *R. eutropha*, which has midpoint potentials such that the proximal $[4\text{Fe}4\text{S}]$ cluster remains oxidized ($S = 0$), when the [NiFe] center is in the Ni–C state, and no spin–spin interaction is observed at low temperatures.

The midpoint potentials for *D. gigas* hydrogenase, at pH 7.0, -270 mV for the appearance and -390 mV for the disappearance of the Ni–C signal, are strongly pH dependent [34]. From the amount of “split” and “unsplit” Ni–C state present in the EPR spectrum at low temperature, the midpoint potential of the $[4\text{Fe}4\text{S}]$ cluster was estimated to be -350 mV (-60 mV/pH unit) [34]. It is therefore possible to carefully set the potential to obtain a maximum amount of “unsplit” Ni–C signal at low temperatures, so that pulsed ENDOR and ESEEM experiments on Ni–C can be recorded [54]. Since these potentials are close together and vary between species, it may not always be possible to obtain unsplit Ni–C signals.

The splitting of the EPR spectrum at low temperature can advantageously be used to measure the spin–spin interaction between the [NiFe] center and the reduced proximal $[4\text{Fe}4\text{S}]^+$ cluster. This has been done by Guigliarelli et al. using multifrequency EPR [52] (see Fig. 8). It was found that the spin–spin interaction

observed in EPR is restricted to that between the [NiFe] center and the proximal [4Fe4S]⁺ cluster; the J coupling constant that leads to the best simultaneous fit of the multifrequency EPR spectra is $40 \times 10^{-4} \text{ cm}^{-1}$ [52,53]. In addition, the relative orientations of the g tensors of the [NiFe] center and the [4Fe4S] cluster in terms of three Euler angles have been elucidated from simulations.

From such measurements information about the identity, coupling strength, distance, and even relative orientation of other paramagnetic centers in the enzyme can, in principle, be obtained. This is of utmost importance for understanding the electron transfer between the metal centers in the enzyme. In this respect, more information is still required for understanding the exact electron transfer pathway in the hydrogenases.

3.4. The Light-Induced State Ni-L

In contrast to the Ni-A and Ni-B redox states, the EPR spectrum of the Ni-C state changes when the sample is illuminated with white light at low temperatures (<180 K) [34,55]. Up to three light-induced states have been identified for [NiFe] hydrogenases [35,56], depending on the temperature at which the illumination was performed, the duration of the illumination, and the source of the enzyme. The light-induced states are commonly referred to as Ni-L1, Ni-L2, and Ni-L3, all of which have different g values. The Ni-L states can be annealed back to Ni-C when the temperature is raised, which shows that the photoprocess is fully reversible. For *T. roseopersicina* hydrogenase, the temperature dependence was investigated by EPR spectroscopy, and a recovery to Ni-C upon annealing was observed at temperatures above ~180 K [57]. The g values of the Ni-L states vary slightly depending on the origin of the enzyme. For *D. gigas* hydrogenase, they are 2.264, 2.113, and 2.044 for Ni-L1, 2.293, 2.124, and 2.045 for Ni-L2, and 2.41 and 2.16 for Ni-L3 (the lowest g value could not be determined for Ni-L3). The values are very similar for *D. vulgaris* Miyazaki F, for which only 2 states were observed (see Table 1) [58]. Compared to Ni-C, the largest g value of the Ni-L states is increased, and also the smallest g value has become larger (typically 2.05). The latter change suggests that the Ni-L states can no longer be described as pure $3d_{z^2}$ ground states [46], since for such states ligand field theory indicates that the smallest g value is equal or very close to $g_e = 2.0023$.

The observation of a g_z value significantly larger than g_e has prompted researchers to suggest that the Ni-L states are formal Ni^I $3d^9$ states, in which the unpaired electron resides in the $3d_{x^2-y^2}$ orbital [59,60]. XAS data, however, indicate that the nickel in Ni-L is slightly more reduced than in Ni-C, but the observed edge shift is too small to justify a description as an Ni^I state [41]. The single-crystal EPR data of Ni-L show that the orientation of the g_z principal axis is still parallel to the bond direction from nickel to the axial cysteine (or to the free coordination position) [51], indicating that the wavefunction of the unpaired electron is still dominated by the $3d_{z^2}$ orbital on nickel. Indeed, ligand field considerations show that only a small admixture of the $3d_{x^2-y^2}$ to the $3d_{z^2}$ orbital is sufficient to shift the g_z value from 2.01 to 2.05 [46]. This situation may be compared to the admixture of

some $3d_{z^2}$ orbital to the $3d_{x^2-y^2}$ ground state in blue copper proteins [61], which introduces a large rhombicity in the g values. Whether the Ni-L states can formally be described as Ni^I or Ni^{III} d_{z^2} states is not clear at present. This depends critically on the relative energies of $d_{x^2-y^2}$ and d_{z^2} , and on the ligand orbitals.

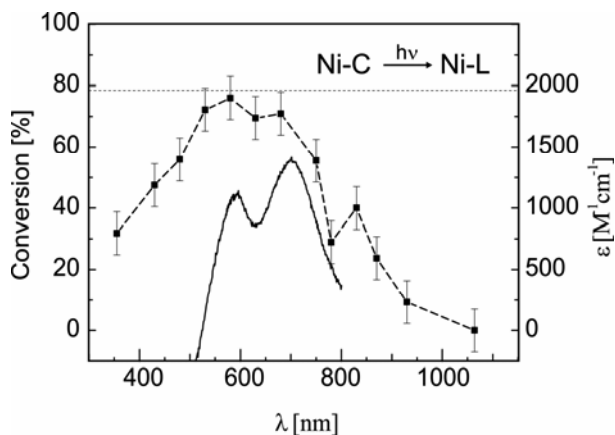


Figure 9. Conversion of Ni-C to Ni-L as derived from EPR decay curves (Ni-C signal decay at $g_x = 2.20$) at different wavelengths of the excitation light (dashed line). Also included is the UV/VIS spectrum of the reduced enzyme (500–800 nm). For further details see [62]. Reproduced with permission [62]. Copyright © 2003, Royal Society of Chemistry.

The action spectrum associated with Ni-C \rightarrow Ni-L2 conversion has recently been investigated by EPR spectroscopy for *D. vulgaris* Miyazaki F [62], and it is illustrated in Figure 9. It turned out that the action spectrum is broad and spans the complete visible range. Nevertheless, some structure was observed with local maxima at 590, 700, and 850 nm. The wavelengths of the first two maxima correspond to those observed in the UV/VIS spectrum of the reduced enzyme, indicating that the conversion process may be a direct process in which the light is absorbed by the [NiFe] center itself. However, based on the available data [62], an additional mechanism according to which the light is absorbed by the nearby [4Fe4S] cluster and the energy is transferred to the [NiFe] center cannot be excluded.

3.5. The Ni-CO State

The [NiFe] hydrogenases are inhibited by CO. Recent x-ray data show that the CO binds at the 6th coordination position (opposite to the axial sulfur) and that it is photolabile [8]. Binding of CO causes a change in the electronic structure and the EPR g -values (2.12, 2.07, 2.02). Addition of ^{13}C [36] results in a large, almost isotropic ^{13}C HFC of 85 MHz. Initially, it was proposed that Ni-C binds the CO. Later work [19] suggested that Ni-L might attach the CO. Best agreement between experimental data and DFT calculations was obtained when the CO is bound to Ni as a π electron acceptor, for which the calculations yield g values of 2.11, 2.06, and

2.00 and a ^{13}C HFC of 72 MHz [63]. So far, a single-crystal EPR study of the Ni-CO state has not been reported.

4. ENDOR AND ESEEM STUDIES OF [NiFe] HYDROGENASE: HYPERFINE STRUCTURE

In this section, hyperfine coupling constants (HFCs) observed by hyperfine resolving techniques such as ENDOR or ESEEM/HYSCORE are discussed. The advantage of these techniques lies in direct determination of the hyperfine coupling parameters, which give information about the spin density distribution over the metal centers and the ligand sphere. Additionally, when applied to single crystals, the techniques also allow elucidation of the principal axes of the hyperfine tensor, which can advantageously be used to determine bond directions or orientations of small molecules bound to or near the active site.

Several specific problems have been addressed using hyperfine spectroscopy on the [NiFe] hydrogenases:

1. Measurement of the HFCs of the metal nuclei by the use of isotopically labeled (^{61}Ni , ^{57}Fe) hydrogenase.
2. Magnitudes of HFCs of ligand nuclei to estimate the spin density distribution.
3. Identification of bridging ligand X by determination of the respective hyperfine data using labeling and exchange procedures.
4. Light sensitivity of Ni-C.
5. Interaction with the protein surrounding.

4.1. Hyperfine Couplings of Metal Nuclei

A question of major importance for the electronic structure of the active center is the spin density distribution over the heterobimetallic [NiFe] center. A direct approach is provided by measuring the spin density at the nickel and at the iron in the paramagnetic states of the enzyme. This has become possible by labeling the enzyme with ^{61}Ni ($I = 3/2$) and ^{57}Fe ($I = 1/2$), respectively. ^{57}Fe ENDOR experiments have shown that the Fe contains a negligible amount of electron spin density in both oxidized states [64]. Similar experiments on the Ni-C state also showed a very small ^{57}Fe HFC (< 1 MHz) [64]. These experiments are in line with iron being in the low-spin Fe^{II} state ($S = 0$) in all redox states of the enzyme. The small amount of spin density at the iron is caused by spin polarization.

^{61}Ni labeling was already employed in early investigations to unambiguously identify the presence of nickel in this class of enzymes [65,66]. For the unready (Ni-A) state of *Methanobacterium thermoautotrophicum* hyperfine coupling constants of $A_x = 21.0$, $A_y = 42.0$, and $A_z = 75.9$ MHz have been elucidated from simulations of cw-EPR experiments [65]. More recently ^{61}Ni labeling of *D. vulgaris* Miyazaki F has been performed and the EPR analysis led to a set of ^{61}Ni HFCs for all paramagnetic states in this hydrogenase [58].

Calculation of the ^{61}Ni HFCs is difficult, in particular for the isotropic part [67]. The data reported recently using DFT [68] are, however, in satisfy-

ing agreement with the available experimental data. This is further evidence that the recent improvements in property calculations of DFT methods [67,69] allows one to reliably predict the observables related to electronic structure of the [NiFe] hydrogenase for small geometry optimized structural models (for details, see [49,63,68,70–81]).

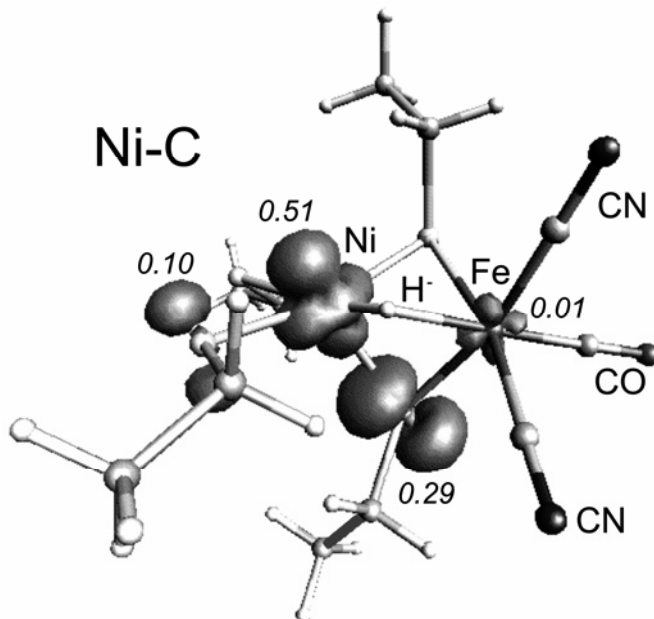


Figure 10. Contour plot of the unpaired spin density distribution ($0.005 e/a_0^3$), DFT (BLYP/DZVP) of a truncated model of the active site in the Ni–C state (Ni^{III} , Fe^{II} , hydride bridge). The Mulliken atomic spin densities are given [76]. In the oxidized ready Ni–B state (OH^- bridge), the spin density at the Ni is almost the same (0.52), at the sulfurs (0.34 and 0.06, axial and equatorial) it is somewhat changed; at Fe and at the bridge it is vanishingly small. For other theoretical results, see [71,78].

The data analysis shows that in the oxidized and the reduced states negligible spin density is found at the Fe. The nickel carries more than 50% of the spin. The remaining spin density is distributed over the (sulfur) ligands of the active site. This is supported by detection of a large ^{33}S HFC in the [NiFe] hydrogenase of *A. vinosum* [82] and also by the ^1H HFCs of the cysteines (see below). A model of the active site used in DFT calculations [76] is shown in Figure 10, depicting the calculated spin density distribution of the Ni–C state ($\text{X} = \text{H}^-$).

4.2. HFCs of Ligand Nuclei

Single-crystal ENDOR studies of the Ni–B state [83] showed two large non-exchangeable ^1H HFCs that could be assigned to the methylene (CH_2) protons of the bridging cysteine axially coordinated to the nickel (Fig. 1). This is in agreement

with earlier ENDOR studies of Ni–B in frozen solutions of *A. vinosum* [84]. The two signals associated with the couplings ($A1 = [17.0, 11.4, 10.9]$ MHz, $A2 = [13.4, 10.1, 10.1]$ MHz) are shown in Figure 11. This finding is in line with the presence of significant spin density at the axial cysteine sulfur. Couplings of similar magnitude are found for Ni–A, [85], and Ni–C [86]. This strongly supports the model of a $\text{Ni}^{\text{III}} d_{z^2}$ ground state with the spin-carrying orbital oriented along an axis pointing toward this sulfur atom. DFT calculations indicate a spin density of up to $\sim 30\%$ at the respective sulfur (Fig. 10); a small amount of spin density is also found at one of the equatorial cysteine sulfur atoms.

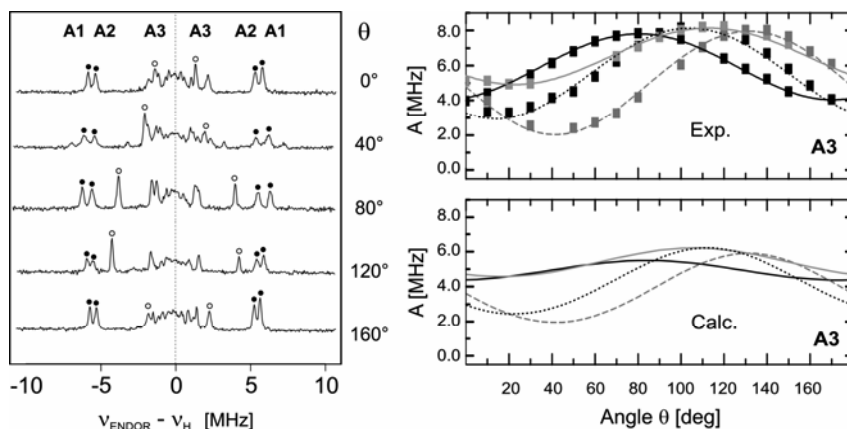


Figure 11. *Left:* Pulse ENDOR spectra for one site of Ni–B in a single crystal of [NiFe] hydrogenase of *D. vulgaris* Miyazaki F (selected traces). The 3 major hyperfine splittings (A1, A2, A3) are indicated by dots. *Right:* angular dependence of the HFC of the exchangeable proton A3 for the four sites in the single crystal (cf. Fig. 6). In the lower panel the orientation dependence of the respective proton HFC obtained from a DFT calculation is shown. Although the absolute magnitude of the HFC is somewhat smaller, the angular dependence is in perfect agreement with the experiment. Based on this comparison, the ^1H HFC has been assigned to the OH^- ligand bridging the Ni and the Fe. The respective proton is located close to the plane of the Ni d_{z^2} orbital. For further details, see [83].

4.3. The Bridging Ligand X

Since it is known that the identity of the 3rd bridging ligand is changed upon activation of the enzyme and also in the catalytic cycle, its clear identification in the different states is of utmost importance. This can be achieved by EPR/ENDOR techniques.

4.3.1. Ni–A/Ni–B

Isotope labeling experiments, using molecular $^{17}\text{O}_2$ for both Ni–A and Ni–B [36], and also H_2^{17}O for Ni–A ($A(^{17}\text{O}) = [5, 7, 20]$ MHz) [87] showed that the

bridging ligand in both states contains an oxygen atom. In the latter study, it was shown that exchange of the bridge to a ^{17}O -labeled one is only possible if a reduction–oxidation cycle is performed, demonstrating the relative inaccessibility of the [NiFe] center in the Ni–A state as compared to the Ni–B state.

The presence of a sulfur species (S^{2-} , SH^- , H_2S) in the bridge between Ni and Fe has been discussed by various authors [6,7,9,21,88]. For the Ni–A and Ni–B states (Fig. 5) this can, however, be excluded based on the ^{17}O data. It is expected that a sulfur-based ligand would lead to an EPR spectrum with different g values. Such minority species with different g values have recently been reported for the oxidized states of *D. vulgaris* Miyazaki F (see, e.g., Fig. 5 and [9,88]). However, up to now the identity of these species remains unclear.

For Ni–A, ENDOR experiments by Fan et al. in combination with deuterium exchange indicated that no exchangeable proton near the [NiFe] center is present [89]. Also with ESEEM, no exchangeable proton has been observed [90]. For Ni–B, the [NiFe] center does have an exchangeable proton, as was found for the enzyme of *A. vinosum* by careful measurement of the g_z signal and examination of the superhyperfine structure [91]. Recently it has been shown that for Ni–A it is also possible to exchange a proton near the active site, by first exchanging the solvent to D_2O , followed by reduction with D_2 gas to remove the bridging ligand and reoxidation to restore an isotopically labeled bridge. With this reduction–reoxidation treatment, a deuterium signal could be observed in ESEEM and HYSORE spectroscopy for Ni–A [80] and an HFC could be estimated. This was fully corroborated by recent single-crystal ENDOR experiments of Ni–A (Ogata et al., unpublished data).

Single-crystal ENDOR experiments of the Ni–B state have been used to elucidate the complete HFC tensor of the proton of the bridging ligand (principal values are $[-8.2, -7.0, +3.6]$ MHz) [83] (see Fig. 11). Early DFT calculations suggested the presence of an OH^- bridge for Ni–B [63,77,92]. By comparison with DFT calculations of the hyperfine tensors in a model of the active site, it was found that Ni–B contains an OH^- bridge and that two possible binding modes for an OH^- exist, and one of them could be favored based on a comparison between experimental and DFT data [83] (see Fig. 11). For the Ni–A state an experimental verification of the identity of the bridging ligand is not yet available. Possible candidates are OH^- , bound in a different conformation, H_2O , or OOH^- [83].

4.3.2. Ni–C

In the Ni–C state, pioneering ENDOR experiments in the groups of Hoffman and Moura have shown for *D. gigas* hydrogenase that a proton with a very large hyperfine coupling constant ($a_{\text{eff}} = 16.8$ MHz) is present, which seems to interact directly with the nickel [89]. This proton was found to be exchangeable, and one of the proposed assignments was that it could belong to an in-plane (i.e., equatorial) hydrogen directly bonded to nickel (e.g., a hydride). This would favor a formal Ni^{III} redox state for Ni–C [89]. A second exchangeable proton with $a_{\text{eff}} \approx 4.4$ MHz was also observed in this work.

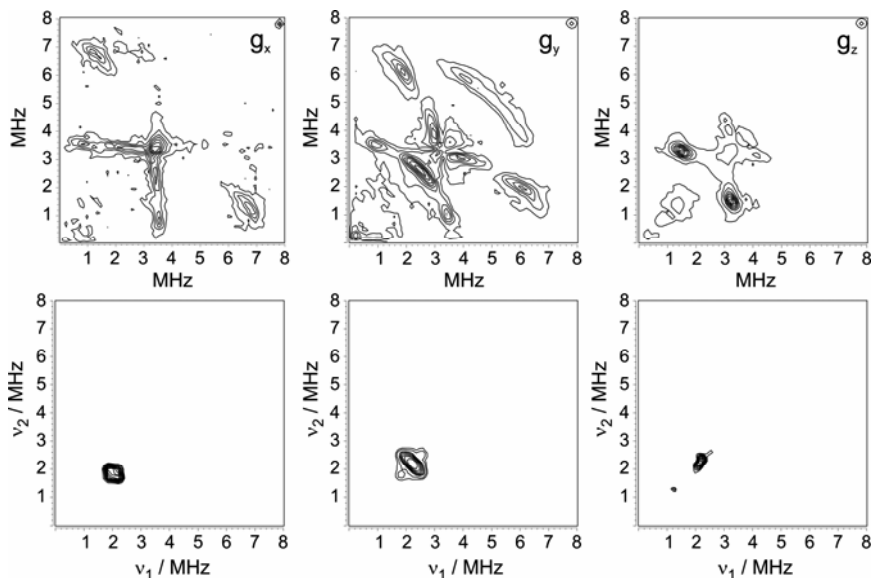


Figure 12. ^2H HYSCORE spectra taken along g_x , g_y , and g_z of the Ni–C and Ni–L1 states of the regulatory hydrogenase of *R. eutropha* in D_2O buffer. The large deuterium coupling of the exchangeable proton (deuteron) observed for Ni–C collapses to a structureless band at the ^2H Larmor frequency (close to 2 MHz), demonstrating the photodissociation of the hydride upon illumination at $T = 77\text{ K}$ in the Ni–C \rightarrow Ni–L1 transition [93]. The process is fully reversible.

In a recent study of the Ni–C state in the RH of *R. eutropha* [23] and in *D. vulgaris* Miyazaki F [86] using orientational selection ENDOR and HYSCORE in combination with H/D exchange, the complete HFC tensor of the exchangeable proton could be determined (principal values are $[\text{+}21.9, \text{−}7.3, \text{−}14.5]$ MHz). The data are only compatible with the presence of a hydrogen in the bridge between Ni and Fe, bound in the equatorial plane of the metal. The obtained tensor is in good agreement with DFT calculations. Illumination of Ni–C removes the signals related to this proton from the spectrum (see Fig. 12). By using the results from the \mathbf{g} tensor analysis in Ni–C [51], this proton is assigned to the hydride in the bridging position, which is derived from the heterolytic splitting of the substrate hydrogen. In these contributions [51,86] a key intermediate in the hydrogenase catalytic cycle has been structurally characterized.

4.4. Light Sensitivity of the Active Intermediate

Illumination of the Ni–C state of all hydrogenases at low temperatures creates a light-induced state (Ni–L) with a significantly different EPR spectrum. Different forms of these species have been reported (Table 1).

In the Ni–L state the large ^1H HFC of the H^- bridge in Ni–C observed by ENDOR and HYSCORE spectroscopy vanishes [23,57,86,89] (see Fig. 12). After annealing of the sample, the Ni–C EPR signal and the large hyperfine interaction is recovered. This observation strongly indicates that the photoconversion of Ni–C to the Ni–L states involves a photodissociation of the bound hydride. With deuterium exchange experiments it was shown that the rich structure in the ^2H region of the HYSCORE spectrum of Ni–C (see Fig. 12) collapses into an unstructured band at the ^2H Larmor frequency [23] for Ni–L. However, signals could still be observed, indicating that upon photodissociation the proton remains in the close vicinity of the center. Since up to three different Ni–L states are observed that are very similar with respect to their spectroscopic properties, it is tempting to speculate that the three equatorial cysteine residues may act as bases and take up the proton. However, at present no experimental data exist to validate this hypothesis. A detailed ENDOR study of the Ni–L states is still lacking [93].

4.5. Interaction of the Active Site with the Protein Surrounding

The [NiFe] center of the hydrogenase is bound to the protein via 4 cysteines, as shown in Figure 1. However, further non-covalent interactions have been identified for this site [3]. The latter include hydrogen bonds to the sulfur and CN^- groups and also hydrophilic and electrostatic interactions. In all catalytic [NiFe] hydrogenases a highly conserved histidine residue is present, which is in a position to form an H-bond to the axial cysteine sulfur with respect to Ni (Fig. 1).

It is interesting to note that 3-pulse ESEEM and HYSCORE spectra of both Ni–A [90] and Ni–B [81] indicated the presence of a nitrogen atom. Since nitrogen is not found in the first ligand sphere of the [NiFe] center, it can only belong to a more remote amino acid ligand, which still interacts with the paramagnetic site. By inspection of the x-ray structure, and determination of the complete hyperfine and quadrupole tensor for ^{14}N ($I = 1$), the nitrogen could be identified as an imidazole (N–H) nitrogen. Moreover, the N–H fragment of the imidazole forms a hydrogen bond to the axial sulfur, which carries a significant amount of electron spin density [81]. The respective histidine ligand is highly conserved in all catalytically active [NiFe] hydrogenases. It is, however, absent in the regulatory hydrogenase of *R. eutropha* [22], where indeed no nitrogen modulations were observed in the ESEEM spectra. It has been discussed that the hydrogen-bonded histidine plays a role in fine tuning the electronic properties of the active site and might therefore have a functional role [81]. The latter point became clear in the Q67H mutant of *R. eutropha* hydrogenase, in which a histidine was introduced in the homologous position of the standard hydrogenases [22]. This mutant showed very similar ESEEM spectra to the standard hydrogenase, indicating that the hydrogen bond had been established in the mutant.

5. DISTANCE STUDIES OF [NiFe] HYDROGENASES

The size of the spin–spin interaction of the [NiFe] center and the [3Fe4S] cluster ($S = 1/2$) is within the range that can be studied by pulse ELDOR spectroscopy. This PELDOR technique allows measurement of the spin–spin interaction and a determination of the effective distance between the two electron spins. Measurements have so far only been performed for *D. vulgaris* Miyazaki F hydrogenase [94] on the as-isolated enzyme (30% Ni–A and 70% Ni–B). The spin delocalization over the [3Fe4S] cluster had to be included for correct data analysis. Spin projection coefficients have been determined that indicate that the largest amount of electron spin density is located on the iron closest to the [NiFe] center.

6. EPR-SILENT STATES

The intermediate states Ni–SU, Ni–SIr, Ni–SIa, and Ni–R, where the number of electrons in the [NiFe] center is even, are commonly denoted as EPR-silent states. X-ray absorption spectroscopy (XAS) experiments are compatible with a formal Ni^{II} in the EPR-silent states (Ni–SU; Ni–SI; Ni–R) [38,41]. With Ni L-edge XAS it was found that the Ni^{II} is most likely in a high-spin state ($S = 1$) [95]. This has so far not been corroborated by EPR spectroscopy, possibly because of the presence of a large zero-field splitting that makes it impossible to detect the signal at X-band frequencies (9 GHz).

The high-spin or low-spin character of the “EPR-silent” Ni^{II} states depends on the energy splitting of the $d_{x^2-y^2}$ and d_{z^2} orbitals (as shown in Fig. 3). When these orbitals are sufficiently close in energy, the high-spin ground state is favored in which each orbital carries one electron. The distortion, which most efficiently brings the $d_{x^2-y^2}$ orbital down in energy, is one toward a trigonal (bi)pyramid [44]. Whether or not the orbitals come close enough to yield the high spin state as the ground state is a question that may have to be addressed by high-field EPR, by which paramagnetic states with a large zero-field splitting can be observed. The possibility to observe the Ni^{II} high-spin states will depend on the magnitude of the zero-field splitting. For a typical value of 3 cm^{-1} , an instrument working at 90 GHz or higher is required.

7. CONCLUSIONS AND OUTLOOK

Based on the single-crystal EPR data collected for the paramagnetic states of the [NiFe] hydrogenase it can be concluded that Ni–A, Ni–B, Ni–C are formally Ni^{III} d^7 species with a $d_{z^2}^1$ ground state ($S = 1/2$). The nickel ion has a square pyramidal coordination geometry, and it is believed that the substrate hydrogen (initially) binds to the sixth (free) coordination position at the Ni. The light-induced Ni–L states have a mixed $d_{z^2}/d_{x^2-y^2}$ ground state. According to crystal field theory, the Ni in Ni–L is in a formal $d^7 \bar{e}_g^1$ Ni^I state. However, the sulfur ligands may lead to strong delocalization of the electrons and a more positive charge at Ni. The iron in the [NiFe] hydrogenase has an octahedral coordination geometry; it is in a d^6 Fe^{II} low-spin state and thus diamagnetic ($S = 0$). This is probably caused by the strong inorganic CO and CN[−] ligands attached to the iron site.

The additional third bridging ligand X between Ni and Fe seems to play an important role for the hydrogenase since it changes its identity in the functional cycle. In the oxidized states this bridging position is occupied by an oxygenic species. For the ready state Ni-B this is a μ -hydroxo (OH^-) [83], while in the unready state Ni-A a final identification has not been achieved. In the activation process of the enzyme the bridging ligand (e.g., OH^- in Ni-B) must be removed. A possible mechanism involves protonation of the OH^- (Ni-B) and subsequent release as water [68], leading to a highly active species (Ni-S1a) that is EPR silent (cf. Fig. 2) [14].

A key intermediate in the reaction cycle is Ni-C, for which it was shown by EPR, ENDOR, and HYSCORE spectroscopy that it carries a μ -hydrido (H^-) bridge between Ni and Fe [23,51,86]. This is most probably directly derived from the substrate hydrogen. In a last reduction step the Ni-R state is reached, which is again EPR silent. The enzyme shuttles between the Ni^{III} (EPR-active) and Ni^{II} (EPR-silent) states in the catalytic cycle (Fig. 2).

Heterolytic H_2 dissociation must occur before the formation of Ni-C in the EPR-silent NiSi states. Mechanistic models for this process have recently been discussed [14,68,79,96]. The paramagnetic light-induced Ni-L states derived from Ni-C have lost the hydride bridge [23,86]. The released proton is attached to a nearby base, possibly one of the sulfurs of the cysteine ligands. The Ni-C to Ni-L conversion process is reversible. The CO-inhibited paramagnetic state Ni-CO is probably derived from the Ni-L state. The CO ligand is attached to the nickel and blocks hydrogen access [8,19]. A similar situation is likely to occur when the enzyme is inhibited by O_2 [9,96]. However, in the case of oxygen additional structural and electronic changes at the cysteines of the enzyme seem to occur as well [5,9].

The EPR studies on the paramagnetic states [98]—together with other investigations using, for example, FTIR and XAS studies that can be applied to the EPR-silent states—have delivered important insight into the catalytic cycle of [NiFe] hydrogenase as well as in activation/deactivation and inhibition of this important enzyme. However, the picture is still far from being complete.

Open questions remain concerning the identity of the bridging ligand in Ni-A. This is important for understanding oxygen sensitivity and inhibition of this enzyme. With the information that the bridging ligand contains oxygen and a proton for both the Ni-A and Ni-B states, likely candidates for the bridge are OH^- and H_2O . However, recent x-ray crystallographic studies on single crystals in the Ni-A state indicate the presence of a bridging ligand, which could be OOH^- [5,9]. The two structures, available for the hydrogenases of *D. fructosovorans* and *D. vulgaris* Miyazaki F, also contain modified cysteines (modeled as oxidized cysteines with an additional oxygen attached to sulfur). Different cysteines were found to be modified in the two structures. Furthermore, it has been discussed that sulfur species (HS^- , S^{2-} , H_2S) might occupy the bridging position in these bacteria [6,7,9,21]. However, a sulfur bridge would probably lead to an [NiFe] center with different EPR characteristics (g values).

It is also unclear what exactly happens to the hydride after it is photodissociated from the [NiFe] center and which amino acid is used as a base in the light-induced Ni–L states. Further studies on Ni–CO structures will provide insight into the mechanism of the catalytic cycle, as CO can inhibit the enzyme only after it has been reduced. The valence of the Ni–CO state is ambiguous, and investigation of the photolability of CO resulting in the same Ni–L structure as that obtained from Ni–C will contribute to understanding the electronic structure of the Ni–L states. Furthermore, the spin multiplicity of the “EPR silent” states is still not known. Though an EPR signal has not been reported, XAS measurements seem to favor a high-spin ground state [95].

The solution of these problems is crucial for formulation of a detailed reliable reaction mechanism that is based on experimental data. More information is also required concerning the H⁺ and e⁻ transfer to the active site of the enzyme and also the H₂ channel (cf. Fig. 1). The influence of the protein surrounding on the structure, function, and dynamics of the hydrogenase has so far been little investigated. Very interesting would also be a comparison of the similarities and differences between the different classes of hydrogenases that use different active sites to convert hydrogen and show substantial differences in enzymatic activity [97,98]. Knowledge of the reaction intermediates is an essential prerequisite for understanding hydrogenase function and for efficiently using this enzyme in future biotechnological processes or as blueprints for designing bioinspired artificial hydrogen catalysts for the production of hydrogen [97].

ACKNOWLEDGMENTS

We gratefully acknowledge Maria E. Pandelia for critically reading and Bärbel Plaschkies and Birgit Deckers for their help with writing the manuscript and for preparing the figures. The authors also want to thank all coworkers who contributed to the results presented in this work and who are named in the respective references. Financial support was provided by the Max Planck Society and the EU (Contract No 516510 (NEST, SOLAR-H)).

REFERENCES

1. Vignais PM, Billoud B, Meyer J. 2001. Classification and phylogeny of hydrogenases. *FEMS Microbiol Rev* **25**:455–501.
2. Volbeda A, Charon M-H, Hatchikian EC, Frey M, Fontecilla-Camps JC. 1995. Crystal structure of the nickel-iron hydrogenase from *Desulfovibrio gigas*. *Nature* **373**:580–587.
3. Volbeda A, Garcin E, Piras C, De Lacey AL, Fernandez VM, Hatchikian EC, Frey M, Fontecilla-Camps JC. 1996. Structure of the [NiFe] hydrogenase active site: evidence for biologically uncommon Fe ligands. *J Am Chem Soc* **118**:12989–12996.
4. Garcin E, Vernede X, Hatchikian EC, Volbeda A, Frey M, Fontecilla-Camps JC. 1999. The crystal structure of a reduced [NiFeSe] hydrogenase provides an image of the activated catalytic center. *Structure* **7**:557–566.
5. Volbeda A, Martin L, Cavazza C, Matho M, Faber BW, Roseboom W, Albracht SPJ, Garcin E, Rousset M, Fontecilla-Camps JC. 2005. Structural difference between the

- ready and unready oxidized states of [NiFe] hydrogenases. *J Biol Inorg Chem* **10**:239–249.
- Higuchi Y, Yagi T, Yasuoka N. 1997. Unusual ligand structure in Ni–Fe active center and an additional Mg site in hydrogenase revealed by high resolution x-ray structure analysis. *Structure* **5**:1671–1680.
 - Higuchi Y, Ogata H, Miki K, Yasuoka N, Yagi T. 1999. Removal of the bridging ligand atom at the Ni–Fe active site of [NiFe] hydrogenase upon reduction with H₂, as revealed by X-ray structure analysis at 1.4 Å resolution. *Structure* **7**:549–556.
 - Ogata H, Mizogushi Y, Mizuno N, Miki K, Adachi S, Yasuoka N, Yagi T, Yamauchi O, Hirota S, Higuchi Y. 2002. Structural studies of the carbon monoxide complex of [NiFe]hydrogenase from *Desulfovibrio vulgaris* Miyazaki F: suggestion for the initial activation site for dihydrogen. *J Am Chem Soc* **124**:11628–11635.
 - Ogata H, Hirota S, Nakahara A, Komori H, Shibata N, Kato T, Kano K, Higuchi Y. 2005. Activation process of [NiFe] hydrogenase elucidated by high resolution x-ray analysis: conversion of the ready to unready state. *Structure* **13**:1635–1642.
 - Montet Y, Amara P, Volbeda A, Vernede X, Hatchikian EC, Field MJ, Frey M, Fontecilla-Camps JC. 1997. Gas access to the active site of Ni–Fe hydrogenases probed by X-ray crystallography and molecular dynamics. *Nat Struct Biol* **4**:523–526.
 - Matias PM, Soares CM, Saraiva LM, Coelho R, Morais J, LeGall J, Carrando MA. 2001. [NiFe] hydrogenase from *Desulfovibrio desulfuricans* ATCC 27774: gene sequencing, three-dimensional structure determination and refinement at 1.8 Å and modelling studies of its interaction with the tetrahaem cytochrome c₃. *J Biol Inorg Chem* **6**:63–81.
 - Bagley KA, Duin EC, Roseboom W, Albracht SPJ, Woodruff WH. 1995. Infrared-detectable groups sense changes in charge density on the nickel center in hydrogenase from *Chromatium vinosum*. *Biochemistry* **34**:5527–5535.
 - Bagley KA, van Garderen CJ, Chen M, Duin EC, Albracht SPJ, Woodruff WH. 1994. Infrared studies on the interaction of carbon monoxide with divalent nickel in hydrogenase from *Chromatium vinosum*. *Biochemistry* **33**:9229–9236.
 - Bleijlevens B, van Broekhuizen F, De Lacey AL, Roseboom W, Fernandez VM, Albracht SPJ. 2004. The activation of the [NiFe]-hydrogenase from *Allochromatium vinosum*: an infrared spectro-electrochemical study. *J Biol Inorg Chem* **9**:743–752.
 - Coremans JMCC, van Garderen CJ, Albracht SPJ. 1992. On the redox equilibrium between H₂ and hydrogenase. *Biochim Biophys Acta* **1119**:148–156.
 - Coremans JMCC, van der Zwaan JW, Albracht SPJ. 1992. Distinct redox behaviour of the prosthetic groups in ready and unready hydrogenase from *Chromatium vinosum*. *Biochim Biophys Acta* **1119**:157–168.
 - George S.J., Kurkin S., Thorneley RNF, Albracht SPJ. 2004. Reactions of H₂, CO, and O₂ with active [NiFe]-hydrogenase from *Allochromatium vinosum*: a stopped-flow infrared study. *Biochemistry* **43**:6808–6819.
 - Kurkin S., George S.J., Thorneley RNF, Albracht SPJ. 2004. Hydrogen-induced activation of the [NiFe]-hydrogenase from *Allochromatium vinosum* as studied by stopped-flow infrared spectroscopy. *Biochemistry* **43**:6820–6831.
 - Happe RP, Roseboom W, Albracht SPJ. 1999. Pre-steady-state kinetics of the reactions of [NiFe]-hydrogenase from *Chromatium vinosum* with H₂ and CO. *Eur J Biochem* **259**:602–608.
 - Roseboom W, De Lacey AL, Fernandez VM, Hatchikian EC, Albracht SPJ. 2006. The active site of the [FeFe]-hydrogenase from *Desulfovibrio desulfuricans*, II: redox prop-

- erties, light sensitivity and CO-ligand exchange as observed via infrared spectroscopy. *J Biol Inorg Chem* **11**:102–118.
21. Bleijlevens B, Buhrke T, van der Linden E, Friedrich B, Albracht SPJ. 2004. The auxiliary protein HypX provides oxygen tolerance to the soluble [NiFe]-hydrogenase of *Ralstonia eutropha* H16 by way of a cyanide ligand to nickel. *J Biol Chem* **279**:46686–46691.
 22. Buhrke T, Brecht M, Lubitz W, Friedrich B. 2002. The H₂ sensor of *Ralstonia eutropha*: biochemical and spectroscopic analysis of mutant proteins modified at a conserved glutamine residue close to the [NiFe] active site. *J Biol Inorg Chem* **7**:897–908.
 23. Brecht M, van Gastel M, Buhrke T, Friedrich B, Lubitz W. 2003. Direct detection of a hydride ligand in the [NiFe] center of the regulatory hydrogenase from *Ralstonia eutropha* in its reduced state by HYSCORE and ENDOR spectroscopy. *J Am Chem Soc* **125**:13075–13083.
 24. Happe RP, Roseboom W, Egert G, Friedrich CG, Massanz C, Friedrich B, Albracht SPJ. 2000. Unusual FTIR and EPR properties of the H₂-activating site of the cytoplasmic NAD-reducing hydrogenase from *Ralstonia eutropha*. *FEBS Lett* **466**:259–263.
 25. Kleihues L, Lenz O, Bernhard M, Buhrke T, Friedrich B. 2000. The H₂ sensor of *Ralstonia eutropha* is a member of the subclass of regulatory [NiFe] hydrogenase. *J Bacteriol* **182**:2716–2724.
 26. Löscher S, Burgdorf T, Buhrke T, Friedrich B, Dau H, Haumann M. 2005. Non-standard structures of the Ni-Fe cofactor in the regulatory and the NAD-reducing hydrogenases from *Ralstonia eutropha*. *Biochem Soc Trans* **33**:25–27.
 27. Pierik AJ, Schmelz M, Lenz O, Friedrich B, Albracht SPJ. 1998. Characterization of the active site of a hydrogen sensor from *Alcaligenes eutrophus*. *FEBS Lett* **438**:231–235.
 28. van der Linden E, Faber BW, Bleijlevens B, Burgdorf T, Bernhard M, Friedrich B, Albracht SPJ. 2004. Selective release and function of one of the two FMN groups in the cytoplasmic NAD⁺-reducing [NiFe]-hydrogenase from *Ralstonia eutropha*. *Eur J Biochem* **271**:801–808.
 29. Lenz O, Friedrich B. 1998. A novel multicomponent regulatory system mediates H₂ sensing in *Alcaligenes eutrophus*. *Proc Natl Acad Sci USA* **95**:12474–12479.
 30. Happe RP, Roseboom W, Pierik AJ, Albracht SPJ, Bagley KA. 1997. Biological activation of hydrogen. *Nature* **385**:126–126.
 31. Frey M, Fontecilla-Camps JC, Volbeda A. 2001. Nickel–iron hydrogenases. In *Handbook of metalloproteins*, Vol. 2, pp. 880–896. Ed A Messerschmidt, R Huber, T Poulos, K Wieghardt. Chichester: John Wiley & Sons.
 32. Volbeda A, Fontecilla-Camps JC. 2005. Structure–function relationship of nickel–iron sites in hydrogenase and a comparison with the active site of other nickel–iron enzymes. *Coord Chem Rev* **249**:1609–1619.
 33. Fernandez VM, Hatchikian EC, Cammack R. 1985. Properties and reactivation of two different deactivated forms of *Desulfovibrio gigas* hydrogenase. *Biochim Biophys Acta* **832**:69–79.
 34. Cammack R, Patil DS, Hatchikian EC, Fernandez VM. 1987. Nickel and iron–sulphur centres in *Desulfovibrio gigas* hydrogenase: ESR spectra, redox properties and interaction. *Biochim Biophys Acta* **912**:98–109.
 35. Medina M, Williams R, Cammack R. 1994. Studies of light-induced nickel EPR signals in *Desulfovibrio gigas* hydrogenase. *J Chem Soc Faraday Trans* **90**:2921–2924.

36. van der Zwaan JW, Coremans JMCC, Bouwens ECM, Albracht SPJ. 1990. Effect of $^{17}\text{O}_2$ and ^{13}CO on EPR spectra of nickel in hydrogenase from *Chromatium vinosum*. *Biochim Biophys Acta* **1041**:101–110.
37. van der Zwaan JW, Albracht SPJ, Fontijn RD, Roelofs YBM. 1986. Electron-paramagnetic-resonance evidence for direct interaction of carbon-monoxide with nickel in hydrogenase from *Chromatium vinosum*. *Biochim Biophys Acta* **872**:208–215.
38. Gu Z, Dong J, Allan CB, Choudhury SB, Franco R, Moura JGG, Moura I, LeGall J, Przybyla AE, Roseboom W, Albracht SPJ, Axley MJ, Scott RA, Maroney MJ. 1996. Structure of the Ni site in hydrogenases by X-ray absorption spectroscopy: species variation and the effects of redox poise. *J Am Chem Soc* **118**:11155–11165.
39. Gu WW, Jacquamet L, Patil DS, Wang HX, Evans DJ, Smith MC, Millar M, Koch S, Eichhorn DM, Latimer M, Cramer SP. 2003. Refinement of the nickel site structure in *Desulfovibrio gigas* hydrogenase using range-extended EXAFS spectroscopy. *J Inorg Biochem* **93**:41–51.
40. Maroney MJ, Bryngelson PA. 2001. Spectroscopic and model studies of the Ni–Fe hydrogenase reaction mechanism. *J Biol Inorg Chem* **6**:453–459.
41. Davidson G, Choudhury SB, Gu Z, Bose K, Roseboom W, Albracht SPJ, Maroney MJ. 2000. Structural examination of the nickel site in *Chromatium vinosum* hydrogenase: redox state oscillation and structural changes accompanying reductive activation and CO binding. *Biochemistry* **39**:7468–7479.
42. De Lacey AL, Hatchikian EC, Volbeda A, Frey M, Fontecilla-Camps JC, Fernandez VM. 1997. Infrared-spectroelectrochemical characterization of the [NiFe] hydrogenase of *Desulfovibrio gigas*. *J Am Chem Soc* **119**:7181–7189.
43. Fichtner C, Laurich C, Bothe E, Lubitz W. 2006. Spectroelectrochemical characterization of the [NiFe] hydrogenase of *Desulfovibrio vulgaris* Miyazaki F. *Biochemistry* **45**:9706–9716.
44. Solomon EI, Pavel EG, Loeb KE, Campochiaro C. 1995. Magnetic circular-dichroism spectroscopy as a probe of the geometric and electronic structure of nonheme ferrous enzymes. *Coord Chem Rev* **144**:369–460.
45. Abragam A, Bleaney B. 1970. *Electron paramagnetic resonance of transition ions*. Oxford: Clarendon Press.
46. Lubitz W, Brecht M, Foerster S, van Gestel M, Stein M. 2003. EPR and ENDOR studies of [NiFe] hydrogenase: contributions to understanding the mechanism of biological hydrogen conversion. *ACS Symp Ser* **858**:128–150.
47. LeGall J, Ljungdahl PO, Moura I, Peck HD, Xavier AV, Moura JGG, Teixeira M, Huynh BH, DerVartanian DV. 1982. The presence of redox-sensitive nickel in the periplasmic hydrogenase from *Desulfovibrio gigas*. *Biochem Biophys Res Comm* **106**:610–616.
48. Geßner C, Trofanchuk O, Kawagoe K, Higuchi Y, Yasuoka N, Lubitz W. 1996. Single crystal EPR study of the Ni center of NiFe hydrogenase. *Chem Phys Lett* **256**:518–524.
49. Cammack R, Patil DS, Aguirre R, Hatchikian EC. 1982. Redox properties of the ESR-detectable nickel in hydrogenase from *Desulfovibrio gigas*. *FEBS Lett* **142**:289–292.
50. Trofanchuk O, Stein M, Gessner Ch, Lenzian F, Higuchi Y, Lubitz W. 2000. Single crystal EPR studies of the oxidized active site of [NiFe] hydrogenase from *Desulfovibrio vulgaris* Miyazaki F. *J Biol Inorg Chem* **5**:36–44.
51. Foerster S, Stein M, Brecht M, Ogata H, Higuchi Y, Lubitz W. 2003. Single crystal EPR studies of the reduced active site of [NiFe] hydrogenase from *Desulfovibrio vulgaris* Miyazaki F. *J Am Chem Soc* **125**:83–93.

52. Guigliarelli B, More C, Fournel A, Asso M, Hatchikian EC, Williams R, Cammack R, Bertrand P. 1995. Structural organization of the Ni and the (4Fe–4S) centers in the active form of *Desulfovibrio gigas* hydrogenase: analysis of the magnetic interactions by electron paramagnetic resonance spectroscopy. *Biochemistry* **34**:4781–4790.
53. Dole F, Medina M, More C, Cammack R, Bertrand P, Guigliarelli B. 1996. Spin–Spin interactions between the Ni site and the [4Fe–4S] centers as a probe of light-induced structural changes in active *Desulfovibrio gigas* hydrogenase. *Biochemistry* **35**:16399–16406.
54. Müller A, Tscherny I, Kappl R, Hatchikian EC, Hüttermann J, Cammack R. 2002. Hydrogenase in the "active" state: determination of *g*-matrix axes and electron spin distribution at the active site by ¹H ENDOR spectroscopy. *J Biol Inorg Chem* **7**:177–194.
55. Cammack R, Fernandez VM, Schneider K. 1988. Nickel in hydrogenases from sulfate-reducing, photosynthetic, and hydrogen-oxidizing bacteria. In *The bioinorganic chemistry of nickel*, pp. 167–190. Ed CRD Lancaster. New York: VCH Publishers.
56. Medina M, Hatchikian EC, Cammack R. 1996. Studies of light-induced nickel EPR signals in hydrogenase: comparison of enzymes with and without selenium. *Biochim Biophys Acta* **1275**:227–236.
57. Whitehead JP, Gurbiel RJ, Bagyinka C, Hoffman BM, Maroney MJ. 1993. The hydrogen binding site in hydrogenase: 35-GHz ENDOR and XAS studies of the Ni–C active form and the Ni–L photoproduct. *J Am Chem Soc* **115**:5629–5635.
58. Foerster S. 2003. EPR spectroscopic investigation of the active site of [NiFe]-hydrogenase: a contribution to the elucidation of the reaction mechanism. PhD dissertation, Technische Universität Berlin.
59. van der Zwaan JW, Albracht SPJ, Fontijn RD, Slater EC. 1985. Monovalent nickel in hydrogenase from *Chromatium vinosum*. *FEBS Lett* **2**:271–277.
60. Sorgenfrei O, Klein A, Albracht SPJ. 1993. Influence of illumination on the electronic interaction between ⁷⁷Se and nickel in active F₄₂₀-non-reducing hydrogenase from *Methanococcus voltae*. *FEBS Lett* **332**:291–297.
61. Gewirth AA, Cohen SL, Schugar HJ, Solomon EI. 1987. Spectroscopic and theoretical studies of the unusual EPR parameters of distorted tetrahedral cupric sites: correlations to X-ray spectral features of core levels. *Inorg Chem* **26**:1133–1146.
62. Fichtner C, van Gastel M, Lubitz W. 2003. Wavelength dependence of the photo-induced conversion of the Ni–C to the Ni–L redox state in the [NiFe] Hydrogenase of *Desulfovibrio vulgaris* Miyazaki F. *Phys Chem Chem Phys* **5**:5507–5513.
63. Stein M, Lubitz W. 2001. DFT calculations of the electronic structure of the paramagnetic states Ni–A, Ni–B and Ni–C of [NiFe] hydrogenase. *Phys Chem Chem Phys* **3**:2668–2675.
64. Huyett JE, Carepo M, Pamplona A, Franco R, Moura I, Moura JGG, Hoffman BM. 1997. ⁵⁷Fe Q-band pulsed ENDOR of the hetero-dinuclear site of nickel hydrogenase: comparison of the NiA, NiB, and NiC states. *J Am Chem Soc* **119**:9291–9292.
65. Albracht SPJ, Graf E-G, Thauer RK. 1982. The EPR properties of nickel in hydrogenase from *Methanobacterium thermoautotrophicum*. *FEBS Lett* **140**:311–313.
66. Moura JGG, Moura I, Huynh BH, Krüger H-J, Teixeira M, DuVarney RC, DerVartanian DV, Xavier AV, Peck Jr HD, LeGall J. 1982. Unambiguous identification of the nickel EPR signal in ⁶¹Ni-enriched *Desulfovibrio gigas* hydrogenase. *Biochem Biophys Res Comm* **108**:1388–1393.
67. Neese F. 2003. Metal and ligand hyperfine couplings in transition metal complexes: the effect of spin-orbit coupling as studied by coupled perturbed Kohn-Sham theory. *J Chem Phys* **118**:3939–3948.

68. Stein M, Lubitz W. 2004. Relativistic DFT calculations of the reaction cycle intermediates of [NiFe] hydrogenase: a model for the enzymatic mechanism. *J Inorg Biochem* **98**:862–877.
69. Neese F. 2001. Prediction of electron paramagnetic resonance g values using coupled perturbed Hartree-Fock and Kohn-Sham theory. *J Chem Phys* **115**:11080–11096.
70. Pavlov M, Siegbahn PEM, Blomberg MRA, Crabtree RH. 1998. Mechanism of H–H activation by nickel-iron hydrogenase. *J Am Chem Soc* **120**:548–555.
71. De Gioia L, Fantucci P, Guigliarelli B, Bertrand P. 1999. Ni–Fe hydrogenases: a density functional theory study of active site models. *Inorg Chem* **38**:2658–2662.
72. Pavlov M, Blomberg MRA, Siegbahn PEM. 1999. New aspects of H₂ activation by nickel–iron hydrogenase. *Int J Quantum Chem* **73**:197–207.
73. Stein M, van Lenthe E, Baerends EJ, Lubitz W. 2001. g- and A-tensor calculations in the zero-order approximation for relativistic effects of Ni complexes (Ni(mnt)₂ and Ni(CO)₃H as model complexes for the active center of [NiFe]-hydrogenase. *J Phys Chem A* **105**:416–425.
74. Stein M, van Lenthe E, Baerends EJ, Lubitz W. 2001. Relativistic DFT calculations of the paramagnetic intermediates of the [NiFe] hydrogenase: implications for the enzymatic mechanism. *J Am Chem Soc* **123**:5839–5840.
75. Stein M, Lubitz W. 2001. The electronic structure of the catalytic intermediate Ni–C in [NiFe] and [NiFeSe] hydrogenases. *Phys Chem Chem Phys* **3**:5115–5120.
76. Stein M. 2001. Insight into the mechanism of [NiFe] hydrogenase by means of magnetic resonance experiments and DFT calculations. PhD dissertation, Technische Universität, Berlin.
77. Stadler C, De Lacey AL, Montet Y, Volbeda A, Fontecilla-Camps JC, Conesa JC, Fernandez VM. 2002. Density functional calculations for modeling the active site of nickel-iron hydrogenases, 2: predictions for the unready and ready states and the corresponding activation processes. *Inorg Chem* **41**:4424–4434.
78. Amara P, Volbeda A, Fontecilla-Camps JC, Field MJ. 1999. A hybrid density functional theory/molecular mechanics study of nickel–iron hydrogenase: investigation of the active site redox states. *J Am Chem Soc* **121**:4468–4477.
79. Bruschi M, Zampella G, Fantucci P, De Gioia L. 2005. DFT investigations of models related to the active site of [NiFe] and [Fe] hydrogenases. *Coord Chem Rev* **249**:1620–1640.
80. van Gastel M, Fichtner C, Neese F, Lubitz W. 2005. EPR experiments to elucidate the structure of the ready and unready states of the [NiFe] hydrogenase of *Desulfovibrio vulgaris* Miyazaki F. *Biochem Soc Trans* **33**:7–11.
81. Goenka Agrawal A, van Gastel M, Gärtner W, Lubitz W. 2006. Hydrogen-bonding affects the [NiFe] active site of *Desulfovibrio vulgaris* Miyazaki F hydrogenase: a hyperfine sublevel correlation spectroscopy and density functional theory study. *J Phys Chem B* **110**:8142–8150.
82. Albracht SPJ, Kröger A, van der Zwaan JW, Uden G, Böcher R, Mell H, Fontijn RD. 1986. Direct evidence for sulfur as a ligand to nickel in hydrogenase: an EPR study of the enzyme from *Wolinella-succinogenes* enriched in ³³S. *Biochim Biophys Acta* **874**:116–127.
83. van Gastel M, Stein M, Brecht M, Schröder O, Lenzian F, Bittl R, Ogata H, Higuchi Y, Lubitz W. 2006. A single-crystal ENDOR and density functional theory study of the oxidized states of the [NiFe] hydrogenase from *Desulfovibrio vulgaris* Miyazaki F. *J Biol Inorg Chem* **11**:41–51.

84. Geßner C, Stein M, Albracht SPJ, Lubitz W. 1999. Orientation-selected ENDOR of the active center in *Chromatium vinosum* [NiFe] hydrogenase in the oxidized "ready" state. *J Biol Inorg Chem* **4**:379–389.
85. Ogata H, et.al. 2006. unpublished data.
86. Foerster S, van Gastel M, Brecht M, Lubitz W. 2005. An orientation-selected ENDOR and HSCORE study of the Ni–C active state of *Desulfovibrio vulgaris* Miyazaki F hydrogenase. *J Biol Inorg Chem* **10**:51–62.
87. Carepo M, Tierney DL, Brondino CD, Yang TC, Pamplona A, Telsler J, Moura I, Moura JGG, Hoffman BM. 2002. ^{17}O ENDOR detection of a solvent-derived Ni–(OH_x)–Fe bridge that is lost upon activation of the Hydrogenase from *Desulfovibrio gigas*. *J Am Chem Soc* **124**:281–286.
88. Vincent KA, Belsey NA, Lubitz W, Armstrong FA. 2006. Rapid and reversible reactions of [NiFe] hydrogenases with sulfide. *J Am Chem Soc* **128**:7448–7449.
89. Fan C, Teixeira M, Moura JGG, Moura I, Huynh BH, LeGall J, Peck Jr HD, Hoffman BM. 1991. Detection and characterisation of exchangable protons bound to the hydrogen-activation nickel site of *desulfovibrio gigas* hydrogenase: a ^1H and ^2H Q-Band ENDOR study. *J Am Chem Soc* **113**:20–24.
90. Chapman A, Cammack R, Hatchikian EC, McCracken J, Peisach J. 1988. A pulsed EPR study of redox-dependent hyperfine interactions for nickel centre of *Desulfovibrio gigas* hydrogenase. *FEBS Lett* **242**:134–138.
91. Bleijlevens B, Faber BW, Albracht SPJ. 2001. The [NiFe] hydrogenase from *Allochromatium vinosum* studied in EPR-detectable states: H/D exchange experiments that yield new information about the structure of the active site. *J Biol Inorg Chem* **6**:763–769.
92. Stadler C, De Lacey AL, Hernandez B, Fernandez VM, Conesa JC. 2002. Density functional calculations for modeling the oxidized states of the active site of nickel-iron hydrogenases, 1: verification of the Method with Paramagnetic Ni and CO complexes. *Inorg Chem* **41**:4417–4423.
93. Brecht M. 2001. Hochfeld- und Puls-EPR-Untersuchungen an den Kofaktoren von [NiFe]-Hydrogenasen: Beiträge zur Klärung des Mechanismus der biologischen Wasserspaltung. PhD dissertation, Technische Universität, Berlin.
94. Elsässer C, Brecht M, Bittl R. 2002. Pulsed electron-electron double resonance on multinuclear metal centers: assignment of spin projection factors based on the dipolar interaction. *J Am Chem Soc* **124**:12606–12611.
95. Wang H, Patil DS, Gu W, Jacquamet L, Friedrich S, Funk T, Cramer SP. 2001. L-edge X-ray absorption spectroscopy of some Ni enzymes: probe of Ni electronic structure. *J Elec Spec Rel Phen* **114–116**:855–863.
96. Lubitz W, van Gastel M, Gärtner W. 2007. Nickel iron hydrogenases. In *Metal ions in life sciences*. Ed A Sigel, H Sigel, RKO Sigel. Chichester: John Wiley & Sons. In press.
97. Morris RH. 2006. Hydrogenase and model complexes. In *Concepts and models in bio-inorganic chemistry*, pp. 331–362. Ed H-B Kraatz, N Metzler-Nolte. Weinheim: Wiley-VCH.
98. Lubitz W, Reiijerse E, van Gastel M. 2007. [NiFe] and [FeFe] hydrogenases studied by advanced magnetic resonance techniques. *Chem Rev* **107**:4331–4365.

UNIQUE SPECTROSCOPIC FEATURES AND ELECTRONIC STRUCTURES OF COPPER PROTEINS: RELATION TO REACTIVITY

Jungjoo Yoon and Edward I. Solomon*

*Department of Chemistry, Stanford University,
Stanford, California*

Copper active sites play a major role in a wide range of biological processes. These include long-range electron transfer, binding, activation, and two-/four-electron reduction of dioxygen, and two-electron reduction of nitrous oxide. Traditionally, copper sites have been classified into three types based on their EPR features: the type 1 “blue,” the type 2 “normal,” and the type 3 “coupled binuclear” sites. However, more recent discoveries of the mixed-valent binuclear Cu_A , the trinuclear Cu cluster in the multicopper oxidases, and the tetranuclear Cu_Z sites show that biological copper centers are even more diverse than previously believed. In this review, EPR and other spectral features of the different copper active sites are developed and compared. The origins of the unique spectroscopic features are discussed with respect to the novel geometric and electronic structures that are intimately coupled to their catalytic functions. High covalency is shown to activate specific pathways for long-range electron transfer and exchange interactions between copper centers to control the two vs. one electron activation of O_2 for different chemistries and the four-electron reduction of O_2 to H_2O . In addition, electron delocalization between mixed-valent copper centers can lower reorganization energy and activate copper clusters for catalysis.

1. INTRODUCTION

Copper proteins are involved in a wide range of biological oxidation-reduction processes. These include long-range electron transfer, dismutation of superoxide, reduction of nitrite and nitrous oxide, and reversible binding, transport, activation,

and $2e^-$ or $4e^-$ reduction of dioxygen to peroxide or water that are coupled to substrate oxidation or proton pumping [1]. This diversity can be attributed to the unique geometric and electronic structures of the copper active sites that are tailored for their specific functions [2,3].

Table 1. EPR Parameters of the Representative Copper Active Sites in Biology

Cu sites ^a	Type	g-values ^b		A values ^c ($\times 10^{-4} \text{ cm}^{-1}$)		Notes
		g_{\parallel}	g_{\perp}	A_{\parallel}	A_{\perp}	
D _{9h} CuCl ₄ ²⁻	Type 2	2.221	2.040	164	35	
Plastocyanin	Type 1	2.226	2.053	63	<17	
Cytochrome <i>c</i> oxidase ^d	Cu _A	2.180	2.015	39	22	7-line hyperfine
Nitrous oxide reductase	Cu _A	2.178	2.022	39	23	7-line hyperfine
	Cu _Z	2.16	2.04	61		
Hemocyanin, oxy-form	Type 3			24		5:2 mixture
						No EPR signal ($2I > -400 \text{ cm}^{-1}$)
Peptidylglycine	Type 2	2.288	2.055	157	11	Two unresolved type 2 centers
α -Hydroxylating monooxygenase (PHM)						
PHM, NO ₂ ⁻ adduct	Type 2	2.265	2.060	160	10	Two perturbed type 2 centers
		2.298	2.060	165	10	
Tree laccase	Type 1	2.30	2.05	43		
	Type 2	2.24	2.05	206		
Tree laccase, Native intermediate	Type 1	2.30	2.05	43		
	Type 2 + Type 3 ^e	2.15	1.86, 1.65			Type 2 + type 3 signal only observable at low temperature (<20 K) and high radiant power (>0.1 mW)

^a Each entry refers to its resting oxidized form, except when otherwise stated. ^b g_{\perp} refers to the average of g_x and g_y , except for the native intermediate of tree laccase. ^c A_{\perp} refers to the average of A_x and A_y .

^d Also contains a Cu_B center, which is EPR silent due to antiferromagnetic coupling to an Fe(III) center in the binuclear heme a₃-Cu_B active site ($S_{\text{tot}} = 2$). ^e The three Cu centers of the type 2 and type 3 sites are antiferromagnetically coupled, with an $S_{\text{tot}} = 1/2$ ground state.

As listed in Table 1, biological copper active sites have been classified by their unique spectral features relative to those of the normal Cu(II) complexes, which typically have tetragonal ligand field environments [4,5]. Classically, these have been divided into type 1 (T1), type 2 (T2), and type 3 (T3) sites [6]. The T2 or “normal” copper sites exhibit spectral features similar to those of small-molecule inorganic Cu(II) complexes. The T2 site exhibits an electron paramagnetic reso-

nance (EPR) signal with $g_{\parallel} > g_{\perp} > 2.0023$ with a four-line hyperfine splitting ($2I + 1$ with $I = 3/2$ for $^{63,65}\text{Cu}$) in the range of $A_{\parallel} \sim 150\text{--}250 \times 10^{-4} \text{ cm}^{-1}$ and $A_{\perp} < 35 \times 10^{-4} \text{ cm}^{-1}$, indicative of a tetragonal Cu(II) center with an $S_{\text{tot}} = 1/2$ ground state reflecting a half-occupied $d_{x^2-y^2}$ orbital. The T2 site often does not have a distinctive feature in its absorption and circular dichroism (CD) spectra, although a number of weak d-d bands are observed in the magnetic circular dichroism (MCD) spectrum. T2 sites are found in Cu/Zn superoxide dismutase [7–9] and nitrite reductase [10], where dismutation of superoxide into dioxygen and hydrogen peroxide and $1e^-$ reduction of nitrite to nitrous oxide occur, respectively. In amine oxidase and galactose oxidase, the T2 sites are present together with covalently bound organic cofactors, topaquinone, and thioether-linked Cys–Tyr ligand, respectively, that are formed in posttranslational modifications of a Tyr residue catalyzed in the presence of both the copper and molecular dioxygen [11–13]. Topaquinone in amine oxidase is involved in substrate oxidation [14], while the Cys–Tyr ligand in galactose oxidase is oxidized to a radical that together with the T2 Cu(II) center catalyze alcohol oxidation [15]. The fully oxidized active form of galactose oxidase is described as a free radical-coupled copper center where the antiferromagnetic coupling of the Tyr radical and the T2 Cu(II) center leads to stabilization of the EPR-silent diamagnetic ground state with singlet–triplet splitting of $>200 \text{ cm}^{-1}$ [13].

Alternatively, the T1 or “blue” copper site exhibits a very small $A_{\parallel} \sim 43\text{--}95 \times 10^{-4} \text{ cm}^{-1}$. It originates from a highly covalent Cu $d_{x^2-y^2}$ –Cys S π bond that is evidenced by an extremely intense absorption band at $\sim 600 \text{ nm}$ with $\epsilon \sim 5000 \text{ M}^{-1} \text{ cm}^{-1}$, which is responsible for its deep blue color [16]. T1 sites are found in the blue copper proteins, such as plastocyanin, azurin, stellacyanin, and cucumber basic blue, and in the multicopper oxidases, such as tree and fungal laccases, ascorbate oxidase, ceruloplasmin, Fet3p, CueO, and CotA, where it functions in inter- or intramolecular electron transfer. The T3 or “coupled binuclear” copper site is characterized by the lack of an EPR signal [1,17]. The T3 site is composed of two Cu(II) centers that are covalently bridged by a peroxide or hydroxide ligand. Due to the covalent overlap between the bridging ligand donor orbitals and two Cu(II) centers, an efficient superexchange pathway mediates strong antiferromagnetic coupling that results in a diamagnetic ground state with $S_{\text{tot}} = 0$. In contrast to the T2 site, the T3 site does exhibit a number of d-d bands in the CD spectrum due to the low-symmetry environment of each Cu center. T3 sites are found in hemocyanin that is involved in binding and transport of dioxygen, and in tyrosinase and catechol oxidase that activate dioxygen for hydroxylation of phenolic substrates (by tyrosinase only) and oxidation of catechol substrates (by both enzymes).

It is interesting to note that in dopamine β -hydroxylase and peptidylglycine α -hydroxylating monooxygenase, two T2 copper centers are present that are magnetically non-interactive but required for catalysis, despite $\sim 11 \text{ \AA}$ Cu–Cu separation and negligible magnetic exchange coupling [18–20]. Thus, these are termed “non-coupled binuclear” Cu sites, contrary to the “coupled binuclear” T3 Cu sites. Dopamine β -hydroxylase and peptidylglycine α -hydroxylating monooxygenase activate dioxygen for water abstraction in the hydroxylation of substrate. The non-coupled nature of these binuclear active sites appears to be closely related to their

ability to form and stabilize a reactive $1e^-$ reduced intermediate species at one Cu center for the H-atom abstraction reaction and to complete the reaction by obtaining the second electron from the other Cu center [14,18,21].

Different types of copper sites are also found in clusters, as in the trinuclear copper cluster site of the multicopper oxidases that are comprised of a T2 and a T3 site [1]. With the involvement of a T1 center ~ 13 Å away, the trinuclear copper cluster site catalyzes the $4e^-$ reduction of dioxygen to water in the multicopper oxidases. Interestingly, while this site exhibits spectral features of isolated T2 and T3 centers in the resting oxidized state, its $4e^-$ reduced oxygen intermediate, called the native intermediate, exhibits unusual spectral features that derive from a spin-frustrated doublet ground state due to μ_3 -oxo-bridge-mediated superexchange interactions among the three Cu(II) centers [22].

In addition to the T1, T2, and T3 sites, recent studies on cytochrome *c* oxidase [23,24] and nitrous oxide reductase [25,26] have revealed new classes of copper sites. These are the binuclear Cu_A and the tetranuclear Cu_Z sites, both of which have mixed-valent $S_{tot} = 1/2$ ground states. (A Cu_B center is also found in the cytochrome *c* oxidase. It forms a binuclear heme a_3 - Cu_B active site where $4e^-$ reduction of O_2 occurs. However, due to the lack of a distinctive spectral feature, studies on the Cu_B center have been limited. Interestingly, it has a covalently linked Tyr residue bound to a His ligand, which is believed to have an important role in the reactivity [27])

The Cu_A site is found in both cytochrome *c* oxidase and nitrous oxide reductase, and is responsible for rapid electron transfer in these enzymes. This binuclear copper site has two bridging Cys S ligands and a short Cu–Cu distance of ~ 2.4 Å. Both the thiolate bridges and a direct Cu–Cu bonding interaction lead to electron delocalization in the low-symmetry protein environment. As a consequence, a seven-line hyperfine pattern is observed in an $S_{tot} = 1/2$ EPR signal in the oxidized form, which indicates a class III mixed-valence system due to spin delocalization in the Cu(+1.5)Cu(+1.5) site ($2nI + 1 = 7$ with $I_{Cu} = 3/2$ and $n = 2$). (Note that in the Robin and Day classification of mixed-valence systems, the extra electron is completely localized in class I, partially delocalized in class II, and completely delocalized in class III [28].) As with the T1 copper center, the Cu_A copper centers have highly covalent Cu–S Cys bonding interactions, evidenced by the low-energy Cys S \rightarrow Cu(II) charge transfer (CT) transitions that are responsible for its purple color.

The Cu_Z site in nitrous oxide reductase catalyzes the $2e^-$ reduction of the greenhouse gas nitrous oxide to dinitrogen and water [29]. Recently solved crystal structures of nitrous oxide reductase have shown that this is a μ_4 -sulfide bridged tetranuclear copper cluster site with seven His ligands and a water-derived ligand [25,26]. In particular, EPR, MCD, and x-ray absorption spectroscopy (XAS) experiments have demonstrated that, while this site in its resting state has an $S_{tot} = 1/2$ ground state with formally one Cu(II) and three Cu(I) centers, the spin is partially delocalized over all four copper centers via the μ_4 -sulfide bridge, rendering it to be a partially delocalized, class II mixed-valent tetranuclear copper site [30–32].

In this review, key spectral features of the copper sites summarized above are presented along with descriptions of their physical origins. In addition to EPR, other spectroscopic methods, such as absorption, CD, variable-field variable-temperature (VTVH) MCD, resonance Raman (rRaman), and XAS, and density functional theory (DFT) will also be presented in order to provide the complementary information necessary for understanding the geometric and electronic structures of these sites.

2. MONONUCLEAR BLUE “TYPE 1” CU SITES

Since the early spectral characterization of copper proteins, the blue copper sites have attracted a major amount of spectroscopic interest [6,33]. These sites exhibit EPR signals at $g_{\parallel} > g_{\perp} > 2.0023$ (Fig. 1c; plastocyanin: $g_z, g_y, g_x = 2.226, 2.059, 2.047$), indicating a $d_{x^2-y^2}$ ground state similar to those of the normal tetragonal Cu(II) complexes. However, the parallel hyperfine splitting is extremely small, reduced by more than a factor of two relative to that of tetragonal Cu(II) complexes (Fig. 1c; plastocyanin: $63 \times 10^{-4} \text{ cm}^{-1}$ vs. CuCl_4^{2-} : $164 \times 10^{-4} \text{ cm}^{-1}$). In addition, there is an intense absorption band at $\sim 600 \text{ nm}$ ($\sim 16000 \text{ cm}^{-1}$) with $\epsilon \sim 5000 \text{ M}^{-1} \text{ cm}^{-1}$, in contrast to the weak d-d transitions of tetragonal Cu(II) complexes.

The crystal structures of blue copper proteins show that the T1 site is in a trigonally distorted tetrahedral environment (Fig. 1a) [34–40]. The trigonal plane has a very short ($\sim 2.1 \text{ \AA}$) Cu–S(Cys) and two typical ($\sim 2.0 \text{ \AA}$) Cu–N His bonds. An additional axial thioether ligand is usually present with a long Cu–S(Met) bond ($\sim 2.8 \text{ \AA}$), although the Met residue is replaced by a non-ligating one, such as Lys or Phe, in some tree and fungal laccases [41–44].

Single-crystal EPR studies on plastocyanin first defined the orientation of g_{\parallel} in the distorted tetrahedral structure of the blue copper site [45]. It showed that the g_{\parallel} EPR signal, with the four-line hyperfine pattern, is observed when the crystal axis corresponding to the long molecular Cu(II)–S(Met) bond is approximately parallel to the field direction, while g_{\perp} , with a broad derivative EPR signal without resolvable hyperfine components, is observed when this crystal axis is approximately 90° off the field direction. Thus, the singly occupied $d_{x^2-y^2}$ orbital is found to be perpendicular to the long Cu–S(Met) bond and close to the plane of the strong S(Cys) and two N(His) ligands.

One of the unique spectroscopic features of the T1 site, as mentioned above, is the small A_{\parallel} compared to that of the normal Cu(II) centers. There are three contributions to account for the metal hyperfine coupling, which are the Fermi contact (A_F), the spin dipolar (A_S), and the orbital dipolar (A_L) terms. The Fermi contact term is isotropic ($A_{\parallel} = A_{\perp}$) and associated with unpaired electron spin density at the nucleus. In a Cu(II) center, this contribution involves the unpaired $3d_{x^2-y^2}$ electron spin polarizing the inner 1s, 2s, and 3s core electron pairs (mostly 2s) to produce a net negative spin density at the nucleus. The spin dipolar term is anisotropic ($A_{\perp} = -1/2A_{\parallel}$) and involves the electron spin, averaged over the shape of its 3d orbital

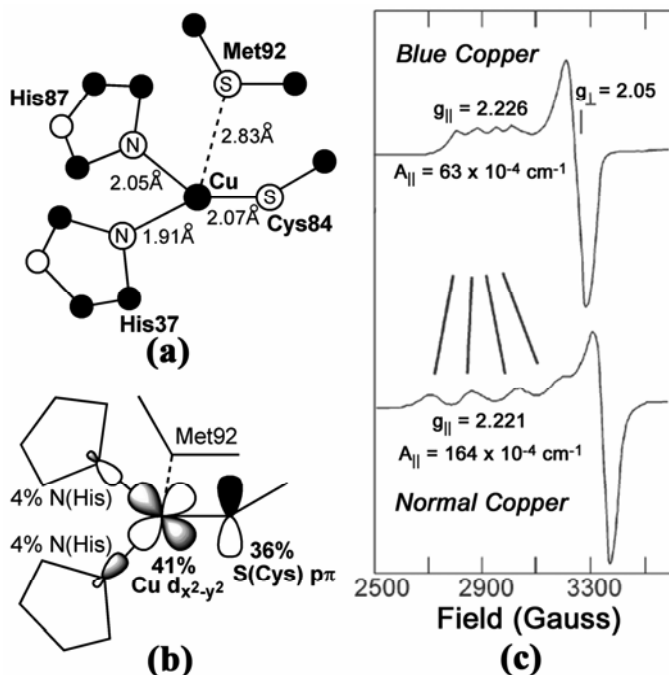


Figure 1. (a) Crystal structure (1PLC, resolution 1.33 Å); (b) ground state wavefunction; and (c, top) X-band EPR spectrum of poplar plastocyanin; (c, bottom) X-band EPR spectrum of a normal copper complex, $D_{4h} [\text{CuCl}_4]^{2-}$.

dipolar coupling to the nuclear spin on the metal center. Finally, the orbital dipolar term is also anisotropic ($A_{\perp} \neq A_{\parallel}$) and involves the electron orbital angular momentum, which is derived from spin-orbit mixing of excited states into the d-electron ground state, dipolar coupling with the nuclear spin on the metal. It is proportional to the g -value deviations from 2.0023. For the D_{4h} CuCl_4^{2-} complex, the contributions from these terms are estimated as: $A_F = -123 \times 10^{-4} \text{ cm}^{-1}$, $A_S = -155 \times 10^{-4} \text{ cm}^{-1}$, and $A_L = +114 \times 10^{-4} \text{ cm}^{-1}$, yielding a total of $A_{\parallel} = -164 \times 10^{-4} \text{ cm}^{-1}$. Here, the A_F and A_S terms are reduced from their values for free Cu(II) ions, $-170 \times 10^{-4} \text{ cm}^{-1}$ and $-230 \times 10^{-4} \text{ cm}^{-1}$, respectively, by covalency from electron delocalization from the Cu 3d orbital to the Cl^- ligands (Cu = 61% and Cl^- = 39%, as indicated by Cu L-edge XAS [46]); the A_L term already contains covalency as it is obtained from the experimental g -values.

Initially, the small A_{\parallel} value of the blue Cu sites had been attributed to the Cu $4p_z$ mixing into the Cu $3d_{x^2-y^2}$ orbital due to the distorted tetrahedral structure of the blue copper site. The spin dipolar interaction of the Cu nuclear spin with the electron in the Cu $4p$ orbital would oppose that of an electron spin vector in the $d_{x^2-y^2}$ orbital [47]. The experimental probe of the $4p$ mixing into the $d_{x^2-y^2}$ or-

bital was conducted via Cu K-edge XAS [48,49]. In Cu K-edge XAS, a weak low-energy peak is observed at 8979 eV, which corresponds to a transition from the Cu 1s orbital to the singly occupied $3d_{x^2-y^2}$ orbital [4]. Since $s \rightarrow d$ is electric dipole forbidden, the dominant electric dipole intensity mechanism contributing to this transition will be $s \rightarrow p$, therefore reflecting the 4p character mixed into the $3d_{x^2-y^2}$ orbital due to the distorted tetrahedral geometry of the blue copper site. In the orientation-averaged XAS edge spectra of plastocyanin, the 8979 eV feature is more intense than that of the D_{4h} $CuCl_4^{2-}$, indicating significant 4p mixing in the blue copper center. However, this 4p mixing in the 8979 eV feature actually originates from the $4p_x/p_y$ orbitals, and not $4p_z$, mixing into the Cu $3d_{x^2-y^2}$ orbital, as determined by single-crystal XAS [48]. The spin dipolar interaction of an electron averaged over the $4p_x$ and $4p_y$ orbitals with the nuclear spin of the copper would complement that of an electron in the $3d_{x^2-y^2}$ orbital, and therefore increase, not decrease, the hyperfine coupling. Thus, the Cu K-edge XAS studies demonstrated that the Cu $4p_z$ mixing model for the small $A_{||}$ value is not valid.

Alternatively, covalent delocalization of the electron onto the ligand will reduce the electron hyperfine coupling to the nuclear spin on the Cu atom and would also lower the A_F and A_S contributions in hyperfine coupling. The quantitative ground state description obtained from DFT calculations shows that the blue copper site is significantly more covalent than $CuCl_4^{2-}$ (41 vs. 61% Cu $d_{x^2-y^2}$) and that the covalency of the blue copper center is anisotropic involving the thiolate–Cu(II) bond [50] (Fig. 1b). These descriptions have been evaluated through Cu L-edge [46] and S K-edge XAS studies [49]. The Cu L-edge spectroscopy allows determination of the Cu d character from an electric dipole-allowed transition ($p \rightarrow d$) from the localized Cu 2p core level to the delocalized singly occupied molecular orbital (MO) based on $3d_{x^2-y^2}$ at ~ 930 eV. The S K-edge spectroscopy allows determination of the ligand S character from an electric dipole allowed transition ($s \rightarrow p$) from the localized S 1s core to the singly occupied MO at ~ 2470 eV [4,51,52]. The intensity of the Cu L-edge for plastocyanin is significantly less than that of D_{4h} $CuCl_4^{2-}$, indicating the blue copper site has less 3d character (Fig. 1b; 41 vs. 61% Cu $d_{x^2-y^2}$) and is therefore more covalent. Complementarily, the intensity of the S K-edge for plastocyanin is ~ 2.5 times more intense than that for a more normal five-coordinate Cu(II)–S(thiolate) model complex (38 vs. 15% S 3p) [53]. In azurin, an S 3p character of $\sim 45\%$ has been determined [54]. Thus, these XAS data demonstrate that the increased delocalization of the electron spin onto the thiolate ligand reduces the electron spin interaction with the nuclear spin on the copper, resulting in the small $A_{||}$ value.

The highly covalent Cu–S bond is also reflected in the intense absorption band at ~ 600 nm. Low-temperature MCD shows that this ~ 600 nm band is associated with a ligand-to-metal CT transition, and not a d–d transition, as its MCD intensity relative to absorption intensity (i.e., C_0/D_0 ratio) is small (~ 0.01) compared to that of the d–d transitions (~ 0.1) [55]. [Note that the MCD C-term intensity is governed by the spin–orbit coupling parameter, and, therefore, the metal-centered d–d bands typically have a higher C_0/D_0 ratio than the ligand-centered CT bands ($\xi[Cu(II)] = 830 \text{ cm}^{-1}$ vs. $\xi[O/N] = 60\text{--}70 \text{ cm}^{-1}$).] This CT band is the Cys S $\pi \rightarrow$ Cu $d_{x^2-y^2}$ CT

transition that originates from the short Cu–S bond. The σ CT transition is observed as a weak higher-energy shoulder on the intense π CT band. The intense π /weak σ CT intensity pattern of the blue copper site requires that the Cu $d_{x^2-y^2}$ orbital be oriented such that its lobes bisect the Cu–S(Cys) bond, giving highly covalent π overlap with the thiolate S ligand.

Upon perturbation of the geometry of the blue copper center, from plastocyanin to cucumber basic blue to nitrite reductase (a green protein), the Cys S $\pi \rightarrow$ Cu $d_{x^2-y^2}$ CT intensity decreases while the Cys S $\sigma \rightarrow$ Cu $d_{x^2-y^2}$ CT intensity increases [56–58]. This indicates that the Cu $d_{x^2-y^2}$ orbital is rotated from a π to σ bonding interaction with the S(Cys) ligand. This dramatic spectral change is associated with a tetragonal distortion of the ligand field of the blue copper site (i.e., blue shift of d–d bands in the MCD spectra) and also weakening of the Cu(II)–S(Cys) bond (i.e., decrease in the associated vibrational frequency from 403 to 394 to 383 cm^{-1} in the rRaman spectra) in going from plastocyanin to cucumber basic blue to nitrite reductase. The strengthening of the axial Cu–S(Met) bond, weakening of the equatorial Cu–S(Cys) bond, and tetragonal Jahn–Teller type distortion have been termed the “coupled distortion” model for the geometric and electronic structures of the blue copper related sites [59]. In the EPR spectrum of nitrite reductase, a rhombic splitting is observed ($\Delta g_{\perp} = 0.04$) [60] that is larger than that for plastocyanin ($\Delta g_{\perp} = 0.017$) [45]. This is the result of the increased ligand field strength along the axial z -direction in nitrite reductase [61], which increases the rhombic d_{z^2} mixing into the $d_{x^2-y^2}$ based singly occupied MO ($\sim 1.8\%$) [59].

The unique spectral features of the blue copper sites reflect geometric and electronic structures that activate the metal site for reactivity. The highly covalent Cu–S Cys thiolate bond activates the superexchange pathways associated with this ligand for long-range electron transfer to specific acceptor sites in or on the protein. The protein environment effects control whether the thiolate is involved in a π (plastocyanin) or σ (nitrite reductase) bonding interaction with the copper, and thus the geometric and electronic structures of this active site.

3. BINUCLEAR Cu_A SITES

As with the blue copper sites, the Cu_A sites found in cytochrome c oxidase (CcO) and nitrous oxide reductase (N_2OR) also have highly covalent Cu–S(Cys) bonding interactions and are involved in long-range electron transfer. The Cu_A site was first observed in CcO [62], but its low g_{\parallel} value of 2.18 with unresolved hyperfine lines could not be readily described within the T1, T2, or T3 copper classification [6,63]. A major advance came when S-band EPR spectroscopy was applied to reduce the contribution from g -strain to the EPR linewidths [64–66]. As a result, the previously unresolved Cu hyperfine structure was observed on the Cu_A signal with $A_{\parallel} \sim 40 \times 10^{-4} \text{ cm}^{-1}$. In particular, seven equally spaced Cu hyperfine lines for all g -values were resolved from the S-band EPR spectrum of the Cu_A site in *Pseudomonas stutzeri* N_2OR (Fig. 2b). The seven-line pattern is indicative of a binuclear Cu site with one unpaired electron equally shared between two Cu atoms ($2nI + 1 = 7$ with $n = 2$ and $I_{\text{Cu}} = 3/2$), forming a mixed-valent binuclear site with a

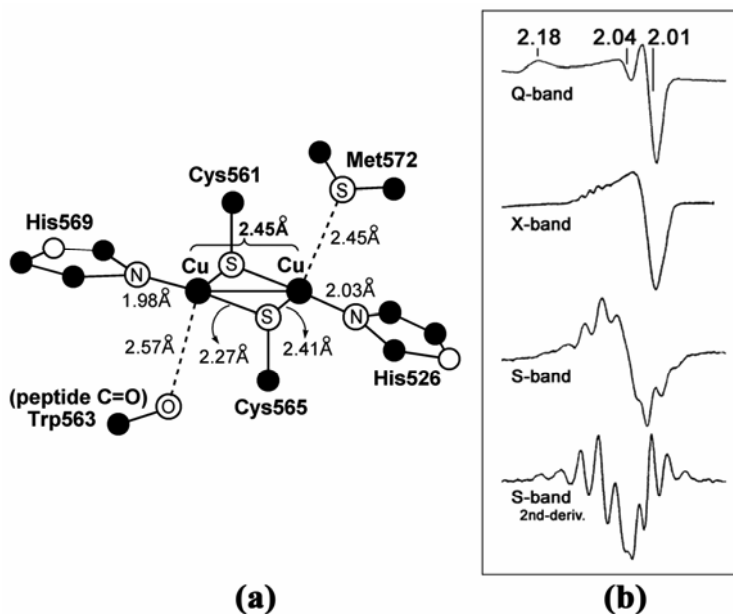


Figure 2. (a) Crystal structure (1FWX, resolution 1.60 Å) and (b) Q-, X-, and S-band EPR spectra of the Cu_A site in nitrous oxide reductase (N₂OR). Spectra adapted from [66].

charge distribution of Cu(+1.5)Cu(+1.5). The small $A_{||}$ reflects an electron delocalization over the two Cu centers that decrease the hyperfine coupling at each center by about half that of a mononuclear Cu(II) center.

The binuclear structure of the Cu_A site has been confirmed by the crystal structures of CcO [23,24] and N₂OR [25,26] that show the two copper centers with two bridging thiolate S(Cys) ligands (Fig. 2a). The crystal structure and extended x-ray absorption fine structure (EXAFS) data indicate that the Cu_A site contains a planar Cu₂S(Cys)₂ core with a Cu–Cu distance of ~2.45 Å in the oxidized form [67,68]. The Cu centers are trigonal, with an N(His) providing the third equatorial ligand. The axial ligand on one Cu is an S(Met), and that on the second Cu is a polypeptide backbone carbonyl oxygen. The short Cu–Cu distance and the presence of two thiolate bridging ligands support the delocalized mixed-valence description of the Cu_A site, as suggested by the EPR studies.

The covalent mixed-valent nature of the Cu_A site implied by its EPR spectrum is supported by excited-state spectroscopic data. The absorption and MCD spectra are dominated by three characteristic strong features: two at ~500 nm and the third at ~750 nm [69,70]. The two bands near 500 nm (~20000 cm⁻¹) originate from the Cys S_{x,y}→Cu CT transitions, where *x* and *y* indicate coordinates in the Cu₂S₂ plane (Fig. 2a). The high intensity of these bands originates from the covalent Cu–S bonds. This is supported by S K-edge XAS on an engineered Cu_A azurin construct

that indicates $46 \pm 2\%$ total S character in the singly occupied MO [71]. The Cu L-edge XAS on the Cu_A azurin also indicates significantly reduced Cu character in the singly occupied MO with $44 \pm 1\%$, in comparison to 61% Cu character in the D_{4h} CuCl₄²⁻ complex [71].

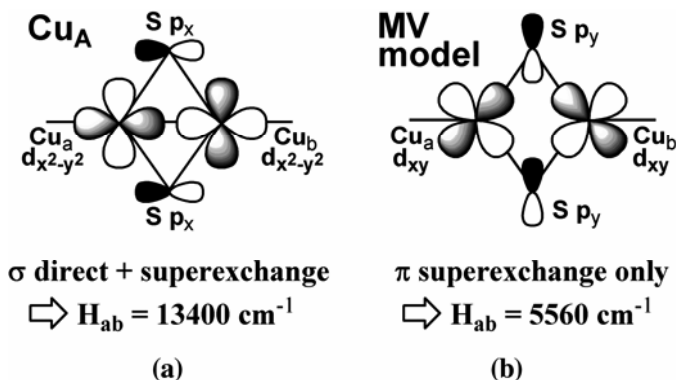


Figure 3. Singly occupied MOs of (a) Cu_A vs. (b) mixed-valence (MV) model complex of Tolman and coworkers [73].

The 750 nm (13400 cm^{-1}) absorption band is assigned as the metal-to-metal intervalence $\psi \rightarrow \psi^*$ transition in the class III mixed-valence site, where ψ and ψ^* refer to the occupied bonding and singly occupied antibonding MOs distributed over the two Cu centers [58,69]. This assignment was made on the basis of the large change in the Cu–Cu separation (distortion in the totally symmetric *a* vibration mode) observed to accompany this excitation in the near-IR in rRaman experiments [72]. Importantly, this intervalence $\psi \rightarrow \psi^*$ transition energy quantifies the electronic coupling matrix element H_{ab} that is associated with bonding interactions between the valence orbitals on the two Cu centers leading to electron delocalization in the Cu_A site. The short Cu–Cu distance and strong thiolate bridging ligands in the Cu_A site provide both the direct and superexchange contributions to this electronic coupling (Fig. 3a). These contributions can either be complementary or oppose one another to produce the final energy splitting $2H_{ab}$. The Cu–Cu distance of 2.45 Å in the Cu_A site (Fig. 3a) allows a direct Cu–Cu bond between the two $d_{x^2-y^2}$ orbitals to be present, with a contribution to $2H_{ab}$ estimated to be $\sim 7000 \text{ cm}^{-1}$. Moreover, the superexchange contribution from the bridging thiolates in Cu_A increases the electronic coupling to the experimental value of $2H_{ab} = 13400 \text{ cm}^{-1}$ (i.e., energy of the $\psi \rightarrow \psi^*$ transition at $\sim 750 \text{ nm}$). This significant electronic coupling results in the Cu_A site being completely delocalized (class III mixed-valence limit) as the H_{ab} value is large enough to overcome the vibronic trapping that induces a double-well potential energy surface to trap the oxidized Cu into either the Cu(II)Cu(I) or Cu(I)Cu(II) state. This lack of vibronic trapping could play a sig-

nificant role in lowering the Franck–Condon barrier to the long-range electron transfer by the Cu_A site [4,58,69].

The relative contributions of the direct Cu–Cu bond and the superexchange interactions to the Cu_A electronic structure have been evaluated via comparative studies on the Cu_A sites from *Bacillus subtilis* CcO, engineered azurin, and amicyanin vs. a mixed-valence model complex by Tolman and coworkers [69,73]. The model complex has two thiolate bridges and complete electron delocalization, evidenced by the characteristic EPR spectrum with a seven-line hyperfine splitting pattern ($g_z, g_y, g_x = 2.204, 2.046, 2.010$, and $A_y = 35 \times 10^{-4} \text{ cm}^{-1}$, $A_z = 51 \times 10^{-4} \text{ cm}^{-1}$). This complex, however, has a relatively long Cu–Cu distance of 2.9 Å that precludes a direct Cu–Cu bonding contribution to H_{ab} . The $\psi \rightarrow \psi^*$ transition is observed at 5560 cm^{-1} , which is $\sim 7800 \text{ cm}^{-1}$ lower in energy than that of the Cu_A sites, due to the lack of a direct exchange interaction. This quantifies the electronic coupling $2H_{ab}$ in the model complex to be $\sim 5560 \text{ cm}^{-1}$ that is associated solely with the superexchange by the bridging thiolates (Fig. 3b). In parallel S K-edge studies on the Cu_A sites and the model complex, very similar pre-edge absorption intensities have been observed [74]. The similar intensities indicate the amount of S character in the ψ^* orbital and its contribution to superexchange and electronic coupling is similar for both the Cu_A site and the model complex. Thus, the difference of $\sim 7800 \text{ cm}^{-1}$ in H_{ab} is due to an additional direct Cu–Cu bonding contribution in Cu_A . From a ligand field analysis, the trigonal ligand field of each copper center in the Cu_A site leads to formation of a direct Cu–Cu σ overlap [69]. Thus, as with the blue copper sites, the protein can influence the ligand interactions at the Cu_A sites that affect the formation of a Cu–Cu bond.

The high covalency of the thiolate bridges of the Cu_A provides two superexchange pathways for electron transfer in CcO: one to the heme *a* acceptor site and the other from the cytochrome *c* electron donor site; the former would be competitive with a shorter His pathway, as only $\sim 1\%$ His is contained in ψ^* as determined by electron nuclear double resonance (ENDOR) experiments [75] compared to 46% from the two Cys S bridging ligands [71], and the latter is required for Cu_A , as it is more buried ($\sim 9 \text{ \AA}$) from the protein surface relative to plastocyanin ($\sim 4.5 \text{ \AA}$). Thus, the presence of both the direct Cu–Cu bond and strong superexchange interactions in Cu_A maintain a delocalized ground state even in the low-symmetry protein environment that is functionally significant.

4. COUPLED BINUCLEAR ‘TYPE 3’ CU SITES

Hemocyanin (Hc), tyrosinase (Tyr), and catechol oxidase (CatOx) are copper proteins that have coupled binuclear T3 Cu sites, where Hc reversibly binds and releases O_2 during its transport, and Tyr and CatOx activate O_2 for substrate hydroxylation (Tyr only) and oxidation (both the Tyr and CatOx) [1,76]. Importantly, these proteins all share a peroxy-level intermediate with a side-on peroxide bridged $[\mu-\eta^2:\eta^2 \text{O}_2^{2-}-\text{Cu}(\text{II})_2]$ oxy-form upon reacting the deoxy-form (i.e., reduced $2\text{Cu}(\text{I})$ form) with O_2 . This intermediate is the most stable oxygen intermediate in

copper proteins and exhibits spectral features that are indicative of the side-on peroxide-bridged structure that plays a key role in reactivity. EXAFS of Hc [77] and crystal structures of oxy Hc and oxy Tyr [78,79] indicate that the two Cu centers (each with three His ligands) are separated by ~ 3.6 Å with a $\mu\text{-}\eta^2\text{:}\eta^2$ $\text{O}_2^{2-}\text{-Cu(II)}_2$ structure (Fig. 4a). As the two Cu centers are greater than 2.5 Å apart, direct overlap of the Cu d-orbitals as in a Cu_A site would be limited. Instead, the two Cu(II) centers are involved in strong antiferromagnetic coupling through the peroxide bridge, which leads to a diamagnetic $S_{\text{tot}} = 0$ ground state, and therefore a lack of an EPR signal [4].

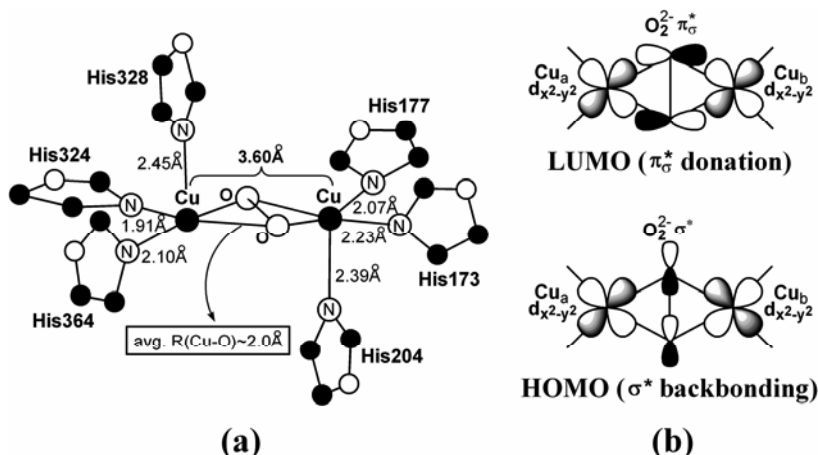


Figure 4. (a) Crystal structure (1OXY, resolution 2.40 Å) of the oxy form of arthropod hemocyanin (Hc). (b) Plots of the lowest unoccupied molecular orbital (LUMO) (top) and highest occupied molecular orbital (HOMO) (bottom) of the side-on $\text{Cu(II)}_2\text{O}_2^{2-}$ species showing highest occupied π_σ^* donation and σ^* backbonding interactions with the Cu(II) $d_{x^2-y^2}$ orbitals.

Experimentally, magnetic susceptibility measurements show that the singlet ground state is below the triplet state in energy by more than 600 cm^{-1} [80], yielding a coupling constant $-2J$ of $>600\text{ cm}^{-1}$. With a Cu-O-Cu angle of $\sim 120\text{--}140^\circ$, this result is consistent with the empirical correlation of Hatfield and Hodgson [81], which indicates that (for hydroxo-bridged Cu(II) dimers) bridging angles greater than 97.5° yield a singlet ground state, whereas those with less than 97.5° have a ferromagnetic triplet ground state. In the framework of MO theory for magnetic exchange by Hay, Thibault, and Hoffmann [82], the strong antiferromagnetism in the $\mu\text{-}\eta^2\text{:}\eta^2$ $\text{O}_2^{2-}\text{-Cu(II)}_2$ originates from the large splitting of the two singly occupied MOs in the single determinantal triplet state. The singly occupied MOs involve bonding interaction between (1) two Cu $d_{x^2-y^2}$ and the $\text{O}_2^{2-} \pi_\sigma^*$ orbital and (2) two Cu $d_{x^2-y^2}$ and the $\text{O}_2^{2-} \sigma^*$ orbital, where π_σ^* refers to one of the doubly degenerate π_σ^* peroxide HOMO that forms σ bonds with the Cu's and σ^* refers to the peroxide LUMO, both of which are in the Cu_2O_2 plane (refer

to the MOs shown in Fig. 4b), where the MOs are designated LUMO and HOMO, respectively, for the singlet wave function). The strong σ -overlap in the MO composed of the $d_{x^2-y^2} - \pi\sigma^* - d_{x^2-y^2}$ anti-bonding interactions would induce destabilization of this MO relative to the MO composed of the weak $d_{x^2-y^2} - \sigma^* - d_{x^2-y^2}$ bonding interaction that reflects a weak π -backbonding interaction, which stabilizes this MO. Overall, the large energy splitting of the two singly occupied MOs results in an antiferromagnetic singlet state.

The strong Cu-peroxide bonding interactions in the $\mu-\eta^2:\eta^2$ -peroxo-dicopper(II) oxy site is evidenced by the intense absorption features at 350 nm with $\epsilon \sim 20000 \text{ M}^{-1} \text{ cm}^{-1}$, and a weak feature at 550 nm with $\epsilon \sim 1000 \text{ M}^{-1} \text{ cm}^{-1}$, both of which are associated with the $\text{O}_2^{2-} \rightarrow \text{Cu}$ CT transitions [83,84]. The doubly degenerate π^* HOMOs of the peroxide are split in energy upon interaction with the binuclear copper site, where one component ($= \pi\sigma^*$; in the Cu_2O_2 plane) forms strong σ -bonds with the Cu centers, while the other component ($= \pi\nu^*$; out of the Cu_2O_2 plane) forms weak π -bonds with the Cu centers. Thus, the intense absorption band at higher energy is assigned as the $\pi\sigma^* \rightarrow \text{Cu(II)}$ CT transition and the weak lower energy as the $\pi\nu^* \rightarrow \text{Cu(II)}$ CT transition [17,76]. The rRaman spectrum exhibits an extremely low O–O stretch vibration at 750 cm^{-1} , which indicates a very weak O–O bond due to π -backbonding from the Cu centers into the σ^* LUMO of the peroxide (Fig. 4b, bottom) [85]. This is activated for O–O cleavage. In addition, the strong $\pi\sigma^*$ donation results in significant peroxide character in the low-energy $d_{x^2-y^2} - \pi\sigma^* - d_{x^2-y^2}$ unoccupied MO, activating it for electrophilic attack on substrate.

A reaction coordinate study on O_2 binding to Hc using DFT calculations has shown that when O_2 approaches the binuclear Cu site with increasing metal–ligand overlap, the coordination mode switches from end-on bridging $\mu-\eta^1:\eta^1$, to $\mu-\eta^1:\eta^2$, then to $\mu-\eta^2:\eta^2$ -butterfly, and finally to the planar side-on $\mu-\eta^2:\eta^2$ -peroxo structure, during which a simultaneous two-electron transfer takes place [86]. The structural changes allow the initially ferromagnetically coupled Cu_2O_2 core in the early stage of O_2 binding (due to near orthogonal magnetic orbital interaction) to progress through the strong antiferromagnetic superexchange coupling between the two Cu centers (due to direct magnetic orbital overlap) and undergo intersystem crossing. Thus, the spin forbiddenness of O_2 binding is overcome through delocalization of unpaired electrons onto the metal centers and the superexchange coupling of the metal centers via the bridging ligand.

5. NON-COUPLED BINUCLEAR CU SITES

The non-coupled binuclear copper enzymes include dopamine β -monooxygenase (D β M) and peptidylglycine α -hydroxylating monooxygenase (PHM). Both enzymes catalyze substrate C–H bond hydroxylation (at a Gly backbone C–H bond in PHM and a dopamine benzylic C–H bond in D β M), and kinetic and mechanistic studies have shown that the reaction mechanisms for both D β M and PHM are very similar [14]. The active site structure from the crystal structures of PHM indicates

that the two Cu centers, Cu_H and Cu_M (alternatively labeled Cu_A and Cu_B , respectively), are $\sim 11 \text{ \AA}$ apart with no bridging ligand and no observable magnetic interaction (Fig. 5a) [19,20,87]. The catalytic hydroxylation reaction occurs at the Cu_M center through an H-atom abstraction mechanism, while the Cu_H center supplies the additional electron required by long-range electron transfer. Because the two Cu centers in $\text{D}\beta\text{M}$ and PHM show no electronic coupling, the mechanism for this inter-copper, long-range electron transfer has been elusive. A superoxide-channeling mechanism [88] and a substrate-facilitated electron transfer mechanism [20,89] have been proposed to account for this intramolecular electron transfer process.

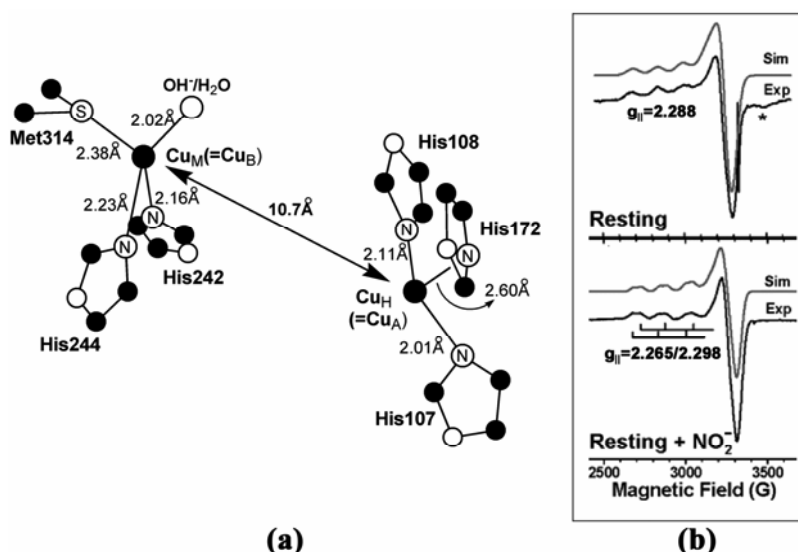


Figure 5. (a) Crystal structure (1OPM, resolution 2.10 Å) of oxidized form of peptidylglycine α -hydroxylating monooxygenase (PHM). (b) X-band EPR spectra of the resting (top) and the nitrite (NO_2^-) adduct forms of PHM. Note that in the NO_2^- adduct, the two perturbed Cu centers are spectroscopically differentiated. Spectra adapted from [93].

Crystal structures of oxidized PHM indicate that the Cu_M center has distorted tetrahedral geometry with one Met, two His, and a water-derived ligand, while the Cu_H center has a nearly square planar geometry, but with only three His ligands in a T-shaped fashion (Fig. 5a) [19,20,87]. The spectroscopic results from EPR, EXAFS, and XAS, however, suggest that both Cu centers should each have an extra water-derived ligand that may not have been observed in the crystallography due to limited resolution [90–92]. Possible Cu_M structures were evaluated using DFT calculations, coupled to a ligand field analysis of EPR and low-temperature MCD data. These calculations have shown that the five-coordinate square pyramidal Cu_M structure with one H_2O and one OH^- in the equatorial positions and a

weak S(Met) ligand in the axial position is consistent with experiment, in particular with the d–d transition energies and the axial g -values observed in the MCD and EPR spectra of PHM [93]. The four-coordinate model with just one water-derived ligand (OH⁻), as suggested by the current crystal structures, underestimates the d–d transition energies and gives rise to significantly rhombic distorted g -values due to the large structural distortion, leading to an inequivalence in the x - and y -directions and d_{z^2} mixing (~19%) into the $d_{x^2-y^2}$ ground state. DFT/ligand field analysis also indicates that the Cu_H site is a four-coordinate, D_{2d} distorted square planar structure, with the H₂O molecule occupying the open coordination site of the Cu_H center described in the crystal structures.

Interestingly, while the Cu_M and Cu_H sites are found inequivalent from the crystal structures, spectroscopic studies on the resting oxidized forms of PHM (and DβM) have shown that these sites are indistinguishable in the EPR, absorption, CD, and MCD spectra [92–94]. In the X-band EPR spectrum of the resting PHM, only one T2 Cu(II) signal is discerned with $g_z = 2.288 > g_{x,y} = 2.050, 2.060$, and $A_z = 157 \times 10^{-4} \text{ cm}^{-1}$ (Fig. 5b, top). Moreover, the d–d transition region in CD and MCD spectra of resting PHM do not provide evidence for two different Cu(II) centers. Alternatively, spectroscopic differentiation of the two sites has been made possible via small molecule binding perturbation of the Cu sites using nitrite (NO₂⁻). As NO₂⁻ is capable of binding in either mono- or bi-dentate fashion to a Cu(II) center, differential perturbation on the Cu_M (with two exchangeable water-derived ligands) and Cu_H (with one exchangeable water ligand) sites was possible. Two sets of signals have been observed in the EPR (Fig. 5b, bottom) and MCD spectra of the NO₂⁻ adduct of PHM [93]. Six transitions are observed in the d–d transition region of the MCD spectrum, as compared to the two-band spectrum of the resting PHM. Since one Cu(II) site can at most contribute four d–d transitions, the presence of six d–d bands in the MCD spectrum indicated that both Cu_M and Cu_H sites in PHM contribute. Also, the X-band EPR spectrum shows two sets of Cu(II) hyperfine couplings with nearly equal intensity, consistent with two inequivalent Cu(II) sites (Fig. 5b, bottom; $g_{1z} = 2.265$, $A_{1z} = 160 \times 10^{-4} \text{ cm}^{-1}$ and $g_{2z} = 2.298$, $A_{2z} = 165 \times 10^{-4} \text{ cm}^{-1}$).

The indistinguishable contribution of the Cu_M and Cu_H sites in the optical and EPR spectra has been ascribed to the very similar overall covalencies and ligand fields of these two Cu sites. In the square planar Cu_H site, the $d_{x^2-y^2}$ orbital has dominant σ interactions with the four ligands (three His and a water). Despite the different number and types of ligands, the d-orbital splitting of the Cu_M site has opposing effects of the square pyramidal distortion by the axial Met ligand and the strong equatorial donation of the OH⁻ ligand. This leads to d–d transition energies similar to those of the Cu_H site. Consequently, the ground state Cu covalencies for the Cu_M and Cu_H sites are very similar, with ~70% Cu character as determined by EPR and ~64% by DFT [93]. Together with their similar d–d transition energies, both the Cu_M and Cu_H sites should exhibit very similar EPR g - and A -values, since these values are dominantly dependent on the d–d energies and covalencies of the ground state.

The non-coupled nature of the PHM and D β M copper active sites is strongly related to their catalytic function. The reaction coordinate generated using DFT [21] suggests that the H-atom abstraction reaction in PHM and D β M involves a mononuclear Cu_M(II)–superoxo species via an almost thermoneutral process with a low reaction barrier of ~ 15 kcal/mole, in contrast to the previously believed Cu_M(II)–OOH intermediate [95], which involves a much higher activation barrier of ~ 37 kcal/mole. The reaction coordinate involving the Cu_M(II)–superoxo species is supported by recent kinetic studies on D β M [96].

Due to the small exchange coupling J , the electronic coupling matrix element H_{DA} contribution to the electron transfer rate is also small ($k_{ET} \propto (H_{DA})^2 \propto -2J$ [97–99]). In addition, significant geometry changes between the reduced and oxidized forms of the Cu_M and Cu_H centers suggest that there is the contribution of a large reorganization energy to further decrease the electron transfer rate. Thus, the catalytically relevant intramolecular electron transfer between the non-coupled Cu_M and Cu_H centers would have to be switched on by a high thermodynamic driving force at the appropriate step in the enzymatic reaction cycle [18,21]. This non-coupled nature of the binuclear Cu active sites in PHM and D β M provides a strategy to reduce O₂ by first forming a reactive 1e[−] reduced Cu_M(II)–superoxo species for the required H-atom abstraction reactivity while maintaining the ability to provide an additional electron from the Cu_H center to complete the reaction. Alternatively, in the strongly coupled binuclear Cu sites of hemocyanin and tyrosinase, the reaction of O₂ with the reduced protein leads to a fast electron transfer from both Cu centers to O₂, generating a 2e[−] reduced binuclear Cu(II)–peroxide species that is effective at electrophilic attack on an aromatic substrate.

6. TRINUCLEAR CU(II) CLUSTER SITES

Trinuclear Cu clusters play a central role in catalytic O₂ reduction in the multi-copper oxidases [1,76]. These enzymes contain at least four Cu centers that are necessary to catalyze the 4e[−] reduction of O₂ to H₂O with concomitant 1e[−] oxidations of various substrates (Fig. 6). The electrons are taken up at the T1 blue copper site and transferred ~ 13 Å to the trinuclear copper cluster site that is comprised of a T2 and a T3 copper center where O₂ reduction occurs [100]. Reaction of the fully reduced enzyme with O₂ involves two 2e[−] intermediate stages, where the first 2e[−] reduction step is rate determining ($k \approx 2 \times 10^6$ M^{−1}s^{−1}) while the second is fast ($k > 350$ s^{−1}), therefore effectively resulting in a single 4e[−] process [101,102].

In the resting oxidized form, two types of EPR signals are observed that originate from the paramagnetic T1 and T2 sites. The other two Cu(II) centers are the coupled binuclear T3 site that are EPR silent due to the strong antiferromagnetic coupling with $-2J > 400$ cm^{−1} through an endogenous OH[−] bridge [80]. The T1 site exhibits an EPR signal at $g_{\parallel} = 2.30$ with $A_{\parallel} = 39 \times 10^4$ cm^{−1} (Fig. 7a) that is consistent with those of the other blue copper proteins (see §2). Alternatively, the T2 site exhibits an EPR signal at $g_{\parallel} = 2.24$ with A_{\parallel} of 180×10^4 cm^{−1} (Fig. 7a). While this

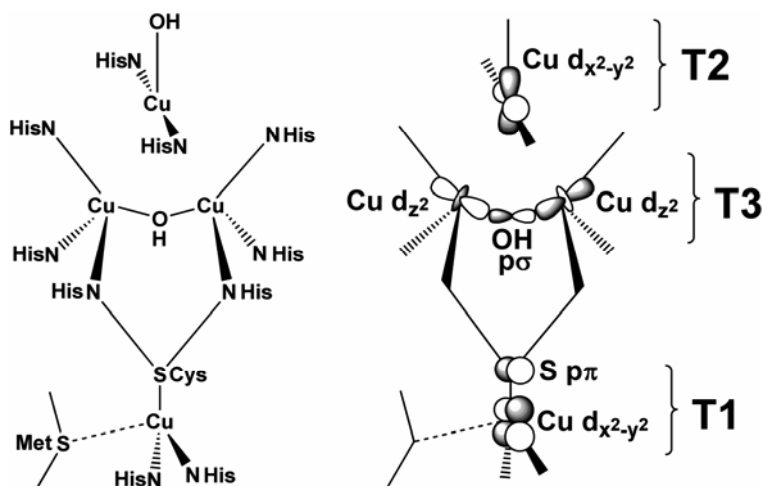


Figure 6. Copper sites in the resting oxidized form of the multicopper oxidases and associated ground state orbitals.

feature is consistent with those of normal tetragonal Cu(II) complexes, it derives from an unusual T-shaped, three-coordinated ligand environment with two His and an OH^- in the x,y -plane (Fig. 6). This structural description is consistent in all reported crystal structures. In addition, a combination of nitrogen electron spin echo envelope modulation (ESEEM), deuterium ENDOR, and MCD spectroscopies has shown that this coordination environment of T2 site is constant over the functional pH range of 5.5 to 7.5 [103]. It has been suggested that the OH^- ligand is stabilized in this pH range by the large inductive effect of the three coordinate T2 Cu(II) ion and hydrogen bonding connectivity to a nearby Asp residue.

It is important to note that the T2 and T3 Cu centers in the trinuclear cluster are all coordinatively unsaturated, with the open sites oriented toward the center of the cluster. The T2 and T3 sites have negligible magnetic influence on each other, and there is no evidence for a bridging ligand (such as H_2O or OH^-) between the T2 and T3 sites, despite the highly positive charge of the cluster. From energetic considerations of the ligand binding at the μ_3 -position (i.e., the center of the cluster) using DFT calculations, it was shown that binding of H_2O or OH^- actually leads to an energetically unfavorable process, after inclusion of the effects of solvation/desolvation, protonation/deprotonation of H_2O and OH^- , and charge stabilization by nearby anionic carboxylate protein residues. In a parallel evaluation of the energetics of fluoride binding (which exhibits a superhyperfine splitting pattern in the EPR spectrum, indicating that it binds equatorially to the T2 site at the μ_3 -position), a very favorable overall energy was obtained that is consistent with its high affinity ($K > 10^4$ higher than for aqueous Cu complexes) [104]. In particular, the possibility of a significant role of the four conserved anionic

Asp/Glu residues within 12 Å in stabilizing the highly charged coordinatively unsaturated trinuclear Cu cluster has been evaluated [103]. The charge stabilization of the cluster contributes to tuning the ligand-binding properties of the cluster, leading to its high affinity for fluoride and its coordination unsaturation that play a key role in its O₂ reactivity.

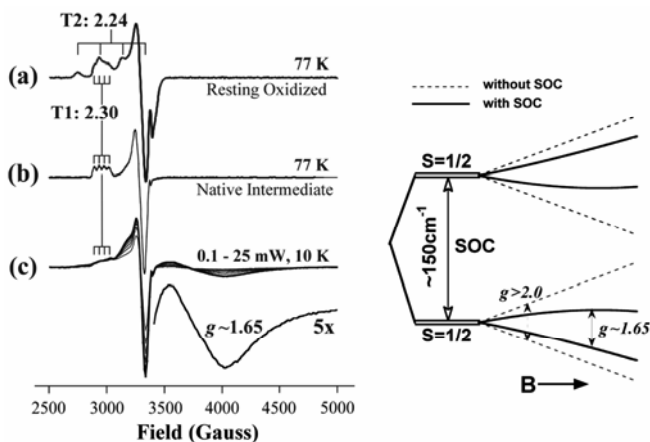


Figure 7. (Left) X-band EPR spectra of the *Rhus vernicifera* tree laccase: (a) the resting oxidized form at 2.02 mW and 77 K, (b) the native intermediate at 2.02 mW and 77 K, and (c) the native intermediate taken at 0.5–25 W at 10 K. (Right) Energy diagram of the ground and low-lying doublet states of the native intermediate, with depiction of the origin of the low g -value observed in (c); see text for details. Spectra adapted from [22].

When the fully reduced enzyme is reacted with O₂, the 4e[−] reduced native intermediate (NI) is formed. This intermediate has been trapped using a rapid freeze-quench technique and spectroscopically characterized using EPR, absorption, CD, VTVH MCD, and XAS [22,105]. It was shown that the NI is a fully oxidized species with the three Cu(II) centers in the trinuclear site mutually bridged by the product of the full 4e[−] O₂ reduction with cleavage of the O–O bond.

One of the characteristic spectroscopic features of the NI is the absence of the T2 signal and the emergence of a broad signal with a low g_{eff} value of 1.65 in the EPR spectrum at low temperature and high radiant power [22,106]. In contrast to the resting oxidized form, the NI at 77 K exhibits only the T1 signal in its EPR spectrum (Fig. 7b). However, as the temperature is lowered, a broad signal at ~4000 G is observed below 20 K (Fig. 7c). This new signal shows rapid relaxation and is difficult to saturate, exhibiting a very different saturation behavior compared to the T1 signal. The $P_{1/2}$, the microwave power at half-saturation, of the broad signal at 8.8 K is > 25 mW, whereas that of the T1 signal is ~0.45 mW and that of the T2 signal in the resting oxidized form is ~0.05 mW. Thus, at high radiant power, the T1 signal is saturated and only the new signal is observed (Fig. 7c). Simulations show that this broad signal has g -values of 2.15, 1.86, and 1.65. Its

Orbach analysis suggests the presence of a low-lying excited doublet state at ~ 150 cm^{-1} above the ground state, which was confirmed by variable-temperature MCD experiments [22].

Earlier studies have attributed this new signal to a three-electron reduced oxyl or hydroxyl species with the T2 Cu center still reduced, based on EPR studies using isotopically enriched $^{17}\text{O}_2$ [106]. However, all four Cu centers in the NI have been determined to be oxidized by XAS edge studies [22]. In addition, a pseudo-A term is observed in the CT region of the MCD spectrum of the NI that is very different from what is observed in the MCD spectrum of a hydroxyl radical [22,105]. Thus, XAS and MCD studies have provided definitive evidence that the NI form is not a radical species produced by a $3e^-$ reduction of O_2 , but rather a $4e^-$ reduced product of O_2 reduction with all four Cu centers oxidized.

The unique spectroscopic and reactivity features of the NI must originate from an all-bridged structure of the trinuclear Cu cluster site. In an all-bridged trinuclear Cu(II) cluster, each of the three spins can interact with its adjacent spins. The two Cu(II) centers with $S = 1/2$ couple to form intermediate spins $S' = 1$ and 0 (Fig. 8, "One Bridge"), which then couple to the third Cu(II) center to give $S_{\text{tot}} = 1/2$ and $3/2$, and another $S_{\text{tot}} = 1/2$ state, respectively (Fig. 8, "Three Bridges"). For the C_3 symmetric trimers with three equivalent exchange coupling interactions, the quartet and doublet ground states are the 4A and 2E states, which are separated by $3|J|$ in energy, when $\hat{H}_{ij} = -2J(\hat{S}_i\hat{S}_j)$ between spin centers i and j (Fig. 8, "Three Equal Bridges"). [Note that the degeneracy in the 2E ground state of the three-bridged case represents what is widely known as *spin frustration*. In the triangular topology of the C_3 symmetric Cu(II) trimers, three $M_S = 1/2$ spin configurations are possible (i.e. $\uparrow\uparrow\downarrow$, $\uparrow\downarrow\uparrow$, and $\downarrow\uparrow\uparrow$), and the competing interactions of these spin configurations often lead to ground states that cannot be described in the conventional spin Hamiltonian and cause a dramatic modification of the magnetic properties.] The bridged structure of the NI would promote strong antiferromagnetic coupling of the three Cu(II) centers, resulting in a doublet ground state accompanied by a low-lying doublet excited state at ~ 150 cm^{-1} (determined by EPR Orbach analysis and variable-temperature MCD) as indicated by a bold arrow in Figure 8. Two possible exchange-coupled structures of the trinuclear Cu cluster in the NI have been proposed based on experiment and consideration of reactivity, one with tris-hydroxo-bridged and the other with a μ_3 -oxo-bridged structure (Fig. 9).

The elucidation of the very low g -value of the NI has been provided by a recent spectroscopic study on the D_3 symmetric tris- μ_2 -hydroxy-bridged trimeric Cu(II) model complex [107] synthesized by Mirica and Stack [108]. In this study, it was shown that the orbitally degenerate 2E ground state of the tris- μ_2 -hydroxy-bridged complex undergoes a zero-field splitting of ~ 65 cm^{-1} , as determined by the field- and temperature-dependent MCD features of the complex. Moreover, the signal observed in the single-crystal EPR spectrum (at $T < 30$ K) is strongly anisotropic, with the g -value shifting from 2.32 down to ~ 1.2 upon rotation of the single crystal from parallel to perpendicular orientation of the molecular C_3 -axis relative to the magnetic field.

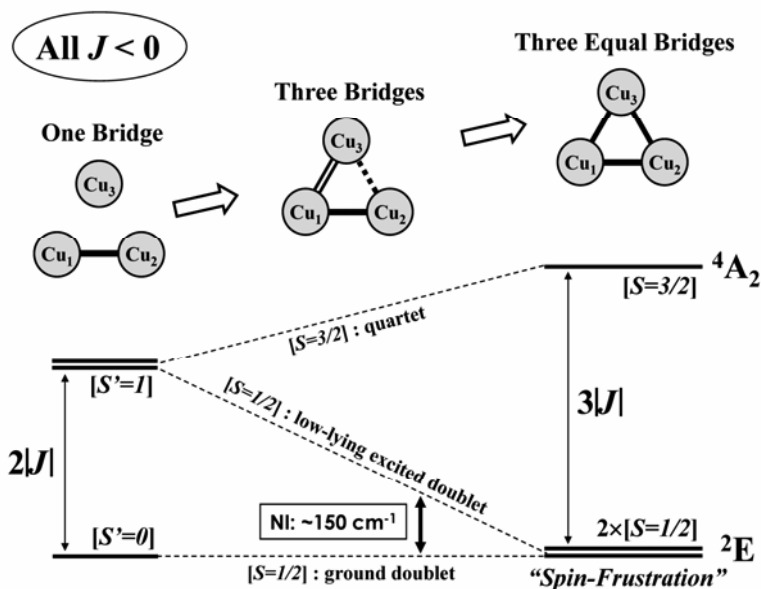


Figure 8. Energy diagram of an antiferromagnetically coupled Cu(II) trimer (all $J < 0$), going from a singly bridged Cu(II) trimer ("One Bridge") to a triply bridged Cu(II) trimer ("Three Bridges"). In the singly bridged case, only the Cu₁ and Cu₂ centers are coupled to give $S' = 0$ and $S' = 1$ states. When the third Cu₃ center is coupled in the triply bridged case, two $S = 1/2$ and one $S = 3/2$ are produced. When the three bridging interactions are equivalent, as in the C_3 or D_3 symmetric trimers, the two doublet states become degenerate, forming a spin-frustrated 2E ground state.

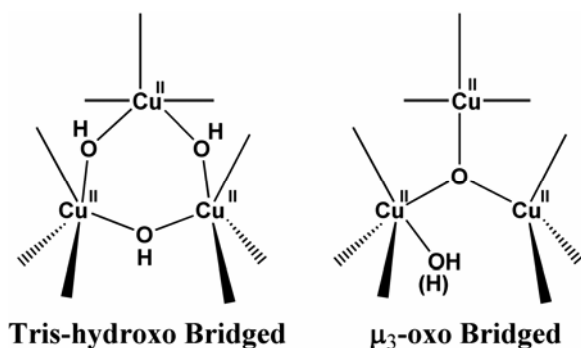


Figure 9. Proposed structural models of the exchange-coupled trinuclear cluster site in the native intermediate of the multicopper oxidases.

The zero-field splitting and the strong anisotropy of the EPR signal originate from antisymmetric exchange [109–111], which is the first-order spin–orbit coupling phenomenon in magnetically coupled pairs that requires the combined effects of local spin–orbit coupling and superexchange interactions between the ground state of one center to both the ground and excited states of the other (and vice versa) with comparable magnitudes. In the 2E ground state of trimeric Cu(II) complexes, the spin–orbit coupling via antisymmetric exchange results in zero-field splitting [112]. In addition, the zero-field split doublets are spin–orbit mixed by the magnetic field and the Zeeman split energy levels of the doublets become nonlinearly dependent on field when the molecular C_3 -axis of the trimer is not aligned with the magnetic field. This results in narrowing of the Zeeman splitting in each doublet and upshift of the resonance field, yielding the low effective g -value down to ~ 1.2 (or even lower but not observed due to line broadening and the detection limit of the instrument). DFT calculations show that the origin of the antisymmetric exchange in the tris- μ_2 -hydroxy complex derives from the efficient superexchange pathway available between the ground and excited state orbitals of adjacent Cu centers, via strong σ -type bonds with the in-plane p-orbitals of the bridging OH⁻ ligands.

Note that the observed EPR signal of the tris- μ_2 -hydroxy complex, which is temperature dependent and observed below 30 K, is the transition between the Zeeman subcomponents of the lower energy zero-field split doublet of the 2E ground state. Importantly, evaluation of the transition probability of this transition requires that symmetry lowering be present in the molecular structure from the crystallographically determined D_3 symmetry. The possibility of magnetic Jahn–Teller effect has been proposed, suggesting that a distortion of ~ 0.01 Å should occur in the ground state of any antiferromagnetically coupled trinuclear complexes to remove the three-fold symmetry [113]. The crystallographically determined D_3 symmetry would reflect either a dynamic or a static Jahn–Teller distortion where the latter would be distributed over the three orientations. However, a very low Jahn–Teller stabilization energy of ~ 4 – 5 cm⁻¹ and small structural distortion of ~ 0.01 Å would be very difficult to distinguish by crystallography even at very low temperature.

Thus, the model study using the tris- μ_2 -hydroxy-bridged model complex has shown that the properties of the ground states of an antiferromagnetically coupled trimeric Cu(II) complex are governed by the complementary effects of antisymmetric exchange and symmetry lowering. These have opposite effects on the spin distribution over the three metal sites where the former tends to delocalize the $S = \frac{1}{2}$ spin over the three metal sites, whereas the latter tends to localize it on a single metal site. In the tris- μ_2 -hydroxy complex, the availability of the efficient ground-to-ground and ground-to-excited superexchange pathways and the high symmetry of the molecular structure result in a relatively large contribution of antisymmetric exchange mixing into the ground state wavefunctions with a significantly delocalized spin distribution over the three Cu centers.

In the NI, on the other hand, the inequivalent Cu centers of the protein active site would allow a dominant contribution of the symmetry lowering effect into the

splitting of the spin-frustrated doublet ground state ($\sim 150\text{ cm}^{-1}$) and to the spin distribution. However, structural distortion alone is insufficient in explaining the low g -value of ~ 1.65 , as it only describes a localized ground state wavefunction equivalent to the individual monomeric Cu centers in the trinuclear cluster with g -values > 2.0 (Fig. 7, right, dotted line). Alternatively, the all-bridged structure of the NI would allow efficient superexchange interactions and thus the antisymmetric exchange to be present. As indicated above, the antisymmetric exchange would induce spin-orbit mixing ($\sim 6\%$) of the ground doublet with the low-lying excited doublet. As a result, the resonance position is shifted up in field, yielding the observed low effective g -value of 1.65 (Fig. 7, right, solid line) [107,114].

The ground state properties of the μ_3 -oxo-bridged structure was also investigated [114] using a C_3 symmetric model complex synthesized by Suh and coworkers [115]. While it has a ferromagnetic 4A ground state ($J = +54.5\text{ cm}^{-1}$), it is the only μ_3 -oxo-bridged trimeric Cu(II) complex available with no other effective bridging ligands that may significantly affect the exchange coupling. DFT calculations have shown that the ferromagnetic ground state is, in fact, not intrinsic to the μ_3 -oxo-bridged structure but derives from the oxo ligand being $\sim 0.5\text{ \AA}$ above the Cu_3 plane, likely "pushed up" by the rigid macrocyclic ligand manifold. It is found that when the oxo ligand is shifted sufficiently into the plane ($< \sim 0.3\text{ \AA}$), the ground state becomes antiferromagnetic, as in the NI.

The ferromagnetic μ_3 -oxo-bridged model complex exhibits two EPR transitions with effective g -values of 3.64 and 2.06 in the X-band and 3.77 and 2.06 in the Q-band. Moreover, a zero-field splitting (2D) of -5.0 cm^{-1} has been estimated from variable-temperature EPR. Interestingly, the g -value of 3.64/3.77 (X-/Q-band) would correspond to a true $g_{x,y}$ of 1.82/1.89 (i.e., half the observed g -value for an axial $S_{\text{tot}} = 3/2$ system) that is too low for individual Cu centers in the trimer. The zero-field splitting and low g -value originate from the second-order spin-orbit coupling phenomenon called the anisotropic exchange. It shares the same physical origin as the first-order antisymmetric exchange, as it also derives from local spin-orbit coupling and ground-to-excited state superexchange interactions [110,111]. Due to the lack of orbital angular momentum in the 4A ground state, the first-order antisymmetric exchange does not exist [112]. The experimental evidence for anisotropic exchange in the ferromagnetic 4A ground state suggests that the first-order antisymmetric exchange would be present in the ground state of an antiferromagnetically coupled μ_3 -oxo-bridged Cu(II) structure, yielding similar ground state properties as those observed for the tris- μ_2 -hydroxy-bridged model.

From the above, it is not possible to determine the geometric structure of the NI from the ground state analyses of the tris- μ_2 -hydroxy-bridged and μ_3 -oxo-bridged complexes alone, as both structures allow large antiferromagnetic and antisymmetric exchange via efficient ground-to-ground and ground-to-excited state superexchange interactions. The determination of the NI structure was possible by excited-state analysis using MCD spectroscopy, which indicated the characteristic MCD pseudo-A term (i.e., a pair of field- and temperature-dependent MCD intensities with opposite signs) of NI is only consistent with the μ_3 -oxo-bridged structure [116]. Elucidation of the orbital origin of the remarkably low effective g -value

for the Cu(II) sites of the NI delineates the important role of the superexchange interactions in the molecular mechanism of O–O bond cleavage and the facile re-reduction of this fully oxidized intermediate in the turnover of the multicopper oxidases (see. [76] for mechanistic details).

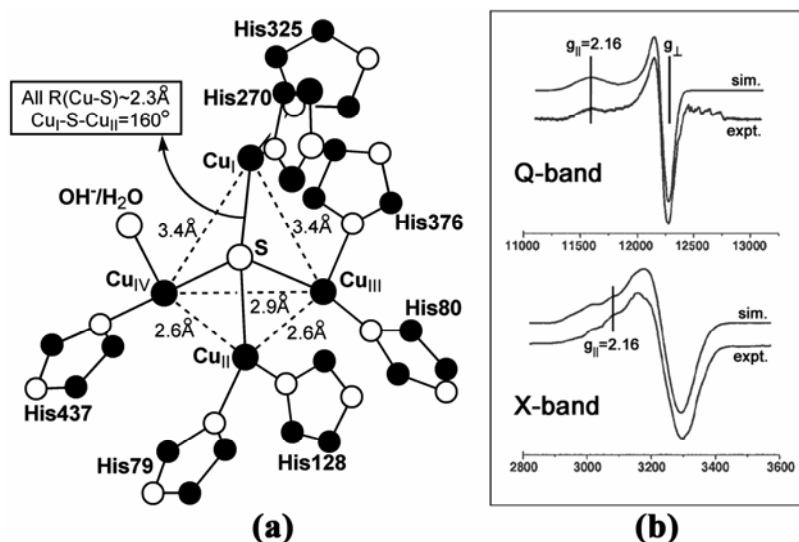


Figure 10. (a) Crystal structure (1FWX, resolution 1.60 Å) and (b) Q- and X-band EPR spectra of the Cu₂ site in nitrous oxide reductase (N₂OR). Spectra adapted from [32].

7. TETRANUCLEAR CU_Z SITES

The Cu_Z site is the second copper active site found in N₂OR, in addition to Cu_A, where the catalytic 2e⁻ reduction of N₂O to N₂ and H₂O occurs [29,30]. This site has been elusive, however, and even its nuclearity was unclear [117,118] prior to the recent release of its crystal structures from *Pseudomonas nautica* and *Paracoccus denitrificans* N₂OR [25,26]. Crystal structures have identified the Cu_Z site to be an unprecedented tetranuclear Cu cluster with a μ₄-sulfide-bridging ligand (Fig. 10a). The Cu₄S core of the Cu_Z structure has approximate C_s symmetry with Cu_I–S–Cu_{II} defining the mirror plane (see Fig. 10a for designation of the Cu centers). While all Cu–S bonds are similar in length, the Cu–Cu distances are very different, with the three Cu centers—Cu_{II}, Cu_{III}, and Cu_{IV}—closer to each other than to the Cu_I center. The Cu_I–S–Cu_{II} angle is ~160°, while the other Cu–S–Cu angles are ~90°. The tetranuclear Cu cluster is coordinated to the protein backbone

by seven His ligands. An additional water-derived ligand is also present at the $\text{Cu}_I/\text{Cu}_{IV}$ edge at which substrate binding is believed to occur.

Most spectroscopic studies have focused on the resting form of the Cu_Z site, which is the form that correlates to the crystal structures [31,32,119]. The X-band EPR spectrum of the resting Cu_Z site exhibits an EPR signal of an $S_{\text{tot}} = 1/2$ system, with some hyperfine features but unresolved g -values (Fig. 10b, bottom) [31]. The total spin of $1/2$ is verified by VTVH MCD, where the MCD intensity of different possible spin states will show different saturation behavior [31]. Analysis of the EPR signal at X-band has been difficult, as the signal is too broad and the g -values are not well resolved. The g -values were resolved by Q-band EPR that showed an axial $g_{\parallel} \approx 2.16 > g_{\perp} \approx 2.04$, indicating that the unpaired electron resides in a $\text{Cu } 3d_{x^2-y^2}$ -derived MO (Fig. 10b, top). The relatively low g -value of resting Cu_Z , compared to that of the normal tetragonal Cu(II) complexes, suggests either a highly covalent metal–ligand bonding interactions or high d–d transition energies, which are the two main factors in the spin–orbit coupling term from second-order perturbation theory that lead to a deviation of the g -values from the free-electron value of 2.0023.

While the g -values are resolved in the Q-band spectrum, the hyperfine splitting is lost due to frequency-dependent g - and A -strain [120]. Thus, the g -values from the Q-band data were mapped back to the X-band spectrum, where the metal hyperfine coupling is somewhat resolved [31]. Simulations show that the g_{\parallel} of 2.16 coincides with a hyperfine feature indicating metal hyperfine pattern with an odd number of lines. This requires electron delocalization to more than one Cu center for the hyperfine splitting. Consequently, a second Cu was included in the analysis to account for the metal hyperfine pattern observed at X-band, with one Cu center dominating the hyperfine splitting ($A_{\parallel} = 61 \times 10^{-4} \text{ cm}^{-1}$) and a second Cu contributing another $\sim 30\%$ of the spin ($A_{\parallel} = 24 \times 10^{-4} \text{ cm}^{-1}$). The two hyperfine splitting values suggest the single electron spin of the Cu_Z center is partially delocalized over at least two Cu centers with a $\sim 5:2$ spin distribution. Therefore, the ground state of the Cu_Z site is a partially delocalized class II mixed-valence system. Inclusion of additional copper(s) (i.e., Cu_{III} and Cu_{IV}) to the spectral simulation did not improve the fit, but could be present with much smaller spin densities [121]. (Note that in a partially delocalized class II system, the interaction between the metal centers is sufficiently weak so that valence trapping or charge localization occurs. In a class III system, such as Cu_A (see §3), the interaction of the donor and acceptor sites is so great that the energy surface features a single minimum, resulting in complete delocalization.)

The partial delocalized description of the resting Cu_Z site is supported by DFT calculations, with the spin density dominantly on the Cu_I center (42%) and delocalized over the Cu_{II} center (16%), while Cu_{III} and Cu_{IV} centers have little spin density [31,32,122]. The calculated spin distribution at the Cu_I and Cu_{II} centers has a $\sim 5:2$ ratio that is consistent with the Q-/X-band EPR results. This is consistent with the Cu K-edge XAS experiment [31], which demonstrated that, of the two possible combinations of the oxidation state of the four Cu centers in the Cu_Z site (i.e., one Cu(II) + three Cu(I) vs. three Cu(II) + one Cu(I)), only the $1\text{Cu(II)}/3\text{Cu(I)}$ model

matches the XAS data obtained, indicating that there is only one dominantly oxidized Cu in the resting Cu_Z site.

The electron delocalization in the Cu_Z cluster is mediated by the μ₄-bridging sulfide ligand. DFT calculations indicate spin density of ~14% at the μ₄-bridging sulfide [31,32,122]. This reflects a dominant σ-bonding interaction (Cu_I-S-Cu_{II} angle ≈ 160°) with the d_{x²-y²} orbitals of Cu_I and Cu_{II} that constitutes an excellent σ superexchange pathway between Cu_I and Cu_{II} for electron delocalization. The electron delocalization is important because it contributes to low reorganization energy during redox processes of the Cu_Z site and leads to stabilization of the oxidized form of Cu_Z after N₂O reduction.

The absorption spectrum of the resting Cu_Z site shows an intense CT band at ~640 nm (~15700 cm⁻¹) that has a corresponding intense feature in the low-temperature MCD spectrum [32]. This band is dominantly the σSp→Cu_I CT transition, in which the transition is made between the S p-orbital along the Cu_I-S-Cu_{II} bond to the Cu_I center where most of the unpaired spin resides. This assignment has been confirmed by rRaman experiments based on stretching frequencies and ³⁴S isotope shifts [32]. The bond-strength pattern of the four Cu-S bonds obtained from the rRaman data reflects the electronic structure description of the resting Cu_Z site with an H₂O at the Cu_I-Cu_{IV} edge.

Since only Cu_I is dominantly oxidized in the resting Cu_Z, the observed d-d transitions in absorption and MCD spectra are attributed to this Cu center. Importantly, the Cu_I d_{xy}→d_{x²-y²} transition is high in energy (at ~18000 cm⁻¹) relative to its energy in normal tetragonal Cu(II) complexes. Its high energy comes from the ligand geometry of the Cu_I center that has two His and one sulfide ligands forming a T-shaped environment with one His distorted out of the molecular plane. The high energy of the Cu_I d_{xy}→d_{x²-y²} transition is a major contribution to the small *g*-value (~2.16) observed for the resting Cu_Z cluster, since the covalency of the bridging sulfide (~15–22% S character in the ground state) is not large enough to account for the low observed *g*-value. Notably, an intervalence transition is observed at ~1000 nm in the absorption spectrum of the resting Cu_Z. The assignment of this band as an intervalence transition is corroborated by the fact that it lacks MCD intensity, indicating that it is a unidirectional electronic transition (MCD intensity requires spin-orbit coupling of two orthogonal transition moments). It corresponds to charge transfer between the Cu_{II} and Cu_I centers and reflects electronic coupling and electron delocalization between the two Cu centers mediated by the bridging sulfide unit.

The ground state wavefunction of the resting Cu_Z provides initial possible insight into the enzymatic reactivity of N₂O reduction. In the catalytic cycle of Cu_Z, the substrate N₂O reacts with the fully reduced form with four reduced Cu(I) centers [123]. The substrate binds at the Cu_I/Cu_{IV} edge of Cu_Z, where a simultaneous 2e⁻ transfer to N₂O occurs. As the Cu_{II} and Cu_{IV} centers have good electron transfer pathways from the neighboring Cu_A center, one electron would be donated directly from the Cu_{IV} center and the other from the Cu_{II} center through the Cu_{II}-S-Cu_I σ superexchange pathway. Importantly, the μ₄-sulfide bridge plays a significant role in the formation of the delocalized electronic structure of the Cu_Z cluster, fa-

ilitating the $\text{Cu}_{\text{II}}\text{-S-Cu}_{\text{I}}$ σ superexchange pathway for transfer of an electron to the substrate and the rapid re-reduction of the Cu_{Z} site during enzymatic turnover. Finally, DFT calculations show the activation of N_2O and the cleavage of its N–O is promoted by a strong backbonding interaction that is induced by bending of the N_2O upon binding to the $\text{Cu}_{\text{I}}/\text{Cu}_{\text{IV}}$ edge in a bent $\mu\text{-}1,3$ bridging mode ($\angle\text{N-N-O} = 139^\circ$), with the terminal nitrogen atom coordinating to the Cu_{I} center. The bending of the bound N_2O causes splitting of the doubly degenerate LUMO of the free N_2O into two non-degenerate π^* orbitals [122]. Consequently, the π^* LUMO in the N–N–O plane is stabilized close in energy to the fully occupied d-orbitals of the reduced Cu_{Z} cluster and, therefore, making the N_2O ligand a very good electron acceptor.

8. CONCLUDING COMMENTS

Biological copper sites are extremely diverse, attaining a wide range of geometric and electronic structures that are tailored for their catalytic functions. With different ligand environments and copper nuclearity, the copper active sites can tune the reduction potentials for long-range electron transfer and promote superexchange interactions and electron delocalization for activation and reduction of dioxygen and nitrous oxide. The complementary information obtained by EPR and other spectroscopic methods and DFT calculations has provided detailed understanding of these geometric and electronic structures and their relationship to catalytic functions. These descriptions provide the basis for insight into the molecular mechanisms and reaction coordinates of catalytic reactions.

ACKNOWLEDGMENTS

E.I.S. wishes to thank his past students and collaborators, as indicated in the references cited, for their outstanding contributions to this field. This work was supported by NIH Grant DK31450. J.Y. gratefully acknowledges a Franklin Veatch Memorial Fellowship.

REFERENCES

1. Solomon EI, Sundaram UM, Machonkin TE. 1996. Multicopper oxidases and oxygenases. *Chem Rev* **96**:2563–2605.
2. Malmstrom BG. 1994. Rack-induced bonding in blue copper proteins. *Eur J Biochem* **223**:711–718.
3. Vallee BL, Williams RJP. 1968. Metalloenzymes: the entatic nature of their active sites. *Proc Nat Acad Sci USA* **59**:498–505.
4. Solomon EI, Hanson MA. 1999. Bioinorganic spectroscopy. In *Inorganic electronic structure and spectroscopy*, pp. 1–129. Ed EI Solomon and ABP Lever. New York: John Wiley & Sons.

5. Solomon EI. 1984. Inorganic spectroscopy: an overview. *Comments Inorg Chem* **3**:225–320.
6. Malkin R, Malmstrom BG. 1970. State and function of copper in biological systems. *Adv Enzymol* **33**:177–244.
7. Holm RH, Kennepohl P, Solomon EI. 1996. Structural and functional aspects of metal sites in biology. *Chem Rev* **96**:2239–2314.
8. Lieberman RA, Sands RH, Fee JA. 1982. A study of the electron paramagnetic resonance properties of single monoclinic crystals of bovine superoxide dismutase. *J Biol Chem* **257**:336–344.
9. Valentine JS, Pantoliano MW, McDonnell PJ, Burger AR, Lippard SJ. 1979. pH-dependent migration of copper(II) to the vacant zinc-binding site of zinc-free bovine erythrocyte superoxide-dismutase. *Proc Nat Acad Sci USA* **76**:4245–4249.
10. Tocheva EI, Rosell FI, Mauk AG, Murphy MEP. 2004. Side-on copper-nitrosyl coordination by nitrite reductase. *Science* **304**:867–870.
11. Matsuzaki R, Fukui T, Sato H, Ozaki Y, Tanizawa K. 1994. Generation of the topa quinone cofactor in bacterial monoamine oxidase by cupric ion-dependent autooxidation of a specific tyrosyl residue. *FEBS Lett* **351**:360–364.
12. Dove JE, Schwartz B, Williams NK, Klinman JP. 2000. Investigation of spectroscopic intermediates during copper-binding and tpq formation in wild-type and active site mutants of a copper containing amine oxidase from yeast. *Biochemistry* **39**:3690–3698.
13. Whittaker JW. 2003. Free radical catalysis by galactose oxidase. *Chem Rev* **103**:2347–2363.
14. Klinman JP. 1996. Mechanisms whereby mononuclear copper proteins functionalize organic substrates. *Chem Rev* **96**:2541–2561.
15. Branchaud BP, Montaguesmith MP, Kosman DJ, McLaren FR. 1993. Mechanism-based inactivation of galactose oxidase: evidence for a radical mechanism. *J Am Chem Soc* **115**:798–800.
16. Solomon EI, Szilagyik RK, George SD, Basumallick L. 2004. Electronic structures of metal sites in proteins and models: contributions to function in blue copper proteins. *Chem Rev* **104**:419–458.
17. Solomon EI, Baldwin MJ, Lowery MD. 1992. Electronic structures of active sites in copper proteins: contributions to reactivity. *Chem Rev* **92**:521–542.
18. Chen P, Solomon EI. 2004. O₂ activation by binuclear Cu sites: noncoupled versus exchange coupled reaction mechanisms. *Proc Nat Acad Sci USA* **101**:13105–13110.
19. Prigge ST, Kolhekar AS, Eipper BA, Mains RE, Amzel LM. 1997. Amidation of bioactive peptides: the structure of peptidylglycine α -hydroxylating monooxygenase. *Science* **278**:1300–1305.
20. Prigge ST, Kolhekar AS, Eipper BA, Mains RE, Amzel LM. 1999. Substrate-mediated electron transfer in peptidylglycine α -hydroxylating monooxygenase. *Nat Struct Biol* **6**:976–983.
21. Chen P, Solomon EI. 2004. Oxygen activation by the noncoupled binuclear copper site in peptidylglycine α -hydroxylating monooxygenase: reaction mechanism and role of the noncoupled nature of the active site. *J Am Chem Soc* **126**:4991–5000.
22. Lee SK, George SD, Antholine WE, Hedman B, Hodgson KO, Solomon EI. 2002. Nature of the intermediate formed in the reduction of O₂ to H₂O at the trinuclear copper cluster active site in native laccase. *J Am Chem Soc* **124**:6180–6193.
23. Iwata S, Ostermeier C, Ludwig B, Michel H. 1995. Structure at 2.8 Å resolution of cytochrome c oxidase from *Paracoccus denitrificans*. *Nature* **376**:660–669.

24. Tsukihara T, Aoyama H, Yamashita E, Tomizaki T, Yamaguchi H, Shinzawaitoh K, Nakashima R, Yaono R, Yoshikawa S. 1995. Structures of metal sites of oxidized bovine heart cytochrome c oxidase at 2.8 Å. *Science* **269**:1069–1074.
25. Brown K, Djjinovic-Carugo K, Haltia T, Cabrito I, Saraste M, Moura JGG, Moura I, Tegoni M, Cambillau C. 2000. Revisiting the catalytic Cu_z cluster of nitrous oxide (N₂O) reductase: evidence of a bridging inorganic sulfur. *J Biol Chem* **275**:41133–41136.
26. Brown K, Tegoni M, Prudencio M, Pereira AS, Besson S, Moura JJ, Moura I, Cambillau C. 2000. A novel type of catalytic copper cluster in nitrous oxide reductase. *Nat Struct Biol* **7**:191–195.
27. Yoshikawa S, Shinzawa-Itoh K, Nakashima R, Yaono R, Yamashita E, Inoue N, Yao M, Fei MJ, Libeu CP, Mizushima T, Yamaguchi H, Tomizaki T, Tsukihara T. 1998. Redox-coupled crystal structural changes in bovine heart cytochrome c oxidase. *Science* **280**:1723–1729.
28. Robin MB, Day P. 1967. Mixed valence chemistry: a survey and classification. *Adv Inorg Chem Radiochem* **10**:247–423.
29. Zumft WG. 1997. Cell biology and molecular basis of denitrification. *Microbiol Mol Biol Rev* **61**:533–616.
30. Chen P, Gorelsky SI, Ghosh S, Solomon EI. 2004. N₂O reduction by the μ₄-sulfide-bridged tetranuclear Cu_z cluster active site. *Angew Chem, Int Ed* **43**:4132–4140.
31. Chen P, George SD, Cabrito I, Antholine WE, Moura JGG, Moura I, Hedman B, Hodgson KO, Solomon EI. 2002. Electronic structure description of the μ₄-sulfide bridged tetranuclear Cu_z center in N₂O reductase. *J Am Chem Soc* **124**:744–745.
32. Chen P, Cabrito I, Moura JGG, Moura I, Solomon EI. 2002. Spectroscopic and electronic structure studies of the μ₄-sulfide bridged tetranuclear Cu_z cluster in N₂O reductase: molecular insight into the catalytic mechanism. *J Am Chem Soc* **124**:10497–10507.
33. Blumberg WE, Peisach J. 1966. Optical and magnetic properties of copper in chenopodium album plastocyanin. *Biochim Biophys Acta* **126**:269–273.
34. Dodd FE, Abraham ZHL, Eady RR, Hasnain SS. 2000. Structures of oxidized and reduced azurin II from alcaligenes xylooxidans at 1.75 Å resolution. *Acta Cryst Sect D* **56**:690–696.
35. Baker EN. 1988. Structure of azurin from alcaligenes denitrificans refinement at 1.8 Å resolution and comparison of the 2 crystallographically independent molecules. *J Mol Biol* **203**:1071–1095.
36. Guss JM, Bartunik HD, Freeman HC. 1992. Accuracy and precision in protein-structure analysis: restrained least-squares refinement of the structure of poplar plastocyanin at 1.33 Å resolution. *Acta Cryst Sect B* **48**:790–811.
37. Guss JM, Freeman HC. 1983. Structure of oxidized poplar plastocyanin at 1.6 Å resolution. *J Mol Biol* **169**:521–563.
38. Inoue T, Sugawara H, Hamanaka S, Tsukui H, Suzuki E, Kohzuma T, Kai Y. 1999. Crystal structure determinations of oxidized and reduced plastocyanin from the cyanobacterium synechococcus sp pcc 7942. *Biochemistry* **38**:6063–6069.
39. Kohzuma T, Inoue T, Yoshizaki F, Sasakawa Y, Onodera K, Nagatomo S, Kitagawa T, Uzawa S, Isobe Y, Sugimura Y, Gotowda M, Kai Y. 1999. The structure and unusual pH dependence of plastocyanin from the fern dryopteris crassirhizoma: the protonation of an active site histidine is hindered by π-π interactions. *J Biol Chem* **274**:11817–11823.

40. Colman PM, Freeman HC, Guss JM, Murata M, Norris VA, Ramshaw JAM, Venkatappa MP. 1978. X-ray crystal structure analysis of plastocyanin at 2.7 Å resolution. *Nature* **272**:319–324.
41. Hakulinen N, Kiiskinen LL, Kruus K, Saloheimo M, Paananen A, Koivula A, Rouvinen J. 2002. Crystal structure of a laccase from melanocarpus albomyces with an intact trinuclear copper site. *Nat Struct Biol* **9**:601–605.
42. Ducros V, Brzozowski AM, Wilson KS, Brown SH, Ostergaard P, Schneider P, Yaver DS, Pedersen AH, Davies GJ. 1998. Crystal structure of the type 2 Cu depleted laccase from coprinus cinereus at 2.2 Å resolution. *Nat Struct Biol* **5**:310–316.
43. Ducros V, Brzozowski AM, Wilson KS, Ostergaard P, Schneider P, Svendsen A, Davies GJ. 2001. Structure of the laccase from coprinus cinereus at 1.68 Å resolution: evidence for different "type 2 Cu-depleted" isoforms. *Acta Cryst Sect D* **57**:333–336.
44. Piontek K, Antorini M, Choinowski T. 2002. Crystal structure of a laccase from the fungus trametes versicolor at 1.90 Å resolution containing a full complement of copers. *J Biol Chem* **277**:37663–37669.
45. Penfield KW, Gay RR, Himmelwright RS, Eickman NC, Norris VA, Freeman HC, Solomon EI. 1981. Spectroscopic studies on plastocyanin single crystals: a detailed electronic structure determination of the blue copper active site. *J Am Chem Soc* **103**:4382–4388.
46. George SJ, Lowery MD, Solomon EI, Cramer SP. 1993. Copper L-edge spectral studies: a direct experimental probe of the ground state covalency in the blue copper site in plastocyanin. *J Am Chem Soc* **115**:2968–2969.
47. Roberts JE, Brown TG, Hoffman BM, Peisach J. 1980. Electron nuclear double resonance spectra of stellacyanin: blue copper protein. *J Am Chem Soc* **102**:825–829.
48. Scott RA, Hahn JE, Doniach S, Freeman HC, Hodgson KO. 1982. Polarized x-ray absorption spectra of oriented plastocyanin single crystals: investigation of methionine copper coordination. *J Am Chem Soc* **104**:5364–5369.
49. Shadle SE, Pennerhahn JE, Schugar HJ, Hedman B, Hodgson KO, Solomon EI. 1993. X-ray absorption spectroscopic studies of the blue copper site: metal and ligand K-edge studies to probe the origin of the EPR hyperfine splitting in plastocyanin. *J Am Chem Soc* **115**:767–776.
50. Penfield KW, Gewirth AA, Solomon EI. 1985. Electronic structure and bonding of the blue copper site in plastocyanin. *J Am Chem Soc* **107**:4519–4529.
51. Wasinger EC, de Groot FMF, Hedman B, Hodgson KO, Solomon EI. 2003. L-edge x-ray absorption spectroscopy of non-heme iron sites: experimental determination of differential orbital covalency. *J Am Chem Soc* **125**:12894–12906.
52. Solomon EI, Hedman B, Hodgson KO, Dey A, Szilagyi RK. 2005. Ligand K-edge x-ray absorption spectroscopy: Covalency of ligand-metal bonds. *Coord Chem Rev* **249**:97–129.
53. Hughey JL, Fawcett TG, Rudich SM, Lalancette RA, Potenza JA, Schugar HJ. 1979. Preparation and characterization of [rac-5,7,7,12,14,14-hexamethyl-1,4,8,11-tetraazocyclotetradecane]copper(II) o-mercaptobenzoate hydrate, [Cu(tet b)(o-SC₆H₄CO₂)]·H₂O, a complex with a CuN₄S (mercaptide) chromophore. *J Am Chem Soc* **101**:2617–2623.
54. George SD, Basumallick L, Szilagyi RK, Randall DW, Hill MG, Nersissian AM, Valentine JS, Hedman B, Hodgson KO, Solomon EI. 2003. Spectroscopic investigation of stellacyanin mutants: axial ligand interactions at the blue copper site. *J Am Chem Soc* **125**:11314–11328.

55. Gewirth AA, Solomon EI. 1988. Electronic structure of plastocyanin: excited state spectral features. *J Am Chem Soc* **110**:3811–3819.
56. Solomon EI, Randall DW, Glaser T. 2000. Electronic structures of active sites in electron transfer metalloproteins: Contributions to reactivity. *Coord Chem Rev* **200**:595–632.
57. LaCroix LB, Randall DW, Nersissian AM, Hoitink CWG, Canters GW, Valentine JS, Solomon EI. 1998. Spectroscopic and geometric variations in perturbed blue copper centers: electronic structures of stellacyanin and cucumber basic protein. *J Am Chem Soc* **120**:9621–9631.
58. Randall DW, Gamelin DR, LaCroix LB, Solomon EI. 2000. Electronic structure contributions to electron transfer in blue Cu and Cu_A. *J Bio Inorg Chem* **5**:16–29.
59. LaCroix LB, Shadle SE, Wang YN, Averill BA, Hedman B, Hodgson KO, Solomon EI. 1996. Electronic structure of the perturbed blue copper site in nitrite reductase: spectroscopic properties, bonding, and implications for the entatic/rack state. *J Am Chem Soc* **118**:7755–7768.
60. Suzuki S, Kohzuma T, Deligeer, Yamaguchi K, Nakamura N, Shidara S, Kobayashi K, Tagawa S. 1994. Pulse radiolysis studies on nitrite reductase from achromobacter cycloclastes IAM 1013: evidence for intramolecular electron transfer from type 1 Cu to type 2 Cu. *J Am Chem Soc* **116**:11145–11146.
61. Gewirth AA, Cohen SL, Schugar HJ, Solomon EI. 1987. Spectroscopic and theoretical studies of the unusual electron paramagnetic resonance parameters of distorted tetrahedral cupric sites: correlations to x-ray spectral features of core levels. *Inorg Chem* **26**:1133–1146.
62. Beinert H, Wharton DC, Griffiths DE, Sands RH. 1962. Properties of copper associated with cytochrome oxidase as studied by paramagnetic resonance spectroscopy. *J Biol Chem* **237**:2337–2346.
63. Peisach J, Blumberg WE. 1974. Structural implications derived from analysis of electron paramagnetic resonance spectra of natural and artificial copper proteins. *Arch Biochem Biophys* **165**:691–708.
64. Kroneck PMH, Antholine WE, Kastrau DHW, Buse G, Steffens GCM, Zumft WG. 1990. Multifrequency EPR evidence for a bimetallic center at the Cu_A site in cytochrome c oxidase. *FEBS Lett* **268**:274–276.
65. Kroneck PMH, Antholine WA, Riestler J, Zumft WG. 1988. The cupric site in nitrous oxide reductase contains a mixed-valence [Cu(II),Cu(I)] binuclear center: a multifrequency electron paramagnetic resonance investigation. *FEBS Lett* **242**:70–74.
66. Antholine WE, Kastrau DHW, Steffens GCM, Buse G, Zumft WG, Kroneck PMH. 1992. A comparative EPR investigation of the multicopper proteins nitrous-oxide reductase and cytochrome c oxidase. *Eur J Biochem* **209**:875–881.
67. Blackburn NJ, Barr ME, Woodruff WH, Vanderroost J, Devries S. 1994. Metal–metal bonding in biology: EXAFS evidence for a 2.5 Å copper–copper bond in the Cu_A center of cytochrome oxidase. *Biochemistry* **33**:10401–10407.
68. Blackburn NJ, deVries S, Barr ME, Houser RP, Tolman WB, Sanders D, Fee JA. 1997. X-ray absorption studies on the mixed-valence and fully reduced forms of the soluble Cu_A domains of cytochrome c oxidase. *J Am Chem Soc* **119**:6135–6143.
69. Gamelin DR, Randall DW, Hay MT, Houser RP, Mulder TC, Canters GW, de Vries S, Tolman WB, Lu Y, Solomon EI. 1998. Spectroscopy of mixed-valence Cu_A type centers: Ligand field control of ground state properties related to electron transfer. *J Am Chem Soc* **120**:5246–5263.

70. Farrar JA, Neese F, Lappalainen P, Kroneck PMH, Saraste M, Zumft WG, Thomson AJ. 1996. The electronic structure of Cu_A: a novel mixed-valence dinuclear copper electron transfer center. *J Am Chem Soc* **118**:11501–11514.
71. George SD, Metz M, Szilagyik RK, Wang HX, Cramer SP, Lu Y, Tolman WB, Hedman B, Hodgson KO, Solomon EI. 2001. A quantitative description of the ground state wave function of Cu_A by x-ray absorption spectroscopy: comparison to plastocyanin and relevance to electron transfer. *J Am Chem Soc* **123**:5757–5767.
72. Gamelin DR, Bominaar EL, Mathoniere C, Kirk ML, Wieghardt K, Girerd JJ, Solomon EI. 1996. Excited-state distortions and electron delocalization in mixed-valence dimers: vibronic analysis of the near IR absorption and resonance Raman profiles of [Fe₂(OH)₃(tmtacn)₂]²⁺. *Inorg Chem* **35**:4323–4335.
73. Houser RP, Young VG, Tolman WB. 1996. Thiolate-bridged, fully delocalized mixed-valence dicopper(I,II) complex that models the Cu_A biological electron transfer site. *J Am Chem Soc* **118**:2101–2102.
74. Williams KR, Gamelin DR, LaCroix LB, Houser RP, Tolman WB, Mulder TC, deVries S, Hedman B, Hodgson KO, Solomon EI. 1997. Influence of copper–sulfur covalency and copper–copper bonding on valence delocalization and electron transfer in the Cu_A site of cytochrome c oxidase. *J Am Chem Soc* **119**:613–614.
75. Gurbiel RJ, Fann YC, Surerus KK, Werst MM, Musser SM, Doan PE, Chan SI, Fee JA, Hoffman BM. 1993. Detection of 2 histidyl ligands to Cu_A of cytochrome oxidase by 35 GHz ENDOR: ^{14,15}N and ^{63,65}Cu ENDOR studies of the Cu_A site in bovine heart cytochrome-aa₃ and cytochrome-caa₃ and cytochrome-ba₃ from thermus thermophilus. *J Am Chem Soc* **115**:10888–10894.
76. Solomon EI, Chen P, Metz M, Lee SK, Palmer AE. 2001. Oxygen binding, activation, and reduction to water by copper proteins. *Angew Chem Int Ed* **40**:4570–4590.
77. Co MS, Hodgson KO, Eccles TK, Lontie R. 1981. Copper site of molluscan oxyhemocyanins: structural evidence from x-ray absorption spectroscopy. *J Am Chem Soc* **103**:984–986.
78. Matoba Y, Kumagai T, Yamamoto A, Yoshitsu H, Sugiyama M. 2006. Crystallographic evidence that dinuclear copper center of tyrosinase is flexible during catalysis. *J Biol Chem* **281**:8981–8990.
79. Magnus KA, Hazes B, Tonthat H, Bonaventura C, Bonaventura J, Hol WGJ. 1994. Crystallographic analysis of oxygenated and deoxygenated states of arthropod hemocyanin shows unusual differences. *Proteins* **19**:302–309.
80. Dooley DM, Scott RA, Ellinghaus J, Solomon EI, Gray HB. 1978. Magnetic susceptibility studies of laccase and oxyhemocyanin. *Proc Nat Acad Sci USA* **75**:3019–3022.
81. Crawford VH, Richardson HW, Wasson JR, Hodgson DJ, Hatfield WE. 1976. Relationship between singlet–triplet splitting and Cu–O–Cu bridge angle in hydroxo-bridged copper dimers. *Inorg Chem* **15**:2107–2110.
82. Hay PJ, Thibeault JC, Hoffmann R. 1975. Orbital interactions in metal dimer complexes. *J Am Chem Soc* **97**:4884–4899.
83. Pate JE, Cruse RW, Karlin KD, Solomon EI. 1987. Vibrational, electronic, and resonance Raman spectral studies of [Cu₂(XYL–O–)O₂]⁺, a copper(II) peroxide model complex of oxyhemocyanin. *J Am Chem Soc* **109**:2624–2630.
84. Eickman NC, Himmelwright RS, Solomon EI. 1979. Geometric and electronic structure of oxyhemocyanin: spectral and chemical correlations to met apo, half met, met, and dimer active sites. *Proc Nat Acad Sci USA* **76**:2094–2098.

85. Baldwin MJ, Root DE, Pate JE, Fujisawa K, Kitajima N, Solomon EI. 1992. Spectroscopic studies of side-on peroxide-bridged binuclear copper(II) model complexes of relevance to oxyhemocyanin and oxytyrosinase. *J Am Chem Soc* **114**:10421–10431.
86. Metz M, Solomon EI. 2001. Dioxygen binding to deoxyhemocyanin: electronic structure and mechanism of the spin-forbidden two-electron reduction of O₂. *J Am Chem Soc* **123**:4938–4950.
87. Prigge ST, Eipper BA, Mains RE, Amzel LM. 2004. Dioxygen binds end-on to mononuclear copper in a precatalytic enzyme complex. *Science* **304**:864–867.
88. Jaron S, Blackburn NJ. 1999. Does superoxide channel between the copper centers in peptidylglycine monooxygenase? a new mechanism based on carbon monoxide reactivity. *Biochemistry* **38**:15086–15096.
89. Bell J, El Meskini R, D'Amato D, Mains RE, Eipper BA. 2003. Mechanistic investigation of peptidylglycine α -hydroxylating monooxygenase via intrinsic tryptophan fluorescence and mutagenesis. *Biochemistry* **42**:7133–7142.
90. Boswell JS, Reedy BJ, Kulathila R, Merkler D, Blackburn NJ. 1996. Structural investigations on the coordination environment of the active site copper centers of recombinant bifunctional peptidylglycine α -amidating enzyme. *Biochemistry* **35**:12241–12250.
91. Blackburn NJ, Rhames FC, Ralle M, Jaron S. 2000. Major changes in copper coordination accompany reduction of peptidylglycine monooxygenase: implications for electron transfer and the catalytic mechanism. *J Biol Inorg Chem* **5**:341–353.
92. Eipper BA, Quon ASW, Mains RE, Boswell JS, Blackburn NJ. 1995. The catalytic core of peptidylglycine α -hydroxylating monooxygenase: investigation by site-directed mutagenesis, Cu x-ray absorption spectroscopy, and electron paramagnetic resonance. *Biochemistry* **34**:2857–2865.
93. Chen P, Bell J, Eipper BA, Solomon EI. 2004. Oxygen activation by the noncoupled binuclear copper site in peptidylglycine α -hydroxylating monooxygenase: spectroscopic definition of the resting sites and the putative Cu_M(II)-OOH intermediate. *Biochemistry* **43**:5735–5747.
94. Blackburn NJ, Concannon M, Shahiyan SK, Mabbs FE, Collison D. 1988. Active site of dopamine β -hydroxylase: comparison of enzyme derivatives containing 4 and 8 copper atoms per tetramer using potentiometry and electron paramagnetic resonance spectroscopy. *Biochemistry* **27**:6001–6008.
95. Tian GC, Berry JA, Klinman JP. 1994. O-18 kinetic isotope effects in the dopamine β -monooxygenase reaction: evidence for a new chemical mechanism in nonheme metal-lomooxygenases. *Biochemistry* **33**:226–234.
96. Evans JP, Ahn K, Klinman JP. 2003. Evidence that dioxygen and substrate activation are tightly coupled in dopamine β -monooxygenase: implications for the reactive oxygen species. *J Biol Chem* **278**:49691–49698.
97. Marcus RA, Sutin N. 1985. Electron transfers in chemistry and biology. *Biochim Biophys Acta* **811**:265–322.
98. Tuzcek F, Solomon EI. 1994. Charge transfer states and antiferromagnetism of bridged Cu dimers: application to oxyhemocyanin. *J Am Chem Soc* **116**:6916–6924.
99. Tuzcek F, Solomon EI. 2001. Excited electronic states of transition metal dimers and the VBCI model: an overview. *Coord Chem Rev* **219**:1075–1112.
100. Messerschmidt A, Ladenstein R, Huber R, Bolognesi M, Avigliano L, Petruzzelli R, Rossi A, Finazziagro A. 1992. Refined crystal structure of ascorbate oxidase at 1.9 Å resolution. *J Mol Biol* **224**:179–205.

101. Cole JL, Ballou DP, Solomon EI. 1991. Spectroscopic characterization of the peroxide intermediate in the reduction of dioxygen catalyzed by the multicopper oxidases. *J Am Chem Soc* **113**:8544–8546.
102. Palmer AE, Lee SK, Solomon EI. 2001. Decay of the peroxide intermediate in laccase: reductive cleavage of the O-O bond. *J Am Chem Soc* **123**:6591–6599.
103. Quintanar L, Yoon J, Aznar CP, Palmer AE, Andersson KK, Britt RD, Solomon EI. 2005. Spectroscopic and electronic structure studies of the trinuclear Cu cluster active site of the multicopper oxidase laccase: nature of its coordination unsaturation. *J Am Chem Soc* **127**:13832–13845.
104. Cole JL, Clark PA, Solomon EI. 1990. Spectroscopic and chemical studies of the laccase trinuclear copper active site: geometric and electronic structure. *J Am Chem Soc* **112**:9534–9548.
105. Clark PA, Solomon EI. 1992. Magnetic circular dichroism spectroscopic definition of the intermediate produced in the reduction of dioxygen to water by native laccase. *J Am Chem Soc* **114**:1108–1110.
106. Aasa R, Branden R, Deinum J, Malmstrom BG, Reinhammar B, Vanngard T. 1976. ^{17}O effect on EPR spectrum of intermediate in dioxygen–laccase reaction. *Biochem Biophys Res Comm* **70**:1204–1209.
107. Yoon J, Mirica LM, Stack TDP, Solomon EI. 2004. Spectroscopic demonstration of a large antisymmetric exchange contribution to the spin-frustrated ground state of a D_3 symmetric hydroxy-bridged trinuclear Cu(II) complex: ground-to-excited state superexchange pathways. *J Am Chem Soc* **126**:12586–12595.
108. Mirica LM, Stack TDP. 2005. A tris(μ -hydroxy)tricopper(II) complex as a model of the native intermediate in laccase and its relationship to a binuclear analogue. *Inorg Chem* **44**:2131–2133.
109. Dzyaloshinsky I. 1958. A thermodynamic theory of weak ferromagnetism of antiferromagnetics. *J Phys Chem Solids* **4**:241–255.
110. Moriya T. 1960. Anisotropic superexchange interaction and weak ferromagnetism. *Phys Rev* **120**:91–98.
111. Moriya T. 1963. Weak ferromagnetism. In *Magnetism*, pp. 85–125. Ed GT Rado and H Suhl. New York: Academic Press.
112. Tsukerblat BS, Belinskii MI, Fainzil'berg VE. 1987. Magnetochemistry and spectroscopy of transition metals exchange clusters. *Sov Sci Rev B Chem* **9**:337–481.
113. Murao T. 1974. Jahn-Teller effect in trinuclear complexes. *Phys Lett A* **49**:33–35.
114. Yoon J, Solomon EI. 2005. Ground-state electronic and magnetic properties of a μ_3 -oxo-bridged trinuclear Cu(II) complex: correlation to the native intermediate of the multicopper oxidases. *Inorg Chem* **44**:8076–8086.
115. Suh MP, Han MY, Lee JH, Min KS, Hyeon C. 1998. One-pot template synthesis and properties of a molecular bowl: dodecaaza macrotetracycle with μ_3 -oxo and μ_3 -hydroxo tricopper(II) cores. *J Am Chem Soc* **120**:3819–3820.
116. Yoon J, Mirica LM, Stack TDP, Solomon EI. 2005. Variable-temperature, variable-field magnetic circular dichroism studies of tris-hydroxy- and μ_3 -oxo-bridged trinuclear Cu(II) complexes: evaluation of proposed structures of the native intermediate of the multicopper oxidases. *J Am Chem Soc* **127**:13680–13693.
117. Farrar JA, Thomson AJ, Cheesman MR, Dooley DM, Zumft WG. 1991. A model of the copper centers of nitrous-oxide reductase (pseudomonas-stutzeri): evidence from optical, EPR and MCD spectroscopy. *FEBS Lett* **294**:11–15.
118. Farrar JA, Zumft WG, Thomson AJ. 1998. Cu_A and Cu_Z are variants of the electron transfer center in nitrous oxide reductase. *Proc Nat Acad Sci USA* **95**:9891–9896.

119. Prudencio M, Pereira AS, Tavares P, Besson S, Cabrito I, Brown K, Samyn B, Devreese B, Van Beeumen J, Rusnak F, Fauque G, Moura JJG, Tegoni M, Cambillau C, Moura I. 2000. Purification, characterization, and preliminary crystallographic study of copper containing nitrous oxide reductase from *pseudomonas nautica* 617. *Biochemistry* **39**:3899–3907.
120. Froncisz W, Hyde JS. 1980. Broadening by strains of lines in the g_{\parallel} region of Cu^{2+} electron paramagnetic resonance. *J Chem Phys* **73**:3123–3131.
121. Oganessian VS, Rasmussen T, Fairhurst S, Thomson AJ. 2004. Characterisation of $[\text{Cu}_4\text{S}]$, the catalytic site in nitrous oxide reductase, by EPR spectroscopy. *Dalton Trans* 996–1002.
122. Gorelsky SI, Ghosh S, Solomon EI. 2006. Mechanism of N_2O reduction by the μ_4 -S tetranuclear Cu_z cluster of nitrous oxide reductase. *J Am Chem Soc* **128**:278–290.
123. Ghosh S, Gorelsky SI, Chen P, Cabrito I, Moura JJG, Moura I, Solomon EI. 2003. Activation of N_2O reduction by the fully reduced μ_4 -sulfide bridged tetranuclear Cu_z cluster in nitrous oxide reductase. *J Am Chem Soc* **125**:15708–15709.

METALS IN MEDICINE

INSULIN-ENHANCING VANADIUM PHARMACEUTICALS: THE ROLE OF ELECTRON PARAMAGNETIC RESONANCE METHODS IN THE EVALUATION OF ANTIDIABETIC POTENTIAL

Barry D. Liboiron

*Centre for Blood Research, Department of Biochemistry
and Molecular Biology, University of British Columbia,
Vancouver, BC, Canada*

Electron paramagnetic resonance spectroscopy has been heavily used for the study of vanadium(IV) compounds in both naturally containing vanadium species and spin-labeled or metal-substituted systems. Vanadium compounds have been shown to possess potent antidiabetic properties such as normalization of blood glucose levels and lipid metabolism. Vanadium compounds, and in particular vanadyl ($V^{IV}O^{2+}$) coordination complexes, represent a potential new treatment option for diabetes mellitus. Understanding of the metabolism and mechanism of these complexes in vivo has been greatly expanded over the past 25 years in large part due to contributions made through the use of EPR spectroscopy. This review will outline the application of EPR to the study of antidiabetic vanadium(IV) compounds and highlight important studies of the in-vitro and in-vivo properties of these complexes in which EPR made a critical contribution. The role of EPR spectroscopy in the field of vanadium antidiabetic pharmaceuticals has led to major advances in the optimization of chemical structure, formulation, and descriptions of vanadium metabolism.

1. INTRODUCTION

The antidiabetic potential of the transition metal vanadium has been known for over 100 years [1], and the last 25 years has marked a period of intense research interest in the development of vanadium salts and complexes as a new treatment for diabetes mellitus. The first report of the strong inhibitory effects of sodium metavanadate ($NaVO_3$) to phosphatases [2,3] was followed by subsequent experiments demonstrating insulin-like effects on isolated adipocytes [4] by vanadyl ion (VO^{2+}). Proof of in-vivo activity after oral administration of a vanadium(V) salt in diabetic rats [5] spurred a flurry of interest in vanadium(V), later followed by sus-

tained interest in the biological activities of V(IV) salts and complexes. A wide variety of vanadyl-based compounds have been synthesized and tested for antidiabetic activity (a sample of which appear in Fig. 1). A number of them have shown promise as antidiabetic therapeutic agents for their ability to enhance the effects of endogenous insulin via oral administration. Vanadium compounds normalize glucose levels in the bloodstream and ameliorate lipid metabolism [6–8] while not increasing the circulating levels of insulin (critical in treatment of Type II, non-insulin-dependent diabetes mellitus) [9,10]. In general, vanadium complexes are orally active [5,11], long-lasting (as much as 16 days after cessation of treatment in diabetic animals [12]), and more effective than VOSO_4 [13,14]; they represent a potential new treatment option for patients with diabetes, particularly Type 2 (non-insulin-dependent diabetes mellitus) diabetics. Frequently in the literature, vanadium compounds are referred to as “insulin-mimics” but these compounds can never truly substitute for insulin [15]. Thus, in this review and now in general use throughout the literature, these compounds will be more properly referred to as insulin-enhancing.

Table 1. Spin Hamiltonian Parameters for Several Classes of Insulin-Enhancing Vanadium Complexes

#	Compound	Coord. mode ^a	g_0	g_x	g_y	g_z	$ A_0 $	$ A_x $	$ A_y $	$ A_z $	Notes	Ref.
1	$\text{VO}(\text{3mpa})_2$	N_2O_2	1.975	1.989	1.989	1.947	92.4	54.5	54.5	168.3	saline	[84]
2	$\text{VO}(\text{5ipa})_2$	N_2O_2	1.976	1.991	1.991	1.945	92.2	52.7	52.7	166.9	1:20 DMSO: H_2O	[12]
3	$\text{VO}(\text{6hpa})_2^b$	N_2O_2	1.966	1.981	1.981	1.936	107.3	72.6	72.6	177.8	saline	[84]
4	$\text{VO}(\text{6mpa})_2$	N_2O_2	1.981	2.002	2.002	1.941	92.2	53.4	53.4	164.0	saline	[12]
5	$\text{VO}(\text{pic})_2$	N_2O_2	1.981	1.998	1.998	1.945	93.4	53.5	53.5	168.2	saline	[12]
6	$\text{VO}(\text{3hpa})_2^c$	NO_3	1.975	1.991	1.991	1.944	95.1	57.7	57.7	172.6	saline	[84]
7	$\text{VO}(\text{2hpo})_2$	O_4	1.967	1.982	1.978	1.942	97.6	61	66	166		[45]
8	$\text{VO}(\text{acac})_2$	O_4	1.966	1.976	1.976	1.946	99.5	59.0	59.0	182.0		[59]
9	$\text{VO}(\text{ema})_2$	O_4	1.966	1.978	1.976	1.938	98	63	63	173		
10	$\text{VO}(\text{ima})_2$	O_4	1.967	1.978	1.978	1.937	101.0	65.8	65.8	175.2	5:1	[23]
11	$\text{VO}(\text{ma})_2$	O_4	1.9646	1.979	1.975	1.938	95.5	62.3	59.4	171.00	MeOH:glycerol 1:1 H_2O : glycerol	[57]
12	$[\text{VO}(\text{H}_2\text{O})_2]^{2+}$	O_4	1.964	1.979	1.979	1.932	106.3	70	70	182.6		[57]
13	$\text{VO}(\text{mpo})_2$	S_2O_2	1.974	1.983	1.983	1.957	89.0	56	56	155		[45]
14	$\text{VO}(\text{tma})_2$	S_2O_2	1.974	1.982	1.982	1.954	85.0	52.0	51.5	153.0		[104]

Parameters were determined from spectra acquired in aqueous solution unless otherwise noted.

^a Equatorial donors only. The influence of the axial ligand on the spin Hamiltonian parameters is minor [21].

^b By ligand set, $\text{VO}(\text{6hpa})_2$ should possess an N_2O_2 coordination set, but water molecules likely displace the weakly bound pyridyl nitrogens in solution.

^c Shown by x-ray crystallography to possess asymmetric ligand coordination; one ligand binds with the 3-hydroxyl and 2-carboxylate oxygens, while the other ligand coordinates via the pyridyl nitrogen and 2-carboxylate oxygen [40].

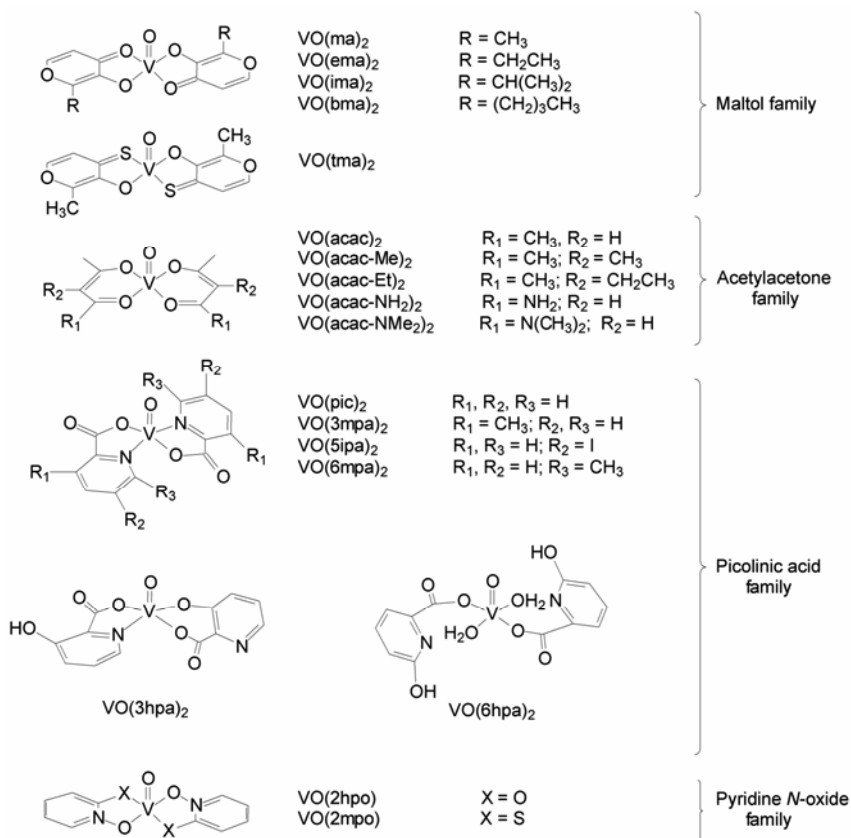


Figure 1. Chemical structures of the main families of insulin-enhancing vanadium(IV) compounds.

1.1. EPR and the Study of Insulin-Enhancing Vanadium Compounds

Electron paramagnetic resonance (EPR) spectroscopy has played a critical role in the development of vanadium(IV) antidiabetic compounds. Ironically, one of the first uses of the vanadyl ion as a spin probe was with the hormone insulin [16]; disfunctions of insulin production and its messaging cascade are the pathogenesis of Type 1 and Type 2 diabetes mellitus, respectively [17]. EPR, and its higher-resolution counterparts electron nuclear double resonance (ENDOR) and electron spin echo envelope modulation (ESEEM), are ideally suited for investigations of the structural, chemical, and biological characteristics of V(IV) compounds. Despite the effectiveness of vanadium compounds in the normalization of blood glucose levels, some resistance to their use remains, mainly due to concerns regarding compound toxicity [17] and a general lack of knowledge of the mechanism of ac-

tion [18]. Therefore, current focal points of the field are: (i) complete description of the solution structures of candidate compounds, (ii) characterization of interactions of the compounds with endogenous ligands by in-vitro and in-vivo methods, (iii) delineation of the absorption, transport, and elimination of vanadium, and (iv) identification of a metabolic target(s) where insulin-enhancing vanadium compounds exert their antidiabetic effects. EPR, ENDOR, and ESEEM have been applied successfully to this range of research topics, and the contributions made to the field of vanadium antidiabetic agents has been critical to its continuing development. In spite of the utility of EPR in these studies, a review of the literature emphasizing its role is lacking, and this review will serve to summarize the important contributions made by EPR in a wide variety of studies.

A brief introduction to the spectroscopic properties of vanadium(IV) is provided, along with identification of key concepts crucial to the successful application of EPR methods to research questions in the field. Specific discussions of EPR spectroscopies, such as continuous wave and pulsed methods, have been recently reviewed [19,20]. The discussion of the use of VO^{2+} ions as spin probes by N.D. Chasteen remains a seminal review paper in the field for its complete overview of the spectroscopic properties of the VO^{2+} ion and application to biological systems [21]. Numerous reviews on the biochemical activity of vanadium compounds are available [22–26], and the rationales for development and synthetic routes to new vanadium compounds are also reported [27,28]. A recent study evaluated the in-vitro activity of 22 compounds currently studied in the literature [29]. In this review, EPR's role in the delineation of structure, chemistry, and in-vivo behavior of vanadium compounds will be discussed. The first section of the review focuses on the use of EPR for the description of solution structures, ternary complex formation, and redox chemistry of vanadium(IV) and (V) compounds, with the general theme of highlighting in-vitro studies. This section is followed by a discussion of the application of EPR for in-vivo investigations of vanadium cellular uptake, pharmacokinetics, and in-vivo coordination structure.

1.2. EPR Properties of the Vanadyl Ion

Vanadium(IV), almost always found as the highly stable oxocation VO^{2+} , is a Kramers doublet, $S = \frac{1}{2}$ system that is very well suited to EPR studies. Following Cu(II), it is the second most-studied $S = \frac{1}{2}$ system. Vanadium(IV) is rarely found without an oxo ligand, and some notable exceptions do occur [26,30], but since all currently reported insulin-enhancing vanadium(IV) compounds are based on the vanadyl ion, the “naked” vanadium(IV) structural motif will not be discussed.

The near-square pyramidal structure of most VO^{2+} complexes yields an orbitally nondegenerate d_{xy} ground state with no low-lying excited states. This leads to slow relaxation behavior in EPR and allows for observation of vanadyl signals at ambient temperatures. Such spectra provide additional structural and/or dynamic information; this spectral property of vanadium compounds has been exploited in studies of protein interactions and cellular uptake of vanadium. The typical room-temperature EPR spectrum of $[\text{VO}(\text{H}_2\text{O})_5]^{2+}$ in acidic solution has eight equally

spaced lines arising from hyperfine coupling to the $I = 7/2$ ^{51}V nucleus (99.75% abundant). The spectrum is nearly isotropic due to rapid tumbling of the ion in solution. A key chemical property of vanadyl ions in solution that affects EPR spectroscopy is the hydrolysis series; as pH is raised in a solution of vanadyl ions in a non-coordinating buffer or solvent, signal intensity is lost due to formation of polymeric $\text{VO}(\text{OH})_2$ and hydroxo-bridged dimers, both of which are EPR silent [31]. This property serves to simplify vanadyl binding experiments to biological ligands as at $\text{pH} > 5$ any unbound VO^{2+} is not observed in the EPR spectrum [21]. Oxidation of vanadyl species to the EPR-silent $\text{V}(\text{V})$ state can be relatively rapid (minutes), so that sample preparation and manipulation should be conducted in an anaerobic atmosphere.

From room-temperature spectra (i.e., free motion regime), the isotropic spin Hamiltonian parameters g_0 and A_0 can be determined either through empirical methods (e.g., $A_0 = [\text{Resonant Field}(7/2 \text{ peak}) - \text{Resonant Field}(-7/2 \text{ peak})/7]$), or through simulation. These parameters are sensitive to the coordination environment of the vanadyl ion. Frozen solution spectra of vanadyl complexes are almost always axial, with $2.0023 > g_{x,y} > g_z$ with rhombicity, uncommonly observed at X-band, usually small at $g_x - g_y \leq 0.006$. Frozen solution spectra appear empirically as two sets of 8 lines each, corresponding to the perpendicular and parallel orientations of the molecule. These anisotropic spectra can also be observed at ambient temperature (i.e., not frozen) if the molecular tumbling rate is slow (i.e., slow-motion regime). Spectra of vanadyl-protein complexes frequently meet this requirement and so are observed as rigid-limit spectra even at room temperature. This property is very useful for the observation of vanadyl coordination to immobile or slowly tumbling moieties in solution as the intensity of the anisotropic signal can be quantified to characterize the binding interaction.

In frozen solution, perpendicular A values are small ($55\text{--}80 \times 10^{-4} \text{ cm}^{-1}$) and largely insensitive to changes in ligand environment. The parallel g and A values, however, show a large range ($1.92 > g_{\parallel} > 1.96$; $130 > A_{\parallel} > 220 \times 10^{-4} \text{ cm}^{-1}$) and are sensitive to the number and type of ligand donor. The relative contributions of any one ligand donor to the observed A_{\parallel} value have been determined for many ligands, which forms the basis of the widely used additivity rule for vanadyl complexes discussed in the next section.

Due to the unpaired electron residing in the essentially non-bonding d_{xy} orbital, ligand superhyperfine splitting is rarely observed, instead metal hyperfine lines are broadened due to unresolved ^1H or ^{14}N ligand superhyperfine coupling. Proton broadening of EPR resonant peaks has been used to quantify coordinated water molecules [32]. Information regarding the magnitude of ligand superhyperfine coupling constants can be obtained through application of pulsed methods, either ENDOR or ESEEM. Recent reviews describe these spectroscopies in greater detail [19,20,33].

1.3. The Additivity Rule

Structural characterization of vanadyl complexes in solution has been greatly assisted through the application of the additivity rule developed by Wüthrich [34] and Chasteen [21], and expanded by several others [35–39]. In its simplest form, values of g_o and A_o , and later, $g_{||}$ and $A_{||}$, can be correlated with particular ligand donor sets, such as S_2O_2 , or N_4 or N_2O_2 , where the subscripts indicate the number of individual donor atoms of that particular element in the equatorial coordination sphere. Figure 2 presents such a correlation for a series of insulin-enhancing vanadium(IV) compounds reported in the recent literature (and shown in Fig. 1), based on spin Hamiltonian parameters reported in Table 1. As shown in the figure, each type of ligand set occupies a discrete region of the plot, such that once the spin Hamiltonian parameters are known for a particular species, some insight can be gained regarding its composition. Combining this knowledge with prior information about possible ligating groups frequently allows for unambiguous assignment of a solution structure. Some caution is in order, however, as shown in Figure 2, as there can be considerable overlap of regions in some cases and it is not always possible to make a clean assignment based on EPR data alone [20,21].

A more advanced method of structural assignment is based on extracted contributions of individual ligand donors to the observed $A_{||}$ value. Ligand contributions have been determined for a wide range of ligands, from water ($45.7 \times 10^{-4} \text{ cm}^{-1}$) to thiols ($31.9 \times 10^{-4} \text{ cm}^{-1}$), with the magnitude of the individual $A_{||}$ contribution inversely correlated with electron donor strength. The sum total of the individual ligand contributions yields an estimated $A_{||}$ value that can be compared to experiment. This method can be a powerful technique for differentiation of coordination modes for multidentate ligands. The generally accepted error, as reported by Chasteen [21], is $\pm 1.5 \times 10^{-4} \text{ cm}^{-1}$ per donor, which is large enough to frequently result in more than one acceptable solution for any given experimental $A_{||}$ value. The additivity rule is discussed in detail by Chasteen [21] and Smith et al. [20], the latter of which includes a table of all currently known extracted $A_{||}$ contributions for a wide range of ligands.

2. IN VITRO STUDIES OF VANADIUM SPECIATION AND REDOX CHEMISTRY

The favorable spectral properties of the vanadyl ion have led to its predominant role as a method for the structural characterization of vanadium(IV) antidiabetic complexes. While crystal structures are available for several compounds [11,40–43], the behavior and structure(s) of the complex in solution must also be elucidated in order to (i) accurately predict interactions in the body, (ii) predict stability to endogenous chelating agents, (iii) determine number and nature (i.e., pH dependence) of structural isomers and solution complexes, and (iv) evaluate the redox activity of the complex. EPR spectroscopy has been used for all of these purposes.

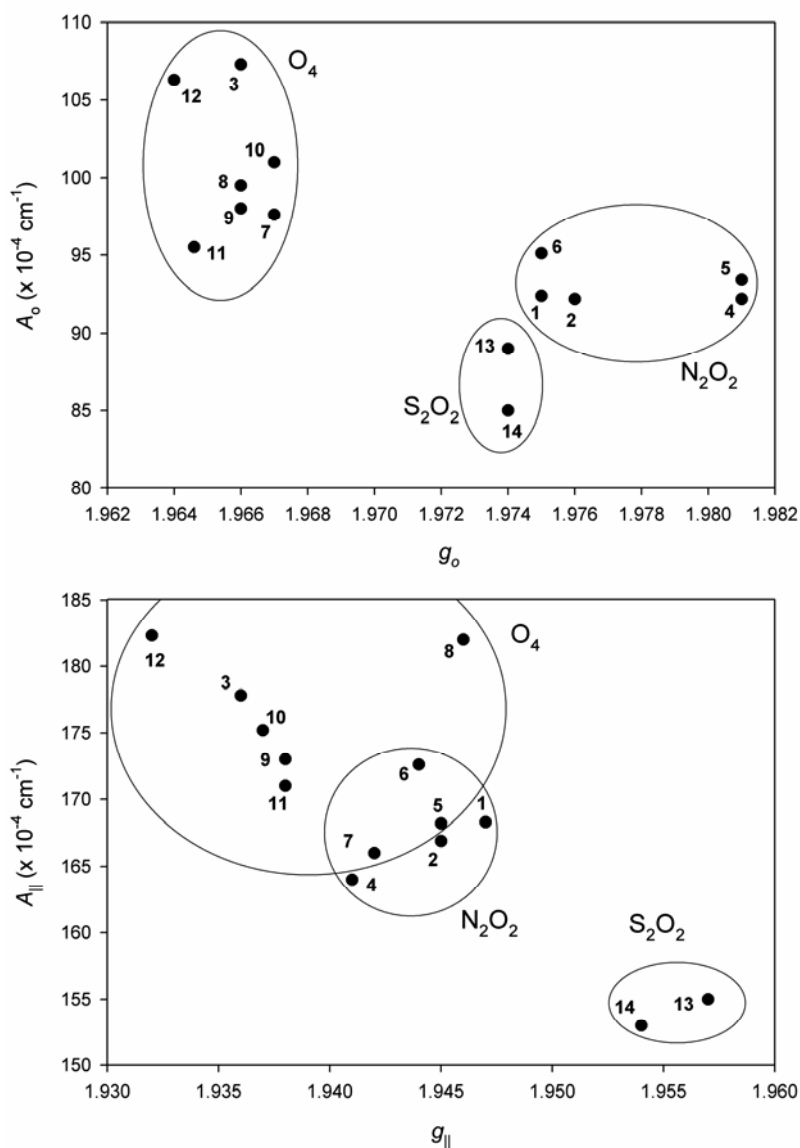


Figure 2. Correlation of spin Hamiltonian parameters of insulin-enhancing vanadium(IV) compounds listed in Table 1 to equatorial donor compositions O_4 , N_2O_2 , and S_2O_2 . Number labels correspond to the number of the complex in the table. The ellipses for each coordination type were drawn arbitrarily to contain all members of the group and are actually stricter boundaries for each coordination type than those shown in [21]. Top: Correlation between A_0 and g_0 for spectra obtained in water. Bottom: Correlation between $A_{||}$ and $g_{||}$ for spectra obtained in frozen aqueous solution (unless otherwise indicated in Table 1).

Despite the utility of the additivity rule, without supporting data occasionally it can be difficult to narrow down possible solution structures to one possibility based on EPR data alone. EPR is frequently paired with other techniques, most often potentiometry [41,42,44–48], to detect the number of species and to use the additivity rule to give insights into the first coordination sphere donor atoms of the moieties in solution. This information can then be used in the fitting of potentiometric titration curves, which reports on the absolute and relative thermodynamic stabilities of species in solution. EPR spectroscopy is also used as a complementary technique to ^{51}V NMR [49–51], allowing for characterization of both V(IV) and V(V) complexes in solution. Other techniques include UV–Vis spectroscopy [41,44,46], circular dichroism [48] and neutron activation analysis [52–56].

2.1. Solution Structures of Insulin-Enhancing Vanadium(IV) Complexes

The most common use of EPR for in-vitro studies of insulin-enhancing vanadium complexes is for detection and characterization of solution structures. The solution chemistry of a number of antidiabetic vanadium compounds, determined by EPR in concert with other techniques, has been reported. Of particular interest is the aqueous solution structure of vanadium compounds, as such knowledge allows for structure/function correlation. As an example, $\text{VO}(\text{ma})_2$ was shown by x-ray crystallography to have a *trans* ligand structure [43], as opposed to *cis*, which has one donor bound in the axial position away from the $\text{V}=\text{O}$ bond (see Fig. 3 for structures of the *cis* and *trans* isomers of $\text{VO}(\text{ma})_2$). A thorough study of $\text{VO}(\text{ma})_2$ in solution by ambient and low temperature EPR demonstrated a 65/35 partiality for the *cis* conformation in water, which reduced to a 55/45 *cis* preference in methanol, detected by fine splittings of the $-7/2$, $-5/2$, $3/2$, $5/2$, and $7/2$ parallel resonances in frozen solution [57]. The presence of coordinating solvent or strong binding ligand such as pyridine increased the proportion of the complex found as *cis* isomer. Other species were also detected and quantified by a variable temperature EPR experiment between 296 and 352 K. At higher temperature, linewidths narrowed due to faster molecular tumbling, allowing for additional spectral detail and clear observation of both structural isomers and a minor contribution from the monoligand species $[\text{VO}(\text{ma})]^+$ (Fig. 3). Accurate simulation of the ambient and frozen solution spectra was essential for determination of the relative proportions of isomers detected in the experimental spectra. $\text{VO}(\text{ma})_2$ showed a strong tendency to form adducts with coordinating solvents or strong monodentate ligands (such as pyridine). These complexes had increased stability to oxidation [43,57,58].

Jakusch et al. coupled a thorough potentiometric study with EPR to delineate the pH-dependent structures of the vanadyl-(2,6-pyridinedicarboxylic acid, H_2dipic) and -(4-hydroxy-2,6-pyridinedicarboxylic acid, $\text{H}_2\text{dipic-OH}$) systems [49]. Starting at low pH, EPR spectra showed the sequential formation of mono and bis(ligand) species, an acid dissociation process, and multiple coordination modes of the dipic^{2-} ligand. Isotropic (A_0) and anisotropic ($A_{||}$) hyperfine coupling constants were used with the additivity rule to propose pH-dependent binding modes. It was found that the protonated bis(ligand) complex, $[\text{VO}(\text{dipic})_2\text{H}]$, contained a

two- and a three-coordinate dipic ligand. Upon deprotonation, both ligands bound in a bidentate fashion [49]. It could be reasonably inferred that this 6-coordinate, protonated species would be more stable to oxidation, as a full coordination shell has been shown to retard oxidation (*vide infra*) [57]. The other system, $H_2dipic-OH$, formed only 1:1 complexes with VO^{2+} . At low pH, $[VO(H_2O)_2dipic-OH]$ was the major species over $[VO(H_2O)_5]^{2+}$, but only a small change in A_0 was observed by EPR. This observation led to the conclusion that the two oxygen-containing function groups of the ligand bound in the equatorial plane, while the pyridine-N was bound in the axial position [49].

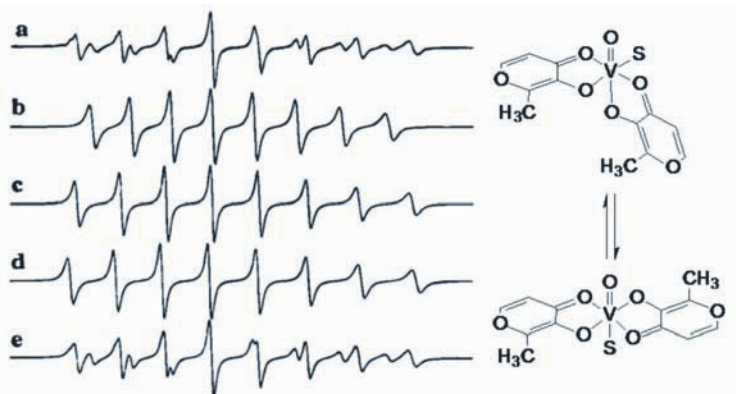


Figure 3. EPR study of the solution structures of $VO(ma)_2$ in aqueous solution. Left: (a) $VO(ma)_2$ at pH 6.0, $T = 352$ K showing peaks due to *cis* isomer (low field peaks, bottom structure) and *trans* isomer (high field peaks, top structure); (b) simulation of *trans* isomer spectrum; (c) simulation of *cis* isomer spectrum; (d) simulation of $[VO(ma)_2]^+$; (e) addition of $c + 0.70 b + 0.10 d$. S = solvent. Right: Equilibrium between the *cis* (top) and *trans* (bottom) isomers of $VO(ma)_2$. Adapted from [57].

Crans and coworkers utilized EPR, ^{51}V NMR, and absorption spectroscopy to observe the solution chemistry of their series of insulin-enhancing complexes based on the acetylacetonate ligand (acac) [46]. Solutions of $VO(acac)_2$ were found to be a mixture of three species, labeled A, B, and C. The B species was observed as a weak shoulder on the resonances attributed to the dominant A EPR signals. Over time, the EPR signal of A(+B) converted to C, and this conversion was studied by EPR and absorption spectroscopy. NMR was used to quantify any oxidation of the complex to a V(V) derivative. Quantification of the EPR signal showed that 90% of the total vanadium was present as A and B, while 10% was EPR silent as a dimer. After 24 days, the solution components had changed to 25% A(+B) and 65% C. This transformation was later shown to be a pH-dependent process. Preparation of $VO(acac)_2$ at a reduced pH produced the C-type EPR spectrum quantitatively [59].

Based on the similarity of water to an alcohol, and the demonstrated preference for the *trans* conformation (with the coordinated alcohol *trans* to the vanadyl oxo) for coordinated alcohols to $\text{VO}(\text{acac})_2$ in organic solvents [60,61], species A was assigned as the *trans* isomer, leaving the minor B species as *cis*. This assignment is in contrast to the isomeric preference of $\text{VO}(\text{ma})_2$ [57]. Species C was shown to be produced under conditions of lower ligand:metal ratios, and was therefore assigned as a hydrolysis product, the 1:1 $[\text{VO}(\text{acac})(\text{H}_2\text{O})_3]^+$ complex [46]. Titration of a solution of $\text{VO}(\text{acac})_2$ with either HCl or NaOH with careful measurement of the peak-to-peak amplitudes of the EPR spectrum led Makinen and Brady to confirm this assignment of C as a 1:1 species that hydrolyzes between pH 1 and 4 [59]. Beyond pH 4, formation of $\text{VO}(\text{acac})_2$ dominates the system. Similar results were also observed for acac-derived ligands of the form R-acac, where R = 3-methyl, 3-ethyl [46] amino, and N,N-dimethylamino [41]. An attempt was made to correlate the compound's efficacy and stability of the 1:1 complex. While the order of stability correlated with the complexes' reported glucose-lowering capacity [14,46], it is difficult to foresee a role for the 1:1 complex, typically found by EPR only in highly acidic conditions (pH < 4), when the action of this class of compounds has been shown to require blood transport (at pH ~ 7.4) for observation of antidiabetic effects.

Investigations of potential biotransformation reactions were carried out through EPR and potentiometric characterization of ternary complex formation between several complexes and low molecular weight biogenic ligands [42,44,45]. Citrate, and to a lesser extent oxalate and lactate, was found to be capable of displacing one of the picolinate or 6-methylpicolinate ligands of $\text{VO}(\text{pic})_2$ and $\text{VO}(\text{6mpa})_2$, respectively, to generate a ternary vanadyl-ligand-citrate complex [44]. This same reaction was also later observed with bis(5-carboxy-picolinato)oxovanadium(IV) ($\text{VO}(\text{5opic})_2$). In the case of lactate, approximately half of the available vanadyl ion at pH 5 is in the form of $[\text{VO}(\text{A})]^+$ (where A = 5opic⁻), while the remainder is found as a ternary $[\text{VO}(\text{A})(\text{B})]$ complex, where B = lactate⁻ [42]. EPR data were critical in these studies for detection of multiple species across a wide range of pH and for measurement of small changes in A_{\parallel} values that accompany changes in the equatorial coordination sphere. These studies indicated that upon introduction of these compounds into the bloodstream, low-molecular-weight bioligands, particularly citrate and lactate, will cause complete decay of the complex into (i) a small portion of ternary $[\text{VO}(\text{A})(\text{B})]$ type complexes and (ii) a major portion forming a bis(ligand) complex with the biological chelator. These calculations, however, neglected the impact of free metal binding capacity of apo-transferrin and albumin, which will be discussed in the next section.

Kiss et al. reported a similar study with a new ligand set, 2-hydroxy-pyridine-N-oxide (2hpo), which was found to form very stable bis(ligand) compounds with VO^{2+} [45]. EPR was again used in conjunction with potentiometry to gain insight into the coordination structure of the complexes formed in mixed ligand (A = 2hpo, B = lactate, oxalate, citrate, phosphate). Due to the high stability of the $\text{VO}(\text{2hpo})_2$ complex ($\log \beta_2 = 16.01(9)$), complete abstraction of the metal ion from the complex to form $[\text{VO}(\text{B})]$ as the major species was not observed for any ligand against

2hpo. Instead, ternary complex formation was observed for oxalate, phosphate, and citrate from pH 2–7, but not for lactate. Due to the $\text{VO}(\text{O}_4)$ coordination sphere of the starting complex, and the fact that ternary complex formation would not radically alter the equatorial coordination sphere (as opposed to picolinate-derived ligands outlined above, with an N_2O_2 ligand set), the authors were careful not to rely solely on EPR data, which in many cases the additivity rule would predict less than $3 \times 10^{-4} \text{ cm}^{-1}$ differences in A_{\parallel} , within the experimental error. Instead, EPR signal intensity was measured as a function of solution pH. Increased stability to hydrolysis at higher pH (which leads to loss of signal to formation of the EPR-silent $[(\text{VO})_2(\text{OH})_2(\text{L})_2]$) over that of the original $\text{VO}(\text{2hpo})_2$ complex was used as evidence of ternary complex formation with a biogenic ligand [45].

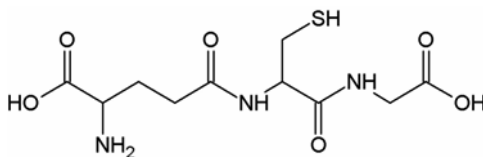


Figure 4. Chemical structure of the linear tripeptide glutathione (GSH). It possesses up to 8 potential metal binding sites and is an important biological reductant of V(V) species *in vivo*.

EPR has shown great utility in the delineation of complicated, biologically relevant systems. Interactions of vanadium complexes with glutathione (GSH, a linear γ -Glu–Cys–Gly tripeptide, Fig. 4) are important owing to observed *in-vivo* reduction of V(V) compounds by GSH and its ability (along with oxidized glutathione, GSSG) to act as a ligand for vanadium(IV) [62–65]. The vanadyl–GSH system serves as an excellent example of the utility of EPR for the simultaneous detection and structural characterization of several components in solution. The vanadyl–GSH system is complicated: GSH and GSSG are not strong ligands for VO^{2+} and therefore cannot prevent hydrolysis of the metal ion above pH 6–8; thus large L:M ratios (typically >10) must be used to study complex formation near physiological pH (~ 7.4). GSH as a ligand possesses 8 potential donor sites (2 terminal carboxylates, terminal amine, thiolate, 2 carbonyl oxygens and 2 deprotonated amides), and both mono(GSH) and bis(GSH) complexes have been observed [38,66,67].

Dessi et al. used a combination of low-temperature EPR and visible absorption spectroscopy of GSH-VO^{2+} solutions and compared the spectra to those of known model complexes [67]. They proposed formation of six EPR-detectable complexes, each with unique equatorial donor sets (ranging from $[4 \times \text{H}_2\text{O}]$ to $[\text{COO}^-, \text{NH}_2, \text{N}_{\text{amide}}, \text{S}^-]$, termed complexes I to VI) appearing sequentially with increasing pH. This number was further refined to 7 complexes (I to VII) [48] using a combination of potentiometry, EPR, Vis, and CD. EPR spectra obtained during pH titrations at different L:M ratios (Fig. 5) clearly demonstrate the sequential formation of these

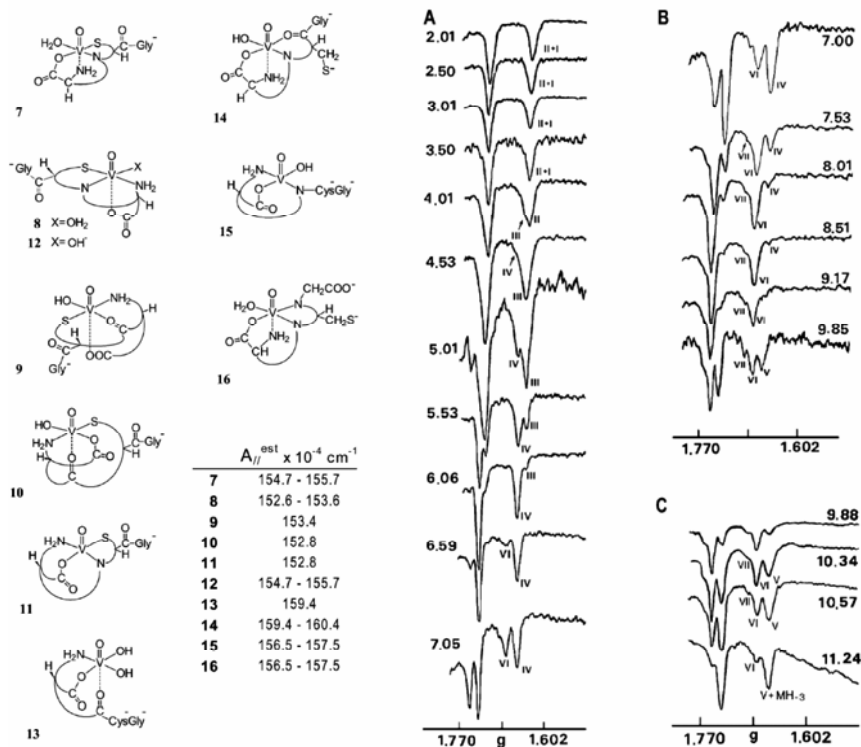


Figure 5. Left: Possible structural isomers for the VO–GSH system for spectra V–VII, with the estimated A_{\parallel} values calculated from the additivity rule. Right: high field (3800–4400 G) region of EPR spectra of VO^{2+} :GSH solutions as a function of pH ($T = 77 \text{ K}$, A: GSH:VO = 10:1; B: GSH:VO = 20:1; C: GSH:VO = 140:1, acquired at pH indicated). Roman numerals indicate unique EPR spectra representing different VO–GSH complexes. Reprinted with permission from [48]. Copyright © 2002, Elsevier.

complexes through observation of new resonances, shoulders, and splittings of the high-field parallel peaks. The additivity rule was used for assignment of likely first coordination sphere donors, although in some cases as many as four possible ligand sets could be proposed due to the predicted A_{\parallel} values for different ligand sets falling within experimental error of each other [48]. Further characterization was provided by comparison to modified systems with a methylated GSH-thiol group [48,68] or ethyl-esterified glutamyl cysteine [48], which allowed determination of the structures that involved thiolate and terminal carboxylate coordination, respectively, in the unmodified system. Figure 5 provides a visual demonstration of the power of EPR for resolving complicated solution chemistries relevant to vanadium(IV) *in vivo*, through the use of additivity rules and complementary spectroscopies and/or potentiometry. On the left, the figure depicts the possible structures of VO–GSH complexes V, VI, and VII, detected at $\text{pH} > 7$, while the right-hand

side displays the high-field resonant peaks of VO–GSH samples as the pH of the solution is raised. The sequential formation of complexes I to VII is indicated. Not shown in the figure are low-pH (<7) structures I–IV; interested readers are referred to the relevant literature for a description of these complexes [38,69,70].

Structures 7 through 10 (O_2SN or OSN_2 eq. donor set, $A_{\parallel}^{est} = 152.8 - 155.7 \times 10^{-4} \text{ cm}^{-1}$) were consistent with EPR spectrum VI, 11 and 12 (O_2SN or OSN_2 eq. donor set, $A_{\parallel}^{est} = 152.8 - 155.7 \times 10^{-4} \text{ cm}^{-1}$) with VII, and 13–16 (O_3N or O_2N_2 eq. donor set, $A_{\parallel}^{est} = 156.5 - 160.4 \times 10^{-4} \text{ cm}^{-1}$) with spectrum V. This system provides an excellent example of both the utility and limitations of the additivity rule: it can distinguish between closely related structural isomers such as structures 10 and 16 in Figure 5, but in several cases the A_{\parallel}^{est} values of any two complexes fall within the experimental error (i.e., distinguishing between structures 12 and 16, $\Delta(A_{\parallel}^{est}) = 0.8 - 2.8 \times 10^{-4} \text{ cm}^{-1}$) or there are more than one possible isomer that fits the experimental A_{\parallel} value (e.g., structures 7–10).

Comparison of these results to vanadyl complexes formed *in vivo* (*vide infra*) demonstrated that complexes assigned as VO–GSH compounds in the cytosol (pH ~ 7.4) [63,64] or detected in the liver and kidney by EPR and ESEEM [54,69,71,72] would only be consistent with structures detected in these studies at pH < 6.5. Other potential bioligands would therefore have to be considered to describe the *in-vivo* coordination of vanadyl ions in cells and organs. These studies serve to highlight the crucial role played by EPR in the delineation of possible physiologically relevant structures in a system with no available x-ray structural data [48].

The redox activity of vanadium compounds is conveniently studied by EPR. Song et al. determined the rate of reduction of $[VO_2(ma)_2]^-$ and $[VO_2(ema)_2]^-$ by the endogenous reductants ascorbic acid and glutathione [51]. The rate of appearance of product was tracked by an increase in EPR signal amplitude over time. Ascorbic acid reduction was found to be too rapid to be able to be studied by EPR under the experimental conditions used. GSH was found to reduce the V(V) equivalent of $VO(ma)_2$ and $VO(ema)_2$ about 2000 times slower than ascorbic acid, and proceeded through an acid-dependent mechanism. The presence of an ethyl or methyl group did not affect the kinetics. Conversely, Castro et al. used EPR to observe the disappearance of the V(IV) signal as bis(3-hydroxy-1,2-dimethyl-4-pyridinoato)oxovanadium(IV) ($VO(dmpp)_2$, the pyridinone analog of $VO(ma)_2$) was oxidized by molecular oxygen in aqueous solution [50]. Oxidation to the V^VO_2L and $[V^VO_2L_2]^-$ species never proceeded to completion, as evinced by a residual EPR signal, due to the reducing capacity of the ligand. The rate of oxidation increased with higher complex and/or oxygen concentration, and with increasing pH. EPR data were complemented by ^{51}V NMR studies of the V(V) products, such that through the combination of both spectroscopies, the solution chemistry and structures of the reactants and products could be characterized [50].

2.2 Interactions of Serum Proteins and Vanadyl Compounds

A major focus of vanadium antidiabetes research is focused on the elucidation of the differences in efficacy between chelated and free vanadium sources. It is known from both in-vivo and in-vitro assays that chelated sources such as $\text{VO}(\text{ma})_2$ or $\text{VO}(\text{pic})_2$ have greater glucose lowering capabilities in vivo and greater inhibition of free fatty acid release from suspended adipocytes (in vitro) than VOSO_4 . Previously, it was proposed that differences in in-vivo efficacy were simply due to the greater absorption from the gastrointestinal tract of chelated vanadyl compounds. Activity differences in cellular studies, however, suggest a role for the intact complex in the mechanism of these compounds. Lastly, biodistribution studies have noted marked differences in the relative proportions of vanadyl ions in body tissues between VOSO_4 and V(IV) complexes [12,73]. These reports suggest that some differences in the metabolism of these compounds must exist to account for the varying activity and tissue accumulation.

A likely difference in the metabolism of free and chelated sources lies in post-absorptive processes, particularly transport in the bloodstream. The study of the interactions of insulin-enhancing compounds with serum proteins has been almost exclusively studied by EPR. Apo-transferrin and albumin have been implicated in the transport of vanadyl ions in the blood, and these proteins represent a significant metal-binding capability in the blood. Considerable interest in the role of these proteins in the transport and biotransformation of administered vanadium compounds has been evident in the recent literature.

Chasteen and coworkers conducted extensive studies on the interactions of VOSO_4 with apo-transferrin (apo-Tf) and albumin (HSA) by EPR [31,50,74–77]. This body of work underpins all current studies of these proteins with insulin-enhancing compounds but will not be reviewed here.

Blood transport of vanadium pharmaceuticals by apo-Tf was first observed by in-vivo EPR of rat blood taken from animals fed a vanadium-supplemented diet for an extended period [78]. Approximately 40–50% of the supplemented vanadyl ions were found bound to transferrin, indicating its major role in scavenging of vanadyl ions from the bloodstream. Takino et al. reported that $\text{VO}(\text{5ipa})_2$ did not interact with either holo- or apo-Tf [12], as the ambient temperature EPR of $\text{VO}(\text{5ipa})_2$ in the presence of either protein was nearly isotropic. Careful examination of the experimental conditions and the spectra themselves reveal, however, that the complex was in a 10:1 molar excess (500 to 50 μM), which, assuming full binding of the complex to apo-Tf, would result in 400 μM of free complex and 100 μM in protein-bound VO^{2+} . This low concentration of the vanadyl–protein adduct relative to the free complex would, in the experience of the author, generally be difficult to detect at ambient temperature. Further, the frozen solution spectra reveal a slight shift in axiality; g_{\perp} and g_{\parallel} appear closer to each other in the spectra of $\text{VO}(\text{5ipa})_2$ with holo- and apo-transferrin than in the low-temperature spectrum of the complex. Therefore, despite this misassignment, this study represents the first report of interactions between a chelated vanadyl source and transferrin. Other

studies involving other insulin-enhancing compounds (i.e., VO(ma)₂) have been reported only recently.

EPR spectroscopy at ambient temperature was used to demonstrate an interaction of VO(ma)₂ with apo-Tf [79]. Addition of VO(ma)₂ to a solution of apo-Tf (in a 1.4:1 ratio) yielded a highly anisotropic spectrum with no residual VO(ma)₂ spectrum remaining. Rudimentary comparison of the solution spectra each of VOSO₄ and VO(ma)₂ with apo-Tf found them to be dissimilar, and the metal-protein adducts formed by VOSO₄ and VO(ma)₂ were concluded to be different. Willsky et al. suggested that a unique complex could be made between VO(ma)₂ and apo-Tf through either ternary complex formation (ma-VO-Tf), or through maltolate acting as a synergistic binding anion, replacing bicarbonate [79].

This result was revised in a recent report, which relied on the higher-resolution and narrower EPR peak widths of frozen solution spectra acquired at 130 K to gain a complete understanding of the maltol-VO-transferrin system [80]. VO(ma)₂ was conclusively demonstrated to bind at the Fe³⁺ sites, and this binding required the presence of bicarbonate. Ambient and frozen solution EPR spectra of VOSO₄ or VO(ma)₂ were virtually identical, in contrast to the earlier report of Willsky et al. [79]. Additionally, a careful comparison of the relative intensities of the $-7/2_{||}$ and $-5/2_{||}$ resonances of both VO(ma)₂ and VOSO₄ with apo-Tf demonstrated that, under the experimental conditions used, VO(ma)₂ and VOSO₄ produced nearly identical proportions of A and B site conformations when bound to apo-Tf. EPR spectra of the low-field parallel peaks, and the results of the intensity fitting for the two vanadyl-protein systems are shown in Figure 6 and Table 2, respectively. Under experimental conditions, VOSO₄ and VO(ma)₂ were bound predominately in the A configuration, with the B conformation approximately 60% of the A fraction. Given all the spectroscopic evidence, the conclusion was that the metal-protein complexes formed between apo-Tf and both vanadyl sources were identical [80].

Table 2. Gaussian fitting results for Determination of Relative proportions of A and B Site Conformations for the Binding of VOSO₄ and VO(ma)₂ to apo-Tf^a

Sample	Resonant field (G)		Peak width ^b (G)		Relative peak area (Area(B)/Area(A), %)
	B	A	B	A	
1:1 VOSO ₄ :Tf	2967.7 (0.3)	2979.5 (0.2)	11.3	6.3	63.5 (5.0)
2:1 VOSO ₄ :Tf	2968.0 (0.3)	2979.6 (0.3)	10.2	6.4	52.5 (2.1)
1:1 VO(ma) ₂ :Tf	2968.0 (0.4)	2979.7 (0.3)	10.8	7.0	66.8 (4.0)
2:1 VO(ma) ₂ :Tf	2968.0 (0.3)	2979.0 (0.4)	10.8	7.2	62.2 (2.8)

Adapted from [80].

^a Error in brackets expressed as the standard deviation over three experiments.

^b Full width at half magnitude.

Investigations have also been made into the interactions of vanadyl complexes and albumin by EPR. Willsky et al. reported that a complex formed between

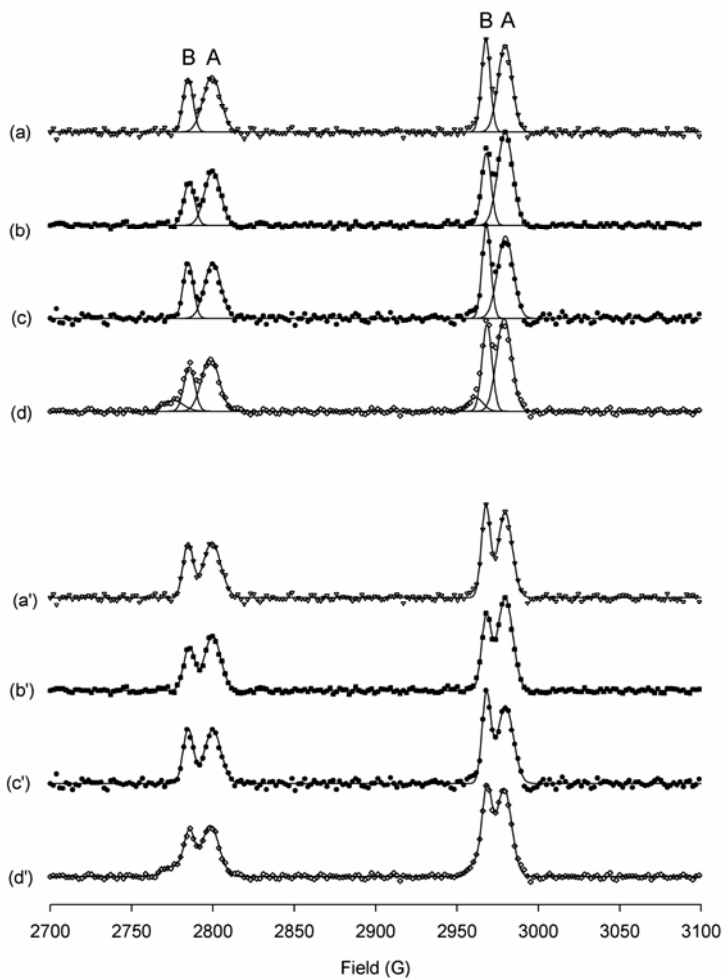


Figure 6. $-7/2_{\parallel}$ and $-5/2_{\parallel}$ low-field parallel resonances lines of the frozen solution ($T = 130$ K) EPR spectrum: (a) 1:1 VOSO_4 and apo-Tf; (b) 2:1 VOSO_4 and apo-Tf; (c) $\text{VO}(\text{ma})_2$ and apo-Tf; (d) 2:1 $\text{VO}(\text{ma})_2$ and apo-Tf, with Gaussian peak fit for determination of the relative amounts of A and B binding conformations (solid lines). Every 4th experimental point is shown. The lower spectra (a'-d') correspond to the sum of the individual Gaussian peaks shown in (a-d). In (d) an additional peak is required to fit the spectrum. Its spin Hamiltonian parameters correlate very well with free $\text{VO}(\text{ma})_2$ in aqueous solution. Reprinted with permission from [80]. Copyright © 2005, American Chemical Society.

$\text{VO}(\text{ma})_2$ and HSA was dissimilar to the one made between VOSO_4 and HAS [79]. Further insight into formation of this new complex, and a potential key difference in in-vivo reactivity between chelated and free vanadyl sources, was provided by Makinen and Brady, who investigated the adduct formed between $\text{VO}(\text{acac})_2$ and bovine serum albumin (BSA) by electron nuclear double resonance (ENDOR) [59],

and by Liboiron and coworkers, who used ambient and low-temperature CW-EPR to elucidate in detail the complicated solution chemistry between $\text{VO}(\text{ma})_2$ and HAS [80].

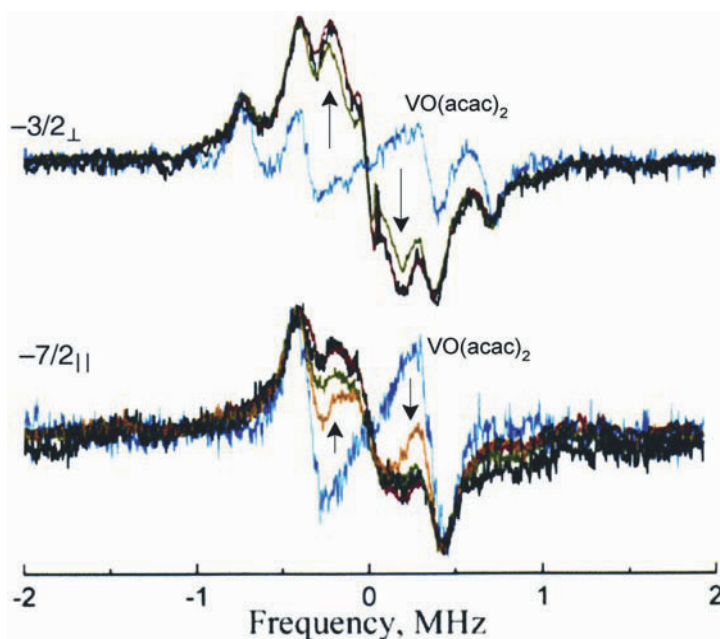
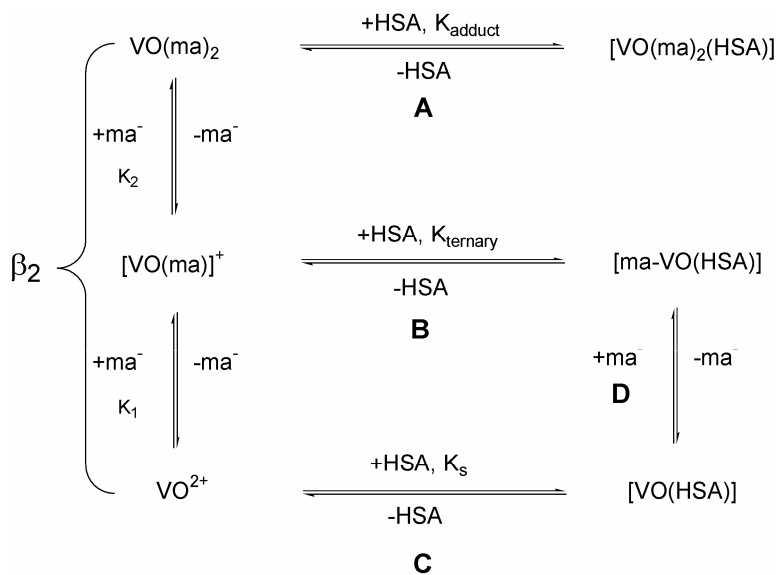


Figure 7. ^1H ENDOR spectra of $\text{VO}(\text{acac})_2$ (labeled) and $\text{VO}(\text{acac})_2$ with increasing BSA (BSA:VO = 1, 2, 5 and 10), acquired at the $-3/2_{\perp}$ and $-7/2_{\parallel}$ peaks of the CW EPR spectrum. The $\text{VO}(\text{acac})_2$:BSA spectra saturate at 2 (top) and 5 (bottom) equivalents. Dashed arrows indicate the direction of changes in peak intensity. The intensity of the acac ligand peaks do not change appreciably, indicating that $\text{VO}(\text{acac})_2$ binds as the intact complex to BSA. Adapted from [59].

Makinen and Brady demonstrated the formation of a 1:1 adduct between $\text{VO}(\text{acac})_2$ and BSA by ^1H ENDOR in deuterated buffer. ENDOR spectra (Fig. 7) showed the appearance of several new peaks upon BSA binding, but clearly no differences in ligand signals, indicating no perturbation or loss of the chelating acetylacetonates upon BSA binding. The hyperfine components of the CW-EPR spectrum of the adduct also showed no broadening relative to the spectrum of the complex alone. This observation supported their assignment that the protein interacts with the complex via the vacant axial position through either a hydrogen bond to the bound water of $\text{VO}(\text{acac})_2$ in the sixth position, or through direct interaction via a protein residue to the complex [59].

Liboiron et al. presented ambient and frozen solution EPR data that showed that the original interpretation of Willsky et al. [79] was not correct, and the maltol–vanadyl–HSA system was in fact more complicated than previously thought

[80]. Frozen solution EPR data revealed small but measurable differences in the high-field parallel peaks. Careful simulation of these spectra revealed that only one equivalent of $\text{VO}(\text{ma})_2$ would bind to HSA, suggested to be at the Cu^{2+} site near the N terminus. No $\text{VO}(\text{ma})_2$ bound nonspecifically to the protein, in contrast to VOSO_4 [31]. Further, provision of $\text{VO}(\text{ma})_2$ to the protein led to formation of an adduct complex, in correlation with Makinen and Brady's results with $\text{VO}(\text{acac})_2$ and HAS [59]. Formation of a ternary complex (maltol–VO–HSA) was demonstrated by titration of maltol into a 1:1 solution of VO^{2+} and HSA. Resonances due to vanadyl bound specifically (i.e., at the Cu^{2+} site) to the protein [31] disappeared and were replaced by increased intensity at peaks corresponding to nonspecific binding sites. It is not possible for metal ions to spontaneously move from a higher-stability site to one of lower stability; therefore, the addition of maltol leads to binding one maltol ligand to VO^{2+} ions bound by the protein. This binding led to generation of an EPR spectrum nearly identical to that of nonspecifically bound VO^{2+} . It was not possible to reform $\text{VO}(\text{ma})_2$ or the $\text{VO}(\text{ma})_2$ –HSA adduct even after addition of high molar equivalents of maltol [80]. This intricate system is summarized in Scheme 1.



Scheme 1. The maltol–vanadyl–HSA system, as delineated by EPR spectroscopy, is governed by several equilibria reactions. (A) formation of the $\text{VO}(\text{ma})_2$ –HSA adduct complex; (B) formation of the ternary complex from $\text{VO}(\text{ma})_2$; (C) binding of VO^{2+} to the strong binding site of HSA (Cu^{2+} site); (D) formation of the ternary complex via titration of maltol. Note that there is no direct connection between the ternary and adduct complexes as titration of maltol to $\text{VO}(\text{HSA})$ yields only ma-VO-HSA , without subsequent formation of $\text{VO}(\text{ma})_2$ and its adduct with HSA. Reprinted with permission from [80]. Copyright © 2005, American Chemical Society.

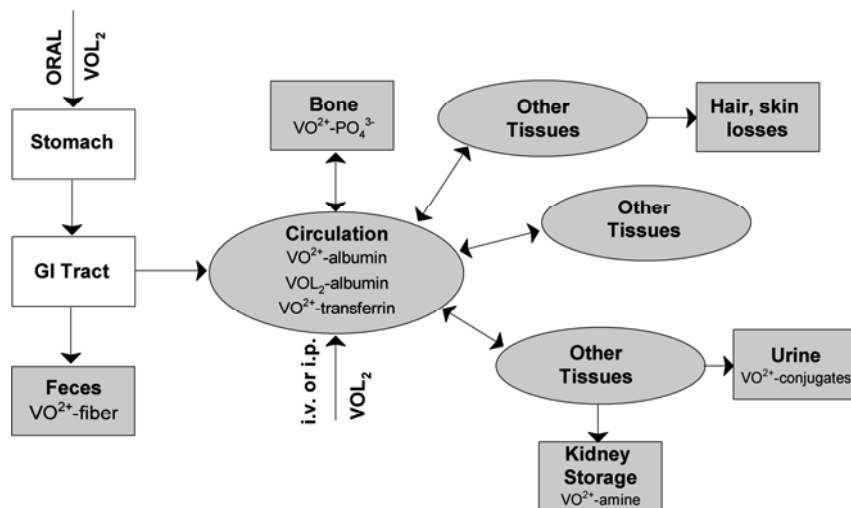
The VO(ma)₂:1-methylimidazole (1-ImMe) system was found to be a good spectroscopic model of the protein adduct formed between VO(ma)₂ and HSA. Simulation of the EPR spectra of all solution components (VO(ma)₂, VO(ma)₂(1-ImMe), VO(HSA)_{strong}, VO(HSA)_{weak}, VO(ma)₂(HSA), and VO(ma)(HSA)) demonstrated the uniqueness of the spin Hamiltonian parameters for both the adduct and ternary complex relative to VO(ma)₂, and the close similarity of parameters between the VO(ma)₂(1-ImMe) and VO(ma)₂(HSA) adducts. Thus, VO(ma)₂ was proposed to form a 1:1 adduct complex with HSA most likely through the H3 imidazole [31] binding to an equatorial position of *cis*-VO(ma)₂ through displacement of the weakly bound water [80].

The interaction of HSA with chelated vanadium sources such as VO(acac)₂ and VO(ma)₂, as identified by EPR and ENDOR spectroscopy, differs considerably from that of VOSO₄, and represents a clear difference in reactivity with a biomolecule of a vanadyl complex versus its inorganic congener. It is unclear, however, whether this reaction is biologically relevant, given the considerable thermodynamic stability of vanadyl transferrin and ternary complex formation reactions with low-molecular-weight chelators such as citrate. These interactions could preclude any binding with HSA. It may be that only a small amount of the total absorbed dose of a vanadyl complex may bind to HAS, which leads to the augmented antidiabetic effects of many vanadyl complexes over VOSO₄. For VO(acac)₂ and VO(ma)₂, antidiabetic activity (as measured by glucose uptake by adipocytes) was increased when administered with BSA over the complex alone, suggesting that adduct formation between the complex and protein may play some role in the mechanism of pharmacological activity [59].

3. USE OF EPR FOR IN VIVO STUDIES OF VANADIUM METABOLISM AND COORDINATION STRUCTURE

Recent developments in the in-vivo characterization of putative vanadium(IV) pharmaceuticals have focused on completion of a metabolic model that fully describes the Absorption, Distribution, Metabolism, and Elimination (ADME) of exogenous vanadium [23]. Such knowledge would assist in the development of compounds with increased efficacy, as direct in-vivo/in-vitro antidiabetic assays combined with complete ADME data for the putative complex would lead to an understanding of the structure/function relationships that determine a complex's insulin-enhancing capability.

Paramagnetic resonance methods have played a central role in furthering our understanding of vanadium species in the biological milieu. Scheme 2 displays a diagram of the ADME properties of a vanadium(IV) complex (such as VO(ma)₂). Highlighted in the figure (by shaded boxes) are those discoveries in which the application of EPR spectroscopy was essential; clearly, the use of paramagnetic resonance has been paramount to further our understanding of vanadium interactions within the body. In this section, a summary of the key studies of vanadium ADME properties as described by EPR methods will be presented.



Scheme 2. Schematic outline of VO_2 absorption, distribution, metabolism, and elimination. Dark shaded compartments indicate regions in which EPR methods played a key role in the description of vanadium behavior in that compartment. Adapted from [23].

3.1. Absorption and in vivo Redox Reactions of Vanadium Compounds

Since both V(V) and V(IV) compounds have been demonstrated to possess insulin-enhancing activity, considerable debate has taken place over the exact chemical form of the active metabolite at or within the target tissue. The biological environment is mainly a reducing one due to the presence of biological reductants such as glutathione and ascorbic acid; however, a significant oxygen tension also exists that may have an effect on the redox state of administered vanadium compounds. EPR has been applied in several studies to observe the interplay between the V(IV) and V(V) oxidation states for several compounds, as well as describing the absorption of these compounds from the GI tract and into the cells of the body.

Absorption of orally administered vanadium compounds has been measured by Cantley and coworkers while investigating the intracellular inhibition of (Na,K)-ATPase activity by sodium vanadate in human erythrocytes [81]. They noted that a significant portion of the administered vanadium was in a form not capable of inhibitory activity. EPR spectra of NaVO_3 -treated erythrocytes showed a characteristic VO^{2+} spectrum, indicating that reduction of V(V) to V(IV) had occurred. In one hour, approximately 30% of the added vanadate was reduced, but only vanadium contained within the cells had undergone reduction. Thus, absorption of vanadate, likely through a cation transport system, must occur before biological reduction could occur [62]. Further study of this reaction by EPR showed

that it proceeded to near completion, and the intracellular vanadyl ions were found bound tightly to hemoglobin [64].

Similar results for rat adipocytes were also noted, though in this study the biological reductant was identified as glutathione [63]. Addition of sodium metavanadate to suspended adipocytes led to the observation of a V(IV) EPR signal within an hour, and transport into the cells was again shown to be required for reduction to occur. Glucose promoted vanadate uptake as followed by EPR. In adipocytes, the produced vanadyl ions were found bound in one of two distinct 1:1 VO(GSH) complexes [63].

The role of GSH in the in-vivo reduction of V(V) to V(IV) was examined by EPR in a study by Lu, Fantus and coworkers [65]. The results of this experiment are shown in Figure 8. In insulin-resistant adipocytes (with naturally lower GSH concentrations, "Resistant" in Fig. 8) or in cells pretreated with buthionine sulfoximine (BSO, a GSH-synthase inhibitor, "GSH-synthase inhibited" in Fig. 8), showed increased sensitivity to vanadate-stimulated phosphorylation of insulin receptors. This result was consistent with EPR spectra showing a decreased intracellular concentration of vanadyl ions that do not promote phosphorylation. Addition of N-acetylcysteine, a precursor of GSH synthesis, to the incubating cells, restored the amount of EPR-detected vanadyl ion within the cells to control levels (compare "Resistant + NAC" to "Resistant" in Fig. 8).

Total vanadium incorporated into the adipocytes did not change between the samples; therefore, this experiment demonstrated the key role of GSH in the intracellular reduction of V(V) species, leading to a decrease in its inhibitory activity toward protein tyrosine phosphatases [65].

Transport of small, neutral V(IV) complexes is thought to take place via a passive diffusion process. Crans and coworkers used a combination of ICP-AES and EPR to track and quantify the membrane transport of VO(acac)₂ and VO(ma)₂, and observe the redox chemistry and interactions with the erythrocyte membrane of these compounds [82]. The intensity of the central signal of the room-temperature EPR spectra of VO(acac)₂ and VO(ma)₂ was used to quantify the amount of V(IV) species during stability tests or membrane transport experiments. For experiments with erythrocytes, transport of the vanadyl compounds into the cytoplasm yielded a highly anisotropic spectrum due to binding of the vanadyl species with cellular components. ICP-AES was used to quantify the total cytosolic vanadium.

Several vanadium(IV) complexes have demonstrated indefinite stability in the blood of rats [40,83,84], and while it was found that VO(ma)₂ was less stable to oxidation in aqueous buffer solution than VO(acac)₂, in the presence of membrane vesicles the differences between the two complexes became insignificant [82]. As a result, maintenance of the V(IV) oxidation state in the blood is achieved through several mechanisms: the presence of biological reductants in the bloodstream, adduct formation with endogenous bioligands, as shown in vitro with pyridine-VO(ma)₂ adducts by Hanson et al. [57], and finally by transport into the cellular component, wherein a reduced oxygen tension is found in the cytosol. This stability toward oxidation is important particularly for VO(ma)₂, whose V(V) congener

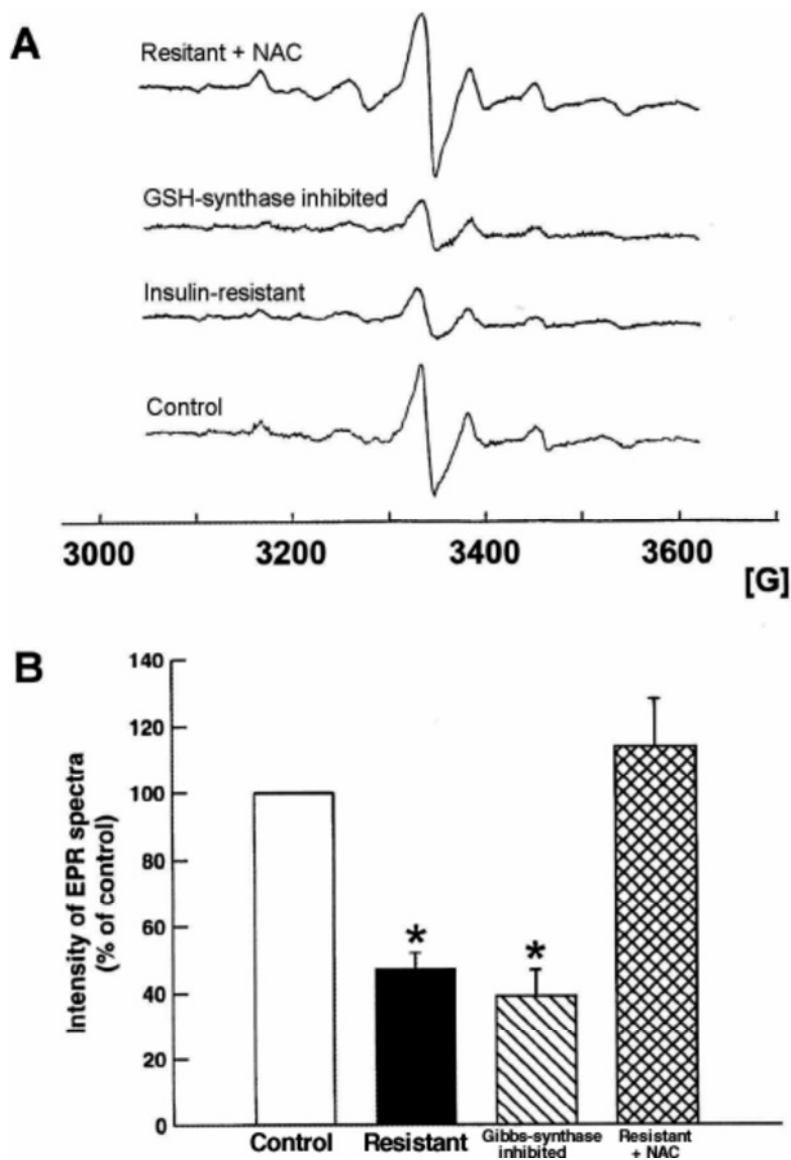


Figure 8. (A) Frozen solution ($T = 223$ K) EPR spectra of vanadate-loaded adipocytes incubated with 15 mM glucose and 100 nM insulin, with (Resistant + NAC) or without (Resistant) 30 mM N-acetylcysteine pretreatment, with 80 μ M BSO (GSH-synthase inhibited), or with 5.6 mM glucose (Resistant). (B) EPR spectral intensity expressed as an average of 3 experiments (* $p < 0.05$ compared with control and R+NAC). Reprinted with permission from [65]. Copyright © 2001, American Society for Biochemistry and Molecular Biology.

$[\text{VO}_2(\text{ma})_2]^-$ was shown to not possess antidiabetic activity [85]. Interestingly, the transport of $\text{VO}(\text{acac})_2$ into erythrocytes was considerably faster than that of $\text{VO}(\text{ma})_2$, likely due to the higher lipophilicity of the former complex. EPR detected an anisotropic signal due to $\text{VO}(\text{acac})_2$ in the cell within 2 minutes; for $\text{VO}(\text{ma})_2$ this process took 12 minutes. Thus, diffusion rates across membranes are considerably faster for $\text{VO}(\text{acac})_2$ [82], although there is no evidence that this effect has any bearing on either complex's antidiabetic activity.

EPR has been used to study the formulation of potential vanadium pharmaceuticals to augment gastrointestinal absorption [86]. A series of three vanadyl compounds (VOSO_4 , $\text{VO}(\text{pic})_2$, and $\text{VO}(\text{6mpa})_2$) were administered to several sites in the GI tract of rats and the appearance of the V(IV) EPR signal in the blood was measured. Differences in absorption for oral, jejunal, and ileal administration were noted: $\text{VO}(\text{6mpa})_2$ had the highest absorption of all complexes for oral and intra-ileal administration, while VOSO_4 was absorbed more rapidly than the chelated compounds after intra-jejunal dosing. Generally, absorption was most effective for all compounds via the ileum [86]. On the basis of this result, enteric-coated capsules of VOSO_4 were prepared and given by oral administration [87]. The encapsulation was expected to allow the administered VOSO_4 to pass through the stomach into the small intestine, where the capsule would begin to slowly release the vanadyl compound at the site of highest absorption. This method of administration resulted in higher blood vanadyl levels, for an extended period of time. Through the observation of vanadyl concentrations in the blood, enteric-coated encapsulation was shown to be an effective method for increasing the absorption of VOSO_4 from the gastrointestinal tract.[87]

3.2. In vivo Pharmacokinetics of Vanadium Species by BCM-EPR

Aside from documented differences in absorption between chelated (i.e., VOL_2) and free (e.g. VOSO_4) vanadium sources [73], several studies have noted efficacy differences between the two forms of vanadium treatment when the compounds are administered intravenously (i.v.) or intraperitoneally (i.p.). Such administration bypasses the gastrointestinal tract and likely complex degradation [73,88] prior to absorption into the bloodstream. Since many chelated vanadyl compounds are more effective as antidiabetic agents (by various assays, both in vitro and in vivo) over inorganic sources by i.v. and i.p. injection, some difference(s) in blood distribution, organ accumulation, and/or biological target must exist to provide explanation for the augmented activity of V(IV) coordination compounds.

Sakurai and coworkers developed a novel pharmacokinetic method for the real-time tracking of the blood distribution of paramagnetic species through EPR. Termed blood-circulation monitoring EPR (BCM-EPR), the method was initially developed for study of ascorbic acid radicals [89] and chromium carcinogens [90]. It has proven, however, to be useful for the study of the distribution and elimination of vanadium(IV) species from the bloodstream of live animals following i.v. injection [83].

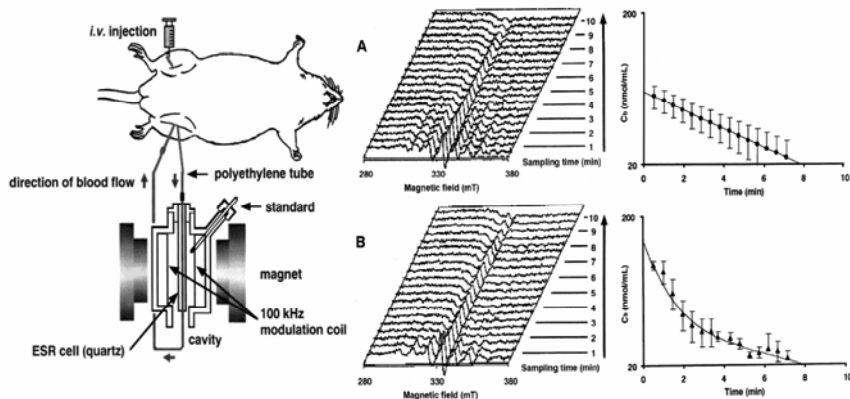


Figure 9. In-vivo blood circulation monitoring electron paramagnetic resonance (BCM-EPR). Left: Schematic diagram of experimental apparatus for real-time measurement of circulating paramagnetic species in the living rat. Center: BCM-EPR spectra of rat blood following i.v. administration of 0.5 mg V/kg of (A) VOSO₄ and (B) VO(pic)₂. EPR spectra were acquired every 30 s. Right: Time courses of vanadyl concentration in the bloodstream following single i.v. administration of (A) VOSO₄ and (B) VO(pic)₂, based on BCM-EPR signal quantification. Reprinted with permission from [84]. Copyright © 2002, Elsevier.

The BCM-EPR method is detailed in Figure 9. Briefly, study animals (Wistar rats) are anesthetized, and polyethylene tubes are cannulated into the left femoral artery and vein. The ends of the cannula are joined with silicone tubing, which in turn is connected to a 20- μ L EPR capillary tube, creating a complete blood circuit outside the body. The rat's own heartbeat drives the blood through the cell, allowing for real-time monitoring of paramagnetic species in the blood. Spectra are acquired at room temperature every 30 seconds [84]. The appearance, and disappearance, of the nearly isotropic vanadyl EPR signal (typically using the intensity of the central $M_I = -1/2$ peak) is plotted as a function of time, yielding time-resolved pharmacokinetic data without the need to draw samples for each time point, or any other additional manipulation that may affect the vanadyl distribution in the bloodstream. For the series of complexes tested in several studies discussed below, a blood challenge (*vide supra*) indicated that all complexes were stable to oxidation in rat blood, and thus disappearance of the vanadyl signal was due to clearance and not oxidation of V(IV) to V(V).

Sakurai and coworkers have used this technique to characterize potential relationships between the insulin-mimetic activity and global distribution of vanadium in the bloodstream [40]. Pharmacokinetic data that can be obtained from the BCM-EPR method include the mean residence time (MRT), area under the concentration curve (AUC), total body clearance (CL_{tot}) and steady-state distribution volume (V_D). These measures are reflections of the ease with which a potential drug is distrib-

uted and ultimately eliminated from the bloodstream, either by excretion, biotransformation or uptake into other compartments (tissues).

Pharmacokinetic parameters derived from BCM–EPR of VOSO_4 in Wistar rats were shown to be consistent with those obtained by radiolabeling methods [73,91]. Careful calibration of the observed EPR signal intensities to known samples of study compounds in fresh blood was carried out to generate a linear correlation region of V(IV) concentration to BCM–EPR signal, typically between 20 and 200 μM V(IV) . The reported detection limit for $S/N = 3$ was 10 μM , while for $S/N = 5$ the minimum V(IV) required was found to be 20 μM [83].

BCM–EPR has been used to systematically and quantitatively determine the pharmacokinetic features of several vanadium(IV) complexes in the bloodstream following i.v. injection, as detailed in Table 3 [40,83,84]. Clear differences in MRT, AUC, and CL_{tot} between VOSO_4 and the picolinate-derived complexes were observed, and it was shown that the main determinant of the pharmacokinetic parameters was CL_{tot} [84]. The signal intensities of the central signal of the vanadyl BCM–EPR spectrum of VOSO_4 decreased in a monophasic pattern; thus a one-compartment model was used to fit the clearance profile. Conversely, signal intensities for VO(pic)_2 decayed in a two-phase pattern, requiring the clearance data to be fit with a two-compartment model [83]. These differences are evident in the right-hand panel of Figure 9, in which the top plot shows the monophasic clearance of VOSO_4 from the bloodstream, while the bottom trace for VO(pic)_2 clearly demonstrates a biphasic clearance mechanism, and overall increased residence time in the blood relative to the inorganic VOSO_4 [83].

Table 3. Metallokinetic Parameters for Antidiabetic Vanadium Compounds as Measured by BCM-EPR^a

Compound	AUC ($\mu\text{mol min mL}^{-1}$)	MRT (min)	CL_{tot} ($\text{mL min}^{-1} \text{kg}^{-1}$)	$t_{1/2}$ (min) ^b	Ref.
VOSO_4	0.26 ± 0.04	4.4 ± 0.7	38.9 ± 5.8	3.0 ± 0.5	[28]
VO(pic)_2	0.65 ± 0.13	9.3 ± 1.7	15.2 ± 2.9	8.2 ± 1.1	[83]
VO(mpa)_2	0.97 ± 0.25	9.6 ± 3.4	10.5 ± 2.3	7.2 ± 2.6	[83]
VO(3hpa)_2	1.02 ± 0.26	14.6 ± 4.6	9.6 ± 2.4	11.6 ± 3.6	[84]
VO(2mpo)_2	1.70 ± 0.17	21.2 ± 2.3	5.8 ± 0.6	14.6 ± 1.6	[28]
VO(2hpo)_2	2.23 ± 0.25	23.3 ± 2.0	4.4 ± 0.5	16.3 ± 1.4	[28]
VO(6mpa)_2	1.45 ± 0.37	19.6 ± 6.9	6.8 ± 1.5	14.8 ± 5.3	[84]
VO(3mpa)_2	2.36 ± 0.52	28.8 ± 5.9	4.2 ± 1.1	20.9 ± 4.1	[84]
VO(5ipa)_2	3.85 ± 0.56	44.9 ± 9.7	2.7 ± 0.8	31.5 ± 7.7	[84]

^aData expressed as means \pm standard deviation. Compounds are listed in order of increasing $t_{1/2}$.

^bBased on the β apparent rate constant for a two-compartment model.

Differences within the picolinate family were also noted, with clearance rates from the bloodstream (related to CL_{tot}) being the fastest for VOSO_4 , followed by

VO(pic)₂, and then finally by VO(3mpa)₂ and VO(5ipa)₂. The AUC and MRT values were also significantly higher for VO(3mpa)₂ and VO(5ipa)₂ [84]. This series correlated linearly with IC_{50} values for suppression of free fatty acid release from rat adipocytes by the vanadyl complexes, where VO(3mpa)₂ and VO(5ipa)₂ were found to be the most effective in this in-vitro assay of antidiabetic activity. Therefore, Yasui et al. reported a significant positive correlation between CL_{tot} and IC_{50} values of vanadyl–picolinate complexes, and that introduction of an electron-withdrawing group (iodo) or an electron-donating group (methyl) at the 5th or 3rd position, respectively, of the picolinate ligand increased the residence time of the complex in the bloodstream, leading to augmentation of the insulinomimetic activity over that of VO(pic)₂ and VOSO₄ [84].

The advantages of BCM–EPR lie in its selectivity and ease of measurement over other common pharmacokinetic methods such as radioactive labeling. Administered complexes need not be radiolabeled, and the method does not require periodic blood sampling for each time point. Since the technique relies on the paramagnetism of the species of interest, it is sensitive only to the complex and interference from other blood components is minimized. Pharmacokinetic measurements can be made in real time, and no further manipulation is needed once the blood circuit is complete. BCM–EPR is limited, though, by a rather poor detection limit (compared to, e.g., ⁴⁸V [73] or ¹³C radiolabeling [88]), which likely precludes oral administration and subsequent BCM–EPR study of vanadium compounds. Both radiolabeling studies used oral administration, considered the *de-rigueur* experiment for the study of an antidiabetic complex touted as an *orally active* pharmaceutical agent, rather than i.v. administration used in the studies detailed above. Therefore, radiolabeling studies could be viewed as yielding more accurate descriptions of uptake, distribution, and elimination of vanadium(IV) complexes, as they take into account the effects of the gastrointestinal tract on these properties. Further, the low S/N of the nearly isotropic spectra in BCM–EPR (see Fig. 9) and the requirement for measurement at ambient temperature does not allow for any meaningful structural interpretation; real-time monitoring of biotransformation reactions (i.e., with serum proteins) of administered complexes would be a useful extension of such an experiment. Nevertheless, the results gained from BCM–EPR emphasize the importance of pharmacokinetic data in the delineation of structure/function relationships that potentially govern the activity of these complexes.

3.3. In-Vivo Structure Determination by CW and Pulsed EPR

3.3.1. In vivo CW-EPR Studies of Vanadium(IV) Distribution

EPR has been a useful in-vivo probe of vanadium metabolism. One of the earliest experiments to study biolocalization of V(IV) species was reported in 1980. After i.p. administration of sodium metavanadate for 3 days, V(IV) species were detected by EPR in the subcellular fraction of rat liver. Using the older structural correlation between A_0 and g_0 values, the detected species was proposed to possess mostly O₄ coordination and be present in a protein-bound form [92].

Later, Chasteen, Lord, and Thompson used EPR to determine the chemical forms of both absorbed vanadium in tissue and excreted vanadium in the urine and feces of rats given VOSO_4 in drinking water over long periods. EPR signals were well defined in the stomach, duodenum, liver, spleen, kidney, lung, and elimination products [78].

EPR spectra of fecal pellets from rats fed a diet supplemented with either VOSO_4 or NaVO_3 showed strong signals due to vanadyl species, evidence of the relatively poor absorption of inorganic vanadium species from the GI tract. The spectrum also demonstrated that most V(V) was reduced to V(IV) prior to fecal excretion. This reaction likely occurred in the stomach, a region of low pH (1.5–4) that stabilizes the vanadyl cation. Vanadyl ions detected in fecal matter appeared to be associated with insoluble fiber. The VO^{2+} spectrum in urine was observed within a few hours of vanadium administration (either +4 or +5 oxidation state). Urine appeared to be the major pathway of elimination. Vanadyl ions observed in urine had a nearly isotropic spectrum at room temperature, indicating formation of a low-molecular-weight complex(es). The kidney, spleen, and liver samples all possessed sharp VO^{2+} EPR spectra, which were found to correspond to the spectrum of a VO^{2+} -ferritin complex reported earlier [93]. In these organs, therefore, absorbed vanadyl ions formed a specific VO -protein complex *in vivo* [78].

Vanadyl sulfate administered via daily *i.p.* injection was detected by EPR in liver, kidney, and serum by Sakurai and coworkers [54]. Spin Hamiltonian parameters were tabulated for the *in-vivo* vanadyl spectra and for several model complexes with known ligand sets to attempt to correlate the *in-vivo* spectra with either O_4 , N_2O_2 , S_2N_2 , or S_2O_2 coordination spheres. Vanadyl ions detected in rat kidney and liver and their subcellular fractions were proposed to possess O_4 coordination with a square pyramidal structure [54]. These studies, while useful for detection and quantification of absorbed vanadyl ions into bodily tissues, also serve to illustrate the limitations of EPR as a stand-alone structural characterization method. Use of EPR alone for assignment of structure carries some risk of misassignment, as was demonstrated recently by Sakurai and coworkers through the application of higher-resolution pulsed EPR methods to an identical system (*vide infra*).

3.3.2. *In-Vivo High-Resolution Pulsed EPR for Structure Determination*

The first application of higher-resolution pulsed EPR techniques was reported by Fukui et al. in 1995, who reported insights into the *in-vivo* coordination structure of vanadyl ions in rat kidney and liver, taken from animals administered a chronic *i.v.* dose of VOSO_4 [69]. ESEEM spectroscopy (2-pulse) was used to detect and quantify small superhyperfine coupling constants of vanadyl compounds in these organs.

Tissue samples were excised from animals following a four-day program of intravenous VOSO_4 injections once per day. CW and 2-pulse ESEEM spectra were measured on the tissue samples directly. Reasonable *S/N* levels were observed in the CW spectra, allowing for orientation selection of the paramagnetic species by measuring the ESEEM spectrum at the parallel and perpendicular features of the

CW spectrum. In both tissues, several peaks were observed at low frequency and were determined to arise from ^{14}N , indicating at least one nitrogen ligating some of the vanadyl ions in each tissue [69], which would appear to contradict earlier CW-EPR work described earlier [54]. This result represented the first direct evidence for nitrogen coordination to vanadyl in the organs of an animal.

In addition, an intense peak at the proton Larmor frequency was observed, and in some spectra this peak appeared to be split. Due to the use of the maximum entropy method (MEM, as opposed to the far more common Fourier transformation) for spectral processing, they could not determine whether the splitting was due to a real physical phenomenon or simply an artifact of the MEM method, precluding further analysis. The appearance of this matrix peak did, however, indicate the presence of waterborne protons weakly coupled to the paramagnetic vanadyl nucleus.

To assist interpretation and to quantify the amount of vanadyl bound by the detected nitrogen ligand, a model complex VO(His) was used. It was found that the spectra of VO(His) and VO^{2+} in the kidney were similar, although the intensity of the ^1H matrix peak was less in VO(His), indicative of fewer water molecules in the VO^{2+} coordination sphere of the model complex. Comparison of the orientation selective spectra of the biological and model samples led to assignment of the low frequency ^{14}N peaks and calculation of anisotropic $A_{(x,y,z)}$ superhyperfine coupling constants. Simulation of the spectra, while successful for the VO(His) model, was not satisfactory for the organ samples (possibly another side effect of MEM processing), and so A_{iso} values for the nitrogen donor in rat kidney and donor were reported, and compared to known model systems with N-amine and N-imine donors. Both rat kidney ($A_{\text{iso}} = 5.2$ MHz) and liver ($A_{\text{iso}} = 5.0$ MHz) samples were proposed to arise from an amine-coordinated vanadyl species, with the donor atom coming from an ϵ -amine of a lysine or N terminal $-\text{NH}_2$ of a protein. Imine coordination (such as from the imidazole group of His) could be excluded as the A_{iso} values for such donors typically exceed 6.5 MHz [94]. Thus, VOSO_4 , administered by i.v. injection, is accumulated in high concentration in the kidney and liver and is bound by protein/peptide moieties in these tissues.

Using the $\nu = 0$ peak amplitude of the VO(His) model, estimates of the amount of nitrogen-coordinated species were made for both kidney and liver samples. After normalization of the peak heights between samples, 50–55% and 70–80% of the total vanadyl in the kidney and liver were present as the nitrogen-coordinated species, indicating that it is the major form of accumulated vanadyl species in these tissues. This elementary method of quantification was later modified [71], and challenged [72] as an inaccurate method of determining this important parameter. These studies are examined below.

This report was followed by several studies that used pulsed EPR spectroscopy to determine the fate of chelated vanadyl complexes in the organs of chronically treated rats. Fukui et al. measured the 2- and 3-pulse ESEEM spectra of rat kidney, liver, and bone from animals treated with VOSO_4 or $\text{VO}(\text{pic})_2$ [71]. Dikanov and coworkers used ESEEM and the two-dimensional ESEEM technique hyperfine sublevel correlation (HYSCORE) spectroscopy to examine in detail the coordina-

tion structure of VO(ema)₂-derived vanadyl ions in rat bone [95] and kidney [72]. Interpretation of the spectra from bone was greatly assisted through a thorough model study of the VO-triphosphate system, also examined by ESEEM and HYSCORE spectroscopies [96]. The results of these studies are summarized in Table 4.

Table 4. Spin Hamiltonian Parameters for VOSO₄, VO(pic)₂, and VO(ema)₂ in Frozen Aqueous Solution and in Rat Tissue Samples

Compound	Tissue	Route	$ A_{\text{iso}} ^a$	g_x^b	g_y	g_z	$ A_x ^b$	$ A_y $	$ A_z $	Ref.
VO(pic) ₂	Complex	--		1.981	1.945		60.5		165.8	[69]
	Kidney	i.p.	4.9	1.98	1.95		58		166	
	Bone	i.p.		1.974	1.935		63.5		173.5	
VO(ema) ₂	Complex	--		1.988	1.976	1.935	60.5	60.0	170.0	[72]
	Kidney	oral	4.9	1.98	1.945		58		168	
	Bone	oral		1.996	1.93		80		190	
VOSO ₄	Complex	--		1.977	1.934		74.0		201.0	[103]
	Kidney	i.v.	5.2	1.98	1.94		61		169	
	Bone	i.p.		1.972	1.935		62.6		173.5	

^a Corresponding to the superhyperfine coupling constant for the coordinated amine only.

^b For $g_{x,y}$ and $A_{x,y}$ values with one entry, this value corresponds to g_{\perp} and A_{\perp} , respectively.

In the case of VO(pic)₂, ESEEM spectroscopy detected similar amine nitrogen coordination in the kidney and liver of treated rats (by i.p. injection), as with VOSO₄, as well as weaker signals that were attributed to residual intact VO(pic)₂ in these organs [71]. This result was further supported by differences in measured phase memory time for the two-pulse ESEEM spectra, where VO(pic)₂ in kidney and liver was found to relax faster than kidney and liver samples derived from VOSO₄-treated rats [71]. For VO(ema)₂, only signals due to equatorial ¹⁴N amine coordination were detected, although it was not possible to detect any residual VO(ema)₂ complexes due to the ESEEM silence of the O₄ (¹⁶O, 99.76% abundant, $I = 0$) coordination sphere [72].

Quantification of the amount of residual VO(pic)₂ (shown in Fig. 10) was conducted through subtraction of normalized time-domain ESEEM spectra of VO(pic)₂ in liver (Fig. 10a) from VOSO₄ in liver (Fig. 10b), yielding the time-domain spectrum of the minor species (Fig. 10c), as described by Eq. (1), where Mod_{norm} corresponds to the normalized time-domain intensity (background decay curve subtracted) extrapolated to $\tau = 0$ and corrected by the preexponential factor obtained from a modified Block-type relaxation equation, for each species. The coefficients α and β were estimated by a linear least-squares method [71]:

$$\text{Mod}_{\text{norm}}[\text{VO}(\text{pic})_2\text{organ}] = \alpha \text{Mod}_{\text{norm}}[\text{VO}(\text{pic})_2\text{intact}] + \beta \text{Mod}_{\text{norm}}[\text{VOSO}_4\text{organ}]. \quad (1)$$

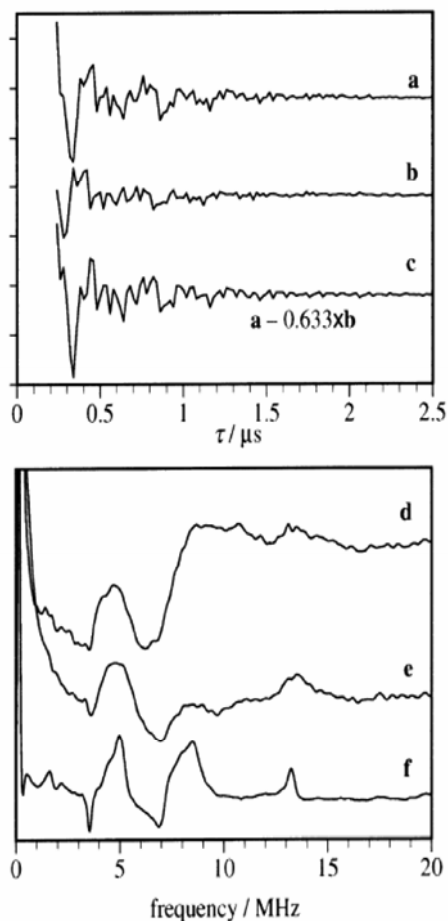


Figure 10. Top: Normalized time-domain ESEEM spectra of (a) $\text{VO}(\text{pic})_2$ in rat liver; (b) VOSO_4 in rat liver; (c) resultant spectrum after subtraction of $0.633(b)$ from (a). Bottom: Frequency-domain difference ESEEM spectra of $\text{VO}(\text{pic})_2$ in kidney (d) and liver (e) after subtraction of amine nitrogen signal; (f) ESEEM spectrum of $\text{VO}(\text{pic})_2$ in ethyleneglycol:water (1:1) glass. Reprinted with permission from [60]. Copyright © 1995, Elsevier.

Fourier transformation of these spectra gave the ESEEM frequency-domain spectrum of the residual $\text{VO}(\text{pic})_2$ in kidney (Fig. 10d) and liver (Fig. 10e). These spectra compared well with the ESEEM spectrum of $\text{VO}(\text{pic})_2$ in ethyleneglycol:water glass (1:1) (Fig. 10f).

Multiplication of the β coefficient for $\text{VO}(\text{pic})_2$ in liver and kidney by the amount of amine-coordinated VOSO_4 in each organ yielded the total percentage of vanadyl ion found coordinated to at least one picolinate ligand. Whether $\text{VO}(\text{pic})_2$ was in the form of the bis or mono complex (and possessing either 2 or 1 imine

donors to VO^{2+}) could not be determined. This procedure revealed that a large proportion of detected vanadyl species from $\text{VO}(\text{pic})_2$ treatment in kidney and liver was in the form of the amine-coordinated compound previously detected in the VOSO_4 study [69] (43–47 and 44–50% respectively [71]). The concentration of $\text{VO}(\text{pic})_x^{2-x}$ species ($x = 1, 2$) [related to α of Eq. (1)] was determined to be 8–16% for kidney and 12–24% for liver, where the smaller number represents the proportion if only the bis complex is present in the organ, and the larger number places an upper limit on the proportion of the monopicolinate complex.

This result was disputed by Dikanov and coworkers, who suggested that use of $\text{VO}(\text{His})$ as a model system for the determination of the amount of amine-coordinated species in rat kidney and liver was a poor choice due to the contribution to the echo decay from both the peptide amine and the imino nitrogen of the imidazole group [69,97]. This contribution from the imine nitrogen affects the observed modulation depth used to normalize the spectra of $\text{VO}(\text{His})$ - and VOSO_4 -treated kidney and liver sample spectra. Dikanov and coworkers corrected for this source of error by using $\text{VO}(1\text{-}^{15}\text{His})$ as an intensity model, and by filtering out high-frequency signals (due to ^1H) from the time domain spectrum of $\text{VO}(\text{ema})_2$ -treated rat kidney prior to fitting the echo decay for the $\nu = 0$ modulation depth [72]. The use of the ^{15}N -labeled model nearly eliminates all contributions to peak intensities < 8 MHz, as well as between 10 and 12 MHz. It is demonstrated that erroneous inclusion of the imine nitrogen modulation depth in the determination of the maximum modulation depth (for subsequent normalization in [69,71]) led to an underestimation of the amount of amine-coordinated species by 10–17% [72]. Thus, a revised value for the amount of amine-coordinated species in VOSO_4 -treated rat kidney and liver would be 70–80 and 90–100%, respectively. This in turn would affect the amount of free $\text{VO}(\text{pic})_2$ detected in these organs.

The use of pulsed EPR conclusively demonstrated that administered vanadyl complexes, whether given by i.p. or oral dose, are accumulated in the liver and kidney tissue, and the majority is found as a protein or peptide-ligated (N_{amine}) species. This result contradicts earlier work with CW-EPR that proposed an O_4 coordination sphere for VO^{2+} ions in kidney and liver based on a $g_{\parallel}\text{-}A_{\parallel}$ correlation diagram [54]. Comparison of these data to the regions of Figure 2 occupied by O_4 and N_2O_2 coordination spheres showed that the spin Hamiltonian parameters for $\text{VO}(\text{pic})_2$ in kidney and liver fall in an intermediate region between pure O_4 and N_2O_2 coordination spheres, consistent with the proposed NO_3 ligand set for the amine-bound vanadyl ions [71]. Clearly, the coordination state of both $\text{VO}(\text{pic})_2$ and $\text{VO}(\text{ema})_2$ has changed since administration. Sakurai and coworkers proposed that the amine-ligated species in liver and kidney corresponded to an inactive form of the drug, and in fact the proportion of the dose that did not go on to form the protein/peptide complex (i.e., $[\text{VO}(\text{pic})]^+$ and/or $\text{VO}(\text{pic})_2$) was in fact the active species [71]. This proposal was supported by the fact that the amount of amine-ligated VO^{2+} was much less for $\text{VO}(\text{pic})_2$ compared to VOSO_4 , which correlates with the increased efficacy [52,98] and the higher concentration in bone of $\text{VO}(\text{pic})_2$ [52,53]. This portion of the administered dose acts as the active species to exert antidiabetic activity, or is left free to circulate in the bloodstream and become

incorporated into bone, thought to contribute to the long-term effect of vanadium compounds upon cessation of treatment [52,73]. Support of this hypothesis could come from further in-vivo ESEEM experiments with other V(IV) insulin-enhancing complexes to attempt to correlate the amount of intact complex after organ uptake with antidiabetic activity. This experiment might shed light on the true role of the amine-ligated species in liver and kidney, if any exists.

Bioaccumulation in bone of chelated and free vanadyl sources was shown to be remarkably similar for VO(ema)₂ [95], VO(pic)₂, and VOSO₄ [71]. CW-EPR spectra of VO(pic)₂ and VOSO₄-treated rat bone samples suggested a complete change in the coordination sphere of VO(pic)₂ (Table 4). The two-pulse ESEEM spectra of the two samples were virtually identical, each containing 2 peaks at ~5.5 and 11 MHz, in addition to the ¹H matrix peak (~13 MHz), as was observed in the kidney and liver samples. No peaks corresponding to ¹⁴N either from the picolinate ligand or an endogenous donor were observed. The two low-frequency peaks varied with applied field precisely as expected for ³¹P nuclei ($I = \frac{1}{2}$), indicating the presence of phosphorus in the coordination sphere of the vanadyl ions. These were assigned as the ³¹P matrix peak (~5.5 MHz) as well as its sum addition peak at ~10.5 MHz that typically appears in the two-pulse spectrum. The ³¹P matrix peak appeared broadened, leading to the conclusion that any hyperfine coupling contained within the signal would be too small to be resolved or the broadness of the signal was a result of a range of ³¹P hyperfine couplings to the vanadyl nuclei [71].

The field-swept electron spin echo (FS-ESE) spectrum (which yields a spectrum similar to that acquired by a CW experiment, but is acquired using a simple two-pulse sequence) of VO(ema)₂-treated rat bone yielded spin Hamiltonian parameters quite different from those obtained with the other two vanadyl compounds (Table 4). As with VO(pic)₂, it was clear that the coordination state of the orally administered VO(ema)₂ had changed [95]. Despite the difference in spin Hamiltonian parameters determined from CW-EPR (VOSO₄, VO(pic)₂) and FS-ESE (VO(ema)₂) spectra, it appears that all three compounds share the same metabolic fate after uptake into bone mineral.

Three-pulse ESEEM spectra of the bone sample collected on the $M_I^V = -1/2$ peak of the FS-ESE spectrum contained a narrow peak at $\nu_p = 5.7$ MHz, corresponding to the phosphorus matrix peak, in addition to the ¹H matrix peak at 14.1 MHz. Sum and/or difference frequencies are suppressed in the three-pulse experiment, which possibly led to the observation of extended peaks at ~1.5 MHz with shoulders to 4 MHz. Peaks in this region, however, were broad and ill defined, which precluded detailed analysis from the three-pulse experiment. Lastly, suggestions of peaks in the region of 8–10 MHz were also observed.

Complete interpretation of the low-frequency peaks was obtained through the application of the two-dimensional four-pulse HYSORE experiment. The HYSORE spectrum of VO(ema)₂-treated rat bone is shown in Figure 11. Three sets of cross-peaks were evident, one of which appeared as an extended arc about the ³¹P matrix peak (Fig. 11, cross-peak 3). Careful selection of the interpulse times led to suppression of the matrix peak to allow for better observation of the third cross-peak. Interpretation of the HYSORE spectrum was carried out using con-

four lineshape analysis [99,100] that allowed for simultaneous determination of two sets of a (isotropic hyperfine coupling constant) and T (anisotropic hyperfine coupling constant) values with opposite relative signs. Such analysis yielded estimates of three ^{31}P hyperfine coupling constants of 14, 9, and 3 MHz [95]. Lastly, HYSCORE results also determined a small 3-MHz coupling arising from ^1H , consistent with a water or hydroxyl ligand in an equatorial position [101].

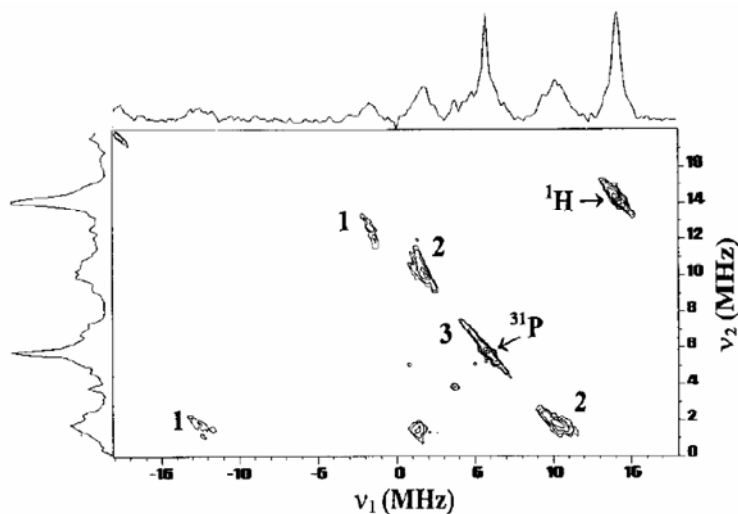
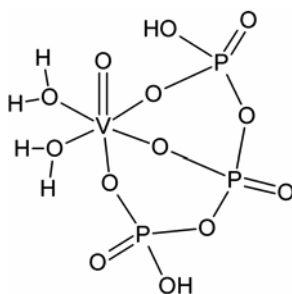


Figure 11. HYSCORE spectrum of $\text{VO}(\text{ema})_2$ -treated rat bone, acquired on the orientation nonselective $M_I^V = -1/2$ peak of the FS-ESE spectrum. Numbers indicate the cross-peak sets corresponding to three different ^{31}P superhyperfine coupling constants. The nuclear matrix peaks of ^{31}P and ^1H are labeled. Reprinted with permission from [95]. Copyright © 1999, American Chemical Society.

Two interpretations could be made. The first is that the administered $\text{VO}(\text{ema})_2$ is completely de-ligated prior to uptake into bone, and is bound by three magnetically distinct phosphate groups in the hydroxyapatitic matrix of bone mineral. The magnitude of the two strongest coupling constants observed were consistent with those reported for $\text{VO}(\text{ADP})_2$ [102] and $\text{VO}(\text{ATP})_2$ [103], indicating that a facial VO -tris(phosphate) moiety with one or two coordinated water molecules in an overall octahedral structure was conceivable.

The second option was that only partial degradation of the complex took place prior to bone uptake, or only partial phosphate coordination takes place in bone mineral. The partial coordination leads to considerable variability in coordination structure and observation of a wide range of ^{31}P coupling constants in the ESEEM/HYSCORE spectra. Such an explanation was offered by Fukui et al. to explain the broad, unresolved signals below 8 MHz that were thought to be due to diversity in phosphate coordination mode [71].

This uncertainty was resolved in a later report of a vanadyl–phosphate model system to investigate the coordination structure of $\text{VO}(\text{ema})_2$ in bone mineral [96]. Two, three, and 1D 4-pulse, along with 2D HYSORE spectroscopies were used to study the coordination structure of the vanadyl–triphosphate system. HYSORE spectroscopy partnered with contour lineshape analysis determined three ^{31}P hyperfine coupling constants of 15, 9, and 1 MHz, in excellent agreement with the *in vivo* results. In addition, detailed analysis of the proton matrix peak by 1D 4-pulse ESEEM led to assignment of at least one, and probably two, water molecules in the equatorial plane. Thus, the VO–triphosphate model system demonstrated that the vanadyl ions in $\text{VO}(\text{ema})_2$ -treated rat bone samples were most likely in a facial tris(phosphate) coordination with water molecules occupying the vacant positions in the equatorial plane, as shown in Scheme 3.



Scheme 3. Proposed solution structure of the dominant species in the vanadyl–triphosphate system at pH 5.0. The structure gives rise to three distinct ^{31}P hyperfine coupling constants of 15, 9, and 1 MHz, in good agreement with those obtained from HYSORE spectra of $\text{VO}(\text{ema})_2$ -treated rat bone (14, 9, and 3 MHz). Adapted from [96].

This model study confirmed bone uptake of vanadium(IV) compounds could lead to formation of a highly stable vanadyl–phosphate complex, and that complex degradation must take place prior to incorporation of the vanadyl ion into the bone matrix. HYSORE spectroscopy was shown to be very powerful for the deconvolution of complicated 1D ESEEM spectra; without the 2D pulse sequence, researchers were only able to confirm the presence of ^{31}P nuclei [71].

4. SUMMARY

EPR methods have uncovered a number of properties of insulin-enhancing vanadium compounds that would otherwise be difficult, if not impossible, to obtain by other methods. The strengths of EPR spectroscopy, such as its natural selectivity, the high-resolving power of closely related structural isomers, and ease of *in vivo* application have been exploited to reveal important details regarding the solution chemistry, absorption, metabolism, and bioaccumulation of antidiabetic vana-

dium species. Still, much remains to be uncovered regarding the mechanism of insulin enhancement by vanadium(IV) compounds, but undoubtedly EPR, ENDOR, and ESEEM spectroscopies will play an important role in its elucidation.

This review has outlined the breadth of studies conducted with paramagnetic resonance methods in the study of antidiabetic insulin enhancing vanadium compounds. It is curious to note that 25 years ago, Chasteen predicted that EPR spectroscopy would remain a central tool for investigations into biological vanadium, and that ENDOR, ESEEM, and ^{51}V NMR had much potential for future studies in the field [21]. As demonstrated throughout this review, this prediction has been borne out, and indeed has led to significant advancement in the field of vanadium antidiabetic agents. Methodological developments such as real-time pharmacokinetic monitoring of in-vivo vanadium(IV), high-resolution in-vivo structure determinations of vanadium species by ENDOR and ESEEM, and multifaceted investigations of the roles of endogenous bioligands in the biotransformation and transport of vanadium pharmaceuticals have proven the utility of EPR methods; it is likely that the important role played by EPR methods will continue in future studies of these compounds.

ACKNOWLEDGMENTS

The author is grateful for the expertise and contributions of past coworkers and collaborators cited in the references, particularly Profs. C. Orvig and G.R. Hanson, and Dr. K.H. Thompson. R. Heffernan is graciously acknowledged for assistance in production of the manuscript.

ABBREVIATIONS

ADME = absorption, distribution, metabolism, elimination

apo-Tf = apo-transferrin

AUC = area under the concentration curve

BCM = blood circulation monitoring

BSA = bovine serum albumin

BSO = buthionine sulfoximine

CD = circular dichroism

CL_{tot} = total body clearance

CW = continuous wave

EPR = electron paramagnetic resonance

ENDOR = electron nuclear double resonance

ESEEM = electron spin echo envelope modulation

GI = gastrointestinal

GSH = glutathione

GSSH = oxidized glutathione

H₂dipic = 2hpo = 2-hydroxypyridine-N-oxide

His = histidine

HAS = human serum albumin

HYSCORE = hyperfine sublevel correlation

IC₅₀ = drug concentration for 50% inhibition

ICP-AES = inductively coupled plasma atomic emission spectrometry

i.p. = intraperitoneal

i.v. = intravenous

MEM = maximum entropy method

MRT = mean residence time

NMR = nuclear magnetic resonance

S/N = signal-to-noise ratio

UV-Vis = ultraviolet/visible electronic absorption spectroscopy

V_D = steady-state distribution volume

Vis = visible electronic absorption spectroscopy

VO(acac)₂ = bis(acetylacetonato)oxovanadium(IV)

VO(acac-Me)₂ = bis(3-methylacetylacetonato)oxovanadium(IV)

VO(acac-Et)₂: bis(3-ethylacetylacetonato)oxovanadium(IV)

VO(acac-NH₂)₂ = bis(acetylacetamido)oxovanadium(IV)

VO(acac-NMe₂)₂ = bis(N,N-dimethylacetylacetamido)oxovanadium(IV)

VO(bma)₂ = bis(n-butylmaltolato)oxovanadium(IV)

VO(dmpp)₂ = bis(3-hydroxy-1,2-dimethyl-4-pyridinato)oxovanadium(IV)

VO(ema)₂: bis(ethylmaltolato)oxovanadium(IV)

VO(3hpa)₂ = bis(3-hydroxypicolinato)oxovanadium(IV)

VO(6hpa)₂ = bis(6-hydroxypicolinato)oxovanadium(IV)

VO(2hpo)₂ = bis(2-hydroxypyridine-N-oxo)oxovanadium(IV)

VO(ima)₂ = bis(isopropylmaltolato)oxovanadium(IV)

VO(5ipa)₂ = bis(5-iodopicolinato)oxovanadium(IV)

VO(ma)₂ = (bis(maltolato)oxovanadium(IV)

VO(3mpa)₂ = bis(3-methylpicolinato)oxovanadium(IV)

VO(6mpa)₂ = bis(6-methylpicolinato)oxovanadium(IV)

VO(2mpo)₂ = bis(2-mercaptopyridine-N-oxo)oxovanadium(IV)

VO(5opic)₂ = bis(5-carboalkoxyxypicolinato)oxovanadium(IV)

VO(pic)₂ = bis(picolinato)oxovanadium(IV)

VO(tma)₂ = bis(thiomaltolato)oxovanadium(IV)

REFERENCES

1. Lyonnet B. 1899. L'emploi therapeutique des derives du vanadium. *Presse Med* 1:191–192.
2. Lopez V, Stevens T, Lindquist RN. 1976. Vanadium ion inhibition of alkaline phosphatase-catalyzed phosphate ester hydrolysis. *Arch Biochem Biophys* 24:31–38.
3. Cantley Jr LC, Josephson L, Warner R, Yanagihara N, Lechene C, Guidotti G. 1977. Vanadate is a potent (Na, K)-ATPase inhibitor found in ATP derived from muscle. *J Biol Chem* 252:7421–7423.
4. Shechter Y, Karlish SJD. 1980. Insulin-like stimulation of glucose oxidation in rat adipocytes by vanadyl(IV) ions. *Nature* 284:556–558.
5. Heyliger CE, Tahiliani AG, McNeill JH. 1985. Effect of vanadate on elevated blood glucose and depressed cardiac performance of diabetic rats. *Science* 227:1474–1477.
6. Brichard SM, Assimacopoulos-Jeannet F, Jeanrenaud B. 1992. Vanadate treatment markedly increases glucose utilization in muscle of insulin-resistant *fa/fa* rats without modifying glucose transporter expression. *Endocrinology* 131:311–317.
7. Blondel O, Simon J, Chevalier B, Portha B. 1990. Impaired insulin action but normal insulin receptor activity in diabetic rat liver: effect of vanadate. *Am J Physiol* 258:E459–E467.
8. Gil J, Miralpeix M, Carreras J, Bartrons R. 1988. Insulin-like effects of vanadate on glucokinase activity and fructose 2,6-bisphosphate levels in the liver of diabetic rats. *J Biol Chem* 263:1868–1871.
9. Ramanadham S, Cros GH, Mongold JJ, Serrano JJ, McNeill JH. 1990. Enhanced *in vivo* sensitivity of vanadyl-treated diabetic rats to insulin. *Can J Physiol Pharmacol* 68:486–491.
10. Bendayan M, Gingras D. 1989. Effect of vanadate administration on blood glucose and insulin levels as well as on the exocrine pancreatic function in streptozotocin-diabetic rats. *Diabetologia* 32:561–567.
11. McNeill JH, Yuen VG, Hoveyda HR, Orvig C. 1992. Bis(maltolato)oxovanadium(IV) is a potent insulin mimic. *J Med Chem* 35:1489–1491.
12. Takino T, Yasui H, Yoshitake A, Hamajima Y, Matsushita R, Takada J, Sakurai H. 2001. A new halogenated antidiabetic vanadyl complex bis(5-iodopicalinato)oxovanadium(IV): *in vitro* and *in vivo* insulinomimetic evaluations and metalokinetic analysis. *J Biol Inorg Chem* 6:133–142.
13. Yuen VG, Orvig C, McNeill JH. 1995. Comparison of the glucose-lowering properties of vanadyl sulfate and bis(maltolato)oxovanadium(IV) following acute and chronic administration. *Can J Physiol Pharmacol* 73:55–64.
14. Reul BA, Amin SS, Buchet JP, Ongemba LN, Crans DC, Brichard SM. 1999. Effects of vanadium complexes with organic ligands on glucose metabolism: a comparison study in diabetic rats. *Br J Pharmacol* 126:467–477.
15. Posner BI, Yang CR, Shaver A. 1998. Mechanism of insulin mimetic action of peroxovanadium compounds. In *Vanadium compounds: chemistry, biochemistry and therapeutic applications*, pp. 316–328. Ed AS Tracey, DC Crans. Washington, DC: American Chemical Society.
16. Chasteen ND, DeKoch RJ, Rogers BL, Hanna MW. 1973. Use of the vanadyl(IV) ion as a new spectroscopic probe of metal binding to proteins: vanadyl insulin. *J Am Chem Soc* 95:1301–1309.

17. Domingo JL, Gomez M, Sanchez DJ, Llobet JM, Keen CL. 1995. Toxicology of vanadium compounds in diabetic rats: the action of chelating agents on vanadium accumulation. *Mol Cell Biochem* **153**:233–240.
18. Willsky GR, Goldfine AB, Kostyniak PJ. 1998. Pharmacology and toxicology of oxovanadium species: oxovanadium pharmacology. In *Vanadium compounds: biochemistry, chemistry and therapeutic applications*, pp. 278–296. Ed AS Tracey, DC Crans. Oxford: Oxford University Press.
19. Deligiannakis YG, Louloudi M, Hadjiliadis N. 2000. Electron spin echo envelope modulation (ESEEM) spectroscopy as a tool to investigate the coordination environment of metal centers. *Coord Chem Rev* **204**:1–112.
20. Smith II TS, LoBrutto R, Pecoraro VL. 2002. Paramagnetic spectroscopy of vanadyl complexes and its applications to biological systems. *Coord Chem Rev* **228**:1–18.
21. Chasteen ND. 1981. Vanadyl(IV) EPR spin probes: inorganic and biochemical aspects. In *Biological magnetic resonance*, pp. 53–119. Ed LJ Berliner, J Reuben. New York: Plenum.
22. Kustin K. 1998. Perspectives on vanadium biochemistry. In *Vanadium compounds: chemistry, biochemistry and therapeutic applications*, pp. 170–185. Ed AS Tracey, DC Crans. Washington, DC: American Chemical Society.
23. Thompson KH, Liboiron BD, Hanson GR, Orvig C. 2005. In vivo coordination chemistry and biolocalization of bis(ligand)oxovanadium(IV) complexes for diabetes treatment. In *Medicinal inorganic chemistry*, pp. 384–399. Ed JL Sessler, SR Doctrow, TJ McMurphy, SJ Lippard. Washington, DC: American Chemical Society.
24. Orvig C, Thompson KH, Battell M, McNeill JH. 1995. Vanadium compounds as insulin mimics. In *Metal ions in biological systems*. Ed H Sigel, A Sigel. New York: Marcel Dekker.
25. Thompson KH, McNeill JH, Orvig C. 1999. Vanadium compounds as insulin mimics. *Chem Rev* **99**:2561–2571.
26. Crans DC, Smee JJ, Gaidamauskas E, Yang Y. 2004. The chemistry and biochemistry of vanadium and the biological activities exerted by vanadium compounds. *Chem Rev* **104**:849–902.
27. Thompson KH, Orvig C. 2000. Design of vanadium compounds as insulin-enhancing agents. *J Chem Soc Dalton Trans*, pp. 2885–2892.
28. Sakurai H, Tamura A, Fugono J, Yasui H, Kiss T. 2003. New antidiabetic vanadyl-pyridone complexes: effect of equivalent transformation of coordinating atom in the ligand. *Coord Chem Rev* **245**:31–37.
29. Rehder D, Costa Pessoa J, Geraldes CFGC, Castro MMCA, Kabanos TA, Kiss T, Meier B, Micera G, Pettersson L, Ranger M, Salifoglou A, Turel I, Wang D. 2002. In vitro study of the insulin-mimetic behaviour of vanadium(IV, V) coordination compounds. *J Biol Inorg Chem* **7**:384–396.
30. Matoso CMM, Pombeiro AJL, da Silva JJRF, da Silva MFCF, da Silva JAL, Baptista-Ferreira JL, Pinho-Almeida F. 1998. A possible role for amavadin in some *Amanita* fungi. In *Vanadium compounds: chemistry, biochemistry and therapeutic applications*, pp. 241–247. Ed AS Tracey, DC Crans. Washington, DC: American Chemical Society.
31. Chasteen ND, Francavilla J. 1976. Electron paramagnetic resonance study of vanadyl(IV)–serum albumin complexes. *J Phys Chem* **80**:867–871.
32. Albanese NF, Chasteen ND. 1978. Origin of the electron paramagnetic resonance line widths in frozen solutions of oxovanadium(IV). *J Phys Chem* **82**:910–914.
33. Telser J. 2003. *Paramagnetic resonance of biomolecules*. Washington, DC: American Chemical Society.

34. Wuthrich K. 1965. Elektronenspinresonanz-Untersuchungen Von VO^{2+} -Komplexverbindungen in Wasseriger Lösung 2. *Helv Chim Acta* **48**:1012–1017.
35. Cornman CR, Zovinka EP, Boyajian YD, Geiser-Bush KM, Boyle PD, Singh P. 1995. Structural and EPR studies of vanadium complexes of deprotonated amide ligands: effects on the V-51 hyperfine coupling constant. *Inorg Chem* **34**:4213–4219.
36. Hamstra BH, Houseman ALP, Colpas GJ, Kampf R, LoBrutto R, Frasch WD, Pecoraro VL. 1997. Structural and solution characterization of mononuclear vanadium(IV) complexes that help to elucidate the active site structure of the reduced vanadium haloperoxidases. *Inorg Chem* **36**:4866–4874.
37. Smith II TS, Root CH, Kampf JW, Rasmussen PG, Pecoraro VL. 2000. Reevaluation of the additivity relationship for vanadyl–imidazole complexes: correlation of the EPR hyperfine constant with ring orientation. *J Am Chem Soc* **122**:767–775.
38. Tasiopoulos AJ, Troganis AN, Evangelou A, Raptopoulou CP, Terzis A, Deligiannakis YG, Kabanos TA. 1999. Synthetic analogues for oxovanadium(IV)–glutathione interaction: an EPR, synthetic and structural study of oxovanadium(IV) compounds with sulfhydryl-containing pseudopeptides and dipeptides. *Chem Eur J* **5**:910–921.
39. Houseman ALP, LoBrutto R, Frasch WD. 1995. Effects of nucleotides on the protein ligands to metals at the M2 and M3 metal binding sites of the spinach chloroplast F1-ATPase. *Biochemistry* **34**:3277–3285.
40. Sakurai H, Yasui H. 2003. Structure–activity relationship of insulinomimetic vanadyl–picolinate complexes in view of their clinical use. *J Trace Elem Exper Med* **16**:269–280.
41. Crans DC, Khan AR, Mahroof-Tahir M, Mondal S, Miller SM, la Cour A, Anderson OP, Jakusch T, Kiss T. 2001. Bis(acetylamido)oxovanadium(IV) complexes: solid state and solution studies. *J Chem Soc Dalton Trans*:3337–3345.
42. Gatzens J, Meier B, Kiss T, Nagy EM, Buglyo P, Sakurai H, Kawabe K, Rehder D. 2003. A new family of insulin-mimetic vanadium complexes derived from 5-carboalkoxypicolinates. *Chem Eur J* **9**:4924–4935.
43. Caravan P, Gelmini L, Glover N, Herring FG, Li H, McNeill JH, Rettig SJ, Setyawati IA, Shuter E, Sun Y, Tracey AS, Yuen VG, Orvig C. 1995. Reaction chemistry of BMOV, bis(maltolato)oxovanadium(IV): a potent insulin mimetic agent. *J Am Chem Soc* **117**:12759–12770.
44. Kiss E, Garribba E, Micera G, Kiss T, Sakurai H. 2000. Ternary complex formation between VO(IV)–picolinic acid or VO(IV)–6-methylpicolinic acid and small blood serum bioligands. *J Inorg Biochem* **78**:97–108.
45. Kiss E, Kawabe K, Tamura A, Jakusch T, Sakurai H, Kiss T. 2003. Chemical speciation of insulinomimetic VO(IV) complexes of pyridine-N-oxide derivatives: binary and ternary systems. *J Inorg Biochem* **95**:69–76.
46. Amin SS, Cryer K, Zhang B, Dutta SK, Eaton SS, Anderson OP, Miller SM, Reul BA, Brichard SM, Crans DC. 2000. Chemistry and insulin-mimetic properties of bis(acetylacetonate)oxovanadium(IV) and derivatives. *Inorg Chem* **39**:406–416.
47. Costa Pessoa J, Gajda T, Gillard RD, Kiss T, Luz SM, Moura JGG, Tomaz I, Telo JP, Torok I. 1998. Oxovanadium(IV) complexes of the dipeptides glycyl-L-aspartic acid, L-aspartylglycine and related ligands: a spectroscopic and potentiometric study. *J Chem Soc Dalton Trans* 3587–3600.
48. Costa Pessoa J, Tomaz I, Kiss T, Kiss E, Buglyo P. 2002. The systems VO^{2+} –glutathione and related ligands: a potentiometric and spectroscopic study. *J Biol Inorg Chem* **7**:225–240.
49. Jakusch T, Jin WZ, Yang LQ, Kiss T, Crans DC. 2003. Vanadium(IV/V) speciation of pyridine-2,6-dicarboxylic acid and 4-hydroxy-pyridine-2,6-dicarboxylic acid com-

- plexes: potentiometry, EPR spectroscopy and comparison across oxidation states. *J Inorg Biochem* **95**:1–13.
50. Castro MMCA, Avecilla F, Galdames CFGC, de Castro B, Rangel M. 2003. Study of the oxidation products of the VO(dmpp)₂ complex in aqueous solution under aerobic conditions: comparison with the vanadate–DMPP system. *Inorg Chim Acta* **356**:142–154.
 51. Song B, Aebischer N, Orvig C. 2002. Reduction of [VO₂(ma)₂][−] and [VO₂(ema)₂][−] by ascorbic acid and glutathione: kinetic studies of pro-drugs for the enhancement of insulin action. *Inorg Chem* **41**:1357–1364.
 52. Fujimoto S, Fujii K, Yasui H, Matsushita R, Takada J, Sakurai H. 1997. Long-term acting and orally active vanadyl–methylpicolinate complex with hypoglycemic activity in streptozotocin-induced diabetic rats. *J Clin Biochem Nutr* **23**:113–129.
 53. Nakai M, Watanabe H, Fujiwara C, Kakegawa H, Satoh T, Takada J, Matsushita R, Sakurai H. 1995. Mechanism of insulin-like action of vanadyl sulfate: studies on interaction between rat adipocytes and vanadium compounds. *Biol Pharm Bull* **18**:719–725.
 54. Sakurai H, Tsuchiya K, Nukatsuka M, Sofue M, Kawada J. 1990. Insulin-like effect of vanadyl ion on streptozotocin-induced diabetic rats. *J Endocrinol* **126**:451–459.
 55. Sakurai H, Yojima Y, Yoshikawa Y, Kawabe K, Yasui H. 2002. Antidiabetic vanadium(IV) and zinc(II) complexes. *Coord Chem Rev* **226**:187–198.
 56. Sakurai H, Watanabe H, Tamura H, Yasui H, Matsushita R, Takada J. 1998. Insulin-mimetic vanadyl–dithiocarbamate complexes. *Inorg Chim Acta* **283**:175–183.
 57. Hanson GR, Sun Y, Orvig C. 1996. Characterization of the potent insulin mimetic agent bis(maltolato)oxovanadium(IV) (BMOV) in solution by EPR spectroscopy. *Inorg Chem* **35**:6507–6512.
 58. Sun Y, James BR, Rettig SJ, Orvig C. 1996. Oxidation kinetics of the potent insulin mimetic agent bis(maltolato)oxovanadium(IV) (BMOV) in water and in methanol. *Inorg Chem* **35**:1667–1673.
 59. Makinen MW, Brady MJ. 2002. Structural origins of the insulin-mimetic activity of bis(acetylacetonato)oxovanadium(IV). *J Biol Chem* **277**:12215–12220.
 60. Linert W, Herlinger E, Margl P, Boca R. 1993. Spectroscopic, electrochemical and quantum mechanical investigations of vanadyl(IV)-acetylacetonate in nonaqueous solutions. *J Coord Chem* **28**:1–16.
 61. Van Willigen H. 1979. Proton ENDOR on VO(acac)₂ in frozen solution. *Chem Phys Lett* **65**:490–493.
 62. Cantley Jr. LC, Aisen P. 1979. The fate of cytoplasmic vanadium: implications of (Na,K)-ATPase inhibition. *J Biol Chem* **254**:1781–1784.
 63. Degani H, Gochin M, D. KSJ, Shechter Y. 1981. Electron paramagnetic resonance studies and insulin-like effects of vanadium in rat adipocytes. *Biochemistry* **20**:5795–5799.
 64. Macara IG, Kustin K, Cantley LC. 1980. Glutathione reduces cytoplasmic vanadate: mechanism and physiological implications. *Biochim Biophys Acta* **629**:95–106.
 65. Lu B, Ennis D, Lai R, Bogdanovic E, Nikolov R, Salamon L, Fantus C, Le-Tien H, Fantus IG. 2001. Enhanced sensitivity of insulin-resistant adipocytes to vanadate is associated with oxidative stress and decreased reduction of vanadate(+5) to vanadyl(+4). *J Biol Chem* **276**:35589–35598.
 66. Goda T, Sakurai H, Yashimura T. 1988. Structures of oxovanadium(IV)-glutathione complexes and reductive complex formation between glutathione and vanadate (+5 oxidation state). *Nippon Kagaku Kaishi* 654–661.

67. Dessi A, Micera G, Sanna D. 1993. EPR investigation of the oxovanadium(IV) complexes formed by the tripeptide glutathione and some related ligands in aqueous solution. *J Inorg Biochem* **52**:275–286.
68. Williams PAM, Baran EJ. 1994. The interaction of the VO^{2+} cation with S-methylglutathione. *J Inorg Biochem* **54**:75–78.
69. Fukui K, Ohya-Nishiguchi H, Nakai M, Sakurai H, Kamada H. 1995. Detection of vanadyl-nitrogen interaction in organs of the vanadyl-treated rat: electron spin echo envelope modulation study. *FEBS Lett* **368**:31–35.
70. Tasiopoulos AJ, Troganis AN, Deligiannakis YG, Evangelou A, Raptopoulou CP, Terzis A, Kabanos TA, Woolins JD, Slavin A. 2000. Synthetic analogs for oxovanadium(IV/V)-glutathione interaction: an NMR, EPR, synthetic and structural study of oxovanadium(IV/V) compounds with sulfhydryl-containing pseudopeptides and dipeptides. *J Inorg Biochem* **79**:159–166.
71. Fukui K, Fujisawa Y, Ohya-Nishiguchi H, Kamada H, Sakurai H. 1999. In vivo coordination structural changes of a potent insulin-mimetic agent, bis(picolinato)oxovanadium(IV), studied by electron spin echo envelope modulation spectroscopy. *J Inorg Biochem* **77**:215–224.
72. Dikanov SA, Liboiron BD, Thompson KH, Vera E, Yuen VG, McNeill JH, Orvig C. 2003. One and two dimensional pulsed electron paramagnetic resonance studies of in vivo vanadyl coordination in rat kidney. *Bioinorg Chem Appl* **1**:69–83.
73. Setyawati IA, Thompson KH, Sun Y, Lyster DM, Vo C, Yuen VG, Battell M, McNeill JH, Ruth TJ, Zeisler S, Orvig C. 1998. Kinetic analysis and comparison of uptake, distribution, and excretion of V-48-labeled compounds in rats. *J Appl Physiol* **84**:569–575.
74. Cannon JC, Chasteen ND. 1975. Nonequivalence of metal binding sites in vanadyl-labeled human serum transferrin. *Biochemistry* **14**:4573–4577.
75. Campbell R, Chasteen ND. 1977. Anion binding study of vanadyl(IV) human serotransferrin: evidence for direct linkage to metal. *J Biol Chem* **252**:5996–6001.
76. Chasteen ND, Lord EM, Thompson HJ, Grady JK. 1986. Vanadium complexes of transferrin and albumin in the rat. *Biochem Biophys Acta* **884**:84–92.
77. White LK, Chasteen ND. 1979. Q-band electron paramagnetic resonance study of vanadyl(IV)-labeled human serotransferrin. *J Phys Chem* **14**:279–284.
78. Chasteen ND, Lord EM, Thompson HJ. 1985. Vanadium metabolism: vanadyl(IV) electron paramagnetic resonance spectroscopy of selected rat tissues in the rat. In *Frontiers in bioinorganic chemistry*, pp. 133–141. Ed A Xavier. Weinheim, Germany: VCH.
79. Willsky GR, Goldfine AB, Kostyniak PJ, McNeill JH, Yang LQ, Khan HR, Crans DC. 2001. Effect of vanadium(IV) compounds in the treatment of diabetes: in vivo and in vitro studies with vanadyl sulfate and bis(maltolato)oxovanadium(IV). *J Inorg Biochem* **85**:33–34.
80. Liboiron BD, Thompson KH, Hanson GR, Lam E, Aebischer N, Orvig C. 2005. New insights into the interactions of serum proteins with bis(maltolato)oxovanadium(IV): transport and biotransformation of insulin-enhancing vanadium pharmaceuticals. *J Am Chem Soc* **127**:5104–5115.
81. Cantley Jr. LC, Resh MD, Guidotti G. 1978. Vanadate inhibits red cell (Na^+ , K^+) AT-Pase from cytoplasmic side. *Nature* **272**:552–554.
82. Yang XG, Wang K, Lu JF, Crans DC. 2003. Membrane transport of vanadium compounds and the interaction with the erythrocyte membrane. *Coord Chem Rev* **237**:103–111.

83. Yasui H, Takechi K, Sakurai H. 2000. Metallokinetic analysis of disposition of vanadyl complexes as insulin-mimetics in rats using BCM-ESR method. *J Inorg Biochem* **78**:185–196.
84. Yasui H, Tamura A, Takino T, Sakurai H. 2002. Structure-dependent, metallokinetics of antidiabetic vanadyl–picolinate complexes in rats: studies on solution structure, insulinomimetic activity, and metallokinetics. *J Inorg Biochem* **91**:327–338.
85. Yuen VG, Caravan P, Gelmini L, Glover N, McNeill JH, Setyawati IA, Zhou Y, Orvig C. 1997. Glucose-lowering properties of vanadium compounds: comparison of coordination complexes with maltol or kojic acid as ligands. *J Inorg Biochem* **68**:109–116.
86. Fugono J, Yasui H, Sakurai H. 2001. Pharmacokinetic study on gastrointestinal absorption of insulinomimetic vanadyl complexes in rats by ESR spectroscopy. *J Pharm Pharmacol* **53**:1247–1255.
87. Sakurai H, Fugono J, Yasui H. 2004. Pharmacokinetic study and trial for preparation of enteric-coated capsule containing insulinomimetic vanadyl compounds: implications for clinical use. *Mini Rev Med Chem* **4**:41–48.
88. Thompson KH, Liboiron BD, Sun Y, Bellman KDD, Setyawati IA, Patrick BO, Karunaratne V, Rawji G, Wheeler J, Sutton K, Bhanot S, Cassidy C, McNeill JH, Yuen VG, Orvig C. 2003. Preparation and characterization of vanadyl complexes with bidentate maltol-type ligands: in vivo comparisons of anti-diabetic therapeutic potential. *J Biol Inorg Chem* **8**:66–74.
89. Takechi K, Tamura H, Yamaoka K, Sakurai H. 1997. Pharmacokinetic analysis of free radicals by in vivo BCM (blood circulation monitoring) ESR method. *Free Rad Res* **26**:483–496.
90. Sakurai H, Takechi K, Tsuboi H, Yasui H. 1999. ESR characterization and metallokinetic analysis of Cr(V) in the blood of rats given carcinogen chromate(VI) compounds. *J Inorg Biochem* **76**:71–80.
91. Sakurai H, Yasui H, Adachi Y. 2003. The therapeutic potential of insulin-mimetic vanadium complexes. *Exp Op Invest Drugs* **12**:1189–1203.
92. Sakurai H, Shimomura S, Fukuzawa K, Ishizu K. 1980. Detection of oxovanadium(IV) and characterization of its ligand environment in subcellular fractions of the liver of rats treated with pentavalent vanadium(V). *Biochim Biophys Res Comm* **96**:293–298.
93. Chasteen ND, Thiel EC. 1982. Iron binding by horse spleen apoferritin: a vanadyl(IV) electron paramagnetic resonance spin probe study. *J Biol Chem* **257**:7672–7677.
94. Eaton SS, Dubach J, More KM, Eaton GR, Thurman G, Ambruso DR. 1989. Comparison of the electron spin echo envelope modulation (ESEEM) for human lactoferrin and transferrin complexes of copper(II) and vanadyl ion. *J Biol Chem* **264**:4776–4781.
95. Dikanov SA, Liboiron BD, Thompson KH, Vera E, Yuen VG, McNeill JH, Orvig C. 1999. In vivo electron spin-echo envelope modulation (ESEEM) spectroscopy: first observation of vanadyl coordination to phosphate in bone. *J Am Chem Soc* **121**:11004–11005.
96. Dikanov SA, Liboiron BD, Orvig C. 2002. Two-dimensional (2D) pulsed electron paramagnetic resonance study of VO²⁺-triphosphate interactions: evidence for tridentate triphosphate coordination, and relevance to bone uptake and insulin enhancement by vanadium pharmaceuticals. *J Am Chem Soc* **124**:2969–2978.
97. Dikanov SA, Samoilova RI, Smiejca JA, Bowman MK. 1995. 2-dimensional ESEEM study of VO²⁺ complexes with imidazole and histidine: histidine is a polydentate ligand. *J Am Chem Soc* **117**:10579–10580.

98. Sakurai H, Fujii K, Watanabe H, Tamura H. 1995. Orally active and long term acting insulin-mimetic vanadyl complex: bis(picolinato)oxovanadium(IV). *Biochem Biophys Res Commun* **214**:1095–1101.
99. Dikanov SA, Bowman MK. 1995. Cross-peak lineshape of 2-dimensional ESEEM spectra in disordered $S = 1/2$, $I = 1/2$ spin systems. *J Magn Reson Ser A* **116**:125–128.
100. Dikanov SA, Bowman MK. 1998. Determination of ligand conformation in reduced [2Fe–2S] ferredoxin from cysteine b-proton hyperfine couplings. *J Biol Inorg Chem* **3**:18–29.
101. Atherton NM, Shackleton JF. 1980. Proton ENDOR of $\text{VO}(\text{H}_2\text{O})_5^{2+}$ in $\text{Mg}(\text{NH}_4)_2(\text{SO}_4)_2 \cdot 6\text{H}_2\text{O}$. *Mol Phys* **39**:1471–1485.
102. Buy C, Matsui T, Andrianambintsoa S, Sigalat C, Girault G, Zimmerman J-L. 1996. Binding sites for Mg(II) in H^+ -ATPase from Bacillus PS3 and in the a_3b_3g subcomplex studied by one-dimensional ESEEM and two-dimensional HYSCORE spectroscopy of oxovanadium(IV) complexes: a possible role for b-His-324. *Biochemistry* **35**:14281–14293.
103. Mustafi D, Telser J, Makinen MW. 1992. Molecular geometry of vanadyl adenine nucleotide complexes determined by EPR, ENDOR and molecular modeling. *J Am Chem Soc* **114**:6219–6226.
104. Monga V, Thompson KH, Yuen VG, Sharma V, Patrick BO, McNeill JH, Orvig C. 2005. Vanadium complexes with mixed O,S anionic ligands derived from maltol: synthesis, characterization, and biological studies. *Inorg Chem* **44**:2678–2688.

CHROMIUM IN CANCER AND DIETARY SUPPLEMENTS

Aviva Levina, Rachel Codd and Peter A. Lay*

Centre for Heavy Metals Research and Centre for Structural Biology and Structural Chemistry, School of Chemistry, The University of Sydney, Sydney NSW 2006, Australia

For many years, the carcinogenicity of Cr(VI) and the antidiabetic effects of Cr(III) compounds were regarded as independent biological activities, but recent evidence suggests that both these types of activities arise from varying amounts of Cr(VI) and reactive intermediates, such as Cr(V) species, which can be formed *in vivo* either by reduction of Cr(VI) or by oxidation of Cr(III) complexes. Applications of EPR spectroscopy for the studies of Cr(V) and other reactive intermediates of relevance to the biological activities of Cr(VI) and Cr(III) compounds have been reviewed. Due to the d^1 electronic structure of Cr(V) complexes, EPR spectroscopy can be used as a highly sensitive and selective tool for the detection of Cr(V) intermediates formed in biological systems exposed to Cr(VI) (and potentially to Cr(III) complexes). Low-frequency (L-band) EPR spectroscopy can be used to detect weak Cr(V) signals in whole living plants or animals. Extensive model studies revealed correlations between the EPR spectroscopic parameters (such as the g_{iso} values and superhyperfine splitting patterns) and the structures of Cr(V) complexes. These correlations were used to identify the Cr(V) complexes with carbohydrate and glycoprotein ligands as the most abundant Cr(V) species formed in biological systems, while Cr(V) thiolato complexes are formed as transient intermediates during the reduction of Cr(VI) by biological thiols (such as glutathione). Applications of EPR spectroscopy for the characterization of biologically-relevant Cr(III) complexes (d^3 systems) are more limited due to the relatively low sensitivity and broadness of the signals. Several reports in the literature on the observation of Cr(IV) intermediates in biological systems by EPR spectroscopy are erroneous, since such species (d^2 sys-

Address all correspondence to Peter A. Lay, Centre for Heavy Metals Research and Centre for Structural Biology and Structural Chemistry, School of Chemistry, The University of Sydney, Sydney NSW 2006, Australia; phone 61-2-93514269, fax 61-2-93513329, email p.lay@chem.usyd.edu.au.

tems) are EPR silent under most conditions. Spin traps can be used to detect the formation of strong oxidant species during the reactions of Cr(VI) or Cr(III) compounds with biological media, but not to establish the nature of such species, since the same EPR-active products can be formed during the reactions of spin traps with either free radical species or reactive Cr intermediates.

1. ROLES OF REACTIVE INTERMEDIATES IN CHROMIUM(VI)-INDUCED TOXICITY AND IN ANTI-DIABETIC EFFECTS OF CHROMIUM(III)

Chromium is probably the most controversial of the transition metal ions in terms of its biological activities [1]. The highest oxidation state of this element, Cr(VI), is a well-established human carcinogen and one of the most commonly encountered occupational hazards [2]. Concerns over the exposure of the general population to Cr(VI)-contaminated water have been highlighted in the film "Erin Brockovich," although the extent of health damage caused by low Cr(VI) concentrations in drinking water is under debate [3]. On the contrary, the most stable oxidation state of chromium, Cr(III), is regarded by most nutritionists as an essential trace element for humans (involved in glucose metabolism) [4], although this opinion has been disputed [5,6]. Production of Cr(III)-containing nutritional supplements for humans and animals forms the basis of a multimillion dollar industry, despite the growing concern over the efficacy and safety of such supplements [1,7,8].

The chemical mechanisms of Cr(VI)-induced cytotoxicity and genotoxicity, based on the efficient cellular uptake of $[\text{CrO}_4]^{2-}$ and its reactions with cellular reductants (Fig. 1) [9], are generally well understood [1,10], although many biochemical details remain to be elucidated [11]. By contrast, the suggested role of Cr(III) in glucose metabolism is difficult to explain from the chemical point of view, given the kinetic inertness of Cr(III) complexes and their inability to enter cells at significant rates [1]. A mechanism based on the selective activation of insulin receptor tyrosine kinase by a specific Cr(III)-containing biomolecule, chromodulin, has been proposed [7,12], but this compound has not been fully characterized to date [13], and its reported isolation procedure is controversial [1]. An alternative mechanism of Cr(III)-induced activation of glucose metabolism, proposed by our group [10,14], is based on extra- and/or intracellular oxidation of Cr(III) to Cr(V) and Cr(VI) species. These species can then act as tyrosine phosphatase inhibitors, via similar mechanisms as V(IV) and V(V) compounds (isoelectronic to Cr(V) and Cr(VI), respectively), which are well-known insulin mimics and antidiabetic agents [15].

Figure 1 summarizes our current hypothesis on the main metabolic pathways of various oxidation states of Cr in mammalian cells (based on the data from [1,8, 10,16–18] and references therein). Chromate ion ($[\text{CrO}_4]^{2-}$) easily penetrates cell

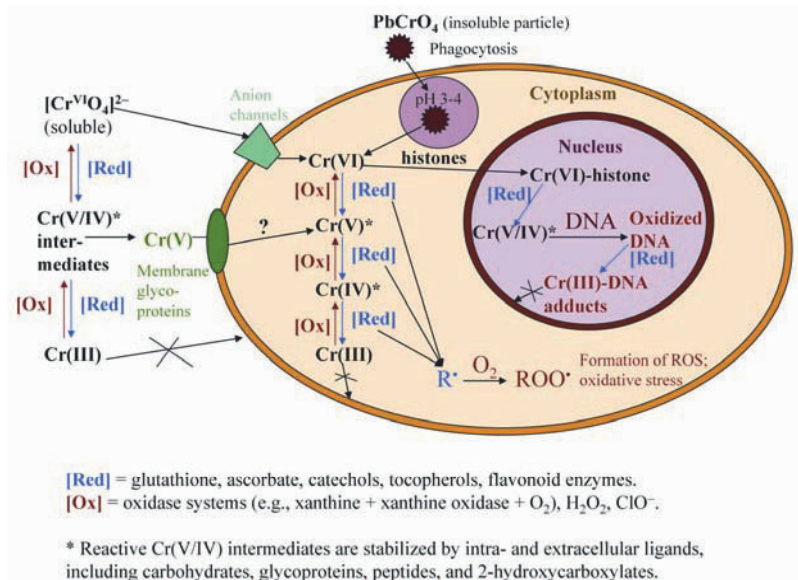


Figure 1. Main biotransformation pathways of Cr complexes (based on data from [1,8,10,16–18] and references therein).

membranes through anion channels, due to its structural similarity to $[\text{SO}_4]^{2-}$ and $[\text{HPO}_4]^{2-}$ ions, while insoluble chromates, such as PbCrO_4 , are likely to enter cells through phagocytosis. Inside the cell, Cr(VI) is reduced to Cr(III) by cellular reductants (listed in Fig. 1) with the formation of reactive Cr(V) and Cr(IV) intermediates. Such intermediates can be relatively long lived due to their stabilization by a variety of intracellular ligands (listed in Fig. 1; see §2 for details). Chromium(V) intermediates produced during the extracellular reduction of Cr(VI) are likely to bind to sialoglycoprotein residues on the cell surface (see §2.3), and can then be transported across the cell membrane [16]. Although Cr(III) is usually considered as a stable final product of Cr(VI) reduction in biological media, both extra- and intracellular re-oxidation of Cr(III) to Cr(VI) (through Cr(IV) and Cr(V) intermediates, Fig. 1) can occur under pathological conditions (e.g., inflammation or diabetes) involving chronic oxidative stress. Such re-oxidation is likely to be involved in the Cr(III)-induced enhancement of glucose metabolism in Type 2 diabetics (not observed in healthy individuals) [8].

Reactions of cellular reductants with Cr(VI), Cr(V), and Cr(IV) species produce organic radicals, which can then react with molecular oxygen, leading to increases in cellular levels of reactive oxygen species (ROS, Fig. 1) and to oxidative stress. However, the main results of Cr(VI) reduction to Cr(III) in the cytoplasm, or within the cell membrane, are likely to be the detoxification of Cr(VI) and the activation of certain cell-signaling pathways, including the insulin pathway that leads to enhancement of glucose metabolism [8,17]. The effects of Cr(VI) on cell signaling can be either direct (through the reactions of Cr(VI) and Cr(V) species with

cysteine residues of tyrosine phosphatases and other regulatory enzymes) [10,19] or indirect (through the formation of ROS) [20]. Higher concentrations of Cr(VI) or longer exposure times overwhelm the cellular protective mechanisms and lead to accumulation of significant amounts of Cr(III) within the cell nucleus [17]. Penetration of Cr into the nuclei of living cells is likely to involve the binding of $[\text{CrO}_4]^{2-}$ to newly synthesized histones and other nuclear proteins (rich in positively charged lysine and arginine residues) in the cytoplasm, followed by the selective transport of Cr(VI)–protein complexes to the nucleus [18]. This event is followed by Cr(VI) dissociation from the proteins (due to the high affinity of nuclear proteins to DNA) and its reduction to Cr(III) in the vicinity of DNA [18], which is likely to lead to Cr(III)–DNA adducts, including DNA–Cr(III)–protein and DNA–Cr(III)–DNA crosslinks. The formation of such adducts, which are highly stable due to the kinetic inertness of Cr(III), is believed to be the main cause of Cr(VI)-induced cytotoxicity and genotoxicity [1,11]. Thus, both toxic (e.g., formation of Cr(III)–DNA adducts) and beneficial (e.g., enhancement of insulin signaling) effects of Cr compounds are likely to arise from varying amounts of Cr(VI) and highly reactive intermediates such as Cr(V/IV) species and organic radicals.

The importance of EPR spectroscopy in the development of Cr bioinorganic chemistry is based on the sensitive detection and speciation of Cr(V) and radical intermediates and (to a lesser extent) Cr(III) products, which are formed in biological and biomimetic systems exposed to Cr compounds. While the technique is very powerful in these studies, it is not without its controversies, such as its purported use for the “detection” of Cr(IV) intermediates and hydroxyl ($\bullet\text{OH}$) radicals in biological systems (see §§3 and 4) [1]. The strength and limitations of EPR spectroscopy in relation to various Cr-derived reactive intermediates are discussed in detail in the following sections.

2. CHROMIUM(V) INTERMEDIATES

2.1. Isolation and Characterization of Chromium(V) Complexes with Biological and Biomimetic Ligands

Due to the d^1 electronic structure of the Cr(V) ion, EPR spectroscopy provides a powerful tool for the selective detection, characterization and speciation of reactive Cr(V) intermediates formed during the reduction of Cr(VI) or oxidation of Cr(III) in a variety of processes. Typical examples include: (i) photocatalytic reduction of Cr(VI) (used in waste water treatment) [21]; (ii) Cr(VI)-based wood fixation [22]; (iii) formation of holographic images in Cr(VI)-treated polyvinyl alcohol films [23]; and (iv) asymmetric epoxidation using chiral Cr(III) complexes as catalysts [24]. However, most attention has been devoted to the studies of Cr(V) formation in Cr(VI)-exposed biological systems, and to the isolation and characterization of biologically relevant Cr(V) complexes [1,25]. Since Cr(V) is a highly reactive oxidation state, it is generally difficult to grow crystals of Cr(V) compounds, suitable for x-ray crystallography. Among ~30 such compounds that have

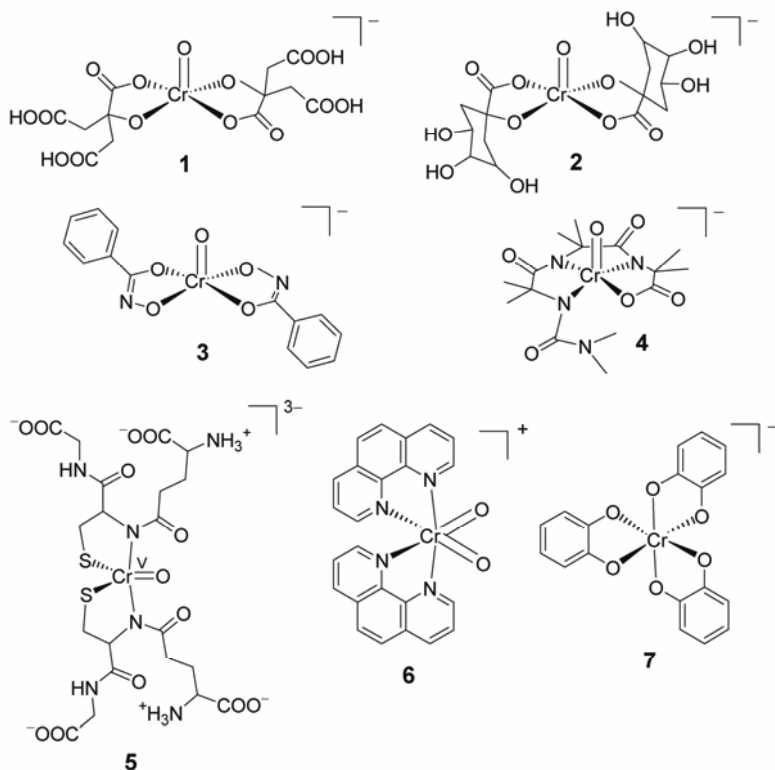


Chart 1. Typical Cr(V) complexes with biological and biomimetic ligands: citric acid (**1**) [27]; quinic acid (**2**) [28]; benzo-hydroxamic acid (**3**) [29]; DMF–Aib–Aib–Aib (**4**; where DMF = *N,N*-dimethylformamide and Aib = 2-amino-2-methylpropanoic acid) [30]; glutathione (**5**) [31]; 1,10-phenanthroline (**6**) [32]; and catechol (**7**) [33,34].

been crystallographically characterized, none possess biological ligands [26]. We have applied a combination of x-ray absorption and EPR spectroscopies, electrospray mass spectrometry, and analytical techniques for the structural characterization of reactive Cr(V) complexes with biological and biomimetic ligands [1]. These complexes can either be rapidly isolated as microcrystalline solids, or generated quantitatively in solutions (followed by snap-freezing for structural studies). Representative structures of such complexes (**1–7**) are shown in Chart 1, and their typical EPR spectra (in solutions, 295 K) are shown in Figure 2 [27–33]. The ligands used include biological 2-hydroxycarboxylates (citrate for **1** and quinate or (1*R*,3*R*,4*R*,5*R*)-1,3,4,5-tetrahydroxycyclohexanecarboxylate for **2**) [27,28], benzo-hydroxamate (a model of siderophores) for **3** [29], a synthetic tripeptide (based on 2-amino-2-methylpropionic acid) for **4** [30], a natural tripeptide (glutathione or γ -glutamyl-cysteinyl-glycine) for **5** [31], 1,10-phenanthroline (a model of biological

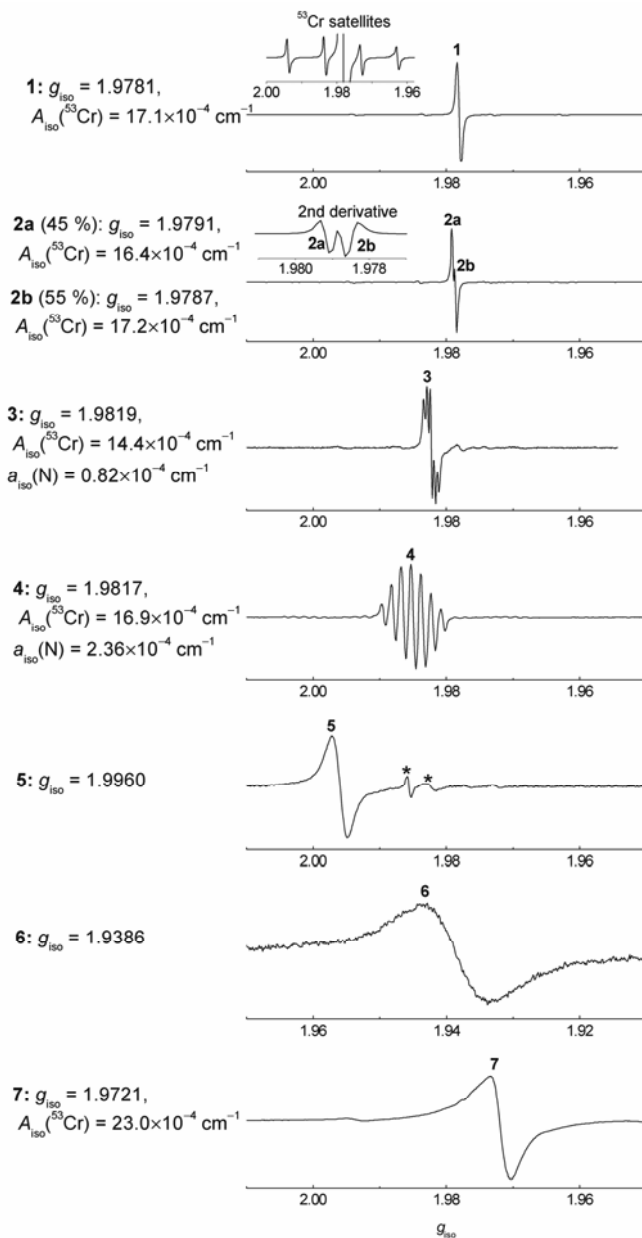


Figure 2. Typical X-band EPR spectra and main spectral parameters of Cr(V) complexes shown in Chart 1 (solutions, $[\text{Cr}] = 10 \text{ mM}$, 295 K) [27–33]. Solvents: H_2O for **1**, **2** and **5**; and DMF for **3**, **4**, **6** and **7**. The spectrum of **7** was recorded in the presence of excess free ligand (20 mM) [33]. Minor signals in the spectrum of **5** (designated by asterisks) are due to hydrolysis of the parent complex [31].

mine ligands such as nucleic bases) for **6** [32], and catechol (a model of catecholato moieties in siderophores and catecholamines) for **7** [33]. In agreement with a common trend for Cr(V) complexes [26], most of the species shown in Chart 1 (**1–5**) are five-coordinate, with one oxo group and the geometry ranging from trigonal bipyramidal to square planar [27–31]. Some exceptions from this rule are a bis-oxo, bis-1,10-phenanthroline Cr(V) complex **6** [32] and an octahedral tris-catecholato Cr(V) complex (**7**, with strong electron density delocalization between the metal ion and the ligands) [33,34]. The high affinity of Cr(V) for deprotonated oxygen-donor ligands (e.g., carboxylato or alcoholato) is illustrated by **1–3** and **7**, but nitrogen (imine or deprotonated amido, **4–6**) and sulfur (thiolato, **5**) donor groups are also represented. Dimeric Cr(V) complexes are EPR silent at ambient conditions due to the spin interactions between the two unpaired electrons [35,37], but such dimers are unlikely to form in biological systems due to the low steady-state concentrations of Cr(V) species [10]. Relations between the structures of Cr(V) complexes (Chart 1) and their EPR spectroscopic parameters (Fig. 2) are discussed in detail in Sections 2.2 and 2.3.

2.2. Application of EPR Spectroscopic Parameters to the Structural Characterization of Chromium(V) Complexes

Several reviews on the subject on this section have been published previously [1,25,36,38]. A typical X-band EPR spectrum of a Cr(V) complex (in solution under ambient conditions) is centered at $g_{\text{iso}} \approx 1.98$, and exhibits an intense narrow line (linewidth $(1–5) \times 10^{-4} \text{ cm}^{-1}$) due to the ^{52}Cr ($n = 50, 52, 54; I = 0$) isotopes, with the appearance of a quartet of hyperfine satellites ($A_{\text{iso}} \approx (16–18) \times 10^{-4} \text{ cm}^{-1}$) due to the ^{53}Cr isotope (natural abundance 9.55%, $I = 3/2$) [25], as shown in the inset for **1** in Figure 2. The isotropic g tensor (g_{iso}) is the most useful EPR spectroscopic parameter for the characterization of Cr(V) complexes, due to its high sensitivity to the nature of the ligands [36,38]. Generally, the g_{iso} values of Cr(V) complexes increase with increasing Lewis basicity of the donor groups (as illustrated in Chart 1 and Fig. 2) [36,38], in agreement with the following empirical correlation:

$$g_{\text{iso}} = 2.0023 - \Sigma \Delta g_{\text{iso}}, \quad (1)$$

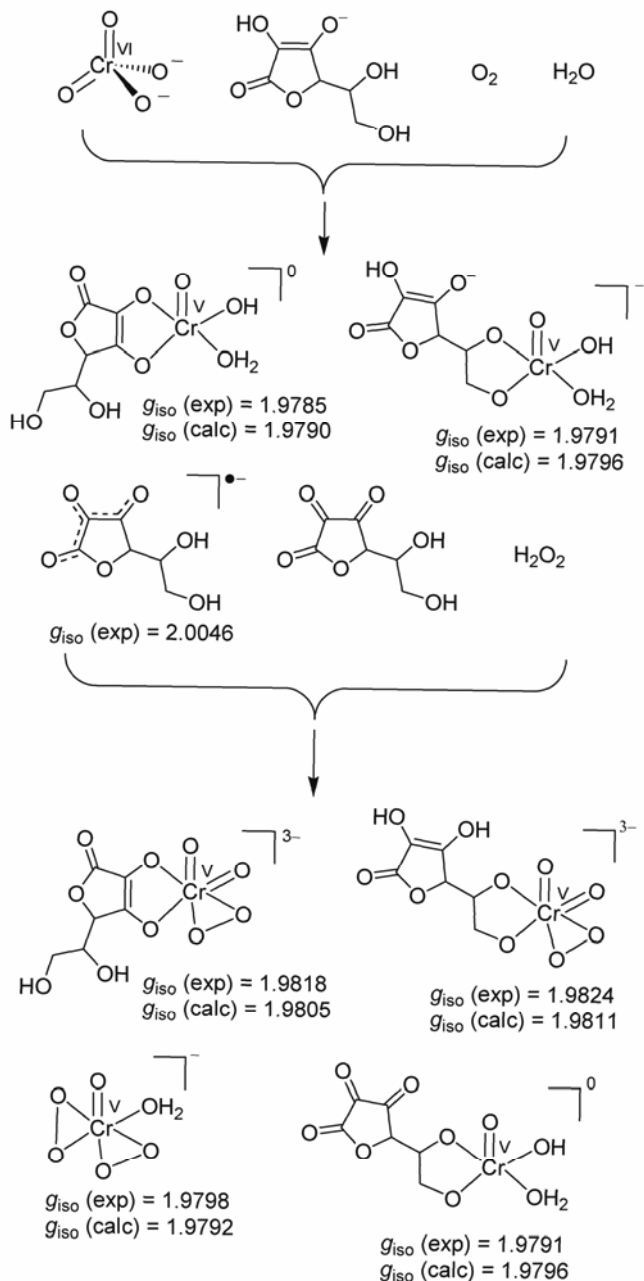
where 2.0023 is the g_{iso} value of a free electron and Δg_{iso} is a spin-orbit-induced g -shift for each donor group (Table 1) [1,26]. Application of Eq. (1) to the prediction of structures of Cr(V) complexes, formed in biological and biomimetic systems, is illustrated by EPR spectroscopic studies of Cr(VI) reduction by ascorbic acid or its derivatives in aerated aqueous solutions (Scheme 1) [1,39]. A direct correlation between the intensity of Cr(V) EPR signals and the extent of DNA damage by the Cr(VI) + ascorbate system was observed [39,40]. Similar studies were performed for the reactions of Cr(VI) with dehydroascorbic acid [41], glutathione, and other thiols [10,42,43], or catechols and catecholamines [44,45], as well as for the oxidation of Cr(III)-peptide complexes to their Cr(V) analogs under biologically relevant conditions [46]. A common method for the studies of speciation in such sys-

tems involves EPR spectroscopic measurements in solutions at varied concentrations of reagents and the pH values [31,39,42,44,46]. The PEST WinSim software [47] provides a convenient tool for the simulation and quantification of EPR spectra of solutions containing up to ten different Cr(V) species (including those possessing ^1H and ^{14}N superhyperfine coupling). Studies on frozen solutions are of limited value in structural assignments of biologically relevant Cr(V) complexes, since most exist as sets of geometric and linkage isomers that give overlapping isotropic signals and for which it is difficult to deconvolute the \mathbf{g} and \mathbf{A} tensors [1,16].

Table 1. Isotropic EPR Δg_{iso} Parameters [Eq. (1)] for Different Donor Groups in Cr(V) Complexes ([26] and references therein)

Donor group	Δg_{iso}	Donor group	Δg_{iso}
R ₃ P	-0.00625	RO ⁻	0.00505
R ₂ S	-0.00083	OH ⁻	0.00505
N ³⁻	0.00000	RCO ₂ ⁻	0.00593
RNCOR ⁻	0.00030	H ₂ O	0.00604
RS ⁻	0.00035	RN ²⁻	0.00630
Cl ⁻	0.00175	RNH ₂	0.00667
O ²⁻	0.00210	R ₂ C=NR	0.00730
R ₂ O	0.00270	O ₂ ²⁻	0.00750
RO ⁻ (enediol)	0.00475		

As shown in Scheme 1, small deviations between calculated and observed g_{iso} values for Cr(V) complexes often occur, due to the steric, electronic, and/or solvent effects that modify the donor properties of the ligands [1]. The influence of steric effects is illustrated by EPR spectroscopic signatures of geometric isomerism in Cr(V) 2-hydroxycarboxylato complexes (Chart 1 and Fig. 2). A Cr(V)-quinato complex **2**, possessing bulky ligands, shows a clear splitting of the main Cr(V) signal due to the presence of two distinct geometric isomers (even more obvious in the second-derivative spectra, see the inset for **2** in Fig. 2) [28,48]. For Cr(V) complexes with more flexible ligands, such as citrate (**1**) [27] or 2-ethyl-2-hydroxybutanoate ($[\text{Cr}^{\text{V}}\text{O}(\text{ehba})_2]^-$) [36,49], only a weak splitting of the outer signals due to the ^{53}Cr satellites is observed (as shown in the inset for **1** in Fig. 2). An example of electronic effects is the decrease in g_{iso} values of Cr(V)-carbohydrate complexes compared with those of model cyclic 1,2-diols, due to the electron-withdrawing effect of the endocyclic oxygen atom in carbohydrates (see also §2.3) [50]. Finally, solvent dependencies of the g_{iso} values (caused by changes in the donor strengths of Cr-ligand bonds due to the variations in hydrogen-bonding properties of the solvents) were demonstrated for Cr(V) 2-hydroxycarboxylato complexes



Scheme 1. Proposed structures of Cr(V) intermediates formed during the reduction of Cr(VI) with ascorbate in neutral aerated aqueous solutions) based on the results of EPR spectroscopic studies [39].

[28,49]. However, the combined electronic, steric, and solvent effects usually cause only small perturbations in the g_{iso} values given by Eq. (1), and as long as they are recognized, this equation holds very well for a large range of mixed-ligand complexes (e.g., those in Scheme 1) [1].

The hyperfine coupling constants (A_{iso}) due to the ^{53}Cr isotopes also provide useful information on the structures of Cr(V) species. The most prominent effect is the increase in the A_{iso} values by $(2-9) \times 10^{-4} \text{ cm}^{-1}$ for six-coordinate versus five-coordinate Cr(V) complexes with O/N donors (see the A_{iso} value for **7** vs. those for **1-4** in Fig. 2) [1,38]. In contrast to the g_{iso} values, the A_{iso} values show only weak correlations with the nature of donor atoms in Cr(V) complexes [36,38], but they are highly sensitive to the coordination geometry. The latter point is illustrated by a significant difference in the A_{iso} (but not in the g_{iso}) values for two related 2-hydroxycarboxylato complexes, $[\text{Cr}^{\text{V}}\text{O}(\text{ehba})_2]^-$ and $[\text{Cr}^{\text{V}}\text{O}(\text{hmba})_2]^-$ (hmba = 2-methyl-2-hydroxybutanoato(2-)) [49]. The A_{iso} values can also be used in the assignment of structures of Cr(V) complexes from those of well-characterized isoelectronic V(IV) complexes, since a linear correlation between the A_{iso} values of Cr(V) and V(IV) complexes of the same structure has been established [38]. A major limitation in the application of A_{iso} values to the structural characterization of Cr(V) complexes, formed in biological systems, is the low abundance of the ^{53}Cr isotope, which in many cases makes the ^{53}Cr satellite signals undetectable without enriching the sample in the ^{53}Cr isotope [31,39,44].

Where observed, superhyperfine coupling involving ligand atoms is a very valuable tool in the determination of structures of biologically-relevant Cr(V) complexes. The superhyperfine coupling due to ^{14}N in nitrogen-donor ligands ($I = 1$, typical $a_{\text{iso}} = (2-3) \times 10^{-4} \text{ cm}^{-1}$) has been particularly useful in determining the number of amide donors in Cr(V) complexes with peptide and macrocyclic ligands [30,51-53], as illustrated for complex **4** in Chart 1 and Figure 2. Notably, superhyperfine splitting was also observed for the N atoms in the second coordination shell of Cr(V)-hydroxamato complexes, such as **3** in Chart 1 and Figure 2, although the a_{iso} values were lower than for N-donor ligands [29]. On the other hand, nitrogen superhyperfine splitting is usually not resolved at X-band frequencies for the Cr(V) complexes with amine or imine ligands, as well as when both amido and thiolato ligands are present. In the both cases, relatively broad EPR signals are observed (**5** and **6** in Chart 1 and Figure 2) [31,32,53]. The analysis of superhyperfine coupling due to ^1H ($I = 1/2$, $a_{\text{iso}} = (0.5-1.0) \times 10^{-4} \text{ cm}^{-1}$) has been crucial in the assignment of structures of biologically important Cr(V) complexes with carbohydrates and their derivatives, as described in detail in Section 2.3.

For complex mixtures of Cr(V) species that are usually obtained in the Cr(VI) reactions with biological reductants, application of multifrequency EPR spectroscopy helps in the determination of the number of Cr(V) species formed. High-frequency (Q-band, 34-35 GHz) measurements were used to address the complexity of EPR signals formed in the Cr(VI) + D-glucose + glutathione systems [38,50]. Q-band EPR spectroscopy provides a higher resolution compared with the conventional X-band (9-10 GHz) measurements, but this is achieved at the expense of

lower sensitivity, such that the concentrations of reagents required to observe Cr(V) signals at Q-band frequencies have to be higher than those that are biologically relevant [38,50]. On the other hand, low-frequency (S- and L-band, ~4 and ~1 GHz, respectively) EPR spectroscopy provides the extra sensitivity (on account of the lower resolution) that is particularly useful for detection of weak Cr(V) signals formed in living cells treated with low concentrations of Cr(VI) (§5). Unless stated otherwise, all the results presented in the following sections were obtained using X-band EPR spectroscopy.

2.3. Chromium(V) Complexes of Carbohydrates and Their Derivatives

Stabilization of Cr(V) by biological 1,2-diolato ligands, including carbohydrates and glycoproteins, is thought to be crucial for the biological activities of both Cr(VI) and Cr(III) compounds [8,10,16]. The predominant binding of Cr(V) to carbohydrate-type ligands has been demonstrated in many EPR-spectroscopic studies of living cells and tissues, treated with Cr(VI) (§5). In addition, a likely formation of Cr(V)–carbohydrate complexes during the oxidation of Cr(III) species by adipocytes (fat-storage cells) has been recently suggested on the basis of microprobe XANES (x-ray absorption near-edge structure) spectroscopy [54]. Although the formation of Cr(V)–carbohydrate complexes can be observed by EPR spectroscopy during the reduction of Cr(VI) by carbohydrates in acidic aqueous solutions (pH ≤ 5) [55–58], a more biologically relevant way of generating such complexes involves the reactions of Cr(VI) with biological reductants (such as glutathione) in neutral aqueous solutions in the presence of an excess of a carbohydrate ligand [38,50,59]. In the case of the reaction with glutathione, a transient Cr(V)–glutathione complex ($g_{\text{iso}} = 1.9858$) is initially formed and then gradually replaced (within minutes at 295 K) with thermodynamically more stable Cr(V)–carbohydrate species ($g_{\text{iso}} \sim 1.9800$) [50]. A general structure of such complexes, $[\text{Cr}^{\text{V}}\text{OL}_2]^-$ (where L^{2-} is the doubly-deprotonated carbohydrate ligand) has been postulated on the basis of EPR spectroscopic studies [38,50] and recently confirmed by electrospray mass spectrometry [60].

The EPR spectroscopic signatures of various types of 1,2-diolato ligands have been established in studies of Cr(V) complexes with model diols [25,48,50,61]. All such complexes possess similar g_{iso} values (~1.9800), but are distinguished by their ^1H superhyperfine coupling patterns (Fig. 3), which arise from the interactions of the protons in the second coordination shell of the ligands with the Cr(V) d_{xy} orbital, containing the unpaired electron density [16,25]. Open-chain 1,2-diolato moieties (such as those present in sialoglycoproteins) [62,63] provide sufficient rotational flexibility of the chelate ring to make all the six protons (three from each ligand) magnetically equivalent on the timescale of X-band EPR measurements, resulting in a septet in the EPR spectrum (Fig. 3a) [16]. For the cyclic ligands like hexoses or their models (*cis*- or *trans*-1,2-cyclohexanediols, Fig. 3b,c), the strain of the ring system imparts inequivalence to the magnetic environments of the protons

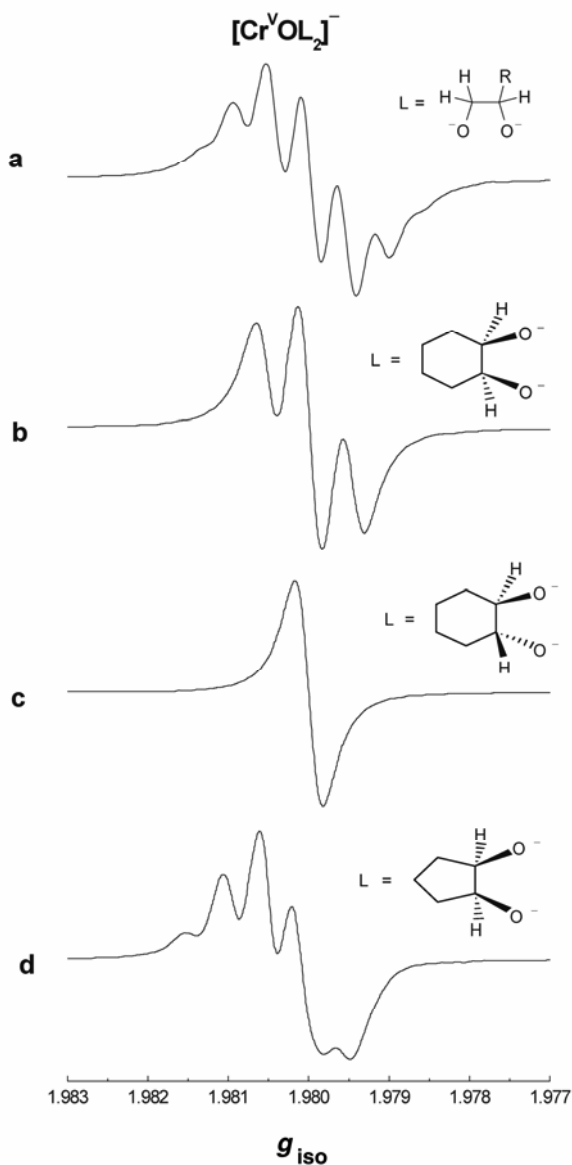


Figure 3. EPR spectroscopic signatures of Cr(V) complexes with various model 1,2-diolato ligands: **(a)** open-chain diols [16,50,63]; **(b,c)** *cis*- and *trans*-1,2-cyclohexanediols [16,50]; and **(d)** *cis*-1,2-cyclopentanediol [61]. A general structure for the complexes is $[\text{Cr}^{\text{V}}\text{OL}_2]^-$, and structures of the ligands are shown in the insets. The complexes were generated in neutral (pH \sim 7) aqueous solutions by the reactions of $[\text{CrO}_4]^{2-}$ (0.50–250 mM) with glutathione (0.50–12.5 mM, used as a reductant) and a large excess of the diol (0.10–5.0 M) at 295 K (reaction time 5–30 min) [16,50,61,63].

in the second coordination sphere, as illustrated in Figure 4 [25,50]. For the Cr(V) complex with *cis*-1,2-cyclohexanediol, two protons (one of each chelate ring) are lying in the Cr(V)-ligand plane, which gives rise to a triplet in the EPR spectrum (Fig. 3b and the associated structure, Fig. 4) [25,50]. In the case of the Cr(V) *trans*-1,2-cyclohexanediolato complex, no protons lie in the Cr(V)-ligand plane, which leads to a singlet in the EPR spectrum (Figs. 3c and 4) [25,50]. Steric considerations also make the complexation of Cr(V) with *trans*-1,2-diols much less efficient than with *cis*-1,2-diols [48,50].

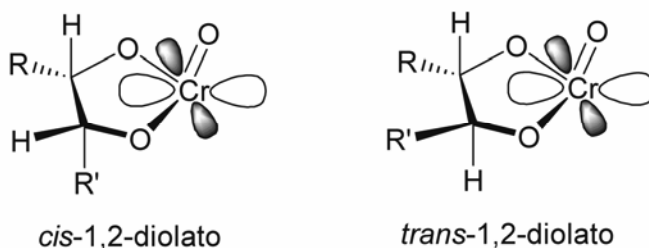


Figure 4. Orbital overlap between a Cr(V) ion and cyclically strained diolato ligands oriented in a *cis*- or *trans*-fashion. Adapted with permission from [25]. Copyright © 2001, Elsevier.

The Cr(V) complex with *cis*-1,2-cyclopentenediol (a model of D-ribose and ribonucleotides) shows a superhyperfine coupling pattern that resembles a mixture of open-chain and cyclically strained diols (Fig. 3d) [61]. This pattern has been interpreted as that arising from two geometric isomers of the Cr(V) complex, with a total of seven inequivalent protons interacting with the d_{xy} orbital of Cr(V) [61,64]. Thus, the cyclopentane ring provides a greater rotational flexibility of the 1,2-diolato moiety compared with the cyclohexane ring. Interestingly, the EPR signal of the Cr(V) complex with *trans*-1,2-cyclopentenediol was apparently the same as that for *cis*-1,2-cyclopentenediol (although it was observed at much higher concentrations of the ligand) [61], which suggests that this signal may be due to a trace of the *cis*-diol present in the sample. The EPR signals of Cr(V) complexes with ribonucleotides closely resembled that for the complex with *cis*-1,2-cyclopentenediol, suggesting that Cr(V) binds exclusively to the *cis*-1,2-diolato moieties of ribonucleotides [64] or RNA [65]. Chromium(V) species formed during the reduction of Cr(VI) by NAD(P)H-dependent enzymes (NAD(P)H are the reduced forms of nicotinamide adenine dinucleotide), such as glutathione reductase [66,67], cytochrome b_5 [68], or nitric oxide synthase [69] are also likely to bind to the *cis*-1,2-diolato moieties of the ribose residues of NAD(P)H.

Typical Cr(V)-binding biomolecules contain several potential coordination modes for the metal ion, as shown in Figure 5. The spectrum of the Cr(V) complex

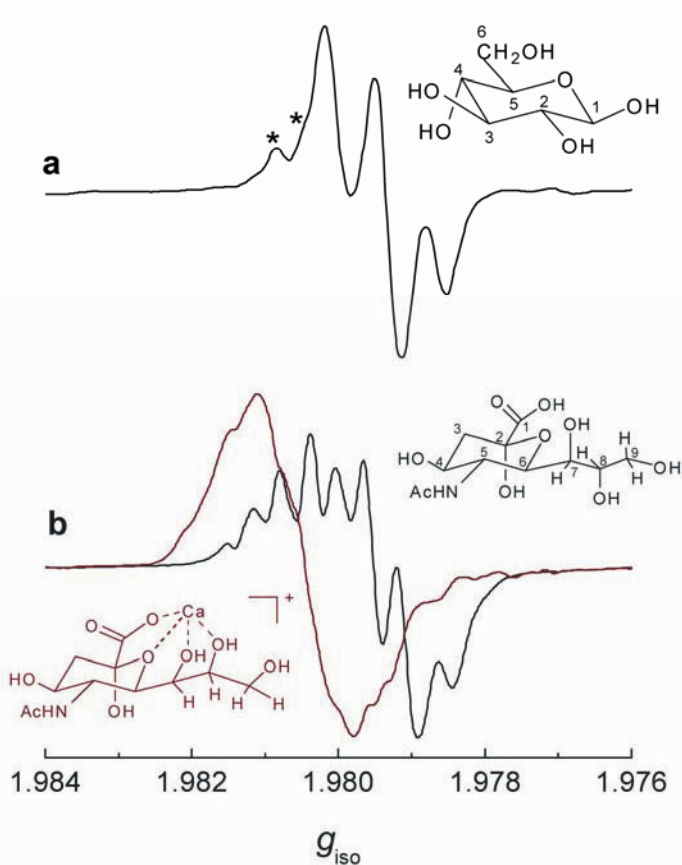


Figure 5. Typical EPR spectra of Cr(V) complexes with biological 1,2-diolato ligands: (a) D-glucose [50] and (b) *N*-acetylneuraminic (sialic) acid in the absence (black line) or presence (red line) of Ca(II) [63,70]. A general structure of the complexes is $[\text{Cr}^{\text{V}}\text{OL}_2]^-$, and structures of the protonated ligands are shown in the insets. Reaction conditions for (a): $[\text{Cr}(\text{VI})] = 0.25 \text{ M}$; $[\text{glutathione}] = 12.5 \text{ mM}$; $[\text{ligand}] = 0.50 \text{ M}$; $\text{pH} = 8.10$ (adjusted with NaOH); reaction time 74 min at 292 K [50]. Reaction conditions for (b): $[\text{Cr}(\text{VI})] = 40 \text{ mM}$; $[\text{glutathione}] = 2.0 \text{ mM}$; $[\text{ligand}] = 0.10 \text{ M}$; $[\text{Ca}(\text{II})] = 1.0 \text{ M}$; $\text{pH} = 7.14$ (adjusted with NaOH), reaction time 3–5 min at 295 K [63,70].

with D-glucose in neutral aqueous solutions is dominated by a triplet due to the only pair of *cis*-OH groups in the 1- and 2-positions of the α -anomer of the ligand (Fig. 5a) [38,50]. Additional signals (designated with asterisks in Fig. 5a) due to linkage isomers with *trans*-diolato and triolato binding moieties become apparent at higher pH values and longer reaction times [38,50]. Sialic (*N*-acetylneuraminic) acid and its derivatives, which play a crucial role in the cell-surface signaling and chemosensing, represent a combination of open-chain 1,2-diolato and 2-hydroxycarboxylato binding motifs, both of which are efficient stabilizers of Cr(V)

(Fig. 5b) [62,63]. The EPR signals of Cr(V) sialato complexes are strongly pH dependent, with the 2-hydroxycarboxylato and 1,2-diolato binding modes being dominant at $\text{pH} < 4$ and $\text{pH} > 8$, respectively [63]. A complicated coupling pattern due to comparable contributions from both binding modes at $\text{pH} \sim 7$ is illustrated in Figure 5b (black line). The EPR spectra of Cr(V) sialato complexes are strongly affected by the presence of excess Ca(II) ion, which is known to bind to sialic acid and its derivatives in biological systems (red line in Fig. 5b) [70]. This competitive Cr(V) binding can potentially be used in the studies of biologically important binding of Ca(II) and Mg(II) ions to sialoglycoproteins and related ligands (termed “metalloglycomics”) [70].

In summary, EPR spectroscopy provides unique insights into the structures of biologically important Cr(V) carbohydrate complexes, but the initial concentrations of Cr(VI) and the carbohydrate ligand, required to observe Cr(V) complexes with clearly resolved superhyperfine coupling patterns, are usually at least an order of magnitude higher than those expected for biological systems (see the captions of Figs. 3 and 5).

3. CHROMIUM(III) AND CHROMIUM(IV) SPECIES

The EPR signals due to Cr(III) (a d^3 ion) are typically very broad and hard to observe in solutions (particularly in water) under ambient conditions, so either solids or frozen solutions are usually used. The resultant anisotropic EPR spectra require extensive computer simulations for the determination of the $g_{x,y,z}$ values and zero-field splitting parameters (D and E). Detailed theoretical descriptions of such spectra have been reported [71–75].

Typical calculated X-band spectra of Cr(III) complexes [76] are shown in Figure 6. A broad isotropic signal with $g \sim 2$ is obtained by assuming that $g_x = g_y = g_z$ and $D = E = 0$ (Fig. 6a), which corresponds to an ideal octahedral geometry of the complex. In practice, EPR spectra close to those in Figure 6a are observed for Cr(III) complexes with six equivalent monodentate ligands (such as $[\text{Cr}(\text{OH}_2)_6]^{3+}$) [76,77]. Distortions from octahedral geometry lead to anisotropy in the g values and to increases in the D and E values, which is manifested in the appearance of a strong positive absorption at $g_{\text{eff}} \sim 4.3$, in addition to a weaker signal at $g_{\text{eff}} \sim 2$ [76]. An increase in the relative intensity of the low-field ($g_{\text{eff}} \sim 4$ –5) signal is likely to indicate a greater distortion from the octahedral structure [74,76] and is due to intra-doublet transitions when $h\nu \gg D$ [72,73].

Some applications of EPR spectroscopy to the studies of Cr(III) coordination environments in the presence of biological or abiological ligands are illustrated in Figure 7. Molecular sieves (APO-5), doped with Cr(III), show a large isotropic and a smaller anisotropic EPR signals, due to two different types of Cr(III) coordination (Fig. 7a) [76]. A complex of Cr(III) with iminodiacetate ($[\text{Cr}(\text{ida})_2]^-$, where $\text{ida} = \text{NH}(\text{CH}_2\text{COO}^-)_2$), in frozen aqueous solution shows a predominantly anisotropic EPR signal (Fig. 7b), probably due to a significant distortion from octahedral

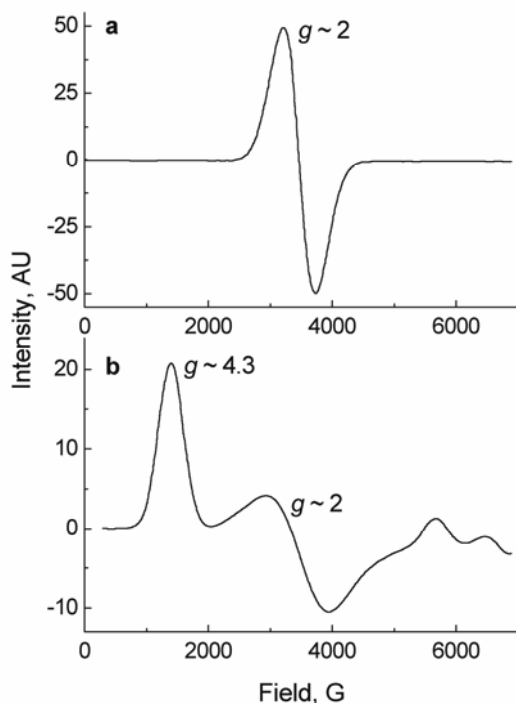


Figure 6. Typical calculated X-band EPR spectra of Cr(III) complexes: (a) an octahedral, isotropically substituted Cr(III) complex ($g_{xx} = g_{yy} = g_{zz} = 1.987$; $D = E = 0.000 \text{ cm}^{-1}$); and (b) a strongly distorted octahedral Cr(III) complex ($g_{xx} = 1.987$; $g_{yy} = g_{zz} = 1.865$; $D = 0.490 \text{ cm}^{-1}$; $E = 0.163 \text{ cm}^{-1}$) [76]. Published spectra were digitized with permission using the WinDIG software [119].

symmetry imposed by a chelating ligand [74]. Similar but much broader spectral features (Fig. 7c) were observed in a solid-state spectrum of Cr(III)–glutathione complexes (probably a mixture of several Cr(III) species, isolated from the reaction of Cr(VI) with excess glutathione) [31]. A frozen solution of Cr(III) complex with transferrin (a 80-kDa protein believed to be the main carrier of Cr(III) in human blood) [1] shows a remarkably similar EPR spectrum to that of $[\text{Cr}(\text{ida})_2]^-$ (Figs. 7d and 7b) [78]. This similarity points to amine and carboxylato groups of transferrin as the most likely binding ligands for Cr(III). The spectra of $[\text{Cr}(\text{ida})_2]^-$ and Cr(III)–transferrin complexes were also similar to those of low-symmetry Co(II) sites in carboxypeptidase A [79]. Kinetics of formation of a Cr(III)–transferrin complex could also be followed by EPR spectroscopy from a gradual replacement of a broad isotropic EPR signal ($g \sim 1.98$, attributed to $[\text{Cr}(\text{OH})_2]^{3+}$ or a similar loosely bound complex) with an anisotropic signal (shown in Fig. 7d) due to a Cr(III)–

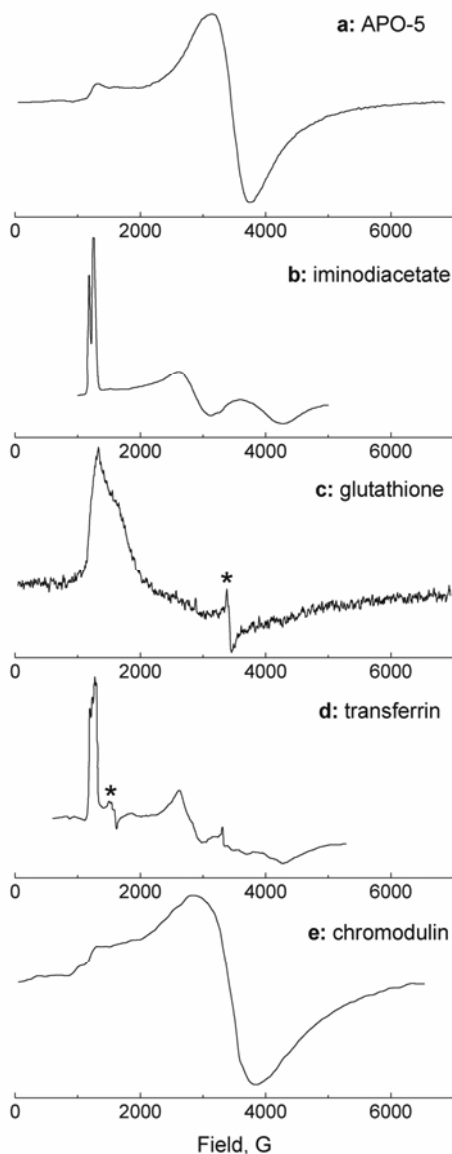


Figure 7. Typical experimental X-band (9.2–9.7 GHz) EPR spectra of Cr(III) complexes with abiological or biological ligands: **(a)** Cr(III) doped into APO-5 molecular sieves, solid, 300 K [76]; **(b)** a frozen solution of $K[Cr(ida)_2]$ (where ida = iminodiacetate) in $H_2O:MeOH:DMF = 1:8:1$, 150 K [74]; **(c)** a solid isolated from the reaction of Cr(VI) (0.10 M) with glutathione (1.0 M) at pH = 7.0, 295 K (a signal designated with an asterisk is due to a trace of Cr(V)) [31]; **(d)** a frozen solution of a Cr(III)–transferrin complex (1.75 mM) at pH = 7.5 and 77 K (a signal designated with an asterisk is due to a trace of Fe(III)) [78]; and **(e)** a frozen solution of chromodulin (a proposed natural Cr(III)-containing oligopeptide; 13.8 mM; in H_2O) at 4.7 K [13]. Published spectra were digitized with permission using the WinDIG software [119].

transferrin complex [78]. The intense low-field ($g_{\text{eff}} \sim 5$, Fig. 7d) EPR signal of this complex was also used to follow the displacement of Cr(III) from the coordination sphere of transferrin with Co(II) or Fe(III) [78]. Finally, the low-temperature (4.2 K) EPR spectrum of chromodulin (a proposed natural Cr(III)-containing oligopeptide) in frozen aqueous solutions (Fig. 7e) [13] is reminiscent of that of Cr(III) adsorbed on molecular sieves (Fig. 7a) [76]. Temperature-dependent EPR spectroscopic studies have shown that the dominant broad signal at $g_{\text{eff}} \sim 2$ and a smaller feature at $g_{\text{eff}} \sim 5$ in the EPR spectrum of chromodulin are due to Cr(III) ions in different magnetic environments, assigned as trinuclear and mononuclear Cr(III) sites, respectively [13].

In summary, only a few EPR spectroscopic studies of Cr(III) complexes with biomolecules have been reported to date [13,78], with the most comprehensive one being published as far back as in 1969 [78]. In addition, Cr(III) complexes with small ligands (usually oxalate) were used as paramagnetic labels in structural studies of proteins and lipids by EPR spectroscopy [80,81]. Given the importance of DNA–Cr(III)–DNA and protein–Cr(III)–DNA crosslinks for Cr(VI)-induced cytotoxicity and genotoxicity (§1) [11], EPR spectroscopy can potentially be applied to the studies of kinetics and mechanisms of the formation of such crosslinks. This method has been previously used in the studies of Cr(III)-induced crosslinking in a non-biological macromolecule (polyacrylamide) used in the petroleum industry [82]. Another potential application of EPR spectroscopy is to follow the changes in the coordination environments of Cr(III) nutritional supplements (such as picolinate or trinuclear propionate) [7,12] in biological media, although quantitative analysis of the EPR spectra produced by mixtures of Cr(III) species is very difficult [74]. A major limitation in the application of EPR spectroscopy to bioinorganic chemistry of Cr(III) is the need to use relatively high (typically 5–10 mM) concentrations of the metal ion [13,78].

Chromium(IV) is a highly reactive oxidation state, which is postulated to play a part, along with Cr(V), in Cr(VI)-induced toxicity (§1) [1]. Applications of EPR spectroscopy to studies of Cr(IV) (a d^2 ion) are very limited. In several cases, signals attributed to Cr(IV) have been observed in Cr-doped solids (such as ruby) at liquid helium temperatures [83,84], but in most systems such signals cannot be observed at all due to the large zero-field splitting [85]. To our knowledge, no EPR spectroscopic data have been reported for any of the well-characterized Cr(IV) complexes ([26] and references therein). Therefore, the reports on EPR spectroscopic observation of Cr(IV) intermediates in Cr(VI)-treated biological systems [86,87] are erroneous. The broad EPR signals at $g \sim 1.96$ – 2.00 , attributed to such intermediates [86,88–91] are in fact due to Cr(III) species (see above) [1,76].

4. FREE RADICALS AS INTERMEDIATES IN CHROMIUM BIOCHEMISTRY

As described in Section 1, reactions of Cr(VI) with cellular reductants are accompanied by the formation of *O*-, *S*- or *C*-based organic radicals, which can then react with O_2 with the formation of reactive oxygen species (ROS, Fig. 1) [1,92].

Some of the *O*-based radicals (derived from ascorbate, tocopherols, or catecholamines) are stable enough to be detected directly by EPR spectroscopy [39,44,93], but in most cases spin traps have to be used for the characterization of such radicals ([1] and references therein). Problems associated with the use of spin traps in the studies of redox reactions involving reactive Cr species have been discussed in detail in recent reviews [1,8]. Briefly, EPR-active forms of spin traps (such as DMPO-OH, where DMPO is 2,2-dimethylpyrrolidine-*N*-oxide) can be formed in the reaction of the corresponding EPR-silent forms with either ROS or reactive Cr species (such as Cr(V)) [1,8,94]. The formation of DMPO-OH (detected by a characteristic four-line spectrum with $a(^1\text{H}) = a(^{14}\text{N}) = 14.0 \times 10^{-4} \text{ cm}^{-1}$) [95] is often considered as “evidence” for the formation of $\cdot\text{OH}$ radicals in biological systems exposed to Cr compounds ([96–98] and references therein). Arguments against the participation of $\cdot\text{OH}$ radicals in Cr biochemistry, and in biological processes in general (except for those caused by γ -irradiation) have been discussed previously [1,8]. The use of inhibitors such as catalase (an enzyme that selectively destroys H_2O_2) or dimethyl sulfoxide (believed to be a selective trap for $\cdot\text{OH}$) to suppress the formation of the EPR signal of DMPO-OH [19] does not directly prove the participation of $\cdot\text{OH}$ in the formation of DMPO-OH. The effect of catalase points to participation of H_2O_2 (but not necessarily $\cdot\text{OH}$) in the oxidation of DMPO, and dimethyl sulfoxide is known to be an efficient scavenger of *C*-based organic radicals [99]. In summary, spin traps can be used to detect the formation of strongly oxidizing species in the Cr(VI) + reductant or Cr(III) + oxidant systems (both in vitro and in vivo), but not to establish the nature of such species [1].

5. LIVING CELL AND ANIMAL STUDIES

Application of EPR spectroscopy provided the first unambiguous evidence for the formation of Cr(V) intermediates during the reactions of Cr(VI) with biological media, such as rat liver microsomes [100]. This observation led Wetterhahn and coworkers to develop the uptake-reduction model of Cr(VI)-induced toxicity [9], which forms the basis of our current understanding of the biological activities of both Cr(VI) and Cr(III) compounds (§1). Following this early work, the formation of Cr(V) intermediates was observed by EPR spectroscopy during the reactions of Cr(VI) with isolated mitochondria [101], whole mammalian cells [102–105], microorganisms (bacteria or yeasts) [88,97,106,107], living plants [108,109], and animals (mice or rats) [66,67,110–112]. Although in most cases these intermediates were observed using conventional X-band EPR spectrometers, an increase in sensitivity was provided by custom-built L-band (~1.2 GHz) spectrometers and was a clear advantage for the whole plant and animal studies [66,67,109,110]. Typical examples of EPR spectra observed in Cr(VI)-treated biological systems are shown in Figure 8.

Exposure of uni- or multicellular organisms (bacteria, yeasts, plants, or animals) to Cr(VI) at 295–310 K typically led to the observation of single Cr(V) signals with $g_{\text{iso}} \sim 1.98$ [66,88,97,106–110], which in some cases showed partially

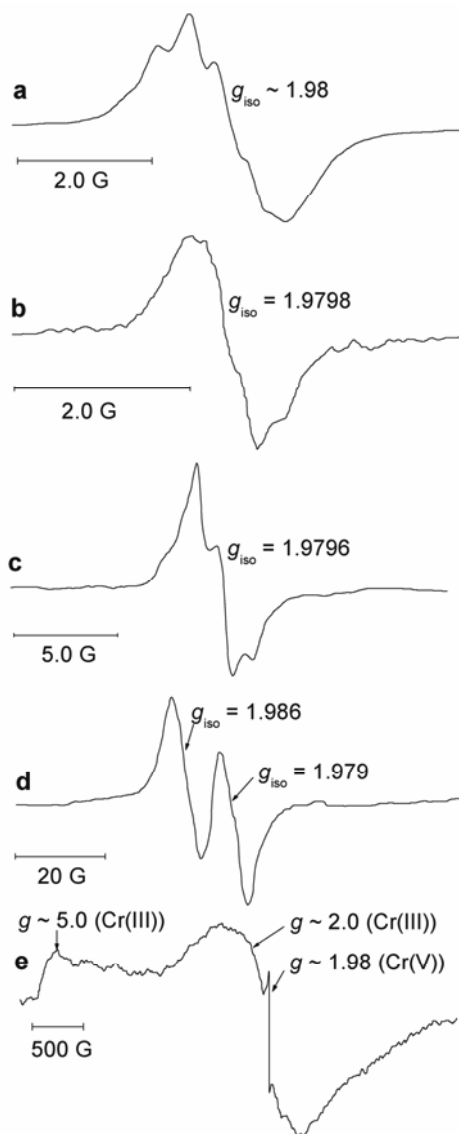


Figure 8. Typical EPR spectra of Cr(VI) biotransformation products in biological systems: (a) roots of a garlic plant after a short treatment with Cr(VI) (250 ppm, 295 K) [108]; (b) a whole living mouse at 5 min after an intravenous injection of Cr(VI) (100 μ L of 200 mM solution, 310 K) [66]; (c) ex-vivo liver homogenate of a Cr(VI)-treated mouse (the same animal as in (b), 295 K) [66]; (d) circulating blood of a living rat at \sim 2 min after an intravenous injection of Cr(VI) (5.0 mg kg^{-1} , 310 K) [111]; and (e) a frozen suspension (153 K, in physiological saline) of V79 Chinese hamster lung cells after a treatment with Cr(VI) (200 μ M for 2 h at 310 K) [104]. All the spectra were acquired at the X-band frequencies (\sim 9.5 GHz), except for (b), which was acquired at the L-band frequency (\sim 1.2 GHz). Published spectra were digitized with permission using the WinDIG software [119].

resolved superhyperfine splitting patterns (Fig. 8a–c) [66,108]. These features point to Cr(V) binding to 1,2-diolato moieties of carbohydrates or glycoproteins (§2.3). A similarity between these signals and those of Cr(V) species formed during the reactions of Cr(VI) with NAD(P)H or NAD(P)H-dependent enzymes led to a suggestion [66,67] that NAD(P)H (not glutathione or ascorbate as thought previously [9]) is the main Cr(VI) reductant in biological systems. However, variations in superhyperfine splitting patterns of the Cr(V) signals dependent on the source of a biological material (Fig. 8a–c) show that these signals are more likely to be due to mixtures of Cr(V) complexes with open-chain and cyclically strained diolato ligands (see Fig. 3 in §2.3). This suggestion is supported by the recent results of computer simulations of Cr(V) EPR signals observed during the reactions of Cr(VI) with rock-inhabiting bacteria, *Arthrobacter oxydans* [113]. Chemical modifications of biological materials can provide more clues for the nature of the resultant Cr(V) species. For instance, deglycosylation of bacterial cell walls led to significant changes in the EPR signals, attributed to Cr(V) binding to *N*-donor residues of proteins [113]. These changes suggest that sialoglycoproteins of bacterial cell walls are at least partially responsible for the stabilization of Cr(V) intermediates during the reduction of Cr(VI) by bacterial cells [16,113].

A different type of Cr(V) EPR spectra, consisting of two signals with $g_{\text{iso}} \sim 1.986$ and ~ 1.979 (e.g., in Fig. 8d), was observed during the reactions of Cr(VI) with isolated red blood cells [102], various lines of cultured mammalian cells [10,105,114], or circulating blood of living rats [111]. In all cases, Cr(V) signals disappeared within several hours at 295–310 K, but relative intensities of the $g_{\text{iso}} \sim 1.979$ signals increased with time [10,105,111]. Based on studies of model systems [31,111], the signal at $g_{\text{iso}} \sim 1.986$ was assigned to a Cr(V) complex with thiolato (most likely glutathione) ligands with a likely structure $[\text{Cr}^{\text{V}}(\text{O})_2(\text{SR})_2(\text{OH}_2)]^-$ (where RSH is glutathione) [10]. The $g_{\text{iso}} \sim 1.979$ signal is probably due to Cr(V) complexes with 1,2-diolato type ligands (§2.3) [16]. These data suggest that glutathione (as the most abundant biological thiol) [115] is likely to be the primary reductant of Cr(VI) in whole blood or cultured animal cells, but subsequent ligand-exchange reactions of the formed Cr(V)–glutathione complex lead to the formation of thermodynamically more stable Cr(V)–carbohydrate complexes [10,16,50]. To support this suggestion, the time-dependent changes in the relative intensities of EPR signals in cellular systems were reproduced in model systems containing physiologically relevant concentrations of glutathione, a model carbohydrate (*cis*-1,2-cyclohexanediol, see §2.3) and a non-reactive protein (bovine serum albumin) [10]. The latter is used to achieve the broadening of Cr(V) EPR signals, which is observed in biological systems compared with low-molecular-weight models [10].

Pretreatment of cultured mammalian cells with dehydroascorbate, which decreases intracellular concentration of glutathione and increases that of ascorbate [116], followed by the exposure of cells to Cr(VI), led to disappearance of the $g_{\text{iso}} \sim 1.986$ signal and to the appearance of a characteristic doublet at $g_{\text{iso}} = 2.0046$ due to the ascorbyl radical, while the signal at $g_{\text{iso}} \sim 1.979$ was still present [114]. These changes point to a switch from glutathione to ascorbate as a primary Cr(VI) reduc-

tant in ascorbate-loaded mammalian cells [114]. The relative contributions of ascorbate and glutathione to Cr(VI) metabolism in exposed humans is likely to be dependent on the nutritional status, since humans are unable to produce ascorbate [116]. The results of EPR spectroscopic studies of whole mice or rats treated with Cr(VI) (Fig. 8b) [66,110] implicate that transient Cr(V) complexes with glutathione or ascorbate, formed in Cr(VI)-exposed humans, will be rapidly converted to Cr(V)-carbohydrate complexes [16]. Decreases in the intensity of Cr(V) signals formed in Cr(VI)-treated cells (bacterial, yeast, or mammalian) after the pretreatments of cells with antioxidant (such as ascorbic acid or vitamin E) can be used in the assessment of the reductive capacity of the cells [97,103,104,117].

A low-temperature (153 K) EPR spectrum of Cr(VI)-treated (200 μ M Cr(VI) for 2 h at 310 K) mammalian cells is shown in Figure 8e [104]. The spectrum is dominated by broad anisotropic signals of Cr(III) at $g_{\text{eff}} \sim 2$ and $g_{\text{eff}} \sim 5$ (cf. Fig. 7), but a sharp signal due to Cr(V) at $g \sim 1.98$ is also visible [104]. The broad features in Figure 8e are probably due to a mixture of Cr(III) species in various coordination environments, so EPR spectroscopy is unlikely to provide much information on the chemical nature of Cr(III) complexes formed in Cr(VI)-treated cells (§3). Recently, x-ray absorption spectroscopy of Cr(VI)-treated cells and model Cr(III) complexes was successfully used to characterize the coordination environment of Cr(III) species, formed in Cr(VI)-treated cells [114]. So far, X-band EPR spectroscopy was not sensitive enough to detect Cr(III) and Cr(V) intermediates formed in Cr(III)-treated cells (such intermediates were detected by microprobe XANES spectroscopy) [54]. In the future, L-band EPR spectroscopy is likely to be used to study the biotransformation products of Cr(III) in biological systems. Magnetic resonance imaging has been used to detect the accumulation of Cr in various organs of Cr(VI)-treated mice or rats, but this method does not distinguish between Cr(V) and Cr(III) species [67,118].

In summary, EPR spectroscopy provides a unique tool for the observation of the Cr(V) intermediates formed in biologically relevant samples, ranging from subcellular fractions [100,101] to living mammals [66,110]. The use of low-frequency (L-band) EPR spectroscopy is particularly promising for the detection of weak Cr(V) signals in whole plants or animals [67,109]. Extensive studies of model Cr(V) complexes (§2) has allowed the assignment of the common Cr(V) signals observed in biological signals ($g_{\text{iso}} \sim 1.979$ and $g_{\text{iso}} \sim 1.986$; Fig. 8) to Cr(V) carbohydrate and glutathione ligands, respectively [10,16]. These results illustrate the use of chemical models to gain insight into the mechanisms of interactions of heavy metal ions with biological systems.

ACKNOWLEDGMENTS

We wish to acknowledge the many contributions of our coworkers and collaborators that are listed in the references. The research has been supported by the Australian Research Council (ARC) Large and Discovery grants (to P.A.L. includ-

ing an ARC Professorial Fellowship), and by ARC RIEFP and Wellcome Trust grants for EPR equipment.

REFERENCES

1. Levina A, Codd R, Dillon CT, Lay PA. 2003. Chromium in biology: toxicology and nutritional aspects. *Prog Inorg Chem* 51:145–250.
2. International Agency for Research on Cancer (IARC). 2001. Overall evaluations of carcinogenicity to humans. <http://www.iarc.fr>.
3. Steinpress MG, Ward AC. 2001. The scientific process and Hollywood: the case of hexavalent chromium. *Ground Water* 39(3):321–322.
4. Anderson RA. 2000. Chromium in the prevention and control of diabetes. *Diabetes Metab* 26(1):22–27.
5. Stearns DM. 2000. Is chromium a trace essential metal? *BioFactors* 11(3):149–162.
6. Martin RB. 2001. Are there proteins containing chromium? In *Handbook on metallo-proteins*, pp.181–192. Ed I Bertini, A Sigel, H Sigel, New York: Marcel Dekker.
7. Vincent JB. 2004. Recent advances in the nutritional biochemistry of trivalent chromium. *Proc Nutr Soc* 63(1):41–47.
8. Levina A, Mulyani I, Lay PA. 2007. Redox chemistry and biological activities of chromium(III) complexes. In *Nutritional biochemistry of chromium(III)*. Ed JB Vincent. Amsterdam: Elsevier Science.
9. Connett PH, Wetterhahn KE. 1983. Metabolism of the carcinogen chromate by cellular constituents. *Struct Bonding (Berlin)* 54:93–124.
10. Levina A, Lay PA. 2005. Mechanistic studies of relevance to the biological activities of chromium. *Coord Chem Rev* 249(3–4):281–298.
11. O'Brien TJ, Ceryak S, Patierno SR. 2003. Complexities of chromium carcinogenesis: role of cellular response, repair and recovery mechanisms. *Mutat Res* 533(1–2):3–36.
12. Vincent JB. 2001. The bioinorganic chemistry of chromium(III). *Polyhedron* 20(1–2):1–26.
13. Jacquamet L, Sun Y, Hatfield J, Gu W, Cramer SP, Crowder MW, Lorigan GA, Vincent JB, Latour J-M. 2003. Characterization of chromodulin by x-ray absorption and electron paramagnetic resonance spectroscopies and magnetic susceptibility measurements. *J Am Chem Soc* 125(3):774–780.
14. Mulyani I, Levina A, Lay PA. 2004. Biomimetic oxidation of chromium(III): does the antidiabetic activity of chromium(III) involve carcinogenic chromium(VI)? *Angew Chem, Int Ed* 43(34):4504–4507.
15. Thompson KH, Orvig C. 2004. Vanadium compounds in the treatment of diabetes. In *Metal ions in biological systems*, pp 221–252. Ed H Siegel, A Siegel, New York: Marcel Dekker.
16. Codd R, Irwin JA, Lay PA. 2003. Sialoglycoprotein and carbohydrate complexes in chromium toxicity. *Curr Opinion Chem Biol* 7(2):213–219.
17. Harris HH, Levina A, Dillon CT, Mulyani I, Lai B, Cai Z, Lay PA. 2004. Time-dependent uptake, distribution and biotransformation of chromium(VI) in individual and bulk human cells: application of synchrotron radiation techniques. *J Biol Inorg Chem* 10(2):105–118.
18. Levina A, Harris HH, Lay PA. 2006. Binding of chromium(VI) to histones: implications for chromium(VI)-induced genotoxicity. *J Biol Inorg Chem* 11(2):225–234.

19. Krepkii D, Antholine WE, Petering DH. 2003. Properties of the reaction of chromate with metallothionein. *Chem Res Toxicol* **16**(6):750–756.
20. Qian Y, Jiang B, Flynn DC, Leonard SS, Wang S, Zhang Z, Ye J, Chen F, Wang L, Shi X. 2001. Cr(VI) increases tyrosine phosphorylation through reactive oxygen species-mediated reactions. *Mol Cell Biochem* **222**(1–2):199–204.
21. Testa JJ, Grela MA, Litter MI. 2004. Heterogeneous photocatalytic reduction of chromium(VI) over TiO₂ particles in the presence of oxalate: involvement of Cr(V) species. *Environ Sci Technol* **38**(5):1589–1594.
22. Humar M, Petrič M, Pohleven F, Šentjurc M. 2002. Consumption of O₂, evolution of CO₂ and reduction of Cr(VI) during fixation of chromium based wood preservatives in wood. *Wood Sci Technol* **36**(4):309–318.
23. Pizzocaro C, Lafond C, Bolte M. 2002. Dichromated poly(vinyl alcohol): key role of chromium(V) in the properties of the photosensitive material. *J Photochem Photobiol A* **151**(1–3):221–228.
24. Bryliakov KP, Talsi EP. 2003. Cr^{III}(salen)Cl catalyzed asymmetric epoxidations: insight into the catalytic cycle. *Inorg Chem* **42**(22):7258–7265.
25. Codd R, Dillon CT, Levina A, Lay PA. 2001. Studies on the genotoxicity of chromium: from the test tube to the cell. *Coord Chem Rev* **216–217**:537–582.
26. Lay PA, Levina A. 2004. Chromium. In *Comprehensive coordination chemistry II: from biology to nanotechnology*, Vol. 4, pp. 313–413. Ed JA McCleverty, TJ Meyer. Amsterdam: Elsevier Science.
27. Cawich CM, Ibrahim A, Link KL, Bumgartner A, Patro MD, Mahapatro SN, Lay PA, Levina A, Eaton SS, Eaton GR. 2003. Synthesis of a pyridinium bis[citrato(2–)]oxochromate(V) complex and its ligand-exchange reactions. *Inorg Chem* **42**(20):6458–6468.
28. Codd R, Levina A, Zhang L, Hambley TW, Lay PA. 2000. Characterization and x-ray absorption spectroscopic studies of bis[quinato(2–)]oxochromate(V). *Inorg Chem* **39**(5):990–997.
29. Gez S, Luxenhofer R, Levina A, Codd R, Lay PA. 2005. Chromium(V) complexes of hydroxamic acids: formation, structures, and reactivities. *Inorg Chem* **44**(8):2934–2943.
30. Barnard PJ, Levina A, Lay PA. 2005. Chromium(V) peptide complexes: synthesis and spectroscopic characterization. *Inorg Chem* **44**(4):1044–1053.
31. Levina A, Zhang L, Lay PA. 2003. Structure and reactivity of a chromium(V) glutathione complex. *Inorg Chem* **42**(3):767–784.
32. Weeks CL, Levina A, Dillon CT, Turner P, Fenton RR, Lay PA. 2004. Synthesis and characterization of a chromium(V) *cis*-dioxo *bis*(1,10-phenanthroline) complex and crystal and molecular structures of its chromium(III) precursor. *Inorg Chem* **43**(24):7844–7856.
33. Levina A, Foran GJ, Pattison DI, Lay PA. 2004. x-ray absorption spectroscopic and electrochemical studies of tris(catecholato(2–))-chromate(V/IV/III) complexes. *Angew Chem, Int Ed* **43**(4):462–465.
34. Milsmann C, Levina A, Harris HH, Foran GJ, Turner P, Lay PA. 2006. Charge distribution in chromium and vanadium catecholato complexes: x-ray absorption spectroscopic and computational studies. *Inorg Chem* **45**(12):4743–4754.
35. Nishino H, Kochi JK. 1990. Unusually stable chromium(V) perfluoropinacolate complexes. *Inorg Chim Acta* **174**(1):93–102.

36. Farrell RP, Lay PA. 1992. New insights into the structures and reactions of Cr(V) complexes: implications for Cr(VI) and Cr(V) oxidations of organic substrates and the mechanisms of chromium-induced cancers. *Comments Inorg Chem* **13**(3–4):133–175.
37. Headlam HA, Weeks CL, Turner P, Hambley TW, Lay PA. 2001. Dinuclear chromium(V) amino acid complexes from the reduction of chromium(VI) in the presence of amino acid ligands: XAFS characterization of a chromium(V) amino acid complex. *Inorg Chem* **40**(20):5097–5105.
38. Barr-David G, Charara M, Codd R, Farrell RP, Irwin JA, Lay PA, Bramley R, Brumby S, Ji J-Y, Hanson GR. 1995. EPR characterisation of the Cr(V) intermediates in the Cr(VI)/Cr(V) oxidations of organic substrates and of relevance to Cr-induced cancers. *J Chem Soc Faraday Trans* **91**(8):1207–1216.
39. Zhang L, Lay PA. 1996. EPR spectroscopic studies of the reactions of Cr(VI) with L-ascorbic acid, L-dehydroascorbic acid and 5,6-O-isopropylidene-L-ascorbic acid in water: implications for chromium(VI) genotoxicity. *J Am Chem Soc* **118**(50):12624–12637.
40. Stearns DM, Kennedy LJ, Courtney KD, Giangrande PH, Phieffer LS, Wetterhahn KE. 1995. Reduction of chromium(VI) by ascorbate leads to chromium-DNA binding and DNA strand breaks in vitro. *Biochemistry* **34**(3):910–919.
41. Stearns DM, Wetterhahn KE. 1997. Intermediates produced in the reaction of chromium(VI) with dehydroascorbate cause single-strand breaks in plasmid DNA. *Chem Res Toxicol* **10**(3):271–278.
42. Zhang L. 1998. EPR and XAFS studies of biologically relevant chromium(V) complexes and manganese(II)-activated aminopeptidase. PhD thesis, The University of Sydney.
43. Levina A, Ludwig C, Lay PA. 2003. Reactive intermediates formed during the reactions of chromium(VI) with glutathione: which species are responsible for the DNA damage? *J Inorg Biochem* **96**(1):177.
44. Pattison DI, Lay PA, Davies MJ. 2000. EPR studies of chromium(V) intermediates generated via reduction of chromium(VI) by DOPA and related catecholamines: potential role for oxidized amino acids in chromium-induced cancers. *Inorg Chem* **39**(13):2729–2739.
45. Pattison DI, Davies MJ, Levina A, Dixon NE, Lay PA. 2001. Chromium(VI) reduction by catechol(amine)s results in DNA cleavage in vitro: relevance to chromium genotoxicity. *Chem Res Toxicol* **14**(5):500–510.
46. Headlam HA. 1998. The role of Cr(III) and Cr(V) peptide and amino acid complexes in Cr-induced carcinogenesis. PhD Thesis, The University of Sydney.
47. Duling D. 1996. PEST WinSim. National Institute of Environmental Health Science, http://epr.niehs.nih.gov/pest_mans/general.html.
48. Codd R, Lay PA. 1999. Competition between 1,2-diol and 2-hydroxy acid coordination in Cr(V)-quinic acid complexes: implications for stabilization of Cr(V) intermediates of relevance to Cr(VI)-induced carcinogenesis. *J Am Chem Soc* **121**(34):7864–7876.
49. Bramley R, Ji J-Y, Judd RJ, Lay PA. 1990. Solvent dependence of the EPR spectra of oxochromate(V) complexes; solution structures and the effects of hydrogen bonding between the solvent and the complex. *Inorg Chem* **29**(17):3089–3094.
50. Irwin JA. 1998. Cr(V)-sugar complexes: possible intracellular intermediates of importance to chromate-induced carcinogenesis. PhD thesis, The University of Sydney.

51. Collins TJ, Slebodnick C, Uffelman ES. 1990. Cr(V)-oxo complexes of macrocyclic tetraamido-N ligands tailored for highly oxidized middle transition metal complexes. *Inorg Chem* **29**(18):3433–3436.
52. Meier-Callahan AE, Di Bilio AJ, Simkhovich L, Mahammed A, Goldberg I, Gray HB, Gross Z. 2001. Chromium corroles in four oxidation states. *Inorg Chem* **40**(26):6788–6793.
53. Headlam HA, Lay PA. 2001. EPR spectroscopic studies of the reduction of chromium(VI) by methanol in the presence of peptides: formation of long-lived chromium(V) peptide complexes. *Inorg Chem* **40**(1):78–86.
54. Wu LE, Levina A, Harris HH, Cai Z, Lai B, Vogt S, James DE. 2006. Adipocytes oxidize a common Cr(III) dietary supplement into carcinogenic Cr(VI) and Cr(V). To be submitted.
55. Branca M, Micera G, Dessì A. 1988. Reduction of chromium(VI) by D-galacturonic acid and formation of stable chromium(V) intermediates. *Inorg Chim Acta* **153**(1):61–65.
56. Signorella S, Daier V, García S, Cargnello R, González JC, Rizzotto M, Sala LF. 1999. The relative ability of aldoses and deoxyaldoses to reduce Cr(VI) and Cr(V): a comparative and mechanistic study. *Carbohydr Res* **316**(1–4):14–25.
57. Signorella S, González JC, Sala LF. 2002. EPR spectroscopic characterization of Cr^V-saccharide complexes. *J Arg Chem Soc* **90**(1–3):1–19.
58. Rizzotto M, Levina A, Santoro M, García S, Frascaroli MI, Signorella S, Sala LF, Lay PA. 2002. Redox and ligand-exchange chemistry of chromium(VI/V)-methyl glycoside systems. *Dalton Trans* **16**:3206–3213.
59. Branca M, Dessì A, Kozłowski H, Micera G, Swiatek J. 1990. Reduction of chromate ions by glutathione tripeptide in the presence of sugar ligands. *J Inorg Biochem* **39**(3):217–226.
60. Bartholomäus R, Levina A, Lay PA. 2006. Unpublished data.
61. Signorella S, Daier V, Santoro M, García S, Palopoli C, González JC, Korecz L, Rockenbauer A, Sala LF. 2001. The EPR pattern of [CrO(*cis*-1,2-cyclopentanediolato)₂][−] and [CrO(*trans*-1,2-cyclopentanediolato)₂][−]. *Eur J Inorg Chem* **7**:1829–1833.
62. Codd R, Lay PA. 2001. Chromium(V)-sialic (neuraminic) acid species are formed from mixtures of chromium(VI) and saliva. *J Am Chem Soc* **123**(47):11799–11800.
63. Codd R, Lay PA. 2003. Oxochromium(V) species formed with 2,3-dehydro-2-deoxy-N-acetylneuraminic or N-acetylneuraminic (sialic) acids: an in vitro model system of oxochromium(V) species potentially stabilized in the respiratory tract upon inhalation of carcinogenic chromium(VI) compounds. *Chem Res Toxicol* **16**(7):881–892.
64. Signorella S, García S, Rizzotto M, Levina A, Lay PA, Sala LF. 2005. The EPR pattern of Cr^V complexes of D-ribose derivatives. *Polyhedron* **24**(9):1079–1085.
65. Meejoo S, Levina A, Lay PA. 2006. Unpublished data.
66. Liu KJ, Shi X, Jiang J, Goda F, Dalal N, Swartz HM. 1996. Low frequency electron paramagnetic resonance investigation on metabolism of chromium(VI) by whole live mice. *Ann Clin Lab Sci* **26**(2):176–184.
67. Liu KJ, Shi X. 2001. In vivo reduction of chromium(VI) and its related free radical generation. *Mol Cell Biochem* **222**(1–2):41–47.
68. Myers CR, Myers JM, Carstens BP, Antholine WE. 2000. Reduction of chromium(VI) to chromium(V) by human microsomal enzymes: effects of iron and quinones. *Toxic Subst Mech* **19**(1):25–51.

69. Porter R, Jáchymová M, Martásek P, Kalyanaraman B, Vásquez-Vivar J. 2005. Reductive activation of Cr(VI) by nitric oxide synthase. *Chem Res Toxicol* **18**(5):834–843.
70. Codd R. 2004. Metalloglycomics: a new perspective upon competitive metal-carbohydrate binding using EPR spectroscopy. *Chem Commun* **23**:2653–2655.
71. Rakitin YV, Yablokov YV. 1982. Distortion of clusters and EPR of trinuclear chromium carboxylates. *Zh Neorg Khim* **27**(1):104–108. Engl transl: *Rus J Inorg Chem* **27**(1):59–62.
72. Pilbrow JR. 1990. *Transition ion electron paramagnetic resonance*, pp. 120–125. Oxford: Clarendon Press.
73. Pilbrow JR. 1978. Effective g Values for $S = 3/2$ and $S = 5/2$. *J Magn Reson* **31**:479–490.
74. Bonomo RP, Di Bilio AJ, Riggi F. 1991. EPR investigation of chromium(III) complexes: analysis of their frozen solution and magnetically dilute powder spectra. *Chem Phys* **151**(3):323–333.
75. Wu S-Y, Gao X-Y, Yan W-Z. 2003. Theoretical studies of the EPR g factors and the hyperfine structure constants of Cr^{3+} in MgS and SrS. *Z Naturforsch A* **58**(9–10):503–506.
76. Weckhuysen BM, Schoonheydt RA, Mabbs FE, Collison D. 1996. Electron paramagnetic resonance of heterogeneous chromium catalysts. *J Chem Soc, Faraday Trans* **92**(13):2431–2436.
76. Thompson M, Connick RE. 1981. Hydrolytic polymerization of chromium(III), 1: two dimeric species. *Inorg Chem* **20**(7):2279–2285.
78. Aisen P, Aasa R, Redfield AG. 1969. The chromium, manganese, and cobalt complexes of transferrin. *J Biol Chem* **244**(17):4628–4633.
79. Martinelli RA, Hanson GR, Thompson JS, Holmquist B, Pilbrow JR, Auld DS, Vallee BL. 1989. *Biochemistry* **28**(5):2251–2258.
80. Della Rocca BM, Lauria G, Venerini F, Palmieri L, Polizio F, Capobianco L, Stipani V, Pedersen J, Cappello AR, Desideri A, Palmieri F. 2003. The mitochondrial oxoglutarate carrier: structural and dynamic properties of transmembrane segment IV studied by site-directed spin labeling. *Biochemistry* **42**(18):5493–5499.
81. Hedin EMK, Hoyrup P, Patkar SA, Vind J, Svendsen A, Fransson L, Hult K. 2002. Interfacial orientation of *Thermomyces lanuginosa* lipase on phospholipid vesicles investigated by electron spin resonance relaxation spectroscopy. *Biochemistry* **41**(48):14185–14196.
82. Montarani L, Scotti R, Lockhart TP. 1994. Kinetics and mechanism of the reaction of hydrated chromium(III) with partially hydrolyzed polyacrylamide. *Macromolecules* **27**(12):3341–3348.
83. Marshall SA, Yu C, Zhang YN. 1988. Comments on the EPR spectrum of tetravalent chromium in ruby. *Phys Stat Sol B* **149**(2):691–695.
84. Reinen D, Kesper U, Atanasov M, Roos J. 1995. Cr^{4+} in tetrahedral coordination of oxidic solids: a spectroscopic and structural investigation. *Inorg Chem* **34**(1):184–192.
85. König E. 1968. Electron paramagnetic resonance. In *Physical methods in advanced inorganic chemistry*, pp. 329–339. Ed HAO Hill, P Day, London: Interscience Publishers.
86. Chiu A, Chiu N, Shi X, Beaubier J, Dalal NS. 1998. Activation of a procarcinogen by reduction: Cr^{6+} – Cr^{5+} – Cr^{4+} – Cr^{3+} : a case study by electron spin resonance (ESR/PMR). *Environ Carcin Ecotox Rev* **C16**(2):135–148.

87. Katz AJ, Chiu A, Beaubier J, Shi X. 2001. Combining *Drosophila melanogaster* somatic mutation-recombination and electron spin resonance spectroscopy data to interpret epidemiologic observations on chromium carcinogenicity. *Mol Cell Biochem* **222**(1–2):61–68.
88. Kalabegishvili TL, Tsibakhashvili NY, Holman H-YN. 2003. Electron spin resonance study of chromium(V) formation and decomposition by basalt-inhabiting bacteria. *Environ Sci Technol* **37**(20):4678–4684.
89. Luo H, Lu Y, Shi X, Mao Y, Dalal NS. 1996. Cr(IV)-mediated Fenton-like reaction causes DNA damage: implication to genotoxicity of chromate. *Ann Clin Lab Sci* **26**(2):185–191.
90. Luo H, Lu Y, Mao Y, Shi X, Dalal NS. 1996. Role of Cr(IV) in the Cr(VI)-related free radical formation, dG hydroxylation and DNA damage. *J Inorg Biochem* **64**(1):25–35.
91. Liu KJ, Shi X, Dalal NS. 1997. Synthesis of Cr(IV)–GSH, its identification and its free hydroxyl radical generation: a model compound for Cr(VI) carcinogenicity. *Biochem Biophys Res Commun* **235**(1):54–58.
92. Lay PA, Levina A. 1998. Activation of molecular oxygen during the reactions of chromium(VI/V/IV) with biological reductants: implications for chromium-induced genotoxicities. *J Am Chem Soc* **120**(27):6704–6714.
93. Dalla-Pozza A-M. 1996. Formation of DNA-damaging Cr(V) complexes during the reactions of Cr(VI) with a vitamin E analogue and D-glucose. BSc(Hons) thesis, The University of Sydney.
94. Sugden KD, Wetterhahn KE. 1996. Reaction of chromium(V) with the EPR spin traps 5,5-dimethylpyrroline *n*-oxide and phenyl-*N*-tert-butyl nitron resulting in direct oxidation. *Inorg Chem* **35**(3):651–657.
95. Buettner G. 1987. Spin trapping: ESR parameters of spin traps. *Free Rad Biol Med* **3**(4):259–303.
96. Antonini JM, Leonard SS, Roberts JR, Solano-Lopez C, Young S-H, Shi X, Taylor MD. 2005. Effect of stainless steel manual metal arc welding fume on free radical production, DNA damage, and apoptosis induction. *Mol Cell Biochem* **279**(1–2):17–23.
97. Poljšak B, Gazdag Z, Jenko-Brinovec Š, Fujs Š, Pesti M, Bélágyi J, Plesničar S, Raspor P. 2005. Pro-oxidative vs antioxidative properties of ascorbic acid in chromium(VI)-induced damage: an in vivo and in vitro approach. *J Appl Toxicol* **25**(6):535–548.
98. Shi H, Hudson LG, Liu KJ. 2004. Oxidative stress and apoptosis in metal ion-induced carcinogenesis. *Free Rad Biol Med* **37**(5):582–593.
99. Levina A, Barr-David R, Codd R, Lay PA, Dixon NE, Hammershoi A, Hendry P. 1999. In vitro plasmid DNA cleavage by chromium(V) and -(IV) 2-hydroxycarboxylato complexes. *Chem Res Toxicol* **12**(4):371–381.
100. Wetterhahn Jennette K. 1982. Microsomal reduction of the carcinogen chromate produces chromium(V). *J Am Chem Soc* **104**(3):874–875.
101. Rossi SC, Gorman N, Wetterhahn KE. 1988. Mitochondrial reduction of the carcinogen chromate: formation of chromium(V). *Chem Res Toxicol* **1**(2):101–107.
102. Branca M, Dessì A, Kozłowski H, Micera G, Serra MV. 1989. In vitro interaction of mutagenic chromium(VI) with red blood cells. *FEBS Lett* **257**(1):52–54.
103. Sugiyama M, Ando A, Ogura R. 1989. Effect of vitamin E on survival, GSH reductase and formation of Cr(V) in Chinese hamster V-79 cells treated with sodium chromate (VI). *Carcinogenesis* **10**(4):737–741.

104. Sugiyama M, Tsuzuki K, Ogura R. 1991. Effect of ascorbic acid on DNA damage, cytotoxicity, glutathione reductase and formation of paramagnetic Cr in Chinese hamster V-79 cells treated with sodium chromate. *J Biol Chem* **266**(6):3383–3386.
105. Witmer C, Faria E, Park H-S, Sadrieh N, Yurkow E, O'Connell S, Sirak A, Schleyer H. 1994. In vivo effects of chromium. *Environ Health Perspect* **102**(2):169–176.
106. Shi X, Dalal NS, Vallyathan V. 1991. One-electron reduction of carcinogen chromate by microsomes, mitochondria and *E. coli*: identification of chromium(V) and OH radical. *Arch Biochem Biophys* **290**(2):381–386.
107. Myers CR, Carstens BP, Antholine WE, Myers JM. 2000. Chromium(VI) reductase activity is associated with the cytoplasmic membrane of anaerobically grown *Shewanella putrefaciens* MR-1. *J Appl Microbiol* **88**(1):98–106.
108. Micera G, Dessì A. 1988. Chromium adsorption by plant roots and formation of long-lived Cr(V) species: an ecological hazard? *J Inorg Biochem* **34**(3):157–166.
109. Appenroth KJ, Bischoff M, Gabrys H, Stoeckel J, Swartz HM, Walczak T, Winnefeld K. 2000. Kinetics of chromium(V) formation and reduction in fronds of the duckweed *Spirodela polyrhiza*: a low-frequency EPR study. *J Inorg Biochem* **78**(3):235–242.
110. Liu KJ, Mäder K, Shi X, Swartz HM. 1997. Reduction of carcinogenic chromium(VI) on the skin of living rats. *Magn Reson Med* **38**(4):524–525.
111. Sakurai H, Takechi K, Tsuboi H, Yasui H. 1999. ESR characterization and metallokinetic analysis of Cr(V) in the blood of rats given carcinogen chromate(VI) compounds. *J Inorg Biochem* **76**(1):71–80.
112. Ueno S, Kashimoto T, Susa N, Furukawa Y, Ishii M, Yokoi K, Yasuno M, Sasaki YF, Ueda J, Nishimura Y, Sugiyama M. 2001. Detection of dichromate(VI)-induced DNA strand breaks and formation of paramagnetic chromium in multiple mouse organs. *Toxicol Appl Pharmacol* **170**(1):56–62.
113. Codd R, Lay PA, Tsiabakhashvili NY, Kalabegishvili TL, Murusidze IG, Holman H-YN. 2006. Chromium(V) complexes generated in *Arthrobacter oxydans* by simulation analysis of EPR spectra. *J Inorg Biochem* **100**(11):1827–1833.
114. Levina A, Harris HH, Lay PA. 2007. x-ray absorption and epr spectroscopic studies of the biotransformations of chromium(vi) in mammalian cells. Is chromodulin an artefact of isolation methods? *J Am Chem Soc*. In press.
115. Kosower EM. 1976. Glutathione. In *Glutathione: metabolism and function*, pp 1–15. Ed IM Arias, WB Jacoby, New York: Raven Press.
116. Quievryn G, Peterson E, Messer J, Zhitkovich A. 2003. Genotoxicity and mutagenicity of chromium(VI)/ascorbate-generated DNA adducts in human and bacterial cells. *Biochemistry* **42**(4):1062–1070.
117. Kartvelishvili T, Abuladze M, Asatiani N, Akhvlediani J, Kiziria E, Asanishvili L, Lejava L, Holman H-YN, Sapojnikova N. 2004. Estimation of the cellular antioxidant response to chromium action using ESR method. *The Scientific World* **4**(Suppl. 2):785–794.
118. Shayer R, Kinchesh P, Raffray M, Kortenkamp A. 2004. Biomonitoring of chromium(VI) deposited in pulmonary tissues: pilot studies of a magnetic resonance imaging technique in a post-mortem rodent model. *Biomarkers* **9**(1):32–46.
119. Lovy D. 1996. WinDIG, University of Geneva, Switzerland. <http://www.unige.ch/sciences/chifi/cpb/windig.html>.

HIGH-FREQUENCY EPR AND ENDOR CHARACTERIZATION OF MRI CONTRAST AGENTS

Arnold M. Raitsimring,¹ Andrei V. Astashkin,²
and Peter Caravan²

¹*EPIX Pharmaceuticals, Cambridge MA;* ²*Department
of Chemistry, University of Arizona, Tucson*

High-frequency EPR and ENDOR techniques have proved useful in characterizing gadolinium-based MRI contrast agents. The result of these studies is a better understanding of the mechanism of action of these contrast agents, and this in turn has aided the design of more potent nuclear relaxation agents. This chapter first takes a broad overview of MRI contrast agents and the need for EPR studies. High-frequency EPR studies of gadolinium contrast agents have focused on four areas: the field-dependent electronic relaxation behavior of Gd(III) complexes in aqueous solution; an understanding of the parameters that define the crystal field interactions (*cfi*) among different contrast agents; the hydration number, i.e., the water coordination number in aqueous and biological matrices; the gadolinium–water proton distance. This chapter reviews each of these subject areas in detail, taking a critical approach and pointing out shortcomings of previous work where applicable. This chapter is aimed at scientists interested in the design of new MRI contrast agents, in EPR of high-spin ions, and/or in the coordination chemistry of lanthanide ions in aqueous media.

1. INTRODUCTION

Magnetic resonance imaging (MRI) is a routine diagnostic tool in modern clinical medicine. MRI has many advantages as a diagnostic imaging modality. It is noninvasive, delivers no radiation burden, and has excellent (submillimeter) spatial resolution. Soft tissue contrast is superb and MRI readily yields anatomical information. Moreover, there are many techniques that can provide contrast in MRI resulting in markedly different images from the same anatomical region. For instance, pulse sequences can be weighted to highlight differences among tissues that

have different proton density, T_1 or T_2 relaxation times, apparent diffusion coefficients, or different chemical shifts (water vs. lipids) [1].

The overriding challenge with MRI is its relatively low sensitivity. In clinical imaging what is primarily observed are hydrogen atoms from water that are present in tissue at $\sim 90\text{M}$. In order to induce additional contrast, a substance is required that will affect some property of the 90M water protons to such an extent that an observable effect is achieved. Such substances are called MRI contrast agents [2,3]. They can be paramagnetic, superparamagnetic, or ferromagnetic compounds that catalytically shorten the relaxation times of bulk water protons. Although there are some manganese- and iron-based contrast agents approved for clinical use, the overwhelming majority of contrast-enhanced clinical exams are performed with gadolinium complexes. More than 10 million MRI studies are performed with gadolinium each year.

It is the action of the contrast agent on the relaxation properties of the water hydrogen nuclei that generates contrast. Since water is present at a much higher concentration than the contrast agent, the contrast agent must act catalytically to relax the water protons in order to observe an effect. The ability of a contrast agent to change the relaxation rate of solvent protons is represented quantitatively as relaxivity, r_1 or r_2 , where the subscript refers to either the longitudinal ($1/T_1$) or the transverse rate ($1/T_2$). Relaxivity is simply the change in water proton relaxation rate after the introduction of the contrast agent $\Delta(1/T_1)$ normalized to the concentration of contrast agent or metal ion (M):

$$r_1 = \frac{\Delta(1/T_1)}{[M]}. \quad (1)$$

Some compounds are better relaxation agents than others. Commercial contrast agents are only effective at high concentrations ($>0.1 \text{ mM}$), and as a result of this there has been considerable effort to increase their sensitivity [4]. Compounds with high relaxivity can be detected at lower doses, or provide greater contrast at equivalent doses to compounds with lower relaxivity.

Relaxation of solvent water (bulk water) by a gadolinium complex is a multifaceted phenomenon. Water in close proximity to the ion is relaxed and then rapidly exchanges with the bulk. For this problem, water can be classified into three categories: inner-sphere water, where the water oxygen is directly coordinated to the Gd(III); 2nd-sphere water, describing water molecules that hydrate the complex and have a finite residency time that is longer than the translational diffusion time of pure water; outer-sphere water, where the interaction of the water with Gd(III) is governed solely by translational diffusion and a distance of closest approach. T_1 relaxation of water hydrogen by Gd(III) occurs via a dipolar mechanism. Relaxation will depend on the number of water molecules (q), their distance to the Gd(III) ion (r_{GdH}), their rate of exchange with bulk solvent ($k_{\text{ex}} = 1/\tau_{\text{m}}$), and some correlation time, τ_{c} .

For Gd(III) complexes there are several processes that can contribute to this correlation time. Electronic relaxation ($1/T_{1,2e}$) at the Gd(III) ion, rotational diffusion ($1/\tau_R$) of the complex, and water exchange in and out of the first ($1/\tau_m$) or 2nd ($1/\tau_m'$) coordination sphere all create a fluctuating field that can serve to relax the hydrogen nucleus. It is the fastest rate (shortest time constant) that determines the extent of relaxation. For water in the second sphere, the relevant correlation time may be the lifetime of this water, which may be on the order of tens of picoseconds. Water in the inner sphere typically has a much longer residency time (1–10,000 ns), so the relevant correlation time is usually rotational diffusion or electronic relaxation.

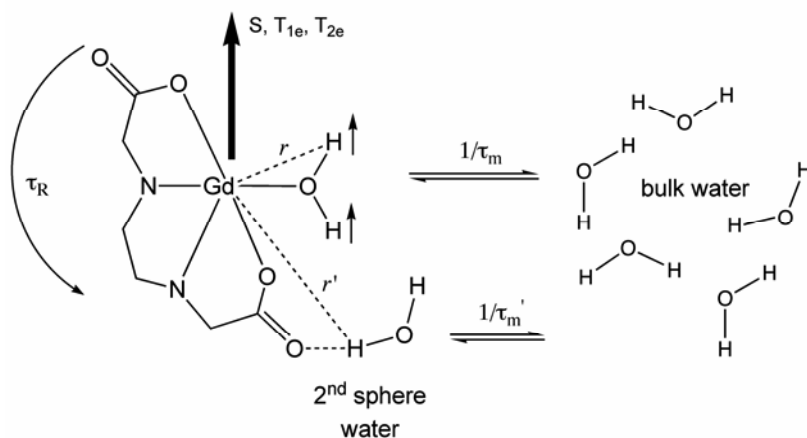


Figure 1. Molecular parameters that contribute to inner- and 2nd-sphere relaxivity.

Figure 1 is an attempt to summarize this problem. The hydrogen nuclei are small magnetic dipoles denoted by the small vectors. There are q waters in the inner sphere with a Gd–H distance r and a residency time τ_m , and q' waters in the second sphere at a Gd–H distance r' and residency time τ_m' . The gadolinium ion is a much larger magnetic dipole denoted by the large vector and characterized by spin S ; it undergoes relaxation that is described by T_{1e} and T_{2e} . Assuming the complex tumbles isotropically, rotational motion is described by a rotational correlation time, τ_R . Water in the outer sphere is described by a translational diffusion correlation time τ_D and a distance of closest approach a . This gives 11 parameters to describe water relaxation at a given applied field B_0 . Moreover, electronic relaxation itself is magnetic field dependent. It is obvious that the relative influence of all these parameters cannot be ascertained by a simple measurement of relaxivity. However, some of these parameters can be determined independently and the effect of others can be simulated. A better understanding of the molecular basis of relaxivity has led to contrast agents with higher relaxivity [5,6].

As an example, it is useful to consider the relaxivity due to the inner-sphere water for fast and slow tumbling complexes. For solvent T_1 nuclear relaxation arising from two-site exchange, the relaxivity due to the inner-sphere water(s) is given by

$$r_1(\text{inner-sphere}) = \frac{q/[\text{H}_2\text{O}]}{T_{1m} + \tau_m}, \quad (2)$$

$$\frac{1}{T_{1m}} = \frac{2}{15} \frac{\gamma_H^2 g_e^2 \mu_B^2 S(S+1)}{r_{\text{GdH}}^6} \left[\frac{7\tau_{c2}}{1 + \omega_s^2 \tau_{c2}^2} + \frac{3\tau_{c1}}{1 + \omega_H^2 \tau_{c1}^2} \right], \quad (3)$$

$$\frac{1}{\tau_{ci}} = \frac{1}{\tau_R} + \frac{1}{T_{ie}} + \frac{1}{\tau_m}; \quad i=1,2. \quad (4)$$

Equations (3) and (4) describe the relaxation of the metal-bound water molecule, where ω_s and ω_H are the electron and proton Larmor frequencies, respectively, γ_H is the proton magnetogyric ratio, g_e is the electron g -factor, and μ_B is the electron Bohr magneton. Figure 3 is a so-called nuclear magnetic relaxation dispersion (NMRD) profile for the contrast agent MS-325 (Fig. 2) either in buffered saline solution or when bound to the protein human serum albumin. In the absence of protein, MS-325 behaves like a small molecule. In the presence of albumin, MS-325 binds to the protein and tumbles more slowly [7]. If the correlation time is static, then one would expect relaxivity to exhibit two dispersions, one at $\omega_s \tau_c > 1$ and the second at $\omega_H \tau_c > 1$. For the albumin-bound complex, relaxivity declines with increasing field, then increases, and then declines again. This is because at low fields electronic relaxation is very fast and is the correlation time governing nuclear relaxation. Electronic relaxation decreases with increasing field to the point where the increasing correlation time causes relaxivity to increase until the inequality $\omega_H \tau_c > 1$ is reached, and relaxivity again disperses. Figure 3 also shows the influence of changing the correlation time (in this case rotation) by binding the Gd(III) complex to a protein. Relaxivity is increased when protein is bound, but also is strongly field dependent.

Magnetic resonance methods have proved useful in better characterizing these contrast agents. There has been considerable effort to optimize the various parameters to increase relaxivity. For instance ^{17}O NMR relaxation is routinely used to estimate the inner-sphere water exchange rate [8,9], and there is now a better understanding of the factors that influence water exchange at Gd(III). EPR methods have also been used. Clarkson and coworkers pioneered the application of EPR to study these molecules, replacing Gd(III) with vanadyl to probe rotational dynamics in solution [10–12], and also by studying the gadolinium complexes directly to estimate electronic relaxation in solution [13–16].

Recent applications of high-frequency EPR to the study of gadolinium contrast agents focused on four areas: the field-dependent electronic relaxation behavior of

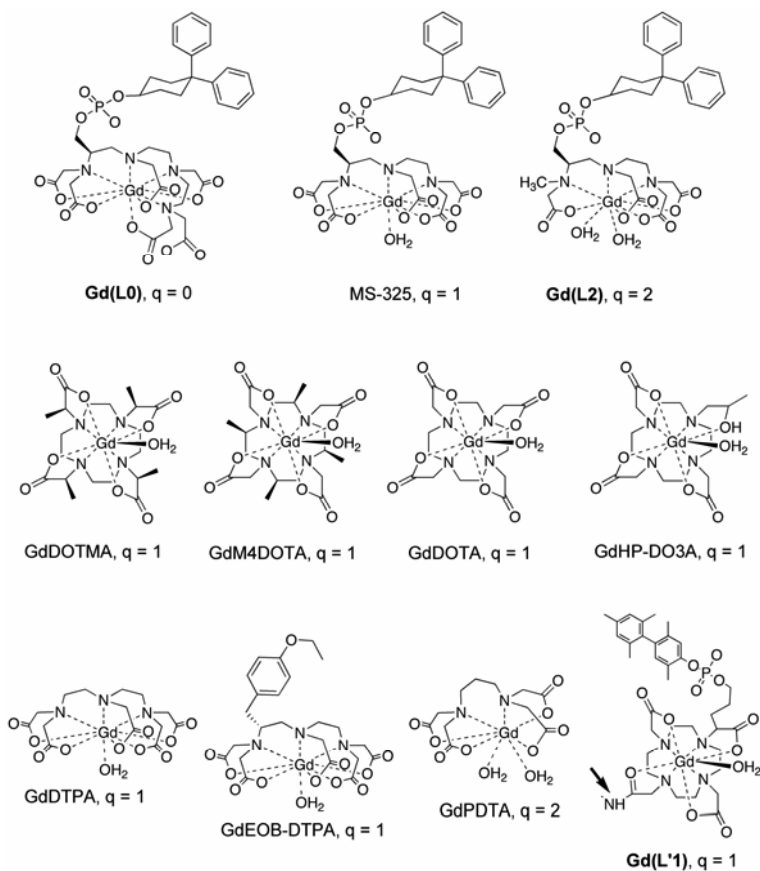


Figure 2. Drawings of gadolinium complexes discussed in this chapter.

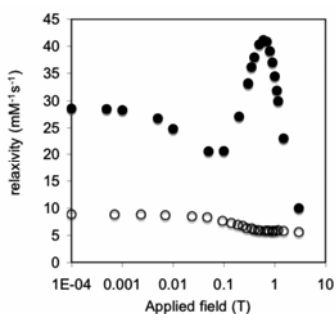


Figure 3. Nuclear magnetic relaxation dispersion (NMRD) of MS-325 in phosphate-buffered saline (○) or in HSA solution (●). Binding to HSA increases the correlation time, increases relaxivity, and alters the field dependence on relaxivity.

Gd(III) complexes in aqueous solution; an understanding of the parameters that define the crystal field interactions (*cfi*) among different contrast agents; the hydration number, i.e., the water coordination number in aqueous and biological matrices; the gadolinium–water proton distance. The first area was reviewed recently by Borel and coworkers [17] in this series, and will only be treated briefly here. The other three areas are covered in more detail.

2. FREQUENCY DEPENDENCE OF GD(III) ELECTRONIC RELAXATION IN AQUEOUS SOLUTION

Electron spin relaxation in aqueous solutions of Gd(III) complexes is too fast to be observed at room temperature by the usual pulsed EPR methods. Two continuous wave (cw) EPR approaches have been used to study electronic relaxation: direct measurement of T_{1e} using Longitudinally Detected EPR (LODEPR) and measuring the frequency dependence of the line shape of the CW-EPR resonance. In LODEPR, the microwave power is subjected to a large amplitude modulation at a frequency on the order of $1/T_{1e}$ before entering the cavity. As a result, the saturation factor is modulated as well, producing corresponding oscillations of the longitudinal spin magnetization M_z . Atsarkin and coworkers [18,19] measured T_{1e} for four Gd(III) complexes at X-band and found T_{1e} in the 1–5 ns range (Table 1).

Table 1. LODEPR Experimentally Determined T_{1e} Values for 4 Gd(III) Complexes in Water at 9.3 GHz and T_{1e} Values Predicted from Lineshape Analysis of Multifrequency Solution EPR Studies [19]

Complex	Peak-to-peak linewidth (mT)	T_{1e} measured (ns)	T_{1e} predicted (ns)
GdDTPA	60	1.2 ± 0.4	0.64
GdDOTA	12.5	4.7 ± 1.0	3.4
GdDOTMA	7.7	3.2 ± 0.3	3.9
GdM4DOTA	15.5	1.9 ± 0.2	1.8

Treatments to interpret the frequency dependence of T_{1e} and T_{2e} have become increasingly sophisticated. The multifrequency studies done in solution define a function of zero-field splitting (ZFS) or the crystal-field interaction (*cfi*) parameters, denoted as Δ^2 . The relationship between the parameters D and E , which account for the quadrupolar part of the *cfi*, and Δ^2 is defined as: $\Delta^2 \equiv (2/3)D^2 + 2E^2$. The *cfi* parameters for Gd(III) complexes are dealt with in much more detail below in Section 3, where we discuss more recent results on frozen glassy solutions. Here we describe efforts to understand electronic relaxation in solution and how this impacts nuclear magnetic relaxation and MRI contrast agents.

Hudson and Lewis [20] showed that the eigenvalues ξ_i of the relaxation matrix \mathbf{R} as defined in Bloch–Wangsness–Redfield theory [21] are functions of a correlation time τ_v and the experimental frequency ω_s , and are related to the relaxation time T_{2ei} of the i th allowed electron spin transition by

$$\frac{1}{T_{2ei}} = -\Delta^2 \tau_v \xi_i. \quad (5)$$

It was assumed that the dominant line-broadening mechanism is provided by the modulation of the quadrupolar term of the cfi and that higher-order contributions are negligible. \mathbf{R} is a 7×7 matrix for the $S = 7/2$ system, with matrix elements written in terms of the spectral densities $J(\omega, \tau_v)$. There are four transitions with nonzero intensity at any frequency resulting in multi-exponential decay of the transverse magnetization. There is not a one-to-one correspondence between the relaxation rates and the degenerate $m_s \leftrightarrow m_s \pm 1$ transitions, and generally one transition is predicted to have a T_{2ei} that is much longer than the other three. At high frequencies (>35 GHz) the difference between the longest T_{2ei} and the other three values is predicted to be greater than 10-fold, resulting in high-frequency CW-EPR spectra consisting of a narrow line superimposed on much broader lines.

In order to calculate the peak-to-peak linewidth, ΔB_{pp} , the EPR line shape must be calculated from T_{2e} values. The values of T_{2ei} and the transition probabilities for all transitions in the system are calculated as a function of magnetic field. The time-dependent magnetization, $\mathbf{M}(\omega, \Delta^2, \tau_v, t)$, can be calculated as a sum of all transitions, followed by a Fourier transformation of the magnetization function, and ΔB_{pp} determined. The experimental data are fitted by varying Δ^2 and τ_v and calculating eigenvalues of the \mathbf{R} -matrix at each τ_v value.

The Hudson and Lewis approach to calculating spin relaxation makes use of the real part of the relaxation matrix \mathbf{R} . Poupko, Barum, and Luz [22] used the complete complex matrix to calculate both the relaxation times and the frequency shifts of the four transitions that give rise to a Gd(III) EPR spectrum in aqueous solution. Their approach predicts changes in the lineshape due to the different transitions and better reproduces the asymmetric lineshapes often observed. By measuring both the dynamic frequency shift (effective g -value, g_{eff}) and the peak-to-peak linewidth, additional information is obtained from the same EPR spectrum. Clarkson and coworkers [13] studied the dependence of g_{eff} with operational frequency for several Gd(III) complexes in aqueous solution and showed that at high frequencies (Q-band and higher) g_{eff} is directly proportional to the ZFS-related parameter, Δ^2 :

$$g_{\text{eff}} = g_e \left(1 - \frac{3\Delta^2}{\omega_s} \right). \quad (6)$$

Values of Δ^2 obtained in this manner are very similar to those obtained from line-shape analysis. This approach was further extended by Borel et al. [23] to include

low-frequency data. Borel et al. [23] combined the shift information with the linewidth data and also recorded spectra at various temperatures as well as frequencies in order better define the system.

In the preceding examples, a single time-varying ZFS, often called the dynamic or transient ZFS, was employed that is described by the square of the trace of this ZFS, Δ^2 , and its correlation time, τ_v . This transient ZFS was invoked [24] in studies of octahedral aqua ions such as Mn^{2+} where, by symmetry, there was no ZFS. In solution, collisions with solvent molecules and vibrations could lower symmetry and induce a ZFS and lead to efficient electronic relaxation. Extending these studies on highly symmetric aqua ions to gadolinium contrast agents, it was often overlooked that these compounds should have some static, time-independent ZFS because of the asymmetric ligand field. The Grenoble group [25–29] has taken this static ZFS into account and constructed a spin Hamiltonian that explicitly considers the random rotational motion of the molecular complex. They identify a magnitude for this static ZFS, called \mathbf{a}_2 for the second-order term, and a correlation time for the rotational motion, called τ_R . They have also included higher-order terms for the static ZFS denoted \mathbf{a}_4 and \mathbf{a}_6 . At the level of 2nd order it can be shown that the \mathbf{a}_2 parameter is equivalent to the parameter D . In their terminology the magnitude of the dynamic ZFS is \mathbf{a}_{2T} . This model provided full EPR spectra that were in very good agreement with the observed, multifrequency spectra. The model also allowed for the prediction of T_{1e} values that were in good agreement with those measured by the LODEPR technique (Table 1). For the range of gadolinium complexes studied, the transient (\mathbf{a}_{2T}) and static (\mathbf{a}_2) ZFS both had similar magnitudes.

For Gd(III) the transverse and longitudinal electron spin relaxation functions are linear combinations of four decreasing exponentials. As discussed above, for transverse relaxation these exponentials have different weightings and are field dependent. On the other hand, Belorizky and Fries [30] showed that in the Redfield limit of the theory of electronic relaxation, the longitudinal relaxation function has a quasi-monoexponential decay characterized by a unique relaxation rate $1/T_{1e}$. Neglecting the higher-order terms of the static ZFS, they showed that $1/T_{1e}$ could be given by a simple analytical expression that is contributed to by static and transient ZFS terms:

$$\frac{1}{T_{1e}} = \frac{2}{5} a_2^2 \tau_R \left[\frac{1}{1 + \omega_s^2 \tau_2^2} + \frac{4}{1 + 4\omega_s^2 \tau_2^2} \right] + \frac{12}{5} a_{2T}^2 \tau' \left[\frac{1}{1 + \omega_s^2 \tau'^2} + \frac{4}{1 + 4\omega_s^2 \tau'^2} \right]. \quad (7)$$

Here ω_s is the electron Larmor frequency; τ_R and τ_2 are correlation times for rotational diffusion that modulate the static ZFS and are related by $\tau_2 \equiv \tau_R/6$ (note that in the NMR literature τ_2 is usually defined as τ_R); τ' is a composite correlation time that modulates the transient ZFS and has contributions from a vibrational correlation time, τ_v , and τ_2 such that $1/\tau' \equiv 1/\tau_2 + 1/\tau_v$. Because rotational diffusion is much slower than vibration ($\tau_2 \gg \tau_v$), the static ZFS only contributes to T_{1e} at low

fields; at higher fields $\omega_s \tau_2 \gg 1$ and the first term in Eq. (7) becomes negligible. Belorizky and Fries [30] further showed that Eq. (7) was valid when the Redfield approximation $\omega_s \gg \mathbf{a}_{2T}$ was met, or when the static ZFS contribution to T_{1e} is small with respect to the transient one.

These findings have significant implications for understanding nuclear relaxation and the efficacy of gadolinium complexes as contrast agents. First, external magnetic fields used for clinical imaging are typically at 0.5 T and higher, with the vast majority of imagers operating at 1.5 T. At these field strengths, the contribution of T_{2e} to nuclear relaxation is negligible ($\omega_s \tau_{c2} \gg 1$, Eq. (3)), and T_{1e} is mono-exponential and well described by Eq. (7). Moreover, at $B_0 \geq 0.5$ T, the contribution of the static ZFS to t_{1e} is negligible and Eqs. (3) and (7) are valid for predicting nuclear relaxation over the range of rotational correlation times encountered with contrast agents. The advent of the field cycling relaxometer has allowed numerous studies with nuclear T_1 data from $B_0 = 0.0002$ T and up. Unfortunately, the majority of these studies use the high-field theory to analyze the data and neglect the existence of the static ZFS and its effect on relaxation. As a result, the magnitude of the transient ZFS is overestimated in these papers on NMRD. Likewise, multi-frequency EPR studies that were interpreted without consideration of the static ZFS have also overestimated the magnitude of the transient ZFS. The consequence of this overestimation of transient ZFS is that it predicts that fast electronic relaxation limits the relaxivity achievable at fields used for clinical imaging. To illustrate this point, Figure 4 shows the high-field NMRD curve of MS-325 bound to serum albumin. The solid line is a fit to the data yielding $\mathbf{a}_{2T} = 2.8 \times 10^9$ rad/s (≈ 0.016 T). The dashed line is the calculated relaxivity using $\mathbf{a}_{2T} = 7 \times 10^9$ rad/s (≈ 0.04 T), a value obtained from multifrequency EPR omitting the static ZFS contribution [31] and also found from low-field NMRD (again omitting the static ZFS) [9]. Neglecting the static ZFS leads to estimates of relaxivity for slow tumbling systems that

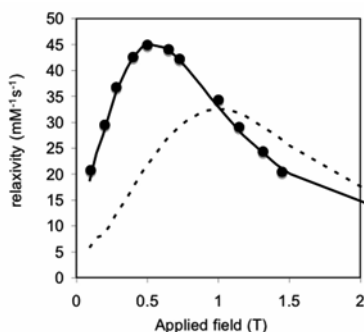


Figure 4. Experimental ^1H relaxivity data (●) for MS-325 bound to HSA [7]. Solid line is fit with $\mathbf{a}_{2T} = 2.8 \times 10^9$ rad/s (≈ 0.016 T). Dashed line is calculated using $\mathbf{a}_{2T} = 7 \times 10^9$ rad/s (≈ 0.04 T) obtained from multifrequency EPR [31] or low-field NMRD [9] studies that omitted static ZFS. Omitting the static ZFS in the multifrequency EPR model leads to T_{1e} values that underestimate proton relaxivity and its field dependence.

are too low and peak at higher frequencies than observed [31]. From the chemist's perspective, it means that electronic relaxation does not limit the relaxivity of GdDTPA-based contrast agents at the common imaging field strength of 1.5 T and that identifying new complexes with longer T_{1e} will not provide any added benefit at 1.5 T and higher fields.

3. CRYSTAL FIELD INTERACTION (*cfi*) PARAMETERS FOR GD(III) COMPLEXES IN GLASSY SOLUTIONS FROM HIGH-FIELD EPR EXPERIMENTS

The importance of accurate estimates for the *cfi* parameters is twofold. As discussed above, the *cfi* affects the electron spin relaxation, and thus contributes to the relaxivity of MRI contrast agents. Second, the *cfi* affects the direction of the electron spin quantization axis, which leads to certain effects in nuclear transition spectra (e.g., electron–nuclear double resonance, ENDOR) that are necessary to take into account in order to accurately determine the electron–nuclear hyperfine interaction (*hfi*) and the distance from the Gd(III) ion to the ligand protons.

As mentioned above, until recently the *cfi* parameters for Gd(III) ions in MRI agents were mainly evaluated in multifrequency continuous wave (CW) EPR measurements, from the dependence of the resonance magnetic field of the $+1/2 \leftrightarrow -1/2$ transition line on the microwave (mw) carrier frequency [13]. For some model complexes of Gd(III), unrelated to the MRI agents, the *cfi* parameters were also determined from CW-EPR measurements performed using magnetically dilute single crystals and glasses [32,33]. Both types of studies are extremely useful in understanding the order of magnitude of the *cfi* parameters; however, neither allows an evaluation of the degree of distribution of these parameters resulting from structural distortions of the complexes. This distribution, however, is of particular relevance for understanding the relaxivity of the MRI agents because it reflects the magnitude of stochastic modulation of the *cfi* in liquids, and is therefore a parameter that has a direct bearing on the relaxivity. While there are no direct experimental ways to measure the dynamics of the *cfi* in liquids, immobilization in frozen glassy solutions (as opposed to single crystals) traps the complexes with different structural conformations that result in statistically distributed magnetic resonance parameters, *cfi* included. Presumably, the distribution range for the structural and magnetic resonance parameters in such a glassy sample approximates that in liquid state, which establishes the relevance of the experiments with glassy samples for elucidating some of the properties of liquid solutions.

With this understanding we initiated a pulsed EPR investigation aimed at evaluating the *cfi* parameters of Gd(III) complexes stabilized in frozen glassy solutions. In our approach, the EPR spectra were recorded as electron spin echo (ESE)-detected field sweeps, which allowed easy detection of the broad featureless components of the EPR spectra of Gd(III) complexes (see below) that are very difficult to observe by CW-EPR.

A combination of cfi and high electron spin of $S = 7/2$ results in the EPR spectra of Gd(III) complexes spreading over the magnetic field range approaching 1 T. To simplify the analysis of such spectra, it is preferable to perform the experiments at a high enough operational mw frequency, ν_{mw} , so that the Zeeman interaction of the electron spin at any EPR position was much greater than the cfi . Therefore, our measurements were performed at $\nu_{mw} \approx 130$ GHz (D-band) [34]. Other authors have used even higher mw frequency of about 240 GHz, although their work was done using CW-EPR [35].

Before considering the results of our pulsed EPR investigations, the necessary theoretical background that will introduce the relevant magnetic resonance parameters and explain the structure of the EPR spectra of Gd(III) complexes is presented. A Gd(III) complex can be adequately characterized by the fine structure spin Hamiltonian

$$H_{FS} = g\beta B_o S_z + D \left(S_{Z_c}^2 - \frac{1}{3} S(S+1) \right) + E(S_{X_c}^2 - S_{Y_c}^2), \quad (8)$$

where g is the electronic g -factor, β is the Bohr magneton, B_o is the external magnetic field, and the parameters D and E account for the quadrupolar part of the cfi . Higher-order terms, although present for Gd(III), are substantially smaller and can be safely neglected [33]. The Hamiltonian, Eq. (8), utilizes two coordinate systems, the laboratory coordinate frame XYZ (where the magnetic field \mathbf{B}_o is parallel to axis Z) and the cfi principal axes frame $X_c Y_c Z_c$. In the conditions of a D-band experiment, for instance, the cfi parameters ($D/g\beta$ and $E/g\beta \sim 50$ mT, see below) are much smaller than the Zeeman term ($B_o \sim 4.5$ T).

The top trace in Figure 5 shows an example of a D-band ESE field-sweep spectrum of a Gd(III) complex in an orientationally disordered system, simulated using the Hamiltonian, Eq. (8), with $D/g\beta = 50$ mT and $E = 0$ (axial cfi tensor). The decomposition of the top spectrum into separate transitions is shown by other traces. To first order in cfi , the singularities of a transition line $m_Z \leftrightarrow m_Z + 1$ ($m_Z = \langle S_Z \rangle$ to first order) are located at

$$\begin{aligned} B_o^\perp &= \frac{h\nu_{mw}}{g\beta} + \frac{1}{2} \cdot \frac{D}{g\beta} (2m_Z + 1), \\ B_o^\parallel &= \frac{h\nu_{mw}}{g\beta} - \frac{D}{g\beta} (2m_Z + 1), \end{aligned} \quad (9)$$

where h is the Planck constant, and B_o^\perp and B_o^\parallel are the resonance magnetic fields corresponding to the perpendicular and parallel orientations of the main cfi axis with respect to \mathbf{B}_o . The total width of the transition line $m_Z \leftrightarrow m_Z + 1$ is thus:

$$\Delta B_o = \left| B_o^\perp - B_o^\parallel \right| = \left| \frac{3}{2} \cdot \frac{D}{g\beta} (2m_Z + 1) \right|. \quad (10)$$

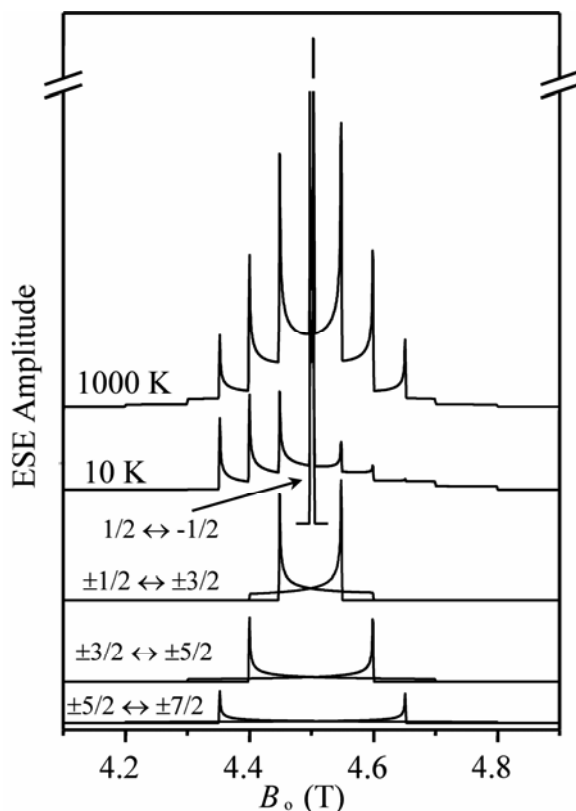


Figure 5. EPR spectra of a Gd^{3+} complex simulated for $\nu_{\text{mw}} = 125.46$ GHz; $g = 1.992$; $D/g\beta = 50$ mT; $E = 0$. The top two traces are the sum of all transitions simulated for the temperatures of 1000 and 10 K, as indicated. Other traces are the contributions of individual EPR transitions to the top spectrum.

Equation (10) predicts a zero width for the $-1/2 \leftrightarrow 1/2$ electron spin transition line, the central line in the EPR spectrum. However, because of second-order effects in *cfi* this width is not exactly zero [36,37], but is about $10D^2/(g\beta)^2B_0$. In high-field experiments this second-order broadening is very insignificant, and this line represents the most narrow and intense feature in the EPR spectrum, unless the experiment is performed at a sufficiently low temperature ($kT < h\nu_{\text{mw}}$, where k is the Boltzmann constant).

The top trace in Figure 5 was simulated for the high-temperature limit ($kT \gg h\nu_{\text{mw}}$). For high-field EPR measurements at cryogenic temperatures, however, the high-temperature approximation is not always valid because the Zeeman energy difference between the states with m_z and $m_z \pm 1$ (expressed in temperature units) is close to 6.2 K for D-band (130 GHz) and 11.5 K for 240 GHz. A more realistic example of the D-band simulation for $T = 10$ K is given by the second trace in Fig-

ure 5. Because significant electron spin polarization takes place, the spectrum for the axial cfi tensor becomes asymmetric. Depending on the sign of D , either the low-field or the high-field side of the spectrum can be prominent. For a rhombic cfi tensor, the spectrum becomes more and more symmetric as E/D approaches $1/3$, and at the limit of $E/D = 1/3$ it is symmetric irrespective of the temperature.

Figure 6 shows the experimental ESE field-sweep spectra of some of the Gd(III) complexes, while Figure 7 gives an expanded view of the central regions of the same spectra. As one can deduce from comparison with Figure 5, the narrow central peak at $g \sim 1.992$ in the experimental spectra belongs to the $-1/2 \leftrightarrow 1/2$ EPR transition. The other transitions contribute to the broad and nearly symmetric background, which is very smooth and virtually featureless, unlike that in Figure 5. Similar featureless spectra were observed by CW-EPR at $\nu_{mw} = 240$ GHz [35].

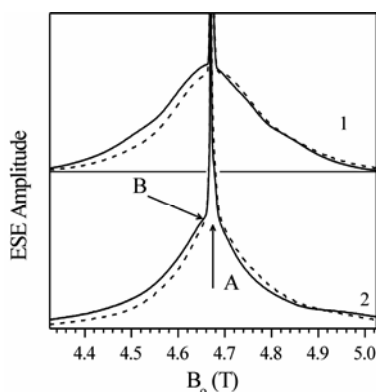


Figure 6. Solid traces 1 and 2, experimental two-pulse ESE field sweep spectra of MRI contrast agent MS-325 and Gd^{3+} aqua complex, respectively. Experimental conditions: $\nu_{mw} = 130.2$ GHz; time interval τ between the mw pulses, 300 ns; durations of the mw pulses, 2×100 ns; temperature, 8 K. Dashed traces 1 and 2, spectra simulated with the parameters D_{cm} and ΔD given in Table 2 for MS-325 and Gd^{3+} aqua complex, respectively. Arrows show field positions (A and B) typical for acquisition of ENDOR spectra.

The featureless appearance of the experimental spectra results from a broad statistical distribution of the cfi parameters. In order to evaluate the cfi parameters from such spectra, the numerical simulations should incorporate two distributions simultaneously, those of D and E/D (the use of independent Gaussian distributions of D and E in [35] was, strictly speaking, incorrect because such an approach did not enforce the condition that $E/D \leq 1/3$). The problem then arises as to which mathematical functions can be used to describe the distributions of D and E/D , and are these distributions correlated or not. While these questions could possibly be dealt with using the method of trial and error, the resulting formal solutions would still require a physical justification. Therefore, we have approached the problem from the opposite direction, by first considering a physical model that would relate

the structure of the Gd(III) complex with the characteristic features of the *cfi* distribution [34]. This model, similar to the superposition approximation of Newman and Urban [38], was based on the assumptions that: (1) the *cfi* tensor associated with a single ligand is axial, with the main axis directed along the Gd–ligand bond; (2) the *cfi* tensors of several ligands are additive, and (3) the *D*-values associated with each ligand, D_1 , are identical.

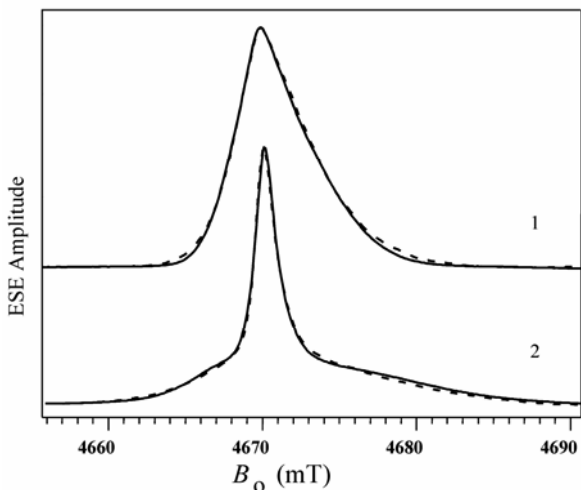


Figure 7. The central region of the experimental and simulated spectra shown in Figure 6.

The superposition model was incorporated in Monte Carlo calculations where the ligands were considered to be randomly distributed on a sphere with the Gd ion in the center. At each step of the calculation, a random structural realization was generated under the constraint that any two ligands should be at least 60° apart, as seen from the center of the sphere. For each realization the *cfi* tensor was calculated and diagonalized. The parameters D and E/D were obtained from the calculated principal values and stored in the D vs. E/D statistical distribution plot. The resulting distributions of D were bimodal (see Fig. 8a) and can approximately be described by two Gaussian functions centered at D_{cnt} and $-D_{\text{cnt}}$, with similar widths (ΔD) and amplitudes. The distributions of E/D (Fig. 8b) can on average be approximated as

$$P(E/D) \propto (E/D) - 2 \cdot (E/D)^2. \quad (11)$$

The numerical simulations of the EPR spectra were performed using the *cfi* distributions predicted by Monte-Carlo structural modeling, with each branch being approximated by a Gaussian function as described above. The purpose of the

simulations was to estimate D_{cnt} and ΔD . The simulations demonstrated that the shape of the $-1/2 \leftrightarrow 1/2$ transition line was sensitive to $\Delta D/D_{\text{cnt}}$, while the shape of the broad background was not, as soon as ΔD was large enough to produce a featureless background. The experimental shape of the $-1/2 \leftrightarrow 1/2$ transition line could usually be reproduced for $|\Delta D/D_{\text{cnt}}| \sim 1/2$. In most cases, a single bimodal distribution was sufficient to describe the EPR spectra (see the simulated spectra for MS-325 shown by traces 1 in Figs. 6 and 7). In some of the complexes, however, the central line itself consisted of a narrow peak and a broader background (e.g., in the Gd(III) aqua complex, Gd_{aq} , see trace 2 in Figs. 6 and 7). In such cases two bimodal distributions were used, with different values of D_{cnt} and ΔD . For simplicity, we will call these distributions tetramodal. The values of D_{cnt} and ΔD obtained in our simulations are summarized in Table 2.

Table 2. *cfi* Parameters D_{cnt} and ΔD Estimated for Various Gd^{3+} Complexes in Glassy Water/Methanol Solutions and in Human Serum Albumin (HSA)^b from Simulations of the ESE Field-Sweep Spectra Using the Superposition Model Described in the Text

Complex	$D_{\text{cnt}}/g\beta$ (mT) ^a	$\Delta D/g\beta$ (mT)	$D (\Delta D)/g\beta$; $E (\Delta E)/g\beta$ (mT) ^c	$\langle D \rangle/g\beta$ (mT)
Gd_{aqua} ^a	28 & 78 (1:2.8)	16 & 34	–	31
GdDOTA	24	12	–20.3 (14.4); 0 (10.0)	23
GdHP-DO3A ^a	30 & 65 (1:1.1)	15 & 32.5	–	–
GdDOTMA	40	20	–	–
GdPDTA ^a	44 & 90 (1:0.82)	20 & 45	–	–
MS-325 ^b	55	26	–	–
GdDTPA	56	26	51.3 (23.5); 13.9 (7.5)	58

Data are compared with the parameters ($D, \Delta D$) and ($E, \Delta E$) from 240 GHz CW-EPR spectra of frozen water/glycerol solutions [35], and the parameter $\langle D \rangle$, calculated using Eq. (13) from the Δ^2 values obtained elsewhere [13].

^a Two bimodal distributions were used in the simulation; relative weight of each distribution is shown in parentheses.

^b MS-325 was measured in both water/methanol glass and in frozen HSA solution and gave the same result in both media.

^c From [35].

The *cfi* parameters obtained this way in D-band experiments were quite close to those later obtained by CW-EPR at 240 GHz (see Table 2) [35]. The latter work, however, did not introduce any physical model to relate the *cfi* parameters with the structure of the complexes, and the EPR simulations were based, as we already mentioned, on formal separate Gaussian distributions of D and E .

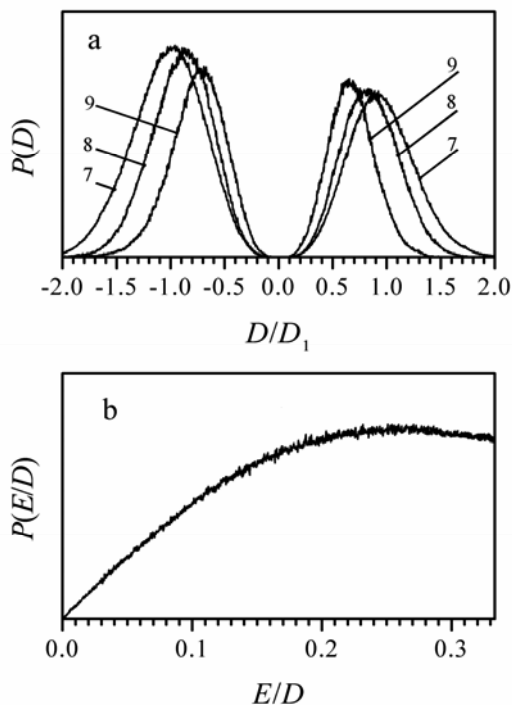


Figure 8. (a) Statistical distributions of D for Gd^{3+} complexes with 7, 8, or 9 (as indicated) ligands stochastically distributed on a sphere around the central ion. D_1 is the D -value for a single ligand. The distributions are obtained by a Monte-Carlo calculation. (b) Statistical distributions of E/D obtained in the same calculation.

The cfi parameters have also been estimated from magnetic relaxation data and from the apparent g -factor shift observed in liquid-state EPR spectra, as described above [13]. In both cases the experimentally determined parameter was $\Delta^2 = \sum D_{ii}^2$, where D_{ii} are the principal values of the cfi tensor that are related to the parameters D and E as

$$\begin{aligned}
 D_{11} &= -\frac{D}{3} + E = -\frac{D}{3} \cdot \left[1 - 3\frac{E}{D} \right], \\
 D_{22} &= -\frac{D}{3} - E = -\frac{D}{3} \cdot \left[1 + 3\frac{E}{D} \right], \\
 D_{33} &= \frac{2D}{3}.
 \end{aligned}
 \tag{12}$$

Assuming, on average, $E/D \sim 1/6$, it is straightforward to estimate the effective value of D that corresponds to a given value of Δ^2 :

$$\langle D \rangle \approx 1.18 \cdot (\Delta^2)^{1/2} \quad (13)$$

The values of $\langle D \rangle$ calculated from the values of Δ^2 given in [13] are given in the last column of Table 2. One can see that they are in good agreement with the D -values found for frozen glassy solutions.

Some of the complexes studied were described by tetramodal cfi distributions. Although the reason for this fact is not immediately clear, the superposition model offers at least one possible explanation. One can see from Figure 8 that D_{cnt} decreases as the number of ligands in the complex increases. Therefore, a tetramodal cfi distribution can, in principle, indicate the existence of two populations of complexes with different numbers of ligands. Another important result that follows from the structural model is that the random distribution of the ligands on a sphere results in a random distribution of orientations of the cfi tensors with respect to any fixed coordinate system. Because of this, the orientation of the cfi tensor becomes completely uncorrelated with the orientation of the hfi tensor of any ligand nucleus (water ligand proton or oxygen), which dramatically simplifies the analysis of the ENDOR spectra.

The distribution of D (and E) determined in frozen glassy solution can be related to the transient ZFS (\mathbf{a}_{2T}) parameter described in Section 2 for aqueous solutions, in that the distribution in D in frozen solution would represent the extent of transient distortions in liquid solution. The results in Table 2 for frozen glassy solutions indicate that ΔD is about half that of D_{cnt} , and this finding is similar to that reported by Rast et al. [25] for GdDTPA and GdDOTA, where their static and transient ZFS parameters \mathbf{a}_2 and \mathbf{a}_{2T} were of similar magnitude.

4. HIGH-FIELD PULSED ENDOR OF WATER LIGANDS IN MRI AGENTS AND THE GEOMETRY OF WATER COORDINATION

4.1. Effect of Weak cfi on Nuclear Transition Frequencies and Appearance of ENDOR Spectra [39]

The theory of ENDOR spectra of high-spin systems with weak cfi is generally similar to that developed for $S = 1/2$. However, there are some cfi -related effects that have to be taken into account in order to be able to accurately estimate the hfi and nqi parameters from the experimental ENDOR spectra. We start with a simple case of nuclear spin $I = 1/2$ (e.g., ^1H , ^{13}C). The spin Hamiltonian appropriate for such nuclei is

$$H_{\text{HF}} = -\nu_1 I_z + a_{\text{iso}} \mathbf{SI} + \mathbf{STI}, \quad (14)$$

where $\nu_1 = g_n \beta_n B_0$ (g_n is the nuclear \mathbf{g} -factor and β_n is the nuclear magneton), a_{iso} is the isotropic hfi constant, and \mathbf{T} is the anisotropic hfi tensor. As in the fine structure

Hamiltonian given by Eq. (8), Z ($\parallel \mathbf{B}_0$) is the axis of the laboratory coordinate frame XYZ.

The ligand *hfi* is considered to be weak compared with the electronic Zeeman and *cf* interactions: $a_{\text{iso}}, T_{ij} \ll g\beta B_0, D, E$. The weak ligand *hfi* practically does not mix electron spin functions, and the various terms of the hyperfine Hamiltonian Eq. (14) can be rearranged as

$$H_{\text{HF}} = (-\nu_I + m_Z A_Z) I_Z + m_Z A_X I_X + m_Z A_Y I_Y, \quad (15)$$

where

$$\begin{aligned} A_X &= T_{ZX} + (a_{\text{iso}} + T_{XX}) \frac{m_X}{m_Z} + T_{YX} \frac{m_Y}{m_Z}, \\ A_Y &= T_{ZY} + T_{XY} \frac{m_X}{m_Z} + (a_{\text{iso}} + T_{YY}) \frac{m_Y}{m_Z}, \\ A_Z &= a_{\text{iso}} + T_{ZZ} + T_{XZ} \frac{m_X}{m_Z} + T_{YZ} \frac{m_Y}{m_Z}, \end{aligned} \quad (16)$$

and the electron spin operators are substituted by their average values: $m_Z = \langle S_Z \rangle$ (to first order), $m_X = \langle S_X \rangle$, and $m_Y = \langle S_Y \rangle$. The nuclear transition frequency for an electron spin manifold with a given m_Z is

$$\nu_{m_Z} = \sqrt{m_Z^2 (A_X^2 + A_Y^2) + (\nu_I - m_Z A_Z)^2}. \quad (17)$$

The electron spin projections on laboratory axes X and Y are generally nonzero and equal to (neglecting the terms quadratic in $(D, E)/g\beta B_0$):

$$\begin{aligned} m_X &\approx \frac{D c_{\theta_c} s_{\theta_c} c_{\varphi_c} - E (c_{\theta_c} s_{\theta_c} c_{\varphi_c} c_{2\psi_c} - s_{\theta_c} s_{\varphi_c} s_{2\psi_c})}{g\beta B_0} (3m_Z^2 - S(S+1)), \\ m_Y &\approx \frac{D c_{\theta_c} s_{\theta_c} s_{\varphi_c} - E (c_{\theta_c} s_{\theta_c} s_{\varphi_c} c_{2\psi_c} + s_{\theta_c} c_{\varphi_c} s_{2\psi_c})}{g\beta B_0} (3m_Z^2 - S(S+1)), \end{aligned} \quad (18)$$

where “*s*” and “*c*” with subscripts φ_c , θ_c , and ψ_c ($2\psi_c$) denote sines and cosines of the Euler angles φ_c , θ_c , and ψ_c describing the orientation of the *cfi*-related coordinate system $X_c Y_c Z_c$ with respect to the laboratory coordinate system XYZ [40]. They are the angles of three consecutive rotations: (1) around Z_c by φ_c , (2) around the new Y_c by θ_c , and (3) around the new Z_c by ψ_c . The situation with all the angles equal to zero corresponds to XYZ coinciding with $X_c Y_c Z_c$.

One can see that the *cfi* contributes to the effective *hfi* values A_k (see Eqs. (16) and (18)), and therefore the nuclear transition frequencies and the shape of ENDOR spectra will depend on the magnitude of the *cfi* parameters and on the orientations of \mathbf{B}_0 and the *hfi* tensor, \mathbf{T} , in the *cfi* reference frame. The effect of the

cfi can be immediately appreciated if we assume $v_1 \gg m_Z A_Z$ (so-called weak hfi limit) and expand Eq. (17) retaining only the terms linear in hfi :

$$\begin{aligned} v_{m_Z} &\approx v_1 - (a_{\text{iso}} + T_{ZZ})m_Z - T_{XZ}m_X - T_{YZ}m_Y \approx \\ &\approx v_1 - (a_{\text{iso}} + T_{ZZ})m_Z - \frac{Dc_{\theta_c}s_{\theta_c}}{g\beta B_o} (3m_Z^2 - S(S+1)) \cdot (c_{\phi_c} T_{XZ} + s_{\phi_c} T_{YZ}), \end{aligned} \quad (19)$$

where we have also assumed for simplicity $E = 0$ and substituted explicit expressions for m_X and m_Y (Eq. (18)). The first two terms in this expression give the usual nuclear transition frequency (accurate to first order in hfi) that would be observed for $D = 0$. The third term gives the correction to the nuclear transition frequency due to the cfi .

The effective magnitude of the cfi -related term relative to that of the anisotropic hfi term is thus given by

$$R_{\text{cfi/hfi}} = \frac{Dc_{\theta_c}s_{\theta_c}}{g\beta B_o} \cdot \frac{(3m_Z^2 - S(S+1))}{m_Z}. \quad (20)$$

With $S = 7/2$, the factor $(3m_Z^2 - S(S+1))/m_Z$ in Eq. (20) equals ∓ 30 , ∓ 6 , ± 1.2 , and ± 6 for the electron spin manifolds with $m_Z = \pm 1/2$, $\pm 3/2$, $\pm 5/2$, and $\pm 7/2$, respectively. One can see that the relative deviations of nuclear transition frequencies from those determined by the hfi only are the largest for the electron spin manifolds with $m_Z = \pm 1/2$. Since $|c_{\theta_c}s_{\theta_c}| \leq 1/2$, one can write

$$\left| R_{\text{cfi/hfi}} \right| \leq \left| \frac{15D}{g\beta B_o} \right|. \quad (21)$$

It follows from Eq. (21) that even if the condition of weak cfi is satisfied very well (e.g., $D/g\beta B_o \sim 0.1$), the cfi -related distortion for $m_Z = \pm 1/2$ may be comparable with the hfi term at least for some relative orientations of the cfi and hfi tensors. This means that the weak interaction condition in terms of EPR does not guarantee the absence of noticeable distortions in an ENDOR spectrum. The situation is substantially better for $m_Z = \pm 3/2$ and $\pm 7/2$, for which $R_{\text{cfi/hfi}}$ is about 80% smaller than that for $m_Z = \pm 1/2$, and the minimal cfi contribution is reached for $m_Z = \pm 5/2$.

These considerations present an experimenter with a choice as to what EPR transition is better to use for pulsed ENDOR measurements. From the standpoint of minimizing the cfi distortions in the ENDOR spectra and simplifying their *analysis*, the best EPR transitions to use are those involving the electron spin manifolds with $m_Z = \pm 5/2$. However, the width of ENDOR lines from $m_Z = \pm 5/2$ manifolds in a disordered system is five times greater, and the amplitude is correspondingly smaller, than those of the lines from the $m_Z = \pm 1/2$ manifolds. On the other hand, unless an extreme electron spin polarization is present, the most intense transition in the EPR spectrum is that between $m_Z = 1/2$ and $-1/2$ (see Fig. 5). Therefore, the

detection of the ENDOR spectra is best achieved for the $-1/2 \leftrightarrow 1/2$ EPR transition. In addition, the ENDOR spectra associated with this transition are the only ones that can be efficiently separated from contributions of other transitions in a system with a distributed *cfi*. This actually makes the $-1/2 \leftrightarrow 1/2$ EPR transition the only practical choice for pulsed ENDOR experiments at the temperatures when this transition dominates the EPR spectrum.

If the $-1/2 \leftrightarrow 1/2$ EPR transition is to be used for pulsed ENDOR measurements, one should obtain a clear idea about the potential distortions of the ENDOR spectrum caused by the *cfi* at given experimental conditions. To address this problem, we performed numerical simulations of ^1H ENDOR spectra of $m_z = \pm 1/2$ manifolds in a disordered system, taking into account the fact that the orientations the *hfi* and *cfi* tensors are mutually uncorrelated (i.e., their orientations are statistically distributed with respect to each other; see the previous section). The *hfi* was taken to be purely anisotropic ($a_{\text{iso}} = 0$) and axial. The axial *hfi* tensor can be fully characterized by its principal components, A_{\perp} and A_{\parallel} :

$$\begin{aligned} A_{\perp} &= a_{\text{iso}} + T_{\perp}, \\ A_{\parallel} &= a_{\text{iso}} - 2T_{\perp}, \end{aligned} \tag{22}$$

which correspond to the perpendicular and parallel orientations of the main *hfi* axis with respect to the magnetic field vector \mathbf{B}_0 . T_{\perp} in Eq. (22) is the perpendicular (minor) principal component of the axial anisotropic *hfi* tensor.

The spectra calculated for various ratios of $D/g\beta B_0$ are shown in Figure 9. Figure 9 (bottom) shows the ENDOR spectrum for $D = 0$. This spectrum is similar to what one expects to observe for an $S = 1/2$ system in the case of purely dipolar coupling between the electron and nuclear spins. The peaks in this spectrum are separated by the *hfi* constant $A_{\perp} = T_{\perp}$, while the shoulders are separated by the *hfi* constant $A_{\parallel} = -2T_{\perp}$. As D increases (Fig. 9, middle and top traces), the A_{\perp} peaks keep their shape and remain at the same positions, while the A_{\parallel} shoulders become progressively broader (as the detailed analysis shows, this broadening is actually caused by the *inner* parts of the ENDOR lines being displaced from their positions by the *cfi* effect) [39]. In such a situation, starting from $D/g\beta B_0 > 0.02$, neglecting the effect of *cfi* can result in slight overestimation of A_{\parallel} and, as a result, in some overestimation of both T_{\perp} and a_{iso} .

For the MRI agents listed in Table 2 the values of $D/g\beta$ are well within 100 mT. Therefore, the $-1/2 \leftrightarrow 1/2$ EPR transition can be readily used for ENDOR measurements of these complexes at the $B_0 > 3$ T, which corresponds to the operational mw frequencies $\nu_{\text{mw}} > 84$ GHz (W-band). The analysis of the ENDOR spectra at such high-field conditions can be performed without taking account of the *cfi*. However, for most of the MRI agents even the K_a band ($B_0 \sim 1$ T, $D/g\beta B_0 < 0.1$) pulsed ENDOR works reasonably well, although in this case it is better if the *cfi* corrections are taken explicitly into account in the numerical simulations. The

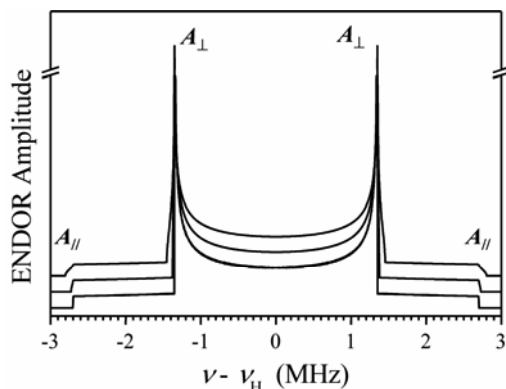


Figure 9. ^1H ENDOR spectra simulated for $B_0 = 4.65$ T, $a_{\text{iso}} = 0$, and $T_{\perp} = -2.7$ MHz. The cfi parameter $D/g\beta = 0, 50$, and 100 mT for the bottom, middle, and top spectra, respectively. The cfi parameter $E = 0$ in all spectra (axial cfi tensor).

historically used K_u band ($B_0 \sim 0.5$ T, $D/g\beta B_0 < 0.2$) probably represents the low-frequency (and field) mw band where meaningful ^1H pulsed ENDOR of some of the MRI agents is still possible, but including the cfi in the analysis of the spectra becomes an absolute necessity [39].

4.2. ^{17}O ENDOR Frequencies at High Field [40]

The previous section dealt with ENDOR spectra of nuclei with spin $I = 1/2$ (^1H , ^{13}C). The general considerations regarding the cfi -related effects made in that section are also applicable to nuclei of higher spin. In this section the expressions for the ENDOR frequencies of the ^{17}O nucleus that has spin $I = 5/2$ and non-negligible nqi are presented. As established above, the interpretation of the high-field ($B_0 > 3$ T, $\nu_{\text{mw}} > 84$ GHz) ENDOR spectra of the MRI contrast agents can be done without taking the cfi into account. In addition, at high fields the nuclear Zeeman interaction of ^{17}O becomes much stronger than the hfi and nqi , which allows one to obtain simple expressions for the ^{17}O ENDOR frequencies using a first order perturbation theory.

The spin Hamiltonian accounting for the ^{17}O Zeeman interaction, hfi , and nqi in the high-field approximation can be written as follows:

$$H = -\nu_0 I_z + m_z (a_{\text{iso}} + T_{zz}) I_z + Q I_z^2, \quad (23)$$

where $Q = \frac{3}{2} k [3b_{zz}^2 - 1 + \eta(b_{xz}^2 - b_{yz}^2)]$, k is the nuclear quadrupole coupling constant ($k = e^2 Q q / [4I(2I - 1)\hbar]$), and η is the asymmetry parameter of the electric field gradient on the ^{17}O nucleus. b_{xz} , b_{yz} , and b_{zz} are the direction cosines of the laboratory axis Z in the nqi principal axes frame $X'Y'Z'$. The frequencies of ENDOR transitions between the energy levels that correspond to the ^{17}O spin projections m_1 and $m_1 + 1$ ($m_1 \equiv \langle I_z \rangle$) are given by

$$\nu_{m_1 \leftrightarrow m_1 + 1} = -\nu_0 + m_z (a_{\text{iso}} + T_{zz}) + Q(2m_1 + 1). \quad (24)$$

Therefore, in this approximation, $\nu_{-1/2 \leftrightarrow 1/2}$ is not affected by the nqi at all, while $\nu_{\pm 1/2 \leftrightarrow \pm 3/2}$ and $\nu_{\pm 3/2 \leftrightarrow \pm 5/2}$ are shifted from $\nu_{-1/2 \leftrightarrow 1/2}$ by $\pm 2Q$ and $\pm 4Q$, respectively. These shifts are orientation dependent, and in an orientationally disordered system the nqi term leads to the broadening and decrease in amplitude of the $\nu_{\pm 1/2 \leftrightarrow \pm 3/2}$ and $\nu_{\pm 3/2 \leftrightarrow \pm 5/2}$ lines. The maximal value of Q is $3k$ (reached for $b_{z'z} = 1$), and for the water oxygen with $k \sim 0.16$ MHz (for H_2O ice [41], $e^2Qq/h \sim 6.5$ MHz) we may expect the shifts of up to $6k \sim 1$ MHz for $\nu_{\pm 1/2 \leftrightarrow \pm 3/2}$ and $12k \sim 2$ MHz for $\nu_{\pm 3/2 \leftrightarrow \pm 5/2}$. The shape of ^{17}O ENDOR spectrum for disordered case calculated in accordance with Eq. (24) is shown in Figure 10.

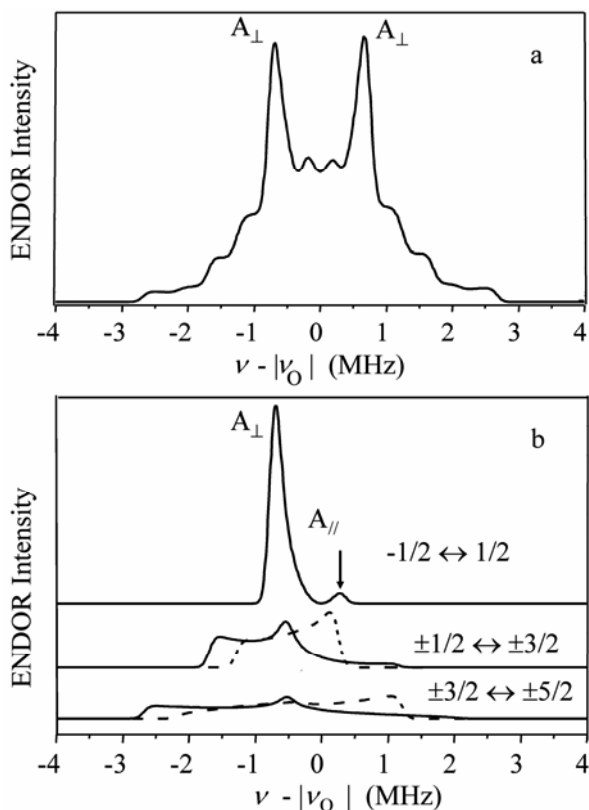


Figure 10. (a) Simulated Mims ^{17}O ENDOR spectrum for the $m_s = \pm 1/2$ electron spin manifolds. Simulation parameters: $a_{\text{iso}} = 0.75$ MHz [51] (central value); $\Delta a_{\text{iso}} = 0.3$ MHz (the width of Gaussian distribution around the central value); $T_{\perp} = 0.69$ MHz; $e^2Qq/h = 6.5$ MHz [41]; $\eta = 1$; $\varphi_{\text{hq}} = 0^\circ$; $\theta_{\text{hq}} = 35^\circ$; $\psi_{\text{hq}} = 0^\circ$. (b) Lines of various ^{17}O transitions within $m_s = -1/2$ electron spin manifold. The m_l values involved in the transitions are shown near the traces. For the two bottom groups of spectra, the solid traces correspond to $m_l < 0$, while the dashed traces correspond to $m_l > 0$. The A_{\parallel} turning point is shown for the $-1/2 \leftrightarrow +1/2$ transition only.

4.3. Practical Aspects of Pulsed ENDOR Spectroscopy of MRI Agents

There are two widely used pulsed ENDOR techniques, one of which after Davies [42] and the other after Mims [43]. The hyperfine interactions of the ligand nuclei we are interested in have magnitudes (see below) that permit the use of both types of pulsed ENDOR spectroscopy. The comparative experiments have shown, however, that better spectra could be obtained using Mims ENDOR, and this was therefore the technique used in all of our practical measurements of MRI agents.

In Mims ENDOR, one monitors the amplitude of the three-pulse (stimulated) ESE signal while sweeping the frequency of the radiofrequency (RF) pulse. The ENDOR effect is observed as a decrease of the stimulated ESE amplitude. For Gd(III) complexes, the ESE signal at virtually any EPR position contains contributions from several different EPR transitions. For example, the center of the EPR spectrum (see Fig. 6, position A) has contributions from all possible transitions: $-1/2 \leftrightarrow -1/2$, $\pm 1/2 \leftrightarrow \pm 3/2$, etc. However, in order to simplify the interpretation of the ENDOR spectra and to enable a quantitative analysis of their amplitudes, we are mostly interested in the spectra associated with the $-1/2 \leftrightarrow 1/2$ EPR transition only. To separate these spectra from those due to other EPR transitions, the following procedure was used. For the Mims ENDOR spectra presented in Figure 11a, traces 1 and 2 were measured at the EPR position A (see Fig. 6), where all transitions contribute, and at EPR position B, where all EPR transitions contribute *except* the $-1/2 \leftrightarrow 1/2$ one. Trace 2, after respective normalization, was then subtracted from trace 1, resulting in the difference spectrum presented in Figure 11b. The difference spectrum contains contributions from the $-1/2 \leftrightarrow 1/2$ EPR transition only. In some applications there was interest in comparing the numbers of ligand nuclei contributing to the ENDOR spectra from different samples. These comparisons are based on the fact that in pulsed ENDOR there is a general proportionality between the amplitude of spectral lines and the number of nuclei contributing to those lines. In addition, the Mims ENDOR effect for a given EPR transition is proportional to the amplitude of the ESE signal from that transition. Therefore, the difference ENDOR spectrum has to be normalized by the amplitude of the ESE signal without RF, or when the RF is not in resonance with any of the magnetic nuclei. For brevity, we will refer in the following text to a such a difference, normalized spectrum, which is related solely to the $-1/2 \leftrightarrow 1/2$ transition, as an "ENDOR spectrum," unless otherwise stipulated.

The purpose of our pulsed ENDOR experiments was to study the MRI contrast agents and their models in frozen glassy aqueous solutions. However, water does not form a glass upon freezing. Therefore, experiments were performed using a 1:1 (v:v) water-methanol solution (WMS). This standard solution (abbreviated as sWMS) has about a minimum methanol content that still allows the solution to form a glass when frozen. The water:methanol molar ratio in sWMS is about 0.7:0.3, and the molar ratio of the water protons to the methanol OH protons is about 0.82:0.18, which ensures that most of the hydroxyl protons in the Gd coordination sphere comes from water. This consideration assumes, however, that H₂O

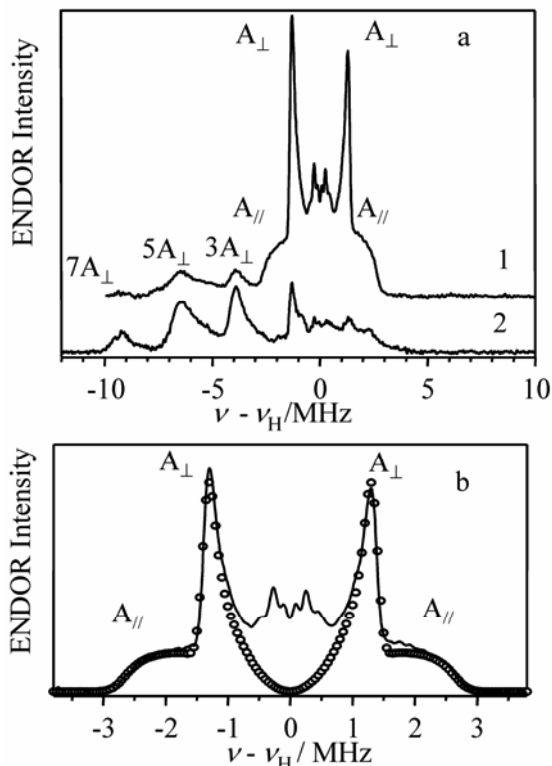


Figure 11. (a) ^1H Mims ENDOR spectra of Gd^{3+} aqua complex. Trace 1, recorded at $B_0 = 4670$ mT (at the maximum of $-1/2 \leftrightarrow 1/2$ electron spin transition line). Trace 2, recorded at $B_0 = 4646$ mT (off the limits of $-1/2 \leftrightarrow 1/2$ electron spin transition line). (See typical field positions in Fig. 6). Experimental conditions: $\nu_{\text{mw}} = 130.2$ GHz; time interval τ between the 1st and 2nd mw pulses, 130 ns; time interval T between the 2nd and 3rd mw pulses, 50 μs ; durations of the mw pulses, 3×50 ns; duration of the RF pulse, 30 μs ; temperature, 8 K. Labels " A_{\perp} " and " A_{\parallel} " denote the A_{\perp} and A_{\parallel} features of the lines of proton transitions within the electron spin manifolds with $m_S = \pm 1/2$. Labels " $3A_{\perp}$ ", " $5A_{\perp}$," and " $7A_{\perp}$ " denote the A_{\perp} features of the lines of proton transitions within the electron spin manifolds with $m_S = -3/2, -5/2,$ and $-7/2$, respectively. (b) Solid trace, the difference between traces 1 and 2 in (a). Before subtraction, the amplitudes of traces 1 and 2 were adjusted in accordance with respective ESE amplitudes. This difference spectrum contributed solely by the proton transitions within the electron spin manifolds with $m_S = \pm 1/2$. Open circles, simulated with the following parameters: $a_{\text{iso}} = 0$ MHz; central $T_{\perp} = -2.7$ MHz; Gaussian distribution width for T_{\perp} , $\Delta T_{\perp} = 0.35$ MHz; $D/g\beta = 30$ mT.

and CH_3OH coordinate to Gd with equal probability. It may thus contain a pitfall because the relative affinities of the Gd(III) ion to water and methanol ligands are not known a priori. This question was addressed in a series of water:methanol titration experiments (described in §4.7), which indicated that water is actually preferred over methanol as a ligand for Gd(III).

4.4. Experimental ^1H ENDOR Spectra

The D-band ^1H Mims ENDOR spectra of the Gd^{3+} aqua ion, Gd_{aq} , obtained at the maximum of the $-1/2 \leftrightarrow 1/2$ EPR transition line (EPR position A in Fig. 6), and at a lower B_0 (EPR position B in Fig. 6) are shown in Figure 11 by traces 1 and 2, respectively. The difference spectrum A–B associated solely with the $-1/2 \leftrightarrow 1/2$ EPR transition is shown by the solid trace in Figure 11b. This spectrum, apart from certain amplitude distortions introduced by Mims ENDOR [43], can be described as a typical “Pake doublet,” which is a powder lineshape in the case of an axial anisotropic *hfi* tensor.

Labels “ A_{\perp} ,” “ $3A_{\perp}$,” “ $5A_{\perp}$,” and “ $7A_{\perp}$ ” in Figure 11 mark the A_{\perp} maxima of the nuclear transition lines that belong to the electron spin manifolds with $m_z = \pm 1/2, -3/2, -5/2,$ and $-7/2$, respectively. Labels “ A_{\parallel} ” indicate the positions of the A_{\parallel} shoulders for the nuclear transitions that belong to $m_z = \pm 1/2$. As the experiments were performed at $\nu_{\text{mw}} \approx 130$ GHz (~ 6 K in the temperature units) and at the temperature of ~ 8 K, there was a considerable difference in the populations of electron spin states and, correspondingly, a substantial difference in the intensities of EPR lines. For this reason, the ENDOR lines “ $3A_{\perp}$,” “ $5A_{\perp}$,” and “ $7A_{\perp}$ ” for $m_z = 3/2, 5/2,$ and $7/2$ (located at $\nu > \nu_{\text{H}}$) are virtually unobservable.

Direct reading of the line positions shows that $|A_{\perp}| \cong |A_{\parallel}|/2$, and therefore $a_{\text{iso}} \approx 0$. Numerical simulations that reproduce the observed linewidth yielded the following *hfi* parameters: $|a_{\text{iso}}| < 0.01$ MHz; $T_{\perp} = -2.70 \pm 0.01$ MHz. In order to reproduce the ENDOR linewidth, the anisotropic *hfi* constant was Gaussian-distributed with a width between the maximum slope points of $\Delta T_{\perp} = 0.35$ MHz. The spectrum simulated using these parameters is shown by open circles in Figure 11b. Assuming that the anisotropic *hfi* is fully determined by the spin population on the central Gd(III) ion, one can estimate the Gd–proton distance as

$$r_{\text{GdH}} \approx \sqrt[3]{\frac{g\beta g_{\text{H}}\beta_n}{hT_{\perp}}}, \quad (25)$$

where g_{H} is the proton *g*-factor, all other parameters having already been defined. The value of r_{GdH} obtained for $T_{\perp} = -2.70$ MHz from this expression equals 3.1 ± 0.05 Å. This distance corresponds to protons of water molecules directly coordinated to the central ion. The accuracy of this estimate will be discussed below.

In the case of MRI agents, the shape of ENDOR spectra is more complicated (see Fig. 12, top panel). Similar to the spectrum of Gd_{aq} , the A_{\perp} peaks separated by ~ 2.65 MHz are present, although they have significantly smaller intensity than those in the spectrum of Gd_{aq} . This is understandable because the MRI agents can coordinate no more than two water molecules, as compared with eight in Gd_{aq} . The spectra also show additional peaks separated by ~ 1.45 and 0.95 MHz that can be attributed to numerous non-exchangeable methylene protons that are rather close to the central ion (Fig. 2 for structures). Indeed, these lines are present in the ^1H ENDOR spectrum recorded for a deuterated solution (Fig. 12, top panel, bottom trace), which confirms that they originate from the non-exchangeable protons of the multidentate ligand.

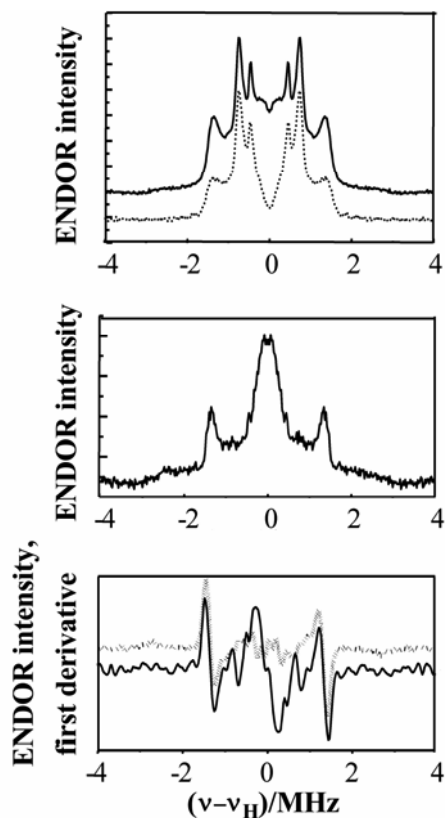


Figure 12. Top panel: ^1H Mims ENDOR spectra of **Gd(L'1)** acquired in protonated ($\text{CD}_3\text{OH}/\text{H}_2\text{O}$, solid line) and deuterated ($\text{CD}_3\text{OD}/\text{D}_2\text{O}$, dashed line) standard water/methanol solutions. Middle panel: ^1H Mims ENDOR spectrum of exchangeable protons obtained as difference of spectra from top panel. Bottom panel, solid line: first derivative of ENDOR spectrum of middle panel; dashed line: ^1H Mims ENDOR spectrum of Gd^{3+} aqua complex, intensity divided by 4.5. Experimental conditions: $\nu_{\text{mw}} = 29.2$ GHz; $B_0 = 1047.5$ mT for maximum of $1/2 \leftrightarrow -1/2$ transition; mw pulses, 3×15 ns; $\tau = 130$ ns; $T = 40$ μs ; $T_{\text{RF}} = 34$ μs ; temperature, 7 K.

Obviously, the spectrum of *exchangeable* protons can be obtained by subtracting the latter from the former, and the result of such a subtraction is shown in Figure 12, middle panel. As seen from Figure 12, the spectrum of exchangeable protons contains a rather broad featureless line from distant protons (second coordination sphere, etc.) that overlaps with the well-defined lines from the protons of directly coordinated water molecules. The *hfi* parameters of the latter protons, within the limits of the experimental accuracy (0.05 MHz), are the same as those for Gd_{aq} , namely $T_{\perp} \approx -2.70$ MHz and $a_{\text{iso}} \approx 0$. The anisotropic *hfi* distribution width in the MRI agents was also found to be similar to that in Gd_{aq} .

The similarity in hfi parameters and hence Gd–H_{water} distance among the various contrast agents studied [34,39,44] has significant implications for the design of new agents and the interpretation of relaxivity data of existing agents. Nuclear relaxation of coordinated water has a $1/r_{\text{GdH}}^6$ dependence, and if this distance could be shortened by structural manipulation, then relaxivity could be significantly increased. Literature values of r_{GdH} ranged from as much as 2.5–3.3 Å [45,46]. Even among very similar complexes such as GdDTPA and its derivatives like MS-325 and GdEOB-DTPA, differences in r_{GdH} as much as 0.3 Å were reported [47,48]. These distances were indirect estimates based often on nuclear relaxation data. The ENDOR studies described above, which measure this key parameter directly, clearly indicate that r_{GdH} is not a value that varies significantly and that differences in relaxivity among different Gd(III) complexes are not a result of different r_{GdH} distances.

4.5. Experimental ¹⁷O ENDOR Spectra

The relationship between the ¹H anisotropic hfi and r_{GdH} may potentially be more complicated than that given by Eq. (25) because of spin delocalization to the oxygen atom directly coordinated to Gd. It is well known from numerous examples of $S = 1/2$ systems that already the spin population on oxygen, ρ_{O} , as small as 4% makes a contribution to the hfi of the ligand proton comparable with that from the central ion [49]. Therefore, the evaluation of ρ_{O} is a crucial element in establishing the relationship between the proton anisotropic hfi and r_{GdH} .

The spin delocalization from f -ions to the ligands is usually extremely small [36]. The analysis of the hfi data for ¹⁹F nuclei in complexes of fluorine with rare earth ions (Tm(II), Yb(III), Eu(II)) shows that the spin population on a fluorine ligand is about $0.2 \pm 0.1\%$ [36,50]. NMR of liquid solutions gives $\rho_{\text{O}} \leq 0.4\%$ [51]. These values are too small to result in any meaningful correction to the Gd–proton hfi . However, the experimental conditions of NMR and ENDOR experiments are different, and therefore this parameter has to be directly determined. This can be achieved by analysis of high-field ¹⁷O ENDOR spectra of Gd_{aq} and MRI agents.

The Gd_{aq} ¹⁷O ENDOR spectrum is presented in Figure 13. Apart from the central broad feature that may be, at least in part, attributed to distant matrix oxygens, this spectrum can be described as consisting of two narrow peaks with a splitting of ~1.33 MHz between them, and two sets of shoulders with splittings of about 3.3 and 5.1 MHz. In view of the preceding theoretical considerations, which have shown that $-1/2 \leftrightarrow 1/2$ nuclear transitions are not affected by nqi (to first order), the narrow peaks can be safely attributed to the $\nu_{-1/2 \leftrightarrow 1/2}$ frequencies at the perpendicular orientation of the hfi tensor axis relative to \mathbf{B}_0 . These peaks are therefore denoted as A_{\perp} to indicate that the splitting between them equals the hfi constant A_{\perp} (see Eq. (22)). Based on analysis of Eq. (24), it is anticipated that the two pairs of shoulders with the splittings of about 3.3 and 5.1 MHz are quite likely to be attributed to $\nu_{\pm 1/2 \leftrightarrow \pm 3/2}$ and $\nu_{\pm 3/2 \leftrightarrow \pm 5/2}$, respectively, and their positions are determined by both hfi and nqi .

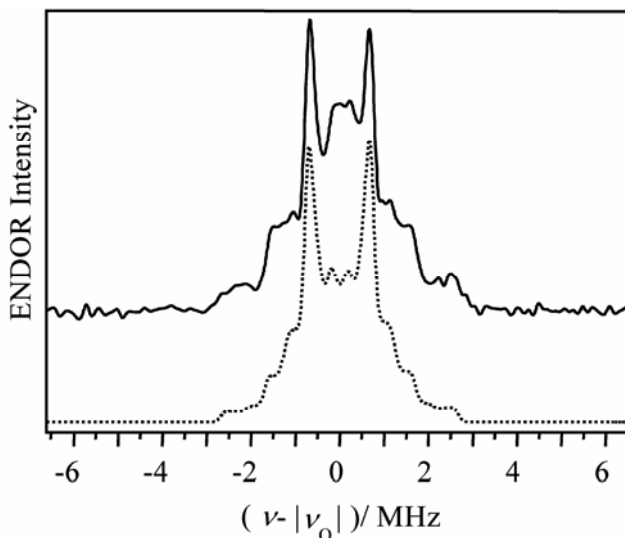


Figure 13. Solid trace: ^{17}O Mims ENDOR spectra of Gd aqua complex. Experimental conditions: mw frequency, 94.7 GHz; durations of the mw pulses, 60 ns; time interval τ between the first and second mw pulses, 200 ns; time interval T between the second and third mw pulses, 40 μs ; rf pulse duration, 35 μs . $B_0 = 3.3966$ T for maximum of $1/2 \leftrightarrow -1/2$ transition; dashed trace: simulated spectrum, which was shown in Figure 6a.

Numerical simulations of the spectra resulted in central hfi values of $a_{\text{iso}} = 0.75 \pm 0.05$ MHz and $T_{\perp} = 0.69 \mp 0.05$ MHz and a Gaussian distribution of a_{iso} with the width between the maximum slope points of $\Delta a_{\text{iso}} = 0.3$ MHz. The derived value of $A_{\perp} = a_{\text{iso}} + T_{\perp} = 1.44$ MHz is slightly greater than the observable splitting of 1.33 MHz as a result of the hfi distribution. The two sets of shoulders in the simulated spectra were sensitive to the nqi parameters. The simulations yielded $k = 0.175 \pm 0.012$ MHz ($e^2Qq/h = 7 \pm 0.5$ MHz) and $\eta \geq 0.8$. An example of a simulated spectrum is shown by the dashed line in Figure 13. The spectra could be successfully simulated for any angle between the Gd–oxygen vector, \mathbf{R}_{GdO} , and the HOH plane (that determines the orientation of the nqi tensor), as long as the HOH plane was perpendicular to the plane formed by \mathbf{R}_{GdO} and the HOH bisector.

The ^{17}O ENDOR spectra of several contrast agents capable of water coordination are shown in Figure 14. Their shape is very close to that of the spectrum of Gd_{aq} , the only difference being the relative amplitude of a central narrow feature due to distant ^{17}O (as confirmed by the spectrum of an MRI agent that does not coordinate water; see Fig. 15). Therefore, within the limits of experimental accuracy, the hfi and nqi parameters of the water ligand ^{17}O in MRI agents are the same as those in Gd_{aq} .

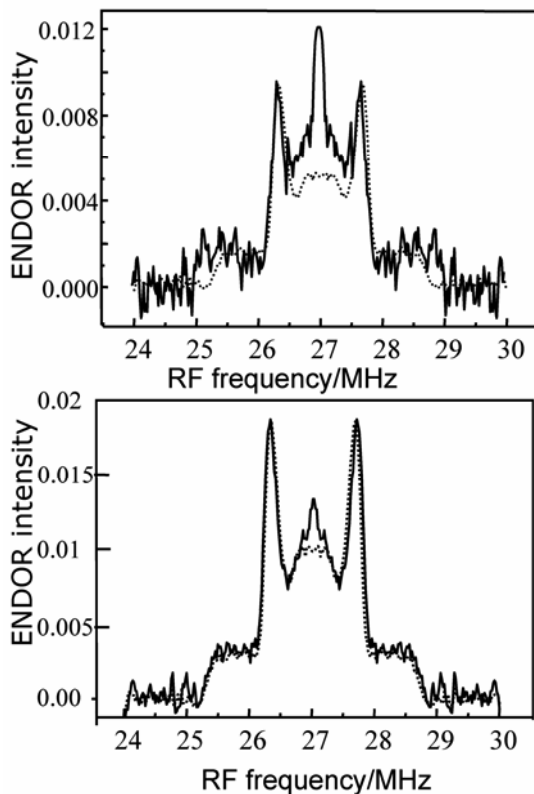


Figure 14. Solid lines, ^{17}O Mims ENDOR spectra of **Gd(L1)** (left panel) and **Gd(L2)** (right panel) in sWMS. Dashed lines, ^{17}O Mims ENDOR spectrum of Gd_{aq} . The amplitude of the Gd_{aq} spectrum is divided by 8 in right panel and by 4 in left panel panels. Experimental conditions: $\nu_{\text{mw}} = 130.2$ GHz ; $B_0 = 4.670$ T (for maximum of $1/2 \leftrightarrow -1/2$ transition); mw pulses, 3×30 ns; $\tau = 200$ ns; $T = 80$ μs ; $T_{\text{RF}} = 72$ μs ; temperature, 8 K.

4.6. Interpretation of ^{17}O hfi and nqi Parameters in Terms of Electronic and Geometrical Structure

The spin population ρ_0 can be evaluated [36] from the experimental a_{iso} :

$$a_{\text{iso}} \approx \frac{1}{2S} [a_s c_s + a_p (1 - c_s)] \rho_0, \quad (26)$$

where, $a_s \approx -5260$ MHz, $a_p \approx -120$ MHz [52,53], S is the electron spin of Gd(III) ($S = 7/2$), and c_s is the s -character of the hybrid orbital where this spin population is located. For an sp^3 hybrid, which is a reasonable approximation for the oxygen

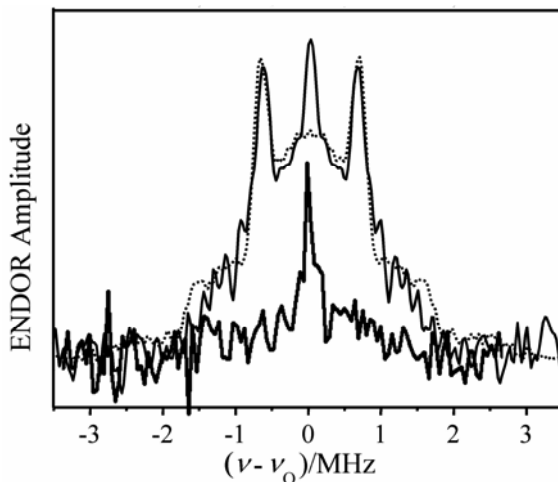


Figure 15. ^{17}O Mims ENDOR spectra of $\text{Gd}(\text{L}'1)$, $\text{Gd}(\text{L}0)$ (top and bottom solid traces), and Gd_{aq} (dashed trace). The amplitude of the Gd_{aq} spectrum is divided by 8. Experimental conditions: $\nu_{\text{mw}} = 94.7$ GHz; $B_0 = 3.3967$ T (for maximum of $1/2 \leftrightarrow -1/2$ transition); mw pulses, 3×30 ns; $\tau = 200$ ns; $T = 40$ μs ; $T_{\text{RF}} = 35$ μs ; temperature, 7 K.

orbitals in a water molecule, $c_s = 1/4$. Using Eq. (26) with $a_{\text{iso}} = 0.75$ MHz, one obtains $\rho_{\text{O}} \approx 4 \times 10^{-3}$.

The ^{17}O anisotropic *hfi* consists mainly of two contributions—from the spin population on Gd(III), ρ_{Gd} , and the spin population ρ_{O} :

$$T_{\perp} \approx -\frac{g\beta g_{\text{O}}\beta_n}{hR_{\text{GdO}}^3}\rho_{\text{Gd}} + \frac{b_p}{2S}(1-c_s)\rho_{\text{O}}, \quad (27)$$

where g_{O} is the ^{17}O nuclear *g*-factor and $b_p \approx 170$ MHz [52,53]. Using $\rho_{\text{O}} \approx -4 \times 10^{-3}$ estimated from Eq. (26), the second term in Eq. (27) is found to be approximately -0.07 MHz, or about 10% of the experimental T_{\perp} value. Neglecting this correction will result in an error in the r_{GdO} estimate of only about 3%. The range of T_{\perp} values obtained from our ENDOR experiments ($T_{\perp} = 0.69 \pm 0.05$ MHz) translates into the range of possible distances r_{GdO} between 2.35 and 2.45 Å that is consistent with the range of distances known from x-ray studies [2].

The contribution of $\rho_{\text{O}} \approx -4 \times 10^{-3}$ to the effective anisotropic *hfi* constant of a water ligand proton, as follows from similar considerations, is entirely negligible. The estimated difference between the two short axes of the proton anisotropic *hfi* tensor resulting from this ρ_{O} is only about 0.1 MHz, significantly smaller than the distribution width of the effective T_{\perp} value ($\Delta T_{\perp} = 0.35$ MHz, see above). This proves the validity of the distance estimate ($r_{\text{GdH}} \approx 3.1$ Å) obtained using Eq. (25) based on a simple point dipole approximation.

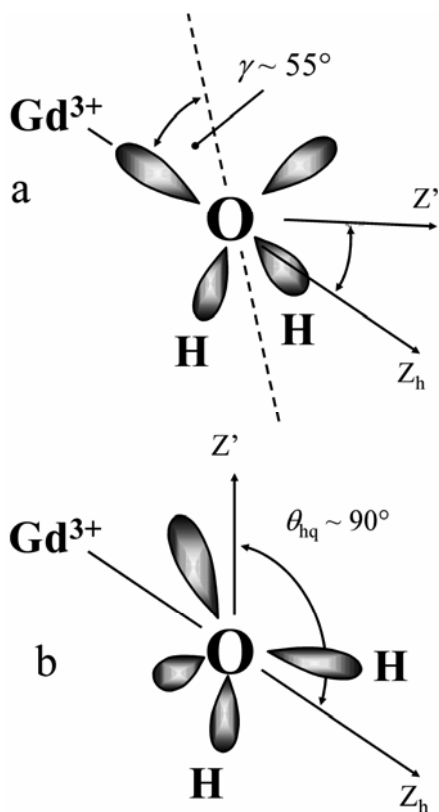


Figure 16. Models of water coordination to Gd^{3+} . In (a) the Gd^{3+} ion is located in the direction pointed by one of the hybrid lone pair orbitals, while in (b) it is located in the HOH plane, on the bisector of the HOH angle. Solid arrows show the main axes of the nqi (Z') and hfi (Z_h) tensors. Dashed line in panel (a) shows the HOH angle bisector that also coincides with the bisector of the angle between the lone pair orbitals. In panel (b) this bisector coincides with the Z_h axis. Angle γ between this bisector and the Z_h axis is $\sim 55^\circ$ in panel (a) and $\sim 0^\circ$ in panel (b). Angle θ_{hq} between the Z' and Z_h axes is $\sim 35^\circ$ in panel (a) and $\sim 90^\circ$ in panel (b).

The determined average distances $\langle r_{GdO} \rangle \approx 2.4 \text{ \AA}$ and $\langle r_{GdH} \rangle \approx 3.1 \text{ \AA}$, together with the water molecule structure ($r_{OH} = 0.96 \text{ \AA}$, $H-O-H \sim 105^\circ$), allow one to obtain detailed information about the geometry of water coordination to Gd. For such distances the bisector of the lone pair orbitals of the water oxygen is directed approximately towards the ion (see Fig. 16), and the ion is located in the HOH plane [54,55]. More detailed analysis including the distributions of r_{GdO} and r_{GdH} and the restrictions provided by the nqi parameters allows one to conclude that the geometry of the water coordination in a glassy sample is actually distributed within rather broad limits [40]. The distribution is described by the conditions that the vector \mathbf{R}_{GdO} is always located within the plane defined by the oxygen lone pair orbitals,

while the angle γ between \mathbf{R}_{GdO} and the bisector of the lone pair orbitals varies from 0° (equivalent bonding to Gd using both lone pairs) to $\sim 55^\circ$ (bonding using only one lone pair, Fig. 16). The statistical weight of smaller angles is large, and it reduces as the angle increases. The effective value of γ is thus close to 26° , found in neutron diffraction experiments [56].

As discussed above, the *hfi* and *nqi* parameters of the water ligand oxygens in MRI agents are the same as those in Gd_{aq} . Therefore, all the conclusions made above about the water coordination geometry apply also to the MRI agents. To conclude this section, we note that because the spin delocalization from Gd(III) to the ligands is so weak, the Gd(III) complexes represent quite a unique example where the ligand anisotropic *hfi* can be directly translated into the distance using a simple point dipole approximation. As a result, high-field pulsed ENDOR of Gd(III) complexes can compete in accuracy with x-ray crystallography, the only difference being that the latter does not work for disordered systems.

4.7. Hydration Numbers of Gd(III) Complexes Determined by High-Field Pulsed ^{17}O and ^1H ENDOR [57,58]

The determination of the hydration number (the number of coordinated water molecules), q , in aqueous solutions and in various biological milieus is important for understanding the mechanism and efficacy of MRI contrast agents in these environments. Lanthanide(III) complexes have coordination numbers ranging from 3 to 12, with coordination numbers of 8 and 9 being the most common [59]. Although q can be predicted from inspection of the number of potential donor atoms (basic nitrogens or oxygens) on the ligand, these estimates are not always accurate [60], because the hydration number can depend on pH [61] and the presence of competing ligands, such as small anions [62,63] or protein sidechains [58,64]. Direct determination of the hydration number of a gadolinium complex in solution is difficult. ENDOR spectroscopy is one of the few techniques available to measure the hydration number of MRI contrast agents.

As mentioned in Section 4.3, there is a general proportionality between the amplitude of normalized pulsed ENDOR spectra and the number of nuclei contributing to those spectra. However, the number of nuclei is not the only parameter affecting the amplitude of ENDOR lines. There are other important factors, mostly those determined by the experimental setup, that have a dramatic impact on the ENDOR amplitudes. The most notorious of these factors is the distribution of the RF field over the sample and the ratio of the RF excitation width to the characteristic width of the ENDOR line under investigation. Since some of these factors (e.g., the RF field distribution) are not known with sufficient accuracy, it is virtually impossible to make direct estimates of the number of nuclei from the absolute ENDOR amplitudes. Therefore, the only realistic way to determine the number of nuclei from an ENDOR spectrum consists in comparison of its normalized amplitude with that obtained for a reference sample where a spectrum of exactly the

same shape is produced by a known number of nuclei. Needless to say, the sample of interest and the reference samples should be of the same size and positioned in the resonator in the same way. The experimental conditions (primarily, the duration of the RF pulse) should also be identical.

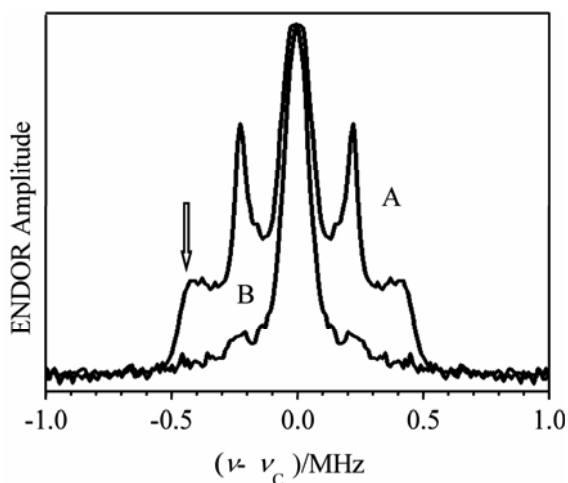


Figure 17. ^{13}C Mims ENDOR spectra of **Gd(L2)** (A) and **Gd(L0)** (B) in 100% ^{13}C methanol. Experimental conditions: $\nu_{\text{mw}} = 29.2$ GHz; $B_0 = 1047.5$ mT (for maximum of $1/2 \leftrightarrow -1/2$ transition); mw pulses, 3×15 ns; $\tau = 500$ ns; $T = 45$ μs ; RF pulse length, $T_{\text{RF}} = 37$ μs ; temperature, 7 K. The arrow marks the spectral feature used to measure the ENDOR amplitude as a function of the methanol content (see Fig.18).

A natural reference system in the case of the MRI agents is Gd_{aq} , for which the number of coordinated water molecules is known with good accuracy. In addition, as shown above, the ENDOR spectra of water ligands are similar for Gd_{aq} and MRI agents. Therefore, q can be estimated from direct comparison of ENDOR spectra of Gd_{aq} and MRI agents. However, before such a comparison is performed we should address the issue mentioned in Section 4.3, which is related to our use of water–methanol solutions and consists of the fact that the relative affinities of Gd(III) to the water and methanol ligands at our experimental conditions are not known. A series of water:methanol titration experiments were performed where the amplitude of ^{13}C ENDOR lines due to coordinated $^{13}\text{CH}_3\text{OH}$ was monitored as a function of methanol content in WMS. Figure 17 shows the ^{13}C Mims ENDOR spectra of two MRI agents, **Gd(L0)** and **Gd(L2)** (see Fig. 2), in 100% ^{13}C methanol. The nominal hydration numbers (i.e., the q -numbers that can be estimated from relaxivity or inferred from the chemical structure) of these complexes are, respectively, equal to $q_{\text{nom}} = 0$ and $q_{\text{nom}} = 2$. The ENDOR spectrum of **Gd(L2)** appears as a typical Pake pattern (neglecting the nonuniform amplitude weighting in

the Mims ENDOR pulse sequence [43]) with an additional peak at the ^{13}C Zeeman frequency. A comparison with the spectrum of **Gd(L0)** ($q_{\text{nom}} = 0$) shows that this Zeeman peak is due to distant ^{13}C in the second and outer coordination spheres.

The Pake pattern in the spectrum of **Gd(L2)** is thus attributed to the coordinated methanol ^{13}C , and the distance between the Gd(III) and the ^{13}C of the methanol ligand(s) is readily evaluated as $\sim 3.4 \text{ \AA}$ using a point dipole approximation. As is evident from Figure 17, the contribution of the distant ^{13}C to the amplitude of the shoulders (marked by an arrow) in the spectrum of **Gd(L2)** is negligible. Therefore, the amplitude of these shoulders was used as a measure of the number of methanol ligands. This is shown in Figure 18, where the amplitude of the shoulders is plotted versus molar methanol content in WMS.

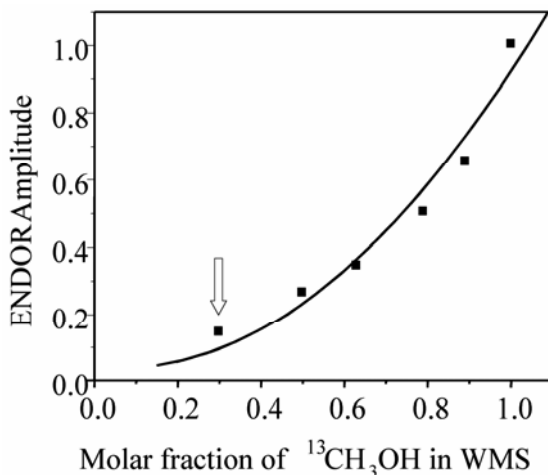


Figure 18. Dependence of the amplitude of ^{13}C Mims ENDOR spectrum of **Gd(L2)** (at the position marked by an arrow in Fig. 17) on the methanol content in WMS. The point taken in sWMS is indicated by an arrow.

It is evident from Figure 18 that the affinity of **Gd(L2)** to water is actually higher than that to methanol, and the equilibrium in sWMS is shifted toward the complexes with water. Indeed, at 30% molar concentration of methanol in sWMS (indicated by an arrow in Fig. 18) only 10–15% of Gd ions are coordinated by methanol molecules. This is in excellent agreement with the results reported for the Eu(III) ion in solution at room temperature [65]. Therefore, the probability of water coordination to Gd(III) in **Gd(L2)** in sWMS is $\sim 85\text{--}90\%$. As for standard $\text{GdCl}_3 \cdot 6\text{H}_2\text{O}$ in similar experiments, it was found that in WMS, water substitutes practically all methanol in the first coordination sphere.

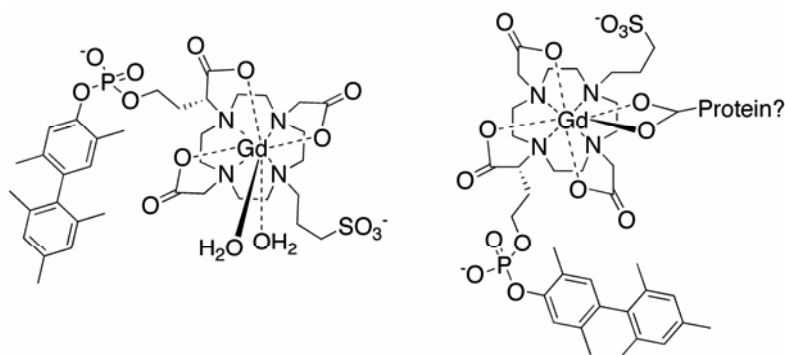
All these considerations allow quantitative determination of the hydration number. An example is shown in Figure 15, where the ^{17}O ENDOR spectrum of

Gd(L'1) is compared with the ^{17}O ENDOR spectrum of Gd_{aq} , indicating $q \approx 1$. This figure also demonstrates that the effect of outer-sphere water on the hydration number estimates can be safely neglected. Other examples are shown in Figure 14. Following from Figure 14, the ^{17}O ENDOR spectrum of **Gd(L1)** was indicative of $q = 1$. The complex **Gd(L2)** is structurally very similar to **Gd(L1)**, except that one of the acetate groups has been replaced by a methyl group, opening up a site for a second water ligand (Fig. 2). Indeed, the ^{17}O ENDOR spectrum of **Gd(L2)** is consistent with $q = 2$.

The above hydration number estimates were based on ^{17}O ENDOR. It is also possible to use ^1H ENDOR for the same purpose. One problem with ^1H ENDOR, however, is that the background from the protons that belong to the outer-sphere water molecules is quite strong (see Fig. 12), and may substantially alter the apparent amplitude of the peaks related to the water ligands. In this situation one still can compare MRI agents with Gd_{aq} , using the first derivatives of the ENDOR spectra. In such an approach the effect of the smooth background on the ligand line amplitudes could be significantly suppressed, however, at the expense of a deteriorated signal/noise ratio. In addition, the amplitudes in a derivative spectrum are more sensitive to small differences in linewidths of the A_{\perp} peaks between Gd_{aq} and the MRI agents, which increases an error of the q estimates. Therefore, the best application of ^1H ENDOR is for a quick qualitative check of the presence or absence of water ligands.

An example of the value of this approach is given for **Gd(L'2)**, shown in Figure 19. As discussed in Section 1, binding to serum albumin dramatically increases relaxivity, e.g., the relaxivity of MS-325 is increased nine-fold at 0.47 T upon binding to serum albumin [7]. However, the relaxivity of **Gd(L'2)** only increased by 30% when bound to albumin (Fig. 19b). Figures 20A and 20B show the ENDOR spectra of the exchangeable protons of **Gd(L'2)** in aqueous solution and bound to HSA, respectively. Interestingly, while the lines related to water ligands are very pronounced in aqueous solution, in the case of HSA-bound complex they are absent. This indicates that in the protein-bound compound both water ligands are replaced, most likely by coordination of the metal to amino acid sidechains. It is thus evident that the protein can have a profound effect on the water coordination number, and hence on the efficacy of protein-targeted MRI contrast agents.

Another interesting ENDOR application is the detection of neighboring exchangeable protons that belong to the multidentate ligand in some MRI agents and are situated at the same distance as directly ligated water protons, which makes them spectroscopically similar. This detection is based on comparison of apparent hydration numbers found from ^{17}O and ^1H ENDOR. For instance, the ^{17}O ENDOR data shown in Figure 15 yield $q = 1$ for **Gd(L'1)**, while the apparent hydration number found from ^1H ENDOR (see Fig. 12, bottom panel) is about 1.7. This indicates the presence of an additional exchangeable proton(s), which can be easily identified upon examining the ligand structure (see arrow in Fig. 2).



a) PBS, pH 7.4, 37 °C.
 $r_1 = 9.1 \text{ mM}^{-1}\text{s}^{-1}$ at 20 MHz

b) PBS, pH 7.4, 37 °C, 0.66 mM HSA,
 0.1 mM Gd. Compound > 99% bound
 to HSA, $r_1 = 12.3 \text{ mM}^{-1}\text{s}^{-1}$ at 20 MHz

Figure 19. $\text{Gd}(\text{L}'2)$ is $q = 2$ in buffered solution but $q = 0$ when bound to a protein. The hydration state is implied by the relaxivity, but confirmed by ^1H ENDOR.

5. CONCLUSIONS

EPR methods have played a key role in understanding the mechanism of action of gadolinium-based MRI contrast agents. There are many parameters that influence the nuclear relaxation enhancing properties of $\text{Gd}(\text{III})$ complexes. The various multifrequency, pulsed or CW, EPR and ENDOR methodologies described here are often the only means of directly probing questions such as the metal-to-hydrogen bond distance. Unlike other physical techniques, these methods are applicable to studying contrast ions in their milieu: biological media at micromolar metal ion concentrations. The findings surveyed in this chapter have broad implications for the design of more potent relaxation agents for MRI. While the genesis of these studies had a very applied focus, solving these problems resulted in some advances in the chemical physics of high-spin ions and an understanding of the bonding of aqua ligands to lanthanide ions. The advances described here have served to make some of these applications routine, to a point where the techniques can be applied by non-spectroscopists working in the contrast agent field.

ACKNOWLEDGMENTS

W-band pulsed EPR measurements were performed at the Weizmann Institute of Science, Rehovot, Israel, in collaboration with Professor D. Goldfarb and Dr. D.

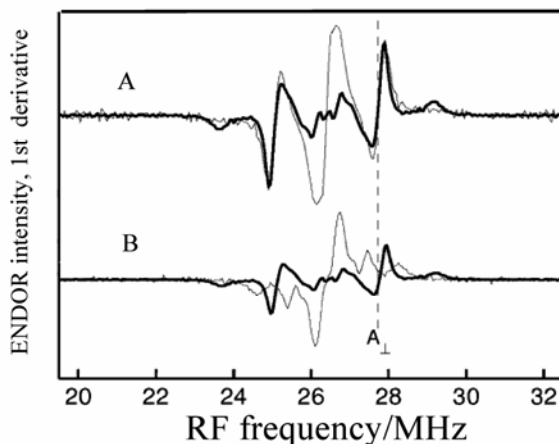


Figure 20. First derivative spectra of the exchangeable protons (thin lines) $\text{Gd}(\text{L}'2)$ in (A) sWMS and (B) in HSA. The thick line represents the spectrum of $[\text{Gd}^{3+}(\text{H}_2\text{O})_8]$, scaled by 1/4 (top), and by 1/8 (bottom) respectively. Experimental conditions: mw frequency $\nu_{\text{mw}} = 17.140$ GHz; magnetic field $B_0 = 6147$ G (for maximum of $1/2 \leftrightarrow -1/2$ transition); mw pulse durations, 10 ns; starting time interval τ between the first and second mw pulses, 130 ns; time interval T between the second and third mw pulses, 30 μs ; RF pulse duration, 18 μs ; temperature, 4.2 K.

Baute. The authors are thankful to both of them for discussion and invaluable help in experiments. This part of the work was supported by Binational Science Foundation (USA-Israel) Grant 2002175 to A.R. and D. Goldfarb. D-band experiments were performed at Argonne National Laboratory under the supervision and direct participation of Dr. O. Poluektov, and was supported by the U.S. Department of Energy, Office of Basic Energy Sciences, Division of Chemical Sciences, Geosciences, and Biosciences, under Contract W-31-109-Eng-38. The funds from the National Science Foundation (DBI-0139459, DBI-9604939 and BIR-9224431) for construction of the pulsed EPR spectrometers at the University of Arizona are gratefully acknowledged.

REFERENCES

1. Edelman RR, Hesselink JR, Zlatkin MB, Crues JV. 2005. *Clinical magnetic resonance imaging*, 3rd ed. Philadelphia: Saunders.
2. Caravan P, Ellison JJ, McMurry TJ, Lauffer RB. 1999. Gadolinium(III) chelates as MRI contrast agents: structure, dynamics, and applications. *Chem Rev* **99**:2293–2352.
3. Caravan P, Lauffer RB. 2005. Contrast agents: basic principles. In *Clinical magnetic resonance imaging*, 3rd ed., pp. 357–75. Ed RR Edelman, JR Hesselink, MB Zlatkin, JV Crues. Philadelphia: Saunders.
4. Caravan P. 2006. Strategies for increasing the sensitivity of gadolinium based MRI contrast agents. *Chem Soc Rev* **35**:512–523.

5. Lauffer RB. 1991. Targeted relaxation enhancement agents for MRI. *Magn Reson Med* **22**:339.
6. Lauffer RB, Parmelee DJ, Dunham SU, Ouellet HS, Dolan RP, Witte S, McMurry TJ, Walovitch RC. 1998. MS-325: Albumin-targeted contrast agent for MR angiography. *Radiology* **207**:529–538.
7. Caravan P, Cloutier NJ, Greenfield MT, McDermid SA, Dunham SU, Bulte JWM, Amedio Jr JC, Looby RJ, Supkowski RM, Horrocks Jr WD, McMurry TJ, Lauffer RB. 2002. The interaction of MS-325 with human serum albumin and its effect on proton relaxation rates. *J Am Chem Soc* **124**:3152–3162.
8. Kotek J, Lebduskova P, Hermann P, Vander Elst L, Muller RN, Geraldes CF, Maschmeyer T, Lukes I, Peters JA. 2003. Lanthanide(III) complexes of novel mixed carboxylic-phosphorus acid derivatives of diethylenetriamine: a step towards more efficient MRI contrast agents. *Chem Eur J* **9**:5899–5915.
9. Powell DH, Ni Dhubhghaill OM, Pubanz D, Helm L, Lebedev YS, Schlaepfer W, Merbach AE. 1996. High-pressure NMR kinetics, Part 74: structural and dynamic parameters obtained from ^{17}O NMR, EPR, and NMRD studies of monomeric and dimeric Gd^{3+} complexes of interest in magnetic resonance imaging: an integrated and theoretically self-consistent approach. *J Am Chem Soc* **118**:9333–9346.
10. Chen JW, Auteri FP, Budil DE, Belford RL, Clarkson RB. 1994. Use of EPR to investigate rotational dynamics of paramagnetic contrast agents. *J Phys Chem* **98**:13452–13459.
11. Chen JW, Belford RL, Clarkson RB. 1998. Second-sphere and outer-sphere proton relaxation of paramagnetic complexes: from EPR to NMRD. *J Phys Chem A* **102**:2117–2130.
12. Wiener EC, Auteri FP, Chen JW, Brechbiel MW, Gansow OA, Schneider DS, Belford RL, Clarkson RB, Lauterbur PC. 1996. Molecular dynamics of ion–chelate complexes attached to starburst dendrimers. *J Am Chem Soc* **118**:7774–7782.
13. Clarkson RB, Smirnov AI, Smirnova TI, Kang H, Belford RL, Earle K, Freed JH. 1998. Multi-frequency EPR determination of zero field splitting of high spin species in liquids: Gd(III) chelates in water. *Mol Phys* **95**:1325–1332.
14. Smirnova TI, Smirnov AI, Belford RL, Clarkson RB. 1997. Interaction of MRI gadolinium contrast agents with phospholipid bilayers as studied by 95 GHz EPR. *Acta Chem Scand* **51**:562–566.
15. Smirnova TI, Smirnov AI, Belford RL, Clarkson RB. 1998. Lipid magnetic resonance imaging contrast agent interactions: a spin-labeling and a multifrequency EPR study. *J Am Chem Soc* **120**:5060–5072.
16. Smirnova TI, Smirnov AI, Belford RL, Clarkson RB. 1999. Interaction of Gd(III) MRI contrast agents with membranes: a review of recent EPR studies. *MAGMA* **8**:214–229.
17. Borel A, Helm L, Merbach AE. 2004. Molecular dynamics of Gd(III) complexes in aqueous solution by HF EPR. In *Biological magnetic resonance: very high frequency (VHF) ESR/EPR*, pp. 207–247. Ed O Grinberg, LJ Berliner. New York: Kluwer.
18. Atsarkin VA, Demidov VV, Vasneva GA, Odintsov BM, Belford RL, Raduechel B, Clarkson RB. 2001. Direct measurement of fast electron spin-lattice relaxation: method and application to nitroxide radical solutions and Gd^{3+} contrast agents. *J Phys Chem A* **105**:9323–9327.

19. Borel A, Helm L, Merbach AE, Atsarkin VA, Demidov VV, Odintsov BM, Belford RL, Clarkson RB. 2002. T1e in four Gd³⁺ chelates: LODEPR measurements and models for electron spin relaxation. *J Phys Chem A* **106**:6229–6231.
20. Hudson A, Lewis JWE. 1970. Electron spin relaxation of ⁸S ions in solution. *Trans Faraday Soc* **66**:1297–1301.
21. Slichter CP. 1980. *Principles of magnetic resonance*. New York: Springer.
22. Poupko R, Baram A, Luz Z. 1974. Dynamic frequency shift in the ESR spectra of transition metal ions. *Mol Phys* **27**:1345–1357.
23. Borel A, Toth E, Helm L, Janossy A, Merbach AE. 2000. EPR on aqueous Gd³⁺ complexes and a new analysis method considering both line widths and shifts. *Phys Chem Chem Phys* **2**:1311–1317.
24. Bloembergen N, Morgan LO. 1961. Proton relaxation times in paramagnetic solutions: effects of electron spin relaxation. *J Chem Phys* **34**:842–850.
25. Rast S, Borel A, Helm L, Belorizky E, Fries PH, Merbach AE. 2001. EPR spectroscopy of MRI-related Gd(III) complexes: simultaneous analysis of multiple frequency and temperature spectra, including static and transient crystal field effects. *J Am Chem Soc* **123**:2637–2644.
26. Rast S, Fries PH, Belorizky E. 1999. Theoretical study of electronic relaxation processes in hydrated Gd³⁺ complexes in solutions. *J Chim Phys Phys-Chim Biol* **96**:1543–1550.
27. Rast S, Fries PH, Belorizky E. 2000. Static zero field splitting effects on the electronic relaxation of paramagnetic metal ion complexes in solution. *J Chem Phys* **113**:8724–8735.
28. Rast S, Fries PH, Belorizky E, Borel A, Helm L, Merbach AE. 2001. A general approach to the electronic spin relaxation of Gd(III) complexes in solutions: Monte Carlo simulations beyond the Redfield limit. *J Chem Phys* **115**:7554–7563.
29. Fries PH, Belorizky E. 2005. Electronic relaxation of paramagnetic metal ions and NMR relaxivity in solution: critical analysis of various approaches and application to a Gd(III)-based contrast agent. *J Chem Phys* **123**:124510.
30. Belorizky E, Fries PH. 2004. Simple analytical approximation of the longitudinal electronic relaxation rate of Gd(III) complexes in solutions. *Phys Chem Chem Phys* **6**:2341–2351.
31. Zhou X, Caravan P, Clarkson RB, Westlund PO. 2004. On the philosophy of optimizing contrast agents: an analysis of ¹H NMRD profiles and ESR lineshapes of the Gd(III) complex MS-325+HSA. *J Magn Reson* **167**:147–160.
32. Brodbeck CM, Iton LE. 1985. The EPR spectra of Gd³⁺ and Eu³⁺ in glassy systems. *J Chem Phys* **83**:4285–4299.
33. Fields RA, Hutchison Jr CA. 1985. The determination of hydrogen coordinates in lanthanum nicotinate dihydrate crystals by gadolinium(III)-proton double resonance. *J Chem Phys* **82**:1711–1722.
34. Raitsimring AM, Astashkin AV, Poluektov OG, Caravan P. 2005. High-field pulsed EPR and ENDOR of Gd³⁺ complexes in glassy solutions. *Appl Magn Reson* **28**:281–295.
35. Benmelouka M. 2006. Multifrequency EPR studies of zero field splitting of Gd(III) based MRI contrast agents in solids and liquids. PhD thesis, École Polytechnique Fédérale de Lausanne.
36. Abragam A, Bleaney B. 1970. *Electron paramagnetic resonance of transition metal ions*. Oxford: Clarendon Press.

37. Bleaney B, Rubins RS. 1961. Explanation of some "forbidden" transitions in paramagnetic resonance. *Proc Phys Soc* **77**:103–112.
38. Newman DJ, Urban W. 1975. Interpretation of S-state ion EPR spectra. *Adv Phys* **24**:793–844.
39. Astashkin AV, Raitsimring AM, Caravan P. 2004. Pulsed ENDOR study of water coordination to Gd^{3+} complexes in orientationally disordered systems. *J Phys Chem A* **108**:1990–2001.
40. Raitsimring AM, Astashkin AV, Baute D, Goldfarb D, Caravan P. 2004. W-Band ^{17}O pulsed electron nuclear double resonance study of gadolinium complexes with water. *J Phys Chem A* **108**:7318–7323.
41. Edmonds DT and Zussman A. 1972. Pure quadrupole resonance of O-17 in ice. *Phys Lett* **41A**:167–169.
42. Davies ER. 1974. A new pulse ENDOR technique. *Phys Lett* **47A**:1–2.
43. Mims WB. 1965. Pulsed ENDOR. *Proc R Soc* **283A**:452.
44. Caravan P, Astashkin AV, Raitsimring AM. 2003. The Gadolinium(III)–water hydrogen distance in MRI contrast agents. *Inorg Chem* **42**:3972–3974.
45. Koenig SH, Brown III RD. 1990. Field-cycling relaxometry of protein solutions and tissue: implications for MRI. *Prog Nucl Magn Reson Spectrosc* **22**:487–567.
46. Yim MB, Makinen MW. 1986. ENDOR study of Gd^{3+} complexes in frozen solutions. *J Magn Reson* **70**:89–105.
47. Muller RN, Radüchel B, Laurent S, Platzek J, Piérart C, Mareski P, Vander Elst L. 1999. Physicochemical characterization of MS-325, a new gadolinium complex, by multinuclear relaxometry. *Eur J Inorg Chem* **11**:1949–1955.
48. Vander Elst L, Maton F, Laurent S, Seghi F, Chapelle F, Muller RN. 1997. A multinuclear MR study of Gd-EOB-DTPA: comprehensive preclinical characterization of an organ specific MRI contrast agent. *Magn Reson Med* **38**:604–614.
49. Getz D, Silver BL. 1974. ESR of $Cu^{2+}(H_2O)_6$, I: the oxygen-17 superhyperfine tensors in $^{63}Cu^{2+}$ doped zinc Tutton's salt at 20 K. *J Chem Phys* **61**:630–637.
50. Ranon U, Hyde J. 1966. Electron-nuclear-double-resonance and electron-paramagnetic-resonance analysis of the ytterbium–fluorine superhyperfine interaction in $CaF_2:Yb^{3+}$. *Phys Rev* **141**:259–274.
51. Reuben J, Fiat D. 1969. Nuclear magnetic resonance studies of solutions of the rare-earth ions and their complexes, III: oxygen-17 and proton shifts in aqueous solutions and the nature of aquo and mixed complexes. *J Chem Phys* **51**:4909–4917.
52. Morton JR, Preston KF. 1978. Atomic parameters for paramagnetic resonance data. *J Magn Reson* **30**:577–582.
53. Zhidomirov GM, Schastnev PV, Chuvylkin ND. 1978. *Quantum chemical calculations of magnetic resonance parameters*. Moscow: Nauka.
54. Chidambaram R, Sequeira A, Sikka SK. 1964. Neutron-diffraction study of the structure of potassium oxalate monohydrate: lone-pair coordination of the hydrogen-bonded water molecule in crystals. *J Chem Phys* **41**:3616–3622.
55. Sikka SK, Momin SN, Rajagopal H, Chidambaram R. 1968. Neutron-diffraction refinement of the crystal structure of barium chlorate monohydrate $Ba(ClO_3)_2 \cdot H_2O$. *J Chem Phys* **48**:1883–1889.
56. Cossy C, Helm L, Powell DH, Merbach AE. 1995. A change in coordination number from nine to eight along the lanthanide(III) aqua ion series in solution: a neutron diffraction study. *New J Chem* **19**:27–35.

57. Raitsimring AM, Astashkin AV, Baute D, Goldfarb D, Poluektov OG, Lowe MP, Zech SG, Caravan P. 2006. Determination of the hydration number of gadolinium(III) complexes by high-field pulsed ^{17}O ENDOR spectroscopy. *Chem Phys Chem* **7**:1590–1597.
58. Zech S, Sun W-C, Jacques V, Caravan P, Astashkin AV, Raitsimring AM. 2005. Probing the water coordination of protein-targeted MRI contrast agents by pulsed ENDOR spectroscopy. *ChemPhysChem* **6**:2570–2577.
59. Cotton FA, Wilkinson G. 1988. *Advanced inorganic chemistry*, 5th ed. New York: John Wiley.
60. Ruloff R, Muller RN, Pubanz D, Merbach AE. 1998. A tripod gadolinium(III) poly(amino carboxylate) relevant to magnetic resonance imaging: structural and dynamical ^{17}O NMR and ^1H NMRD studies. *Inorg Chim Acta* **275–276**:15–23.
61. Lowe MP, Parker D, Reany O, Aime S, Botta M, Castellano G, Gianolio E, Pagliarin R. 2001. pH-dependent modulation of relaxivity and luminescence in macrocyclic gadolinium and europium complexes based on reversible intramolecular sulfonamide ligation. *J Am Chem Soc* **123**:7601–7609.
62. Bruce JI, Dickins RS, Govenlock LJ, Gunnlaugsson T, Lopinski S, Lowe MP, Parker D, Peacock RD, Perry JJB, Aime S, Botta M. 2000. The selectivity of reversible oxy-anion binding in aqueous solution at a chiral europium and terbium center: signaling of carbonate chelation by changes in the form and circular polarization of luminescence emission. *J Am Chem Soc* **122**:9674–9684.
63. Supkowski RM, Horrocks Jr WD. 1999. Displacement of inner-sphere water molecules from Eu^{3+} analogues of Gd^{3+} MRI contrast agents by carbonate and phosphate anions: dissociation constants from luminescence data in the rapid-exchange limit. *Inorg Chem* **38**:5616–5619.
64. Aime S, Gianolio E, Terreno E, Giovenzana GB, Pagliarin R, Sisti M, Palmisano G, Botta M, Lowe MP, Parker D. 2000. Ternary Gd(III)L-HSA adducts: evidence for the replacement of inner-sphere water molecules by coordinating groups of the protein: implications for the design of contrast agents for MRI. *J Biol Inorg Chem* **5**:488–497.
65. Kimura T, Nagaishi R, Kato Y, Yoshida Z. 2001. Luminescence study on preferential solvation of europium(III) in water/non-aqueous solvent mixtures. *J Alloys Compd* **323–324**:164–168.

CONTENTS OF PREVIOUS VOLUMES

VOLUME 1

Chapter 1

NMR of Sodium-23 and Potassium-39 in Biological Systems

Mortimer M. Civan and Mordechai Shporer

Chapter 2

High-Resolution NMR Studies of Histones

C. Crane-Robinson

Chapter 3

PMR Studies of Secondary and Tertiary Structure of Transfer RNA in Solution

Philip H. Bolton and David R. Kearns

Chapter 4

Fluorine Magnetic Resonance in Biochemistry

J. T. Gerig

Chapter 5

ESR of Free Radicals in Enzymatic Systems

Dale E. Edmondson

Chapter 6

Paramagnetic Intermediates in Photosynthetic Systems

Joseph T. Warden

Chapter 7

ESR of Copper in Biological Systems

John F. Boas, John R. Pilbrow, and Thomas D. Smith

VOLUME 2

Chapter 1

Phosphorus NMR of Cells, Tissues, and Organelles

Donald P. Hollis

*Chapter 2***EPR of Molybdenum-Containing Enzymes***Robert C. Bray**Chapter 3***ESR of Iron Proteins***Thomas D. Smith and John R. Pilbrow**Chapter 4***Stable Imidazoline Nitroxides***Leonid B. Volodarsky, Igor A. Grigor'ev, and Renad Z. Sagdeev**Chapter 5***The Multinuclear NMR Approach to Peptides: Structures, Conformation, and Dynamics***Roxanne Deslauriers and Ian C. P. Smith***VOLUME 3***Chapter 1***Multiple Irradiation ^1H NMR Experiments with Hemoproteins***Regula M. Keller and Kurt Wüthrich**Chapter 2***Vanadyl(IV) EPR Spin Probes: Inorganic and Biochemical Aspects***N. Dennis Chasteen**Chapter 3***ESR Studies of Calcium- and Protein-Induced Photon Separations in Phosphatidylserine–Phosphatidylcholine Mixed Membranes***Shun-ichi Ohnishi and Satoru Tokutomi**Chapter 4***EPR Crystallography of Metalloproteins and Spin-Labeled Enzymes***James C. W. Chien and L. Charles Dickinson**Chapter 5***Electron Spin Echo Spectroscopy and the Study of Metalloproteins***W. B. Mims and J. Peisach*

VOLUME 4*Chapter 1***Spin Labeling in Disease***D. Allan Butterfield**Chapter 2***Principles and Applications of ^{113}Cd NMR to Biological Systems***Ian M. Armitage and James D. Otvos**Chapter 3***Photo-CIDNP Studies of Proteins***Robert Kaptein**Chapter 4***Application of Ring Current Calculations to the Proton NMR of Proteins and Transfer RNA***Stephen J. Perkins***VOLUME 5***Chapter 1***CMR as a Probe for Metabolic Pathways *in Vivo****R. L. Baxter, N. E. Mackenzie, and A. L. Scott**Chapter 2***Nitrogen-15 NMR in Biological Systems***Felix Blomberg and Heinz Rüterjans**Chapter 3***Phosphorus-31 Nuclear Magnetic Resonance Investigations of Enzyme Systems***B. D. Nageswara Rao**Chapter 4***NMR Methods Involving Oxygen Isotopes in Biophosphates***Ming-Daw Tsai and Larol Bruzik**Chapter 5***ESR and NMR Studies of Lipid-Protein Interactions in Membranes***Philippe F. Devaux*

VOLUME 6*Chapter 1***Two-Dimensional Spectroscopy as a Conformational Probe of Cellular Phosphates***Philip H. Bolton**Chapter 2***Lanthanide Complexes of Peptides and Proteins***Robert E. Lenkinski**Chapter 3***EPR of Mn(II) Complexes with Enzymes and Other Proteins***George H. Reed and George D. Markham**Chapter 4***Biological Applications of Time Domain ESR***Hans Thomann, Larry R. Dalton, and Lauraine A. Dalton**Chapter 5***Techniques, Theory, and Biological Applications of Optically Detected Magnetic Resonance (ODMR)***August H. Maki***VOLUME 7***Chapter 1***NMR Spectroscopy of the Intact Heart***Gabriel A. Elgavish**Chapter 2***NMR Methods for Studying Enzyme Kinetics in Cells and Tissue***K. M. Brindle, I. D. Campbell, and R. J. Simpson**Chapter 3***Endor Spectroscopy in Photobiology and Biochemistry***Klaus Möbius and Wolfgang Lubitz**Chapter 4***NMR Studies of Calcium-Binding Proteins***Hans J. Vogel and Sture Forsén*

VOLUME 8*Chapter 1***Calculating Slow Motional Magnetic Resonance Spectra:
A User's Guide***David J. Schneider and Jack H. Freed**Chapter 2***Inhomogeneously Broadened Spin-Label Spectra***Barney Bales***Chapter 3****Saturation Transfer Spectroscopy of Spin-Labels: Techniques and
Interpretation of Spectra***M. A. Hemminga and P. A. de Jager**Chapter 4***Nitrogen-15 and Deuterium Substituted Spin Labels for Studies of
Very Slow Rotational Motion***Albert H. Beth and Bruce H. Robinson**Chapter 5***Experimental Methods in Spin-Label Spectral Analysis***Derek Marsh**Chapter 6***Electron–Electron Double Resonance***James S. Hyde and Jim B. Feix**Chapter 7***Resolved Electron–Electron Spin–Spin Splittings in EPR Spectra***Gareth R. Eaton and Sandra S. Eaton**Chapter 8***Spin-Label Oximetry***James S. Hyde and Witold S. Subczynski**Chapter 9***Chemistry of Spin-Labeled Amino Acids and Peptides: Some New Mono-
and Bifunctionalized Nitroxide Free Radicals***Kálmán Hideg and Olga H. Hankovský**Chapter 10***Nitroxide Radical Adducts in Biology: Chemistry, Applications, and Pitfalls***Carolyn Mottley and Ronald P. Mason*

*Chapter 11***Advantages of ^{15}N and Deuterium Spin Probes for Biomedical Electron Paramagnetic Resonance Investigations***Jane H. Park and Wolfgang E. Trommer**Chapter 12***Magnetic Resonance Study of the Combining Site Structure of a Monoclonal Anti-Spin-Label Antibody***Jacob Anglister**Appendix***Approaches to the Chemical Synthesis of ^{15}N and Deuterium Substituted Spin Labels***Jane H. Park and Wolfgang E. Trommer***VOLUME 9***Chapter 1***Phosphorus NMR of Membranes***Philip L. Yeagle**Chapter 2***Investigation of Ribosomal 5S Ribonucleotide Acid Solution Structure and Dynamics by Means of High-Resolution Nuclear Magnetic Resonance Spectroscopy***Alan G. Marshall and Jiejun Wu**Chapter 3***Structure Determination via Complete Relaxation Matrix Analysis (CORMA) of Two-Dimensional Nuclear Overhauser Effect Spectra: DNA Fragments***Brandan A. Borgias and Thomas L. James**Chapter 4***Methods of Proton Resonance Assignment for Proteins***Andrew D. Robertson and John L. Markley**Chapter 5***Solid-State NMR Spectroscopy of Proteins***Stanley J. Opella**Chapter 6***Methods for Suppression of the H_2O Signal in Proton FT/NMR Spectroscopy: A Review***Joseph E. Meier and Alan G. Marshall*

VOLUME 10

*Chapter 1***High-Resolution ^1H -Nuclear Magnetic Resonance Spectroscopy of Oligosaccharide-Alditols Released from Mucin-Type O-Glycoproteins***Johannis P. Kamerling and Johannes F. G. Wiegenthart**Chapter 2***NMR Studies of Nucleic Acids and Their Complexes***David E. Wemmer*

VOLUME 11

*Chapter 1***Localization of Clinical NMR Spectroscopy***Lizann Bolinger and Robert E. Lenkinski**Chapter 2***Off-Resonance Rotating Frame Spin-Lattice Relaxation: Theory, and *in Vivo* MRS and MRI Applications***Thomas Schleich, G. Herbert Caines, and Jan M. Rydzewski**Chapter 3***NMR Methods in Studies of Brain Ischemia***Lee-Hong Chang and Thomas L. James**Chapter 4***Shift-Reagent-Aided ^{23}Na NMR Spectroscopy in Cellular, Tissue, and Whole-Organ Systems***Sandra K. Miller and Gabriel A. Elgavish**Chapter 5****In Vivo* ^{19}F NMR***Barry S. Selinski and C. Tyler Burt**Chapter 6****In Vivo* ^2H NMR Studies of Cellular Metabolism***Robert E. London**Chapter 7***Some Applications of ESR to *in Vivo* Animals Studies and EPR Imaging***Lawrence J. Berliner and Hirotsada Fujii*

VOLUME 12*Chapter 1***NMR Methodology for Paramagnetic Proteins***Gerd N. La Mar and Jeffrey S. de Ropp**Chapter 2***Nuclear Relaxation in Paramagnetic Metalloproteins***Lucia Banci**Chapter 3***Paramagnetic Relaxation of Water Protons***Cathy Coolbaugh Lester and Robert G. Bryant**Chapter 4***Proton NMR Spectroscopy of Model Hemes***F. Ann Walker and Ursula Simonis**Chapter 5***Proton NMR Studies of Selected Paramagnetic Heme Proteins***J. D. Satterlee, S. Alam, Q. Yi, J. E. Erman, I. Constantinidis,
D. J. Russell, and S. J. Moench**Chapter 6***Heteronuclear Magnetic Resonance: Applications to Biological and Related Paramagnetic Molecules***Joël Mispelter, Michel Momenteau, and Jean-Marc Lhoste**Chapter 7***NMR of Polymetallic Systems in Proteins***Claudio Luchinat and Stefano Ciurli***VOLUME 13***Chapter 1***Simulation of the EMR Spectra of High-Spin Iron in Proteins***Betty J. Gaffney and Harris J. Silverstone**Chapter 2***Mössbauer Spectroscopy of Iron Proteins***Peter G. Debrunner*

*Chapter 3***Multifrequency ESR of Copper: Biophysical Applications***Riccardo Basosi, William E. Antholine, and James S. Hyde**Chapter 4***Metalloenzyme Active-Site Structure and Function through Multifrequency CW and Pulsed ENDOR***Brian M. Hoffman, Victoria J. DeRose, Peter E. Doan, Ryszard J. Gurbiel, Andrew L. P. Houseman, and Joshua Telser**Chapter 5***ENDOR of Randomly Oriented Mononuclear Metalloproteins: Toward Structural Determinations of the Prosthetic Group***Jürgen Hüttermann**Chapter 6***High-Field EPR and ENDOR in Bioorganic Systems***Klaus Möbius**Chapter 7***Pulsed Electron Nuclear Double and Multiple Resonance Spectroscopy of Metals in Proteins and Enzymes***Hans Thomann and Marcelino Bernardo**Chapter 8***Transient EPR of Spin-Labeled Proteins***David D. Thomas, E. Michael Ostap, Christopher L. Berger, Scott M. Lewis, Piotr G. Fajer and James E. Mahaney**Chapter 9***ESR Spin-Trapping Artifacts in Biological Model Systems***Aldo Tomasi and Anna Iannone***VOLUME 14****Introduction: Reflections on the Beginning of the Spin Labeling Technique***Lawrence J. Berliner**Chapter 1***Analysis of Spin Label Line Shapes with Novel Inhomogeneous Broadening from Different Component Widths: Application to Spatially Disconnected Domains in Membranes***M. B. Sankaram and Derek Marsh*

*Chapter 2***Progressive Saturation and Saturation Transfer EPR for Measuring Exchange Processes and Proximity Relations in Membranes***Derek Marsh, Tibor Páli, and László Horváth**Chapter 3***Comparative Spin Label Spectra at X-band and W-band***Alex I. Smirnov, R. L. Belford, and R. B. Clarkson**Chapter 4***Use of Imidazoline Nitroxides in Studies of Chemical Reactions: ESR Measurements of the Concentration and Reactivity of Protons, Thiols, and Nitric Oxide***Valery V. Khrantsov and Leonid B. Volodarsky**Chapter 5***ENDOR of Spin Labels for Structure Determination: From Small Molecules to Enzyme Reaction Intermediates***Marvin W. Mäkinen, Devkumar Mustafi, and Seppo Kasa**Chapter 6***Site-Directed Spin Labeling of Membrane Proteins and Peptide–Membrane Interactions***Jimmy B. Feix and Candice S. Klug**Chapter 7***Spin-Labeled Nucleic Acids***Robert S. Keyes and Albert M. Bobst**Chapter 8***Spin Label Applications to Food Science***Marcus A. Hemminga and Ivon J. van den Dries**Chapter 9***EPR Studies of Living Animals and Related Model Systems (*In-Vivo* EPR)***Harold M. Swartz and Howard Halpern***Appendix***Derek Marsh and Karl Schorn*

VOLUME 15*Chapter 1***Tracery Theory and ^{13}C NMR***Maren R. Laughlin and Joanne K. Kelleher**Chapter 2* **^{13}C Isotopomer Analysis of Glutamate: An NMR Method to Probe Metabolic Pathways Intersecting in the Citric Acid Cycle***A. Dean Sherry and Craig R. Malloy**Chapter 3***Determination of Metabolic Fluxes by Mathematical Analysis of ^{13}C Labeling Kinetics***John C. Chatham and Edwin M. Chance**Chapter 4***Metabolic Flux and Subcellular Transport of Metabolites***E. Douglas Lewandowski**Chapter 5***Assessing Cardiac Metabolic Rates During Pathologic Conditions with Dynamic ^{13}C NMR Spectra***Robert G. Weiss and Gary Gerstenblith**Chapter 6***Applications of ^{13}C Labeling to Studies of Human Brain Metabolism *in Vivo****Graeme F. Mason**Chapter 7****In-Vivo* ^{13}C NMR Spectroscopy: A Unique Approach in the Dynamic Analysis of Tricarboxylic Acid Cycle Flux and Substrate Selection***Pierre-Marie Luc Robitaille***VOLUME 16***Chapter 1***Determining Structures of Large Proteins and Protein Complexes by NMR***G. Marius Clore and Angela M. Gronenborn*

*Chapter 2***Multidimensional ^2H -Based NMR Methods for Resonance Assignment, Structure Determination, and the Study of Protein Dynamics***Kevin H. Gardner and Lewis E. Kay**Chapter 3***NMR of Perdeuterated Large Proteins***Bennett T. Farmer II and Ronald A. Venters**Chapter 4***Recent Developments in Multidimensional NMR Methods for Structural Studies of Membrane Proteins***Francesca M. Marassi, Jennifer J. Gesell, and Stanley J. Opella**Chapter 5***Homonuclear Decoupling to Proteins***Eriks Kupce, Hiroshi Matsuo, and Gerhard Wagner**Chapter 6***Pulse Sequences for Measuring Coupling Constants***Geerten W. Vuister, Marco Tessari, Yasmin Karimi-Nejad, and Brian Whitehead**Chapter 7***Methods for the Determination of Torsion Angle Restraints in Biomacromolecules***C. Griesinger, M. Hennig, J. P. Marino, B. Reif, C. Richter, and H. Schwalbe***VOLUME 17***Chapter 1***Aspects of Modeling Biomolecular Structure on the Basis of Spectroscopic or Diffraction Data***Wilfred F. van Gunsteren, Alexandre M. J. J. Bonvin, Xavier Daura, and Lorna J. Smith**Chapter 2***Combined Automated Assignment of NMR Spectra and Calculation of Three-Dimensional Protein Structures***Yuan Xu, Catherine H. Schein, and Werner Braun*

*Chapter 3***NMR Pulse Sequences and Computational Approaches for Automated Analysis of Sequence-Specific Backbone Resonance Assignments of Proteins***Gaetano T. Montelione, Carlos B. Rios, G. V. T. Swapna, and Diane E. Zimmerman**Chapter 4***Calculation of Symmetric Oligomer Structures from NMR Data***Seán I. O'Donoghue and Michael Nilges**Chapter 5***Hybrid–Hybrid Matrix Method for 3D NOESY–NOESY Data Refinements***Elliott K. Gozansky, Varatharasa Thiviyanathan, Nishantha Illangasekare, Bruce A. Luxon, and David G. Gorenstein**Chapter 6***Conformational Ensemble Calculations: Analysis of Protein and Nucleic Acid NMR Data***Anwer Mujeeb, Nikolai B. Ulyanov, Todd M. Billeci, Shauna Farr-Jones, and Thomas L. James**Chapter 7***Complete Relaxation and Conformational Exchange Matrix (CORCEMA) Analysis of NOESY Spectra of Reversibly Forming Ligand–Receptor Complexes: Application to Transferred NOESY***N. Rama Krishna and Hunter N. B. Moseley**Chapter 8***Protein Structure and Dynamics from Field-Induced Residual Dipolar Couplings***James K. Prestegard, Joel R. Tolman, Hashim M. Al-Hashimi, and Michael Andrec**Chapter 9***Recent Developments in Studying the Dynamics of Protein Structures from ^{15}N and ^{13}C Relaxation Time Measurements***Jan Engelke and Heinz Rüterjans**Chapter 10***Multinuclear Relaxation Dispersion Studies of Protein Hydration***Bertil Halle, Vladimir P. Denisov, and Kandadai Venu**Chapter 11***Hydration Studies of Biological Macromolecules by Intermolecular Water–Solute NOEs***Gottfried Otting*

VOLUME 18*Chapter 1***Introduction to *in Vivo* EPR***Harold M. Swartz and Lawrence J. Berliner**Chapter 2***Principles of *in Vivo* EPR***Sankaran Subramanian, James B. Mitchell, and Murali C. Krishna**Chapter 3***Frequency and Power Considerations for *in Vivo* EPR and Related Techniques***James M. S. Hutchison**Chapter 4***CW EPR Signal Detection Bridges***Janusz Koscielniak**Chapter 5***Resonators for Low Field *in Vivo* EPR***Kenneth A. Rubinson**Chapter 6***Principles of Imaging: Theory and Instrumentation***Periannan Kuppasamy, Michael Chzhan, and Jay L. Zweier**Chapter 7***Time-Domain Radio Frequency EPR Imaging***Sankaran Subramanian, James B. Mitchell, and Murali C. Krishna**Chapter 8***Stable Soluble Paramagnetic Compounds***Howard J. Halpern**Chapter 9***Stable Particulate Paramagnetic Materials as Oxygen Sensors in EPR Oximetry***R. B. Clarkson, Paul Peroke, Shong-Wan Norby,
and B. M. Odintsov**Chapter 10***Packaging of Stable Paramagnetic Materials in Oximetry and Other Applications***Bernard Gallez*

*Chapter 11***Spin Trapping *in Vivo*: Facts and Artifacts***Graham S. Timmins and Ke Jian Liu**Chapter 12****Ex Vivo* Detection of Free Radical Metabolites of Toxic Chemicals and Drugs by Spin Trapping***Ronald P. Mason and Maria B. Kadiiska**Chapter 13***Chemistry and Biology of Nitric Oxide***Andrei M. Komarov**Chapter 14****In Vivo* and *in Vitro* Detection of NO by EPR***Hirotsada Fujii and Lawrence J. Berliner**Chapter 15***The Measurement of Oxygen *in Vivo* Using *in-Vivo* EPR Techniques***Harold M. Swartz**Chapter 16***Cardiac Applications of *in-Vivo* EPR Spectroscopy and Imaging***Jay L. Zweier, Alexandre Samouilov, and Periannan Kuppusamy**Chapter 17***Applications of *in-Vivo* EPR Spectroscopy and Imaging in Cancer Research***Howard J. Halpern**Chapter 18***Applications of *in-Vivo* EPR Spectroscopy and Imaging to Skin***Jürgen Fuchs, Norbert Groth, and Thomas Herrling**Chapter 19***Pharmaceutical Applications of *in-Vivo* EPR***Karsten Mäder and Bernard Gallez**Chapter 20***Proton–Electron Double-Resonance Imaging (PEDRI)***David J. Lurie**Chapter 21***Combining NMR and EPR/ESR for *in-Vivo* Experiments***Jeff F. Dunn and Harold M. Swartz*

*Chapter 22***Potential Medical (Clinical) Applications of EPR: Overview and Perspectives***Harold M. Swartz***VOLUME 19***Chapter 1***Distance Measurements by CW and Pulsed EPR***Sandra S. Eaton and Gareth R. Eaton**Chapter 2***Relaxation Times of Organic Radicals and Transition Metal Ions***Sandra S. Eaton and Gareth R. Eaton**Chapter 3***Structural Information from CW-EPR Spectra of Dipolar Coupled Nitroxide Spin Labels***Eric J. Hustedt and Albert H. Beth**Chapter 4***Determination of Protein Folds and Conformational Dynamics Using Spin-Labeling EPR Spectroscopy***Hassane S. Mchaourab and Eduardo Perozo**Chapter 5***EPR Spectroscopic Ruler: The Deconvolution Method and Its Applications***Wenzhong Xiao and Yeon-Kyun Shin**Chapter 6***TOAC: The Rigid Nitroxide Side Chain***Joseph C. McNulty and Glenn L. Millhauser**Chapter 7***Depth of Immersion of Paramagnetic Centers in Biological Systems***Gertz I. Likhtenshtein**Chapter 8***Determination of Distances Based on T_1 and T_m Effects***Sandra S. Eaton and Gareth R. Eaton*

*Chapter 9***Double-Quantum ESR and Distance Measurements***Petr P. Borbat and Jack H. Freed**Chapter 10***"2+1" Pulse Sequence as Applied for Distance and Spatial Distribution Measurements of Paramagnetic Centers***A. Raitsimring**Chapter 11***Double Electron–Electron Resonance***Gunnar Jeschke, Martin Pannier, and Hans W. Spiess**Chapter 12***Electron Paramagnetic Resonance Distance Measurements in Photosynthetic Reaction Centers***K. V. Lakshmi and Gary W. Brudvig**Chapter 13***Photo-Induced Radical Pairs Investigated using Out-of-Phase Electron Spin Echo***Sergei A. Dzuba and Arnold J. Hoff***VOLUME 20***Chapter 1***Transverse Relaxation Optimized Spectroscopy***Konstantin V. Pervushin**Chapter 2***Segmental Isotopic Labeling: Prospects for a New Tool to Study the Structure-Function Relationships in Multi-Domain Proteins***Jennifer J. Ottesen, Ulrich K. Blaschke, David Cowburn, and Tom W. Muir**Chapter 3***Characterization of Inter-Domain Orientations in Solution Using the NMR Relaxation Approach***David Fushman and David Cowburn**Chapter 4***Global Fold Determination of Large Proteins using Site-Directed Spin Labeling***John Battiste, John D. Gross, and Gerhard Wagner*

*Chapter 5***Solid State NMR Studies of Uniformly Isotopically Enriched Proteins***Ann McDermott**Chapter 6***NMR Spectroscopy of Encapsulated Proteins Dissolved in Low Viscosity Fluids***A. Joshua Wand, Charles R. Babu, Peter F. Flynn,
and Mark J. Milton**Chapter 7***Angular Restraints from Residual Dipolar Couplings for Structure Refinement***Christian Griesinger, Jens Meiler, and Wolfgang Peti**Chapter 8***Protein Structure Refinement using Residual Dipolar Couplings***Angela M. Gronenborn**Chapter 9***Hydrogen Bond Scalar Couplings — A New Tool in Biomolecular NMR***Stephan Grzesiek, Florence Cordier, and Andrew Dingley**Chapter 10***NMR Methods for Screening the Binding of Ligands to Proteins: Identification and Characterization of Bioactive Ligands***Thomas Peters, Thorsten Biet, and Lars Herfurth***VOLUME 21***Chapter 1***Microwave Engineering Fundamentals and Spectrometer Design***C. J. Bender**Chapter 2***EPR Spectrometers at Frequencies below X-Band***G. R. Eaton and S. S. Eaton**Chapter 3***Frequency Dependence of EPR Sensitivity***G. A. Rinard, R. W. Quine, S. S. Eaton, and G. R. Eaton*

*Chapter 4***ENDOR Coils and Related Radiofrequency Circuits***C. J. Bender**Chapter 5***The Generation and Detection of Electron Spin Echoes***C. J. Bender**Chapter 6***Convolution-Based Algorithm: From Analysis of Rotational Dynamics to EPR Oximetry and Protein Distance Measurements***A. L. Smirnov and T. I. Smirnova**Chapter 7***1d and 2d Electron Spin Resonance Imaging (ESRI) of Transport and Degradation Processes in Polymers***M. V. Motyakin and S. Schlick**Chapter 8***Peptide Aggregation and Conformation Properties as Studied by Pulsed Electron–Electron Double Resonance***Y. D. Tsvetkov***VOLUME 22***Chapter 1***The Early Years***Oleg Y. Grinberg and Alexander A. Dubinskii**Chapter 2***The Development of High-Field/High-Frequency ESR***Jack H. Freed**Chapter 3***Primary Processes in Photosynthesis: What Do We Learn from High-Field EPR Spectroscopy?***Klaus Möbius, Anton Savitsky, and Martin Fuchs**Chapter 4***High Field ESR: Applications to Protein Structure and Dynamics, HF-ESR Protein Structure and Dynamics***Keith A. Earle and Alex I. Smirnov*

*Chapter 5***The Use of Very High Frequency EPR (VHF-EPR) in Studies of Radicals and Metal Sites in Proteins and Small Inorganic Models***Anne-Laure Barra, Astrid Gräslund, and K. Kristoffer Andersson**Chapter 6***Time-Resolved High-Frequency and Multifrequency EPR Studies of Spin-Correlated Radical Pairs in Photosynthetic Reaction Center Proteins***Marion C. Thurnauer, Oleg G. Poluektov, and Gerd Kothe**Chapter 7***Molecular Dynamics of Gd(III) Complexes in Aqueous Solution by HF-EPR***Alain Borel, Lothar Helm, and André E. Merbach**Chapter 8***Pulse High-Frequency EPR***Thomas F. Prisner**Chapter 9***High-Frequency EPR, ESEEM and ENDOR Studies of Paramagnetic Centers in Single-Crystalline Materials***Edgar J. J. Groenen and Jan Schmidt**Chapter 10***W-Band Pulse ENDOR of Transition Metal Centers in Orientationally Disordered Systems and Single Crystals***Daniella Goldfarb and Vladimir Krymov**Chapter 11***Sample Resonators for Quasioptical EPR***David E. Budil and Keith A. Earle**Chapter 12***The Bruker ELEXSYS E600/680 94 Ghz Spectrometer Series***P. Höfer, A. Kamlowiskil, G. G. Maresch, D. Schmalbein, and R. T. Weber**Chapter 13***HF-EPR Spectra of Spin Labels in Membranes***V. A. Livshits and D. Marsh*

*Chapter 14***Modern Developments and Prospects in Multi-Frequency High Field EMR**

Louis-Claude Brunel, Anna Lisa Maniero, Alexander Angerhofer, Stephen Hill, and J. (Hans) van Tol

VOLUME 23**SECTION I: JAMES S. HYDE AND BIOMEDICAL EPR***Chapter 1***Helmut Beinert***Chapter 2***An Incomplete History of Jim Hyde and the EPR Center at MCW**

Harold M. Swartz

SECTION II: BIOLOGICAL FREE RADICALS AND MEDICINE*Chapter 3***Free Radicals and Medicine**

Harold M. Swartz, Ronald P. Mason, Neil Hogg, Balaraman Kalyanaraman, Tadeusz Sarna, Przemyslaw M. Plonka, Mariusz Zareba, P. L. Gutierrez, and Lawrence J. Berliner

*Chapter 4***Superoxide Generation from Nitric Oxide Synthase: Role of Cofactors and Protein Interaction**

Jeannette Vásquez-Vivar, Pavel Martásek, and B. Kalyanaraman

*Chapter 5****In Vivo* Spin Trapping of Free Radical Metabolites of Drugs and Toxic Chemicals Utilizing *Ex Vivo* Detection**

Ronald P. Mason and Maria B. Kadiiska

*Chapter 6***Post Processing Strategies in EPR Spin-Trapping Studies**

Agnes Keszler and Neil Hogg

*Chapter 7***Biophysical Studies of Melanin: Paramagnetic, Ion-Exchange and Redox Properties of Melanin Pigments and Their Photoreactivity**

Tadeusz Sarna and Przemyslaw M. Plonka

*Chapter 8***Application of Spin Labels To Membrane Bioenergetics: Photosynthetic Systems of Higher Plants***Alexander N. Tikhonov and Witold K. Subczynski***SECTION III: *IN VIVO* EPR AND PHYSIOLOGY***Chapter 9***EPR Spectroscopy of Function *in Vivo*: Origins, Achievements, and Future Possibilities***Harold M. Swartz and Nadeem Khan**Chapter 10***EPR Oximetry in Biological and Model Samples***Witold K. Subczynski and Harold M. Swartz**Chapter 11****In Vivo* EPR Imaging***Benjamin B. Williams and Howard J. Halpern**Chapter 12***Time-Domain Radio Frequency EPR Imaging***Sankaran Subramanian and Murali C. Krishna***SECTION IV: METALS***Chapter 13***Copper Biomolecules in Solution***Riccardo Basosi, Giovanni Della Lunga, and Rebecca Pogni**Chapter 14***Low-Frequency EPR of Cu^{2+} in Proteins***William E. Antholine**Chapter 15***Electron Spin-Echo Envelope Modulation Studies of ^{14}N in Biological Systems***Michael J. Colaneri and Jack Peisach*

VOLUME 24

SECTION I: INSTRUMENTATION AND METHODOLOGY

*Chapter 1***Saturation Recovery EPR***Sandra S. Eaton and Gareth R. Eaton**Chapter 2***Loop-Gap Resonators***George A. Rinard and Gareth R. Eaton**Chapter 3***EPR Interfaced To Rapid Mixing***Charles P. Scholes**Chapter 4***Application of Angle-Selected Electron Nuclear Double Resonance to Characterize Structured Solvent in Small Molecules and Macromolecules***Devkumar Mustafi and Marvin W. Makinen**Chapter 5***Solution-ENDOR of Some Biologically Interesting Radical Ions***Fabian Gerson and Georg Gescheidt**Chapter 6***Electron–Electron Double Resonance***Lowell D. Kispert**Chapter 7***Digital Detection by Time-Locked Sampling in EPR***James S. Hyde, Theodore G. Camenisch, Joseph J. Ratke,
Robert A. Strangeway, and Wojciech Froncisz**Chapter 8***Measurement of Distances Between Electron Spins Using Pulsed EPR***Sandra S. Eaton and Gareth R. Eaton*

SECTION II: MOTION, PROTEINS, AND MEMBRANES

*Chapter 9***ESR and Molecular Dynamics***Jack H. Freed*

*Chapter 10***SDSL: A Survey of Biological Applications***Candice S. Klug and Jimmy B. Feix**Chapter 11***Saturation Transfer Spectroscopy of Biological Membranes***Derek Marsh, László I. Horváth, Tibor Páli, and
Vsevolod A. Livshits**Chapter 12***Saturation Transfer EPR: Rotational Dynamics of Membrane Proteins***Albert H. Beth and Eric J. Hustedt**Chapter 13***Trends in EPR Technology***James S. Hyde**Chapter 14***Prognosis***Sandra S. Eaton and Gareth R. Eaton***VOLUME 25***Chapter 1***Microwave Amplitude Modulation Technique to Measure Spin–Lattice (T_1) and Spin–Spin (T_2) Relaxation Times***Sushil K. Misra**Chapter 2***Improvement in the Measurement of Spin–Lattice Relaxation Time in Electron Paramagnetic Resonance***Robert Lopez — translated by Sushil K. Misra**Chapter 3***Quantitative Measurement of Magnetic Hyperfine Parameters and the Physical Organic Chemistry of Supramolecular Systems***Christopher J. Bender**Chapter 4***New Methods of Simulation of Mn(II) EPR Spectra: Single Crystals, Polycrystalline and Amorphous (Biological) Materials***Sushil K. Misra**Chapter 5***Density Matrix Formalism of Angular Momentum in Multi-Quantum Magnetic Resonance***H. Watari and Y. Shimoyama*

VOLUME 26

Chapter 1

Ultra High Field Magnetic Resonance Imaging: A Historical Perspective

Pierre-Marie L. Robitaille

Chapter 2

Design Considerations for Ultra High Field MRI Magnet Systems

*John Bird, Darren Houlden, Nick Kerley, David Rayner,
David Simkin, and Simon Pittard*

Chapter 3

**Hardware Considerations in Ultra High Field MRI:
An Overview of System Integration**

Douglas A. C. Kelley

Chapter 4

Aspects of Clinical Imaging at 7 T

*Franz Schmitt, Andreas Potthast, Bernd Stoeckel, Christina Triantafyllou,
Christopher J. Wiggins, Graham Wiggins, and Lawrence L. Wald*

Chapter 5

The Challenges of Integrating a 9.4T MR Scanner for Human Brain Imaging

Keith R. Thulborn

Chapter 6

Ultra High Field MRI: High-Frequency Coils

J. Thomas Vaughan

Chapter 7

A Perspective into Ultra High Field MRI RF Coils

Tamer S. Ibrahim

Chapter 8

Radiofrequency Field Calculations for High Field MRI

Christopher M. Collins

Chapter 9

Magnetic Susceptibility Effects in High Field MRI

Qing X. Yang, Michael B. Smith, and Jianli Wang

*Chapter 10***High Magnetic Fields for Imaging Cerebral Morphology, Function, and Biochemistry**

Kâmil Uğurbil, Gregor Adriany, Can Akgün, Peter Andersen, Wei Chen, Michael Garwood, Rolf Gruetter, Pierre-Gilles Henry, Malgorzata Marjanska, Steen Moeller, Pierre-François Van de Moortele, Klaas Prüssmann, Ivan Tkac, J. Thomas Vaughan, Florian Wiesinger, Essa Yacoub, and Xiao-Hong Zhu

*Chapter 11***High-Resolution and Microscopic Imaging at High Field**

Lawrence L. Wald, Bruce Fischl, Bruce R. Rosen

*Chapter 12***In-Vivo NMR Spectroscopy of the Brain at High Fields**

Rolf Gruetter, Pierre-Gilles Henry, Hongxia Lei, Silvia Mangia, Gülin Öz, Melissa Terpstra, and Ivan Tkac

*Chapter 13***Clinical Promise: Clinical Imaging at Ultra High Field**

Vera Novak and Gregory Christoforidis

VOLUME 27*Chapter 1***Introduction and Future of Site-Directed Spin Labeling of Membrane Proteins**

Marcus A. Hemminga

*Chapter 2***Instrumentation and Experimental Setup**

Gunnar Jeschke

*Chapter 3***Advanced ESR Spectroscopy in Membrane Biophysics**

Janez Štrancar

*Chapter 4***Practical Pulsed Dipolar ESR (DEER)**

Piotr G. Fajer, Louise Brown, and Likai Song

*Chapter 5***Membrane Protein Structure and Dynamics Studied by Site-Directed Spin-Labeling ESR**

Enrica Bordignon and Heinz-Jürgen Steinhoff

*Chapter 6***High-Field ESR Spectroscopy in Membrane and Protein Biophysics***Tatyana I. Smirnova and Alex I. Smirnov**Appendix 1***Molecular Modeling of Spin Labels***Mikolai I. Fajer, Kenneth L. Sale, and Piotr G. Fajer**Appendix 2***SIMPOW6: A Software Package for the Simulation of ESR Powder-Type Spectra***Mark J. Nilges, Karen Mattson, and R. Linn Belford**Appendix 3***ACERT Software: Simulation and Analysis of ESR Spectra***Jack H. Freed**Appendix 4***DeerAnalysis 2006: Distance Measurements on Nanoscopic Length Scales by Pulse ESR***Gunnar Jeschke**Appendix 5***EWVoigt and EWVoigt_n: Inhomogeneous Line Shape Simulation and Fitting Programs***Alex I. Smirnov**Appendix 6***EasySpin: Simulating cw ESR Spectra***Stefan Stoll and Arthur Schweiger**Appendix 7***EPRSIM-C: A Spectral Analysis Package***Janez Štrancar*

INDEX

- α -subunit hemoglobin spectrum, 425–430
 a_2 parameter, 588
 a_{2T} parameter, 588–589
 a_4 parameter, 588
 a_6 parameter, 588
Aasa-Vännegård factor, 246–247
Acetylacetonate ligand in insulin-enhancing vanadium(IV) complexes, 515–516
Acinetobacter radioresistens S13, 298
Additivity rule, 512, 518–519
Adrenodoxin, 87
Alanine (Ala) 91, 185, 294
Albumin interacting with vanadyl compounds, 520–525
Alkane ω -hydroxylase, 291–293
 biochemical and structural characterization, 291–292
 flavoprotein rubredoxin component (AlkT), *see* AlkT
 mechanistic insights, 292
 membrane bound oxygenase component (AlkB), *see* AlkB
 soluble rubredoxin component (AlkG), *see* AlkG
 spectroscopic characterization, 292
AlkB, 291–292
Alkene monooxygenase (AMO), 293–295
 biochemical and structural characterization, 293–294
 mechanistic insights, 294–295
 spectroscopic characterization, 294
AlkG, 291
AlkT, 291
Alternative oxidase (AOX), 353–355
 biochemical and structural characterization, 353–354
 mechanistic implications, 354–355
 spectroscopic characterization, 354
Amino acid free radicals, 106, 308–313
Amino acid radicals in ribonucleotide reductase, 308–313
p-Aminobenzoate oxygenase, 355, 395
1-Aminocyclopropane-1-carboxylic acid oxidase (ACCO), 259–260
Aminopyrrolnitrin oxygenase, 355
AmoB, 294
AmoD, 294
Antibiotics, 348
Anticancer drugs, 303
Antidiabetic pharmaceuticals, 8, 507–508
Antiferromagnetic coupling, 278–280
Antisymmetric exchange interaction, 130–132
Apo-transferrin interacting with vanadyl compounds, 520–525
Aquometmyoglobin, 406, 408
Archaeal Rieske center, 33
Arthrospira platensis, 82–83
Arylamino oxygenases, 355
Arylnitro compounds, 355
Asymmetry parameters, 197, 216–217
A tensor, 77–78
Atom isotopes in computer simulation software, 127–128
Aureothin, 355
Axial anisotropic exchange interaction, 130–132
Axial ligand orientation, 403–405
Axial symmetry, 122–123
Azide binding to hemerythrin, 339
Azidosemimethemerythrin, 340
Azurin, 5
 β -subunit hemoglobin spectrum, 425–430
B3LYP functional, 199–202, 219
Bacterial multicomponent monooxygenases, 274–303
Bacterioferritins, *see* Ferritins
Basis set in Spin Hamiltonian, 200–201
Basis set limit, 179
BCM–EPR of vanadium compounds, 529–532
Benzene, 220
Binuclear Cu_A sites, 478–481
Binuclear metalloenzymes, 165
Binuclear metallohydrolases, 346
Binuclear non-heme iron enzymes, 6, 269–356
 classes, 273
 reactions, 270–272
 representative, 269–272

- Blind spots
 in ENDOR, 43
 in ESEEM, 34
- Bloch–Wangsness–Redfield theory, 587
- Blood-circulation monitoring EPR. *See* BCM-EPR
- Bond addition in computer simulation software, 129
- Born–Oppenheimer Hamiltonian operator, 177–178
- BP86 functional, 199–200, 219
- Bridging ligands, 344, 346, 458–460, 463, 489–490
- Buthionine sulfoximine, 527
- Carbohydrate complexes with chromium(V), 561–565
- CASSCF method, 221
- Catechol, 296
- Catechol oxidase, 165–166, 481
- Chemical shift, 176
- Chiral epoxides, 293–294
- Chirp-ENDOR-HYSCORE sequence, 51
- Chlorinated alkenes, 295
- Chromatium vinosum, 94, 96
- Chromium complexes, 9, 552–554
 in cell and animal studies, 569–572
- Chromium(III) complexes, 163–164, 565–568, 572
 in glucose metabolism, 552–554
 with glutathione, 566–567
 with transferrin, 566–568
- Chromium(IV) complexes, 565–568
- Chromium(V) complexes, 571
 EPR spectroscopy, 557–561
 with biological and biomimetic ligands, 554–557
 with carbohydrates 561–565
 intermediates of, 554–565
- Chromium(VI) complexes, 571–572
 reactive oxygen species (ROS), 568–569
 intermediates of, 552–554
- Chromodulin, 568
- Citrate and insulin-enhancing vanadium(IV) complexes, 516–517
- Coenzyme M reductase (MCR), 2
- Coherence transfer pathways, 158
- Combination frequencies, 23
- Combination peak experiments, 25–27
- Common Object Request Broker Architecture (CORBA) daemons, 110, 112, 115
- Computer simulation – Molecular Sophie 105–171
- Configuration interaction, 181
- Continuous-wave electron paramagnetic resonance. *See* CW EPR
- Continuous wave ENDOR. *See* CW ENDOR
- Contrast agent for MRI, 582
- Coordination structure of vanadyl ions, 534–535, 537
- Copper hyperfine tensor, 215–216
- Copper proteins, 8
 classification of, 471–475
 binuclear Cu_A sites, 478–481
 non-coupled binuclear copper sites, 473–474, 483–486
 tetranuclear Cu_Z sites, 493–496
 trinuclear Cu cluster sites, 474, 486–493
 type I (T1) copper active site, 472–473, 486–488
 EPR analysis of, 475–478
 type II (T2) copper active site, 472–473, 486–489
 type III (T3) copper active site, 472–474, 481–483, 487
- Copper(II) cyclic peptide complexes, 164–165
- Correlation energy, 181
- Correlation error, 181
- COSMO model, 209–213
- COSMO-RS model, 210–213
- Coulomb operators, 179
- Coupled binuclear copper sites, 473, 481–483
- Coupled-cluster (CC) theory, 181
- Coupled distortion model, 478
- Coupled-perturbed self-consistent field methods, 188
- Couplings in iron–sulfur proteins, 84–86, 93
- Cross-peaks in HYSCORE, 32–33
- Cr(V)–2-hydroxycarboxylato complexes, 558–560
- Crystal field description of spin Hamiltonian parameters, 161–162
- Crystal field interactions
 in Gd(III) complexes, 590–597
 in water ligands, 598–601
- Cubane structure
 in iron–sulfur proteins, 90–94
 in metalloproteins, 66
- Cu_A site, 474
- Cu_H structure, 484–485
- Cu_I site, 494–495
- Cu_{II} site, 494–495
- Cu_M structure, 484–485
- Cu_Z sites, 474, 493–496
- CW ENDOR, 64, 72
 of iron–nitric oxide complexes, 259–260
 use in heme systems, 401–402

- CW EPR spectroscopy, 1, 105, 152–156, 397, 590
analysis of complex spectra, 156
automatic fitting of, 167–171
computer simulation of spectra, 109–111
of dinuclear iron centers, 279–280
experiment in computer simulation software, 133–135
field segmentation, 152–153
line width models, 156
matrix diagonalization, 152–156
mosaic misorientation line width model, 153–156
Molecular Sophe simulations, 159–165
in SOPHE, 152–156
of vanadium(IV), 532–533
- Cyclam derivatives, 257
- cys*-1,2-cyclopentanediol complexing with chromium(V), 563
- Cysteine (Cys) 313, 439
binding protons 84–85
dihedral angle in cysteine radicals, 203–204
residues in ferritin, 337
- Cytochromes, 34
- Δ° desaturase
acetate complex, 316–317
azide complex, 316–317
ENDOR, 318
- Davies ENDOR, 41–43, 48–49, 71–72, 399
- DEFENCE, 25–26
and decoupling, 38
- Density Functional Theory (DFT), 2, 4, 17, 177, 181, 195, 215–217
calculations, 161–163
cysteine radicals, 203–207
electronic structure theory of spin Hamiltonian parameters, 177–201
of [NiFe] hydrogenases, 456–457
nitroxide radicals, 207–212
in organic radicals, 220
in transition metal complexes, 222
phenoxyl radicals, 201–203
practical aspects, 198–201
solvent effects, 207–212
- Density matrix, 180
- Deoxyhemerythrin, 339
- Desulfovibrio* species, 442–443
- Desulfovibrio vulgaris*, 326
- D-glucuronate, 320
- Dicopper complexes, 165–166
- Diferric cluster, 335
- Diferric MMOH, 281–282
- Diferric transferrin, 234–235
- Diferric transferrin carbonate, 244–245
- Diferrous MMOH, 282
- Diferrous R2 subunit of ribonucleotide reductase, 305–306
- Dihedral angle in cysteine radicals, 203–204
- Diiron flavoproteins, 350–351
- Diiron site
in AlkB, 292
in *myo*-inositol oxygenase (MIOX), 321–322
in phenol hydroxylase, 297–298
in ribonucleotide reductase, 304–305
in rubrerythrin, 326–328
in stearyl-acyl carrier protein Δ° desaturase, 316–318
in T4MOH, 300
in ToMOH, 301–302
- Dinuclear copper(II) EPR spectra, 165–167
- Dinuclear iron EPR spectra, 277–278
- 1,2-Diolato ligands, 561–565
- Dioxygen mimicked by nitric oxide, 287
- Diphenyl nitric oxide (DPNO), 208–211
- Dipolar interactions in hyperfine tensor, 72
- Dipole–dipole interactions, 114, 192–193
in computer simulation software, 129
- Diradicals and zero-field splittings, 217–220
- Direct magnetic dipolar spin–spin interaction, 184
- Di-*tert*-butyl nitric oxide (DTBNO), 208–209
- DMP phenol hydroxylase, 296
- DmpK, 296
- DmpLNO, 296–298
- DmpM, 296
- DmpP, 296
- DMSO, 285–286
- DONUT, 37
- DONUT-HYSCORE, 37
- Dopamine β -hydroxylase, 473
- Dopamine β -monooxygenase, 483–486
- Double nuclear-coherence transfer. *See* DONUT
- Double perturbation theory, 188
- Double quantum transitions, 18, 31–32, 38–40
- D* parameters
for benzene and polyacenes, 220
in non-heme iron proteins, 236–240
- D** tensor, 193–194
- EasySpin, 55
- Echo modulation, 23
- Ectothiorhodospira halophila*, 90–93, 97–98
- EDRF, 419
- Eight histidine motif, 291–292
- ELDOR detected NMR, 399, 408
- ELDOR spectroscopy of [NiFe] hydrogenases, 462

- Electric field gradient (EFG), 197–198
- Electric field gradient (**Q**) tensor, 197–198
- Electric field-like perturbations, 191
- Electron interaction with nuclei, 107, 178
in metal ions, 64
- Electron nuclear distance, 16
- Electron Nuclear Double Resonance. *See*
ENDOR
- Electron nuclear double (triple) resonance
spectroscopy, 112
- Electron paramagnetic resonance. *See* EPR
- Electron spin
decoupling, 37
density, 16
in ENDOR, 66, 68
in Gd(III) complexes, 590–591
manifolds, 51
quantum number, 52
vector operator, 15–40
- Electron Spin Echo Envelope Modulation. *See*
ESEEM
- Electron Zeeman interaction, 15–16, 107, 185
in computer simulation software, 121–122
- Electron Zeeman-resolved EPR, 54
- Electron Bohr magneton, 176
- Electronic coupling matrix element, 486
- Electronic relaxation, 583
of Gd(III) complexes, 586–590
- Electronic structure theory of spin Hamiltonian
parameters, 177–201
additional spin Hamiltonian terms, 182–185
methods, 177–182
practical aspects, 198–201
self consistent field methods, 192–198
sum over states theory of spin Hamiltonian
parameters, 185–192
- Electrostatic interactions, 177–178
- ENDOR, 1–3, 13–14, 40–52, 55–56, 65–73, 112,
114
advantages of, 64–65
applications of, 82–99
baseline artifacts in, 43–44
blind spots, 43
chirp-ENDOR-HYSCORE sequence, 51
of Δ^9 desaturase, 318
Davies, 41–43
 ^{57}Fe , 94–98
 ^1H , 82–94, 605–607, 612–616
high-field, 48–50
hyperfine-correlated, 44–46
hyperfine enhancement of radio frequency
pulses, 50
of iron–nitric oxide complexes, 258–260
of mixed-valence MMOH, 284
of [NiFe] hydrogenases, 456–461
of iron sulfur proteins, 82–98
 ^{17}O , 601–602, 607–609
orientation selection in, 76–82
simulated by computer software, 77–82,
143–145
spin densities, 98–100
substrate/product interactions with MMOH,
285–287
theory of, 65–73
time-domain, 50–52
transitions, 65, 67–68
triple resonance, 46–47
of vanadyl compounds, 523
variable mixing time, 47
- Endothelium-derived vascular relaxing factor.
See EDRF
- Energies of states of paramagnetic species, 15
- Energy level diagrams, 156
in computer simulation software, 146–147
- Energy levels
diagrams, 156, 146–147
transitions, 240–244
in zero-field splitting, 236–238
- Enterobactin, 247
- Epoxidation of alkenes, 299
- Epoxygenase component of alkene monooxy-
genase, 294–295
- EPR
amino acid radicals in ribonucleotide reduc-
tase, 308–313
analysis of NO-ligated heme proteins, 408–
410
applications of, 13–14
in cell and animal studies, 569–572
characterization of chromium compounds, 9
characterization of FprA and FIRd, 352
characterization of **g** tensors of [NiFe] hy-
drogenases, 448–456
electron Zeeman resolved, 54
field-swept, 52–54
for detection of nitric oxide and hemoglobin
interactions, 419–432
high-frequency, 244–246
line shapes, 246–250
multifrequency analysis, 163–164
of chromium(V) complexes, 557–561
of chromium(V) complexes with carbohy-
drates, 561–563
of chromium(V) intermediates, 554–561
of copper active sites, 471–472
of crystal field interactions, 590–597
of dinuclear iron centers, 277–278
of gadolinium contrast agents, 584–586

- of iron–nitric oxide complexes, 254–258
- of mononuclear low-spin ferric non-heme proteins, 251
- of mononuclear high spin non-heme iron proteins, 233–264
- of [NiFe] hydrogenases, 441–464
- of nitric oxide and hemoglobin interactions, 424–431
- of non-coupled binuclear copper sites, 484–485
- of photosynthetic reaction centers, 251–254
- of redox cofactors in metalloproteins, 107
- of semiquinone–iron interactions, 253–254
- of tetranuclear Cu_z sites, 494
- of trinuclear copper cluster sites, 486–493
- of vanadium compounds, 507–541
- orientation selection in, 74–82
- simulations of, 115
- solution structures of insulin-enhancing vanadium(IV) complexes, 514–519
- transitions, 20–22
- EPR-II basis set, 201, 219
- EPR-III basis set, 201, 219
- EPR-silent states, 462
- ESE-field sweep, 590–593
- ESE signal, 603
- ESEEM, 1, 13–14, 54–55, 112, 114
 - automatic fitting of spectra, 170
 - basics of, 20–40
 - blind spots, 34
 - in high-spin ferric heme proteins, 407–408
 - matched, 35–37
 - mixed valence MMOH, 282–283
 - of [NiFe] hydrogenases, 459
 - of NO-ligated heme proteins, 409–410
 - of vanadyl ions, 533–536
- Euler angle rotation, 121–122
- Exact cancellation condition, 33
- EXAFS. *See* Extended x-ray absorption fine structure (EXAFS)
- Exchange interaction, 8
 - dinuclear iron centers, 278–281
 - in computer simulation software, 130–132
 - operators, 179
 - strong exchange regime, 278–281
 - weak exchange regime, 281
- Exchangeable protons, 82, 606
- Excitation bandwidth, 19
- Experiment addition in computer simulation software, 132–135
- Extended x-ray absorption fine structure (EXAFS), 6
- Facial triad oxygenases, 258–260
- Fatty acid desaturases, 314, 316
- Fe, 334, 337–339
- [2Fe2S] clusters, 87–89
 - interactions, 94–98
 - and spin densities, 98–99
 - Rieske iron sulfur cluster, 66, 89–90
- [4Fe4S] clusters, 90–92
 - in HiPIP proteins, 96–98
- FeFur, 262–264
- Fe(II) interactions, 94–96, 99
- Fe(III) interactions, 94–96, 99
- Fermi contact term, 184, 187, 475
- Ferredoxins, 66, 98
 - g-tensor in, 86–90
 - and proton hyperfine interactions, 82–85
- Ferric iron pairs, 90–91, 96–97, 99
- Ferric mouse neuroglobin, 34
- Ferric non-heme proteins
 - EPR characterization of, 233–236
 - low-spin, 251
- Ferritins, 332–337
 - biochemical and structural characterization, 332–335
 - mechanistic implications, 337–337
 - spectroscopic characterization, 335–337
- Ferromagnetic coupling, 278–280
- Ferrous iron, radical probes of, 251–264
- Ferrous protocatechuate 3,4-dioxygenase (3,4-PCD), 261–262
- Ferroxidase center, 334–335
- Ferroxidase reaction, 336
- Field-frequency plot, 84–85
- Field gradient operator, 184–185
- Field gradients, 188
- Field segmentation algorithm, 135–136, 152–153
- Field-swept electron spin echo (FS-ESE), 538
- Field-swept EPR, 52–54
- Fine structure interaction in computer simulation software, 123–124
- First-order nuclear frequencies, 17
- Flavorubredoxin (FIRd), 351–352
- Floquet segments, 137
- Floquet theory, 137, 158
- Fluoride and purple acid phosphatases (PAPs), 344
- Fluorometmyoglobin, 406–407
- Four-pulse ESEEM, 25–26, 399
- FprA, 350–353
- Free evolution time of nuclear coherence, 51
- Free radicals, 106–107
 - as intermediates in chromium complexes, 568–569

- Frequency space, 109–110
 Frequency-swept spectra and line shapes, 246–247
- Fur, 254
 binding with nitric oxide, 262–264
- Fur–(NO)₂, 262
- Gadolinium. *See* Gd
- Gauge including atomic orbitals (GIAOs), 196
- Gd
 complexes, 582–585
 ¹⁷O ENDOR spectra, 607–609
- Gd(III) complexes, 9–10, 586–590
 crystal field interactions, 590–597
 frequency dependence of electronic relaxation, 586–590
 high field EPR, 590–597
 hydration numbers of, 612–616
- Gd(L0), 613–614
 Gd(L2), 613–617
- Geometry
 of cysteine radicals, 203–205
 in Spin Hamiltonian, 198–199
- Glassy solutions and crystal field interaction parameters, 590–597
- Gloxyase II (GOX II), 348–350
- Glucose complexing with chromium(V), 564
- Glutathione
 complex with chromium, 561
 and vanadium compounds, 517–519, 527–528
- Glycol-cleavage reaction, 323–325
- g*-sphere in ENDOR, 74
- g*-tensor, 3, 64–65, 67–70, 176, 187, 193, 196–197
 and spin densities, 98–99
 characterization of [NiFe] hydrogenases, 446–456
 in cysteine radicals, 203–207
 in ENDOR, 74
 in 2Fe₂S clusters, 94–96
 in ferredoxins, 86–90, 93
 in iron–sulfur proteins, 85
 in low-spin ferric heme systems, 405
 in phenoxyl radicals, 201–203
 of nitroxides, 207–212
 of plastocyanin, 215
- g* values, 67, 77–78, 206–207
 for low-spin ferric heme centers, 400–401
 of [NiFe] hydrogenases, 444
 of ribonucleotide reductase, 310–311
 of tetranuclear Cu_z sites, 494
 of trinuclear copper cluster sites, 491–492
- g*_{iso} curve, 74–75, 77–81
*g*_{iso} line, 68–69
- HALS (highly anisotropic low-spin) species, 398, 400
- Hartree–Fock (HF) method, 4, 178–182, 189
- Hellman–Feynman theorem, 169
- Heme–Fe(II)NO spectral components, 424–427
- Heme–Fe(II)NO subunit selectivity, 427–430
- Heme–Fe(II)NO subunit spectral editing, 430–431
- Heme proteins, 6–7, 34
 distance measurements in, 410–411
 ferric forms of, 398–408
 high spin forms, 406–408
 low spin forms, 398–406
 NO ligated, 408–410
 structure–function relationship, 397–412
- Hemerythrin, 6, 337–341
 azide binding, 339
 biochemical and structural characterization, 337–339
 deoxyhemerythrin, 339
 forms of, 339–340
 iron active site, 340–341
 mechanistic implications, 340–341
 semimethemerythrin, 340
 spectroscopic characterization, 339–340
- Hemocyanin, 481
- Hemoglobin (Hb), 34
 EPR spectroscopy of NO Hb, 424–431
 α-subunit hemoglobin spectrum, 425–430
 β-subunit hemoglobin spectrum, 425–430
 subunit selectivity, 427–430
 subunit spectral editing, 430–431
 evolution of NO Hb interactions, 431–432
 interactions with nitric oxide, 420–432
 S-nitrosylated Hb (SNO Hb), 421–422
 SNO Hb function, 422–423
- Heterobimetallic center, 441
- High-field ENDOR, 48–50
- High-field EPR of crystal field interaction parameters, 590–597
- High Potential Iron sulfur Proteins. *See* HiPIP proteins
- High-field pulsed ENDOR
 and ¹⁷O ENDOR frequencies, 601–602, 612–616
 of water ligands, 597–615
- High-spin ferric forms of heme proteins, 406–408
- High-spin ferric proteins, 233–250
- High-spin nitric oxide complexes and non-heme iron proteins, 258–261

- High-spin states in [NiFe] hydrogenases, 462
- HiPIP proteins, 3, 90–92
4Fe4S clusters in, 96–98
- Hohenberg–Kohn theorems, 181
- HOMO, 482–483
- HOMO–LUMO gap, 160
- Human p53 ribonucleotide reductase, 303
- Hybrid functionals, 182
- Hydration numbers of Gd(III) complexes, 612–616
- Hydrogenases, 442–445
- Hydrolytic enzymes, 6, 273, 341–350
- 2-Hydroxy-pyridine-N-oxide (2hpo), 516–517
- Hydroxyl radicals, 569
and ferritin, 337
- HYEND, 44–46
- Hyperfine-correlated ENDOR spectroscopy, 44–46
- Hyperfine coupling, 13–16, 21, 36, 54–55, 107, 122, 176, 184, 187–188, 197, 405
decoupling, 37–40
enhancement of radio frequency pulses, 50
⁵⁷Fe, 94–96
in chromium(V) complexes, 560
in computer simulation software, 122–123
in four-pulse ESEEM, 26
in HYSCORE, 33
in [NiFe] hydrogenases, 448
in [NiFe] structure, 456–458
in proteins, 216–217
in ribonucleotide reductase, 310–311
in Type I copper active site, 475–477
in vanadium compounds, 539
of binuclear copper sites, 478–479
of ¹⁷O ENDOR spectra, 609–612
of [NiFe] hydrogenases, 456–461
of MRI agents, 597–601, 606–607
of protons, 82–94
of tetranuclear Cu₂ sites, 494
- Hyperfine Sublevel Correlation Spectroscopy.
See HYSCORE
- Hyperfine (A) tensors, 64–65
effect of spin population, 76
in ENDOR, 72–73
in [4Fe4S] clusters, 96–97
in ribonucleotide reductase, 310–311
- HYSCORE, 1–2, 25–34, 55
applications of, 33–34
computer simulation of, 132
cross-peaks in 32–33
DONUT-HYSCORE, 37
of low-spin ferric heme systems, 403–405
of [NiFe] hydrogenases, 459–461
of NO-ligated heme proteins, 409–410
orientation selective simulation, 142–143
peak analysis in spectra, 28–29
powder patterns, 29–30
simulated by computer software, 138–143
SMART, 403, 408
of vanadium compounds, 538–540
of vanadyl ions, 534
- IGLO-II basis set, 201
- IGLO-III basis set, 201
- Imidazole in [NiFe] hydrogenases, 461
- Iminodiacetate, 565, 567
- Independent gauge for localized orbitals (IGLOs), 196
- Inner-sphere water, 582, 584
- Insulin-enhancing vanadium compounds
acetylacetonate ligand in, 515–516
citrate, 516–517
EPR, 509–514
oxalate, 516–517
solution structures of, 514–519
structure of, 508–509
- Intensity factor, 241–242
- Intermediate G, 323
- Intermediate H, 323
- Intermediate P, 308, 313
- Intermediate U, 306
- Intermediate X, 306–309, 313–314
- Inversion pulse, 41
- Iron
and EPR spectra of ferric proteins, 235–236
in facial triad oxygenases, 258–260
in hydrogenase, 441
interactions in ENDOR, 70–71
interactions in iron–sulfur proteins, 94–98
intermediate states of, 5
- Iron enzymes, binuclear non-heme, 269–356
- Iron–nitric oxide as model of iron–reactive oxygen intermediates, 258
- Iron nitrosyls, 255–258
- Iron oxidation, 334–337
- Iron proteins
and high-spin nitric oxide complexes, 258–261
low-spin, 251
- Iron-reactive intermediates and iron–nitric oxide, 258
- Iron reduction in iron–sulfur proteins, 85
- Iron–semiquinone interactions, 251–254
- Iron storage proteins, 332–337

- Iron–sulfur proteins
 cubane structure, 90–94
 effect of spin population, 76
 and ENDOR spectroscopy, 65–73, 82–94
 high potential, 90–92
 spin densities, 98–99
- Iron transport
 and storage enzymes, 273
 and storage proteins, 6
- Iron–tyrosinate complex, 335–336
- Iron uptake by ferritin, 336
- Isotopes in computer simulation software,
 127–128
- Isotropic exchange, 130–131, 278
- Isotropic g tensor, 557–560
- Isotropic hyperfine coupling, 200–201
- Isotropic hyperfine coupling constant, 16
- Isotropic interactions in hyperfine (A) tensor,
 72
- Iterative bisection method, 152
- Kohn–Sham equations, 162
- Kronecker delta function, 73
- Lactate and insulin-enhancing vanadium(IV)
 complexes, 516–517
- Lanthanide(III) complexes, 612
- Ligand field splitting, 445–448
- Ligand nuclei and hyperfine coupling constants,
 457–458
- Linear response theory, 188–192
- Linear scaling approach, 181
- Lineshape, 246–250
 Aasa–Vänngård factor, 246–247
 distributions in zero-field splitting, 248–249
 function, 109–110
 looping transitions, 249–250
 relaxation, 247
- Linewidth
 calculation of, 153–156
 parameters in computer simulation software,
 126–127
- Lipid biosynthesis, 314, 316
- Lipoxygenase, 236
 in nitric oxide complexes, 254–255
- LODEPR, 586
- Longitudinally detected EPR. *See* LODEPR
- Looping transitions, 240–242, 249–250
- Low-spin ferric forms of heme proteins,
 398–406
- Low-spin ferric non-heme proteins, 251
- Low-spin nitric oxide complexes with non-heme
 iron proteins, 261–262
- LUMO, 482–483
- μ -hydroxo bridging ligand, 344, 346
- μ -oxo bridging ligand, 317–318
- Magnesium in hydrogenases, 443
- Magnetic circular dichroism (MCD), 6
 of trinuclear copper cluster sites, 488–489,
 492
- Magnetic dipole moments, 107–108
- Magnetic field-like perturbations, 191
- Magnetic flux density, 176
- Magnetic resonance imaging. *See* MRI
- Maltol binding to vanadyl compounds, 524
- Manganese lipoxygenase, 243–244, 246
- Many-body perturbation theory (MBPT), 181
- Many-electron wavefunction, 178
- Matched ESEEM, 35–37
- Matched HYSCORE, 399
- Matrix diagonalization, 110, 135, 151–156
- Maxi-ferritins, 333
- Maximum frequency shift, 29
- MCD. *See* Magnetic circular dichroism (MCD)
- Membrane-bound diiron proteins, 353–355
- Membrane transport of vanadium compounds,
 527–529
- Metal ions in metallo- β -lactamases, 348–350
- Metal nucleus in orientation selection, 74
- Metallo- β -lactamases, 348–350
 biochemical and structural characterization,
 346–348
 spectroscopic characterization, 348–350
- Metalloflavoproteins, 350
- Metallohydrolases, 341
- Metalloproteins, 2, 105–106
 characterization by HYSCORE, 33
 computer simulation of structural characteri-
 zation, 105–171
 in ENDOR, 65
- Methane conversion to methanol, 274–275
- Methane monooxygenase (MMO), 274–291
 biochemical and structural characterization,
 274–277
 catalytic cycle of, 289–291
 component B (MMOB), *see* MMOB
 diferric form, 281–282
 diferrous form, 282
 hydroxylase component (MMOH), *see*
 MMOH
 interactions with MMOB, 288–289
 mixed valence form, 282–285
 nitric oxide complexes, 287

- reductase component (MMOR), *see* MMOR
- spectroscopic characterization, 277–289
- substrate and product interactions, 285–287
- Methane thiosulfonate, 288
- Methanotrophic bacteria, 275
- Methyl-coenzyme M reductase (MCR), 30, 36
- Methylococcus capsulatus, 275
- Methylosinus trichosporium, 275
- Microwave attenuation, 145
- Microwave frequency for heme protein analysis, 402–403
- Microwave pulses in Davies ENDOR, 71
- MIMS ENDOR, 41–43, 167–168, 399, 603–604
 - 2D, 44
 - simulated by computer software, 143–145
- Mini-ferritins, 333
- Mixed-valence iron pairs, 90–91, 93, 96–97, 99
 - MMOH, 282–285
 - R2 subunit of ribonucleotide reductase, 306
- MMOB, 275, 277, 301
 - interactions with MMOH, 288–289
- MMOH, 275–277, 301
- MMOR, 275, 289
- Mn(acac)₃, 221
- Modulation depth, 35
- Molecular model choice for calculation of Spin Hamiltonian parameters, 198
- Molecular orbitals (MOs), 178
- Molecular sieves, 565, 567
- Molecular Sophe software, 3–4, 114–171
 - adding atoms, 119–120
 - adding bonds, 129
 - adding experiments, 132–133
 - atom form, 121
 - atom isotopes, 127–128
 - computational parameters, 135–137
 - control bar in, 149
 - CW EPR experiment simulation, 133–135
 - and dinuclear exchange coupled copper(II) EPR spectra, 165–167
 - electron Zeeman interaction, 121–122
 - energy level diagrams, 146–147
 - examples of, 159–167
 - exchange interaction, 130–132
 - experiment form, 133
 - fine structure interaction, 123–124
 - hyperfine interaction, 122–123
 - HYSORE simulation, 138–142
 - linewidth parameters, 126–127
 - main menus in, 147–148
 - MIMS ENDOR simulation, 143–145
 - molecule form, 119
 - orientation selective HYSORE simulation, 142–143
 - overview, 114–116
 - position form, 128
 - project form, 117
 - pulsed EPR experiments, 138–145
 - quadrupole interaction, 124–126
 - resonator configuration, 138, 141
 - sample form, 118
 - simulation form, 117–118
 - SOPHE computational parameters, 135–137,
 - spectra input/output, 137–139
 - spin Hamiltonian parameter optimization, 167–171
 - superhyperfine interactions, 129–139
 - Sydney OPerA HousE method, *see* SOPHE
 - tool bar in, 147, 149
 - units conversion calculator, 145–146
 - use in copper(II) cyclic peptide complexes, 164–165
 - use in CW-EPR spectroscopy, 159–165
- Møller–Plesset perturbation theory, 181
- Molybdopterin cofactor protein aldehyde oxidoreductase, 87–89
- Molybdopterin hydroxylases, 87, 95–96
- Mononuclear blue copper proteins, 475–478
- Mononuclear non-heme iron and nitric oxide, 261
- Mononuclear non-heme iron proteins, 233–264
- Mononuclear copper(II) Westiellamide complex, 164–165
- Mosaic misorientation linewidth model, 153–156
- Mo(V) model complexes, 159–162
- Magnetic Resonance Imaging (MRI), 9
 - overview of, 581–582
- MRI contrast agents, 582
 - high field pulsed ENDOR of, 603–616
 - effect of weak crystal field interactions - on nuclear transition frequencies, 597–601
 - ¹⁷O ENDOR spectroscopy, 601–602, 607–616
 - practical aspects, 603–604
 - ¹H ENDOR spectroscopy, 605–607, 612–616
 - hydration numbers of Gd(III) complexes, 612–616
 - MS-325, 584
- Multidimensional pulsed EPR, 112
- Multifrequency EPR, 6–7
- Mycobacterium tuberculosis, 316
- Myo-inositol, 320–322
- Myo-inositol oxygenase (MIOX), 320–325
 - biochemical and structural characterization, 320–321
 - catalytic mechanism of, 323–325

- mixed-valence form, 322–323
 - oxidation of, 322–323
 - spectroscopic characterization, 321–323
 - substrate binding, 322
- Myoglobin, 398
- N_2O , 495–496
- N-acetylcysteine, 527–528
- N-confused tetraphenylporphyrin (NCTPP)
 - complex, 32
- Neuroglobin, 398
- Newton–Raphson method, 152
- [NiFe] hydrogenases, 7–8, 34, 441–464
 - active site interaction with surrounding protein, 461
 - bridging ligand X, 458–460
 - center, 442–443
 - classification, 442–445
 - composition, 442–445
 - density functional theory (DFT), 456–457
 - distance studies of, 462
 - electronic structure of, 445–448
 - ELDOR spectroscopy, 462
 - ENDOR, 456–461
 - EPR-silent states, 462
 - ESEEM, 459
 - g tensors characterization, 448–456
 - high-spin states in, 462
 - hyperfine coupling, 448, 456–461
 - ligand nuclei, 457–458
 - metal nuclei, 456–457
 - imidazole, 461
 - interaction of active site with surrounding protein, 461
 - light sensitivity of active intermediate, 460–461
 - Ni-A, 443–444, 448–452, 458–459, 463
 - Ni-B, 443–444, 448–452, 458–459, 463
 - Ni-C, 459–460, 463
 - reduced state, 452
 - split signal, 452–454
 - Ni-CO state, 444–445, 455–456, 463–464
 - Ni-L, 444–445, 451, 454–455, 460–461, 463
 - Ni-L1, 454
 - Ni-L2, 454, 455
 - Ni-L3, 454
 - Ni-R, 444–445
 - Ni-Sir, 443–444
 - Ni-SU, 443–444
 - redox states of, 443–444
 - spin density, 456–458
 - sulfur bridge, 463
 - structure, 442–445
- Nigerythrin, 330–332
 - biochemical and structural characterization, 330–331
 - mechanistic implications, 331–332
 - spectroscopic characterization, 331
- Nitric oxide, 7
 - binding to Fur, 262–264
 - complexing with facial triad oxygenases, 258–260
 - and ferritin, 335
 - and hemerythrin, 340
 - interactions with hemoglobin, 420–432
 - ligand to mononuclear non-heme iron, 261
 - ligated to heme proteins, 408–410
 - as mimic for dioxygen, 287
 - and non-heme ferrous centers, 254–258
 - protocatechuate 3,4-dioxygenase, 261–262
 - reductases, 350–353
 - biochemical and structural characterization, 350–352
 - mechanistic implications, 352–353
 - spectroscopic characterization, 352
 - response regulons, 254
 - responsive transcription factor, 261
- Nitrile hydratase, 5, 251
- Nitrite reductase, 473, 478
- Nitrogen hyperfine coupling, 164
- Nitrogen HYSCORE simulations, 167
- Nitrogen in [NiFe] hydrogenases, 461
- Nitrogen interactions in ENDOR, 70–71
- Nitrosobenzene (NOB), 291
- Nitroxide radicals, g-tensors of, 207–212
- NMR 6, 201, 607
 - chemical shifts 196
 - ELDOR detected 399, 408
 - paramagnetic 85, 92–94, 100
 - parameters 177, 188
 - solution structures 275, 277, 296, 299
 - transitions 14, 18, 21, 67
- Non-coupled binuclear copper sites, 473–474, 483–486
- Non-heme diiron carboxylate-bridged proteins, 273
- Non-heme ferrous centers and nitric oxide, 254–255
- Non-heme iron proteins
 - and high-spin nitric oxide complexes, 258–261
 - with low-spin nitric oxide complexes, 261–262
 - relaxation in line shapes, 247
- Non-interacting reference system, 181
- Norcarane, hydroxylation of, 292–293
- NorR, 254, 261

- Nuclear Bohr magneton, 176
- Nuclear coherence, 24
in HYSCORE, 27–29
- Nuclear coherence generator, 51
- Nuclear coherence transfer echo, 25
- Nuclear frequencies, 21–22, 25
in DONUT-HYSCORE, 37
in HYSCORE, 33
- Nuclear frequency spectra, 17–18
- Nuclear magnetic relaxation dispersion (NMRD) profile, 584–585, 589
- Nuclear magnetic resonance. *See* NMR
- Nuclear modulation effect, 20–22
- Nuclear-orbit interaction, 184
- Nuclear quadrupole coupling constants, 216–217
- Nuclear quadrupole interactions, 13, 16
- Nuclear quadrupole resonance (NQR) frequencies, 33
- Nuclear spin, 16
in ENDOR, 66, 68
- Nuclear spin decoupling, 37–40
- Nuclear spin vector operators, 15
- Nuclear transition frequencies, 14
- Nuclear Zeeman
frequency, 67
interactions, 16, 108
splitting, 48
- Nuclei interaction with electrons, 107–108, 176
- Nutation experiments, 52–54
- One-electron functions, 179
- Orbital dipolar term, 475–476
- Orbital energies, 212
- Orbitals, perturbation of, 188–192
- ORCA, 4, 176, 218
- Organic radicals and zero-field splittings, 217–220
- Organic triplets and zero-field splittings, 217–219
- Orientation-dependent modulation depth parameter, 23
- Orientation selection, 65
in ENDOR, 74–82
in EPR, 74–82
in pulse EPR, 18–20
of spectra, 2
- Orientation selective HYSCORE simulation, 142–143
- Orthorhombic symmetry, 121
- Ox1 complex, 34
- Oxalate and insulin-enhancing vanadium(IV) complexes, 516–517
- Oxidation in phenoxyl radicals, 202
- Oxygen activation by R2 subunit of ribonucleotide reductase, 313–314
- Oxygen and hemerythrin, 338–341
- Oxygen intermediates in R2 subunit of ribonucleotide reductase, 306–308
- Oxygen rebound mechanism, 292–293
- Oxygen reduction in trinuclear copper cluster sites, 486–490
- Oxygen storage and transport enzymes, 273
- Oxygen storage and transport proteins, 6
- Oxygenases, 6, 273
- Pake doublet, 605
- p*-aminobenzoate oxygenase, 355
- PAP, *see* Purple Acid Phosphatase
- Parallel mode EPR spectroscopy, 163–164
- Paramagnetic centers
and computer simulation, 115
exchange interaction of, 130
and spin Hamiltonian, 108–109
- Partition scheme in SOPHE, 150–151
- PCU-L, 213–215
- PCU-S, 213–215
- PEANUT spectrum, 53–54
- PELDOR, 312–313
- Peptidylglycine α -hydroxylating monooxygenase, 473, 483–486
- Periodic table in computer simulation software, 120
- Peroxidation
and nigerythrin, 331–332
and rubrerythrin, 328–330
- Peroxide binding to copper sites, 482–483
- Peroxo diferric intermediate, 319, 336–337
- Peroxo diiron intermediates, 302–303
- Perpendicular mode EPR spectroscopy, 163–164
- Perturbation in linear response theory, 188–192
- Perturbation theory, 110, 152, 185–186, 205
- Perturbed density matrix, 190
- Phase cycling in pulsed EPR experiments, 158
- Phe208Tyr, 311
- Phenol, degradation of, 296–297
- Phenol hydroxylases, 296–299
biochemical and structural characterization, 296–297
spectroscopic characterization, 297–298
- Phenoxyl radicals, 201–203
- Phenylalanine hydroxylase (PAH), 235–236
- PHI, 298
- PHO, 298
- Phosphorylcholine esterase (Pce), 348
- Photosynthetic reaction centers, 114, 251–254
- Planck's constant, 73

- Plastocyanin, 5, 213, 475–477
- Point–dipole approximation, 73
- Polarization in ENDOR, 41–42
- Polyacenes, 220
- Preparation regime in ENDOR, 71–72
- Primary echo in two-pulse ESEEM, 22–23
- Proton hyperfine interactions, 73, 82–94
- Proton HYSCORE simulations, 167
- Protons
- coupling in iron–sulfur proteins, 93
 - cysteine binding, 84–85
 - in high potential iron sulfur proteins (HiPIP), 91
 - interactions in spin densities, 98
 - and nitrogen interactions in ENDOR, 70–71
- Pseudomonas putida* GPO1, 291
- Pseudomonas* sp. OX1, 297
- Pseudomonas* sp. Strain CF600, 296
- 2-Pulse ESEEM, 402
- 3-Pulse ESEEM, 402
- Pulse sequence, 114
- in ENDOR, 40–42, 45
 - in HYSCORE, 35–37
 - in pulsed EPR simulations, 156–158
 - in time-domain ENDOR, 51–52
 - in triple resonance, 46–47
 - in variable mixing-time ENDOR, 47
- Pulsed electron electron double resonance (PELDOR) spectroscopy.
See PELDOR
- Pulsed ENDOR, 1, 64
- Davies ENDOR, 89
 - of MRI agents, 603–604
- Pulsed EPR, 105
- for structure determination of vanadyl ions, 533–540
 - orientation selection in, 18–20
 - simulations of, 138–145, 156–159, 167–168
 - use in heme proteins, 397–412
- Purple acid phosphatases (PAPs), 6, 322, 341–346
- active sites of, 342–343
 - biochemical and structural characterization, 341–343
 - fluoride and purple acid(PAPs), 344
 - hydrolysis by, 346–347
 - mechanistic implications, 346
 - red kidney bean PAP, 342–343
 - spectroscopic characterization, 343–345
- Putidaredoxin, 87
- Pyrrrole nitrogen, 36
- Q-band frequency
- in EPR spectra, 30–31, 163–164, 560–561
 - for heme proteins, 402–403
 - of tetranuclear Cu_z sites, 494
- Quadrupole coupling, 70, 108, 124–126, 176, 184–185, 197
- Quantum mechanical/molecular modeling (QM/MM) approach, 199, 212–217
- Quasi-restricted orbitals (QROs), 196
- Quinol, 355
- Quinoline oxidoreductase, 95–96
- Quinone–iron interactions, 251–254
- R1 subunit of ribonucleotide reductase, 303–305, 311
- R2 subunit of ribonucleotide reductase, 6, 303–305, 311
- activation of oxygen, 313–314
 - diferrous, 305–306
 - diferrous R2, 306
 - mixed-valence R2, 306
 - oxygen intermediates in, 306–308
 - spectroscopic characterization of, 305–313
- Radical clock probes, 300
- Radical probes of ferrous iron, 251–258
- of photosynthetic reaction centers, 251–254
 - nitric oxide and non-heme ferrous centers, 254–255
 - model compounds, 255–258
- Radiofrequency pulses in Davies ENDOR, 71
- Radiolytic reduction, 284–285
- Rayleigh-functional, 178
- Reactive intermediates in Cr(VI) induced toxicity, 552–554
- Reactive oxygen species (ROS), 106, 341, 568–569
- Red kidney bean PAP, 342–343
- Redox
- active cofactors, 112
 - activity of vanadium compounds, 519
 - chemistry of vanadium compounds, 527–529
 - cofactors in metalloproteins, 106–107
 - induced toggling, 331
 - states of [NiFe] hydrogenases, 443–444
- Reductase component of alkene monooxygenase, 294–295
- Relaxation matrix **R**, 587–588
- Relaxation of lineshapes, 247
- Relaxivity in MRI imaging, 582–590
- Remote echo detection, 34–35
- Residual hyperfine coupling, 38, 39

- Resonance lines in ENDOR, 82–86
Resonance Raman spectroscopy, 6
Resonant field positions, calculation of, 152–153
Resonator, 18, 138, 141
 quality factor, 18
Restricted open-shell HF (ROHF) method, 179–181
Rhodococcus rhodochrous B-276, 293
Rhombic symmetry in **g**-tensor, 74
Ribonucleotide reductase, 6
 biochemical and structural characterization, 303–305
 catalytic cycle of, 315
 class I, 303–314
 hyperfine coupling, 310–311
 mechanistic insights, 313–314
 oxygen activation by R2 subunit, 313–314
 R1, 303–305, 311
 R2 subunit, 6, 303–305, 311
 spectroscopic characterization of R2, 305–313
 amino acid radicals in, 308–313
 diferric form, 305–306
 diferrous form, 306
 mixed valence form, 306
 oxygen intermediates, 306
Ribonucleotides complexing with chromium(V), 563
Ricinus communis, 314, 316
Rieske iron sulfur cluster, 33, 66, 89–90, 301, RNase Z, 348
ROBP86, 219–220
Rubredoxin, 350
Rubredoxin oxygen oxidoreductase (ROO), 348, 350–353
 biochemical and structural characterization, 350–352
 mechanistic implications, 352–353
 spectroscopic characterization, 352
Rubrerythrin, 326–330
 biochemical and structural characterization, 326–227
 mechanistic implications, 328–330
 spectroscopic characterization, 327–328
6-31G* basis set, 200
Saturation-recovery EPR, 288
Scalar relativistic zero-order regular approximation (ZORA), 162, 213, 217
Scalar relativity, 213–214
Second rank **D** tensor, 107
SECSY, 167–168
Segmental length, 80
Segmentation method, 152
Selenocysteine, 442
Self-consistent field ground state, 189–190
Self-consistent field methods, 192–198
Semimethemerythrin, 340
Semioccupied molecular orbitals (SOMOs), 207–208
Semiquinone–iron interactions, 251–254
Serum proteins interactions with vanadyl compounds, 520–525
Sialic acid, 564
Single Crystal ENDOR, 64–65
Single-quantum transitions, 18, 31–32, 38–40
Slater-determinant, 178
SMART HYSOCORE, 403, 408
S-nitrosothiols, 420–421
S-nitrosylated-hemoglobin. *See* SNO-hemoglobin
SNO-hemoglobin, 421–422
 function of, 422–423
SOC, 220–222
Software for structural characterization, 105–171
Solution structures of insulin-enhancing vanadium(IV) complexes, 514–519
Solvent effect on nitroxide radicals, 207–212
SOPHE software,
 computational code, 150–159
 computational parameters, 135–137
 computer simulation, 110–113
 and CW EPR spectroscopy, 152–156
 grid, 137, 150–151
 and mosaic misorientation linewidth model, 153–156
 and pulsed EPR simulations, 156–159
SORCI method, 221
Spectra input/output in computer simulation software, 137–139
Spectrometer deadtime, 23–24
Spectrum simulation, 55–56
Spin density, 194, 212
 distribution, 13, 16, 114
 in ENDOR, 73
 in iron–sulfur proteins, 82, 98–99
 in [NiFe] hydrogenases, 456–458
 in tetranuclear Cu₂ sites, 494–495
 matrix, 180
Spin dipolar term, 475–476
Spin-down orbitals, 179

- Spin frustration, 489
- Spin Hamiltonian, 2, 5, 15–20, 110, 130, 137, 158, 597
 and automatic fitting of CW EPR spectra, 169, 171
 case studies, 201–222
 choice of basis set, 200–201
 choice of geometry, 198–199
 choice of molecular model, 198
 choice of theoretical method, 199–200
 in dicopper complexes, 166–167
 direct magnetic dipolar spin–spin interaction, 184
 electronic structure theory of, 177–201
 electronic Zeeman interaction, 185
 in ENDOR, 65
 hyperfine coupling, 184
 for insulin-enhancing vanadium complexes, 508, 512–513
 linear response theory, 188–192
 for Mo(V) model complexes, 161–162
 in multifrequency EPR spectra, 163–164
 nuclear–orbit interaction, 184
 parameters, 175–177
 in proteins, 212–217
 quadrupole coupling, 184–185
 for self-consistent field methods, 192–198
 simulation of, 107–109
 spin Hamiltonian parameter optimization, 167–171
 spin–orbit coupling, 183–184
 sum-over states theory of, 185–188
 for vanadium compounds, 535, 537
 zero-field splittings, 217–222
- Spin in iron–sulfur cubane proteins, 90–91
- Spin label and distance measurements, 410–411
- Spin–orbit coupling, 183–184, 193, 491
- Spin–orbit mean-field approximation (SOMF), 183–184
- Spin-other-orbit, 183
- Spin population, 16, 609–610
 and hyperfine (**A**) tensor, 76
 in proteins, 213–215
- Spin projection coefficients, 94, 99
- Spin relaxation, 586–590
- Spin-same-orbit, 183
- Spin–spin interactions, 176, 185–187
 in iron–semiquinone interactions, 252–253
- Spin state of heme proteins, 398–408
- Spin systems, 110
 and decoupling, 37–40
 nuclear frequency spectra of, 17–18
- Spin-trap probes, 291, 569
- Spin-unrestricted Kohn–Sham equations, 181–182
- Spin-unrestricted (UHF) method, 179–180
- Spin-up orbitals, 179
- Static spin Hamiltonian, 15–17
- Stearoyl–acyl carrier protein Δ^9 desaturase, 314–320
 biochemical and structural characterization, 314–317
 spectroscopic characterization, 317–318
 mechanistic implications, 318–320
- Stimulated echo in three-pulse ESEEM, 24
- Sulerythrin, 332
- Sulfur bonding in type I copper active site, 477–478
- Sulfur bridge in [NiFe] hydrogenases, 463
- Sum-combination frequency, 39
- Sum-over states theory, 185–188
- Superhyperfine interactions, 107
 in computer simulation software, 129–130
- Superoxide
 dismutase, 473
 intermediates, 258
 reductase (SOR), 233–234, 248, 254
- Superoxidiferic complex, 325
- Superpropagator in pulsed EPR, 157–158
- SVP basis set, 200
- Sweet potato PAP, 343
- T2MO, 298
- T4MOC, 299–300
- T4MOD, 299–300
- T4MOF, 299–300
- T4MOH, 299–300
- Temperature and EPR resonances, 239–240, 279–281
- Tetranuclear Cu_z sites, 493–496
- Theoretical method in Spin Hamiltonian, 199–200
- Thiomolybdenyl complexes in simulated CW-EPR spectroscopy, 159–163
- Thiyl radicals, 303, 313
- Three-pulse ESEEM, 24, 26, 399
 and NO-ligated heme proteins, 409
- Time-domain ENDOR, 50–52
- Toluene, metabolism of, 298–299
- Toluene-2-monooxygenase (T2MO), 298
- Toluene-4-monooxygenase (T4MO), 299–300
 biochemical and structural characterization, 299
 mechanistic insights, 300
 spectroscopic characterization, 300
- Toluene *o*-monooxygenase, 298

- Toluene/*o*-xylene monooxygenase (ToMO),
300–303
 biochemical and structural characterization,
 300–302
 coupling protein (ToMOD), 301–302
 hydroxylase component (ToMOH),
 301–302
 oxidoreductase component (ToMOF),
 301
 Rieske type ferredoxin (ToMOC), 301
 spectroscopic characterization, 302–303
 ToMOH–azide complex, 301
- Topaquinone, 473
- Tp*Mo^{VI}SX₂ complexes, 159–160
- Transferrin,
 diferric, 234–235
 diferric carbonate, 244–245
 EPR spectra of, 233–235
 oxalate, 240–241
- Transition frequencies in ENDOR, 65, 67–68
- Transition metal complexes, 14
 and zero-field splittings, 220–222
- Transition probability, 109–110
- Transition selection rules, 14
- Transition surfaces in Molecular Sophe, 156
- Transition roadmaps, 156
- Transitions in EPR spectroscopy, 163–164
- Transverse nuclear relaxation time, 24
- Trichloroethylene, 298
- Triclinic symmetry, 122
- Trinuclear Cu cluster sites, 474, 486–493
- Triple resonance, 46–47
- Truth tables, 400
- Two-dimensional HYSORE spectroscopy,
 399
- Two-pulse ESEEM, 22–25, 399
- Type I (T1) copper active site, 472–473,
 486–488
 EPR analysis of, 475–478
- Type II (T2) copper active site, 472–473,
 486–489
- Type III (T3) copper active site, 472–474,
 481–483, 487
- Type I ferric heme centers, 398, 400–401
- Type II ferric heme centers, 400–401
- Type III ferric heme centers 201–202, 313,
 354, 400–401
- Tyrosine (Tyr), 201–202, 311, 313, 354
 radicals, 303–304, 310–314
- Tyrosinase, 481
- TZVP basis set, 200–201
- U*-coefficients, 194–195
- Unit sphere partition, 150–151
- Units conversion calculator, 145–146
- Uteroferrin, 345
- Vanadium compounds, 8
 absorption and in vivo redox reactions
 of, 526–529
 as antidiabetic agents, 507–508
 with glutathione, 517–519
 metabolic properties, 525–529
 redox activity of, 519
 interactions with serum proteins,
 520–525
 in vitro studies of, 512, 514–525
 in vivo distribution of, 532–533
 CW EPR, 532–533
 pulsed EPR, 533–540
 in vivo pharmacokinetics of, 529–532
 in vivo studies of vanadium metabolism,
 525–526
 solution structures, 514–519
 speciation and redox chemistry, 512–514
- Vanadyl compounds
 additivity rule, 512
 albumin interaction, 520–525
 BCM–EPR, 529–532
 coordination complexes, 507
 EPR properties, 510–514
 interactions with serum proteins,
 520–525
 phosphate complex, 539–540
- Variable mixing time, 47
- Vasodilation, 421–422
- VO(3-mpa)₂, 532
- VO(5-ipa)₂, 520, 532
- VO(6-mpa)₂, 529
- VO(acac)₂, 523–525, 527, 529
- VO(ema)₂, 538
- VO(His)₂, 534, 537
- VO(ma)₂, 514–515, 520–523, 527, 529
- VO(ma)₂:1-methylimidazole (1-ImMe)
 system, 525
- VO(pic)₂, 520, 529, 531, 535–538
- VOSO₄, 520–525, 529, 531, 535–538
- Water coordination to Gd, 611
- Water ligands in MRI contrast agents,
 597–615
- W-band EPR spectra, 163–164
- XAMO, 295
- X-ray absorption near edge spectroscopy
 (XANES), 561
- Xanthobacter Py2, 295

- X-ray absorption spectroscopy (XAS) of
 - trinuclear copper cluster sites, 488–489
- X-band, 30–31, 33
 - CW ENDOR and NO-ligated heme proteins, 409–410
 - CW EPR of high-spin ferric forms of heme proteins, 406–407
 - Davies-ENDOR spectroscopy for heme proteins, 402
 - in ENDOR, 64
 - in EPR, 163–164, 569–570
- XeprView[®], 110, 112, 115, 137
- XSophe, 3, 55, 110–113

- Zeeman term, 236–240
 - in high-frequency EPR, 244–246

- Zero-field splitting, 13, 15–16, 176, 186–187, 192–196
 - assignment, 236–244
 - high-frequency EPR, 244–246
 - distributions in, 248–249
 - in Gd(III) complexes, 588–589
 - high-frequency EPR, 244–246
 - in iron–semiquinone interactions, 252–253
 - in non-heme iron proteins, 233–244
 - in organic triplets and diradicals, 217–220
 - parameters, 406
 - parameter space, 233–236
 - in transition metal complexes, 220–222
 - in trinuclear copper cluster sites, 491–492
- Zinc binding to Fur, 262–263
- Zinc in metallo- β -lactamases, 348–350
- ZORA, 162, 213, 217